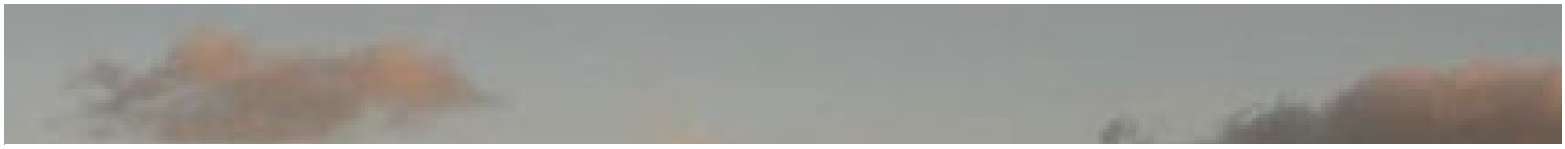

Free Access to the whole issue

E3S Web of Conferences

Volume 334 (2022)

EFC21 - European Fuel Cells and Hydrogen Piero Lunghi Conference

Virtual Conference, December 15-17, 2021

V. Cigolotti (Ed.)

Export the citation of the selected articles Export

Select all

Open Access

Statement of Peer review

Published online: 10 January 2022

PDF (198 KB)

- *Hydrogen Production*

Demonstration and analysis of a steam reforming process driven with solar heat using molten salts as heat transfer fluid 01004
Alberto Giaconia, Giampaolo Caputo, Primo Di Ascenzi, Giulia Monteleone and Luca Turchetti
Published online: 10 January 2022
DOI: https://doi.org/10.1051/e3sconf/202233401004
PDF (1.340 MB) | References | NASA ADS Abstract Service

Open Access
On-site solar powered refueling stations for green hydrogen production and distribution: performances and costs 01005
Simona Di Micco, Mariagiovanna Minutillo, Alessandra Perna and Elio Jannelli
Published online: 10 January 2022
DOI: https://doi.org/10.1051/e3sconf/202233401005
PDF (405.6 KB) | References | NASA ADS Abstract Service

Open Access
Thermochemical cycle based on solid intermediates for hydrogen storage and on-demand production 01006
Anna Chiara Tizzoni, Emiliana Mansi, Salvatore Sau, Annarita Spadoni, Natale Corsaro, Michela Lanchi, Gianremo Giorgi, Luca Turchetti and Tiziano Delise
Published online: 10 January 2022
DOI: https://doi.org/10.1051/e3sconf/202233401006
PDF (247.4 KB) | References | NASA ADS Abstract Service

- Power-to-X Conversion Technologies

Open Access
Smart Design of Green Hydrogen Facilities: A Digital Twin-driven approach 02001
Bruno Gerard, Eduardo Carrera, Olivier Bernard and Denis Lun
Published online: 10 January 2022
DOI: https://doi.org/10.1051/e3sconf/202233402001
PDF (379.3 KB) | References | NASA ADS Abstract Service

Open Access
Economic appraisal of Power-to-Liquid Fischer-Tropsch plants exploiting renewable electricity, green hydrogen, and CO_2 from biogas in Europe 02002
Marco Marchese, Paolo Marocco, Andrea Lanzini and Massimo Santarelli
Published online: 10 January 2022
DOI: https://doi.org/10.1051/e3sconf/202233402002
PDF (576.1 KB) | References | NASA ADS Abstract Service

Open Access
Benefits of the multi-modality formulation in hydrogen supply chain modelling 02003
Federico Parolin, Paolo Colbertaldo and Stefano Campanari
Published online: 10 January 2022
DOI: https://doi.org/10.1051/e3sconf/202233402003
PDF (2.210 MB) | References | NASA ADS Abstract Service

- Hydrogen Storage and Handling

Open Access
Towards stable and highly active IrO_2 catalysts supported on doped tin oxides for the oxygen evolution reaction in acidic media 03001
Sofia Delgado, Paranjeet Lakhtaria, Eva Sousa, Tiago Lagarteira, K.A. Friedrich and Adélio Mendes
Published online: 10 January 2022
DOI: https://doi.org/10.1051/e3sconf/202233403001
PDF (618.8 KB) | References | NASA ADS Abstract Service

Open Access
Optimized design and simulation of a hybrid storage system based on hydrogen as an energy carrier 03002
Maria Alessandra Ancona, Michele Bianchi, Lisa Branchini, Francesco Catena, Andrea De Pascale, Federico Ferrari, Francesco Melino and Antonio Peretto
Published online: 10 January 2022
DOI: https://doi.org/10.1051/e3sconf/202233403002
PDF (415.4 KB) | References | NASA ADS Abstract Service

Open Access
Pressure management in smart gas networks for increasing hydrogen blending 03003

Marco Cavana, Enrico Vaccariello and Pierluigi Leone
Published online: 10 January 2022
DOI: https://doi.org/10.1051/e3sconf/202233403003
PDF (326.1 KB) | References | NASA ADS Abstract Service

Open Access
Hydrogen emission in enclosed volume (tunnel for mobility) 03004
Farhad Farajimoghadam, Matteo Testi and Luigi Crema
Published online: 10 January 2022
DOI: https://doi.org/10.1051/e3sconf/202233403004
PDF (1.539 MB) | References | NASA ADS Abstract Service

- *Fuel Cell Technologies*

Open Access
Composite chitosan and quaternary ammonium modified nanofibrillar cellulose anion exchange membranes for direct ethanol fuel cell applications 04001
Maša Hren and Selestina Gorgieva
Published online: 10 January 2022
DOI: https://doi.org/10.1051/e3sconf/202233404001
PDF (907.6 KB) | References | NASA ADS Abstract Service

Open Access
The efficiency of chitosan-graphene oxide composite membranes modified with genipin in fuel cell application 04002
Selestina Gorgieva, Azra Osmić, Boštjan Genorio, Viktor Hacker, Sigrid Wolf and Silvo Hribernik
Published online: 10 January 2022
DOI: https://doi.org/10.1051/e3sconf/202233404002
PDF (2.010 MB) | References | NASA ADS Abstract Service

Open Access
Characterization and experimental comparison of commercial PEMFC stacks for marine applications 04003
Eleonora Gadducci, Thomas Lamberti, Loredana Magistri, Massimo Rivarolo, Andrea Dellacasa, Barbara Campora, Gerardo Borgogna, Agnese Lancella, Enrico Speranza and Andrea Voiello
Published online: 10 January 2022
DOI: https://doi.org/10.1051/e3sconf/202233404003
PDF (557.2 KB) | References | NASA ADS Abstract Service

Open Access
Thermal integration of PEM Fuel Cells and metal hydrides storage system for Zero Emission Ultimate Ship (ZEUS) 04004
Matteo Cavo, Eleonora Gadducci, Massimo Rivarolo, Loredana Magistri, Andrea Dellacasa, Matteo Romanello, Gerardo Borgogna and Christian Davico
Published online: 10 January 2022
DOI: https://doi.org/10.1051/e3sconf/202233404004
PDF (590.3 KB) | References | NASA ADS Abstract Service

Open Access
Single step polyol synthesis of highly stable Pt/C/SiO_2 catalysts for use in PEMFCs: effects of pH, temperature and W/EG ratio 04005
Eva Sousa, Sofia Delgado, Tiago Lagarteira and Adélio Mendes
Published online: 10 January 2022
DOI: https://doi.org/10.1051/e3sconf/202233404005
PDF (481.9 KB) | References | NASA ADS Abstract Service

Open Access
Response Surface Methodology for 30 kW PEMFC stack characterization 04006
Eleonora Gadducci, Stefano Saccaro, Massimo Rivarolo and Loredana Magistri
Published online: 10 January 2022
DOI: https://doi.org/10.1051/e3sconf/202233404006
PDF (1.466 MB) | References | NASA ADS Abstract Service

Open Access
Success factors for demonstration projects of small-scale stationary fuel cells in residential buildings 04007
Guenter Simader and Patrick Vidovic
Published online: 10 January 2022

DOI: https://doi.org/10.1051/e3sconf/202233404007
PDF (1.071 MB) | References | NASA ADS Abstract Service

Open Access

Exsolution in La and Ni co-doped strontium titanate: a suitable anode for running SOFCs on ammonia as alternative fuel 04008

Jonathan Cavazzani, Enrico Squizzato, Elena Brusamarello and Antonella Glisenti

Published online: 10 January 2022

DOI: https://doi.org/10.1051/e3sconf/202233404008

PDF (840.5 KB) | References | NASA ADS Abstract Service

Open Access

Comparison of different infiltration amounts of CeO_2 inside Ni-YSZ anodes to improve stability and efficiency of Single-Chamber SOFCs operating in methane 04009

Giovanni d'Andrea, Enrico Squizzato and Antonella Glisenti

Published online: 10 January 2022

DOI: https://doi.org/10.1051/e3sconf/202233404009

PDF (884.6 KB) | References | NASA ADS Abstract Service

Open Access

Graphite/epoxy composite for building Bipolar Plates 04010

Luca Spinelli, Fabrizio Roncaglia, Roberto Biagi, Alessandro di Bona, Marcello Romagnoli and Adele Mucci

Published online: 10 January 2022

DOI: https://doi.org/10.1051/e3sconf/202233404010

PDF (449.8 KB) | References | NASA ADS Abstract Service

Open Access

Degradation of Ni-YSZ and Ni-GDC fuel cells after 1000 h operation: Analysis of different overpotential contributions according to electrochemical and microstructural characterization 04011

Aiswarya Krishnakumar Padinjarethil, Fiammetta Rita Bianchi, Barbara Bosio and Anke Hagen

Published online: 10 January 2022

DOI: https://doi.org/10.1051/e3sconf/202233404011

PDF (511.0 KB) | References | NASA ADS Abstract Service

Open Access

Nanostructured gas diffusion layer to improve direct oxygen reduction reaction in Air-Cathode Single-Chamber Microbial Fuel Cells 04012

Giulia Massaglia, Eve Verpoorten, Candido F. Pirri and Marzia Quaglio

Published online: 10 January 2022

DOI: https://doi.org/10.1051/e3sconf/202233404012

PDF (547.7 KB) | References | NASA ADS Abstract Service

Open Access

High temperature fuel cells to reduce CO_2 emission in the maritime sector 04013

Maurizio Archetti, Emilio Audasso, Barbara Bosio and Dario Bove

Published online: 10 January 2022

DOI: https://doi.org/10.1051/e3sconf/202233404013

PDF (861.4 KB) | References | NASA ADS Abstract Service

Open Access

Effects of $(Li\text{-}Na)_2CO_3$ on The Electrical Properties of Calcia-Stabilized Zirconia/Carbonate Composite Electrolytes 04014

Aiman Iqbal, Pramujo Widiatmoko and Hary Devianto

Published online: 10 January 2022

DOI: https://doi.org/10.1051/e3sconf/202233404014

PDF (150.9 KB) | References | NASA ADS Abstract Service

Open Access

Redox Cycling for SOFC Accelerated Degradation 04015

Daria Vladikova, Blagoy Burdin, Asrar Sheikh, Paolo Piccardo, Milena Krapchanska and Dario Montinaro

Published online: 10 January 2022

DOI: https://doi.org/10.1051/e3sconf/202233404015

PDF (179.4 KB) | References | NASA ADS Abstract Service

Open Access

Distribution of current density across the active area at various stoichiometry ratios using the JRC ZERO∇CELL single cell PEM fuel cell testing hardware 04016

Tomasz Bednarek

Published online: 10 January 2022

DOI: https://doi.org/10.1051/e3sconf/202233404016

PDF (819.2 KB) | References | NASA ADS Abstract Service

Open Access

High-temperature PEM Fuel Cell Characterization: an Experimental Study Focused on Potential Degradation due to the Polarization Curve 04017

Mathieu Baudy, Amine Jaafar, Christophe Turpin, Sofyane Abbou and Sylvain Rigal

Published online: 10 January 2022

DOI: https://doi.org/10.1051/e3sconf/202233404017

PDF (1.683 MB) | References | NASA ADS Abstract Service

Open Access

An efficient composite membrane to improve the performance of PEM reversible fuel cells 04018

Gabriele G. Gagliardi, Carlotta Cosentini and Domenico Borello

Published online: 10 January 2022

DOI: https://doi.org/10.1051/e3sconf/202233404018

PDF (549.7 KB) | References | NASA ADS Abstract Service

Open Access

Ionomer Films Impact on The Structure, Flow Regime, and The Wettability of The Catalyst Layer of PEMFC 04019

Karrar Alofari, Ezequiel Me´dici, Kazuya Tajiri and Jeffrey Allen

Published online: 10 January 2022

DOI: https://doi.org/10.1051/e3sconf/202233404019

PDF (806.9 KB) | References | NASA ADS Abstract Service

Open Access

Experimental study of gas diffusion layers nonlinear orthotropic behavior 04020

Marwa Ouerghemmi, Christophe Carral and Patrice Mele

Published online: 10 January 2022

DOI: https://doi.org/10.1051/e3sconf/202233404020

PDF (1.298 MB) | References | NASA ADS Abstract Service

Open Access

Impedance-based Solid Oxide Fuel Cell testing as scalable and reliable Quality Control tool for cell and batch manufacturing: first findings 04021

Davide Pumiglia, Della Pietra Massimiliano, Andrea Monforti Ferrario, Stephen McPhail and Sergii Pylypko

Published online: 10 January 2022

DOI: https://doi.org/10.1051/e3sconf/202233404021

PDF (2.539 MB) | References | NASA ADS Abstract Service

- Power Generation

Open Access

Knowledge Based Engineering for Hydrogen Gas Turbines and Burners Design: a review 05001

Corallo Angelo, Dibiccari Carla, Lazoi Mariangela, Starace Giuseppe and Laforgia Domenico

Published online: 10 January 2022

DOI: https://doi.org/10.1051/e3sconf/202233405001

PDF (107.4 KB) | References | NASA ADS Abstract Service

Open Access

Experimental characterization of a PEM fuel cell for marine power generation 05002

Andrea Pietra, Marco Gianni, Nicola Zuliani, Stefano Malabotti and Rodolfo Taccani

Published online: 10 January 2022

DOI: https://doi.org/10.1051/e3sconf/202233405002

PDF (1.092 MB) | References | NASA ADS Abstract Service

- *Hydrogen Mobility*

Open Access

An algorithm for comparative analysis of power and storage systems for maritime applications 06001

Massimo Rivarolo, Federico Iester and Aristide F. Massardo

Published online: 10 January 2022

DOI: https://doi.org/10.1051/e3sconf/202233406001

PDF (838.9 KB) | References | NASA ADS Abstract Service

Open Access

Pilot autonomous hybrid hydrogen refueling station utilizing a metal hydride compressor covering local transportation needs 06002

Nikolaos Chalkiadakis, Athanasios Stubos, Emmanuel I. Zoulias and Emmanuel Stamatakis

Published online: 10 January 2022

DOI: https://doi.org/10.1051/e3sconf/202233406002

PDF (2.533 MB) | References | NASA ADS Abstract Service

Open Access

Digital Twin of Fuel Cell Hybrid Electric Vehicle: a detailed modelling approach of the hydrogen powertrain and the auxiliary systems 06003

Lorenzo Bartolucci, Edoardo Cennamo, Stefano Cordiner, Vincenzo Mulone, Ferdinando Pasqualini and Marco Aimo Boot

Published online: 10 January 2022

DOI: https://doi.org/10.1051/e3sconf/202233406003

PDF (907.4 KB) | References | NASA ADS Abstract Service

Open Access

Investigation of gas purging and cold storage impact on PEM fuel cell system performance for aeronautical applications 06004

Gema Montaner Ríos, Florian Becker, Anna Vorndran, Christoph Gentner and Syed Asif Ansar

Published online: 10 January 2022

DOI: https://doi.org/10.1051/e3sconf/202233406004

PDF (1.170 MB) | References | NASA ADS Abstract Service

Open Access

Characterization of a metallic interconnect operated in stack during 40,000 hours in SOFC mode 06005

Paolo Piccardo, Roberto Spotorno, Valeria Bongiorno, Daniele Paravidino, Christian Geipel, Greta Patrone and Francesca Valente

Published online: 10 January 2022

DOI: https://doi.org/10.1051/e3sconf/202233406005

PDF (2.499 MB) | References | NASA ADS Abstract Service

Open Access

A hydrogen generator coupled to a hydrogen heater for small scale portable applications 06006

Dirk Hufschmidt, Gisela M. Arzac, Maria Carmen Jiménez de Haro and Asunción Fernández

Published online: 10 January 2022

DOI: https://doi.org/10.1051/e3sconf/202233406006

PDF (1.140 MB) | References | NASA ADS Abstract Service

Open Access

Ammonia-based Solid Oxide Fuel Cell for zero emission maritime power: a case study 06007

Simona Di Micco, Mariagiovanna Minutillo, Luca Mastropasqua, Viviana Cigolotti and Jack Brouwer

Published online: 10 January 2022

DOI: https://doi.org/10.1051/e3sconf/202233406007

PDF (332.7 KB) | References | NASA ADS Abstract Service

Open Access

Four years of operational data for five hydrogen refueling stations 06008

Roberta Caponi, Andrea Monforti Ferrario, Enrico Bocci and Kristina Fløche Juelsgaard

Published online: 10 January 2022

DOI: https://doi.org/10.1051/e3sconf/202233406008

PDF (1.734 MB) | References | NASA ADS Abstract Service

Open Access

Characterization and modelling of air humidification in Fuel Cell System for transport sector 06009

Amedeo Grimaldi, Lorenzo Villa, Andrea Baricci, Stefano De Antonellis, Claudio Oldani and Andrea Casalegno
Published online: 10 January 2022
DOI: https://doi.org/10.1051/e3sconf/202233406009
PDF (242.4 KB) | References | NASA ADS Abstract Service

Open Access
Analysis of MEA's durability under Accelerated Stress Tests that mimic realistic automotive operations 06010
Elena Colombo, Andrea Baricci and Andrea Casalegno
Published online: 10 January 2022
DOI: https://doi.org/10.1051/e3sconf/202233406010
PDF (134.5 KB) | References | NASA ADS Abstract Service

Open Access
Hydrogen-based technologies in maritime sector: technical analysis and prospective 06011
Mariagiovanna Minutillo, Viviana Cigolotti, Giovanni Di Ilio, Arianna Bionda, Erik-Jan Boonen and Thomas Wannemacher
Published online: 10 January 2022
DOI: https://doi.org/10.1051/e3sconf/202233406011
PDF (1.391 MB) | References | NASA ADS Abstract Service

Open Access
Design of a hydrogen-powered bicycle for sustainable mobility 06012
Paolo Di Giorgio, Giovanni Di Ilio, Gabriele Scarpati, Giovanni Erme, Elio Simeoni and Elio Jannelli
Published online: 10 January 2022
DOI: https://doi.org/10.1051/e3sconf/202233406012
PDF (5.368 MB) | References | NASA ADS Abstract Service

Open Access
Development of a plug-in fuel cell electric scooter with thermally integrated storage system based on hydrogen in metal hydrides and battery pack 06013
Paolo Di Giorgio, Gabriele Scarpati, Giovanni Di Ilio, Ivan Arsie and Elio Jannelli
Published online: 10 January 2022
DOI: https://doi.org/10.1051/e3sconf/202233406013
PDF (4.715 MB) | References | NASA ADS Abstract Service

- Microbial & Enzymatic Biolectrochemical Systems

Open Access
Bioelectricity production of PMFC using Lobelia Queen Cardinalis in individual and shared soil configurations 08001
Grégory Bataillou, Naoufel Haddour and Christian Vollaire
Published online: 10 January 2022
DOI: https://doi.org/10.1051/e3sconf/202233408001
PDF (740.4 KB) | References | NASA ADS Abstract Service

Open Access
Development of Flexible, Conductive and Biocompatible Chitosan-Based Miniaturized Bioelectrodes for Enzymatic Glucose Biofuel Cells 08002
Laura García-Carmona, Mireia Buaki-Sogó, Marta Vegas-García, Mayte Gil-Agustí, Pedro Llovera-Segovia and Alfredo Quijano-López
Published online: 10 January 2022
DOI: https://doi.org/10.1051/e3sconf/202233408002
PDF (684.4 KB) | References | NASA ADS Abstract Service

Open Access
Assessing the effect of the electrode orientation on the performance of soil microbial fuel cells 08003
Jakub Dziegielowski, Gresa Bregu, Luke Hulse and Mirella Di Lorenzo
Published online: 10 January 2022
DOI: https://doi.org/10.1051/e3sconf/202233408003
PDF (398.8 KB) | References | NASA ADS Abstract Service

Open Access
Minimalistic soil microbial fuel cells for bioremediation of recalcitrant pollutants 08004
Arpita Nandy, Bongkyu Kim and Mirella Di Lorenzo
Published online: 10 January 2022

DOI: https://doi.org/10.1051/e3sconf/202233408004
PDF (2.280 MB) | References | NASA ADS Abstract Service

Open Access

Modelling Miniature Microbial Fuel Cells with Three-dimensional Anodes 08005

Elisa Casula, Michele Mascia, Giorgia De Gioannis, Mirella Di Lorenzo, Marco Isipato, Aldo Muntoni and Daniela Spiga

Published online: 10 January 2022

DOI: https://doi.org/10.1051/e3sconf/202233408005

PDF (512.0 KB) | References | NASA ADS Abstract Service

Open Access

Versatile Bioelectrochemical system for heavy metals removal 08006

Martí Aliaguilla, Daniele Molognoni, Pau Bosch-Jimenez and Eduard Borràs

Published online: 10 January 2022

DOI: https://doi.org/10.1051/e3sconf/202233408006

PDF (219.1 KB) | References | NASA ADS Abstract Service

Open Access

Towards cost-effective soil microbial fuel cell designs 08007

Jakub Dziegielowski and Mirella Di Lorenzo

Published online: 10 January 2022

DOI: https://doi.org/10.1051/e3sconf/202233408007

PDF (498.8 KB) | References | NASA ADS Abstract Service

Open Access

The different behaviour of *Thermotoga neapolitana* in the anodic and cathodic compartment of a bioelectrochemical system 08008

Pierangela Cristiani, Laura Malavola, Silvia Franz, Massimiliano Bestetti, Giuliana D'Ippolito, Nunzia Esercizio, Mariamichela Lanzilli and Angelo Fontana

Published online: 10 January 2022

DOI: https://doi.org/10.1051/e3sconf/202233408008

PDF (1.514 MB) | References | NASA ADS Abstract Service

Open Access

Performance of Reduced Titanium Oxide and Boron Doped Diamond as anodes in hyperthermophilic bioelectrochemical systems 08009

Laura Malavola, Silvia Franz, Massimiliano Bestetti, Nunzia Esercizio, Giuliana D'Ippolito and Pierangela Cristiani

Published online: 10 January 2022

DOI: https://doi.org/10.1051/e3sconf/202233408009

PDF (4.746 MB) | References | NASA ADS Abstract Service

Open Access

Long-term experience in anoxic wastewater treatment plants of planar MFC with Ce-doped cathodes 08010

Andrea Franzetti, Anna Espinoza, Enrico Barontini, Matteo Tucci, Paolo Bonelli and Pierangela Cristiani

Published online: 10 January 2022

DOI: https://doi.org/10.1051/e3sconf/202233408010

PDF (1.909 MB) | References | NASA ADS Abstract Service

Open Access

Performance assessment of stacked air-cathode microbial fuel cells under series and parallel electrical connections 08011

Simona Di Micco, Pasquale De Falco, Mariagiovanna Minutillo, Antonio Bracale, Pierluigi Caramia, Angelo Gifuni and Giuseppe Grassini

Published online: 10 January 2022

DOI: https://doi.org/10.1051/e3sconf/202233408011

PDF (1.505 MB) | References | NASA ADS Abstract Service

Open Access

Testing novel multicomposite materials for electromethanogenesis 08012

Giorgia Ghiara, Stefano Trasatti, Andrea Goglio and Pierangela Cristiani

Published online: 10 January 2022

DOI: https://doi.org/10.1051/e3sconf/202233408012

PDF (2.008 MB) | References | NASA ADS Abstract Service

- *Cross-Cutting and Overarching*

Open Access

Social Life Cycle Assessment of a Proton Exchange Membrane Fuel Cell stack 09001

Eleonora Bargiacchi, Felipe Campos-Carriedo, Diego Iribarren and Javier Dufour

Published online: 10 January 2022

DOI: https://doi.org/10.1051/e3sconf/202233409001

PDF (324.4 KB) | References | NASA ADS Abstract Service

Open Access

Assessment of Hydrogen and LNG buses adoption as sustainable alternatives to diesel fuel buses in public transportation: Applications to Italian perspective 09002

Michele Vincenzo Migliarese Caputi, Rossana Coccia, Paolo Venturini, Luca Cedola and Domenico Borello

Published online: 10 January 2022

DOI: https://doi.org/10.1051/e3sconf/202233409002

PDF (2.063 MB) | References | NASA ADS Abstract Service

Open Access

Comparative study of Global, European and Italian Standards on Hydrogen Refueling Stations 09003

Matteo Genovese, Viviana Cigolotti, Elio Jannelli and Petronilla Fragiacomo

Published online: 10 January 2022

DOI: https://doi.org/10.1051/e3sconf/202233409003

PDF (444.2 KB) | References | NASA ADS Abstract Service

Statement of Peer review

In submitting conference proceedings to E3S Web of Conferences, I certify to the Publisher that I adhere to the **Policy on Publishing Integrity** of the journal in order to safeguard good scientific practice in publishing.

1. All articles have been subjected to peer review administered by the proceedings editors.
2. Reviews have been conducted by expert referees, who have been requested to provide unbiased and constructive comments aimed, whenever possible, at improving the work.
3. Proceedings editors have taken all reasonable steps to ensure the quality of the materials they publish and their decision to accept or reject a paper for publication has been based only on the merits of the work and the relevance to the journal.

Title, date and place of the conference

EFC21 - European Fuel Cells and Hydrogen Piero Lunghi Conference
15th - 17th December 2021
Virtual Conference

Proceedings editor(s):

Viviana Cigolotti, PhD
ENEA - Italian National Agency for New Technologies, Energy and Sustainable Economic Development

Date and editor's signature

15/12/2021

Techno-economic analysis of hydrogen production from PV plants

Angelica Liponi[1], *Andrea* Baccioli[1], *Lorenzo* Ferrari[1,*], and *Umberto* Desideri[1]

[1]Department of Energy, Systems, Territory and Construction Engineering, University of Pisa, Pisa, Italy

Abstract. Hydrogen production through electrolysis from renewable sources is expected to play an important role to achieve the reduction targets of carbon dioxide emissions set for the next decades. Electrolysers can use the renewable energy surplus to produce green hydrogen and contribute to making the electrical grid more stable. Hydrogen can be used as medium-long term energy storage, converted into other fuels, or used as feedstock in industry thus contributing to decarbonise hard-to-abate-sectors. However, due to the intermittent and variable nature of solar and wind power, the direct coupling of electrolysers with renewables may lead to high production fluctuations and frequent shutdowns. As a consequence, accelerated electrolyser degradation and safety issues related to low load operation may arise. In this study, simulations of hydrogen production with an electrolyser fed by a PV system are performed in Matlab for a reference year. The effect of PV power fluctuations on the electrolyser operation and production is investigated. The impact of the electrolyser size for a fixed nominal power of the PV plant is also analysed from both energetic and economic points of view.

1 Introduction

In order to keep global warming below 2°C and limit climate changes, carbon emissions must be drastically reduced. As a consequence, the share of renewable energies (RE) in electricity production is increasing with the associated need to cope with their variability and unpredictability. In this context, hydrogen production through electrolysis from RE can play a key role. Electrolysers can use the RE overproduction and contribute to making the electrical grid more stable. The green hydrogen produced can be used as energy storage, converted into other compounds (e.g. power to fuel [1]) such as methane, methanol, or ammonia or used as feedstock in the industry contributing to the decarbonize this sector.

Water electrolysis technologies can be divided into low-temperature (alkaline and polymer electrolyte membrane (PEM) electrolysers) and high-temperature electrolysers (solid oxide electrolysers). Alkaline electrolysers are the most mature and widespread technology [2]. However, they have some limitations that must be taken into account when operating with fluctuating REs. They must operate in the range of 20-100% of the nominal power. Indeed, there is the risk of formation of potentially flammable mixtures of hydrogen and oxygen due to the diffusion of these gases through the membranes when the operating current is relatively low [3]. Furthermore, the number of start-ups and stops must be limited since it is associated with a reduction of the electrolyser lifetime [3].

Solar photovoltaics (PV), along with wind energy, are the most widespread REs and are expected to increase in the next years. However, their intermittent and unpredictable nature can affect the electrolyser operation and lifetime.

In recent years, several studies dealt with the coupling of PV power and hydrogen production through electrolysis. Gutiérrez-Martín et al. [4] proposed two configurations for an off-grid PV-electrolyser system: direct coupling and battery-assisted electrolysis and found hydrogen production costs of around 6–7 €/kg H_2. They asserted that batteries can support cost reductions by increasing the capacity factors of electrolysers, depending on the specific costs of these components. Schnuelle et al. [5] developed a model for both alkaline and PEM electrolysers and performed dynamic simulations with PV and wind power input datasets. They found that the better operational flexibility of PEM is generally not advantageous in terms of hydrogen production quantities and hydrogen production costs. Yates et al. [6] made a techno-economic analysis of stand-alone hydrogen production system from PV energy using Monte-Carlo-based uncertainty analysis; they found that the most important drivers of the LCOH are system size, capital cost, and electrolyser efficiency. Khalilnejad et al. [7] performed an optimization of a directly coupled PV-electrolyser system with a hydrogen storage tank to maximum hydrogen production of electrolyser with minimum excess power production of a PV system and minimum power transfer loss finding the optimal PV size.

The choice of the relative sizes of the electrolyser and the PV plant is a key issue, made complicated by the high variability of solar energy. In this study, a system consisting of an alkaline electrolyser fed by a PV plant for hydrogen production is investigated. Annual simulations

* Corresponding author: lorenzo.ferrari@unipi.it

for different electrolyser sizes are performed for a case study to analyse the size effect on some key performance indicators such as the total hydrogen production, the electrolyser efficiency, the number of shutdowns, and the levelized cost of hydrogen. The results obtained are related to the case study and the chosen site, but some general considerations can be drawn.

2 Method

The system under study consists of a 1 MW PV power plant providing electrical energy to an alkaline electrolyser for hydrogen production.

Annual simulations of the hydrogen production were performed in Matlab for different electrolyser sizes expressed as a percentage of the PV nominal power and ranging from 20% to 100% with 5% steps.

5-minute power production data of one year of a solar PV plant (Fig. 1) taken from the NREL database [8] were scaled to the nominal power of the PV plant. Not all the PV energy can be used by the electrolyser due to the electrolyser technical limitations, in particular, its operating power range. Therefore, the energy that could not be used by the electrolyser was supposed to be released to the grid.

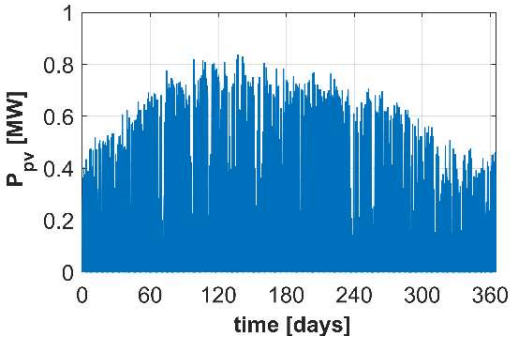

Fig. 1. PV power production.

An alkaline electrolyser model was adopted from [9] and scaled for the different sizes. An operating power range between 20%-100% of the nominal power was imposed as typical range for alkaline electrolyser. When PV power is below the lower power limit, the electrolyser is turned off while, over the maximum power limit, the excess of PV energy is released to the grid. The hydrogen production and the efficiency were calculated at each 5-minute time step given the electrical power input and the nominal electrolyser power. Inside the model the cell current (I_{cell}) and voltage (V_{cell}) are determined by solving the system of Eqs. (1) and (2) by means of the Newton iteration method:

$$V_{cell} = V_{rev} + C_1 \cdot \log_{10}(C_2 \cdot I_{cell} + 1) + R \cdot I_{cell} \quad (1)$$

$$\mathrm{P} = n_{cell}\, V_{cell}\, I_{cell} \quad (2)$$

where n_{cell} is the number of cells in series, and P is the power input to the electrolyser, that is the PV power minus the power required for the balance of the plant ($\mathrm{P_{aux}}$), expressed as a percentage of the total power, decreasing for increasing loads as in [10].

The coefficients of Eq. (1) are determined from the model adopted in [9] assuming an operating temperature of 70°C and a pressure of 5 bar. The resulting polarization curve is shown in Fig. 2.

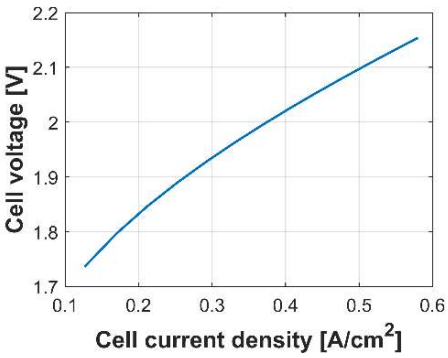

Fig. 2. Electrolyser's current – voltage curve.

The hydrogen production rate ($\dot{n}_{H_2}$), expressed in [mol/s], and the electrolyser efficiency (η_{LHV}) are then calculated for each time step as:

$$\dot{n}_{H_2} = \eta_F\, I_{cell} / (2\ \mathrm{F}) \quad (3)$$

$$\eta_{LHV} = \dot{n}_{H2}\, \mathrm{LHV} / \mathrm{P} \quad (4)$$

where F is the Faraday constant, and LHV is the lower heating value of hydrogen (241 kJ/mol). The Faraday efficiency, η_F, is expressed with a 5-parameters model, as a function of the current density ([9]).

The electrolyser efficiency, shown in Fig. 3 is a function of the load and has a maximum for a power input of about half the nominal power.

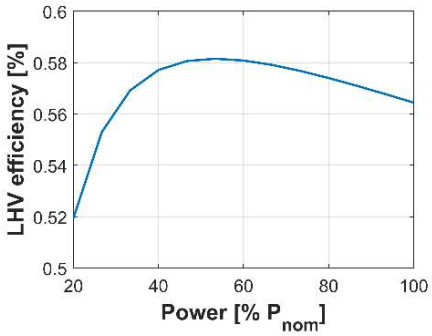

Fig. 3. Electrolyser efficiency as function of the power input.

For each simulation, the capacity factor, the number of shutdowns, the total operating time, and the percentage of PV energy used for water electrolysis are determined as important indicators of the electrolyser operation.

The levelized cost of hydrogen (LCOH) was evaluated for each electrolyser size as the sum of the contribution of the electrolyser cost (including annualized capital cost, operation and maintenance cost, and stack replacement cost), $\mathrm{LCOH_{electr}}$, and of the production cost of electrical energy, $\mathrm{LCOH_{el\ en}}$.

$$\mathrm{LCOH} = \mathrm{LCOH_{electr}} + \mathrm{LCOH_{el\ en}} = \frac{C_{el,ann}}{V_{H2,ann}} + \frac{\mathrm{LCOE} \cdot E_{PV,ann}}{V_{H2,ann}} \quad (5)$$

where $\mathrm{E_{PV,ann}}$ is the annual electrical energy produced by the PV plant and $\mathrm{V_{H2,ann}}$ is the annual hydrogen

production, expressed in [kg]. A levelized cost of energy (LCOE) of 60 €/MWh [11] is considered for the PV energy production.

The annualized cost for the electrolyser was evaluated as:

$$C_{el,ann} = \mathrm{CRF}\,[\,C_{cap,el} + C_{rep,el}\,(1+\mathrm{IR})^{-10}] + C_{O\&M,el} \quad (6)$$

where $C_{cap,el}$ is the electrolyser capital cost, $C_{rep,el}$ is cost of stack replacement (supposed to be after 10 years), and $C_{O\&M,el}$ is the operation and maintenance cost. The capital recovery factor, CRF, is given by:

$$\mathrm{CRF} = \mathrm{IR}(1+\mathrm{IR})^{\mathrm{Lt}}/[(1+\mathrm{IR})^{\mathrm{Lt}} - 1] \quad (7)$$

Table 1 shows the main assumptions for the economic evaluation.

Table 1. Economic parameters.

Parameter	Value	Ref.
Lifetime, Lt	20 years	[5]
Interest rate, IR	5%	[5]
Specific capital cost	750 €/kW	[12]
O&M cost, $C_{O\&M,el}$	2%/year of the capital cost	[13]
Stack replacement cost (1 repl.)	30% of the capital cost	[14]

LCOH defined by Eq. 5 assumes to have no gain from selling the PV energy not used by the electrolyser.

Then, in order to take into account the possible gain from selling the electrical energy surplus to the grid, a new LCOH (LCOH*) was evaluated assuming a selling price for the energy released to the grid, by Eq. 8:

$$\mathrm{LCOH}^* = \mathrm{LCOH} - p_{sell} \cdot \frac{E_{PV,ann} - E_{el,ann}}{V_{H2,ann}} \quad (8)$$

Several selling prices (p_{sell}) for the energy released to the grid were considered to see how they can affect the LCOH and the choice of the electrolyser size.

3 Results and discussion

Results show that the average operating power of the electrolyser (Fig. 4) initially increases with the nominal power since the maximum power limit increases allowing the electrolyser to operate at higher powers. At higher nominal powers, the increase of the average operating power becomes less marked. Indeed, most of the highest PV power values can be already completely absorbed by electrolysers with a lower nominal power; thus, the slight increase of the average power is mainly due to the cut of the lowest PV powers.

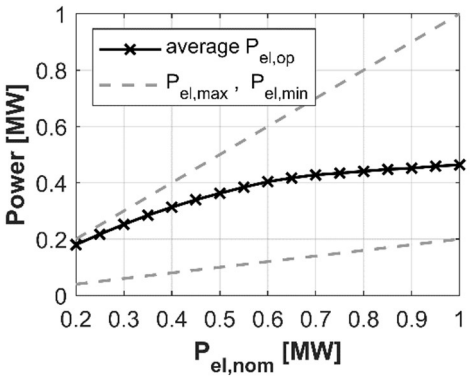

Fig. 4. Average operating power of the electrolyser and operating power limits as function of the electrolyser nominal power.

Furthermore, at lower nominal powers, the electrolyser operates averagely nearer to its maximum power at lower efficiencies (Fig. 5). At higher nominal powers, the electrolyser works more often at part-load conditions and averagely at higher efficiencies.

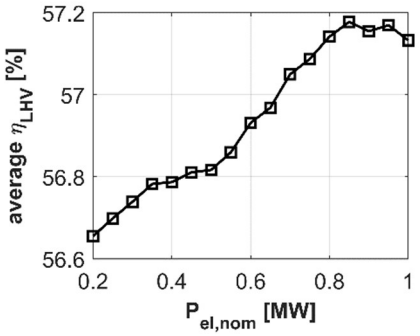

Fig. 5. Average efficiency of the electrolyser.

On one hand, electrolysers with lower nominal powers operate for a longer time and are closer to the nominal power, thus showing higher capacity factors as shown in Fig. 6. On the other hand, they can use only a small part (E_{el}) of the total energy produced by the PV plant (E_{pv}).

The maximum percentage of energy used by the electrolyser is reached for a nominal power of 0.7 MW. At higher power values, the cut of the lowest PV powers due to the greater minimum power limit of the electrolyser is not compensated by the increase of the maximum power limit.

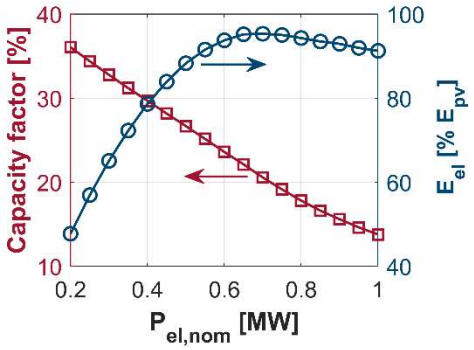

Fig. 6. Capacity factor and percentage of PV energy used by the electrolyser.

The annual hydrogen production (Fig. 7) increases with the nominal power of the electrolyser until reaching a maximum for a nominal power of 0.7 MW, the same value that maximizes the amount of PV energy used by the electrolyser. However, at this nominal power, the electrolyser has a low capacity factor (Fig. 6), slightly higher than 20% that can increase the payback time.

Nominal power higher than 0.7 MW showed even lower operating time. These electrolyser sizes should be therefore avoided from all the points of view.

The results obtained suggest that the best choice for the electrolyser size is a trade-off between the maximization of the hydrogen production and the maximization of the electrolyser capacity factor.

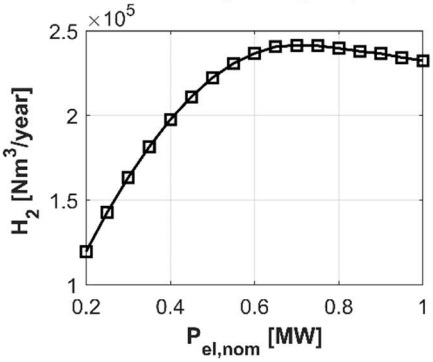

Fig. 7. Annual hydrogen production.

Another important parameter is the number of electrolyser on/off, which must be as low as possible to avoid fast performance degradation and consequent reduction of the stack lifetime.

Due to the nature of solar energy, the electrolyser is shut down at least one time per day. However, the number of on/off can be higher, especially in the case of cloudy days. Results show an increase in the annual number of on/off with the nominal power of the electrolyser (Fig. 8). Indeed, the PV power becomes more frequently lower than the minimum operating power in the case of higher nominal powers.

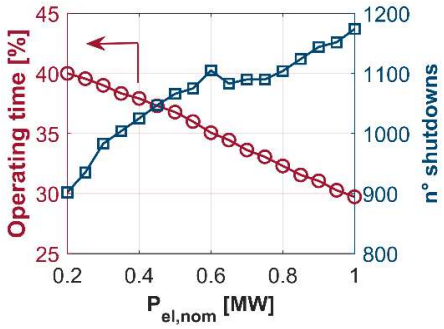

Fig. 8. Operating time percentage and annual number of shutdowns.

The levelized cost of hydrogen (Fig. 9) reaches a minimum at a nominal power of the electrolyser of 0.55 MW for a LCOE of 60 €/MWh. Indeed, on the one side, the contribution associated with the electrolyser cost grows with the size since the increasing annualized cost is not balanced by the increase in hydrogen production (because the capacity factor of the electrolyser decreases). On the other side, the contribution of the electrical energy cost to LCOH decreases with the electrolyser nominal power since the cost of the electrical energy produced by the PV plant is constant while the annual hydrogen production increases for nominal powers lower than 0.7 MW.

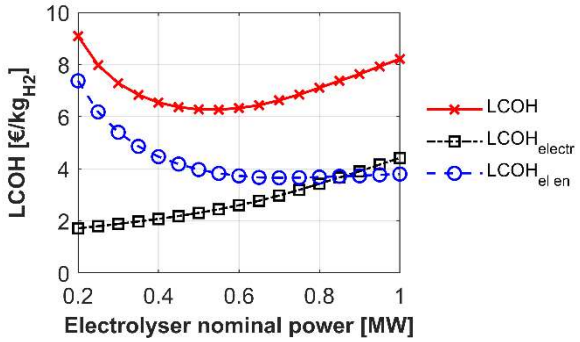

Fig. 9. Levelized cost of hydrogen (LCOH) and electrolyser- and electrical energy contributions (LCOE=60 €/MWh).

The electrolyser nominal power giving the minimum LCOH increases with LCOE (Fig. 10). The reason is that the weight of the contribution of the production cost of the electrical energy to LCOH increases with LCOE and has decreasing trend with the electrolyser nominal power.

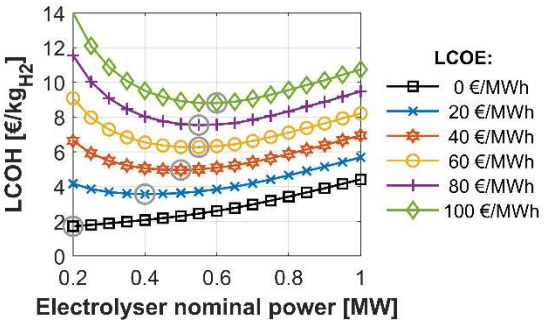

Fig. 10. Levelized cost of hydrogen (LCOH) for different LCOEs.

Finally, LCOH* (Fig. 11) shows a minimum for intermediate values of the nominal power of the electrolyser when the selling price of electrical energy is lower than LCOE. As the nominal power of the electrolyser increases, the beneficial effect of the selling price to reduce the LCOH decreases because the amount of electrical energy sold decreases.

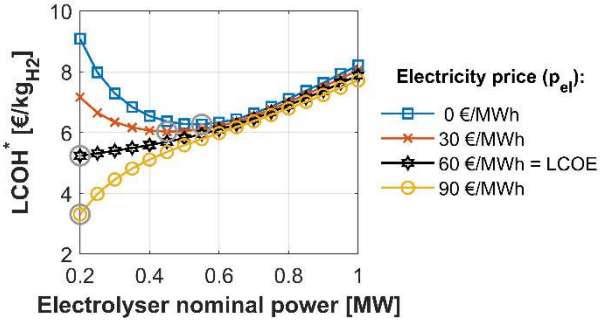

Fig. 11. Levelized cost of hydrogen (LCOH*) taking into account different selling price of electrical energy (LCOE=60 €/MWh).

4 Conclusion

The hydrogen production by an alkaline electrolyser fed by a 1 MW PV plant was simulated for different electrolyser nominal powers. For the studied case, the annual hydrogen production was maximized for a nominal power of the electrolyser of 0.7 MW. However, the increase of the electrolyser size leads to a decrease in the electrolyser capacity factor. Furthermore, the number of electrolyser shutdowns increases at higher electrolyser nominal powers leading to faster degradation. From an economic point of view, higher electrolyser sizes are related to higher capital costs that are not compensated by the increase in hydrogen production.

Assuming to not have a gain from selling the PV energy surplus, the minimum LCOH was obtained for an intermediate electrolyser nominal power, lower than that maximizing the hydrogen production. Even if the results are obtained for a specific site, some outcomes can be generalized. The best choice for the electrolyser size should be the result of a trade-off between the maximization of hydrogen production and the need of limiting the number of shutdowns and of having a sufficiently high capacity factor of the electrolyser in order to keep the LCOH down.

References

1. E. Bargiacchi, M. Antonelli, U. Desideri, Energy **183**, 1253–1265 (2019).
2. Á. Hernández-Gómez, V. Ramirez, D. Guilbert, Int. J. Hydrogen Energy **45**, 14625–14639 (2020).
3. A. Ursúa, E.L. Barrios, J. Pascual, I. San Martín, P. Sanchis, Int. J. Hydrogen Energy **41**, 12852–12861 (2016).
4. F. Gutiérrez-Martín, L. Amodio, M. Pagano, Int. J. Hydrogen Energy **46**, 29038–29048 (2021).
5. C. Schnuelle, T. Wassermann, D. Fuhrlaender, E. Zondervan, Int. J. Hydrogen Energy **45**, 29938–29952 (2020).
6. J. Yates, R. Daiyan, R. Patterson, R. Egan, R. Amal, A. Ho-Baille, N.L. Chang, Cell Reports Physical Science **1**, 100209 (2020).
7. A. Khalilnejad, A. Abbaspour, A.I. Sarwat, Int. J. Hydrogen Energy **41**, 11884–11894 (2016).
8. NREL, Solar Power Data for Integration Studies. https://www.nrel.gov/grid/solar-power-data.html (accessed 29 March 2021).
9. M. Sánchez, E. Amores, L. Rodríguez, C. Clemente-Jul, Int J Hydrogen Energy **43**, 20332–20345 (2018).
10. A. Liponi, G.F. Frate, A. Baccioli, L. Ferrari, U. Desideri, Green hydrogen from wind energy: mitigation of operating point fluctuations, in: Proceedings of ECOS - The 34th International Conference, Italy (2021).
11. IRENA, Renewable Power Generation Costs in 2019, Abu Dhabi, 2020.
12. J. Proost, Int J Hydrogen Energy **44**, 4406–4413 (2019).
13. J. Armijo, C. Philibert, Int J Hydrogen Energy **45**, 1541–1558 (2020).
14. B. Olateju, A. Kumar, M. Secanell, Int J Hydrogen Energy **41**, 8755–8776 (2016).

Carbon-coated stainless steel as a bipolar plate material in PEM water electrolyzers

Sebastian Proch[1,*], *Ulf* Bexell[1], *Claire* Moffatt[1], *Mikael* Stenström[1], *Carlos* Bernuy-Lopez[1], *Jörgen* Westlinder[1], *Hans* Becker[2], *Graham* Smith[2], *Edmund J.F.* Dickinson[2], *Gareth* Hinds[2], *Vincent* Wilke[3], *Svenja* Stiber[3], and *Aldo* Gago[3]

[1]Surface Research, Strategic Research, AB Sandvik Materials Technology, 81181 Sandviken, Sweden
[2]National Physical Laboratory, Hampton Rd, TW11 0LW, Teddington, United Kingdom
[3]German Aerospace Center (DLR), Institute of Engineering Thermodynamics, Pfaffenwaldring 38-40, 70569 Stuttgart, Germany

Abstract. The kinetically sluggish oxygen evolution reaction in proton exchange membrane water electrolyzers (PEMWEs) leads to ***high potentials*** of >1.5 V vs RHE at the ***anode electrode*** during operation. In contrast, an investigation with an *in situ* reference electrode indicates a much ***lower potential*** at the anode side of the ***bipolar plate*** which would allow the use of stainless steel and carbon as the bipolar plate materials. This decoupling is induced by the low conductivity of the circulating deionized water. In single cell electrolyzer tests, we show that ***carbon-coated 316L*** (C-316L) ***stainless steel*** is suitable as a ***bipolar plate material*** in contact with the anode and cathode sides of the PEMWE. The coating remains stable throughout the experiments, i.e., 720 h at the anode and 1000 h at the cathode side. Based on these results we regard ***carbon-coated stainless steel*** as a sustainable solution for the ***large-scale application of PEM water electrolysis*** since it might replace (Pt-coated) titanium in the bipolar plate.

1 Introduction

Hydrogen production via electrolysis of water has the potential to make a significant contribution to decarbonization of energy. The two mature electrolysis technologies are alkaline electrolysis using concentrated aqueous KOH as electrolyte and PEM electrolysis, which replaces the aqueous electrolyte with a proton conducting membrane [1]. The low ohmic resistance of thin polymer membranes, e.g., Nafion, in comparison to aqueous solutions facilitates higher current densities and, therefore, a smaller physical footprint of PEMWEs. Moreover, it has been proposed that membrane electrolysis allows faster response towards electricity from renewable sources [2]. Hence, PEM electrolysis is considered a promising option for green hydrogen production.

However, competitive costs for H_2 need to be achieved, which can be accomplished by lowering the electrolyzer's operational and capital expenditures (OPEX and CAPEX). OPEX is mainly associated with input electricity driving the endoergic water splitting reaction. Renewable electricity costs will drop in the future due to falling prices of solar PV panels [3] and other renewable electricity sources like wind turbines [4] due to their continued deployment. Consequently, it seems more beneficial to focus on decreasing the CAPEX.

A major cost driver of PEMWEs is the need for highly corrosion-resistant (Pt-coated) titanium components used within the anode compartment; they are often used on the cathode side too. Their use is based on the widely accepted perception that the high potential at the anode electrode (> 1.5 V vs RHE [5]) leads to an exceptionally corrosive environment across all the anode components [6]. This view of the anode has been challenged recently by experiments in which an *in situ* reference electrode demonstrates decoupling of the current collector from the catalyst layer. The observed 'galvanic' decoupling is attributed to the very low ionic strength of the electrolyzer feed water [7].

This effect results in a potential at the bipolar plate that is less oxidative than expected, creating the opportunity to use less corrosion-resistant and, therefore, more cost-effective materials, like stainless steel and carbon, in the anode compartment. In other words, the complete bipolar plate and parts of the porous transport layer could be substituted by stainless steel and carbon components with significant opportunity for cost reduction. We demonstrate the validity of one part of this suggestion by investigating the use of 316L and carbon-coated 316L (C-316L) stainless steel flow plates at the anode and cathode side in single cell PEM water electrolysis experiments.

2 Experimental

C-316L was manufactured by removing the oxide layer of a bright-annealed 316L strip (plasma etching) and subsequently coating it with a metallic adhesion layer and

* Corresponding author: sebastian.proch@sandvik.com

carbon in a coil-to-coil, high-throughput physical vapor deposition (PVD) coating line. The production process aims to achieve a 35 nm carbon layer and a 95 nm adhesion layer, but variations of these values are to be expected over large areas.

Single cell experiments at the anode side with and without an *in situ* reference electrode were presented previously [5]. The *in situ* reference electrode comprises a reversible hydrogen electrode (RHE, Hydroflex, Gaskatel, Germany) immersed in a chamber filled with 0.5 M H_2SO_4 connected to the cell using a Nafion tube sealed with an O-ring and a polyetheretherketone (PEEK) monofilament to prevent acid leakage. The measured current collector potential (E_{BPP}) is the potential between the anode current collector (working electrode) and the reference electrode. The end tip of the salt bridge is positioned at the surface of the metal sheet sample facing the expanded Ti metal mesh. A schematic representation of the anode side components is shown in Fig. 1.

Auger electron spectroscopy (AES) sputter depth profiling, catalyst coated membrane (CCM) digestion and subsequent trace metal analysis by inductively coupled plasma sector-field mass spectrometry (ICP-SFMS) [8] and *ex situ* contact resistance (CR) determination [9] have been described elsewhere.

Single cell experiments at the cathode side were carried out with a commercial CCM based on Nafion 115. Platinum-coated Ti mesh-type PTLs were used on both sides and, additionally, carbon paper was sandwiched between the PTL and the CCM at the cathode side. Testing was carried out in ultra-pure water at 60°C and ambient pressure. A mixed bed (strong acid/strong base) ion-exchange resin was deployed in the cell setup for inline water purification. Contact resistance of 316L and C-316L was measured by sandwiching them between two carbon paper sheets between two identical gold-plated copper cylinders. The assembly was installed in a hydraulic press and pressure was applied in 16 N cm^{-2} steps from 16 N cm^{-2} to 160 N cm^{-2}. The gold-plated copper cylinders were connected to a current source and a constant current was applied. The resulting voltage drop was recorded for each pressure step to calculate the total resistance. The contact resistance can be calculated by comparison of the total resistance of the setup and a single carbon paper sheet.

3 Results and Discussion

Fig. 1 presents the results of PEM electrolysis single cell tests in which 316L and C-316L were used as end-flow plates. In addition, an *in situ* reference electrode [5] was placed at the surface of the respective plates and, as expected, the potential at the plate surface was far below the potential in the anode catalyst layer. An additional 30-day (720 h) test with C-316L was carried out (not shown).

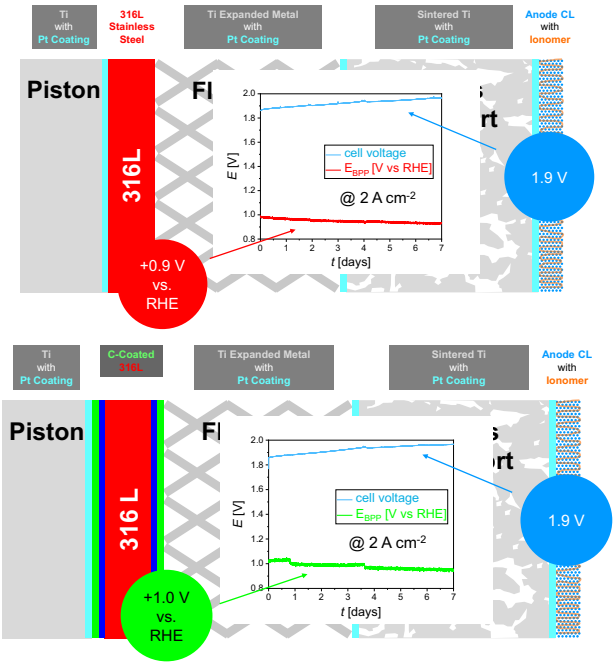

Fig. 1. Ionic decoupling in single cell PEMWE experiments with an *in situ* reference electrode at the anode side, with 316L (top) and C-316L (bottom) flow plates. The potential at the end-flow plates, red trace (top) and green trace (bottom) is much less oxidative than suggested by the cell voltage, blue trace (top and bottom). The results indicate relatively mild conditions under which both stainless steel and carbon are stable.

Post mortem analysis of the plates via AES sputter depth profiling indicated the absence of corrosion of the 316L material and the absence of bulk carbon oxidation on C-316L in all cases (7 and 30 days). Furthermore, digestion and ICP-SFMS analysis of the CCMs at the end of the tests showed no contamination with typical elements present in stainless steel, i.e., Cr, Mn, and Fe. The clear advantage of the carbon-coated material over its uncoated counterpart is found in substantially reduced contact resistance, which was measured *ex situ* under conditions obtained from the *in situ* experiments in Fig. 1 (7 days, 60°C, 0.9 V vs RHE, sulfuric acid pH 4.5). The *ex situ* measurements were necessary due to surface contamination of the *in situ* plates with Ru deposits likely originating from the CCM.

By definition, a bipolar plate is exposed to both anode and cathode conditions. Thus, the behaviour of 316L and C-316L was also investigated as end-flow plate at the cathode side of a PEMWE. Fig. 2 shows the temporal evolution of the cell voltage of two single cell PEM electrolysis experiments at a constant applied current density of 2 A cm^{-2} with 316L and C-316L, respectively, as cathode flow plates. The cell voltage degradation is in both cases about 77 µV per hour and both plates exhibit similar behaviour. The notion that cell degradation is independent of the choice of the cathode end-flow plate (316L vs. C-316L) is corroborated in polarization curves and electrochemical impedance spectroscopy (not shown).

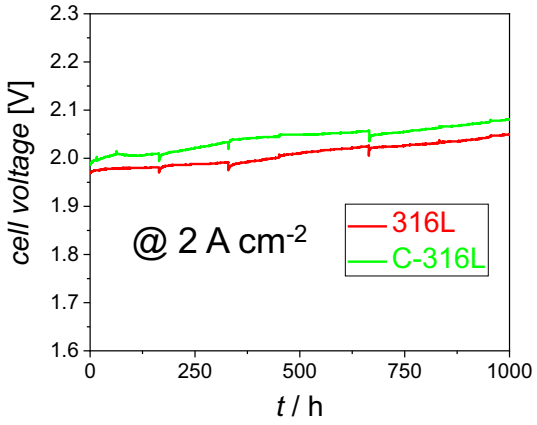

Fig. 2. PEMWE single cell experiments with 316L (red trace) and C-316L (green trace) as end-flow plates at the cathode side.

Contact resistance measurements for the cathode flow plates are presented in Fig. 3. The C-316L plate shows a significantly lower CR than 316L while in both cases deterioration of the CR due to electrolyzer operation is absent. The difference in contact resistance is small in single cell tests but becomes more important in the construction of stacks from cells connected in series. The plates will be investigated by AES sputter depth profiling to investigate changes in the oxide (passive) layer of the stainless steel and the carbon-coating.

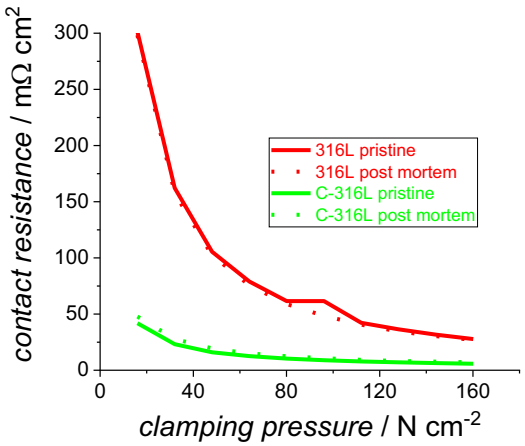

Fig. 3. Contact resistance measurements of 316L and C-316L flow plates before (pristine) and after (post mortem) 1000 h operation at the cathode of a PEMWE at 2 A cm^{-2}.

In summary, the suitability of C-316L as the end plate material at the anode and cathode side of a PEM water electrolyzer has been demonstrated. Hence, we suggest carbon-coated stainless steel as a cost-effective and scalable solution to replace Pt-coated titanium bipolar plates. The ionic decoupling effect which makes the substitution possible also holds great promise to reduce costs of the anode PTL.

References

1. K. Ayers, Curr. Opin. Electrochem., **18**, 9 (2019)
2. M. Carmo, D.L. Fritz, J. Mergel, D. Stolten, Int. J. Hydrogen Energy, **38**, 4901 (2013)
3. International Technology Roadmap for Photovoltaic (ITRPV) 2020 Results (2021)
4. J. Arbib, A. Dorr, T. Seba, Rethinking Climate Change, RethinkX, 26 (2021)
5. E. Brightman, J. Dodwell, N. van Dijk, G. Hinds, Electrochem. Commun. **52**, 1 (2015)
6. Q. Feng, X.Z. Yuan, G. Liu, B. Wie, Z. Zhang, H. Li., J. Power Sources, **366**, 33 (2017)
7. H. Becker, L. Castanheira, G. Hinds, J. Power Sources, **448**, 227563 (2020)
8. T. Novalin, B. Eriksson, S. Proch, U. Bexell, C. Moffatt, J. Westlinder, C. Lagergren, G. Lindbergh, R. Wreland-Lindström, Int. J. Hydrogen Energy, **46**, 13855 (2020)
9. S. Proch, M. Stenström, L. Eriksson, J. Andersson, G. Sjöblom, A. Jansson, J. Westlinder, Int. J. Hydrogen Energy, **45**, 1313 (2020)

Experimental validation of a dynamic modelling of a Reversible Solid Oxide Cells (rSOCs)

Michele Bolognese[1,*], *Matteo Testi*[1], *Lorenzo De Bortoli*[1] ,*Ruben Bartali*[1] and *Luigi Crema*[1]

[1] Fondazione Bruno Kessler, Via Sommarive 18, 38123 Povo, Trento, Italy

Abstract. The integration of Hydrogen technologies in different end-uses such as transport, electric microgrids, residential and industrial applications, will increase exponentially soon. Hydrogen as energy carrier allows more favourable energy conversion than other conventional systems and is crucial in worldwide decarbonize end uses. The production of green hydrogen, using RES, is a key area for the evolution of this technology. In this context, SWITCH is a Horizon 2020 European Project that aims to design, build and test an in-situ fully integrated and continuous multisource hydrogen production system, based on solid oxide cell technology. Reversible Solid Oxide Cell (rSOCs) technologies allow to convert renewable energy as hydrogen in the power-to-gas application (P2G) and in reversible mode is able to produce electricity from hydrogen stored, power-to-power application (P2P). rSOCs are really interesting to stabilize the random nature of RES because a combined electrolysis and fuel cell system should be able to switch between the two modes as quickly as possible in order to optimize the integration and the use of RES. However, rSOCs need a complex BoP from the thermal point of view, able to guarantee high efficiency even at partial load mode as well as easy start-up and shutdown procedures. In this work, a Stack Box Module dynamic model was developed in Modelica environment as a dynamic tool for the definition and optimization of BoP requirements. Stack model was validated in SOFC (Solid Oxide Fuel Cell) and SOE (Solid Oxide Electrolyser). The results of the simulation provide verification of the technical/thermodynamic behaviour and flexibility of a stack box of 70 cells. Dynamic modelling allows to evaluate the effect of the reagent inlet temperatures on the operation and hydrogen production/consumption in terms of yield as well as the transients between the different operative modes. Model has been validated by experimental measurements performed in the laboratory. In particular, the kinetics of the reactions governing steam methane reforming (SMR) was considered from data found in the literature, while the ASR (Area Specific Resistance) value was calibrated according to experimental data. The results of the dynamic model show as model can be a useful design and optimization tool for the SOCs technology.

1 Introduction

According to the European Hydrogen Strategy, mass production of electrolysers is expected to be deployed on the market with capacities of 6 GW by 2024 and 40 GW by 2030 [1]. Reversible Solid oxide cells (rSOCs) occurs in electrochemical devices that operate at high temperature (800-1000 °C). They are particularly attractive as electrochemical devices since they can operate both as fuel cells and as electrolysers depending on the application and needs. The behaviour of both Solid oxide fuel cells (SOFCs) and Solid oxide electrolyser (SOE) has been studied and reported in many articles [2][3][4][5] and the reversibility has been investigated since the 1980s when both steam[6][7]. The reversible working mode is gaining interest due to its high flexibility of operation than which supports the integration of fluctuating energy produced from renewable energy sources (RES). In fact, rSOCs can work as electrolysers when there is excess production from RES. The hydrogen produced during periods of RES abundance can be stored in dedicated systems until RES can meet the energy demand, at which point the stored hydrogen is used for energy production [8]. However, a limited amount of studies has been carried out on the combined design of a reversible fuel cell characterized by SOFC and SOE behaviour like the one that the SWITCH project aims to implement.[9][10][11]. In this study, values of area specific resistance at temperature T0 (T0 =1073K) ASR_0 and activation energy (Ea) valid for the calculation of area specific resistance (ASR) for the SOE and SOFC cases respectively were extrapolated through laboratory tests and used to validate the model and the simulation results of rSOFC behaviour.

2 Methodology

The dynamic modelling of the Reversible Solid Oxide Cells (rSOCs) was developed by using Modelica language [12] with the Dymola software[13].
The one-dimensional models and sub-models that characterizes the system is discretized over space with a number of *n* intervals. The choice of this discretization number is set at the top level of the model's system and then it results equal for each subsystem and sub model. In addition, a kinetic model for the reactions describing the steam methane reforming was considered within the anode channel of the stack and within an external reformer while a reversible equivalent electrical model for the water electrolysis and fuel cell operation was considered within the elementary cell model. The general layout used in the model is presented in Figure 1.

* Corresponding author: mbolognese@fbk.eu

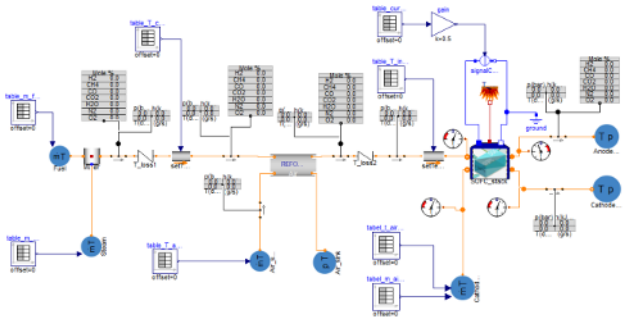

Figure 1: Layout of the general model

The general layout consists in different blocks as the stack, the external reformer, the mixer, the hydraulic losses blocks, the temperature sensors, the sinks and the fluid sources. In the hydraulic losses blocks the pressure difference between the inlet and the outlet port is caused by friction losses. In the friction model the mass flow rate (m_{flow}) is in first approximation function of nominal operating point specified by mass flow rate (m_{flow0}), density(ρ_0) and pressure drop (dp_0) :

$$m_{flow} = m_{flow0} \left(\frac{dp}{dp_0}\right)\left(\frac{\rho}{\rho_0}\right)$$

The diagram and the breakdown of the stack is shown in Figure 2. The Stack model (1) consists of other sub-models such as one relating to thermal losses (4) with the environment and one relating to the sub-stack model(2). The sub-stack is itself composed of a model relating to the anode and cathode channels (3) and one relating to the elementary cell model (4), as is possible to see in Figure 2.

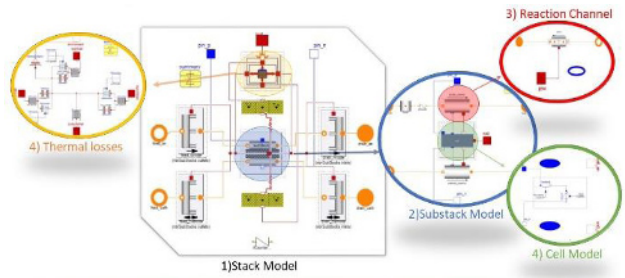

Figure 2: Diagram and breakdown of the model that describes the stack

In the model that describes the stack it is possible to link several sub-stacks in parallel. The mass ports (orange circles) used for the flow of fuel and air to the anode and cathode, respectively, are connected to particular manifolds that consider the number of sub-stacks chosen. According to SOE/SOFC modes, gases can exit or enter the sub-stack and then are collected in the exhaust manifolds, at the exit of the stack. The heat exchange between manifolds and the sub-stack is accounted in the manifold model. Moreover, a medium (*NASA reformate long*) from the Modelon fuel cell library [14][15] was used for the fuel that feeds the anode in both SOE and SOFC phases, while a medium with a fixed composition was used for the air. In the SOFC phase a mixer is used to mix steam and methane in order to have a Steam Carbon (S/C) ratio of about 2.3, while in the SOE phase water is used with a mass fraction of about 12% to avoid undesirable phenomena at the cathode that can cause irreversible damage [16]. The compositions and mass fractions of inlet fuel and air for the SOE and SOFC case are expressed in the following Table 1 and Table 2.

Table 1: Mass Fraction of the fuel in SOE and SOFC mode

Fuel Supply Channel	Mass Fraction (%)						
	H_2	CH_4	CO	CO_2	H_2O	N_2	O_2
SOFC	0	0.303	0	0	0.697	0	0
SOE	0.12	0	0	0	0.88	0	0

Table 2: Mass Fraction of the air

Air Supply Channel	Mass Fraction (%)				
	Ar	CO2	H20	N2	O2
Air	0	0	0	0.767	0.233

Three main hypotheses are made in the model:

1. All the gases in the model are considered to be ideal gases ;
2. Equidistant one-dimensional discretization for the stack cells and channels is considered ;
3. Concentrated parameters model, physical phenomena occur only in the respective component ;
4. Diffusion phenomena are not considered.

A cell area A_{cell} of 80 cm^2 I provided by the LSM during SOFC operation I_{SOFC} and that absorbed by the SOE mode I_{SOE} is an input data of the model, taken by experimental data. The current sign indicates the outgoing (positive) or incoming (negative) direction as per the standard. The number of H_2 moles, n_{H_2}, is calculated considering the Faraday's law as follows:

$$n_{H_2} = \frac{|I_{SOE}|}{F_u\, 2F}\, n_{cell}\, n_{sub}$$

Where F_u is the fuel utilization of 0.75, F is the Faraday constant ($F = 96485.3\ C/mol$), n_{cell} is the number of cells (70), and n_{sub} is the number of sub-stacks. The input for anode channel mass flowrates of the fuel are defined as follows:

$$\dot{m}_{H_2} = n_{H_2}\ MM_{H_2}$$

$$\dot{m}_{H_2O} = \frac{n_{H_2}}{2}\ MM_{H_2}$$

$$\dot{m}_{CH_4} = \frac{n_{H_2}}{4}\ MM_{CH_4}$$

Where MM is the molar mass of the different elements.

2.1. Cell model

The single elementary cell model is the lowest modelling level developed for this study. The single cell can be traced back to an electrical circuit with voltage and resistance generator. The voltage delivered from the cell is closely related to the electrical resistance of the cell, the current density, and the molar flows coming from the upper level of the sub-stack. In the elementary cell model, the open circuit potential at various temperatures can be evaluated with Nerst's equation, considering the evolution of the oxidation-reduction reaction:

$$H_2 + \frac{1}{2} \leftrightarrow H_2O \quad (1)$$

With the Nerst's equation:

$$V_{Nerst} = -\frac{\Delta G^0}{2F} - \frac{RT}{2F} ln\left(\frac{p_{H_2O}}{p_{H_2} p_{O_2}^{0.5}}\right) \quad (2)$$

where F is the Faraday constant ($F = 96485.3\ C/mol$), R is the universal constant of gas ($R = 8.314\ J/K\ mol$) [17]while ΔG^0 is the Gibbs free energy for the complete reaction (1) calculated by using the difference between the enthalpy formation (ΔH^0) and the product of cell temperature and formation entropy ($T\ \Delta S^0$) of both anode and cathode semi-reactions [18]. In addition, for the calculation of the enthalpy and entropy of formation, polynomials which are functions of the cell temperature were used [19]. The partial pressures of both reactants and products are evaluated for each segment of the one-dimensional discretization with a penalty to avoid negative pressure values :

$$p_{H_2O}=p_{cath}\ y_{H_2O}\ ;\ p_{H_2}=p_{cath}\ y_{H_2}\ ;\ \ p_{O_2}=p_{anod}\ y_{O_2}$$

In this way, by using Nernst equation, the cell equilibrium potential is calculated as a function of temperature and partial pressures. In real conditions, irreversible voltage losses occur when an electrical load is connected to the cell and a current flow through the cell. The overall voltage losses can be divided in three main categories: ohmic losses related to the resistivity of the solid oxide cell materials, electrode activation losses, and concentration losses. In this model, only an ohmic loss term (η_{ohmic}) is considered and represents all the voltage losses occurring in the SOE/SOFC model. The voltage at the cell external connectors is calculated by Kirchhoff voltage law (KVL) on the circuit [20], shown in Figure 3, as follows:

$$V = V_{Nerst} \mp R_{int}\ I_{cell} \quad (3)$$

The second term is positive for SOE and negative for SOFC since the resistances must be overcome to allow the reactions to occur. Each cell is discretized by dividing the spatial domain in N equivalent elements cells (i.e. n_{cell} = 70). Therefore, the single-cell resistance is given by the sum of the resistances over the N cell elements. As a consequence, the computation of the overall stack resistance (R_{int}) is given by :

$$R_{int=}\frac{n_{cell} ASR}{A_{cell}}$$

Where ASR is the area-specific resistance of each cell and A_{cell} is the equivalent active area of the stack. An empirical law [4] is used to describes the ASR as a function of the cell temperature (T_{cell}):

$$ASR = ASR_0 - \exp\left[\frac{E_a}{R}\left(\frac{1}{T_{cell}} - \frac{1}{T_0}\right)\right]$$

where ASR_0 is the area specific resistance at temperature T0 (T_0 =1073 K) [9]. The data extrapolated from the laboratory experiments are expressed in Table 3

Table 3: Experimental value of ASR_0 and E_a for SOFC and SOE case

	ASR_0 (Ω/cm²)	E_a (J/mol)
SOFC	0.2785 ± 0.0030	53680
SOE	0.3529 ± 0.0300	70489

Once the electrical model is defined, the current density (j_{ionic}) is defined as follows:

$$j_{ionic} = \frac{I_{cell}}{A_{cell}}$$

Where I_{cell} is the current applied to the whole cell. Depending on the current direction, the ASR0 and Ea values associated with the electrolyser or fuel cell mode are considered within the elementary cell model. Therefore, the equivalent electrical circuit with the voltage generator represented by the potential of Nerst and an electrical resistance that depends on the current (pin_n.i) and the system temperature through the ASR, is represented in the block diagram in Figure 3.

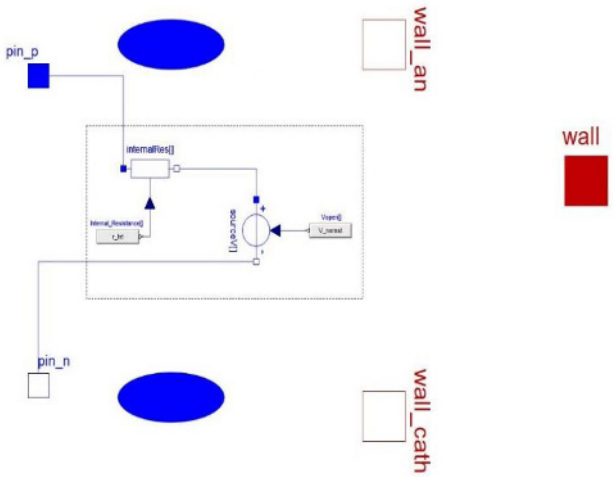

Figure 3: Block diagram of the i-th elementary cell element

The current generator (*source.V*) is connected to the electric connectors (pin_p, pin_n), passing through the internal resistance block (*internalRes*). T_{cell} is defined as the temperature of the cell that is directly connected to the thermal port wall (wall.T = Tcell). A thermal port allows temperature and heat flow continuity. Moreover, two mass ports that allow only the stoichiometric mass flow to diffuse from the cell to the channels and vice-versa according to hydrogen consumption or production. The temperature of the cell is calculated by the following expression for each element of discretization :

$$\frac{M_{cp}}{N}\frac{dT_{cell}}{dt} = Q_{an} + Q_{cath} + Q_{wall} + Q_{cell} \quad (4)$$

where M_{cp} is the thermal capacity (400 J/K), Q_{an} is the heat flux between the cell and the anode, Q_{cat} is the heat flux between the cell and the cathode, Q_{cell} is the heat produced in the i-th cell, and Q_{wall} is the heat exchanged between cell and external environment. The thermal ports referred to heat transfer between the cell and the anode or cathode (wall_an and wall_cath, respectively) are characterized by temperatures (T_{wall_an} and T_{wall_cat}). The heat fluxes are defined:

$$Q_{an} = K_c \frac{n_{cell}\, A_{cell}}{N}\left(T_{wall\_an} - T_{cell}\right) \quad (5)$$

$$Q_{cath} = K_c \frac{n_{cell}\, A_{cell}}{N}\left(T_{wall\_cath} - T_{cell}\right) \quad (6)$$

where K_c = 250 W/(m^2 K) is defined as the heat transfer coefficient between fluid and substrate and A_{cell} = 80e-4 m^2.

$$I = nF\,\frac{dZ}{dt} \quad (7)$$

$\frac{dZ}{dt}$ represents the speed with which reagent species are consumed and produced, i.e. the kinetic speed of reaction (mol/s). The global reaction introduced before can be split in the following two semi-reactions :

$$2O_2^{2-} \rightarrow O_2 + 4\,e^- \quad (8)$$

$$2H^+ + 2\,e^- \longrightarrow H_2 \quad (9)$$

The mass flow rate of H2O consumed can be evaluated according to Faraday's law, which allows at the same time to evaluate the O2 and H2 produced:

$$\dot{m}_{H_20} = \frac{j_{ionic} A_{cell}}{2F}\, MM_{H_20}\, \frac{n_{cell}}{N} \quad (10)$$

$$\dot{m}_{H_2} = -\frac{j_{ionic} A_{cell}}{2F}\, MM_{H_2}\, \frac{n_{cell}}{N} \quad (11)$$

$$\dot{m}_{O_2} = -\frac{j_{ionic} A_{cell}}{4F}\, MM_{O_2}\, \frac{n_{cell}}{N} \quad (12)$$

The sign is positive (+) for substances entering into a block and negative (-) for those exiting the block, i.e. positive for H_2O and negative for H_2 and O_2. Therefore, it is possible to determine the flow through the mass ports and the bulk enthalpy of the mixture ($\dot{H_{cath}}$ and $\dot{H_{anod}}$), since specific enthalpy of each component is known.

$$\dot{H_{cath}} = \sum_i \dot{m}_i\, h_i \qquad for \qquad i = H_2; H_2O \quad (13)$$

$$\dot{H_{anod}} = \dot{m}_{O_2}\, h_{O_2} \quad (14)$$

Finally, Q_{cell} is defined through the following energy balance:

$$Q_{cell} = \dot{H_{cath}} + \dot{H_{anod}} + P_{cell} \quad (15)$$

Where $P_{cell} = V_{cell}\, I$ is the cell power while V_{cell} is calculated as potential difference between the two electric connectors (pin_p, pin_n).

2.1. Reaction channel model

In the SOFC mode, the reactions describing the steam methane reforming will take place in the anode channel and in the external reformer. Subsequently, the hydrogen produced by these reactions will be converted into electricity produced from the fuel cell by using the equivalent electrical approach described in the elementary cell model. The stoichiometric coefficients of the following reactions are defined at first in the reaction channel:

$$CH_4 + H_2O \leftrightarrow CO + 3H_2 \qquad \Delta H = 206.2\ kJ/mol$$
$$CH_4 + 2H_2O \leftrightarrow CO_2 + 4H_2 \qquad \Delta H = 164.9\ kJ/mol$$
$$CO + H_2O \leftrightarrow CO_2 + H_2 \qquad \Delta H = -41.1\ kJ/mol$$

The reaction rates are expressed as R_1, R_2 and R_3, respectively and defined as follows [4]:

$$R_1 = \frac{k_1}{p_{H_2}^{2.5}}\left(p_{CH_4} p_{H_2O} - \frac{p_{H_2}^3 p_{CO}}{K_I}\right)\frac{1}{\Omega^2} \cdot S_{Cat} \quad (16)$$

$$R_2 = \frac{k_2}{p_{H_2}^{3.5}}\left(p_{CH_4} p_{H_2O}^2 - \frac{p_{H_2}^4 p_{CO}}{K_{II}}\right)\frac{1}{\Omega^2} \cdot S_{Cat} \quad (17)$$

$$R_3 = \frac{k_3}{p_{H_2}}\left(p_{CO} p_{H_2O} - \frac{p_{H_2} p_{CO_2}}{K_{III}}\right)\frac{1}{\Omega^2} \cdot S_{Cat} \quad (18)$$

Where S_{Cat} is a coefficient that represents the effect of a possible catalyzer, and in this model, it has been fixed with a different constant value in external reformer and in internal anode channel of the stack (4e-5 and 1e-5 respectively). Ω is a parameter expressed by the following equation:

$$\Omega = 1 + K_{CO}\, p_{CO} + K_{H_2} p_{H_2} + K_{CH_4} p_{C_{H_4}} + K_{H_2O}\frac{p_{H_2O}}{p_{H_2}} \quad (19)$$

Moreover, k_j is the Arrhenius reaction constant and is defined as follow:

$$K_i = K_{0i} \cdot exp\left(\frac{-\Delta H_i}{RT}\right) \quad (20)$$

The values of k_j are calculated by using the parameters listed in Table 4 [9]

Table 4: Arrhenius kinetic parameters

Reaction j	k_{0j}	$E_j(J/mol)$	Equilibrium Constants
1	1.17 E+15	240100	$K_I = exp\left(\frac{-26830}{T[i]} + 30.114\right)$
2	2.83 E+14	243900	$K_{II} = K_I\, K_{III}$
3	5.43 E+5	67130	$K_{III} = exp\left(\frac{-4400}{T[i]} - 4036\right)$

K_I, K_{II} and K_{III} are the equilibrium constant related to the corresponding reactions and are expressed as a function of the cell temperature. On the other hand, the Van't Hoff species adsorption constants (K_i) introduced for the definition of **Ω** are calculated with a similar Arrhenius expression by using the parameters listed in Table 5 [11].

Table 5: Van't Hoff parameters

Substance i	$k_{0j}(bar^{-1})$	$\Delta H_i(J/mol)$
CH_4	6.65 E-04	-38280
CO	8.23 E-05	-70650
H_2	6.12 E-09	-82900
H_20	1.77 E+05	88680

The reaction molar rate (rZ) are expressed as follows:

$$r_{CH_4} = -v_1R_1 - v_2R_2$$
$$r_{CO_2} = v_2R_2 + v_3R_3$$
$$r_{H_2O} = -v_1R_1 - 2v_2R_2 - v_3R_3$$
$$r_{H_2} = 3v_1R_1 + 4v_2R_2 + v_3R_3$$
$$r_{CO} = v_1R_1 - v_3R_3$$

With $v_1 = 0.07$, $v_2 = 0.06$ and $v_2 = 0.7$. These reaction molar rates are considered in the consumption or production rates of each substance by the following equation:

$$\frac{dZ}{dt} = Zx_{flow} + rZ \cdot deplZ \quad (21)$$

Where *deplZ* is a protection factor used against depleted species. It is calculated by using the smoothing splice function present in the math library of Modelon library while Zx_{flow} is the molar fraction and is defined as:

$$Zx_{flow} = \frac{mX_{flow}}{MMX} \quad (22)$$

In which MMX is the molecular weight of the medium while mX_{flow} is the mass flow rate that is defined in the reaction channel as the product of mass flow by the mass fraction.

$$mX_{flow} = m_{flow}\, X_j \quad (22)$$

3 Results and Discussion

In this section, simulation results are presented in comparison with experimental results. The results referring to the behaviour of the rSOCs refer to SOFC behaviour with a current ramp delivered from 1 to 9 A and SOE behaviour with a current ramp from 0.5 to 3.5 A. In the first case, an increase and decrease of the supplied current within the declared limits was considered, with a trapezoidal trend, while in the second case only a linear increase of the absorbed current was considered. Simulation times in accordance with those of the experiments have a duration of 3450 and 22900 s for SOFC and SOE, respectively. The voltage trend as a function of time is presented in Figure 4 for the SOFC case (top) and for the SOE case (bottom).

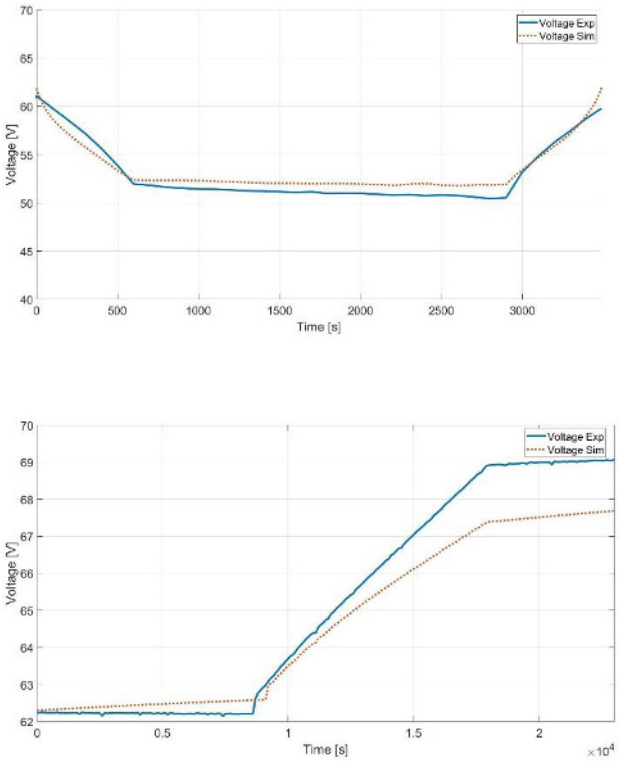

Figure 4: Voltage trend as a function of time for SOFC (top) and SOE (bottom) respectively

It is possible to notice that the trend of the simulated voltage (*Voltage Sim*) in both cases is very consistent to that of the experimental voltage (*Voltage Exp)*. In the SOFC case there is an increase and subsequent decrease in voltage of approx. 8.5 V, while in the SOE case there is an increase of approx. 7 V. The Figure 5 shows the relative error (gap) between the simulated and experimental voltage in the SOFC case (top) and in the SOE case (bottom).

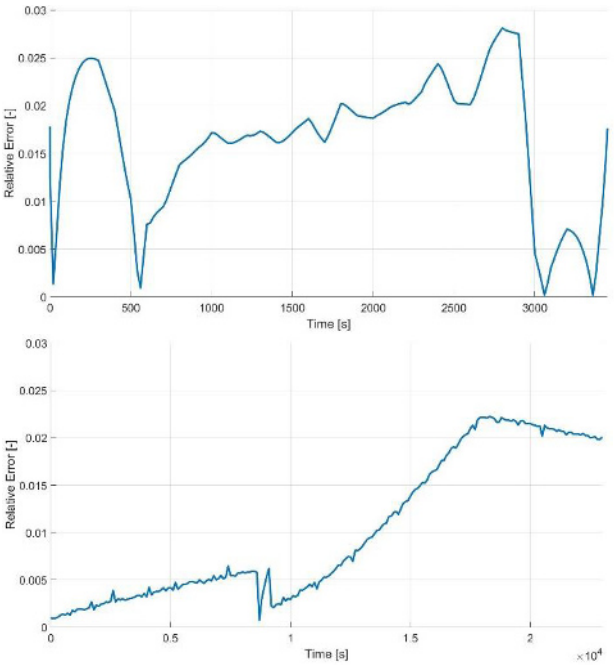

Figure 5: Relative error trend as function of time for SOFC (top) and SOE (bottom) respectevely

It can be observed that in both cases, the relative error is less than 3%. In the SOFC case when the current reaches plateaux and is stationary with a value of 9 A, the relative error increases from a value close to zero to a maximum value slightly higher than 2.5%. In the SOE case instead, the relative error varies from a minimum value of about 0.25% to a maximum value of about 2.25%.
In Figure 6, the evolution of voltage versus current (V-I trend) in the SOFC case (top) and in the SOE case (bottom) is presented. The trend of the polarization curve allows appreciating the nature of the ohmic losses. These in fact present a typically linear trend both in the experimental case (*linear lines*) and in the simulated case (*dotted lines*).

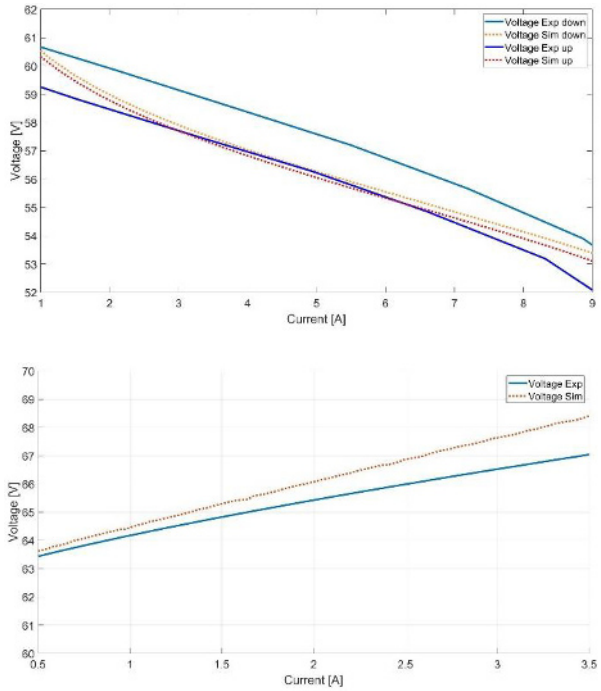

Figure 6: Voltage-Current trend for SOFC (top) and SOE (bottom)

Particularly in the SOFC case, it is possible to appreciate a difference in the V-I trend in the ramp-up and ramp down phases. For the first phase, the lines have a blue and red (dotted) colour, while for the second phase they have light blue and orange (dotted) color. It can be noticed that the curves have a parallel trend in the current range from 3 to about 7 A, while outside this range the curves have a slight deviation from the experimental data. For the SOE case, on the other hand, the curves show a linear trend for the complete current range. Finally, with this model it was possible to demonstrate that the system can work reversibly as a fuel cell or electrolyser. The calculation and the relative error estimation allow the model to be considered robust as the simulation results converge with the experimental ones with a maximum margin of error about 0.028.

4 Conclusions

In this paper a dynamic model of a reversible Solid Oxide Cells (rSOCs) has been developed in Dymola [13]. The dynamic model results were validated through experimental data with a relative error of less than 3 % The model constructed in this way is enough precise to simulate rSOCs for different applications as in power to power system, or to study the integration of rSOCs systems in electrical grid to manage in smart way the use of renewable energy. The reversible behaviour between electrolyzer (SOE) and fuel cell (SOFC) has been implemented in the elementary cell sub-model using experimental data. This would allow to simulate the storage of a surplus of energy produced by renewable sources [21] in the form of hydrogen and vice versa the conversion of hydrogen into electrical energy The use of SOCs systems at high operating temperatures shows a low impact of activation overvoltages compared to low temperature systems [9] and these systems show negligible mass transport effects at high currents and low fuel utilization (steam or natural gas). Moreover, the experimental data used for the validation of the model did not cover this type of case and for these reasons, the use of a simple ohmic model does not introduce significant errors. However, since the ASR used is determined by experimental data and is a function of temperature, inaccuracies in the model may arise if current and fuel utilization values are used outside the range of the experimental values. To achieve greater flexibility in the behaviour of the modelled current-voltage curve, it would be appropriate to implement more complex functions to describe the overvoltage losses due to activation and mass transfer [22][2]. However, in reality, the operating condition of an LSM is usually handled within a certain current range for which the ASR function used can be adjusted although there are obviously deviations that are considered negligible.

Acknowledgements

Authors acknowledge that CH2P and SWITCH projects have received funding from the Fuel Cells and Hydrogen 2 Joint Undertaking under grant agreements nos. 735692 and 875148. This Joint Undertaking receives support from the European Union's Horizon 2020 research and innovation program, from Hydrogen Europe and Hydrogen Europe Research.

References

[1] "A Hydrogen strategy for a climate-neutral Europe." [Online]. Available: https://ec.europa.eu/energy/ sites/ener/files/hydrogen_strategy.pdf1.

[2] P. Aguiar, C. S. Adjiman, and N. P. Brandon, "Anode-supported intermediate temperature direct internal reforming solid oxide fuel cell. I: model-based steady-state performance," *J. Power Sources*, vol. 138, no. 1–2, pp. 120–136, Nov. 2004.

[3] H. Zhu and R. J. Kee, "A general mathematical model for analyzing the performance of fuel-cell membrane-electrode assemblies," *J. Power Sources*, vol. 117, no. 1–2, pp. 61–74, May 2003.

[4] D. Andersson, E. Åberg, J. Eborn, J. Yuan, and B. Sundén, "Dynamic modeling of a solid oxide fuel cell system in Modelica," 2011, pp. 593–602.

[5] A. Hauch, S. D. Ebbesen, S. H. Jensen, and M. Mogensen, "Highly efficient high temperature electrolysis," *J. Mater. Chem.*, vol. 18, no. 20, p. 2331, 2008.

[6] A. ISENBERG, "Energy conversion via solid oxide electrolyte electrochemical cells at high temperatures," *Solid State Ionics*, vol. 3–4, pp. 431–437, Aug. 1981.

[7] W. DONITZ, G. DIETRICH, E. ERDLE, and R. STREICHER, "Electrochemical high temperature technology for hydrogen production or direct electricity generation," *Int. J. Hydrogen Energy*, vol. 13, no. 5, pp. 283–287, 1988.

[8] L. Crema, M. Testi, and M. Trini, "5 High-temperature electrolysis: efficient and versatile solution for multiple applications," in *Utilization of Hydrogen for Sustainable Energy and Fuels*, De Gruyter, 2021, pp. 219–268.

[9] J. Saarinen, M. Halinen, J. Ylijoki, M. Noponen, P. Simell, and J. Kiviaho, "Dynamic Model of 5kW SOFC CHP Test Station," *J. Fuel Cell Sci. Technol.*, vol. 4, no. 4, pp. 397–405, Nov. 2007.

[10] X. Xing, J. Lin, N. Brandon, A. Banerjee, and Y. Song, "Time-Varying Model Predictive Control of a Reversible-SOC Energy-Storage Plant Based on the Linear Parameter-Varying Method," *IEEE Trans. Sustain. Energy*, vol. 11, no. 3, pp. 1589–1600, Jul. 2020.

[11] S. Santhanam, M. P. Heddrich, M. Riedel, and K. A. Friedrich, "Theoretical and experimental study of Reversible Solid Oxide Cell (r-SOC) systems for energy storage," *Energy*, vol. 141, pp. 202–214, Dec. 2017.

[12] P. Fritzson and V. Engelson, "Modelica — A unified object-oriented language for system modeling and simulation," 1998, pp. 67–90.

[13] Dassault Systèmes, "Dymola Systems Engineering," 2017. [Online]. Available: https://www.3ds.com.

[14] "Modelon." [Online]. Available: https://www.modelon.com/library/fuel-cell-library/. [Accessed: 01-Aug-2021].

[15] "Modelon libraries." [Online]. Available: https://www.modelon.com/products-services/modelon-library-suite-modelica-libraries/.

[16] Manohar Sohal, "Degradation in Solid Oxide Cells During High Temperature Electrolysis," May 2009.

[17] W. B. Jensen, "The Universal Gas Constant R," *J. Chem. Educ.*, vol. 80, no. 7, p. 731, Jul. 2003.

[18] B. Cheng and M. Ceriotti, "Computing the absolute Gibbs free energy in atomistic simulations: Applications to defects in solids," *Phys. Rev. B*, vol. 97, no. 5, p. 054102, Feb. 2018.

[19] NIST Standard Reference Database Number 69, *NIST Chemistry WebBook*. 2021.

[20] L. E. Woodman, "Teaching Kirchhoff's Laws," *Am. J. Phys.*, vol. 2, no. 4, pp. 161–163, Dec. 1934.

[21] T. D. Hutty, S. Dong, and S. Brown, "Suitability of energy storage with reversible solid oxide cells for microgrid applications," *Energy Convers. Manag.*, vol. 226, p. 113499, Dec. 2020.

[22] M. Noponen, M. Halinen, and J. Kiviaho, "Electrochemical characterization and modeling of anode supported solid oxide fuel cell," *Proc. - Electrochem. Soc.*, vol. PV 2005-07, pp. 544–553, 2005.

Demonstration and analysis of a steam reforming process driven with solar heat using molten salts as heat transfer fluid

Alberto Giaconia[1,*], *Giampaolo* Caputo[1], *Primo* Di Ascenzi[1], *Giulia* Monteleone[1], and *Luca* Turchetti[1]

[1] ENEA, Italian National Agency for New Technologies, Energy and Sustainable Economic Development, Department of Energy Technologies and Renewable Sources (TERIN), Casaccia Research Center, via Anguillarese 301, 00123 Rome, Italy

Abstract. Solar reforming of biogas or biomethane represents an example hydrogen production from the combination of renewable sources such as biomass and solar energy. Thanks to its relatively low-cost and flexibility, solar-reforming can represent a complementary source of hydrogen where/when the demand exceeds the green hydrogen availability from water electrolysis powered by PV or wind. Molten salts can be used as heat transfer fluid and heat storage medium in solar-driven steam reforming. The main units of the process have been developed at the pilot scale and experimentally tested in a molten salt experimental loop at ENEA-Casaccia research center: a molten salt heater and a molten salt membrane reformer. After experimental validation, techno-economic studies have been carried out to assess the solar reforming technology on commercial scale and exploitation opportunities have been analysed.

1 Introduction

The growing interest on hydrogen requires evaluating all possible conversion processes for its production. Technologies developed so far allow hydrogen production from renewable (carbon-free or carbon-neutral) sources using electrochemical, photochemical, thermochemical or biochemical pathways; however, there are opportunities for further improvement of green hydrogen production in terms of costs reduction and efficiency in the deployment of primary sources [1].

Besides water-splitting by electrolysis driven by renewable power sources, steam reforming of biomass-derived methane represents a reliable and complementary thermochemical route, provided that this heat-demanding process is supplied with renewable heat to obtain 100% "green" hydrogen.

Today, steam methane reforming is the most used industrial process for hydrogen production. The core of the reforming plants is represented by catalytic reactors where the Steam Methane Reforming (SMR) reaction (1), which is highly endothermic, and the Water Gas Shift (WGS) reaction (2), which is moderately exothermic, take place:

$CH_4 + H_2O \rightarrow CO + 3H_2$ (1)

(SMR reaction, ΔH^0_{298K} = +206 kJ/mol, 750-950°C)

$CO + H_2O \rightarrow CO_2 + H_2$ (2)

(WGS reaction, ΔH^0_{298K} = -41 kJ/mol, 250-450°C)

Process heat is mainly needed to drive the highly endothermic SMR reaction (1) and to generate the reactant steam fed to reactors (steam is the excess reactant, in order to improve the hydrocarbons conversion and prevent any carbon deposition over the SMR catalyst).

Replacing fossil methane (e.g. from natural gas) with biomass-derived methane (i.e., biomethane) as feedstock allows to apply the same process scheme to green hydrogen production. However, in order to best valorise the available biomethane (i.e., to maximize the biomethane-to-hydrogen conversion) it is possible to use other renewable heat sources to partially or totally supply the process heat. One option consists in using high-temperature solar concentrating solar thermal (CST) systems to drive the thermochemical process. In this case, the issues raised by the intermittent nature of the primary renewable source can be smoothed out by applying suitable Thermal Energy Storage (TES) systems and Heat Transfer Fluid (HTF) to steadily transfer the renewable heat to the thermochemical process.

A substantial revision of the layout of the chemical process is however required for its adaptation to the new heat source, mostly related to the lower temperature achieved in the current CST plants compared to the conventional steam reforming operating conditions. With this purpose, ENEA has developed a new process scheme to drive methane steam reforming with solar heat [2]: the solar heat from the CST system equipped with TES is transferred at constant rate to the chemical process by using a molten salt mixture ($NaNO_3/KNO_3$, 60/40 %wt) as HTF at a temperature up to 550°C. The use of a membrane reformer heated with molten salt [3] allows to overcome the hydrogen yield limitations related to such low operating temperature.

The implementation of the above-described process scheme requires innovative heat-transfer equipment, which was also developed by ENEA in previous research actions:

- a molten salt heated Steam Generator (SG);
- a molten salt heater (MSH) to guarantee the continuity of hydrogen production also during periods with low or no

* Corresponding author: alberto.giaconia@enea.it

solar irradiance by using a fuel as back-up energy source.

This paper presents the state of the art of research activities carried out by ENEA on renewable-heated steam reforming and the perspectives for process optimization to obtain cost-competitive green hydrogen production.

2 Process description and state of the art

Figure 1 presents a conceptual scheme of the SMR process heated with molten salts. The molten salt captures the intermittent renewable heat up to 550°C, in a CST system. Hot molten salts are stored in a TES tank . A molten salt heater (MSH), including a gas fuel combustion chamber and a gas/molten salt heat exchanger, is used as back-up to heat the molten salt up to 550°C in case of lack of renewable energy from the TES system. Then, the hot molten salt stream is fed to the SMR process units. A single membrane reformer is used to carry out the SMR and WGS reactions with satisfactory final methane conversion (exceeding the value that can be obtained with a conventional reformer operating under the same conditions) thanks to the continuous removal of hydrogen from the reaction environment [2]. A pre-reformer can be included in order to feed the membrane reformer with an hydrogen-containing mixture; this ensures a better exploitation of the membrane and avoids sharp temperature gradients near the inlet section of the reactor. The residual sensible heat of the molten salt is used to generate the process steam.

Besides the outlet hydrogen permeate stream, a retentate stream is also obtained from the membrane reformer. This stream contains produced CO_2 and CO, unreacted CH_4 and H_2O, and non-permeated H_2. Depending on the operation mode, this retentate stream can be used in two different ways:

1) burnt as fuel in the MSH;
2) sent to a CO_2 separation unit to recover and recycle a $CH_4/H_2/CO$ mixture.

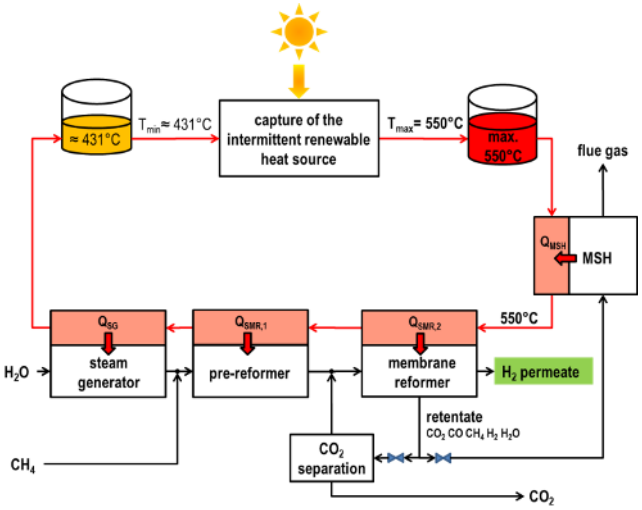

Fig. 1. Conceptual scheme of the SMR process driven with renewable heat using molten salt up to 550°C as heat transfer fluid. Red lines: molten salt streams; black lines: process streams.

The above described process scheme includes several innovative process units integrated in the molten salt loop: the CST system with TES, the MSH, the steam generator and the steam reformers heated with the molten salt. These key units have been individually developed and successfully tested at the pilot or pre-commercial scales by ENEA in different projects.

The molten salt heated membrane reformer integrated with the pre-reformer has been developed and successfully demonstrated at the pilot scale (up to 3 Nm^3/h H_2 permeate production) in a molten salt loop in the project CoMETHy [3,4]. Figure 2 shows the tube sheet of the molten salt heated steam reformer with catalyst and membranes in the inner tubes [4].

Fig. 2. Tube sheet of the molten salt heated steam reformer with catalyst and membranes in the inner tubes developed in the project CoMETHy [4].

The molten salt heater (MSH) has been developed and successfully demonstrated by ENEA in the projects MATS and Hysol: Figure 3 shows the 90 kW (thermal) gas/molten salt heat exchanger installed in the molten salt loop to validate heat transfer correlations prior to process scale-up [5]. In this case, gas fuels were burned in a combustion chamber and the generated hot gases up to 632°C used to heat the molten salt in the convective section of the back-up unit [5].

Fig. 3. Finned tube bundle of the MSH prototype developed in the projects MATS and Hysol [5].

Concentrating solar systems with "solar salt" and TES up to 550°C have been developed in several projects by different players worldwide. In the project MATS, ENEA has specifically developed and demonstrated an innovative approach that integrates the following units at the 5 MW (thermal) scale: parabolic linear concentrators with direct solar heating of molten salt up to 550°C, a gas fuelled MSH, and single-tank TES integrated with a super-heated steam generator (Figure 4). The mentioned units are integrated in a cogenerative plant to produce 1 MW of power and 250 m^3/d of desalinated water [6].

The CO_2 separation unit shown in Figure 1 can be based on mature technologies such as PSA or amine systems.

Fig. 4. Underground molten salt TES system (14 MWh thermal) integrated with super-heated steam generator developed in the project MATS [6].

3 Development perspectives

The previous section reports that the different units of the SMR process scheme shown in Figure 1 have been tested and validated at the pilot or demonstration scale: up to 3 Nm^3/h hydrogen production for the SMR reactors and up to 5 MW thermal for the heat supply units (solar concentrators, MSH, TES, SG). Additionally, tests carried out with the molten salt heated SMR pilot reactors did not show any significant performance loss after about 150 hours of operation [4]; however, it is worth underlying that the durability/reliability of membrane reactors has yet to be validated for at least 5,000 hours-on-stream.

Assuming a plant with 1,500 Nm^3/h capacity, a preliminary techno-economic assessment resulted on Levelized Costs of Hydrogen (LCOH) from 2.4 to 4.7 €/kg for the solar SMR process [7]. This wide range is mainly due to the different assumptions made on the utilization factor and the cost of the CST plant. Table 1 summarizes the results in terms of LCOH and average specific CO_2 emissions under different scenarios:

- "solar-only" case considers minimal use of the back-up, i.e. when solar heat is not available the hydrogen production is stopped and reactors maintained in a "hot stand-by" condition;
- "hybrid" case considers 8,000 hours/year continuous hydrogen production with broad use of the back-up system when solar heat is not available.

Clearly, the hybrid case entails combustion of the retentate during the operating hours, when solar heat is no longer available and, hence, specific CO_2 emissions increase from 5.7 to 10.2 kg_{CO2}/kg_{H2} (yearly average) [7]. Compared to a conventional (non-solar) SMR process with typical overall CO_2 emissions in the flue gases of 11.7 kg_{CO2}/kg_{H2}, in the solar hybrid case only 4.3 out of the total 10.2 kg_{CO2}/kg_{H2} produced are emitted with the flue gases of the MSH; the residual CO_2 is recovered as nearly pure stream in a carbon capture and utilization (CCU) scenario.

Table 1 shows that a reduction of the unit costs of the CST system from 231 to 100 €/m^2 (installed, including solar collectors, receiver tubes, piping and ancillary equipment) will lead to a more competitive hydrogen production costs: from 2.8-4.7 €/kg to 2.4-3.4 €/kg (CH_4 cost: ~0.25 €/kg). This is due to the significant impact of the CST cost on the capital expenditure of the plant [7].

Table 1. Levelized Cost of Hydrogen and specific CO_2 emissions obtained for the solar SMR under different assumptions [7].

			yearly operation hours	
			solar-only 4,456 hr/year	hybrid 8,000 hr/year
LCOH	CST plant cost	100 €/m^2	3.4 €/kg_{H2}	2.4 €/kg_{H2}
		231 €/m^2	4.7 €/kg_{H2}	2.8 €/kg_{H2}
Specific CO_2 emissions			5.7 kg_{CO2}/kg_{H2}	10.2 kg_{CO2}/kg_{H2}

Based on these preliminary results, development pathways can be identified to further reduce the hydrogen production costs. Due to the significant impact of the CST system on the cost of hydrogen, it is recommended to investigate solutions that improve the thermal efficiency of the process. As a matter of fact, the overall thermal efficiency of the preliminary SMR scheme being around 60% [7] can be improved with an optimized thermal integration.

A major source of efficiency loss derives from cooling and steam condensation prior low-temperature separation of CO_2 from the retentate and H_2 from the sweep steam in the permeate. Here, CO_2 separation can be optimized, investigating different options such as the PSA or innovative approaches based on regenerative CO_2 sorption at relatively high temperatures (>300°C): in this latter case, it will be possible to avoid condensation of residual steam in the retentate and allow its recirculation (with residual CH_4 and H_2) to the reactor, thus increasing the overall efficiency of the SMR process.

Operating pressures in both reaction and permeate sides of the reformer (assumed 10.5 and 1.4 bar in the

preliminary layout) can be optimized too in order to minimize the amount of sweep steam to be generated and downstream condensed for hydrogen removal.

Finally, it is worth underlying that the proposed flowsheet implies relevant power consumption (~430 kWe for a 1,500 Nm^3/h SMR plant) being the second highest operating cost (after methane feedstock), which can also be reduced with an optimized integration of the SMR plant with a hybrid CST/PV plant [8].

4 Conclusions

In this paper, an innovative approach to solar steam reforming of (bio)methane is presented. This process makes use of a molten salt mixture up to 550°C as solar heat transfer fluid and heat storage medium. Research, development and demonstration activities carried out by ENEA led to the experimental validation of the single units of the process: the concentrating solar system with heat storage and steam generator have been demonstrated to the pre-commercial scale, while the solar back-up unit and the steam reforming reactor have been experimentally validated at the pilot scale in a molten salt experimental loop at the ENEA-Casaccia research center. After experimental validation, techno-economic studies have been carried out to assess the solar reforming technology on commercial scale and exploitation opportunities have been analysed. Results show the interesting opportunities for solar SMR to reach the target of 2 €/kg for green hydrogen production.

This research has been initially funded through the FCH JU project CoMETHy (Compact Multifuel-Energy To Hydrogen converter, Grant Agreement n. 279075), and the 7FP projects Hysol (Innovative Configuration for a Fully Renewable Hybrid CSP Plant, Grant Agreement n.308912) and MATS (Multipurpose Applications by Thermodynamic Solar, Grant Agreement n. 268219). Experimental results have been further analysed in the project 1.9 “Concentrating Solar Power” and 1.2 “Energy storage”, under the “Electric System Research” program 2019–2021, with the financial support of Italian Ministry for Ecological Transition.

References

1. M. van de Voorde. “Hydrogen Production and Energy Transition, Volume 1”, De Gruyter (2021). https://doi.org/10.1515/9783110596250.
2. A. Giaconia, M. De Falco, G. Caputo, R. Grena, P. Tarquini, L. Marrelli. AIChE J., 54, 1932 (2008). https://doi.org/10.1002/aic.11510.
3. A. Giaconia, G. Monteleone, B. Morico, et al. Energy Procedia, 69, 1750 (2015). https://doi.org/10.1016/j.egypro.2015.03.144.
4. A. Giaconia, G. Iaquaniello, G. Caputo, B. Morico, A. Salladini, L. Turchetti, G. Monteleone, A. Giannini, E. Palo. Int. J. Hydrogen Energy, 45, 33088 (2020). https://doi.org/10.1016/j.ijhydene.2020.09.070
5. A. Giaconia, I. Balog, G. Caputo. Energies. 14, 7652 (2021). https://doi.org/10.3390/en14227652.
6. A. Giaconia, G. Iaquaniello, A. Amin Metwally, G. Caputo, I. Balog. Solar Energy. 211, 622 (2020). https://doi.org/10.1016/j.solener.2020.09.091.
7. A. Giaconia, G. Iaquaniello, B. Morico, A. Salladini, E. Palo. Int. J. Hydrogen Energy, 46, 35172 (2021). https://doi.org/10.1016/j.ijhydene.2021.08.096.
8. A. Giaconia, R. Grena. Solar Energy. 2021, 224, 159 (2021) https://doi.org/10.1016/j.solener.2021.05.043.

On-site solar powered refueling stations for green hydrogen production and distribution: performances and costs

Simona Di Micco[1,*], *Mariagiovanna* Minutillo[2], *Alessandra* Perna[3] and *Elio* Jannelli[1]

[1] University of Naples "Parthenope", Naples, Italy
[2] Department of Industrial Engineering, University of Salerno, Salerno, Italy
[3] University of Cassino and Southern Lazio, Cassino, Italy

Abstract. Today, the hydrogen is considered an essential element in speeding up the energy transition and generate important environmental benefits. Not all hydrogen is the same, though. The "green hydrogen", which is produced using renewable energy and electrolysis to split water, is really and completely sustainable for stationary and mobile applications. This paper is focused on the techno-economic analysis of an on-site hydrogen refueling station (HRS) in which the green hydrogen production is assured by a PV plant that supplies electricity to an alkaline electrolyzer. The hydrogen is stored in low pressure tanks (200 bar) and then is compressed at 900 bar for refueling FCHVs by using the innovative technology of the ionic compressor. From technical point of view, the components of the HRS have been sized for assuring a maximum capacity of 450 kg/day. In particular, the PV plant (installed in the south of Italy) has a size of 8MWp and supplies an alkaline electrolyzer of 2.1 MW. A Li-ion battery system (size 3.5 MWh) is used to store the electricity surplus and the grid-connection of the PV plant allows to export the electricity excess that cannot be stored in the battery system. The economic analysis has been performed by estimating the levelized cost of hydrogen (LCOH) that is an important economic indicator based on the evaluation of investment, operational & maintenance and replacement costs. Results highlighted that the proposed on-site configuration in which the green hydrogen production is assured, is characterized by a LCOH of 10.71 €/kg.

1 Introduction

The transition to a hydrogen-based mobility requires the development of an infrastructure that must be able to satisfy the hydrogen demand. Hydrogen refueling stations (HRSs) with on-site production from electric renewable energy sources (RES) are an interesting solution for assuring green hydrogen with zero CO_2 emissions [1-4] The advantages achievable by adopting this solution are: i) increasing the share of electricity produced by renewable sources, ii) helping the integration of the fluctuating and non-programmable renewables (solar and wind) in the electric grid, iii) providing grid balancing services, iv) producing "green hydrogen" able to assure a sustainable mobility. The main issue of these on-site RES powered HRSs is the green hydrogen cost that is currently too high and depends on both the plant size (hydrogen production capacity) and on the hydrogen source [4].
In recent scientific literature, several studies have been focused on techno-economic analysis of this type of plants, aiming to evaluate the levelized cost of hydrogen (LCOH). Gökçek and Kale [5] proposed a wind/solar/battery hybrid renewable energy powered refueling station on the island of Gökçeada, (Turkey). The hydrogen refueling station was sized for servicing 25 vehicles per day each having a 5 kg tank. The LCOH values were equal to $ 8.92/kg and $ 11.08/kg for the wind-PV-battery power system and the wind-battery system, respectively.
Zhao and Brouwer [6] evaluated the feasibility of a self-sustained hydrogen refueling station, in which a proton exchange membrane electrolysis unit fed by renewable sources (wind and photovoltaic plants) produced the specified hydrogen amount. Results showed that, for the photovoltaic (PV) system, the estimated LCOH was equal to $20.22/kg (by assuming an average levelized cost of electricity of $0.280/kWh). The LCOH dropped to 9.14 $/kg by reducing this cost to $0.103/kWh.
In [7] the authors studied an electrolysis/PV-Wind plant installed in Belgium. The estimated LCOH varied with the costs of electricity and the annual operation time, ranging from 10.3 €/kg to 18.0 €/kg.
In this study, a techno-economic assessment of an on-site hydrogen refueling station, based on hybrid PV-battery system integrated with an alkaline electrolysis unit and sized for a maximum hydrogen production of 450 kg/day, has been performed. In particular, in order to properly supply the electrolysis unit, a management strategy to optimize the electricity sharing between the PV field and the battery system has been defined. Moreover, in order to evaluate the contribution of each plant section (production section and compression & dispensing section) to the LCOH, a detailed costs analysis has been carried and the LCOHs of the plant sections have been calculated.

* Corresponding author: simona.dimicco@studenti.uniparthenope.it

2 Plant layout description and design

The proposed on-site HRS is based on a hybrid PV-battery system integrated with an electrolysis unit, to be installed in the South of Italy. Figure 1 shows the conceptual scheme of the proposed HRS. The electrolysis unit has a modular architecture consisting of 18 modules (the size of each module is 118 kW_p) operating a 16 bar and produces 450 kg/day (207 Nm^3/h) by converting 5040 liters/day of water in hydrogen and oxygen with an AC power consumption of 5.1 kWh/Nm^3. The produced hydrogen is pre-compressed up to 200 bar before entering the ionic compression unit IC90 (Linde technology), where it is compressed and stored up to 900 bar. During the refueling, the hydrogen is cooled at -40 °C according to the SAE J2601 protocol.

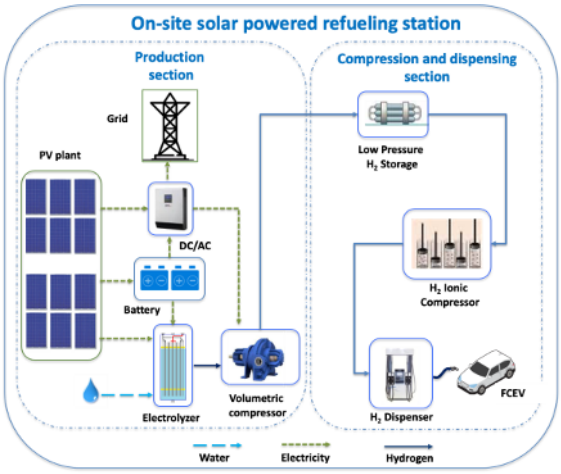

Figure 1: Scheme of the proposed on-site HRS station

The required electric power for the hydrogen production and compression is supplied by 8 MW peak PV plant and a 3.5 MWh Li-ion battery pack. In particular, each module of the PV plant consists of 250 W_p peak power mono-crystalline unit (Model 1Soletech 1STH-240-WH, Anodized Aluminum Alloy) with a fixed both azimuthal angle and tilt angle equal to 157.5° and 33°.

In Fig.2 the PV plant monthly electricity production is reported, while table 1 summarizes the size of the HRS components.

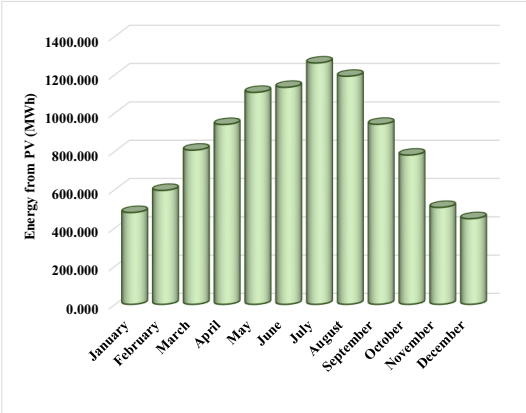

Figure 2: PV monthly electricity production.

Table 1. Size of HRS components.

Component	Size
PV (MWp)	8
Alkaline Electrolyzer (MW)	2.1
Pre-Compressor (kW)	23
Ionic Compressor IC90 (kW)	15
Li-ion battery (MWh)	3.5

3 Methodology

In order to properly supply the electrolysis unit for the hydrogen production, a management strategy for electricity sharing between PV plant and battery has been defined. The flowchart of the proposed management strategy is depicted in Fig.3. When the electric power generated by the PV plant is in the range 25-100% of the electrolyzer rated power, hydrogen is produced and stored; when the produced electric power is greater than the electrolyzer rated power (>100%), the electricity surplus is stored in the battery (considering that its initial charging state is 650 kWh) or delivered to the grid.

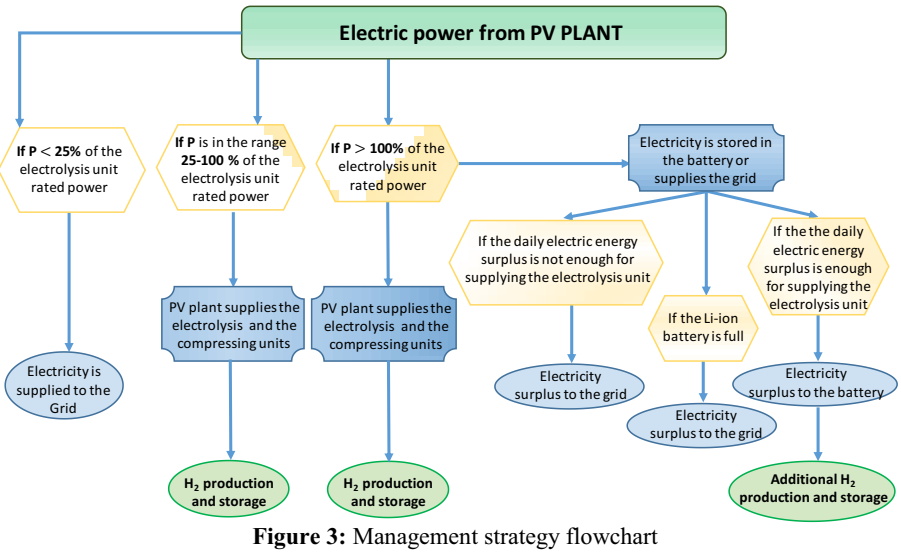

Figure 3: Management strategy flowchart

Moreover, when the electric power production is lower than the minimum load of the electrolysis unit (<25% of the rated power), the electric energy generated is diverted to the grid.
Figs.4 and 5 illustrate the results of the management strategy for the days of maximum and minimum hydrogen production, respectively.

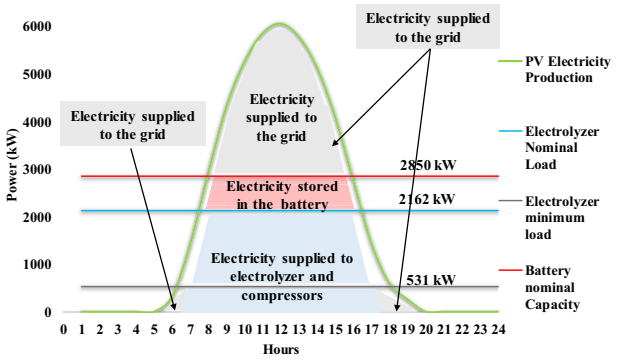

Figure 4: Day of maximum H_2 production

In Fig.4 it can be noticed that the PV field produces more electricity than that required by the plant (electrolyzer and compressors), allowing for the maximum hydrogen production of 400 kg. The electricity excess is partly stored in the Li-ion battery and partly delivered to the grid, according to the aforementioned management strategy. In particular, in this day, the battery allows to have an additional H_2 production of about 50 kg, allowing a maximum annual daily production of 450 kg, whereas the electricity surplus that has to be delivered to the grid is 20.4 MWh.

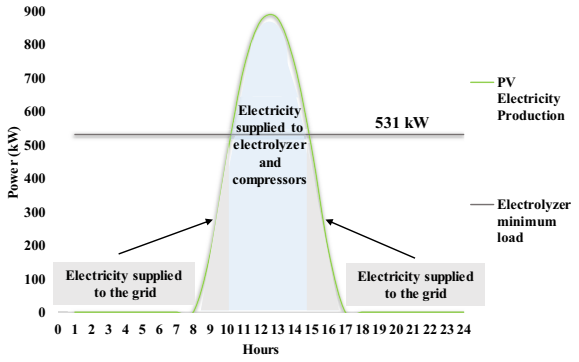

Figure 5: Day of minimum H_2 production

It is worth noticing that in the worst irradiation day (Fig, 5) the electricity generated by the PV field is always lower than that required by the electrolyzer at full load, and in some hour ranges (8h-10h; 15h-17h), the electricity generation is lower than that needed to supply the electrolyzer operating at minimum load. In this last condition, the electricity generated by the PV is diverted to the grid (1.3 MWh). On the other hand, when the electricity is greater than the minimum load of the electrolyzer (531 kW), the hydrogen production is assured, amounting for 56 kg in time range 10h-15h.

Fig.6 shows the annual hydrogen production, equal to 123.1 tons. Thanks to the battery pack it is possible to obtain an increase of the annual hydrogen production of about 11% corresponding to 14 tons.
The daily minimum and maximum hydrogen availability in the refueling station (or the capacity range of the station) are 56 kg and 450 kg, respectively.

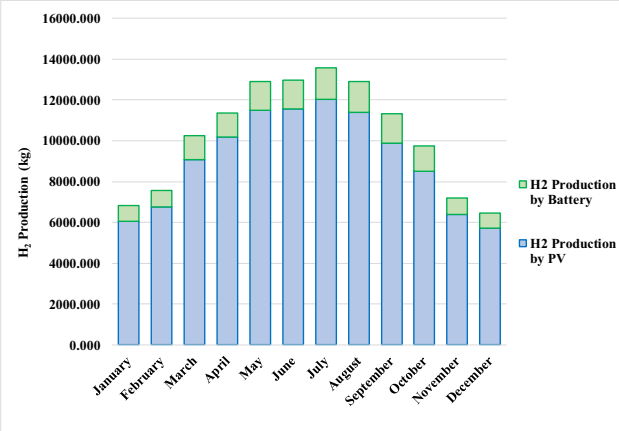

Figure 6: Monthly distribution of the annual hydrogen production

3 Economic Assessment

In order to define the HRS economic feasibility, the analysis has been performed by estimating the Capital Expenditure (CAPEX), the Operational Expenditure (OPEX), the Replacement Expenditure (REPLEX), and then by calculating the levelized cost of hydrogen LCOH that is the more important indicator among the economic evaluation indexes.

3.1 Plant cost definition

The costs of PV and electrolyzer have been assumed equal to 950 €/kW and 1100 €/kW respectively [8,9]. As concern the IC-90 Compressor, a capital investment cost of 648,000 € is assumed, according to ref [10]. For the Li-ion battery pack, a cost of 800 €/kW is assumed. According to the nominal HRS capacity, 2 Dispensing systems, with 4 nozzles are considered, each of which has a capital investment cost of 65,000 €.
The O&M cost of each component has been evaluated on yearly basis as a proper percentage of its initial investment cost. The percentages assumed for each plant component have been widely discussed by the authors in a previous paper [11]. For evaluating the cost due to the water consumption (computed as operating costs), the tariffs defined by the Italian Company ABC (sited in Naples) have been assumed [12] Based on these data, this cost consists of a fixed annual cost (€/year) and a cost variable according to water consumption (€/m^3). Considering that the annual water consumption is 1379 m^3/year, the fixed annual cost is equal to 18.12 €/year and the variable cost is equal € 1.006 for each consumed water cubic meter (m^3). Therefore, the total annual operating expenditure for water consumption results equal to 1,405 €/year.
As concern the electricity delivered to the grid, the

* Corresponding author: simona.dimicco@studenti.uniparthenope.it

assumed remuneration electricity price is equal to 50 €/MWh [13,14]. According to this value, the annual remuneration for the electricity sale amounts to 154,000 €/year.
Referring to the Replex, only one replacement (after 10 years) has been considered for the electrolyzer, compressors, Li-ion battery, dispensing and water system. Table 2 lists the CAPEX, OPEX and REPLEX for each plant's component.

Table 2. Total costs for HRS configuration.

Components	**CAPEX (k€)**	**OPEX (k€)**	**REPLEX (k€)**
PV modules	7600.0	120.1	-
Electrolyzer	2336.4	46.7	368.0
Compressor	239.6	19.2	239.6
Low pressure Storage System	450.0	9.0	-
IC90	648.0	25.9	-
Li-ion battery	2800.0	84.0	2800.0
Dispenser	260.0	7.8	260.0
Water System	7.83	0.3	7.83
Total (k€)	14,341.8	313.0	3,675.4

3.1 Levelized Cost of Hydrogen

The levelized cost of hydrogen ($LCOH$) methodology allows for accounting all the capital and operating costs of hydrogen supply chain. It is calculated as:

$$LCOH = \frac{Total\ Costs\ (€) - Electrical\ Revenue\ (€)}{H_2\ Annual\ Production\ (kg)} = \frac{C_{inv,a} + C_{rep,a} + C_{O\&M} - Rev_{el}}{M_{H_2}} \quad (1)$$

$C_{inv,a}$ represents the annual capital repayment, which is calculated by taking into account the total plant capital investment costs (C_{inv}), the plant lifetime (n), and the nominal interest rate (i):

$$C_{inv,a} = \frac{i\cdot(1+i)^n}{(1+i)^n-1}\cdot C_{inv} \quad (2)$$

In particular, a plant lifetime equal to 20 years and a nominal interest rate equal to 3% have been assumed [15,16].

$C_{rep,a}$ is the annualized replacement cost and represents the annual cost rate to replace all components and parts that wear out during the plant lifetime. It is calculated as:

$$C_{rep,a} = \frac{i\cdot(1+i)^n}{(1+i)^n-1}\cdot\frac{C_{rep}}{(1+i)^t} \quad (3)$$

where C_{rep} and t are the replacement cost and related year, respectively.
$C_{O\&M}$ represents the cost to guarantee the normal operation and maintenance of the plant; it is calculated on yearly basis.
Finally, Rev_{el} represents the annual revenue obtained by selling "electricity excess" to the grid. This term is considered in the eq. (1) as a negative cost.
In this analysis, in order to evaluate the cost incidence of each hydrogen supply chain section (fig.1), the $LCOH$ has been calculated as:

$$LCOH = LCOH_P + LCOH_{C\&D} \quad (4)$$

where $LCOH_P$ refers to the hydrogen production section and $LCOH_{C\&D}$ refers to the hydrogen compression and dispensing section.
Tables 3 and 4 list the cost items for the $LCOH_P$ and $LCOH_{C\&D}$ calculation, respectively.

Table 3: Individual cost item for $LCOH_P$ calculation

$C_{inv,a}$ (k€/year)	$C_{rep,a}$ (k€/year)	$C_{O\&M}$ (k€/year)	Rev_{el} (k€/year)	$LCOH_P$ (€/kg)
872.7	181.2	271.5	154.0	9.52

Table 4: Individual cost item for $LCOH_{C\&D}$ calculation

$C_{inv,a}$ (k€/year)	$C_{rep,a}$ (k€/year)	$C_{O\&M}$ (k€/year)	Rev_{el} (k€/year)	$LCOH_{C\&D}$ (€/kg)
91.3	13.0	42.7	-	1.19

The $LCOH$ for the considered HRS is 10.71 €/kg. This is a good value considering that the hydrogen production is totally renewable.
Fig.7 shows the $LCOH_P$ and $LCOH_{C\&D}$ incidence on the total $LCOH$. It is worth noticing that the production section affects the total $LCOH$ for about 89%, showing the greatest incidence compared to the compression and dispensing section.
The higher incidence on the $LCOH_P$ is due to $C_{inv,a}$, which affects it for about 66%.

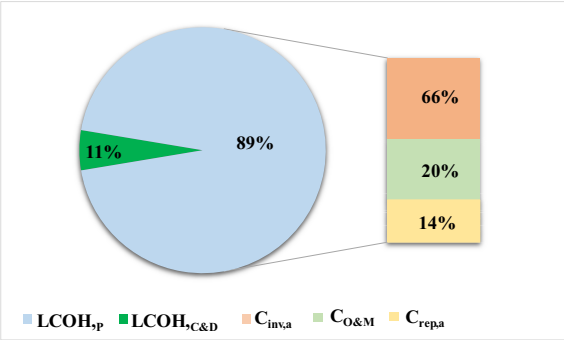

Figure 7: Incidence of items cost on the $LCOH$ of each section plant

4 Conclusion

This paper is focused on the techno-economic analysis of an on-site hydrogen refueling station (HRS) in which the green hydrogen production is assured by a PV plant that supplies electricity to an alkaline electrolyzer. A Li-ion battery pack is used to store the electricity surplus, while the grid-connection mode of the PV plant allows to export the electricity excess that cannot be stored in the battery system. The HRS consists of two main sections: the production section and the compression and dispending section. To properly supply the electrolysis unit a management strategy able to optimize the electricity sharing between the PV field and the battery system has been defined. According to this strategy the annual hydrogen production in the proposed HRS is equal to 123.1 tons. The daily minimum and maximum hydrogen availability in the refueling station (or the capacity range of the station) are 56 kg and 450 kg, respectively and thanks to the battery unit the annual hydrogen production increases of about 11% (14 tons).

The economic analysis has allowed to estimate the LCOH; in particular, the contributions of each plant section (production section and compression & dispensing section) on the LCOH value have been calculated, underlying the prevailing incidence of the production section.

Results highlighted that the proposed on-site configuration in which the production of green hydrogen is performed, is characterized by a LCOH of 10.71 €/kg.

2 References

[1] Alessandra Perna, Mariagiovanna Minutillo, Simona Di Micco, Viviana Cigolotti, Adele Pianese. E3S WEB OF CONFERENCES, 197, (2020)

[2] Dimitrios Apostolou, and George Xydis. Renewable and Sustainable Energy Reviews 113, 109292. (2019)

[3] Alessandra Perna, Mariagiovanna Minutillo, Simona Di Micco, Pasquale Di Trolio, Elio Jannelli. AIP Conference Proceedings 2191. 2201, p. 020127-020136, (2019)

[4] Alessandra Perna, Mariagiovanna Minutillo, Pasquale Di Trolio, Simona Di Micco, Elio Jannelli. Int J Hydrogen Energy, 46 (16),10059–10071 (2021)

[5] Gökçek, Murat, and Cihangir Kale. Energy Conversion and Management 161 (2018): 215-224

[6] Zhao L, Brouwer J. Int J Hydrogen Energy 2015;40:3822–37.

[7] Viktorsson L, Heinonen JT, Skulason JB, Unnthorsson R. Energies 10,1–15, (2017).

[8] Staffell I, Green R. Int J Hydrogen Energy 2013;38:1088e102.

[9] Schmidt O, Gambhir A, Staffell I, Hawkes A, Nelson J, Few S. Int J Hydrogen Energy2017;42:30470e92.

[10] Edmund G. Brown Jr., Governor, Calif. Energy Comm. (2019)

[11] Mariagiovanna Minutillo, Alessandra Perna, Antonio Forcina, Simona Di Micco, Elio Jannelli. Int J Hydrogen Energy 46(26):13667-13677 (2020).

[12] Napoli ABC. Adeguamento tariffario 2019.

[13] GESTORE MERCATI ENERGETICI (GME)-Mercato del Giorno Prima (MGP)

Thermochemical cycle based on solid intermediates for hydrogen storage and on-demand production

Anna Chiara Tizzoni[1*], *Emiliana* Mansi[1], *Salvatore* Sau[1], *Annarita* Spadoni[1], *Natale* Corsaro[1], *Michela* Lanchi[1], *Gianremo* Giorgi[1], *Luca* Turchetti[1] *and Tiziano* Delise[1]

[1] ENEA – Italian National Agency for New Technologies, Energy and Sustainable Economic Development, Via Anguillarese, 301, 00123 Rome, Italy

Abstract. Thermochemical water splitting processes based on Sulfur-Iodine cycle can be conveniently improved using solid intermediates, in order to increase the global yield and avoid the use of concentrated acid at high temperatures. In this context, an innovative process has been conceived, where a metal oxide, namely NiO, is reduced into oxygen and the correspondent metal, which can be suitably stored and reacted with steam into hydrogen when and where necessary. Data previously obtained and published, together with the integration of experimental results have been used to evaluate the technical feasibility and the heat duties of each step of the proposed cycle. The starting point was a Nickel compounds based process already extensively characterized, which has been modified using low toxic Iron (III) species as intermediates for oxygen formation. Based on the theoretical and experimental analysis carried out, the resulting cycle thermal efficiency is quite promising, about 19%, also taking into account the hydrogen generation step.

1 Introduction

Solar driven thermochemical water splitting cycles (TWSC) are considered a valid alternative to the direct thermal water splitting, which can only occur at about 3500°C, in very severe operating conditions which lead to serious issues related to materials and products separations [1]. Moreover, solar receivers present a limited thermal efficiency above 1000°C [2]. For these reasons, several TWSC processes were proposed in the last years, and, among them, the so called "Sulfur-Iodine" cycle [3][4][5] can be operated at relatively limited temperatures (<900°C). In this cycle the water molecule is "incorporated" into sulfuric and hydriodic acids by the "Bunsen reaction". Then, both are thermally decomposed, the former at around 900°C into oxygen and sulfur dioxide, and the latter at about 500°C, leading to hydrogen and iodine. Iodine and sulfur dioxide are recirculated to the Bunsen section, to be converted again into the two acid solutions. The cycle is schematized in Figure 1.

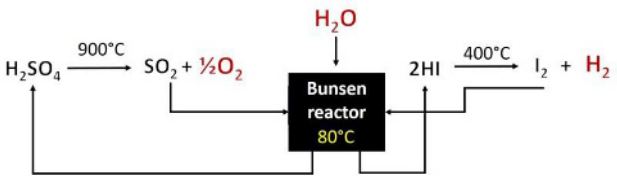

Fig. 1. Scheme of the "Sulfur Iodine" cycle

Compared to other TWSC, this process presents the advantage to employ commonly chemicals as intermediates, but also the drawback of a relative great number of reactive and separative phases, quite corrosive compounds at high temperatures, and the requirement of specific heterogeneous catalysts, with an important thermodynamic limitation for hydriodic acid cracking [4].

In this regard, the use of solid intermediates was investigated as an alternative solution to overcome some of the described issues, and Nickel compounds were proposed at this aim by Prosini et al [6]. The modified cycle is illustrated in Figure 2. Hydrogen is quantitatively produced at high purity and low temperature by reacting metallic Nickel with sulfuric acid, and a sulfate and an iodide are decomposed in place of the related acids. However, it is necessary to reduce the toxicity of the employed intermediates and it is important to consider a proper method to store and transport the hydrogen produced.

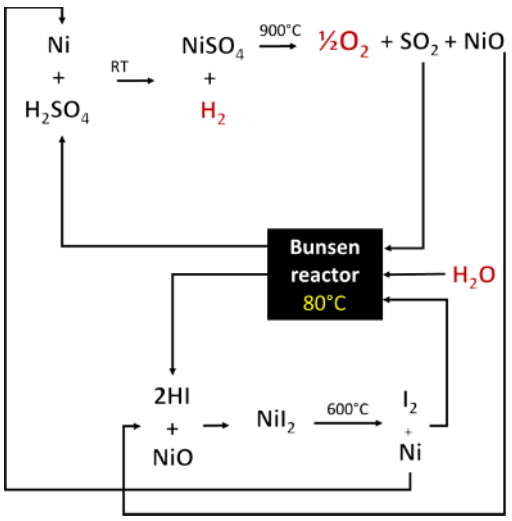

Fig. 2. Scheme of the "Sulfur-Iodine" cycle modified by using Nickel based intermediates [6]

ENEA, in the contest of the "Electric System Research Program", funded by the Italian Ministry of Ecological Transition (Implementation plan 2019-2021), has been continuing to investigate modified "Sulphur-Iodine" schemes, and, as a first result, as presented in the present

* Corresponding author: annachiara.tizzoni@enea.it

paper, an innovative one has been conceived to limit the use of Nickel only to the HI section. This metal, being stable and dense, can be easily transported and used as reactant to obtain hydrogen "on-demand" when and where necessary, just reacting it with water. Available literature data were employed to demonstrate the feasibility of the process, integrated with a necessary experimental evaluation, that is, the study of the reaction yield between Iron (III) oxide and Sulfuric acid 50 wt%.

2 Materials and methods

Analytical grade Iron (III) oxide (Fe_2O_3) was purchased by Sigma-Aldrich, Sulfuric acid 96 wt% (Carlo Erba) was used to prepare the 50 wt% solution.
The production yield of Iron (III) sulfate ($Fe_2(SO_4)_3$) was determined by using a Mettler-Toledo thermogravimetric system, TGA/DSC1, with 70µl alumina crucible and chromatographic air as carrier gas (40 Nml/min).

3 Results and discussion

As discussed in the previous paragraph, it is necessary to reduce, at least partly, the toxicity of the employed intermediates and it is important to consider a proper method to store and transport the hydrogen produced. Regarding the former, only Nickel iodide decomposition has to date been investigated [7], but it is still possible to utilize a different and safer sulfate, namely the Ferric salt ($Fe_2(SO_4)_3$). Moreover, the cycle can be modified in order to obtain the cracking of Nickel oxide (NiO), producing Nickel to be employed as hydrogen store source on demand. This way, the resulting metal can be easily accumulated and transported, aso considering its high density and stability, thus providing a suitable method for hydrogen storage.
The involved reactions, balanced to achieve one mole of Nickel and half mole of Oxygen, are summarized in Table 1. The core of the process is the Bunsen reaction (Eq. I), where aqueous solutions of Sulfuric acid (H_2SO_4) and Hydriodic acid (HI) are produced, at a concentration of about, respectively, 50wt% and 57wt%. In order to separate the two phases, an excess of iodine must be introduced, with a ratio of around 3.5:1 (mol I_2/mol HI)[8][9]. The two acids are purified according to the scientific literature[10] and reacted following equations III and VI.

Table 1. Reactions, steps and heat duties for the proposed thermochemical cycle

	Step	T (°C)	Heat duty (kJ)	Ref.
I	$3.4\ H_2O\ (l) + (1 + exc)I_2(aq) + 1.4\ SO_3(aq) + SO_2(aq) \rightarrow (2HI + exc\ I_2)(aq) + 2.4\ H_2SO_4(aq)$	80÷120	Exothermic	[5]
II	$2.4\ H_2SO_4$ (50wt%)heating from 100 to 170°C	100→170	11	[11]
III	$0.8\ Fe_2O_3(s) + 2.4\ H_2SO_4(aq) \rightarrow 0.8\ Fe_2(SO_4)_3(s) + 2.4\ H_2O\ (g)$	170	185	[12][13]
IV	$0.8\ Fe_2(SO_4)_3(s)$ heating from 120 to 675°C	170→675	173	[14]
V	$0.8\ Fe_2(SO_4)_3(s) \rightarrow 0.8\ Fe_2O_3(s) + SO_2(g) + 1.4\ SO_3(g) + 0.5\ O_2(g)$	675	412	[12]
VI	$NiO(s) + 2\ HI(aq) + exc\ I_2(aq) \rightarrow NiI_2(s) + H_2O(g) + exc\ I_2(s)$	100	-63	[6] [13][15]
VII	$NiI_2(s)$ Iodine removal by evaporation	100→180	235	[15]
VIII	$NiI_2(s)$ heating from 100 to 600°C	100→600	42	[16]
IX	$NiI_2(s) \rightarrow Ni(s) + I_2(g)$	600	141	[6]
Sum I÷IX	$\mathbf{NiO(s) \rightarrow Ni(s) + 0.5\ O_2(g)}$		**1199**	
X	On demand: $Ni(s) + H_2O(g) \rightarrow NiO(s) + H_2(g)$	200	63	[13][15] [16][17][18]
Sum I÷X	$\mathbf{H_2O \rightarrow H_2 + \frac{1}{2}\ O_2}$		**1262**	

In reaction III, Ferric oxide (Fe_2O_3) reacts with the aqueous sulphuric acid solution producing the corresponding sulfate, which, in turn, is heated up to 675°C (step IV). The heat duty reported for reaction II includes also the enthalpy necessary to evaporate the formed water. $Fe_2(SO_4)_3$ is then decomposed under air atmosphere into sulphur dioxide (SO_2), sulphur tri-oxide (SO_3) and oxygen (reaction V). At that temperature, the molar ratio between the produced SO_2 and SO_3 is about 0.42/0.58[12]. It is important to note that the reaction III can occur with H_2SO_4 at 50wt%[12], so avoiding an energetic costly sulfuric acid concentration. While the formation of the Iron(III) sulfate phase was demonstrated[12], no data were available about the actual reaction temperature and to confirm a quantitative neutralization between Iron(III) oxide and H_2SO_4 under those conditions. For this reason, a specific experimental verification was carried out for this work. Figure 3 shows the formation of Iron (III) sulfate, starting from Fe_2O_3 and using H_2SO_4 50%wt, carried out in a TGA equipment using three different temperature ramps.

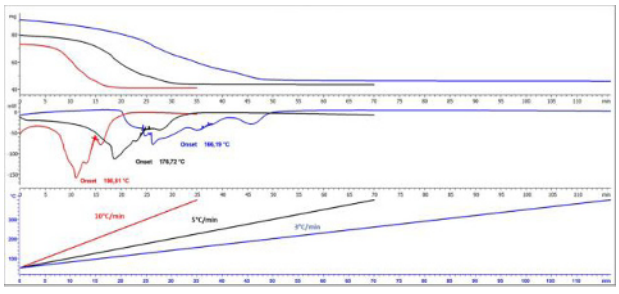

Fig. 3. TGA analysis of Iron (III) Sulfate formation, starting from Fe_2O_3 and using stoichiometric H_2SO_4 50%wt; from top to bottom are shown: gravimetric curves, calorimetric curves and temperature ramps used (3°C/ min, 5°C/min and 10°C/min, N_2 carrier gas 40 Nml/min)

Two processes occur simultaneously: the concentration of sulfuric acid with H2O loss and the reaction with oxide to give sulfate (with further water release). Table 2 reports the yields and reaction times for the three ramps considered. The formation rates were calculated considering the mass and molar balances below:

$$mol\ Fe_2O_3 initial = \frac{weight\ Fe_2O_3}{MW\ Fe_2O_3} + \frac{weight\ Fe_2(SO_4)_3}{MW\ Fe_2(SO_4)_3} \quad (1)$$

$$weight\ final\ from\ TGA = weight\ Fe_2O_3 + weight\ Fe_2(SO_4)_3 \quad (2)$$

$$yield\ of\ Fe_2(SO_4)_3 formation = \frac{weight\ Fe_2(SO_4)_3}{weight\ final\ from\ TGA} \quad (3)$$

Table 2. Reaction yields and times for: $Fe_2O_3 + 3H_2SO_4$ 50%wt

Temperature ramp	3°C/min	5°C/min	10°C/min
Yield	1	1	1
Reaction time (min)	42.25	31.19	18.23

Clearly, an unitary conversion could be established even at the smallest reaction time. Regarding the actual neutralization temperature, since the evaporation of H_2O is obviously endothermic, it can be assumed that the weak exothermic peak correspond to the formation of sulphate. Therefore, from Figure 3, it was possible to assume a realistic value of 170°C for the step III.

In reaction VI, Nickel oxide is quantitatively converted to Nickel iodide at the same temperature of the Bunsen reaction[6]; this neutralization is exothermic[6] but water and excess of Iodine (step VII) present in the HI phase are to be evaporated, leading to a global endothermic process. NiI_2 is then heated up 600°C and quantitatively decomposed into metallic Nickel and iodine[6] (steps VIII and IX). All reactions in this part of the cycle are performed under Nitrogen.

All the gaseous products from III, V, VI, VII and IX are cooled down and reintroduced in the Bunsen reactor, where Sulfur dioxide, Sulfur trioxide and Iodine are absorbed and make available for the redox step. Iron (III) oxide from V is also brought back to 170°C, that is, at the reaction III temperature.

The total balance of steps I-IX correspond to the reduction of Nickel oxide, obtaining Nickel as hydrogen source to be used on-demand (step X). Using the available thermodynamic data, this process is endoergonic and slightly endothermic[15][18][19]. The heat duty included in Table 1 considers the reaction enthalpy along with the energy necessary to heat Nickel and Water up to the reaction temperature, and the water vaporization heat. A temperature of 200°C is indicated by Yavor et al. for this step[17].

Assuming an unitary conversion of Nickel into Hydrogen, which might be achieved by removing the gaseous products during the reaction, and considering the ratio of the hydrogen low heating value (240.4 kJ/mol) to the overall energy inputs, it is possible to preliminarily estimate the cycle global efficiency, equal to about 0.19. If, on one hand, the heat duty of step X can be underestimated, given the realistic necessity to operate the reaction in an excess of water, on the other hand, also advantageous heat recoveries might be conceived to increase the cycle efficiency.

4 Conclusions

Using both literature and experimental data, the global thermal efficiency of a sulphur-iodine modified thermochemical cycle, was assessed. The proposed cycle is based on the adoption of an intermediate metal, which can be reacted with water to quantitatively produce hydrogen on demand, with the purpose to facilitate the storage and improve the dispatchability of this solar fuel.

Clearly, the use of Nickel leads to safety and environmental issues: to overcome this problem a dedicated work is now on-going to modify the proposed process employing low or no-toxic intermediates, maintaining, at the same, a high global cycle efficiency.

Acknowledgments

The activity presented in this paper have been obtained in the framework of the Project 1.2 “Heat accumulation, including electrochemical and power to gas systems, and relative interfaces with distribution networks”, under the “Electric System Research” program 2019–2021, with the financial support of Italian Ministry for Ecological Transition

References

1 S. Ihara, “Feasibility of hydrogen production by direct water splitting at high temperature,” *Int. J. Hydrogen Energy*, vol. 3, no. 3, pp. 287–296, 1978.

2 R. Pitz-Paal, “Concentrating Solar Power Systems,” 2017.

3 D. W. J.H. Norman, K.J. Mysels, R. Sharp, “Studies of the sulfur-iodine thermochemical water-splitting cycle,” *Int. J. Hydrogen Energy*, vol. 7, no. 7, pp. 545–556, 1982.

4 L. T. Salvatore Sau, Anna Chiara Tizzoni, Alberto Giaconia, Michela Lanchi, “Splitting water with renewable heat: green hydrogen beyond electrolysis,” *Energia, ambiente e innovazione 1/2021*, 2021. https://www.eai.enea.it/component/jdownloads/?task=download.send&id=1220&catid=61&Itemid=101 (accessed Aug. 30, 2021).

5 P. Liberatore, R., Lanchi, M., Caputo, G., Felici, C., Giaconia, A., Sau, S., Tarquini, “Hydrogen production by flue gas through sulfur-iodine thermochemical process: Economic and energy evaluation,” *Int. J. Hydrogen Energy*, vol. 37, no. 11, pp. 8939–8953, 2012.

6 S. S. Pier Paolo Prosini, Cinzia Cento, Alberto Giaconia, Giampaolo Caputo, “A modified sulphur–iodine cycle for efficient solar hydrogen production,” *Int. J. Hydrogen Energy*, vol. 34, no. 3, pp. 1218–1225, 2009.

7 M. Lanchi *et al.*, “Use of metallic Ni for H2 production in S-I thermochemical cycle: Experimental and theoretical analysis,” *Int. J. Hydrogen Energy*, vol. 34, no. 3, pp. 1200–1207,

2009, doi: 10.1016/j.ijhydene.2008.10.044.

8 G. Caputo, C. Felici, A. Giaconia, M. Lanchi, R. Liberatore, and S. Sau, "Experimental study of the bunsen reaction for the S-I thermochemical cycle," in *AIChE Annual Meeting Conference Proceedings*, 2005, vol. 2005.

9 A. Giaconia *et al.*, "Experimental study of two phase separation in the Bunsen section of the sulfur-iodine thermochemical cycle," *Int. J. Hydrogen Energy*, vol. 32, no. 5, pp. 531–536, 2007, doi: 10.1016/j.ijhydene.2006.08.015.

10 A. Giaconia, S. Sau, G. Caputo, C. Felici, and P. Tarquini, "Continuous flow operation of a bunsen reactor in the sulfur-iodine thermochemical water-splitting cycle," 2007.

11 "Sulfuric Acid-Water Chemical Energy Storage System," Redmond, Washington, 1976.

12 P. T. A.C. Tizzoni, N. Corsaro, C. D'Ottavi, S. Licoccia, S. Sau, "Oxygen production by intermediate metal sulphates in sulphur based thermochemical water splitting cycles," *Int. J. Hydrogen Energy*, vol. 40, no. 11, pp. 4065–4083, 2015.

13 "The engineering toolbox, Water - Heat of Vaporization." https://www.engineeringtoolbox.com/water-properties-d_1573.html (accessed Nov. 24, 2021).

14 J. Majzlan, A. Navrotsky, R. Stevens, M. Donaldson, B. F. Woodfield, and J. Boerio-Goates, "Thermodynamics of monoclinic Fe2(SO4)3," *J. Chem. Thermodyn.*, vol. 37, no. 8, pp. 802–809, 2005, doi: 10.1016/j.jct.2004.11.021.

15 D. R. Lide, *CRC handbook of chemistry and physics. Vol. 85*. 2004.

16 R. L. and W. P. Heinz Gamsjäger (Chairman), Jerzy Bugajski, Tamas Gajda, *Chemical Thermodynamics Of Nickel-Chemical Thermodynamics Volume 6*. .

17 D. L. F. Yinon Yavor, Sam Goroshin, Jeffrey M. Bergthorson, "Comparative reactivity of industrial metal powders with water for hydrogen production," *Int. J. Hydrogen Energy*, vol. 40, no. 2, pp. 1026–1036.

18 K. H. Stern, *High temperature properties and thermal decomposition of inorganic salts with oxyanions*. 2000.

19 B. J. Boyle, E. G. King, and K. C. Conway, "Heats of Formation of Nickel and Cobalt Oxides (NiO and CoO) of Combustion Calorimetry," *J. Am. Chem. Soc.*, vol. 76, no. 14, pp. 3835–3837, 1954, doi: 10.1021/ja01643a072.

Smart Design of Green Hydrogen Facilities: A Digital Twin-driven approach

Bruno Gerard[1], *Eduardo* Carrera[1,2], *Olivier* Bernard[1,2], and *Denis* Lun[1,*]

[1]Envision Digital, 1 passerelle des reflets, 92400 Courbevoie, France
[2]Capgemini Engineering, 2 Rue Paul Dautier, 78140 Vélizy-Villacoublay, France

Abstract. This work studies the potentials of Digital Twin solutions for the design of competitive and reliable green hydrogen facilities. A digital twin based on stochastic simulations is proposed to address the uncertainties associated with investment and operating costs, to increase confidence and stimulate investments. Several input assumptions are involved (i.e., capital and operational costs, energy consumption, available energy, among others) to analyse their influence on financial indicators. A set of facility designs with equipment redundancy, and thus different system availabilities, was proposed. Monte Carlo simulation method is chosen to propagate uncertainties onto the project bankability assessment. By applying the proposed methodology, the opportunity index and internal rate of return (IRR) are calculated. A sensibility analysis is also carried out. The simulations illustrate that the design of a facility can be optimized to achieve higher profits, based on a trade-off between investment and availability. This study concludes that digital twin solutions are an opportunity for reducing the uncertainties associated with green hydrogen facility design. Improvements to the proposed model can be achieved by performing a refined simulation, in relation to the calculation of system availability and maintenance costs.

1 Introduction

By 2050, global final energy consumption is expected to increase by about 30% and the production of electricity is projected to double [1]. However, currently, it is based on intensive exploitation of fossil energy sources. Approximately 81% of the world's energy consumption stem from coal, crude oil, and natural gas, which are at the origin of most of the greenhouse gas emissions that cause climate change [2]. Within the framework of the Paris Agreement aimed at a temperature increase of less than 2°C [3], numerous actions have been taken to achieve a decarbonized economy, mainly proposing an increase in the use of renewable energy sources [4]. However, this drastic change implies significant challenges to meet the growing demand for energy, from the point of view of security of supply, availability of resources and robustness of the power network.

Hydrogen has been identified as a key energy carrier to drive the energy transition and achieve the sustainable development goals [5,6], being a long-term opportunity to move to cleaner energy and transport systems [7]. Through water electrolysis, green hydrogen is produced from renewable electricity. Among the main benefits are:

- Provision of long-term energy storage solutions for renewable energy sources [6].
- Diverse roles in different energy systems and industries (e.g., heat generation, low-carbon fuel supply, electricity generation, feedstock in chemical industry, etc.) [6].
- Hydrogen only emits water as a byproduct without any greenhouse gas emissions when it is used in a fuel cell [8].
- It possesses a high energy density (140 MJ/kg), being more than twice the energy density of typical energy carriers (e.g., 50 MJ/kg for methane) [8].

Nonetheless, green hydrogen technologies face multiple challenges. A major issue is the economic viability of water electrolysis using renewable electricity compared to other hydrogen production technologies (e.g., steam methane reforming) [9]. In this regard, significant cost reductions and efficiency improvements will be necessary before green hydrogen facilities can be economically competitive [10,11]. Furthermore, the Technology Readiness Level (TRL) of these technologies are at Level 3 to 7 [12], implying that a limited amount of historical data is available. This fact leads to poor estimates of system performance and thus represents investment risks. It is then crucial to evaluate the impact of input uncertainty on performance indicators related to decision-making.

* Corresponding author: denis.lun@envision-digital.com

Digital Twin (DT) technologies have been successfully implemented for the intelligent use of available data. By using the internet of things (IoT), software simulation, and data analytics, DT technologies create a digital replica of a physical object or system [13]. Its use is gaining momentum due to rapidly evolving simulation and modelling capabilities, better coupling between interoperability and IoT sensors, and increased availability of infrastructure for the use of digital devices [14]. Furthermore, DT technologies have proven to offer advantages in accelerating technology growth, optimizing design, and improving return on capital [15–18]. Despite the potential offered by DT technologies, few attentions have been given to their application in green hydrogen facility design. To address these gaps, this works proposes a DT-driven approach based on stochastic simulations for the smart design of green hydrogen facilities.

This paper is divided into six sections. Following this introduction, a literature review is presented in Section 2. The main five steps of the methodology are described in Section 3. The case study chosen to illustrate the methodological framework is shown in Section 4. In Section 5, the main results and a sensibility assessment are analyzed. Finally, conclusions and perspectives are drawn in Section 6.

2 Literature review

Since its concept was introduced by Michael Grieves in 2002 [19], the Digital Twin technology has been applied to different fields of engineering [13–18]. They are the result of a continuous improvement of design, optimization and simulation methods used in industry, being part of what today is called Industry 4.0 paradigms [20]. DT concepts have been involved in energy systems and chemical industry mainly for the development of optimal management strategies [18,21,22], which is also the case for green hydrogen technologies:

- Ogumerem et al. propose an optimal thermal management for Proton Exchange Membrane Water Electrolysis (PEMWE) systems driven by DT technologies [23]. Their study shows that it can attenuate the long-term effects of high operating temperatures or rapid temperature changes on the polymer membranes.
- DT concepts for the optimal operation of hydrogen storage systems have been successfully developed [13]. The DT real-time connection to hydrogen vessels provides condition monitoring, allowing the operator to receive intelligent insights to reduce risk.
- Kang et al. presented a dynamic DT of a 25 kW Solid oxide fuel cells (SOFC) plant as a simulator to help operators safely and stably determine the operating conditions for a real commercial SOFC plant [24]. The results show that the on-site operation prediction is highly accurate, helping operators to determine operation strategies.
- Meraghni et al. propose a data-driven DT prognostics method for proton-exchange membrane fuel cells (PEMFCs). A DT is applied to establish an ensemble remaining useful life prediction system [25]. Its implementation achieves a high prediction accuracy. Furthermore, the predicted results are proved to be less affected even with limited measurement data.

Some studies focus on the design and simulation of hydrogen production plant components. For example, Wang et al. develops a high-accuracy data-driven surrogate model of proton exchange membrane fuel cells (PEMFCs) [26]. Their model has a comparable accuracyto a comprehensive 3D physical model. However, it considerably reduces the cost of computation and time.

As seen, methodologies based on data-driven DT approaches have been applied for the optimal management and simulation of green hydrogen technologies. However, this approach has not necessarily been applied to the design and evaluation of entire facilities. In the next section, a methodology to address some of these aspects is presented.

3 Methodological framework

A methodological framework for the smart design of green hydrogen facilities based on stochastic simulations and data-driven DT approach is presented. The methodology consists of five steps as described in Fig. 1.

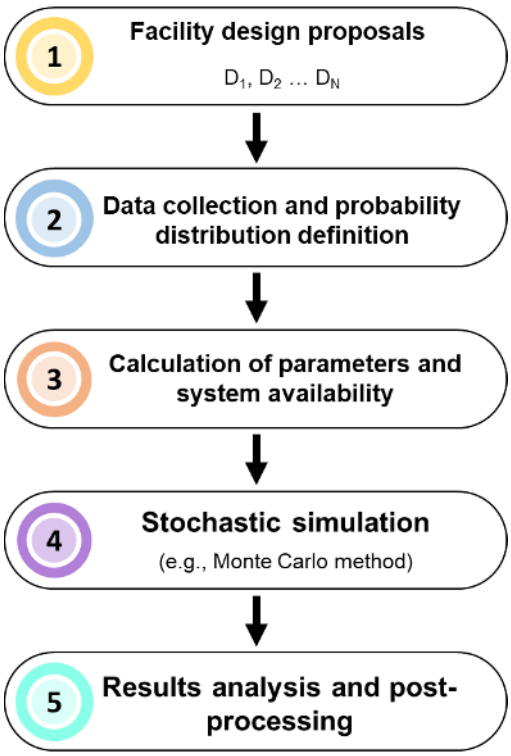

Fig. 1. Methodological framework

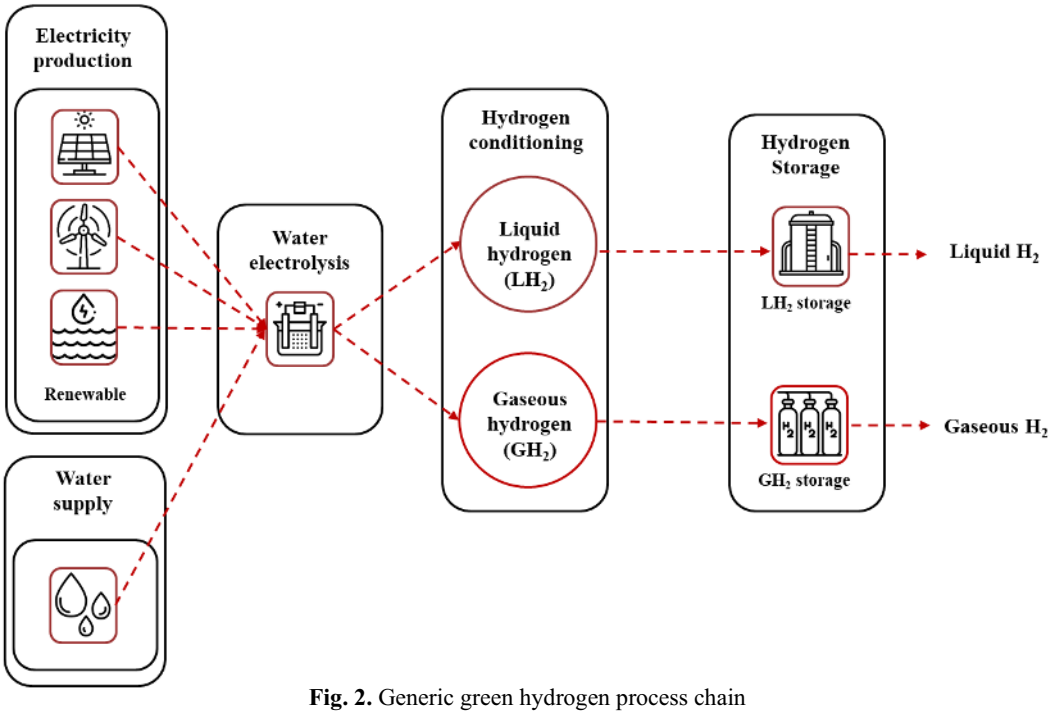

Fig. 2. Generic green hydrogen process chain

3.1. Facility design proposals

A green hydrogen production system typically consists of five main echelon [27], which are illustrated in Fig. 2. Renewable electricity and water are used to produce hydrogen through electrolysis. Hydrogen is then conditioned to obtain the desired physical form at specific conditions (i.e., pressure, temperature, residue gas composition, among others), which will determine the subsequent stages of the process chain. Hence, hydrogen could be compressed or liquefied, and stored.

Given the set of equipment that composes each of the echelons (e.g., compressors, pumps, heat exchangers, electrolyzers, etc.), several configurations are possible. Thus, different plant designs can be proposed with various level of redundancy of the equipment, which can be in series or in parallel. This leads to a trade-off between system availability and invested capital, being a key aspect to be addressed in order to increase the financial performance of the project. The following sections will address these issues.

3.2 Data collection and probability distribution definition

A set of techno-economic data is necessary to carry out the bankability analysis. It corresponds to the acquisition costs of each equipment, operating costs, main time to failure, main time to repair, process efficiencies, production rates, among others. It comes from direct monitoring of industrial systems. However, in case of insufficient information coming directly from operating facilities, data from manufacturers and expert consultation can be included. In this sense, some assumptions are made about the probabilistic distribution function (PDF) of the data involved (i.e., triangular, Gaussian, constant, among others) [28].

The subsequent incorporation of data from industrial projects operating under real conditions allows to refine previous assumptions, which leads to updating the PDF of inputs. For this purpose, there is a set of strategies such as Bayesian network modelling, which have demonstrated their applicability to this type of self-learning process [29,30].

3.3 Calculation of system availability

The calculation of the system availability of the design facilities is the next step in the proposed methodology. The availability of a repairable system can be defined as the probability that the system will be operational at a given time "t" [31]. An analytical approach to calculating availability is presented in Eq. (1) to (5). The Main Time to Failure ($MTTF_i$) and Main Time to Repair ($MTTR_i$) for each equipment "i" are used in Eq. (1) and (2) to calculate their failure (λ_i) and repair rate (μ_i), respectively. In this case, they are assumed to be constant. These parameters are used to determine the availability of each equipment through Eq. (3). Finally, the system availability is calculated considering series (A_s) or parallel (A_p) configurations by using Eq. (4) and (5), respectively.

$$\lambda_i = \frac{1}{MTTF_i} \quad (1)$$

$$\mu_i = \frac{1}{MTTR_i} \quad (2)$$

$$a_i(t) = \frac{\lambda_i}{\lambda_i + \mu_i} + \frac{\mu_i}{\lambda_i + \mu_i} exp(-\lambda_i + \mu_i)t \quad (3)$$

$$A_s(t) = \prod_{i=1}^{n} a_i(t) \quad (4)$$

$$A_p(t) = 1 - \prod_{i=1}^{n} \left(1 - a_i(t)\right) \quad (5)$$

3.4 Stochastic simulation

Stochastic simulations are used to consider uncertainty on several input parameters. Thus, the simulation output will have an inherent variability due to the stochastic nature of the system under study, which is referred to as stochastic uncertainty [32]. Renewable energy systems exhibit these characteristics due to the intermittency of the renewable energy sources (e.g., solar and wind sources). The algorithms used to deal with this type of problem are well known and are generally based on statistical approaches [32].

This study proposes the use of Monte Carlo simulations as stochastic method [33], which is well-known and successfully applied to similar energy systems [34,35]. It can be summarized as follow:

- Define input parameters and probability distribution functions (as described in Section 3.2. and 3.3.).
- Find the cumulative distribution function (CDF) for each parameter.
- Sample from the CDF using a random number generator (between 0 and 1).
- Perform simulations with the generated samples to obtain the CDF of the outputs. The number of simulations will depend on the level of precision required.

3.5 Results analysis and post-processing

The application of a stochastic simulation, in this case, the Monte Carlo method, allows to obtain the CDF of the outputs. Several outputs can be evaluated for further analysis. In this case, the internal rate of return (IRR) and the "opportunity index" are proposed as the main performance indicators.

3.5.1 Internal rate of return

The internal rate of return (IRR) is the discount rate that would yield a net present value (NPV) of zero over the planning period. A zero NPV value means that the discounted cashflows generated by the project are equivalent to the cashflows obtained with an investment on a bank account serving an interest rate equivalent to IRR [36].

3.5.2 Opportunity index

The opportunity index corresponds to the probability of achieving a value equal to or lower than the desired output value.

4 Case study

In order to demonstrate the usefulness of the proposed methodology, an analysis was carried on a project located in the south of Spain. This region is one of the most suitable for the deployment of photovoltaic systems in Europe, thanks to its highest levels of solar radiation. As results, it is one of the regions that have been allocated the highest volumes of the EU funds to promote solar energy projects [37].

The project to be evaluated consists of the production of green hydrogen from solar electricity (i.e., photovoltaic). The data considered involve each of the echelon in the green hydrogen production chain: energy production, water supply, water electrolysis, hydrogen conditioning and buffer storage. The data comes from consultation with manufacturers, experts and industrial data. The main parameter inputs are given below:

- The technology used for the electrolysis of water corresponds to pressurized alkaline electrolysis.
- The facility's capacity is 100 MWh, which corresponds to 20 electrolyzers of 5 MW each.
- 100% of the electricity used comes from solar energy source.
- The final physical form of hydrogen is gaseous.
- Hydrogen is compressed from 30 to 70 bar.
- The target IRR is 5%.
- The lifespan of the project is 35 years.

Three green hydrogen facility design configurations are tested, considering redundancy in key equipment (i.e., electrolyzers and compressors), which implies a trade-off between CAPEX and system availability. They are shown in Table 1.

Table 1. Green hydrogen facility design configurations

Design	Description
--- 1 (Base case)	Project in the south of Spain
--- 2 (Hypothetical A)	Design 1 with 20% increase in hydrogen production capacity.
--- 3 (Hypothetical B)	Design 2 with doubled compression capacity

5 Results

The results obtained by applying the proposed methodology are shown in this section. Table 2 presents the CAPEX and system availability of each design. System availability in Design 2 and 3 increases by 2.5 and 3.5% compared to the baseline design, respectively. Nevertheless, an increase in availability implies a higher investment. CAPEX in Design 2 and 3 rises by 20 €/kW (5.4%) and 70 €/kW (19%) compared to Design 1, respectively.

Table 2. Availability and CAPEX for each design (hydrogen production)

Design scenario	System availability (%)	CAPEX (€/kW)
--- 1 (Base case)	96.0	370
--- 2 (Hypothetical A)	98.5	390
--- 3 (Hypothetical B)	99.5	440

As indicated in Section 3.5, the IRR and the opportunity index were defined as the main performance indicators. Fig. 2 (a) then shows the opportunity index vs IRR for the base design. It reflects a potential business for the project under study. It is observed that An IRR of 5% leads to an opportunity rate of 70%, thus showing the robustness of the basic design. To study the most critical drivers to achieve the targeted IRR, a sensitivity analysis was carried out, which is presented in Fig. 3 (b). It shows that the investment costs of electrolyzers, their power consumption, and the annual solar energy available represent the three critical parameters affecting the IRR, which can have an impact of up to +/- 0.23%. This implies that in order to obtain competitive green hydrogen plants, it is necessary to prioritize the reduction of the investment costs of the electrolyzers, which has also been indicated by other studies [38]. The energy consumed in the electrolysis process has also been identified in the literature as a key factor in increasing the profitability of green hydrogen production systems [11,38,39]. This should be a core aspect in the technological development of the future generation of electrolyzers. In addition, this parameter, as well as the annual solar energy available, also implies an operational optimization of the system. The development of technologies such as DT can be useful for such purposes, which has already been highlighted in other studies [23–25].

A comparison between the three proposed designs is carried out in Fig. 4. Their IRR and opportunity index are shown in Fig. 4 (a). “Design 2” allows to obtain a higher opportunity rate despite having a higher CAPEX (see Table 2), thanks to an increase in the system availability compared to the “Design 1”. “Design 3” decreases the opportunity index and therefore the probability of achieving higher IRR values. A comparison of the three configurations was made at P90 (chance ratio equal to 90%). The IRR as a function of CAPEX is shown in Fig. 4 (b). The IRR in “Design 2” increases by 0.24%, while it decreases by 0.43% in “Design 3”.

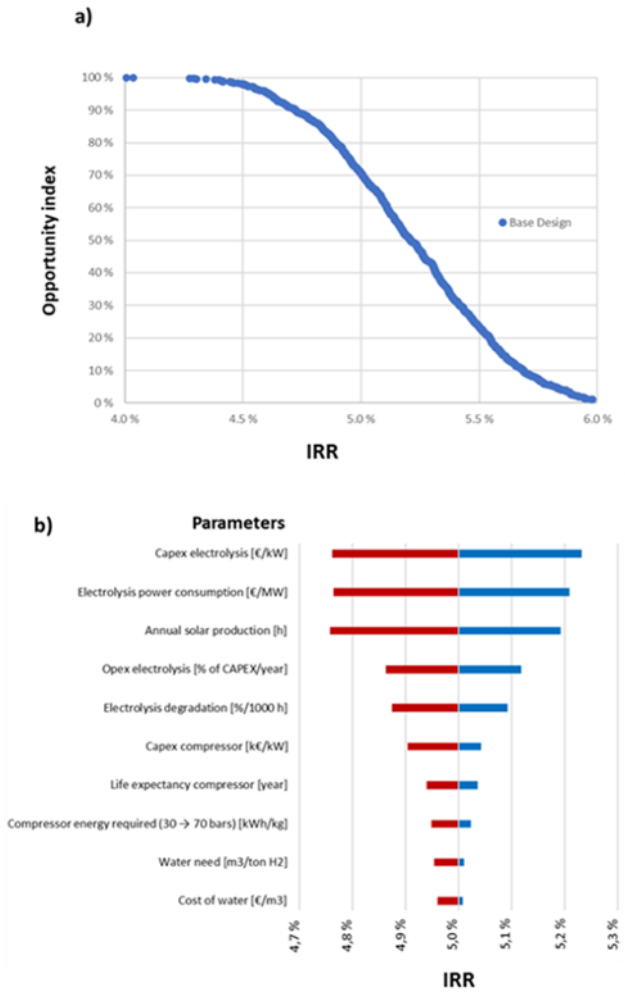

Fig. 3. (a) Opportunity index as a function of IRR for the base case (Design 1); **(b)** Sensitivity analysis

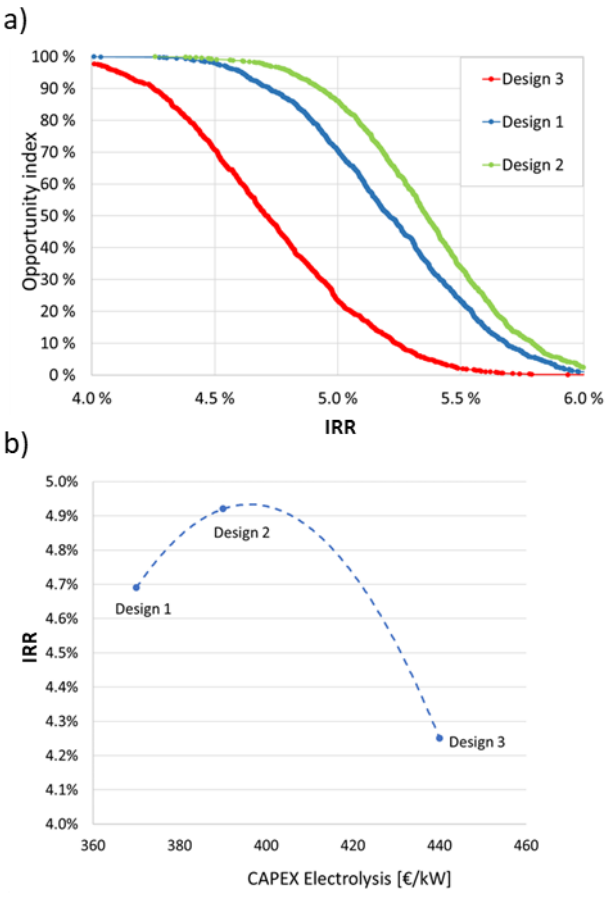

Fig. 4. (a) Opportunity index as a function of IRR for the three designs proposed; **(b)** IRR as a function of CAPEX.

According to this analysis, “Design 2” would be the green hydrogen facility design to be considered. This illustrates that an increase in the availability of the electrolyzers is enough to improve the financial performance of the hydrogen facility. In this sense, one aspect to consider would be the possibility of evaluating different hydrogen production technologies (i.e., PEMWE and solid oxide electrolysis cells), in order to compare the results with the precedent designs.

6 Conclusions

With the outputs of the proposed methodological framework applied to the green hydrogen facility design, we were able to demonstrate that an approach driven by DT technologies and stochastic analysis generates substantial value-added insights to decision-makers. Firstly, the approach developed allows addressing the uncertainty inherent in the input parameters and its consequences on key financial performance indicators. Secondly, the probability of reaching a given value using an indicator such as the opportunity index provides confidence intervals. Thus, the risk associated with the project can be mitigated. Finally, different designs can be proposed and evaluated, which allows to find trade-offs between the capital invested and the system availability. Consequently, the proposed approach contributes to optimal, coherent, and robust decision making.

The usefulness of the methodology was shown in a case study. Three green hydrogen facility design were tested. When comparing the designs, it was determined that "Design 2" presented the best business opportunity, thanks to an improved trade-off between capital investment and system availability compared to the base case. The calculation of its opportunity index shows that higher IRR can be attained with lower risk. Besides, a sensitivity analysis was performed to identify the parameters that have the major impact on the IRR. The capital cost of electrolyzers is the main parameter that needs to be improved to increase business opportunities and is a key issue for the development of the next generations of electrolyzers.

Future research will be conducted on the treatment of the input data when it will come from direct monitoring of different hydrogen production systems, since the simulation output data, and hence the performance measures, are directly affected by the probability distributions (i.e., input models) from which the sample paths are generated in simulation [32]. In this sense, a key aspect to be addressed will be the appropriate selection of probability models that will adequately characterize the stochastic behavior of the system, in order to reduce uncertainty. Among the major issues to be considered are the calculation of system availability and operating costs.

The authors would like to thank the team of experts from Corporate Value Associates (CVA), Capgemini Engineering and Envision Digital, whose comments contributed to enrich the work carried out.

References

1. IAEA, *Energy, Electricity and Nuclear Power Estimates for the Period up to 2050* (Vienna, 2020)
2. IEA, *Key World Energy Statistics 2020* (Paris, 2020)
3. United Nations, *Paris Agreement* (Paris, 2015)
4. IRENA, (2020)
5. European Commission, (2020)
6. A. Lewandowska-Bernat and U. Desideri, Appl. Energy **228**, 57 (2018)
7. T. da Silva Veras, T. S. Mozer, D. da Costa Rubim Messeder dos Santos, and A. da Silva César, Int. J. Hydrogen Energy **42**, 2018 (2017)
8. S. Shiva Kumar and V. Himabindu, Mater. Sci. Energy Technol. **2**, 442 (2019)
9. E. Carrera and C. Azzaro-Pantel, Comput. Chem. Eng. **153**, 107386 (2021)
10. T. Egeland-Eriksen, A. Hajizadeh, and S. Sartori, Int. J. Hydrogen Energy **46**, 31963 (2021)
11. E. Carrera and C. Azzaro-Pantel, Comput. Aided Chem. Eng. **50**, 1859 (2021)
12. R. Pinsky, P. Sabharwall, J. Hartvigsen, and J. O’Brien, Prog. Nucl. Energy **123**, 103317 (2020)
13. A. Jaribion, S. H. Khajavi, M. Öhman, A. Knapen, and J. Holmström, in (2020), pp. 369–375
14. J. Leng, D. Wang, W. Shen, X. Li, Q. Liu, and X. Chen, J. Manuf. Syst. **60**, 119 (2021)
15. C. K. Lo, C. H. Chen, and R. Y. Zhong, Adv. Eng. Informatics **48**, 101297 (2021)
16. Y. Wang, X. Wang, and A. Liu, Procedia CIRP **93**, 198 (2020)
17. M. Liu, S. Fang, H. Dong, and C. Xu, J. Manuf. Syst. **58**, 346 (2021)
18. E. Örs, R. Schmidt, M. Mighani, and M. Shalaby, in *2020 IEEE Int. Conf. Eng. Technol. Innov.* (2020), pp. 1–8
19. M. Grieves, White Pap. **1**, 1 (2014)
20. H. Lasi, P. Fettke, H.-G. Kemper, T. Feld, and M. Hoffmann, Bus. Inf. Syst. Eng. **6**, 239 (2014)
21. A. Ebrahimi, in *2019 IEEE 28th Int. Symp. Ind. Electron.* (2019), pp. 1059–1066
22. E. O’Dwyer, I. Pan, R. Charlesworth, S. Butler, and N. Shah, Sustain. Cities Soc. **62**, 102412 (2020)
23. G. S. Ogumerem and E. N. Pistikopoulos, J. Process Control **91**, 37 (2020)
24. J.-L. Kang, C.-C. Wang, D. S.-H. Wong, S.-S. Jang, and C.-H. Wang, J. Taiwan Inst. Chem. Eng. **118**, 60 (2021)

25. S. Meraghni, L. S. Terrissa, M. Yue, J. Ma, S. Jemei, and N. Zerhouni, Int. J. Hydrogen Energy **46**, 2555 (2021)
26. B. Wang, G. Zhang, H. Wang, J. Xuan, and K. Jiao, Energy AI **1**, 100004 (2020)
27. E. Carrera and C. Azzaro-Pantel, Chem. Eng. Sci. **246**, 116861 (2021)
28. J. S. Arora, *Introduction to Optimum Design*, Fourth edi (Elsevier, Iowa, 2017)
29. M. Borunda, O. A. Jaramillo, A. Reyes, and P. H. Ibargüengoytia, Renew. Sustain. Energy Rev. **62**, 32 (2016)
30. T. Adedipe, M. Shafiee, and E. Zio, Reliab. Eng. Syst. Saf. **202**, 107053 (2020)
31. Y. Hou, M. Sallak, and W. Schön, IFAC-PapersOnLine **28**, 1315 (2015)
32. C. G. Corlu, A. Akcay, and W. Xie, Oper. Res. Perspect. **7**, 100162 (2020)
33. A. F. Magnússon, R. Al, and G. Sin, Comput. Aided Chem. Eng. **48**, 451 (2020)
34. E. J. da S. Pereira, J. T. Pinho, M. A. B. Galhardo, and W. N. Macêdo, Renew. Energy **69**, 347 (2014)
35. Y. Gu, X. Zhang, J. Are Myhren, M. Han, X. Chen, and Y. Yuan, Energy Convers. Manag. **165**, 8 (2018)
36. E. H. Macdonald, Handb. Gold Explor. Eval. 553 (2007)
37. C. Perpiña Castillo, F. Batista e Silva, and C. Lavalle, Energy Policy **88**, 86 (2016)
38. H. Böhm, A. Zauner, D. C. Rosenfeld, and R. Tichler, Appl. Energy **264**, 114780 (2020)
39. A. Buttler and H. Spliethoff, Renew. Sustain. Energy Rev. **82**, 2440 (2018)

Economic appraisal of Power-to-Liquid Fischer-Tropsch plants exploiting renewable electricity, green hydrogen, and CO_2 from biogas in Europe

Marco Marchese[‡], *Paolo* Marocco[‡*], *Andrea* Lanzini, and *Massimo* Santarelli

Energy Department DENERG, Politecnico di Torino, Italy, Corso Duca degli Abruzzi 24, 10129, Torino (IT)

[‡] *These authors contributed equally to this work.*

Abstract. The present work analyses the techno-economic potential of Power-to-Liquid routes to synthesize Fischer-Tropsch paraffin waxes for the chemical sector. The Fischer-Tropsch production unit is supplied with hydrogen produced by electrolysis and CO_2 from biogas upgrading. In the analysis, 17 preferential locations were identified in Germany and Italy, where a flow of 1 t/h of carbon dioxide was ensured. For each location, the available flow of CO_2 and the capacity factors for both wind and solar PV were estimated. A metaheuristic-based approach was used to identify the cost-optimal process design of the proposed system. Accordingly, the sizes of the hydrogen storage, electrolyzer, PV field, and wind park were evaluated. The analysis studied the possibility of having different percentage of electricity coming from the electric grid, going from full-grid to full-RES configurations. Results show that the lowest cost of Fischer-Tropsch wax production is 6.00 €/kg at full-grid operation and 25.1 €/kg for the full-RES solution. Wind availability has a key role in lowering the wax cost.

1 Introduction

To reduce the impact of climate change derived from human activities, several solutions are being proposed and studied with different levels of maturity at international level. In this context, the reduction of carbon dioxide (CO_2) emissions towards the environment, together with a rise in the installation of renewable energy and the deployment of innovative technologies are paramount to reach such a goal [1]. Accordingly, the International Energy Agency (IEA) has proposed a possible pathway for the implementation of different technologies to reach carbon neutrality in various industrial sectors by the year 2050 [2]. Power-to-X (PtX) and carbon capture and utilization (CCU) routes have been identified as crucial solutions.

Power-to-X routes combine several technologies to deliver the product "X", exploiting renewable energy sources (RES). Such pathways involve hydrogen obtained through electrolysis fed with RES (i.e., green hydrogen). H_2 can be further mixed with CO_2 to promote carbon dioxide utilization and synthesize non-fossil marketable compounds. In this regard, Power-to-Liquid solutions aiming at Fischer-Tropsch (FT) favour the generation of carbon-neutral hydrocarbons to decarbonize the heavy transport and chemical sector with a single application [3]. While the decarbonization of the transport sector has been widely investigated, the decarbonization of the chemical sector is non-trivial, with the FT being one of the few technologies that allows producing long-chain hydrocarbons (i.e., paraffin waxes) destined to the chemical sector [4]. Additionally, a rise in the demand for such products is forecasted, with a market expansion from 5.1 billion € in 2018 to 7.5 billion € in 2025 [5]. However, at the current date, no alternative-to-fossil commercial production for these compounds is available.

Parallelly, there exists a high availability of biogas plants (i.e., anaerobic digestors) installed in Europe, with a growing trend in the installation of upgrading facilities to obtain biomethane (for gas grid injection) and carbon dioxide (which is typically vented to the atmosphere). Thus, there is a large amount of potential carbon dioxide that can be utilized to generate further products and makes it advantageous to study solutions that use biogas-derived CO_2 [6].

Moreover, RES-based solutions involving the production of FT material are seldom found in literature [7], with none found dedicated to the waxes production. However, given the wide range of products generated by the FT technology, it becomes relevant to investigate solutions that involve such a technology fed by RES to decarbonize several sectors at once.

Accordingly, the present work analyses Power-to-Liquid routes installed in Europe to synthesize FT paraffin waxes destined to the chemical sector. More in detail, it studies routes that combine renewable energy production (wind and/or solar power), green hydrogen generation via low temperature electrolysis, hydrogen storage, and FT product generation with CO_2 coming from anaerobic digestion processes (Fig 1). Such routes are being

* Corresponding author: paolo.marocco@polito.it

investigated ranging from full-grid to full-RES conditions, with cost-optimal economic considerations on the cost of FT waxes production.

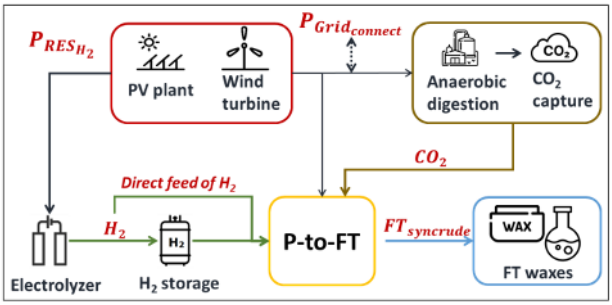

Fig. 1. Schematic of the plant investigated in this analysis.

2 Methodology

17 preferential locations were identified throughout Germany and Italy (12 in Germany, 5 in Italy), the two European countries with the largest number of installed biogas plants. Each of the selected sites presents an anaerobic digester with an installed biogas upgrading unit that provides a flow of clean CO_2 equal to or higher than 1000 kg/h [8]. This CO_2 flow threshold was set based on previous results obtained for a CCU plant converting CO_2 from biogas into FT hydrocarbons with relevant industrial size [9]. Geographical locations are shown in Fig. 2.

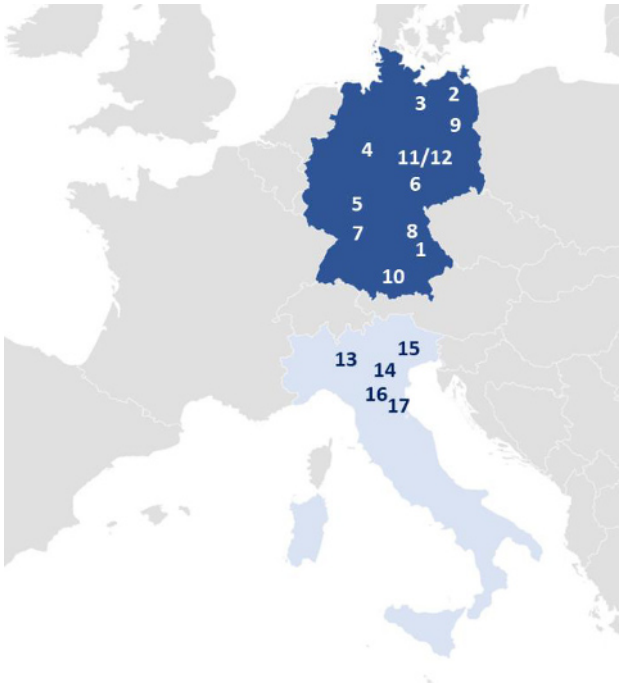

Fig. 2. Locations used in the present analysis, where an anaerobic digestor is present, with an existing biogas upgrading unit with a minimum flow of CO_2 of 1 t/h.

For each location, the availability of CO_2 was estimated. Similarly, the potential production of renewable electricity was evaluated, and capacity factors (CF) for both wind and solar PV were derived exploiting yearly profiles of irradiance and wind speed data taken from the online PVGIS tool [10]. The wind turbine corresponded to model v27 from Vestas producer [11]. Wind speed data were corrected to the turbine height of 30 m. CO_2 flow and capacity factor for each location are listed in Table 1. Locations in Germany present a higher availability of wind energy compared to Italy, but lower PV capacity factors.

Table 1. Wind and PV capacity factors and carbon dioxide evaluated for each investigated location.

State	Code	Location	CO_2 flow	Wind CF	PV CF
			[t/h]	[%]	[%]
DE	1	Aiterhofen Niederbayern	1.35	2.71%	11.39%
DE	2	Dargun	1.54	11.23%	11.43%
DE	3	Güstrow	6.34	10.52%	11.06%
DE	4	Horn Bad Meinberg	1.38	4.60%	10.02%
DE	5	Industriepark Hoechst	1.04	5.92%	10.92%
DE	6	Könnern 2	2.28	5.18%	11.55%
DE	7	Schwaigern	1.23	4.06%	11.61%
DE	8	Schwandorf	1.35	3.72%	11.57%
DE	9	Schwedt	3.8	5.12%	11.36%
DE	10	Wolnzach	1.36	3.01%	11.32%
DE	11	Zörbig 1	3.8	5.18%	11.57%
DE	12	Zörbig 2	3.14	5.18%	11.57%
IT	13	Montello	2.62	0.92%	12.90%
IT	14	Este	2.62	1.48%	14.99%
IT	15	Maniago	3.93	0.18%	12.55%
IT	16	Faenza	4.91	0.09%	10.41%
IT	17	Sant'Agata Bolognese	1.12	0.71%	14.85%

2.2 System optimization

Employing PV/Wind producibility data, the analysis utilized an optimization model based on a metaheuristic algorithm to identify the cost-optimal design of the system. More specifically, this model (adapted from Ref. [12]), employs the particle swarm optimization (PSO) algorithm to determine the system configuration that allows a certain objective function (OF) to be minimized. In this work, the wax cost was considered as OF to perform the optimal design (i.e., Eq. 3). Hence, the sizes of the hydrogen storage, alkaline electrolyzer, PV field, and wind farm were evaluated.

All the CO_2 available at each site was exploited, and the H_2-storage guaranteed a constant flow of hydrogen needed by the FT reactor when its direct production was

not doable from the electrolyser. Additionally, in case of extra hydrogen produced by the electrolyser, this was stored in the storage unit until reaching its maximum capacity. Electric energy generated by RES was fed to the CCU plant and electrolyser for hydrogen generation. Extra RES was curtailed to the grid once the storage was full, and the hydrogen load covered. The system was grid-connected, to allow for the sale of curtailed renewable electricity not utilized by the system, or to buy electricity when RES power was not available or not investigated (e.g., 100% grid connection configuration). An electrolyser efficiency of 51 kWh/kg_{h2} was considered [13]. Moreover, the electrolyser operation was set to null when its input power was lower than 15% of its nominal power [13].

The CCU-to-FT section operated at steady-state conditions for constant output of FT compounds, utilizing a reverse water gas shift (RWGS) reactor for the generation of syngas followed by a Co-based FT reactor and FT products distillation into naphtha (C_5-C_{11}), middle distillates (C_{11}-C_{20}), and waxes (C_{20+}). FT gas fraction was internally recirculated. At the reference size of 1 t/h of CO_2 at the inlet of the CCU plant, 79.9 kg/h, 93.7 kg/h and 85.7 kg/h of naphtha, middle distillates and waxes were produced, respectively. A detailed description of the CCU-to-FT plant together with an energy analysis can be found at [9,14]. The FT synthesis accounted for a carbide mechanistic kinetic model for the description of the FT products generation [15].

For each location, sensitivities on the fraction of electricity coming from the grid were accounted for while estimating the waxes cost. Hence, the cost-optimal system composition was studied ranging from full-grid to full-RES configurations. The full-RES solution was assumed to be connected to the electric grid only to sale the curtailed RES.

2.3 Economic analysis

Based on CAPEX, OPEX, and revenues values, the wax production cost was evaluated for each site and for different scenarios with rising levels of RES exploitation. The annuity method was utilized, with a plant life of 25 years (N_{rt}) and a weight average cost of capital (WACC) of 4.0% in the baseline configuration. Accordingly, the wax production cost (in €/kg_{wax}) was obtained as follows:

$$TIC_{inv}=(\sum C_{P,i}) (1+f_{site}) (1+f_{cont}+f_{eng}) (1+f_{com}) \quad (1)$$

$$CAPEX_{ANN}=TIC_{inv} (WACC (1+WACC)^(N_{rt}))/ ((1+WACC)^(N_{rt})]-1) \quad (2)$$

$$\text{Wax cost}=(CAPEX_{ANN}+C_{OP}-\text{Revenues})/(\text{FT Wax Production Rate}) \quad (3)$$

Where TIC_{inv} (in €) is the total investment cost and $C_{P,i}$ (in €) is the purchase cost of the i-th component (see Table 2). The f_j parameters account for site preparation (0.2), contingencies (0.2), engineering (0.1) and commissioning (0.1) costs. $CAPEX_{ANN}$ was derived by correcting TIC_{inv} by the annuity coefficient.

OPEX costs (C_{OP}, in €/y) included the yearly sum of operation and maintenance, labour cost, electricity costs, catalysts replacements, components replacement (e.g., electrolysers), and raw material costs (e.g., water, biogas). Revenues accounted for the sale of by-product oxygen from electrolysis, curtailed electricity, naphtha, and middle distillate, and credits from the sale of biomethane to the gas grid. BioCH_4 credits were included for the injection of biomethane into the gas grid:

- German policies, bioCH_4 sale price of 31.6 €/kWh with 20 years sale credits for 61.6 €/MWh [16–18];
- Italian policies, sale price of CH_4 of 20.9 €/kWh, with credits of 62.7 €/MWh for 10 years and 0.305 €/m^3 for each subsequent year [16,19].

Baseline electricity was purchased at 100 €/MWh and sold at 80 €/MWh [20]. Other relevant costs are listed in Table 2 and Table 3.

Table 2. Cost used for CAPEX evaluation.

System	Investment cost	Ref.
PV power plant	800 €/kW	[21]
Wind power plant	1100 €/kW	[22]
Electrolyser	$1437 Palk_{nom}^{-0.095}$ €/kW	[14]
H_2 Storage	470 €/kg	[23]
CCU (Biogas up.+RWGS+FT)	8878.2 k€/(t_{CO2}/h)	[14,24]

Table 3. OPEX and revenues costs used in the analysis.

Cost item	Value	Ref.
O&M	3% TIC (€/y)	[25]
PV Repl.	80 €/kW (10 y)	[26]
Electrolyser Repl.	26.6% Elect Inv. Cost (9 y)	[27]
Biogas	50 / 44.3 €/MWh (DE / IT)	[16,17,19]
Water	2 €/m^3	[28]
Labour	49500 / 75000 €/Op/y*4 operators (IT / DE)	[14]
Cat. Repl.	1% CCU Inv. Cost (3 y)	[14]
O_2 sale	0.15 €/kg	[29,30]
Naphtha sale	0.31 €/l	[31]
Midd. Dist sale	0.60 €/l	[32]

3 Results and discussion

3.1. Grid connection effect

For each location, the cost of FT wax production was evaluated, by varying the share of grid electricity from 0%

to 100%. The resulting Pareto fronts for all the 17 locations are reported in Fig. 3. It can be noted that the wax cost increases as direct RES electricity is used, with an almost constant wax cost in the range 75% to 100% of electricity from the grid. Accordingly, bigger sizes of PV, wind, H_2-storage, and electrolysers are needed to sustain the system operation when increasing the share of electricity from local RES.

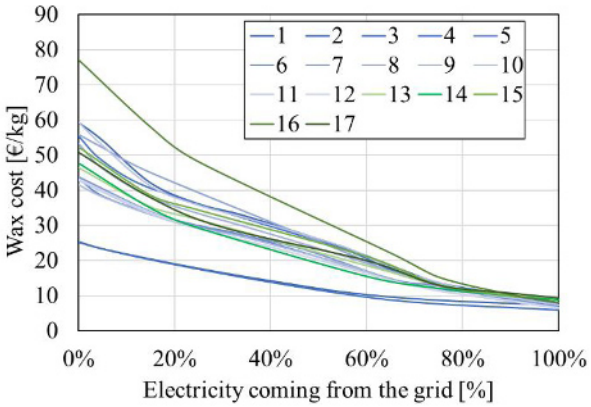

Fig. 3. Cost of FT wax at different grid connection values.

For the sake of comparison, the wax costs for the full-grid and full-RES cases are graphically displayed in Fig. 4. With 100% electricity from the grid, all the locations provide a cost of wax production lower than 10 €/kg. Moreover, the most economic locations in Germany and Italy correspond to Güstrow (6.00 €/kw_{wax}) and Montello (8.05 €/kw_{wax}), respectively. However, electricity coming from the grid might not be of renewable source, increasing the carbon footprint of the generated products. In this regard, a solution with 0% grid electricity utilization (i.e., full-RES configuration) ensures only green energy consumption. Due to the installation of PV, wind, and H_2-storage units, the rise in the wax cost ranges from 254% to 857%, with the two most economically feasible solutions corresponding to Dargun and Güstrow, in Germany. Moreover, it is to note that the cost of wax production is poorly affected by the amount of carbon dioxide entering the unit, and the main key factor is the percentage of grid electricity purchased. Accordingly, Dargun has flow of carbon dioxide of 1.54 t/h, while Güstrow presents 6.34 t/h of CO_2. And they reach similar costs of waxes at full-RES operation (25.44 €/kg and 25.12 €/kg, respectively). With 100% grid electricity, the difference in cost of waxes between the two locations becomes more remarkable, with values of 7.18 for Dargun and 6.00 €/kg Güstrow.

Concerning the optimal sizes of the different components, Table 4 lists the cost-optimal values of the full-grid and full-RES scenarios for all the locations. The resulting production of FT products is instead presented in Fig. 5. Expectedly, locations with high CO_2 availability result in high FT products generation. Moreover, with 100% electricity from the grid, the only component required in addition to the CCU unit is the electrolyser. For full-RES operation, all the other components (i.e., PV, wind and hydrogen storage) become relevant.

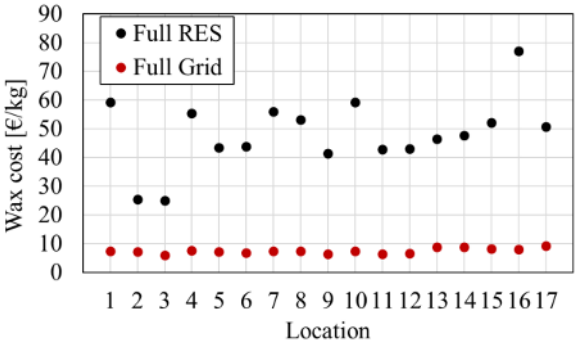

Fig. 4. Wax production cost for the full-grid and full-RES cases.

Table 4. Components size and wax cost at each location.

Code	Grid	Wax	PV	Wind	Alk	H_2 Storage
	[%]	€/kg	MW	MW	MW	MWh
1	100	7.3	0.0	0.0	9.2	0.0
	0	59.3	87.7	101	32.8	9503.8
2	100	7.2	0.0	0.0	10.5	0.0
	0	25.4	24.6	199	21.5	1989.1
3	100	6.0	0.0	0.0	43.3	0.0
	0	25.1	115.4	735	98.6	8234.8
4	100	7.6	0.0	0.0	7.1	0.0
	0	55.4	46.3	147	21.3	5680.3
5	100	7.3	0.0	0.0	9.4	0.0
	0	43.4	44.0	201	28.5	3150.5
6	100	6.8	0.0	0.0	15.6	0.0
	0	43.8	78.4	310	46.7	6357.3
7	100	7.4	0.0	0.0	8.4	0.0
	0	56.0	55.3	140	26.1	8989.7
8	100	7.3	0.0	0.0	9.2	0.0
	0	53.2	63.0	150	28.5	7780.8
9	100	6.4	0.0	0.0	25.9	0.0
	0	41.5	113.0	517	77.7	10082.5
10	100	7.3	46.2	75	11.7	16.0
	0	59.3	84.3	115	31.6	9948.2
11	100	6.4	0.0	0.0	25.9	0.0
	0	42.9	130.3	517	76.4	10711.1
12	100	6.5	0.0	0.0	21.4	0.0
	0	43.1	109.6	411	63.8	9255.1
13	100	8.9	0.0	0.0	17.9	0.0
	0	46.4	181.7	0.0	72.7	10471.4
14	100	8.8	0.0	0.0	17.9	0.0
	0	47.7	156.4	0.0	68.0	18589.6
15	100	8.2	0.0	0.0	26.8	0.0
	0	52.3	285.3	0.0	105.1	27747.9
16	100	8.1	0.0	0.0	33.5	0.0
	0	77.1	461.6	0.0	148.9	73825.6
17	100	9.3	0.0	0.0	7.6	0.0
	0	50.8	68.8	0.0	28.8	8435.7

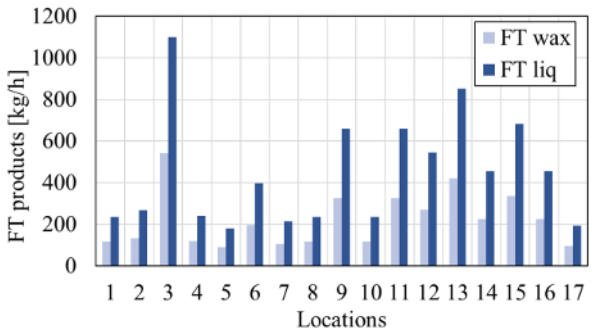

Fig. 5. FT products generation at each location.

3.2. Renewable energy capacity factor

For the various locations, a different capacity factor for wind and PV power is available. Accordingly, Fig. 6 shows the cost of waxes production at full-RES conditions together with the RES capacity factors. As a matter of fact, the PV capacity factor is similar for all the selected locations (range of 10 to 13%), while there exist a much higher variability considering the wind power capacity factor. In this regard, the selected Italian locations have low to null wind power availability. This results in zero MW of wind power installed for locations 13 to 17, with a consequent PV size to be installed very large (bigger than German locations). On the contrary, locations 2 and 3 have the highest availability of wind power, resulting in low cost of wax production. These results suggest that the implementation of these CCU-PtL plants – specifically aiming at FT waxes for the chemical sector – is more effective in locations where high wind power capacity factors are available.

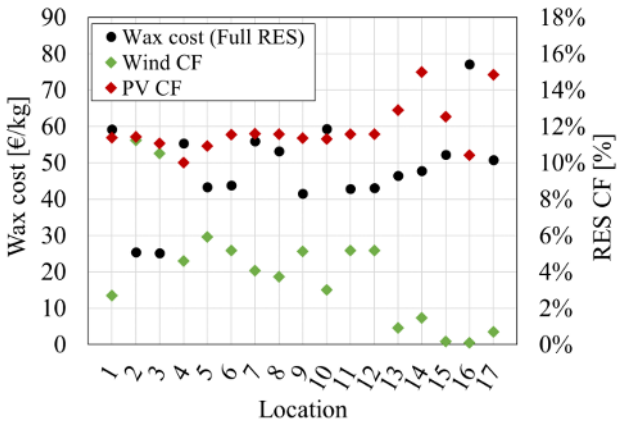

Fig. 6. Cost of wax production for the full-RES configuration against the wind and PV capacity factors.

3.3. Güstrow location

Specific results about system sizing are provided for the most performing location (Güstrow, DE), but similar results could be derived for all the 17 locations. Fig. 7 depicts the PV and wind power generation profiles over the year for Güstrow to ensure full-RES operation.

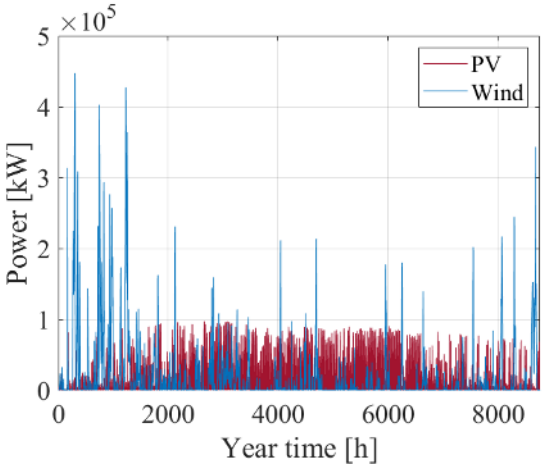

Fig. 7. PV and wind power for the full-RES configuration in Güstrow.

The TIC breakdown of the full-RES configuration is reported in Fig. 8. It can be observed that the green hydrogen production step (i.e., RES generators, electrolysis unit, and hydrogen storage) is the greatest contributor, accounting for around 97% of the TIC. Specifically, wind power represents the most impacting element (with about 74% of the CAPEX). This is connected to the need of having high-RES capacities to ensure a cost-effective full-RES solution.

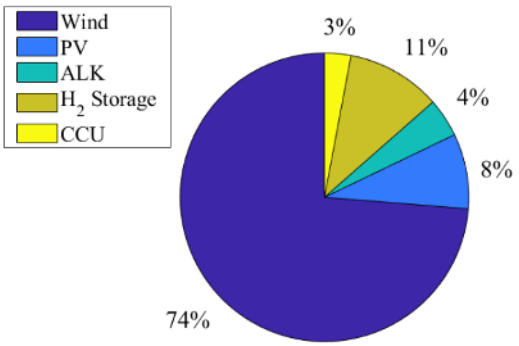

Fig. 8. CAPEX breakdown for the full-RES configuration in Güstrow.

It should be noted that the resulting wax cost of 25.12 €/kg is related to the full-RES case where the RES curtailment is sold to the electric grid. In the case of a completely off-grid system (i.e., no power exchanges with the grid) no extra RES can be sold to the grid. In this case, the wax cost would become 28.12 €/kg, which is slightly higher than the baseline case selling extra RES (the component sizes are around the same for the two options).

Additionally, further sensitivity analyses can be carried out. In this regard, economic parameters assumptions play a vital role in the evaluation of the cost of wax production. Accordingly, the WACC was varied from 2.0% to 10.0% at full-RES operation (i.e., 0% electricity from the grid). As visible from Fig. 9, more favourable conditions for the synthesis of waxes come at low WACC values. Such result is in line with literature studies involving PtX units [7]. Moreover, a compensation

derived by the utilization of CO_2 could be included. Accordingly, the German Power-to-X alliance has proposed an initial credit value of 300 €/kg of carbon dioxide utilized in PtX units [33]. With this credit, the reduction in cost of wax production would be of about 0.6 €/kg regardless of the WACC value.

Thus, to reach a breakthrough of such plant design to be competitive with the current fossil production route (2.50 €/kg_{wax}), credits higher than 300 €/kg of CO_2 would be needed. Alternatively, a solution with high grid electricity share for FT production could be preferential over the full-RES one, provided that the electricity used has a low carbon footprint. As shown before, the wax production cost would become lower at higher share of grid electricity. However, it is to point out that such processes involve technologies that are expected to have a reduction in their cost and operations (i.e., RES generators and electrolysers), and can impact the cost of heavy FT compounds. Lastly, complete decarbonization of the chemical sector would not be reached without FT long chain carbon-neutral hydrocarbons.

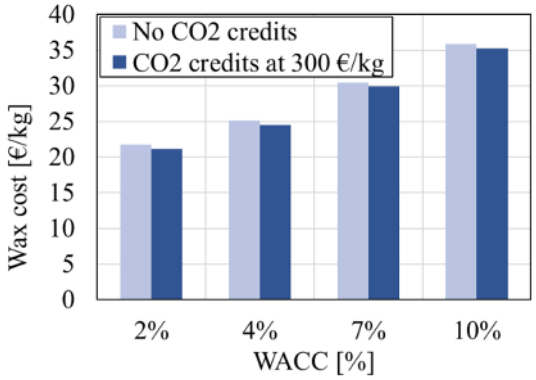

Fig. 9. Effect of WACC variation and carbon dioxide credits on the cost of wax production (full-RES configuration in Güstrow).

4 Conclusion

The present study investigates the production of FT compounds (i.e., liquid fuels and chemicals) with a focus on FT waxes destined to the chemical sector in a CCU and Power-to-Liquid framework. At current date, no alternative to fossil route is commercially available for these products. In this analysis, hydrogen from electrolysis and CO_2 separated from biogas are the material feedstocks for the FT production unit.

A cost-optimal optimization was performed in 17 locations in Europe, exploiting a flow of clean carbon dioxide available from the upgrading of biogas into biomethane. The optimal design of the wind and PV rated power, H_2-storage size, and electrolyser nominal power was carried out, with plant configurations ranging from 0% (full-RES) to 100% (full-grid) electricity from the grid. Accordingly, full-grid configurations have a cost of wax production (around 6 to 10 €/kw_{wax}) closer to the fossil route. However, full-RES solutions ensure having carbon neutral production of FT waxes. Lastly, the analysis shows that RES-based configurations require a high capacity factor of wind power generation, constraining the synthesis of FT waxes to places with high wind availability. In this regard, the analysis provides evidence of the convenience of installing these units in the north of Germany compared to Italy.

Further investigation will include the evaluation of optimal PV/wind power capacity factors to make the RES-based FT wax synthesis competitive with the fossil route. Suitable locations will be then identified as a support for decision makers to foster the complete decarbonization of chemical pathways.

The authors want to acknowledge the EU Horizon 2020 projects ICO2CHEM (From industrial CO2 streams to added value Fischer-Tropsch chemicals; grant agreement No 768543) and REMOTE (Remote area Energy supply with Multiple Options for integrated hydrogen-based Technologies; grant agreement No 779541).

References

1. K. Andersson, S. Brynolf, J. Hansson, and M. Grahn, Sustainability **12**, 3623 (2020)
2. International Energy Agency (IEA), *Net Zero by 2050 - A Roadmap for the Global Energy Sector* (2050)
3. G. Herz, E. Reichelt, and M. Jahn, Energy **132**, 370 (2017)
4. M. Marchese, S. Chesta, M. Santarelli, and A. Lanzini, Energy **228**, 120581 (2021)
5. Grand View Research, *Global Paraffin Wax Market* (2019)
6. E. Billig, M. Decker, W. Benzinger, F. Ketelsen, P. Pfeifer, R. Peters, D. Stolten, and D. Thrän, J. CO2 Util. **30**, 130 (2019)
7. M. Decker, F. Schorn, R. C. Samsun, R. Peters, and D. Stolten, Appl. Energy **250**, 1099 (2019)
8. EBA-GIE, Gas Infrastruct. Eur. 1 (2020)
9. M. Marchese, E. Giglio, M. Santarelli, and A. Lanzini, Energy Convers. Manag. X 100041 (2020)
10. PVGIS Hub, Eur. Comm. (2021)
11. Wind-Turbine-Models.Com/Turbines/9-Vestas-V27 (2021)
12. P. Marocco, D. Ferrero, A. Lanzini, and M. Santarelli, Energy Convers. Manag. **238**, 114147 (2021)
13. Tractebel and Hinicio, *Study on Early Business Cases for H2 in Energy Storage and More Broadly Power to H2 Applications* (2017)
14. M. Marchese, PhD Thesis, Politec. Di Torino (2021)
15. M. Marchese, N. Heikkinen, E. Giglio, A. Lanzini, J. Lehtonen, and M. Reinikainen, Catalysts **9**, 717 (2019)
16. Regatrace, *Mapping the State of Play of Renewable Gases in Europe* (n.d.)
17. F. M. Baena-Moreno, D. Sebastia-Saez, Q. Wang, and T. R. Reina, (2020)
18. J. Daniel-Gromke, V. Denysenko, J. Liebetrau, B. And, and B. I. Europe, *Biogas and Biomethane in Europe: Lessons from Denmark, Germany, and Italy* (2019)
19. E. Barbera, S. Menegon, D. Banzato, C.

D'alpaos, and A. Bertucco, (2018)
20. A. Berrada, A. Emrani, and A. Ameur, J. Energy Storage **40**, 102825 (2021)
21. D. G. Caglayan, H. U. Heinrichs, M. Robinius, and D. Stolten, Int. J. Hydrogen Energy (2021)
22. E. Crespi, P. Colbertaldo, G. Guandalini, and S. Campanari, (2020)
23. Tractebel, Engie, and Hinicio, *Study on Early Business Cases for H_2 in Energy Storage and More Broadly Power To H_2 Applications* (2017)
24. M. Marchese, G. Buffo, M. Santarelli, and A. Lanzini, J. CO2 Util. **46**, 101487 (2021)
25. L. J. F. Comidy, M. D. Staples, and S. R. H. Barrett, Appl. Energy **256**, 113810 (2019)
26. P. Marocco, D. Ferrero, M. Gandiglio, M. M. Ortiz, K. Sundseth, A. Lanzini, and M. Santarelli, Energy Convers. Manag. (2020)
27. J. Proost, Int. J. Hydrogen Energy **44**, 4406 (2019)
28. F. G. Albrecht, D. H. König, N. Baucks, and R. U. Dietrich, Fuel **194**, 511 (2017)
29. A. Hassan, M. K. Patel, and D. Parra, Int. J. Hydrogen Energy (2018)
30. D. Parigi, E. Giglio, A. Soto, and M. Santarelli, J. Clean. Prod. **226**, 679 (2019)
31. M. Hillestad, M. Ostadi, G. d. Alamo Serrano, E. Rytter, B. Austbø, J. G. Pharoah, and O. S. Burheim, Fuel **234**, 1431 (2018)
32. J. Kärki, T. Thomasson, K. Melin, M. Suomalainen, H. Saastamoinen, M. Hurskainen, and S. Mäkikouri, in *14th Greenh. Gas Control Technol. Conf. Melb.* (2018)
33. G. Herz, E. Reichelt, and M. Jahn, Appl. Energy **215**, 309 (2018)

Benefits of the multi-modality formulation in hydrogen supply chain modelling

Federico Parolin[1], *Paolo* Colbertaldo[1,*], and *Stefano* Campanari[1]

[1]Group of Energy Conversion Systems (GECOS), Department of Energy, Politecnico di Milano, 20156 Milan, Italy

Abstract. Hydrogen is recognized as a key element of future low-carbon energy systems. For proper integration, an adequate delivery infrastructure will be required, to be deployed in parallel to the electric grid and the gas network. This work adopts an optimization model to support the design of a future hydrogen delivery infrastructure, considering production, storage, and transport up to demand points. The model includes two production technologies, i.e., steam reforming with carbon capture and PV-fed electrolysis systems, and three transport modalities, i.e., pipelines, compressed hydrogen trucks, and liquid hydrogen trucks. This study compares a multi-modality formulation, in which the different transport technologies are simultaneously employed and their selection is optimized, with a mono-modality formulation, in which a single transport technology is considered. The assessment looks at the regional case study of Lombardy in Italy, considering a long-term scenario in which an extensive hydrogen supply chain is developed to supply hydrogen for clean mobility. Results show that the multi-modality infrastructure provides significant cost benefits, yielding an average cost of hydrogen that is up to 11% lower than a mono-modality configuration.

1 Introduction

With the European Green Deal, the European Union has committed to reach carbon neutrality by 2050, calling all the energy-consuming sectors to a paradigm-shifting transition towards decarbonization [1].

The development of a hydrogen economy is expected to be one of the pillars of the energy transition, as hydrogen can be employed in a variety of applications, allowing to abate emissions in diverse sectors [2]. This energy vector appears particularly promising for the decarbonization of the transport sector, which alone accounts for more than 30% of CO_2 emissions in Europe [3]. Hydrogen-powered fuel cell electric vehicles (FCEVs) ensure zero tailpipe emissions, offering higher mileage and faster refuelling if compared to battery electric vehicles (BEVs). In addition to passenger cars, FCEVs are highly suitable for buses and heavy-duty transport, where weight constraints are relevant and payload reductions must be avoided [4].

The realization of an extensive delivery infrastructure is of paramount importance to assist the development of a hydrogen-based clean mobility, as the lack of a distributed supply chain currently limits the access to this energy vector. Accordingly, the topic of the hydrogen supply chain (HSC) has drawn increasing interest in the scientific community, and different authors developed modelling tools to design and analyse the hydrogen infrastructure. The HSC modelling features an inherent complexity, as each stage (production, transport, storage, and consumption) may take place with competing alternatives, each coming with advantages and drawbacks, as well as different costs and industrial maturity.

The existing literature features a variety of approaches to deal with such complexity, and each work addresses different aspects with distinct assumptions. The majority of the studies consists of mono-objective optimization models, aimed at minimising the total cost of the infrastructure [5]–[18]. A few works deal with multi-objective optimization, in which the cost minimisation is combined with environmental, financial, or safety concerns [19]–[25], while others focus on parametric analyses, to compare alternative infrastructure configurations [26], [27].

Many works analyse a snapshot of the infrastructure, i.e., a representative steady-state condition with time-invariant quantities [5], [6], [9]–[11], [15], [24], [26], [27], thus sizing the HSC according to the condition identified as the most stressful moment throughout the year, e.g., in terms of highest demand and/or lowest production. While this approach allows to reduce the computational complexity of the model, it fails to track the optimal design and operation of storage units, which is paramount when dealing with hydrogen production from intermittent renewable energy sources (RES). An alternative approach is to consider a year-long analysis, tracking the variation of quantities according to a certain time resolution [17], [18], thus obtaining a more accurate description of the HSC, at the expenses of a higher model complexity. A further alternative is to analyse the evolution of the infrastructure over a long time horizon through a multi-period analysis, which consists of dividing the considered timeframe in intervals of equal

* Corresponding author: paolo.colbertaldo@polimi.it

duration, treated similarly to snapshots [7], [14], [16], [20]–[23], [25].

The spatial modelling of the HSC is often addressed by adopting schematized networks with a restricted number of points and connections to limit the number of variables and equations [7], [10], [14]–[17], [20], [21], [23]–[25], [27]. A more accurate, yet more computationally demanding, approach is to define the candidate infrastructure network on the basis of actual spatial data through a Geographic Information System (GIS), thereby introducing territorial constraints in the model.

A crucial aspect in the HSC modelling is the multiplicity of hydrogen transport modalities. Since these are not alternative, but rather competing, it would be beneficial to optimize also the selection of the transport technologies for each stage of the supply chain in a multi-modality formulation. However, since this approach significantly increases the model complexity and computational requirements, it is featured in a limited number of studies [7], [8], [10], [11], [14], [16], [19]–[21], [23], [24], which typically introduce other simplifying modelling assumptions, whereas the majority considers a single transport modality at a time in mono-modality formulations.

This work adopts a spatially and temporally resolved mixed integer linear programming (MILP) model to optimize the design and operation of a hydrogen infrastructure to supply a network of hydrogen refuelling stations (HRS) [28]. The model includes all the stages of the HSC (production, transport, storage, and demand) and optimizes the infrastructure taking into account the candidate HSC networks based on GIS data, considering a year-long analysis with daily resolution. Two production technologies are considered in this analysis (although the model could also include a larger variety of options), (i) steam methane reforming equipped with carbon capture and (ii) electrolysis fed by dedicated solar photovoltaic (PV) plants. The included transport modalities are hydrogen pipelines, compressed hydrogen trucks, and liquid hydrogen trucks, and a multi-modality formulation is developed to optimize their selection. The adopted tool also allows to impose the selection parameters at start, in order to perform mono-modality simulations, i.e., considering only one transport mode.

After presenting an overview of the model formulation, the article focuses on the comparison between the multi- and the mono-modality formulations, according to the results obtained from the model applications to the case study of the Italian region of Lombardy, considering a long-term scenario in which a 25% FCEV stock share is assumed among passenger cars.

Compared to other works in the existing literature that presented a multi-modality formulation, the added value of the adopted model is the combination of the multi-modality formulation, the detailed description of the HSC pathways, the inclusion of territorial constraints through GIS data, and the time-variant analysis, as these characteristics are not simultaneously featured by any of the studies identified in the literature survey.

2 Problem statement

The adopted model minimizes the total cost of the infrastructure. The objective function is set equal to the average cost of hydrogen delivered to demand points, considering investment and operational costs for hydrogen production, conditioning, transport, and storage:

$$f_{ob} = \min\left\{\frac{\sum_i CAPEX_i \cdot CRF_i + \sum_i OPEX_i}{\sum_n \sum_t q_{dem}^{n,t}}\right\} \quad (1)$$

Figure 1 summarizes the technological options considered for each stage of the HSC. Hydrogen production in the model can exploit two different technologies. The first option is steam methane reforming equipped with carbon capture and storage (SMR-CCS), which ensures a flexible production of blue hydrogen within the plant nominal capacity. The second option is electrolysis (EL) fed by dedicated PV plants (PV-EL), which produces green hydrogen with a constrained output that depends on the availability of solar radiation. The purchase of grid electricity is allowed to partially compensate this issue, while revenues can be obtained from the sale of surplus electricity that may result due to the PV vs. EL nominal capacity ratio or in periods of low hydrogen demand and large availability of solar radiation.

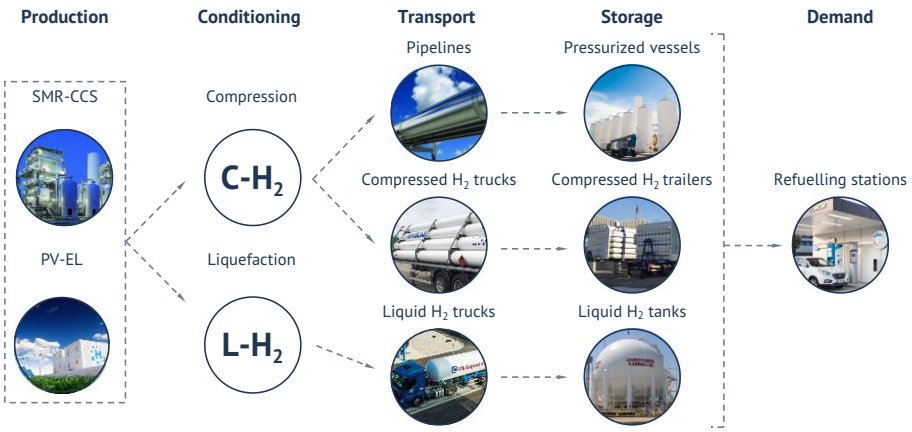

Figure 1. Scheme of the HSC stages, depicting the included technological options.

Conditioning to compressed or liquid hydrogen is performed at production sites, according to the subsequent transport technology. In particular, hydrogen can be delivered as a gas via pipeline (GP), as a gas in a compressed hydrogen truck (GT), or as a liquid in a cryogenic truck (LT). Depending on the employed modality (see Figure 1), hydrogen is stored in pressurized vessels at 160 bar, in the trailer vessels themselves, or in cryogenic insulated tanks.

The end point of hydrogen pathways are the HRSs. Each HRS can be supplied exclusively via one of the three included transport modalities, and the selection is optimized. The internal station structure is not investigated and the installation costs are left out of the boundaries of the analysis since they do not vary significantly between the different types of stations [9]. Storage needs at HRSs are instead included, setting an upper boundary to the installed capacity depending on the maximum daily demand of each node, since the space availability of HRSs is typically constrained. The daily demand profiles for each station are provided as input to the model, and they vary depending on the time of year, whereas the annual demand depends on the station location.

3 Model structure

The HSC is modelled as a network of nodes and edges. In order to model the infrastructure components represented in Figure 1, the network topology comprises four node types: production, demand, intermediate storage, and transit. Except for transit nodes, all node types feature a storage section and a virtual sub-node, which is responsible for the connection with the network edges. According to this approach, the node mass balance is defined by two equations, one for the storage section, and one for the virtual sub-node. In a general form, the equations for each node n and each transport modality m, at each time step t are:

$$\begin{cases} Q_s^{n,m,t+1} = Q_s^{n,m,t} + \left(q_{in,s}^{n,m,t} - q_{out,s}^{n,m,t} - \xi_{dem}^{m} q_{dem}^{n,t}\right) \cdot \Delta t \cdot N_{td} \\ Y^{n,m} \cdot q_{edg}^{e,m,t} = q_{out,s}^{n,m,t} - q_{in,s}^{n,m,t} + \xi_{prd}^{m} q_{prd}^{m,t} \end{cases} \quad (2)$$

where q_{dem} is the hydrogen demand, q_{prd} is the production flow, q_{edg}^{e} is the flow along edge e, Q_s is the storage content, $q_{in,s}$ and $q_{out,s}$ are the inlet and outlet storage flows, ξ_{dem} and ξ_{prd} are equal to 1 for demand and production nodes, respectively, and zero otherwise, and Y is the incidence matrix of the graph representative of the transport network.

The terms Δt and N_{td} in Eq. (2) are related to the model timescale and deserve a separate discussion. The model considers the infrastructure operation over a year-long timeframe, and, since the quantities are tracked according to a daily resolution, the parameter Δt is equal to 1 day. In order to limit the number of variables and equations, the typical day approach is followed. This consists of identifying a set of typical days, each representative of a period of the year, and to repeat them identically for a certain number of times, in terms of demand, production, and flows, up to representing the entire year. In this analysis, 52 typical days are identified, and each of them is repeated $N_{td} = 7$ times to form the 52 weeks of the year. The advantage of this approach is that it allows to substantially reduce the computational complexity while preserving a sufficient level of detail. The intra-week variation of the demand is neglected, whereas the year-long fluctuation of PV generation is preserved.

Figure 2 outlines the high level representation of the HSC in the model. Road and pipeline delivery occur on two parallel graphs, while production and demand nodes are unique and shared between the two networks. In particular, the production flow is injected in the respective graph through conditioning, after which variables become separated, according to the transport modality. As can be noted from Figure 2, intermediate storage is not envisaged for compressed hydrogen trucks, as it is preferable to store the trailers at production sites and transport them to demand points when required than deliver them to an intermediate hub and move them again later.

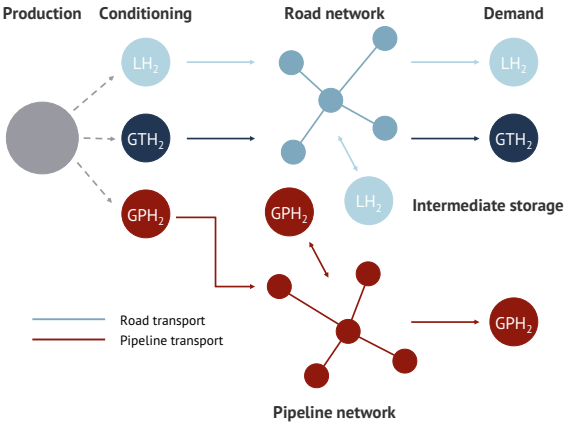

Figure 2. High level representation of the HSC as structured in the model.

Territorial constraints are included by building the candidate transport networks from GIS spatial data, which are available as shapefiles [29]. Candidate truck routes run along the existing road infrastructure, under the hypothesis that it is not saturated, while the current railroad network is adopted as candidate example of graph for pipeline routes, considering it conceptually suitable as it consists of pathways where rights of way already exist and that exclude forbidden or implausible areas. A more plausible alternative could be the current natural gas grid network; however, the access to detailed spatial information on pipeline routes is restricted. At any rate, the main aim in this analysis is to define a candidate network for hydrogen transport via pipeline that differs from the road infrastructure, includes a lower number of edges, and involves areas where infrastructural intervention already occurred. The road and railroad shapefiles are converted into directed graphs by means of dedicated Matlab® functions, which also allow to add production and demand nodes by connecting them to the nearest nodes of the graph. To reduce the size and complexity of the model, the resulting networks are then simplified by maintaining only the transit nodes that host

multiple intersections of edges. Furthermore, the *minimum spanning tree* algorithm is applied to extract the subset of edges that yields the minimum network extent, accepting the risk of losing some potentially usable pathways to improve the computational tractability of the model.

To complete the model presentation, the HSC optimization problem is here summarized. The required input data are:

- the set of available hydrogen production, storage, and transport technologies, together with their techno-economic data;
- the topology of the candidate transport networks, the position of production sites, potential intermediate storage hubs, and demand points;
- the demand profiles of HRSs;
- the upper boundaries of production and storage nominal capacities;
- the PV electricity generation profiles and the PV-EL nominal capacity ratio.

Then, the infrastructure is designed by the model, while solving also the year-long operation, by optimizing the following:

- the employed production, transport, and storage technologies;
- the installed production capacities;
- the installed storage capacities at production, demand, and intermediate hub nodes;
- the exploited transport pathways and modalities, and the delivered quantities;
- the hydrogen flows for each component of the HSC.

As previously discussed, the analysis presented in this work focuses on the comparison between the mono- and multi-modality formulations. Accordingly, although the model was developed following a multi-modality formulation, its implementation allows to perform also mono-modality simulations, by transforming the variables of the excluded modalities into parameters before running the model.

4 Case study: assumptions and data

For the purpose of comparing the mentioned mono-/multi-modality formulations, the model is applied to the regional case study of Lombardy in Italy, considering a long-term scenario (2050) in which FCEVs account for 25% of the passenger car stock share in the country, with small deviations among provinces based on population, population density, vehicle ownership rate, and income per capita [30]. Note that this assumption could be turned into an equivalent distributed consumption e.g. of heavy-load trucks or other hydrogen demands, without changing the validity of the example.

The position of HRSs is identified assuming that 10% of existing gasoline and diesel refuelling stations (i.e., 366 stations) will host hydrogen refuelling, selecting them to guarantee an even spatial presence. Hydrogen demand is computed for each province and distributed uniformly among the stations, which feature an annual demand in the range 0.2-1.1 kt/y, leading to a total of 145 kt/y in the region.

As far as production is concerned, SMR-CCS plants are assumed to be sited at the existing refineries of ENI Sannazzaro and MOL Mantova [31], while the centroid of each province is selected as candidate location for a centralized PV-EL facility. In terms of maximum capacity, a cap is introduced for (i) the upper boundary for SMR-CCS, which is set to 20% of today's refinery hydrogen production, and (ii) the dedicated PV capacity in each province, which cannot exceed 5 times the installed PV capacity in 2018, thus also preserving the proportion among provinces. In the case of PV-EL systems, the hydrogen production is bounded in terms of daily production via an intra-hour analysis that assumes a PV-EL capacity ratio equal to 2 [32].

To complete the networks, 15 candidate intermediate storage sites are identified through a random extraction among transit nodes for both the pipeline and the road delivery graph, considering a minimum distance of 20 km between them to obtain a homogeneous distribution. This set of nodes is supplied as input to the model, which optimizes the installed capacities and the actual use.

The main techno-economic data are reported in Table 1. In order to be consistent with the assessment of a long-term scenario, values are selected considering available projections or optimistic values among short- and medium- term estimates. All costs have been reported to $€_{2019}$ through inflationary adjustments for both the EU [33] and the US [34].

Table 1. Main techno-economic data.

Parameter	Value	Unit	Reference
EL CAPEX*	580	€/kW$_e$	[35]
EL consumption	49	kWh$_e$/kg$_{H2}$	[35]
PV-EL capacity ratio	2	-	[32]
PV LCOE	51	€/MWh$_e$	[36]
PV LCOE – CAPEX share	75%	-	[37]
Grid electricity purchase cost	150	€/MWh$_e$	Assumed
PV surplus electricity sale price	30	€/MWh$_e$	Assumed
SMR-CCS H_2 production cost	1.9	€/kg$_{H2}$	[38]
Liquid H_2 truck CAPEX	207	€/kg$_{H2}$	[39]
Liquid H_2 truck capacity	4.3	t$_{H2}$/vehicle	[39]
Compressed H_2 truck CAPEX	355	€/kg$_{H2}$	[40]
Compressed H_2 truck capacity	1	t$_{H2}$/vehicle	[40]
Gaseous H_2 pipeline CAPEX	$4 \cdot 10^3\ A + 336$ €/km, with A in m^2		[5]

*Includes stack replacement after 10 years

5 Comparison and discussion

The study investigates four cases, considering, at first, a mono-modality simulation for each of the three included transport technologies, and, then, a complete multi-modality simulation that optimizes the selection of the transport technology. All simulations are performed with a workstation equipped with an Intel Xeon W-2123 3.6 GHz processor and 32 GB RAM. Due to the high model complexity and size that result from the detailed spatial and temporal resolutions, the integer variables representing the number of travelling trucks are relaxed to continuous values. With this adjustment, the mono-modality simulations are each completed in about 10 minutes, whereas 43 hours are required for the multi-modality case, thus proving the necessity of such a simplification to comply with the available resources.

As Figure 3 shows, the multi-modality simulation (labelled "Multi") yields the lowest average cost of hydrogen (5.83 €/kg_{H2}), while all mono-modality configurations (labelled "Mono -" with a suffix indicating the mode type) are more expensive, with values 4-11% higher. The multi-modality infrastructure exploits all the three transport technologies, with a predominance of pipeline and liquid hydrogen truck delivery, which meet the demand of 173 and 171 stations, respectively, while the remaining 22 receive compressed hydrogen via truck. Although the number of stations supplied via pipeline is almost the same as those that receive hydrogen via liquid hydrogen trucks, pipeline delivery accounts for more than 60% of the total hydrogen consumption, whereas liquid hydrogen represents only 25%. This result is due to the fact that most of the stations supplied via liquid hydrogen truck are located in the southern provinces of the region (see Figure 4), which are characterised by a lower demand than the central provinces that are supplied via pipeline.

The comparison of the cost breakdown of the mono-modality simulations (see Figure 3) shows the advantages and drawbacks of the different transport technologies. The share of the transport cost is considerably higher for pipeline and compressed hydrogen truck delivery. As far as the former is concerned, the large expense is due to the high investment costs required for pipeline installation, while the cost item 'Transport' in the case of compressed H_2 truck delivery also covers the storage expenditure at demand nodes, since storage is performed with the same trailers that are used for transport. On the other hand, liquid hydrogen truck delivery benefits from lower specific costs for both transport and storage (see Table 1), but liquefaction is more capital and energy intensive than compression, leading to higher investment and operational cost, and, thus, to a significantly higher conditioning share. Production costs are slightly less impacting in the Mono-LT configuration, as the lower storage cost allows to better exploit PV plants, minimizing the purchase of grid electricity.

In the multi-modality simulation, the advantages of each technology are exploited, and each performs the tasks it is most suited for, yielding the overall lowest-cost infrastructure configuration. The cost breakdown is compared to that of the mono-modality configurations in Figure 3. In the multi-mode, since liquid hydrogen is employed to satisfy only a fraction of the total demand, the higher cost and consumption of liquefaction are compensated by the favourable economics of liquid transport and storage, as the combined share of production and conditioning is in line with those of the Mono-GP and Mono-GT scenarios, while the transport and storage at HRS costs are lower.

As opposed to all mono-modality configurations, the multi-modality infrastructure exploits four intermediate storage sites, with capacity of 1000, 1000, 405, and 183 t_{H2}, respectively, which absorb the hydrogen overproduction from PV-fed electrolysis systems during summer to redistribute it in periods of lower solar radiation. The selected storage form is liquid due to the much lower investment costs, despite the boil-off. Such option is not exploited in the Mono-LT configuration, since, in the analysed case study, it becomes economically favourable when the production of liquid hydrogen is limited to few plants, as in the multi-modality case, in order to maximise its contribution.

By looking at the exploited transport networks (Figure 4), it emerges that the installed pipelines cover most of the region, consistently with the fact they are suitable to deliver large quantities over long distances, while compressed hydrogen trucks travel along a less extensive network and supply a limited number of stations, confirming that this transport modality is appropriate to meet relatively small delivery requirements.

In all the cases, the highest-share cost item is production, which is strongly based on PV-fed electrolysis systems, which account for about 95% of the delivered hydrogen quantities. In the production cost, the impact of the investment is nearly twice the operational expenditure, and all the infrastructure configurations feature a similar proportion.

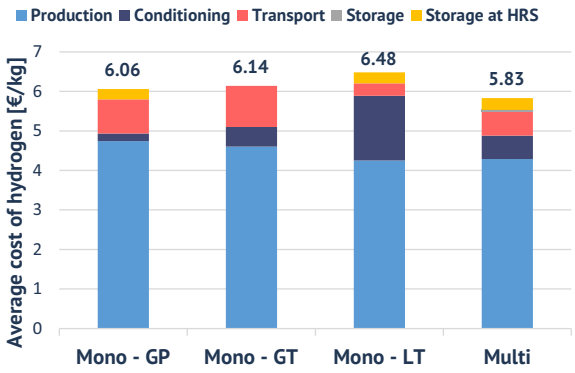

Figure 3. Average cost of hydrogen with cost breakdown for the different configurations. In the 'Mono-GT' case, the item 'Transport' covers also the storage needs at demand sites.

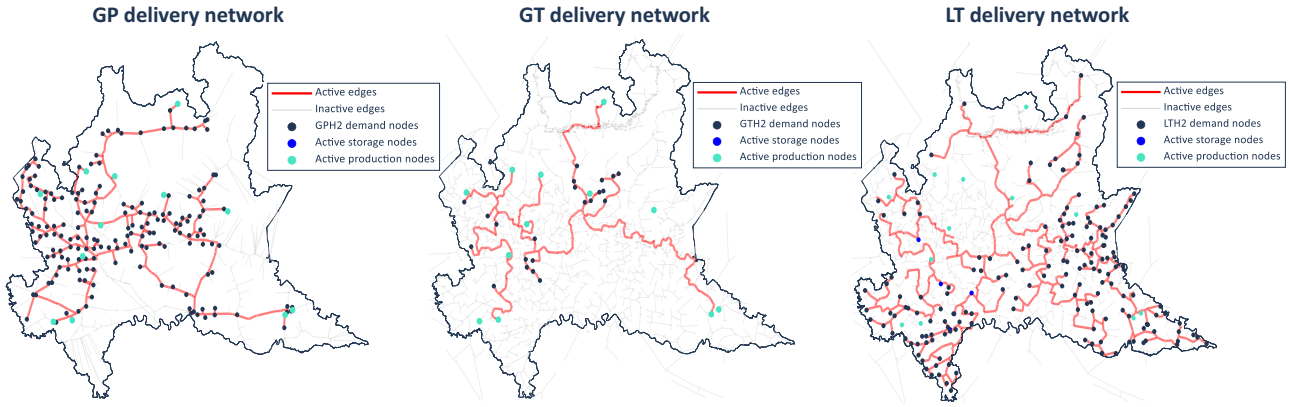

Figure 4. Optimized transport network for each transport technology in the multi-modality configuration.

6 Conclusions

By means of an optimization model of the hydrogen supply chain, this study investigated the infrastructural needs related to the widespread adoption of hydrogen as a fuel for clean mobility, focusing on the comparison between the mono- and multi-modality formulations. The former consider a single transport technology at a time, while the latter optimizes the choice of the transport technology within the overall system simulation.

The analysis developed as an example the case study of the Italian region of Lombardy, considering a long-term scenario (2050) featuring a distributed demand of hydrogen for FCEVs, accounting for 25% of the passenger car stock. The study considered four simulations, comparing three mono-modality scenarios in which either hydrogen pipelines, compressed hydrogen trucks, or liquid hydrogen trucks are adopted separately, and a multi-modality configuration in which the three transport modalities are allowed together and their selection is optimized. Results showed that the multi-modality infrastructure yields the lowest average cost of hydrogen delivered to refuelling stations, with a value of 5.83 €/kg_{H2}, whereas the mono-modality cases are 4%-11% more expensive. The multi-modality configuration simultaneously exploits all the three included technologies, with 47.3% of stations supplied via pipeline, 46.7% via liquid hydrogen truck, and 6.0% via compressed hydrogen truck.

Beyond the specific case study, the model application proves the relevance of the multi-modality formulation, showing that the multiplicity of transport options cannot be disregarded when modelling the HSC, as the cost-optimal alternative cannot be predicted *a priori* and the cheapest solution is likely a combination of different modalities. On the other hand, the multi-modality formulation significantly increases the model complexity, as, in the case study, the solution is obtained in dozens of hours, whereas mono-modality simulations require few minutes. Accordingly, conventional computational resources become no longer suitable to dealing with a wider spatial scale (e.g., considering a national case study) or with a broader set of transport modalities (e.g., including also liquid organic hydrogen carriers or shipping) while maintaining the proposed model detail, thus requiring to look into high-performance computing clusters for applications of increasing size.

Further analyses will investigate hydrogen storage at intermediate sites, evaluating the cost impact and the required cost reduction to attain overall advantages, e.g., by considering alternative technologies such as underground storage in lined rock caverns, which could provide cheaper seasonal storage and, thus, a better integration with RES-based hydrogen production.

References

[1] European Commission, “European Green Deal,” 2020. https://ec.europa.eu/info/strategy/priorities-2019-2024/european-green-deal_en.

[2] Fuel Cells and Hydrogen Joint Undertaking (FCH), “Hydrogen Roadmap Europe,” 2019.

[3] IEA, “Europe: key energy statistics.” https://www.iea.org/regions/europe.

[4] G. Guandalini and S. Campanari, “Well-to-wheel driving cycle simulations for freight transportation: Battery and hydrogen fuel cell electric vehicles,” *2018 Int. Conf. Electr. Electron. Technol. Automotive, Automot. 2018*, no. ii, pp. 0–5, 2018.

[5] C. Yang and J. Ogden, “Determining the lowest-cost hydrogen delivery mode,” *Int. J. Hydrogen Energy*, vol. 32, no. 2, pp. 268–286, 2007.

[6] S. Baufumé *et al.*, “GIS-based scenario calculations for a nationwide German hydrogen pipeline infrastructure,” *Int. J. Hydrogen Energy*, vol. 38, no. 10, pp. 3813–3829, 2013.

[7] H. Talebian, O. E. Herrera, and W. Mérida, “Spatial and temporal optimization of hydrogen fuel supply chain for light duty passenger vehicles in British Columbia,” *Int. J. Hydrogen Energy*, vol. 44, no. 47, pp. 25939–25956, 2019.

[8] N. Strachan, N. Balta-Ozkan, D. Joffe, K. McGeevor, and N. Hughes, “Soft-linking energy systems and GIS models to investigate spatial hydrogen infrastructure development in a low-carbon UK energy system,” *Int. J. Hydrogen Energy*, vol. 34, no. 2, pp. 642–657, 2009.

[9] P. Colbertaldo, S. Cerniauskas, T. Grube, M.

Robinius, D. Stolten, and S. Campanari, "Clean mobility infrastructure and sector integration in long-term energy scenarios: The case of Italy," *Renew. Sustain. Energy Rev.*, vol. 133, p. 110086, 2020.

[10] L. Li, H. Manier, and M. A. Manier, "Integrated optimization model for hydrogen supply chain network design and hydrogen fueling station planning," *Comput. Chem. Eng.*, vol. 134, 2020.

[11] A. Almansoori and A. Betancourt-Torcat, "Design of optimization model for a hydrogen supply chain under emission constraints - A case study of Germany," *Energy*, vol. 111, pp. 414–429, 2016.

[12] S. Samsatli, I. Staffell, and N. J. Samsatli, "Optimal design and operation of integrated wind-hydrogen-electricity networks for decarbonising the domestic transport sector in Great Britain," *Int. J. Hydrogen Energy*, vol. 41, no. 1, pp. 447–475, 2016.

[13] A. Ochoa Bique and E. Zondervan, "An outlook towards hydrogen supply chain networks in 2050 — Design of novel fuel infrastructures in Germany," *Chem. Eng. Res. Des.*, vol. 134, pp. 90–103, 2018.

[14] M. Moreno-Benito, P. Agnolucci, and L. G. Papageorgiou, "Towards a sustainable hydrogen economy: Optimisation-based framework for hydrogen infrastructure development," *Comput. Chem. Eng.*, vol. 102, pp. 110–127, 2017.

[15] J. Kim, Y. Lee, and I. Moon, "Optimization of a hydrogen supply chain under demand uncertainty," *Int. J. Hydrogen Energy*, vol. 33, no. 18, pp. 4715–4729, 2008.

[16] M. Dayhim, M. A. Jafari, and M. Mazurek, "Planning sustainable hydrogen supply chain infrastructure with uncertain demand," *Int. J. Hydrogen Energy*, vol. 39, no. 13, pp. 6789–6801, 2014.

[17] W. Won, H. Kwon, J. H. Han, and J. Kim, "Design and operation of renewable energy sources based hydrogen supply system: Technology integration and optimization," *Renew. Energy*, vol. 103, pp. 226–238, 2017.

[18] L. Welder, D. S. Ryberg, L. Kotzur, T. Grube, M. Robinius, and D. Stolten, "Spatio-temporal optimization of a future energy system for power-to-hydrogen applications in Germany," *Energy*, vol. 158, pp. 1130–1149, 2018.

[19] A. Ochoa Bique, L. K. K. Maia, F. La Mantia, D. Manca, and E. Zondervan, "Balancing costs, safety and CO2 emissions in the design of hydrogen supply chains," *Comput. Chem. Eng.*, vol. 129, 2019.

[20] N. Sabio, A. Kostin, G. Guillén-Gosálbez, and L. Jiménez, "Holistic minimization of the life cycle environmental impact of hydrogen infrastructures using multi-objective optimization and principal component analysis," *Int. J. Hydrogen Energy*, vol. 37, no. 6, pp. 5385–5405, 2012.

[21] Z. Li, D. Gao, L. Chang, P. Liu, and E. N. Pistikopoulos, "Hydrogen infrastructure design and optimization: A case study of China," *Int. J. Hydrogen Energy*, vol. 33, no. 20, pp. 5275–5286, 2008.

[22] S. De-León Almaraz, C. Azzaro-Pantel, L. Montastruc, and M. Boix, "Deployment of a hydrogen supply chain by multi-objective/multi-period optimisation at regional and national scales," *Chem. Eng. Res. Des.*, vol. 104, pp. 11–31, 2015.

[23] G. Guillen-Gosalbez, F. D. Mele, and I. E. Grossman, "A Bi-Criterion Optimization Approach for the Design and Planning of Hydrogen Supply Chains for Vehicle Use," *AIChE J.*, vol. 56, no. 3, pp. 650–667, 2010.

[24] J. H. Han, J. H. Ryu, and I. B. Lee, "Multi-objective optimization design of hydrogen infrastructures simultaneously considering economic cost, safety and CO2 emission," *Chem. Eng. Res. Des.*, vol. 91, no. 8, pp. 1427–1439, 2013.

[25] J. O. Robles, C. Azzaro-Pantel, and A. Aguilar-Lasserre, "Optimization of a hydrogen supply chain network design under demand uncertainty by multi-objective genetic algorithms," *Comput. Chem. Eng.*, vol. 140, 2020.

[26] M. Reuß, T. Grube, M. Robinius, and D. Stolten, "A hydrogen supply chain with spatial resolution: Comparative analysis of infrastructure technologies in Germany," *Appl. Energy*, vol. 247, no. December 2018, pp. 438–453, 2019.

[27] C. Wulf *et al.*, "Life Cycle Assessment of hydrogen transport and distribution options," *J. Clean. Prod.*, vol. 199, pp. 431–443, 2018.

[28] F. Parolin, P. Colbertaldo, and S. Campanari, "Design and Optimization of a Multi-Mode Hydrogen Delivery Infrastructure for Clean Mobility," accepted paper SDEWES2021.0753 at 16th Conference on Sustainable Development of Energy, Water, and Environment Systems (SDEWES2021), Dubrovink, Croatia, Oct 2021.

[29] ESRI, "ESRI Shapefile Technical Description," 1998.

[30] P. Colbertaldo, "Power-to-hydrogen for long-term power and transport sector integration," Politecnico di Milano, 2019.

[31] Il Sole 24 Ore, "Le raffinerie e l'indotto arrancano," 2014. https://www.infodata.ilsole24ore.com/2014/07/31/le-raffinerie-e-lindotto-arrancano/.

[32] P. Colbertaldo, G. Guandalini, G. Lozza, and S. Campanari, "Sizing of integrated solar photovoltaic and electrolysis systems for clean hydrogen production," in *EFC2019 European Fuel Cell Technology & Applications - Piero Lunghi Conference EFC2019*, 2019, pp. 2019–2020.

[33] European Commission, "Eurostat." https://ec.europa.eu/eurostat/home.

[34] United States Department of Labor, "U.S. Bureau of Labor Statistics." https://www.bls.gov/.

[35] IRENA, "Hydrogen From Renewable Power," 2018.
[36] W. Zappa, M. Junginger, and M. van den Broek, "Is a 100% renewable European power system feasible by 2050?," *Appl. Energy*, vol. 233–234, no. November 2018, pp. 1027–1050, 2019.
[37] IRENA, "Renewable Power Generation Costs in 2018," 2019.
[38] IEAGHG, "Techno - Economic Evaluation of SMR Based Standalone (Merchant) Hydrogen Plant with CCS," 2017.
[39] M. Reuß, T. Grube, M. Robinius, P. Preuster, P. Wasserscheid, and D. Stolten, "Seasonal storage and alternative carriers: A flexible hydrogen supply chain model," *Appl. Energy*, vol. 200, pp. 290–302, 2017.
[40] Fuel Cells and Hydrogen 2 Joint Undertaking (FCH JU), "Addendum to the Multi-Annual Work Plan 2014-2020," 2018.

Towards stable and highly active IrO_2 catalysts supported on doped tin oxides for the oxygen evolution reaction in acidic media

Sofia Delgado[1,2], *Paranjeet* Lakhtaria[1], *Eva* Sousa[1], *Tiago* Lagarteira[1], *K.A.* Friedrich[2] and *Adélio* Mendes[1*]

[1]Laboratory for Process Engineering, Environmental, Biotechnology and Energy (LEPABE), Faculty of Engineering of University of Porto, Rua Dr. Roberto Frias s/n, 4200-465 Porto, Portugal
[2]Institute of Engineering Thermodynamics, German Aerospace Center (DLR), Pfaffenwaldring 38-40, 70569 Stuttgart, Germany

Abstract. Iridium oxide is the preferred catalyst for water oxidation but it is required to maximize its utilization to deploy Proton Exchange Membrane Water Electrolyzers (PEMWEs) into the large-scale applications panorama. A promising pathway for dispersing this precious catalyst is on an electric conductive and stable support. However, there is a lack of understanding how the support-catalyst interactions affect the stability/activity of the electrocatalyst under anodic conditions. This work discloses a modified, easy-scalable, polyol synthesis protocol to produce a highly active and stable iridium-based catalyst, supported on metal-doped tin oxides. The loading of Ir was reduced 30 wt.% compared to the reference IrO_2, and dispersed on Sb-SnO_2 (IrOx/ATO), In-SnO_2 (IrOx/ITO) and SnO_2 supports. All synthesized electrocatalysts not only surpassed the OER-mass activity of a commercial catalyst (IrO_2) – reference – but also reached higher electrochemical active surface areas and enhanced stability under the OER conditions. The highest performance was achieved with Ir NPs supported on ITO (176 A/g_{Ir} *vs.* 15.5 A/g_{Ir} for the reference catalyst @ 1.51 V *vs.* RHE) and both IrOx/ITO and IrOx/SnO_2 catalysts demonstrated remarkable stability after cycling the electrode and performing long-term chronopotentiometry. ITO is, therefore, an auspicious support to serve Ir-based catalysts as it favors a good bargain between activity and stability, while drastically reducing the amount of noble metal.

Keywords. Proton Exchange Membrane Water Electrolyzer; Oxygen evolution reaction; Supports, Tin oxide

1 Introduction

Proton exchange membrane water electrolyzers (PEMWEs) exhibit excellent features for the production of green hydrogen, by mitigating the intermittency and fluctuation of renewable energy sources, and thus allowing the decarbonization of the electrical grids[1]. The oxygen evolution reaction (OER), considers the use of high noble metal loadings (*ca.* 2 to 4 $mg_{Ir}\cdot cm^{-2}$); even though the cost breakdown for the electrolyzer system addresses solely 5 % to the catalysts for small scale systems, considering the increasing energy demand and the needed widespread commercialization of PEM electrolysis, the catalysts still pose the major contributors for the prohibitive costs (1.9-2.3 k€/kW) [2–4]. For lowering the loading of such PGMs, the development of highly-structured catalysts that utilize PGM more effectively, the catalyst must display high mass activities, while being durable and possessing low volumetric packing density [5]. Overcoming these challenges will push PEM electrolysis into an economically feasible panorama to serve the large-scale production of green hydrogen.

By dispersing Ir catalysts onto high electrical conductive, large surface area (m^2/g) and highly corrosion resistant supports, there is a possibility to reduce the Ir-loading, while ensuring the maximum utilization of the noble metal to increase the OER mass activity [6]. These approaches are required to achieve the target for the reduction of today's Ir-specific power density in *ca.* 50-fold, down to *ca.* 0.01 g_{Ir}/kW while maintaining high efficiency (assuming electrolyzer efficiency of 70 % LHV – cell potential of *ca.*1.79 V) [7].

Non-noble metal oxides, specifically doped tin oxides (M-SnO_2) with hypovalent or hypervalent ions such as Sb, Nb, F, In, or Ta have been gaining momentum as they show great stability in strong acidic

* Corresponding author: mendes@fe.up.pt

media and delivering noteworthy electronic conductivities, surpassing 0.2 $S \cdot cm^{-1}$ [8–10]. As most metal oxides are semiconductors, doping them with such types of ions present the ultimate pre-requisite to allow an increase of electrical conductivities without compromising a path-free interconnected structure compatible with facile mass transport rates (water and oxygen).

The main objective of this work was to prepare highly active and stable IrO_2-based electrocatalysts via a facile modified polyol synthesis route and screen their activity and stability by carrying out different accelerated stress tests. In this regard, Ir- salt precursors were dispersed on different tin oxide-based nanoparticles, SnO2, SnO_2:Sb_2O_5 (-ITO) and SnO_2:In_2O_3(-ATO). A prepared 30 wt.% IrO_2 catalyst supported on SnO_2: In_2O_3 (1:1)/ 30IrO2/ITO allows to achieve a *ca.*11.5-fold larger OER activity and enhanced stability compared to a commercial benchmark catalyst, IrO_2. Moreover, remarkably *ca.* 3-fold larger BET surface area and electrochemical available surface areas could be achieved with IrOx/SnO_2 and IrOx/ITO, comparatively to IrO_2.

Extensive physico-chemical characterization acquired from TEM, TGA, ICP-OES, XPS, XRD and B.E.T physisorption analyses corroborate with the electrochemical measurements. To the best of the authors knowledge, the OER-mass activities herein reported of as-prepared catalysts (30IrO_2/ITO) are the highest at such operating conditions.

2 Experimental

2.1 Catalyst Preparation

Synthesis of electrocatalysts was carried out by adding 0.6 g of sodium hydroxide into 75 mL of ethane-1,2-diol (vwr) to produce a 0.2 M NaOH solution. This solution was sonicated and stirred for 3 hours. Antimony tin oxide (Sigma Aldrich, < 50 nm diameter), indium tin oxide (Sigma Aldrich, < 50 nm diameter) and tin oxide (Alfa Aesar, <30 nm) were used as received, added to the solution which was then sonicated for 45 minutes. The catalysts were then prepared via a chemical reduction of an IrO_2 salt precursor - $IrCl_3 \cdot xH_2O$ (Alfa Aesar) - in an ethane-1-2-diol solution kept at 175 °C for three hours. After the synthesis, 1 M nitric acid was added to adjust the pH of the solution to *ca.* 1 while stirring it for 4 h. The ratio of the salt precursor: support was maintained as 1:1 m/m. Later, the solution was filtrated and thoroughly washed using 1.5 L of ultra-pure water. The collected IrO_2 based nanoparticles were dried in an oven at 100 °C for 5 h.

2.2 Textural and physico-chemical characterization

Thermogravimetric analyses (TGA) were performed using a thermogravimetric analyser (TG 209 F1 iris, NETZSCH) under 30 cm^3 min^{-1} of airflow, and heating from room temperature to 1000 ºC at 2 ºC min^{-1}. *Ca.* 10 mg of catalyst powder was used in each analysis. The textural properties of each sample were evaluated by N_2 physisorption (-196 °C) in a Quantachrome Autosorb-1 Instruments device. The S_{BET} was obtained from the Brunauer-Emmett- Teller (BET) equation for a nitrogen partial pressure range of (P/P^0) from 0 to 1. The samples (*ca.* 50 mg) were outgassed in vacuum at 200 ºC overnight. Ir wt.% in each synthetized catalyst was confirmed with inductively coupled plasma – optical emission spectroscopy (ICP-OES; Thermo iCAP 7000). The solid samples of catalysts were completely dissolved in *aqua regia*, and, subsequently, diluted in deionized water prior to ICP-OES analyses, using a microwave digestor (Milestone, Start D). The bulk elemental composition of the IrO_2/M-SnO_2 catalysts was analyzed by energy dispersive X-ray spectroscopy (EDS) which was integrated in a Phenom ProX desktop scanning electron microscope (SEM).

2.3 Electrochemical characterization

2.3.1 OER activity and cyclic voltammograms - Cu_{UPD}

A catalyst suspension consisting of 5 mg of electrocatalyst, Nafion ionomer suspension (Quintech, 5 wt.%) and a mixture of ultrapure water (Millipore) and isopropanol (Merck) 1:4 was prepared via ultrasonication for 20 min at 20 kHz. Then, 20 µL of the prepared suspension containing 2.8 ± 0.1 μg_{Ir} was deposited and dried under rotation at 700 RPM on top of a 0.196 cm^2 Au working electrode tip. Electrochemical characterization was carried out in a rotating disk electrode (RDE) from PineResearch, equipped with a Gamry jacketed cell, a carbon rod and saturated Ag/AgCl in 3 M $KCl_{(aq)}$ which served as reference electrode. The bulk electrolyte 150 mL of 0.1 M $HClO_4$ solution was firstly saturated with Ar (mL/min) and a conditioning step took over consisting of 100 cycles from 0 V to 1.4 V vs RHE at 100 $mV \cdot s^{-1}$. Immediately after 3 cyclic voltammograms were retrieved at the same potential window at 20 mV/s.

An electrochemical impedance spectrum (EIS) was recorded to retrieve the ohmic resistance contribution from the electrolyte at 1 kHz with 10 mV of amplitude. Three linear sweep voltammograms were recorded at 2 mV s^{-1} to measure the OER specific activity at 1.51 V vs. RHE, and the ohmic resistance contribution was subtracted. The electrochemical performance of the prepared catalysts was compared with that of a commercially available IrO2 from Premetek, Co. To estimate the number of active sites available to process

the OER, a separate Cu_{upd} method was followed. The electrode was kept in a purged (Ar) 0.1 M H_2SO_4 electrolyte at 0.05 V *vs.* RHE for 10 minutes to reduce the reversible iridium oxide species formed throughout the synthesis. The electrode was cycled in the potential range from 0.2 V to 0.72 V *vs.* RHE at 20 mV for obtaining a first background CV. Afterwards, the electrode was reduced again for 15 min at 0.05 V. The first electrolyte was replaced by other containing 0.5 M H_2SO_4 and 5 mM of Cu_2SO_4 (Alfa Aesar). The electrode was cycled for 5 times (0.2 V to 0.72 V *vs.* RHE at 20 $mV \cdot s^{-1}$) to retrieve the Cu UPD voltammogram. Copper has a similar radius to that of metallic Iridium, 128 pm and 136 pm, respectively. By initially keeping the electrode at 0.05 V and then cycling it under these potentials, each Cu atom will adsorb/desorb on the surface of each iridium atom. By integrating the UPD (stripping) peak area it was possible to retrieve the amount of active Ir sites from each catalyst.

2.3.2 Stability Protocols

The first accelerated stress test (AST1) consisted of a controlled current electrolysis at 10 $mA \cdot cm^{-2}$ for 2 h under Ar saturated electrolyte, while keeping the electrode rotating at 1600 RPM [11] to avoid the accumulation of O_2 bubbles on top of the electrode. EIS, LSV and CV were again recorded to compare with initial performance. A second, separate AST, consisted of cycling the potential from 0.8 V – 1.0 V for 10 k cycles at the scan rate of 100 $mV \cdot s^{-1}$, while rotating the electrode at 200 RPM [11]; the latter serves as benchmark degradation protocol for heterogeneous catalysts to perform OER and therefore deeply understand the interaction between support and the catalyst.

3 Results and Discussion

3.1 Characterization of synthetised electrocatalysts

IrO_2 based catalysts supported on tin doped oxide nanoparticles were prepared following a polyol chemical reduction in alkaline media, as depicted in Fig. 1. The effective loading of Ir on each electrocatalyst was very similar for each prepared sample, *ca.* 30 ±2.3 wt.% as confirmed with ICP-OES. This proves that the synthesis was successful and the reaction conversion mostly complete.

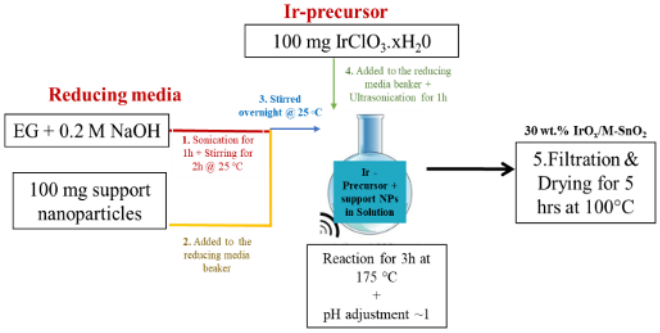

Fig. 1. Synthesis pathway to prepare IrO_2 supported on tin oxide-based nanoparticles via a polyol reduction in NaOH.

EDS analysis to the supports provided information regarding the weight concentration ratio of the dopants, Sn and In, Fig. 2; both represented 18 ± 0.06 wt.% of Sn and 47.6 ± 0.13 wt.% of the overall weight of the support, respectively.

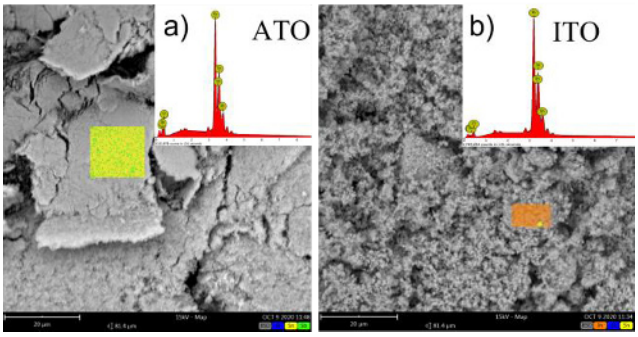

Fig. 2. EDS chemical mapping obtained for the supports a) ATO and b) ITO.

The thermal gravimetric decomposition curves of the synthesized catalysts and commercial IrO_2 demonstrate mainly two weight loss regions (as seen in Fig. 3). An immediate weight loss was detected for all the electrocatalysts except for IrO_2, from 90 °C to 220 °C and is attributed to the release of moisture from the 3D microstructure. As perceived from Table 1, $30IrO_2$/ATO demonstrates the steepest weight loss (~8 %) due to the desorption of interstitial water and that could be attributed to its microstructure, as it is the one evidencing the largest pore volume and hence porosity; the latter is opposed to IrO_2 which appears to possess a more hydrophobic metallic nature and is, amongst all, the one owning the lowest pore volume and average pore diameter. From *ca.* 850 °C to 1000 °C, iridium tends to degrade from IrO_2 to IrO and the fact that Ir is dispersed on a tin oxide support enables to increase the thermal stability as the weight drop is less significant for all the prepared electrocatalysts comparatively, to non-supported commercial IrO_2 [12].

Overall, ITO containing catalyst depicted remarkable thermal stability up to 1000 °C with no significant weight variation (loss of *ca.* 3 % of initial weight).

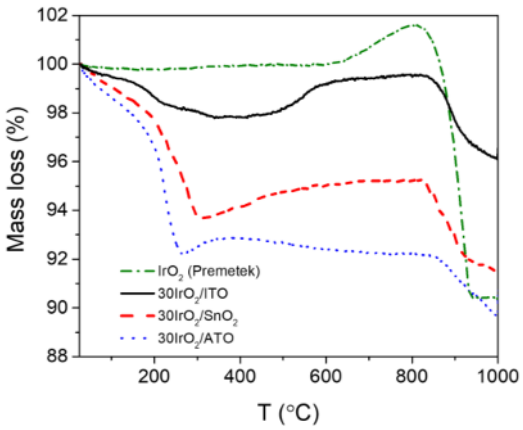

Fig. 3. TG curves for the prepared electrocatalysts from room temperature to 1000 °C under air flow – 200 mL·min^{-1}.

The activity of the synthesised electrocatalysts towards the OER, was derived from the average value of current at 1.51 V vs. RHE from three LSVs normalized by the mass of Ir in the working electrode. A scan rate of 2 mV·s^{-1} at 1600 RPM was used and the loading of the active metal, Ir, was kept similar throughout the experiments with the different electrocatalysts (10 μg_{Ir}·cm^{-2}). Fig. 4a) shows the OER polarisation curves and all the prepared electrocatalysts demonstrate an evident earlier onset happening at *ca.* 1.48 V vs. RHE comparatively to the benchmark catalyst. In fact, solely after an overpotential of nearly 390 mV does IrO_2 initiate the OER.

The kinetic mechanisms are facilitated for the remaining catalysts as a much lower overpotential is required to deploy the reaction, in detail: 30IrO_2/ITO (η=240 mV) < 30IrO_2/SnO_2 (255 mV) < 30IrO_2/ATO (η *ca.* 270 mV). Moreover, considerably higher limiting current densities can be achieved at such lower overpotentials, specially for ITO and SnO_2 supported IrO_2 catalysts, both reaching *ca.* 55 mA·cm^{-2} @ 1.58 V vs. RHE.

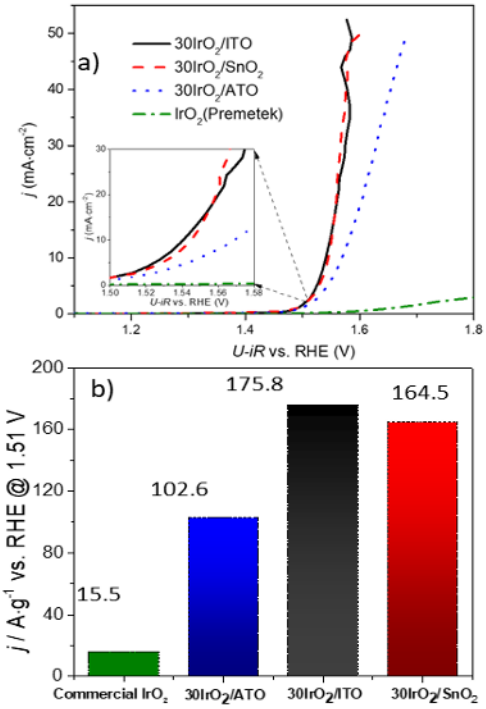

Fig. 4. a) OER polarisation curves for the studied catalysts retrieved at 2mV/s in Ar- saturated electrolyte 0.1 M $HClO_4$ at 1600 RPM and b) OER-mass specific activities retrieved at 1.51 V vs RHE normalized per the equal mass of Ir (2 ± 0.2 μg_{Ir}) in the Au tip (0.196 cm^2) for each catalyst.

The OER-mass specific activity for each catalyst is described in detail in Fig. 4b). A 11.5-fold higher MA could be attained with the prepared catalyst consisting of 30 wt.% of Ir(Ox) supported on ITO (where the dopant In represents *ca.* 33.4 % of the total electrocatalyst weight) vs the commercially available catalyst. Therefore, this electrocatalyst together with the dopant free SnO_2 IrO_2-based catalyst emerge as some of the highest and most promising OER supported catalysts ever reported at low Ir loadings at such operating conditions (175.8 and 164.8 mA/g @1.51 V for 10µg·cm^{-2} at 1600 RPM). Fig. 5 shows the CV curves for the prepared electrocatalysts and the commercial IrO_2 at 20 mV·s^{-1} in 0.1 M $HClO_4$.

Undoubtedly, the type of support deeply influences the reversibility of the system, as the redox couples shift slightly in the potential window to more reducing or oxidative potentials. However, the most symmetric CV and most likely electrochemically reversible electrocatalyst appears to be 30IrO_2/ITO since the peak-to-peak potential difference is small (certainly below < 57 mV at 25 °C) and the ratio between the anodic and cathodic peak/ forward-reverse scan peak current ratios reaches the ideality ($i_{pa}/i_{pc} \approx 1$) [13,14]; ITO-based electrocatalyst is the one exhibiting the more evident and symmetric set of redox peaks from 0.85 V to 0.95 V vs RHE attributed to the Ir^{3+}/Ir^{4+} redox reaction whilst the defined peaks emerging at 1.2 V to 1.35 V refer to the oxidation of Ir from Ir^{+4} to Ir^{5+} (forward scan) [15]. Several works report iridium valence states of $n \geq +4$ as

OER active but unstable, as dissolution mechanisms are generally triggered by the appearance of higher oxidation states.

Thereupon, among the synthesized catalysts, it is predictable that the catalyst $30IrO_2$/ITO may be more stable although not necessarily more active, at higher potentials comparatively to SnO_2 or ATO-supported catalysts [16]. All the catalysts have originated a hydrous Ir oxide (IrOx) specie. as if there was any Ir metallic character. The respective set of peaks would have appeared at low potentials 0.05 V < *U*< 0.35 V vs RHE.

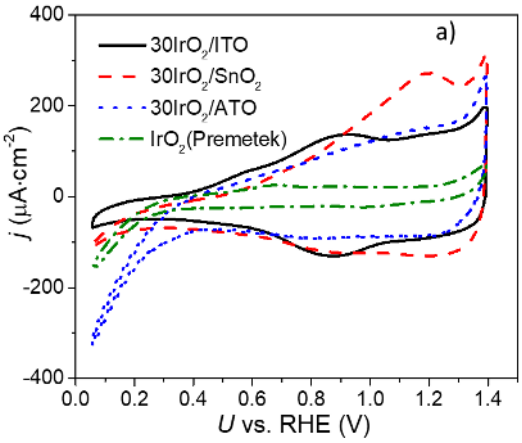

Fig. 5. Cyclic voltammograms of the synthetized electrocatalysts under Ar- saturated 0.1 M $HClO_4$ electrolyte at 20 $mV \cdot s^{-1}$ potential scan rates.

Cu_{UPD} was used as *in-situ* method to derive the active surface area of each catalyst. Table 1 presents the results for the attained charge related to the adsorption of Cu^{2+} ions on each iridium atom. Both SnO_2 and ITO display the greatest adsorbed charge, which is proportional to a larger number of effective active crystal planes from the supported IrO_2 (*ca.* 3-fold and 2-fold higher electrochemical total charge for $30IrO_2/SnO_2$ and $30IrO_2$/ITO, respectively and relatively to the commercial IrO_2). These results corroborate BET results and, although the OER-MA is slightly higher for $30IrO_2$/ITO while the surface areas are marginally superior for $30IrO_2/SnO_2$, it is important to address the morphology of the catalysts as it may be that the crystallinity and number of most active Ir facets is superior for the former ($30IrO_2$/ITO).

Besides, IrO_2 nanoparticles dispersed on ITO and SnO_2 revealed an average particle size of 2.4 nm and 2.9 nm compared to *ca.* 6.3 nm for those supported on ATO; all the former also approached a more acicular/round shape utterly distinct from the ordered IrO_2 nanoclusters, which present an average diagonal length of about 21.8 nm; typically, the electrochemical active area decreases with increasing average particle size.

Table 1. B.E.T estimated surface area, pore volume, average pore diameter and effective charge associated to Cu_{UPD}.

	IrO_2	**IrO_2/ATO**	**IrO_2/ITO**	**IrO_2/SnO_2**
B.E.T surface area ($m^2 \cdot g^{-1}$)	96.4	135.4	150.1	152.0
Pore Volume ($cm^3 \cdot g^{-1}$)	0.140	0.245	0.192	0.158
Avg. Pore Diameter (nm)	2.96	3.11	3.30	3.12
Cu_{UPD} adsorbed charge ($C \cdot s^{-1}$)	36.1	57.4	73.5	100.8

3.2 Stability tests

Concerning the first degradation protocol and the figure of merit for the OER activity Fig. 6a), which correlates the overpotential required to reach 10 $mA \cdot cm^{-2}$ after a specific period (2 h), it is possible to rapidly assess the stability of the stressed catalysts. The centred dashed line represents the potential dependant ideal catalyst response.

The overpotential of $30IrO_2$/ITO throughout the chronopotentiometry remained practically unchanged and therefore the deviation from the ideal behaviour is small, comparatively to the remaining electrocatalysts, as their final overpotential reached *ca.* 1 V *vs* RHE, including the commercial catalysts. By analysing the OER LSVs at Beginning of Life (BoL) and then at End of Life (EoL), Fig. 6b) and the limiting current density variation values from Table 2, it is quite noticeable the increment in mass transport limitations in all of them after the AST1. The commercial catalyst though, could barely endure the entire protocol, as there was no evident onset, and no current limited plateaux could be attained. The justification may rely in the fact that the mechanical integrity of the unsupported catalyst became compromised, perhaps due to the continuous entrapped bubbles of O_2 which may have triggered a dissolution mechanism or mechanical detachment from the working electrode into de bulk electrolyte - loss of 94 % of the initial limiting current density and 48 % of OER-MA loss with the long-term test. However, the presence of ITO, SnO_2:In_2O_3(1:1) as support appears to stabilize IrO_2 NPS thus contributing to the visible smallest drop in OER-activity (15 %).

But, overall, no evident conclusions may be associated with the fact that the use of dopants triggers dissolution mechanisms of Iridium, as described in recent works [17]; nonetheless the synthesis pathway is very distinct. On the other hand, OER activity and stability of the electrocatalyst $30IrO_2$/ITO is even superior compared to that of the undoped support (SnO_2); even so, the

30IrO_2/ATO, which contains a different dopant and lower ratio of Sb on the catalyst, delivers a lower performance comparatively to the undoped electrocatalyst. These results infer therefore, that the stability and OER-activity is highly dependent on the synthesis procedure and on the ratio between dopant and the active metal.

iR-corrected Tafel plots, Fig.6c) that display geometric normalized current on logarithmic scale, demonstrate a linear fit of the Butler-Volmer equation applied to potentials ranging from 1.45 V to 1.6 V vs RHE. Noticeable lower Tafel slopes at BoL could be acquired for the catalysts 30IrO_2/ITO (41.4 mV·dec^{-1}) < 30IrO_2/ATO (59.4 mV·dec^{-1}) < 30IrO_2/SnO_2 (67.5 mV·dec^{-1}) < IrO_2 (93.1 mV·dec^{-1}), which corroborates to the 86 mV·dec^{-1}obtained in other works considering the same overpotentials [18].

After the AST, all the Tafel slopes increased at the same potential window indicating more complicated electron transfer processes possibly indicating the deterioration of the electrocatalysts; the causes for higher Tafel slopes may be attributed to increased mass transport resistance caused by the deterioration and rearrangement of the electrocatalysts' microstructure, loss of crystallinity, growth of Ir average particle size and consequently lower number of active sites or even detachment of active material from the WE surface.

Still, ITO supported IrO_2 catalyst shows the smallest increment in the Tafel slope (44.2 mV·dec^{-1}, *ca.* + 7 %), followed by 30IrO_2/SnO_2 (83.3 mV·dec^{-1}= + 23.3 %), 30IrO_2/ATO (81.9 mV·dec^{-1}= + 37.9 %). The unsupported commercial IrO*2* catalyst clearly suffered excessive and evident undesirable modifications in the reaction mechanisms, as a much higher Tafel slope was originated (*ca.* 192 mV·dec^{-1} after the AST2). This indicates that consecutively higher overpotentials are needed as higher energy barrier is imposed to deploy OER. In this regard, ITO stands a reliable support to stabilize IrO_2 NPs for long term operation at steady current densities.

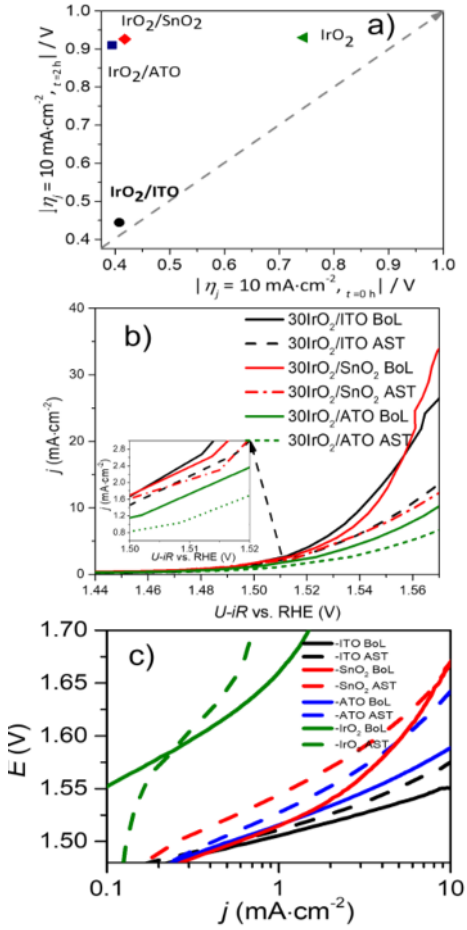

Fig. 6. a) Universal plot of merit for OER-MA activity and stability - the xx axis stands for the overpotential needed to achieve 10 mA/cm^{2}geo when t=0. The yy axis is the overpotential required to reach 10 mA·cm^{-2} time t=2 h; grey dashed diagonal represents the ideal output from a stable catalyst; b) OER polarisation curves at Beginning of Life (BoL) and after the AST1, End of Life (EoL) of the supported catalysts; c) corresponding Tafel plots for all the studied electrocatalysts (commercial IrO_2, 30IrO_2/SnO_2, 30IrO_2/ATO and 30IrO_2/ITO) , before (bold) and after (dashed lines) the AST1 recorded at 2 mV·s^{-1} and 1600 RPM.

Table 2. Variation of current density values at plateaux and loss of OER mass activity after AST1.

AST1	**IrO_2**	**30IrO_2 /ATO**	**30IrO_2 /ITO**	**30IrO_2 /SnO_2**
Limiting current density at **BoL** (mA·cm^{-2})	10.8	21.7	52.4	49.7
Limiting current density at **EoL** (mA·cm^{-2})	0.66 (-94 %)	15.2 (-30 %)	22.3 (-57 %)	21.1 (-58 %)
OER-mass activity loss at EoL @ 1.51 V vs. RHE (%)	48	34	15	21

AST2 consisted of extensively cycling the potential for 10 k cycles from 0.8 V to 1.0 V vs RHE at 100 mV·s^{-1}. The potential window at which occurs the cycling stands for the conventional Ir(III)/Ir(IV) redox couple corresponding to the formation of the hydrous Ir – $IrO_x(OH)_y(H_2O)_z$.

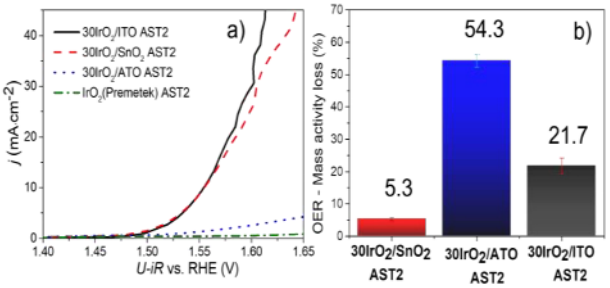

Fig. 7. a) OER polarisation curves EoL after the AST2; c) loss of OER mass activity, recorded at 1.51 V vs RHE at 2 mV·s^{-1} and 1600 RPM (10 µgIr·cm^{-2}).

Interestingly, the shape of CVs varied deeply, especially for the ATO supported and unsupported IrO_2 electrocatalysts, as an eminent loss of peaks could be perceived with a slightly shift to more oxidative potentials of the commercial catalyst. The later hints for the formation of unstable Ir oxidation states ($n \geq +4$), known to trigger degradation mechanisms and cause the loss of activity and inability of reaching a limiting current density plateaux, evident from Table 3 and Fig. 7a).

Table 3. Variation of current density values at plateaux and OER after AST2.

AST2	**IrO_2**	**30IrO_2/ ATO**	**30IrO_2/ ITO**	**30IrO_2/ SnO_2**
Limiting current density loss at **EoL** (%)	- 95	- 89	- 36	-51
OER-mass activity loss at EoL (%)	- 56	-54.3	-21.7	- 5.3

Once again, the catalyst 30IrO_2/ITO demonstrated superior stability and activity after the AST2, although the non-doped SnO_2 based catalyst demonstrated higher mass-activity – and a smaller performance drop after cycling (5.3% comparatively to BoL) - which might had been a direct cause of porosity increment throughout the catalyst´s microstructure, mainly micropores; in fact, higher MA may be associated to the a greater availability of active sites or reorientation of Ir facets to more active states, due to the intensive cycling on this region. However, 30IrO_2/SnO_2 demonstrate slightly higher mass transport limitations, comparatively to 30IrO_2/ITO (see Fig. 7b and limiting current density drop in Table 3).

4 Conclusion

A modified polyol chemical reduction synthesis route was effectively utilized to produce highly active and stable electrocatalysts consisting of 30 wt. % of noble Ir metal dispersed on ATO, ITO and SnO_2 nanoparticles.

The prepared catalysts not only demonstrated remarkably higher BET surface areas and larger effective electrochemical areas which in turn enabled these electrocatalysts to surpass the initial OER-activity of commercial IrO_2 in a maximum of *ca.*12-fold. Overall, dispersing Ir salt precursor onto these supports had a positive impact on the performance and stability of the prepared electrocatalysts. Important observations are:

- The stability of an electrocatalyst after either current controlling or potential cycling and the immediate EoL OER-activity is highly dependent on the synthesis procedure and on the ratio between dopant and the electrochemical active metal.
- The catalyst 30IrO_2/ITO with a dopant ratio of *ca.* 33 % on the overall electrocatalyst weight demonstrated the greatest initial OER-MA activity and showed comparable results in terms of activity and stability with the undoped counterpart, 30IrO_2/SnO_2, on delivering the best stability after both ASTs.
- AST2 caused the highest impact on loss of performance overall; the formation of less stable Iridium species (n >+4) was mainly triggered on unsupported IrO_2 and Sb doped (*ca.* 15 % dopant on total weight of catalyst) based catalysts.

In depth, investigations on the optimum ratio of In dopant/Iridium loading should be led following this synthesis method to tune this promising electrocatalysts and pave the way for the mass commercialization of PEMWEs for large scale applications.

Acknowledgment

This work was financially supported by the project UID/EQU/00511/2020 of the Laboratory for Process Engineering, Environment, Biotechnology and Energy – LEPABE - funded by national funds through FCT/MCTES(PIDDAC). Eva Sousa and Sofia Delgado are grateful to the Portuguese Foundation for Science and Technology (FCT) for the doctoral grants (references SFRH/BD/145412/2019 and SFRH/BD/144338/2019, respectively).

References

1. F. Smolinka, Tom.;Wiebe Nikolai.; Sterchele Philip.; Palzer, Andreas. ; Lehner, Franz.; Jansen, Malte.; Kiemel, Steffen.; Miehe, Robert.; Wahren, Sylvia.; Zimmermann, *Industrialisation of Water Electrolysis in Germany: Opportunities and Challenges for Sustainable Hydrogen for*

Transport, Electricity and Heat (Berlin, 2018)
2. U. Babic, M. Suermann, F. N. Büchi, L. Gubler, and T. J. Schmidt, J. Electrochem. Soc. **164**, F387 (2017)
3. M. Carmo, D. L. Fritz, J. Mergel, and D. Stolten, Int. J. Hydrogen Energy **38**, 4901 (2013)
4. K. E. Ayers, J. N. Renner, N. Danilovic, J. X. Wang, Y. Zhang, R. Maric, and H. Yu, Catal. Today **262**, 121 (2016)
5. C. Spöri, J. T. H. Kwan, A. Bonakdarpour, D. P. Wilkinson, and P. Strasser, Angew. Chemie - Int. Ed. **56**, 5994 (2017)
6. L. Wang, P. Lettenmeier, U. Golla-Schindler, P. Gazdzicki, N. A. Canas, T. Morawietz, R. Hiesgen, S. S. Hosseiny, A. S. Gago, and K. A. Friedrich, Phys. Chem. Chem. Phys. **18**, 4487 (2016)
7. M. Bernt, A. Siebel, and H. A. Gasteiger, J. Electrochem. Soc. **165**, F305 (2018)
8. H. Ohno, S. Nohara, K. Kakinuma, M. Uchida, and H. Uchida, (2018)
9. S. Geiger, O. Kasian, A. M. Mingers, K. J. J. Mayrhofer, and S. Cherevko, Sci. Rep. **7**, 1 (2017)
10. H.-S. Oh, H. N. Nong, and P. Strasser, Adv. Funct. Mater. **25**, 1074 (2015)
11. M. CC, J. S, P. JC, and J. TF, J. Am. Chem. Soc. **135**, 16977 (2013)
12. F. Karimi, B. A. Peppley, and A. Bazylak, ECS Trans. **69**, 87 (2015)
13. R. G. Compton and C. E. Banks, Underst. Voltammetry, 2nd Ed. 1 (2010)
14. A. J. Bard, J. Am. Chem. Soc. **129**, 242 (2007)
15. B. Zhang and D. S. Su, ChemCatChem **7**, 3639 (2015)
16. N. Danilovic, R. Subbaraman, K.-C. Chang, S. H. Chang, Y. J. Kang, J. Snyder, A. P. Paulikas, D. Strmcnik, Y.-T. Kim, D. Myers, V. R. Stamenkovic, and N. M. Markovic, J. Phys. Chem. Lett. **5**, 2474 (2014)
17. G. C. da Silva, S. I. Venturini, S. Zhang, M. Löffler, C. Scheu, K. J. J. Mayrhofer, E. A. Ticianelli, and S. Cherevko, ChemElectroChem **7**, 2330 (2020)
18. Z. Ma, Y. Zhang, S. Liu, W. Xu, L. Wu, Y. C. Hsieh, P. Liu, Y. Zhu, K. Sasaki, J. N. Renner, K. E. Ayers, R. R. Adzic, and J. X. Wang, J. Electroanal. Chem. **819**, 296 (2018)

Optimized design and simulation of a hybrid storage system based on hydrogen as an energy carrier

Maria Alessandra Ancona[1*], *Michele* Bianchi[1], *Lisa* Branchini[1], *Francesco* Catena[1], *Andrea* De Pascale[1], *Federico* Ferrari[1], *Francesco* Melino[1] and *Antonio* Peretto[1]

[1]DIN – Università di Bologna, Viale del Risorgimento 2, 40136 Bologna, Italy

Abstract. The integration of renewable energy sources into the electricity system can contribute to the development of a low-carbon economy. However, due to the intermittency and non-programmability of these sources, problems related to the management of local electricity grids may occur. A possible solution or limitation to these issues is given by the electrical storage. In addition, in the next future, domestic micro-grids are expected to play a fundamental role in electric power networks, driving both the academic and industrial research interests in developing highly efficient and reliable conversion and storage technologies. In this study, the behavior of a small-scale hybrid energy system for hydrogen production and storage has been predicted, by means of a developed calculation model, and the operational strategy of the system has been optimized with the aim to maximize the hydrogen production. In addition, with the aim to maximize the overall solar-to-hydrogen chain efficiency, the whole system model has been applied to different operating scenarios, to identify the optimal management strategy to control it.

1 Introduction

In the last years, the growing attention to the environmental issues, such as the need to reduce pollutant emissions or to find alternatives to the fossil fuels, has led to an increase in the efforts of the scientific research to improve the Renewable Energy Sources (RES) utilization [1, 2]. These resources, especially wind and solar, in addition to their characteristic of zero emissions production during their operation, present the advantage that they can be employed in those applications where there is no connection to the electricity grid, such as in rural areas [3, 4]. However, the main limit of the renewables is represented by their non-programmability. Consequently, the problem of mismatch between the energy available from the renewables and the energy demand of the users is one of the main issues related to the increase in the RES exploitation. A possible solution to the mismatch problem can be the implementation of Electrical Energy Storage (EES) systems [5-8]. These systems allow to store the energy produced by the renewable sources when it is higher than the one required by the user; then, the stored energy can be used when the renewable source production is not sufficient to satisfy the user's demand. For a photovoltaic system, a common solution is the utilization of a battery bank. The batteries show a fast charge/discharge capacity and a good round-trip efficiency. On the other hand, batteries are not indicated for long-term storage, mainly for leakage phenomena and low energy density [9, 10]. Thus, a viable solution can be represented by hybrid battery/hydrogen systems, which combine the good performance of the battery for the short-term storage with the one of the hydrogen for long-term storage. Indeed – being one of the leading options to store energy from renewables and looking promising as low-cost option to store electricity over days, weeks or even months – the hydrogen production may increase the share of renewables [11]. In addition, hydrogen is very versatile. Technologies already available today enable hydrogen to produce, store, move and use energy in different ways: indeed, it can be employed to produce electricity (via fuel cells) or methane, to power homes and feed industry or to fuel cars, trucks, ships and planes.

Concerning the hydrogen storage for a subsequent electricity production, the system is usually made up of an electrolyzer, in order to produce hydrogen through the electrolysis of the water, a hydrogen storage system – e.g. metal hydrides canisters – and a fuel cell. In literature, the optimization of these systems is widely studied [12 - 19].

One of the key aspects to be considered for the hybrid systems is the choice of the Power Management Strategy (PMS). Indeed, in these systems there are many solutions to distribute the energy from the renewable source to the several storage devices and to the electrical load. The choice of the PMS depends on the system configuration and on the aim of the application [20 - 24].

In this context, the aim of this paper is the analysis of an experimental hybrid system set-up, composed of photovoltaic panels, batteries and an electrolyzer, in order to define the optimal operational strategy. In detail, different scenarios have been defined in terms of PV panels and electrolyzer off-design operation, allowing to optimize the PMS of the whole system with the purpose of maximizing the hydrogen production and, consequently, also the overall solar-to-hydrogen chain efficiency. The detail of the novelty of the proposed study is discussed in the following paragraph.

* Corresponding author: maria.ancona2@unibo.it

The study proposed in this paper analyses a small-scale hybrid photovoltaic/battery/hydrogen system, which consists of PV panels, a battery bank, an electrolyzer and metal hydrides canisters for the hydrogen storage. This paper represents a prosecution of the Authors' previous studies [25, 26]. While in these previous works [25, 26] the models and characterization of each component has been presented, in terms of efficiency evaluation as a function of the boundary and operational conditions, the aim of this paper is to develop a calculation code for the system management, able to simulate the behavior of the whole system and to evaluate the performance of the micro-grid operating with various strategies, to define the optimal one. In particular, the optimization of the management strategy of the system is made to maximize the hydrogen production and thus the system efficiency.

As for the Authors' best knowledge, the main contribution of this work with respect to the literature stands in the proposed method, giving the possibility of evaluating and comparing several management strategies on the same system with the aim to maximize the hydrogen production. The proposed approach is general and can be applied both for the short-term and for the long-term storage. In addition, the relevance of this paper stands in the laboratory size scale analyzed (micro-size) with respect to the large-scale systems usually studied, as a starting point to test the employment of the hybrid storage technology for residential applications. Then, different scenarios – in terms of strategy for the control of the operation of the PV panels, battery bank and hydrogen generator – have been evaluated and compared, with the aim to figure out how the selected strategy influences the system performance. In particular, the performance indicators overall defined for the comparison are the solar-to-hydrogen chain efficiency and the storage efficiency, as well as the hydrogen production. The validation of the management strategies for the hybrid system overall are the object of experimental tests which are in progress now and the related results will be presented in future studies. As a support for this study, an experimental test bench is being set up dedicated to the emulation of the physical devices that are part of the microgrid, with the aim of optimizing the management and control strategies of the entire system.

2 Microgrid description

The Figure 1 shows a schematic layout of the micro-grid installed at the laboratory of the University of Bologna. The micro-grid is composed by the following devices:

- two PV panels parallel connected;
- two batteries (lead-acid gel technology);
- a solar charge regulator to connect the PV panels to the batteries; • a DC/DC Converter to feed a DC load;
- a DC/AC inverter;
- an electrolyzer (PEM technology);
- three metal hydrides canisters for the hydrogen storage.

In Figure 1 the measuring sensors are indicated by the red circles: it can be noticed that voltage (ER) and current (IR) values are measured in every system branch. In addition, the ambient temperature (TR1), the PV panels operating temperature (TR2) and the solar radiation (RR) are measured by means of a pyranometer equipped with thermocouples. Finally, the sensors installed within the hydrogen generator measure the quality of the water (QR) and the volumetric flow rate (LR).The PV panels are made of polycrystalline silicon and are parallel connected. The rated power of a single panel in Standard Test Conditions (STC: Solar radiation 1000 W/m2, Cell Temperature 25 °C with a spectrum of AM 1.5) is equal to 220 W, while the rated efficiency is equal to 15 %. The solar charge regulator has the aim to couple the PV panels to the batteries.

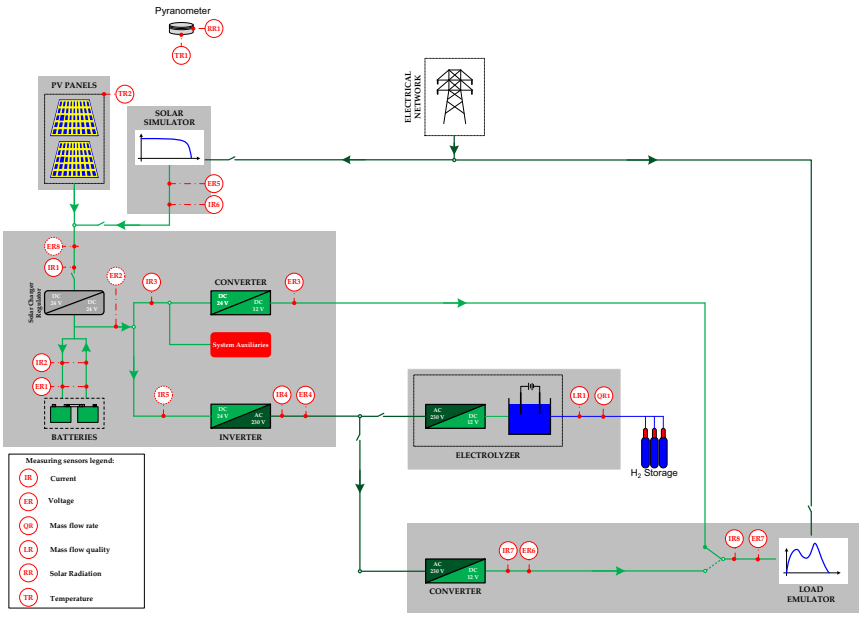

Fig. 1. Layout of the integrated laboratory micro-grid with the installed measuring sensors.

Its control strategy is the Pulse Width Modulation (PWM) mode. This, in addition to the controller protection functions (including the overcharge and the deep discharge protection) ensures the optimal operating conditions of the batteries. These, each one with a capacity of 55 Ah and a nominal voltage equal to 12 V, are coupled in series; therefore, the resulting voltage is 24 V. The system has a DC/DC converter (Meanwell SD-25B-12) to feed a DC load and a DC/AC inverter (Meanwell TS-700-224B) for an AC load. Finally, there is an electrolyzer within an internal AC/DC converter to feed the electrolysis process. The produced hydrogen is stored into three metal hydrides canisters at a storage pressure of 10 bar. A more detailed description of the experimental microgrid test bench system can be found in a previous Authors' publication [25], reporting mathematical models of each component and their experimental characterization [26].

3 Management strategy analysis

For a system that couples solar arrays, batteries and an electrolyzer, several possible management strategies are available in literature [20-24]. The strategies analyzed in this paper, presented in Figure 2, are focused on the handling of the PV panels and of the electrolyzer. In more detail, the PV panels operating mode is determined by the solar charge regulator: indeed, they can operate in MPP or in PWM mode, related to the possibility of maintaining a different voltage between the PV panels and the batteries. If they are independent from the battery voltage, they can work in MPP mode producing as much power as possible. On the other hand, if their voltage has to be the same as the one of the battery, they work in PWM mode to ensure optimal operating conditions of the batteries. Therefore, their performance depend on the battery State Of Charge (SOC), which is correlated to the voltage. On the other hand, the electrolyzer can work at fixed-point mode or at variable-point: in the first case (Figure 2a) a constant input power feeds the electrolyzer, which works at its maximum efficiency point; in the second case (Figure 2b) the electrolyzer is able to work within a power supply range, then the maximum efficiency is not guaranteed. In all the analyzed strategies, the electrolyzer power supply has the priority.

In particular, in the developed management strategies the power provided by the PV panels is checked for each time step of the considered time horizon:

- if, in the considered time-step, the power produced by the PV panels is lower than the minimum operating power of the electrolyzer, then: if the battery SOC is higher than the minimum admissible SOC value (equal to 30 % for the considered system), the power produced by the PV panels is integrated by the batteries; if the battery SOC is lower than the minimum admissible SOC value, the battery discharge is interrupted in order to avoid a deep discharge of the battery;
- if, in the considered time-step, the power produced by the PV panels is within the operating range of the electrolyzer, then all the produced electric power is employed by the electrolyzer;
- if, in the considered time-step, the power produced by the PV panels is higher than that required by the electrolyzer, then: if the battery SOC is lower than the maximum admissible SOC value (equal to 100 % for the considered system), the difference between the power produced by the PV panels and the maximum operating power of the electrolyzer is employed to charge the batteries; if the battery SOC reaches the maximum admissible SOC value, the battery charge is interrupted and the excess power is wasted.

The power required by the electrolyzer depends on its operating mode. If it works at fixed-point mode the reference parameter for the energy flow management is the supply power corresponding to the maximum hydrogen generator efficiency. On the contrary, if the electrolyzer works at variable-point mode, the reference parameters for the energy flow management are the minimum and the maximum allowed supply powers of the hydrogen generator. In this case, when the power produced by the PV panels is outside of the operating range of the electrolyzer, then the latter is supplied at the maximum power.

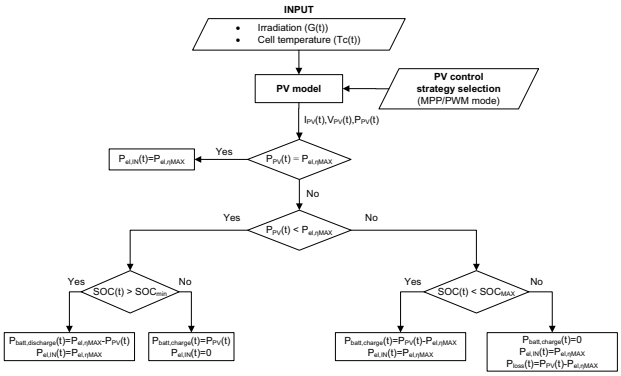

a) MPP/PWM strategy with hydrogen generator at fixed-point (HGF).

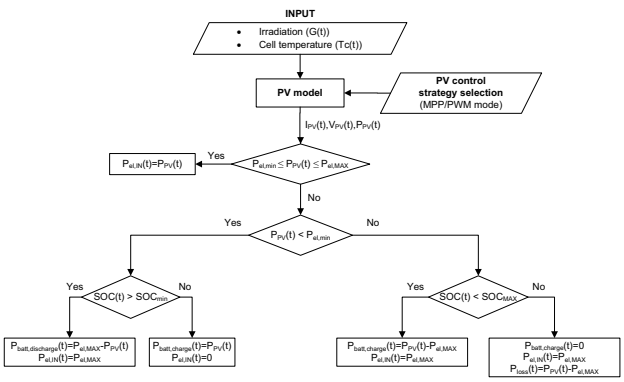

b) MPP/PWM strategy with hydrogen generator at variable-point (HGV).

Fig. 2. Flow chart of the analyzed management strategies.

* Corresponding author: maria.ancona2@unibo.it

In this study four different strategies have been analyzed. In addition, for each strategy, the electrolyzer has been evaluated in two operating modes: fixed-voltage mode and variable-voltage mode. Then, a total of eight cases have been considered. The Table 1 summarizes the features of the eight case studies.

A system simulation model has been developed to manage the power fluxes through the different components. Since the model has to simulate the behavior of the PV panels, it requires the values of the irradiation (RR) and of the cell temperature (T_{cell}) as external inputs Indeed, starting from these values it is possible to estimate the power produced by the PV panels and feeding the system. The values of the irradiation and of the cell temperature used in this analysis have been recorded during laboratory tests; the same values have been used to compare the different case studies. Figure 3 shows the trend of the irradiation recorded during the tests as a function of the time (time step equal to 5 seconds). In order to compare the management strategies above described, first of all the overall solar-to-hydrogen efficiency (η_{tot} [-]) has been used [25]:

$$\eta_{tot} = \frac{m_{H_2} \cdot HHV_{H_2}}{\int_0^t RR \cdot S_{PV} dt} \quad (1)$$

where m_{H_2} [kg] is the hydrogen produced during the considered time horizon (t), HHV_{H_2} [kJ/kg] is the higher heating value of the hydrogen, RR [W/m^2] is the time varying solar radiation and S_{PV} [m^2] is the total surface of the PV panels. The results in terms of η_{tot} are shown in Figure 4 for each simulated scenario. In addition, in order to better explain these results, the hydrogen production, as a function of the power at the inlet of the electrolyzer, is presented in Figure 5, while the trend of the state of charge of the batteries, as a function of the time step, is presented in Figure 6.

Table 1. Features of the eight analyzed management strategies.

Case	PV panels	Hydrogen generator	
MPP-HGF fixed-voltage	MPP	Fixed-point	Fixed-voltage
MPP-HGF variable-voltage	MPP	Fixed-point	Variable-voltage
MPP-HGV fixed-voltage	MPP	Variable-point	Fixed-voltage
MPP-HGV variable-voltage	MPP	Variable-point	Variable-voltage
PWM-HGF fixed-voltage	PWM	Fixed-point	Fixed-voltage
PWM-HGF variable-voltage	PWM	Fixed-point	Variable-voltage
PWM-HGV fixed-voltage	PWM	Variable-point	Fixed-voltage
PWM-HGV variable-voltage	PWM	Variable-point	Variable-voltage

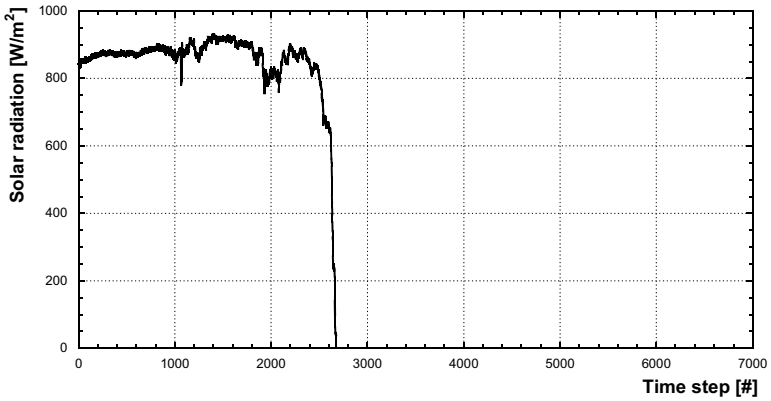

Fig. 3. Experimental trend of the irradiation in the considered time horizon (each time step corresponds to 5 s).

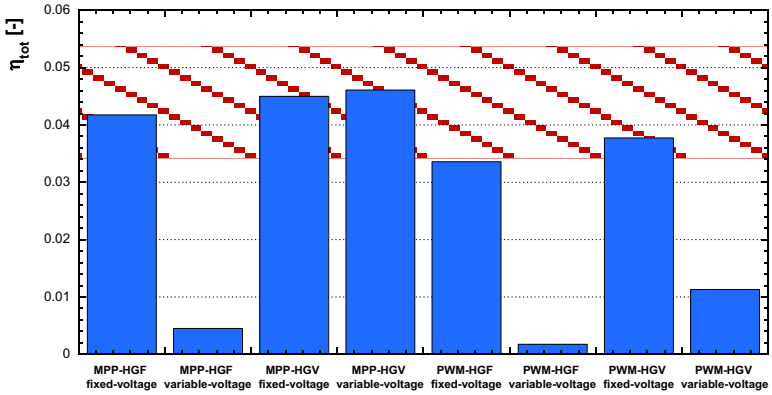

Fig. 4. Overall solar-to-hydrogen efficiency obtained for the analyzed scenarios. The red area represents the efficiency range experimentally evaluated in [25].

* Corresponding author: maria.ancona2@unibo.it

As it can be observed in Figure 4, the best scenario is the MPP-HGV at variable-voltage, with the PV panels working at the maximum power and the hydrogen generator at variable-point and at variable-voltage, with a value of η_{tot} of about 0.046.

Indeed, in this case, the PV power production is at the maximum (MPP) and – depending on the considered time step and except for a few instants – the panels and/or the batteries can provide a higher value of power with respect to the upper limit of the electrolyzer operating range. To this respect, in the first part of the analyzed period the PV panels production is high and quite stable (see Figure 3) allowing to feed the electrolyzer and to charge the batteries (see Figure 6). Indeed, in this stage the batteries show the maximum SOC during the tests, with a value of about 0.6 for the scenario MPP-HGV at variable-voltage. On the other hand, in the second part of the analyzed period, no production from PV is registered and the batteries can provide power to the electrolyzer, depending on the considered strategy; this behavior can be seen in Figure 6, in which the SOC of the batteries starts to decrease in correspondence of the PV panels inactivity. Consequently, in the MPP-HGV at variable-voltage case, the electrolyzer can be operated at its maximum power for the larger part of the analyzed period, allowing at the same time to reach the maximum hydrogen production (see Figure 5).

The small difference between this case and the scenario MPP-HGV at fixed-voltage is given by the different couple voltage-current at the inlet of the electrolyzer and by the conversion efficiency of the converter. On the contrary, in the other scenarios the variable-voltage mode is disadvantageous, especially when the hydrogen generator works at fixed-point (HGF). This evidence can be explained considering that the electrolyzer always works at the point of maximum efficiency, also when the power available from the PV panels and the batteries is higher with respect to the operating point of the electrolyzer.

This assumption – being the PV production, in the first part of the analyzed time period, always higher than the electrolyzer required input power – causes a faster charge of the batteries for HGF variable voltage strategies with respect to the corresponding fixed-voltage ones (see Figure 6a), since the power corresponding to the maximum efficiency point is lower for the variable voltage operation than for the fixed voltage operation. For the same reason, the discharge process of the HGF variable voltage scenarios results slower. Furthermore, in the case of fixed-voltage, the operating point of the variable-voltage scenario (120 W) causes the minimum production of hydrogen (Figure 5).

The explanation of the cases PWM-HGV is similar to the one of the cases MPP-HGV, even if the results are quite different. Indeed, in these cases the number of intervals in which the PV panels directly supply the electrolyzer is larger (the PV panels work in PWM mode and then produce a lower quantity of power) and then there are more time steps in which the electrolyzer is not supplied by the maximum power.

Finally, relating to the HGV scenarios, from Figure 6 it can be observed the same batteries behavior for fixed PV operating mode, independently from the electrolyzer voltage management. Indeed, when the PV panels produce a value of power higher or lower compared to the operating range of the electrolyzer, then, in this scenarios (HGV), the latter is supplied by the maximum operating power (it's the same value for fixed-voltage and variable-voltage); the only difference stands in the PV operating mode.

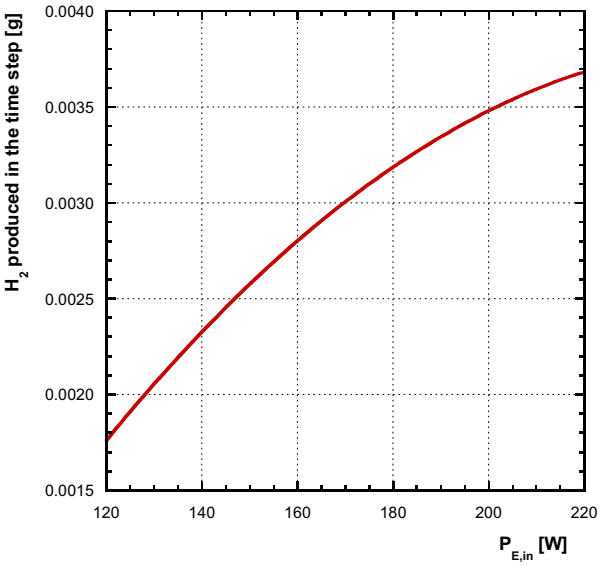

Fig. 5. Hydrogen production as a function of the power at the inlet of the electrolyzer.

In addition, in Figure 4 it is also shown the overall solar-to-hydrogen efficiency range evaluated experimentally in [25] (red area in the figure). This range goes from 3.4 % to 5.3 %, on the basis of the operating conditions. To this respect, some of the strategies analyzed in this paper present a value of the efficiency included in this range, but the considered strategies are quite different from the experimental process.

Indeed, the PV panels in the experimental set-up works in PWM mode but the charging and discharging processes are different from the studied strategies: the charging process consists in directing the solar radiation energy, converted by the PV panels, to the batteries by means of the solar charge regulator and once the batteries are completely charged, the PV panels are disconnected and the stored energy is discharged to the hydrogen generator.

* Corresponding author: maria.ancona2@unibo.it

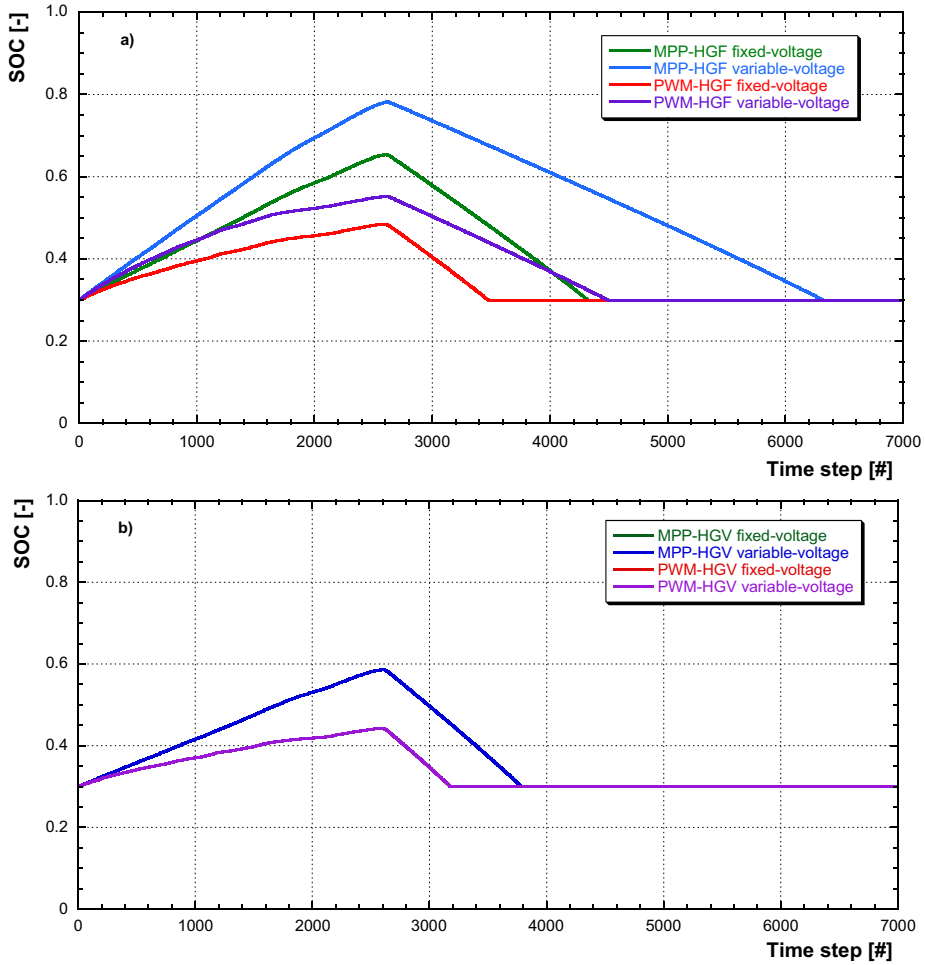

Fig. 6. Trend of the batteries SOC as a function of the time step for: a) HGF strategies and b) HGV strategies.

Furthermore, a second performance parameter has been considered, in order to evaluate the system as a storage itself. In particular, the storage efficiency (η_{sto} [-]) takes into account the energy provided in input to the system by the PV panels (instead of the solar radiation), as an integral of the power produced (P_{PV} [kW]) during the considered time horizon:

$$\eta_{sto} = \frac{m_{H_2} \cdot HHV_{H_2}}{\int_0^t P_{PV} dt} \quad (2)$$

In Figure 7 the values of the storage efficiency for the analyzed scenarios are shown. The trend of this parameter as a function of the considered strategy is similar to the one of the solar-to-hydrogen overall chain efficiency, but the values are evidently higher since the PV panels efficiency is not taken into account. Due to this, the strategies based on the PWM mode are more competitive with respect to the strategies based on the MPP mode. Indeed, the MPP mode shows better PV panel efficiency with respect to the PWM mode and in the storage efficiency this penalizing factor is not accounted. Then, in this case the better strategy is the PWM-HGV with fixed-voltage, showing a value of efficiency equal to about 35 %.

1. CONCLUSIONS

In the last years, the increase in the penetration of renewable energy sources into the electrical system has been promoted, due to the need of reducing pollutant emissions and finding alternatives to the fossil fuels employment. However, as a consequence of the intermittency and non-programmability of these sources, issues related to the management of local and regional electric networks has been registered, such as the mismatch between the energy available from the renewables and the energy demand of the users. In order to limit (or avoid) these problems, the electrical energy storage is recognized as a fundamental solution.

In this paper, an experimental micro-grid composed of photovoltaic panels, batteries and an electrolyzer has been modelled and analyzed.

In addition, the model has been applied to different scenarios – in terms of the whole system operation management – with the aim to maximize the hydrogen production (*i.e.* the overall solar-to-hydrogen chain efficiency) and, consequently, to identify the optimal management strategy to control the system.

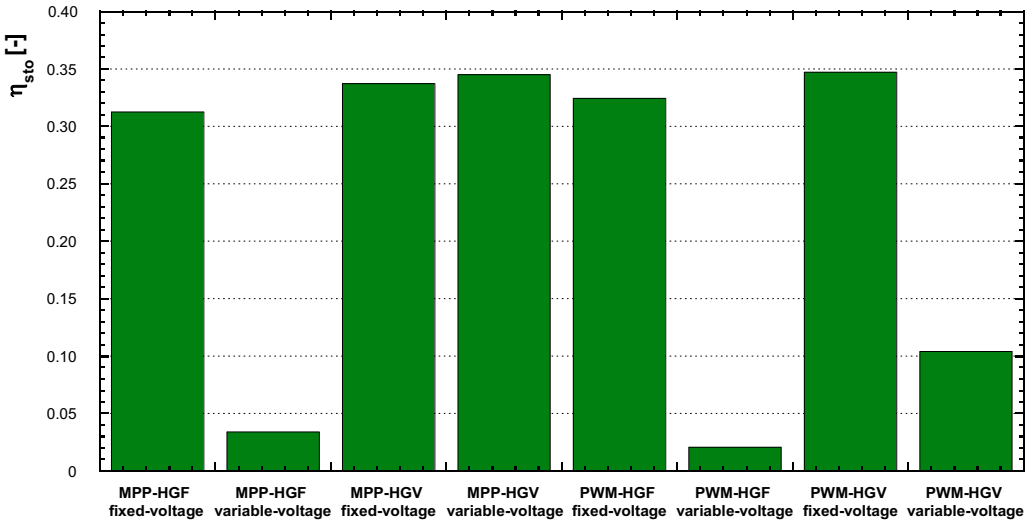

Fig. 7. Storage efficiency obtained for the analyzed scenarios.

To this respect, eight scenarios have been simulated and analyzed, considering the photovoltaic panels operating in maximum power point (MPP) or pulse width modulation (PWM) mode, the hydrogen generator operating at fixed (HGF) or variable point (HGV) and at fixed or variable voltage. In order to compare the analyzed cases, two performance indexes have been considered: the overall solar-to-hydrogen chain efficiency and the storage efficiency (which exclude the photovoltaic conversion efficiency by considering the photovoltaic panels production as energy input of the system).

The best scenario resulting from the carried out analysis is the MPP-HGV at variable-voltage, with the photovoltaic panels working at the maximum power and the hydrogen generator at variable-point and at variable-voltage, with a value of the overall solar-to-hydrogen chain efficiency equal to about 4.6 %. Indeed, in this case, the PV panels work at the maximum power production and – except for a few instants – along with the batteries always provide a higher value of power with respect to the upper limit of the electrolyzer operating range. Consequently, the electrolyzer can be operated at its maximum power for the larger part of the analyzed period, allowing at the same time to reach the maximum hydrogen production. This scenario is one of the best also from the storage efficiency viewpoint, even if the maximum value of this performance parameter is obtained for the PWM-HGV with fixed-voltage scenario (slightly lower than 35 %), since the lower PV efficiency characterizing the PWM mode with respect to the MPP mode is not accounted in the storage efficiency evaluation.

Finally, it must be pointed out that the obtained results – in terms of identified optimal management strategy – are obviously affected by the sizes of the systems composing the laboratory set-up and, in particular, by the correlation of the sizes between the considered energy systems. For this reason, to give a complete optimization of the management strategy, future works will aim at the integration, within the microgrid, of some electronic devices for the emulation of energy systems inspired by the logic of hardware in the loop, in order to better test the management algorithms developed.

NOMENCLATURE

Acronyms

AC	Alternate Current
DC	Direct Current
EES	Electrical Energy Storage
FC	Fuel Cell
HGF	Hydrogen Generator Fixed-point
HGV	Hydrogen Generator Variable-point
MPPT	Maximum Power Point Tracking
PEM	Proton Exchange Membrane
PMS	Power Management Strategy
PV	Photovoltaic
PWM	Pulse Width Modulation
RES	Renewable Energy Sources
SOC	State Of Charge
STC	Standard Test Conditions

References

1. Wang, J., Zhong, H., Ma, Z., Xia, Q., Kang, C. Review and prospect of integrated demand response in the multi-energy system. *Applied Energy*, 202 (2017) 772-782.
2. Zia, M. F., Elbouchikhi, E., Benbouzid, M. Microgrids energy management systems: A critical review on methods, solutions, and prospects. *Applied Energy*, 222 (2018) 1033-1055.
3. Bhandari, B., Lee, K. T., Lee, C. S., Song, C. K., Maskey, R. K., Ahn, S. H. A novel off-grid hybrid power system comprised of solar photovoltaic, wind, and hydro energy sources. *Applied Energy*, 133 (2014) 236-242.
4. Yan, J., Zhai, Y., Wijayatunga, P., Mohamed, A. M., Campana, P. E. Renewable energy integration with mini/micro-grids. *Applied Energy*, 201 (2017) 241-244.

* Corresponding author: maria.ancona2@unibo.it

5. Aneke, M., Wang, M. Energy storage technologies and real life applications–A state of the art review. *Applied Energy*, 179 (2016) 350-377.
6. Bianchi, M., Branchini, L., Ferrari, C., Melino, F. Optimal sizing of grid-independent hybrid photovoltaic–battery power systems for household sector. *Applied Energy*, 136 (2014) 805-816.
7. Bianchi, M., Branchini, L., De Pascale, A., Melino, F. Storage solutions for renewable production in household sector. *Energy Procedia*, 61 (2014) 242-245.
8. Akinyele, D. O., Rayudu, R. K. Review of energy storage technologies for sustainable power networks. *Sustainable Energy Technologies and Assessments*, 8 (2014) 74-91.
9. Zhou, K., Ferreira, J. A., De Haan, S. W. H. Optimal energy management strategy and system sizing method for stand-alone photovoltaic-hydrogen systems. *International Journal of Hydrogen Energy*, 33(2) (2008) 477-489.
10. Spiers D. Chapter II-2-B – Batteries in PV Systems. In: McEvoy's Handbook of Photovoltaics (Third Edition); 2018, p.789-43. https://doi.org/10.1016/B978-0-12-809921-6.00021-5.
11. Report IEA – The Future of Hydrogen (2019), https://www.iea.org/hydrogen2019/
12. Han, Y., Chen, W., Li, Q., Yang, H., Zare, F., Zheng, Y. Two-level energy management strategy for PV-Fuel cell-battery-based DC microgrid. *International Journal of Hydrogen Energy*, 44 (2019) 19395-19404.
13. Parra, D., Walker, G. S., Gillott, M. Modeling of PV generation, battery and hydrogen storage to investigate the benefits of energy storage for single dwelling. *Sustainable Cities and Society*, 10 (2014) 1-10.
14. Zhou, M., Liu, Y. Theoretical study on direct coupling of a PV array to a PEM electrolyser. In: *2013 International Conference on Materials for Renewable Energy and Environment.* IEEE, 1 (2013) 52-56.
15. McDonagh, S., Ahmed, S., Desmond, C., Murphy, J. D. Hydrogen from offshore wind: Investor perspective on the profitability of a hybrid system including for curtailment. *Applied Energy*, 265 (2020) 114732.
16. Li, C. H., Zhu, X. J., Cao, G. Y., Sui, S., Hu, M. R. Dynamic modeling and sizing optimization of stand-alone photovoltaic power systems using hybrid energy storage technology. *Renewable Energy*, 34(3) (2009) 815-826.
17. Han, G., Kwon, Y., Kim, J. B., Lee, S., Bae, J., Cho, E., Lee, B. J., Cho, S., Park, J. Development of a high-energy-density portable/mobile hydrogen energy storage system incorporating an electrolyzer, a metal hydride and a fuel cell. *Applied Energy*, 259 (2020) 114175.
18. Firtina-Ertis, I., Acar, C., Erturk, E. Optimal sizing design of an isolated stand-alone hybrid wind-hydrogen system for a zero-energy house. *Applied Energy*, 274 (2020) 115244.
19. Esfahani, I. J., Ifaei, P., Kim, J., Yoo, C. Design of hybrid renewable energy systems with battery/hydrogen storage considering practical power losses: a MEPoPA (modified extended-power pinch analysis). *Energy*, 100 (2016) 40-50.
20. Behzadi, M. S., Niasati, M. Comparative performance analysis of a hybrid PV/FC/battery stand-alone system using different power management strategies and sizing approaches. *International Journal of Hydrogen Energy*, 40(1) (2015) 538-548.
21. Cano, M. H., Kelouwani, S., Agbossou, K., Dubé, Y. Power management system for off-grid hydrogen production based on uncertainty. *International Journal of Hydrogen Energy*, 40(23) (2015) 7260-7272.
22. Ipsakis, D., Voutetakis, S., Seferlis, P., Stergiopoulos, F., Elmasides, C. Power management strategies for a stand-alone power system using renewable energy sources and hydrogen storage. *International Journal of Hydrogen Energy*, 34(16) (2009) 7081-7095.
23. dos Santos Neto, P. J., Barros, T. A., Silveira, J. P., Filho, E. R., Vasquez, J. C., Guerrero, J. M. Power management techniques for grid-connected DC microgrids: A comparative evaluation. *Applied Energy*, 269 (2020) 115057.
24. de la Hoz, J., Martín, h., Alonso, A., Luna, A. C., Matas, J., Vasquez, J. C., Guerrero, J. M.Regulatory-framework-embedded energy management system for microgrids: The case study of the Spanish self-consumption scheme. *Applied Energy*, 251 (2019) 113374.
25. Ancona, M. A., Bianchi, M., Branchini, L., De Pascale, A., Melino, F., Peretto, A., Rosati, J., Scarponi, L. B. From solar to hydrogen: Preliminary experimental investigation on a small scale facility. *International Journal of Hydrogen Energy*, 42(33) (2017) 20979-20993.
26. M. A. Ancona, M. Bianchi, L. Branchini, F. Catena, A. De Pascale, F. Melino, A. Peretto. Modelling and validation of a small-scale hybrid photovoltaic-battery-electrolyzer system. *Proceedings of the 8th European Fuel Cell Piero Lunghi Conference - EFC2019,* 9-11 December, 2019, Naples, Italy.

Pressure management in smart gas networks for increasing hydrogen blending

Marco Cavana[1,*], *Enrico* Vaccariello[1], and *Pierluigi* Leone[1]

[1]Department of Energy, Politecnico di Torino, 10129 Torino, Italy

Abstract. The injection of hydrogen into existing gas grids is acknowledged as a promising option for decarbonizing gas systems and enhancing the integration among energy sectors. Nevertheless, it affects the hydraulics and the quality management of networks. When the network is fed by multiple infeed sites and hydrogen is fed from a single injection point, non-homogeneous hydrogen distribution throughout the grid happens to lead to a reduction of the possible amount of hydrogen to be safely injected within the grid. To mitigate these impacts, novel operational schemes should therefore be implemented. In the present work, the modulation of the outlet pressures of gas infeed sites is proposed as an effective strategy to accommodate larger hydrogen volumes into gas grids, extending the area of the network reached by hydrogen while keeping compliance with quality and hydraulic restrictions. A distribution network operated at two cascading pressure tiers interfaced by pressure regulators constitutes the case study, which is simulated by a fluid-dynamic and multi-component model for gas networks. Results suggest that higher shares of hydrogen and other green gases can be introduced into existing distribution systems by implementing novel asset management schemes with negligible impact on grid operations.

1 Introduction

While there has been a consensus of fact that natural gas would have been the energy source for the transition, now that the decarbonization goals have become higher and aims to the complete decarbonization by 2050, the natural gas industry is seen as a threat against a quicker transition towards the net-zero energy system.

However, the full electrification of the energy sector appears to be, if not unfeasible, not viable at all [1],[2]. There are sectors such as the transports (especially the heavy ones) and energy-intensive industries which are defined the “hard-to-abate” as the ones, for which molecule-based energy carriers appear to be the most viable solutions.

In this context, renewable gases such as green hydrogen and biomethane appear to be the perfect compromise between sustainability, storability, and flexibility of use. What is more, these gases are expected to be integrated within the current gas network system, contributing to enhancing the strategic value of the whole infrastructure, avoiding the risk of stranded assets.

Within renewable gases, hydrogen is the most promising one to become the energy vector of the future [3]. In the past few years, it has gained more and more momentum among stakeholders and institutions so that roadmaps at the national and European levels have been published [4]. In [4], the evolution of the gas network infrastructure towards a European-wide hydrogen backbone is described. The practice of blending hydrogen within the current natural gas flows is expected as a viable contribution to the market uptake of green hydrogen during the 2020s.

However, hydrogen is to be considered an unconventional gas in the traditional natural gas system. A strong effort needs to be put in place for harmonization of natural gas regulation to include hydrogen and to allow cross-border exchanges. The latest achievement of the European Committee for Standardization (CEN) is the publication of the norm EN 16726:2019 [5] on standardization of gas quality (group H) which concludes the impossibility of setting a common limiting value, as presented in [6]. This shall go together with the research on the impact of hydrogen presence on the infrastructure’s materials, valves and fittings as well as on the appliances of the final users.

Hydrogen blends up to 5-10% are commonly considered possible and already feasible. An extensive literature review across all the sectors of the natural gas system that might be impacted by hydrogen presence made by Marcogaz (European gas industry association) showed that criticalities are a few [7]. These appear among end-users such as compressed natural gas (CNG) vehicles and gas turbines. Problems with CNG vehicles are related to the onboard pressurized tanks which are made of high-strength steel for which a limit of 2% H_2 is set by the ISO Standard 11439. As for turbines instead, according to [8] which reviewed manufacturer’s catalogs,

* Corresponding author: marco.cavana@polito.it

the new Dry Low Emission turbines on the market may accept hydrogen up to 30%. Still, problems with installed ones may exist.

For what concerns the household appliances, the ones installed after the 90s should fall within the Gas Appliances Directive (Directive 2009/142/EC) which foresees a test on flashback with a 77%/23% CH_4-H_2 mixture. About indoor piping, which is usually made of copper, hydrogen presence does not affect the integrity of the material [9]. In terms of safety, even though the flammability range of hydrogen and natural gas – hydrogen blends is wider than the natural gas one, the Lower flammability limit of hydrogen blend is very similar to the one of natural gas. This factor, together with the fact that common odorants such as THT and TBM do not interact with hydrogen ([10] [11]) indicates that current procedures for natural gas may be suitable also for hydrogen blends.

As for the gas metering aspects, according to [12] gas meters do not experience significant metrological differences for concentration up to 20%. In [13] a slight undercounting is registered but it is still within the range of the specification of EN 1359

Given the complexity and the diversity of stakeholders and appliances connected to the natural gas infrastructure, injection at the distribution level may be a useful starting point to demonstrate the feasibility of hydrogen blending while maintaining the impacts at a local level. Similar projects have already been set up in The Netherlands (2011) [14] and in UK (2019) [15]. Distribution system operators have to equip themselves with the expertise and tools to manage these innovative practices. Works on distributed injection of renewable gases have already been published. In [16], the distributed injection of hydrogen within a test case distribution network is performed. The pressure level is on the order of 75mbar, thus representing a very lolcal portion of the network: it is representative of a neighbour. The case study aims at studying the impact of hydrogen injection on the pressure and gas flow fields with a steady state show case. In [17], a medium pressure (5 bar-g) infrastructure is addressed. The hydrogen injection scenario originates from a sector coupling tentative: a few hydrogen injection pattern and injection location have been tested in order to assess the hydrogen injection impact both in space and in time. Both works are based on the analysis of gas networks fed by only one citygates. Other works about gas network modelling focussing on distribution or regional networks may be found in [18] and [19]. Both assess multiple gas entry point networks, highlighting the potential to track gas quality of the network simulation softwares with multiple sources of renewable gases (i.e. biomethane and hydrogen).

Differently from the previous works, this one aims at combine the quality trascking fature and the fluid-dynamic results of a in-house built network simulation software to highlight possible grid management measures in order to enhance the hydrogen injection and consumption within an existing infrastructure, while maintaining a maximum share of hydrogen in the blending.

In this work, the goal is to underline that the limited hydrogen receiving potential of a real distribution network can be increased by the correct management of pressure levels. Furthermore, by using a multi-component fluid-dynamic network model, the increasing complexity of gas quality distribution within the network is shown, highlighting the need for smart approaches to gas network management. With respect to the state-of-the-art approaches on distribution network management, the simulation tools here showcased allow the tracking of the hydrogen blending front throughout the whole network at steady-state conditions, as infeed pressure levels are varied. In the perspective of multi-gas networks, the tracking capability of different quality of gases will be fundamental for the correct allocation of energy consumption and final users' billing. What is more, the results show that by performing dynamic pressure regulation among the different regulation stations, it is possible to allow more or less renewable gas within the grid or to control which areas will be interested with blends and which others will not, giving a powerful tool to distribution system operators.

2 Methodology

The proposed technique of smart gas network management to increase the amount of hydrogen that is acceptably injectable within a gas network has been tested by means of a numerical simulation on an existing network asset.

2.1. Gas network model

The simulation of the gas networks consists of the calculation of the gas flow rates through all the pipelines of the infrastructure and the determination of the pressure level at all the ends of each pipeline (also called nodes of the networks) once all the outlet gas flow rates (at users' nodes) are defined and the pressures at the gas inlet nodes are given as boundary conditions. This is possible by jointly solving the equations of conservation of mass (the continuity equation) and conservation of momentum applied on each node and each pipeline of the network respectively. The closure of the mathematical problem is given by the equation of state which describes the thermodynamic behavior of the gas (or the mixture of gases) flowing within the infrastructure.

Given that the aim of this study is hydrogen blending and its propagation throughout the network, the multi-component feature has been implemented so that the simulation tool is able to manage different gases within the same infrastructure. Natural gas is thus considered as a mixture of different chemical species whose concentration is defined at the inlet point of the network (given as further boundary condition) and calculated as a required output for all the nodes of the infrastructure.

The one dimensional (1-D) system of partial differential equations composed of the continuity and conservation of momentum equations has been simplified considering the following assumptions:

1) Isothermicity of the gas flowing in the pipelines;

2) Horizontal pipes;
3) Negligible effect of the convective term (kinetic energy variation);
4) Steady-state condition.

These assumptions are commonly used in the literature [16],[20],[21], and by distribution system operators (DSOs) when running their commercial software for their business-as-usual activities. Thanks to these simplifications, the fluid-dynamic problem has been solved by the adaptation of the SIMPLE algorithm [22], which has been developed for incompressible fluids applications, to the case of networks of compressible fluids [23].

The specific case requires a network simulation tool that allows variable gas composition throughout the network caused by the presence of a hydrogen injection which is set to form a natural gas-hydrogen blend containing 10%mol of hydrogen. Thus, the boundary conditions of users' consumption are given in terms of thermal energy demand rather than flow rates of natural gas. This is due to the unknown distribution of the gas quality. At the hydrogen injection point, the inflow hydrogen flow rate is also given as a boundary condition, coming from the fixed condition of hydrogen share of the network blend. Starting from an initial guess in which the whole network is filled with 100% natural gas, the fluid-dynamic solver is solved to define a first approximation of the pressure field and the gas flow rate throughout the network. Based on these tentative results, once the gas flow rates in all the branches are known, the solution of the "mixing problem" is possible. This consists of the solution of the conservation of mass for each chemical species of the gas flow for each node of the network, thus allowing the calculation of the updated gas composition at each node. This information allows the updating of the gas flow rates requested at each consumption node based on the updated heating value of the gas mixture, thus requiring an iteration of the fluid-dynamic problem. Using this new composition map as input thus, the fluid-dynamic problem is solved iteratively until convergence is reached, meaning that a configuration of equilibrium regarding the gas composition map has been achieved and the steady-state of the network is fully represented.

2.2. Case Study description

An urban area of around 40,000 inhabitants, covering about 7.6 km^2 has been considered as a case study. The area is served by a distribution network operated at two cascading pressure tiers interfaced by pressure regulators. The network is fed by three city booths (gas entry points) directly feeding the higher pressure tier of the infrastructure. The higher pressure tier is designed to be operated within a pressure range between 5 and 1.5 bar-g. It is composed of the main backbone to which two city booths out of three are connected and a shorter duct that connects the third entry points directly to a peripheral section of the lower pressure tiers distribution infrastructure.

The lower pressure tiers, which are designed to be operated within a pressure range between 0.5 – 0.04 bar-g consists of two highly meshed infrastructures: the main one serving the main urban area and a much smaller one that serves a satellite urban conglomerate. The lower pressure network of the urban area is fed by six pressure regulators which are connected to the main higher pressure backbone plus one pressure regulator delivering the gas from the higher pressure duct connected to the third city booth. The lower pressure network of the satellite urban conglomerate is fed by a single pressure regulation station connected to the main higher pressure backbone by means of a branch pipe. The total number of pressure regulators in the distribution network is eight.
In Figure 1 a distorted version of the network structure is given.

Fig. 1. Distorted representation of the topology of the distribution gas network infrastructure.

The total number of active gas meters in the area is around 10,300 and it has been assumed they are all connected to the lower pressure tiers of the network. It has been assumed that all the gas users are evenly distributed all over the lower pressure infrastructure: each node of the lower pressure distribution grid is associated with a number of gas meters and a consumption flow rate. It has also been assumed that all the gas users have the same gas consumption flow rate. All the simulated scenarios presented in this work share these homogeneity assumptions on the distribution of gas consumption.

The annual gas consumption of the whole area is 4.2 MSm^3. The steady-state fluid-dynamic simulations have been performed referring to the expected peak gas consumption, which has been evaluated as about 3,900 Sm^3/h for each gas user.

2.3. Simulated scenarios

The gas infrastructure as described in the previous paragraph has been modeled under the condition of hydrogen injection at a single point of the infrastructure. Furthermore, the hydrogen flow rate to be injected has been fixed by setting the maximum hydrogen share in the blend to 10%$_{mol}$. Since the distribution network has three gas entry points, when keeping the same hydrogen injection position, the amount of hydrogen that is possible to inject depends on the fluid-dynamic

configuration of equilibrium reached by the network depending on the pressure regulators settings.

At first, the gas network is simulated by setting the same value of the pressure set-point at the outlet of each reduction station. Then, the pressure set-point of the reduction station in which hydrogen blending is performed is increased. Furthermore, also the pressure set point of the secondary reduction station (feeding the lower pressure tiers) which is nearest to the hydrogen injection point is kept at a higher level than the others.

Variations of the distribution of the gas flow rates are observed, modifying the amount of hydrogen which can have access to the grid.

3 Results

The peak natural gas consumption of the whole area has been assumed to be equal to 3,900 Sm^3/h, which corresponds to 42.2 MW_{th}. In case the same amount of energy would be fed by a hydrogen-natural gas mixture with 10% hydrogen share, the total amount of hydrogen to be injected into the infrastructure would be 420 Sm^3/h.

When dealing with a gas network having multiple gas entry points and choosing one single hydrogen injection point, the amount of hydrogen to be injected in order to form a gas mixture with a maximum hydrogen share equal to 10% is dramatically reduced.

The first network simulation has been conducted setting the pressure set-points of the three reduction stations which feed the higher pressure tier all equal to 3 bar_g. Similarly, the outlet pressure of all the secondary pressure reduction stations feeding the lower pressure tier has been set equal to 0.5 bar_g. The hydrogen injection is located at the reduction station labeled “C” in Figure 1. The fluid dynamic configuration of the network is such that the reduction station “C” contributes to the fulfillment of the whole gas flow request by 12%, being the minimum share with respect to reduction stations A and B which respectively contribute by 38% and 50%. This implies that the amount of hydrogen that is possible to inject in the area is also reduced to 12% with respect to the value given above, being thus equal to 51.4 Sm^3/h. As it is possible to observe in Figure 1, the spreading of the hydrogen-natural gas blend affects only a limited portion of the network: the tree-shaped branch to the right of the secondary reduction station following the reduction station “C” and part of the ducts flowing towards the meshed network receives exactly 10% hydrogen blend. This corresponds to 11% of the users of the network. A smaller portion of nodes and branches are instead reached by a mixture that underwent further blending, as an effect of the network topology. Thus, 3% of the users are reached by a hydrogen-natural gas mixture with 2% hydrogen share.

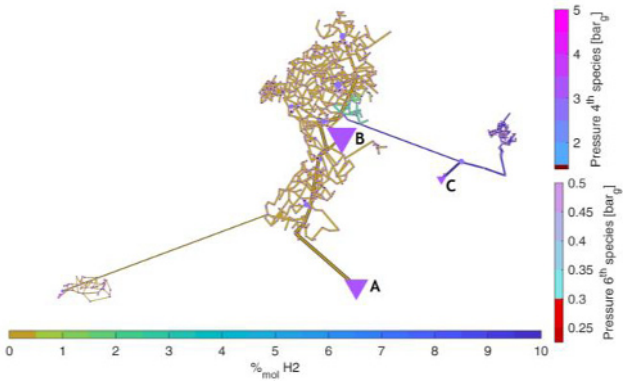

Fig. 2. Fluid-dynamic and quality tracking results of the first simulated scenario: all the pressure regulation stations have the same set-point.

By managing the pressure more smartly, it is possible to enhance the network's capability to receive and distribute hydrogen.

The second network simulation has been conducted by increasing the pressure set-point of the reduction station “C” to the maximum admissible value: 5 bar_g. The other pressure reduction stations (A and B) have been kept to 3 bar_g. As for the secondary reduction stations, the one directly connected to reduction station “C” has been kept a 0.5 bar_g set-point, while all the others have been set to 0.4 bar_g.

In Figure 2, the results of the fluid-dynamic simulation are given. While the pressure and velocity fields are still within the range of acceptability for the safe and correct operation of the network, the balance of gas flows has changed. In particular, the reduction station “C” contributes by 29% to the fulfillment of the total gas request in this case. The acceptable hydrogen flow rate is increased to 128.4 Sm^3/h. As it is possible to see from Figure 2, the hydrogen is much more spread throughout the network. However, the highly meshed feature of the network generates a further dilution of hydrogen, generating areas with lower hydrogen share as the distance from the injection point increases. In particular, with respect to the previous simulation, the total share of users who are reached by hydrogen concentration at least higher than 1% are 44% of the total. However, only 16% are reached by an exact 10% hydrogen blend. The remaining 11% and 17% are reached by hydrogen-natural gas mixtures with hydrogen share between 10% and 5% and between 5% and 1% respectively.

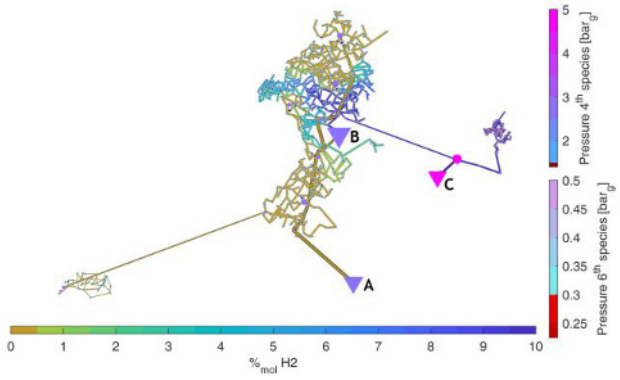

Fig. 3. Fluid-dynamic and quality tracking results of the second simulated scenario: the pressure regulation station in which hydrogen blending is performed has a higher pressure set-point.

4 Conclusion

The hydrogen injection within the gas network at the distribution level has the advantage of delimiting the impacts on gas quality variations to a local level, without affecting the higher pressure transmission infrastructure. This aspect can ease the roll-out of blending projects without the need for national or international standardization process and technical regulation revision. However, the magnitude of acceptable hydrogen injection flow rates, which is already lower, may be further lowered because of the peculiarity of the fluid-dynamic equilibrium of the distribution network, especially in those networks with multiple gas entry points.

In this work, these aspects have been highlighted and an approach in order to alleviate these bottlenecks has been proposed. The coordinated management of pressure set-points of the gas reduction stations at all pressure tiers is shown to be a valid management scheme in order to enhance the hydrogen injection and distribution throughout the network. The specific example showed that the hydrogen injection rate has been increased by a factor of 2.5 by setting different pressure set-points, with negligible impacts on grid operations.

The multi-component fluid-dynamic modeling showed also the increase of complexity the distribution grids are going to face in the framework of hydrogen injection, in terms of gas quality distribution. The gas network operator will have to handle networks with non-homogeneous quality as well as dynamically manage the possible different sources of gases, by tuning pressures and gas flows. The evolution towards a smarter gas network will be fundamental for the management of the multi-gas networks of the future.

References

[1] ewi Energy Research & Scenarios gGmbH, The energy market in 2030 and 2050 – The contribution of gas and heat infrastructure to efficient carbon emission reductions (2018).
[2] Pöyry, Fully decarbonising Europe's energy system by 2050 Decarbonising Europe's energy system (2018).
[3] I. Staffell, D. Scamman, A. Velazquez Abad, P. Balcombe, P.E. Dodds, P. Ekins, N. Shah, K.R. Ward, Energy Environ. Sci. 12 (2019)
[4] Enagás, Energinet, Fluxys Belgium, Gasunie, GRTgaz, NET4GAS, OGE, ONTRAS, Snam, Swedegas, Teréga, European Hydrogen Backbone (2020)
[5] UNI/EN, UNI 16726:2018, (2018).
[6] K. Altfeld, D. Pinchbeck, Gas Energy (2013)
[7] Marcogaz, Overview of available test results and regulatory limits for hydrogen admission into existing natural gas infrastructure and end use (2019).
[8] E. Giacomazzi, G. Messina, Energia, Ambient. e Innov.(2021)
[9] EIGA, Hydrogen transportation pipelines (2004)
[10] A. Huszal, J. Jaworski, Energies (2020)
[11] Marcogaz, Odorisation Of Natural Gas And Hydrogen Mixtures (2021).
[12] J. Jaworski, P. Kułaga, T. Blacharski (2020)
[13] GRTgaz, Report on the impact of renewable gases, and mixtures with natural gas, on the accuracy, cost and lifetime of gas meters. Literature overview for renewable gases flowmetering. (2020).
[14] M.J. Kippers, J.C. De Laat, R.J.M. Hermkens, J.J. Overdiep, A. Van Der Molen, W.C. Van Erp, A. Van Der Meer, Int. Gas Res. Conf. 2011 Proc., Seoul (2011)
[15] T. Isaac, Clean Energy (2019)
[16] M. Abeysekera, J. Wu, N. Jenkins, M. Rees, Appl. Energy. 164 (2015)
[17] M. Cavana, A. Mazza, G. Chicco, P. Leone, Appl. Energy. 290 (2021)
[18] C. Fiebig Hielscher A. Span R. Gulin A. Rickelt S. Schley P., Int. Gas Union Res. Conf. (2014)
[19] P. Schley, A. Hielscher, C.F.M. Sc, S. Rickelt, World Gas Conference, (2018)
[20] M. Chaudry, N. Jenkins, G. Strbac, Electr. Power Syst. Res. 78 (2008)
[21] A.J. Osiadacz, M. Chaczykowski, Chem. Eng. J. 81 (2001)
[22] S. V. Patankar, D.B. Spalding, Int. J. Heat Mass Transf. 15 (1972)
[23] M. Cavana, Gas network modelling for a multi-gas system, Politecnico di Torino, 2020.

Hydrogen emission in enclosed volume (tunnel for mobility)

Farhad Farajimoghadam[1,*], *Matteo* Testi[1], and *Luigi* Crema[1]

[1]Sustainable energy group, Fondazione Bruno Kessler, Via Sommarive, 18, 38123, Povo (TN), Italy.

Abstract. Fuel cell vehicles and trains (FCVs) are seen as a viable alternative to fossil fuel-powered vehicles, with the potential to help the automotive and transport industry grow sustainably. Because of their zero emissions, great efficiency, and diverse hydrogen sources, they are an ideal solution to climate change and the global energy issue. In this study, the simulation of releasing hydrogen from a moving vehicle inside a tunnel has been done. For this purpose, two scenarios have been considered. In the first one, it assumed that hydrogen propagates inside a tunnel without ignition and in the second approach, hydrogen released considered to be combusted. The effect of this combustion on the tunnel and train wall has been investigated. For this goal, two different mass flow rates of hydrogen were considered and results were compared together. Moreover, pressure contours have been shown to represent the overpressure phenomenon and it is resulted that in the area of hydrogen dispersion, there will be high pressure.

1 Introduction

As hydrogen fuel cell vehicle technology advances, it is evident that this mode of transportation will become increasingly widespread in the future. The influence of HFCVs on various road infrastructure must be studied in order to achieve that goal. Tunnels are a major concern because hydrogen might be released and then confined, potentially posing a serious threat[1].

Governments and major vehicle companies have placed a high priority on research and development of FCV-related technology in recent years. Furthermore, hydrogen seems to be the most acceptable answer for overcoming the current energy and environmental crises from the standpoint of clean energy generation. It may be extracted using solar, wind, or other sustainable energy sources and is commonly available in the form of water. As a result, hydrogen energy and hydrogen FCVs are optimal. This remark ignores the dangers that arise during the manufacturing, storage, transit, and usage processes. Although hydrogen is less likely to create a fire or explosion in an open or well-ventilated room (owing to its ease of diffusion and low density), it can pose a safety danger if it piles up in a confined or poorly ventilated space. While hydrogen is released from the valve, the hydrogen concentration rises for as long as the hydrogen is released. When hydrogen is no longer released, diffusion causes the hydrogen-air mixture to slowly drop. The hydrogen will become homogeneously mixed with the air in the confined space after a long period (far longer than the duration of the discharge). But all this scenario happens if there is not an ignition. When a leak takes place in a hydrogen carrying vehicle, a flammable hydrogen–air mixture might build up within the tunnel, posing a safety threat. Because if the concentration of hydrogen will be more than 4%, the combustion probability of hydrogen-air mixture is so high[2].

When releasing hydrogen, release rate (expressed in g/s or kg/s) has a decisive impact on the way in which hydrogen-rich layers form below the ceiling or roof of a space during the release phase[3]. At high release rates, there is usually a lot of turbulence, in which case the hydrogen spreads along the ceiling and walls of the room and descends until the room is homogeneously filled. At low release rates, there is much less turbulence and the hydrogen rises to the ceiling where it forms layers of varying concentrations (stratification). The highest hydrogen concentrations can be found in the layers directly below the ceiling[4]–[6].

Hydrogen dispersion can either be turbulent or laminar in nature. A laminar flow is a steady flow going in one direction, whereas a turbulent flow is much more unpredictable and can go in multiple directions. The higher the pressure of the released gas, the more turbulent the release will be. In the case of a release rate on the order of 1 litre per hour, the flow will be laminar. In the case of more major leaks, the flow will be turbulent[7], [8].

Several research investigations have been conducted both experimentally and numerically that some of them are as follows. Groethe et al. [9] conducted experiments in a 78.5 m long tunnel with section equal to 3.74 m2. The tunnel represented approximately 1/5th scaled real tunnel for vehicles.

In order to validate the dispersion/deflagration modelling, a set of experiments were performed at the SRI Corral Hollow Experiment Site by Houf et al [10]. A set of scaled tunnel tests were performed to approximate the full-scale dimensions of the tunnel from the modelling effort. The hydrogen mass, release rate, initial tank

* Corresponding author: ffarajimoghadam@fbk.eu

pressure, and TPRD release diameter were scaled to approximate the modelling parameters.
Other experiments were performed by Kumar et al. [11]to evaluate the influence of congestion and ventilation flow rates on the over-pressure produced from ignition of hydrogen stoichiometric clouds. Quiescent experiments were performed in a sealed enclosure with a stoichiometric hydrogen/air mixture and different congestion volumes/configurations. Also, a set of steady-state experiments were performed with various hydrogen leak rates and ventilation flow rates.
Friedrich et al. [12] and Seike et al. [13] examined deflagration in stratified hydrogen layers to evaluate the potential of selfsustained detonation in flat mixture layers. The hydrogen concentrations used in these experiments ranged between 15% and 25% (by volume in air). Hao et al. [14] has been done the experiments related to dispersion of hydrogen from fuel cell vehicles in confined spaces recently.
In terms of numerical investigations, a lot of researchers put efforts as well as Li et al. [15] that simulated combustion of dispersed hydrogen with CFD code GASFLOW and Choi et al. [16] that did the same for emission of hydrogen from fuel cell vehicles.
Lowesmith et al. [17] worked on the combustion of air hydrogen and methane mixtures with different ratios in the confined spaces and also they investigated the explosion results. Bauwens et al. [18] and Gamezo et al. [19] did some similar studies to define the results regrading the concentration of hydrogen inside confined places.
Computational fluid dynamics is utilized in this study to look into transient and steady-state hydrogen release, dispersion, and explosion in a tunnel for fuel cell moving vehicles.

2 Modelling of the tunnel

In this study, computational fluid dynamics has been used to evaluate releasing hydrogen from a moving vehicle like train inside a tunnel. The main objective was obtaining tunnel and train wall temperature considering two cases. These two modes of simulation were consisted of performing calculation with and without burning of hydrogen. The main idea behind this assumption was based on the fact that hydrogen is a very flammable gas with a very little activation energy. Therefore, both cases considering only releases of hydrogen without any ignition and with the spontaneous ignition and combustion were simulated.

2.1 Geometry

The geometry information for the tunnel and its cross-section area are given in Fig. 1 and Fig. 2.

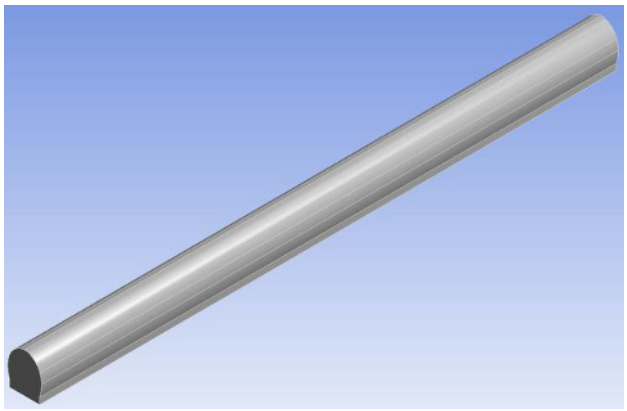

Fig. 1 Tunnel Geometry

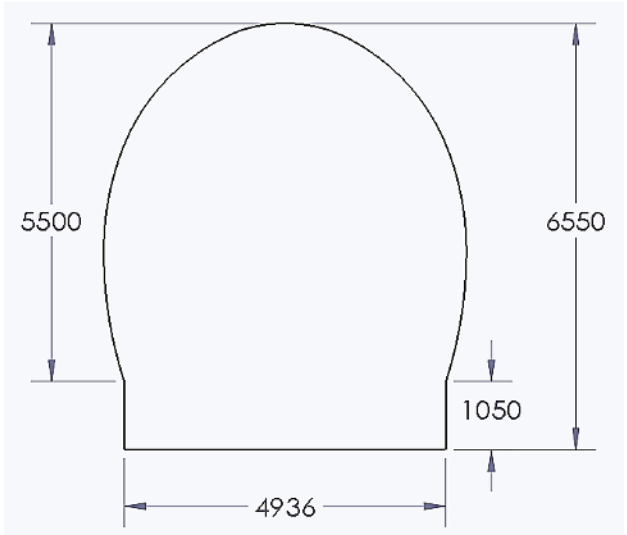

Fig. 2 Cross-section of the tunnel (Dimensions are in millimeters)

Total train length considering the space between wagons is about 100 meters and for this reason a tunnel with the length of more than 100 meters has been chosen to perform all the simulation.
The train composed of several wagons and the middle wagon is the place which hydrogen tanks are and the release of hydrogen happens in the middle of its ceiling.

2.2 Mesh

After creating fluid volume from the geometry of tunnel and train, meshing has been done using unstructured meshing technique. For investigating mesh independency, three different mesh from coarse grid to fine have been considered and by comparing the results, it was decided to use the medium mesh with about 7.5 million total nodes. In the Fig. 3, a cross section of mesh is shown:

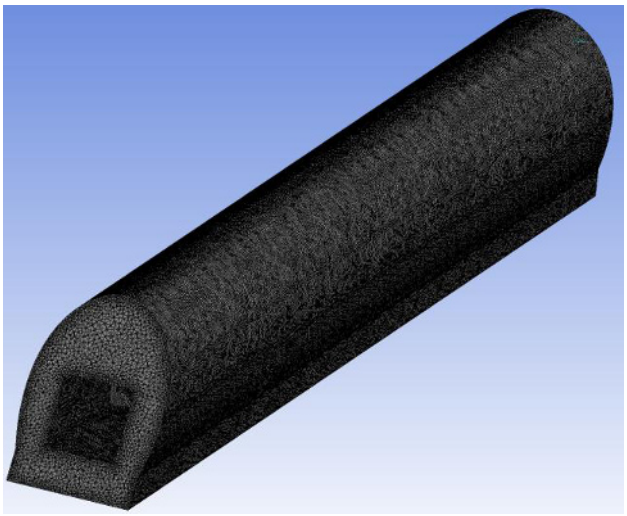

Fig. 3 Cross-section of fluid volume mesh

2.3 Boundary conditions and assumptions

A study of hypothetical hydrogen vehicle fire situations in tunnels was undertaken to determine the maximum amount of hydrogen that might be burned in a short period of time.

This research has been done using computational fluid dynamics which is on the basis of finite volume method. First of all, domain is discretized into a finite set of control volumes, after that, general conservation (transport) equations for mass, momentum, energy, species, etc. are solved on this set of control volumes solved on this set of control volumes. Partial differential equations are discretized into a system of algebraic equations and all algebraic equations are then solved numerically to render the solution field.

In this study, it is assumed that train is moving inside the tunnel with the velocity of 80 Km/hr. and hydrogen is released while it is moving. For this reason, for the simulation train was considered stable and instead the flow inside the tunnel is moving with the same velocity. As a result, there is an inlet boundary in one side of tunnel which is considered to be velocity inlet and on the opposite side there should be outlet with the ambient pressure.

For modeling hydrogen, there is another inlet on the train ceiling. Two different amounts of hydrogen were simulated with and without ignition. These two numbers are related to the amount of hydrogen inside the tanks and should be chosen based on this decision that how much hydrogen must be burned or released two alleviate the pressure of the tanks.

Hydrogen release pipe has the diameter of 12 millimeter based on the chosen thermal pressure relief device (TPRD) and it is exactly in the middle of the small coach.

This whole idea of releasing hydrogen is due to high pressure of tanks inside the train which can be around 350 bar and if it exceeds from this number, it is so dangerous.

Temperature of air outside tunnel is equal to 300 K which is ambient temperature and convection heat transfer between burned hydrogen and the outside air was considered.

After burning, fluid is turbulent and for modeling turbulence K-e realizable has been used together with scalable wall functions[20]. The simulation tool extrapolates value of convection heat transfer coefficient based on the various temperatures.

Mass flow rate of hydrogen is constant and two scenarios were evaluated: 1) 140 g/s of hydrogen release and 2) 720 g/s of hydrogen. Contours are shown and explained in the next section.

3 Results and discussion

Release of hydrogen is considered in two ways in this study, first without ignition and second with ignition.

3.1 Hydrogen release without ignition

In this section, the released hydrogen will not be burned and a transient simulation has been done in order to know the concentration of hydrogen inside tunnel. Because if the concentration of hydrogen goes over 4 % it is very dangerous and flammable. In this regard, a transient study was carried out and results were extrapolated to know the total time after the first second of hydrogen dispersion to understand the exact of time of reaching this concentration.

Mass flow rate of hydrogen in this section was 140 g/s and molar concentration contours has been shown in respect to time in the Fig. 4 .

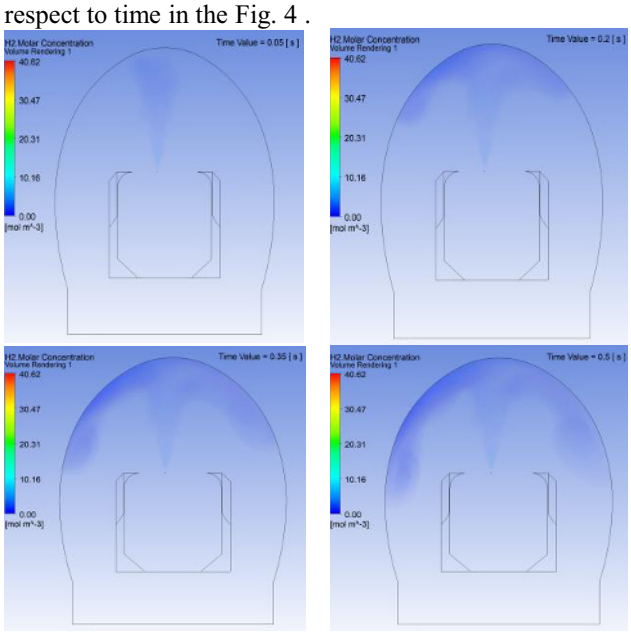

Fig. 4 Hydrogen molar concentration in mol/m3 in different times

From data above a relation has been derived that shows the relation of hydrogen concentration inside tunnel in respect to time which is shown in the Fig. 5.

As it is obvious, Concentration of hydrogen increases gradually and after one minute it goes higher than 4 %, exactly 4.2 %. A linear relationship was found between time and concentration since the mass flow rate of hydrogen dispersioni s constant during the time.

As a matter of fact, it seems that after one minute or 60 seconds the mixture of hydrogen and air in the tunnel has become extremely flammable. It is better to note that the concentration of hydrogen is based on total volume of tunnel and it is average. As a result, in some parts of tunnel ceiling it can be higher.

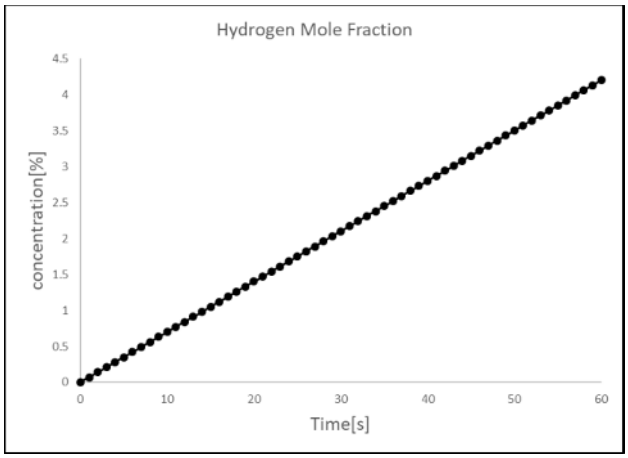

Fig. 5 Concentration of hydrogen in the tunnel

3.2 Hydrogen release with ignition

In this part, the effect of burning hydrogen after dispersion will be shown. For burning the stoichiometric ratio of hydrogen and air was considered and all the simulations have been carried out in steady state mode.

The main goals were calculating adiabatic hydrogen flame temperature and evaluation train and tunnel wall temperature. For this reason, two cases were examined. Hydrogen mass flow rate for these cases was 140 g/s and 720 g/s respectively.

Contour of adiabatic flame temperature for the first case is shown in the Fig. 6.

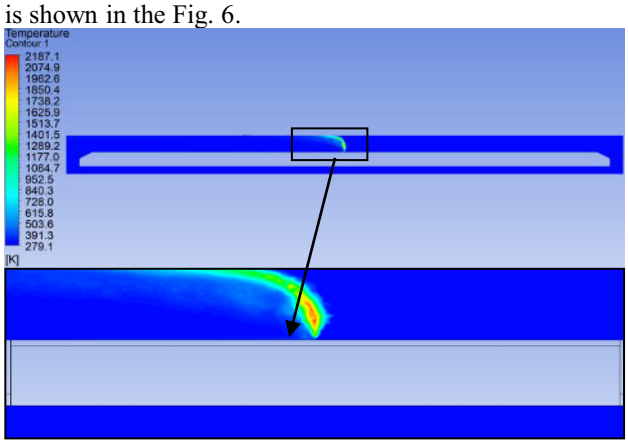

Fig. 6 Hydrogen flame temperature in the tunnel centerline (for 140 g/s of hydrogen)

Maximum flame temperature is around 2200 K which is close to the hydrogen adiabatic flame temperature, furthermore, the effect of burning hydrogen on the tunnel ceiling is exhibited in the Fig. 7.

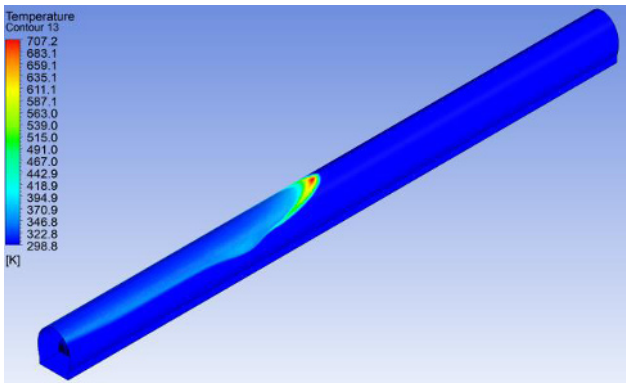

Fig. 7 Train and tunnel wall temperature (for 140 g/s of hydrogen)

As it can be seen, the steady state effect of burning 140g/s hydrogen is clear with a hot spot area just above the release point and maximum temperature on the tunnel wall is equal to 707 K which represents 434 degrees centigrade.

In the figure Fig. 8, contours of water and oxygen mass fraction can be seen. As it is expected, in the area of combustion, oxygen fully consumed and water was produced as a product of combustion.

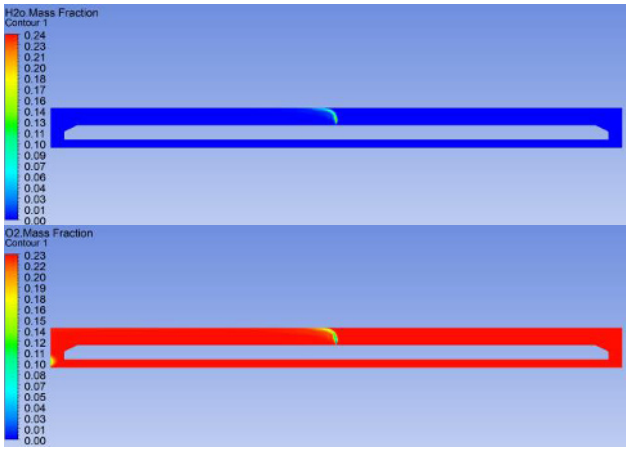

Fig. 8 Water and oxygen mass fraction in tunnel centerline

In the figure Fig. 9, volume rendering temperature inside the tunnel is exhibited which can be a representative of the temperature in every point of tunnel.

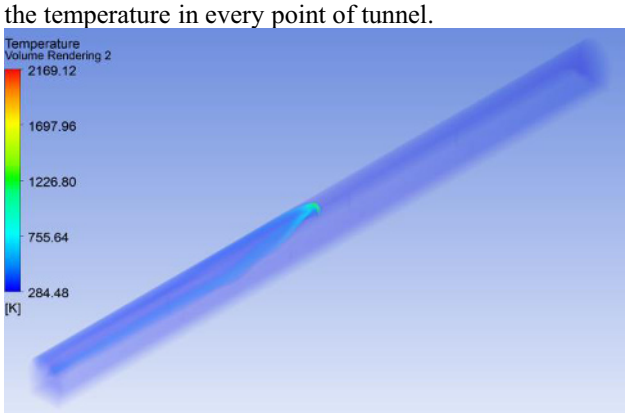

Fig. 9 Volume rendering temperature of train and tunnel (for 140 g/s of hydrogen)

For digging in about the pressure in the tunnel, three different section were chosen along the tunnel including the central section. In the figure **Error! Reference source not found.**, overpressure can be observed in middle section due to the release of hydrogen from a very little 12 mm diameter pipe. In the other sections, contours of pressure show the pressure difference with the reference.

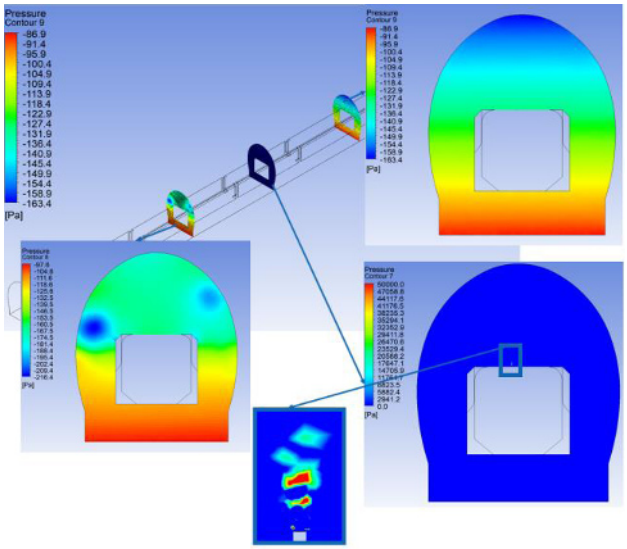

Fig. 10 Pressure contours in three different sections (for 140 g/s of hydrogen)

In the second case, everything is the same unlss the mass flow rate of hydrogen which is 720 g/s.
Contour of tempreature in the tunnel centerline is shown in the Fig. 11, the only difference is the total area which had been covered by the heat and as it is obvious a very bigger area has high temperature. Additionally, maximum flame temperature is almost constant and is around 2200 K like before, because it should not be dependent to the amount of burned hydrogen.

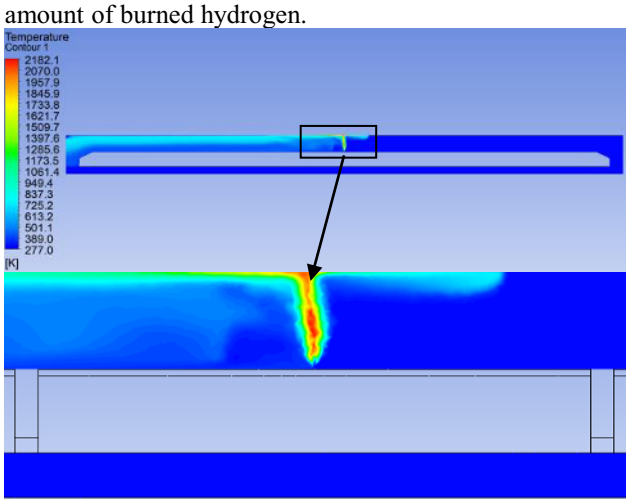

Fig. 11 Hydrogen flame temperature in the tunnel centerline (for 720 g/s of hydrogen)

In the , temperature contour is exhibited on the train and tunnel wall. In this regarad, with increasing the amount of burned hydrogen, maximum flame temperaure does not change but maximum tunnel wall temperature shows a significant change which is a consequence of more heat produced by hydrogen burning.

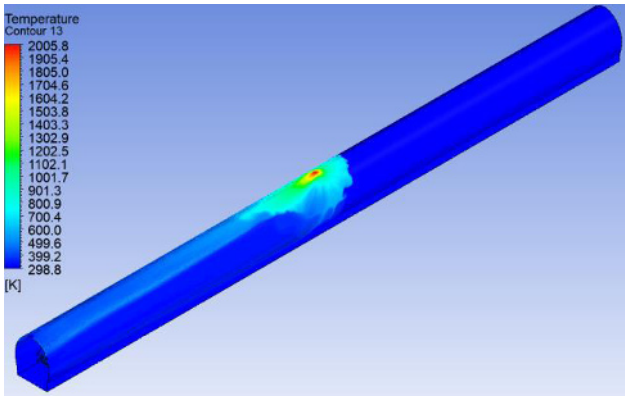

Fig. 12 Train and tunnel wall temperature (for 720 g/s of hydrogen)

Water and oxygen mass fraction do not represent a huge deviation with previouse results due to the similarity of the sotoichiometric ratio and they will not be shown again. On the other side, it is interesting to depict the volume rendering temperature in the new case while more volume of fluid inside the tunnel have been affected by the combustion.

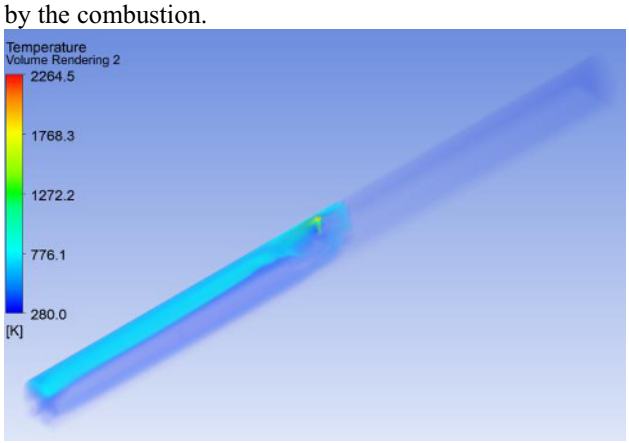

Fig. 13 Volume rendering temperature of train and tunnel (for 720 g/s of hydrogen)

Regarding pressure contours, the same ones have been depicted for the second case and what is significant is that in general, pressure is higher which easily can be explained. The diameter of release point is constant but amount of hydrogen flow rate is more. Therefore, overpressure happens. They were exhibited in Fig. 14.

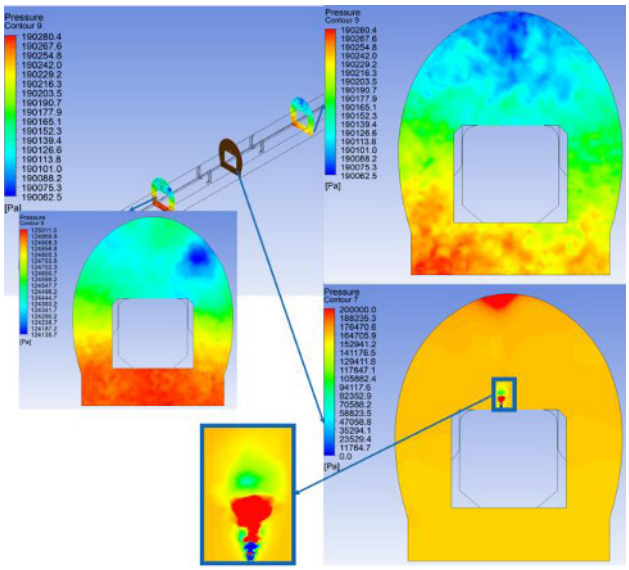

Fig. 14 Pressure contours in three different sections (for 720 g/s of hydrogen)

In the pressure contours, negative pressure shown in the contour is due to the relative pressure in comparison with working pressure. Also, the blue holes in pressure contours are related to the velocity of combution products which are obvious only in the plane after releasing hydrogen.

4 Conclusions

In this research, computational fluid dynamics is used to investigate transient and steady-state hydrogen release, dispersion, and explosion in a tunnel for fuel cell moving vehicles. The following are some of the inferences that can be drawn:

•Releasing hydrogen into air without ignition, apparently does not have a big effect on growing train wall temperature, but after one minute it can cause an auto-ignition of hydrogen because the concentration of hydrogen inside tunnel goes above 4% after 1 minute and it could be dangerous.

•Increasing mass flow rate of hydrogen, increases maximum train wall temperature and approximately does not have a big effect on flame temperature because the hydrogen adiabatic flame temperature depends on stoichiometric ratio of fuel and air.

•It is assumed that releasing of hydrogen starts when the train is in the middle of tunnel but in reality, it can happen in any point of tunnel and has the same effect of increasing temperature of train and tunnel.

•After passing a few seconds, increasing time of simulation does not change maximum temperature.

•Increasing the velocity and pressure of flow inside the tunnel is due to the very small release diameter of hydrogen and from the simulation it is concluded that in other parts of tunnel high pressure and velocity does not exist as it was shown in the pressure and velocity contours.

5 References

[1] KIWA, “Future-proof gas distribution networks,” 2018, Accessed: Sep. 02, 2021. [Online]. Available: www.kiwatechnology.nl.

[2] BRHS, “BASICS OF HYDROGEN SAFETY FOR FIRST RESPONDERS Lecture. Hydrogen properties relevant to safety Content.”

[3] V. Molkov, “Fundamentals of Hydrogen Safety Engineering I,” 2012.

[4] B. Cariteau and I. Tkatschenko, “Experimental study of the concentration build-up regimes in an enclosure without ventilation,” *Int. J. Hydrogen Energy*, vol. 37, no. 22, pp. 17400–17408, Nov. 2012, doi: 10.1016/J.IJHYDENE.2012.03.156.

[5] M. De Stefano, X. Rocourt, I. Sochet, and N. Daudey, “HYDROGEN DISPERSION IN A CLOSED ENVIRONMENT.”

[6] J. M. Lacome, Y. Dagba, D. Jamois, L. Perrette, and C. H. Proust, “LARGE-SCALE HYDROGEN RELEASE IN AN ISOTHERMAL CONFINED AREA.”

[7] R. W. Schefer, W. G. Houf, B. Bourne, and J. Colton, “Spatial and radiative properties of an open-flame hydrogen plume,” *Int. J. Hydrogen Energy*, vol. 31, no. 10, pp. 1332–1340, Aug. 2006, doi: 10.1016/J.IJHYDENE.2005.11.020.

[8] DNV GL, “Gedrag van waterstof bij lekkages in het gasdistributienet Netbeheer Nederland,” 2020, Accessed: Sep. 02, 2021. [Online]. Available: www.dnvgl.com.

[9] M. Groethe, E. Merilo, J. Colton, S. Chiba, Y. Sato, and Iwabuchi, “LARGE-SCALE HYDROGEN DEFLAGRATIONS AND DETONATIONS.”

[10] W. G. Houf, G. H. Evans, E. Merilo, M. Groethe, and S. C. James, “Releases from hydrogen fuel-cell vehicles in tunnels,” *Int. J. Hydrogen Energy*, vol. 37, no. 1, pp. 715–719, Jan. 2012, doi: 10.1016/J.IJHYDENE.2011.09.110.

[11] S. Kumar, S. D. Miles, P. Adams, A. Kotchourko, D. Hedley, and P. Middha, “Hytunnel project to investigate the use of Hydrogen Vehicles in Road Tunnels,” *International Conference on Hydrogen Safety (ICHS3)*, 2009. https://businessdocbox.com/Green_Solutions/81570426-Hytunnel-project-to-investigate-the-use-of-hydrogen-vehicles-in-road-tunnels.html (accessed Sep. 02, 2021).

[12] K. S. and G. A. Friedrich, J. Grune, T. Jordan, A. Kotchourko, N. K. M. Kotchourko and Stern, “EXPERIMENTAL STUDY OF HYDROGEN-AIR DEFLAGRATIONS IN FLAT LAYER,” 2007.

[13] M. H. and H. T. M. Seike, Y. Ejiri, N. Kawabata, “"Fire experiments of carrier loaded FCV in full-scale model tunnel - Estimation of heat release rate and smoke generation rate,” 2014.

[14] D. Hao, X. Wang, Y. Zhang, R. Wang, G. Chen,

and J. Li, "Experimental Study on Hydrogen Leakage and Emission of Fuel Cell Vehicles in Confined Spaces," *Automot. Innov. 2020 32*, vol. 3, no. 2, pp. 111–122, May 2020, doi: 10.1007/S42154-020-00096-Z.

[15] Y. Li *et al.*, "Numerical analysis of hydrogen release, dispersion and combustion in a tunnel with fuel cell vehicles using all-speed CFD code GASFLOW-MPI," *Int. J. Hydrogen Energy*, vol. 46, no. 23, pp. 12474–12486, Mar. 2021, doi: 10.1016/J.IJHYDENE.2020.09.063.

[16] J. Choi, S. Kang, N. Hur, E. D. Lee, and K. B. Lee, "A NUMERICAL SIMULATION OF HYDROGEN DIFFUSION FOR THE HYDROGEN LEAKAGE FROM A FUEL CELL VEHICLE IN AN UNDERGROUND PARKING GARAGE."

[17] B. J. Lowesmith, C. Mumby, G. Hankinson, and J. S. Puttock, "Vented confined explosions involving methane/hydrogen mixtures," *Int. J. Hydrogen Energy*, vol. 36, no. 3, pp. 2337–2343, Feb. 2011, doi: 10.1016/J.IJHYDENE.2010.02.084.

[18] C. R. Bauwens, J. Chao, and S. B. Dorofeev, "EFFECT OF HYDROGEN CONCENTRATION ON VENTED EXPLOSION OVERPRESSURES FROM LEAN HYDROGEN-AIR DEFLAGRATIONS."

[19] V. N. Gamezo, T. Ogawa, and E. S. Oran, "Numerical simulations of flame propagation and DDT in obstructed channels filled with hydrogen-air mixture," doi: 10.1016/j.proci.2006.07.220.

[20] T. J. Bardina, J.E., Huang, P.G., Coakley, "Turbulence Modeling Validation, Testing, and Development," *NASA Technical Memorandum 110446.*, 1997. https://www.researchgate.net/publication/24296213_Turbulence_Modeling_Validation_Testing_and_Development (accessed Sep. 07, 2021).

Composite chitosan and quaternary ammonium modified nanofibrillar cellulose anion exchange membranes for direct ethanol fuel cell applications

Maša Hren[1], *Selestina* Gorgieva[1,2,*]

[1]Faculty of Mechanical Engineering, University of Maribor, Smetanova ulica 17, 2000 Maribor, Slovenia
[2]Faculty of Electrical Engineering and Computer Science, University of Maribor, Koroška cesta 46, 2000 Maribor, Slovenia

Abstract. Fuel cells are a promising technology for energy production, but their commercialization is hindered mainly due to high costs. Direct alkaline ethanol fuel cells (DAFC) are receiving increasing attention as they can utilize cheaper, non-precious metal catalysts. A vital component of a DAFC is the anion exchange membrane (AEM). Currently, the commercially available AEMs don't possess satisfactory properties. This indicates a need for the development of new highly efficient, environmentally friendly, and economically viable AEMs. Synthesis of synthetic polymer AEMs is usually complex and time-consuming, as well as environmentally unfriendly. Therefore, it is highly desired that the membrane material is bio-renewable, non-toxic and environmentally benign. In this work, a series of biopolymer membranes were designed by a simple, cost-effective, dispersion-casting procedure, fully complying with green-chemistry principles. Design of experiments was used as a methodology for identifying optimal combinations of influencing factors and their relations within selected responses. The obtained chitosan-$Mg(OH)_2$ composite membranes containing modified nanofibrillar cellulose (CNF) fillers with quaternary ammonium groups were investigated for their mechanical properties, swelling ratio, ethanol permeability and ion exchange properties. Obtained data suggest the applicability of newly prepared, biopolymeric composites as eco-friendly AEMs in DAFC technologies.

1 Introduction

Among the most significant societal challenges nowadays are CO_2 emissions and global warming, so a lot of attention is directed towards the use of alternative energy sources. To this end, much of the research focus has been aimed at fuel cells, electrochemical devices that can be used for alternative energy production. It is a device that uses fuel and an oxidant to produce electrical energy through an electrochemical reaction. [1] Similar to batteries, which power portable devices and electrical vehicles, also fuel cells convert chemical energy into electrical energy. There are many different types of fuel cells, but all of them have the same basic structure: two electrodes and an electrolyte between them. They are mainly differentiated by the type of electrolyte, which is responsible for ion transport, and by the operating temperature. A fuel cell with a polymer electrolyte (PEFC) can operate in an acidic or alkaline environment, depending on the properties of the polymer. A PEFC with an anion exchange membrane (AEM) operating in alkaline conditions has benefits in comparison to a PEFC operating in acidic conditions, as the OH^- anions pass through the AEM in the opposite direction as fuel. In addition, cheaper non-noble catalysts can be used. [2] The basic structure of AEMs for alkaline fuel cell applications is a hydrophobic polymer backbone with added positively charged hydrophilic functional groups, one of them being the quaternary ammonium group, which is permanently positively charged. AEMs need to have a high ion conductivity, be mechanically stable and have a low ethanol permeability as well as good stability in an alkaline environment. [3]

Biopolymer-based membranes are renewable and eco-friendly alternatives to synthetic membranes, offering a reasonable cost/effectiveness ratio. [4] Chitosan membranes have already been included in different fuel cell set-ups, including alkaline anion exchange membrane fuel cells (AAEMFCs). [5] Chitosan is a low-cost non-toxic biopolymer with high chemical stability, which can readily form films. Chitosan membranes on their own do not possess appropriate mechanical properties and conductivity properties; therefore, the introduction of fillers can be beneficial to improve those properties. [1] Nanofibrillar cellulose (CNF) is a biomaterial with a high aspect ratio and has the potential to improve the chitosan membrane's shortcomings, such as mechanical stability. Additionally, CNF can be readily modified on the abundant -OH groups, thus formulating the positively charged fillers, which can improve the conductive properties of the AEM.

Herein we report the preparation of composite chitosan membranes with (modified) CNF fillers for the

* Corresponding author: selestina.gorgieva@um.si

application of AEMs in AAEMFCs. The properties of resultant nanocomposites relevant for AEM applications were investigated, in terms of tensile strength, EtOH fuel permeability, swelling ratio, and ion exchange capacity.

2 Methods

2.1. Membrane production

Chitosan-$Mg(OH)_2$ dispersion was used as a base for composite membrane preparation. The membranes have been prepared similarly as described in our previous work [3]. Chitosan was dissolved in Mili-Q water by adjusting the pH to 2.0 (with 1M HCl) at room temperature under stirring. The solution was stirred overnight until a transparent homogenous solution was obtained. Next, 1 wt.% $Mg(OH)_2$ dispersion was added until a pH value of 6.0 – 6.2 had been reached, and the dispersion was diluted to a final 1.wt.% of chitosan. Design of Experiments was used to determine the relations between different membrane production factors and membrane properties in order to obtain appropriate AEM properties for fuel cell applications (low fuel permeability, high ion conductivity, etc.). The experimental design consisted of 17 membranes with different contents of modified or unmodified fillers. Membranes with a modified filler (CNF polyDADMAC) content from 0 – 0.125 g and unmodified filler (CNF) content from 0 – 0.375 g were prepared. The resulting dispersions have been cast as membranes and dried at different temperatures. When dry, the membranes were neutralized with 1 M NaOH and subsequently washed with Mili-Q water and left to air dry. The modified fillers were obtained by adsorption between CNF and polydiallyldimethylammonium chloride (polyDADMAC) under vigorous stirring. The resulting CNF polyDADMAC was washed with Mili-Q water.

2.2 Zeta potential

The zeta potential of monodispersed CNF and CNF polyDADMAC particles in water dispersion with a concentration of 0.001 wt.% was obtained as streaming potential in a DLS apparatus at different pH values set by 0.1 M NaOH or 0.1 M HCl.

2.3 Ethanol permeability

Ethanol (EtOH) permeability through CS nanocomposite membranes has been measured in temperature-controlled diffusion cells at 25 °C ± 1 °C. [6], [3] The diffusion cell consisted of two glass compartments (source and receiving compartment), each 25 ml in volume, and the membrane sample separating the two compartments in between. Before each experiment, the membrane was equilibrated in Mili-Q water for 24 h. The source compartment was filled with 25 ml of 2 M EtOH in 6 M KOH solution (i.e., 8.5 w/w % EtOH), and the receiving compartment was filled with 25 ml of 6 M KOH. Both compartments have been filled simultaneously in order to apply the same pressure on the membrane from both sides. The membrane sample had an effective surface area of 7.026 cm^2. The concentration of permeated EtOH was obtained based on the conductivity measurements, measured by a conductometer, in the receiving compartment at different time intervals. The permeability coefficient of EtOH, P $(cm^2\ s^{-1})$ was calculated using the equation below

.

$$P\left(\frac{cm^2}{s}\right) = \frac{(C_B - C_{B0})}{(t - t_0)} \times \frac{V_B \cdot l}{A \cdot C_{A0}} \quad (1)$$

where C_{A0} represents the initial concentration of EtOH in the source compartment, and V_B represents the volume of KOH in the receiving compartment. A and l represent the area and thickness of the membrane, respectively.

2.4 Ion exchange capacity (IEC)

To obtain the titrated gravimetric IEC values, AEMs were weighed to determine the dry mass and then converted to the OH^- form in 1 M KOH solution for 24 hours, washed with Mili-Q water, and subsequently immersed in 40 ml of 0.01 M HCl standard solution for 24 h. The solutions were then titrated with a standardized KOH (0.1 M) solution. Following the potentiometric titration, parameter IEC was calculated in terms of mili-equivalents (meq) of OH^- ions per gram of dry AEM from the following equation:

$$IEC\left(\frac{meq}{g}\right) = \frac{(V_{blank} - V_{membrane}) \cdot c_{HCl}}{m_{dry\ membrane}} \quad (2)$$

where V_{blank} and $V_{membrane}$ represent the consumed volumes [ml] of 0.1 M KOH solution for the blank and sample membranes, respectively. c_{HCl} represents the molar concentration [mol/l] of HCl solution, and $m_{dry\ membrane}$ represents the mass of dry membrane samples [g].

2.5 Mechanical properties

The tensile strength at maximum (MPa) of the membranes was determined by Shimadzu, AG-X plus 10 kN electromechanical universal testing machine. Membrane samples with specimen dimensions: 10 mm × 20 mm were vertically mounted. Application of tensile force proceeded at 5 mm min^{-1}. Three specimens were tested per sample and average values and standard deviations were calculated. Prior to testing, membrane samples were equilibrated in liquid water and ambient air at room temperature for 3 h.

2.6 Swelling ratio

Swelling ratio measurements were performed in 6 M KOH at 60 °C. Membrane samples with dimensions of 1 × 1 cm^2 (A_{dry}) were immersed in an alkaline medium (6 M KOH at 60 °C.) After immersion, the surplus alkaline solution on the membrane surface was removed with a paper towel, and then the surface area (A_{wet}) of the wet membranes was determined at room temperature after 24 hours. In-plane swelling ratio (SR) of the membranes has been determined

after 24 hours when equilibrium was reached from the following equation.

$$SR_{In-plane} = \frac{A_{wet} - A_{dry}}{A_{dry}} \cdot 100\ \% \quad (3)$$

3 Results

Figure 1 shows the zeta potential of CNF and CNF polyDADMAC dispersion which were used as a filler in the composite chitosan membranes. The successful modification of CNF by the reagent polyDADMAC was observed as an obtained positive zeta potential value on the purified product. A positive zeta potential correlates to a positive charge but not also to the quantity of charge. The neat CNF dispersion shows a negative zeta potential in all pH ranges except for pH 2, where it is close to zero, therefore differentiating in charge from the modified CNF. The opaque appearance of the resulting composite chitosan membrane with CNF fillers is shown in Figure 2.

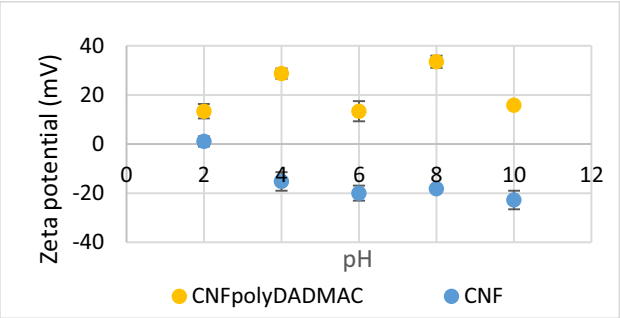

Fig. 1. Zeta potential of modified and un-modified fillers

Fig. 2. Composite chitosan CNF membrane

Fuel permeability is an undesirable property as a high membrane fuel permeability can lead to a decreased fuel cell performance. Fuel permeability expressed as EtOH permeability of the composite membranes is shown in Figure 3. A higher amount of unmodified filler increases the EtOH permeability in comparison to a chitosan membrane without fillers. In contrast, with the addition of modified CNF polyDADMAC fillers, EtOH permeability is decreased in comparison to a pure chitosan membrane. Fuel permeability in membranes is linked to different factors, and the 3D structure of the membrane with formed channels and clusters has a huge role on the permeability. The addition of un-modified un-charged CNF fillers can result in a bigger chain spacing between chitosan chains, and the charged modified CNF fillers can diminish the effect.

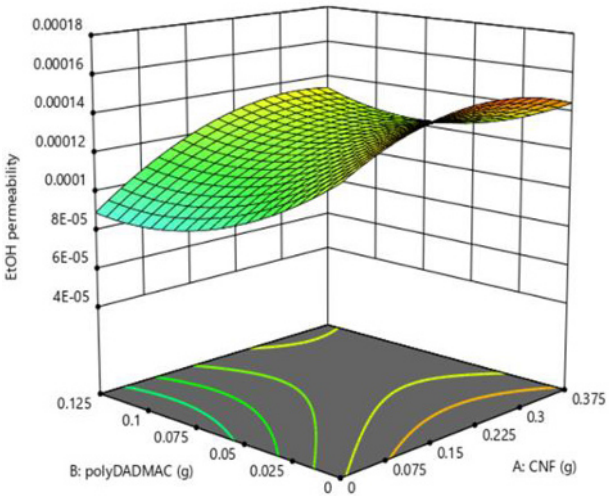

Fig. 3. EtOH permeability of membranes with different filler contents

Ion exchange capacity (IEC) corresponds to the ion exchangeable groups present in the membrane. IEC calculated from titration measurements of the composite membranes is shown in Figure 4. With the introduction of unmodified fillers, IEC significantly decreased in comparison to a pure chitosan membrane; however, the inclusion of modified fillers caused only a minor decrease in IEC. The highest amount of modified filler had a similar IEC to a membrane without fillers.

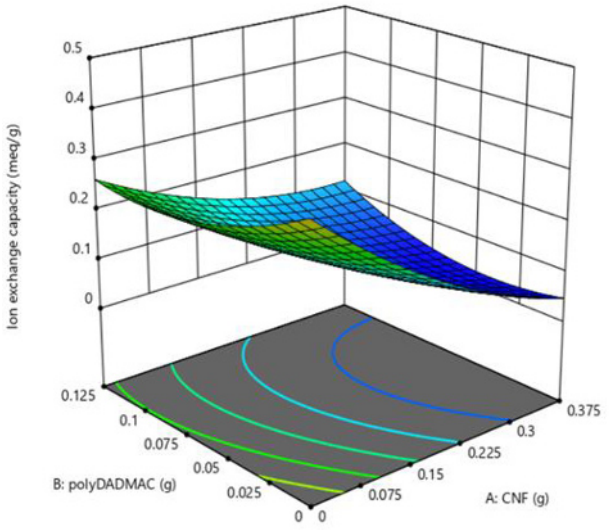

Fig. 4. Ion exchange capacity of membranes with different filler contents.

The mechanical properties of the composite membranes were determined by a tensile strength test. Results of the tensile strength tests of the composite membranes are shown in Figure 5. The tensile strength is greatly improved with the addition of a higher amount of filler. The greatest improvement in tensile strength is seen for the membranes with the highest loading of unmodified and modified CNF fillers, which is directly related to the excellent mechanical and physical properties of CNF.

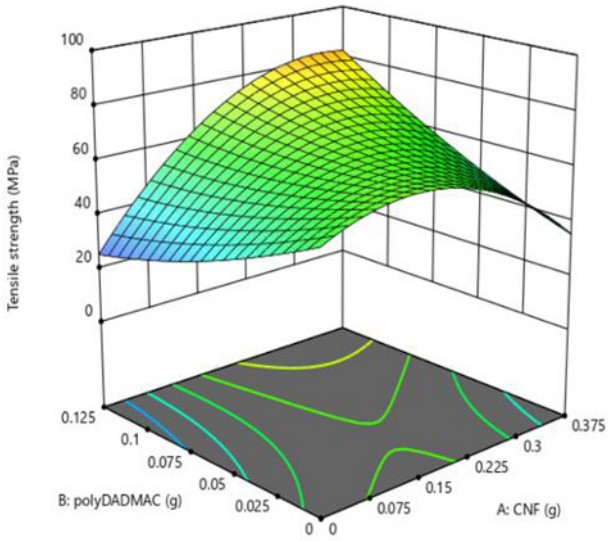

Fig. 5. Tensile strength of membranes with different filler contents.

The in-plane swelling of the membranes might loosen the contact between current collectors and membrane electrode assembly in the fuel cell. In-plane swelling ratio (SR) of the composite membranes is shown in Figure 6. The SR was decreased with the presence of unmodified and modified CNF fillers, making the inclusion of both types of fillers beneficial in the composite chitosan AEMs. The highest amount of un-modified and modified fillers resulted in the lowest SR.

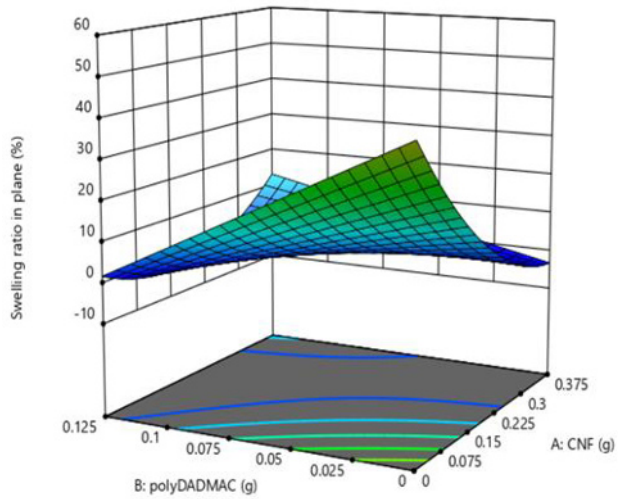

Fig. 6. In-plane swelling ratio of membranes with different filler contents.

4 Conclusions

A series of composite chitosan membranes with different amounts of unmodified and modified CNF fillers were prepared by a simple dispersion casting technique. The inclusion of fillers enables the tuning of membrane properties for AAEMFC applications. The lowest EtOH permeability of $8.97 \cdot 10^{-5}$ cm^2/s and in-plane swelling ratio of 1.78 % was observed for the chitosan membranes with the highest amount of CNF polyDADMAC. The highest IEC of 0.35 meq/g was observed for the chitosan membrane. Tensile strength of the highest CNF and CNF polyDADMAC filler loading in the composite chitosan membrane corresponded to 82.36 MPa. In comparison, in a product sheet for a commercially available proton exchange membrane Nafion™ 117 [7] it can be found that the commercial membrane has almost a half lower tensile strength (43 MPa) and a higher (10%) in-plane swelling ratio and a commercial AEM fumasep® FAA-3-50 [8] also has a lower tensile strength (25-40MPa) and has a comparable swelling (0-2%); although testing should be done in the same conditions to offer a reliable comparison. The results demonstrate that the obtained membranes are promising AEM candidates for alkaline alcohol fuel cell applications. Additionally, cell tests will need to be performed to showcase the AEMs behaviour in actual fuel cell set-ups.

Financial support was received in the frame of the Slovenian Research Agency Young Researcher Programme (P2-0118/0795) and project “GO DEFC” (Grant number N2-0087).

References

[1] M. Hren, M. Božič, D. Fakin, K. S. Kleinschek, and S. Gorgieva, “Alkaline membrane fuel cells: Anion exchange membranes and fuels,” *Sustain. Energy Fuels*, vol. **5**, no. 3, pp. 604–637, 2021.

[2] J. Cheng, G. He, and F. Zhang, “A mini-review on anion exchange membranes for fuel cell applications: Stability issue and addressing strategies,” *Int. J. Hydrogen Energy*, vol. **40**, no. 23, pp. 7348–7360, 2015.

[3] M. Hren *et al.*, “Chitosan-Mg(OH)2 based composite membrane containing nitrogen doped GO for direct ethanol fuel cell,” *Cellulose*, vol. **28**, no. 3, pp. 1599–1616, 2021.

[4] N. A. Hanna Rosli *et al.*, “Review of chitosan-based polymers as proton exchange membranes and roles of chitosan- supported ionic liquids,” *International Journal of Molecular Sciences*, vol. **21**, no. 2. MDPI AG, Jan-2020.

[5] L. W. XuYing Zheng, ChenShi Shang, JiaRui Yang, JiLin Wang, “Preparation and characterization of chitosan-crown ether membranes for alkaline fuel cells,” *Synth. Met.*, vol. **247**, pp. 109–115, 2019.

[6] B. Kaker *et al.*, “Novel Chitosan–Mg(OH) 2 -Based Nanocomposite Membranes for Direct Alkaline Ethanol Fuel Cells,” *ACS Sustain. Chem. Eng.*, vol. **7**, no. 24, pp. 19356–19368, Dec. 2019.

[7] FuelCellStore, “Nafion N115, N117, N1110 Ion

exchange Materials.” .

[8] FuelCellStore, “Technical Data Sheet - fumasep FAA-3-50.” .

The efficiency of chitosan-graphene oxide composite membranes modified with genipin in fuel cell application

Selestina Gorgieva[1,2*], *Azra* Osmić[1], *Boštjan* Genorio[3], *Viktor* Hacker[4], *Sigrid* Wolf[4] and *Silvo* Hribernik[1,2]

[1]Faculty of Electrical Engineering and Computer Science, University of Maribor, Koroška cesta 46, 2000 Maribor, Slovenia
[2]Faculty of Mechanical Engineering, University of Maribor, Smetanova 17, 2000 Maribor, Slovenia
[3]Faculty of Chemistry and Chemical Technology, University of Ljubljana, Večna pot 113, SI-1000 Ljubljana, Slovenia
[4]Graz University of Technology, Institute of Chemical Engineering and Environmental Technology Inffeldgasse 25/C, 8010 Graz, Austria

Abstract. The paper reports on the processing of chitosan N-doped reduced graphene oxide (CS/N-rGO) nanocomposite membranes prepared by a facile, dispersion-casting procedure aimed as anion exchange membranes in fuel cells. Genipin (GEN) was used as a crosslinking agent to ameliorate mechanical weakens of nanocomposite membranes, while the N-rGO filler, aside of its role as a mechanical enhancer, is expected to improve the ionic conductivity of membranes. The resulting properties of processed membranes in terms of morphology, tensile strength, elasticity, and ethanol permeability were examined. The relevance of the membranes in terms of efficiency and performance was demonstrated in a single cell test.

1 Introduction

As promising technology for (chemical to electrical) energy conversion, with extremely low pollutant emissions and environmental impact, the fuel cells are on the right track to dominate relevant market segments. Yet, improvements in efficiency/cost ratio of fuel cell components and the whole set-up are still necessary to reach market competitiveness against current technologies for energy production, such as the internal combustion engine and the gas turbine. Anion exchange membranes (AEMs) are among the core components of the alkaline fuel cell, acting as separators among anode and cathode and transporters of OH- ions. In seeking sustainability and green development, the investigation on biopolymeric AEMs nowadays becomes actual among the research community. [1] Natural polymers, such as chitosan (CS), have been recognised as a potential alternative to synthetic AEMs. [2] CS is a deacetylated chitin product found in the exoskeleton of invertebrates and the cell walls of fungi, consisting predominantly of 2-amino-2-deoxy-D-glucopyranose units, linked by ß-1,4-bond. Aside from the reported attributes of this material in fuel cell applications, its mechanical weakness and swelling related to OH-groups abundance and lack of ion-transporting moieties seek its augmentation into a more complex molecular arrangement. Our approach introduces an inorganic component, N-doped reduced graphene oxide (N-rGO), combined with genipin (GEN)-crosslinking chemistry. GEN is a natural and biodegradable alternative to synthetic crosslinking agents which reacts with primary and secondary amines [3], offering improved mechanical, chemical and thermal stability of the material. [4]

2 Methods

2.2 Membrane preparation

Neat CS membranes were prepared according to our recently published approach. [2] For the preparation of CS/GEN and CS/GEN/N-rGO membranes, the 1 wt. % GEN solution in ethanol and 1 % N-rGO dispersion were respectively added to 25 mL of 1 % CS dispersion, to final concentration of 0.002 % (denominated as 100 µL), 0.004 % (200 µL), 0.020 % (500 µL) and 0.040 % w/v (1000 µL) for GEN and 0.01 %, 0.04 % and 0.07 % w/v for N-rGO. Final dispersion was vortexed at 3000 min^{-1} to obtain a homogeneous dispersion. The membranes were dried on-air and stored for future characterisations.

2.2 Attenuated Total Reflectance Fourier Transform Infrared Spectroscopy (ATR-FTIR)

ATR-FTIR spectra were obtained on a Spectrum One FTIR spectrometer (Perkin-Elmer) with a Golden Gate ATR attachment and a diamond crystal for all components and CS membranes, containing a variable concentration of N-rGO and GEN. The absorbance measurements were recorded within the 650 - 4000 cm^{-1} region, with 16 scans at a resolution of 4 cm^{-1}.

* Corresponding author: selestina.gorgieva@um.si

2.3 Mechanical measurements

The membranes' tensile strength (MPa) and elastic elongation (%) were determined by testing machine Shimadzu, AG-X plus 10 kN. Membranes samples with specimen dimensions: 10 mm × 20 mm were vertically mounted. The effective clamping distance was 25 mm. Application of tensile force (10 kN load cell) proceeded at 1 mm min^{-1}. Prior to testing, the membranes were equilibrated in distilled water.

2.4 Scanning Electron Microscopy (SEM)

The field eFE-SEM analysis was performed using a Carl Zeiss FE-SEM SUPRA 35 VP electron microscope to visualise membranes' microstructure. Imaging was performed at 1 kV accelerating voltage at an approximately 4.5 mm working distance. The membranes were attached to aluminium sample holders via conductive carbon adhesive tape. Before analysis, a layer of palladium was sputtered on the surface of membrane samples.

2.5 Ethanol permeability

Ethanol permeability through 1 % CS membrane with different N-rGO and GEN was measured in a temperature probe at 25 °C in two temperature-controlled diffusion cells. The membrane was located between the two temperature-controlled diffusion cells (the volume of each cell unit is 25 mL). Reservoir A was filled with 25 mL of 6 M KOH; reservoir B was filled with 25 mL of 2 M EtOH/6 M KOH (8.5 w/w % ethanol). To create the same pressure on the membrane, both reservoirs were filled simultaneously, as this represents the natural working environment of the fuel cell. The ethanol concentration was determined using a conductometer at different time intervals. The permeability coefficient of ethanol, P *(cm^2 s^{-1})* was calculated using the equation below.

$$P\left(\frac{cm^2}{s}\right) = \frac{(C_B - C_{B0})}{(t - t_0)} \times \frac{V_B \cdot l}{A \cdot C_{A0}} \quad (1)$$

where C_{A0} represents the initial concentration of ethanol in the source compartment, and V_B represents KOH volume in the receiving chamber. A and l represent the area and thickness of the membrane, respectively.

2.7 Cell performance measurement (Single-cell testing, DAEFC performance)

Before the fuel cell experiments, the membranes were doped with OH- by immersion in 1 M KOH for 24 h and extensive washing with distilled water. Electrodes were prepared as described in our previous work. [2] The Membrane Electrode Assemblies (MEAs) with 2 x 2 cm^2 were prepared by placing the membrane electrolyte between the electrodes. The MEAs were assembled in a self-constructed DAEFC. Pure oxygen gas (5.0, 99.995 %) with a constant flow rate of 25 mL min 1 was used as a cathode feed gas. A mixture of 1 M ethanol in 1 M KOH served as anode fuel (5 mL min^{-1}). The membranes were tested additionally in 3 M EtOH/5 M KOH to determine the influence of the fuel concentration on the cell performance. To evaluate the temperature dependence, experiments were conducted at room temperature, as well as at 35 °C, 43 °C, 50 °C and 57 °C. The current densities (I) and cell potentials (V) of the single cells were determined using a Reference 600TM Potentiostat/Galvanostat/ZRA from Gamry instruments. The results were plotted in a current density–potential diagram, indicating the power density.

3 Results and discussion

Due to the fragility of thin CS membranes, especially after immersion in water or water /KOH mixtures, the crosslinking with GEN was examined, alongside the introduction of inorganic N-rGO filler. The GEN molecule can react with the primary amino group in CS in a neutral or acidic environment, resulting in heterocyclic amines forming and developing deep-blue colour, as seen on membrane on Figure 1. The heterocyclic amines can further associate to form crosslinked networks with short (dimmer, trimer, and tetramer) bridges.

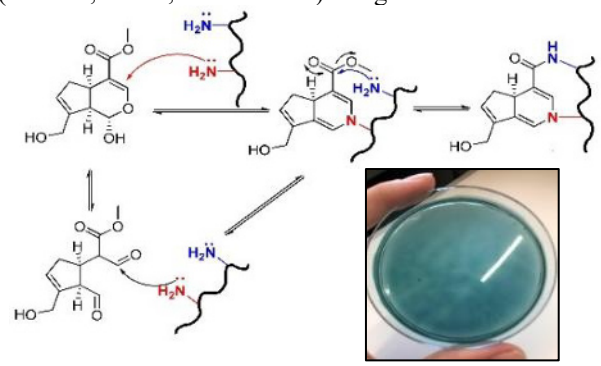

Fig. 1. Tentative scheme for GEN crosslinking in NH_2-containing polymers. Insert: CS membrane crosslinked with GEN.

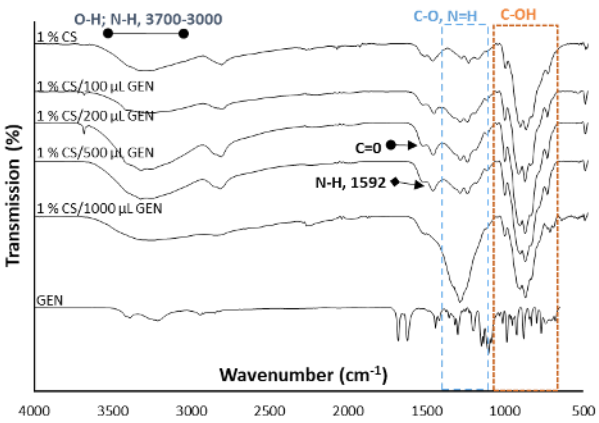

Fig. 2. ATR-FTIR spectra of CS membrane with different concentrations of GEN, including the GEN powder as control.

ATR-FTIR spectra (Figure 2) demonstrate GEN concentration-dependent spectral changes in GEN-containing membranes in comparison to neat CS membrane, which suggest on molecular interaction among the components. As explained in our previous work [5],

two-way reaction mechanisms are possible in GEN – CS system. Herein, the spectral lines demonstrate an increase of ratio between the area of absorption bands at 1640–1650 cm^{-1} and 1570–580 cm^{-1} assigned to υ(C=O) and υ(N-H), respectively, in crosslinked, relative to neat CS. Latter can be attributed to the formation of secondary amino groups among CHT amines and ester groups of GEN, being identified as a second, slower reaction under which a single, bi-functional crosslink between CHT molecules are formed. The mechanical data in Figure 3 evidence that GEN presence significantly improve the tensile strength in N-rGO – free membranes, while filler addition brings the opposite effect. In contrary, the membrane elasticity significantly decreased by GEN addition, suggesting the formation of bridges, which secures the polymer distances, restricting the membrane elongation on macro scale.

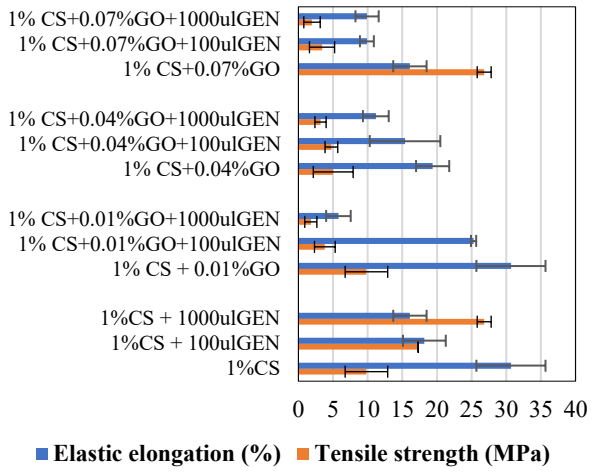

Fig. 3. Tensile strength (MPa) and elastic elongation (%) of CS membranes with different concentrations of GEN and N-rGO.

Previous studies [6] utilising CS and rGO demonstrate that at low content, rGO can be dispersed in the polymer solution more uniformly, which may improve the adhesion with the polymer matrix, while, with the further increase of the rGO content, dispersibility within the polymer solution deteriorated, resulting in much weaker interaction with the polymer. Our results do not confirm this, and tensile strength increases with N-rGO increment in GEN-free samples, suggesting that the nature of filler in terms of shape, size, and charge has a dominant influence on its efficiency as a mechanical enhancer.

SEM micrographs in Figure 4 demonstrate the smoothening effect of GEN; herein, we speculate that the presence of GEN bridges controls the membrane shrinking during the drying process, which is the leading cause for shrinking of neat CS membranes, thus positively contributing to tensile strength. Upon addition of N-rGO, the bridges may restrict the continuous assembling of filler, promoting the phase separation into condensed, N-rGO - rich areas on one side and N-rGO - lean areas on another, forming the weak points and tensile strength reduction.

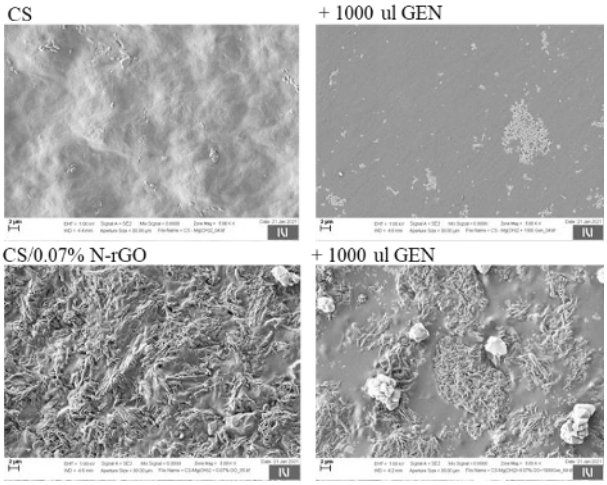

Fig. 4. ATR-FTIR spectra of CS membrane with different concentrations of GEN, including the GEN powder as control.

The fuel (ethanol) permeability is one of the critical parameters affecting the membrane performance, as the same can accelerate the degradation process of the membrane, interfere with the cathode reaction, and cause electrocatalyst poisoning. [2] It was found that the permeability was slightly increased by the addition of N-rGO and was not affected by addition of GEN crosslinking agent, irrespective of concentration. As seen by SEM image, the fillers are expected to cause the formation of intermediate spaces in the membranes, which do not restrict the migration of ethanol molecules, resulting in increased permeability values.

The membrane performance in fuel cells is determined in direct alkaline ethanol test cells, where the effect of different loading concentrations of N-rGO and GEN concentration were investigated, as well as the influence of temperature and fuel concentration on the DAEFC membrane performance. In summary, the CS/N-rGO with the lowest graphene loading (0.01 %) at a temperature of 57 °C and the concentrated 3 M EtOH/5 M KOH anode fuel presented the best overall performance (Figure 5). The best Pmax. Of 17.7 mW cm^{-2} could be achieved at a current density of 97.39 $mAcm^{-2}$.

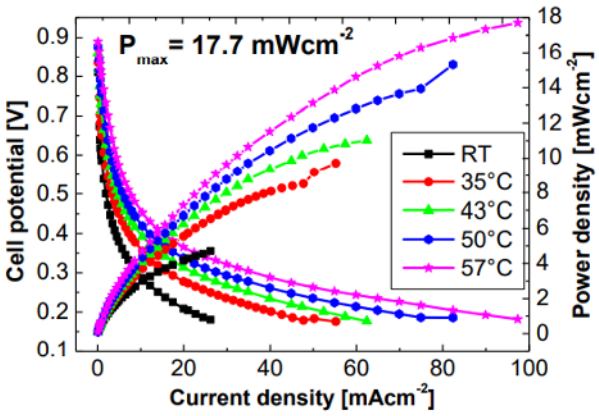

Fig. 5. DEAFC discharged cell voltage and power density of 1% CS/N-rGO (0.01%) membranes at different temperatures with 3 M EtOH/5 M KOH.

Very comparable are values with the addition of 100 ul GEN, without N-rGO loading (Pmax. of 17.2 mW cm^{-2} at a current density of 96.90 mA cm^{-2}). Latter, suggest on the potential action of GEN or GEN-product in ion conduction, as also suggested by ionic conductivity study (not presented here). Yet, the GEN presence at higher concentrations increases membrane fragility and their disintegration under a highly alkaline medium.

4 Conclusion

We demonstrated that CS-based nanocomposite membranes containing N-rGO and/or GEN significantly outperform the fuel cell performance of the pristine CS membrane. In previous studies [19], the highest reported power density value for CS-based membranes was 62.2 mW cm^{-2} (current density 174 mA cm^{-2}) at 60 °C and 72.7 mW cm^{-2} (current density 209 mA cm^{-2}) at 80 °C. Compared to these investigations, lower temperatures (57 °C instead of 60 °C and 80 °C), a lower oxygen fuel rate (25 mL min^{-1} instead of 100 mL min^{-1}) and lower metal loading for the anode (0.75 mg cm^{-2} instead of 2 mg cm^{-2}) and the cathode (0.5 mg cm^{-2} instead of 1 mg cm^{-2}) were used showing the relevance of the tested sustainable bio-based membranes for use in energy conversion applications.

The authors would like to acknowledge the financial support from Slovenian Research Agency, in the frame of project »Graphene Oxide-based MEAS for the Direct Ethanol Fuel Cell« (grant number N2-0087), the Textile Chemistry Program (P2-0118) and from the Austrian Science Fund (FWF) under project number I 3871-N37.

References

1. M. Hren, M. Božič, D. Fakin, K.S. Kleinschek, S. Gorgieva, Alkaline membrane fuel cells: Anion exchange membranes and fuels, *Sustain. Energy Fuels*. **5** (2021) 604–637.

2. S. Gorgieva, A. Osmić, S. Hribernik, M. Božič, J. Svete, V. Hacker, S. Wolf, B. Genorio, Efficient Chitosan/Nitrogen-Doped Reduced Graphene Oxide Composite Membranes for Direct Alkaline Ethanol Fuel Cells, *Int. J. Mol. Sci.* **22** (2021).

3. V.G. Tacias-Pascacio, E. García-Parra, G. Vela-Gutiérrez, J.J. Virgen-Ortiz, Á. Berenguer-Murcia, A.R. Alcántara, R. Fernandez-Lafuente, Genipin as an emergent tool in the design of biocatalysts: Mechanism of reaction and applications, *Catalysts.* **9** (2019).

4. a Bigi, G. Cojazzi, S. Panzavolta, N. Roveri, K. Rubini, Stabilisation of gelatin films by crosslinking with genipin., *Biomaterials.* **23** (2002) 4827–32.

5. S. Gorgieva, T. Vuherer, V. Kokol, Autofluorescence-aided assessment of integration and μ-structuring in chitosan/gelatin bilayer membranes with rapidly mineralised interface in relevance to guided tissue regeneration, *Mater. Sci. Eng. C.* **93** (2018) 226–241.

6. X. Qian, N. Li, Q. Wang, S. Ji, Chitosan/graphene oxide mixed matrix membrane with enhanced water permeability for high-salinity water desalination by pervaporation, *Desalination.* **438** (2018) 83–96.

Characterization and experimental comparison of commercial PEMFC stacks for marine applications

Eleonora Gadducci*[1], *Thomas* Lamberti[2], *Loredana* Magistri[1], *Massimo* Rivarolo[1], *Andrea* Dellacasa[3], *Barbara* Campora[3], *Gerardo* Borgogna[3], *Agnese* Lancella[3], *Enrico* Speranza[3]and *Andrea* Voiello[3]

[1]Thermochemical Power Group (TPG), DIME, University of Genoa, Via Montallegro 1, 16145 Genoa, Italy
[2]BluEnergy Revolution Scarl, Viale Nazario Sauro 5/2A, 16145 Genoa, Italy
[3]Fincantieri S.p.A., via Cipro 11, 16129 Genoa, Italy

Abstract. PEM Fuel Cells are considered among the most promising technologies for hydrogen utilization in both stationary and automotive applications. The number of FC installations on board ships – alone or in hybrid configuration with batteries – is increasing significantly, although international regulations that drive their installation are still missing. In this scenario, the project TecBia aims to identify a dedicated test protocol and the best commercial PEMFC technology for marine applications, assessing the integration of a 140 kW PEMFC system on the Zero Emission Ultimate Ship (ZEUS) vessel. The system design and technology provider has been chosen after a technical comparison based on a dedicated experimental campaign. The experimental campaign had two goals: (i) analyse the performance of the different PEMFC systems to define the best characteristics for maritime applications; (ii) verify the compliance with naval requirements with reference to current and future standards. The present study shows the resulting test protocol for FC Systems (FCS) for maritime applications, defined starting from the existing international regulations on FCS installations and on naval environment requirements; the results of its application on the commercial system chosen for the installation on ZEUS are reported.

1 Introduction

The use of alternative fuels on-board ships has become crucial to decrease navigation's strong impact on the environment, as issued by the International Maritime Organization (IMO) [1,2], and to follow the recent restrictions on Green House Gases (GHG) emissions [3]. In this context, hydrogen is one of the most promising fuels for marine applications [4][5], and Polymeric Electrolyte Membrane FC (PEMFC) can be a promising technology to be employed for propulsion [6-12], also coupled with batteries, and evaluating the best hydrogen storage technology, to increase the practicable navigation distance [13-21]. In this context, many research projects have deepened the topic of experimental PEMFC systems for maritime applications [22-25], but the absence of a shared international legislation specific for fuel cells on marine vessels can create issues in the design phase of real-scale systems. Indeed, the IMO has not made available any guideline for the installation for FC Systems (FCS) on marine vessels, nor guidelines for the Type Approval Test (TA), which is the totality of the tests that an FCS should withstand in order to obtain a Type Approval Certificate (TAC). For this reason, the present work – which is part of the national research project TecBia (*Technologies at low environmental impact for energy production on ships*), financed by Fincantieri-Isotta Fraschini Motori S.p.A. and Italian Ministry of Economic Development (MISE) as part of "National Operational Programme (PON) 2014/2020 Large R&D Projects" [26] – aims to define a testing routine which can be crucial to carry out a technical comparison between different commercial PEMFC systems and to evaluate their suitability for shipping installations. Starting from the legislations available for fuel cell installations and from the aspects related to naval environment regulations, the main aspects to be checked via the testing protocols have been individuated. The previous experience of the research team in terms of experimental know-how for designing, building up and testing a FCS for maritime application in the HI-SEA UniGe-Fincantieri joint laboratory [27] has been a fundamental prerequisite to the output of the study [22-25]. This operation can lay the foundations of a future and specific international standard, defining the experimental steps necessary to assess the suitability of FC stacks for shipping requirements.

After the definition of dedicated test protocols, the different available FC technologies have been tested following the outlined procedure. This allowed to individuate the best commercially available PEMFC technology, which is going to be installed onboard the ZEUS research vessel, which is the main outcome of the TecBia project. This work presents the results of the application of the testing protocol of the chosen FCS,

* Corresponding author: eleonora.gadducci@edu.unige.it

which justify the choice for its installation onboard the ZEUS.

1.1 Existing legislations considered

Nowadays, as a dedicated regulation does not exist, every integration process of Fuel Cell and hydrogen systems must follow the Alternative Design procedure (AD), a general procedure based on Risk Assessment (RA) that allows the introduction of limited and unregulated variants within the project if they demonstrate, through the RA, a level of security equal or higher than the one required by the regulations for traditional design. To proceed with an objective evaluation of the performance of FCS, it is therefore not possible to refer to any internationally recognized technical document. It is consequently necessary to carry out an analysis of the regulations and available standards published by Classification Societies (CS) and standardization (ISO, IEC) recognized at European (EU) and national level. Indeed, while an international legislation is expected in the next future, the CS such as the Italian Naval Register (RINA) are equipping themselves with internal rules that define the safety requirements that FC systems must comply with in order to be installed on board.

To consider in the broadest but most precise way possible both the aspects related to the naval legislation (as for the environmental conditions) and those related to the rules and standards of FC technology (as regards the operational conditions), the regulations of the CS and the standards related to fuel cells have been taken into account, in particular:

- IACS UR-E10: it defines the test specifics for the TA of electrical systems.
- RINA-FC: it is specific for FCS and gives important guidelines for their installation onboard ships, citing the IEC 62282 as a reference for the TA.
- RINA RULES, PART C: these regulations referred to all the machinery, electrical installations and the automation installed on board; it has also been used as a guideline for the design of the test stations, and it has provided multiple indications and specifications of completion to the IACS UR-E10.
- IEC 62282: it describes the TA for FCS for the installation in stationary, portable, micro and vehicles applications.

The latter has been considered also for what concerns the environmental conditions – vibrations, temperature, and wind) – which the FCS should withstand to, comparing these conditions to the ones applicable to Auxiliary Power Units (APU) on heavy-duty transport installations [28].

1.2 FCS characteristics

Table 1 reports the main technical data for the FCS investigated in this work: the data are referred to a system which can provide a maximum electrical power of 36 kW, 30 kW considering the Balance of Plant (BoP) consumption.

Table 1. FCS technical data. [29]

Parameter	Range
Current range [A]	50 - 500
Power range [kW]	5.1 – 36
Voltage range [V]	71 – 102
H_2 mass flow [kg/h]	0.2 – 2.3
BoP consumption [kW]	1 – 6

2 Experimental

The outcome of the study of the available legislation, as described in Section 1.1, is the definition of a test list, which can be divided into six different typologies:

- Environmental
- Operative
- Emissions
- Normal conditions
- Failure conditions
- Routine tests

The experimental test rig has been designed and built with the support of BluEnergy Revolution (BER [30]), an emerging company operating in the field of hydrogen applications on marine vessels.

To estimate the effects of static inclination on the FCS performance, BER designed a dedicated platform able to withstand 500 kg and to offer two different inclination degrees: 30 and 45°. The Table 2 summarizes the experimental tests – which were reproducible in BER's test rig – that have to be carried out on the FCS to evaluate their suitability for maritime applications:

Table 2. Experimental tests performed.

Typology	Test description	Regulation
Environmental tests	Cooling temperature: ±2°C from setpoint	RINA PartC, Vol II, Sec2
	Static inclination: startup+constant load at 30°	IACS UR E-10
Operative tests	Efficiency: calculated at 25%, 50%, 75% and 100% of nominal power	EC 62282-3-200
	Power response (electrical and thermal, time needed), minimum to nominal power and reverse	EC 62282-3-200
	Start-up/shutdown: time response of the net electrical power	EC 62282-3-200
Emissions tests	Maximum noise: during operation and in background with FCS off	EC 62282-3-200
	Maximum vibrations: during operation and background with FCS off	EC 62282-3-200
	Exhaust reaction water: quantity and quality	-
Normal conditions	Polarization curve	-

	Constant load (minimum time: 15 minutes)	-
	Typical navigation profile simulation	-
Failure conditions tests	Emergency shutdown: time needs to conclude procedure	EC 62282-3-200
Routine tests	Visual inspection (agreement with technical schemes)	IACS UR E-10
	Voltage variation measure	-
	Gas leakage assessment test (on FC stack)	-

The tests results have been the key for the evaluation of the different technologies available. In this work, the most interesting outputs of the test protocol on the FCS are reported and described in the following sections: efficiency calculation, polarization curve and operative profile.

2.1. Test rig integration scheme

Depending on the design chosen by the supplier, each FCS can be already provided with different components and connections. In order to prepare a test rig where the technology under investigation can be easily integrated, it is necessary to define a generic integration scheme. Despite the absence of technical prescriptions for this, the authors faced the challenge thanks to the experience acquired by working on previous projects on the same topic [22,23,25].

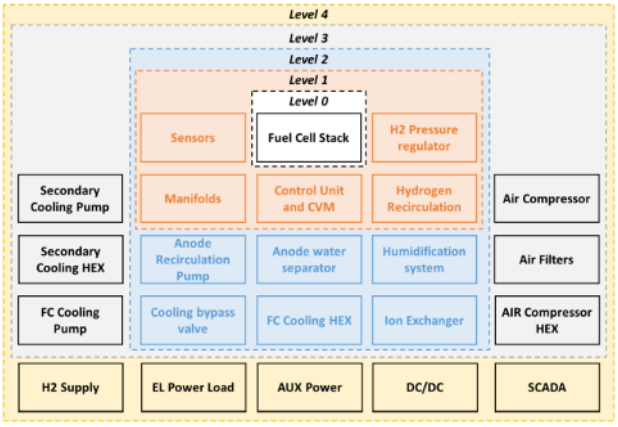

Fig. 1. Generic FCS integration scheme.

Figure 1 shows the generic integration scheme adopted to design the test rig. The scheme not only divides the integration levels but identifies the various integration modules for the various connection lines between the FCS system and the laboratory.

2.2. Comparison of tests results

To compare the performance of the different systems, it is necessary to normalize the dimensions on which carry out the comparative study. The comparative analysis mainly concerns the performance, in terms of voltage and current ranges, as well as the system efficiency. The latter is given by the difference between the net power and the gross power, thus the power absorbed by the auxiliaries. Since the power, both the nominal one and the measured one, absorbed by the BoP components has different levels of uncertainty, to make the analysis meaningful it was chosen to proceed with the comparison of the electrical performance measured with respect to the stack, excluding the consumption of the BoP.

2.2.1 Efficiency calculation

According to [31], the efficiency is calculated based on the Higher Heating Value (HHV) of hydrogen, and the calculation requires the following measures:

- Hydrogen inlet flow rate
- Heat supplied/absorbed externally
- Flow rate of the oxidant (air) entering the system
- Electrical power absorbed by auxiliaries
- Electrical power generated by the system
- The efficiency test should be conducted in accordance with the following procedure:
- Start the system and require a constant power
- Verify that the system operates in stable conditions, i.e., within the limits of variability imposed by the [31] regulation
- Measure the parameters necessary for the calculation of efficiency for no less than 1 hour.

The electrical efficiency η_{el} of the system is therefore calculated by using the following formula:

$$\eta_{el} = \frac{P_n}{P_{in}} * 100 = \frac{(P_{el,out} - P_{el,aux})}{(P_{fuel,in} + P_{air,in})} * 100 \qquad (1)$$

Where P_n is the net electrical power generated by the system, and P_{in} is the total power input to the system. The thermal efficiency of the system is calculated as:

$$\eta_{th} = \frac{P_{HR}}{P_{in}} * 100 \qquad (2)$$

Where P_{HR} is the recoverable thermal power output from the system, and it is obtained by the following equation:

$$P_{HR} = \dot{m}_{HR} * c_{HR} * (T_{HR1} - T_{HR2}) \qquad (3)$$

knowing the mass flow $\dot{m}_{HR}$ of the cooling fluid [kg/s], its specific heat c_{HR} at given temperature and pressure [J/(kgK)], and the temperature difference $(T_{HR1} - T_{HR2})$ between entrance and exit of the system under consideration.

2.2.2 Polarization test

Experimentally reproducing a polarization curve implies that a FC (single cell or stack) will be subjected to the

operation at subsequent current setpoints, from zero to the nominal value and back to zero. This procedure allows the operator to draw for the tested device the V-I curve, which varies slightly for FC technologies by different manufacturers. In general, the goal of measuring the polarization curve is the determination of the Membrane-Electrode Assembly (MEA) performance in terms of cell voltage and power density considering the current density as a reference. The residence time of each set-point should be long enough to ensure the stabilization of cell voltages in ±5 mV in a time range between 2 and 15 minutes, except for the Open Circuit Voltage (OCV) measure, which must not exceed 1 minute of stay. The set-points proposed by the EU Harmonised Test Protocols for PEMFC-MEA Testing in Single Cell Configuration for Automotive Applications [32] are summarized Figure 2: the y-axis represents the current density at which the FC must be tested, while the x-axis indicates the subsequent test steps. This harmonized test protocol is designed for single cell tests and for this reason the possibility to make slight changes on the protocol is allowed, in order to apply it in the best possible way to the characteristic limitations of the individual FC modules: minimum operating electrical power, longer possible operation at minimum power, etc.

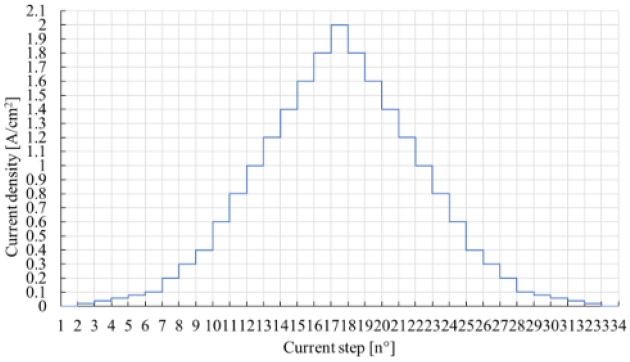

Fig. 2. Set-points for the polarization curve testing [32].

2.2.3 Operative profile test

To verify the adequacy of the performance of the FC module in a real on-board application, part of a typical naval cargo load energy demand profile – agreed with Fincantieri – is considered, which had been successfully adopted also in a previous project [25]. This profile can be divided into two parts: the first one, where first some increasing and later some decreasing load steps are present, represents the dynamic load that can be required during manoeuvring. The second one simulates navigation after manoeuvring inside the port, where the system works for a longer period at constant load and at 100% of its capabilities. It may represent the load request during navigation at constant speed for propulsion, or the case where the system is employed as an auxiliary to cover the hotel load. The profile can be obtained thanks to the implementation of the electrical control of the systems (including the FC and DC/DC module coupling).

Figure 3 shows the shipping load profile cited, to be applied to the PEM fuel cell systems under consideration for 4300 seconds.

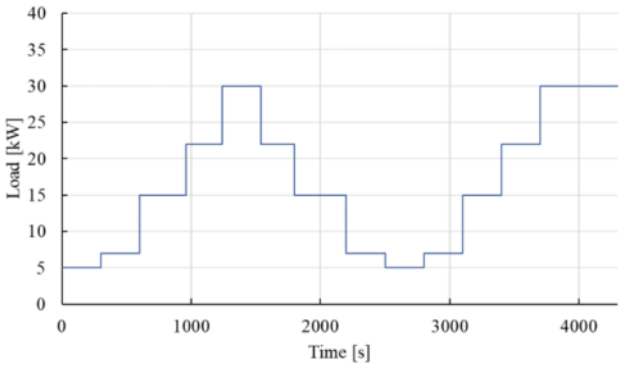

Fig. 3. Shipping load profile assumed to be tested on the FCSs.

2.2.4 Static inclination test

To assess the ability of the FCS to work while inclined, it has been installed and tested on the Test Bench developed by BER. The angle of inclination tested was 22.5°, and the load request during this part of the assessment was constant for a prolonged period (around 20 minutes), to verify the good operation of the system in this condition. The main concerns that may arise from this type of operation are linked to the efficient delivery of the reactants and cooling flows to the FCS. The results of this test are compared with the implementation of the same load profile implemented with the non-inclined stack.

3 Results

Hereby are reported the results of the calculation of the FCS efficiency and the most relevant experimental results.

In order to compare the performance of FC systems, it is necessary to normalize the dimensions on which carry out the comparative study. The comparative analysis mainly concerns the performance in terms of voltage and current ranges, as well as system efficiency. The latter is given by the net system power output divided by the gross power input, that accounts for the power absorbed by auxiliaries. Since the powers absorbed by the BoP have different levels of uncertainty and changes depending on the components installed, to make the analysis meaningful it was chosen to proceed with the calculation of the electrical performance measured with respect to the stack, excluding the consumption of the BoP. Figure 4 shows the trend of η_{el} as calculated from the experimental data.

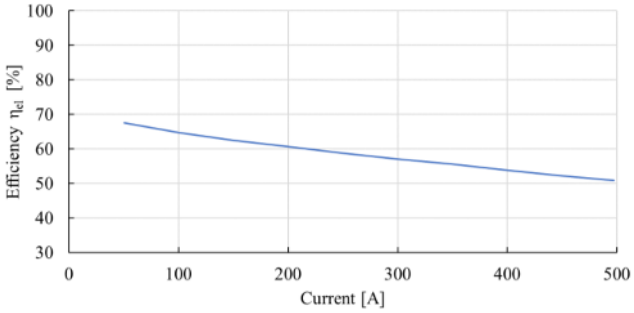

Fig. 4. η_{el} for the tested FCS.

The objective of the polarization tests is to get to the definition of the polarization curve, to have a reliable reference of the voltage as a function of current that must be verified during operation. Figure 5 shows the experimental V-I points collected during the dedicated tests (blue dots), compared with two reference curves named "FAT", which stands for Factory Tests. The yellow and orange lines represent in fact the results of the FATs that have been implemented by the FCS supplier, and which are given together with the specifics of the system. The two curves represent respectively the implementation of the first half of the current profile shown in Figure 2 (orange line), and the second descending half (yellow line). It is possible to notice from Figure 5 that FAT's results and the ones obtained inside BER's test rig are similar; the slight difference is mainly due to the lower temperature of the FCS (air, cooling fluid, components) during the test.

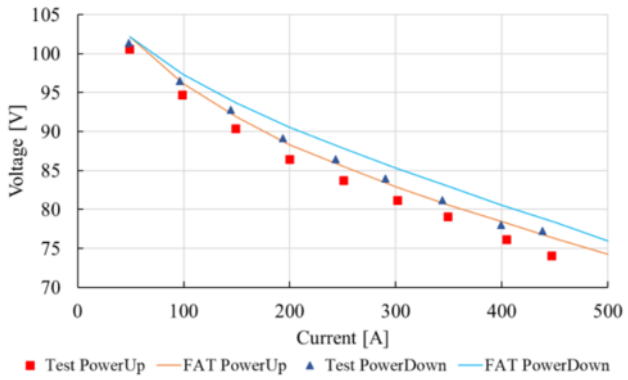

Fig. 5. Polarization test results.

The system's ability to respond to typical naval load profiles has been tested as well. The profile aims to represent the typical operating conditions that can be found on board (hotel load, manoeuvre, propulsion). Unlike tests in stationary and dynamic conditions, the operating profile represents a mix that can positively or negatively affect stack performance. The tests have been conducted in ideal conditions, with the objective of evaluating the global average performance of the FC system during the implementation of the operative profile. In Figure 6, it is reported the trend of the electrical power output – P_{el} – and of the thermal power – P_{th} – exchanged by the cooling circuit during the development of the naval profiles tested. The load request is always guaranteed, while the thermal power follows the trend of the electrical power output and is always managed correctly by the cooling loop. The FC stack voltage reaches a stable value during the implementation of each load step, despite the short time. This is especially appreciable at the end of the test, where a high and constant load is requested after the more stressing dynamic load, demonstrating that the FCS is able to withstand a similar load profile.

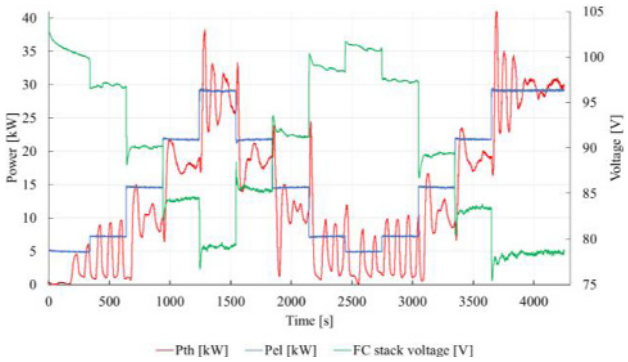

Fig. 6. Operative profile test results.

The FCS has eventually been tested under static conditions (stable load levels) for prolonged periods of time, on a 22.5° inclined plane, to evaluate the proper functioning of the system at all current densities. During these tests, the specific consumption, the efficiencies of the system, the analysis of the purges, the temperatures and operating pressures of the FC system, the temperatures and flow rates of the cooling output to the FC system, the measurement of water produced at the cathode, and the measurement of the water purged at the anode have been defined. No abnormal operating conditions have been encountered, confirming the good setting and operation of the stack control system which automatically manages the cooling, the air flow rates and the current supply ramp. Figure 7 shows the test results. The constant load has been maintained for a long time without major fluctuations but, most important, no difference in the stack voltages has been measured, proving that the humidity management of the system is optimal.

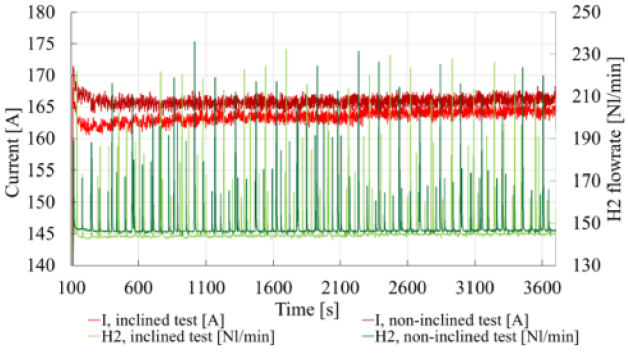

Fig. 7. Static inclination test results : current and H_2 flowrate.

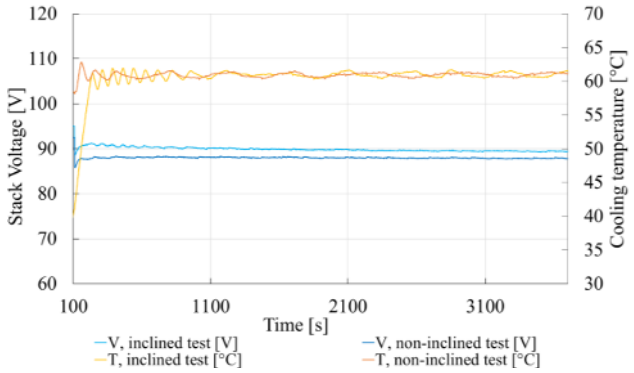

Fig. 8. Static inclination test results : cooling temperature and stack voltage.

4 Conclusions

The activities carried out for the TecBIA project, and described in this work, show the results of the definition of a test protocol for FCS installation in a ship environment – starting from the available international regulations – and its application to the system chosen for the installation onboard the ZEUS vessel. The test protocol can hint technical differences between FCS designed by different suppliers which make one technology more suitable than another; it will provide a guidance to integrators and to ranking institutes for the evaluation of the performance of PEMFC systems for marine application.

A dedicated Test Bench was developed, specifically designed to check and test FC systems, allowing the operator to test them even in static inclinations. The test protocol developed has been therefore applied to the commercial FCS chosen for the application on ZEUS, and the main outputs of the experimental campaigns are reported. From an environmental point of view, the tests conducted during the TecBIA project certify that the PEM technology can operate in naval use conditions without problems. In particular, it is confirmed that the system chosen for the installation onboard the ZEUS vessel is able to operate in the entire operative range maintaining a good performance, as well as it can withstand an operative profile comparable to the ones required to shipping power systems.

References

1. International Maritime Organization (IMO). Third greenhouse gas study. 2015.

2. https://www.imo.org/en/MediaCentre/HotTopics/Pages/Reducing-greenhouse-gas-emissions-from-ships.aspx, International Maritime Organization (IMO) official website, last access 22/01/2021

3. https://ec.europa.eu/commission/presscorner/detail/en/IP_20_1599

4. K. Kołwzan, M. Narewski, Latv J Chem; **51** ; 398-406 (2013)

5. Veldhuis IJS, Richardson RN, Stone HBJ. Int J Hydrogen Energy; **32 ;** 2553-66 (2007)

6. T. Tronstad, H. Astrand, G. Haugom, L. Langfeldt; www.emsa.europa.eu (2017)

7. M. Rivarolo, D. Rattazzi, L. Magistri, A.F. Massardo, En. Conv. And Management, 244, 114506 (2021)

8. M. Rivarolo, D. Rattazzi, T. Lamberti, L. Magistri. Int J Hydrogen Energy;**45** ;25747-57 (2020)

9. O.B. Inal, C. Deniz; J Clean Prod;**265**:121734 (2020)

10. Y. Bicer, I. Dincer, C. Zam, G. Vezina, F. Raso ; **135** ; 1379-1395 (2016)

11. H. Nazir, N. Muthuswamy, C. Louis, S. Jose, J. Prakash, M.E.M. Buan, et al., Int J Hydrogen Energy; **45** ; 28217-39 (2020)

12. A. Pfeifer, P. Prebeg, N. Duic ; E Transportation; **3 ;** 100048 (2020)

13. C. Nuchturee, T. Li, H. Xia ; Renew Sustain Energy Rev; **134** ; 110145 (2020)

14. S.E. Hosseini ; *Reference Module in Earth Systems and Environmental Sciences*, Elsevier (2020)

15. P. Wu, R. Bucknall ; Int J Hydrogen Energy; **45** ; 3193-208 (2020)

16. M. Cavo, E. Gadducci, D. Rattazzi, M. Rivarolo, L. Magistri ; Int H Hydrogen Energy, 46, 32630-32644 (2021)

17. A. Bouakkaz, A.J.G. Mena, S. Haddad, M.L. Ferrari ; Journal of Energy Storage, **33**, 101887_1-13 (2021)

18. A.L. Dicks ; *Reference Module in Earth Systems and Environmental Sciences*, Elsevier (2020)

19. J.J. De-Troya, C. Alvarez, C. Fernandez-Garrido, L. Carral ; Int J Hydrogen Energy; **41 ;** 2853-66 (2016)

20. M. Rivarolo, D. Rattazzi, T. Lamberti, L. Magistri ; Int J Hydrogen Energy; **45 ;** 25747-57 (2020)

21. C.H. Choi, S. Yu, I.S. Han, B.K. Kho, D.G. Kang, H.Y Lee, et al. ; Int J Hydrogen Energy; **41**;3591-9 (2016)

22. G. Borgogna, E. Speranza, T. Lamberti, A.N. Traverso, L. Magistri, E. Gadducci, et al. ; E3S Web Conf.;**113**:1-8 (2019)

23. E. Gadducci, T.Lamberti, D. Bellotti, L. Magistri, A.F Massardo ; Int J Hydrogen Energy ;**46 ;** 24305-17 (2021)

24. TESEO project (2012-2015) PON02_00153_2939517, http://www.ponrec.it

25. Gadducci, T. Lamberti, L. Magistri ; *Proceedings of EFC2019,* 235-236 (2020)

26. www.fincantieri.com, last access 12 September 2021

27. http://www.tpg.unige.it/TPG/

28. IEC 62282-4-101:2016 https://webstore.iec.ch/ (TRUCK&APU) (2016)

29. https://www.proton-motor.de/

30. https://bluenergyrevolution.com/

31. IEC 62282-3-200:2016 https://webstore.iec.ch/ (paragraph 9.2.6) (2016)

32. G. De Marco, T. Malkow, G. Tsotridis, A. Pilenga ; https://ec.europa.eu/jrc (2015)

Thermal integration of PEM Fuel Cells and metal hydrides storage system for Zero Emission Ultimate Ship (ZEUS)

Matteo Cavo[1], Eleonora Gadducci[1], Massimo Rivarolo[1], Loredana Magistri[1], Andrea Dellacasa[2], Matteo Romanello[2], Gerardo Borgogna[2], and Christian Davico[2]

[1]Thermochemical Power Group (TPG), DIME, University of Genoa, Via Montallegro 1, 16145 Genoa, Italy
[2]Fincantieri S.p.A., via Cipro 11, 16129 Genoa, Italy

Abstract. The ZEUS (Zero Emission Ultimate Ship), developed in the framework of the national research project TecBia conducted by Fincantieri and co-founded by Italian Ministry of Economic Development, is a 25m length vessel characterized by a zero-emissions propulsion system. The on-board power generation is provided by 4 PEM Fuel Cell modules (140 kW power installation) fed by hydrogen stored into 48 Metal Hydride tanks (MH). PEMFC and MH thermal systems are coupled to recover the heat produced by PEMFC and to feed the endothermic dissociation reactions of hydrogen from MHs. This paper provides a Matlab-Simulink model to simulate the dynamic behaviour of the PEMFC power generation system and the thermal coupling with MH racks installed onboard. Three typical operative profiles are simulated to verify the thermal management control system and the impact of transient conditions on the propulsion plant. Furthermore, the effects of the major exogenous parameters are investigated. Results verify that thermal coupling between the two systems is guaranteed; however, an excessive load increase can lead the stacks to operate under non-optimal conditions for significant periods of time. The effect of exogenous parameters has been verified to be negligible and does not significantly affect the control system.

1 Introduction

In the last years, global CO_2 emissions have been growing significantly due to anthropogenic activities, reaching the record values of 33.5 and 33.4 Gtons in 2018 and 2019 respectively [1]. The impact of maritime transportation has increased in the last years, due to the fact that 99% of the ships in operation still employ traditional high-pollutant fuels for propulsion, as reported in [2]. In the Fourth Greenhouse Gas Study (2020), the International Maritime Organization (IMO) has recently reported that Greenhouse Gas (GHG) emissions of total shipping have increased from 977 million tonnes in 2012 to almost 1.1 Gtons in 2018 (9.6% increase) [3]. The same IMO, as main regulator authority at international level in maritime sector, has recently defined long-term targets to reduce by 50% GHG emissions from shipping by 2050, compared to 2008 levels [4].

To reach this ambitious target, the introduction of alternative fuels and the diffusion of new technologies has a primary importance role. The introduction of LNG to replace fuel oil in internal combustion engines (ICE) will help to reduce CO_2 emissions, but it is not sufficient to reach the target: thus, different more sustainable solutions are under analysis. Recent studies in literature highlighted the possibility of employing fuel cell systems, fed by methanol [5,6], biogas [7,8] or hydrogen [9,10], while other authors developed algorithms to compare different fuels by adopting multi-criteria approaches [11,12], considering technical, environmental and economic aspects [13,14]. Among the different choices, Proton Exchange Membrane Fuel Cells (PEMFC), fed by pure hydrogen, present several advantages, such as low noise and vibrations, zero pollutant and CO_2 emissions, fast response to load variations and high compactness. Considering their strong potential, their possible application in ships, in particular for sizes up to 1 MW, has been investigated by many authors [15,16,17,18,19].

A critical point in the use of PEMFC in maritime application is the high volumes related to hydrogen storage: this aspect can be a limitation both in case of compressed high-pressure tanks and liquid storage at cryogenic vessels for liquid storage (20 K). Metal Hydrides (MH) represent an interesting alternative storage method, as they allow for a good energy storage in terms of volume, without needing high amounts of energy since H_2 is stored at limited pressure (<40 bar) and ambient temperature [20,21,22]. The main drawback is the considerable weight of MH tanks; however, this aspect can be limited by properly positioning the tanks onboard the ship [23,24].

As H_2 release by MH needs thermal energy and the PEMFC is characterized by heat production during operations, their thermal coupling has been investigated by many authors [25,26,27], mostly in stationary applications; more recently, the authors developed a model for the integration for maritime application, referred to the ZEUS research vessel [28], developed in

* Corresponding author: matteo.cavo@edu.unige.it

the framework of the national research project *TecBia* (*Technologies at low environmental impact for energy production on ships*), financed by Fincantieri-Isotta Fraschini Motori S.p.A. and Italian Ministry of Economic Development (MISE), as part of "National Operational Programme (PON) 2014/2020 Large R&D Projects". The ZEUS is fully powered by PEMFCs (installed power 140 kW) and H_2 is stored onboard by MH.

Fig. 1 shows the simplified system layout. The two PEMFC modules are connected to the main hydraulic system through the WGHE heat exchangers, where a mix 50% water- 50% glycol circulates. The main hydraulic system is responsible for the heat transfer from the PEMFC to the MH tanks, in a closed-loop system. Depending on the thermal energy available, the MH tanks release a determined amount of hydrogen, which is needed to supply the PEM stacks. The heat exchanger WHSE, fed by seawater at the cold side, assures the thermal equilibrium in the whole system, dissipating the eventual exceeding heat.

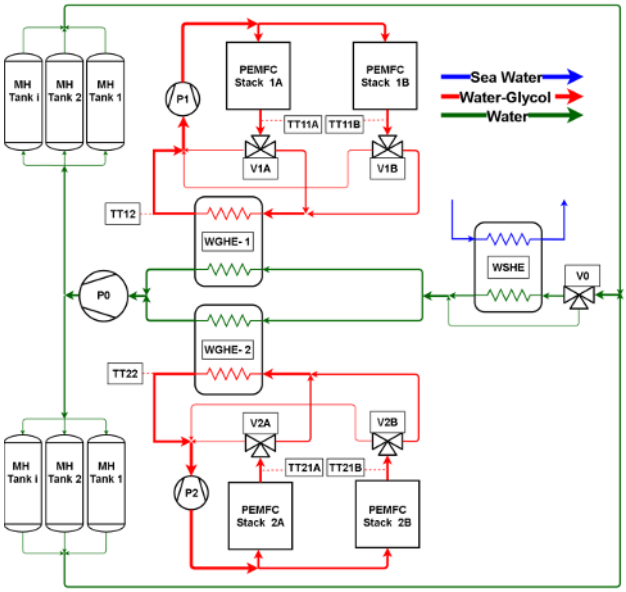

Fig. 1. ZEUS energy system description.

This paper aims to investigate the interaction between the PEMFC system and the MH considering different load profiles, to verify possible critical conditions.

2 Model based approach

In this section the main operating and modelling approaches of the PEM fuel cell and metal hydride thermal coupling system are discussed. Additionally, a description of the control logic to guarantee the proper operation of the PEMFC modules is presented: in this application, a proportional-integral (PI) control logic is proposed. The aim of this study is to verify the ability of the heat dissipated by the PEMFCs to activate and sustain the endothermic hydrogen release reactions involving the metal hydride cylinders. Critical conditions may occur in case of excessive power ramps: temperature peaks lead to irreversible deterioration of the polymeric membrane of the fuel cell stacks. In addition, the effect of an exogenous parameter affecting the system's ability to release heat is investigated: the seawater temperature.

2.1. Model description and control strategy

The assumptions used to develop the model are set out below.

- All models are 0D representations of real components; therefore, temperature gradients and velocity profiles are not considered.
- Heat losses to the environment are neglected.
- The representation of the thermal control circuit of the PEMFC modules and the MH heating circuit does not consider the fluid-dynamic delays. This is justified by the fact that the delays due to fluid accumulation are several orders of magnitude lower than the thermal dynamics affecting the working fluid.

The physical and mathematical approaches are described in [28]. The fuel cell and metal hydride tank models were validated according to experimental data provided by the respective suppliers, as shown in [28]. The control strategy designed for the system must guarantee the temperature set points required by the cells to ensure the correct humidity condition of the polymer membrane. The control is performed through two basic logics:

- Temperature control at PEMFC stacks outlet: to avoid irreversibly damaging the polymeric membranes due to temperature peaks at high load, the temperature of the water-glycol at stacks outlet must be controlled. As shown in Fig. 1, this is possible through the partialisation of valves V1A and V1B of branch 1 and V2A and V2B of branch 2. Integral proportional controllers measure the error between the temperature signal of TT11A and TT11B at branch 1, TT21A and TT21B at branch 2: then it regulates the mass fraction which bypasses the WGHE.
- Temperature control at the outlet of the WGHE: to avoid critical operating conditions of stacks temperature control valves, the temperature of the water-glycol at WGHE outlet must be controlled. The V0 actuator modifies the fluid flow rate that passes through the water-sea exchanger according to the difference between the mean temperature measured by the TT12 and TT22 sensors and the set point temperature.

The mathematical approach of PI controllers can be described by transfer functions in relation to the error [29]. The characteristic parameters of the controller are derived following the "Ziegler-Nichols Oscillatory" calibration method.

2.2 Case studies

In this section, the case studies are described; all the data required to carry out the simulations are provided in [28]. The forcing of the system is the current set on the stacks. Since every current point corresponds to an electrical power (as in Table 1), for each forced current ramp there is an electrical power ramp. The first case study (CASE A) refers to a current ramp which leads the stacks to deliver the minimum power, starting from the nominal

power. The second case study (CASE B) refers to a current ramp that leads the stacks to deliver the nominal power, starting from the minimum power. Finally, in CASE C the effect on the main control variables of the system caused by variations in seawater temperature is investigated. All simulations are based on the assumption of equilibrium conditions and a 100% initial metal hydride state of charge. Ramps proceed at a 50A/s velocity: this is the limit suggested by the PEMFC supplier.

Table 1. Summary of working points and case studies.

Current	Power
400 A	Nominal Power (~60 kW)
120 A	Minimum Power (~17 kW)
Case studies	
CASE A	Nominal Power → Minimum Power
CASE B	Minimum Power → Nominal Power
CASE C	Effects of seawater temperature

3 Results

The simulations carried out aim to investigate the most critical operating conditions of the thermal management system of the PEMFC plant coupled to the metal hydride racks. Results are hereby presented, some important considerations must be pointed: (i) CASE A can be considered a safe and suitable ramp for the thermal management system; (ii) CASE B outcomes critical operating conditions of fuel cell stacks during transients; (iii) CASE C simulations prove the robustness of the thermal management system, which reacts appropriately to different sea water temperatures.

3.1. CASE A

The system is considered to be in equilibrium at nominal power and MHs fully charged. The aim is to verify that the control system can handle the load variation and move the plant to a balanced state avoiding critical operating conditions.

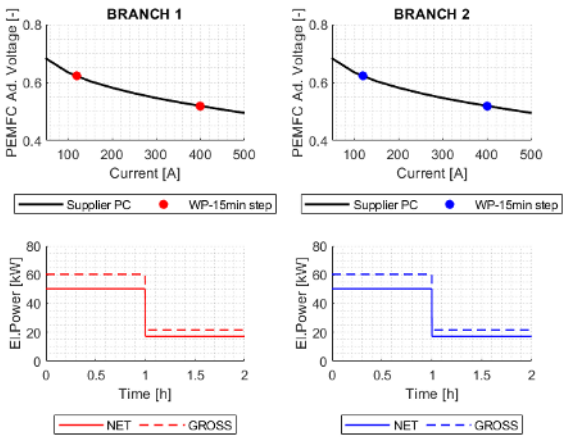

Fig. 2. Forcing and electrical power as a function of simulation time (CASE A). PEMFC Ad.Voltage has been obtained dividing cell voltage by Nernst electric potential.

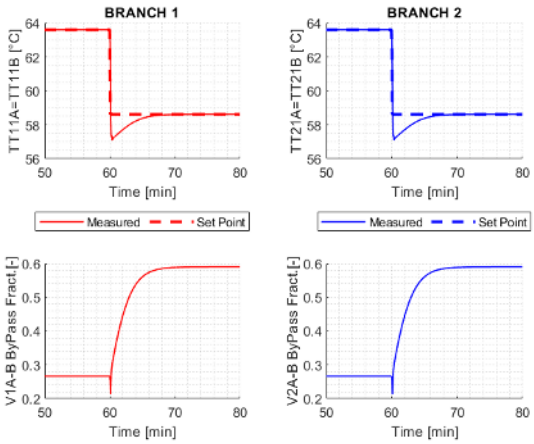

Fig. 3. PEMFC outlet temperature and V2 bypass mass fraction as function of simulation time (CASE A).

Figures 2 and 3 show the electrical power and stacks outlet temperature during CASE A current ramp. The working point (WP) is plotted every 15 min above the polarization curve (PC) provided by the stack supplier. As the current gets lower, the electrical power decreases as well (Figure 2); also, the heat dissipated by the fuel cells drops, so the control system must react to guarantee the set point temperature (Figure 2). V2A and V2B valves regulate the amount of water-glycol which bypasses the heat exchanger; so, for lower loads more fluid has to skip the WGHE (Figure 3). The control system restores the equilibrium in about 3 minutes. The maximum temperature variation with respect to the set point desired by the cells is about 1.5 °C: this working condition does not cause stress to the PEMFC modules.

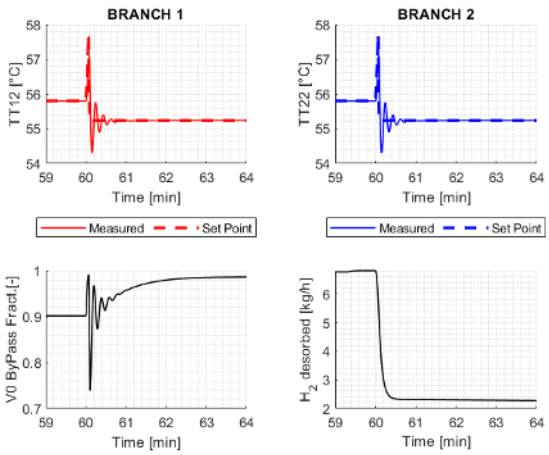

Fig. 4. WGHE glycol outlet temperature, V0 bypass mass fraction and hydrogen desorption flow as function of simulation time (CASE A).

Figure 4 shows the behaviour of the water-glycol temperature at WGHE outlet. Restricting this temperature is essential to prevent excessive stress on the control system of the V2A and V2B valves. During load drops, the flow rate through the WGHE is lower; therefore, in order to guarantee the set point temperature, it is necessary to decrease the inlet water temperature of the heat exchanger's cold side. So, valve V0 bypasses less water to the seawater exchanger. Metal hydrides release less hydrogen due to a reduction of thermal power dissipated from the fuel cells; anyway, it is sufficient to feed the electrochemical reactions happening in the working stacks at the PEMFC standard operating pressure. The simulation outcomes that the temperature measured by TT3A is handled promptly and efficiently by the control system.

3.2. CASE B

The system is considered to be in equilibrium at minimum power and MHs fully charged. Under this operating condition, it is important to verify that the rise in electrical load does not lead to a substantial raise in stack cooling circuit temperatures for extended periods of time; otherwise, the membrane would dry out and this shortens the lifetime of the cell.

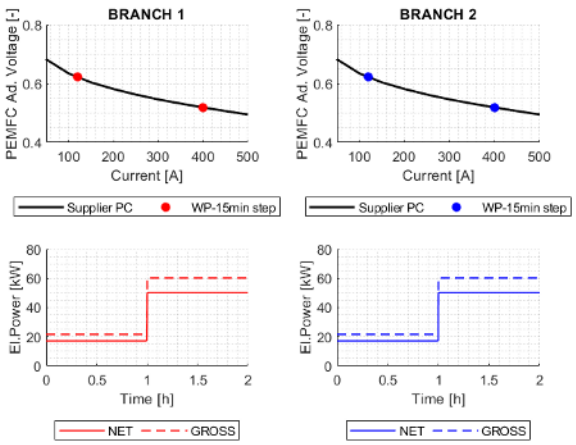

Fig. 5. Forcing and electrical power as a function of simulation time (CASE B). PEMFC Ad.Voltage has been obtained dividing cell voltage by Nernst electric potential.

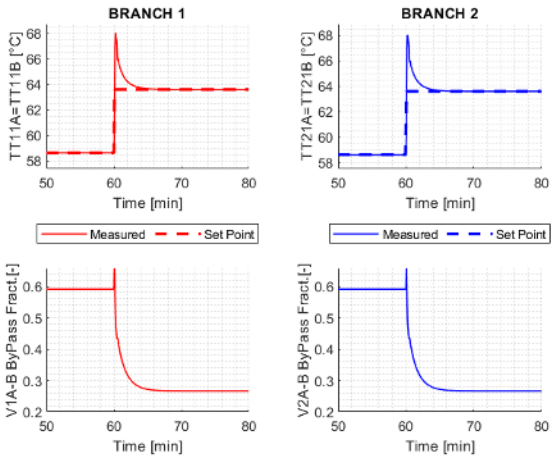

Fig. 6. PEMFC outlet temperature and V2 bypass mass fraction as a function of simulation time (CASE B).

Figures 5 and 6 outline the effects of load increase during transient conditions. The working point (WP) is plotted every 15 min above the polarization curve (PC) provided by the stack supplier. Since the electrical power output rises, the heat produced by the stack increase. V2A and V2B valves tends to let pass more fluid to the WGHE (Figure 6) to reach the set point desired, but mechanical delays and the dynamic of the system lead to a peak of water-glycol temperature at stack inlet: 4°C higher than the desired one. The overall time to reach the new equilibrium point is about 3 minutes. So, it results that the cells work under critical conditions for a long time at CASE B. Two possible solutions can be adopted to avoid this phenomenon: reducing the speed of power increment or introducing intermediate load steps. Here, the battery shall offset the lack of energy for the duration required to attain the nominal operating condition.

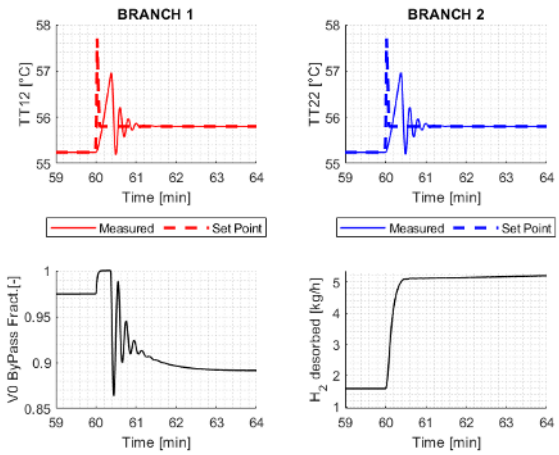

Fig. 7. WGHE glycol outlet temperature, WSHE water flow and hydrogen desorption flow as a function of simulation time (CASE B).

WGHE outlet temperature is controlled properly, and the maximum deviation is neglectable. Control valve V0 manages to guarantee the set point by increasing the water flow to the WSHE (Figure 7). Differently from CASE A, as the load rises, the heat flux dissipated by the fuel cells increases, resulting in more hydrogen being extracted from the metal powder.

3.3. CASE C

PI are robust control systems which base their response on the error between a measured variable and the desired set point. Therefore, any exogenous component might overcome the control systems. Sea water temperature is one of the most influencing factors: in the Mediterranean Sea it ranges from an average value of approximately 15°C during winter to 25°C for summer. In this section different load ramps are computed from minimum to nominal power at three different sea water temperatures: 15°C, 20°C and 25°C. The role of V0 valve is to adjust the mass fraction bypassing the WSHE to avoid temperature fluctuations and critical operations in the stack water-glycol cooling circuit. As shown in Figure 8, the behaviour of valves V1A, V1B and V2A, V2B is not affected by the variation of the seawater temperature: the V0 control system acts promptly and efficiently (Figure 9). Furthermore, the water flow rate through the sea-water exchanger decreases as the sea temperature increases, while the hydrogen released by the MHs is not affected.

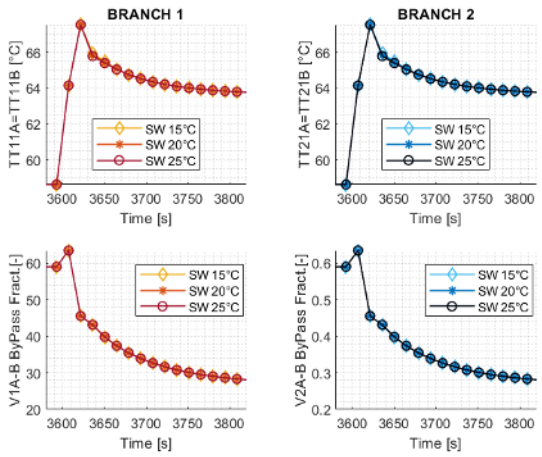

Fig. 8. Comparison of V1A, V1B, V2A and V2B control valves at different sea water temperatures.

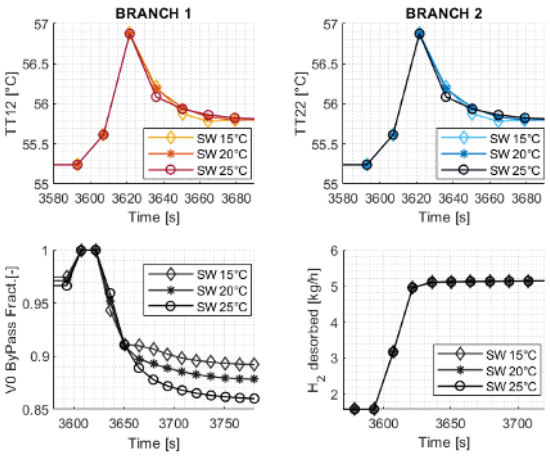

Fig. 9. Comparison of V0 control valve and hydrogen desorption at different sea water temperatures.

4. Conclusions

Exploring critical areas of operation of the ZEUS propulsion system and determining their causes is the first step towards a robust and effective control system. In this paper, a Matlab Simulink dynamic model is employed to analyse the behaviour of the thermal coupling system between PEM-type fuel cells and metal hydride tanks. The main elements constituting the circuit have been realised and validated based on data provided by the suppliers. The simulations computed explore the most severe operating conditions the yacht may experience, moving from nominal to minimum load and vice versa. Also, the effect of an important exogenous parameter that can affect system operation is analysed: the seawater temperature is varied from 15°C to 25°C in the worst operating condition (load increment).

Results show that, when the boat switches from nominal to minimum power, the control system manages this new equilibrium point avoiding critical transients. When the system switches from minimum to nominal power, a long-lasting temperature peak occurs in the cooling circuit of the PEMFC stacks. Temperature set

points are determined by the manufacturer to ensure an ideal membrane humidity level; therefore, this phenomenon could cause permanent degradation of the polymer membrane contained in the fuel cells. A few possible solutions have been identified and will be tested in future works: introducing intermediate steps, load ramps with reduced advance rates or analysing the performance of a model predictive controller (MPC) and comparing this control technique to the previous one. Finally, it has been highlighted the effect of sea water on the control system does not have a significant impact. This proves the robustness of the PI control under environmental conditions beyond the design point.

This work becomes particularly relevant as it explores the operational limits of the hybrid PEMFCs energy system installed on board the ZEUS. In addition, it will be possible to test the reliability of the model computations basing on the ship real data, providing a powerful tool to perform predictions leading to improvements in the control system, preventing from damage, extending both PEMFC and MH lifetimes.

This work has been partially supported by Fincantieri S.p.A. and Italian Ministry of Economic Development through the research project TecBia, CUP n.B98I17000680008.

References

1. www.iea.org last access 8/9/2021.
2. Maritime forecast to 2050, DNV, available at https://eto.dnv.com/2021.
3. https://www.imo.org/en/OurWork/Environment/Pages/Fourth-IMO-Greenhouse-Gas-Study-2020.aspx last access 8/9/2021.
4. https://www.imo.org/en/MediaCentre/HotTopics/Pages/Reducing-greenhouse-gas-emissions-from-ships.aspx last access 8/9/2021.
5. N.R. Ammar, Transportation Research, Transport Environ., 69 (2019), 66-76.
6. M. Santin, A. Traverso, L. Magistri, App. Energy, 86 (2009), 2204-2212.
7. L. Mantelli, M.L. Ferrari, A. Traverso, App. Thermal Engineering, 191 (2021), 1-14.
8. A.F. Massardo, L. Magistri, Int. J. of Engineering for gas Turbine and Power, 125 (2003), 67-74.
9. L.E. Klebanoff, J.W. Pratt, C.M. Leffers, K.T. Sonerholm, T. Escher, J. Burgard, S. Ghosh, Transportation Research, Transport Environ., 54 (2017), 250-268.
10. M. Rivarolo, D. Rattazzi, T. Lamberti, L. Magistri, Int. J. of Hydrogen En., 45 (2020), 25747-25757.
11. M. Baumann, M.Weil, J.F. Peters, N. Chibeles-Martins, Antonio B. Moniz, Renewable and Sust. En. Reviews, 107 (2019), 516-534.
12. R. Chauvy, R. Lepore, P. Fortemps, G. De Weireld, Sust. Prod. and Consumption, 24 (2020), 194-210.
13. A. Priftis, E. Boulougouris, O. Turan, A. Papanikolau, Ocean Engineering, 156 (2018), 347-357.
14. M. Rivarolo, D. Rattazzi, L. Magistri, A.F. Massardo, En. Conv. And Management, 244 (2021), 114506.
15. O.B. Inal, C. Deniz, J. of Cleaner Prod., 265 (2020), 121734.
16. Nazir H, Muthuswamy N, Louis C, Jose S, Prakash J, Buan MEM, et al., Int J Hydrogen Energy, 45 (2020), 28217–28239.
17. Pfeifer A, Prebeg P, Duić N., ETransportation, 3 (2020), 100048.
18. Nuchturee C, Li T, Xia H., Renew Sustain Energy Rev, 134(2020), 110145.
19. Wu P, Bucknall R., Int J Hydrogen Energy, 45(2020), 3193–3208
20. Chabane D., et al., Int. J. of Hydrogen Energy, 44 (2019), 1034-1046.
21. K. Manickam et al., Int. J. of Hydrogen Energy, 44 (2019), 7738-7745.
22. S.N. Nyamsi, M. Lototskyy, I. Tolj, Int. J. of Hydrogen Energy, 43 (2018), 22568-22583.
23. J.B. von Colbe, et al., Int. J. of Hydrogen Energy, 44 (2019), 7780-7808.
24. C. Fiori, A. Dell'Era, F. Zuccari, A. Santiangeli, A. D'Orazio, F. Orecchini, Int. J. of Hydrogen Energy, 40 (2015), 11879-11889.
25. P. Rizzi, E. Pinatel, C. Luetto, P. Florian. A. Graizzaro, S. Gagliano, M. Baricco, , J. of Alloy and Compounds, 645 (2015), 338-342.
26. F. Mahmoodi, R: Rahimi, App. Thermal Engineering, 178 (2020), 115490.
27. T. Førde, J. Eriksen, A.G. Pettersen, P.J.S. Vie, Ø. Ulleberg, Int. J. of Hydrogen En., 34 (2009), 6730-6739.
28. M. Cavo, E. Gadducci, D. Rattazzi, M. Rivarolo, and L. Magistri, Int. J. Of Hydrogen Energy, 46 (2021), 32630-32644.
29. G. Goodwin, S. Graebe, M. Salgado, Control System Design (Valparaiso: Prentice Hall, 2000).

Single step polyol synthesis of highly stable Pt/C/SiO_2 catalysts for use in PEMFCs: effects of pH, temperature and W/EG ratio

Eva Sousa, *Sofia* Delgado, *Tiago* Lagarteira, and *Adélio* Mendes*

LEPABE - Laboratory for Process Engineering, Environment, Biotechnology and Energy Faculty of Engineering of the University of Porto, Rua Dr. Roberto Frias, 4200-465 Porto, Portugal

Abstract. Hybrid supports have been proposed as a new alternative to increase the stability of ORR catalysts used in PEMFCs for automotive applications since they are known to be stable under harsh conditions. In this work, Pt nanoparticles were deposited over C/SiO_2, via single-step polyol method, to take advantage of the corrosion-resistance properties of silica nanoparticles. In fact, the synthesis parameters, namely, pH, temperature, and glycol concentration had a remarkable impact on the Pt size-distribution, crystallinity, and dispersion over the C/SiO_2 supports. A maximum ORR activity and stability was obtained for Pt/C/SiO_2 catalysts produced at 1:6 W/EG (v/v). The addition of SiO_2 nanoparticles to the carbon structure showed their ability to effectively inhibit support corrosion and Pt nanoparticles detachment and/or growth, with the pH adjustments being critical for obtaining highly stable C/SiO_2 supports. Pt/C/SiO_2 synthetized under acidic conditions revealed the highest stability when subjected to accelerated stress tests (ASTs), losing only 30 % of the initial electrochemically active surface area (ECSA) of Pt after 4 000 cycles from 0.6 to 1 V (*vs* RHE), whereas the commercial Pt/C revealed > 50 % of ECSA loss.

1 Introduction

Polymer Electrolyte Membrane Fuel Cells (PEMFCs) will be an important choice for the future of the transport sector due to their low operation temperature, high power density and cold-start withstand. PEMFCs are especially suited for trucks, buses, ships, trains and larger cars. However, the main technical challenge for automotive PEMFCs commercialization is the insufficient stability of the cathodic electrodes; usually, Pt-based electrocatalysts supported on carbon materials [1]. The reason for not meeting durability targets set by the US Department of Energy (DoE; 5 000 h; 0.44 $A \cdot mg^{-1}_{Pt}$ and < 40 % loss in mass activity after 30 000 cycles) has been assigned to the carbon corrosion and insufficient anchoring strength of the active sites, resulting in Pt nanoparticles growth in size due to coalescence and dissolution/agglomeration or in Pt detachment from the support [2]. Hence, the development of robust and stable supports is a priority in the design of new electrocatalysts for mobile applications.

Despite their poor conductivity and low surface area, the use of metal oxides - such as SnO_2 [3], TiO_2 [4], Nb_2O_5 [5] or SiO_2 [6] - as supports has attracted special attention since they are known to be stable under highly acidic pH and humidified media. In fact, the addition of metal oxide nanoparticles to the carbon support is a promising pathway to increase the stability of Pt-based electrocatalysts [7]. These hybrid supports are able to keep the carbon structure main properties – porosity and high surface area, conductivity, anchoring sites – while the corrosion-resistance is provided by the metal oxide.

Particularly, Pt/C/SiO_2 electrocatalysts have been prepared by covering Pt/C with thin silica layers, using silicon alkoxides (MTEOS, TEOS, APTES, among others) as precursors [8]. The presence of hydrophilic silanol groups (Si-OH) in the final silica layers improves the catalyst wettability, allowing operation at higher current densities due to lower mass-transport overpotentials [9]. However, these electrocatalysts should be carefully prepared since the coverage of the whole surface of Pt/C with thick silica layers might lower its electrical conductivity, leading to insufficient ORR performance.

In this work, Pt/C/SiO_2 electrocatalysts were prepared by performing a single step polyol method. Instead of using silicon alkoxides to obtain a silica coating, this new approach considers the addition of SiO_2 as a binding element between carbon and Pt nanoparticles. Hence, SiO_2 nanoparticles were directly added to the support, avoiding the insulating effect produced by the hydrolysis of silicon precursors. Moreover, the polyol reduction temperature (which depends of the glycol concentration on water) and the pH of the polyol solution are parameters that deeply impact electrocatalysts performance and stability [10,11]. This study reports for the first time the effects of these key synthesis conditions on Pt/C/SiO_2 catalysts. The as-prepared catalysts were analyzed with ICP-OES, TGA, TEM, XRD, BET and XPS. Furthermore, their corrosion-resistance was studied performing accelerated stress tests

* Corresponding author: mendes@fe.up.pt

(ASTs) by cycling the potential between 0.6 and 1.0 V (*vs* RHE) during 4000 cycles.

2 Experimental Section

2.1. $Pt/C/SiO_2$ synthesis by single step polyol method

The prepared platinum-based catalysts (40 wt.%) supported on carbon-silica materials were denoted as $Pt/C/SiO_2$. Initially, the support nanoparticles - 16 mg of SiO_2 (Sigma Aldrich) and 30 mg of carbon (Ketjenblack EC-600J from Tanaka) - were dissolved in an aqueous solution of ethane-1,2-diol (EG; VWR Chemicals) and blended for 6 h. The platinum precursor, $H_2PtCl_6{\cdot}6H_2O$ (Sigma Aldrich) was added to the support nanoparticles and stirred during 12 h. After the pH adjustment, the synthesis was performed at the boiling point of the colloidal solution for 6 h under continuous stirring. Lastly, after the reacting mixture reached room temperature, the obtained powder was filtered and washed with MilliQ-water several times; the electrocatalyst was collected and dried at 100 ºC overnight [12]. The electrocatalysts were produced under different glycol concentrations, namely 1:4 Water/EG (W/EG), 1:6 and 1:8 (v/v), which also changed the temperature of the reduction process. The pH was adjusted to produce catalysts at acidic pH=2, alkaline pH=10 and sequential pH=10 to pH=2 (defined as alkaline-acidic medium; the pH was adjusted to alkaline before the synthesis using NaOH (Alfa Aesar) and at the end of the reaction was set again to pH=2, using $H_2SO_{4(aq)}$ (VWR Chemicals)) [13].

For a real assessment, a Pt/C without silica produced under similar conditions and a commercial 40 wt.% Pt/Ketjenblack (Premetek) were used as benchmark catalysts.

2.2 Electrochemical Measurements

A three-electrode configuration was prepared using a Rotating Disk Electrode (RDE) from Pine Research Instrumentation. For that, a carbon rod was used as a counter electrode, a saturated Ag/AgCl in 3 M $KCl_{(aq)}$ as reference electrode, and a glassy carbon surface (GCE, 0.196 cm^2) as working electrode. A small quantity of catalyst powder (5 mg) was dispersed using a 1:4 (v/v) isopropanol/water solution; 20 µL were further dropped onto the GCE and dried at 700 rpm and 25 °C. A potentiostat - Zahner IM6-ex - was used to perform the electrochemical measurements. Firstly, the working electrode was activated by cycling the potential between 50 mV and 1 V (*vs* RHE) at 100 $mV{\cdot}s^{-1}$ during 100 cycles under inert atmosphere. The ohmic resistance of the electrolyte - 0.1 M $HClO_{4(aq)}$ (70 % conc. Sigma Aldrich) - was obtained by performing electrochemical impedance spectroscopy (EIS) at 0.4 V *vs* RHE using a small amplitude perturbation of 5 mV at 1 kHz. Cyclic voltammograms (CVs) were obtained under Ar-saturated 0.1 M $HClO_{4(aq)}$ at 25 °C using a scan rate of 20 $mV{\cdot}s^{-1}$. The electrochemical surface area (ECSA) was calculated from the hydrogen desorption peaks from 0.05 to 0.4 V (*vs* RHE), assuming a fully hydrogen-covered platinum (111) monolayer of 210 $\mu C{\cdot}cm^{-2}$. Linear Sweep Voltammograms (LSVs) were performed in O_2-saturated 0.1 M $HClO_{4(aq)}$ electrolyte at 25 °C. LSVs were obtained from 0.05 to 1 V *vs* RHE at a scan rate of 20 $mV{\cdot}s^{-1}$ and 1600 rpm. Background currents were obtained by performing the same test in inert atmosphere - Ar-saturated 0.1 M $HClO_{4(aq)}$ electrolyte. Electrochemical performance was evaluated during ASTs, by cycling the potential between 0.6 and 1.0 V *vs* RHE for 4000 cycles at a scan rate of 100 $mV{\cdot}s^{-1}$ in O_2-saturated electrolyte.

3 Results and Discussion

$Pt/C/SiO_2$ catalysts were extensively analyzed using morphological characterization (including XRD, XPS, BET, ICP, TGA, among others; not shown). These analyses were further correlated with the electrochemical results. As expected, temperature, glycol concentration and pH adjustments generated important differences on the size-distribution, crystallinity, and dispersion of Pt nanoparticles on C/SiO_2 supports, which in turn impacts electrocatalysts ORR performance.

Fig. 1. a) and b) show CVs obtained for the catalysts produced under alkaline-acidic sequence pH and acidic pH, respectively; both exhibited well-shaped peaks of hydrogen adsorption/desorption, which indicates that the silica nanoparticles did not hinder O_2 diffusion to the Pt active sites.

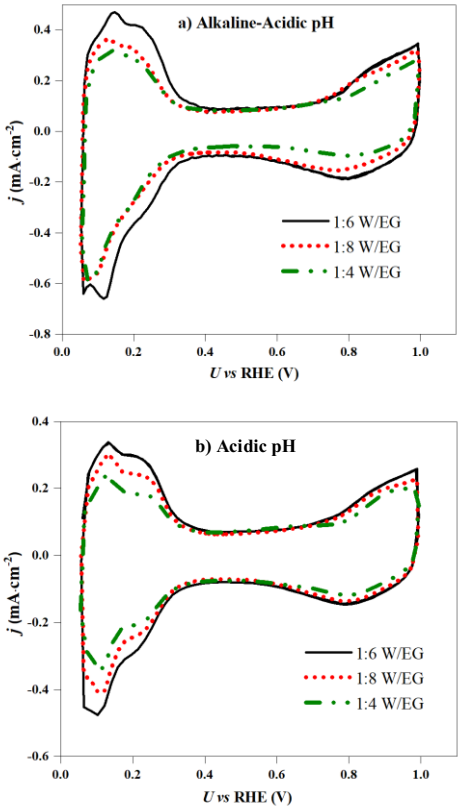

Fig. 1. CVs for a) $Pt/C/SiO_2$ prepared under 1:4, 1:6, 1:8 W/EG concentration and alkaline-acidic conditions, b) $Pt/C/SiO_2$ prepared using 1:4, 1:6 and 1:8 W/EG and acidic medium; in Ar-purged 0.1 M $HClO_4$ electrolyte. Scan rate of 20 $mV{\cdot}s^{-1}$.

In fact, the alkaline-acidic pH control delivered catalysts with improved ECSA and ORR mass-activity due to a better dispersion of Pt over the support, as shown in TEM images, **Fig. 2**. During the synthesis under alkaline medium, Pt cations are surrounded by negatively charged acetaldehyde species, which in turn hinders coalescence or agglomeration of Pt precursor; thus, high pH contributes to a better dispersion of the active sites over the support [14]. However, such effect also produces repulsive electrostatic forces between Pt and support nanoparticles, caused by their same electric surface charge. Hence, after carrying out the reaction under alkaline medium, the pH can be changed to acidic, to allow the complete nucleation of Pt on the anchoring sites of the support. The alkaline-acidic process and the acidic pH control allowed a complete utilization of Pt precursor [13]. On the other hand, an incomplete Pt deposition was verified for the electrocatalysts prepared under alkaline pH, thus making the production of these catalysts uncompetitive.

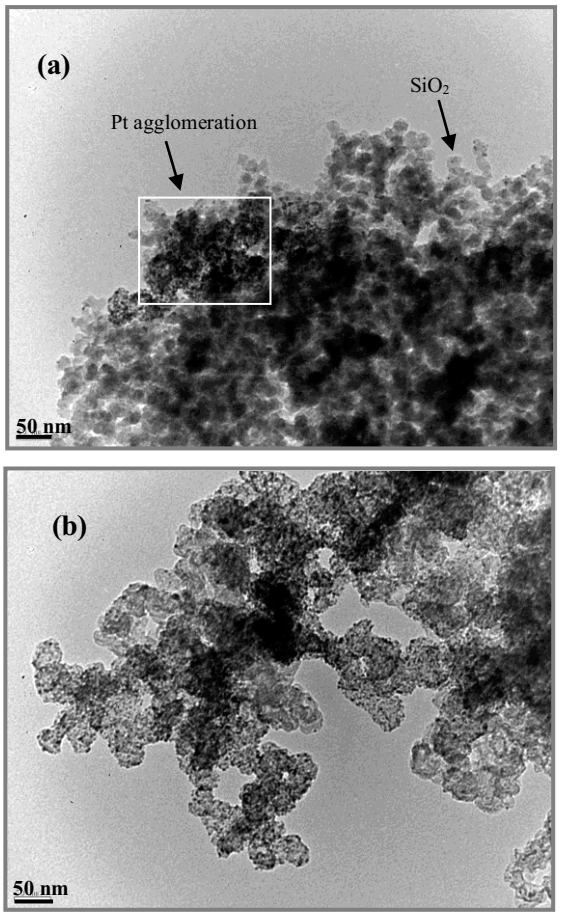

Fig. 2. TEM images of a) 1:8 W/EG Pt/C/SiO_2 prepared under acidic conditions; and b) 1:8 W/EG Pt/C/SiO_2 prepared using the sequential alkaline-acidic method.

Higher glycol concentration means higher reduction temperature of the polyol process (set by the boiling point of the reaction solution). The faster reduction kinetics under higher temperature delivers smaller Pt nanoparticles, but can also produce agglomerates of individual Pt, which compromises ECSA and ORR mass-activity [15]. **Fig. 3.** shows that a proportion of 1:6 W/EG results in the highest ECSA and ORR mass-activity, regardless of the pH medium, during Pt/C/SiO_2 synthesis. ECSA and ORR mass-activity values of 58.0 $m^2 \cdot g_{Pt}^{-1}$ and 83.3 $mA \cdot mg_{Pt}^{-1}$ were achieved for the acidic pH, respectively; and 85.2 $m^2 \cdot g_{Pt}^{-1}$ and 93.1 $mA \cdot mg_{Pt}^{-1}$ for the alkaline-acidic 1:6 W/EG Pt/C/SiO_2 catalyst. The larger ORR mass-activity at 1:6 W/EG reveals improved mass diffusion pathways and porosity, which provide better access of oxygen to the active sites. Despite the presence of silica nanoparticles, 1:6 Pt/C/SiO_2 catalysts reached higher ORR mass-activity than the commercial 40 % Pt/Ketjenblack (65.6 $mA \cdot mg_{Pt}^{-1}$).

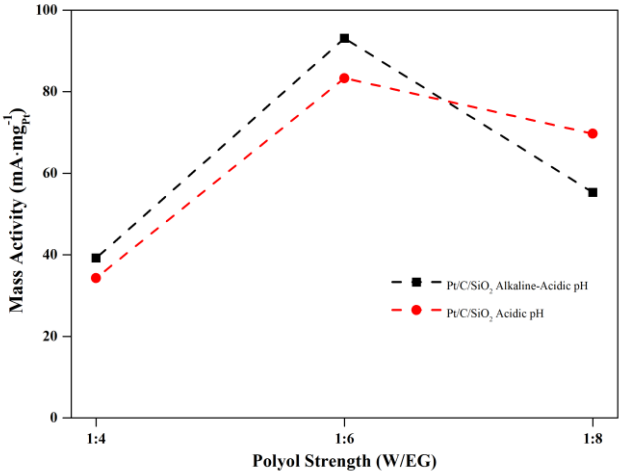

Fig. 3. ORR mass-activity as function of the polyol strength, considering both acidic and alkaline-acidic pH.

Stability of Pt/C/SiO_2 catalysts was evaluated by performing potential cycling between 0.6 - 1 V *vs* RHE in O_2-saturated 0.1 M $HClO_{4(aq)}$ electrolyte during 4 000 cycles. The acidic Pt/C/SiO_2 catalysts revealed the best stability under stress conditions; **Fig. 4.** shows its performance upon degradation.

In detail, silica nanoparticles have silanol groups (Si-OH) at their near-surface, that can change their electric charge according to the pH of the reactive solution [16]. Therefore, during the alkaline-acidic sequence, silica and carbon nanoparticles are initially both negatively charged, which can contribute to a weakened bond between the final C/SiO_2 support. The latter can be confirmed by TEM images that revealed silica nanoparticles well incorporated in carbon in the catalysts prepared under acidic pH, but in the alkaline-acidic catalysts, silica is only present in specific regions. Besides, ECSA and mass-activity values upon ageing revealed the poor stability of the alkaline-acidic 1:6 W/EG Pt/C/SiO_2 catalyst; its ECSA decreased from 85 to 40 $m^2 \cdot g_{pt}^{-1}$ upon 4 000 cycles (53 % loss), **Fig. 5**. Instead, the loss of ECSA of catalysts obtained under acidic pH was inhibited from 58 $m^2 \cdot g_{pt}^{-1}$ to 37 $m^2 \cdot g_{pt}^{-1}$ (32 % loss). It is evident that C/SiO_2 produced under acidic pH promotes a stronger corrosion-resistant behavior. Also, according to its LSV, **Fig. 4.** b), the small loss in the mass transport region suggests a slight modification in the microstructure of the catalyst upon degradation.

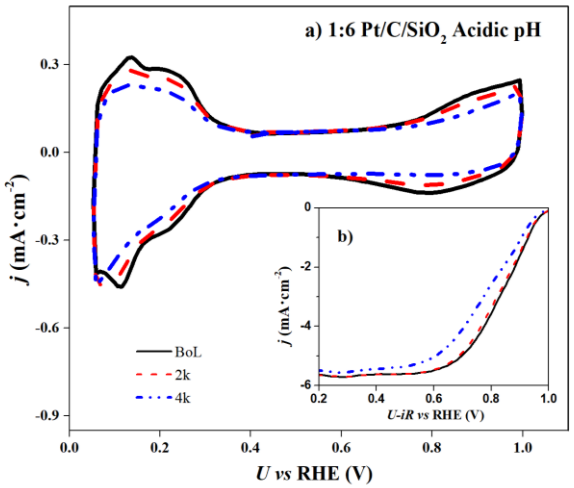

Fig. 4. a) CVs for $Pt/C/SiO_2$ prepared under 1:6 W/EG and acidic medium; in Ar-purged 0.1 M $HClO_4$ electrolyte, before and after ASTs; b) LSVs obtained in O_2-purged 0.1 M $HClO_4$ electrolyte. Scan rate of 20 $mV \cdot s^{-1}$.

The same stability protocol was applied to the 1 :6 W/EG Pt/C prepared under similar conditions of pH, glycol concentration and without silica. The electrochemical results were compared with those obtained for the commercial 40 % Pt/Ketjenblack, **Fig. 6**. ECSA for the Pt/C catalyst decreased after 4 000 cycles to 36 $m^2 \cdot g_{pt}^{-1}$ (41 % loss); its ORR mass-activity loss was also very significant, almost 70 %, which shows the greatly superior stability of acidic $Pt/C/SiO_2$ - lost only 38 % of its initial mass-activity.

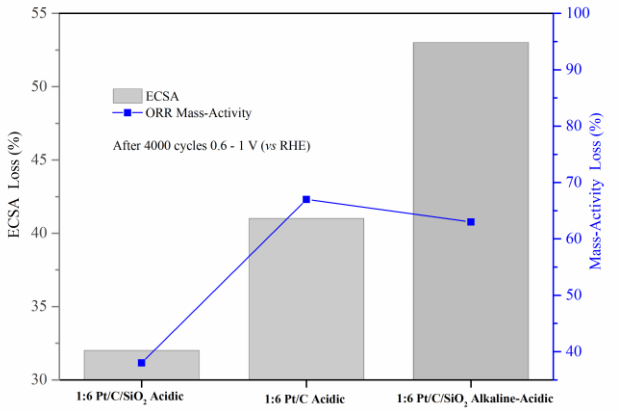

Fig. 5. ORR mass-activity and ECSA of electrocatalysts with and without silica, prepared using 1:6 W/EG, upon ageing.

Typically, Pt nanoparticles detachment or sintering/agglomeration during catalysts degradation significantly contributes to a decrease of the active surface area available for ORR, resulting in substantial losses of ORR mass-activity [2]. It was verified a remarkably higher loss of active surface area in the catalysts without silica. Hence, the addition of SiO_2 nanoparticles leads to higher binding strength between carbon and Pt nanoparticles, effectively inhibiting support corrosion and Pt degradation mechanisms, which might include migration, detachment, and sintering/agglomeration phenomena.

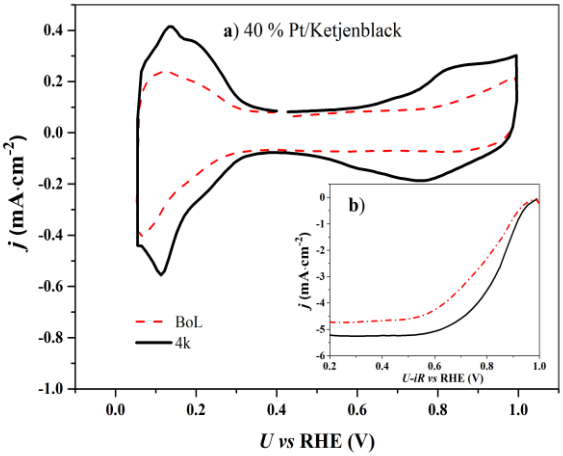

Fig. 6. a) CVs for commercial Pt/C in Ar-purged 0.1 M $HClO_4$ electrolyte, before and after ASTs; b) LSVs obtained in O_2-purged 0.1 M $HClO_4$ electrolyte. Scan rate of 20 $mV \cdot s^{-1}$.

Moreover, the ECSA of the commercial 40 % Pt/Ketjenblack decreased 52 % after 4 000 cycles, confirming the improved stability of acidic $Pt/C/SiO_2$ catalysts at PEMFC cathodic conditions.

4 Conclusion

$Pt/C/SiO_2$ catalysts were successfully produced via single step polyol method. Glycol concentration and pH of polyol solution strongly impacted Pt size-distribution, and its dispersion over C/SiO_2 supports. The maximum ORR mass-activity was achieved at 1:6 W/EG (v/v). Moreover, highly stable C/SiO_2 supports were obtained under acidic pH conditions, due to favorable electrostatic forces between silica and carbon nanoparticles displayed under such medium. A sequential alkaline-acidic process delivers $Pt/C/SiO_2$ with improved ECSA and ORR mass-activity, but its degradation under stress was significantly higher (> 50 % ECSA losses). Instead, the acidic $Pt/C/SiO_2$ catalysts lost only 30 % of its initial ECSA, with the interactions between carbon and silica enhancing support stability and inhibiting Pt degradation mechanisms.

Acknowledgments

This work was financially supported by the project UID/EQU/00511/2020 of the Laboratory for Process Engineering, Environment, Biotechnology and Energy – LEPABE - funded by national funds through FCT/MCTES (PIDDAC).
Eva Sousa and *Sofia* Delgado, are grateful to the Portuguese Foundation for Science and Technology (FCT) for the doctoral grants (references SFRH/BD/145412/2019 and SFRH/BD/144338/2019, respectively).

References

1. B. G. Pollet, S. S. Kocha, and I. Staffell, Curr. Opin. Electrochem. **16**, 90 (2019)
2. E. Padgett, V. Yarlagadda, M. E. Holtz, M. Ko, B. D. A. Levin, R. S. Kukreja, J. M. Ziegelbauer, R. N. Andrews, J. Ilavsky, A. Kongkanand, and D. A. Muller, J. Electrochem. Soc. **166**, F198 (2019)
3. G. Cognard, G. Ozouf, C. Beauger, L. Dubau, M. López-Haro, M. Chatenet, and F. Maillard, Electrochim. Acta **245**, 993 (2017)
4. Y. Dai, B. Lim, Y. Yang, C. M. Cobley, W. Li, E. C. Cho, B. Grayson, P. T. Fanson, C. T. Campbell, Y. Sun, and Y. Xia, Angew. Chemie - Int. Ed. **49**, 8165 (2010)
5. A. Ishihara, C. Wu, T. Nagai, K. Ohara, K. Nakada, K. Matsuzawa, T. Napporn, M. Arao, Y. Kuroda, S. Tominaka, S. Mitsushima, H. Imai, and K. ichiro Ota, Electrochim. Acta **283**, 1779 (2018)
6. S. Takenaka, D. Mikami, E. Tanabe, H. Matsune, and M. Kishida, Appl. Catal. A Gen. **492**, 60 (2015)
7. E. Antolini and E. R. Gonzalez, Solid State Ionics **180**, 746 (2009)
8. S. Takenaka, R. Akiyama, I. T. Kim, H. Matsune, and M. Kishida, Chem. Lett. **46**, 851 (2017)
9. S. Takenaka, H. Miyamoto, Y. Utsunomiya, H. Matsune, and M. Kishida, J. Phys. Chem. C **118**, 774 (2014)
10. X. Li and I. M. Hsing, Electrochim. Acta **51**, 5250 (2006)
11. C. C. Chou, C. H. Liu, and B. H. Chen, Energy **70**, 231 (2014)
12. P. Dhanasekaran, A. Shukla, S. V. Selvaganesh, S. Mohan, and S. D. Bhat, J. Power Sources **438**, (2019)
13. H. S. Oh, J. G. Oh, and H. Kim, J. Power Sources **183**, 600 (2008)
14. L. Pak Hoe, M. Boaventura, T. Lagarteira, L. Kee Shyuan, and A. Mendes, Int. J. Hydrogen Energy 1 (2018)
15. L. S. and G. V. F. Fievet, S. Ammar-Merah, R. Brayner, F. Chau, M. Giraud, F. Mammeri, J. Peron, J.-Y. Piquemal, (2018)
16. J. Cloarec, J. Genest, J. Beauvais, and H. Chamas, (2014)

Response Surface Methodology for 30 kW PEMFC stack characterization

Eleonora Gadducci*, *Stefano* Saccaro, *Massimo* Rivarolo, *Loredana* Magistri

DIME, University of Genoa, Via Montallegro 1, 16145 Genoa, Italy

Abstract. Hydrogen is a promising energy carrier to allow the reach of the zero-emission targets established for the next years. Polymeric Electrolyte Membrane FC are studied inside the HI-SEA laboratory of the University of Genoa, to assess the opportunities of this technology on marine applications. Here, 8 PEMFC stacks, sized 30 kW each for a total power installation of 240 kW, have been tested to draw guidelines for the best system design onboard ships and to deepen the know-how on the experimental management of the technology. During the tests, it was possible to observe the reciprocal influence of some parameters, which may influence the system efficiency. In this work, a statistical investigation is developed to quantify the cell voltage variation correlated to the values of temperature and current. This has been possible thanks to Design Expert (DE), a software developed by Stat-EASE, Inc. Through the Design of Experiment approach, it is possible to evaluate the significance of variables in the FC system, called factors. The experiment under consideration is also characterized by non-controllable factors, cause of disturbances that induce further variability in the response. Eventually, it was possible to analyse the significance of the parameters involved, to build a regression model by performing the analysis of variance with which the significant values are identified, and to assess the presence of outliers.

1 Introduction

The impact of the shipping sector on global Green House Gases (GHG) emissions is not negligible, and actions must be taken in order to reach the ambitious targets on emissions set at 2050 [1,2]. Indeed, under a business-as-usual scenario, emissions could increase between 50 and 250% by 2050, [3,4], mining the Paris Agreement objectives [5].

Under these new constraints, innovative technologies are studied that employ alternative and low-carbon fuels. Among others, hydrogen is a very promising energy carrier; it can be employed as a reactant in Fuel Cell (FC) technology, where it undergoes an electrochemical reaction producing an outlet flow and electrical energy. Polymeric Electrolyte Membrane FCs (PEMFC) are in particular interesting for transport applications, where they can be employed to power low and heavy-duty vehicles, trains as well as shipping vessels of different sizes [6-8]. For this reason, different studies have been focusing on assessing the use of this technology on real scale applications even in hybrid configurations coupled with batteries [9-16], also detailing the different opportunities and limitations of producing [17] and storing the hydrogen gas safely onboard [18].

However, the lack of international legislations regarding the installation of Fuel Cell Systems (FCS) on ships, together with a poor experience on real-size systems, are delaying the spread of the technology and the optimization of dedicated control systems. In this context, the HI-SEA (Hydrogen Initiative for Sustainable Energy Applications) Laboratory of the University of Genoa [19] offers an interesting opportunity to deepen the research on a 240 kW FCS, complete with auxiliary components. This infrastructure has seen different experimental campaigns developing the assessment of the Balance of Plant (BoP) components adequacy to withstand naval environmental and operative conditions [20,21]. The results obtained also gave some hints to identify the most influent operative parameters that determine the global efficiency of the system, which are taken as the starting point for the present study.

1.1. Design of Experiments and Response Surface Methodology

In stochastic systems, such as the one under consideration, specific statistical techniques are used to determine the effect that input parameters have on the output variable (objective function). The aim of the Design of Experiments (DoE) techniques, is to determine the influence on a selected objective function for one or more independent variables (named factors), varying among different levels or treatments. The significance of such factors is determined through a statistical comparison of the average of the observations under each treatment [22,23]. This process is carried out in order to establish which factors determine a significant variation of the objective function. The experiment is also characterized by uncontrollable factors, which are the

* Corresponding author: eleonora.gadducci@edu.unige.it

cause of disturbances or background "noises", which induce further variability of the response.

An important evolution of DoE is the so-called Response Surface Methodology (RSM) that aims to define the optimal design (the grid of candidate points in the experimental region) in order to build regression models for the objective function.

To fit a first-order regression model, the RSM identifies as best experimental design the Two-Level Factorial Design. To fit second order regression models, the Central Composite Design (CCD) or the Face-Centered Central Composite (FCC) design are adopted.

The statistical analysis and graphical analysis of the data were performed by using Design Expert software (Version 12.0, Stat-Ease, USA).

Thanks to the development of experimental tests on the HI-SEA system, a number of different parameters can be collected. The postprocessing of these data can be employed to create a regression model of the system, as the ones developed in previous studies such as [24-33]. In this work, the effect of cooling temperature on cell voltage has been deepened.

2 The HI-SEA system

The HI-SEA system is made up by 8 PEMFC stacks supplied by Nuvera Fuel Cells, model Orion®. All auxiliaries and fuel cells that make up a single entity capable of delivering power are identified with the name of FC "stack". The latter operate with pure hydrogen and air as reactants, producing water as the only exhaust. These stacks, born for automotive applications, have been described in detail in a previous work by the authors [21]; each of them is sized 30 kW and has around 200 cells. The cells work with a slight excess of hydrogen and with a more significant excess of air with respect to stoichiometric requirements. The unreacted hydrogen is recirculated, while unreacted air is eliminated through the same line designated for the exhaust reaction water produced by the electrochemical reactions. The whole system has been designed to simulate the installation on a real vessel, and therefore it is assembled inside a 30 ft container. The cathodic delivery line is supplied by an industrial compressor to simulate the connection to the compressed air line present onboard, the cooling temperature is regulated by a two-stage cooling circuit that simulates the heat exchange with sea water, and finally the load profiles can be tested through a resistive electric load to prove the ability of the installation to follow different power requests. The previous experimental campaigns have confirmed that the system is compliant with shipping operation requirements [21,35], however some general instabilities emerged. The latter were mainly due to the intrinsic behaviour of the air delivery circuit, where the industrial compressor follows a start and stop dynamic, and to the cooling temperature control. The effect was especially visible on the value of cell voltage, which during the tests is taken as the reference to evaluate the general performance of the FC, and it was amplified by the natural aging of the cells themselves. In fact, the cells were assembled first in 2014, then they underwent harsh test conditions and eventually were left unemployed during three years before their rearrangement inside the HI-SEA Lab. Although a dedicated test campaign managed to re-establish a good system performance through a recovery procedure [34], the cells weakness remains visible and is influenced by other components of the system.

2.1. System layout and control

The FCS is made up of 8 stacks, divided into 2 parallel branches. Inside a branch they are connected in electrical series, and the parallel operation is possible thanks to the presence of 2 DC/DC converters, that set the voltage output on the same value so that the load is equally shared. In this way, voltage differences between the stacks – that may arise from different aging of the cells or from temporary unfavourable operating conditions – are not an issue to load repartition.

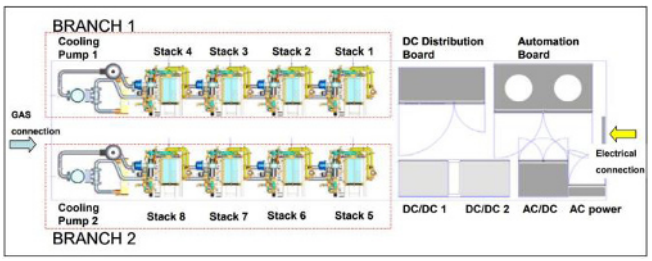

Fig. 1. Layout of the HI-SEA system.

The control of the HI-SEA system consists of a supervision system and a local panel that contains the Programmable Logic Controller (PLC) type GE IP Rx3i, an I/O field, power supplies and all auxiliary accessories for the management of communication lines; the supervisory computer interfaces to the PLC and performs the monitoring and historicization of all process variables, as well as manages the Human-Machine Interface (HMI) also implementing all the procedures to provide standard security levels for the access to the information. The control PLC performs the interfacing, management, and coordination of field devices, using when necessary different communication standards.

One of the tasks assigned to the system is to control and regulate the control circuits of fuel cells; the software is designed to control up to 8 stacks, however the operating logic of all stacks is perfectly identical to each other. One of the most important parts of the control system is the Cell Voltage Monitoring (CVM). As cell voltage is a very important indicator of the performance as well as of the state of health of cells [36,37], this value must be carefully handled and considered. The CVM chosen by Nuvera Fuel Cells acquires every second the voltage value of each cell in the stacks; therefore, it saves and communicates to the control system – for each FC stack – the following data:

- Minimum cell voltage: the lowest voltage value measured in a stack, and the ID of the cell where it is measured

- Maximum cell voltage: the highest voltage value measured in a stack, and the ID of the cell where it is measured
- Average cell voltage: obtained dividing the total stack voltage by the number of cells.

The cell voltage values are therefore employed in the analysis described in this work, to evaluate the influence of other parameters on the global FC performance. Minimum cell voltage is particularly interesting for the study, as it is usually linked to the weakest cell in a stack. In this case, it will immediately hint the presence of a non-optimized operating condition.

Another crucial aspect of the control system is the cooling circuit. The most suitable operating temperature has been set by the FC supplier to keep the ideal relative humidity on the membranes. The maintenance of the correct cell temperature is ensured by the cooling circuit, which regulates the temperature and mass flow rate of the cooling flow that removes the excess heat from the cells by means of a heat exchanger. The regulation is led by the measured current.

2.2. Tests description

To evaluate the influence of the operative conditions on cell voltage, a dedicated test campaign has been defined. In normal operation, the cell's potential follows a well-known trend that depends on the current density. The generic polarization curve represented in Figure 2 describes the typical correlation between current and voltage in a PEMFC.

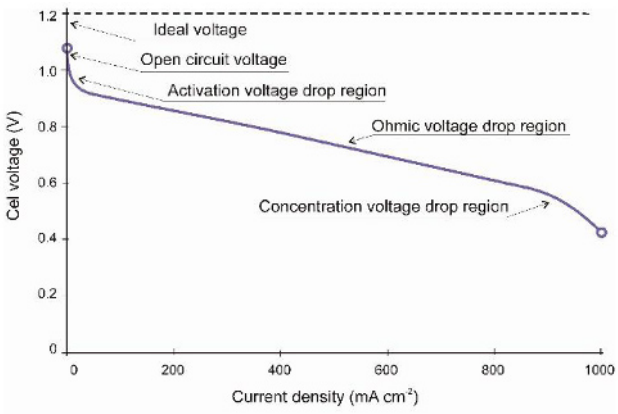

Fig. 2. Typical polarization curve of a PEMFC [38].

Due to the different losses – namely activation, ohmic and concentration losses [38] – the voltage tends to decrease with the increasing current, but with a different slope depending on the value of the latter. For this reason, in order to start the RSM analysis on the HI-SEA system, it was chosen to initially develop constant load tests, to avoid incurring in misleading cell voltage variations due to different load request and not to the system's instabilities under investigation. The constant load tests have the objective of verifying if the system is adequate for the operation. The tests have been implemented at different loads: 10, 20, and 30 kW per stack. This choice was made to ensure that the whole operative range indicated by the FC supplier was actually exploitable, kept a good performance and would not cause excessive stress to the cells. After the development of the tests, the acquired data has been postprocessed and inserted in DE software. To analyse the total stack voltage as a function of temperature and current, the following steps are taken:

- Current and cooling temperature are considered as the quantitative independent variables to be analysed.
- Maximum and minimum values of the independent variables are identified.
- Total stack voltage is considered as the objective function.
- The presence of outliers is issued, as they can distort the results of the analyses.
- The software DE evaluates the significance of the analysed variables and builds a representative regression model.
- The ANOVA allows the evaluation of significative and non-significative terms (p-value > 0,05).

This process has been applied to all the stacks, whereas only the results related to one stack of the system (number 7) for an output power of 20 kW are reported in the results, as this FC stack is the most stable during operation, considering the average quadratic deviation relative to the stack voltage.

3 Results

After analyzing the influence of the cooling temperature, a regression model is built. The V-I correlation is carried out using the temperature as a parameter, with the aim of building a map through the characteristic curves drawn at different power setpoints; through this map, it will be possible to act on the control system to implement a more precise performance monitoring.

The three main outputs of the study are:

- The survey domain, represented in Figure 3: relative to the total cell voltage, it shows the contour lines and, depending on the red or blue colour, it gives an indication of the increase or decrease of the objective function (voltage) linked to the parameters change (current and temperature).

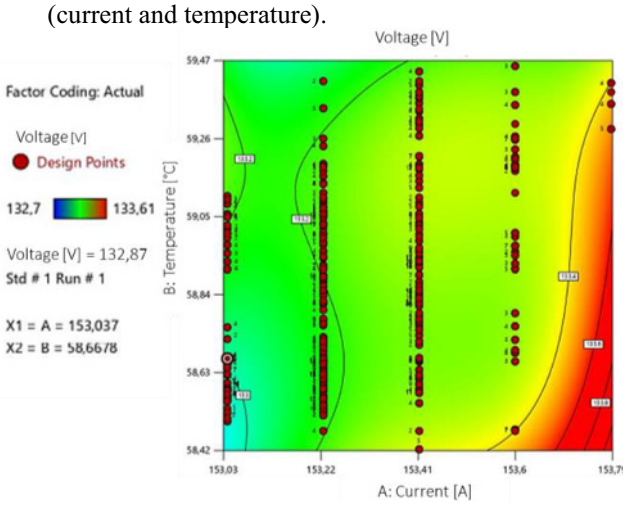

Fig. 3. Survey domain of total stack voltage, stack n.7, 20 kW.

- Response surface, represented in Figure 4: for each investigation domain, Design Expert builds a response surface that represents the behaviour of the output variable as a function of the input factors in the investigated ranges. The surface is represented through a 3D graph. For this analysis, it must be considered that the sampled data, being collected during the tests on the HI-SEA system, can make the experiment result unbalanced. This means that in the domain there are some areas where no experimental answers are available, and where an incorrect approximation of the response is verified leading to an unreliable response surface at those points. To delimit the problem, an appropriate domain cut can be made in order to analyse only the area where the experimental data are located, in order to make the statistical analysis more reliable.

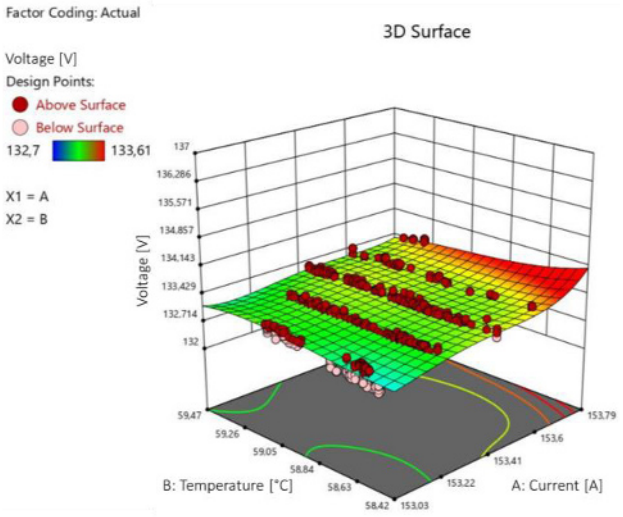

Fig. 4. Response surface, stack n.7, 20 kW.

Since no imbalance areas to be cut have been identified, the analysis is carried out of the confidence interval.

- Confidence interval, represented in Figures 5 and 6: once the most suitable response surface has been identified, the confidence intervals are analyzed, which represent the fields of variation where one expects to find the answers of the system. Each interval has a confidence level associated with it that represents the statistical probability that that range contains the true value of the answer; specifically, the level used is equal to 95%.

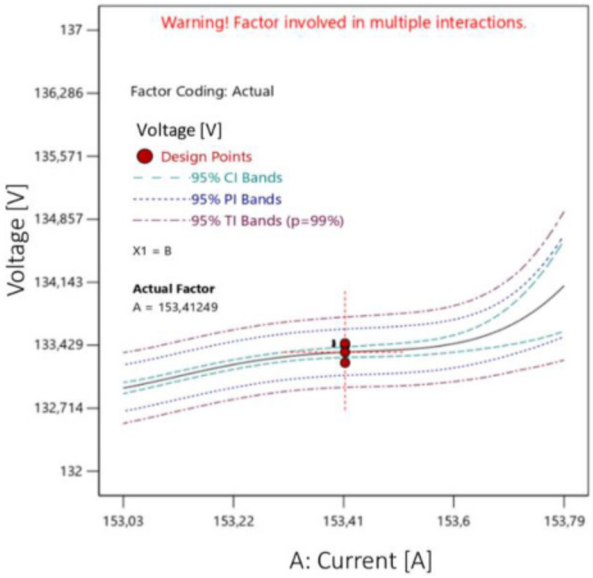

Fig. 5. Confidence interval for total stack voltage, stack n.7, 20 kW; current is set at 153,41 A.

For each domain, one single current value is set, as the variations for this parameter are small and mainly due to the control of the resistive load. The current value for the confidence interval is set at 153.41 A, as this value was the most measured during the tests at 20 kW. As regards the cooling temperature, it is set at 58,42 °C, corresponding to the most measured value assumed during the tests at 20 kW. The lines in figures 4 and 5 represent the trend of total voltage of stack n.7 and its confidence intervals for a 20 kW power output. These maps can be the starting point to develop a precise monitoring system: when voltage is measured, if it lays within the confidence interval thus the system is operating correctly. Otherwise, a warning is reported as some anomalies may be ongoing.

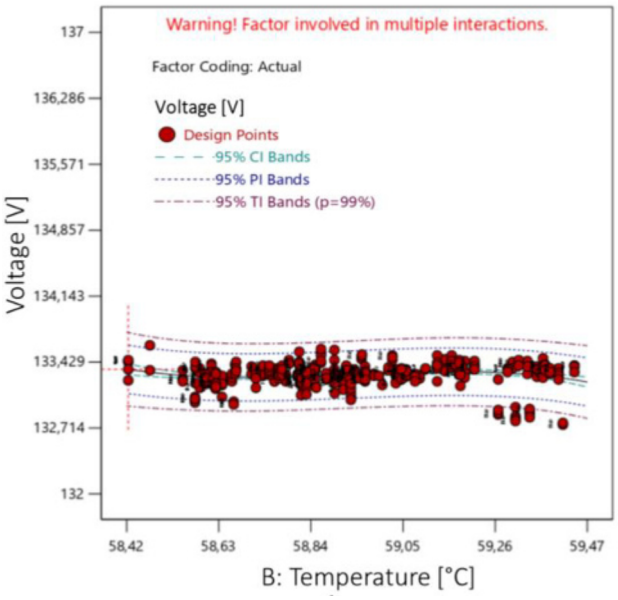

Fig. 6. Confidence interval for total stack voltage, stack n.7, 20 kW; cooling temperature is set at 58,42 °C.

4 Conclusions

The HI-SEA system is a real scale laboratory sized 240 kW of a PEMFC installation for shipping applications. The size of the FC system is compliant with the adopted ones in real world applications: PEMFC systems of similar size are already installed or are planned for future hydrogen-based vessels, such as the Italian ZEUS vessel by Fincantieri (tests in open sea are foreseen in 2022) [18]. For this reason, the HI-SEA system acquires relevance as a baseline study for the future of PEMFC applications in the maritime field, considering the lack of experimental results on real-scale systems in literature. Its BoP is made up of components that represent the naval environment; however, such components can create instabilities on the system which have an effect on the FC performance and in particular on the voltage. A Design of Experiment approach has been applied to the experimental data acquired during constant load tests, to verify the influence of current and cooling temperature oscillations, classified as the independent variables, on the objective function – the total stack voltage. The results, reported for the representative case study of stack n.7 for a power output of 20 kW, are obtained through the software Design Expert. The latter allowed to draw the survey domain, the Response Surface and the confidence intervals of the stack voltage for the case study and can become the reference for the creation of a precise performance monitoring system for the PEMFC installation: if the stack voltage lays out of the confidence intervals, anomalies can be rapidly detected, reducing significantly the operation in stressing conditions that can affect the state of health of the PEMFCs.

References

1. International Maritime Organization (IMO). Third greenhouse gas study. 2015.
2. https://www.imo.org/en/MediaCentre/HotTopics/Pages/Reducing-greenhouse-gas-emissions-from-ships.aspx, International Maritime Organization (IMO) official website, last access 22/01/2021
3. Maritime forecast to 2050-Energy transition outlook. DNV-GL Maritime (2019)
4. Setting the course to low carbon shipping. American Bureau of Shipping (ABS); (2019)
5. United Nations. Framework convention on climate change (UNFCCC). Paris Agreement; (2015)
6. M. Rivarolo, D. Rattazzi, T. Lamberti, L. Magistri. Int J Hydrogen Energy;**45** ;25747-57 (2020)
7. H. Sapra, J. Stam, J. Reurings, L. van Biert, W. van Sluijs, P. de Vos, et al. Appl Energy;281:115854 (2021)
8. M. Rivarolo, D. Rattazzi, L. Magistri, A.F. Massardo, En. Conv. And Management, **244**, 114506 (2021)
9. O.B. Inal, C. Deniz, J Clean Prod; **265** ; 121734 (2020)
10. P. Wu, R. Bucknall, Int J Hydrogen Energy;**45**:3193-208 (2020)
11. H. Nazir, N. Muthuswamy, C. Louis, S. Jose, J. Prakash, M. Buan, et al. Int J Hydrogen Energy; **45** ; 28217-39 (2020)
12. A. Pfeifer, P. Prebeg, N. Duic, E Transportation;**3**:100048 (2020)
13. C. Nuchturee, T. Li, H. Xia, Renew Sustain Energy Rev;**134**:110145 (2020)
14. S.E : Hosseini, Modul. Earth syst. Environ. Sci.. Elsevier; (2020)
15. A.L. Dicks, Modul. Earth syst. Environ. Sci.. Elsevier; (2020)
16. A. Bouakkaz, A.J.G. Mena, S. Haddad, M.L. Ferrari, Journal of Energy Storage, **33**, pp.101887_1-13 (2021)
17. D. Bellotti, M. Rivarolo, L. Magistri, A.F. Massardo, International Journal of Hydrogen Energy, **40**, pp.2433-2444 (2015)
18. M. Cavo, E. Gadducci, D. Rattazzi, M. Rivarolo, L. Magistri, Int H Hydrogen Energy, **46**, 32630-32644 (2021)
19. http://www.tpg.unige.it/TPG/
20. G. Borgogna, E. Speranza, T. Lamberti, A.N. Traverso, L. Magistri, E. Gadducci, et al. E3S Web Conf.;**113**:1-8 (2019)
21. E. Gadducci, T.Lamberti, D. Bellotti, L. Magistri, A.F : Massardo, Int J Hydrogen Energy ;**46(47):**24305-17 (2021)
22. D.C. Montgomery, John Wiley & Sonc, Inc. (1997/2005)
23. R.H. Meyers, D.C. Montgomery, John Wiley & Sons, Inc. (1995)
24. S.J. Cheng, J.M. Miao, S.J. Wu, Applied Energy, **105**, 161-169 (2013)
25. M. Ghasabehi, M. Shams, H. Kanani. Energy Conversion and Management, **230**, 113798 (2021)B. Wahdame, D. Candusso, F. Harel, X. François, M.C. Péra, D. Hissel, J.M. Kauffmann, Journal of Power Sources, **182**, 429-440 (2008)
26. H. Kanani, M. Shams, M. Hasheminasab, A. Bozorgnezhad, Energy Conversion and Management, **93**, 9-22 (2015)
27. G. Correa, F. Borello, M. Santarelli, International Journal of Hydrogen Energy, **40**, 10354-10365 (2015)
28. L. Jin, X.J. Wang, J.W. Zhu, et al. Energy Conversion and Management, **228**, 113727 (2021)
29. K. Charoen, C. Prapainainar, P. Sureeyatanapas, et al. Journal of Cleaner Production, **142**, 1309-1320 (2017)
30. T. Jahnke, G. Futter, A. Latz, et al. Journal of Power Sources, **304**, 207-233 (2016)
31. F. Mahmoodi, R. Rahimi, Applied Thermal Engineering, **178**, 115490 (2020)
32. S. Jeon, D. Cha, H. Kim, Y. Kim, Applied Energy, **166**, 165-173 (2016)

33. M. Moein-Jahromi, M.J. Kermani, Energy Conversion and Management, **231**, 113837 (2021)
34. E. Gadducci, T. Lamberti, L. Magistri, *Proceedings of EFC2019,* 231-232 (2020)
35. Gadducci, T. Lamberti, L. Magistri, *Proceedings of EFC2019,* 235-236 (2020)
36. P. Pei, Y. Li, H. Xu, Z. Wu, Appl Energy, **173**, 366-385 (2016)
37. E. Ramschak, V. Peinecke, P. Prenninger, T. Schaffer, W. Baumgartner, V. Hacker, Fuel Cell Bull, 12-15 (2006)
38. J.C. Amphlett, J Electrochem Soc, **142**, 9 (1995)

Success factors for demonstration projects of small-scale stationary fuel cells in residential buildings

Guenter Simader[1,*], Patrick Vidovic[1]

[1]Austrian Energy Agency, Mariahilfer Straße 136, 1150 Vienna, Austria

Abstract. Worldwide small-scale micro-CHPs account for the largest share in the fuel cell market by units of installation (not by installed power output). Notably, the Japanese Ene-Farm program is responsible for over 400.000 micro-CHP fuel cell installations (until the end of June 2021). This is the largest worldwide deployment program and it reflects the long- and outstanding commitment of both the Japanese government and the Japanese industry to form a 'Hydrogen Society'. In Europe, the situation is entirely different. European projects like PACE financed by the European joint undertaking for hydrogen and fuel cells give a positive impulse for fuel cell based micro-CHP, however it has to be judged as insufficient for a market transformation measure. Presently, only Germany, notably by the KFW433 program, is providing frame conditions for a rollout of fuel cell based micro-CHP systems. This article analyses the success factors for the implementation of Ene-Farm systems in Japan. It compares the different frame conditions of Japan and European countries like Austria and discusses the question whether an Ene-Farm project based on the Japanese success factors could be replicated in Austria. On a bird's eye, a European perspective will be derived from the analysis.

1 Introduction

Typical use cases for stationary fuel cells are large stationary prime power plants, combined heat and power (CHP), uninterruptible power supplies (UPS), larger 'permanent' APUs and small scale stationary micro-CHP supplies. Small-scale micro-CHPs account for the largest share in the fuel cell market by units of installation (not by installed power output). (1)

Notably, the Japanese Ene-Farm program is responsible for over 400.000 micro-CHP fuel cell installations (until the end of June 2021). (2) This is the largest worldwide deployment program for residential fuel cells and it reflects the long- and outstanding commitment of both the Japanese government and the Japanese industry to form a 'Hydrogen society'.

This high-volume market also made it possible to drive the technology along the learning curve and generate substantial economies of mass production. Successful product developments could be achieved in highly competitive markets.

The prime products of Ene-Farm program are presently a PEM-based technology from Panasonic and a SOFC-based technology from Aisin and Kyocera. The products have a typical electrical power output of 700 W (and even lower). They operate on natural gas or LPG. Japan's gas companies, like Tokyo Gas or Osaka Gas, mainly supply the units.

The climate conditions in Central and Northern European countries (like Austria) make heating systems necessary to cover the heating and domestic hot water demand. However, with exception of Germany, fuel cell based micro-CHP systems (or conventional ones) are not installed in large quantities in residential and/or non-residential buildings like in Japan.

This article analyses the success factors for the implementation of Ene-Farm systems in Japan. It compares the different frame conditions of Japan and European countries like Austria and discusses the question whether an Ene-Farm project based on the Japanese success factors could be replicated in Austria. On a bird's eye, a European perspective will be derived from the analysis.

2 Success factors of the Japanese Ene-Farm project

For the Japanese Ene-Farm project, the following success factors could be identified:

- Clear strategic positioning with clear strategic goals (embedded in an overall country's R&D strategy) by establishing a level playing field for micro-C
- Ene-Farm systems are recognized as greenhouse-gas abatement technology (contributing to national energy and climate policy goals)

* Corresponding author: guenter.simader@energyagency.at

- Excellent product quality and availability, simple distribution channels and system installation (by one-stop-shops)
- Product characteristics (power output of micro-CHPs) meet the market requirements of Japanese households/buildings (domestic hot water demand and electricity demand)
- High-volume markets enable product standardisation, product iterations/improvements and significant cost reductions
- Micro-CHP systems increase the resilience of the energy system (in case of natural disasters like earthquakes, hurricanes, …)

In the following, the success factors are analyzed and the applicability and replicability for the Austrian (European) market are examined.

2.1 Clear strategy and clear goals for micro-CHP systems

As already pointed out, hydrogen and fuel cells are central elements of the Japanese energy and climate policy to form a 'Hydrogen Society'. Goals for stationary fuel cells ('Ene-Farms') are the implementation of 5.3 million systems until 2030 (10 % of Japanese households). The target price for PEM based Ene-Farm systems is ¥ 800.000 (ca. € 6.500) and ¥ 1.000.000 (ca. € 8.000) for SOFC based systems. The payback period of 5 years should be achieved at this time. (3)

In Europe, the frame conditions are (entirely) different to the Japanese ones. Although there is a hydrogen strategy in place, the primary goal is to achieve the reduction of CO_{2eq} by 55 % until 2030 and to achieve climate neutrality by 2050 (with hydrogen as one element in the puzzle). (4, 5) Austria, even more ambitious, has the goal of climate neutrality by 2040. The discussion of the role of 'green' hydrogen is still ongoing.

In order to reach the goal of climate neutrality, fossil fuels should continuously phase-out from all sectors. In Austria, there is a Renewable Heat Act in preparation to ban fossil fuels by 2040. Prior to this, a commandment for systems based on renewable energy sources will be implemented accompanied by extensive subsidy schemes in order to start to phase-out fossil fuels by 2025. These systems are seen to result in CO_2 lock-in effects of fossil fuels and to prevent the transition to climate neutrality.

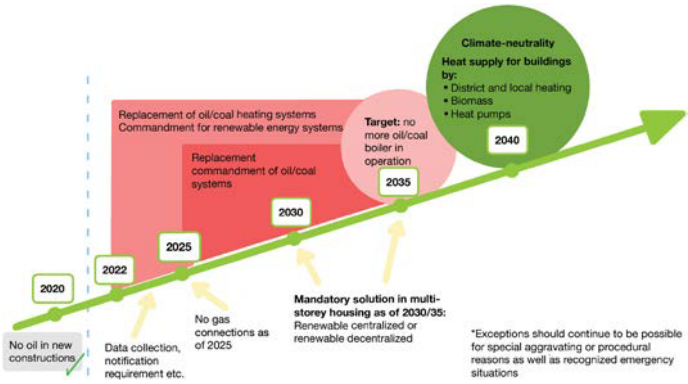

Fig. 1. Key points of the planned Austrian Heat Act implementing renewable based heating systems to reach climate neutrality by 2040

'Green'-hydrogen or 'renewable gases or E-fuels' will fit into the strategy of climate neutrality. However, the quantities of 'green' gases/fuels are presently classified as very limited and expensive. Significant quantities of 'green' hydrogen are expected by 2030.

Moreover, this 'green' hydrogen (also applicable for renewable gases or E-fuels) are foreseen to be used in sectors with no other technological options. Examples for sectors with limited technological options to become climate neutral are seen in the heavy industry (e.g., steel industry, cement industry,) or in the transportation sector (long distance freight transportation).

The use cases in the building sector offer many technological options for fossil-free heating systems (like heat pumps, biogenic systems, etc.). Many innovations based on renewable energy sources are presently tested and implemented in Austria. (6)

2.2. Ene-Farm systems are recognized as greenhouse-gas abatement technology (contributing to national energy and climate policy goals)

Fossil generation capacities account for more than 80 % (mainly coal and gas) in the Japanese power generation. In Austria, this share is only about 17% (regardless of imports). Accordingly, the CO_{2eq} intensities of grid electricity in the two countries differ significantly. While Japan had a high value of 464 g/kWh CO_{2eq} in 2017 (7), Austria was most recently at 227 g/kWh CO_{2eq}.

When operating an Ene-Farm system based on fossil fuels in Japan, the achievable savings in greenhouse gases are much higher than in Austria. In Austria, only marginal savings can be achieved. Using renewable gases or 'green' hydrogen in micro-CHP systems could increase these savings tremendously (see figure 3). However, as already pointed out, the building sector is not seen as priority use case for the deployment of 'green' hydrogen or renewable gases.

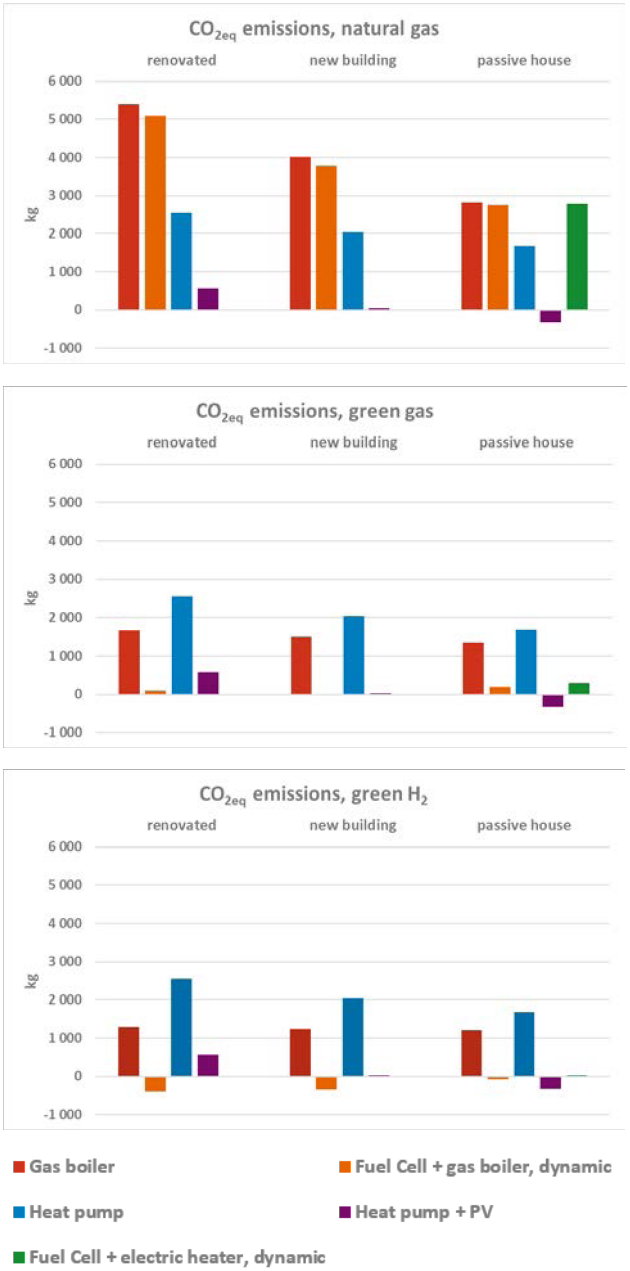

Fig. 2. Comparison of CO_{2eq} emissions of fuel cell based micro-CHP heating systems with competing technologies in single family houses in Austria (for three building standards: renovated, new building and passive house) fuelled by natural gas, 'green' gas and 'green' hydrogen with competing technologies (like gas condensing boiler, heat pump w/o PV) (8) Reading: The second column shows the results of the micro-CHP system, respectively. Only when fuelled with 'green' gas or 'green' hydrogen significant CO_{2eq}-savings can be achieved.

2.3 Excellent product quality and availability, simple distribution channels and system installation (by one-stop-shops)

The distribution channels of Ene-Farm products are very simple for end customers. There are currently three manufacturers of Ene-Farms (Aisin, Kyocera and Panasonic), and sales are handled entirely by local gas utilities (e.g., Osaka Gas, Tokyo Gas, etc.).(3)

The utilities also take care of the installation and maintenance of the equipment as well as of suitable energy supply contracts, thus forming a one-stop shop for customers. Furthermore, the installation of Ene-Farm devices are not very costly, as the investment costs are low (compared to Europe) and they are mainly installed outside of the buildings. Thanks to the optimized systems, durability of the cell stack, that is the main device of the system, the service life of the power generation unit has been extended from 10 to 12 years. (10)

The typical system configuration of an Ene-Farm system is shown in the figure below.

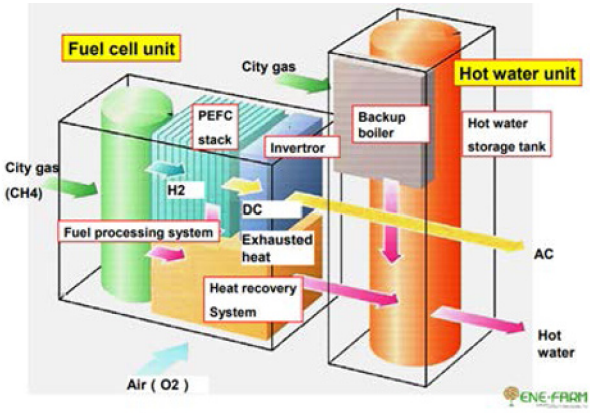

Fig. 3. Typical system configuration of an Ene-Farm system (3)

In Austria, stationary micro-CHP systems based on fuel cells are mainly sold directly by the manufacturers or their installer companies (no one-stop store). Usually, the manufacturers or their installers have a product portfolio of different heating systems (from heat pumps, biogenic-based systems to gas condensing boilers, and micro-CHP systems). The owner must conclude gas supply contracts and network access contracts.

In contrast to Japan, heating systems in Austria are installed indoors. The regulatory requirements for indoor installations are notably higher (due to safety regulations) and the installations are more complex than outdoors. In addition, there are bureaucratic barriers in Austria that make the installation of a micro-CHP system in buildings more difficult (e.g., issuance of an energy performance certificate (EPC) in case of a new building or a deep renovation).

Thus, there is a very competitive environment for micro-CHP systems offering very weak unique selling propositions to the end user.

2.4 Product characteristics of Ene-Farm systems are optimized to the required Japanese demand profiles in residential buildings

Ene-Farm systems in Japan are operated following the electrical demand of the building as long as the required hot water demand is produced. First and foremost, the hot water demand is provided by the Ene-Farm system, during this time the system also provides power to the building. In case of a higher hot water demand, a backup boiler provides this demand. The power grid covers a higher electricity demand.

The operating modes of Ene-Farm systems are shown exemplarily for two single-family houses (in the following figure). The use of Ene-Farm systems in condominiums is also possible (if space conditions allow the installation of the system).

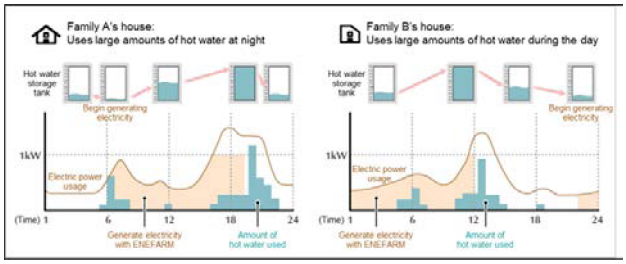

Fig. 4. Typical operation modes of Ene-Farm systems (8)

The following table lists the product characteristics of the three relevant manufacturing companies. The power ratings of Ene-Farm systems were optimized in order to meet the daily hot water demand (about 150 liters and lower) and to achieve a long daily operation period. Over the years, the electrical power output decreased slightly from 1 kW to 700 W). Kyocera's system with 400 W has been dimensioned smaller enabling even longer daily operating periods.

Table 1. Product characteristics (2)

Company	Type	Electrical Power kW	Electrical Efficiency %	Total %
Panasonic	PEFC	0,7	40	97
Aisin	SOFC	0,7	55	87
Kyocera	SOFC	0,4	47	80

Due to the climate conditions in Austria the energy demand for heating in single family houses (50 – 225 kWh/m^{2}a) is significantly higher than in Japan (about 12 GJ/household year).[a] The domestic hot water demand is about 10 kWh/m^{2}a, only a small part compared to the heating demand.

In Austria, central heating systems (including boiler, distribution and dissipation system – radiators) are the standard to cover the heat and domestic hot water demand. Presently, typical central heating systems are fossil-fuelled (oil, gas), renewable energy-based (biomass, heat pumps) or connected to the district heating system.

The central heating system continuously charges the hot water storage tank. In case of using condensing gas combi boilers, a storage system is not even required. In fewer cases, electric water heaters or instantaneous water heaters are used. Investment costs for these systems are quite low (about € 100 and above). Another – more efficient and more expensive – option are domestic hot water heat pumps (about € 1.000 to € 2.000).

Comparing the total costs of ownership of different heating options in single family houses (including micro-CHP systems) show very limited economic performance (see next chapter). The economic advantages that can be realized for users of Ene-Farm systems in Japan cannot be transferred to the Austrian situation.

2.5 Market volume generates improved product iterations and competitive product prices

As already pointed out, over 400,000 Ene-Farm systems were successfully installed in Japan by 2020 (mainly outside of buildings). Although Japan was not able to reach its own target of 1.4 million systems by 2020, a mass market was established for fuel cell based micro-CHP systems.

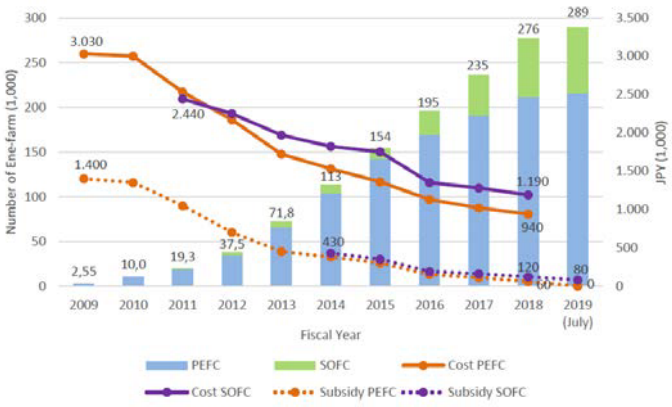

Fig. 5. Commercialisation of Ene-farm stationary fuel cell systems in Japan until 2019, evolution of costs and subsidies [3]

By 2030, a target of 5.3 million installations (about 10% of Japanese households) were announced by METI as part of the strategic roadmap for hydrogen and fuel cells. The clear framework conditions enable the manufacturing companies to establish mass production of these systems,

[a] The way of looking to the energy consumption in buildings, respectively households is different in Austria compared to Japan. In Austria, the typical usable floor area in single-family houses is between 115 and 150 m^2 (to make the numbers between Austria and Japan comparable).

to significantly reduce the price of the systems (between € 7,000 and € 9,300 by 2021), and to develop business models for distribution. (3)

By achieving a mass market, it was possible to continuously improve the product characteristics in terms of compactness, integration into the building automation, higher supply security, higher efficiency and improved sale possibilities of produced electricity. In terms of cost-effectiveness, payback periods below 10 years (goal 5 years by 2030) were achieved.

In Europe, the situation is entirely different. European projects like PACE financed by the European Joint Undertaking for hydrogen and fuel cells give a positive impulse for fuel cell based micro-CHP, however it has to be judged as insufficient for a market transformation measure. Presently, only Germany, notably by the KFW433 program, provided frame conditions for a rollout of over 15.000 fuel cell based micro-CHP systems in the last few years.

The typical investment costs of fuel cell based micro-CHP systems for single-family houses are much higher in Austria (but also in Germany) than in Japan. Depending on the system configuration, the manufacturer announces system prices between € 25.000 and € 35.000 (incl. VAT). The following figure shows the fuel cell based micro-CHP system installed most often in Austria (from Viessmann Company).

@courtesy of Viessmann Company

Fig. 6. Vitovalor PT 2 based on PEM-LT technology P_{el}: 750 W, P_{th}: 1,1 kW_{th} P_{th} from gas boiler: individual scalable from 11,4 kW, 24,5 kW to 30,8 kW Hot water storage tank: 220 l

The prices for electricity and gas is unfavourable for realising benefits of produced electricity (ratio: electricity/gas is in Austria 2:1; in Germany much better with 4:1). A comparison of the total cost of ownership (TCO) of different heating systems shows that a fuel cell-based micro-CHP system is challenging (see Figure 8).

For this comparison, three scenarios were developed, comparing micro-CHP fuel cell systems with gas condensing boilers and heat pumps (w/o photovoltaic):

Scenario 1: Austrian prices: for the investment of the heating system, for gas and electricity (purchase and feed-in) and for O&M (operation and maintenance)

Scenario 2: Scenario 1 using Japanese Ene-Farm investment costs for the micro-CHP system, all other parameters follow Scenario 1

Scenario 3: Scenario 1 including a subsidy scheme (similar to the KfW 433 scheme[b]) and German prices for gas and electricity

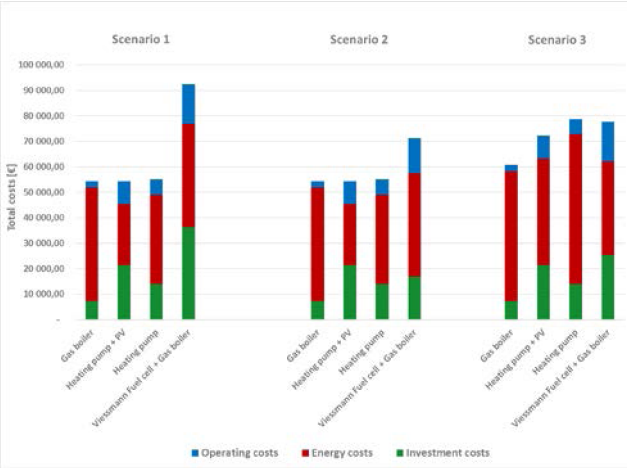

Fig. 7. Comparison of the total cost of ownership (TCO) between micro-CHP system (incl. gas boiler) and gas condensing boiler, electrically heat pump (w/o photovoltaic) in single-family houses. Reading: Only with a subsidy scheme like Germany's KfW 433 and ratios of gas/electricity prices of 4:1, the micro-CHP system can achieve a similar economic performance like a heat pump (scenario 3). Presently, competing systems have a very similar TCO level in Austria (scenario 1). Scenario 2 shows that even with price levels for the fuel cell like in Japan, a fuel cell micro-CHP achieves no economic advantage (due to other unfavourable economic frame conditions).

In Austria, subsidy schemes similar to the German KfW 433 program must be implemented in order to achieve similar TCO for fuel cell based micro-CHP systems.

Economic analysis of fuel cell systems with a higher power output deployed in larger buildings (more family houses and/or non-residential buildings) with long annual operation hours of the fuel cell improve the economic performance of micro-CHP fuel cell systems.

[b] The subsidy scheme of KfW 433 provides a fixed amount of € 6.800 and additionally a power-dependent amount of € 550 per 100 W of electrical power or part thereof.

2.6 Micro-CHP systems increase the resilience of the energy system (in case of natural disasters like earthquakes, hurricanes …)

The resilience of power systems due to natural disasters (such as earthquakes, hurricanes, etc.) has a completely different meaning in Japan compared to Austria (or Europe). In Japan, long outages of the power grid with far-reaching consequences can occur (in case the transmission system is affected). Accordingly, decentralized systems for energy supply that increase the resilience of the energy system are regarded as very positively by the society.

Ene-Farms can be operated in parallel to the grid as emergency power systems. If a power failure occurs, the Ene-Farm system will take over the energy supply. This allows the use of, for example, smaller electrical appliances and/or the lighting system (even during a power outage). In addition, domestic hot water is produced. This feature offers an excellent additional selling point for Ene-Farm systems in Japan. Ene-Farm companies receive very often awards like the "Japan Resilience Award".

In Austria, power outages due to unplanned regional extraordinary events such as floods, snowstorms are less frequent (between 10 to 20 minutes per year in the last 10 years). The importance of using a stationary fuel cell as emergency power system is less relevant and is not a common purchase argument.

3 Conclusions

Hydrogen and fuel cells are central elements of the Japanese energy and climate policy to form a 'Hydrogen Society' in all sectors. The implementation of the 'Ene-Farms' project resulted in over 400.000 installed units by the End of June 2021. By 2030, a target of 5.3 million installations (about 10% of Japanese households) were announced by METI.

The clear frame-conditions made it possible to achieve a mass market for Ene-Farm systems in the residential sector. It was possible to continuously improve the product characteristics in terms of compactness, integration into the building automation, higher supply security (resilience), higher efficiency and improved sale possibilities of produced electricity. In terms of cost-effectiveness, lower prices were achieved and payback periods of 7 to 8 years are reported (with the target of 5 years in 2030).

The Ene-Farm project may be characterised as a success story yet unequalled in the world!

In Europe, the frame conditions are (entirely) different to the Japanese ones. Although, there is a hydrogen strategy in place, the primary goal is to achieve the reduction of CO_{2eq} by 55 % until 2030 and to achieve climate neutrality by 2050 (with hydrogen as one element in the puzzle). (4, 5) Austria, even more ambitious, has the goal of climate neutrality by 2040.

Presently, the discussion of climate neutrality unfavourable influences the usage of micro-CHP systems based on fossil fuels. These systems are seen to result in CO_2 lock-in effects of fossil fuels and to prevent the transition to climate neutrality. The role of 'green' hydrogen in our future energy system is still ongoing.

The question whether the Japanese Ene-Farm project can/should be replicated in Austria's residential building sector is very difficult to be answered positively. Identified success factors for the Japanese Ene-Farm project cannot be transferred to Austria. Besides the mentioned unfavourable political frame-conditions, many barriers were identified concerning technological requirements for heating systems, economic competitiveness and acceptance as climate abatement technology.

Nevertheless, the future of stationary fuel cells is seen very positive (but not based on fossil fuels). The strategy of climate neutrality will increase the amounts of renewable energy sources in our energy system in the next few years significantly. In parallel to the generated electrical energy, energy vectors like hydrogen and/or other synthetic fuels are regarded to be necessary for our future energy system.

Looking to a fossil-free energy future, fuel cells in combination with hydrogen from renewable energy sources (like photovoltaic, wind, small hydropower) will be the core element of decentralised, hydrogen-based eco-systems providing electricity (and waste heat) to households, mobility applications as well as the trade and commerce sector.

Acknowledgement

This project receives support by the Austrian IEA research cooperation on behalf of the Federal Ministry for Climate Action, Environment, Energy, Mobility, Innovation and Technology.

Federal Ministry
Republic of Austria
Climate Action, Environment,
Energy, Mobility,
Innovation and Technology

IEA Research Cooperation
Part of open4innovation

FFG
Promoting Innovation.

References

1. E4 Tech, The Fuel Cell Industry Review 2020, March 2021, ()
2. The Japan Gas Association, news release, Cumulative sales of household fuel cell "ENE-FARM" exceeded 400,000 units, 5th August 2021 (https://www.gas.or.jp/newsrelease/)
3. J. Arias, Hydrogen and Fuel Cells in Japan. Report from the EU-Japan Centre for Industrial Cooperation 2019
4. European Commission, European Green Deal: Commission proposes transformation of EU economy and society to meet climate ambitions, Brussels, 14th July 2021 (https://ec.europa.eu/commission/presscorner/detail/en/IP_21_3541)
5. European Commission, The role of hydrogen in meeting our 2030 climate and energy targets, Brussels, July 2021 (https://ec.europa.eu/commission/presscorner/detail/en/fs_21_3676
6. Showcase projects using renewable energy sources in the city of Vienna, 2021 (https://www.wien.gv.at/stadtentwicklung/energie/wissen/erneuerbar/index.html
7. Ministry of Economy, Trade and Industry (METI), Agency for Natural Resources and Energy. Japan's Energy 2018. 10 questions for understanding the current energy situation. 2019. (https://www.enecho.meti.go.jp/en/category/brochures/pdf/japan_energy_2018.pdf)
8. G. Simader, et.al., Conception of an Austrian fuel cell demonstration project – Ene-Farm Austria, Report, Vienna, 2022 (in preparation)
9. Itochu Enex Co. Ltd, ENEFARM (Residential Fuel Cells), July 2021 (https://www.itcenex.com/en/business/detail/enefarm/index.html)
10. Osaka Gas Co., News release, February 2020 (https://www.osakagas.co.jp/en/whatsnew/__icsFiles/afieldfile/2020/03/03/20200225.pdf)
11. K. Kordesch, G. Simader, Fuel Cells and their Applications, Wiley-VCH, 1996

Exsolution in La and Ni co-doped strontium titanate: a suitable anode for running SOFCs on ammonia as alternative fuel

Jonathan Cavazzani[1,*], *Enrico* Squizzato[1], *Elena* Brusamarello[1] and *Antonella* Glisenti[1,2]

[1]Department of Chemical Science, University of Padova, Via F. Marzolo 1, 35131, Padova, Italy
[2]ICMATE - Department of Chemical Science, University of Padova, Via F. Marzolo 1, 35131, Padova, Italy

Abstract. Ammonia exhibits interesting features as fuel to feed Solid Oxide Fuel Cell. Herein, Ni and La co-doped strontium titanate was synthetized using wet chemistry route. Ni nanoparticles emerged via exsolution in reducing environment to decorate the surface. X-Ray Diffraction measurements exhibits perovskite structure was also preserved after the exsolution, as expected. H_2 – Temperature Programmed Reduction highlights the great resistance of titanates in anode operation condition. Ammonia conversion in nitrogen and hydrogen were investigated by catalytic tests. It begins to decompose at 560°C and the full yield was achieved at 720°C. Electrochemical measurements were recorded at 800°C using 10% of ammonia in Ar. They were analysed though the model of equivalent circuit and two processes were attributed. Results certify Ni exsolution strongly enhances the hydrogen oxidation and the total polarisation resistance in ammonia approaches to the one in hydrogen.

1 Introduction

During the current transition towards renewable energy sources, the demand for versatile devices able to store and re-use the excess of energy production is increasing [1–4]. In this scenario, Solid Oxide Fuel Cells (SOFCs) exhibit tempting features, such as high efficiency and low environmental impact [5–8].

Although hydrogen is the most conventional and studied fuel for this application, ammonia is constantly gaining more attention as alternative [9–14]. Ammonia is mainly synthetized though Haber-Bosch method , however more environmentally friendly routes are under investigation [15,16]. Ammonia is largely used in household cleaning products, fertilizers and nitric acid production [17]. It does not present severe safety concerns: it is toxic but human nose is sensible below a concentration of 1 ppm so the detection of leakage is easy [9]. In addition, ammonia has a narrower combustion range than hydrogen [14]. All these features promote the ammonia as an interesting hydrogen carrier and then it deserves a deeper study in SOFC technology.

In 1980, Farr and Vayenas [18] investigated the odds to synthetize NO and obtaining an electrical current during the same process. In the early 2000s, Wojcik and co-workers [19] explored the use of ammonia as fuel to feed a SOFC and they collected promising results.

It has been proposed a two-step mechanism when anode is fed by ammonia in oxygen anion conducting SOFC: first ammonia cracks in nitrogen and hydrogen via thermal decomposition mediated by a catalyst. Then the hydrogen diffuses across the interface reacting with the oxygen to form water [12]. Ni cermet, such as Ni-Yttria Stabilized Zirconia (YSZ) and Ni-Gadolinium Doped Ceria (GDC), have been largely studied for running SOFC on ammonia as fuel [20–23].

Hereby, we propose Ni and La co-doped strontium titanate as anode material. We already investigated $SrTiO_3$ – based materials showing interesting properties for this application [24]. In the current work, we try to impart new functionalities using the method of the exsolution [25–29]. It has been recently employed for anode application in SOFC technology and it allows to realize high dispersive nanoparticles on the surface of the catalyst for preventing drawbacks connected to sintering in long-term operation [30,31].

Ni exsolution in titanates – based materials have been studied as alternative to state-of-art Ni-YSZ for working as anode in high temperature SOFC [27,32,33]. Lanthanum aims to promote the formation of the redox couple of the titanium Ti (IV)/ Ti (III) [34].

In this contribution, we focus our attention on the response of La and Ni co-doped titanates towards ammonia decomposition. The material demonstrates suitable features in reducing environment under operation condition preserving the perovskite structure, as H_2 – Temperature Programmed Reduction (TPR) establish. Catalytic tests prove a totally conversion of ammonia at working temperature (800°C), although the whole decomposition, in nitrogen and hydrogen, occurs at 720°C. From the measurements Ni exsolved nanoparticles do not affect the catalytic activity towards the ammonia cracking. Instead, Ni nanoparticles strongly boost the electrochemical performances, as detected in

impedance measurements at 800°C. To increase furtherly the temperature would enhance the cell tests; for this reason, other tests are under investigation.

2 Experimental

2.1 Synthesis

Regarding the synthesis of $La_{0.45}Sr_{0.45}Ti_{0.90}Ni_{0.10}O_3$, (LSTNO) stoichiometric amounts of La_2O_3 (Sigma-Aldrich, 99.9%) $SrCO_3$ (Sigma-Aldrich, 98%), $C_{12}H_{28}O_4Ti$ (Sigma-Aldrich, 97.0%) and $Ni(NO_3)_2{\cdot}6H_2O$ (Sigma-Aldrich, 97.0%) were dissolved in distilled water and nitric acid under continuous heating and stirring. Precursor's solutions were added to a solution of citric acid; precursors/citric acid ratio is 1/1.8. Subsequently, ammonium hydroxide was added to adjust the pH between 7 and 8. The solution was heated and stirred at 80°C to permit the solvent evaporation and then left to age for 24 hours. Self-combustion was ignited increasing the temperature above 300°C. The ashes-like material was then grinded and calcined at 1000°C for 12 hours (rate 6°C min^{-1}). $La_{0.45}Sr_{0.45}TiO_3$ (LSTO) was synthetized using the same method. The calcined $La_{0.45}Sr_{0.45}Ti_{0.90}Ni_{0.10}O_3$ was treated in 5% H_2/Ar flow to promote the exsolution at 900°C for 20 hours (rate 7°C min^{-1}), as reported in [27]. After the reducing treatment, material has been named $La_{0.45}Sr_{0.45}Ti_{0.90}Ni_{0.10-\delta}O_3$ (LSTNOH).

2.2 Characterization

Crystalline structure of the powders was characterized by X-Ray Diffraction (XRD) using a Brucker D8 Advance diffractometer with Bragg-Brentano geometry and Cu Kα radiation (40 kV, 40 mA, λ = 1,54 Å). H_2 - Temperature Programmed Reduction measurements were carried out through an Autochem II 2920 Micromeritics equipped with a thermal conductivity detector (TCD). H_2 – TRP measurements were led in a quartz tube with 50 mg of the sample powder. The heating goes from room temperature (RT) to 900°C at 10°C/min under a constant flow of 5 vol% H_2/Ar and a flow rate of 50 sccm.

2.3 Catalytic measurements

The sample powder (50 mg) was loaded in quartz tube reactor of 6 mm internal diameter and was exposed to a flow of 10 vol% NH_3/Ar balance helium (He is also the gas carrier). All gas flows were monitored by a thermal mass flow meter and the total inlet flow is 100 sccm. Analysis were performed from RT to 800°C. Samples were pre-treated in He for 1 hour at 100°C before the measurements. The composition of the outlet gas was measured with an Agilent 7890 A gas chromatograph equipped with a TCD and two columns (molecular sieve 13X, 60/80 mesh, 1.8; Porapak Q, 1.8 m). Calibration was carried out using standard gases containing known concentration of the components. NH_3 conversion yield was calculated as reported in [22], F indicates the fraction of fuel (ammonia, 10% in this work) in the flow:

$$NH_3 \text{ conversion yield (\%)} = [(F\ NH_3 \text{ inlet} - F\ NH_3 \text{ unreacted}) / F\ NH_3 \text{ inlet}] * 100 \quad (1)$$

2.4 Cell manufacturing and measurements

The electrochemical tests were carried out on symmetric button cell. Thick electrolyte was prepared by pressing a commercial 8 mol% Yttria-stabilized Zirconia (8YSZ) powder (Fuel Cell Materials) in to pellet and fired in air. Symmetric electrodes were deposited a homemade screen-printing machine and then fired in air at 1200°C for 2 hours. Final circular electrodes have an area of 1,13 cm^2. Electrodes are composite made up by the anodic material and 8YSZ (50:50). Ink preparation involved mixing the powders with a proper amount of binder to adjust the viscosity and 3 wt% of carbon soot to guarantee the porosity to the electrodes. Gold paste was deposited as electron collector and treated at 800°C. Symmetric cell tests were carried out in a home-made single chamber set up using a flow rate of 100 sccm. Electrochemical Impedance Spectroscopy (EIS) measurements were performed through an Autolab Frequency Response Analyser in a frequency range of 10^{-2} – 10^{-6} Hz. The values of area specific resistance (ASR) were calculated considering one electrode in the symmetric cell and its surface area (1.13 cm^2), starting from polarization resistance (R_p) values obtained from impedance measurements.

3 Characterization

3.1 XRD

XRD analysis were performed at room temperature. Diffractograms are displayed in Fig. 1. La – doped $SrTiO_3$, LSTO, shows the characteristic reflections of perovskite crystal structure. The structure is also maintained when Ni is added. Moreover, it has been likely incorporated in the lattice because no further phases appear in the diffractogram. It suggests that 10 mol% of Ni is completely soluble in $La_{0.45}Sr_{0.45}TiO_3$. The insertion in Fig. 1 exhibits an enlargement of the reflection at ~ 46.5° (2θ) The diffractograms in samples containing nickel, LSTNO and LSTNOH, are shifted towards lower angle respect to LSTO. Here, this shift in normally attributed to the substitution of Ti^{4+} atoms, 61 pm, with those larger of Ni^{2+}, 69 pm [35]. This effect indicate that the Ni atoms have been successfully merged in the perovskite lattice producing a consequent expansion of the unit cell [27,36].
Reducing treatment for the exsolution, 900°C for 20 hours in 5% H_2/Ar, causes the release of Ni atoms which move towards the surface forming metal nanoparticles. The reflections in LSTNOH diffractograms demonstrate that the perovskite has been preserved and Ni phase

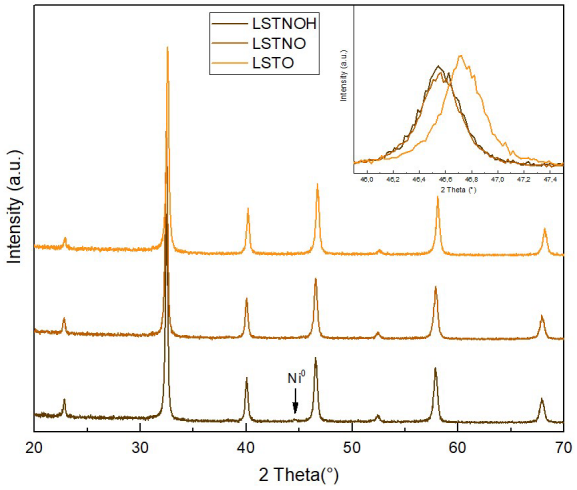

Fig. 1: room temperature XRD of $La_{0.45}Sr_{0.45}TiO_3$ and $La_{0.45}Sr_{0.45}Ti_{0.90}Ni_{0.10}O_3$ calcination at 1000°C in air (LSTO and LSTNO, respectively); LSTNO was furtherly treated at 900°C for 20 h in 5% H_2/Ar: $La_{0.45}Sr_{0.45}Ti_{0.90}Ni_{0.10-\delta}O_3$ (LSTNOH). Insertion: closer inspection of reflection at ~ 46.6° (2θ).

appears at ~ 44.5° (2θ), the most intense reflection, as identified from JCPDS database (# 96-901-3025).

3.2 H_2 – TPR

All TPR measurements were carried out in 5% H_2/Ar from room temperature to 900°C with a ramp of 10°C/minute. Moreover, for LSTNOH sample, a pre – treatment in He at 300°C for 1 hour was also carried out before the TPR analysis in order to remove molecules eventually adsorbed after the exposition with the air, as suggested from the literature [37]. However, it is not reported in Fig. 2 because no variations in the profile have been detected. All TPR profiles are displayed in Fig. 2 (all detectable signals occur between 250 – 750°C). It is well-known that titanate-based materials show high stability in reducing environment, this the reason why they are largely studied for anode application in fuel cells. Indeed, literature works attribute a slightly consumption of hydrogen in LSTO to the reduction from Ti^{4+} to Ti^{3+} [38]. However, in this current work, it is really difficult to distinguish the hydrogen consumption and the background noise because the signal is very low and no well-defined peaks appear. Some considerations can be achieved: in the TPR profile of LSTNO, the peak at ~ 475°C can be associated to the reduction of different nickel oxide species. In particular this signal can be ascribed to surface NiO that might had not been fully incorporated in the perovskite structure [37,39,40]. LSTNO might be exploited to achieve information for the exsolution. Since the condition for this process are stronger (900°C for 20 hours), in the current case, the TPR profile is not diagnostic for this process because there is not any clear variation in the TCD signal. Analysing LSTNOH, two peaks at ~ 375°C and 530°C might correspond to the reduction of nickel oxide state, different to those in LSTNO [40]. No deeper investigations were carried out to identify the phases.

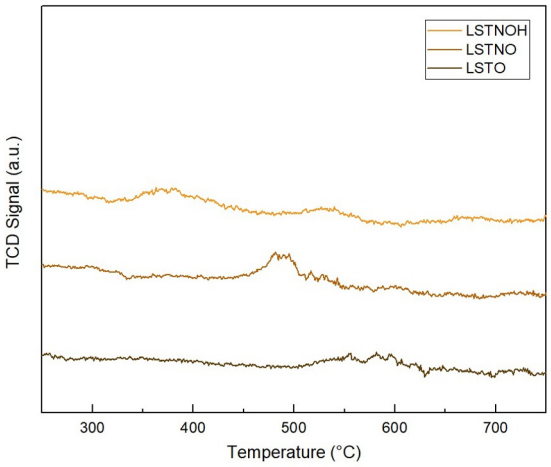

Fig. 2: H_2 - TPR curves obtained for the samples: the $La_{0.45}Sr_{0.45}TiO_3$ (LSTO), $La_{0.45}Sr_{0.45}Ti_{0.90}Ni_{0.10}O_3$ (LSTNO) and $La_{0.45}Sr_{0.45}Ti_{0.90}Ni_{0.10-\delta}O_3$ (LSTNOH); all profile were reported from 250 to 750°C.

4 Catalytic tests

Catalytic tests were carried out though a Gas Chromatograph with aim to evaluate the conversion yield of the inlet ammonia (10%) in nitrogen and hydrogen. Conversion yield was calculated using Eq. (1), as reported in the Experimental section (2.3). In Fig. 3 the results of the catalytic tests are displayed. Observing the conversion curves, both powders show a really close activity towards ammonia decomposition. In particular, ammonia starts to crack at 560°C and it is completely decomposed at 720°C. In this case, Ni nanoparticles do not affect the reaction yield. Ammonia decomposition tests were led by Song *et al.* [41]. They evaluate the catalytic activity of infiltrated Ni, Co and NiCo doped lanthanum strontium titanate on Samarium Doped Ceria (SDC) scaffold. They highlight how the NiCo alloy nanoparticles shows the superior conversion (95,3% at 800°C), while pure SDC scaffold exhibits the lowest, 5,8% at 800°C. This demonstrate that electrolyte oxides show really poor catalytic activity, it must be imparted by the anodic material. However, Molouk and co-workers [22] study the ammonia decomposition on Ni-YSZ and Ni-GDC.
They evidence that Ni-GDC, thanks to a larger number of basic sites on GDC, has higher catalytic activity compared to Ni-YSZ. The choice of the electrolyte affects the ammonia conversion yield.

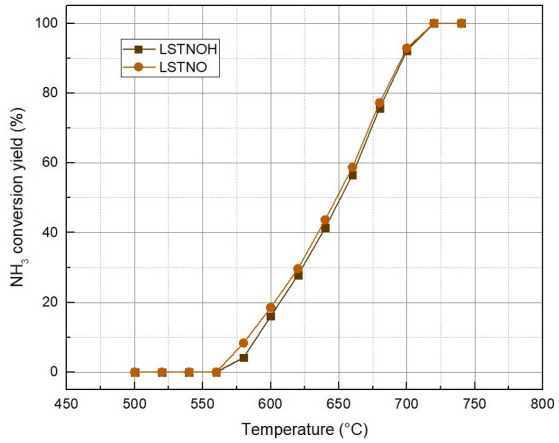

Fig. 3: NH_3 conversion yield as a function of the temperature. Ammonia content in the flow (100 sccm) was 10%.

5 Electrochemical tests

Electrochemical investigations were carried out at 800°C on LSTO, LSTNO and LSTNOH. They were studied forming a composite with 8YSZ (50:50) with the purpose to provide ionic conductivity to the electrode [24]. In Fig. 4 impedance spectra are displayed using 10% NH_3/Ar as fuel. Hydrogen is reported for comparison. Spectra were analysed by mean the method of equivalent circuit. In literature, the most used model circuit [33,42] is made up by a resistor R_1, which refers the resistance of the electrolyte, and then two resistor-constant phase elements (R-CPE) in series to describe the semicircles at high frequency (~ 10^4 - 10^3) and medium frequency (~ 10 – 1 Hz) region. There are no further processes when the cell works with ammonia instead of hydrogen, although the ammonia oxidation involves two steps. The process in high frequency region may be attributed to a not perfect adhesion at the interface between the electrode and electrolyte [42]. Decreasing the amount of soot in order to diminish the porosity may improve the goodness of the interface. Another solution could be a buffer layer between the electrode and the electrolyte with the aim to increase the ion diffusion. However, the main contribute to the total resistance derives from the second process [33]. It could be assigned to the reduction and oxidation cycles of the couple Ti (IV)/Ti (III), which governs the electrical conductivity in the material. The resistance would decrease raising the operation temperature [32,34].
In Table 1, all tested cells are reported highlighting their composition and summing up the performances. From the values of polarization resistance is clearly visible that Ni nanoparticles on the surface, in LSTNOH, strongly improve the electrochemical performances. This consideration is valid both when ammonia and hydrogen have been used as fuel. However, considering the catalytic results discussed above, the behaviour of LSTNO and LSTNOH are totally overlapped. In the light of these results, the Ni nanoparticles boost the performance of the electrode: they are more active towards hydrogen oxidation rather than the ammonia decomposition, where the conversion is not affected by Ni nanoparticles. Although, the completely decomposition of ammonia make possible to study the cell performance at lower temperature, likely the cell performance will be worse because titanate-based materials assume high temperature for operation.

Table 1: cell measurements are sum up and cell composition is highlighted. * Polarization resistance values were collected using EIS.

Symmetric cell	% fuel (in Ar)	Rp (Ω)*	ASR (Ω cm^2)
LSTNOH+8YSZ (50:50) | 8YSZ	10 H_2	22,6	12,8
LSTNOH+8YSZ (50:50) | 8YSZ	10 NH_3	24,2	13,7
LSTNO+8YSZ (50:50) | 8YSZ	10 NH_3	79,1	44,7
LSTO+8YSZ (50:50) | 8YSZ	10 NH_3	126,2	71,4

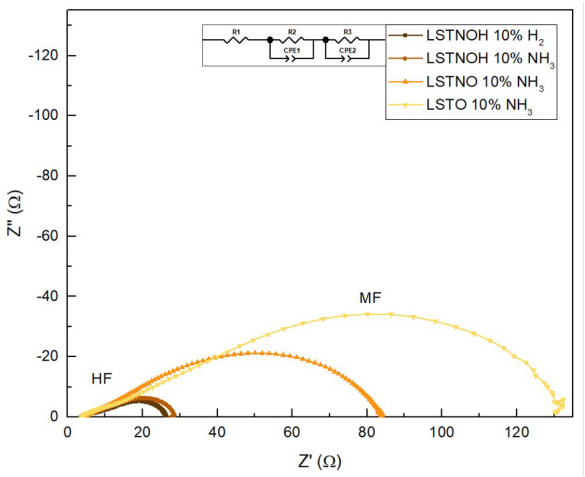

Fig. 4: EIS spectra for the anode composite materials at 800°C using NH_3 (in Ar). Also 10% of H_2 in Ar is reported as reference. The model circuit used for the fitting is displayed.

6 Conclusions

In this contribution we synthetized La and Ni co-doped strontium titanate by means wet chemistry route, a robust and suitable potential anode for SOFC technology. Ni has been exsolved from the perovskite crystal structure through a reducing treatment forming metallic nickel nanoparticles on the surface, as shown in XRD diffractograms. We focused the work on ammonia as alternative fuel. The catalytic behaviour of the material was evaluated by tests measuring the ammonia conversion. LSTNO and LSTNOH exhibit a really close activity. They start to decompose the ammonia at 520°C and the conversion reaches the full yield at 720°C. Instead, LSTNOH shows superior results during electrochemical measurements at 800°C, both in ammonia and hydrogen. Increasing temperature would

diminish the polarization resistance. In the light of these results, ammonia demonstrates interesting properties and deserves a deep investigation, for example using high working temperature. Further work is in progress in order to collect more data in electrochemical measurements. Complete cell tests will be early carried out for measuring the density power and to have clearer the potential of ammonia to feed SOFC.

7 References

[1] M.S. Dresselhaus, I.L. Thomas, Nature **414** (2001) 332–337.

[2] A.M. Abdalla, S. Hossain, A.T. Azad, P.M.I. Petra, F. Begum, S.G. Eriksson, A.K. Azad, Renew. Sustain. Energy Rev. **82** (2018) 353–368.

[3] F. Nadeem, S.M.S. Hussain, P.K. Tiwari, A.K. Goswami, T.S. Ustun, IEEE Access **7** (2019) 4555–4585.

[4] A.G. Olabi, C. Onumaegbu, T. Wilberforce, M. Ramadan, M.A. Abdelkareem, A.H. Al – Alami, Energy **214** (2021) 118987.

[5] S.C. Singhal, Solid State Ionics **135** (2000) 305–313.

[6] N. Mahato, A. Banerjee, A. Gupta, S. Omar, K. Balani, Prog. Mater. Sci. **72** (2015) 141–337.

[7] M. Mehrpooya, M. Sadeghzadeh, A. Rahimi, M. Pouriman, Energy Convers. Manag. **198** (2019) 111767.

[8] A.B. Stambouli, E. Traversa, Renew. Sustain. Energy Rev. **6** (2002) 433–455.

[9] A. Fuerte, R.X. Valenzuela, M.J. Escudero, L. Daza, J. Power Sources **192** (2009) 170–174.

[10] M. Ni, M.K.H. Leung, D.Y.C. Leung, Int. J. Hydrogen Energy **33** (2009) 943–959.

[11] A. Valera-medina, H. Xiao, M. Owen-Jones, W.I.F. David, P.J. Bowen, Prog. Energy Combust. Sci. **69** (2018) 63–102.

[12] O. Siddiqui, I. Dincer, Therm. Sci. Eng. Progess **5** (2018) 568–578.

[13] Q. Ma, R.R. Peng, L. Tian, G. Meng, Electrochem. Commun. **8** (2006) 1791–1795.

[14] G. Jeerh, M. Zhang, S. Tao, J. Mater. Chem. A **9** (2021) 727–752.

[15] E. Morgan, J. Manwell, J. McGowan, Renew. Energy **72** (2014) 51–61.

[16] C. Smith, A.K. Hill, L. Torrente-Murciano, Energy Environ. Sci. **13** (2020) 331–344.

[17] T.E. Bell, L. Torrente-Murciano, Top. Catal. **59** (2016) 1438–1457.

[18] R.D. Farr, C.G. Vayenas, Energy Dev. Japan **4** (1981) 111–128.

[19] A. Wojcik, H. Middleton, I. Damopoulos, J. Van herle, J. Power Sources **118** (2003) 342–348.

[20] G.G.M. Fournier, I.W. Cumming, K. Hellgardt, J. Power Sources **162** (2006) 198–206.

[21] Q. Ma, J. Ma, S. Zhou, R. Yan, J. Gao, G. Meng, J. Power Sources **164** (2007) 86–89.

[22] A.F.S. Molouk, J. Yang, T. Okanishi, H. Muroyama, T. Matsui, K. Eguchi, J. Power Sources **305** (2016) 72–79.

[23] J. Yang, A.F.S. Molouk, T. Okanishi, H. Muroyama, T. Matsui, K. Eguchi, ACS Appl. Mater. Interfaces **7** (2015) 28701–28707.

[24] G. Carollo, A. Garbujo, F. Mauvy, A. Glisenti, Energy and Fuels **34** (2020) 11438–11448.

[25] D. Neagu, G. Tsekouras, D.N. Miller, H. Ménard, J.T.S. Irvine, Nat. Chem. **5** (2013) 916–923.

[26] D. Neagu, T.S. Oh, D.N. Miller, H. Ménard, S.M. Bukhari, S.R. Gamble, R.J. Gorte, J.M. Vohs, J.T.S. Irvine, Nat. Commun. **6** (2015) 1–8.

[27] G. Tsekouras, D. Neagu, J.T.S. Irvine, Energy Environ. Sci. **6** (2013) 256–266.

[28] B.A. Rosen, Electrochem **1** (2020) 32–43.

[29] D. Neagu, E.I. Papaioannou, W.K.W. Ramli, D.N. Miller, B.J. Murdoch, H. Ménard, A. Umar, A.J. Barlow, P.J. Cumpson, J.T.S. Irvine, I.S. Metcalfe, Nat. Commun. **8** (2017) 1–8.

[30] K. Kousi, C. Tang, I.S. Metcalfe, D. Neagu, Small **17** (2021) 2006479.

[31] J.T.S. Irvine, D. Neagu, M.C. Verbraeken, C. Chatzichristodoulou, C. Graves, M.B. Mogensen, Nat. Energy **1** (2016) 1–13.

[32] D. Neagu, J.T.S. Irvine, Chem. Mater. **22** (2010) 5042–5053.

[33] D.N. Miller, J.T.S. Irvine, J. Power Sources **196** (2011) 7323–7327.

[34] O.A. Marina, N.L. Canfield, J.W. Stevenson, Solid State Ionics **149** (2002) 21–28.

[35] B.H. Park, G.M. Choi, Solid State Ionics **262** (2014) 345–348.

[36] B.H. Park, G.M. Choi, J. Power Sources **293** (2015) 684–691.

[37] M. Toscani, F. Volpe, N. Nichio, Int. J. Hydrogen Energy **5** (2020) 23433–23443.

[38] J. Li, T. Lv, N. Hou, P. Li, X. Yao, L. Fan, T. Gan, Y. Zhao, Y. Li, Int. J. Hydrogen Energy **42** (2017) 22294–22301.

[39] J. Marrero-Jerez, E. Chinarro, B. Moreno, M.T. Colomer, J.R. Jurado, P. Núñez, Ceram. Int. **40** (2014) 3469–3475.

[40] A. Mizera, E. Drożdż, Ceram. Int. **46** (2020) 24635–24641.

[41] Y. Song, H. Li, M. Xu, G. Yang, W. Wang, R. Ran, W. Zhou, Z. Shao, Small **16** (2020) 1–8.

[42] C. Arrivé, T. Delahaye, O. Joubert, G. Gauthier, J. Power Sources **223** (2013) 341–348.

Comparison of different infiltration amounts of CeO_2 inside Ni-YSZ anodes to improve stability and efficiency of Single-Chamber SOFCs operating in methane

Giovanni d'Andrea[1,*], *Enrico* Squizzato[1], and *Antonella* Glisenti[1,2]

[1] Department of Chemical Sciences, University of Padova, Via F. Marzolo 1, 35131, Padova, Italy
[2] ICMATE - Department of Chemical Sciences, University of Padova, Via F. Marzolo 1, 35131, Padova, Italy

Abstract. Electrochemically active oxide-based anodes capable of working in Single-Chamber Solid Oxide Fuel Cells (SC-SOFCs) were developed. Their performance is related to the selectivity of the electrodes. Tests are carried out on lab-scale devices with YSZ pellets as solid electrolytes in electrolyte supported cells. Selecting methane as a fuel, a gas mixture in the ratio $CH_4/O_2 = 2$ was chosen. The Ni-YSZ (NiO:YSZ=60:40) anode was optimized through CeO_2 nanocatalysts infiltration to enhance the anode catalytic activity and make its reduction easier. Several infiltration amounts were compared, from null to 15% of the electrode weight. Both symmetric and complete cells (with LSCF-based cathodes) were tested in H_2 and CH_4/O_2. For increasing amounts of infiltrated CeO_2, symmetric cells tests describe an area specific resistance (ASR) reduction from 40 Ω cm^2 to 1.7 Ω cm^2 in hydrogen and from 11 Ω cm^2 to 3.9 Ω cm^2 in the methane/oxygen mixture. While complete cells tests displayed an ASR drop from 30 Ω cm^2 to 2.9 Ω cm^2 in H_2, and from 8.7 Ω cm^2 to 4.3 Ω cm^2 in the methane/oxygen mixture, while OCP and power grew from 478 mV and 3.7 mW cm^{-2} to 766 mV and 13 mW cm^{-2}.

1 Introduction

Single Chamber Solid Oxide Fuel Cells (SC-SOFCs) represent a particular branch of SOFCs technologies that aims to overcome the main flows of the dual chamber devices, mainly due to the sealing, that makes the device design more complex and make it hard to be employed for portable applications [1]. Some of the greatest benefits of single chamber SOFCs are the easier fabrication, the great potential for miniaturization, the easier preparation of a stack assembly and the presence of exothermic reactions to sustain the cell temperature [2,3]. Despite the advantages, the main challenges bound to this technology are the intrinsic necessity for highly selective and catalytically active materials, the lower fuel utilization and efficiency, due to parasitic reactions, and the risk of explosion due to fuel and air being mixed together at high temperatures [4,5]. These critical aspects made research on single chambers to become little appealing in the latest years [6], yet its employment for specific applications would make it a competitive technology, as in portable power applications [7], cogeneration [8] or in a context where the high fuel use efficiency is not a fundamental requirement, as sensors [9] or in residual fuel in engine exhaust [10].

Of all possible fuels, methane is a largely available and safe one. In fact, methane must undergo partial oxidation on the anode surface to produce syngas, which is the actual fuel [4,5]. Because of catalytic activity toward the partial oxidation of methane, Ni is the most used catalyst [11,12], despite it is far from being an ideal catalyst [13,14]. Ni-YSZ is one of the most employed anodic materials, even though YSZ is not an ideal material for intermediate temperature applications, below 700°C [4], however, this ionic conductor has great chemical and mechanical stability. Metal oxides can boost the activity of the anode [15–17]. They are often investigated and represent ideal catalysts whenever balance between costs and performance improvement is reached. Doping with precious metals like Pd or Ru, is not a preferential option though. A material often accounted for in catalysis is CeO_2 [18], a promising material for improving Ni-YSZ anode efficiency. Different approaches have been followed to couple these materials, i.e. preparing a solid solution [19] and by infiltration [20]. In this last case, in the work of Yang *et al.* (2014), it was emphasized the stability of the infiltrated CeO_2 nano-catalysts, their ability to catalyse the deep oxidation of methane and their ability in helping the reduction of NiO to Ni. The infiltrated amount was 3% of the weight (3wt%) of the NiO-YSZ unreduced electrode.

Aim of this work, was to test the correlation between the anode performance in SC-SOFCs and the increasing infiltration amount of CeO_2 into the electrode (3wt%, 6wt%, 9wt% and 15wt%). This was mainly done by means of Electrochemical Impedance Spectroscopy (EIS) where the spectra variation can give insights on a modified ability of the electrode to retain and conduct electrical charge and influence the reaction rate of the fuel. It was chosen to employ a CH_4/O_2=2 ratio for safety reasons, to work above the upper flammability level [2], and to avoid the redox

* Corresponding author: giovanni.dandrea.1@unipd.it

oscillatory behaviour, but it is still high enough to avoid carbon deposition [21]. To maximize the TPB density, it was chosen to employ YSZ as electrolyte, limiting the ability of the material to work on lower temperatures. LSCF was chosen as cathode material. Considering different parameters, like activity towards the oxidation of methane and stability in CH_4/O_2 mixtures, seems to be one of the most promising material for SC-SOFCs applications [22]. Due to compatibility issues, a GDC interlayer was employed, paying attention to thermal gradients, for the different thermal expansion coefficient between GDC and YSZ may give rise to complications [23]. The final cathode was LSCF:GDC (50:50) to avoid delamination of pure LSCF cathodes after thermal treatment.

2 Experimental

Electrolyte supported cells consisted in YSZ pellets, 1.4 mm thick and 19 mm in diameter, with 12 mm electrodes deposited above via tape casting. YSZ powder was chosen in the stoichiometric ratio of 8YSZ ($(Y_2O_3)_{0,08}$ $(ZrO_2)_{0,92}$) (fuelcellmaterials, US). 2.5 g of powder were pressed by a hydraulic press to obtain the pellets that were later oven sintered at 1500°C and eventually polished on P220 sandpaper. Anode powder was produced by impregnation, starting from YSZ powder and $Ni(II)(NO_3)_2 \cdot 6H_2O$ (Sigma-Aldrich, US). To achieve the anode material, with chosen ratio of NiO:YSZ=60:40, the Nickel precursor was mixed with YSZ powder, water and twice its mole amount of citric acid. Keeping the reaction slurry heated and under stirring, basification occurred to obtain pH = 7. After that, the slurry was dried and taken to the ignition point through heating. Eventually, the powder was milled with a mortar and calcinated for 6 hours at 900°C, delivering a pale green powder. To produce the ink, the powder was mixed with 3wt% of carbon soot as a pore former, half its weight in a thinner ink (fuelcellmaterials, US) and a few drops of terpineol based ink vehicle to adjust viscosity (fuelcellmaterials, US). Cathode and interlayer (IL) inks preparation followed the same route, with the cathode consisting in a 50:50 (weight) mixture of LSCF ($La_{0.6}Sr_{0.4}Co_{0.2}Fe_{0.8}O_{3-\delta}$) powder (Sigma-Aldrich, US) and GDC ($Ce_{0.9}Gd_{0.1}O_{1.95}$) powder (fuelcellmaterials, US) and the IL in pure GDC. The electrode inks were deposited above the electrolyte surface with a tape casting technique, where a 12 mm in diameter mask consisted in a punched through piece of packaging tape, and the spreader, in a razor blade. Eventually, the anode was calcinated at 1400°C, while the cathode and the IL, at 1200°C. For complete cells, the cathode was deposited above the GDC interlayer, for which, a 14 mm in diameter mask was used to avoid contact between the cathode and the electrolyte [24]. In fact, as a compatibility test proved, LSCF and YSZ are not compatible materials at 1200°C. In Figure 1, it is reported the XRD pattern of LSCF and YSZ powders mixed together and treated at 1200°C, proving that, even though no insulting phase $La_2Zr_2O_7$ [25], was observed, LSCF structure was completely lost, in favour of simple oxides structures. Cathode calcination at a lower temperature was tested, at 850°C, but no adhesion was achieved, making it impossible to be used in a cell. Even

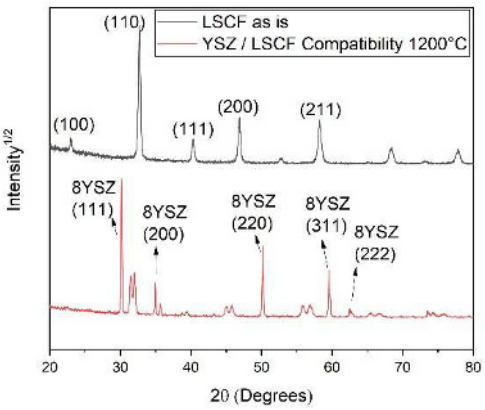

Figure 1: Comparison between pure LSCF (black) and the LSCF/YSZ compatibility test at 1200°C powders (red) XRD patterns. LSCF is completely lost after treatment at 1200°C when mixed with YSZ.

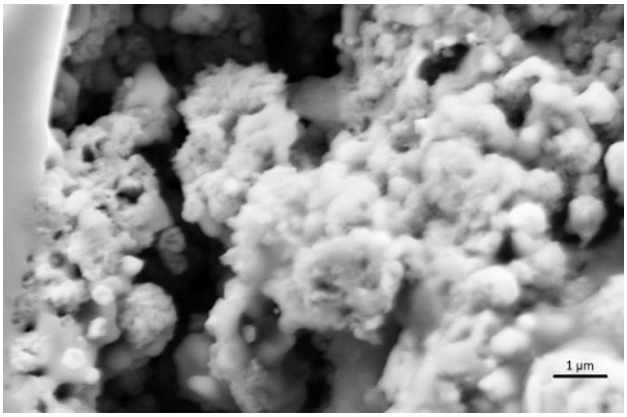

Figure 2: SEM image of the NiO-YSZ anode 3wt% CeO_2 infiltrated. On the bottom left corner, it is easy to identify the CeO_2 nanoparticles.

though, the mixed powders at 850°C did not react together and the two phases remained unchanged. At first an attempt with a CeO_2 interlayer was made [26], calcinating the powder at 1200°C, but there was no adhesion on the pellet. The GDC interlayer calcinated at 1200°C have a fair adhesion, but a small portion of powder can be easily removed from the calcinated layer with scotch tape or friction. Since the interlayer, due to its thickness and limited conductivity, decreases the ability of the material to deliver power, it is desirable to keep it as porous and thin as possible, reason why a higher calcination temperature, to give more compactness to the material, was not tested. Also, at higher temperatures it is likely favoured the reaction between Ceria and Zirconia.

Subsequent infiltrations were carried out through weighting the anode, with one measurement of the cell before deposition and after calcination. Infiltration volumes of a 0.5 M $Ce(III)(NO_3)_3$ solution were evaluated on the weight amount of CeO_2 expected to be present inside the electrode. After the infiltration of no more than 3wt% at a time, to allow the solution to permeate, the cell was heated to 450°C to let the nitrates decompose and leave CeO_2 alone in the structure. In Figure 2, the anode at the interface with the electrolyte is seen and on the bottom

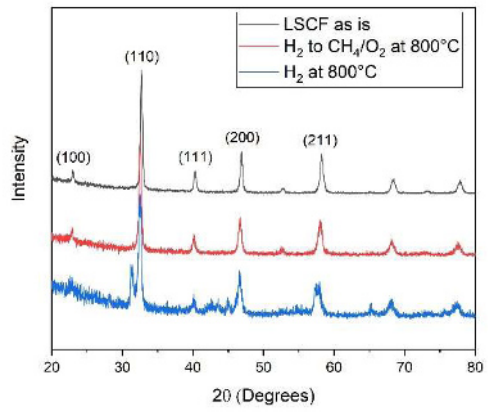

Figure 3: Comparison of the XRD patterns for pure LSCF powders (black); the LSCF powders treated at 800°C in H_2 first and in CH_4/O_2 later (red), preserving the original pattern; and LSCF powders treated at 800°C in H_2 (blue), losing the original pattern, showing the formation of new phases.

left corner it is possible to identify the infiltrated CeO_2 nanoparticles.

The electrical contacts were obtained using a gold paste (fuelcellmaterials, US) spread on top of the electrodes, then treated at 780°C to decompose the organic carrier, and a gold wire cemented in contact with it.

The first challenge was to identify the best reduction conditions for the NiO in the anode, to obtain Ni(0), the active phase. Several reduction methods have been employed over time, both in-situ and ex-situ [2]; in our case, the chosen route was the employment of a diluted hydrogen mixture at high temperature. To make sure the anode was fully reduced, it was chosen to raise the temperature of the chamber while fluxing a 30% diluted hydrogen gas mixture in argon before proceeding in raising temperature to 700°C, at which the first measurements is carried out. The symmetric cells were taken to 550°C and stationed at that temperature for three hours to achieve full reduction of the anode, expecting that this temperature would not negatively affect the cathode. XRD patterns were obtained on powders treated for one hour in H_2 at 500°C, yet the conditions did not allow for a full reduction. For this reason, the temperature was raised to 550°C and the stationing time was increased up to 3 hours, just before taking the cell to a higher temperature. TPRs displaying the reduction of nickel oxide in YSZ show different behaviour depending on the state of the material, on the stoichiometric ratio between the two components and whether it is found in powder state or in a low or high temperature sintered state. For an analogous material 61% NiO in YSZ calcinated at 1450°C, the TPR main reduction peak is found at 800 K [27], just below the selected temperature of 550°C.

The reduction process is mainly a problem for complete cells, in presence of the cathode, which behaves differently from the anode in a reducing atmosphere. For LSCF, TPRs were examined to determine the temperature at which a reducing atmosphere would induce a stoichiometric variation of the material. Reduction of the material occurs at about 860°C, in particular on Co and Fe sites, while on lower temperatures, at 640°C a reduction peak is observed, and below 400°C, only excessive non-stoichiometric oxygen is removed from inside the structure [28,29]. A modification of the structure was observed after treatment of LSCF powders up to 800°C, with a 5°C/min ramping, in a 100 sccm, 30% H_2 atmosphere in Ar, and cooling in pure argon flow. No specific phases were identified, but a new crystalline component did arise. A second test was carried out, though, to confirm whether or not it is possible to achieve reoxidation of the powder. Here, the commercial powder was treated in H_2 up to 800°C, with a 5°C/min ramping (same treatment of the previous powder sample), then kept for one hour at the same temperature in a CH_4/O_2=2 working gas mixture, then cooled in a pure argon flow. As the diffraction patterns reported in Figure 3 show, the structure of the powder treated with the working mixture of methane and oxygen, differently from the sample treated in hydrogen alone, shows the same crystalline structure of the commercial powders, confirming the reoxidation of the material.

3 Results and discussion

3.1 Symmetric cells

The main goal of this work was observing the effects of increasing infiltration amounts on impedance spectra and, particularly, resistance of the electrodes. Symmetric cells were tested, starting from a non-infiltrated (0wt% CeO_2) Ni-YSZ electrode, then 3wt%, 6wt%, 9wt% and eventually a 15wt% CeO_2 infiltrated cell. Cells were tested in hydrogen at three different increasing temperatures, 700°C, 750°C and 800°C, and only at 800°C the cells were also tested in the working gas mixture (CH_4/O_2=2). This was done to prevent the electrodes degradation given by carbon deposition that may arise with oxidation of methane or re-oxidation of the anode that may proceed with the employment of an oxidating atmosphere [21,30].

The tests on symmetric cells were planned to use a ramp of 2°C/min from room temperature to 550°C with a dwelling of 3 hours, then 1.5 hours at 700°C, 1.5 hour at 750°C and finally reaching 800°C with ramps of 2°C/min and a flow set to 100 sccm with a composition of 30% hydrogen and 70% argon. At 800°C, after the EIS measurements in hydrogen, the gas was switched to 100 sccm of a gas mixture composed of 20% in pure methane, 10% oxygen, introduced by flowing air, and argon as completion gas. Both gas mixtures went through a bubbler to humidify the mixture (about 3%) before the inlet of the chamber. The Electrochemical Impedance Spectroscopy (EIS) measurements were obtained with an Autolab PGSTAT204 (Metrohm, CH) potenziostat/galvanostat with 20 mV AC amplitude in a frequency range of 10^6 Hz to 10^{-2} Hz, always displayed, for decreasing frequencies from left to right. Measurements were taken in sequence at each temperature, always with the same setting, to follow all possible variations in behaviour over time of the cells.

All Area Specific Resistance (ASR) values reported are associated to circular electrodes of 1.2 cm in diameter. When possible, resistance values were obtained by fitting the curves with ZView (3.5e version). The most frequently

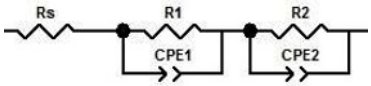

Figure 4: Equivalent circuit used to fit the EIS spectra. R_S is associated to the resistance of the electrode, the two elements with a Resistance in parallel with a constant phase element (CPE) are associated to the semi-circles at the different frequencies.

employed associated circuit follows the scheme reported in Figure 4. It was often not possible to retrieve a resistance value from the fits because of the issues encountered with fitting specific shapes of the spectra or because of the signal instability at low frequencies, that did not allow for the semicircles to reach an ordinate value tending to 0 Ω at frequencies close to 10^{-2} Hz. In these cases, the resistance is determined by the difference between the lowest frequency point following the curve and the highest frequency point (with–Z''≥0). Concerning the significant figures, always 2 are reported. Temperature increase induces a lowering in the electrolyte resistance, referred to the gap between the abscissa values of 0 Ω and that of the first point at high frequencies (with –Z''≥0).

The cell without CeO_2 infiltration (0wt%), at 700°C delivers a spectrum that reaches about 300 Ω (over 160 in ASR Ω cm^2) a value that discourages the exploitation of the material, despite the temperature is suited for YSZ electrolytes [2,3]. At 750°C, though, the resistance is halved with an ASR of 75 Ω cm^2, and eventually, 40 Ω cm^2 at 800°C. These resistances are higher than the expected ones, in the range of a few ohms, but considering the preparation steps, the materials and the experimental conditions are the same for all measurements, they serve as a valid reference for the measurements on infiltrated cells. The spectra are reported in Figure 5, above. The employment of the chosen methane gas mixture (CH_4/O_2=2) drastically diminishes the resistance observed down to an ASR of 11 Ω cm^2. The comparison between the spectra at 800°C for the cell tested in H_2 and in CH_4/O_2 are reported in Figure 5, below.

The interpretation of the EIS spectra relies on computational models. Different works in literature link different frequency ranges to different chemical processes, so the interpretation given is not univocal. EIS spectra can change across the whole frequency range just by a change in the chemistry and the structure of the material [31]. The first semicircle on the left is that for high frequencies (HF), describing a range around 10^6 Hz – 10^4 Hz. This is generally described as due to charge transfer process and electrical double layer. Its value is also proportional to the triple phase boundary (TPB) density in the material [32]. The next semicircle on the right, is that for medium frequencies (MF), in a range around 10^4 Hz – 10^1 Hz. Sometimes it is also visible a smaller arch at the highest measured Z' values, for the low frequencies (LF), in the range 10^1 Hz – 10^{-2} Hz. These two semi-circles are generally associated with mass transfer processes, the one at MF depends on the micro-structure of the material and is due to gas diffusion through the electrode and the current collector, while the LF arch is associated to the diffusion of gases on top of the electrodes [31,33].

The behaviour of the cell 3wt% CeO_2 infiltrated was stable in hydrogen at all temperatures, both at 700°C, 750°C and

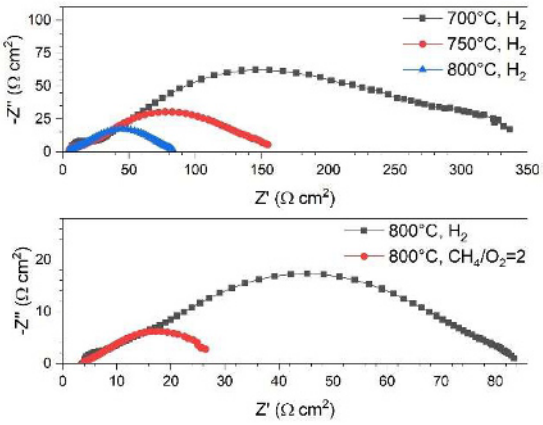

Figure 5: Above: EIS spectra for the 0wt% infiltrated symmetric cell at the different temperatures in H_2, 700°C (black), 750°C (red) and 800°C (blue). Below: EIS spectra for the same cell obtained at 800°C in H_2 (black) first, and in a CH_4/O_2=2 gas mixture (red) later.

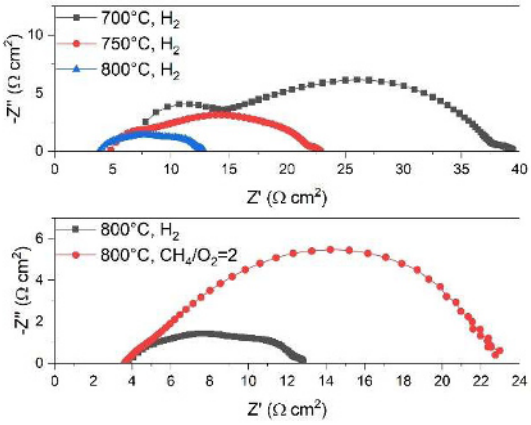

Figure 6: Above: EIS spectra for the 3wt% infiltrated symmetric cell at the different temperatures in H_2, 700°C (black), 750°C (red) and 800°C (blue). Below: EIS spectra for the same cell obtained at 800°C in H_2 (black) first, and in a CH_4/O_2=2 gas mixture (red) later. These spectra are representative of all those for infiltrated cells, all having similar behaviour qualitatively and being different only quantitatively.

800°C, not increasing their resistance over time. The Area Specific Resistance (ASR) reduction is consistent between the different temperatures: 16 Ω cm^2 at 700°C, 9.0 Ω cm^2 at 750°C and 4.8 Ω cm^2 at 800°C. The values reported are referred to Figure 6, above. When employing the methane gas mixture, the ASR is doubled, with a value of 9.6 Ω cm^2. The comparison between the spectra at 800°C for the cell (3wt%) tested in H_2 and in CH_4/O_2 are reported in Figure 6, below. In addition to the resistance, also the ordinate values of the spectra consistently increase, from 1.3 Ω to 4.8 Ω, denoting a larger capacitance of the electrodes. The curves at high frequencies, though, are not relevantly different in shape, but they both appear as almost overlapped by the arches at medium frequencies, the ones displaying the largest increase in real and complex impedance values. The same trend is repeated also for all the symmetric cells whose anodes were infiltrated with larger percentages of CeO_2, meaning that working in

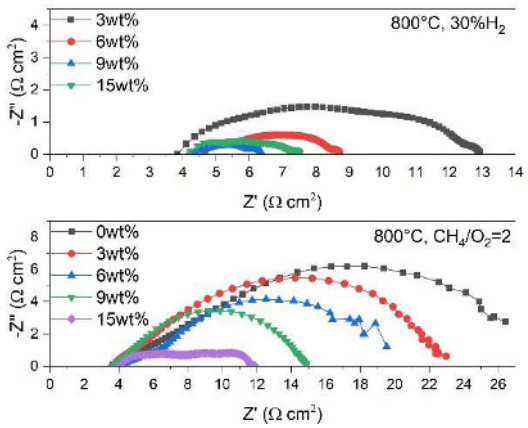

Figure 7: Above: comparison of the EIS spectra for the 3wt%, 6wt%, 9wt% and 15wt% infiltrated symmetric cell at 800°C in H_2. Below: comparison of the EIS spectra for the 0wt%, 3wt%, 6wt%, 9wt% and 15wt% infiltrated symmetric cell at 800°C in in the CH_4/O_2=2 gas mixture.

methane, for these cells, make the resistance double and the capacitance to grow larger as well. This behaviour is the exact opposite of that observed for the non-infiltrated cell in Figure 5. The reasons for this effect are unclear, but undeniably, the CeO_2 infiltration has an effect over this. Several hypotheses can be drawn on the matter, but the most convincing one is that CeO_2 strongly influences the oxidation process, taking methane to full oxidation and leaving the electrodes free from carbon; in doing so, the impedance spectra show the resistance of the electrode itself, which is expected to be higher at low frequencies because partial reforming and full oxidation of methane are more complex processes than hydrogen oxidation and because of a more size hindered transport of the gases inside the electrodes, while the cell without infiltration is not as-efficient in oxidizing methane, comporting a thin carbon layer to grow on top of the anodic material [34], which is thin enough to boost conduction. In fact, all HF and MF points in the EIS plots are found at smaller values and all high frequencies are denser for the non-infiltrated cell, while this does not happen for the infiltrated ones, where the HF semi-circles are almost superimposed (in position and density).

The cells with increased infiltration amounts, in EIS spectra measured at the three different temperatures in hydrogen, all follow the same trend observed for those with a 3wt% infiltrated CeO_2 infiltration, with a great reduction of both the visible semi-circle, especially the HF one. For this reason, they are not reported. All cells with different infiltration amounts tested in hydrogen at 800°C are reported and compared in Figure 7, above. The cell without infiltration, with an ASR of 40 Ω cm^2, had a resistance that was too high compared to the other ones, so it is not reported in the graph. In Figure 7, below, the same cells, plus the non-infiltrated one, are compared for measurements carried out at 800°C employing the CH_4/O_2 gas mixture. The signal for the cells in the new environment inside the chamber takes a while before it become stable, still, some of the cells went through a quick degradation of the electrodes. To balance these boundaries, all measurements reported are acquired after about 20 minutes after the introduction of the methane gas mixture.

Table 1: ASR values obtained for the cells with increasing infiltrations, both in H_2 and in CH_4/O_2=2.

CeO_2 infiltration	ASR in H_2 (Ω cm^2)	ASR in CH_4/O_2=2 (Ω cm^2)
0wt%	40	11
3wt%	4.5	9.7
6wt%	2.1	7.7
9wt%	1.1	5.6
15wt%	1.7	3.9

The ASR values observed for the different cells at 800°C, both in hydrogen and in methane, are reported in Table 1. For the cells tested in hydrogen, the resistance is constantly lowered until the 9wt% infiltrated cell, suggesting that the infiltration process helped the material to work more efficiently. Yet the 15wt% infiltrated displays a higher resistance than the 9wt% one in hydrogen. A difference that is not observed in methane, where the 15wt% one has the lowest resistance observed. This cell, it is assumed, received too much infiltration for the porosity that can be achieved with this preparation route, and the CeO_2 nanoparticles managed to reduce the TPB density in the anode, driving the efficiency lower. Indeed, both the HF and the MF semi-circles grow, meaning that both the charge transfer and the gas permeability in the material are negatively affected. In methane, on the other hand, the advantages of having CeO_2 to help methane oxidation is much more important than the reduced TPB density, as the consistent reduction of the spectrum size in CH_4/O_2 suggests. After the infiltration process in some of the 15wt% infiltrated cells, it was possible to see a faint white halo above the anode, probably due to a portion of CeO_2 that did not menage to enter inside the porosities and remained on top of the anode. If this is the case, infiltrations should only be used for highly porous materials or for lower amounts of CeO_2, otherwise, different preparation processes are recommended.

The EIS spectra in Figure 7, show that the infiltration process was successful in decreasing the resistance of the electrodes in a methane/oxygen mixture, which translates in a better performance of the material due to an increased efficiency of the physical and chemical processes involved during the employment of a SOFC with these conditions. Also, when comparing the 0wt% infiltrated cell to the others, despite the different behaviour in methane/oxygen previously discussed, its resistance turns out to be higher than those for infiltrated cells.

Despite the promising results of these tests, the ASR could still be reduced and since the MF semi-circles appear to be large enough to hide the HF and LF ones, the cells could be improved with a better control over porosity to allow a better permeation of the gas through the material.

3.2 Complete cells

Some tests were carried out on complete cells to test their performance. Successful tests include three cells with

anodes infiltrated with 0wt%, 6wt% and 9wt% CeO_2. These tests were carried out with the intent to make a comparison in stability and efficiency between the different cells. As for symmetric cells, despite the working conditions and preparation process were kept the same for every cell (except for the infiltration amount), the reproducibility of the process is limited, and different parameters may change. However, the results are representative of the cells behaviour and may give several insights. The tests on complete cells followed the following steps. The cell with an unreduced anode is brought directly from room temperature to 800°C with a ramp of 2°C/min with a variable dwelling of at least 2 hours. For these cells, the degradation was very quick and, despite other data were retrieved for lower temperatures, cannot be considered reliable to a critical loss in OCP after treatment at 800°C, indicating a substantial modification of the cells that can't be described a priori, despite different processes may occur [35]. Another important effect to consider is that the LSCF-based cathode had been in contact with a reducing atmosphere for several hours. Even though the cathode, as previously explained, should quickly recover from any minor reduction, the measurements required several minutes before they could be carried out. Meanwhile, the OCP variation was a good indicator of the materials condition. Up to 800°C, the flow was set to 100 sccm with a composition of 30% hydrogen and 70% argon. At 800°C, after the EIS measurements in hydrogen, the gas was switched to 100 sccm of the same methane/oxygen gas mixture previously used for symmetric cell tests. The Electrochemical Impedance Spectroscopy (EIS) measurements, as in the previous case, were obtained in a frequency range of 10^6 Hz to 10^{-2} Hz with 20 mV AC amplitude. After testing the cells in H_2 at 800°C, the OCP was measured, and the methane/oxygen gas mixture was introduced to keep track of its growth and the signal stability. After that, an alternation on EIS and Linear Sweep Voltammetry (LSV) measurements occurred until deactivation, after which only EIS measurements were made.

The complete cell without infiltration (0wt%) displayed the same behaviour observed for the symmetric cell counterpart, with a consistent reduction in resistance in switching from hydrogen to the methane/oxygen mixture. A comparison of the behaviour in the two atmospheres is reported in Figure 8, above. The cell at 800°C in hydrogen displayed an ASR of 30 Ω cm^2, while it was of 8.7 Ω cm^2 in CH_4/O_2. In the methane mixture, the cell appeared very stable, displaying a maximum observed ASR of 10 Ω cm^2 after 2 hours in this gas mixture, however, the performance dropped down in the same time range. In Figure 9, it is reported the OCP growth observed for this cell, with the CH_4/O_2 mixture being employed within the first minute. After a sharp growth, the signal proved itself unstable, with wide oscillations for some minutes, eventually stabilizing within a range of about 20 mV around 500 mV. After about 25 minutes, an OCP of 478 mV was observed, with a power of 3.7 mW cm^{-2}. After about 40 minutes the OCV peaked at 614 mV delivering a power of 6.7 mW cm^{-2}, then went back to the previous values, after about 55 minutes, with 473 mV OCP and 3.6 mW cm^{-2} in power, and

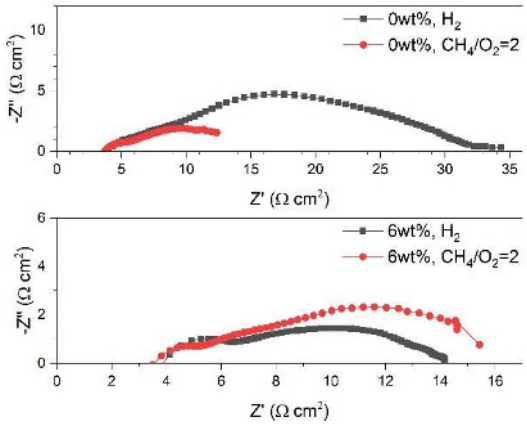

Figure 8: Above: comparison of the EIS spectra for the 0wt% infiltrated complete cell tested in H_2 and CH_4/O_2=2 at 800°C. Below: comparison of the EIS spectra for the 6wt% infiltrated complete cell tested in H_2 and CH_4/O_2=2 at 800°C. The 9wt% infiltrated complete cell, in the same conditions display the same behaviour shown by the 6wt%, except for the quantitative values.

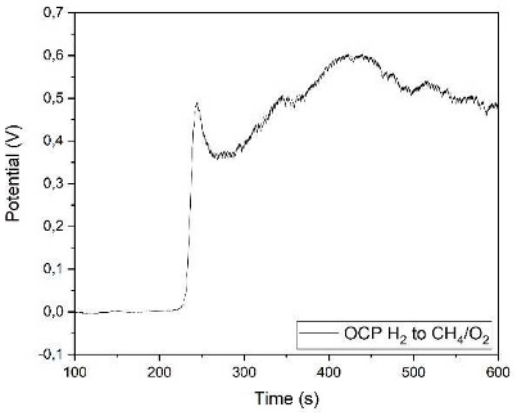

Figure 9: Rising and stabilization of the 0wt% infiltrated complete cell OCP after introducing the CH_4/O_2=2 gas mixture into the chamber.

eventually decreased to 398 mV and 2.4 mW cm^{-2} after about 2 hours.

The complete cell with a 6wt% CeO_2 infiltration at the anode was the most unstable of the complete ones. The ASR at 800°C in H_2 was 10 Ω cm^2, higher than the value obtained for the non-infiltrated cell, then it rose to 12 Ω cm^2 after about 30 minutes in CH_4/O_2, showing again a behaviour with the gas switch that is the opposite of that observed for the 0wt% complete cell. These results are shown in Figure 8, below, and can be compared to the results for the 0wt% cell in the graph above. After a couple of hours, the ASR increased up to 20 Ω cm^2, almost doubling the initial resistance. The OCP was very unstable, with oscillations up to 30 mV after about 10 minutes in CH_4/O_2. After 30 minutes of methane gas mixture flowing in the chamber, an LSV measurement showed an OCP of 610 mV and a power of 5.6 mW cm^{-2}. The OCP and the power quickly decreased and after about 70 minutes it reached 435 mV in OCP and 3.0 mW cm^{-2} in power. Eventually, after a couple of hours the OCP dropped below 200 mV. A test was carried out to attempt a re-activation

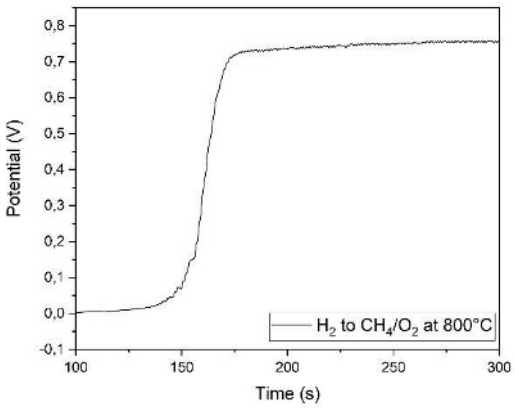

Figure 10: Rising and stabilization of the 9wt% infiltrated complete cell OCP after introducing the CH_4/O_2=2 gas mixture into the chamber.

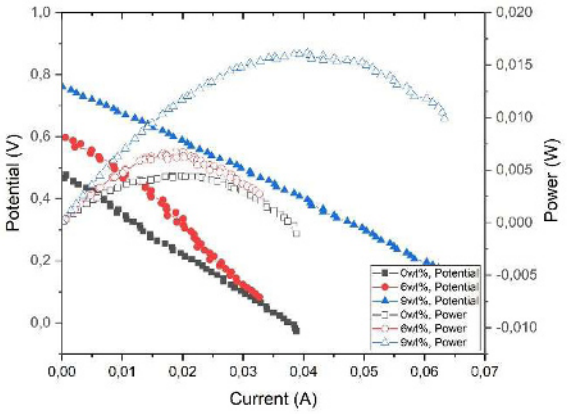

Figure 11: LSV and power obtained after about 20-25 minutes from the employment of the CH_4/O_2=2 gas mixture for the 0wt%, 6wt% and 9wt% complete cells. A correlation between increasing OCP and power with the increasing amount of infiltration can be observed.

of the material in hydrogen, but after the CH_4/O_2 mixture was re-introduced, it did not manage to make the OCP increase again, as is remained below the 100 mV.
The complete cell with an anode infiltration of 9wt% CeO_2 managed to deliver the highest power of the three cells. At 800°C in H_2 the cell displayed an ASR of 2.9 Ω cm^2 that rose to 4.3 Ω cm^2 after the CH_4/O_2 mixture was employed. These values are low compared to the previous ones for complete cells, yet the EIS measurement in methane had an unstable signal. The instrument was unable to retrieve meaningful data around frequencies of 5 Hz, with the beginning of the LF range. So, the last point following the trend was chosen as limit for determining the ASR. Despite the instability of EIS spectra at LF, the OCP measured with the transition between the two gas mixtures was the most stable with oscillations below 10 mV, as shown in Figure 10. After 20 minutes stabilization, LSV measurements determined an OCP of 766 mV and a power of 13.3 mW cm^{-2}. The cell was stable enough to avoid a constant drop in performance, despite temporary losses, and reaching the highest values of OCP and power of 776 mV and 14 mW cm^{-2}. Eventually, after a couple of hours, the cell abruptly broke, delivering meaningless values.
In comparing the results for the different complete cells, it is chosen to look at the results obtained after about 20-25 minutes after switching to the methane/oxygen gas mixture, neglecting the best performances obtained, being transient phenomena, and considering the quick degradation that the cells face, especially the 6wt% one. With these considerations, in Figure 11, it is seen the correlation between an increased performance and an increasing amount of infiltrated CeO_2 into Ni-YSZ cermet anodes. For more consistent results, further tests with other infiltration percentages should be carried out.
An issue that occurred for all cells used in a methane/oxygen mixture at 800°C was a quick degradation of the cells. The problem is supposed being due to surface segregation of anodic Ni on top of the gold paste employed. This hypothesis is confirmed by X-ray Photoelectron Spectroscopy (XPS) measurements, where on top of the cell, where nothing but gold should be seen, almost no gold was found and nickel is present, while above the scratched surface, the spectra revealed the absence of nickel and presence of gold, with the patterns being the same as those obtained on the gold paste that was not deposited in contact with the anode. However, the results of these tests are not reported since this work does not discuss on the current collector properties.

Conclusions

The correlation between performance and increasing CeO_2 infiltration amounts in Ni-YSZ anodes in SC-SOFCs was tested. In symmetric cells, low percentage infiltration amounts drastically decreased the resistance of the electrodes in H_2, with best results for the 9wt% cell. Increasing infiltration induced a continuous improvement in CH_4/O_2=2, with best results for the 15wt% cell, with a reduction of EIS spectra semi-circles both at HF and MF. Complete cells confirmed the observations on symmetric cells, with increased performance for higher infiltrations, both in OCP and power, despite transient instabilities in performance. EIS tests were not as clarifying, even though they were not against the trend observed for symmetric cells. However, measurements on complete cells were not comprehensive of the whole infiltration range tested for symmetric cells and results should be confirmed.

Acknowledgements

The authors thank the Veneto region for financial support of this study in the frame of the “POR FSE 2014-2020” project.

References

[1] A. Hagen, A.C. Wulff, P. Zielke, X. Sun, B. Talic, I. Ritucci, H.L. Frandsen, S.H. Jensen, W.R. Kiebach, P. V. Hendriksen, Int. J. Hydrogen Energy **45** (2020) 29201–29211.
[2] M. Kuhn, T.W. Napporn, Energies **3** (2010) 57–134.
[3] M. Yano, A. Tomita, M. Sano, T. Hibino, Solid State Ionics **177** (2007) 3351–3359.

[4] I. Riess, J. Power Sources 175 (2008) 325–337.
[5] Y. Hao, D.G. Goodwin, J. Power Sources **183** (2008) 157–163.
[6] M. Kamvar, M. Ghassemi, R. Steinberger-Wilckens, Int. J. Hydrogen Energy **45** (2020) 7077–7087.
[7] Z. Shao, S.M. Haile, J. Ahn, P.D. Ronney, Z. Zhan, S.A. Barnett, Nature **435** (2005) 795–798.
[8] B. Morel, Ŕ. Roberge, S. Savoie, T.W. Napporn, M. Meunier, Electrochem. Solid-State Lett. **10** (2007) 2006–2008.
[9] L.N. Van Rij, J. Le, R.C. Van Landschoot, J. Schoonman, J. Mater. Sci. **36** (2001) 1069–1076.
[10] M. Yano, M. Nagao, K. Okamoto, A. Tomita, Y. Uchiyama, N. Uchiyama, T. Hibino, Electrochem. Solid-State Lett. **11** (2008) 29–33.
[11] Y. Lu, Y. Liu, S. Shen, J. Catal. **177** (1998) 386–388.
[12] C. Zhang, Y. Lin, R. Ran, Z. Shao, Int. J. Hydrogen Energy **35** (2010) 8171–8176.
[13] Z. Jiao, N. Shikazono, N. Kasagi, J. Electrochem. Soc. **159** (2012) B285–B291.
[14] B. Morel, R. Roberge, S. Savoie, T.W. Napporn, M. Meunier, J. Power Sources **186** (2009) 89–95.
[15] T. Hibino, A. Hashimoto, M. Yano, M. Suzuki, S. Yoshida, M. Sano, J. Electrochem. Soc. **149** (2002) A133.
[16] M.D. Cabezas, D.G. Lamas, M.G. Bellino, R.O. Fuentes, N.E. Walsöe De Reca, S.A. Larrondo, Electrochem. Solid-State Lett. **12** (2009) 35–38.
[17] C. Zhang, L. Sun, R. Ran, Z. Shao, Electrochem. Commun. **11** (2009) 1563–1566.
[18] A. Trovarelli, Catal. Rev. **38** (2006) 439–520.
[19] H. Takahashi, T. Takeguchi, N. Yamamoto, W. Ueda, Solid State Ionics **185** (2011) 52–57.
[20] G. Yang, C. Su, W. Wang, R. Ran, M.O. Tadé, Z. Shao, J. Power Sources **264** (2014) 220–228.
[21] Z. Wang, Z. Lü, B. Wei, K. Chen, X. Huang, W. Pan, W. Su, Electrochim. Acta **56** (2011) 6688–6695.
[22] D. Rembelski, J.P. Viricelle, L. Combemale, M. Rieu, Fuel Cells **12** (2012) 256–264.
[23] A. Atkinson, A. Selçuk, Acta Mater. **47** (1999) 867–874.
[24] S.Y. Park, J.H. Ahn, C.W. Jeong, C.W. Na, R.H. Song, J.H. Lee, Int. J. Hydrogen Energy **39** (2014) 12894–12903.
[25] A. Chen, J.R. Smith, K.L. Duncan, R.T. DeHoff, K.S. Jones, E.D. Wachsman, J. Electrochem. Soc. **157** (2010) B1624.
[26] S. Elangovan, J.J. Hartvigsen, L.J. Frost, Int. J. Appl. Ceram. Technol. **4** (2007) 109–118.
[27] H. Mori, C.J. Wen, J. Otomo, K. Eguchi, H. Takahashi, Appl. Catal. A Gen. **245** (2003) 79–85.
[28] A.P. Jamale, C.H. Bhosale, L.D. Jadhav, J. Alloys Compd. **623** (2015) 136–139.
[29] L.F. Liotta, F. Puleo, V. LaParola, S.G. Leonardi, N. Donato, D. Aloisio, G. Neri, Electroanalysis **27** (2015) 684–692.
[30] A. Faes, A. Hessler-Wyser, A. Zryd, J. Van Herle, Membranes (Basel). **2** (2012) 585–664.
[31] S. Gewies, W.G. Bessler, J. Electrochem. Soc. **155** (2008) B937.
[32] B. Song, E. Ruiz-Trejo, A. Bertei, N.P. Brandon, J. Power Sources **374** (2018) 61–68.
[33] A. Bertei, E. Ruiz-Trejo, F. Tariq, V. Yufit, A. Atkinson, N.P. Brandon, Int. J. Hydrogen Energy **41** (2016) 22381–22393.
[34] A. Lanzini, P. Leone, C. Guerra, F. Smeacetto, N.P. Brandon, M. Santarelli, Chem. Eng. J. **220** (2013) 254–263.
[35] X. Jacques-Bédard, T.W. Napporn, R. Roberge, M. Meunier, J. Power Sources **153** (2006) 108–113.

Graphite/epoxy composite for building Bipolar Plates

Luca Spinelli[1,*], *Fabrizio* Roncaglia[1,*], *Roberto* Biagi[2,3], *Alessandro* di Bona[3], *Marcello* Romagnoli[4],and *Adele* Mucci[1]

[1]Dipartimento di Scienze Chimiche e Geologiche, Università di Modena e Reggio Emilia, 41125 Modena, Italy
[2]Dipartimento di Scienze Fisiche, Informatiche e Matematiche, Università di Modena e Reggio Emilia, 41125 Modena, Italy
[3]CNR - Istituto Nanoscienze - Centro S3, 41125 Modena, Italy
[4]Dipartimento di Ingegneria "Enzo Ferrari", 41125 Modena, Italy

Abstract. Bipolar plates (BPs) are important components of Proton Exchange Membrane Fuel Cells (PEMFC). Graphite-epoxy composites, having a better corrosion resistance than metal-based BPs and better mechanical properties than graphite BPs, are a promising alternative. In this study, we tried to develop graphite-epoxy composites meeting the technical US DOE targets for 2020, with a proper choice of manufacturing conditions that ensure a good compromise between conductivity, flexural strength, and gas permeability. In particular, we studied the influence of the filler to binder ratio, changed the molding temperature and time, and investigated the effects of increasing pressure both on in-plane conductivity and on helium permeability. We found that both formulation and molding pressure are crucial in determining the permeability of the graphite-epoxy composites, whereas molding temperature and time seem to play a minor role.

1 Introduction

Hydrogen powered electric vehicles rely mainly on Proton Exchange Membrane Fuel Cells (PEMFC) that are reaching the commercialization phase. Bipolar plates (BPs) are important components of PEMFC where they distribute the gases (hydrogen and oxygen or air) uniformly, support the membrane electrode assemblies, collect and conduct electric current, connect the stacks, allow proper water management, remove heat and sustain the clamp pressure [1].

Graphite-based BPs can be used in place of the metal-based ones but suffer from inherent brittleness, while graphite-epoxy composites, combining a better corrosion resistance than metals and better mechanical properties than graphite, are emerging as promising alternative materials for BPs [1]. In our effort to develop graphite-epoxy composites meeting the US DOE technical targets for 2020 [2], we are searching for an optimal compromise between conductivity, flexural strength, and gas permeability. To this end, we are looking for synergistic combinations in the preparation phases (i.e., composite formulation, mixing, molding).

We already proved the evident advantages coming from wet mixing compared to the dry one [3]. In this work, the search spanned over different resin to filler ratios, and higher molding temperature and pressure. We found that the molding pressure and composition play a crucial role in determining the gas permeability of the formed BP, whereas in-plane conductivity (IPC) can be maintained at values well above the DOE targets.

2 Materials and methods

2.1 Composite discs fabrication

2.1.1 Materials

Diglycidylether of bisphenol A (DGEBA) resin D.E.R. 311® (187 g/eq) was from Dow Chemicals; isophoronediamine (IPDA) was from Merck; GraphCOND® 45/98 X, D50 75 µm, 98% carbon (G45) was from LUH (www.luh.de); GraphTERM® 23/99.9, D50 18-25 µm, 99,9% carbon (G23) was from LUH; carbon black (CB) PBX 51, D50 17 µm, was from Cabot.

2.1.2 Mixing

A 100 mL screw cap container was equipped with a mechanic stirrer using a three-blade propeller. Carbon black PBX51 (0.249 g), G23 (0.679 g) and G45 (3.322 g) and dichloromethane (40 mL) were introduced, and the solution was stirred at 360 rpm for 15 min. Then DGEBA epoxy resin (0.612 g, dissolved in 2 mL of dichloromethane) was added under stirring. Ten minutes later, IPDA (0.138 g, dissolved in 2 mL of dichloromethane) was slowly dropped while maintaining the mixing. The mixture was further stirred for 5 min. The solvent was removed by means of a rotary vacuum evaporator and 1.00 g of the obtained powder was transferred in the mold and pressed as described below. This amount permits to prepare 4 replicates.

* Corresponding author: luca.spinelli@unimore.it;fabrizio.roncaglia@unimore.it

2.1.3 Molding

Each dried powder sample (1.00 g) was pressed by means of a custom-made pressing machine (Graf S.p.A.) [3], The machine's mold (2 cm id) can operate between room temperature and 160 °C, and with an applied force up to 96 kN (corresponding to a maximum of 306 MPa). Temperature, pressure, and time were managed and recorded by a custom-made software (Labview® based) via an interfaced PC. The obtained discs were post-cured in oven (60 °C) for 2 days.

2.2 In-plane conductivity (IPC) measurements

IPC was measured by means of a digital source meter (Keithley 2400) equipped with a four-point probe, as described [3]. Each sample was produced in four replicates and probed in eight different points, four per side. IPC (S cm^{-1}) was obtained using equation (1) by correcting the measured resistivity ρ (Ω cm), accordingly to the geometry of the sample [4].

$$IPC = \frac{1}{\rho} \quad where \quad \rho = \frac{\pi}{ln\,2} \cdot F\left(\frac{t}{s}\right) \cdot \frac{V}{I} \cdot t \qquad (1)$$

where t is the sample thickness (cm), s is the distance between two probe contacts (cm), V is the measured voltage (mV), I is the measured current (mA) and F(t/s) is the correction factor tabulated by F.M. Smits [4].

2.3 Permeation coefficient (HP) measurements

Different studies use hydrogen to obtain the gas permeability of BP. Supported by its lower kinetic diameter [5], we opted to utilize helium instead of hydrogen at this stage, since it allows safer and simpler handling conditions.

The permeation coefficient (HP), defined as in ref. [6], was measured by means of a helium leak detector (BALZER HLT-150) equipped with a customized sample holder (schematic is shown in Figure 1). The detector works in high vacuum and is able to provide a quantitative measure of the helium flux. The sample is placed between two chambers: the first one connected to the detector and the second one attached to a line switched either to an external vacuum pump or to a helium bottle. Each sample was produced in four replicates and each one was tested.

The measurement procedure is described below: the sample is placed in the sample holder within two O-rings to guarantee the gas-tight closure. The area of the surface exposed to helium is kept always the same for all samples. The sample holder is then placed between the two chambers and the enclosure secured with an external mechanical lock. The detector was then switched to READ mode, it evacuates the second chamber and starts measuring the helium flux. At the same time, also the external vacuum pump is activated for evacuating the first chamber. When the detector reading stabilizes at the background value (about $2*10^{-9}$ sccm s^{-1}) the first chamber was switched to the helium bottle and filled at 1 atm. After some seconds needed to stabilize the reading, the helium flux is acquired.

HP was calculated according to equation (2), where the helium leak detector response is Ans, the flow of helium detected expressed in sccm s^{-1}; the exposed area of the sample (determined by the O-ring id) is A (1.539 cm^2); the atmospheric pressure of helium in the corresponding chamber is P (101325 Pa).

$$HP\ [sccm\ (s^{-1}cm^{-2}Pa^{-1})] = \frac{Ans}{A \cdot P} \qquad (2)$$

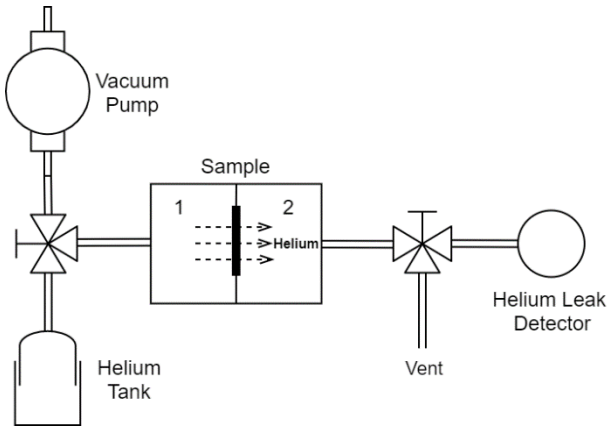

Fig. 1. Schematic of the helium leak detector and customized system to record permeation coefficient.

2.4 Scanning electron microscopy (SEM)

The surface morphology of the bipolar plates was investigated by a JEOL JSM-6010LA InTouchScope, using a back-scattered electron detector (BSED).

3 Results and discussion

In this work we mainly investigated the role played by composition and pressure used in the molding process on IPC and HP of graphite-epoxy composites for BPs. We started from a formulation with a filler to binder ratio of 91/9 (referred to as C0 in Table 1), molded at 80 °C and 30 MPa for 2 h, very similar to that developed in a previous study [3] and that guarantees both good conductivity (> 160 S cm^{-1}) and flexural strength (nearly 50 MPa).

Table 1. Composition (percent by weight) of the composites used in the present study.

	C0 (% wt)	C1 (% wt)	C2 (% wt)
G45	89.3	85	66.4
CB	1.7	1.7	5.0
DGEBA	7.3	12.4	12.2
IPDA	1.7	3	2.8
G23	-	-	13.6

Nevertheless, when we were able to measure the HP of discs of this composition, it resulted unacceptably high. Some tests on C0 samples, produced at increasing pressures, gave their best HP in the range 80-145 MPa, with a minimum value around 10^{-11} sccm (s^{-1} cm^{-2} Pa^{-1}) (the US DOE target for 2020 is 1.3 * 10^{-14} sccm (s^{-1} cm^{-2} Pa^{-1}) [2].

SEM micrographs, obtained with back-scattered electrons, showed that cracks were present around the graphite flakes (Figure 2). In addition, we did not observe an optimal reproducibility in conductivity performances.

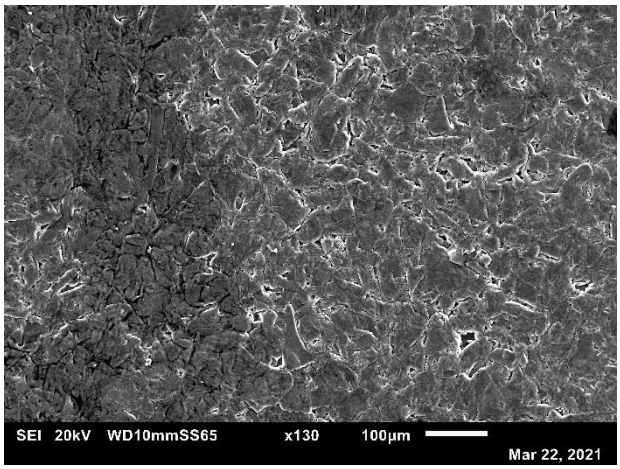

Fig. 2. SEM micrograph of a disc of composition C0 obtained at 26 MPa.

This scarce reproducibility was attributed mainly to the time elapsing between composite preparation and molding, that was then reduced shortening the molding time and enhancing the molding temperature. Shorter time and higher temperature and pressure are also closer to the usual industrial fabrication conditions for this class of materials and increase the production rate. To test both the effect of these different molding conditions and of a higher binder content, some tests were carried out on samples with a 15% of epoxy resin (composition C1, Table 1), at 150 °C and 160 MPa for 5-10 min obtaining IPC of 160-180 S cm^{-1}, very similar to that of discs of C0 or similar composition [3]. HP was found around 10^{-14} sccm (s^{-1} cm^{-2} Pa^{-1}), improving of three orders of magnitude. At this stage, no evidence of detrimental effects on IPC and mechanical properties were observed by increasing molding temperature and pressure and decreasing molding time.

Then, we enhanced the carbon black content (to 5%) to reduce the costs, introduced a secondary filler (G23), thinner, cheaper than the primary one (G45) and optimized for thermal conductivity, in the view of future studies on thermal conductivity and of industrial applications. After further tests, we decided to work at t = 5 min, T= 150 °C, P < 200 MPa and 13.6% of G23 (composition C2, Table 1). This change in formulation did not improve IPC or HP but improved the preparation, because it allowed the reduction of about 30 % of the amount of solvent required to obtain a proper dispersion while mixing. We focussed then on the effects of increasing pressure on IPC and HP on samples with this last composition (C2). We observed that with the new setup IPC is almost independent from pressure (Figure 3), except at the lowest values (< 60 MPa). A narrow IPC range is observed at P > 60 MPa (170 ± 4 S cm^{-1}), meaning that the integrity of the conductive network is well maintained in a broad range of pressure. Interestingly, IPC shows a linear correlation with density (R^2 = 0.97, Figure 4) and, as expected, a higher density results in a more efficient conducting network.

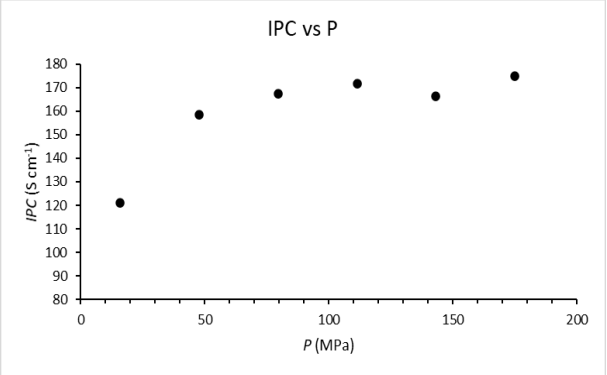

Fig. 3. IPC of discs of composition C2 obtained at increasing molding pressures.

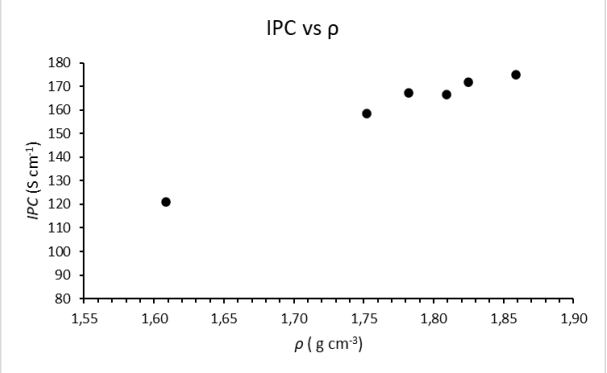

Fig. 4. IPC of discs of composition C2 vs density (ρ).

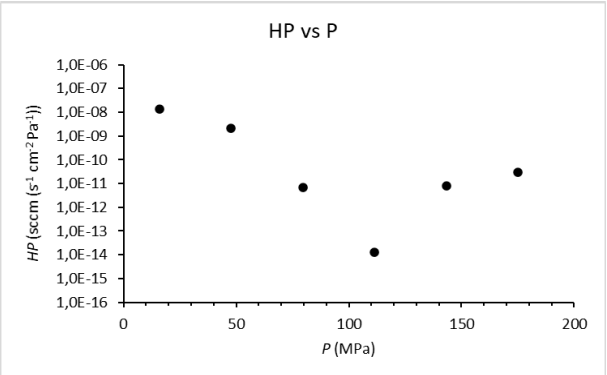

Fig. 5. Helium permeability (HP, logarithmic scale) of discs of composition C2 obtained at increasing molding pressures.

At a 15 % of binder and with 5% of carbon black and 13.6 % of G23 (C2) the HP of the discs had still a huge decrease of 1-3 orders of magnitude (Figure 5) with respect to that of samples of composition C0, reaching values close to the permeability targets [2]. These results

show that good permeability is obtainable at intermediate pressure. The best result was obtained at 111 MPa where the permeability reaches values around $1.2*10^{-14}$ sccm (s^{-1} cm^{-2} Pa^{-1}). Nevertheless, the fluctuations of HP observed for similar pressure values, indicates that there is still room for improvement of the standardization of the whole fabrication/testing process.

4 Conclusions

High electric conductivity and low gas permeability are among the most important characteristics required to BPs to be used in PEMFC, together with good mechanical performances. In this study, we showed that a moderate increase in the epoxy resin content, the use of mixtures of properly chosen fillers and of appropriate pressure hugely improves the permeability of the composite, several orders of magnitude, while maintaining IPC values well above US DOE targets (> 100 S cm^{-1}). This is probably due to the fact that amounts of resin too small are not able to wet properly the graphite flakes, leaving void paths that permit gas diffusion, whereas addition of a filler with a low granulometry helps in better distributing the binder. Molding pressures in the range 110 -160 MPa and epoxy resin around 15% seem to be appropriate to obtain low gas permeability. Carbon black amounts up to 5% are compatible with low HP and good IPC values. In addition, short cycle production conditions (high temperatures and short times) seem not to influence significantly neither IPC nor HP. Further optimization of the formulation and fabrication process are in progress to improve the reproducibility of the properties of the graphite-epoxy resin composites.

Acknowledgments

The authors are thankful to Fondazione Cassa di Risparmio di Modena for funding the CARCOM project (grant LINEAFCRM2019FARINTERDMUCCI).

References

1. N. Saadat, H.N. Dhakal, J. Tjong, S. Jaffer, W. Yang, M. Sain, Renew. Sustain. Energy Rev. **138**, 110535, (2021)
2. Hydrogen and Fuel Cell Technologies Office, Electrolyte Membrane Fuel Cell Components, https://www.energy.gov/eere/fuelcells/doe-technical-targets-polymer-electrolyte-membrane-fuel-cell-components
3. F. Roncaglia, M. Romagnoli, S. Incudini, E. Santini, M. Imperato, L. Spinelli, A. di Bona, R. Biagi, A. Mucci, Int. J. Hydrogen Energy, **46**, 4407, (2021)
4. F.M. Smits. Bell Syst. Tech. J. **37**, 711 (1958)
5. S. Matteucci, Y. Yampolskii, B.D. Freeman, I. Piannau, *Transport of Gases and Vapors in Glassy and Rubbery Polymers* chapter **1** (John Wiley & Sond, Ltd, Eds: Y. Yampolskii, B.D. Freeman, I. Piannau, 2006)
6. R. Blunk, F. Zhong, J. Owens, Journal of Power Sources, **159**, 533 (2006)

Degradation of Ni-YSZ and Ni-GDC fuel cells after 1000 h operation: Analysis of different overpotential contributions according to electrochemical and microstructural characterization

Aiswarya Krishnakumar Padinjarethil[1], *Fiammetta Rita* Bianchi[2,*], *Barbara* Bosio[2], and *Anke* Hagen[1]

[1] Department of Energy Conversion and Storage, Technical University of Denmark, Building 310, Fysikvej, DK-2800 Lyngby, Denmark
[2] DICCA, University of Genoa, Via Opera Pia 15b, 16145 Genoa, Italy

Abstract. Solid Oxide Fuel Cell (SOFC) technologies are emerging as potential power generation units with limited environmental impacts. However, the main challenges towards large scale commercial applications are high costs and low lifetime compared to currently used technologies. The present study aims at understanding degradation mechanisms in SOFCs through both experimental and modelling approaches. For this purpose, two state of the art fuel cell configurations based on Ni cermet fuel electrode (either YSZ-Yttrium Stabilised Zirconia or GDC-Gadolinium Doped Ceria), YSZ electrolyte and LSCF (Lanthanum Strontium Cobalt Ferrite oxide) air electrode were chosen. The cells were tested for 1000 hours with H_2 rich mixture as fuel feed and air as oxidant. Cells were characterised at several H_2/H_2O ratios and temperatures with air or oxygen fed to the air electrode using different techniques. These allowed the identification of kinetic parameters to be implemented in an in-house 2D Fortran based model. The model was able to successfully simulate global cell behaviour as a function of local features, and it was validated with experimental I-V curves recorded prior and post durability operation. Moreover, post-mortem microstructure characterisation was also performed to fine-tune the model towards a more accurate prediction of the degradation influence on cell performance.

1. Introduction

Solid Oxide Fuel Cells (SOFCs) are promising energy conversion devices suited for future energy scenarios. Indeed, SOFCs provide a high electrical efficiency of about 60% with minimum greenhouse gas emissions from a range of possible fuels [1]. To ensure longer operating times of more than 60,000 hours as required target for the commercialization of this technology, there is a need to understand the fundamental degradation mechanisms [2]. It is known that SOFC performance strongly depends on the cell microstructure and its changes under different operation conditions. Past studies have identified several degradation mechanisms associated with the long-term stability of SOFCs under a wide range of operating conditions in terms of temperature, gas composition, fuel utilization etc [3]. These studies have indicated that the most significant changes occur at the fuel electrode in case of the conventional Ni based SOFCs. Indeed, Ni shows a high mobility between 650-950 ˚C, resulting in (i) Ni particle coarsening or agglomeration [4-6], (ii) Ni migration from the active reaction zone close to electrode-electrolyte interface [7-9].

For instance, in Ni-YSZ based fuel electrodes Simwonis et al. [4] showed a decrease of electrical conductivity of 33% over 4000 h operated under 4%mol H_2 and 3%mol H_2O in Argon at 1000 ˚C. This loss was correlated to the reduced number of Ni active particles due to its migration accompanied with agglomeration; here the decrease of Triple Phase Boundary (TPB) length resulted in a worse electrochemical performance as well. Indeed, when the volume fraction of the ionic or electronic phases is below the percolation threshold of 20-35%, a drastic reduction in the TPB length is expected [10]. Hagen et al. [11] also observed changes in the Ni particle diameter and a broader distribution of particle sizes under current densities above 0.75 Acm^{-2} at both 750 ˚C and 850 ˚C. In addition, local Ni depletion was noted at higher operating temperatures in humid conditions, which was attributed to the formation of volatile Ni hydroxide species. Several studies have shown the effect of overpotential on the Ni migration on Ni-YSZ cells. For instance, Hauch et al. [12] detected a significant Ni migration when the fuel electrode overpotentials were between 160 mV and 300 mV. Whereas Sun et al. [13] presented the post-mortem results on 4400 h electrolysis operated cells. In this case, both loss of Ni percolation and increased porosity were observed within the active electrode as consequences of imposed load. Another possible driving force for detected Ni mobility and agglomeration consists of the minimization of surface energy in view of the particle contact areas [14,15]. To validate this hypothesis, Faes et al. [15] studied the grain growth trend for both fine and coarse initial particle size distributions in the Ni cermet electrode. Fine Ni particle sizes resulted in a higher coarsening in the initial 240 h operation as compared to the coarse microstructure of the pristine fuel electrode; the maximum grain size was reached at close to 1000 h. This time profile was simulated using a ‘charging capacitor’ model that assumed the maximum Ni particle growth to be dependent on stable YSZ backbone influence. Monaco et al. [7] recently performed long-term operation tests on Ni-YSZ based cells aged in both fuel cell and electrolysis mode. The Ni particle growth within

* Corresponding author: fiammettarita.bianchi@edu.unige.it

the bulk of the electrode was attributed to local sintering processes due to Ni-YSZ interfacial adhesion gradient, whereas the local overpotential was proposed as the driving force for the Ni detachment and migration at the electrode/electrolyte interface.
Despite the desired target of more than 60,000 h, only few tests exceeding several 1000 hours have been performed in previous scientific literature. For instance, a recent work by Menzler et al. [16] tested a SOFC short stack for 100,000 h at 700 °C, 0.5 Acm^{-2} with humidified H_2 obtaining an overall degradation of 0.5 V% kh^{-1}. Looking at post-mortem analysis, Ni presence increased from 32% to 40% close to the electrolyte/electrode interface with a reduction in the porosity, differently from common reference observations. These uncertainties confirm the need of further studies to obtain a deeper knowledge of occurring mechanisms.
Similar Ni evolution effects were observed also in case of Ni-GDC based fuel electrodes. Holzer et al. [17] studied quantitatively the changes in Ni-GDC cermet under dry and humid conditions (until 40%mol of H_2O). In the first case a rapid reduction of the TPB length was noted due to Ni coarsening in the initial 200 h through Ostwald ripening mechanism [8,18]. At higher operating hours, from 1023 h to 2286 h, Ni volatilization was identified as the main cause for Ni cermet changes resulting in an increase of local Ni-GDC ratio. Whereas, in the humid case GDC formed a layer around the Ni particles which hindered the particle growth. Iwanschitz et al. [19] studied Ni coarsening effects as a function of reduction temperatures for Ni/GDC40 electrode composition, confirming the significant effect of high sintering temperatures on the Ni particle size. Aiming at the validation of cell long-term behaviour Zekri et al. [20] tested Ni-GDC based ESCs with operation times by 20,000 h observing Ni depletion up to 6-10 µm from the electrolyte. Further particle agglomeration effects were observed for both Ni as well as GDC particles throughout the electrode in turn, leading to a higher Ni agglomeration and increased porosity.
Only few studies have shown a direct comparison between the two considered Ni based cermets. For instance, Sciazko et al. [21] analysed Ni-YSZ and Ni-GDC electrode behaviour under both fuel cell and electrolysis operations. Although a better initial performance was observed for the GDC electrodes, Ni-YSZ was concluded to be more durable. Indeed, the YSZ stable backbone limited Ni coarsening effects [15,22]. Whereas the variation of GDC particles resulted in a thicker layer formation outside the reaction zone, which led to a thin more tortuous GDC layer close to the interface.

In this work, the authors aim at studying and comparing 1000 h operated solid oxide fuel cells based on both Ni-YSZ and Ni-GDC fuel electrodes at a fixed fuel feed of 96/4 mol/mol composition of H_2/H_2O and air as the oxidant. An in-situ evaluation of electrochemical performance through voltage measurements and EIS spectra was carried out. A detailed post-mortem analysis of fuel electrode side was also performed showing the main structural changes. These experimental outcomes formed the basis for the tuning of parameters requested into simulation tool. Indeed, a previously validated 2D model, SIMulation of Fuel Cells-SIMFC, was here improved by specifying some kinetic parameters as function of microstructural features to understand the direct correlation between the microstructure variation and the loss of electrochemical performance.

2. Experimental setup

The experimental data were recorded at Technical University of Denmark (DTU) on 4 cm x 4 cm planar commercial cells involving a Ni-YSZ based anode supported cell and a Ni-GDC based electrolyte supported cell. The detailed description of the test setup as well as the characterisation prior and post durability, by varying temperatures, reactant compositions and utilizations, are described elsewhere [23]. The cells were tested under H_2/H_2O molar ratio of 96/4 with air as the oxidant for 1000 hours, as per manufacturer protocols (Table 1). During the durability operation, the cells were characterised using Electrochemical Impedance Spectroscopy (EIS) at intervals of about 8 hours. In case of the ESCs, a N_2 flow was added in order to have the minimum total flows within the test setup. With the added N_2 flow, the effective p_{H2O} in ESC was reduced slightly to ~0.03 atm.

Table 1: Summary of test conditions for the long-term operation of both ASC and ESC configurations.

Parameters	**ASC**	**ESC**
H_2 flow [lh^{-1}]	19.2	9.6
H_2O flow [lh^{-1}]	0.8	0.4
Air flow [lh^{-1}]	140	140
H_2/H_2O ratio [mol/mol]	96/4	96/4
N_2 flow [lh^{-1}]	0	4.6
Total fuel flow rate [lh^{-1}]	20	14.6
Temperature [°C]	750	850
Current density [Acm^{-2}]	0.4	0.2
Fuel utilization [-]	~14%	~14%

Performance characterization both prior to, after and during durability test was derived by applying a suitable Equivalent Circuit Model (ECM) and Complex Nonlinear Least Squares (CNLS) fitting on recorded EIS spectra. The quantification of different resistances allowed for identification of kinetic parameter dependences on operation conditions. The proposed ECM consists of an inductance element in series with a single ohmic resistor for electrolyte performance and four sub-circuits built up with resistors and constant phase elements in parallel and a Gerischer element in series for behaviour of the electrode [24]. Post-mortem cell analysis was performed by Scanning Electron Microscopy (SEM) and Energy Dispersive X-Ray Analysis (EDS) techniques on a Zeiss Ultra. Secondary electron imaging (SE) was used at high accelerating voltages to study the surface feature changes,

while the percolation network was studied using low accelerating voltages < 1 keV through an in-lens detector. Computed particle sizes and volume fractions were also useful for modelling purposes.

3. Modelling

SOFC performance was simulated based on a 2D approach through SIMFC (SIMulation of Fuel Cells), an in-house developed Fortran code. Dividing the cell plane in an optimised number of sub-cells, the global behaviour derives from a local analysis of conservation equations resolved in each specific subdomain [25]. Here the cell voltage is evaluated through ad hoc formulated electrochemical kinetics and knowing the gradients of main physicochemical features, such as current density, gas composition and temperature, as well as microstructure parameters. Considering an isopotential system, the model assumes Fickian diffusion as the gas transport mechanism inside electrodes, a reaction rate following Butler-Volmer equation and a thermal activated process for the charge transfer. Here SOFC voltage V_{SOFC} results as summarised in Equation 1, then specifying Open Circuit Voltage (OCV), diffusion, activation and ohmic overpotential, η, formulations valid for both anodic and cathodic side in Equations 2, 3, 4 and 5, respectively [26].

$$V_{SOFC} = OCV - \eta_{diff} - \eta_{act} - \eta_{ohm} \quad (1)$$

$$OCV = (RT/zF) \ln [p_{H2,bulk} (p_{O2,bulk})^{0.5} / p_{H2O}] \quad (2)$$

$$\eta_{diff} = (RT/zF) \ln[\Pi (p_{i,bulk}/p_{i,TPB})^{2\alpha i}] \quad (3)$$

$$\eta_{act} = (2RT/zF) \sinh^{-1}(J/J_0) \quad (4)$$

$$\eta_{ohm} = R_{ohm} J = AT \exp(B/T)\, J \quad (5)$$

Where R is the ideal gas constant, T the temperature, z the charge number, p the gas partial pressure, J the current density, J_0 the exchange current density, R_{ohm} the ohmic resistance, A, B and α some kinetic parameters.
Starting from the previously validated approach at time equal to zero for a wide range of working points [23], the model was tuned to simulate the cell behaviour under long-term operation considering the main degradation mechanisms that could penalise the obtainable power. For this purpose, the kinetic parameters obtained from EIS deconvolutions before and after testing were implemented in SIMFC electrochemical kinetics core. Moreover, some empirical coefficients were now formulated as a function of microstructure parameters in order to consider how material changes influence the electrocatalyst active site distribution as well as the conductivity. Here the exchange current density results in function of available active site, namely TPB length l_{TPB}, (Equation 6) or the ohmic term depends on the conductivity σ of each layer (Equation 7).

$$J_0 = 2\gamma l_{TPB} \Pi y_{i,bulk}^{\alpha i} \exp(-E_{act}/RT) \quad (6)$$

$$R_{ohm} = \Sigma (d_j/\sigma_j) \quad (7)$$

Where γ is the preexponential coefficient, E_{act} the activation energy, d the thickness of a specific layer and y the gas molar fraction.
The analysis focused mainly on fuel electrode side which showed a higher variation of performance and microstructure according to experimental observations. Here, for instance the TPB length as well as the cermet conductivity were expressed in terms of particle radius and phase fractions [27].

4. Results and Discussions

The fuel cell performance for both cells was evaluated through electrochemical characterization based on voltage measurements and EIS spectra along with additional information obtained by the SIMFC code, such as the distinction of different polarization losses and their contribution on global cell performance.
Looking at initial operation before durability tests, the Ni-YSZ based anode supported cell shows lower polarization losses as compared to the electrolyte supported cell. For instance, at 800 °C and a current density 0.2 Acm^{-2} the voltage is equal to around 1 V for Ni-YSZ based cell compared to 0.94 V of Ni-GDC based one. According to modelling, indeed the ohmic term increases by a factor of four when moving from the anode supported (Ni-YSZ) to the electrolyte supported (Ni-GDC) design (Figure 1). In addition to the electrolyte thickness effect, also the use of different ceramic materials at the fuel electrode affects the ohmic resistance, since YSZ has a higher conductivity value than GDC (4.2 vs. 2.5 S m^{-1}) [27,28]. Whereas the activation overpotentials are quite similar as well as the diffusion terms that are negligible in both cases.

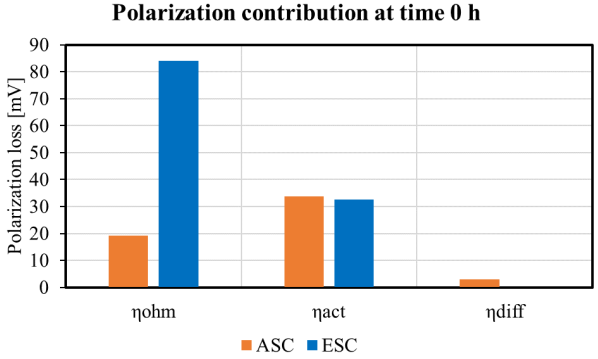

Figure 1. Comparison of polarization losses (ohmic overpotential "ηohm", activation overpotential "ηact" and diffusion overpotential "ηdiff") at 800 °C and 0.2 Acm^{-2} feeding 96/4 H_2/H_2O and air according to SIMFC results.

Durability tests were performed in fuel cell mode avoiding any stressful working conditions such as excessive loads (i.e., cause of fuel starvation), redox and thermal cycles (i.e., cause of delamination and microcracking formation). Here, all detected changes should be specifically correlated to variations in the chosen materials and cell configurations. Figure 2 shows the measured voltage profiles along more than 1000 h operation. In both cases, a gradual reduction is visible

(higher voltage values for Ni-GDC based cell are due to the selected operating conditions specified in Table 1).

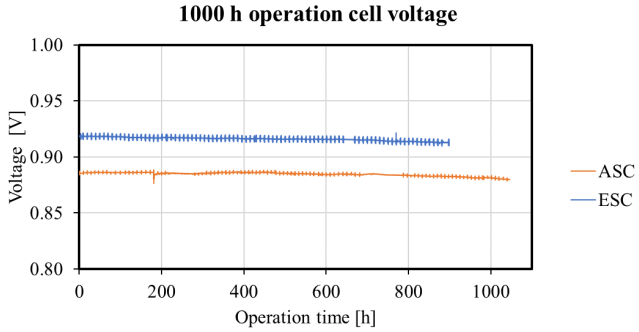

Figure 2. Voltage profiles for cells operated along 1000 h with 96/4 H_2/H_2O fuel composition and air as oxidant at 750 °C under 0.4 Acm^{-2} for ASC (orange line) and at 850 °C under 0.2 Acm^{-2} for ESC (blue line).

A common index of performance variation is the degradation rate *DR* which evaluates the absolute difference between the measured value $V_{SOFC,t}$ at time *t* and the initial voltage $V_{SOFC,0}$, normalised to $V_{SOFC,0}$ assuming a reference time step of 1000 h (Equation 8).

$$DR = \left|(V_{SOFC,t} - V_{SOFC,0})/V_{SOFC,0} \cdot (1000/t)\right| \quad (8)$$

Considering global *DR*, the Ni-YSZ based cell shows a slightly lower value than the Ni-GDC based cell: 0.5 V% kh^{-1} vs. 0.7 V% kh^{-1}. Moreover, the degradation mechanisms are characterised by different trends. The Ni-YSZ based configuration has a larger *DR* in the first 100 operation hours, followed by a fairly stable operation until a further increase of the voltage degradation rate after 350 h. In the last part, *DR* is quite negligible. In comparison, the Ni-GDC based cell shows a continuously decreasing trend until a quite stable *DR* value, suggesting the occurrence of a main degradation processes in the initial test period where *DR* exceeds 10 V% kh^{-1}. Only after 500 h the *DR* becomes always lower than 1 V% kh^{-1} (value reached after only 100 h in ASC case).

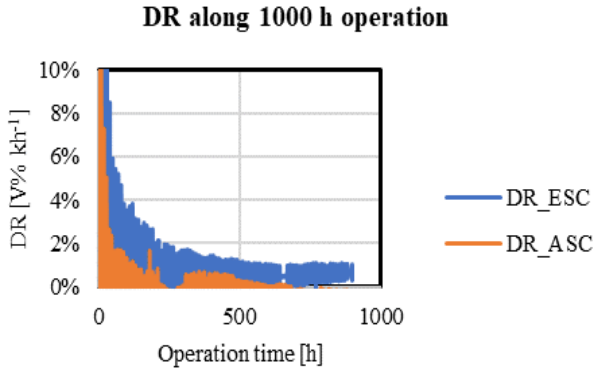

Figure 3. Comparison of degradation rate trends along durability tests.

Figure 4 shows the evolution of the ohmic and polarisation resistances for both configurations. In case of ASC (Figure 4.a), the initial polarisation term is higher than ohmic one of ~0.06 Ωcm^2. This was expected because of the major electrode contribution in terms of activation overpotential (Figure 1). The change of the ohmic resistance decreases from ~145 $m\Omega cm^2kh^{-1}$ in the initial 100 hours to ~4.5 $m\Omega cm^2kh^{-1}$ at 1000 h. Whereas the polarisation resistance shows a linear increasing slope of ~20 $m\Omega cm^2kh^{-1}$ throughout the whole operation. This suggests the main role of electrode degradation to the overall voltage decrease.

In the ESC cell (Figure 4.b), the ohmic contribution is about 1.7 times higher than the polarisation one due to a thicker electrolyte support. Looking at the durability test, the ohmic resistance changes only slightly throughout the whole operation with ~7 $m\Omega cm^2kh^{-1}$ as the maximum value (however it was a smaller degradation rate than ASC cell case). Similar to Ni-YSZ based cell, the polarization resistance has a linear trend with a lower slop equal to ~12 $m\Omega cm^2kh^{-1}$. Despite smaller detected degradation rates for Ni-GDC based cell, more detrimental effects are evident on a global SOFC behaviour due to its higher resistance values.

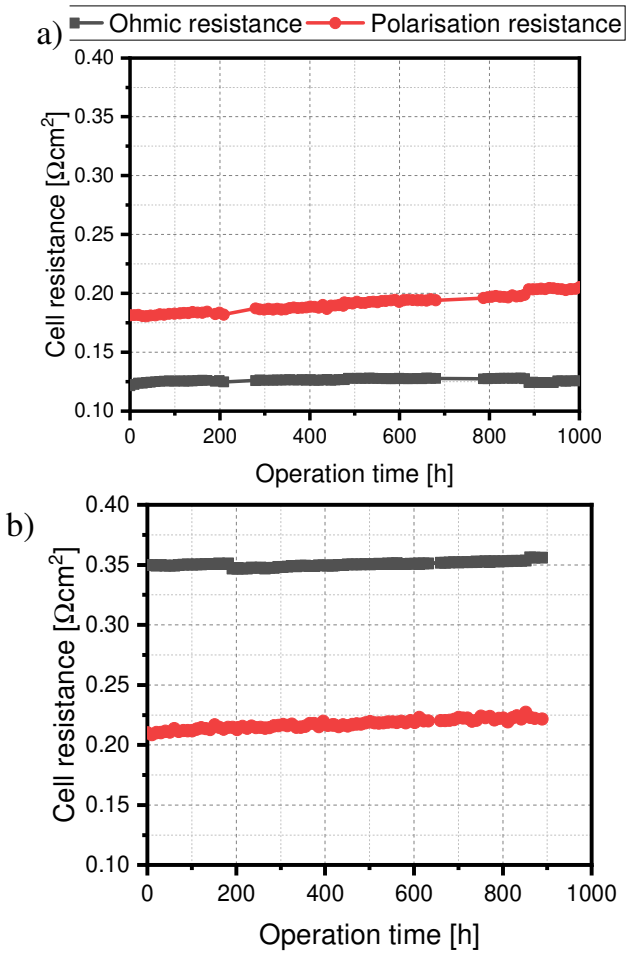

Figure 4. Evolution of ohmic and polarisation resistances over 1000 h operation for a) ASC and b) ESC.

After these preliminary analysis on electrochemical performance of the cells, a detailed post-mortem analysis allowed for the identification of main degradation processes focusing on the fuel electrode structure as discussed earlier. Here SEM image analysis was fundamental to elaborate a more detailed simulation tool where kinetics parameters were expressed as a function also of microstructural features. Since their variations on

the cell plane are not homogeneous, showing different particle sizes and component phases by comparing inlet and outlet sections, the SIMFC local modelling proved to be a suitable tool to represent the cell effective behaviour in long-term operation. Here, maps of main physical, chemical and geometrical features were implemented as inputs for electrochemical kinetics, allowing a correlation between observed microstructural changes and polarization losses.

As an example of this approach, Ni agglomeration and migration detected in the active zone by experimental observations were correlated to TPB length to adjust the anodic overpotential term in ASC case (Equations 4 and 6).

Through post-test SEM analysis, the mean particle diameters and the mean linear intercepts over 1000 particles were determined (Table 2). The global Ni phase fraction is almost unchanged although a more relevant variation in terms of percolating Ni was observed in the samples. Considering particle diameters, Ni underwent coarsening resulting in an overall size increase (a bit higher in the outlet section). Differently the dimension of pores rises in quite homogeneous way showing the same value on the whole cell plane.

Table 2. Microstructure parameters in term of phase fraction and particle size for Ni and pores in ASC.

	Reference	**Inlet after 1000 h**	**Outlet after 1000 h**
	Phase fraction [-]		
Total Ni	40%	39%	37%
Pore	15%	21%	16%
	Mean linear intercept [µm]		
Ni	0.80	1.09	1.15
Pore	0.30	0.49	0.50

These local variations were implemented into the model to evaluate how TPB length changes and to compare the effective anodic overpotential before and after the durability test. At time equal to zero the microstructure is homogeneous in the whole electrode, so a constant value of l_{TPB} was computed equal to 7 µm^{-2}. Whereas for post-test simulation, maps were imposed for Ni radius and fraction distribution as Figure 5.a and Figure 5.b show respectively. According to SIMFC outcomes (Figure 5.c), the availability of TPB active sites decreases as result of the degradation: a Ni radius increase of 35% as well as a Ni percolating phase decrease of 70% cause the l_{TPB} reduction of about 7 times. Looking at specific local values after 1000 h operation, a small increase is observed along the cell feed side due to a higher percolating Ni fraction (27% inlet vs. 30% outlet), indicating a higher impact compared to the increase in particle diameter.

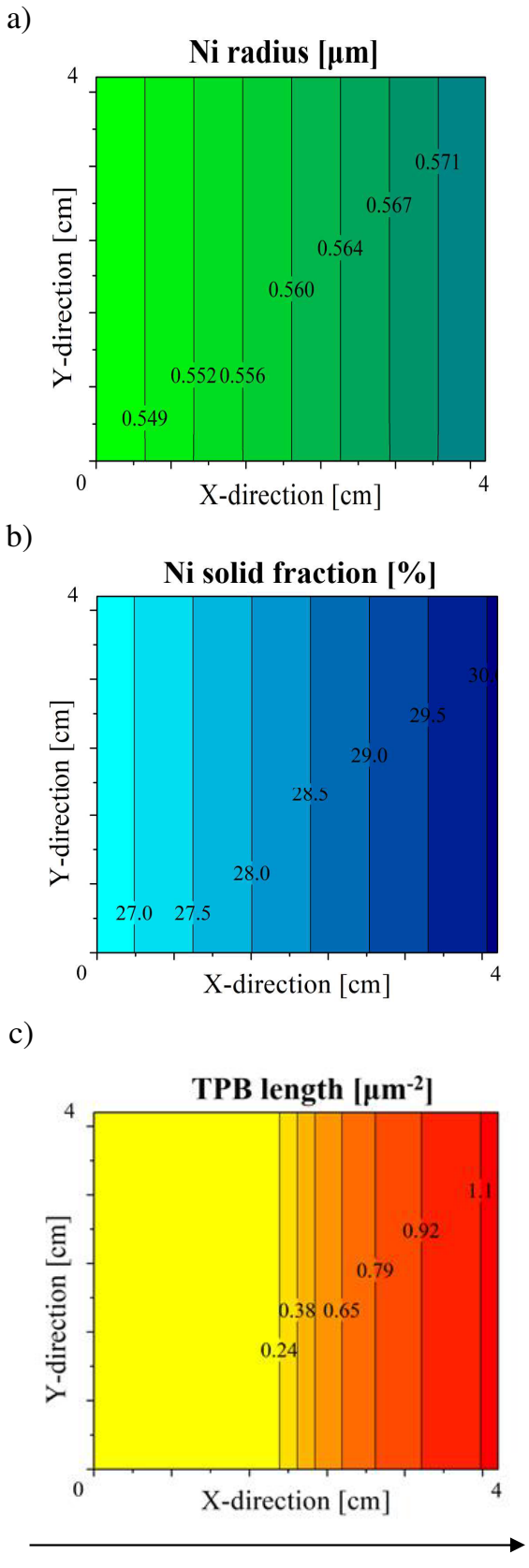

Figure 5. Local maps of imposed a) Ni radius and b) percolating Ni fraction derived from SEM images and c) resulting TPB length computed through SIMFC.

Translating this variation in terms of cell performance and not changing any other kinetic parameter, the

activation overpotential at fuel electrode has a considerable increase by comparing values at time 0 and 1000 operation hours. Considering the case at 750 °C in 96/4 H_2/H_2O fuel composition and dry air as oxidant, Figure 6 shows the increase of η_{act} at fuel electrode under common working points. Here the previously detected increase of TPB length equal to 7 times (at OCV) causes a higher value of activation term around 10 times.
Similar approaches based on experimental observations on microstructural variation and local level modelling could be applied also to determine how material conductivity as well as gas transport phenomena changes influence other polarization losses.

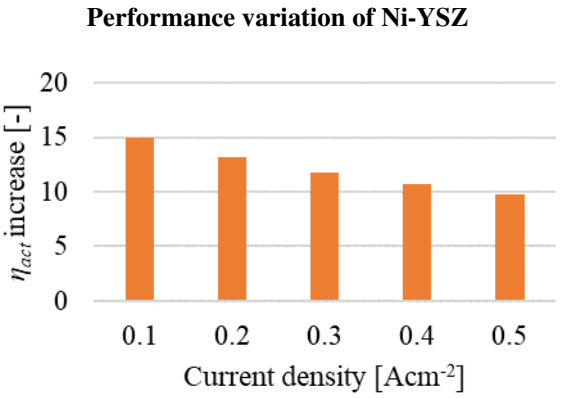

Figure 6. Variation of Ni-YSZ activation overpotential in view of TPB length decrease after 1000 in operation hours.

The results of this research were obtained thanks to received funding from the European Horizon 2020 – Research and Innovation Framework program (H2020-JTI-FCH-2018-1) under grant agreement n°825027 (AD ASTRA project).

References

[1] Elmer, T., M. Worall, S. Wu, S.B. Riffat, Appl. Therm. Eng., 2015, 90, 1082.
[2] Office of energy efficiency & renewable energy. Available online: https://www.energy.gov/eere/fuelcells/downloads/hydrogen-and-fuel-cell-technologies-office-multi-year-research-development. (Accessed on 2020 -11 -24).
[3] Mogensen, M.B., M. Chen, H.L. Frandsen, C. Graves, A. Hauch, P. Vang Hendriksen, T. Jacobsen, S.H. Jensen, T.L. Skafte, X. Sun. Fuel Cells. 2021, 1–15.
[4] Simwonis, D., F. Tietz, D. Stöver, Solid State Ion., 2000, 132(3–4), 241.
[5] Sehested, J., Catal. Today, 2006, 111(1–2), 103.
[6] Yokokawa, H., H. Tu, B. Iwanschitz, A. Mai, J. Power Sources, 2008, 182(2), 400.
[7] Monaco, F., M. Hubert, J. Vulliet, J.P. Ouweltjes, D. Montinaro, P. Cloetens, P. Piccardo, F. Lefebvre-Joud, J. Laurencin, J. Electrochem. Soc., 2019, 166(15), 1229.
[8] Gubner, A., H. Landes, J. Metzger, H. Seeg, R. Stübner, ECS Proc. Vol., 1997, 1997–40(1), 844.
[9] Hauch, A., S.D. Ebbesen, S.H. Jensen, M. Mogensen, J. Electrochem. Soc., 2008, 155(11), B1184.
[10] Martinez, A.S., J. Brouwer, Electrochim. Acta, 2008, 53(10), 3597.
[11] Hagen, A., R. Barfod, P.V. Hendriksen, Y.-L. Liu, S. Ramousse, J. Electrochem. Soc., 2006, 153, A1165.
[12] Hauch, A., K. Brodersen, M.Chen, M.B. Mogensen, Solid State Ion., 2016, 293, 27–36.
[13] Sun, X., P.V. Hendriksen, M.B. Mogensen, M. Chen, FUEL CELLS 19, 2019, 6, 740–747.
[14] Holzer, L., B. Iwanschitz, T. Hocker, B. Münch, M. Prestat, D. Wiedenmann, U. Vogt, P. Holtappels, J. Sfeir, A. Mai, T. Graule, J. Power Sources, 2011, 196(3), 1279.
[15] Faes, A., A. Hessler-Wyser, D. Presvytes, C.G. Vayenas, J. Van herle, Fuel Cells, 2009, 9(6), 841.
[16] Menzler, N.H., D. Sebold, Y.J. Sohn, S. Zischke, J. Power Sources, 2020, 478, 228770.
[17] Holzer, L., B. Münch, B. Iwanschitz, M. Cantoni, T. Hocker, T. Graule, J. Power Sources, 2011, 196(17), 7076–7089.
[18] Ioselevich, A., A.A. Kornyshev, W. Lehnert, J. Electrochem. Soc., 1997, 144(9), 3010.
[19] Iwanschitz, B., L. Holzer, A. Mai, M. Schütze, Solid State Ion., 2012, 211, 69.
[20] Zekri, A., K. Herbrig, M. Knipper, J. Parisi, T. Plaggenborg, Fuel Cells, 2017, 17(3), 359.
[21] Sciazko, A., T. Shimura, Y. Komatsu, N. Shikazono, Bull. JSME J. Therm. Sci. Technol., 2021, 16(1), 2021.
[22] Hubert, M., J. Laurencin, P. Cloetens, B. Morel, D. Montinaro, F. Lefebvre-Joud, J. Power Sources, 2018, 397, 240.
[23] Padinjarethil, A.K.; F.R. Bianchi, B., Bosio, A. Hagen, Conference: European Fuel Cell Forum, 2020.
[24] Graves, C., J. Hjelm, Conference: European Fuel Cell Forum, 2014.
[25] Conti, B., B. Bosio, S.J. McPhail, F. Santoni, D. Pumiglia, E. Arato, Catalysts, 2019, 9(1), 36.
[26] Bianchi, F.R., A. Baldinelli, L. Barelli, G. Cinti, E. Audasso, B. Bosio, Energies, 2020, 13(19), 5058.
[27] Chen, D., W. Bi, W. Kong, Z. Lin, J. Power Sources, 2010, 195(19), 6598–6610.
[28] Leah, R.T., N.P. Brandon, P. Aguir, J. Power Sources, 2005, 145, 336–352.

Nanostructured gas diffusion layer to improve direct oxygen reduction reaction in Air-Cathode Single-Chamber Microbial Fuel Cells

Giulia Massaglia[1,2*], Eve Verpoorten[1,2], Candido F. Pirri[1,2], and *Marzia* Quaglio[1,2]

[1]Department of Applied Science and Technology, Politecnico of Turin, 10129, Corso Duca degli Abruzzi 29, Italy
[2]Center for Sustainable Future and Technologies, Italian Institute of Technology, 10100, Via Livorno 60, Italy

Abstract. The aim of this work is the development of new nanostructured-gas-diffusion-layer (GDL) to improve the overall behaviour of Air-Cathode Single-Chamber-Microbial-Fuel-Cells (SCMFCs). The design of new nanostructured-GDL allowed exploiting all nanofibers 'intrinsic properties, such as high surface ratio to volume, high porosity, achieving thus a good oxygen diffusion into the proximity of catalyst layer, favouring thus the direct oxygen-reduction-reaction (ORR). Nanostructured-GDLs were prepared by electrospinning process, using a layer-by-layer deposition to collect 2 nanofibers' mats. The first layer was made of cellulose nanofibers able to promote oxygen diffusion into SCMFC. The second layer, placed outwards, was based on polyvinyl-fluoride (PVDF) nanofibers to prevent the electrolyte leakage. This nanostructured-GDL plays a pivotal role to improve the overall performance of Air-Cathode-SCMFCs. A maximum current density of 20 mA m^{-2} was obtained, which is higher than the one reached with commercial-GDL, used as reference material. All results were analysed in terms of energy recovery parameter, defined as ratio of generated power integral and the internal volume of devices, evaluating the overall SCMFC performance. SCMFCs with a nanostructured-GDL showed an energy recovery equal to 60.83 mJ m^{-3}, which was one order of magnitude higher than the one obtained with commercial-GDL, close to 3.92 mJ m^{-3}.

1 Introduction

Renewable energy sources play a pivotal role to ensure the transition from carbon-based economies towards sustainable human development [1]. Among all possible renewable energy sources, like wind, solar, hydro-and geo-thermal and biomass, microbial fuel cells (MFCs) have gained great interest in recent years since they are able to combine the power production with some processes like water treatments, bio-remediation and sensing, obtained by involving a particular class of bacteria into MFCs [2-3]. In general, MFCs are bio-electrochemical devices that directly transduce the chemical energy, entrapped into organic matter, into energy one thanks to the metabolic activity of a particular kind of bacteria, named exo-electrogenic bacteria [4-6]. These microorganisms, indeed, are able to release all produced electrons outside their cells to anode electrode surfaces [4-6]. This kind of bacteria proliferated onto the anode surfaces, leading thus to the formation of a biofilm, whose exocellular electron transfer ensured the power output production. In the present work, an open-air cathode configuration MFCs is used, where direct oxygen reduction reaction (ORR) occurred into the cathodic compartment [7]. As investigated in several works in the literature, the optimization of cathode electrodes, with the main purpose to improve the diffusion layer, which plays a crucial role into the diffusion of oxygen from outside into the devices and apply a proper catalyst layer able to ensure the achievement of ORR, is mandatory. In this context, the activation losses at the cathode are minimized and the overall MFCs performance is improved [8-9]. The catalyst layer must provide a number of electrons that are as close as possible to the theoretical value of 4, favouring the direct ORR and avoiding the intermediate 2-electrons reduction reaction, which releases H2O2, a toxicant for microorganisms [8-9]. A catalyst layer based on platinum results to be the best performing class of catalyst for this reaction [9]. On the contrary, the common gas diffusion layer (GDL) is composed by polytetrafluoroethylene (PTFE), that is deposited onto carbon-based electrode. PTFE ensures the oxygen diffusion into the cathodic compartment, avoiding/reducing as much as possible the electrolyte leakage. The aim of the present work is the development of a new nanostructured-gas-diffusion-layer (GDL) to improve the overall behaviour of Air-Cathode Single-Chamber-Microbial-Fuel-Cells (SCMFCs). The design of new nanostructured-GDL allowed exploiting all nanofibers 'intrinsic properties, such as high surface ratio to volume, high porosity and light weight, achieving thus a good oxygen diffusion into the proximity of catalyst layer, ensuring and favouring the direct oxygen reduction reaction (ORR). Nanostructured-GDLs were prepared by electrospinning process, using a layer-by-layer deposition to collect 2 different nanofibers' mats. The first layer was made of cellulose nanofibers that play a crucial role to promote oxygen diffusion into SCMFC. The second layer, placed outwards, was based on polyvinyl-fluoride (PVDF) nanofibers with the main purpose to prevent the electrolyte leakage, while allowing oxygen free to flow. Cellulose nanofibers were obtained starting from a polymeric solution of cellulose-acetate (CA). To employ final cellulose nanofibers, as fabricated-CA nanofibers were hydrolysed in 0.05 mol/L NaOH/ethanol solution for 24 h at room temperature, followed by thoroughly washing with double-distilled water until the supernatant reached neutral. Both of 2 nanostructured layers were

* Corresponding author: giulia.massaglia@polito.it

directly deposit onto carbon paper. Onto the inner side of carbon paper electrode, a catalyst layer made of Pt/C was applied to ensure the direct ORR. To demonstrate how nanostructured GDL can improve the overall performance of Air-Cathode-SCMFCs, this cathode electrode was applied into the devices and compared with the one that presents a commercial GDL, made of polytetrafluoroethylene (PTFE). A maximum current density of 35.71 mA m-2 was obtained, which is higher than the one reached with commercial-GDL, used as reference material. All reached results were analysed in terms of the energy recovery parameter, defined as the ratio of the generated power integral and the internal volume of the devices, evaluating the overall SCMFC performance. SCMFCs with a nanostructured-GDL showed an energy recovery equal to 60.83 mJ m-3, which was one order of magnitude higher than the one obtained with commercial-GDL, close to 3.92 mJ m-3. All these latter results open the doors to design the entire nanostructured cathode electrode in SCMFCs. The nanostructured cathode electrode may be done by carbon nanofibers doped with nitrogen (N-CNFs), which play a pivotal role as promising catalyst layer for direct ORR as demonstrated in our previous work [11] and can be employed as a carbon backbone to ensure the electron transfer produced and released by microorganisms into the anode compartment.

2 Materials and Methods

2.1 Materials and nanofibers synthesis

The layer-by layer deposition is ensured by implementing the electrospinning process (NANON 01A electrospinning apparatus MECC, LTD). One of the great advantages of this technology, indeed, consist into ability to ensure a layer-by layer deposition without the using of binder to ensure the connection between dried nanofiber mats and CP material. In particular, two different layers were obtained: *i)* the first layer is made of cellulose nanofibers, obtained by a starting polymeric solution based on cellulose acetate (Mw=, Sigma Aldrich) dissolved into N-N DMF (assay 99.8%, Sigma Aldrich); *ii)* the second layer, on the contrary, is composed by 2g of polyvinyl fluoride (PVDF, Mw=, Sigma Aldrich) dissolved into a mixture of N-N DMF and acetone with a volume ratio of 1:1. During the electrospinning process, the working voltage between the needle and planar counter electrode is fixed at 26 kV with a flow rate of 0.5 mL h-1. The working distance between the needle and substate is equal to 15 cm. After the deposition of first layer made of cellulose acetate nanofibers must be properly hydrolysed with the main purpose to obtain a final mat of cellulose nanofibers. As fabricated-CA nanofibers were hydrolysed in 0.05 mol/L NaOH/ethanol (Sigma Aldrich) solution for 24 h at room temperature, followed by thoroughly washing with double-distilled water until the supernatant reached neutral. After this post-process treatment, a deposition of PVDF nanofibers is achieved to prevent possible leakage of electrolyte solution.

2.2 SCMFCs architecture and operation

As deeply used in our previous work [10-11], a squared shape open-air cathode SCMFCs is used during the whole experiment. The devices 'case is realized by 3D printer (OBJET 30]. SCMFCs are composed by 3 different compartments and the devices are membrane-less cell with electrolyte in common between anode and cathode. The total internal volume is equal to 12.5 mL and both anode and cathode electrodes show a geometric surface area close to 5.76 cm2. The anode electrodes is a carbon based materials, carbon paper (CP, purchased from Fuel Cell Earth, USA), on which a biofilm is formed. In the present work, all anode electrodes have been obtained from previous experiments, conducted in our laboratories. In this scenario, microbial biofilm is formed on anodes surfaces. The cathode electrodes are modified by applying a catalyst layer based on platinum (0.5mg cm-2 of Pt/C obtained by Sigma Aldrich) and 5wt% of Nafion (Sigma Aldrich), as discussed in the literature [9]. Moreover, on the inner side of CP a gas diffusion layer is deposited. The commercial GDL, composed by PTFE layer, was directly compared with the new designed nanostructured-GDL. The electrolyte is a water-based solution containing 12mM of sodium acetate, used as organic matter, and other compounds (5.8 mM of ammonium chloride and phosphate buffer saline solution (PBS) [10-12]) suitable for the preservation of metabolic activity of microorganisms. Titanium wires were used to ensure a good electrical contact and both anode and cathode were connected with a multichannel data acquisition unit (Agilent 34972 A). an external load of 1kΩ is applied. Moreover, during the whole experiments, a fed bath mode is implemented to substitute the old electrolyte with the new one. According to this method, the replacement of electrolyte is carried out when voltage reaches a values close to 0V. all the experiments were conducted in duplicate.

2.3 Characterizations and measurements

Field Emission Scanning Electron Microscopy (FESEM, Supra), operating from 5 kV to 10 kV, is used to evaluate the morphological properties of nanostructured gas diffusion layer (GDL). In order to evaluate how nanostructured-GDL can affect SCMFCs performance, polarization curves are defined through Linear Sweep Voltammetry (LSV) performed by using Palmsens potentiostat (Palmsens4, Netherlands)). LSV characterizations performed at the end of experimental study. Moreover, in the present work LSV characterization is provided by implementing a voltage range from open circuit to a short circuit with a rate of 0.1 mV s-1. The catalytic properties of the diverse cathodes were assessed through electrochemical impedance spectroscopy (EIS), employing a Palmsens potentiostat. For EIS, the sinusoidal signal had an

amplitude of 25 mV and the frequency was spanned between 150 kHz and 200 mHz; the fixed resistor method [12] (100 **Ω**) was employed. All experimental data were fitted by defining the equivalent circuit, as reported in in Scheme 1, in order to quantitatively evaluate the electrical parameters; R1 represent the series resistance (accounting for electrolyte and wiring resistances), R2 and R3 denote the charge transport (in the electrode) and the charge transfer (at the electrode/electrolyte interface) resistances, respectively. Due to porous nature of catrhode electrodes, constant phase elements, Q1 and Q2 are used to model the corresponding double layer capacitances [12]). Low frequency feature, corresponding to the species diffusion, was modelled by Warburg element, as included in the fitting.

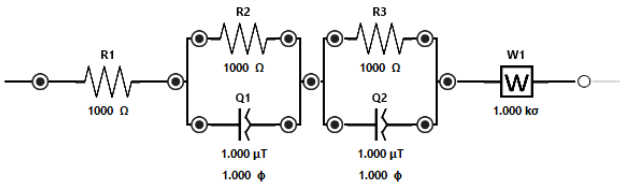

Scheme 1. Equivalent circuit used to fit the impedance spectra.

3 Results and Discussion

3.1 Morphological properties of nanostrucutred-GDL

The morphological properties of nanostructured-GDL is reported in **Fig. 1a**). FESEM images highlight the pore distribution in this samples. Indeed nanostructured-GDL are characterized by pores with dimensions in the range of few micrometres, leading thus to exhibit a higher surface area to volume ratio than the one obtained with commercial gas diffusion layers (see **Fig. 1b**) These intrinsic properties of nanofibers play a pivotal role into the enhancement of oxygen diffusion inside the devices, improving thus direct ORR.

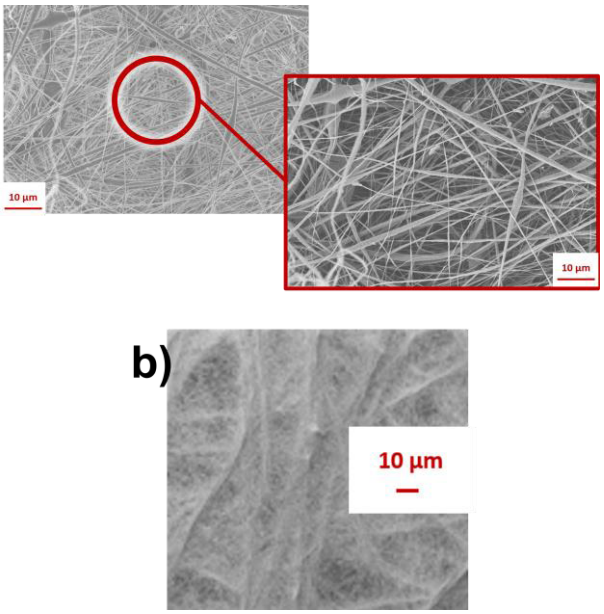

Fig. 1. a) Morphological properties of nanostructured-GDL, confirming high porosity of samples, as highlighted from higher magnification, underlined by red box. b) morphological properties of commercial GDL applied onto carbon paper CP. b) commercial carbon paper with commercial gas diffusion layer

3.2 SCMFCs performance

As previously described, at the beginning of experiments, anodes were obtained by preceding experiments, leading thus to employ a biofilm formation onto all anode surfaces. For all cathode electrodes, a catalyst layer based on platinum is applied, while nanostructured-GDL and commercial GDL were compared, to evaluate how can affect the overall performance of SCMFCs. **Fig**.**2**. represents the current density trends over time. Nanostructured-GDL reached a maximum current density equal to (35.7±2.3) mA m-2, which is double of the one reached with commercial GDL (maximum current density close to (15.22± 0.21) mA m-2), used as reference material. Since the anodic compartments of both kinds of devices are nominally identical, the differing performance of the SCMFCs can be directly attributed to the use of diverse GDLs applied onto cathode electrodes.

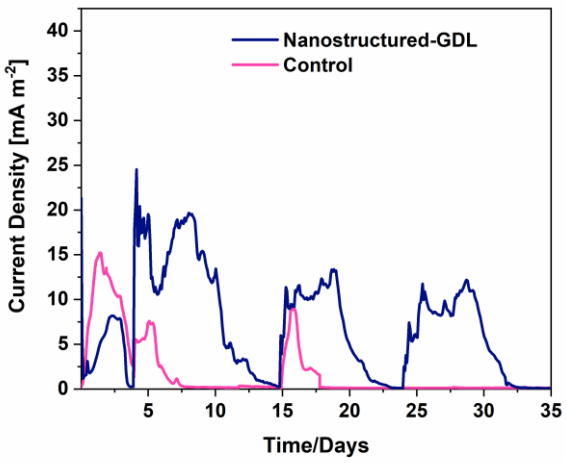

Fig. 2. Comparison of average current density trend of SCMFCs with nanostructured-GDL and current density trend reached by SCMFCs with commercial GDL, defined as reference cathode electrode.

In **Fig.3.a)** LSV curves, related to both GDLs, are reported. It is possible to notice that the maximum power density with nanostructured-GDL was up to the double of the ones reached by SCMFCs with commercial GDL, defined as control device for the whole experiment. Both of SCMFCs devices reach a similar open circuit voltage (OCV) close to 0.4V, while SCMFCs with nanostructured-GDL achieved a higher short circuit current that the one obtained with control material. Since nanostructured-GDL can affect and favour the direct ORR, ensuring the best oxygen diffusion into SCMFCs, the variation of total cathodic resistance over time was investigated through EIS. Typical Nyquist plots are represented in Fig.3b), comparing nanostructured-GDL and commercial one. The curves obtained by fitting procedure are overlaid on the experimental data (see Fig.3b). Table 1, on the contrary, summarized all resistance values.

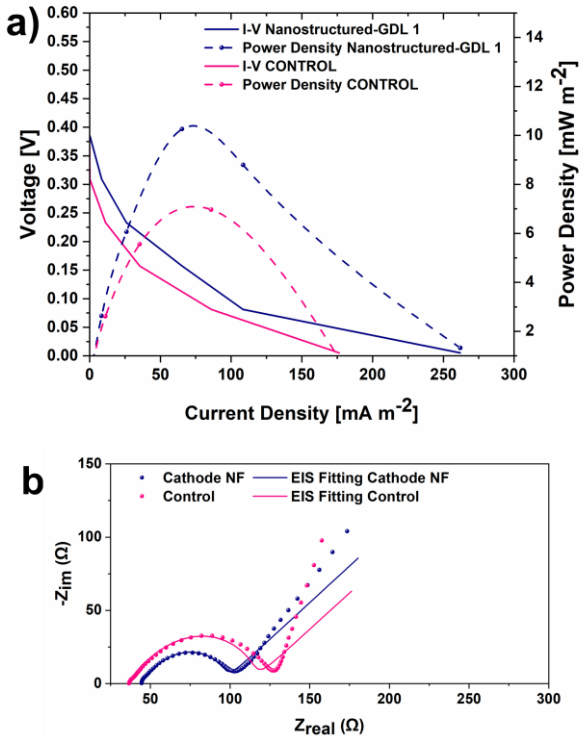

Fig. 3. a) Polarization curves obtained by LSV characterization. Potential vs. current density curves (left axis, straight lines) and power density vs. current density (right axis, dash lines) curves of SCMFCs with nanostructured-GDL and commercial GDL, used as reference. b) Typical impedance spectra of nanostructured-GDL (blue dot and line) and commercial-GDL (pink dot and line).

As highlighted in Fig.3b), all SCMFCs show a similar value of series resistance R1, independently of cathode electrodes. This is to be expected, since electrolyte, wires and electrical connection are identical for all SCMFCs. Moreover, the lower is the charge transfer at the electrode/electrolyte interface R3, higher is the capacity of cathode electrode to ensure a faster electrons flow. This result demonstrates the effectiveness of nanostructured-GDL to ensure an enhancement of oxygen diffusion, improving consequently the occurring of direct-ORR and the overall SCMFCs performance. A similar trend is observed for the transport resistance R2, which is visible in the high-frequency smaller arc sketched in fig.3b). A lower R2 defines an increasing of electrode transport properties and since all other aspects of cathode electrodes are the same, it is possible to confirm how nanostructured-GDL results to be more efficient in carrying out ORR.

Table 1. Typical resistance values (R1, R2 and R3) calculated from the fitting procedure on Electrochemical Impedance Spectroscopy (EIS) data. For each parameter, the maximum variation observed between three nominally identical Microbial Fuel Cells (MFCs) was 10%.

Cathode electrodes	R1	R2	R3
	[Ω]	[Ω]	[Ω]
Nanostructured-GDL	44.3	12.04	38.4
Commercial-GDL	36.93	25.69	50.45

Moreover, in line with all obtained results, the analysis performed in terms of energy recovery parameter, defined as ratio of generated power integral and the internal volume of devices, allow evaluating the overall SCMFC performance. SCMFCs with a nanostructured-GDL showed an energy recovery equal to 60.83 mJ m-3, which was one order of magnitude higher than the one obtained with commercial-GDL, close to 3.92 mJ m-3

4 Conclusion

In the present work, nanostructured-GDL was designed as new gas diffusion layer to improve the oxygen diffusion inside SCMFCs, exploiting the intrinsic properties of nanofibers, such as high porosity, high surface area to volume ratio and light weight. Moreover, through electrospinning process, a direct deposition of nanofiber mats can be collected onto carbon based materials, used as cathode electrodes, without the necessity of binder to bond GDL with the carbon backbone. Morphological properties confirm a higher porosity obtained with nanostructured-GDL, than the one reached when commercial-GDL is applied as reference results. Moreover, all obtained results demonstrate that nanostructured-GDL play a pivotal role to improve all SCMFCs performance. Indeed, SCMFCs with nanostructured-GDL reach a maximum current density which is double of the value achieved when commercial GDL is analyzed. Since all other aspects are in common between all cathode electrodes, it is possible to confirm that all difference can be addicted to the presence of nanofiber mats as GDL. All obtained results demonstrate the effectiveness of nanostructured-GDL to ensure an enhancement of oxygen diffusion, improving consequently the occurring of direct-ORR and the overall SCMFCs performance.

Reference

[1] B. Walsh, P. Ciais, I.A. Janssensz,; J.Penuelas, J, K. Riahi, F. Rydza, D.P. Van Vuuren, M. Obersteiner. *Nature Communications* (2017), **8**, 14856-68
[2] Logan, B.E.; Rabaey, K. *Science* (2012), **337**, 686-690
[3] Logan, B.E. Microbial Fuel Cells, New York: John Wiley & Sons; 2008
[4] Logan, B.E.; Hamelers, B.; Rozendal, R.; Schroder, U.; Keller, J.; Freguia, S.; Aelterman, P.; Verstraete, W.; Rabaey, K. *Environmental Science and Technology* (2006), **40**, 5181-92
[5] Babauta, J.; Renslow, R.; Lewandowski, Z.; Beyenal, H.. *Biofouling* (2012), **28**, 789-812
[6] Harnisch, F.; Aulenta, F.; Schroeder, U. Comprehensive Biotechnology 2nd ed; Elsevier: Amsterdam, 2011, p. 644-659
[7] Santoro C, Stradlhofer A, Hacker V, Squadrito G, Schroder U, Li B. *Journal of Power Sources (*2013); **243**:499-507
[8] Oh S, Min B, Logan BE. *Environmental Science Technology* (2004); **38**: 4900-4904
[9] Cheng S, Liu H, Logan BE. *Electrochemistry communications* 2006; 8:489-494
[10] Massaglia G, Chiodoni A, Salvador GP, Delmondo L, Munoz-Tabares JA, Bocchini S, Sacco A, Bianco S, Saracco G, Quaglio M. *RSC Adv*. (2017);**7**:38812-38818
[11] Massaglia G., Margaria V., Sacco A., Castellino M., Chiodoni A., C.F. Pirri, Quaglio M., *IJHE* **44** (2019) : 4442-9
[12] Jackson A, Strickler A, Higgins D, Jaramillo TF.. *Nanomaterials* (2018); **8**: 38-53

High temperature fuel cells to reduce CO_2 emission in the maritime sector

Maurizio Archetti[1], *Emilio* Audasso[2], *Barbara* Bosio[2,*], and *Dario* Bove[2]

[1]Ecospray Technologies s.r.l., Alzano Scrivia (AL), Italy
[2]Department of Civil, Chemical and Environmental Engineering (DICCA), University of Genoa, Genoa, Italy

Abstract. Recently the interest in the sustainability of the maritime sector has increased exponentially. The International Maritime Organization (IMO) set as objective the reduction of CO_2 emissions by 2030 by a margin of 40% compared to 2008. Recent studies showed that, according to the ships and the emission mitigation method applied, only 15-25% of CO_2 reduction is de facto needed. Fuel cells represent an answer to meet this regulation. We propose two different solutions: (i) produce with SOFCs instead of engines the minimum power necessary to cut 20% of the emissions, or (ii) reduce the engine power of about 10% balancing the power requirement using MCFCs with CO_2 capture. Using Aspen Plus each solution was investigated. The analysis contemplated LNG steam reforming to produce the H_2 necessary for cell operation and the separation and liquefaction of CO_2. Two case studies were considered comparing existing passenger ships with engines working on HFO and on LNG respectively. Although both solutions showed potential for the reduction of CO_2 emissions respecting the IMO regulations, the SOFC solution requires a major change in the design of the ship, while MCFCs are proposed as an urgent solution allowing ship retrofitting without demanding update.

1 Introduction

The maritime sector has an essential role in the transport of both goods and passengers across the globe. Maritime transport of goods constitutes the most significant fraction of the transportation sector with a 90% share of global trade [1–3]. Accordingly, the naval shipping industry consumes the largest amount of fuel in the transportation sector and generates 3% of the global CO_2 emissions [1]. This fuel consumption is also responsible such for the release into the atmosphere of large amount of greenhouse gases (GHG) and other regulated emissions as nitrogen oxides (NOx), sulphur oxides (SOx), CO, and particulate matter (PM)[2]. In comparison, the transport of passengers generates lower CO_2 emission since the number of vessels employed is significantly lower, however its total GHG emissions have a very high impact at local level especially in port areas [4,5].

Due to this large number of emissions, in the last years, the interest in the environmental sustainability of the maritime sector has increased exponentially. To encourage this effort, the International Maritime Organization (IMO) has set as objective the reduction of CO_2 emissions per transport work by 2030 by a margin of 40% compared to 2008 [2]. Subsequently, it pursues to increase this reduction to 70% by 2050, while also halving the total annual GHG emissions [2]. According to age, design and quality of the ships and considering additional mitigation method such as speed reduction or route optimization, only 15-25% of CO_2 emission reduction is required by the development of new technological solutions.

Fuel cells can provide a valid answer to meet the IMO regulations by allowing the required CO_2 emission reduction. Indeed, compared to the traditionally used internal combustion engines, fuel cells grant a sensibly lower amount of emissions coupled with higher efficiency [6]. Moreover, fuel cells are highly modular thus allowing a smart use of the limited space typical of vessels [7]. For this reason, in literature there have been already different studies that consider the use of fuel cells on ships. Inal et al. [7] studied the substitution in a chemical tanker ship of a 4-stroke diesel engine with 2880 kW output power with an LNG fuelled molten carbonate fuel cell (MCFC) with same output power. The results of their investigation showed that it is possible to effectively reduce GHG emission and particularly CO_2, although more studies on the overall needs of the equipment for a smooth substitution are required. Haseltalab et al. [8] studied the component sizing, energy and power management of solid oxide fuel cells (SOFCs) as the main source integrated into the liquefied natural gas fuelled Power and Propulsion System of vessels. As results they confirmed that the adoption of SOFCs in combination with batteries can effectively address the challenges of the maritime sector in term of emission reductions, despite the need for improvements in the design of the SOFC system to reduce the impact on vessel design and operation. Wu et al. [9] investigated a hybrid proton-exchange membrane fuel cell

* Corresponding author: barbara.bosio@unige.it

(PEMFC) and battery propulsion system in Matlab for use on a coastal ferry. They showed that the proposed propulsion system can achieve at least a 65% life-cycle greenhouse gas reduction. However, also in this case, more investigation is needed to improve the system. Coupled with this theoretical studies, in the last years also numerous projects have been conducted with practical investigations [6]. Among these, based on the Zemships project [10], a PEMFC power system (maximum power output of 100 kW) was developed for the passenger ship FCS Alsterwasser. The fuel cell system was used to power the propulsion motor directly or charge the lead-gel battery packs that served as a back-up option if the fuel cells failed. The H_2 stored onboard allowed for 2 to 3 days of ship operation. Then, under the FellowSHIP project, the offshore supply vessel Viking Lady was the first to use MCFCs as auxiliary power systems (320 kW for 500 cells) to dual fuel engines propulsor [11]. The system operated for 18 hours [7]. Furthermore, under the METAPHU project, while a conceptual study of a 250 kW SOFC auxiliary power systems using methanol was completed, the practical operation of a 20 kW SOFC unit onboard the car carrier MV Undine were conducted. The SOFC unit was aimed at testing the performance and emissions under real-life conditions onboard a ship and at assessing the maturity of methanol-based technology in the shipping sector [12].

However, a complete substitution of the combustion engines with fuel cells may not be easy to apply because the required spaces and costs could be excessive, and existing ships would have to be completely redesigned or put out of use. In this work, the authors propose two different solutions: (i) relying on solid oxide fuel cells instead of engines just the minimum power necessary to cut emissions of about 20%, or (ii) reduce the engine power around 10% while balancing the power requirement using MCFCs for CO_2 capture. Using both solutions two case studies were studied comparing existing passenger ships where engines working on HFO, typical of more traditional ships, and on LNG, currently emerging for emission reduction, are used respectively.

2 Fuel cells

Fuel cells are electrochemical devices that allows the production of electrical power exploiting the electrochemical reaction between a fuel, usually H_2, and an oxidant, usually O_2 [13]. There is a large variety of fuel cells that differ by components and catalyst materials used, charge carriers, operating temperatures, and range of applications [13]. Among these, high temperature fuel cells are considered those type of cells that operate between 500-1200°C. For this reason, compared to low temperature fuel cells (operating temperature 20-200°C), they do not need the use of noble metal as catalysts highly affecting the prices and can work with carbon containing components allowing a more diverse range of possible fuels [6]. They can be divided into two subclasses according to the electrolyte that they use to operate: solid oxide and molten carbonate fuel cells.

Solid oxide fuel cells (SOFCs) use as electrolyte solid oxide materials such as YSZ, GDC, or LSGM. According to the electrolyte materials used and the dopant applied, the temperature range at which SOFCs can operate varies between 1200°C and 500°C. Thanks to the high operating temperature and the Ni based anode catalysts usually used, SOFCs can work also with carbon containing fuels (i.e.: CH_4, CH_3OH) in addition to the commonly used H_2 thanks to internal reforming reactions. As in any other kind of fuel cells, the global reaction that provides energy is the formation of H_2O from reduction of O_2 and oxidation of H_2 at the respective electrodes, as described by Eq. 1 where the subscripts A and C indicate anode and cathode sides.

$$H_{2,A} + \frac{1}{2} O_{2,C} \leftrightarrow H_2O_{2,A} \qquad (1)$$

Molten carbonate fuel cells (MCFCs) are characterized by the use of a eutectic alkali carbonate mixture as electrolyte of which Li_2/K_2CO_3 and Li_2/Na_2CO_3 are the most common. To both keep the electrolyte in its liquid form and avoid extreme evaporation, they are limited to work in the 580-700°C temperature range. In the specific case of MCFCs, CO_2 serves as an additional reactant with O_2 to form, at the cathode, the carbonate ions (CO_3^{2-}) that function as the anion carrier through the electrolyte and matrix. The total MCFC reaction is thus described in Eq. (2, where the subscripts again refer to anode and cathode.

$$H_{2,A} + \frac{1}{2} O_{2,C} + CO_{2,C} \leftrightarrow H_2O_{2,A} + CO_{2,A} \qquad (2)$$

This migration of CO_2 from a CO_2 poor stream (cathode inlet) to an enriched stream (anode outlet) allows for MCFC to be used as CO_2 capture tools. The anode inlet constitutes a stream with concentrated CO_2 that can be more easily treated for sequestration.

3 Proposed solutions

As mentioned, the authors propose two different paths to meet new IMO regulation. Both are aimed to reduce CO_2 emission by the necessary percentage which cannot be achieved thanks to conventional ship design and management optimisation, that means around 20%.
The first path consists in reducing the power provided by the combustion engines while covering this decrease using a more efficient technology such as SOFCs. The second path adds to this concept the ability offered by MCFCs to capture the excess CO_2 from the engine exhausts. This second path will be slightly more complex because it requires a step of separation and liquefaction of CO_2, but it can also favour the start of a virtuous chain of CO_2 recovery. For both solutions, two case studies will be analysed comparing existing passenger ships where engines working on Heavy Fuel Oil (HFO), typical of more traditional ships, and on LNG (Liquified Natural Gas), currently emerging for emission reduction, are used respectively. Both solutions in both cases will also be studied to determine the additional required fuel for operation at same overall CO_2 emission reduction.

The schematic of how the SOFC fuel cell systems is added to the combustion engines is shown in Fig. **1**. As previously mentioned, the SOFC overall reaction see the oxidation of H_2 to water. This required fuel can be fed either directly or in the form of light hydrocarbons such as CH_4 that due to the high temperature and appropriate catalysts materials can undergo a reforming reaction. Since LNG is already present on ships or of easier storage compared to H_2 [7], the authors decided to use it as fuel. However, as internal reforming fuel cells are more complex to deal with, the authors decided to have the reforming reaction required to produce H_2 before the cell stack. For this scope, water vapour from utilities is mixed with LNG, then they are preheated and sent to a reformer unit. The reformed gas (a mixture of mainly H_2, CO, CO_2 and H_2O) is then cooled and sent to the anode side of the cell as fuel.

For the oxidant at the cathode side, air is used after being preheated.

The anode outlet of the cell is cooled with sea water to favour the separation of water in a subsequent step. The dry current is then sent to a membrane to separate part of the non-combusted H_2. This H_2-upgraded current is sent back to the SOFC inlet. The H_2-deprived current is sent to a burner together with the cathode outlet for combustion. This stream of exhaust is used to heat up the stack inlets and the reforming unit before release in the atmosphere.

The schematic of how the MCFC fuel cell systems is added to the combustion engines is shown in Fig. **2**.

A fraction of the exhausted gases from the combustion engines is used as oxidant at the cathode side of the MCFCs.

Before entering the stack, such exhausts are preheated because in the case of HFO fuelled engines the exhausted gases must be treated to remove sulphur and other pollutants using scrubbers that decrease the temperature to about 30°C, while in the case of LNG fuelled engines the final combustion temperature is usually lower (about 300°C) than the one required for MCFC operation.

As for the SOFCs, also in the case of MCFCs H_2 is the fuel required by the main reactions and can be either fed directly or through light hydrocarbons that can be internally reformed. In similar manner of what presented for the SOFC systems, also in this case the production of H_2 is obtained in an external steam reforming of LNG. The anode inlet production process is like the one previously described for SOFC, however in this case the final reformed gas is cooled down to a lower temperature of 580°C which is suitable for MCFC operation.

As it is done in the SOFC case, after reaction in the cell stack, the anode outlet is cool down using sea water to facilitate the separation of H_2O in a subsequent step and the separation of the H_2. However, in this MCFC case, the CO_2 rich stream (poor in H_2) is sent to a liquefaction system to obtain liquid CO_2. Then, the not liquefied part of the steam and the separated H_2 rich flow rate are sent together with the cathode outlet to a burner where additional LNG is fed to enhance combustion. The cell exhaust is used to warm up the cell inlets and provide heat to the reformer. Eventually, it is released into the atmosphere.

Fuel cell stack sizes, operating conditions and flow rate management have been optimised so that, as result of these overall processes, the total exhaust gas (from combustion engines + cell stack) contains an amount of CO_2 that will respect the regulations set by the IMO.

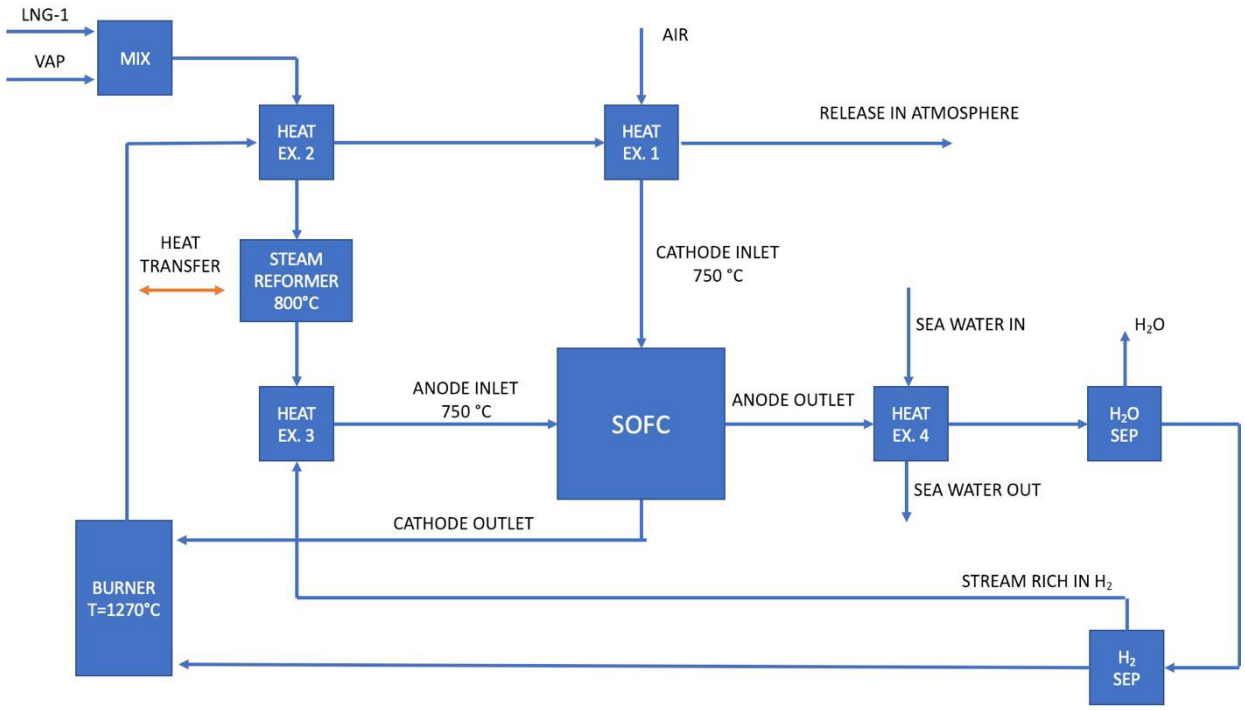

Fig. 1: Schematic representation of the SOFC system downstream the combustion engines.

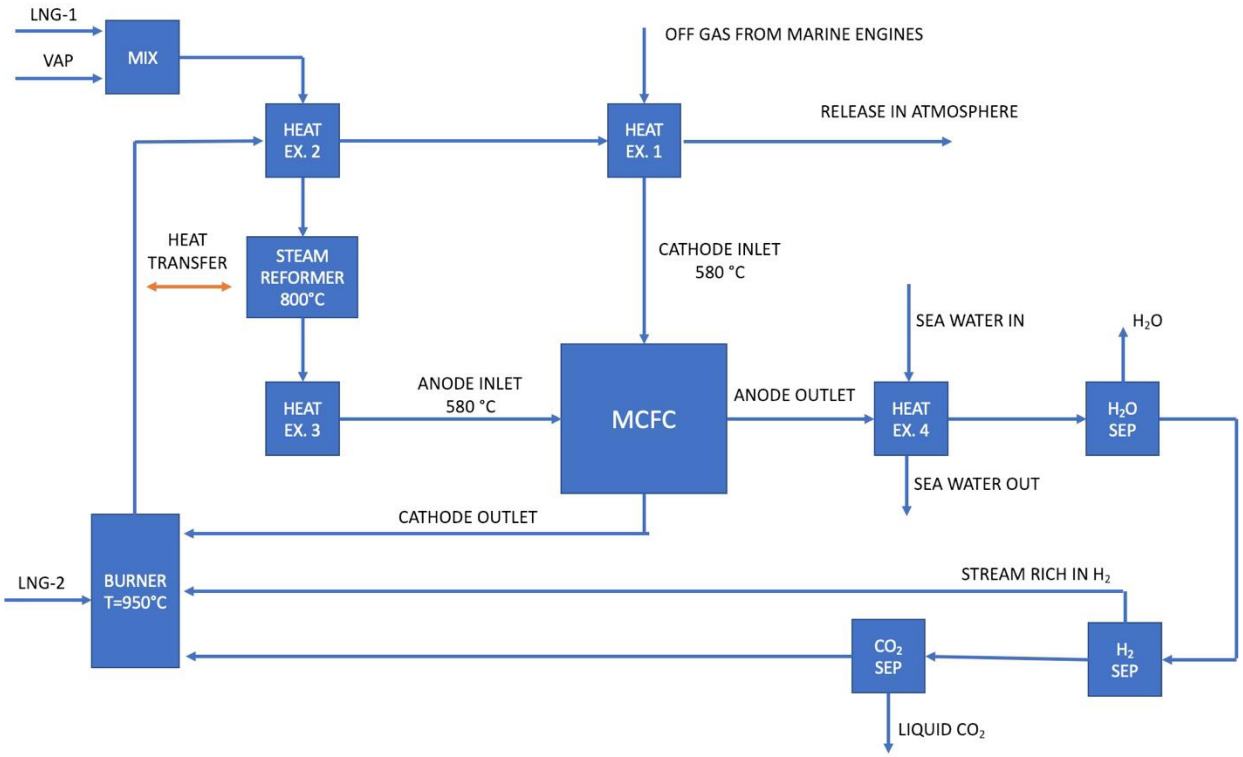

Fig. 2: Schematic representation of the MCFC system downstream the combustion engines.

4 Simulation and results

4.1 Detail of the simulation

To study the feasibility of the proposed solutions, the software Aspen Plus was used for the modelling of the fuel cell systems.

The steam reformer reactor used to produce H_2 from LNG (assumed at 15°C and 1 atm) and steam (available from the ship utilities at 4 bar and 140°C) was simulated using a Gibbs reactor at the pressure of 1 atm and 800°C.

Steam:LNG molar ratio has been guaranteed 3.5:1 to avoid carbon deposition.The reactions are not defined inside of Gibbs reactor but, according to the literature [14], the main reactions assumed are: :

$$CH_4 + H_2O \leftrightarrow 3H_2 + CO \quad (3)$$

$$CO + H_2O \leftrightarrow H_2 + CO_2 \quad (4)$$

A Gibbs reactor was also used for the simulation of the burner, considered operating with a small negative duty of about -5 kW but slightly different in all the encountered cases. The main reactions supposed for the burning process are the following:

$$CH_4 + 2O_2 \leftrightarrow 2H_2O + CO_2 \quad (5)$$

$$CO + \frac{1}{2} O_2 \leftrightarrow CO_2 \quad (6)$$

$$H_2 + \frac{1}{2} O_2 \leftrightarrow H_2O \quad (7)$$

The heat exchangers needed to increase the anode and cathode inlet streams to the desired temperature for correct cell operations were set to have both outlet temperature of 750°C in case of SOFC and 580°C in case of MCFC. The heat exchanger that cools the anode inlet is considered to exchange heat with the utilities of the vessels. Instead, the heat exchanger after the mixer of water vapour and LNG prior to the reforming reactor was imposed to have 50°C as difference between the cold and the warm streams. The heat exchanger with sea water at the anode outlet was set to have a gas outlet temperature of 30°C. The following water separation was simulated with a simple flash.

In this initial phase the membrane for H_2 separation was simulated using a simple separator unit imposing the 65% efficiency coupled with 65% purity as per literature [15].

Between the reforming and the exhaust gas coming from the burner there is exchange of heat that has been set to provide 10% heat in excess compared to the total duty required by the reforming reactor.

The separation of the CO_2 was modelled using a separator unit and considering the need of 0.2kWh for the liquefaction of 1 kg of CO_2. The liquid CO_2 is obtained at 25 bar and -40°C.

Finally, for the simulation of the fuel cell stacks a 0D simplified version of the home-made code called SIMFC was used. Developed and tested by the authors, it is based on mass, energy, and momentum balances and is capable to simulate the performance of high temperature fuel cells. The fundamental equations that describe the kinetics of the fuel cells are presented in previous works by the authors for both SOFCs [16] and MCFCs [17–19]. The main operating parameters and evaluated performances of the proposed configurations are reported in Table 1.

Table 1. Main parameters and evaluated performances of MCFC and SOFC in HFO and LNG cases

	HFO Case - MCFC	HFO Case - SOFC	LNG Case - MCFC*	LNG Case - SOFC*
Utilization of CO_2 [%]	85	/	83	/
Utilization of H_2 [%]	76,5	75,5	76,5	75,5
Current density [A/m^2]	1000	5000	1400	5000
Voltage single cell [V]	0,76	0,83	0,76	0,83
Area of single cell [m^2]	1	0,04	1	0,04
Number of cell [-]	1102	22360	2500	105810
Power [kW]	842	3693	2651	17474
*during navigation				

4.2 Heavy Fuel Oil (HFO) case

The reference passenger ship fuelled with HFO uses a main engine with MCR (Maximum Continuous Rating) power of about 11060 kW. For one day its operation time can be divided between navigation (18 hours with engine load of 59%), manoeuvring (2 hours with engine load of 27%) and port operations (4 hours with engine load of 27%). To avoid too stressed operating conditions during manoeuvring and in port, it was decided to act only on the exercise in navigation to meet the overall 20% reduction of the weekly emissions as averaged on all the operation time.

As the total emission of the ship without any modification are of about 538 t week^{-1} that can be divided between 479 t week^{-1} during navigation and 59 t week^{-1} during port operation and manoeuvring, to achieve the 20% weekly reduction, the cell stacks have to reduce the navigation CO_2 emission to 372 t week^{-1} as it is shown in Fig. ***3***-A. Fixing this value, calculations have been made to evaluate the SOFC and MCFC stack requirements, the percentage at which the engines should work, and new fuel requirements.

As shown in the graph Fig. ***4***, in the case of SOFC, it was determined that to meet such requirements the stack must provide a total energy output of about 66.5 MWh day^{-1}, that can be provided using 45 modules, each made of 500 cells having area of 0.04 m^2 and working with a current of 5000 A m^{-2}. This quite small size of each single cell is dictated by the current technological state of the art.

In these conditions, the engine must provide 50.5 MWh day^{-1}, which means that the engine would work with a load of about 25% (total maximum energy provided is of about 199 MWh day^{-1}).

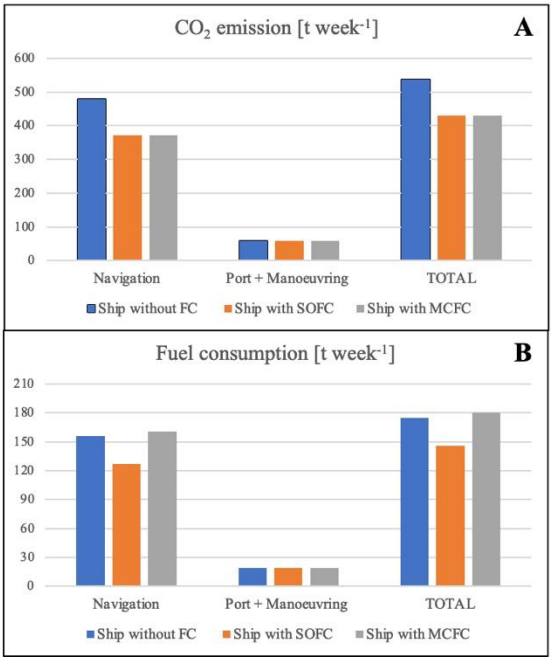

Fig. 3: Weekly CO_2 emission (A) and fuel consumption (B) of the HFO fuelled ship using the traditional combustion engine only, and the engines integrated with an SOFC or an MCFC system.

In such operating conditions, as shown in the graph B of Fig. ***3***, the fuel consumption of the systems considering both the HFO fed to the engines and the LNG fed to the stack decreases of about 16.6%. However, since the engine would need to work at 25% of its total load, this solution does not seem practical for retrofitting on this kind of ship. In fact, it is usually desirable to not operate the combustion engines with load lower than 40%, while it can be accepted just for short periods of time such as during manoeuvring or port operations. So, in this case, it would be preferable to substitute the engines with smaller ones to avoid excessive losses or directly substitute the engines with an opportune SOFC stack.

In the case of MCFC, as shown in the graph Fig. ***4***, it was determined that to meet CO_2 emission requirements the stack must provide a total energy output of about 15 MWh day^{-1} that can be provided using 2 modules, each made of 550 single cells having area of 1 m^2 and working with a current of 1100 A, according with the technology state of the art. In these conditions, the engine must provide 105 MWh day^{-1}, which means that the engine would work with a load of about 52.8%. Of this power, it is to be noted that about 3 MWh day^{-1} are needed for the liquefaction of CO_2, and this explains why thy energy required in this case is slightly higher than in the other cases. In such operating conditions, as shown in the graph B of Fig. ***3***, the fuel consumption of the systems considering both the HFO fed to the engines and the LNG fed to the stack increases of about 3.2%.

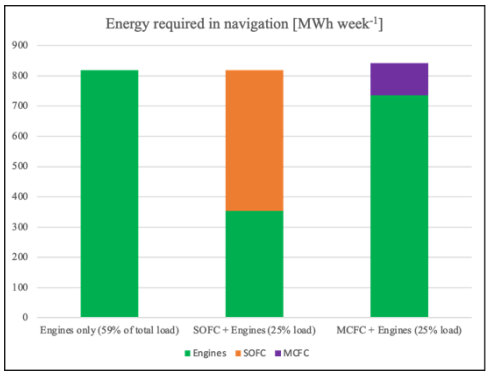

Fig. 4: Total daily energy required by the HFO fuelled ship during navigation using traditional engines only, and the engines integrated with an SOFC or an MCFC system.

4.3 Liquified Natural Gas (LNG) case

The reference passenger ship fuelled with LNG uses two main engines with total MCR power of about 30880 kW. For one day its operation time can be divided between navigation (15.5 hours with engines load of 78%), and manoeuvring as well as port for which only one of the two engines is used (8.5 hours with engine load of 50%). In this case, it was possible to reduce the emission of both phases to achieve a reduction in total CO_2 weekly emission of 20%.

As shown in the graph A of Fig. 5, the total emission of the ship without any modification are of about 1656 t week^{-1} that can be divided between 1398 t week^{-1} during navigation and 258 t week^{-1} during port operation and manoeuvring.

As only the final emission reduction value of 20% is known, the desired result was achieved through iterative calculations.

In the SOFC case it was determined that a stack made of 212 modules using 500 cells having area of 0.04 m^2 and working with a current of 5000 A m^{-2} during navigation and the same stack using only 20 modules during port operation and manoeuvring are suitable for achieving the desired CO_2 emission reduction. When the vessel is in navigation, the stack will provide a total energy of about 271 MWh day^{-1} with the engines that would consequently need to provide 102.5 MWh day^{-1}, which is about 21% of the total load (around 479 MWh day^{-1}). When the vessel is manoeuvring or doing port operation, the stack will provide a total energy of about 13.6 MWh day^{-1} with the engines that would consequently need to provide 52 MWh day^{-1} which is about 40% of the total load (around 131 MWh day^{-1}). Both these results are shown in graphs A and B of Fig. ***6***. Under these operating conditions, the emission are reduced to 1084 t week^{-1} (22%) during navigation and 242 t week^{-1} (6%) during manoeuvring and port operation, for a total of about 1325 t week^{-1} that corresponds to the desired 20% reduction, as shown in graph A of Fig. 5. As in the previous case with ship fuelled with HFO, as shown in Fig. 5, the total fuel consumption, which in this case is represented only by LNG, is reduced of about 8.8%.

Also in this case using an SOFC stack the reduction target is achievable, but the load of the engines results too low, so that a retrofitting approach seems not suitable.

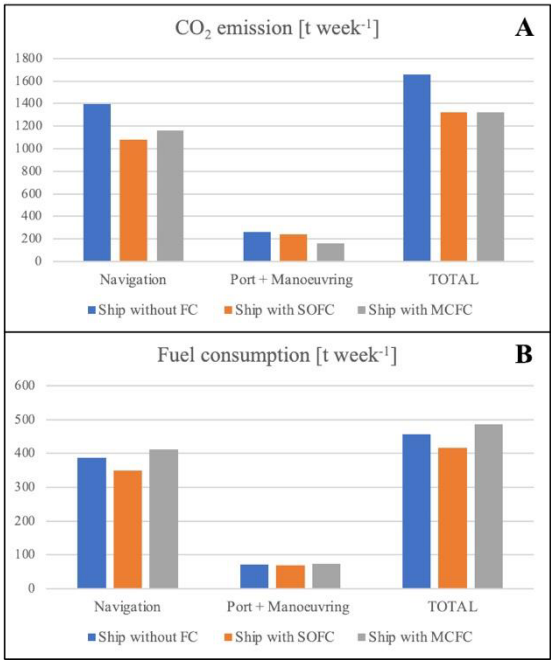

Fig. 5: Weekly CO_2 emission (A) and fuel consumption (B) of the LNG fuelled ship using the traditional combustion engine, and the engines integrated with an SOFC or an MCFC system.

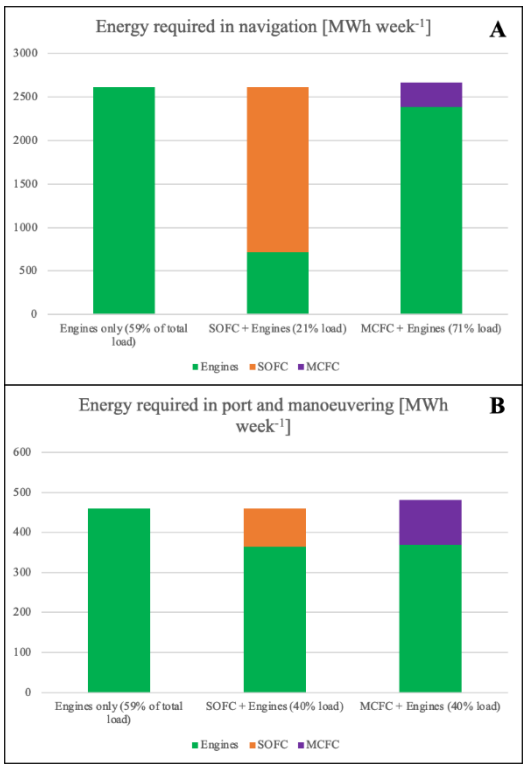

Fig. 6: Total daily energy required by the LNG fuelled ship during navigation (A) and during manoeuvring and port activities using traditional engines only, and the engines integrated with an SOFC or an MCFC system.

In the MCFC case it was determined that a stack made of 5 modules using 500 cells having area of 1 m^2 and working with a current density of 1400 A m^{-2} during navigation and the same stack using 1000 A m^{-2} during port operation and manoeuvring are suitable for achieving the desired CO_2 emission reduction. When the vessel is in navigation, the stack will provide a total energy of about

41.1 MWh day^{-1} with the engines that would consequently need to provide 340.5 MWh day^{-1}, which is about 71% of the total load (around 479 MWh day^{-1}). Of this amount 8 MWh day^{-1} will be used for CO_2 liquefaction. When the vessel is manoeuvring or doing port operation, the stack will provide a total energy of about 16.1 MWh day^{-1} with the engines that would consequently need to provide 52.7 MWh day^{-1} which is about 40% of the total load (around 131 MWh day^{-1}). Of this amount 3.2 MWh day^{-1} will be used for CO_2 liquefaction. Both these results are shown in graphs A and B of Fig. ***6***. Under these operating conditions, the emission are reduced to 1163 t week^{-1} (16.8%) during navigation and 161 t week^{-1} (37.7%) during manoeuvring and port operation, for a total of about 1324 t week^{-1} that corresponds to the desired 20% reduction, as shown in graph A of Fig. 5. As in the previous case with ship fuelled with HFO, as shown in Fig. 5, the total fuel consumption, which in this case is represented only by LNG, increases of about 6.2%.

5 Conclusions

In this work, the authors presented a new approach for the mitigation of CO_2 emission in the maritime sector by coupling high temperature fuel cells and combustion engines with the aim to minimise the impact on the traditional ship design.

To study the feasibility of this proposal, the author investigated two systems: one coupling combustion engines and SOFC stacks to provide the required power, and one coupling combustion engines and MCFC stacks to provide the required power as well as to segregate the produced CO_2.

Both systems were studied considering two passenger ships operating with combustion engines fuelled using either LNG or HFO.

The results of the study showed both the solutions have potential for the reduction of CO_2 emissions respecting the IMO regulations.

Nevertheless, the SOFC solution resulted not suitable for simple ship retrofitting, as it would involve a too extreme reduction of the working load of the engines (about 20% during navigation) thus requiring either the substitution of the engines with smaller ones or a complete substitution of the engines with SOFC stack of appropriate size.

On the over hand, the simulation showed that an MCFC stack can be effectively used to reduced CO_2 emission while maintaining the same combustion engines operating at reduced load. Although this solution involved a higher fuel consumption (3.2% in the HFO fuelled ship case and 6.2% in the LNG fuelled ship case), its benefits make it interesting for more detailed investigation using more detailed modelling (i.e.: 2D or 3D model of the cell stack) and focusing more the attention on the energy balance for better integration with the utilities of the ship.

Thus, MCFC is proposed as a valid solution to mitigate the CO_2 emissions with a ship retrofitting policy which allows urgent and efficient actions and follows the energy transition phase.

References

[1] C. Deniz, B. Zincir, Environmental and economical assessment of alternative marine fuels, J. Clean. Prod. 113 (2016) 438–449. https://doi.org/https://doi.org/10.1016/j.jclepro.2015.11.089.

[2] International Maritime Organization, Fourth IMO GHG Study 2020, 2021. https://www.imo.org/en/OurWork/Environment/Pages/Fourth-IMO-Greenhouse-Gas-Study-2020.aspx.

[3] O.B. Inal, C. Deniz, Assessment of fuel cell types for ships: Based on multi-criteria decision analysis, J. Clean. Prod. 265 (2020) 121734. https://doi.org/https://doi.org/10.1016/j.jclepro.2020.121734.

[4] F. Murena, L. Mocerino, F. Quaranta, D. Toscano, Impact on air quality of cruise ship emissions in Naples, Italy, Atmos. Environ. 187 (2018) 70–83. https://doi.org/https://doi.org/10.1016/j.atmosenv.2018.05.056.

[5] B. Dragović, E. Tzannatos, V. Tselentis, R. Meštrović, M. Škurić, Ship emissions and their externalities in cruise ports, Transp. Res. Part D Transp. Environ. 61 (2018) 289–300. https://doi.org/https://doi.org/10.1016/j.trd.2015.11.007.

[6] H. Xing, C. Stuart, S. Spence, H. Chen, Fuel Cell Power Systems for Maritime Applications: Progress and Perspectives, Sustain. . 13 (2021). https://doi.org/10.3390/su13031213.

[7] O.B. Inal, C. Deniz, Emission Analysis of LNG Fuelled Molten Carbonate Fuel Cell System for a Chemical Tanker Ship: A Case Study, Mar. Sci. Technol. Bull. 10 (2021) 118–133. https://doi.org/https://doi.org/10.33714/masteb.827195.

[8] A. Haseltalab, L. van Biert, H. Sapra, B. Mestemaker, R.R. Negenborn, Component sizing and energy management for SOFC-based ship power systems, Energy Convers. Manag. 245 (2021) 114625. https://doi.org/https://doi.org/10.1016/j.enconman.2021.114625.

[9] P. Wu, R. Bucknall, Hybrid fuel cell and battery propulsion system modelling and multi-objective optimisation for a coastal ferry, Int. J. Hydrogen Energy. 45 (2020) 3193–3208. https://doi.org/https://doi.org/10.1016/j.ijhydene.2019.11.152.

[10] Zemships. One Hundred Passengers and Zero Emissions: The First Ever Passenger Vessel to Sail Propelled by Fuel Cells., n.d.

https://webgate.ec.europa.eu/life/publicWebsite/index.cfm?fuseaction=search.dspPage&n_proj_id=3081.

[11] E. Ovrum, G. Dimopoulos, A validated dynamic model of the first marine molten carbonate fuel cell, Appl. Therm. Eng. 35 (2012) 15–28. https://doi.org/https://doi.org/10.1016/j.applthermaleng.2011.09.023.

[12] C. Strazza, A. Del Borghi, P. Costamagna, A. Traverso, M. Santin, Comparative LCA of methanol-fuelled SOFCs as auxiliary power systems on-board ships, Appl. Energy. 87 (2010) 1670–1678. https://doi.org/https://doi.org/10.1016/j.apenergy.2009.10.012.

[13] I. EG&G Technical Services, Fuel Cell Handbook, Fuel Cell. (2004). https://doi.org/10.1002/zaac.200300050.

[14] M. Buga, M. Balan, I. Iordache, M. Varlam, A comparative simulation and sensitivity analysis study of hydrogen production by steam methane reforming, Prog. Cryog. Isot. Sep. 17 (2014) 15-22. https://link.gale.com/apps/doc/A434414210/AONE?u=anon~dcc0994f&sid=googleScholar&xid=8927d964

[15] K. Yang, Y. Ban, A. Guo, M. Zhao, Y. Zhou, N. Cao, W. Yang, In-situ interfacial assembly of ultra-H2-permeable metal-organic framework membranes for H2/CO2 separation, J. Memb. Sci. 611 (2020) 118419. https://doi.org/https://doi.org/10.1016/j.memsci.2020.118419.

[16] F.R. Bianchi, A. Baldinelli, L. Barelli, G. Cinti, E. Audasso, B. Bosio, Multiscale modeling for reversible solid oxide cell operation, Energies. 13 (2020). https://doi.org/10.3390/en13195058.

[17] T.A. Barckholtz, H. Elsen, P.H. Kalamaras, G. Kiss, J. Rosen, D. Bove, E. Audasso, B. Bosio, Experimental and Modeling Investigation of CO3=/OH– Equilibrium Effects on Molten Carbonate Fuel Cell Performance in Carbon Capture Applications, Front. Energy Res. 9 (2021) 235. https://www.frontiersin.org/article/10.3389/fenrg.2021.669761.

[18] E. Audasso, B. Bosio, D. Bove, E. Arato, T. Barckholtz, G. Kiss, J. Rosen, H. Elsen, R. Blanco Gutierrez, L. Han, T. Geary, C. Willman, A. Hilmi, C.Y. Yuh, H. Ghezel-Ayagh, New, dual-anion mechanism for Molten Carbonate Fuel Cells working as carbon capture devices, J. Electrochem. Soc. (2020). https://doi.org/https://doi.org/10.1149/1945-7111/ab8979.

[19] E. Audasso, B. Bosio, D. Bove, E. Arato, T. Barckholtz, G. Kiss, J. Rosen, H. Elsen, R. Blanco Gutierrez, L. Han, T. Geary, C. Willman, A. Hilmi, C.Y. Yuh, H. Ghezel-Ayagh, The effects of gas diffusion in Molten Carbonate Fuel Cells working as carbon capture devices, J. Electrochem. Soc. 167 (2020) 114515. https://doi.org/https://doi.org/10.1149/1945-7111/aba8b6.

Effects of $(Li\text{-}Na)_2CO_3$ on The Electrical Properties of Calcia-Stabilized Zirconia/Carbonate Composite Electrolytes

Aiman Iqbal [1], *Pramujo* Widiatmoko[1], and *Hary* Devianto[1,*]

[1] Department of Chemical Engineering, Faculty of Industrial Technology, Institut Teknologi Bandung, Jl. Ganesha No. 10, Bandung 40132, Indonesia.

Abstract. Calcia-Stabilized Zirconia (CSZ) is potential as low-cost electrolytes material for Solid oxide fuel cell (SOFC). It is fluorite structure widely known as oxygen ion conductors. Addition of carbonate salt into fluorite-based electrolyte is common to overcome low conductivity of CSZ as well as to decrease sintering temperature. Increase of ionic conductivity in the SOFC electrolyte is also influenced by presence of protons (H^+), so it is called mixed-ion electrolytes. In this study, the effect of sintering temperature and carbonate content prepared from mixture of Li_2CO_3 and Na_2CO_3 on the relative density, ionic conductivity and microstructure of electrolyte and fuel cell performance was investigated. The sintered CSZ/carbonate samples were examined physically and electrochemically by using SEM, TEM, XRD, and EIS. The unique detail of nanostructure for CSZ/carbonate was investigated by TEM. The XRD is to observed peak associating with CSZ, Li_2CO_3, and Na_2CO_3, as well as its crystallinity. Moreover, the electrolyte resistance was measured by EIS so that the proton conductivity and oxygen conductivity of CSZ/carbonate can be calculated. The improvement of low-cost electrolyte material such as CSZ can be realized by providing protons pathway.

1. Introduction

Fuel cell is an energy conversion device that produces electricity by electrochemical reaction. A fuel cell consist of two electrodes and electrolyte. Fuel is fed to the anode where it is oxidized and oxidant is fed to the cathode where it is reduced. Fuel cells are classified by electrolyte and temperature consist of polymer electrolyte membrane fuel cells (PEMFC), alkaline fuel cells (AFC), molten carbonate fuel cells (MCFC) and solid oxide fuel cells (SOFC). Among the types of fuel cells, SOFC offer diversified advantages such as fuel flexibility, desirable energy (chemical-to-electrical) conversion efficiency that unlimited by Carnot cycle, chemically-non pollutant, lower emission of gases, generation of heat and electricity [1].

SOFC are one of the most promising fuel cell technology. The electrolytic material, being the heart of an SOFC unit has been a topic of interest and continuous development among many researchers. Nernst, in the 1890s, recognized yttria-stabilized zirconia (YSZs) as a potential electrolyte material owing to its property of oxide ion conductivity [2]. For high-temperature cells operating above 800^0C, doped zirconia, and especially yttria-stabilized zirconia (YSZ), remains the material of choice for the electrolyte. The long-term chemical stability of YSZ and compatibility with electrode materials are well proven. The synthesis of reactive zirconia powder and thin dense electrolyte film fabrication by tape casting, screen printing, calendaring, and chemical–electrochemical vapor deposition (EVD) processes are also well understood for implementation in large-scale manufacturing [3]. But the problems are caused by electrolyte material that function only a high temperature and lower ionic conductivity at lower temperature.

Stabilized-zirconia (ZrO_2), especially yttria-stabilized zirconia, is the most common electrolyte in SOFCs because the material possesses an adequate level of oxygen-ion conductivity and exhibits desirable stability in both oxidizing and reducing atmospheres. The properties of stabilized zirconia have been extensively studied. Currently applicated SOFC are based on oxides, for example YSZ and ceria with a fluorite structure. Fluorite has a simple structure group F*m3m.*

ZrO_2, in its pure form, does not serve as good electrolyte, primarily because its ionic conductivity is too low. At room temperature, ZrO_2 has a monoclinic (*m*) crystal structure. The monoclinic structure changes to a tetragonal (t) form above 1170^0C and to a cubic fluorite structure above 2370^0C. The cubic phase exists up to the melting point of 2680^0C. However, the addition of certain aliovalent oxides stabilizes the cubic fluorite structure of ZrO_2 from room temperature to its melting point and, at the same time, increases its oxygen vacancy concentration [4]. The most commonly used dopants are CaO, MgO, Y_2O_3 and Sc_2O_3.

* Corresponding author: hardev@che.itb.ac.id

Yttria-stabilized zirconia material has been widely used in SOFC as electrolyte. However, yttria material is expensive and it is not widely available especially in Indonesia. Calcia can stabilize zirconia to become CSZ in cubic phase, which is the most stable phase to allow the flow of oxygen ions. Calcia has an advantage as it can be operated at a lower temperature if it is combined with other material with high ionic conductivity [5]. Therefore calcia-stabilized zirconia is potential as low-cost material for electrolytes material for SOFC.

Electrolyte conductivity has been found to be greatly influenced by the grain boundary and grain resistance that are, in turn, affected by the grain size [6]. Grain boundaries or interior contacts between particles are barriers to limit the ionic conductivity since the grain boundary conductivity is much lower than (order) that of the grain thus blocks the ionic transport. Engineering of the grain boundaries is a top option to improve and develop material ionic conductivity [7]. In single phase materials, the nanosized particles expose large surfaces leading to high surface energy [6]. Second phase material can create interfaces and surface with effective functions. Addition of carbonate salt into fluorite based given proton pathway.

Wang et al. [8] fabricated SDC/carbonate (SDC/sodium carbonate) electrolytes based on core-shell type of particles. The particle size was < 100 nm and thickness of amorphous sodium carbonate shell varied from four to six nm. Proton conductivity (10^{-2} S cm^{-1} at 350^0C) varies from one to two orders of magnitude higher than oxygen conductivity in the temperature range 200-600^0C. Huang [9] was investigated about the cell with SDC/$(Li–Na)_2CO_3$ composite electrolyte showed the best performances, and the cell with SDC/$(Li–K)_2CO_3$ composite electrolyte showed slightly higher performances than the cell with SDC/$(Li–K)_2CO_3$ composite electrolyte. It indicates that the conduction mechanism of SDC/carbonate composite electrolytes is distinct in an air atmosphere and in a H_2/air fuel cell atmosphere. The possible oxygen ion/proton conduction in SDC/carbonate composites and excellent cell performances make them a novel electrolyte for cost-effective low-temperature SOFC.

Fuel cells with such an electrolyte have delivered attractive power output at low temperature. The dual ion electrolytes can combine the advantages of proton and oxygen ion conduction. Due to the dual ion conductivity, D-SOFCs no longer require an external humidification device, which can simplify the systems. By optimizing electrode materials and stability, D-SOFCs can achieve better performance at intermediate to low temperatures [10].

In this study, the effect of sintering temperature and carbonate content prepared from mixture of Li_2CO_3 and Na_2CO_3 on the relative density, ionic conductivity and microstructure of electrolyte and fuel cell performance was investigated. Li_2CO_3 and Na_2CO_3 in the molar ratio of 52Li:48Na to form a binary carbonate eutectic with a melting point temperature around 490^0C [11]. The sintered CSZ/carbonate samples were examined physically and electrochemically by using SEM, TEM, XRD, and EIS.

2. Methodology

The process of producing CSZ/carbonate consist of milling, dry pressing, and sintering. First step of the research was started with milling ZrO_2, CaO, PEG, PVA, Li_2CO_3 and Na_2CO_3. ZrO_2 and CaO materials were mixed with a weight ratio of 97:3. After that, PVA was added as a binder as much as 1% by weight and PEG as a plasticizer as much as 1% by weight. Li_2CO_3 and Na_2CO_3 materials were added with a molar ratio of 52:48. The composition of Li_2CO_3 and Na_2CO_3 was varied at 5,5%, 6,5% and 7,5% total weight from CSZ. Then all materials were mixed with ethanol as medium. The milling process was carried out using a ball milling for 12 hours and speed 40 rpm rotation. The process was then followed by filtration to obtain CSZ/carbonate powder. The next step was to produce electrolyte powder by drying process in oven at the temperature of 100^0C for 24 hours. The powder was dry pressed at 500 bar during 5 minutes. The last step CSZ/carbonate powder was sintered at various temperature such as 900, 1000, and 1100^0C.

Characterization was carried out on CSZ/carbonate electrolyte, including crystal structure analysis using x-ray diffractometer (XRD) along with microstructure and nanostructure analysis using scanning electron microscopy (SEM) and transmission electron microscopy (TEM). The electrolyte resistance was measured by electrochemical impedance spectroscopy (EIS) in a temperature range of 600-800^0C. Silver paste was painted on both surfaces of electrolyte. The resistivity under reducing or oxidizing atmosphere was monitored by continuously supplying anode gas (5% H_2, 95% N_2) or cathode gas (static air) to both sides of the electrolyte.

3. Result and Discussion

Through the review of CSZ electrolyte which has a single-phase material, the approach taken is to develop a material with two phases to form a strong interface. The carbonate salts bring some interesting results such as lowering sintering temperature, increasing ionic conductivity and enhancing the mechanical properties. This technology can realize superionic materials by building interfaces to form ion highways. As illustrated in Fig.1, the positive ions or protons (H^+) pass through the interfaces of the particles while oxygen ions (O^{2-}) pass through the host particles of CSZ. A Swing Model was further proposed for explaining the proton conduction in the CSZ/carbonate such as the mechanism that occurs in the Samarium-Doped Ceria/carbonate.

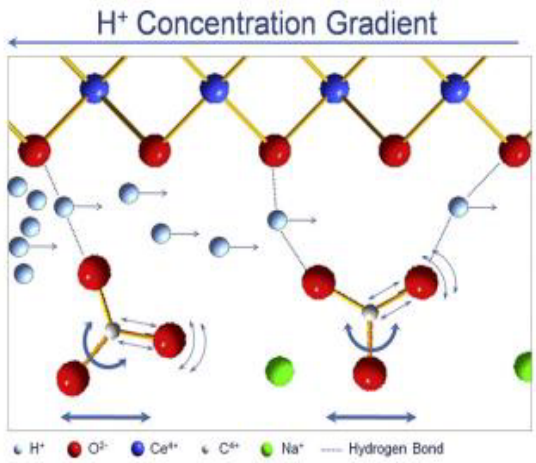

Fig. 1. Swing model pathway for SDC/carbonate [8].

Chen et al [11] investigated that the molten carbonate contributes to the total ionic conductivity of the composite, besides the oxygen ionic conductivity. While it is worthy to point out that only the source ions (oxygen ions, here) can dedicate the effective ionic conductivity and power output. When the temperature overcomes 500^0C, the solid oxide serves as a matrix with liquid carbonate phase surrounded. Continuous phase interface is consequently formed. Both the SDC and interface phase provide percolated networks for ions to pass through. Some pores existing in the electrolyte are observed in the cross-sectional images. Due to the low sintering temperature of only 700^0C which is restrained by the carbonate in the electrolyte, it is hard for the electrolyte to be fully dense. However, the composite electrolyte can still be used as an electrolyte of SOFC because the carbonates melt at working temperature and serve as seals to avoid gas crossover. When the temperature lowers down, the carbonates become solid and shrank, leading to residual pores in the composite electrolyte [12]. So therefore, adding salt carbonate especially Li_2CO_3 and Na_2CO_3 can serve a matrix in the CSZ electrolyte. The performance of CSZ electrolyte, which was originally a conductor of oxygen ions, was later improved to deliver protons so that it became a mixed ion electrolyte which enhanced total ionic conductivity and mechanical properties. While still speculative, these findings are interesting, and further research is in progress

References

1. Hussain, S. & Yangping, L. Review of solid oxide fuel cell materials: cathode, anode, and electrolyte. *Energy Transitions* **4**, 113–126 (2020).
2. Nernst, W. Uber die elektrolytische leitung fester körper bei sehr hohen temperaturen. *Zeitschrift für Elektro Chemie* **6**, 41–43 (1899).
3. Singh, P. & Minh, N. Q. Solid oxide fuel cells: Technology status. *Int. J. Appl. Ceram. Technol.* **1**, 5–15 (2004).
4. Minh, N. Q. Ceramic Fuel Cells. *J. Am. Ceram. Soc.* **76**, 563–588 (1993).
5. Nurbanasari, M., Syarif, D. G. & Irwan, Y. Characterization of Calcia Stabilized Zirconia as a solid Electrolyte Made through a sol gel Method in Solid Oxide Fuel Cell. 3056–3060 (2019).
6. Mahato, N., Gupta, A. & Balani, K. Doped zirconia and ceria-based electrolytes for solid oxide fuel cells: a review. *Nanomater. Energy* **1**, 27–45 (2012).
7. Zhu, B. No. *Int. J. ENERGY Res.* **33**, 1126–1137 (2009).
8. Wang, X. *et al.* Ceria-based nanocomposite with simultaneous proton and oxygen ion conductivity for low-temperature solid oxide fuel cells. *J. Power Sources* **196**, 2754–2758 (2011).
9. Huang, J., Gao, Z. & Mao, Z. Effects of salt composition on the electrical properties of samaria-doped ceria/carbonate composite electrolytes for low-temperature SOFCs. *Int. J. Hydrogen Energy* **35**, 4270–4275 (2010).
10. Shi, H., Su, C., Ran, R., Cao, J. & Shao, Z. Progress in Natural Science : Materials International Electrolyte materials for intermediate-temperature solid oxide fuel cells. *Prog. Nat. Sci. Mater. Int.* 0–1 (2020).
11. Chen, M., Zhang, H., Fan, L., Wang, C. & Zhu, B. Ceria-carbonate composite for low temperature solid oxide fuel cell: Sintering aid and composite effect. *Int. J. Hydrogen Energy* **39**, 12309–12316 (2014).
12. Di, J. *et al.* Samarium doped ceria-(Li/Na)2CO3 composite electrolyte and its electrochemical properties in low temperature solid oxide fuel cell. *J. Power Sources* **195**, 4695–4699 (2010).

Redox Cycling for SOFC Accelerated Degradation

Daria Vladikova[1]*, *Blagoy* Burdin[1], *Asrar* Sheikh[1], *Paolo* Piccardo[2], *Milena* Krapchanska[1], and *Dario* Montinaro[3]

[1] Institute of Electrochemistry and Energy Systems - Bulgarian Academy of Sciences, 10 Acad. G. Bonchev, 1113 Sofia, Bulgaria
[2] Dipartimento di Chimica e Chimica Industriale - University of Genova, via Dodecaneso 31, I-16146 Genoa, Italy
[3] SOLIDpower S.p.A, Viale Trento 117, 38017, Mezzolombardo, Italy

Abstract. This work aims at development of Accelerated Stress Tests for SOFC via artificial aging of the fuel electrode applying chemical and electrochemical (hydrogen starvation) redox cycling. In principle the degradation processes follows that of calendar aging (Ni coarsening and migration), but in addition it can bring to irreversible damages caused by the development of cracks at the interface anode/electrolyte due to the expansion/shrinkage of the Ni network. The challenge is to introduce conditions which will prevent the formation of cracks which can be done by partial oxidation. The advantage of the proposed methodology is that a mild level of oxidation can be regulated by direct impedance monitoring of the Ni network resistance changes during oxidation/reduction. Once the redox cycling conditions are fixed on bare anode and checked on anode/electrolyte sample for eventual cracks, the procedure can be introduced for AST in full cell configuration. The developed methodology is evaluated by comparative impedance analysis of artificially aged and calendar aged button cells. The results for 20 redox cycles which can be performed for 24 hours are comparable with those obtained for about 1600 hours operation in standard conditions which ensures more than 50 times acceleration.

1. Introduction

Among fuel cells SOFC is an emerging technology for the efficient production of electricity [1] and hydrogen [2] implying low CO_2 emissions [1]. Moreover, the possibility of being operated with different fuels [3] and in two modes - fuel cell and steam electrolysis, makes them perspective [2]. The SOFC technology is still away from commercialization mainly due to the problem of durability and lifetime [4]. Currently the lifetime requirement for SOFC is at least 40,000 hours [5], but testing for such long lifetimes is not viable. This problem can be overcome by the introduction of Accelerated Stress Tests (AST), which should ensure the investigation of long term phenomena in a shorter time.

This work aims at presenting an approach for AST based on artificial redox cycling of the anode in cell configuration before operation. Principally the same approach can be applied also for stack configuration. There are intensive studies of the anode degradation, since it influences strongly the durability of the fuel cell. The most often used anode material is Nickel-yttria stabilized zirconia (Ni-YSZ) cermet. The anode is a multifunctional component which has high catalytic activity and electronic conductivity coming from the Ni network, optimized porosity ensuring the fuel input and the exhaust water output combined with strong mechanical stability, since it is most often used as cell support.

The main degradation of the anode during operation comes from the microstructural changes in the Ni network, due to both Ni agglomeration resulting in a phase coarsening and migration and volatilization changing the Ni distribution in the electrode. The Ni mean particle diameter increases due to the sintering of the smaller particles. The global effect is decrease of the triple phase boundaries (TFB) and of the Ni/gas specific surface area [6-20]. The migration over long distances can bring to Ni depletion near the electrolyte interface [8].

During long term operation the fuel electrode degrades due to Ni re-oxidation that causes microstructural changes [21,22] that bring to accelerated degradation. This

* Corresponding author: d.vladikova@iees.bas.bg

phenomenon can be caused by leakage, fuel starvation, increased oxygen partial pressure, accidental switch off, etc. The repetitive changes of Ni volume damage the cermet structure in two directions: (i) reduction of the TPB density due to accelerated Ni coarsening and (ii) production of cracks at the electrode/electrolyte interface [23-28]. The degradation can be evaluated by electrochemical testing followed by microstructural post mortem characterization based on comparative analysis between pristine and cycled samples. Dynamic in situ analyses recording the changes in the microstructure exposed to different redox conditions are also reported, however, they are performed in conditions which strongly differ from the operating environment [28-31]. Most often the chemical oxidation is performed in a furnace at high temperature and enough long time which brings to oxidation of the entire Ni network. There are some studies where partial oxidation is carried out [32] which report that when the oxidation of about 25 % at 800^{o}C, no cracks are observed at the interface electrode/electrolyte. At lower temperatures the deepness of oxidation with no cracks formation could be even higher.

The analysis of the degradation caused by redox cycling shows that this approach which also causes Ni coarsening and migration can be used as a tool for accelerated degradation. However, the Accelerated Stress Tests should cause changes of the system similar to those obtained during calendar aging, i.e. the redox cycling conditions should prevent from cracking at the electrode/electrolyte interface which can be achieved by partial re-oxidation.

The challenge of the redox cycling approach is the governance of the process which should reproduce standard aging. This work proposes a method for artificial aging via redox cycling which can be governed and fine-tuned applying impedance monitoring of the oxidation level. Two approaches are selected: (i) chemical oxidation which starts from the outer part of the anode and influences the whole volume of the fuel electrode and (ii) electrochemical redox cycling via hydrogen starvation which localizes the redox cycling area in the vicinity of the interface electrode/electrolyte.

2. Experimental

The chemical oxidation is performed by consecutive change of the anode compartment gas flow from N_2+H_2 blend to air. A three-step procedure is applied:

- The redox cycling conditions which should determine the oxidation deepness are defined on experiments performed on bare anode mounted between two Pt nets [33]. This configuration ensures direct monitoring of the Ni network formation and changes during oxidation by impedance measurements of its resistance which has the typical for metallic conductivity inductive behavior. Fig. 1 shows a selected change of the Ni network resistance during oxidation. For ensuring partial oxidation the level of oxidation should not change the inductive behavior of the impedance which guarantees that the Ni network is not totally destroyed (Fig. 1). It should be noted that the absolute value of the Ni network resistance in the anode matrix is much lower than the measured one which includes also the ohmic resistance of the test rig. However, this parameter is very sensitive to the changes of the Ni network in respect to oxidation and can be used as internal standard for governing and monitoring of the process. Once the oxidation conditions are selected, high level of reproducibility is ensured (Fig. 1). They are further used for the redox cycling experiments in cell configuration. The level of aging is controlled by the number of redox cycles.
- The selected redox cycling regime is applied on anode/electrolyte sample for checking the interface anode/electrolyte which should not be influenced by the aging conditions and cycling. In this configuration (as well as in full cell) the Ni oxidation/reduction cannot be any more directly monitored and the measured impedance registers the effect of the governed oxidation/reduction on the total behavior of the investigated configuration.
- The final stage is the redox cycling on full cell.

The monitoring of the level of aging is performed by measurements of current voltage (*i-V*) curves after selected number of redox cycles and analysis of the impedance diagrams measured after every cycle at OCV (Fig. 2) and periodically in different working points. After the final redox cycle post mortem analysis for microstructural characterization is also performed.

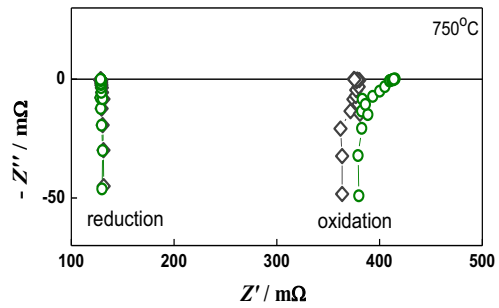

Fig. 1. Bare anode during redox cycling: two consecutive redox cycles – Cycle 7 (◊) and Cycle 8 (o).

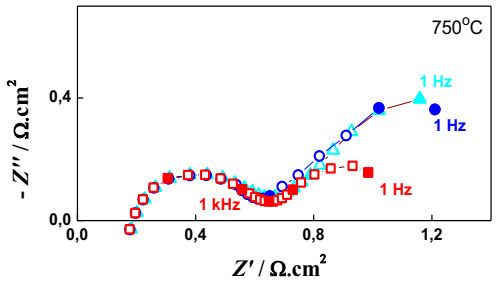

Fig. 2. Redox cycling of button cell at OCV: Oxidation 1 (▲), Oxidation 6 (●), Reduction 6 (■).

The chemical redox cycling was carried out on button cells at 750°C. More detailed information about the redox cycling procedure is described in [33].

The electrochemical redox cycling was performed directly on button cell configuration under load at 800°C - the temperature of the initial reduction. On the cathode side there is constant air gas flow. On the anode side the selected blend of hydrogen and nitrogen is periodically replaced with pure nitrogen which is accompanied by voltage drop.

The sample configurations were prepared by SOLIDpower according to a technological procedure which is subjected to proprietary information: NiO-YSZ anode pellets (bare anode) with diameter 20 mm and thickness 250 µm; anode/electrolyte with the same anode and 10 µm thick electrolyte (8 mol % Y_2O_3 stabilized zirconia) with GDC barrier layer; anode supported button cell with the same anode/electrolyte and oxygen electrode $(La,Sr)(Co,Fe)O_{3-\delta}$ (LSCF) perovskite with active surface area 0,28 cm^2 and $(La,Sr)CoO_{3-\delta}$ (LSC) layer on top for efficient current collection.

The test rig consists of a completely ceramic housing. The cell is sealed on the cathode side by ceramic paste (Ceramabond) following the procedure of the producer (Aremco products Inc). The testing was performed at 750°C and gas flows: air 435,7 $Nml.min^{-1}.cm^{-2}$ and hydrogen 102,9 $Nml.min^{-1}.cm^{-2}$.

The impedance measurements were carried out on IVIUM CompactStat in a frequency range from 1 MHz down to 1 Hz with density 5 points/decade in the temperature range from 22 to 800°C and amplitude of the AC signal depending on the impedance of the sample. A furnace with DC power supply and temperature drift during measurements less than 0,5°C ensures reproducible data with high quality. For the redox cycling experiments Pt meshes were used for contacts which makes the system stable in both oxidizing and reducing atmosphere.

Post mortem microstructure and porosity analysis were performed on Scanning Electron Microscope (SEM) Zeiss EVO 40 with acceleration voltage of 20 kV, equipped with an energy dispersive X-ray spectroscope (EDXS Pentafet). SEM BSE pictures with magnification 5000x were collected for quantitative image analyses and treated with Zeiss Axiovision software to estimate the porosity and Ni crystals volume fraction.

3. Results and discussion

3. 1. Chemical redox cycling

The chemical aging of button cells via redox cycling was performed in two regimes that ensure partial oxidation: Regime 1 with 2 times increase of the initial resistance of the Ni network and Regime 2 with 4 times increase. The two selected oxidation depths do not change the inductive behavior of the bare anode impedance diagrams during oxidation which shows that the Ni network is not destroyed, i.e. that partial oxidation is kept (Fig. 1).

SEM images register Ni coarsening after 20 redox cycles of bare anode performed according to Regime 1. Since the Ni grains have irregular shape, their size is presented as surface area (μm^2). The comparison of the distribution of pristine (reduced) anode and the aged one shows more irregular distribution with a tendency for rearrangement and increase of the fraction with larger grains for the redox cycled sample (Fig. 3).

The most challenging moment in the AST performance by redox cycling is the governing of the degradation level. On this stage a comparison with calendar aged cells based on impedance measurements is applied. The samples are prepared by the same technology and have the same composition. However, the information is selected from experiments performed in different operating conditions and test benches. Especially for impedance analysis the diagrams depend on the selected

working point (Fig. 4). That is why the comparison was made based on the Area Specific Resistance (ASR) change in percentage (%) after a definite number of cycles. Table 1 presents a summary of the experimental results performed applying Regime 2, while Table 2 gives similar information for calendar aging reaching 1200 hours.

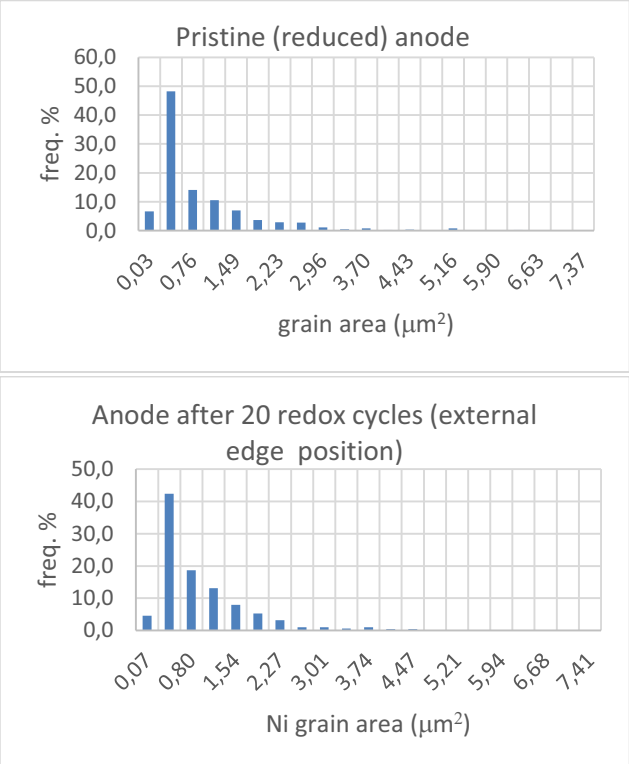

Fig. 3. Ni grain size distribution of bare anode before and after 20 redox cycles presented as grain area (µm²).

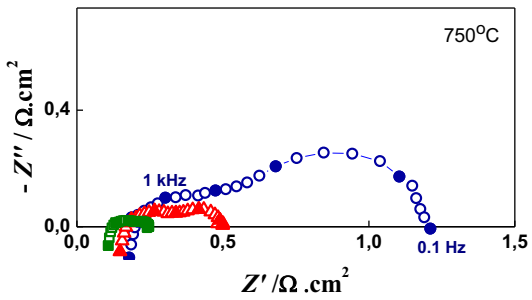

Fig. 4. Impedance diagrams of button cell recorded before redox cycling at 3 Working points: OCV (●); 0,11 A.cm^{-2} (▲); 0,29 A.cm^{-2} (■).

The experimental results show that between the 1st and the 6th redox cycle the ohmic resistance of the cell decreases (Fig. 5, Table 1) which is typical for the first 1000 hours of calendar aging, as it is presented in Fig. 6 and Table 2. Although the total resistance does not increase drastically and even may decrease (Table 2 - 600 hours), the increase of the polarization resistance is significant. Further and more detailed comparative analysis of the impedance data is under performance for extraction of additional information about the aging caused by the cell anode. The semiquantitative comparison between the data presented in Tables 1 and 2 can bring to the conclusion that the 20 redox cycles performed by Regime 2 can be compared with calendar aging exceeding 1200 hours. If we accept that the accelerated aging corresponds to about 1600 hours calendar operation, and taking into account that the performance of the 20 cycles needs 3 working days, i.e. about 24 hours, the acceleration factor could be evaluated on 66 which is very promising result. For more precise calculations, the number of redox cycles should be further increased.

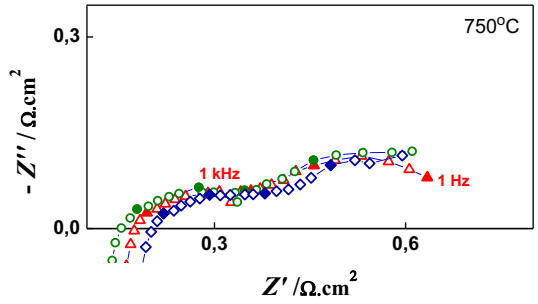

Fig. 5. Impedance diagrams of button cell at OCV during redox cycling: reduction 1 (▲); reduction 6 (●); reduction 8 (◆).

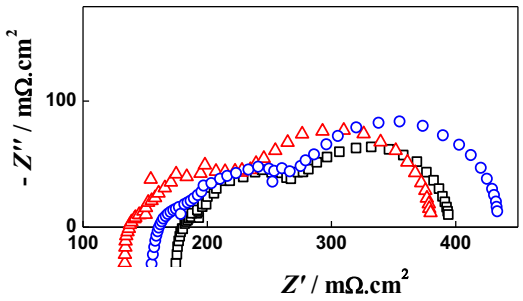

Fig. 6. Impedance spectra of calendar aged cell operated 1200 hours: 0h (□); 600h (△); 1200h (○).

3. 2. Electrochemical redox cycling via hydrogen starvation

In respect to the electrochemical redox cycling, preliminary experiments were performed on button cell operated at 180 mA.cm^{-2} by replacing the H_2 gas flow

with N_2 (435,7 ml.min^{-1}.cm^{-2}) for 480 sec., divided in 3 cycles of 160 sec. During every cycle the OCV was left to decrease down to 100 mV thus introducing conditions of hydrogen starvation in the reaction area. After every cycle, due to diffusion of hydrogen from the neighbouring regions, the OCV was increasing. After the last cycle it was established at 716 mV. The anode reduction takes place in the first 2 minutes when the cell resistance sharply decreases and OCV jumps from 716 up to 1040 mV. In the next 28 minutes, the polarization resistance slightly increases, which may be related to the release of the extra water formed during the reduction and the OCV reaches its initial value (1120 mV). The cell impedance before, during and after electrochemical oxidation is presented in Fig. 7 and Table 1. The comparison between the initial and final state shows high level of degradation (about 100% increase of the polarization resistance) which is confirmed also by the break of the sample in the end of the experiment. The results confirm the applicability of the electrochemical reoxidation. However, the experimental conditions should be adjusted towards those obtained by the chemical reduction in respect to oxidation depth which should not bring to cracks and delamination at the anode/electrolyte interface. A more precise procedure and criterion for oxidation depth, i.e. for level of hydrogen deficiency are under development.

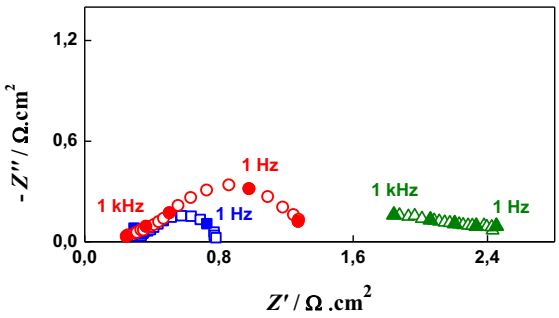

Fig. 7. Impedance diagrams of cell subjected to electrochemical redox cycling: before oxidation (□), end of oxidation (△), after 30 minutes reduction (○).

Table 1. Chemical and electrochemical aging via redox cycling.

Parameter	**R (mΩ.cm^2)**							**% Change (vs. 0 cycles)**			
	0 cycles **	*6 cycles* **	*0 cycles* *	*7 cycles* *	*20 cycles* *	*0 cycle* ***	*1 cycle* ***	*6 cycles* **	*7 cycles* *	*20 cycles* *	*1 cycle* ***
R_Ω	174,2	156,5	58,7	59,8	63,5	288,4	254,8	-10,2	+1,9	+8,2	-11,7
R_p	568,1	666,2	59,8	39,7	42,5	492,8	1016,4	+17,3	+16,4	+24,5	+106,3
R_T	742,3	822,7	92,8	99.5	106,0	781,2	1271,2	+10,8	+7,2	+14,2	+62,7

*i = 510 mA.cm^{-2}
** OCV
*** H_2 starvation (i = 180 mA.cm^{-2})

Table 2. Calendar aging of button cell (i = 500 mA.cm^{-2}).

Parameter	**R (mΩ.cm^2)**			**% Change (vs. 0 pristine sample)**	
	0 h	*600 h*	*1200 h*	*600 h*	*1200 h*
R_Ω	180,6	137,0	160,2	-14,1	-11,4
R_p	212,8	242,8	272,8	14,1	28,2
R_T	393,4	393,4	433,0	-3,5	10,0

4. Conclusions

The developed procedure for accelerated degradation via artificial aging of the anode by chemical redox cycling confirms the applicability of the approach, which shows very high level of acceleration. The selected oxidation depths are reasonable and well reproducible. The efforts should be concentrated on the correlation between the redox cycles and the degradation level for which additional comparative studies with calendar aged cells are needed. For better comparison with field tests, button cells are produced from aged stacks. They will be tested in the same testing conditions, including equipment. The microstructural changes are also reliable information source which will be used more intensively. On this stage of development, the procedure demonstrates more than 50 times acceleration of the degradation which determines the artificial aging of the anode via redox cycling as a powerful tool for accelerated stress tests.

5. Acknowledgements

The research leading to these results received funding from the Fuel Cells and Hydrogen 2 Joint Undertaking under grant agreement № 825027. This Joint Undertaking receives support from the European Union's Horizon 2020 research and innovation program and Hydrogen Europe. The experiments were performed with equipment supported by the Bulgarian Ministry of Education and Science under the National Roadmap for Research Infrastructure 2017-2023 “Energy storage and hydrogen energetics (ESHER)”, approved by DCM № 354/29.08.2017.

6. References

1. E. Pahon, N. Yousfi Steiner, S. Jemei, D. Hissel, M.C. Pᵉra, K. Wang, P. Moçoteguy, Int. J. Hydrogen Energy, 2016, **41,** 13678.
2. J. Laurencin, M. Hubert, D. Ferreira Sanchez, S. Pylypko, M. Morales, A. Morata, B. Morel, D. Montinaro, F. Lefebvre-Joud, E. Siebert, Electroc. Acta, 2017, **241,** 459.
3. Y. Heo, J. Lee, S. Lee, T. Lim, S. Park, R. Song, C. Park, D. Shin, Int. J. Hydrogen Energy, 2011, **36**, 797.
4. A. Hagen, J. Hogh, R. Barfod, J. Power Sources, 2015, **300,** 223.
5. A. Ploner, A. Hagen, A. Hauch, J. Power Sources, 2018, **395,** 379.
6. S. J. Kim, M. Choi, M. Park, H. Kim, J. Son, J. Lee, B. Kim, H. Lee, S. Kim, K. J. Yoon, J. Power Sources, 2017, **360**, 284.
7. R. Vaßen, D. Simwonis and D. Stöver, J. Materials Science, 2001, **36**(1), 147.
8. M. Ananyev, D. Bronin, D. Osinkin, V. Eremin, R. Steinberger-Wilckens, L.G.J. de Haart, J. Mertens, J. Power Sources, 2015, **286**, 414.
9. P. Tanasini, M. Cannarozzo, P. Costamagna, A. Faes, J. Van Herle, A. Hessler-Wyser, C. Comninellis, Fuel Cells, 2009, **9**(5), 740.
10. M. Hubert, J. Laurencin, P. Cloetens, J. Mougin, D. Ferreira Sanchez, S. Pylypko, M. Morales, A. Morata, B. Morel, D. Montinaro, E. Siebert, F. Lefebvre-Joud, ECS Transactions, 2017, **78**, 3167.
11. J. Villanova, J. Laurencin, P. Cloetens, P. Bleuet, J. Delette, H. Suhonen, F. Usseglio-Viretta, J. Power Sources, 2013, **243**, 841.
12. M. Hubert, J. Laurencin, P. Cloetens, B. Morel, J. Power Sources, 2018, **397,** 240.
13. R. Spotorno, T. Ferrari, C. Nicolella, P. Piccardo, Proceedings of the 12th European SOFC & SOE Forum, 5-8 July 2016, Lucerne/Switzerland, B1216.
14. M. Hubert, J. Laurencin, P. Cloetens and J. Mougin, ECS Transactions, 2017, **78**(1), 3167.
15. A. Hauch, M. Mogensen, A. Hagen, 2011, **192**(1), 547.
16. F. Monaco, M. Hubert, J. Vulliet, J. Ouweltjes, D. Montinaro, P. Cloetens, P. Piccardo, F. Lefebvre-Joud, J. Laurencin, J. Electrochemical Society, 2019, **166**(15), F1229.
17. M. Trini, A. Hauch, S. De Angelis, X. Tong, P. Vang Hendriksen, M. Chen, J. Power Sources, 2020, **450**, 227599.
18. G. Rinaldi, A. Nakajo, P. Caliandro, L. Navratilova, ECS Transactions, 2019, **91**, 641.
19. M. Laguna-Bercero, J. Power Sources, 2012, **203**, 4.
20. A. Faes, A. Hessler-Wyser, D. Presvytes C. Vayenas, J. Van Herle, Fuel Cells, 2009, **9**(6), 841.
21. A. Nakajo, Z. Wuillemin, J. Van Herle, D. Favrat, J. Power Sources, 2009, **193**(1), 203.
22. A. Nakajo, Z. Wuillemin, J. Van Herle, D. Favrat, J. Power Sources, 2009, **193**(1), 216.
23. A. Nakajo, A. Kiss, A. Cocco, W. Harris, M. DeGostin, F. Greco, G. Nelson, A. Peracchio, B. Cassenti, A. Deriy, S. Wang, Y. Chen-Wiegart, J. Wang, J. Van Herle, W. Chiu, ECS Transactions, 2015, **68**(1), 1069.

24. M. Pihlatie, A. Kaiser, M. Mogensen, M. Chen, Solid State Ionics, 2011, **189**, 82.
25. D. Waldbillig, A. Wood, D. Ivey, J. Power Sources, 2005, **145**, 206.
26. Y. Nakagawa, K. Yashiro, K. Sato, T. Kawada, J. Mizusaki, ECS Transactions, 2007, **7**, 1373.
27. D. Sarandaridis, R. Rubkin, A. Atkinson, ECS Transactions, 2007, **7**, 1491.
28. J. Laurancin, V. Roche, C. Jaboutian, I. Kieffer, J. Mougin, M. Steil, Int. J. Hydrogen Energy, 2012, **37**, 12557.
29. F. Greco, A. Nakajo, Z. Wuillemin, J. Van Herle, ECS Transactions, 2015, **68**(1), 1921.
30. Q. Jeangros, A. Faes, J. Hansen, U. Aschauer, J. Van Herle, A. Hessler-Wyser, R. Dunin-Borlowski, Acta Materialia, 2010, **58**, 4578.
31. B. Liu, Y. Zhang, B. Tu, Y. Dong, M. Cheng, J. Power Sources, 2007, **165**, 114.
32. M. Ettler, H. Timmermann, A. Weber, N.H. Menzler, J. Power Sources, 2010, **195**, 5452.
33. B. Burdin, A. Sheikh, M. Krapchanska, D. Montinaro, R. Spotorno, P. Piccardo, D. Vladikova, ECS Transactions, 2021, **103**, 1137.

Distribution of current density across the active area at various stoichiometry ratios using the JRC ZERO∇CELL single cell PEM fuel cell testing hardware

Tomasz Bednarek*

European Commission, Joint Research Centre (JRC), Directorate C Energy Transport and Climate, The Netherlands

Abstract. The performance of the PEM fuel cell directly depends on the partial pressure of provided reactants, namely hydrogen and oxygen. Since reactants are consumed in the fuel cell reaction, partial pressure of reactants decreases in the direction of reactants flow. This well-known mechanism makes the performance of the fuel cell dependent on the stoichiometry ratios of input reactants. The JRC ZERO∇CELL, a single cell PEM fuel cell testing setup, is developed to provide as much as possible uniform operating conditions at the 10cm^2 active area specimen, hence giving uniform current density across the active area of the cell. To investigate what is the real gradient of current density across the active area for the JRC ZERO∇CELL at various reactant stoichiometry ratios, segmented bi-polar plates and current collectors are developed.

This study presents experimental investigation of the current density distribution across the active area of the JRC ZERO∇CELL setup at range of reactant stoichiometry ratios from λ=2 up to λ=15. Current density gradients are considered along the gas flow as well as in the transverse direction. The experimental results show that the current density gradient across the active area, although dependant on the reactants stoichiometry ratios, is relatively small as compared with a wide range of investigated stoichiometry ratios.

1 Introduction

The JRC ZERO∇CELL has been developed [1,2] with the purpose to minimise the influence of the testing hardware on the performance and durability test results. The features of this hardware setup ensure that the tested Membrane Electrode Assembly (MEA) is exposed to possibly uniform distribution of operating conditions in terms of temperature, pressure and reactant gases composition across the active area, therefore showing the "real" characteristics of the tested specimen. Hence, the JRC ZERO∇CELL has the potential to be used as a reference testing hardware for PEM single cell testing.

However, the presented up-to-date results [1,3], do not provide experimentally measured voltage and current density distribution across the active area of the MEA.

The aim of the current study is to provide an information how reactant stoichiometry ratios influence current density distribution across the active area of the MEA. For this purpose, a segmented current collector has been developed, allowing to measure voltage and current distribution along as well across the parallel channels at the MEA active area.

2 Design criteria and hardware setup

Measurements of voltage and current distribution across the active area of the tested MEA required a modification of the current collector and the bi-polar plate of the JRC ZERO∇CELL testing setup. The other parts of the testing hardware remained unchanged. The experiments were done with regular non-segmented MEA.

The principle of the segmented measuring circuits are presented in Fig. 1. It is assumed the experiment is carried out using a single electronic bank, hence all gradients of current and voltage result from the features and operation of the testing setup. It can be seen in Fig. 1, that voltage and current measurement circuits are separated. This is to avoid possible effects of the current measurement circuit to the voltage measurements. The current measurements are done using high-precision shunt resistors with additional possibility of calibration.

The sketch of measuring segments is shown in Fig.2a. The current collector, presented in Fig. 2b, is a Printed Circuit Board (PCB) with imprinted voltage sensing and current lines and sockets for sensing and current cables. The voltage sensing lines and current lines are as much as

* Corresponding author: Tomasz.Bednarek@ec.europa.eu

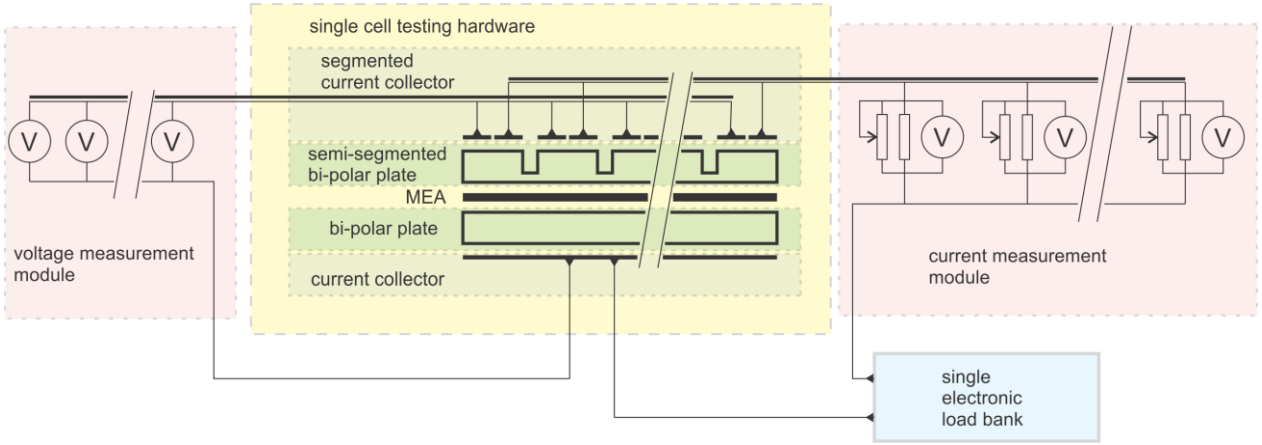

Fig. 1. Circuits for current and voltage distributions measurements.

possible separated to minimise all possible interferences, i.e. for Electro-Impedance Spectroscopy (EIS) measurements. In this purpose, the voltage senses socket and current lines socket are placed on separate sides of the testing setup.

Current measurement shunts are located in separated current measurement module. Such configuration avoids effects of shunts on voltage measurements and allows for more compact design of the current collector PCB. Additional calibration of each individual shunt is possible using multi-turn calibration potentiometers.

Both, voltage and current recordings are done using external data acquisition system NI CompactDAQ. It is worth to mention, that relatively high currents produced by the JRC ZERO∇CELL, in extreme cases up to 50A, turn out in considerable electromagnetic fields around the testing setup. Such conditions make precise measurements difficult. The correct shielding and earth grounding of all current and sensing lines was of importance there. Finally, it was possible to make voltage measurements with accuracy ±1mV and current measurements ±3mA. Additional post-process time averaging of the obtained results allowed further improvement of the obtained results accuracy.

As the first try, due to difficulties to achieve full segmentation, a semi-segmentation of the bi-polar plate was done, see Fig. 3. In the solid block of graphite bi-polar plate, on the opposite side to the gas channel grooves, segments were milled matching to the measuring points in the segmented current collector. Such approach, considering also non-segmented MEA used for tests, provides uniform voltage across the whole active area. Therefore, segmented measurements are limited only to current distribution.

It is worth to be noted, that such semi-segmented bi-polar plate approach with uniform voltage distribution is suitable for both, potentiostatic as well as galvanostatic operation modes. In galvanostatic mode, although voltage across the active area is uniform, the result consist of current distribution across the active area, while integral of current going through each segment gives the total current applied to the cell.

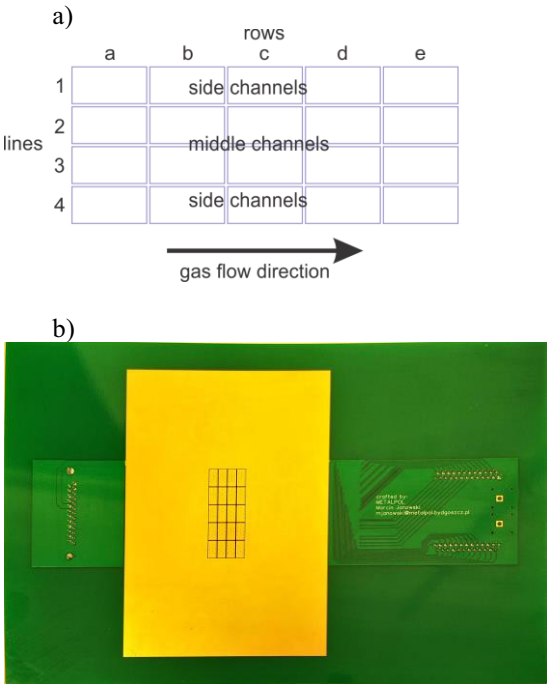

Fig. 2. Segmented current collectors, (a) localisation of segments, (b) current collector PCB plate.

3 Results and discussion

The JRC ZERO∇CELL testing setup with segmented current collector installed in the testing bench is presented in Fig. 4. The experiments were done using the 10 cm^2 (20 mm width, 50 mm length) active area MEA. The active area was divided into 20 equal segments, 0.5 cm^2 (5×10 mm) each. There are 4 segments in the transverse direction to the gas channels and 5 segments along gas channels, see segmentation sketch in Fig. 2. Operating conditions for the tests are listed in Fig. 5.

In order to get reference performance of the tested MEA, polarisation IV curves experiments were made for range reactant stoichiometry ratios, from λ_{an}=4, λ_{cath}=5 up to λ_{an}=12, λ_{cath}=15. The polarisation curves were obtained at galvanostatic mode.

It can be seen, Fig. 5, that the effects of stoichiometry ratio on the performance of the cell are visible at rather low current densities, up to 1.0 Acm^{-2} and at the highest current densities above 2.5 Acm^{-2}. At the moderate

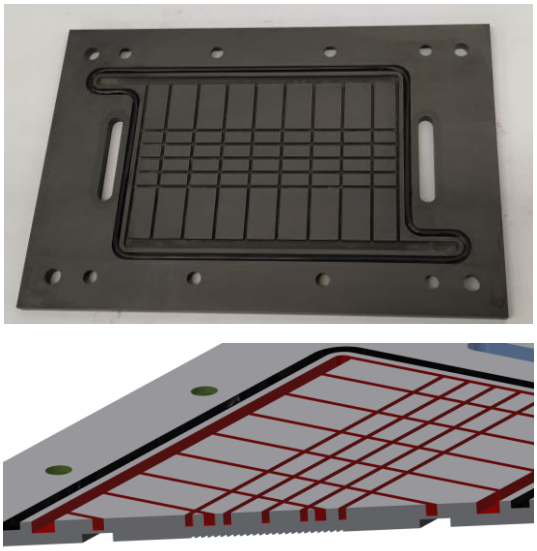

Fig. 3. Semi-segmented graphite bi-polar plate.

current densities between 1.0 Acm^{-2} and 2.5 Acm^{-2}, the effects of the reactant stoichiometry on the performance of the MEA are less pronounced.

At the lowest current densities, namely 0.5 Acm^{-2} and 1.0 Acm^{-2}, the difference between the best performance (λ_{an}=12, λ_{cath}=15) and the lowest (λ_{an}=4, λ_{cath}=5) is about 14 mV and 17 mV respectively. Although those differences are clearly visible on the plot, Fig. 5, the variations of the total output power density do not exceed ±1.5% and ±1.3% at current densities 0.5 Acm^{-2} and 1.0 Acm^{-2} respectively.

Considering that at moderate current densities, from 1.5 Acm^{-2} up to 2.5 Acm^{-2}, the effects of reactants stoichiometry ratios on MEA performance nearly disappear (variations below 0.6%), the effects of reactant stoichiometry ratios at lower current densities might be associated with low mass flow rate of reactant gasses. Due to employed parallel channels flow field pattern, at low current densities, the pressure drop or reactant gasses is relatively small, which in turn limits a driving force for liquid water removal. Therefore, the product liquid water at the active area of the MEA is evacuated less effectively as compared with higher mass flow rates at moderate current densities.

At high current densities above 3.0 Acm^{-2}, it is observed that reactant stoichiometry ratios start affecting the cell performance. At the highest current density, namely 4.0 Acm^{-2}, the difference between the highest performance at λ_{an}=12, λ_{cath}=15 and the lowest performance at λ_{an}=4, λ_{cath}=5 (extrapolated) is about 450 mV, which affects the affects the performance of the MEA by ~12%.

The loss of performance for low stoichiometry ratios at high current densities might be associated with two reasons. The first is due to lower feed of reactants. The reactants are consumed along the channels hence causing a descending partial pressure in the gas channels. Additionally high mass transport of reactants form the through gas diffusion layer provokes reactants concentration gradient between the gas channel and the catalyst layer. This results in lowering of the overall

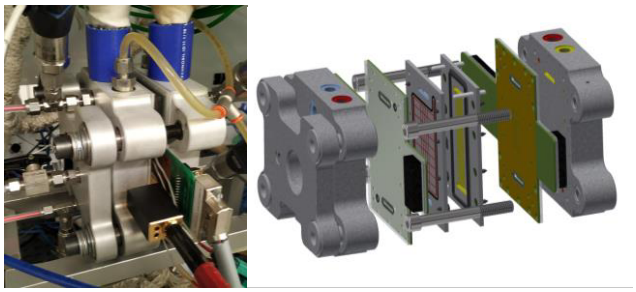

Fig. 4. Assembly of segmented current collector for the JRC ZERO∇CELL and its installation on the testing station.

MEA performance. The second reason could be associated with less efficient removal of product liquid water at low stoichiometry ratios. The lower mass flow rate of reactant gasses results in lower pressure drop, which in turn has an effect on the efficiency of liquid water evacuation form the active area of the MEA. Nevertheless, considering wide range of considered reactant stoichiometry ratios (from λ_{cath}=12 down to λ_{cath}=4), the effect on the performance equal to ~12% at the highest current densities only can be considered as relatively low.

The current density gradients across the MEA active area can be considered in two directions: along the gas channels (lines *1-4*) and perpendicular to the parallel channels in the flow field, namely rows *a* to *e*, Fig. 2a. The distribution on the current density along gas channels shows the MEA performance change due to changes in reactant gas composition and liquid water effects. On the other hand, the current density distribution in transverse direction is able to investigate the uniformity of MEA performance at comparable gas/liquid composition (among parallel channels) and identify effects of the active area sides. In order to further extend the range of investigated current densities, the evaluation of the current density distribution at various reactant stoichiometry ratios were done at fixed operating voltage of 0.3 V, which corresponds to current density range of 3.7÷4.8 Acm^{-2}, depending on applied reactant stoichiometry ratio.

The plots of the current density distribution in both considered directions for a range of reactant stoichiometry ratios are presented in Fig. 6. It is clearly visible, see Fig. 6a, that distribution of current densities

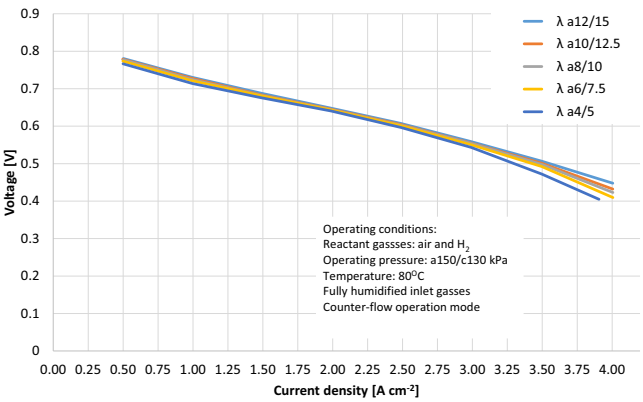

Fig. 5. Polarisation IV curves for a range of reactant stoichiometry ratios, from λ_{an}=4, λ_{cath}=5 up to λ_{an}=12, λ_{cath}=15.

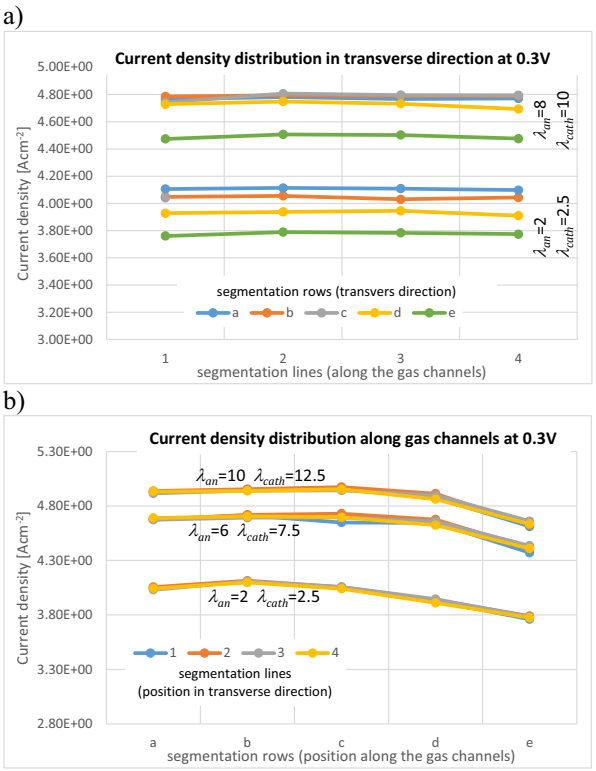

Fig. 6. Distribution of current density at steady operation at 0.3V for selected stoichiometry ratios: (a) in transvers direction and (b) along the gas channels,

in the transverse direction is nearly uniform in consecutive positions along the channel. Spread of the corresponding values slightly exceeds measurement accuracy, namely ±3 mA. Therefore, it is shown that working conditions in all individual parallel channels are equal and there are no further effects of the sides of the active area.

The current density distribution for selected reactant stoichiometry ratios in longitudinal direction (lines 1-4) is presented in Fig. 6b. Since the current density distribution in transverse direction is rather uniform, the lines 1-4 at corresponding operating stoichiometry ratios are overlapping. It can be seen, Fig 6b, that in the first three rows the current density is rather uniform independently on the operating stoichiometry ratio. This would mean that reactant concentration in the gas channel is still high enough to efficiently feed the fuel cell reaction in the catalyst layer. However, in the following rows *d* and *e* the performance of the MEA slightly decreases, depending on the applied reactants stoichiometry ratio. Such performance loss can be associated with both, decrease of partial pressure of reactants due to their consumption and limited diffusion of reactants to the catalyst layer due to hindering effects of liquid water accumulated already in the gas channel from rows *a* to *c*.

However, comparison of current distribution curves is difficult due to different values of the total current produced by the MEA. In order to enable fair evaluation of the effects of the reactant stoichiometry ratios on current density distribution, its longitudinal gradient is being calculated and presented in Fig. 7. It can be seen that the current density gradients are rather independent of the operating stoichiometry ratio. Additionally, current

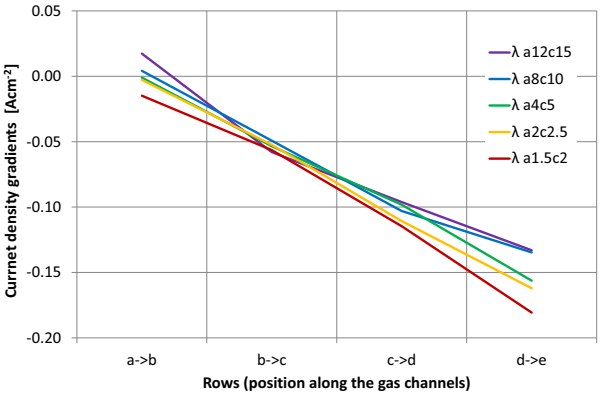

Fig. 7. Current density gradients along the gas channels at various reactant stoichiometry ratios.

density gradients show linear behaviour from the beginning of the active area (row *a*) down to the end of the active area (row *e*), what could suggest linear reasons of performance loss along the channels. Such linear reasons could be associated with linearly descending partial pressure of reactants, as opposite to negative effects of liquid water affecting diffusion of reactants, which are expected to be non-linear. However, in order to separate effects due to liquid water and reactants consumption a more detailed analysis is required using i.e. computer simulations.

Conclusions

The evaluation of current density distribution across the active area of the JRC ZERO∇CELL single cell PEM fuel cell testing hardware was done using segmented current collector and semi-segmented bi-polar plate at a range of reactant stoichiometry ratios. The results show that the overall cell performance, although dependant on reactant stoichiometry ratios, varies ~12% in the stoichiometry ratios range from λ_{an}=2, λ_{cath}=2.5 up to λ_{an}=12, λ_{cath}=15. Current density distribution in the direction transverse to the gas channels is uniform, hence there are no effects of the active area sides, neither other effects affecting performance across the active area of the testing hardware. In the direction along the gas channels, gradients of current density show linear behaviour in the whole range of investigated stoichiometry ratios. That would suggest linear phenomena causing decrease of the cell performance along the channel such as decreasing reactants partial pressure and diffusion resistance, as opposite to liquid water effects, which are expected to be non-linear.

The design documentation of the JRC ZERO∇CELL is publicly available at DOI: 10.17632/c7bffdv7yb.1 under CERN Open-Hardware licence.

References

1. T. Bednarek. G. Tsotridis, J. Power Sources, **473**, (2020)
2. T. Bednarek, DOI: 10.17632/c7bffdv7yb.1
3. T. Bednarek. G. Tsotridis, Data Brief, **27**, (2020)

High-temperature PEM Fuel Cell Characterization: an Experimental Study Focused on Potential Degradation due to the Polarization Curve

Mathieu Baudy[1,*], *Amine* Jaafar[1], *Christophe* Turpin[1], *Sofyane* Abbou[2] and *Sylvain* Rigal[1]

[1]LAPLACE, Université de Toulouse, CNRS, INPT, UPS, Toulouse, France
[2]Safran Power Units, F-31019 Toulouse, France

Abstract. High-Temperature Proton Exchange Membrane Fuel Cell constant current ageing tests highlighted that the characterizations used to monitor the state of health of single cells could be potentially degrading. An experimental campaign to analyze potential degradation due to polarization curves was carried out. More exactly, four methodologies to generate a polarization curve including Electrochemical Impedance Spectroscopies (EIS) were cycled 30 times. The tested single cells were based on a commercial PBI Membrane Electrodes Assembly (MEA) with an active surface of 45 cm² (BASF Celtec®-P 1100 type). Before the first cycling test and after the last cycling one, complete characterizations, composed by a voltammetry and a polarization curve including EIS, were performed. The results show that one of the MEA has a voltage which increased for one of the four methods to obtain the polarization curve. This growth is linked to a decrease of ohmic losses: in an unexpected way, it could be considered as a way to improve the break-in period. Similarly, the monitoring of CO_2 emission (as corrosion has been suspected to be involved at high voltage, i.e. low current density) confirms the potential degradation of the electrodes during the measurement of the polarization curve.

1 Introduction

1.1 Study context

The use of fuel cells for aeronautical applications is proposed as one of the technological solutions, in order to decarbonize this sector responsible for 2-6 % of the global radiative forcing [1]. In 2018, 11 % of the world's population flew at least once, while only 1 % emits 50 % of CO_2 from commercial aviation [2]. In this context, aircraft manufacturers are predicting a doubling of the global fleet by 2035 [3,4]. The scenarios envisaged in order to achieve the decarbonization objectives set by the European Commission, propose using fuel cells to power electric engines of light (<80 passengers), short and medium-haul (<1000 km) aircrafts [5]. This use should reduce the impact on the climate of this market segment by 75 to 90 % [5].

As part of the PIPAA ("PIle à combustible Pour Applications Aéronautiques") project led by Safran Power Units, a fuel cell system is to be developed to supply a number of secondary loads on a business aircraft [6]. These may be, for example, galley equipment, entertainment equipment or auxiliary power units [7]. For these uses, the main characteristics expected from a power generation system are to be as compact and light as possible.

Developed in the 1990s, the HT-PEMFC (High Temperature Proton Exchange Membrane Fuel Cell) operates between 120 and 200 °C thanks to a PoliBenzImidazole (PBI) polymer membrane doped with phosphoric acid (H_3PO_4). The HT-PEMFC provides several advantages compared to the LT-PEMFC (Low Temperature Proton Exchange Membrane Fuel Cell): (i) a better tolerance to carbon monoxide CO [8-10], which allows it, for example, a facilitated use with H_2 coming directly from the steam-reforming of hydrocarbide (95 % of the current world production) or biomethane, (ii) a use with dry gases [10,11] (it is not necessary to use a gas humidification system), (iii) a simplified thermal management (an easier cooling at higher ambient temperatures that could be a real advantage for transport applications with very high ambient temperature as an aircraft on the tarmac of an airport in an arid zone). Its main disadvantages compared to the LT-PEMFC are: (i) its longer start-up time (the fuel cell must be preheated to avoid the presence of liquid water harmful to the electrolyte) [9], (ii) accelerated degradative side reactions (catalyzed by the higher temperature) [9], (iii) decreased kinetics of the oxygen reduction reaction (by adsorption of H_3PO_4 on the platinum catalyst of the electrode) [12-14]. Despite these drawbacks, the HT-PEMFC advantages make it an interesting candidate to meet the different expectations.

* Corresponding author: baudy@laplace.univ-tlse.fr

1.2 Study issues

Since 2015, several research works at the LAPLACE laboratory have been focused on the HT-PEMFC study. In particular, the work done by S. Rigal et al [15,16] has validated the use of a semi-empirical model, for the analysis of quasi-static performance, as a function of the operating conditions. The model was developed from a design of experiment carried out by varying the current, the temperature and the stoichiometry of the reactive gases. This work allowed mapping the operating ranges of different HT-PEMFC Membrane-Electrode Assembly (MEA) technologies, in order to compare their performances. In addition, ageing tests at different constant currents for about 540 hours (see Fig. 1) were performed on commercial MEAs of the BASF Celtec®-P 1100 type (manufactured by the Advent company). In order to monitor the health of the MEAs, several experimental characterizations were performed: (i) polarization curves, named *v*(*i*) (to describe the quasi-static state, representing the evolution of the voltage as a function of the current density), (ii) Electrochemical Impedance Spectroscopies named EIS (to describe the dynamic state, by representing the response of the system to a sinusoidal solicitation of low amplitude in current, between 20 kHz and 1 Hz around an operating point), (iii) sinusoidal scans in current of high amplitude at low frequency, (iv) cyclic voltammetries (potentiostatic scans in H_2/N_2). The ageing rates calculated from the fuel cell voltage, over the duration of the tests and for the different MEAs, are five times greater than those commonly found in the literature (e.g., -25 µV.h^{-1} at 0.2 A.cm^{-2} instead of -5 µV.h^{-1} [10,17-20]). Also, following the characterization phases, voltage drops have been observed (see Fig. 1).

In the work of S. Rigal et al [16], a first degradation path is proposed as being the corrosion of carbon. It occurs usually at high voltages (>0.8 V) in presence of water [21]. These high voltages are explored during the various characterizations and particularly at Open Circuit Voltage (OCV). A complementary aging test of 540 h on a new MEA with truncated *v*(*i*) (i.e. the high voltages are explored by limiting the current density to 0.2 A.cm^{-2}, noted MEA0.2* in Fig. 1) has been performed. The observed effect is particularly important at high current densities: 30 % less voltage degradation, calculated from the polarization curves at 1.1 A.cm^{-2} (about +23 mV). In addition, an aging test with a new MEA under the same conditions (160 °C, H_2/AIR at 1.2/2 stoichiometry and without pressure regulation) was also performed. This test lasted 2400 h at four successive current densities (0.2, 0.4, 0.6 and 0.2 A.cm^{-2}) every 600 h and without any follow-up characterizations. Only reference characterizations truncated at 0.2 A.cm^{-2} were performed, at the beginning and at the end of the test. Ageing rates close to those reported in the literature were obtained for the different tested currents. Thus, the main hypothesis for the origin of the observed degradations, is related to the characterizations. Consequently, it was decided to verify and quantify the potential degrading character of one of the characterizations carried out during the ageing tests: the polarization curve.

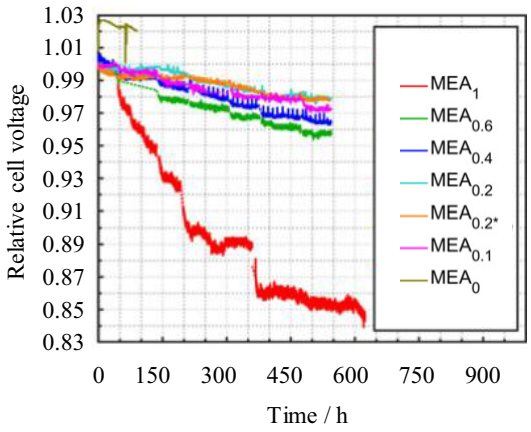

Fig. 1. Voltages referred to the initial voltage of 7 MEAs aging at different constant currents (from 0.1 to 1 A.cm^{-2}, at 160 °C, in H_2/AIR at stoichiometries of 1.2/2 and without pressure regulation). The characterizations have been replaced by dotted lines for better lisibility. Figure from [16].

Several methodologies for realizing the polarization curve have been identified in the literature. Two projects, funded by the Fuel Cells and Hydrogen Joint Undertaking (FCH-JU), named respectively CISTEM (Construction of Improved HT-PEM MEAs and Stacks for Long Term Stable Modular CHP Units, 2013-2016) and DEMMEA (Understanding the Degradation Mechanisms of Membrane-Electrode-Assembly for High Temperature PEMFCs and Optimization of the Individual Components, 2010-2012) were specifically interested in the HT-PEMFC technology and more particularly in the implementation of standardized operating procedures to carry out characterizations. The procedure concerning the polarization curve is inspired by an old version of the AFNOR 62282-7-1 standard which has been adapted for the HT-PEMFC. This procedure has been included, in a specific chapter on characterization, in the 2016 reference book on HT-PEMFC from the publisher Springer [21].

The proposed methodologies mainly ensure the quasi-static character of the polarization curve. Following the first observations made previously, different phenomena specific to the HT-PEMFC must also be taken into account when choosing a methodology for the realization of the polarization curve. It must, for example, be the least intrusive possible. For that, it must avoid degrading the fuel cell. Therefore, it is important to know the degradation mechanisms that the polarization curve is likely to solicit and to avoid or minimize them. For example, in the case of carbon corrosion, which often occurs at high voltages, truncating the polarization curve in current can be justified to avoid degradation. The use of discharge resistors can then avoid the HT-PEMFC to explore these high voltages, as it was already done for PAFCs.

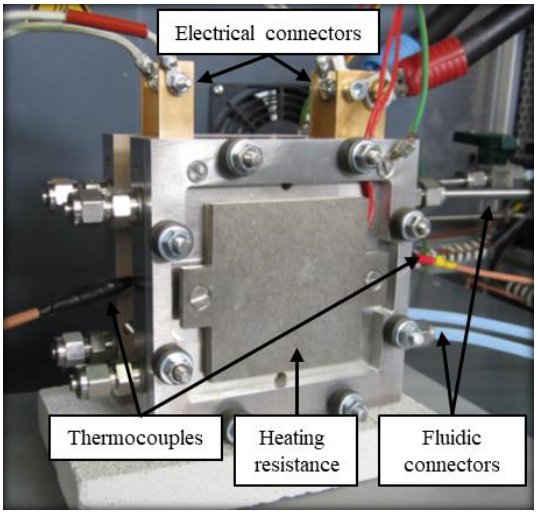

Fig. 2. Photo of the BASF HT-PEMFC single-cell fuel cell installed in the Laplace lab test bench.

2 Experimental tests

2.1 Test specimen and test bench

Commercial MEAs of the BASF Celtec®-P 1100 type (manufactured by Advent) with an active surface area of 45.2 cm^2 are used to perform these tests. They are installed in a single-cell box, manufactured by BASF (see Fig. 2). This box is made of graphite gas flow plates, copper current collector plates and clamping end plates including the distribution and extraction of the fuel cell gases.

The single cell box is installed in an in-house test bench that can operate with H_2, air and N_2 gases. It includes fluidic equipment to distribute and extract these gases and to carry out the flow regulation. It also has electrical equipment to regulate the fuel cell current and the fuel cell temperature. An atmospheric pressure sensor is installed in the test bench since the fuel cell anodic and cathodic compartments are not regulated. It should be noted that the exhaust pipes are immersed in water pots in order to purify the gases before rejecting them to the atmosphere. This system generates very little pressure drop and consequently the anode and the cathode outlet pressures are very close to atmospheric pressure.

2.2 Initial phase and baseline characterizations

For the test campaign performed during this study, particular attention is given to the development of operating procedures for the test initial phase. The aim is to limit the degradation during this step. The test initial phase is composed of different parts: (i) the assembly of the MEA in the box, (ii) the box installation in the test bench, (iii) the temperature rise followed by the fuel cell start-up, (iv) the break-in (specific early life operation to improve reproducibility and performance), (v) an initial characterization phase. The main changes, compared to the operating procedures of the previously presented campaigns [15,16], consisted in: (i) limiting the generation of local high potentials (during gas changes occurring for start-ups and voltammetries) by using a discharge resistor connected to both MEA electrodes during transient phases when the fuel cell current is not regulated, (ii) perform active gases at 120 °C to limit the degradation linked to secondary reactions (catalyzed by the high temperature), (iii) use the break-in procedure specifically proposed by the MEA manufacturer (14 h at 0.2 $A.cm^{-2}$ and 180 °C). Following the fuel cell break-in, a cyclic voltammetry (in H_2/N_2 at 0.2 $NL.min^{-1}$, from 30 mV to 800 mV and at a speed of 40 $mV.s^{-1}$) is performed, followed by an initial reference $v(i)$ (identical for each cycle). The characterization phase including the cyclic voltammetry and the $v(i)$ is performed at the end of the test. The aim is to make a comparison of the collected data, by carrying out the same procedure whatever the test.

2.3 Cycling test

Four MEAs are used to cycle four different current profiles 30 times (see Fig. 3). Each current profile allows to perform a polarization curve (four polarization curves are obtained in total) and then finishes with a stabilization phase (see Fig. 4). This phase takes place at constant current. Its duration is determined so that the cycle lasts 70 h in total (see Fig. 3 and Table 1). It is therefore different for each cycle. All the tests are carried out at 160 °C, in H_2/AIR at respective stoichiometries 1.2/2 and without pressure regulation. Each cycle will be named $v(i)\_j$ where j represents the number of the MEA used (between 1 and 4 inclusive). The MEA will also be identified by MEA j. The number of repetitions of the current profile related to each $v(i)$ has been chosen by taking into account the perspective of performing aging tests of 3000 h. Indeed, by monitoring the MEA health every 100 h, 30 $v(i)$ will be performed. Thus, it seems interesting to study the impact of these $v(i)$ on the ageing tests. To perform a $v(i)$, each current profile starts from the first indicated current density value and finishes with the final current density, shown in Table 1. Several current ramps are therefore performed to reach the levels where a stabilization and voltage reading are performed. The ramps and stabilizations are defined to achieve stable operating conditions for the $v(i)$ steps. Current ramps are also performed, to reach and return to the stabilization phase current.

The cycles can be differentiated by several characteristics: (i) the direction of the imposed current profile ($v(i)\_1$ and $v(i)\_2$ perform the current profile in an increasing way and inversely for the cycles $v(i)\_3$ and $v(i)\_4$, cf. Fig. 4), (ii) the passage or not to 0 $A.cm^{-2}$ (only $v(i)\_3$ performs OCV measurements), (iii) the passage to the low current densities lower than 0.2 $A.cm^{-2}$ ($v(i)\_4$ is truncated in current), (iv) the passage to a current density of 1.1 $A.cm^{-2}$ ($v(i)\_3$ and $v(i)\_4$ stabilize at 1.1 $A.cm^{-2}$ after the current ramp performed between the stabilization point and the starting point of $v(i)$), (v) the stabilization current density ($v(i)\_2$ has exactly the same current profile as $v(i)\_1$ but stabilizes at 0.6 $A.cm^{-2}$). Note that it is the $v(i)\_1$ current profile (see Fig. 4) that is used

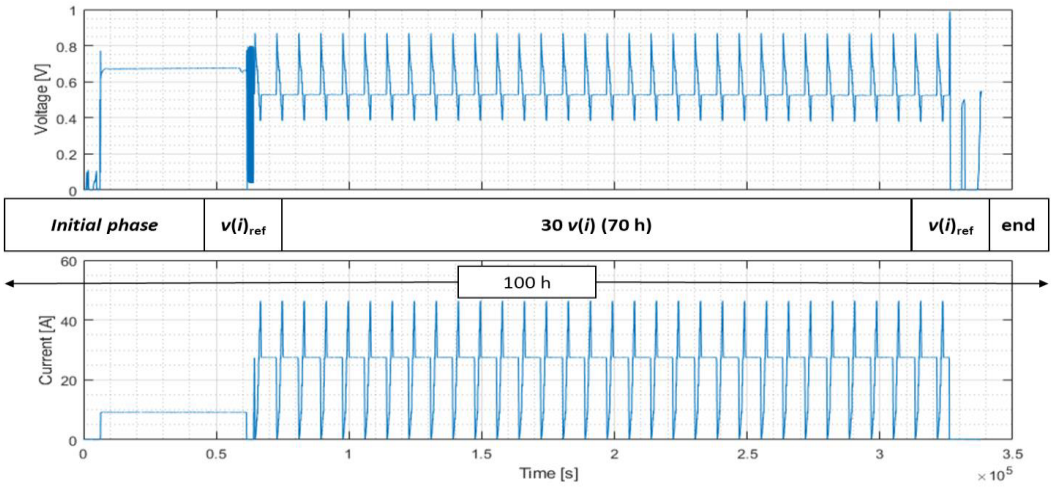

Fig. 3. *v*(*i*)_2 cycle current profile and fuel cell voltage response.

Table 1. Definition of the four performed cycles.

Cycle	Current profile and duration of the *v*(*i*)	Current density and duration of the stabilization.
v(*i*)_1	0.004 to 1 A.cm^{-2} (40 min)	0.2 A.cm^{-2} (95 min)
v(*i*)_2	0.004 to 1 A.cm^{-2} (40 min)	0.6 A.cm^{-2} (95 min)
v(*i*)_3	1.1 to 0 A.cm^{-2} (82 min)	0.2 A.cm^{-2} (53 min)
v(*i*)_4	1.1 to 0.2 A.cm^{-2} (58 min)	0.2 A.cm^{-2} (87 min)

to make the initial and final reference polarization curves. In addition, EIS (from 20 kHZ to 1 Hz) are performed during some steps of the polarization curves (not shown in Fig. 4). The EIS is used to measure the high frequency resistance (R_{HF}). This resistance is taken at the frequency where the fuel cell impedance spectrum is composed of only a real part.

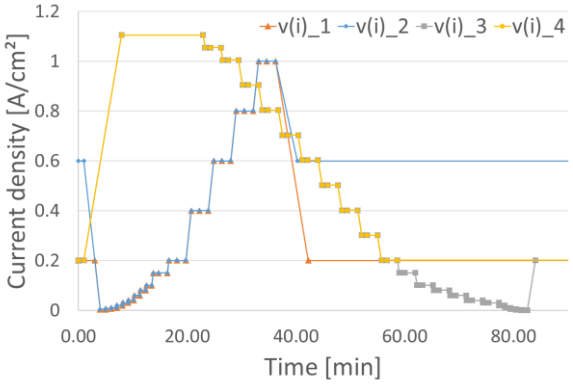

Fig. 4. Current profiles used for the four cycles.

3 Results

3.1 Reproducibility of the initial test phase

We observe, in Fig. 5, the increase of the voltage, during the break-in period. This increase is similar for the four MEAs. It should be noted that the atmospheric pressure has an impact on the voltage, by its direct effect on the partial pressures of the gases within the electrodes. At constant flow rate, an increase of the atmospheric pressure will lead to an increase of the voltage. Moreover, at constant atmospheric pressure, the increase in flow will also generate greater pressure drops.

The implementation of the operating procedures at the beginning of the tests allows a good reproducibility between each MEA, following the initial reference *v*(*i*) (cf. Fig. 6). Indeed, the maximum deviation from the mean value is obtained at 1 A.cm^{-2}. It is equal to 7 mV, i.e. 1.86 % relative to the mean voltage (with a standard deviation of 5.5 mV). It can be noted that it is the MEA 4, which does not come from the same batch, which increases this deviation (1 mV of maximum deviation from the mean without MEA 4).

3.2 Comparison of initial and final reference *v*(*i*)

To compare the different cycles, the voltages recorded for each current of the steps of the reference polarization curves are subtracted. Also, a particular interest is given to the results at 1 A.cm^{-2} where the voltage differences are the most important (see Table 2). The aging rates μ are calculated from the voltages at 1 A.cm^{-2} of the initial $U_{init}(i)$ and final $U_{final}(i)$ reference polarization curves, with a test duration of Δt=70 h in accordance with equation 1. The atmospheric pressures P_{atm}, at the time of the voltages reading, are given as an indication.

$$\mu=[U_{final}(1\ \text{A.cm}^{-2})-U_{init}(1\ \text{A.cm}^{-2})]\ \Delta t^{-1} \quad (1)$$

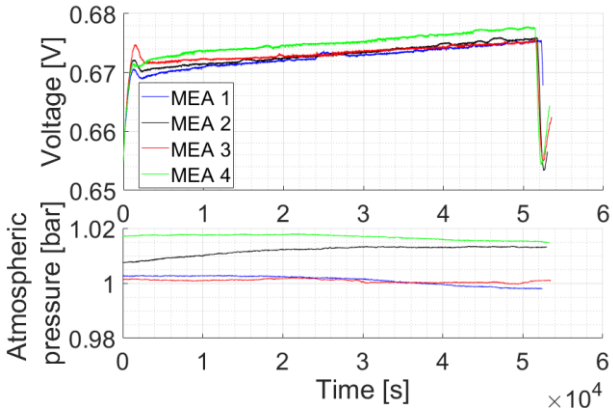

Fig. 5. Voltage and atmospheric pressure during the break-in period of the four MEAs at 180 °C, at 9 A or 0.2 A.cm^{-2} during 14 h.

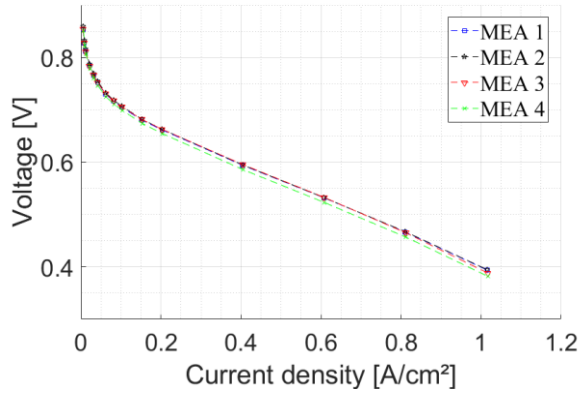

Fig. 6. Initial reference polarization curves of the 4 MEAs (cycle current profile *v*(*i*)_1, 160 °C, in H_2/AIR at 1.2/2 stoichiometries). Atmospheric pressures are given as an indication.

3.3 Evolution of the *v*(*i*) regarding each cycles

As can be observed in Fig. 7, the disparities are relatively small between the different sets composed by the *v*(*i*) of each cycle. It is interesting to note that the obtained voltages on the polarization curves *v*(*i*)_1 and *v*(*i*)_2 cycles (where the *v*(*i*) are realized by current increase) are slightly better at high current densities. Also, the *v*(*i*) voltages of the *v*(*i*)_3 and *v*(*i*)_4 cycles are slightly better at low current densities.

3.4 Evolution of the stabilization phases

Analysis of the stabilization phases (see Fig. 8) shows similar changes in relative voltages for the *v*(*i*)_1 and *v*(*i*)_3 cycles. The cycle *v*(*i*)_4 has a voltage that decreases slightly before stabilizing. Finally, the *v*(*i*)_2 cycle has a decreasing relative voltage. Note that the voltages were related to the voltage measured at the end of the first stabilization phase, after the initial reference polarization curve. Indeed, since the *v*(*i*)_2 cycle performs its stabilization at a higher current density (0.6 A.cm^{-2}), this allows us to compare the evolution of the four cycles along the time.

Table 2. Voltages measured at 1 A.cm^{-2} and ageing rate.

	***v*(*i*)_1**	***v*(*i*)_2**	***v*(*i*)_3**	***v*(*i*)_4**
U_{init} (1 A.cm^{-2}) [mV]	393	394	388	381
P_{atm} [barA]	0.997	1.012	1.001	1.014
U_{final} (1 A.cm^{-2}) [mV]	401	390	388	387
P_{atm} [barA]	1.007	0.982	1.009	1.002
μ [µV.h^{-1}]	114	-57	0	85

The voltage of cycles *v*(*i*)_1 and *v*(*i*)_4 have increased, cycle *v*(*i*)_3 remained globally neutral and cycle *v*(*i*)_4 lost voltage. Fig. 9 shows the evolution of atmospheric pressure along the time. It is interesting to note that the evolution of the relative voltages, seems similar to that of the atmospheric pressures.

4 Results analysis and discussion

4.1 Comparison of cycles

The results, from the comparison of the initial and final reference *v*(*i*), allow distinguishing two cycles that improve the voltage (*v*(*i*)_1 and *v*(*i*)_4) and two others that slightly degrade it (v(i)_2 and *v*(*i*)_3). The only difference between *v*(*i*)_1 and *v*(*i*)_2 is the stabilization current. Also, the stabilization current of *v*(*i*)_2 at 0.6 A.cm^{-2} seems to have been degrading for the voltage. However, this result must be nuanced. Indeed, the impact of the variation of the atmospheric pressure can have a significant effect on the voltage. Particularly, if we analyze the atmospheric pressures in Table 2, which can also be seen in Fig. 9, the final reference polarization curve of the *v*(*i*)_2 cycle is performed at a low atmospheric pressure.

Comparing the references of the v(*i*)_4 cycle (characterized by a current-truncated v(*i*)) with the other cycles, it can be seen that it does not necessarily seem more degrading to explore high voltages. If we observe the evolution of the *v*(*i*) voltages for the *v*(*i*)_4 cycle, we can see that they decrease during the test. Nevertheless, by comparing the reference polarisation curves, a voltage improvement is noted. It is indeed the final reference *v*(*i*) that has a beneficial effect on the voltages. This suggests that the repetition of the *v*(*i*)_4 cycle current profile results in an accumulation of reversible losses. This idea is reinforced by the fact that *v*(*i*)_1 also increased in performance during each *v*(*i*) cycle (as a reminder, this is the current profile used for the reference polarization curves). In addition, the *v*(*i*)_3 cycle had no overall effect

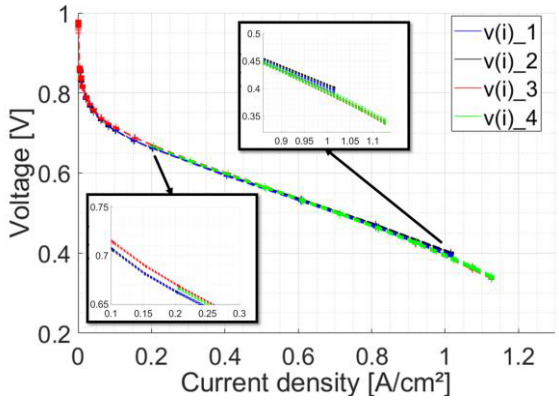

Fig. 7. All 30 polarization curves performed for each cycle (reference polarization curves are not plotted).

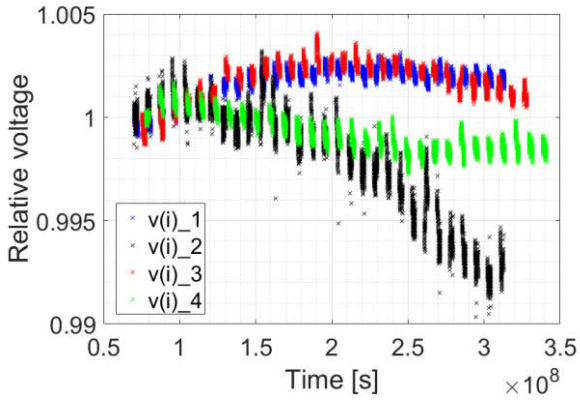

Fig. 8. Voltage evolution of the stabilization phases of the four cycles. The $v(i)$ have been removed to improve readability.

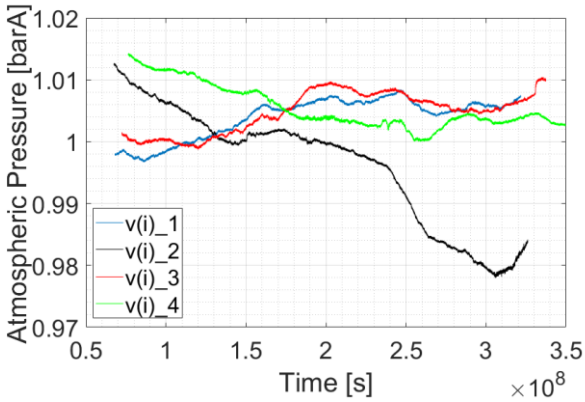

Fig. 9. Variation of the atmospheric pressure during the different cycles. A similar evolution of pressure and voltage is observed, particularly visible for the cycle $v(i)$_2.

on the voltages. This was the only current profile that measures open circuit voltage. As with the $v(i)$_4 cycle, the $v(i)$ started at high currents (1.1 A.cm^{-2}). It thus seems that the switch to low current densities did have a negative effect. This is the hypothesis that had already been considered by Rigal et al [15,16]. Moreover, if we establish that the final reference $v(i)$ eliminates the reversible losses, we could think that these are irreversible losses, which impact the $v(i)$_3 cycle. However, this statement should be tempered because MEA 4 comes from a different production batch. This could have an effect on its behaviour that makes the comparative analysis questionable.

Comparison of $v(i)$_1 and $v(i)$_3, performed in a different current direction, i.e. exploring the currents in an increasing manner and vice versa, confirms that this technology does not exhibit significant hysteresis. This can be seen in Fig. 7 where the first $v(i)$ of these two cycles are well superposed.

4.2 Proposal to improve the break-in process

The realization of EIS on the different steps of the $v(i)$ revealed an interest, to carry out $v(i)$ in cycling in order to extend the running-in procedure of the MEA manufacturer. Indeed, the EIS allows the access to the measurement of the high-frequency resistance R_{HF}, which is identified in the models with a R_{cell} resistance, attributed to the resistive phenomena taking place in the fuel cell [15]. It can be observed to decrease over time before stabilizing during the $v(i)$_1 and $v(i)$_2 cycles. This resistance is used in the quasi-static modeling of the HT-PEMFC, in a voltage loss term which is subtracted to the reversible voltage (see equation 2) [15].

$$\eta_{ohm}=R_{cell}\, j_{cell} \tag{2}$$

For the $v(i)$_1 cycle, the voltage gain provided by the R_{HF} decrease is then maximal at 1 A.cm^{-2} (+5 mV). It is a part of the gain that is also observed between the initial and the final reference $v(i)$ of the $v(i)$_1 cycle (+8 mV, cf. Table 2). Thus, a perspective is considered to extend the break-in period. The $v(i)$_1 cycle could therefore be performed, after the break-in period proposed by the manufacturer. It would improve performance and ensure good repeatability of the $v(i)$, by measuring the R_{HF}. This cycle would then stop at the moment of stabilization of this resistance and validation by the repeatability of the $v(i)$. This last $v(i)$ would then constitute the initial reference polarization curve of the test.

4.3 About degradation

The test campaign presented was also carried out on a similar test bench in order to check the reproducibility of the results. The different cycles were performed at the same time in order to be at the same atmospheric pressure. Moreover, this second test bench presented a CO_2 sensor at the cathode gas outlet. In order to protect the sensor from humidity, additional condensation and liquid purging equipments are also present. Due to current regulation problems, all results are unfortunately not usable. However, we note similarities in the results for the initial phases of the tests and for the voltage variations during the first half of the cycles.

If we look at the measurements of the CO_2 sensor, it seems that the degradation observed by S. Rigal et al is at least partly caused by carbon corrosion. Indeed, above a certain voltage, a CO_2 emission (attributed to the carbon corrosion reaction) has been observed. This emission seems to be more important, following the transition to the open circuit voltage (see Fig. 10). Note that the sensor

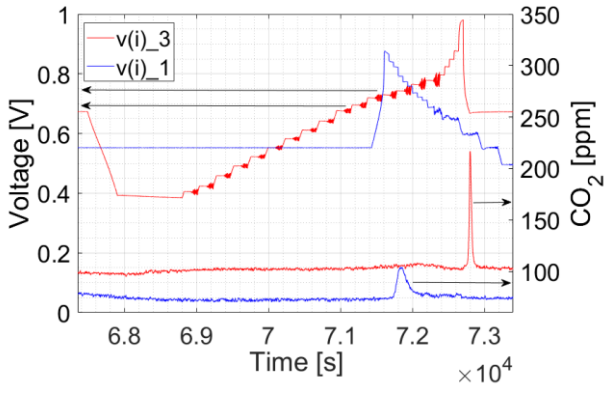

Fig. 10. Voltages recorded during two different $v(i)$ (from $v(i)\_1$ and $v(i)\_3$) and the corresponding CO_2 peaks).

is not located directly after the fuel cell cathode outlet. There is therefore a time lag between the CO_2 emission by the fuel cell and its reception by the sensor. Consequently, this time lag depends on the gas flow and the pipe volume. Thus, it explains why the cycle $v(i)\_3$ is not at the same global voltage gain level as $v(i)\_1$ and $v(i)\_4$.

5 Conclusion

The proposed cycling method is therefore validated in order to compare $v(i)$. However, the analysis will have to be prolonged with regard to the stabilities of the operating conditions and the modelling to be truly complete. Meanwhile, this investigation has helped to better understand in which way a $v(i)$ could be more or less degrading. The degradation linked to the passage to low current densities has been highlighted as being CO_2 emitting by the carbon corrosion mechanism. It seems to be intensified by the passage to the open-circuit voltage. Thus, the use of these MEA at OCV, even for short times during the realization of the $v(i)$, should be prohibited. Also, cycling of $v(i)$ could have a beneficial effect on the fuel cell. An extension of the break-in period could then consist in performing several polarization curves, until the R_{HF} parameter is stabilized and the $v(i)$ are superposed in repeatability. This could improve the reproducibility at the beginning of the MEA life, thanks to the monitoring of the R_{HF}. Finally, thanks to the observations and analyses, it will be possible to design a $v(i)$ methodology for future tests that is the less degrading as possible. This $v(i)$ can then be experimented on stack. It will also be interesting to analyze the other characterizations, by the experimental methodology proposed in this article.

The authors would like to express their sincere thanks to all the members of the PIPAA project, it is to say Safran Power Units, the LAPLACE laboratory and to the PBI (Banque Publique d'Investissement). The authors would like also to thank all the public funders (FEDER, Occitanie Region, French Government, and Toulouse Metropole) of the LAPLACE Hydrogen Platform used for all tests during the PIPAA project.

References

1. D. S. Lee, D. W. Fahey, A. Skowron, M. R. Allen, U. Burkhardt, Q. Chen, S. J. Doherty, S. Freeman, P. M. Forster, J. Fuglestvedt, A. Gettelman, R. R. De León, L. L. Lim, M. T. Lund, R. J. Millar, B. Owen, J. E. Penner, G. Pitari, M. J. Prather, R. Sausen, and L. J. Wilcox, Atmospheric Environment **244**, 117834 (2021)
2. S. Gössling and A. Humpe, Global Environmental Change **65**, 102194 (2020)
3. Airbus, Global Market Forecast (2019-2038), airbus.com (2019)
4. Boeing, Commercial Market Outlook (2021-2040), boeing.com (2021)
5. McKinsey & Company, Hydrogen-powered aviation, fch.europa.eu (2020)
6. Safran, Le projet collaboratif PIPAA, safran-group.com (2017)
7. DOE, Workshop on Fuel Cells in Aviation, energy.gov (2011)
8. J. R. Vang, F. Zhou, S. J. Andreasen, and S. K. Kaer, ECS Transactions **68**, 13 (2015)
9. A. Chandan, M. Hattenberger, A. El-kharouf, S. Du, A. Dhir, V. Self, B. G. Pollet, A. Ingram, and W. Bujalski, Journal of Power Sources **231**, 264 (2013)
10. T. J. Schmidt and J. Baurmeister, Journal of Power Sources **176**, 428 (2008)
11. T. J. Schmidt, in *Polymer Electrolyte Fuel Cell Durability*, edited by F. N. Büchi, M. Inaba, and T. J. Schmidt (Springer, New York, NY, 2009), pp. 199–221
12. S. Authayanun, K. Im-orb, and A. Arpornwichanop, Chinese Journal of Catalysis **36**, 473 (2015)
13. K. Scott, S. Pilditch, and M. Mamlouk, J Appl Electrochem **37**, 1245 (2007)
14. R. Sood, *Electrolytes polymère nano-structurés à base de liquides ioniques pour les piles à combustible hautes températures*, phdthesis, Université de Grenoble (2012)
15. S. Rigal, C. Turpin, A. Jaafar, N. Chadourne, T. Hordé, and J.-B. Jollys, in *2019 IEEE 12th International Symposium on Diagnostics for Electrical Machines, Power Electronics and Drives (SDEMPED)* (2019), pp. 439–445
16. S. Rigal, C. Turpin, A. Jaafar, T. Hordé, J.-B. Jollys, and N. Chadourne, Fuel Cells **20**, 272 (2020)
17. A. D. Modestov, M. R. Tarasevich, V. Ya. Filimonov, and N. M. Zagudaeva, Electrochimica Acta **54**, 7121 (2009)
18. Y. Oono, A. Sounai, and M. Hori, Journal of Power Sources **189**, 943 (2009)
19. Z. Qi and S. Buelte, Journal of Power Sources **161**, 1126 (2006)
20. S. Galbiati, A. Baricci, A. Casalegno, and R. Marchesi, International Journal of Hydrogen Energy **38**, 6469 (2013)
21. Q. Li, D. Aili, H. A. Hjuler, and J. O. Jensen, *High Temperature Polymer Electrolyte Membrane Fuel Cells: Approaches, Status, and Perspectives* (2016)

An efficient composite membrane to improve the performance of PEM reversible fuel cells

Gabriele G. Gagliardi[1], *Carlotta* Cosentini[1] *and Domenico* Borello[1]

[1]Department of Mechanical and Aerospace Engineering, University of Rome La Sapienza, Rome, Italy

Abstract. The aim of this study is to develop composite Nafion/GO membranes, varying GO loading, to be used in a Unitized reversible fuel cell comparing its performance with the baseline Nafion. Water uptake, ion exchange capacity (IEC), tensile strength, and SEM (scanning electron microscope) analysis are discussed. The SEM analysis revealed how the GO is homogeneously disposed into the Nafion matrix. The addition of GO improves the membrane tensile strength while reducing the elongation ratio. Water uptake, IEC enhance with the increasing of GO content. Regarding fuel cell mode, the performance is analysed using a polarization curve on a MEA with an effective area of 9 cm^2. The composite membrane demonstrated higher mechanical strength, enhanced water uptake so higher performance in fuel cell mode. Despite the power absorbed from the electrolysis is higher when using a composite membrane, the beneficial effect in FC mode resulted in a slightly higher round trip efficiency. The GO-Nafion membrane was not able to maintain its performance with increasing the operating time, so potentially leading to a lower lifetime than the Nafion bare.

1 Introduction

Considering the global warming, new technologies must be efficient and especially respectful of the environment. Indeed, the emissions of greenhouse gas, like carbon dioxide, carbon monoxide or other like SOx and NOx, must be avoided at all costs. The energy also must be produced without fossil fuel because the latter's reserves diminish and come dangerously to their ends. Then, renewable energies are worthwhile because of the tremendous and limitless amount of energy that can be produced. New technologies like electrolysers (and fuel cells), can be linked to renewable sources, which have non-continuous production [1] to store the surplus of energy in the form of gas that can be used in a second time with fuel cells. Among different types of fuel cells, the Unitized Reversible Fuel Cells (RFCs) are an innovative and promising technology able to accomplish two different tasks: power production (fuel cell mode) and energy storage (electrolyser mode) in one device [2]. In addition to the versatility and the reversibility, this technology is characterized by several advantages such as low operating temperature, fast start ups, sustainable operation at a high current density, low volume, low weight of the stack and suitability for discontinuous operation. However, some technical challenges are still to be overcome. The basic challenges are related to the materials cost and to the durability. To date, the operational lifetime for real life application does not meet the requirements for the art technologies state, such as 40,000 h for stationary applications, 20,000 h and 5000 h for mobile applications [3]. Despite many efforts to develop the URFC-PEM fuel cell technology in past decades, its major barriers including durability and cost for commercialization purpose have not been solved. To overcome those issues, research has investigated ways of modifying the Nafion matrix for many reasons: (a) compared to other fuel cell components, the production cost of Nafion is significantly higher; (b) the durability is not efficient for long cycle unit cell operation due to the swelling nature of the membrane; and (c) fuel permeability. Although many investigations have been undertaken, up to now, not many membrane-based studies have been reported for URFC applications. A low-cost, highly stable advanced composite-structured membrane should be proposed to replace the more expensive Nafion membranes. Sulfonated polyether ether ketone (sPEEK) and sulfonated polyphenylene oxide (SPPO) can be considered as efficient organic compounds instead of conventional Nafion due to their low cost, availability, and easy sulfonation processes. The sulfonated polymer membrane can increase the proton conductivity, flexibility, and stability of the membrane. To augment the advanced properties in the membrane, functionalized inorganic materials must be dispersed in the polymer membrane matrix. The inorganic materials can enhance the mechanical and thermal stability of the polymer membrane due to strong interfacial interaction between the polymer main chain and inorganic functional properties. Furthermore, the incorporation of inorganic material can act as a barrier for the fuel crossover in the membrane [4]. Graphene Oxide (GO) is a highly hydrophilic material and exhibits a reasonable level of proton conductivity. It was reported

* Corresponding author: gabriele.gagliardi@uniroma1.it

that the incorporation of GO into the Nafion electrolyte increases the mechanical strength and gas impermeability of the membrane so enhancing the performance in fuel cell mode giving the opportunity to reduce the thickness of the membrane so reducing the total cost [5]. The work reported here is aimed to improve the performance and the durability of Nafion membranes for URFC application. Therefore, Nafion and GO-Nafion composite membranes with variable GO loading were fabricated, characterised, and tested in-situ.

2 Materials and method

2.1. Materials

Materials and precursor were obtained from several companies: GO sheets and hydrogen peroxide (34%) from Sigma Aldrich; sulfuric acid (98%) from Alfa Aesar; Nafion dispersion, GDL and catalysts, PtC at the anode and the cathode, from Fuel cell store.

2.2. Preparation of membranes

Nafion and composite Nafion-GO membranes were prepared using casting method, the process of formation of film or membrane on a flat surface by the evaporation of the solvent [6]. Regarding Nafion-GO membranes, three different loading were considered: 0.5, 1 and 1.5%. For membrane preparation the following procedure was adopted: a) pour Nafion solution in a flat petri dish; b) dry for 2 hours at 100°C; c) dry it at 120°C for 1 hour in the oven to anneal. Afterwards, the membranes were treated at 80 °C by immersion in the following sequence (each procedure lasted 1 h): in water, in 3% H_2O_2, in water, in 0.5 M H_2SO_4 and in water. Then, the membranes were immersed in water overnight.

2.3. Characterization

The main properties, such as water uptake (WU), ion exchange capacity (IEC), microscopic structure and tensile strength, were evaluated. WU and IEC are relevant tests to characterize a membrane as proton exchange membrane due to the influence of water on the proton transport. Microscopic structure and tensile strength measurement were carried out to understand the dispersion of GO in the Nafion matrix and the improvement of mechanical properties. For a better comprehension, all the data are compared with that of the commercial membrane and a casted Nafion.

2.3.1 Water uptake

Water uptake (WU) was determined gravimetrically by recording the wet and dry mass of the membranes using the following steps (repeated three times): the membranes were placed in water at room temperature for 24 h, and then their wet weight was measured. To measure the wet weight, the water on the surface was absorbed using dry filter paper. After this, the wet membrane samples were dried at 100 °C (until no more 75 weight variation was detected) and their dry weight was recorded. The water uptake (WU) was measured using the Equation 1, where WE_w and WE_d denote the wet weight and the dry weight, respectively.

$$WU = (WE_w - WE_d)/ WE_d \quad (1)$$

2.3.2 Ion exchange capacity

The ion exchange capacity (IEC), expressed as milliequivalent of ion exchange groups per gram of the membrane (meq/g), is an important parameter because the ionic transport properties depend on the amount of the ion exchange groups. The IEC and WU are usually correlated: an increase of IEC induces high water content, but the mechanical strength of the membrane drops [7]. Membranes Ion Exchange Capacity was evaluated by acid-base titration method. The desired membrane was soaked in 0.1 M HCl for 24 h. After thoroughly rinsing the membrane with water, it was immersed in saturated NaCl for 72 h to exchange the H^+ ions for Na^+ ions. Then, the proton release was evaluated by titrating the solution with 0.01 M NaOH at room temperature with phenolphthalein as indicator. The IEC was obtained by using the Equation 2:

$$IEC = (VOL_{NaOH} \, x \, M_{NaOH})/ WE_d \quad (2)$$

2.3.3 Scanning electron microscope

Scanning electron microscope (SEM) was used to record surface morphology information of the sample by recording secondary electrons emitted from the material due to inelastic scattering [8]. Using this method, the primary electron beam is scanned across the sample, exciting the electrons on the surface, which are then detected to produce 3D images. SEM can successfully be used to investigate particle distribution throughout the thickness of the membranes at both nanometre and micrometre scale. The analysis is carried out through Electron microscopy analyzer using a Zeiss EM10 SEM, in the following operating conditions: 20 kV acceleration voltage, beam current between 6 and 14 pA and BSD detector with four elements, gain +3. By analysing the cross sections of the composite membranes by SEM, the distribution of the filler particles could be evaluated.

2.3.4 Tensile strength

Tensile strength and elongation are both important mechanical properties regarding polymeric membrane because they indicate the maximum stress to which a material can resist before breaking. This test was performed using a Zwick/Roel Z010 following the standard method D882-02. 5 samples were cut in strips of uniform width, 11 mm, placed in the grips of the machine and tested at a strain rate of 1 mm/min.

2.3. Fuel cell tests

The MEA was obtained by hot pressing the membrane sandwiched between the commercial electrodes purchased from Fuelcellstore. The electrochemical performance (cell voltage and electrical current) of the fuel cell were measured by using a test station consisting of an Agilent E3631A DC power supply to perform the electrolysis and the TTi LD300 Electronic DC Load to carry out the polarization curve in the fuel cell mode. The power density was calculated as the product of cell voltage and current density. The power density was plotted against the current density (P–I curve) to determine the peak power density (Pmax) at each test.

3 Results and discussion

3.1. Membrane characterization

SEM images of the GO-Nafion composite membranes with different loading (0.5, 1 and 1.5%) are presented in Fig. 1. The composite membrane showed the GO sheets dispersed horizontally in the polymer layer and perpendicular to the direction of reactant supply to electrodes.

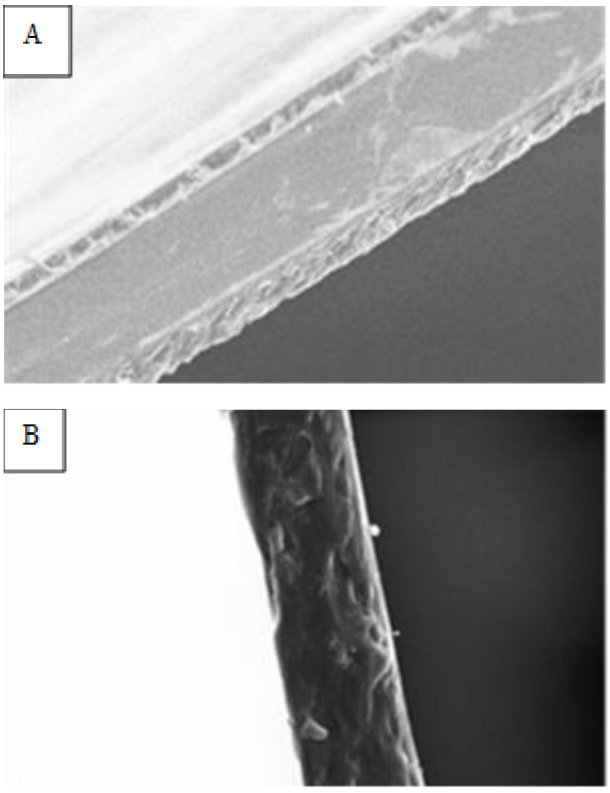

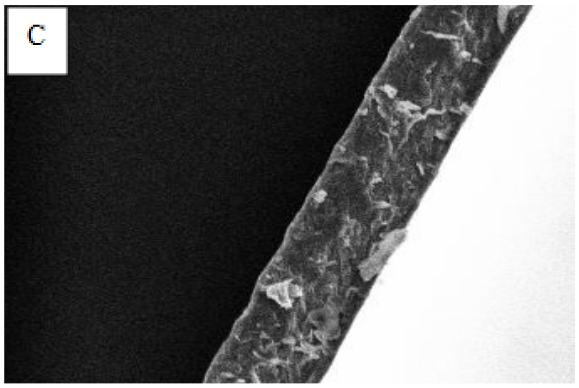

Fig. 1. SEM images for recast and GO membranes. A for 0.5%, B for 1% and Cf or 1.5%.

Table 1 displays the membrane characteristics of water uptake, swelling, and IEC. For all loading, the presence of GO in the polymer structure has led to an increase in swelling and has improved water uptake due to the hydrophilic nature of graphene oxide.

Table 1. Water uptake, swelling, and ion exchange capacity of the fabricated membranes.

Membrane	Water uptake %	Swelling ratio (%)	IEC (meq/g)
Nafion	16.55	24.07	0.80
Nafion-GO (0.5%)	28.10	25.37	0.87
Nafion-GO (1%)	31.16	27.38	0.89
Nafion-GO (1.5%)	31.88	29.63	0.91

The beneficial effect of GO on the IEC is controversial. Some authors [5] claimed that the IEC decreased with the addition of GO, when compared to the recast Nafion, due to the less Nafion amount in the GO membranes and a reduction in ionic channels. However, authors [9] claimed that s non-uniform dispersion with agglomerates could potentially have a higher IEC as less ionic channels are obstructed by the graphene oxide. The tensile strength and elongation ratio data of the recast Nafion and composite membrane were summarized in Table 2.

Table 2. Tensile strength and elongation ratio of the fabricated membranes.

Membrane	Tensile strength [MPa]	Elongation ratio (%)
Nafion	16.55	75
Nafion-GO (0.5%)	28.10	65
Nafion-GO (1%)	31.16	50

Nafion-GO (1.5%)	31.88	40

All GO/Nafion membrane showed a tensile strength higher than the bare Nafion membrane due to the inclusion of GO into the perfluorosulfonic matrix. The more GO is included in the membrane, the higher tensile strength is obtained, as stated by several authors [10-11]. However, as can be observed, the elasticity of the GO membrane is very low compared to Nafion. This result is in agreement with literature. In fact, Bayer et al. [11] claimed that the elongation of the GO membrane before rupture is only 22 ± 1%, compared with 411 ± 14% in Nafion, so the introduction of GO results in a decrease in elongation. To obtain good performances, membrane should have high elongation ratio and high tensile strength. However, high tensile strength is often chosen over the elongation ratio. A good compromise between a gain obtained from the water uptake, IEC, and tensile strength and the loss of the elongation rate, is obtained by using the membranes with 1 and 1.5% of GO loading, which represent the optimum range. In this work, MEAs were fabricated using GO membranes with 1% of loading, a compromise solution between the enhancement obtained and material quantity, so costs.

3.2. In-situ tests

The current-voltage (I-V) characteristics curves for the prepared GO and Nafion casted composite membrane are studied in both electrolysis and fuel cell mode. Single cell water electrolysis polarization curves were depicted in Figure 2.

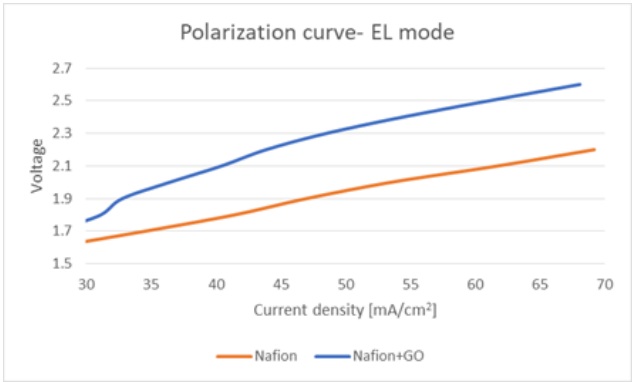

Fig. 2. Water electrolysis polarization curves

The current onset in the activation region is slightly favourable for the cell with plain Nafion, whereas at higher current densities, higher voltages are required for the cell assembled with the GO composite membrane. To the best of our knowledge, there are no studies in the literature on the use of graphene oxide as a polymer electrolyte in water electrolysis. Therefore, this phenomenon needs to be better elucidated, carrying out tests at different temperature and different GO loading, because on a first attempt the analysed behaviour could be due to the presence of the functionalized inorganic filler dispersed in the polymer matrix, which lowers the proton conductivity of the membrane, phenomenon emphasized at low temperature. From the polarization curves obtained in the fuel cell mode, the trend observed is the opposite (Figure 3).

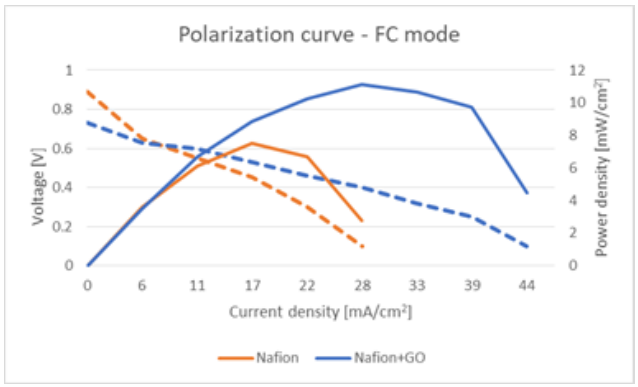

Fig. 3. Fuel cell polarization curves

The composite GO membrane showed higher performance than that of recast Nafion. The maximum power density of the composite membrane and the operating range were 48% and 57% more than those recorded for the bare Nafion. This was because the graphene oxide retained more water and enhance the ion exchange capacity, so those beneficial effects mitigate the drop in the proton conductivity [12]. Figure 4 shows the maximum FC generated power density for more than 15 cycles to investigate the energy performance drop of the device when it performs numerous continuous cycles.

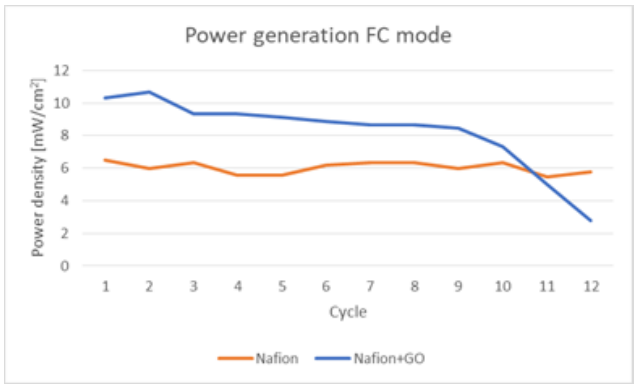

Fig. 4. Maximum power output over cycles

As is clear from the above figure, the maximum power density delivered by the fuel cell assembled with the GO membrane was initially higher than that of the bare Nafion. However, the performance started to drop after the tenth cycle reaching a maximum value of 8 mW/cm^2 then collapsing up to 3 mW/cm^2 at the twelfth cycle. This trend was expected due to electrochemical carbon corrosion at high voltage, one of the critical determinants of the lifetime of polymer electrolyte membrane fuel cells [13]. Considering the results obtained in both WE and FC, the round-trip efficiency (RT) for the Nafion membrane was 21%, slightly lower than the RT efficiency of the GO composite membrane that reached a value of 23%. Despite the small improvement, the RT is

still far from being an acceptable value for URFC commercialisation and global uses besides the fact that is should be kept constant for hundreds of hours. However, this was a first study performed on the application of GO membranes for URFC application that requires further investigation.

4 Conclusion

In this study, Nafion and GO-Nafion membranes were fabricated via solution casting to be tested in a PEM reversible fuel cell. The membranes were characterised, and it was confirmed SEM that graphene oxide was successfully incorporated into the Nafion structure. The composite membranes exhibited better tensile strength and higher swelling and water uptake, but with lower tensile strength. In-situ testing revealed that the composite membrane generally had higher FC performance, leading to an initial slight improvement in term of efficiency, even if with a lower durability due to the carbon corrosion that occurs during the WE mode. It is important to note that the development of GO-Nafion composite membranes for URFC is not present in literature so the behaviour of the composite membranes presented here should be deepen in term of different operating conditions and different filler loading.

References

[1] T. Sadhasivam, K. Dhanabalan , S. Roh , T. Kim et al.. International Journal of Hydrogen Energy, **42** (2017)
[2] P. Biddyut, J. Andrews. Renewable and Sustainable Energy Reviews **79,** (2017)
[3] G. Mohamed, et al. International journal of hydrogen energy **39,** (2014)
[4] H. Junoh et al. Membranes **10**, (2020)
[5] A. Ibrahim et al.. International Journal of Hydrogen Energy, **45** (2020)
[6] Jung, H.-Y.; Cho, K.-Y.; Lee, Y.M.; Park, J.-K.; Choi J.-H.; Sung Y.-E. Journal of Power Sources **163**, (2007)
[7] Yasukawa, M.; Suzuki, T.; Higa, M. Membrane-Based Salinity Gradient Processes for Water Treatment and Power Generation 1st edition (2018)
[8] Leng, Y.; Materials Characterization. 2008, Singapore:John Wiley & Sons (Asia) Pte Ltd.
[9] Kumar, R.; Xu, C.; Scott, K. RSC Adv, (2012).
[10] Wang, L.; Kang, J.; Nam, J.; Suhr, J.; Prasad, A.; Advani, S. ECS Electrochemistry Letters **4**, (2015).
[11] Bayer, T.; Bishop, S.R.; Nishihara, M.; Sasaki, K.; Lyth, S.M. Journal of power sources **272**, (2014)
[12] Kumar, R.; Xu, C.; Scott, K. RSC Adv. **2**, (2012)
[13] S. Jang, H.Kim. J. Am. Chem. Soc. **132**, (2010)

Ionomer Films Impact on The Structure, Flow Regime, and The Wettability of The Catalyst Layer of PEMFC

Karrar Alofari[1, *], *Ezequiel* Me´dici[1], *Kazuya* Tajiri[1], and *Jeffrey* Allen[1]

[1]MTU, ME-EM Department, 49931 Houghton MI, USA

Abstract. Percolation testing and contact angle measurements have been used to investigate the role of relative humidity on structure, mass transport, and wettability of a PEM fuel cell catalyst layer and membrane. Four samples were tested, two catalyst layers and two membranes. Structure and mass transport changes in the catalyst layers resulting from RH changes were studied in terms of percolation pressure. A clear change in the structure between low and high RH conditioning was observed. Relative humidity (RH) cycling also impacted percolation pressures with an indication of catalyst layer cracking. In addition, RH effect on wettability of both catalyst layers and membranes was studied by measuring contact angles of sessile drops.

1 Introduction

Ionomer in the catalyst layer form nano-scale thin films [1, 2] that often have the same chemistry as the much thicker electrolyte membranes, though a distinctive difference in properties such as water uptake and conductivity are observed [3, 4]. The chemical structure of the ionomer consists of hydrophilic sulfonic group clusters that work as a protonic path, which are connected by a side chain to a hydrophobic fluorocarbon backbone that keeps the ionomer both mechanically and chemically stable [5, 6]. Transport properties of the ionomer are affected by hydration [4, 7, 8]. Both thin (7nm [1]) and thick (> 10m [9, 10]) ionomer films interact with vapor to alter the orientation of sulfonic acid side chains [5, 11]. This affects wettability and conductivity in the ionomer films [12, 13].

The ionic domains in the ionomer retains water, where the number of water molecules per sulfonic acid group can reach up to 8 as in ionomer thin films in the catalyst layer [4], and 15in electrolyte membrane [10, 14] when saturated with vapor. Thus, the pore size distribution of a catalyst layer may be shifted towards a lower average effective radius as the ionomer swells [15, 16]. This will have an impact on reactant transport resistances [17, 18, 19]. Cycling the relative humidity of the catalyst layer results in the absorption/release of water to/from ionomer films, which in turn leads to structural stresses and potential defect (crack) growth [20].

In order to macroscopically probe the effect of RH on catalyst layers, percolation testing was conducted using a modified Hele-Shaw arrangement. Percolation behaviour and projected wetted area will help investigate the internal structural changes and the flow regimes as the RH condition changes. Similarly, the sessile drop method is adapted to observe the macroscopic changes in the wettability over a range of RH conditioning.

2 Experimental Section

2.1 Percolation Testing

Figure 1 illustrates the modified Hele-Shaw approach used for percolation testing. A catalyst layer sample is compressed between two transparent PMMA platens and liquid is injected at a constant rate through a 2mm diameter hole located in the middle of the lower platen. RH conditioning is achieved by injecting gas nitrogen through the test setup prior to liquid injection. RH conditioning occurred at room temperature (22 to 25 ◦C).

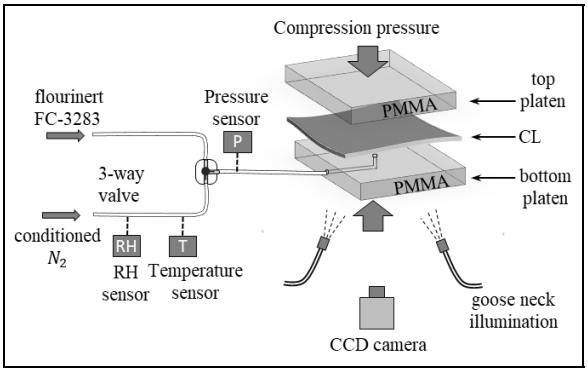

Fig. 1. Percolation setup using a modified Hele-Shaw apparatus.

* Corresponding author: ktalofar@mtu.edu

Table 1. Catalyst Layers data.

Sample	Pt loading	EW	I/C
CL725	–	725	0.8
CL825	0.19 mg/cm2	825	0.9

RH of the nitrogen was measured using a Mega 2560 R3 board that was connected to an Arduino computer. After sufficient RH conditioning, an inert liquid (FC3283 Fluorinert, 3M) was injected at a constant flow rate using an ultra-low flow rate syringe pump (Harvard Apparatus, 2274). Injection pressure (i.e., percolation pressure) is measured using a pressure transducer (Omega 209-30V15G10V) located just upstream of the sample injection location. The projected area of the catalyst layer containing liquid was recorded using a CCD camera (Panasonic GP-KS125) at 30 frames per second. Further details of the test apparatus are provided in Alofari et al. [21] and Medici and Allen [22].

Two catalyst layers with equivalent weights of 725 and 825 (provided by 3M) were tested over a range of RH conditioning. Samples were conditioned at low and high RH as shown in Figure 2 for up to three hours. Pertinent material properties for the catalyst layers are listed in Table 1. CL725 and CL825 refer to catalyst layers with equivalent weights (EW) of 725 and 825, respectively. The ionomer-to-carbon (I/C) ratio for CL725 and CL825 are 0.8 and 0.9, respectively, and CL725 does not include any platinum catalyst.

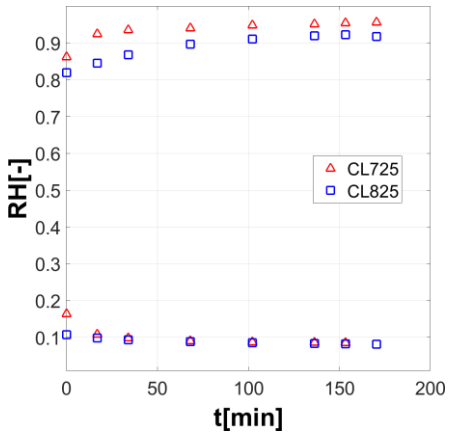

Fig. 2. Measured RH versus time while conditioning the CLs.

2.2 Contact Angle Measurement

Wettability of the catalyst layer samples CL725 and CL825 as well as electrolyte membranes with the same chemistry and equivalent weight, PEM725 and PEM 825, respectively, was measured using the sessile drop method. Drop profile images were measured using a long working distance microscope paired with a CCD camera with a uniform backlight. Consistent, accurate, and repeatable drop sizes were deposited using a precision threaded syringe (Hamilton 1750TPLT) in which one plunger rotation is equivalent to 5.27µL. Drop size control is illustrated in Figure 3.

Catalyst layer and membrane samples were conditioned

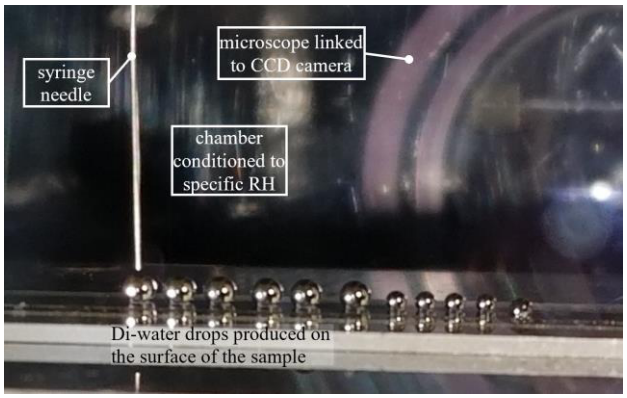

Fig. 3. Water drops on catalyst layer sample for contact angle measurements.

by first drying in a desiccator for two days. Samples were placed into a sealed chamber that enclosed the sample platform. Humidified air flowed through the chamber for a minimum of 60 minutes before drop deposition to ensure constant humidity conditions. The exception was the 0% RH samples that did not use conditioned air circulation. RH measurements were the same as for percolation testing. After conditioning, multiple drops of deionized water were placed on the catalyst layer or membrane surface and imaged.

Contact angles were determined by fitting a Laplace curve to the drop profile, then intersecting the curve at the substrate location. The static contact angle is determined by the value of the Laplace curve at the intersection. For each measurement, a minimum of three independent images were captured within 5 seconds to minimize effects of evaporation. The reported contact angle is the average of the three contact angles and uncertainty is related to the standard deviation.

The rough, heterogeneous surfaces of catalyst layers results in a drop size dependence of the measured contact angle [23, 24]. Therefore, drop deposition volume was carefully controlled for consistency with 3.96 µL for catalyst layers and 1.32 µL for membranes.

3 Results and Discussion

3.1 Percolation Test Results

Table 2 shows the details of the RH conditioning and percolation flow rate for each test. Transient percolation pressure changes dramatically with RH conditioning, indicating structural changes in the catalyst layer. Figure 4a shows percolation pressure at low (9%) and high (95%) RH conditioning for CL725. The injection rate of

Table 2. RH Conditioning and Percolation Flow Rate.

Sample	Sample Size	RH %	Injection Flow Rate
CL725	3.8 cm × 3.8 cm	9	0.396 mm3/min
CL725		95	
CL825		9	
CL825		92	

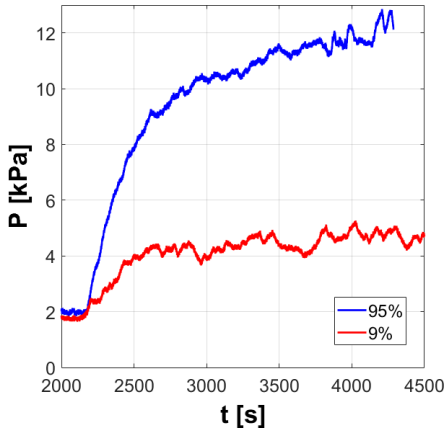

(a) CL725

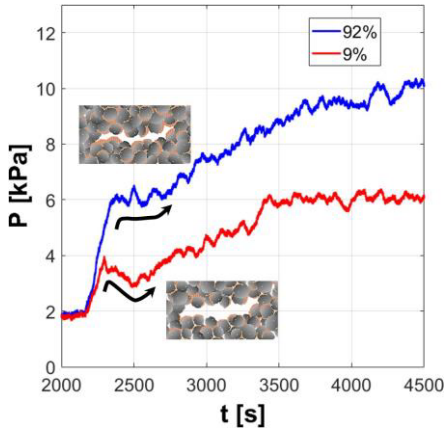

(b) CL825

Fig. 4. Percolation pressure at low and high RH conditioning at constant injection rate of 0.396 mm3/min for (a) CL725 and (b) CL825.

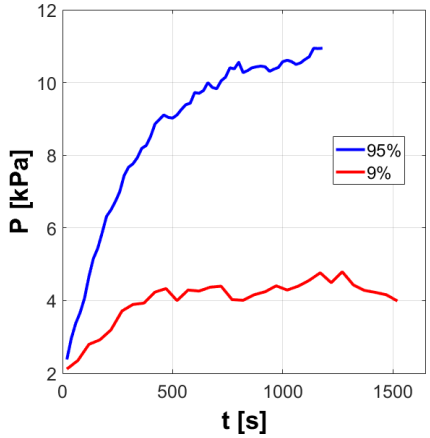

(a) Percolation pressure.

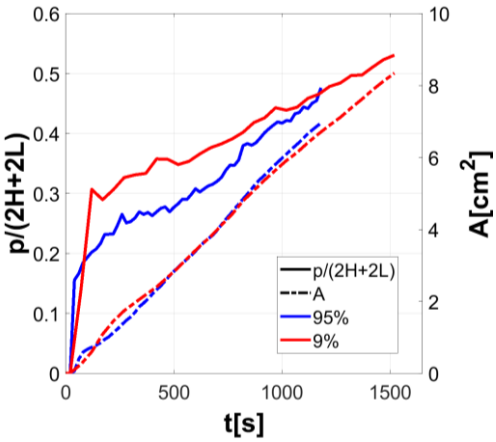

(b) Wetted perimeter and projected area.

Fig. 5. The data include the beginning of the percolation of the liquid phase until the break through. (a) Transient percolation pressure and (b) scaled wetted area and wetted perimeter for CL725 at an injection rate of 0.396 mm3/min. The perimeter of the wetted area, P, is scaled by the perimeter of the catalyst layer sample, 2H + 2L.

FC3283 was 0.396 mm3/min for all tests shown. The percolation pressure curve for CL725 at 9% condition levels off after approximately 2500 seconds, whereas the 95% test exhibits a continuous rise at much higher pressures. The difference in percolation pressure is likely due to ionomer swelling resulting in a smaller average pore size. The result is an increase in mass transport resistance within the catalyst layer at high RH conditioning. A similar effect is observed in CL825, which had a defect (crack) in the catalyst layer. The instant FC3283 encountered this defect is easily detected in the transient percolation pressure as shown in Figure 4b. After the defect, or crack, fills, then the pressure curves exhibit a similar trend as for the CL725 sample.

Transient percolation pressure data in Figure 4a indicate that imbibition changes with RH conditioning. At 9% conditioning, the pressure curves exhibit a classic capillary fingering response and at 95% the pressure curves exhibit a stable displacement response [22]. In stable displacement, viscous effects dominate the advancing liquid front and liquid is invading most, if not all, pores. For a fixed flow rate, the injection pressure continuous to increase as the liquid advances. In capillary fingering, at the liquid-gas interface, fingers form with a nearly levels off percolation pressure to a constant value. The stable displacement and capillary fingering response is reinforced in the imaging data. Figure 5a compares the injection pressure for CL725 at high and low RH conditioning with wetted area and perimeter data for the same tests in Figure 5b. The wetted area follows the same trend, is the same for high and low RH conditioning, which is expected for a constant rate of injection. The rate that they advanced is not the same, though with the 95% RH test ending earlier than the 9% RH test. A percolation test ends when liquid reaches the edge of the catalyst layer sample. The wetted area results are indicative of a smaller average pore size for the high RH sample as compared to the low RH sample. There is less overall void volume in the high RH sample, so at a constant rate of injection the test will end earlier.

The scaled perimeter (perimeter of the projected wetted area divided by perimeter of sample) in Figure 5b, like the pressure response, indicates a difference in imbibition flow regime. A dry catalyst layer, such as the 9% RH sample, has a relatively large average pore size that more readily facilitates capillary fingering. In contrast, the relatively small average pore size of the wet catalyst layer (95% RH sample), resulting from the

hypothesized ionomer swelling, increases the local viscous stresses at the advancing liquid-vapor interface resulting in stable displacement.

The hypothesized shift in average pore size due to ionomer swelling in the catalyst layer is supported by varying measured water uptakes with RH. Figure 6 shows the water content, λ, of nafion for thick membranes [14, 25] and for ultrathin ionomer films with similar equivalent weight as CL725 [4]. As RH is increased, more water retained by hydrophilic sulfonic acid clusters in the ionomer, which results in internal structural changes. As RH decreases, the absorbed water is released. Water uptake and release with RH is repeatable, but the cyclic effect on catalyst layer structure might not be.

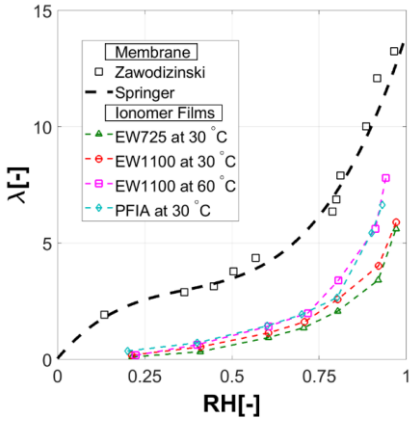

Fig. 6. RH effect on the water content (λ) in the hydrophilic sulfonic acid side chain clusters for thick nafion membrane [14, 25] and ultra-thin ionomer films [4].

3.2 RH Effects on Wettability

Sessile drop contact angle measurements were conducted on catalyst layers (CL725 and CL825) and membranes (PEM725 and PEM825) for a range of RH conditioning, see Figure 7. For both catalyst layer and membrane samples the static contact angle increased then decreased with increasing RH conditioning. The lowest values of contact angle for the catalyst layers occurs at 0% RH conditioning. This is also where there is minimal difference between CL725 and CL825, less than 1◦ and within the measurement uncertainty.

For both catalyst layers, as RH increases from 0%, there is an immediate difference in static contact angle that can likely be attributed to the dispersed Pt catalyst particles present in the CL825 sample, as shown in Figure 7a, where the maximum static contact angle that occurs is approximately 50 to 60% RH. As RH is further increased the static contact angle decreases. The difference in the I/C ratio between the two catalyst layers does not appear to have any significant effect since the trends are the same.

Despite good repeatability, changes in static contact angle for the heterogeneous surfaces of these catalyst layers are difficult to explain. Based on preliminary results from laser surface profiling there is no measurable change in surface roughness (0.29µm ± 0.37 for CL725, and 0.75µm ± 0.93 for CL825) with RH conditioning. Our hypothesis is sulfonic acid side chains become less exposed at the catalyst layer surface as the ionomer films take up additional water as RH conditioning increases. For RH conditions above 50-60%, morphological alterations associated with the non-linear increase in water uptake, shown in Figure 6, there is a decrease in the catalyst layer's surface hydrophobicity.

Figure 7b shows the static contact angle measurements for the membrane samples PEM725 and PEM825. The static contact angles are approximately 50◦ less than those on the catalyst layer. This is largely due to the absence of surface roughness on the membranes so there is no structural component to the contact angle measurement. There is a slight increase in static contact angle with increased RH conditioning from 0% to 25%. Unlike the catalyst layer samples, static contact angles are relatively constant with increased RH conditioning. The exception is at the highest RH of 90% for which an absorbed water film may have begun to form on the membrane surface. PEM725 exhibits overall larger contact angles as compared to PEM825, which was unexpected, though this is consistent with the results of water content in the ionomer films shown in Figure 6, where the calculated λ at $30\ ^{\circ}C$ for EW725 is less than EW1100. With higher the EW there are less sulfonic acid groups (hydrophilic part) and less water content [26].

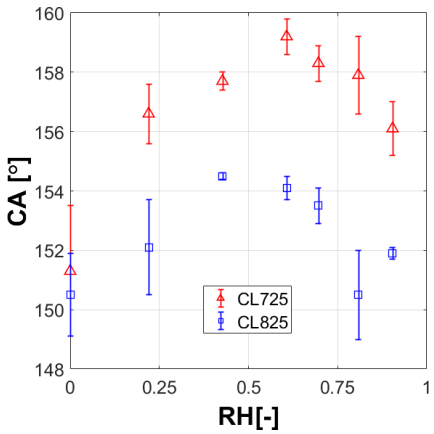

(a) Catalyst layers

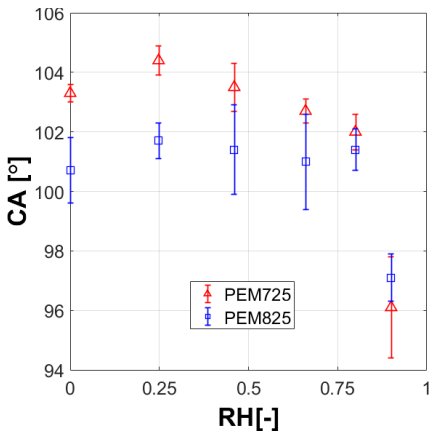

(b) Membranes

Fig. 7. Static contact angles on (a) catalyst layer samples and (b) membranes for range of RH conditioning.

There is a possibility of changes in the chemical structure orientation in the membrane similar to the observations of Bass et al. [5].

3 Conclusion

Changes in mass transport resistance and wettability of catalyst layers and membranes were studied using macroscopic observations of percolation and contact angle testing. Percolation pressure and liquid front dynamics for low and high RH conditioning indicate structural changes are occurring in the catalyst layer samples. These changes are significant enough to alter the imbibition flow regime for the same liquid injection rates. Static contact angle measurements on the catalyst layer surfaces also indicate possible morphological changes.

Acknowledgement

This work was supported in part by The Department of Energy, Office of Energy Efficiency and Renewable Energy (EERE) under award number DE-EE0007650. Additional support was provided by the Higher Committee for Education Development (HCED) of the Iraq Ministry of Higher Education, the Department of Mechanical Engineering – Engineering Mechanics at Michigan Tech, and funds from the John F. and Joan M. Calder Professorship. The authors thank Dr. Andrew Haug for supply the test samples and Dr. Kevin Cooper of Scribner Associates, Inc. for providing a gas humidifier for sample conditioning.

References

1. Lopez-Haro, M., Guétaz, L., Printemps, T., Morin, A., Escribano, S., Jouneau, P.H., Bayle-Guillemaud, P., Chandezon, F. and Gebel, G., *Nature communications*, **5,** 1 (2014).
2. Paul, D. K., Karan, K., Docoslis, A., Giorgi, J. B., and Pearce, J. *Macromolecules*, **46**, 9 (2013).
3. Paul, D. K., McCreery, R., and Karan, K. *Journal of the electrochemical society*, **161**,14 (2014).
4. Shrivastava, U. N., Fritzsche, H., and Karan, K.. *Macromolecules*, **51**,23 (2018).
5. Bass, M., Berman, A., Singh, A., Konovalov, O., and Freger, V., *Macromolecules*, **44,** 8 (2011).
6. Weber, A. Z. and Newman, J.. *Journal of the Electrochemical Society*, **151**, 2 (2004).
7. Shrivastava, U. N., Suetsugu, K., Nagano, S., Fritzsche, H., Nagao, Y., and Karan, K., *Soft Matter*, **16**, 5 (2020).
8. Nguyen, H.-D., Porihel, R., Brubach, J.-B., Planes, E., Soudant, P., Judeinstein, P., Porcar, L., Lyonnard, S., and Iojoiu, C., *ChemSusChem*, **13**, 3 (2020).
9. Gierke, T.D., Munn, G.E. and Wilson, F., *Journal of Polymer Science: Polymer Physics Edition*, **19,** 11 (1981).
10. He, Q., Kusoglu, A., Lucas, I.T., Clark, K., Weber, A.Z. and Kostecki, R., *The Journal of Physical Chemistry B*, **115**, 40 (2011).
11. Van Nguyen, T., Nguyen, M. V., Lin, G., Rao, N., Xie, X., and Zhu, D.-M., *Electrochemical and Solid State Letters*, **9**, 2 (2005).
12. Paul, D. K. and Karan, K., *The Journal of Physical Chemistry C*, **118**, 4 (2014).
13. Bass, M., Berman, A., Singh, A., Konovalov, O., and Freger, V., *The Journal of Physical Chemistry B*, **114**, 11 (2010).
14. Zawodzinski Jr, T. A., Neeman, M., Sillerud, L. O., and Gottesfeld, S., *The Journal of Physical Chemistry*, **95**, 15(1991).
15. Kusoglu, A., Kushner, D., Paul, D. K., Karan, K., Hickner, M. A., and Weber, A. Z., *Advanced Functional Materials*, **24**, 30 (2014).
16. Ahangar, S. B., Bellur, K., Medici, E., Tajiri, K., Allen, J. S., and Choi, C. K., *ECS Transactions*, **92**, 8 (2019).
17. Wang, G., Osmieri, L., Star, A. G., Pfeilsticker, J., and Neyerlin, K. C., *Journal of The Electrochemical Society*, **167**, 4 (2020).
18. Zhang, F.-Y., Spernjak, D., Prasad, A. K., and Advani, S. G., *Journal of The Electrochemical Society*, **154**, 11 (2007).
19. Deevanhxay, P., Sasabe, T., Tsushima, S., and Hirai, S., *Electrochemistry communications*, **22** (2012).
20. Chang, Y., Liu, J., Li, R., Zhao, J., Qin, Y., Zhang, J., Yin, Y., and Li, X., *Energy Conversion and Management*, **189** (2019).
21. Alofari, K. T., Medici, E., Tajiri, K., and Allen, J. S., *ECS Transactions*, **92**, 8 (2019).
22. Medici, E. and Allen, J. (2009). *Journal of Power Sources*, 191(2):417– 427.
23. Drelich, J. and Miller, J. D. *Journal of colloid and interface science,* **164**, 1 (1994).
24. Wang, X., Wang, W., Qu, Z., Ren, G., and Wang, H., *International Journal of Hydrogen Energy,* (2021).
25. Springer, T. E., Zawodzinski, T., and Gottesfeld, S. *Journal of the electrochemical society*, **138**, 8 (1991).
26. Ramaswamy, N., Kumaraguru, S., Koestner, R., Fuller, T., Gu, W., Kariuki, N., Myers, D., Dudenas, P. J., and Kusoglu, A. *Journal of The Electrochemical Society*, **168,** 2 (2021).

Experimental study of gas diffusion layers nonlinear orthotropic behavior

Marwa Ouerghemmi, *Christophe* Carral*, and *Patrice* Mele
Univ. Grenoble Alpes, Univ. Savoie Mont Blanc, CNRS, Grenoble INP, LEPMI, Grenoble, 38000, France

Abstract. One of the most important components of PEMFC is the gas diffusion layer (GDL), owing to its key role in the reactant diffusion, water management, thermal and electron conductivity. Therefore, the GDL must have an optimal stiffness to ensure these transport functions during numerous hydrothermal cycles.
The understanding of its behavior is still a remaining issue. Its orthotropic mechanical behavior requires a series of mechanical characterizations in the plane of the fibers and out of plane. In addition, there are different manufacturing processes for GDL in sheet or roll form to optimize its functional properties. A macro porous layer (MPL) or different PTFE contents might be added by different manufacturers to optimize its performance. In this study, we have performed several mechanical tests differentiating between in plane and out of plane properties in order to characterize different GDLs available on the market. All of the experimental work has been done in the machine (MD) and cross machine direction (CD) according to the fiber orientation. The different GDL types were then classified into categories presenting similar mechanical response.

1 Introduction

The PEMFC is subjected to different range of stresses induced by its assembly process and then by its operating conditions, which have a direct impact on its performance and durability [1,2]. Different studies have shown that the response to the mechanical stress is different from a layer to another in the stack [3,4]. Understanding the mechanical response of the GDL to the different stresses it undergoes during operation cycles will help identify the origin of morphological changes that may impact the performance of the PEMFC [5,6]. For example, cyclic compression causes significant and irreversible changes in the GDL's structure and properties, surface morphology and pore size, which inhibit the gas circulation and blocks the water evacuation. Moreover, it induces a nonlinear decrease in the contact electric resistance between the bipolar plate and GDL [7-11].

Some GDLs undergo hydrophobic treatment or have an additional microporous layer for better efficiency. However, during the manufacturing process, several heterogeneities can appear, such as thickness variation or non-homogeneous distribution of the hydrophobic treatment, which makes its characterization difficult besides its orthotropic criterion.

In this study, the experimental behavior of GDLs has been investigated, in both in plane as well as out of plane according to the machine and cross machine directions. The Young moduli, shear moduli and Poisson's ratios were determined. As a perspective of this work, the properties determined will be implemented in a numerical model to predict the different mechanical behavior of the membrane electrode assembly (MEA) different layers.

2 Experimental details

2.1. Materials

A range of the most commercialized references of GDL has been characterized, from different manufacturers, with varying PTFE content, and exhibiting or not a MPL (Table1). X-ray tomography observations of these different GDLs have been made and are shown in Figure 1.

Table 1. Description of GDLs samples

GDL type	References	PTFE	MPL
Roll	AvCarb EP40 SGL 28AA SGL 29AA SGL 36AA SGL 38AA SGL 39AA	0	No
Roll+PTFE	SGL 28AA-09 SGL 28AA-18 SGL 28AA-29 SGL 28AA-32	9 % -30%	No
Roll+PTFE +MPL	SGL 22BB SGL 28BB SGL 36BC SGL 39BC	13%-15%	Yes
Sheet	Spectracarb 2050A-0850 TorayH060 TorayH090	0.4-10%	No

* Corresponding author: christophe.carral@univ-smb.fr

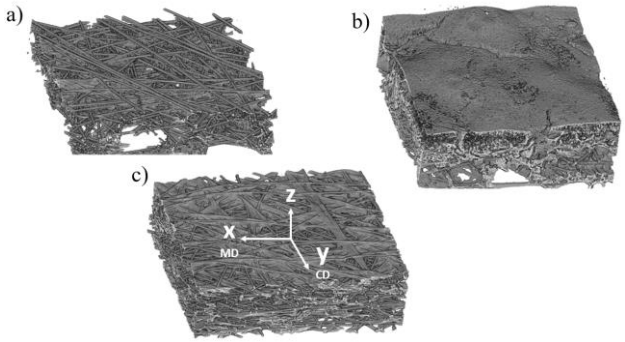

Figure 1. Tomographic images of (a) a roll GDL (39AA), (b) a roll GDL with PTFE and MPL (39BC) and (c) a sheet GDL (Toray H090)

2.2 Tensile test

The tensile tests were carried out on a Metravib-Acoem VA4000 machine with a 140N force sensor, the displacement speed was 1 mm/min.

A study on the optimization of the sample dimensions was performed during the implementation of the experimental protocol based on the ISO 1924 [12]. This analysis was used to verify the good repeatability of the results. The chosen dimensions for the tensile specimen were 5mm of width and 40mm for the gauged length.

The nominal strain (ε_x) and stress (σ_x) were calculated with the following equations:

$$\sigma_x = \frac{F_t}{A} \quad (1)$$

$$\varepsilon_x = \frac{\Delta l}{l_0} \quad (2)$$

where F_t is the tensile force, A is the cross sectional area, Δl is the change in length and l_0 is the initial length.

2.3 Poisson's ratio

Tensile tests were carried out on a Shimadzu AGS-X equipped with a video extensometer (Figure 2) to measure the longitudinal and transverse displacements in order to estimate the Poisson's ratio. A force sensor of 100N and displacement speed equals to 1mm/min were employed. The specimens were cut in both MD and CD directions and had a rectangular shape with a width (30mm) greater than that of the tensile tests in order to increase the amplitude of the transverse displacement for the determination of the Poisson's ratio. Tensile tests were performed cyclically: 2 cycles per specimen. The longitudinal and transverse strains were then determined from the changes in the displacements locations of the vertical and horizontal marker points (Figure 3) during the test given by the extensometer, respectively. The displacements were normalized by the initial length values between marks to obtain the strains. It should also be noted that for GDLs with an MPL, tests were carried out on both sides, in order to analyze the possible influence of this layer.

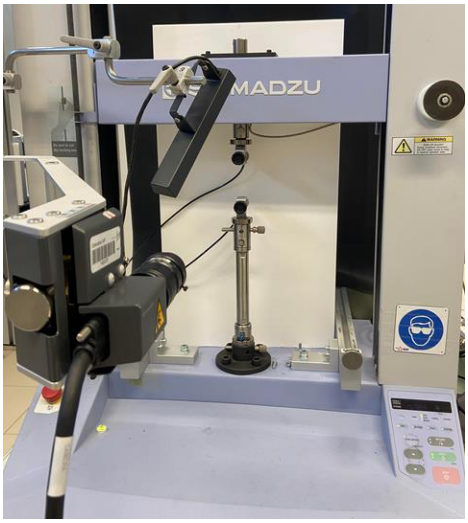

Figure 2. Tensile test bench equipped with a video extensometer

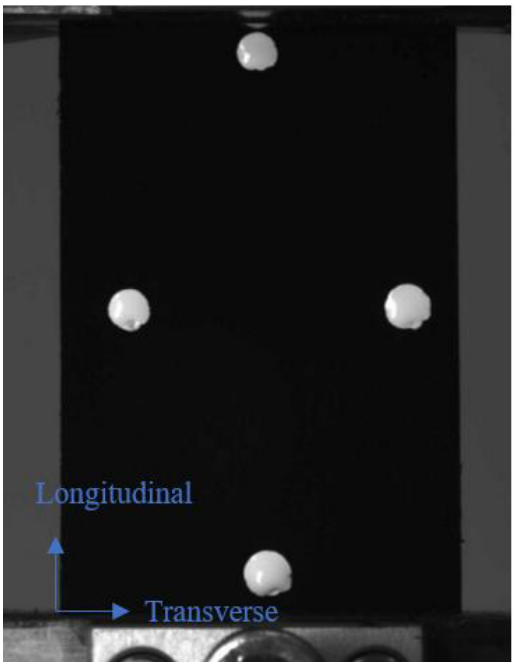

Figure 3. Extensometer image of the MPL side on a roll GDL (SGL 22BB)

2.4 Shear test

Shear tests were performed on the same machine as the tensile tests with specific in plane and out of plane shear devices (Figures 4 and 5). The out of plane shear test is based on the method described in references [13,14]. Samples were rectangular with dimensions of 30mm×15mm for the in plane shear tests and 30mm×25mm for the out of plane shear test. Shear stress (τ) and strain (γ) were calculated as follow:

$$\tau = \frac{F_s}{2A} \quad (3)$$

$$\gamma = \frac{d}{g} \quad (4)$$

where F_s is the shear force, A is the cross-sectional area, d is the vertical displacement, and g is the air gap between the jaws. g is equal to 2mm and 0.2mm for the in plane and out of plane shear test set-ups, respectively.

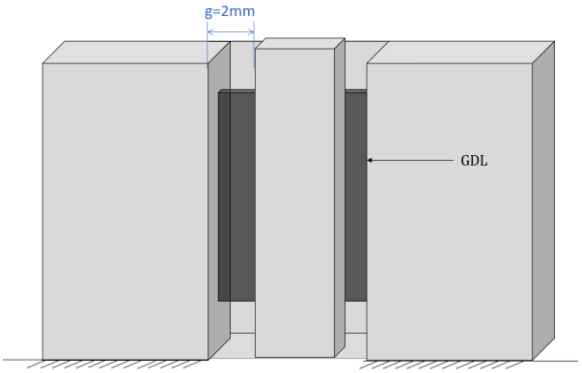

Figure 4. Schematic representation of the in-plane shear test

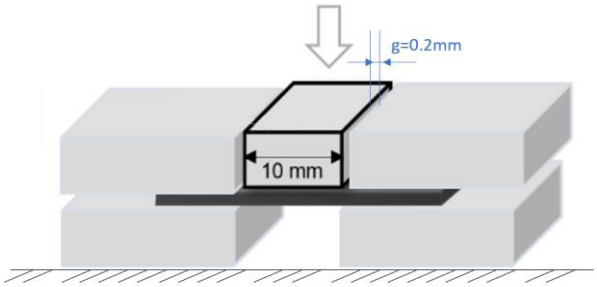

Figure 5. Schematic representation of the out of plane shear test

2.5 Compression test

The compression tests were carried out on an Instron 8872 machine, equipped with a 5kN force sensor. The displacement was measured with clip-on extensometer installed on the compression plate. Tests were performed on a stack of 6 GDLs of 16 mm diameter, with aluminum spacers of 100 µm thickness (Figure 6). These spacers were used to separate the samples and prevent the interpenetration of carbon fibers.

Only the loading part of the compression of the stack was analyzed with a stress ranging from 0.01MPa up to 20MPa, 0.01 being the contact pressure at which the stack thickness was measured. Compressive stress and strain were calculated as follows:

$$\sigma_z = \frac{F_c}{A} \quad (6)$$

$$\varepsilon_z = \frac{\Delta t}{t_0} \quad (7)$$

where F_c is the compressive force, A is the specimen area, Δt is the variation in thickness and t_0 is the initial thickness.

The stress can be represented as a function of relative density, as proposed by Carral et al [4]. This representation allows to take into account the fibrous structure of the different GDL.

The relative density ρ can be calculated with the following equation:

$$\rho = \frac{Aw}{t_0(1-\varepsilon_z)\rho_f} \quad (8)$$

where Aw is the areal weight and ρ_f is the fiber density equal to 1.8 g cm^{-3}[15].

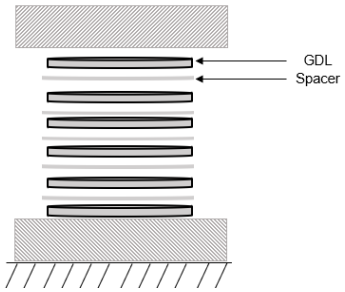

Figure 6. Schematic representation of the compression test setup

3 Results and discussion

The GDLs exhibit a linear behavior in the MD and CD directions under tensile and shear stresses. Tensile moduli in both directions can be then determined and are shown for the different types of GDL (roll, roll + PTFE, roll + PTFE and MPL and sheet) in Figure 7. The highest elastic properties are obtained for sheets, where a graphitization step is performed on the materials. We can also note the absence of a significant influence of the hydrophobic treatment or the presence of MPL on these properties, for both in plane and out of plane directions. Finally, a weak anisotropy of the elastic properties can be observed with higher properties in the x direction, i.e. in the machine direction.

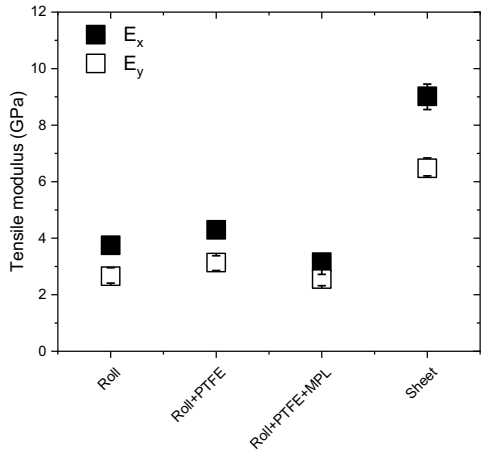

Figure 7. Tensile moduli for the different types of GDL

These results are confirmed in Figures 8 and 9 showing the evolution of in plane and out of plane shear moduli for the different types of GDL respectively. We can also notice that the anisotropy of the elastic properties in shear is significant (factor 100) between the in-plane (between 0.1 and 0.3 GPa) and out of plane properties (between 1 and 4 MPa).

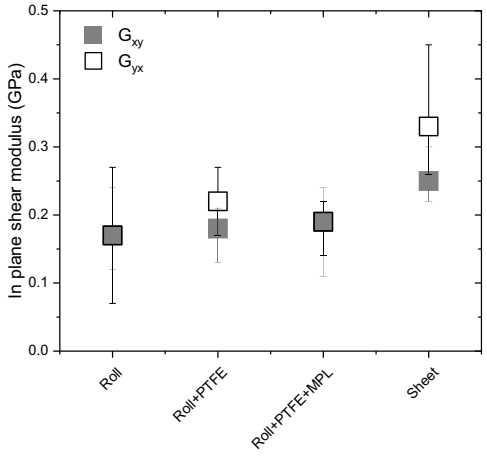

Figure 8. In plane shear moduli for the different types of GDL

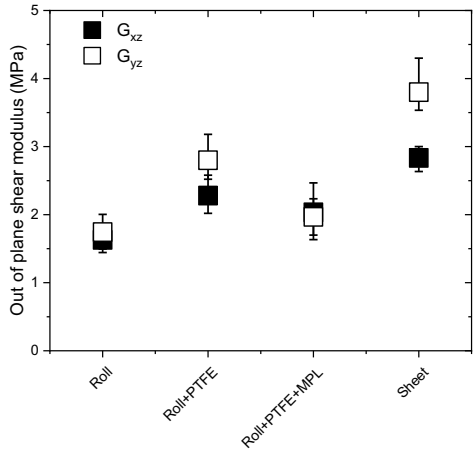

Figure9. Out of plane shear moduli for the different types of GDL

3.1. Poisson's ratio

The evolution of the transverse deformation as a function of the longitudinal deformation of a roll GDL (SGL 22 BB) on the fibers side and on the MPL side are shown in Figures 10a and 10b, respectively. We can observe a low amplitude of the transverse strain of the GDL on the fibers side (10a) while they are insignificant on the MPL side. This result shows that the GDL with MPL should be considered as a composite structure with different properties. The values of the Poisson's ratio estimated from these curves are collected in Table 2, with values between 0.2 and 0.3 for the fibers part of roll GDLs, and close to 0 for sheets GDL and for the MPL side.

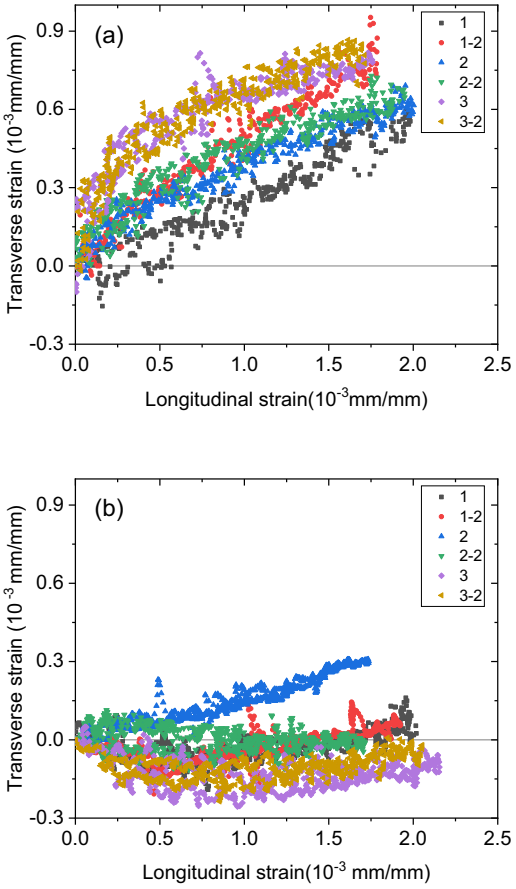

Figure 10. Evolution of the transverse strain with the longitudinal strain, (a) on the fibers side and (b) on the MPL side for the reference SGL 22BB in the cross-machine direction

Table 2. Values of measured in-plane Poisson's ratio for 2 GDL types (roll/sheet)

GDL	ν	Fibers	MPL
Roll SGL 22BB	ν_{MD}	$0.19^{+0.09}_{-0.03}$	$0.07^{+0.05}_{-0.03}$
	ν_{CD}	$0.35^{+0.08}_{-0.06}$	$0.06^{+0.12}_{-0.06}$
Sheet TorayH090	ν_{MD}	≤ 0.05	N/A
	ν_{CD}	≤ 0.05	

3.2. Nonlinear compression behavior

The GDL's behavior under compression (out of plane direction) is non-linear (Figure 11). This non-linearity is related to the porous structure of the material, as shown by different authors [16-19]. In fact, the compression leads to the decrease of porosity and therefore the increase of the contacts between fibers.

The results show a minor impact of the hydrophobic treatment under compression loading since the behavior depends mainly on the contact points between the fibers.

From the previous curve, the tangent modulus (Et) is calculated for the different types of GDL and represented in Figure 12 as function of the stress calculated.

Two different regions can be separated from these curves:

- The first region: at stress values below 5 MPa where Et reaches a constant value ranging from 2.5 and 20 MPa for the different types of GDL, this behavior has been linked in the literature to the mechanical history of the GDL during processing [4].

-The second region: at stress values over 5 MPa, linked to the native behavior of GDL for stress greater than the process stress (Figure 13).

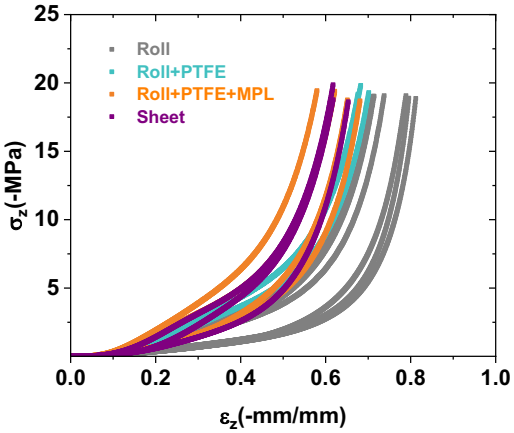

Figure 11. Stress-strain curve of the compression test for the different types of GDL

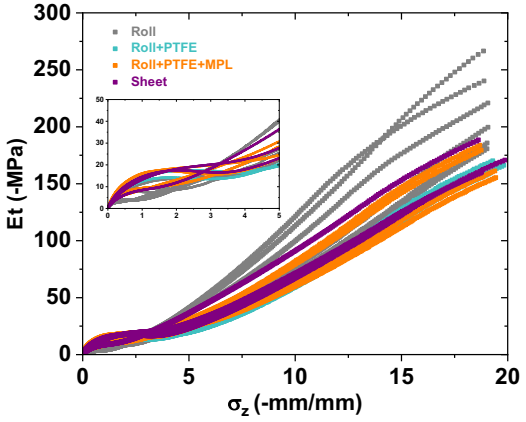

Figure 12. Evolution of the tangent modulus vs σ_z for the different types of GDL

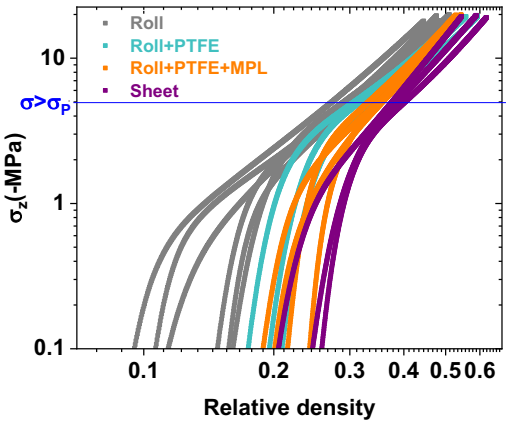

Figure 13. Evolution of σ_z as a function of relative density for the different types of GDL

Conclusion

The complex structure of GDL made of dispersed carbon or graphite fibers, requires a meticulous characterization. To study its orthotropic mechanical behavior, we performed a series of mechanical in plane and out of plane tests. The developed method was, then, applied on different types of GDL, from several suppliers. Our reference set included GDLs in sheet and roll form, with different PTFE contents and with or without MPL layer.

All experimental works were performed in the machine and cross machine directions, depending on the fibers orientation.

Through this study, different GDL types were classified into categories depending on their mechanical elastic behavior. Results showed that GDLs in sheet form had a higher in-plane stiffness than GDLs in roll form, under tensile and shear stresses. The non-linear behavior of the GDLs observed under compression was also characterized. The in-plane anisotropy of the GDLs behavior was not significant compared to its anisotropy between the in plane and out of plane directions, the mechanical moduli ranging from several GPa to few MPa respectively.

A specific tensile test was developed in order to determine the Poisson's ratio for the different GDL references, via the use of an extensometer video able to measure the low transverse displacements (few micrometers) of these materials. In our knowledge, for the first time, values of in plane Poisson's ratio of GDLs were thus obtained and presented in this article.

For sheets GDL, and the MPL side of roll GDLs, very low transverse displacements were measured, indicating that the in plane Poisson's ratios for these materials tended to be close to a zero value. A value in the range of 0.2-0.4 was estimated for the in-plane Poisson's ratio of the rolls GDL fibers' part.

In conclusion, this study has enabled the creation of a database of the orthotropic mechanical properties of the most commercially available GDL references allowing the selection of the best GDL for optimized PEMFC performances. These data will also be used to refine the mechanical modelling of PEMFC, by introducing the experimental orthotropic mechanical properties of the different types of GDL.

References

1. Ozden et al. Progress in Energy and Combustion Science, 2019, 74, 50-102
2. Wu et al. Journal of Power Sources, 2020, 476, 228724
3. Carral et Mélé, International Journal of Hydrogen Energy, 2014, 39, 4516–4530
4. Carral et al., International Journal of Hydrogen Energy, 2018. 43, 19721–19729.
5. Irmscher et al. International Journal of Hydrogen Energy, 2019, 44, 23406–23415
6. Zhang et al. International Journal of Hydrogen Energy, 2020, 45, 23480–23489
7. Radhakrishnan et al. International Journal of Hydrogen Energy,2010, 35, 11107-11118.
8. Bouziane et al. Renewable Energy, 2020, 153, 349–361.
9. Toghyani et al. International Journal of Hydrogen Energy, 2018, 43, 4534–4545.
10. Dafalla et al. International Journal of Hydrogen Energy, 2018, 43, 2327–2348.
11. Zhou et al. Journal of Power Sources, 2017, 163, 874–881.
12. ISO 1924-2: 2008. Paper and board: Determination of tensile properties.
13. Lai et al. Journal of Power Sources, 2008, 184, 120–128
14. Chen et al. Journal of Solid State Electrochemistry, 2019, 23, 2021–2030
15. Mathias et al. Handbook of fuel cells, 42, 2003, 517-37.
16. Norouzifard et al. Journal of Power Sources 2014, 264, 92-99.
17. Kleemann et al. Journal of Power Sources 2009;190, 92-102.
18. El Oualid et al. International Journal of Hydrogen Energy, 2017, 42, 23920-23931.
19. Escribano et al. Journal of Power Sources, 2006, 156, 8-13.

Impedance-based Solid Oxide Fuel Cell testing as scalable and reliable Quality Control tool for cell and batch manufacturing: first findings

Davide Pumiglia[1], Massimiliano Della Pietra[1], *Andrea* Monforti Ferrario[1,2,*], *Stephen* McPhail[1] and *Sergii* Pylypko[3]

[1] ENEA, Laboratory of Energy Storage, Batteries and Hydrogen Production & Use, Department of Energy Technologies and Renewable Sources (TERIN-PSU-ABI), C.R. Casaccia, Via Anguillarese 301, 00123 Rome, Italy
[2] Department of Industrial Engineering and Mathematical Sciences (DIISM), Università Politecnica delle Marche, Via Brecce Bianche 12, 60131 Ancona, Italy
[3] Elcogen AS, Valukoja 23, 11415 Tallinn, Estonia

Abstract. Testing is a necessary step in the manufacturing process of Solid Oxide Fuel Cells (SOFC) to assess the performance of the produced cells before on-field deployment. In this work, the implementation of Electrochemical Impedance Spectroscopy (EIS) and subsequent data elaboration via Equivalent Circuit Modelling (ECM) is evaluated as a viable experimental framework for characterization and Quality Control (QC) of cells or cell batches, complemented to standard polarization-based methods. By performing a statistical analysis of the ECM parameters (representative of each physico-chemical process) the cell and batch operational parameters can be determined and compared. The validity of the proposed methodology is assessed using a wide experimental dataset of a significant number of SOFC samples (20 cells from 3 batches – two of which identical and the third with an intentional modification in the manufacturing process in order to validate the proposed methodology) tested in identical conditions. Results show that the impedance-based method provide detailed information in terms of impedance breakdown (anode gas diffusion process resulting the main criticality), as well as confirming the preliminary results obtained from the polarization approach (Batch#2 showing the lowest total performance and highest uniformity). Highly reproducible intra-batch distributions of the ECM parameters encourage the applicability of such methodology for QC purposes, even with few data collected only in Open Circuit Voltage (OCV) conditions. A relevant deviation of charge transfer and diffusion resistances in Batch#3 respect to other batches is observed (not visible from the polarization curves), which is reconducted to the modified anode functional layer, opening potential applications of the proposed methodology to assess the impact of targeted modifications of manufacturing methods on specific cell electrochemical performances.

* Corresponding author: andrea.monfortiferrario@enea.it

1 Introduction

Testing is a necessary step in the manufacturing process of Solid Oxide Fuel Cells (SOFC) to assess the performance of produced cells before on-field deployment [1]. Currently, production batches are typically characterized by randomly extracting sample cells from the batch which are tested in terms of output performances at a macro-scale (output power and fuel consumption) in long-term stationary operating conditions and compared with the design parameters. However, such characterization method requires long testing periods to obtain meaningful results (especially for high temperature cells which present a high thermal inertia and require long start-up and stabilization times [2]), representing a challenge for Quality Control (QC) when scaling-up production capacity.

Different SOFC characterization methodologies have been developed, among which polarization-based and impedance-based methods are the most widespread [3]. On the one hand, polarization-based methods are simpler and provide a direct indication of the cell performance under load, however only overall performance indicators can be extracted, and little can be said with respect to any specific process occurring within the cell [4]. On the other hand, albeit providing results that are complex to interpret, impedance-based methods based on Electrochemical Impedance Spectroscopy (EIS) provide more detailed data regarding both the ohmic (ionic conduction) and polarization (charge transfer, mass transfer) processes, as well as providing also information in terms of frequency response of the cell [5–7]. The EIS data can be further deconvoluted via different mathematical formulations, obtaining the breakdown of the impedance response for each physico-chemical process (charge or mass transfer) occurring at the electrolyte or at each electrode [8–10].

Impedance-based testing methods present several similarities with other typical QC techniques. In fact, the performance parameters can be obtained with relatively fast and highly replicable measurements (with respect to endurance testing). Furthermore, since the cell is not loaded, EIS can be almost considered a non-destructive test (with exception of a thermal cycle to reach the operating temperature) [6,11].

In this work, the implementation of EIS and subsequent data elaboration via Equivalent Circuit Modeling (ECM) is evaluated as a viable experimental framework for characterization and Quality Control (QC) of cells or cell batches, respect to standard polarization methods. The applicability of the proposed methodology is analysed applied on an experimental dataset obtained from a significant number of IT-SOFC samples (20 cells from 3 production batches) tested in identical experimental conditions (test setup and operating conditions). The quantitative parameters obtained from each characterization technique are analysed statistically to analyse the intra-batch parameter homogeneity – to confirm the applicability of the proposed methodology – and subsequently implemented to spot recurrent parameter deviations between batches.

2 Materials and methods

Within the qSOFC project, several IT-SOFC button cells provided by Elcogen AS were tested by ENEA for electrochemical characterization. The cells present an Anode Supported Cell (ASC) configuration, with an active surface of 2 cm^2 (cathode limited). The thicker supporting anode substrate, together with a very thin layer of electrolyte allows lower operating temperatures (between 650-700 °C) [12], with respect to other manufacturers. In particular, the SOFC samples were supplied from three different production batches (Batch#1, Batch#2 and Batch#3). For Batch#1 and Batch#2 the manufacturing process was identical, whereas for Batch#3 a slight modification of the anode functional layer morphology was intentionally introduced in the manufacturing process in order to validate the proposed methodology. The modification resulted in a denser anode layer at the interface with the electrolyte with the aim of impacting the hydrogen electro-oxidation charge transfer kinetics due to an increase in the active surface and Triple Phase Boundary (TPB) length.

2.1 Experimental setup

The cells were tested in the High Temperature Fuel Cells Operating and Testing Laboratory of ENEA C.R. Casaccia, where two identical test benches were setup. The test bench scheme is illustrated in Figure 1.

The gas distribution system supplies gas from external gas bottles, separate Mass Flow Controllers (MFC - Bronkhorst EL-Flow) are installed in each line to control the flow rate of the gases to the anode and cathode compartment. The total flow rates are set to 150 Nml/min at the anode and 250 Nml/min at the cathode; which are intentionally abundant with respect to the cell surface to ensure ideal performances [13]. The hydrogen content at the anode fuel gas is controlled by varying the relative flow of H_2 and N_2 at equal total flow rate, since N_2 behaves as an inert gas. Likewise, the oxidant composition can be varied by diluting air with N_2. The anode and cathode feeds are supplied to the fuel cell sample through an alumina ceramic housing, placed inside a temperature-controlled furnace (Evenheat Kiln Hot Box) where the cells are mounted vertically, through the use of a high temperature refractory paste (Aremco Ultra-temp 516) which ensures both mechanical support and gas tightness of both anode and cathode chambers.

The electrical interface is composed of an DC electronic power load (Agilent E3634A DC) together with a datalogger (Agilent 34970A) and a LABVIEW-based control system which is used to perform the polarization curves and a separate Impedance Analyzer module (Solartron 1260) coupled with an Electrochemical Interface (Solartron 1287) for the Electrochemical Impedance Spectroscopy (EIS) measurements. The instrumentation is connection to the cell via separate current and voltage wires, attached to current collector meshes to ensure uniform current distribution (Ni and Au for anode and cathode side). Separate current and voltage wires reduce voltage perturbation from current flow and allow to perform 4-point impedance measurements.

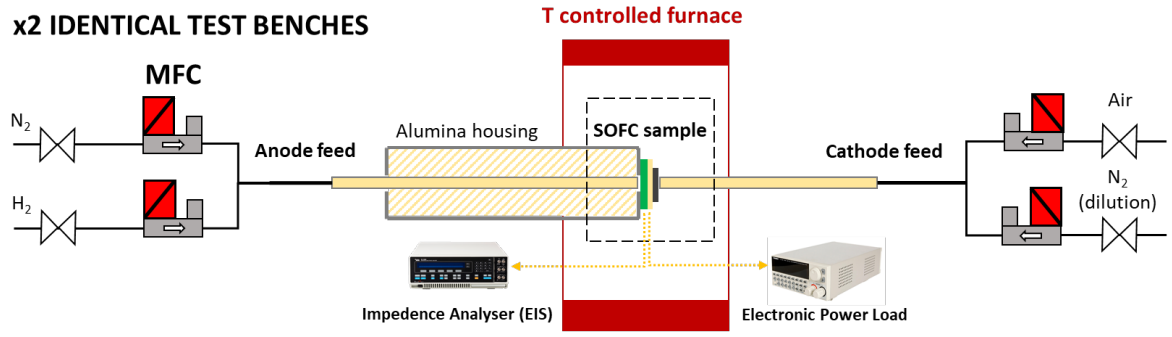

Figure 1. SOFC Test Bench scheme

2.2 Electrochemical characterization techniques and data elaboration methods

Each cell is mounted in the experimental setup and characterized with a homogeneous experimental procedure, which is here described.

After following the start-up procedure (controlled 1°C/min temperature ramp; gradual reduction of the NiO at the fuel electrode) each cell is preliminarily characterized in standard conditions (H_2/N_2 50/50%; 700 °C) with polarization and EIS methods before and after a stabilization period of 50-100 h under a load current of 0.5 A/cm^2, to ensure that stationary conditions have been reached.

Polarization measurements are carried out in galvanostatic mode (step-wise), until reaching 1 A/cm^2 with current in steps of 50 mA/cm^2 or until a cell voltage below 700 mV is reached. After each polarization curve, the cell is stabilized in standard conditions, to remove the produced steam from within the cell which might affect other measurements.

The EIS measurements are carried out in OCV conditions with a frequency range between 100 kHz – 10 mHz (10 points per decade) with an applied voltage perturbation amplitude of 10 mV by using the ad-hoc ZPlot/ZView software by Scribner Associates. By analysing the current response, it is possible to map the impedance in the complex plane. The EIS measurements are carried out in OCV conditions to ensure quasi-static operating conditions, avoiding perturbations due to water and heat formation from the electrochemical reaction, which might alter the cell impedance response.

The EIS data can be elaborated with different techniques to obtain even more detailed information on the cell electrochemical parameters:

- By mathematical elaboration, it is possible to transform the complex impedance data into a frequency-dependant function, namely Distribution of Relaxation Times (DRT), whose intensity can be correlated to each separate impedance contribution, attributed to each physico-chemical process occurring at a certain characteristic frequency. An in-house DRT tool developed in MATLAB has been used to derive the DRT function for all EIS measurements [8], implementing adaptive Tikhonov regularization and K-K tests to ensure the quality of the output DRT functions.
- By means of Equivalent Circuit Modeling (ECM) method the EIS data can be used to determine quantitative values of the impedance contribution of each physico-chemical process [5,9,10]. In fact, a SOFC can be modelled with a well-known equivalent circuit (illustrated in Figure 2), where each circuit element represents a separate physico-chemical process:
  - ➢ The impedance of the electrical connection of the test setup is represented by an ideal inductance L_1, which provides an impact only at high very frequencies for positive values of the imaginary part of the impedance (not significative in terms of cell response);
  - ➢ The impedance of the electrolyte, associated to the ionic conductivity/resistivity of the YSZ electrolyte, can be considered constant with frequency and represented by an ideal resistance;
  - ➢ The charge transfer impedance contributions (for both anode – within the TPB and at the interface - and cathode) can be considered as a RC-parallel, whose frequency response is suitable to represent high-frequency phenomena. Instead of an ideal double layer capacitance, a Constant Phase Element CPE is used to assess non-ideal capacitive behaviour;
  - ➢ The gas diffusion impedance contributions (for both anode and cathode) can be represented by a semi-infinite Warburg element, which is an equivalent electrical circuit component that models the diffusion process in porous media. The Warburg diffusion element mainly contributes to the frequency response at lower frequencies, which are the characteristic frequencies of the diffusion phenomena.

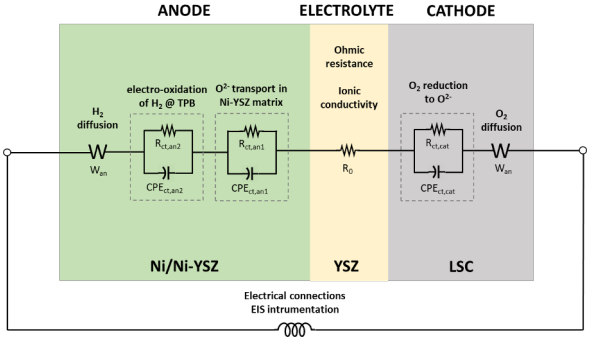

Figure 2. Equivalent Circuit Modeling scheme – association of circuit elements to physico-chemical processes

Given the equivalent circuit topology, the value of each circuit element can be determined via Complex Nonlinear Least Squares (CNLS) fitting method ("Equivalent Circuits" module implemented in ZView software). From the preliminary analysis of the DRT function, initial values for capacitances and resistances can be calculated, rather than being estimated, thus making the fitting more reliable. The numerical algorithm is solved iteratively on gradually wider portions of the frequency range to refine the fitting (according to the preliminary DRT analysis), manually checking for inconsistent values which may arise (since multiple fits can provide the same overall frequency response). The main indicators which are controlled during the fitting process is the χ^2 value of the overall fit, the residual (absolute and relative error) of the fit as a function of frequency with respect to the experimental data and the deviation (absolute and relative error) of each circuit element with respect to the initial calculation. An example of the fitting procedure is illustrated in Figure 3.

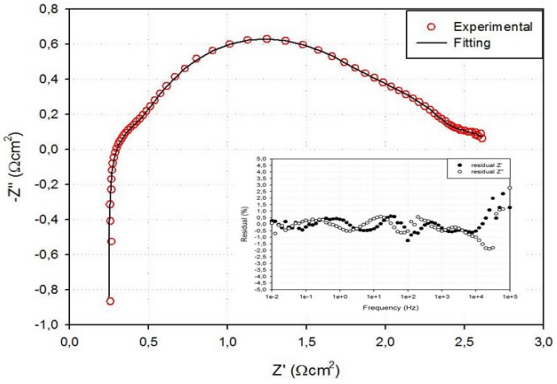

Figure 3. Fitting verification – comparison of the experimental vs. fitted EIS spectra.

With a sufficiently large dataset, the quantitative parameters obtained from each characterization technique (e.g. ASR from polarization, R_0 and R_{pol} from EIS measurements, circuit elements from ECM) can be analysed statistically to assess the similarity/differences between cells and batches [11,14]. As a preliminary analysis, the average value, distribution (variability assessed in terms of standard deviation σ) and percentile analysis is performed according to classical statistical analysis method.

From a QC perspective, a high degree of similarity within a same batch is an indicator of high manufacturing quality (all cells present homogeneous electrochemical performances); instead, relevant differences could indicate two aspects: *i)* low manufacturing quality (cells present heterogeneous electrochemical performances) or *ii)* presence of outliers (differences are recorded only for specific samples). Furthermore, recurrent differences across batches may identify and quantify the impact modifications of the manufacturing process (e.g. modifications in terms of cell design, morphology, architecture and so on), especially in cases when the overall performance (output voltage) is not modified substantially.

2.2 Experimental campaign design

Within the qSOFC project 27 cells samples from 3 batches have each been tested, 20 samples were successful in providing coherent results. In Table 1 the tested cells are reported (only the successfully tested cells are included). Overall, a similar number of cell tests were successful on either test bench (12 cells for Test Bench 1 and 8 cells for Test Bench 2) with consistent results, confirming that the test benches can be considered by all means equivalent in terms of performance and do not introduce an experimental offset. More cells from Batch#2 have been tested due to longer testing time available. At least 5 cells/batch have been tested successfully, to obtain sufficient data for each batch.

Table 1. Tested cell samples and batches*.

Batch#1	Batch#2		Batch#3**
BC_01_09_TB1	BC_02_05_TB1	BC_02_14_TB2	BC_03_02_TB2
BC_01_11_TB1	BC_02_07_TB1	BC_02_15_TB1	BC_03_03_TB1
BC_01_12_TB2	BC_02_08_TB2	BC_02_17_TB1	BC_03_04_TB2
BC_01_13_TB1	BC_02_11_TB1		BC_03_05_TB1
BC_01_14_TB2	BC_02_12_TB2		BC_03_08_TB2
BC_01_15_TB1	BC_02_13_TB1		

* Nomenclature: ButtonCell_Batch#_Cell#_TestBench#
** Batch#3 modifications are introduced to validate the proposed methodology – thus do not correspond to the Elcogen commercial product specifications

In this work the analysis is focused only on experimental data collected in standard conditions (H_2/N_2 50/50%; T=700°C; stabilized conditions) in the perspective of QC of cell and batch manufacturing.

Thanks to fast EIS measurements, the testing time (including the start-up and stabilization period) can be strongly reduced with respect to performance-based cell characterization.

3 Results and discussion

In Section 3.1 the preliminary results from the polarization characterization methods are presented, followed by more detailed results obtained from impedance-based methods in Section 3.2. A statistical analysis of the results is performed to analyse the parameters obtained by each testing method.

Cells with a very high value of R_0 (>0.5 Ω cm^2 – from EIS spectra) were excluded from the analysed dataset to avoid skewed results, attributing the low performance to testing setup or procedural issues.

It should be noted that results should be assessed on a comparative basis rather than on a quantitative basis, which might be affected by the test setup

3.1 Preliminary results from polarization methods

A preliminary analysis of the stabilized polarization curves in standard conditions (H_2/N_2 50/50%; T=700°C) provides a first indication of the overall electrochemical performance of the tested samples. In Figure 4 the performances of the cells and batches are compared.

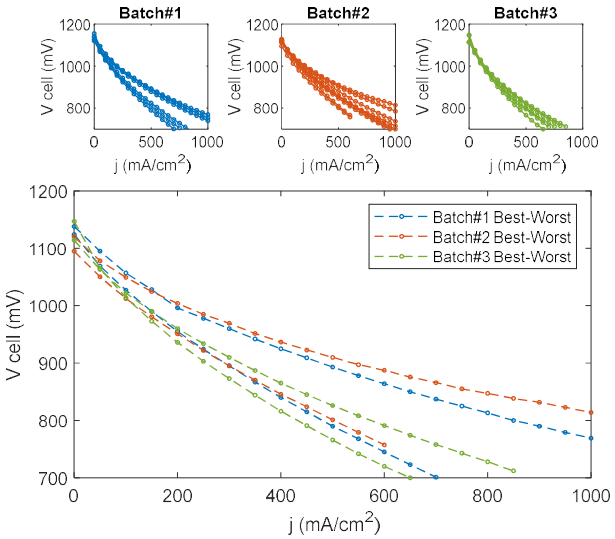

Figure 4. Polarization curves of each cell (top); comparison of best-worst Batch performance range (bottom)

In Figure 5 the OCV and ASR parameters obtained from the IV curves are reported for each Batch. The average OCV and ASR values are summarized in Table 3.

Table 3. Average OCV and ASR parameters obtained by the polarization characterization method.

Parameters	OCV (V)	ASR (Ω cm²)
Batch#1	1.13	0.44
Batch#2	1.12	0.33
Batch#3	1.13	0.52
Variability	σ(OCV)	σ(ASR)
	(V)	(Ω cm²)
Batch#1	0.013	0.098
Batch#2	0.009	0.183
Batch#3	0.018	0.056

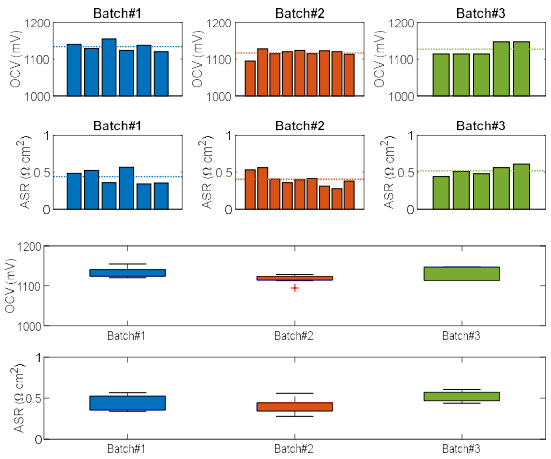

Figure 5. OCV and ASR parameters for each cell (top); Statistical analysis of OCV and ASR for each batch (bottom)

The OCV values are consistently high (between 1.11-1.15 V - close to the thermodynamic limit [15]), confirming that the gas supply and experimental conditions are suitable for all cells and batches.

By analysing the compared IV curves and electrochemical parameters it is possible to observe that cells from Batch#2 achieve the highest performances both in terms of average (average ASR equal to 0.33 Ω cm²) and best-performing cell (minimum ASR equal to 0.28 Ω cm²) performances. However, it can also be seen that Batch#2 ASR shows also quite a high variability (σ equal to 0.183 Ω cm²), comprising also worse performing cells (maximum ASR equal to 0.56 Ω cm²), which could be related to the fact that more cells were tested from Batch#2 respect to other batches, increasing the batch performance variability. Cells from Batch#1 show intermediate performances, substantially similar to Batch#2 (average ASR equal to 0.44 Ω cm²), with high homogeneity (σ equal to 0.098 Ω cm²). Batch#3, on the other hand, shows a slightly worse average IV performance (average ASR equal to 0.52 Ω cm²) close to the lower boundary of Batch#1 and Batch#. However, Batch#3 shows the highest homogeneity (σ equal to 0.056 Ω cm²) of all Batches, meaning that the cells are very performing consistently in the observed performance range. The ASR parameter shows a high variability among cells (σ between 0.05-0.2 Ω cm²), denoting that such parameter is not suitable as indicator for QC purposes.

Although the obtained results are coherent with the modification of the manufacturing process for Batch#3, with the performance-based characterization methods it is difficult to provide additional information, since the output measured signal (IV curve) is a result of a convoluted effect of many different phenomena occurring simultaneously in the cell. In order to obtain more detailed and deconvoluted results, impedance-based methods should be used as described in Section 3.2.

3.2 Detailed results from Impedance-based methods

In Figure 6 the complex impedance response for each batch obtained from the EIS measurements in standard stabilized conditions are compared in the Nyquist plane. The impedance contribution can be differentiated between the internal resistance R_0 (equal to the intercept of the complex impedance at high frequency) associated to the ionic conduction in the electrolyte and by the electrical resistance of the setup and the polarization resistance R_{pol} (equal to the intercept of the complex impedance at low frequency), associated to the activation and concentration overpotentials. The summary of the R_0, R_{pol} and R_{tot} values are reported in Table 4 for each batch.

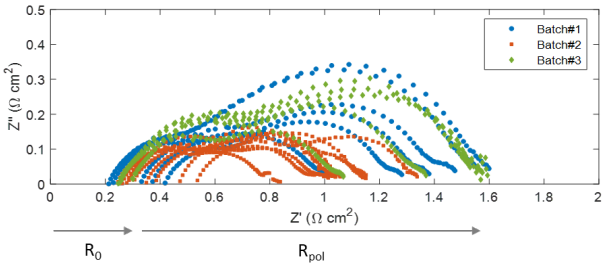

Figure 6. EIS measurements for each cell

Well-performing cells are typically those showing the lower values of R_0 (ca. 0.2 Ω cm^2), which mainly defines the IV curve slope (however, R_0 is not exactly equal to the IV curve slope since also the activation and concentration regimes are mutually present). A high value of internal resistance can arise from misalignment between the cathode and the cathodic current collector (because of the vertically oriented cell set up) related to the experimental setup. Nevertheless, a good voltage performance can also be obtained in cells with high R_0 if R_{pol} is low enough to counterbalance the ohmic losses.
All tested cells show appropriate R_0 values (between 0.2-0.5 Ω cm^2) with low internal variability (σ<0.1 Ω cm^2). Thanks to the similar values of R_0 for all batches, the trends previously identified on the ASR are reflected on R_{pol} which can be used as a relevant indicator for cell quality (provided that the R_0 is within the acceptable range). As previously identified from the analysis of the ASR values, Batch#2 shows consistently lower R_{pol} values (between 0.6-0.9 Ω cm^2) with respect to Batch#1 and Batch#3 (around 0.8-1.2 Ω cm^2), highlighting that Batch#2 is better performing than Batch#1 and Batch#3 as well as also presenting the least variability in terms of R_{pol} (σ<0.1 Ω cm^2).

Table 3. Average R_0, R_{pol} and R_{tot} parameters obtained by the impedance characterization method.

Parameters	R_0	R_{pol}	R_{tot}
	(Ω cm^2)		
Batch#1	0.304	1.081	1.385
Batch#2	0.347	0.717	1.064
Batch#3	0.272	1.166	1.438
Variability	σ(R_0)	σ(R_{pol})	σ(R_{tot})
	(Ω cm^2)		
Batch#1	0.083	0.239	0.215
Batch#2	0.100	0.093	0.138
Batch#3	0.026	0.220	0.227

The variability rate of R_{pol} (consequently also R_{tot}) within each batch is still quite high (σ between 0.1-0.2 Ω cm^2) denoting that the R_{pol} is still not suitable as quantitative QC indicator (at least with the tested setup) – unless a very wide variability range is considered. Rather, the use of EIS parameters as QC indicators can be done qualitatively to assess cell and batch quality, with the possibility to discern between R_0 and R_{pol} (as done in the case of Batch#2, for which the improvement is ascribed to R_{pol} rather than R_0, which presents higher and less consistent values with respect to other batches).
The analyses of the EIS spectra confirm that impedance spectroscopy is a powerful tool for SOFC electrochemical characterization, however it is challenging to determine which specific physico-chemical process (charge or mass transfer) changing between cells and batches. To do so an even more accurate analysis of each deconvoluted impedance contribution is required, analysing the ECM elaborated data, which is presented in Subsection 3.2.1.

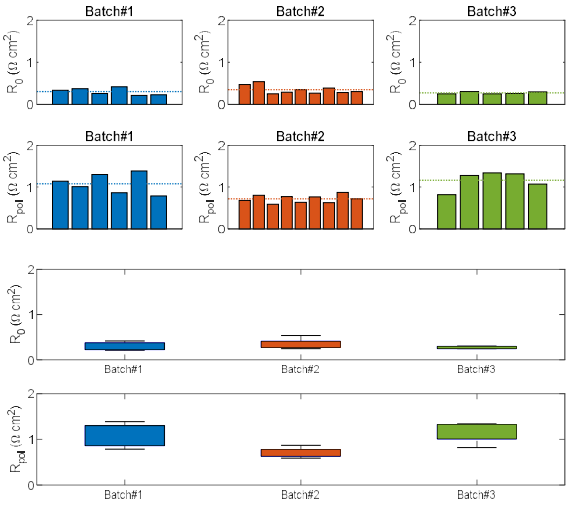

Figure 7. R_0 and R_{pol} parameters for each cell (top); Statistical analysis of R_0 and R_{pol} for each Batch (bottom)

3.2.1 ECM results – Quantitative analysis of deconvoluted Impedance contributions

Applying the model reported in Figure 2 to the EIS spectra obtained for all the cells in standard conditions, the circuit element parameters – representative of the impedance contribution of each physico-chemical process – can be calculated and compared on a quantitative basis for each cell and batch. The ECM parameters in standard conditions are reported in Figure 8 as well as in Table 5.
The R_0 range observed in the ECM results (between 0.2-0.5 Ω cm^2) is consistent with the one observed in the EIS spectra, confirming that the fitting procedure with respect to this parameter is correctly performed.
Breaking down the polarization resistance it is possible to observe that the main contribution for all batches is related to the mass transport phenomenon at the anode side ($R_{diff,an}$ up to 0.9 Ω cm^2 – composing up to 60% of R_{pol}), followed by the charge transfer mechanism at the anode functional layer (combined $R_{ct,an}$ up to 0.4 Ω cm^2 – composing up to 35% of R_{pol}). Other processes have a smaller impact in the tested conditions (<0.2 Ω cm^2). The main limiting process is the gas diffusion in the anode, which is reasonable considering that the cells are ASC and the gas diffusion paths are longer throughout the thicker bulk anode substrate. On the other hand, the charge transfer mechanism at the anode is slightly limiting (possibly due to 50% H_2 fuel), while charge transfer at the cathode does not represent a limitation (possibly due to highly over-stoichiometric oxidant flow). The cathode diffusive contribution $R_{diff,cat}$ is not a limiting factor, showing much lower values than the anodic one ($R_{diff,cat}$ <0.15 Ω cm^2) for all cells. In fact, the cathode – contrarily to the anode – is a thin layer which does not have to provide mechanical support to the cell, therefore the diffusion paths are shorter, allowing the oxidant to easily reach the active layer. However, it must be noted that the cathode diffusive phenomena typically happen at very low frequency (order of mHz), where the EIS spectra can present measurement noise which affects the interpretation.

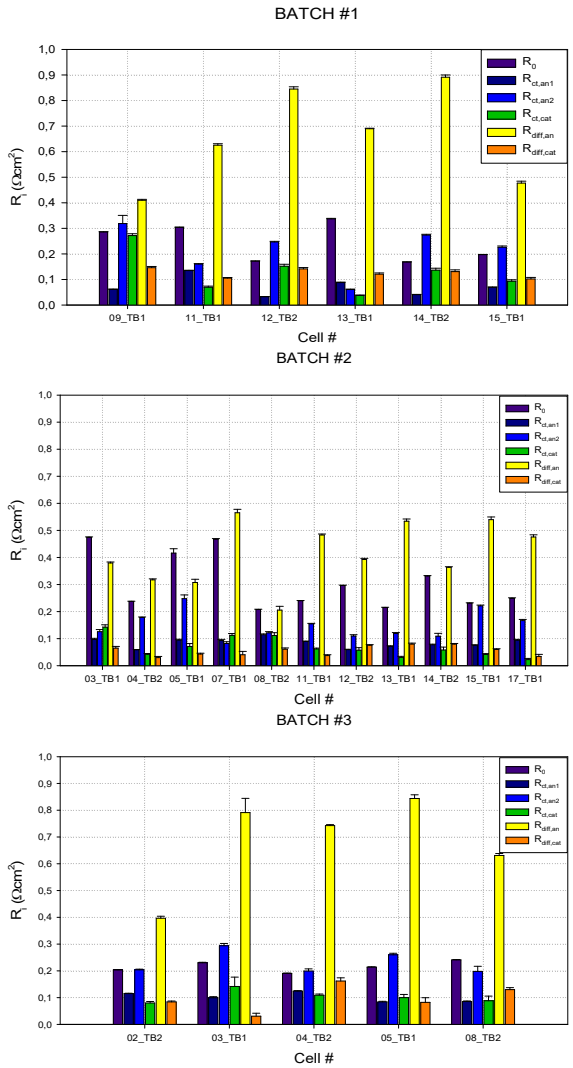

Figure 8. ECM parameters of each cell for Batch#1 (top); Batch#2 (middle); Batch#3 (bottom)

Table 5. Average R_0, R_{pol} and R_{tot} parameters obtained by the impedance characterization method.

Parameters	R_0	$R_{ct,an1}$	$R_{ct,an2}$	$R_{ct,cat}$	$R_{diff,an}$	$R_{diff,cat}$
	(Ω cm^2)					
Batch#1	0.244	0.071	0.214	0.127	0.656	0.124
Batch#2	0.295	0.086	0.148	0.063	0.430	0.057
Batch#3	0.216	0.102	0.231	0.104	0.681	0.098
Variability	$\sigma(R_0)$	$\sigma(R_{ct,an1})$	$\sigma(R_{ct,an2})$	$\sigma(R_{ct,cat})$	$\sigma(R_{diff,an})$	$\sigma(R_{diff,cat})$
	(Ω cm^2)					
Batch#1	0.074	0.037	0.092	0.083	0.193	0.018
Batch#2	0.093	0.016	0.055	0.032	0.121	0.019
Batch#3	0.020	0.018	0.044	0.024	0.177	0.050

In general, Batch#2 show slightly lower and less variable ECM results than other batches, indicating better performance and more homogeneity, confirming that the quality of Batch#2 – in terms of average electrochemical performance – is higher than that from Batch #1 and Batch#3.

As previously discussed, the ECM results of Batch#1 are slightly higher (especially in terms of charge transfer and diffusion resistances) than the ones of Batch#2. Also, the variability range is slightly higher (average σ related to all resistances equal to 0.083 Ω cm^2) respect to Batch#2 (average σ equal to 0.056 Ω cm^2), denoting slightly lower manufacturing quality.

Comparing the ECM results of Batch #3 with the ones from Batch #2 and Batch#1, it is possible to highlight that $R_{ct,an2}$, as well as $R_{diff,an}$, show a larger contribution to the overall impedance. The deviations observed from this quantitative comparison are coherent with a modified anode active layer, which mostly affects the related charge transfer mechanism at the TPB. However, the modification seems to have been unsuccessful, resulting in a recurrent increase of $R_{ct,an2}$ (0.2-0.3 Ω cm^2 vs. 0.1-0.2 Ω cm^2 obtained for other batches). A possible hypothesis could be that the modification in the manufacturing process resulted in a more coarsened (lower TPB length) anode functional layer, less effective from an electrochemical point of view. Moreover, also $R_{diff,an}$ seems to increase for all cells (maximum value of around 0.9 Ω cm^2 vs. 0.6 Ω cm^2 previously obtained for other batches), indicating that the structural modification also affected the gas diffusion process in the anode, possibly in relation to a reduced porosity caused by the denser Ni grains. On the other hand, a stable value of R_0 and a homogeneous batch performance (average σ equal to 0.056 Ω cm^2 – in alignment with Batch#2) was obtained, denoting high batch quality, within its measured operating parameters.

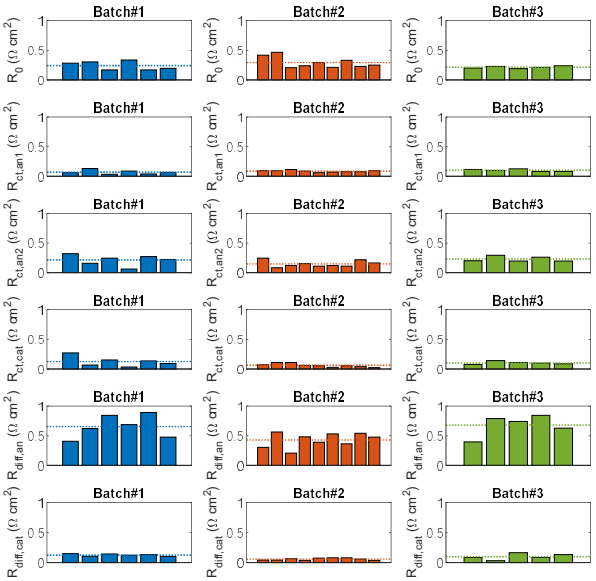

Figure 9. ECM parameters for each cell

Analysing the results under a QC perspective, the intra-batch distribution of the disaggregated ECM parameters (shown in Figure 9 and Figure 10) is much more homogeneous with respect to the parameters that can be obtained from polarization curves (ASR) and from EIS measurements (R_0, R_{pol}). In fact, all ECM parameters - with exception of $R_{diff,an}$, which is the main impedance contribution for all cells – are highly replicable

presenting a very low variability range (σ<0.1 Ω cm^2). This means that (despite the potential introduction of additional errors caused by the numerical fitting procedure) the ECM parameters are much more suitable to be used as quantitative indicators for QC. In addition, the availability of six parameters instead of one or two global parameters is extremely helpful to analyse similarities/differences of cell and batch performances in relation to specific physico-chemical processes and not only from an overall perspective (different cells could lead to similar aggregated results).

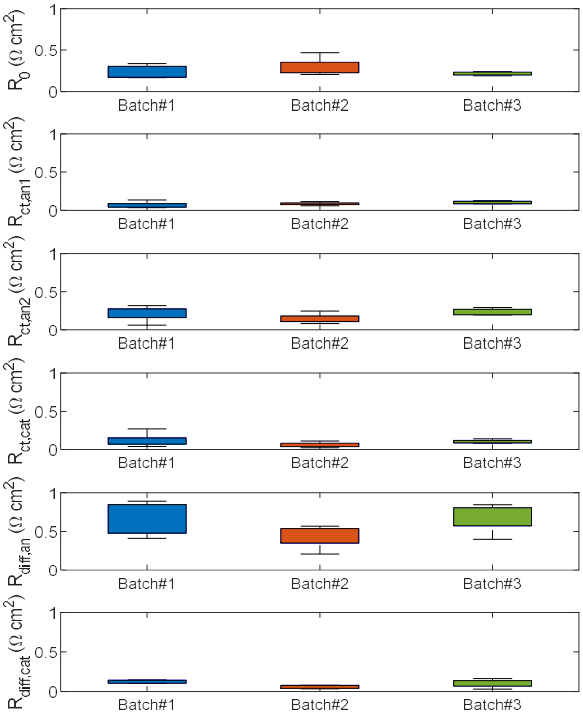

Figure 10. Statistical analysis of the ECM parameters for each Batch

Ideally, from the statistical analysis of a large enough ECM dataset, quantitative threshold limits could be determined and implemented as a scalable and reliable QC tool [11]. Clearly, datasets obtained at laboratory level are insufficient in terms of both data amount (considering equipment availability and testing time constraints) and data quality (considering issues of data replicability), where this methodology can be only demonstrated in principle – as done in this work. Implemented at industry level (with dedicated testing apparatus and implementing automation processes), larger and more consistent ECM datasets could be built, broadening the potential use of such methodology. Advanced data-driven and real-time learning models could be complementarily implemented to improve the dataset generation and management to further enhance the potential of the proposed method as QC tool [14].

4 Conclusions and future work

An impedance-based experimental framework has been analysed for the characterization of SOFC cells and batches as an improvement of standard polarization-based methods. A wide experimental dataset composed of 20 IT-SOFC cells from 3 production batches has been used to assess the validity of the proposed methodology.

With respect to the polarization-based method, the impedance-based approach provides detailed and deconvoluted information with respect to each physico-chemical process occurring within the cell. Through the calculation of the ECM parameters from EIS data in OCV conditions (which present high intra-batch replicability) it is possible to quantitatively assess the quality and homogeneity of the SOFC operational performances with high reliability, without having to actually operate the cells. By analysing the distribution of the ECM parameters, it is also possible to successfully identify and quantify differences between batches, identifying the impact on electrochemical performances caused by specific modifications of the manufacturing process.

It was possible to assess product quality both within a production batch and between different production batches. Batch#2 shows lower and more homogeneous R_i values, denoting higher quality with respect to other batches, which is reflected in terms of electrochemical performances. Instead, the modified Batch#3 exhibits a relevant deviation of $R_{ct,an2}$ and $R_{diff,an}$, which is reconducted to a modified anode functional layer.

Future work will focus on the implementation of a larger experimental dataset, also in different parametric operating conditions as well as improving the statistical analysis to further improve the robustness of the proposed methodology as a reliable QC tool.

This research has been carried out below the EU project qSOFC (Horizon 2020; Grant ID: 735160) which is kindly acknowledged.

References

1. US Fuel Cell Council. Introduction to Solid Oxide Fuel Cells Button Cell Testing. **2007**
2. Mcphail SJ, Aarva A, Devianto H, Bove R, Moreno A.. Int J Hydrogen Energy **2010**;36:10337–45.
3. Klotz D, Weber A, Ivers-Tiffée E. Electrochim Acta **2017**;227:110–26.
4. Joint Research Centre, JRC Sci Tech Reports **2010**.
5. Padinjarethil AK, Bianchi FR, Bosio B, Hagen A. Front Energy Res **2021**;9:1–19.
6. Barai A, Uddin K, Dubarry M, Somerville L, McGordon A, Jennings P, et al. Prog Energy Combust Sci **2019**;72:1–31.
7. Barfod R, Mogensen M, Klemensø T, Hagen A, Liu YL, Vang Hendriksen P. Proc - Electrochem Soc **2005**.
8. Boigues-Muñoz C, Pumiglia D, McPhail SJ, Santori G, Montinaro D, Comodi G, et al. J Power Sources **2015**
9. Boigues Muñoz C, Pumiglia D, McPhail SJ, Montinaro D, Comodi G, Santori G, et al. J Power Sources **2015**;
10. Leonide A, Apel Y, Ivers-Tiffee E. ECS Trans **2019**.
11. Lang M, Bohn C, Couturier K, Sun X, Mcphail SJ, Malkow T, et al. J. Electr. Soc., 166-15 (**2019**)
12. Silva-Mosqueda DM, Elizalde-Blancas F, Pumiglia D, Santoni F, Boigues-Muñoz C, McPhail SJ. Appl Energy **2019**;235:625–40.
13. Del Zotto L, Monforti Ferrario A, Hatunoglu A, Dell'era A, McPhail S, Bocci E. Energies **2021**;14:1–19.
14. Padinjarethil AK, Hagen A. Fuel Cells **2021**:1–11.
15. Khotseng L. Thermodyn Energy Eng **2020**:1–17.

Knowledge Based Engineering for Hydrogen Gas Turbines and Burners Design: a review

Corallo Angelo[1], *Dibiccari* Carla[1], *Lazoi* Mariangela[1,*] *Starace* Giuseppe[2] and *Laforgia* Domenico[1],

[1]Dipartimento di Ingegneria dell'Innovazione, Università del Salento, via per Monteroni, sn., 73100, Lecce (LE), Italy

[2]Dipartimento di Management, Finanza e Tecnologia, Università LUM, km 18 SS.100, 70019 Casamassima (BA), Italy

Abstract. Hydrogen gas turbines and burners need high attention and their appropriate realization, yet during their design, can lead important benefits for the whole sector. Realizing the best design, the first time, reduces reworks and requests of design changes from the manufacturing departments. In this field, Knowledge Based Engineering is a good strategy for embedding, in an automatic way, experts' knowledge into CAD models during the design of a component. It enables a reduction of human errors and costs in several design tasks and improving the final quality of a component model. With these premises, the aim to the study is to lead improvements and appropriate actions in the design and re-configuration of hydrogen power generation systems (i.e. gas turbines and burners) by means of KBE, leading improvements yet in this early phase of the global race for hydrogen. A systematic literature review is carried out to explore the current state of art for the application of KBE for the design of turbines and burners in different industrial sectors. Evidences from the practice are collected in a structured classification and elaborated and summarized for application in the design of gas turbines and burners for the hydrogen production.

1 Introduction

Researches on hydrogen power generation systems (HPG) systems currently play a relevant role in assuring appropriate levels of productivity and sustainability. Compared to power generation based on traditional hydrocarbon fuels, HPG systems, coupled with the use of renewable energy sources for hydrogen production, could dramatically reduce greenhouse gases emissions, relying on a completely CO2 free energy source [1].

The major global industrial players in power generation, like GE Power [2], Mitsubishi Power [3] and Ansaldo Energia [4], are dealing with the conversion of traditional gas turbines to the combustion of mixed-fuel. The challenges of this transition are mostly related to the specific combustion characteristics of high hydrogen fuels. A new configuration of the fuel accessory system is, thus, needed in order to adjust the traditional gas turbines for hydrogen flow rates. The sealing systems should be reconsidered and replaced with welding or other specifically designed components. For example, the combustor component should be adapted for preventing flashback issues [2] [3] [5].

Gas turbines and burners are key components of HPG systems. They are products resulting by the assembly of different components that are specified through dimensional and geometrical values to guide their physical realization. Variations in the components can lead to problem in the assembly requiring re-works of parts with higher costs for a company. Accurately design the product, its physical elements and how to assembly them in a main architecture, it's a critical activity for avoiding changes during the manufacturing where reworks and stops require higher cost. Computer aided design (CAD) systems supported by other CAX technologies (Computer Aided Technologies) to define engineering, manufacturing or testing data are used during the design. CAD is referred to the math-based definition of the physical architecture of the product and can use two-dimensional (i.e. an engineering drawing with geometrical and dimensional values) or three dimensional space (i.e. a solid model for virtual test and analysis) to define and allocate the product and the elements shapes [6].

In Computer-aided technologies (CAx) systems, Knowledge Based Engineering (KBE) covers a relevant role. It is related to the application of knowledge to automate or assist the engineering tasks [7]. KBE can be integrated in CAD software for capturing engineering knowledge and for integrating the entire design process in a single data model [8]. According to Yao et al. [9], KBE supports the designers by decreasing the repeated design work, that represent about 80% of engineering activity [10] [11]. It automates the non-creative and repetitive tasks in the design phase by integrating multidisciplinary concepts [12].

In the current state of art, a study providing guidelines for improving the design of hydrogen power generation components with KBE is currently missing. This paper

* Corresponding author: mariangela.lazoi@unisalento.it

aims to reduce this gap extending the discussions of the relevance of an appropriate design also to the hydrogen field considering KBE as a relevant method to support it. A systematic literature review is carried out on papers published on the topic of KBE for turbine and burners design.

From the analysis of the papers, evidences from the practice are collected in a set of insights highlighting type of product, type of KBE, managed issues and benefits. These contents are then elaborated and summarized in a set of guidelines applicable in the design of gas turbines and burners for the hydrogen production.

Industrial practioners can benefit from this study for leading their design and configuration activities introducing innovations and best practices from others industrial fields while academia researchers can consider this study as a main reference for defining future researches.

2 KBE Overview

Very often companies launch new products that are evolutions of existing products, re-applying components and engineering techniques in multiple designs. In these cases, the new product development process can lead to sub-optimal use of company knowledge, devoting hours of work by highly experienced designers to activities of little value, like routine calculation, part catalog browsing and update of CAD models. KBE is able to automate routine engineering tasks, allowing the reduction of the design cycle and the engineers to spend time and resources on creative tasks. Therefore, considering the definition of La Rocca [13]*, "KBE is a technology based on the use of dedicated software tools that can capture and reuse product and process engineering knowledge*." Two main features enable KBE to achieve its goals of reducing time and costs in new product development: "*automation of repetitive and non – creative design task; and support of multidisciplinary design optimization in all the phases of the design process* » [13].

KBE systems are implemented as software environments that tightly integrate an object-oriented programming component in a geometric modelling tool [13 - 14]. KBE leverages the parametric modelling feature used by mechanical CAD allowing generative modelling. In generative modeling, design requirements are encoded in computer readable rules, enabling design automation. Moreover, thanks to KBE, CAD objects are enriched with information that can optimize decisions and changes along the lifecycle of the product. Specific skills are required to create KBE applications in these environments and a new, dedicated figure emerged: the KBE engineer. KBE applications developed by KBE engineers can be applied by different company's roles, like designers and product managers, in their daily activities [15].

Several benefits are associated with KBE: 1) *KBE improves product quality*. Appling KBE to the product development process leads to a dramatic increase of the overall products' quality. Task automation can remarkably increase the number of design and simulation iterations. Embedding computer rules to design can avoid possible design mistakes or detect errors more easily and in the earlies design phases. Moreover, KBE decodes and stores designers experience, making it more effective [16]. This consideration leads to a second particular benefit of KBE.

2) *KBE gathers engineering expertise and supports knowledge reuse*. KBE applications are containers of engineering knowledge which is formally translated in rules and algorithms. The particular development process of a KBE application involves an experienced designer describing his activities in terms of functional requirements which are then translated in design rules and software functionalities. The KBE application can be then used by less experienced designers allowing the experienced resources to focus on high-end design activities.

3) *KBE allows to reduce design cost.* Most of a product's lifecycle cost is determined in the earliest design phases. Decisions and trade-off considerations taken as early as the preliminary design stage commit between 60 % and 80% of the final cost [17]. Exploring multiple design alternatives would limit cost compromises identifying optimum solutions for design parameters and cost at once. Design alternatives are often produced and testes through a chain of repetitive, time-consuming CAx-based tasks, leading designers to develop only a limited amount of design solutions and settle for a non-optimal one. Considering KBE in the design process allows the production and the evaluation of a high number of design solutions in a short time, using automation and enriching design models with knowledge.

4) *KBE enables Concurrent Engineering*. It is a paradigm of product development based on the notion of performing simultaneously and collaboratively tasks that were usually performed in sequence and individually by different disciplinary teams [14]. KBE environments provide specific functionalities for setting up collaboration on a product model. Rule and constraint setting for each discipline, change management, change detection, model checking and update functionalities allows for consistent collaboration during design.

It is important to note, however, that when applying KBE design tasks should be carefully chosen. A number of authors identified a set of cases when KBE would not be convenient [14, 17, 18]. More specifically, Stokes [10] identifies the following situations where the use of KBE is not appropriate: 1) when the functionality that should be automated using KBE is already offered by Commercial-Of-The-Shelf (COTS) applications; 2) if the design processes and products, are highly subject to change; 3) when the design processes are blurry and not well defined; 4) if it is not possible to clearly outline and isolate a particular design stage; and 5) when the technology in the design process is constantly changing.

3 Research Method

In order to address KBE issues for Gas Turbines and Burners design, a systematic literature review was carried out. It consisted in a replicable process aimed at guiding decisions, procedures and conclusions [20] in the analysis of the scientific state of art.

Among the different systematic literature review strategies, in this study the strategy suggested by Corallo et al. [21]was adopted. It is composed by four steps:

1. *Review Planning*. In this step, the objectives are defined, the source of information to be consulted are selected, the search keywords are chosen, the filters for the results are identified, the qualitative mechanism for contents selections are planned, the way to track the reference is defined.
2. *Search Execution*. During this step, the sources are interrogated with search queries, the results are preliminarily filtered and selected.
3. *Documents Analysis*. In this step, the selected documents are examined, specific contents, elements and key concepts are detected and the final selection of documents is defined. Furthermore, relationships among papers are compared and a critical analysis of papers contents is done.
4. *Results Reporting*. In this step, the results are summarized and the consulted reference tracked.

The described steps represent the reference to execute the study with a predefined logical and temporal flow.

3.1 Papers Selection and Analysis

According to the described systematic literature review strategy, after the definition of the objective of analysis, the search process starts with a selection of scientific papers. In this study, Scopus (www.scopus. com) was used as main electronic scientific indexed database and all queries were launched on September 2021.

The search criteria and the related results are reported in Table 1.

Table 1. Search criteria and results.

ID	Query	#Results	#Filtered Results
1	Title-Abs-Key("Hydrogen") And Title-Abs-Key(Kbe) Or Title-Abs-Key(« Knowledge Based Engineering »)	5	0
2	Title-Abs-Key("Power Generation System*") And Title-Abs-Key(Kbe) Or Title-Abs-Key(« Knowledge Based Engineering »)	0	0
3	Title-Abs-Key("Turbin*") And Title-Abs-Key("Kbe") Or Title-Abs-Key("Knowledge Based Engineering")	19	17
4	Title-Abs-Key("Burner*") And Title-Abs-Key("Kbe") Or Title-Abs-Key("Knowledge Based Engineering")	1	1
Total		25	18

To find the most suitable study in the field of analysis, a first query was made on hydrogen and KBE, in order to explore existing studies treating KBE in the hydrogen field. The result of this query was of five papers but out of scope. In these papers, KBE was treated with different meanings (e.g. Kadanoff-Baym Equations). Another query explored the existence of studies about power generation systems and KBE, but no result was reported. A good number of studies was instead, selected using a third query combining Gas Turbines and KBE. Only two papers were excluded: one was out of scope and the other a replication. The last query, with Burner and KBE, extended the selection of one more paper.

Therefore, 18 papers were considered relevant to the analysis of the KBE role on HPGS design, mainly considering Gas Turbines and Burners. In Table 2, information on the 18 papers are provided.

Table 2. Selected Papers.

ID	Reference	Type	Year	Country
1	[22]	Conference Paper	2018	USA
2	[23]	Article	2015	China
3	[24]	Conference Paper	2015	Germany
4	[25]	Conference Paper	2014	China
5	[26]	Conference Paper	2013	Germany
6	[27]	Conference Paper	2010	Netherlands
7	[28]	Article	2010	China
8	[29]	Conference Paper	2007	USA, Netherlands
9	[30]	Article	2006	China
10	[31]	Conference Paper	2001	USA
11	[32]	Article	2001	USA
12	[33]	Conference Paper	2000	USA
13	[34]	Conference Paper	1995	USA
14	[35]	Article	1994	USA
15	[36]	Article	1993	USA
16	[37]	Conference Paper	1993	USA
17	[38]	Conference Paper	1989	USA
18	[39]	Conference Paper	2005	USA

The papers selected in this study were red and the contents analysed comparing similar and different results. In particular, the evaluation of the papers was based on four topics: 1) type of product; 2) type of KBE solution or approach; 3) managed issues; and 4) benefits.

As a result, a set of insights was defined, collecting the most relevant evidence for leading future research and design applications and decisions.

4 Results and Discussion

The studies available in the current literature exploring KBE application for gas turbines and burners design are mainly focalized on the aerospace, energy and automotive sectors. As illustrated in table 3, the analyzed papers address many different types of product. In general, they are complex products [40] characterized by high technology value, several customizable parts and high investments.

Table 3. Type of product.

Type of Product	Reference
Bulb Turbine	[22]
Combustor	[24]
Airfoils shapes	[24, 28]
Rotating Machines	[25]
Turbine Blade	[22, 27, 32, 37]
Turbine Impeller	[29]
Compressor Rotor and Compressor Blades	[30]
Micromachined Atomizers (e.g. for gas turbine engines)	[31]
Turbine Engines	[33]
Gas-Turbine Nozzles	[34 – 36]
Utility Boiler Burners	[38]

The performed KBE solutions, to support the design of the cited product, are of different types. In [23], a KBE interface-tool and a database are implemented, using also automation script based on interface-tool input and database information. Context-sensitive allocation of design-relevant knowledge was realized in [25] for the identification of components of complex machineries. In [27], instead, after the definition of design process and domain knowledge, case-based reasoning is combined with rule-based reasoning, for improving the efficiency in the retrieval of information. Knowledge fusion is also a topic associated to KBE. It is used in [29] for the combination of knowledge and CAD software through a blurry inference mechanism. Neural networks' learning ability and fuzzy's logic are also applied for automatic acquire knowledge in a KBE solution [31] as well as Rule Stream's database architecture [38].

Some papers illustrate the steps for KBE application. Reference [24] describes the steps for the KBE implementation (i.e. structure-behavior function model definition, neural rules deduction, design method establishment, dimensional model set-up, algorithm of geometric parameters proposal) contestualized for the design of airfoils variable pitch wind turbines. In [22], the main steps are also described. They are summarized in 1) knowledge acquisition, 2) knowledge representation, 3) knowledge reasoning, 4) establishment of knowledge base. In this last step, the knowledge base is considerd as a set of experience, rules case and other knowledge applicable in a specific domain. These steps are applied for the selection of the type of bulb turbine generator in the hydraulic field.

For the development of these KBE solutions several issues have been managed related to the design process and the engineers' tasks.

Table 4. Managed Issues.

Managed Issues	Reference
Performing several refinement studies	[22 – 23]
Knowledge Acquisition Bottlenecks	[31]
Long Design Time	[22, 37]
Lacking of Expert Experience	[27]
Low Level of Intelligence	[27]
Fuzzy Inferences	[29]
Reparametrization of scalable products for family of parts	[34 – 36]

In almost all the papers, benefits are cited and described for the application of KBE solution. They are mainly related to the re-use of experts (design engineers) knowledge that have to be captured and automatized in the solutions. Using KBE, the design quality is increased as well as the efficiency of the realized design that avoids drop backs to the conceptualization phases, increasing the design time. The CAD models are better developed and debugged using in some case minimal source code, independent of proprietary CAD systems. KBE solutions helps to reduce the learning curves for new employees working in the design and manufacturing field; it can enrich the model with information also about why and how activities that have to be performed and choices that have to be taken. A detail of the main reference and associated benefits are available in Table 4.

Table 4. Benefits.

Benefits	Reference
Reduction of the risk of a drop back to the conceptual phase	[25]
Capture and reuse the expert experience efficiently	[27, 31, 33, 37]
Heighten the design efficiency and quality	[27, 37]
Portable web-based development and runtime environments	[28]
Independence from proprietary CAD systems	[28]
Automatic caching and dependency tracking for scalable runtime performance of large models	[28]
Minimal source code volume	[28]
More efficient, clearer and easier model development and debugging	[22, 26, 28, 31, 34, 35, 36]
More information on the model (what, why, how)	[30]

Shorten learning curves for novice engineers	[22, 31]
Shorten Design cycle time	[22, 34, 35, 36, 37]

Given the peculiar features of hydrogen combustion, existing gas turbines can be adapted for using hydrogen as a fuel integrating improved burners that are able to work at high temperature. Therefore, one of the major design challenge is related to re-configure existing gas turbines and to integrate new burners/combustor with them. KBE can provide tools to address this challenge with an easier approach. A KBE solution can assist the designer in evaluating the change in the product model based on hydrogen features and also, power generation requirements. For example, a widget can accompany the designers to take the right choices that are automatically translated in changes on the model, to shift in dimensions, tolerances or other geometrical features. Defining rules to guide the assembly of the different parts that refer to a main product structure made of all the possible combinations could be also possible.

In the definition of new burners, KBE can support the check of the points of integration with gas turbines, can support scalability of the dimensions and evaluation of performance. Guiding the designers during the design process, KBE can provide custom integration of CAx systems enabling, for example, the automation of the configuration of multiphysics simulations, taking boundary conditions and initial settings directly from the product model, allowing for multiple iterations.KBE can also automate shape optimization, formalizing rules for a geometrical interpretation of simulation results. Furthermore, in HPG systems design, KBE can support the design phase through the implementation of methodologies and tools aimed at integrating and assessing the environmental aspect at early stages of product lifecycle, for example, by providing a precise calculation of CO2 emissions related to the use of mixed-fuels using alternative design configurations of the combustor component.

Most researches have investigated the integration of specific themes as embedding an LCA (Life-Cycle Assessment) instrument and CAD software [41], linking PLM (Product Lifeycle Management) systems and Ecodesign tools and data mapping PLM and LCA databases [42]. KBE can be a good strategy for embedding environmental knowledge (e.g. data from LCA databases) into CAD models thus enabling a concurrent interaction between the design feature and a set of environmental metrics. A KBE application can address diverse product development tasks at once, such as environmental performance indicators (e.g. material recovery, remanufacturing, environmental regulations, economic metrics). The application can suggest how these indicators varied based on design decisions.

5 Conclusion

KBE for HPG systems is a widely explored topic in the literature. literature general analysis revealed that there is a large number of studies addressing the use of KBE for gas turbines and burners design but no one of these was in the hydrogen field.

This paper fills this gap by investigating the KBE concept for generic gas turbines and burners to build lead guidelines for HPG systems as well. The proposed results provide a preliminary contribution to the state of art of HPG systems design by KBE and want to support the discussion about the use of purposely set up IT solutions (such as KBE) aimed at improving design tasks of gas turbines and burners of HPG systems.

Future research can consider the contribution of this study, as a preliminary reference to address innovative solutions for the design stage of HPG systems. Managers and product designers can consider future application of KBE in their activities in collaboration with the IT staff that can support the source code development. Theoretician can study KBE methods and tools for more efficient and sustainable gas turbines and burners of HPG systems.

References

1. Y. Matsuo, S. Endo, Y. Nagatomi, Y. Shibata, R. Komiyama, and Y. Fujii, *Energy*, **165**, 1200–1219, (2018).
2. D. J. Goldmeer, GE Power, *GEA33861*, (2019).
3. K. Inoue, K. Miyamoto, S. Domen, I. Tamura, T. Kawakami, and S. Tanimura, *Mitsubishi Heavy Industries Technical Review*, **55**, 6, (2018).
4. Ansaldo Energia, *PowerGeneration News*, **2**, 10-12, (2018).
5. M. R. Bothien, A. Ciani, J. P. Wood, and G. Fruechtel, *J. Eng. Gas Turbines Power*, **141**,(2019).
6. M. Grieves, *Product Lifecycle Management: Driving the Next Generation of Lean Thinking*. (New York: McGraw-Hill, 2006).
7. C. Danjou, J. Le Duigou, and B. Eynard, *Int. J. Comput. Integr. Manuf.*, **30**, 995–1009, (2017).
8. A. Corallo, M. Marra, and C. Pascarelli, *Aerospace*, **6**, 41-58, (2019).
9. G. La Rocca and M. van Tooren, *Adv. Eng. Inform.*, **26**, 157–158, (2012).
10. D. E. Calkins, N. Egging, and C. Scholz, *Int J Eng Ed*, **16**,21–38, (2000).
11. M. Stokes, *Managing Engineering Knowledge: MOKA Methodology for Knowledge Based Engineering Applications*. (Wiley Publishing,Inc, 2001).
12. A. H. Van Der Laan and M. J. Van Tooren, *J. Aircr.*, **42**, 1605–1613, (2004).
13. G. La Rocca, *Adv. Eng. Inform.*, **26**, 159–179, (2012).
14. C. B. Chapman and M. Pinfold, *Knowl.-Based Syst.*, **12**,. 257–267, (1999).

15. S. Cooper, I.S. Fan, and G. Li, *Achieving Competitive Advantage through Knowledge-Based Engineering* p. 21
16. H. T. Dinh, *Improving product design phase for engineer to order (ETO) product with knowledge base engineering (KBE)*, (2015).
17. J. Pokojski, S. Fukuda, and J. Salwiński, Eds., *New World Situation: New Directions in Concurrent Engineering: Proceedings of the 17th ISPE International Conference on Concurrent Engineering*, (2010).
18. P. Bermell-Garcia and I.-S. Fan, *J. Prod. Lifecycle Manag.*,**3**,3-20, (2008).
19. D. S. Darai, S. Singh, and S. Biswas, *Int. J. Comput. Sci. Inf. Technol*, **1**, 230-234, (2010).
20. A. Bryman and E. Bell, *Business Research Methods*, (Oxford University Press, 2015).
21. C. Angelo, C. A. Maria, D. V. Vito, L. Mariangela, and M. Manuela, *IEEE Trans. Eng. Manag.*, 1–13, (2021).
22. H. Ram and S. Krumdieck, *GRC Transactions*, **42**. (2018) .
23. W. Guo, J. Wen, H. Shao, and L. Wang, *Adv. Mech. Eng.*, **7**, (2015).
24. M. Gessel, M. Pfitzner, and R. Eggels, *ASME Turbo Expo 2015: Turbine Technical Conference and Exposition*, (2015).
25. H. Xie and W. Zeng, *Adv. Mater. Res.*, vol. **1030**, 1342–1347, (2014).
26. C. Küstner, T. Breitsprecher, and S. Wartzack, *Proceedings of the International Conference on Engineering Design, ICED*, **5,** 81–90, (2013).
27. I. Sanya, E. Shehab, D. Lowe, M. Maksimovic, and A. Al-Ashaab, *Improving Complex Systems Today*, London, , 285–292. (2011).
28. R. Jiang, D.-H. Zhang, and W.-H. Wang, " *Hangkong Dongli XuebaoJournal Aerosp. Power*, **25**, 1061–1067, (2010).
29. D. Cooper and G. La Rocca, *7th AIAA ATIO Conf, 2nd CEIAT Int'l Conf on Innov and Integr in Aero Sciences,17th LTA Systems Tech Conf; followed by 2nd TEOS Forum*, (2007).
30. T. Guo, H.-L. Yang, and S.-G. Tong, *J. Harbin Inst. Techno.,* **38**, 1809–1812, (2006).
31. P. J. Röhl, R. M. Kolonay, M. J. Paradis, and M. W. Bailey, *ASME 2001 International Design Engineering Technical Conferences and Computers and Information in Engineering Conference* " 789–798 (2001).
32. S. Huang, X. Hao, and M. Benjamin, *J. Intell. Manuf.*, **12**, 377–391, (2001).
33. P. Roehl, R. Kolonay, R. Irani, M. Sobolewski, K. Kao, and M. Bailey, *8th Symposium on Multidisciplinary Analysis and Optimization*, (2000).
34. J. Marra, *ASME 1995 International Gas Turbine and Aeroengine Congress and Exposition*, (1995).
35. M. Saxena and R. K. Irani, *Concurr. Eng.*, **2**, 45–57, Mar. (1994).
36. M. Saxena and K. Irani Rohinton, *Mech. Eng.*, vol. **115,** 84–90, (1993).
37. M. Saxena and R. K. Irani, *International Design Engineering Technical Conferences and Computers and Information in Engineering Conference* , **97645**, 385–395. (1993).
38. K. Kessel-Hunter, *Society of Manufacturing Engineers. AUTOFACT89 conference,* 22, *(*1989).
39. T. Capozzi, *ASME Power Conference*, **41820**, 1107-1114, (2005).
40. M. Hobday, *Res. Policy*, **26**, 689–710, (1998).
41. H. Ostad-Ahmad-Ghorabi, D. Collado-Ruiz, and W. Wimmer, *Proc. ICED 09 17th Int. Conf. Eng.*,**7** 301–310, (2009).
42. J.-P. Theret, D. Evrard, F. Mathieux, Y. Le Guern, and P. Chemla, *EnviroInfo2011. Workshop: "Trends in IT for Life Cycle Assessment",* 799-808, (2011)

Experimental characterization of a PEM fuel cell for marine power generation

Andrea Pietra[1,2], Marco Gianni[1,2], Nicola Zuliani[2], Stefano Malabotti[3], Rodolfo Taccani[2].*

[1]Merchant Ship Division, Fincantieri S.p.A., Trieste, Italy
[2]Department of Engineering and Architecture, University of Trieste, Trieste, Italy
[3]CEnergy, Trieste, Italy;

Abstract. This study is focused on the possible application of hydrogen-fed PEM fuel cells on board ships. For this purpose, a test plant including a 100 kW generator suitable for marine application and a power converter including a supercapacitor-based energy storage system has been designed, built and experimentally characterised. The plant design integrates standard industrial components suitable for marine applications that include the technologies with the highest degree of maturity currently available on the market. Fuel Cell generator and power converter have been specifically designed by manufacturers to fit the specific plant needs. The experimental characterisation of the plant has been focused on the evaluation of the efficiency of the single components and of the overall system. Results shows a PEM fuel cell efficiency of 48% (when all auxiliaries are included) and an overall plant efficiency, including power conditioning, of about 45%. From load variation response tests, the fuel cell response time was maximum 2 seconds without supercapacitors and increased up to 20 seconds with supercapacitors connected, reducing the stress on the fuel cell generator. Experimental results confirm that PEM fuel cells, when supported by a suitably sized energy storage system, represent a viable technical solution for zero-emission power generation on board ships.

1 Introduction

International maritime transport accounts for about 2 % to 3 % of global Green House Gas (GHG) emissions. Also, in 2015, shipping was responsible for almost 13 % of the total GHG emission from transportation in the European Union (EU) [1]. According to the fourth International Maritime Organization (IMO) GHG Study, emissions have increased of almost 10 % between 2012 and 2018 as a result of the growth in shipping activities. This study also highlights a sharp increase in short-lived climate pollutants, like methane and black carbon [2]. In the next years, shipping is expected to grow and thus its emissions are expected to increase up to 50% by 2050 if no proactive actions will be put in place [1]. For this reason, IMO has set a 50% reduction target for the global shipping sector by 2050 and a 40% reduction target for emissions per transport unit by 2030 and a 70% reduction target by 2050 in order to reach zero emissions from international shipping as soon as possible by the end of this century.
Innovative technologies, carbon-free fuels and efficiency gains are paramount for reducing maritime transport GHG emissions. In this context Proton Exchange Membrane (PEM) fuel cells are considered a novel technology even if they have been employed since 1960s especially for aerospace applications. This type of generator requires high purity hydrogen as fuel and therefore it can be considered a key enabling technology for carbon-free fuels. There have been some niche applications of PEM fuel cells in the maritime sector during last years, mainly as submarine's Air Independent Propulsion (AIP) system or small demonstration projects. Starting from 1980s, PEM fuel cell based AIP fuelled by hydrogen has been tested on board submarines. The nominal power installed has progressively increased during the years reaching a maximum of 300 kW on board class U-212A submarines developed for German and Italian Navies since 2002 [3]. Then, in 2003, a system based on the same technology has been installed on the Autonomous Underwater Vehicle (AUV) Urashima by the Japan Agency for Marine Earth Science and Technology. The PEM fuel cell power installed as main source of power on Urashima was limited to 4 kW and integrated with a lithium-ion rechargeable battery storage system [4-5]. Small but successful applications of PEM fuel cell powered passenger boats have been developed starting from the beginning of the 21st century. The most noteworthy project in such field are: the Duffy-Herreshoff DH 30 water-taxi developed in 2003 for operations in San Francisco bay (3 kW), the project Xperiance NX hydrogen developed in 2006 in Netherlands (1.2 kW), the ZemShip project operated in Hamburg, Germany between 2008 and 2010 (2 x 48 kW) [6] and Nemo H2 project, which run from 2008 to 2011 in Amsterdam, Netherlands (60 kW) [7]. Since these first applications, projects were focused on system's overall energy efficiency. For example, on ZemShip project, different energy management systems have been tested in order to evaluate the best possible operative solutions to minimise hydrogen fuel consumption and fuel cells degradation [8]. In more recent years, other projects regarding maritime utilisation of PEM fuel cells fed by hydrogen have not yet passed from the design phase to the building one, like the SF-Breeze and Zero-V projects, both from Sandia National Laboratories [9-10]. In 2018, Swedish-Swiss company ABB and Canadian Ballard Power Systems have announced to have signed a Memorandum of Understanding (MoU) to design, develop and validate a 3

MW PEM fuel cell power generation system specifically for marine applications [11]. At the moment of the development of this paper, no real application or details about the design and the validation of the ABB-Ballard PEM power system has been disclosed to the public. All these studies and project did not publish any significant experimental result about efficiency, transient load response and procedures for marine application classification. One of the main problems that naval engineers meet during their effort to decarbonise ships, is the lack of recognised international standards or guidelines for testing, modelling and certifying a fuel cell and all its related equipment. As far as the characterization of fuel cell systems is concerned, the availability of sources represents a further obstacle to ship designers. Among the researches available on this topic, the study [12] describes a PEM fuel cell's polarisation curve measurement and the statistical analysis of tests performed on this kind of power generator varying different parameters like temperature, pressure, flows of all fuel cell's interfaces and ambient conditions. Another report describes the experimental characterisation of a 1.2 kW PEM fuel cell and the modelling of its performances [13]. In order to improve efficiency, increase lifetime and reduce cost of PEM fuel cells for automotive market, Swiss Federal Office of Energy developed a time dependent numerical model [14]. An analysis of potential application of fuel cells in ferries and cruise ship can be found in [15] and [16]. Since the beginning of this project, authors have focused their work in developing a modular and easily scalable PEM power plant suitable for marine application. The elementary unit of this system is a 100 kW PEM fuel cells based power plant which has been designed, built and experimentally characterised. All components are able to withstand the harsh on board conditions, such as strong mechanical and environmental stresses (salty atmosphere, vibrations, inclinations, etc) and have been designed minimising their weight and volume. In particular, this power plant has been designed to be easily integrated on board minimising interfaces with systems already available on a ship. Also, this generation system is independent since has a dedicated cooling system without any impact on machinery spaces. Power converter which interfaces the fuel cell power plant with the onboard existing electrical network has been specifically designed by manufacturer to fit specific plant needs minimising conversion stages and including a supercapacitor-based energy storage system. The supercapacitors have been included in order to improve the system response to load change and, at the same time, reduce fuel cell degradation conditions that can arise when high load change are applied [17]. Considering the state of the art of the regulatory framework and the most recent literature available, the authors tested a marine-ready power generation plant following test methods and procedures which are currently not used for marine applications, bringing a useful contribution to the possible wider employment of PEM fuel cells and hydrogen on board ships. Authors have employed the international recognised standards IEC 62282-3-200 [18] and the European Community testing procedure document Test Module PEFC ST 5-3 [19]. In this work, authors have summarised experimental results obtained by tests carried out on the PEM power plant provided with field instrumentation and a dedicated automation system.

2 Test plant

The investigated test plant, shown in Fig. 1, consists of:

- a 200 bar g, 16 cylinders storage system of about 128 Nm^3 of hydrogen capacity;
- a 100 kW_{el} PEM fuel cell generator (2 strings in parallel, each composed of 6 stacks in series, 1152 cells in total);
- a DC/AC power converter including a supercapacitor-based energy storage;
- an electronic load bank;
- a fuel cell dry cooler;
- an electric board and a control system

The fuel cell is a commercially available generator fed with pure hydrogen at a pressure of about 4 bar g. Process air entering the stacks is provided by means of an internal centrifugal blower. Air is filtered before entering the fuel cell. The DC power produced by the fuel cell is converted to a three phase 440 V AC power by means of a DC/AC power converter. This equipment includes a supercapacitor-based energy storage system to improve the dynamic behaviour of the fuel cell. The AC power is delivered to an electronic load bank, whereas the fuel cell thermal power is dissipated by means of a dry cooler. All the Balance Of Plant (BOP) devices, such as cooling circuit water pump and dry cooler, as well as the fuel cell internal ancillaries and overall plant control system are electrically powered by a dedicated electric board.

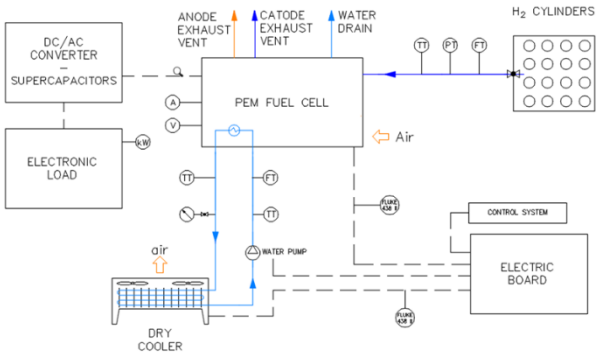

Fig. 1. *P&ID of the investigated test plant.*

Table 1. *System efficiency test: gross and net fuel cell and system electrical efficiency at 100% and 50% fuel cell nominal power.*

FC power	FC gross el. eff.	FC net el. eff.	System gross el. eff.	System net el. eff.
100%	54,5 %	47,8 %	52,2 %	45,3 %
50%	58,5 %	47,5 %	56,6 %	45,6 %

3 Experimental analysis and results

In order to investigate the performance of the system the following tests have been carried out:

- Fuel cell and system electrical efficiencies evaluation;
- fuel cell polarization curve plotting;
- system start-up and shut-down characterization;
- discharge water quality test;
- fuel cell electric load response analysis;
- load cycle test;
- DC/AC converter characterization.

3.1 Metrological characteristics of main instrumentation

The accuracy and repeatability of the main instruments used to characterise the test plant are shown in Table 2.

Table 2. *Metrological characteristics of main instrumentation.*

Component	Feature	Value
H_2, thermal mass flowmeter	Accuracy Repeatability	±0.5% Rd plus ±0.1% FS <0.2% Rd
H_2 piezoresistive pressure sensor	Accuracy Repeatability	±0.50% FS <0.1% FS
BoP power Portable network analyser	Accuracy	±1% ±10 counts
FC voltage	Accuracy	< 1 %
FC current	Precision class	1

3.2 Fuel cell and system electrical efficiency evaluation

Fuel Cell (FC) and system electrical efficiencies have been calculated at 100% and 50% nominal power (100 kW_{el} DC) referring to hydrogen Lower Heating Value (LHV) equal to 120 MJ/kg. Table 1 shows gross and net FC and system electrical efficiency at 100% and 50% nominal power.
Fuel cell gross electrical efficiency has been defined as:

$$\eta_{FC\_gross} = \frac{P_{elFC}}{P_{in}} \cdot 100 = [\%] \quad (1)$$

Fuel cell net electrical efficiency has been calculated according to the formula indicated in IEC 62282-3-200:

$$\eta_{FC\_net} = \frac{P_{elFC} - P_{elin}}{P_{in}} \cdot 100 = [\%] \quad (2)$$

Similarly, the system gross and net electrical efficiencies has been defined as:

$$\eta_{el\_gross} = \frac{P_{elSYS}}{P_{in}} \cdot 100 = [\%] \quad (3)$$

$$\eta_{el\_net} = \frac{P_{elSYS} - P_{elin}}{P_{in}} \cdot 100 = [\%] \quad (4)$$

The description of the symbols used in equations (1) to (4) are listed in Table 3. Fuel cell electrical efficiency is in line with data declared by other stationary systems fuel cell producers. The difference between the FC gross and net electrical efficiency is higher at 50% nominal power output. This is due to the BOP and ancillaries power consumption, which increases less than linearly with respect to the FC power output.

Table 3. *Description of the symbols used in equation (1) to (6).*

Symbol	Description	Unit
P_{elFC}	FC DC power output	kW_{el}
P_{elSYS}	System AC power output	kW_{el}
P_{in}	Fuel power input on LHV basis	kW
P_{elin}	BOP AC input power	kW

3.3 Fuel cell polarization curve plotting

FC polarization curve has been plotted following the guidelines included in the European Community (EC) Joint Research Centre test module PEFC ST 5-3 [19].

Table 4. *Load bank power set point imposed for measuring the fuel cell polarization curve.*

Set point number	Load bank power kW_{el}	Set point number	Load bank power kW_{el}
1	5	**7**	40
2	10	**8**	50
3	15	**9**	60
4	20	**10**	70
5	25	**11**	80
6	30	**12**	93

The polarization plotting process requires that the supercapacitors are charged and then that the fuel cell gets to its operational temperature. Fig. 2 shows fuel cell and system AC power output versus time during fuel cell polarization curve test. On the left side of Fig. 2 it is possible to observe the peak power delivered by the fuel cell to charge the supercapacitors. Then the fuel cell heats up delivering about 40 kW_{el} DC power. Fuel cell system warming phase lasts about 25 minutes. After the fuel cell has warmed up, the procedure for plotting of the polarization curve is started by increasing first and then decreasing the power absorbed by the load bank in steps, as indicated in Table 4.

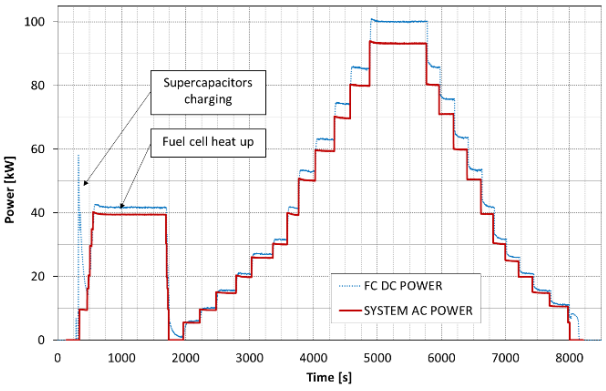

Fig. 2. *Fuel cell and system power output versus time.*

Fig. 3 shows the fuel cell polarization curve recorded during the test. In the same figure the FC DC power variation with current is presented. Fuel cell polarization curve is in line with producer's data. Nominal power is delivered at about 250 A. At this operating point, considering that each fuel cell system consist of 2 string connected in parallel of 6 stacks in series and that the total number of cells is 1152, the single cell voltage is about 0.7 V. The data recorded for the polarization curve plotting allows to calculate also the FC and system electrical efficiency at different FC operating point. Fig. 4 shows FC and system gross and net electrical efficiencies variation at different FC power. It is possible to observe that FC and system gross electrical efficiencies decrease as power increase while FC and system net electrical efficiencies increase with power. As already mentioned in section 3.1, this behaviour is due to the higher influence of BOP power consumption at low loads. The highest FC gross electrical efficiency (about 60%) is reached at 30% nominal load. System net electrical efficiency remains almost constant from about 60% to 100% fuel cell power.

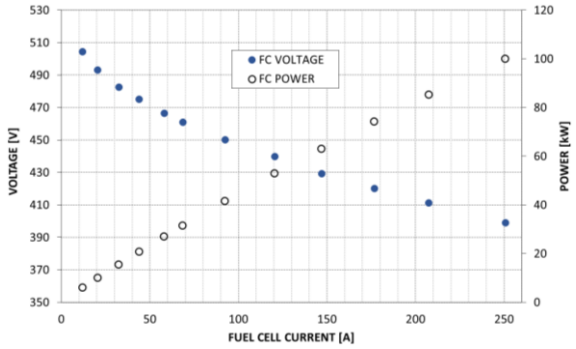

Fig. 3. *Fuel cell voltage and power variation with current.*

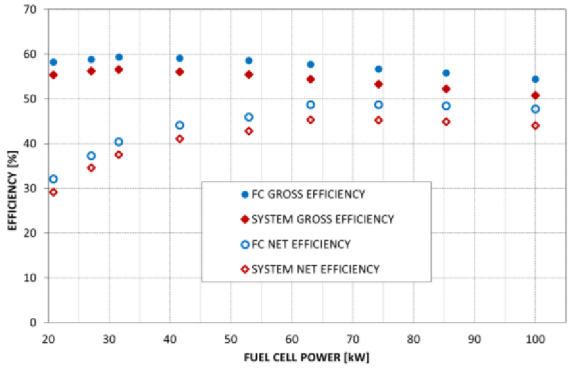

Fig. 4. *Fuel cell and system gross and net electrical efficiency.*

3.4 System start-up and shut-down characterization

System start-up and shut-down characterization test was developed to investigate energy and fuel consumption during these operational phases. In order to improve fuel cell expected life, the system is being flushed with hydrogen every time it is started or shut-down. In both cases hydrogen is discharged in atmosphere. An evaluation of the discharged hydrogen volume is essential to allow the calculation of the extension of any dangerous areas onboard, as required by Classification Societies. This parameter is also fundamental for the proper sizing of the hydrogen storage system. During the same test the BOP energy consumption and power demand were recorded as well in order to compare them with the ship power and energy availability. For the purpose of the test, the start-up period has been considered as the time interval between the issuing of the start signal and the reaching of a stable 15 kW_{el} AC power output. Similarly, the shut-down period has been considered as the time interval between load disconnection and the interruption of hydrogen consumption. In Table 5 and Table 6 hydrogen consumption, average and peak BOP electric power consumption and BOP electric energy demand at system start-up and shut-down are recorded. Total hydrogen consumption at start-up is 0.33 Nm^3, while hydrogen consumption at shut-down is 0.24 Nm^3. Maximum recorded peak BOP consumption is equal to 10 kW_{el}.

Table 5. *Hydrogen consumption, average and peak BOP electric power consumption and BOP electric energy demand at system start-up.*

	Unit of measure	Value
Time	s	120
Hydrogen consumption	Nm^3	0.33
Average BOP consumption	kW_{el}	3.3
Peak BOP consumption	kW_{el}	10
BOP electric energy demand	kWh_{el}	0.11

Table 6. *Hydrogen consumption, average and peak BOP electric power consumption and BOP electric energy demand at system shut-down.*

	Unit of measure	Value
Time	s	175
Hydrogen consumption	Nm^3	0.24
Average BOP consumption	kW_{el}	3.8
Peak BOP consumption	kW_{el}	9.6
BOP electric energy demand	kWh_{el}	0.19

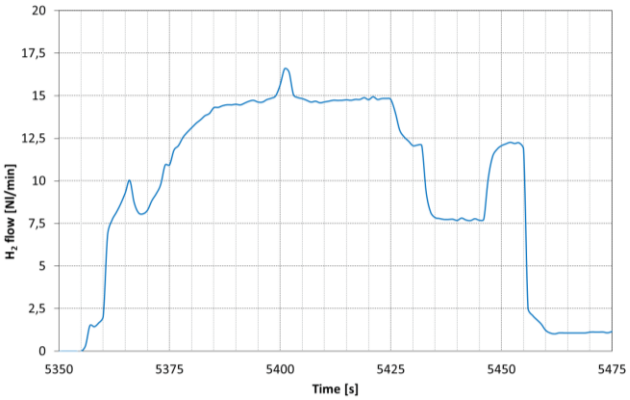

Fig. 5. *System start-up: hydrogen flow rate variation with time.*

Fig. 5 and Fig. 6 show hydrogen flow rate variation at start-up and shut-down respectively. It is possible to observe that the highest peak flow rate was measured at system shut-down and is higher than 25 Nl/min. Hydrogen flow peaks are due to the fuel cell manufacture's control strategy that aims to remove every unwanted residue from the anode side before the fuel cell shuts down.

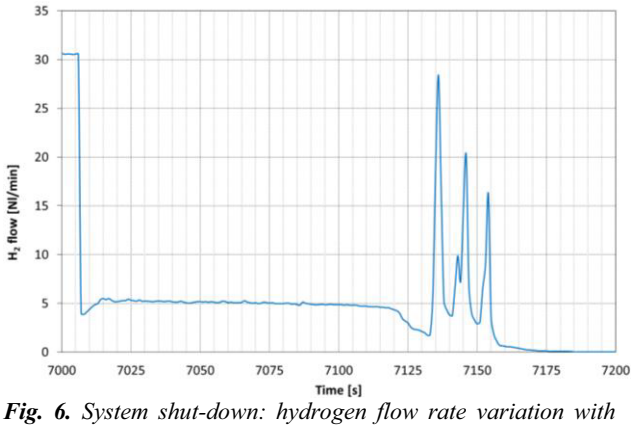

Fig. 6. *System shut-down: hydrogen flow rate variation with time at system shut-down.*

3.5 Discharge water quality test

This test was performed for measuring the quality of water discharged from the fuel cell in order to verify the possibility to collect this excess of product water into the onboard grey water collecting system. The test was carried out by analysing the water taken from the system internal process tank. As expected, the water analysis has shown that the fuel cell produced water can be considered demineralized water except for the presence of negligible quantities of iron, lead, zinc and nickel, probably originating from the cooling system pipes materials. Concentration of such contaminants is lower than values given in a study focused on the impact of grey water discharge in the Baltic Sea [20] and others stated in a document issued by United States Environmental Protection Agency [21].

Table 7. *FC electrical load response time and FC delivered power for different load power variations. Supercapacitors connected.*

Load power variation		FC response time	FC delivered power
from	to		
kW	kW	s	kW
0	15	-	17.80
15	45	19	47.75
45	75	15	79.92
75	93	10	99.09
93	33	18	38.79
33	15	21	20.12
15	45	10	47.76
45	75	15	79.66
75	93	9	98.94
93	33	20	40.22
33	15	24	20.16
15	45	10	47.77
45	75	15	78.96
75	93	10	99.07
93	33	20	40.23
33	15	22	20.29
15	45	9	46.63
45	75	17	79.66
75	93	11	100.4
93	33	21	38.98
33	15	23	20.23

Table 8. *FC electrical load response time and FC delivered power for different load power variations. Supercapacitors disconnected.*

Load power variation		FC response time	FC delivered power
from	to		
kW	kW	s	kW
0	15	-	15.84
15	45	≤ 1	47.21
45	75	2	80.78
75	93	≤ 1	99.65
93	33	≤ 1	33.34
33	15	≤ 1	15.83
15	45	2	48.13
45	75	≤ 1	80.32
75	93	≤ 1	99.27
93	33	≤ 1	34.48
33	15	≤ 1	15.83
15	45	2	48.10
45	75	≤ 1	80.36
75	93	≤ 1	99.26
93	33	2	34.50
33	15	≤ 1	15.82
15	45	≤ 1	48.13
45	75	2	80.22
75	93	≤ 1	99.24
93	33	≤ 1	34.52
33	15	≤ 1	15.80

3.6 Fuel cell electric load response analysis

This test was performed for measuring the FC power response time, which is defined as the time interval necessary to reach a FC electric power output steady-state value starting from the moment in which a change of electric power output is started. The test has been carried out both with supercapacitor storage system connected and disconnected. For the purpose of the test, it has been chosen not to apply a load power increase higher that 30 kW_{el} in order to preserve system integrity. Table 7 and Table 8 shows FC electrical load response time and FC delivered power with supercapacitor storage system connected and disconnected respectively. With supercapacitors connected, the longest FC response time was 24 seconds with a step load reduction from 33 to 15 kW_{el}. The shortest FC response time was 9 seconds and it was recorded with a step load increase from 15 to 45 kW_{el} and from 75 to 93 kW_{el}. With supercapacitors disconnected, the longest FC response time was about 2 seconds. Fig. 7 and Fig. 8 show the fuel cell power variation during the FC electric load response test with supercapacitor storage system connected and disconnected respectively. Comparing Fig. 7 and Fig. 8 it is evident how the supercapacitor energy storage system integrated in the DC/AC converter smoothens the FC delivered power output.

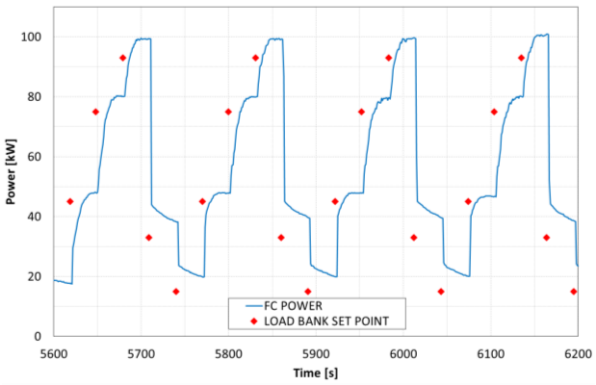

Fig. 7 *Fuel cell power variation for the FC electrical load response time test with supercapacitor storage system.*

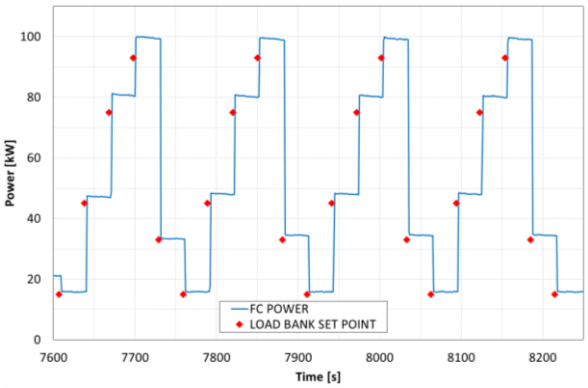

Fig. 8. *Fuel cell power variation for the FC electrical load response time test without supercapacitor storage system.*

3.7 Load cycle test

A load cycle test consisting in periodically changing the power required from the generator has been performed to evaluate the dynamic response of the generator when following a continuously variable load, i.e. a load cycle.

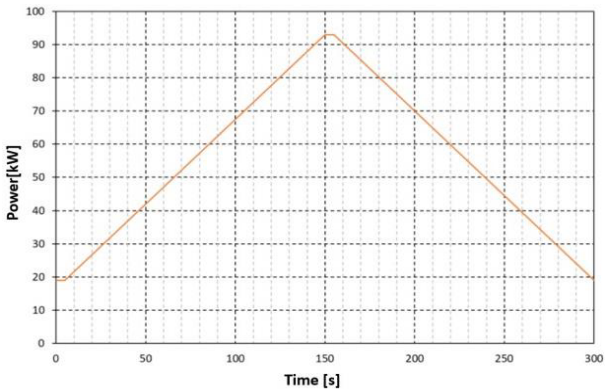

Fig. 9. *Load cycle test: load profile applied at the load bank.*

Load profile applied at the load bank had a triangular shape, with power output varying from a minimum value of 19 kW_{el} to the load bank rated power (93 kW_{el}), as shown in Fig. 9. The load cycle has a period of 5 minutes. The test was carried out with the supercapacitors in operation. Fig. 10 shows the fuel cell delivered power variation during the load cycle test. The system is capable of following the proposed triangular-shaped load cycle without any issue.

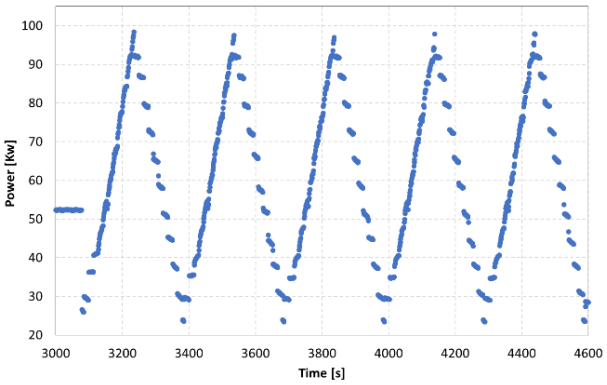

Fig. 10. *Fuel cell delivered power variation during the load cycle test.*

3.8 DC/AC converter characterization

The test for the characterization of the DC/AC converter was carried on in order to:

- characterize the charging process of supercapacitors;
- evaluate the efficiency of DC/AC converter at different loads;
- analyse the system current and voltage behaviour at different power factors.

3.9 Supercapacitors charging process characterization

The characterization of the supercapacitor charging process aims to evaluate the supercapacitors voltage variation with time, the time required for charging them and the current and voltage at the fuel cell output during such process.

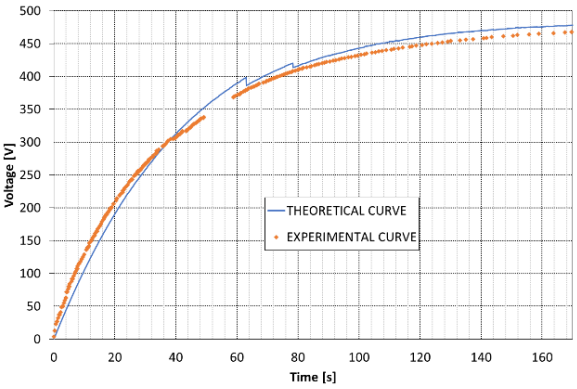

Fig. 11. *Experimental and theoretical supercapacitors voltage variation with time.*

In Fig. 11 is shown the measured supercapacitors voltage variation with time. In the same figure, the theoretical supercapacitors voltage variation with time of an equivalent Resistor-Capacitor (RC) circuit is also plotted. It is possible to observe a good correspondence between the experimental and the theoretical curves. The charging process is considered completed when the power delivered by the fuel cell is equal to the setting point of the load bank and the voltage reading across the supercapacitors is constant. It has been observed that the charging process takes about 175 s. The final

supercapacitors voltage is 470 V. Fig. 12 shows fuel cell current and voltage variation with time during the supercapacitors charging period. Fuel cell voltage initially increases, then becomes stable at 470 V. Instead, the fuel cell current decreases as supercapacitors charge. It is also possible to notice two discontinuities in the fuel cell current and voltage curves. These are due to the supercapacitors charging strategy adopted. At the beginning of the charging process the fuel cell delivers about 20 kW_{el} to charge the supercapacitors. As the energy storage system is being charged, the power delivered by the fuel cell decreases. In order to avoid high fuel cell potential that can negatively affect fuel cell performance and that can accelerate degradation, a load is applied during the supercapacitors charging period.

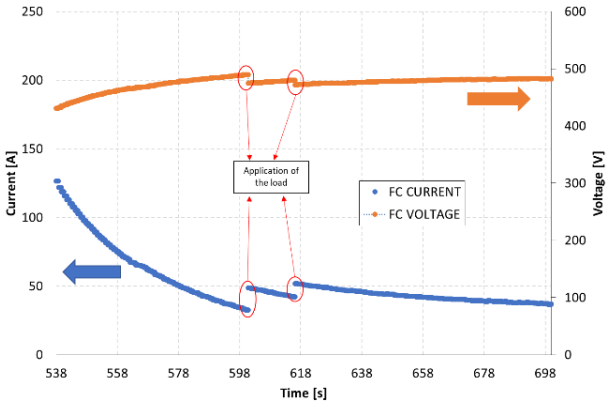

Fig. 12. *Fuel cell current and voltage behaviour during the supercapacitors charging period.*

3.9.1 Converter efficiency evaluation

In Table 9 conversion efficiency, converter average power and FC average power at two different load bank set points (45 kW_{el} and 80 kW_{el}) are presented. Average values are calculated on a 10 minutes basis. Results show that the maximum conversion efficiency is reached at 45 kW_{el} output and is equal to 96.2 %. Considering that the DC/AC converter is a prototypal unit, this value could be further improved.

Table 9. *Conversion efficiency, converter and FC average power at different load bank set point.*

Load bank set point	Average FC power	Converter average power	Conversion efficiency
kW_{el}	kW_{el}	kW_{el}	%
45	46.9	45.1	96.2
80	85.5	81.2	94.9

3.9.2 System current and voltage behaviour at different power factors

The power factor variation test was performed to evaluate the response of the system under real operating conditions, when a reactive electrical load component is present. The influence of the power factor variation on the power generation system behaviour is evaluated by measuring converter reactive power output and fuel cell power output when the power factor changes. The considered system load is 50 kW_{el}.

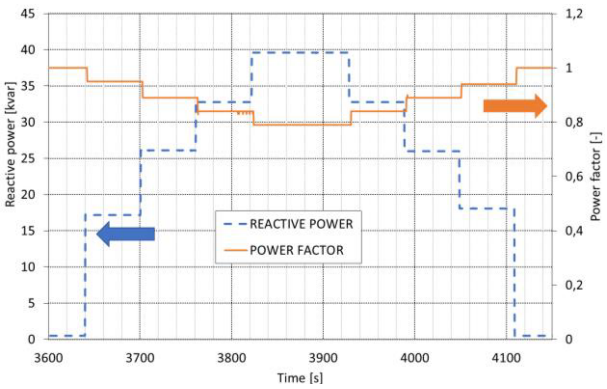

Fig. 13. *Converter reactive power output variation as load bank power factor changes. Considered system load: 50 kW_{el}*

Fig. 13 shows converter reactive power output variation as power factor changes: converter reactive power increases up to 38.9 kvar when power factor decrease to 0.8. Fig. 14 shows FC power output and load bank power factor variation with time: as the power factor varies, the effect on the fuel cell is negligible, with small oscillation of the produced output power.

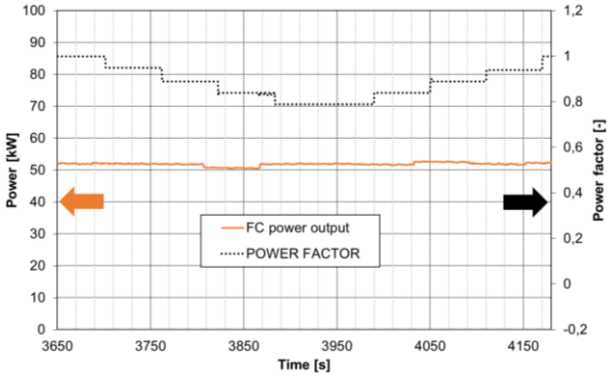

Fig. 14. *FC power output and load bank power factor variation with time.*

4 Discussion and conclusion

In the past years, applications of marine-ready PEM fuel cell based systems have been limited to niche vessels, like inland small passenger vessels or naval submarines, and in literature, very little experimental data is available especially regarding experimental characterization of marine-ready systems for seagoing vessel or cruise ships. In this work, in order to widen the knowledge on PEM fuel cell based generators suitable for such applications, a 100 kW_{el} PEM fuel cell test plant including a power DC/AC converter with a supercapacitors energy storage system, has been designed, built and experimentally characterized in order to ease the approval process for on board installation and the integration with the ship electrical system. The obtained data demonstrates that plant efficiency is comparable with commercial heavy-duty systems. It has been also observed that, as expected, the system load response time is noticeably improved by the supercapacitors based energy storage that, at the same time reduces the stress on the fuel cell generator.

Nevertheless, the PEM fuel cell generator still shows good response time even when supercapacitors are not activated. The analysis on the fuel cell start-up and shut-down procedures highlights that some hydrogen used to flush the fuel cells internal channels is discharged into the atmosphere. The largest volume of hydrogen is flushed at system start-up and is about 0.33 Nm^3. This value has to be taken into account in order to calculate the extension of any dangerous area that can arise at fuel cell anode exhaust on board of a ship, as required by Classification Societies. The DC/AC power converter and system start-up analysis show that the time to recharge the supercapacitors is about 175 s and the time to warm up the fuel cell system is about 25 minutes. A BOP peak power of about 10% of the plant nominal power should be made available for the start-up. The load cycle test confirms the capability of the system to follow a cyclical load variation. However, further tests should be done in order to evaluate fuel cell degradation when a variable load is applied over a longer period of time, as it could happen on board of a ship. Authors are anyway confident that the already obtained data could help the process of integrating a PEM fuel cell based system on board of seagoing ships. The next step of the experimentation is the installation of the system on board for testing its response to the marine environment.

5 References

1. M. Pape for EPRS (European Parliamentary Research Service); *decarbonising maritime transport: the EU prespective*, 2020. Available at: https://www.europarl.europa.eu/RegData/etudes/BRIE/2020/659296/EPRS_BRI(2020)659296_EN.pdf ;
2. International Maritime Organisation, *Fourth IMO Greenhouse Gas Study*, 2020. Available at: https://wwwcdn.imo.org/localresources/en/OurWork/Environment/Documents/Fourth%20IMO%20GHG%20Study%202020%20-%20Full%20report%20and%20annexes.pdf;
3. J. B. Lakeman, D. J. Browning; *The Role of Fuel Cells in the Supply of Silent Power for Operations in Littoral Waters*. Proceedings of NATO RTO AVT Symposium on "Novel Vehicle Concepts and Emerging Vehicle Technologies", 47, 1-18, 2004;
4. T. Sawa, T. Aoki, I. Yamamoto et al.; *Performance of the fuel cell underwater vehicle URASHIMA*. Acoustic Science & Technologies 26, 249-257, 2005;
5. T. Maeda, S. Ishiguro, K. Yokoyama et al.; *Fuel Cell AUV "Urashima"*. Mitsubishi Heavy Industries, Ltd. Technical Review Vol. 43 No. 1, 2006;
6. K. T. Hammou; *One hundred passengers and zero emissions*, 2008. Available at: https://webgate.ec.europa.eu/life/publicWebsite/project/details/2657 ;
7. EMSA, Study on the use of fuel cells in shipping, 01/2017. Available at: http://www.emsa.europa.eu/publications/download/4545/2921/23.html;
8. A. Bassam, S. R. Turnock, A. Phillips, P. Wilson; *Development of a multi-scheme energy management strategy for a hybrid fuel cell driven passenger ship*. International Journal of Hydrogen Energy 42, 2016. DOI: 10.1016/j.ijhydene.2016.08.209
9. J. W. Pratt, L. E. Klebanoff; *Feasibility of the SF-BREEZE: a Zero-Emission, Hydrogen Fuel Cell, High-Speed Passenger Ferry*. Sandia National Laboratories, 2016;
10. L. E. Klebanoff, J. W. Pratt, R. T. Madsen et al.; *Feasibility of the Zero-V: A Zero-Emission, Hydrogen Fuel-Cell, Coastal Research Vessel*. Sandia National Laboratories, 2018;
11. ABB press release on 27th June 2018, available online at: https://new.abb.com/news/detail/5360/abb-and-ballard-power-systems-to-jointly-develop-zero-emission-fuel-cell-power-plant-for-shipping-industry;
12. L. Placca, R. Kouta, D. Candusso, J. F. Blachot, W. Charon; *Analysis of PEM fuel cell experimental data musing Principal Component Analysis and Multi linear regression*. International Journal of Hydrogen Energy 35, 4582–4591, 2010. DOI: ff10.1016/j.ijhydene. 2010.02.076
13. I. San Martìn, A. Ursùa, P. Sanchis; *Modelling of PEM Fuel Cell Performance: Steady-State and Dynamic Experimental Validation*. Energies 2014, 7; 670-700, 2014. DOI: doi:10.3390/en7020670
14. J. O. Schumacher, R. Herrendörfer for the Swiss Federal Office of Energy, *ACTIF: Advanced CharacTerIsation of Fuel Cell Stacks for Automotive Applications*, 2019. Available online at: https://www.aramis.admin.ch/Default?DocumentID=66024&Load=true
15. C., Dall'Armi, D. Micheli, R. Taccani, Comparison of different plant layouts and fuel storage solutions for fuel cells utilization on a small ferry, 2021 International Journal of Hydrogen Energy, 46(26), pp. 13878-13897.
16. M. Gianni, A. Pietra, R. Taccani, Outlook of future implementation of PEMFC and SOFC onboard cruise ships, Proceeding of Applied Energy Symposium (ICAE), 100RES, Pisa 29 October 2020.
17. 15. P.Pei, X. Yuan, J. Gou and P. Li, *Dynamic Response during PEM Fuel Cell Loading-up*, Materials 2009, 2, 734-748; doi:10.3390/ma2030734
18. International Electrotechnical Commission; IEC 62282-3-200:2015 *Fuel Cell Technologies – Part 3-200: Stationary Fuel Cell Power Systems – Performance test methods*;
19. European Commission Joint Research Centre; *PEFC power stack performance testing procedure Measuring voltage and power as function of current density. Polarisation curve test method Test Module PEFC ST 5-3*, 2013;
20. E. Ytreberg, M. Eriksson, I. Maljutenko et al.; *Environmental impacts of grey water discharge from ships in the Baltic Sea*. Marine Pollution Bulletin 152, 2020. DOI: https://doi.org/10.1016/j.marpolbul.2020.110891
21. United States Environmental Protection Agency, *Greywater Discharge from Vessels*. 2011, available online at: https://www3.epa.gov/npdes/pubs/vgp_graywater.pdf

An algorithm for comparative analysis of power and storage systems for maritime applications

Massimo Rivarolo[1], Federico Iester[1], Aristide F. Massardo[1]

[1]Thermochemical Power Group (TPG), DIME, University of Genoa, Via Montallegro 1, 16145 Genoa, Italy

Abstract. This paper presents an innovative algorithm to compare traditional and innovative energy systems onboard for maritime applications. The solutions are compared adopting a multi-criteria method, considering four parameters (weight, volume, cost, emissions) and their relevance according to the kind of ship and navigation route. The algorithm, which includes a large and updated database of market solutions, leads to the implementation of HELM (Helper for Energy Layouts in Maritime applications) tool. HELM was conceived to support the design of maritime systems: it chooses the best technology comparing traditional marine diesel engines, propulsion systems with alternative fuels (methanol, ammonia, LNG) and innovative low-emission technologies (fuel cell and batteries). Two case studies are investigated: (i) a small passenger ship for short routes (ii) and a large size ro-ro cargo ship. For case (i), fuel cells represent a competitive solution, in particular considering navigation in emission control areas. For case study (ii) Internal Combustion Engines shows are the best solution. The evaluation of alternative fuels is performed, considering a sensitivity analysis on emissions' importance: methanol, LNG, and ammonia are promising solutions. For case (i), the installation of electrical batteries is also evaluated to analyse potential advantages to reduce the amount of H_2 stored onboard.

1 Introduction

As the emission of Green House Gases (GHG) are increasing more and more in last years, reaching the record values of 33.5 Gtons in 2018 and 33.4 Gtons in 2019 in terms of CO_2 [1], both international associations and governments are adopting environmental and energy strategies to reduce their growth. According to the last data, the impact of maritime sector is growing as well, with an increase of GHG emissions from 977 million tonnes in 2012 up to nearly 1.1 Gtons in 2018 (+9.6%) [3]. Today almost the total (99.5%) of maritime vessels in operation employ Internal Combustion Engines (ICEs) for propulsion fed by high pollutant fuel oils (Heavy Fuel Oil, HFO, or Marine Diesel Oil, MDO) [3]. In the last twenty years, the International Maritime Organization (IMO) set many regulations to limit the impact of maritime sector. The document MARPOL Annex VI established limitations SOx and NOx emissions. Since 2020, SOx maximum content in terms of weight in the fuel has been set to 0.5% (previous limit was 3.5%), with a further limitation of 0.1% in Emission Control Areas (ECA). Concerning NOx emissions, new ships (construction since 2016) must comply with the TIER 3 limit in ECA, which implies a reduction from 14 g/kWh to 4 g/kWh for navigation at low rated engine speeds (<150 rpm). In 2018, IMO has also established long-term targets to reduce 50% GHG emissions in shipping sector by 2050, compared to 2008 levels.

Recent studies demonstrated that the introduction of alternative fuels and the diffusion of new technologies is mandatory to reach the long-term targets set by IMO. Although the introduction of LNG to replace HFO in ICEs will help to reduce CO_2 emissions [5][6], it is not sufficient: thus, the use of more sustainable solutions must be considered as well. The potential of many possible fuels, such as ammonia and methanol, has been investigated in [7][8][9]. In recent years, the introduction of fuel cells as energy generation systems for propulsion or auxiliary power units (APU) for maritime vessels has been investigated by many authors, in particular PEMFC and SOFC technologies appear to be the most promising ones [10][11][12][13][14][15][16]. Fuel cells present many interesting features for maritime applications, such as high efficiency (also at partial loads), low level of emissions, noise and vibrations. However, it should be noted that this technology is currently available only for limited power range, up to 1-2 MW, thus they cannot substitute traditional ICE for propulsion on large size ships (i.e. containerships, tankers, large cruise ships).

As many solutions for both energy generation and storage onboard are available on the market and new innovative solutions are under analysis, it is important to adopt instruments and software tools to compare them with state-of-the-art solutions and find out the most promising ones, also according to the operating scenario and the vessel navigation route. For maritime applications, a holistic evaluation is mandatory to consider many relevant parameters, such as costs,

* Corresponding author: massimo.rivarolo@unige.it

emissions, volumes and weights. In this research paper a simple but reliable method for a preliminary evaluation of the solutions currently available on the market is presented: the developed approach allows for calculating the values of these parameters for different technologies, based on a strong database implemented inside the software tool and based on real market data for each storage and energy generation technology. The algorithm is based on a multi-criteria decision method, which is employed to compare many solutions, also in maritime applications [17][18][19].

2 Algorithm description

The HELM algorithm is based on a wide specifics database of different power systems and their corresponding fuel storage. Once obtained the data from the literature the software creates a set of maps with information that covers a large range of sizes. The main inputs are the power required by the ship and the hours of operation. In the latest version of the software, there is one more feature required as input that leads to the possibility of introducing the use of the battery, covering variable percentages, as a second technology in the same study case to help innovative ones like fuel cells.

Figure 1. shows the flow chart that describes the algorithm on which the software depends that was already explained in previous works by the authors' research group [20][21][22]. It starts from the main inputs, then entering the maps, evaluates the weight, volume, and cost of the system including both the energy consumption unit and the fuel supply and storage systems. Furthermore, there are maps used to estimate the emissions as a function of the fuel and the type of generating system.

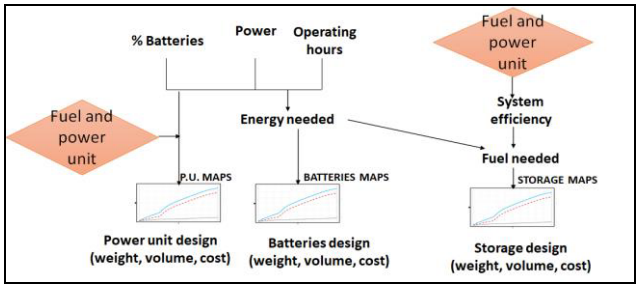

Fig. 1. Algorithm flow chart

The second part of the software code establishes a comparison between the different technologies considered in the first part. To implement this phase, four areas of comparison are considered, which are the same outputs described above (weight, volume, cost, and emissions), then the software gives scores according to the performance of each technology for all the four fields and after rates are added.

Table 1. describes the criteria by which the scores are awarded. The scores range from 1 up to 10 for each class, the technology with the best performing value takes 10, used a reference value (Vbest) to evaluate the scores of the other technologies (Vi) using the following formula:

$$X_i = V_i / V_{best}$$

To expand the case study and to adapt the computation to different situations, the software uses references that are nothing more than weights, which give different importance to the various parameters (weight, volume, cost, and emissions). The reference value ranges from 1 to 5 and multiplies the corresponding score. In this way, new low RTL technologies with performances that are not as excellent as those of traditional systems but with low polluting emissions can withstand and in some cases win the comparison.

Table 1. Scores in function of the X range of a certain output variable.

Value	*Score*	*Value*	*Score*
$1 < X \leq 1.1$	10	$3 < X \leq 4$	5
$1.1 < X \leq 1.3$	9	$4 < X \leq 5$	4
$1.3 < X \leq 1.6$	8	$5 < X \leq 6$	3
$1.6 < X \leq 2$	7	$6 < X \leq 8$	2
$2 < X \leq 3$	6	$X > 8$	1

One of the greatest advantages of HELM, besides its ease of use, is that its database can be constantly updated to provide reliable data and solutions able to consider even the most recent technologies in the maritime sector, with also the possibility of analysing hybrid solutions (i.e., combining batteries and fuel cells). It is possible to include a new technology simply by inserting the maps in the program code. The functions are periodically updated based on the most recent market values: the detailed maps for each energy generation and storage technology concerning volume, weights, costs, and emissions are reported in [21]. At present, HELM database is made by hundreds of commercial solutions: for innovative technologies (i.e. SOFC), only a few market solutions exist, while for traditional ones (i.e. ICE fed by MDO) nearly 100 market values are included in the database. The possible different solutions are reported in Table 2.

Table 2. Technologies implemented in HELM database

Power generation system	**Storage system**
PEM Fuel Cells (PEMFC)	Liquid H2 (LH2)
PEM Fuel Cells (PEMFC)	Compressed H2 (CH2)
Solide Oxyde Fuel Cells (SOFC)	Liquid Natural Gas (LNG)
microGT (mGT)	Liquid Natural Gas (LNG)
Int. Comb. Engine (ICE)	methanol
Int. Comb. Engine (ICE)	ammonia
Int. Comb. Engine (ICE)	Liquid Natural Gas (LNG)
Int. Comb. Engine (ICE)	Marine Diesel Oil (MDO)

To facilitate the use of the software and speed up data collection, additional functions have been implemented to calculate all the possible input ranges and then to represent the results, indeed some graphical representations are reported in the following chapters.

3 Case studies

Two case studies have been chosen for presentation in this paper, based on their size and on the characteristics of their operative usage.

3.1 Small size case study: passenger ship for fluvial transport, Jules Verne 2

This case study is a small sized ship for public fluvial transport in Nantes, France. This bus-ship has been in operation since August 2019, and it is one of the first passenger ships in the world fully powered by hydrogen. It operates throughout the whole year to connect Port-Boyer and Petit Port on the river Erdre, at one kilometre, and it is powered by PEM fuel cells (installed power 10 kW) that enable the ship to transport up to twelve passengers and eight bikes.

Observing the ship's most recent navigation activity [23], the operating hours are assumed equal to 24. Since ships rarely need to exploit their power units to the maximum of their capabilities, a load profile has been investigated based on the methodology described in [24], and later processed via a weighted average of the energy loads during the navigation, yielding a corrective energy factor, expressed in percentage, and applied to the operative hours of the case study. Fig. 2 shows the load profile for two passenger ship types, coastal and ocean-going vessels, through which the equivalent hours turned out to be equal to 19% and 28% of the whole navigation time respectively. In this case, the weighted average considered is the first one, bringing the 24 hours mentioned above to 5 equivalent hours.

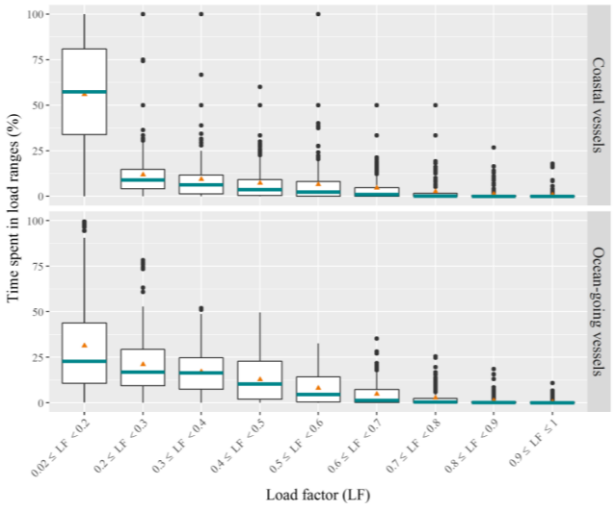

Fig. 2. Load factor for two passenger ships classes [24].

After defining power (10 kW) and equivalent hours (5), the relevance of the four parameters used in HELM has to be set. As this ship needs to operate always in urban areas, a high relevance must be considered for emissions, which has been set to 5. Volumes must have a high relevance as well because space is a critical factor for passenger transportation, and the same can be said, to a lesser extent, for the weight, resulting in volume having a relevance of 3, and weight being assigned 2. Costs are less relevant than the other parameters for such a small sized ship, thus relevance is set to 1, also thanks to incentives.

3.1.1 Simulation results

In this case study's results (Fig. 3), PEMFC showed great potential due to the nature of the ship, requiring low power and only few equivalent operating hours. Among the other technologies, the fuel oil ICE obtains a high score thanks to its maturity, which leads to low volume, weight and cost, while emissions are its weakness. It is worth analysing the absolute values for the best potential choices (PEMFC fed by liquid or compressed hydrogen and ICE fed by fuel oil), comparing the impact of both storage and propulsion systems on the results. As far as volume and weight are concerned, Fig. 4 shows that the largest impact is due to the propulsion unit in case of ICE; on the other hand, the impact of the storage system is considerable in case of PEMFC solutions, due to the large volumes and weight required for H_2 storage onboard. Concerning costs, it is evident that the propulsion system represents the largest amount for each technology, because the required autonomy is limited (5 hours) and the related size of storage system does not affect significantly total costs.

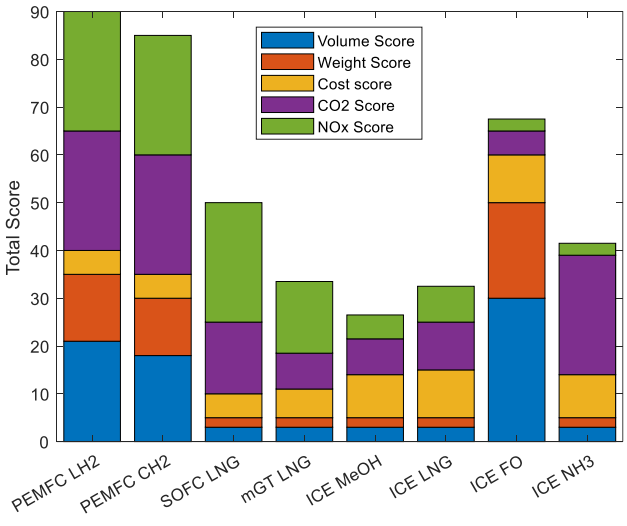

Fig. 3. Comparative HELM results for small case study (Jules Verne 2)

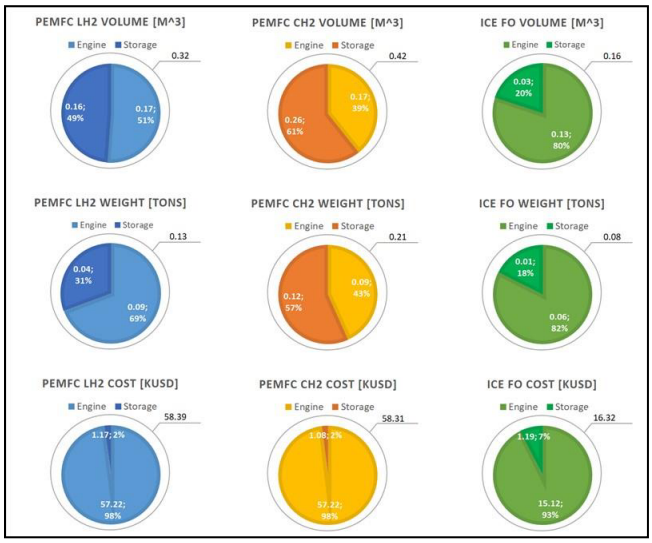

Fig. 4. Propulsion and storage systems comparison for the best technologies (Jules Verne 2)

To further analyse the results' range of validity, a parametric analysis has been conducted (Fig. 5) repeating the simulation while assigning every time a different emissions relevance (1, 3 and 5) and normalising the scores of all technologies of each simulation so that their sum would be the same with the three different relevance sets, in order to make the changes easily noticeable. It is worth noting that the fuel oil ICE is the best choice only in a scenario with very low relevance for emissions; PEMFC fuelled by hydrogen are a competitive solution for this application, as the limited power demand and autonomy required does not require large volumes for hydrogen storage onboard.

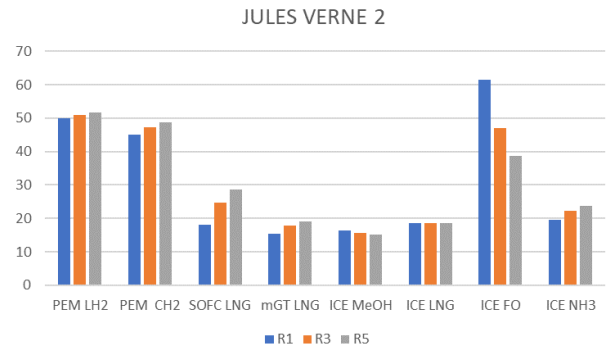

Fig. 5. Parametric analysis of the scores of the small sized case study, with the relevance of the emissions being set to 1, 3 and 5 (blue, orange and grey bars).

3.2 Large size case study: Ro-Ro ship, F. A. Gauthier

This case study is a large size ship operating in Canadian waters since 2015, connecting Bas-Saint-Laurent to Godbout and Baie-Comeau, and built in 2013 in Italy by Fincantieri. With a length of 130 meters and a width of 25, it can transport up to 800 passengers and 180 cars. It has been the first LNG-powered ferry used in North America, and the first one of this kind to be built in Italy. It's propelled by 4 Wärtsilä Dual Fuel LNG/MDO engines, with a total power of 20880 kW.

Searching for the ship's most recent navigation activity, it has been assigned 48 operating hours. Following the same process described for the first case study [23], a load profile has been searched for and processed, obtaining a corrective consumed energy factor of 33% that correspond to the Ocean-going vessels case shown in Fig. 6. The final equivalent hours amount to roughly 16.

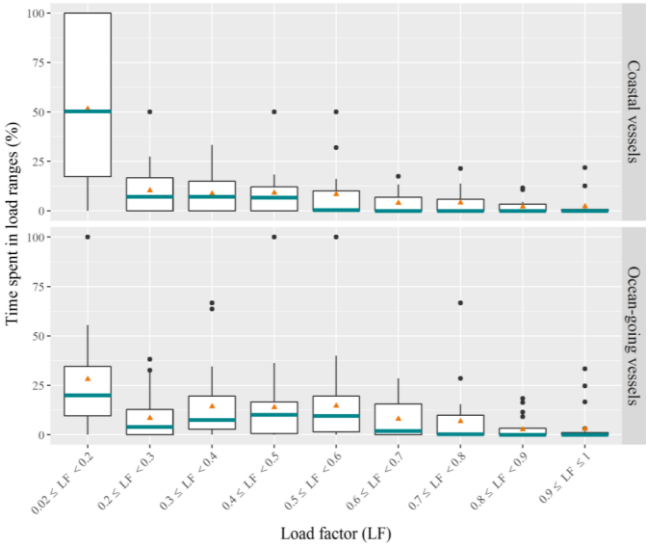

Fig. 6. Load factor for two Ro-Ro ships classes [24].

With power (20880 kW) and equivalent hours (16) defined, the relevance of the four parameters needed to be defined. In this case, as this ship needs to be able to store a large number of vehicles and passengers, volume is critical, thus a relevance of 4 has been assigned. For such a large ship, costs are also an important factor, leading to an assigned relevance of 3, while weight is less critical than volume, therefore relevance 2 has been assumed. The same value has been imposed for emissions, as navigation does not occur in ECA zones or in locations with specific requirements.

3.2.1 Simulation results

In this case study's results (Fig. 7), the combination of medium-high power requirements and few equivalent hours set up the field for a good result for LNG ICEs. The absence of SCR systems makes the typical advantage of FO engines in terms of weight and volume vanishes, as the storage does not need to be particularly large. As the required power is quite high (about 20 MW), fuel cell solutions are not particularly competitive, confirming that nowadays they are an interesting alternative to traditional ICEs only for small size applications.

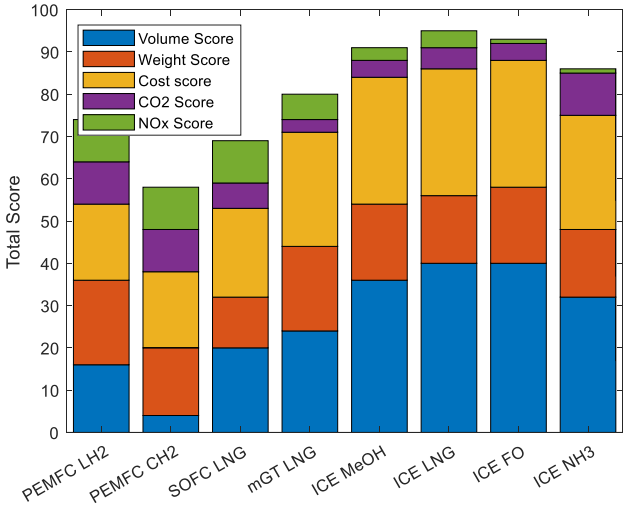

Fig. 7. Comparative HELM results for small case study (Gauthier Ro-Ro ship)

Tab. 3 shows the impact of propulsion and storage systems for the solutions that obtain the highest score (Fig. 7). Fuel oil is slightly superior to LNG and methanol in terms of volume, weight and costs, but the difference is limited; from the environmental standpoint, LNG and MeOH arouse interest, thus they can both represent an interesting alternative for the present scenario as well.

Tab. 3. Propulsion and storage systems comparison for the best technologies (Gauthier Ro-Ro ship)

		ICE LNG	ICE FO	ICE MeOH
Volume [m^3]	*Engine*	578.65	686.95	643.10
	Storage	274.27	101.60	277.63
	Total	**852.92**	**788.55**	**920.73**
Weight [tons]	*Engine*	600.44	555.41	553.32
	Storage	31.38	10.26	14.76
	Total	**631.82**	**565.67**	**568.08**
Cost [kUSD]	*Engine*	12058.16	11483.96	11943.32
	Storage	238.33	50.45	21.16
	Total	**12296.48**	**11534.41**	**11964.47**

It is interesting to note that, by looking at the parametric analysis data presented (Fig. 8), LNG ICEs show the same score as FO ICEs in the case of emissions having minimum relevance (R1). This shows that LNG is now a viable and convenient solution for ships operating in similar conditions as those presented in this case study, not needing a strong importance in emissions restrictions to be competitive.

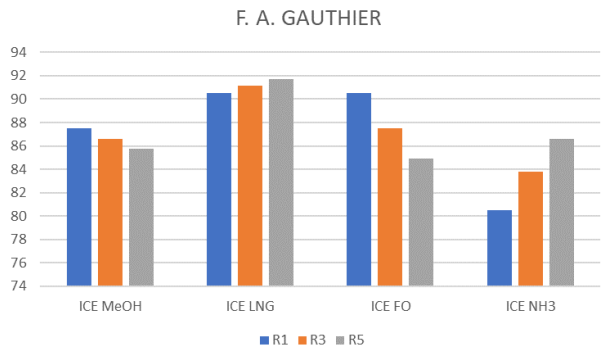

Fig. 8. Parametric analysis of the scores of the large sized case study, with the relevance of the emissions being set to 1, 3 and 5 (blue, orange and grey bars).

3.3 Batteries analysis

In order to investigate the level of maturity of Li-Ion batteries for maritime application, an analysis in two steps has been performed. Initially, batteries have been applied to the case study described in section 3.1 (Jules Verne 2); then, a large parametric dataset has been produced to investigate the conditions in which the batteries excel or show their drawbacks.

3.3.1 Batteries applied to a small sized case study

The Jules Verne 2 ship represents a good case study to investigate the effect of the adoption of batteries on small ships with low power and operating hours requirements. With the parametric analysis performed (Fig. 9), it becomes apparent how adopting batteries does not increase the overall performance, because of the weight being considerably higher (batteries are characterised by low gravimetric energy density [25]) and the volume being slightly higher as well, due to the low convenience of using both fuel cells (with hydrogen storage) and batteries in parallel considering such a low energy storage requirement. The main advantage in using batteries is due to the possibility of having an additional option during operations, increasing flexibility. On the other hand, they represent an extra cost, volume and weight onboard.

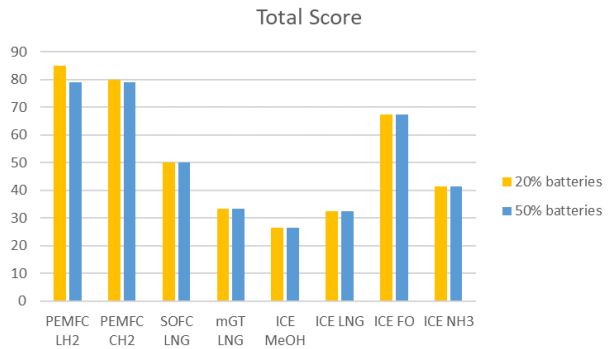

Fig. 9. Results of the small sized case study when imposed 20% and 50% batteries usage over the total of consumed energy.

3.3.2 Parametric dataset analysis

From the parametric analysis (Fig. 10), it is evident that batteries show better performance for low powers and high operating hours values. When the operating hours increase, the volume of the storage of hydrogen grows so much that batteries, even if much heavier, show better results. On the other hand, for low operating hours, fuel cells show significantly better scores, thanks to their lower weight. Concerning costs, batteries have lower costs compared to PEMFC and hydrogen storage systems.

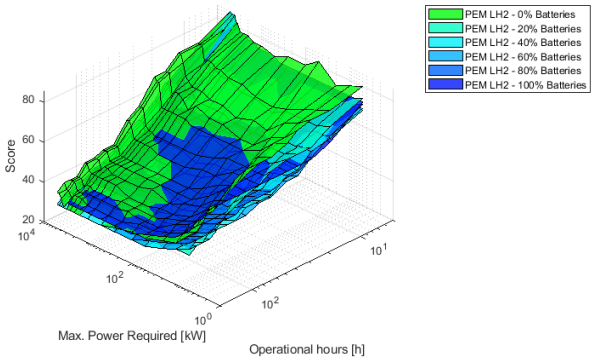

Fig. 10. 3D representation of the parametric dataset for PEMFC solutions paired with LH2 showing different score surfaces for different percentages of batteries, generated with a fixed relevance set of 4 for volume, 2 for weight and emissions, and 3 for cost.

4 Conclusions

This paper investigates the potentiality of the multi-criteria decision method-based software HELM, which identifies the most suitable power system to be used in specific applications in the maritime field. Two applicative cases have been investigated.

In the first case study, a small passenger ship operating in urbas anreas, where the reduction of emissions has a high relevance, was considered. The simulation suggested the use of hydrogen fueled PEMFC as an excellent alternative to traditional FO engines. To investigate a different condition, the second case study is a large sized ship, where ICE is identified as the best technology due to the more stringent limits on volume and cost. However, a very good alternative to FO is a different fuel as LNG, which allows for a reduction in CO_2, NOx and SOx emissions.

Finally, the use of batteries was investigated for small size ships: from the analysis, batteries result suitable in a small range of sizes and operational hours, anyway they are included in the options available in HELM.

The study cases analyzed are only two of all those considered during research activities conducted by the authors' research group. The decisional criterion has been tested on many cases, always returning results that are likely, proving the reliability of the algorithm. Furthermore, by inserting technologies with reduced environmental impact in the HELM database, the software shows unconventional options suitable for particular applications, in order to move towards decarbonization in the maritime field and a more sustainable future.

The Authors wish to thank Lorenzo Clerici and Stefano Bottino, graduated students at University of Genoa, for their contribution to this research activity.

References

1. https://www.iea.org/statistics/ International Energy Agency (IEA) official website, last access 8/9/2021.
2. Maritime forecast to 2050-Energy transition outlook (2021), DNV Maritime.
3. MARPOL Annex VI - Prevention of Air Pollution from Ships (2020), International Maritime Organization (IMO).
4. https://www.imo.org/en/MediaCentre/HotTopics/Pages/Reducing-greenhouse-gas-emissions-from-ships.aspx International Maritime Organization (IMO) official website, last access 8/9/2021.
5. T. Ouyang, J. Tan, S. Xie, W. Wu, Z. Su, Energy Conversion and Management, 229 (2021), 113770.
6. J.E. Fokkema, P. Buijs, I.F.A. Vis, Transportation Research, Transport Environ., 56 (2017), 229-240.
7. P. Balcombe et al, En. Conv. and Manag., 182 (2019), 72-88.
8. M. Prussi, N. Scarlat, M. Acciaro, V. Kosmas, J. of Cleaner Production, 291 (2021), 125849.
9. N.R. Ammar, Transportation Research, Transport Environ., 69 (2019), 66-76.
10. L. van Biert, M.Godjevac, K.Visser, P.V.Aravind, Journal of Power Sources, 327 (2016), 345-364.
11. Rivarolo M, Rattazzi D, Magistri L, Int. J. of Hydrogen En., 43 (2018), 23500-23510.
12. H. Sapra, J. Stam, J. Reurings, L. van Biert, W. van Sluijs et al., App. En., 281 (2021), 115854.
13. Gadducci E, Thomas L, Bellotti D, Magistri M, Massardo AF, Int J. of Hydrogen En., 46 (2021), 24305-24317.
14. O.B. Inal, C. Deniz, Journal of Cleaner Production, 265 (2020), 121734.
15. A. Bouakkaz, A.J.G. Mena, S. Haddad, M.L. Ferrari, 2021, J. of En. Storage, 33 (2021), 1-13.
16. A.F. Massardo, L. Magistri, J. of Eng. For Gas Turbine and Power, 125 (2003), 67-74.
17. R. Chauvy, R. Lepore, P. Fortemps, G. De Weireld, Sustainable Prod. and Cons., 24 (2020), 194-210.
18. A. Priftis, E. Boulougouris, O. Turan, A. Papanikolau, Ocean Eng., 156 (2018), 347-357.
19. M. Pesce, S. Terzi, R.I.M. Al-Jawasreh, C. Bommarito, L. Calgaro, et al., Science of the Total Environment, 642 (2018), 668-678.
20. http://www.tpg.unige.it/TPG/portfolio-item/helm/ last access 31/7/2021.
21. M. Rivarolo, D. Rattazzi, L. Magistri, A.F. Massardo, En. Conv. And Management, 244 (2021), 114506.
22. M. Rivarolo, D. Rattazzi, L. Magistri, Int. J. of Hydrogen En., 45 (2020), 25747-25757.

23. www.vesselfinder.com last access 31/7/2021.
24. S. Jafarzadeh, I. Schjølberg, Transp. Research Part D: Transport and Env., 65 (2018), 500-523.
25. O'Hayre et al, Fuel Cell Fundamentals, 2016.

Pilot autonomous hybrid hydrogen refueling station utilizing a metal hydride compressor covering local transportation needs

Nikolaos Chalkiadakis[1,*], *Athanasios* Stubos[1], *Emmanuel I.* Zoulias, and *Emmanuel* Stamatakis[2]

[1] NCSR "DEMOKRITOS", Athens, Greece
[2] New Energy & Environmental Solutions & Technologies - NEEST, Athens, Greece
[3] Institute of Petroleum Research / Foundation for Research and Technology - Hellas (IPR/FORTH), Chania, Greece

Abstract. The need for decreasing carbon emissions in the transportation sector in order to meet the targets of the European Union by 2030, inevitably leads to the large scale adoption of cleaner alternatives. Hydrogen fueled vehicles could possibly provide one such alternative, if we could assume that the necessary infrastructure would be widely available throughout Europe. Already, the European Union has committed to the construction of a significant number of Hydrogen Refueling Stations (HRS) by year 2025 and in view of that, there is a need of developing suitable configurations for the production, compression, storage and dispensing of green hydrogen to hydrogen fueled vehicles. This work presents an autonomous hybrid system which produces green hydrogen by PV- powered water electrolysis (PEM), which is subsequently compressed by a novel metal hydride hydrogen compressor to pressures up to 200 bar. This pilot HRS will meet the daily demand of 2 scooters and a golf cart which have been transformed, in order for their electric motor to be powered by a hydrogen fuel cell instead of a battery. An important element of the work which is presented, revolves around the integration of the metal hydride compressor with the rest of the system, and how this integration won't hinder its functionality. The complete system design and layout is presented, while the results from the system operation could give a good idea regarding the optimal system sizing for similar large scale applications.

1 Introduction

Worldwide, there is an obvious effort for the minimization of the gas emissions which are produced by all aspects of human activity. The main reason for this is the increasing presence of the effects of climate change which are already starting to be felt, which are in large due to carbon dioxide emissions (Fig.1).
The above mentioned effort is evident if one looks at the relevant decisions of most governments, the most notable example being the targets defined by the European Union for the decrease in greenhouse gas (GHG) emissions by 2030 and 2050.
More specifically, the E.U. has defined its 2030 targets as:

- 40% reduction in GHG emissions in relation to the 1990 levels
- At least 32% renewable energy share
- At least 32.5% improvement in energy efficiency

Currently, one of the sectors of human activity with the most GHG emissions is the transportation sector. Although common sense would lead to the expectation of decreasing levels of emissions due to measures similar to those which are mentioned above, the reality is that they remain relatively the same. This fact can be attributed to several causes, the most likely of which are:

- The trend of consumers selecting larger and heavier vehicles (not just in the USA but in Europe and Asia as well). This trend is in part counterbalanced by the increasing penetration of electric vehicles and the subsequent decrease of the share of Diesel vehicles.
- The growth of the global GDP, combined with the rise of e-commerce which requires fast product delivery, resulting in the increase of emissions due to transportation of goods.

The above lead to the realization of the importance of the transportation sector in shaping the worldwide GHG emissions and for this reason the E.U. has set specific targets to be met by years 2030 and 2050. These are

- 30% decrease of CO_2 emission by 2030 and
- 60% decrease of CO_2 emissions by 2050

In order meet these targets, hydrogen could be the fuel of choice for the transportation sector, but in order for it to have an expanded role as a fuel in the future, an extensive refueling network must be developed. There is also the counter-argument that without a sufficient number of hydrogen fueled vehicles, refueling infrastructure is not financially viable, which leads to a chicken and egg problem [1]. A way to avoid this problem is the gradual development of stations which could meet the demand for hydrogen of smaller vehicle fleets, or of vehicles such as scooters, hydrogen bicycles

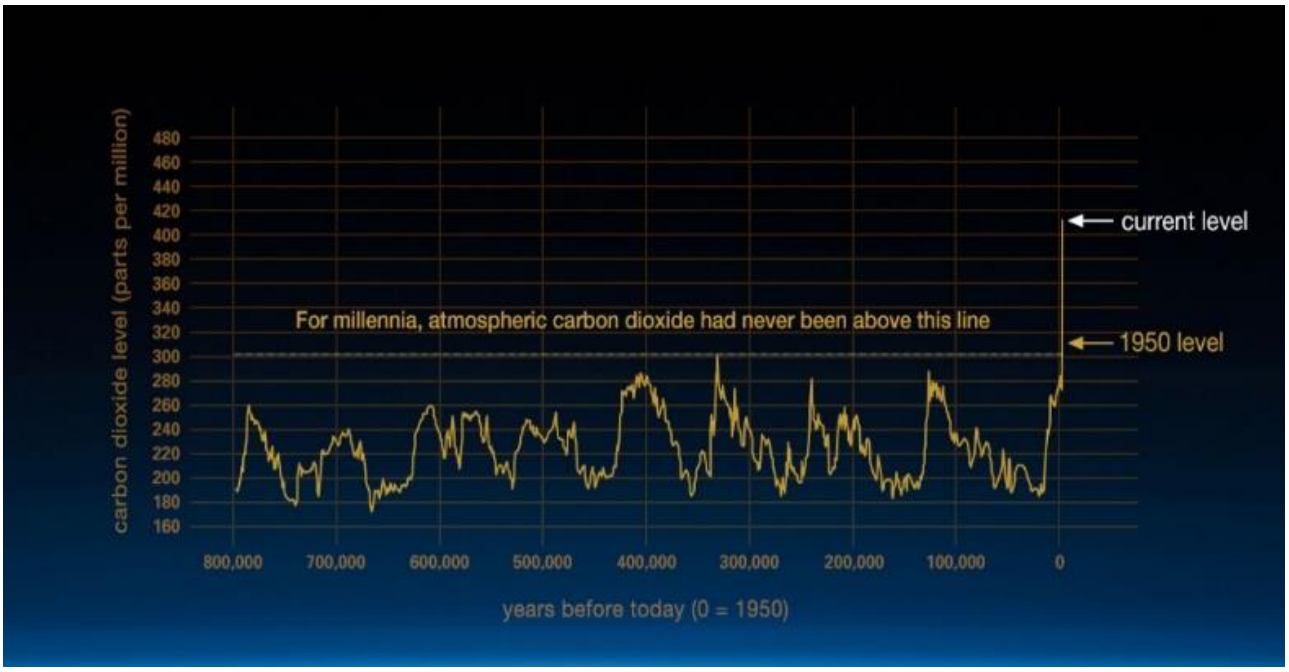

Fig. 1. Carbon Dioxide levels over the years (climate.nasa.gov)

and other light duty vehicles, eventually expanding to larger automotive applications once the financial viability of the smaller stations has been showcased.

An added benefit of this scenario is the acquisition of the relevant knowhow through numerous projects and different configurations, leading to the identification of the optimal case specific layout for future installations.

The project which will be analyzed throughout this paper, aims to showcase the design and construction of the first autonomous HRS for hydrogen fueled vehicles in Greece.

2 The HRS subsystems

The pilot refueling station which has been developed for the purpose of the H2TRANS project is designed to cover the daily hydrogen demand of two scooters and a golf cart, both of which have been configured in a way that their electric motors are powered by hydrogen fuel cells instead of batteries. As a result the whole system has been sized accordingly. The components that the system is comprised of are the following:

- Water treatment unit
- PV panels
- PEM water electrolysis
- Buffer and Low/High pressure hydrogen tank
- Metal Hydride Compressor
- Hot/Cold water tanks for the compressor function
- Hydrogen Dispenser

The above components are interconnected by a gas network which consists of various valves, flow regulators, flow meters, pressure/temperature transmitters and vents. In the following paragraphs, the exact role and specifications of each component will be detailed.

2.1 Water treatment

Water quality is an important aspect of a PEM electrolyzer's function and the threshold in which it can operate is strictly determined by the manufacturer. The most important characteristic for the water used in PEM electrolysis is its high resistivity, which is achieved by low content in contaminants such as electrolytes, ions, sodium and chlorides. Such contaminants are removed in the water treatment unit by filtering and deionizing water by using mixed bed resins and carbon filters. Also in order to desterilize water a UV lamp is used, which kills bacteria and microorganisms. The water which has passed though the treatment unit enters the electrolysis with an electrical conductivity lower than 0.1μS and concentration of sodium and chlorides lower than

Fig. 2. Water Treatment

5μg/L. The unit which is used in this case is depicted in Figure 2.

2.2 Hydrogen Production

Despite hydrogen being the most abundant element in the universe, the only form in which it can be found on earth is as part of a compound with other elements. Thus in order to isolate it for the purposes of using it as fuel, certain chemical reactions should be utilized, which depend on the compound that hydrogen is found in. The compounds in which hydrogen is most frequently found in are hydrocarbons (be it fossil fuels or biomass) and water. The most common methods for producing hydrogen through hydrocarbons are steam methane reforming (SMR), thermo cracking (TC), partial oxidation (POX) and coal gasification (CG). For the case of water electrolysis, the main methods for the production of hydrogen are PEM and alkaline electrolysis, while different approaches include photoelectrolysis (PHE) or photolysis, water thermolysis (WT), and photobiological processes [2].

The hydrogen production unit of the installation has been selected to be a PEM electrolysis unit. The reasoning behind choosing PEM electrolysis as a means of hydrogen production is the fact that it presents an ideal solution for coupling with renewable sources in order to produce green hydrogen. After leaving the water treatment unit, water enters the PEM electrolysis (Figure 3) which is made of three 1.3 kW stacks, each of which produces hydrogen at 16 bar at a purity greater than 99.99999%. The maximum flow rate of each stack is 3300 cc/min or 0.714 kg/h in terms of mass flow with a mean output of 0.127 kg/h throughout the day. The electrolysis unit has a modular design that allows for the installation of more stacks in order to increase the hydrogen flow rate. In its current size though, the daily amount of hydrogen produced can meet the respective demand of the vehicles used in the project.

2.3 Hydrogen storage

There are several ways to store hydrogen, some of which are pretty mainstream and have been used numerous times and some which are being currently tested and evaluated. A critical parameter for the assessment of a storage technology has to do with the suitability of the materials which are used, its volumetric density, as well as the reversibility of uptake and release [3]. The most popular storage methods, are compressed gas, liquefied and metal hydrides.

For the purposes of this project, hydrogen is stored as a compressed gas. The storage system (Figure 4) is divided in two parts, one used as a buffer and dedicated for low pressure storage at 16 bar. Basically, hydrogen flowing out of the electrolysis unit is stored in the low pressure compartment before entering the compressor. The low pressure storage ensures that regardless of whether the electrolysis operates or not, there is a sufficient quantity of hydrogen to feed the compressor. After compression hydrogen is stored at the second compartment at the pressure of 200 bar. Both compartments have a total volume of 300L, while the tanks are made of steel.

2.4 Hydrogen Compression

Hydrogen compression constitutes the main barrier regarding the large scale adoption of hydrogen as a fuel, not just for transportation applications but for stationary applications as well. For this reason, improvements in the efficiency, durability and reliability of hydrogen compressors is of utmost importance. Currently, the most commonly used hydrogen compression technologies in HRSs are based on mechanical compression. These include either reciprocating or diaphragm compressors, both of which despite being relatively mature technologies, have several drawbacks, most of which stem from the presence of moving parts. The most notable related issues are [4]

a) the high mechanical stresses which unavoidably lead to the need for lower speeds, which in turn leads to relatively low flow rates
b) high manufacturing and maintenance costs
c) high noise and vibration
d) potential diaphragm rupture [5]

We are thus lead to the conclusion that there exists the need for identifying and developing different solutions for hydrogen compression, which will tackle all the above issues in an efficient way. The most promising alternatives for hydrogen compressors include ionic liquid, metal hydride and electrochemical compressors, all of which will be discussed in the following paragraphs.

The compressor technology used in this case is the Metal Hydride compressors (MHC). MHCs base their operation on the property of metal hydrides of absorbing/desorbing hydrogen depending on their temperature, thus they are classified as thermal compressors. Compression is achieved by a reversible heat-driven interaction of a hydride forming metal or alloy or intermetallic compound with hydrogen to form MH. Since their operation is based on thermal

Fig. 3. Electrolysis Stacks

Fig. 4. Hydrogen storage tanks

processes, they could potentially utilize waste heat and/or excess renewable energy (e.g. solar thermal) for the required heating and cooling of the MH tanks, which reduces significantly their operational cost and increases the overall efficiency of the system [6].

Metal hydrides which are used in such compressors are special alloys like AB5-type (example, (La-Ce)(Ni-$Al)_5$) or AB2-type (for example, (Ti-Zr)(Mn-Cr-Fe-Co-$V)_2$) which can chemically store hydrogen in their metallic lattice [7]. Notable advantages of MH compression include their simple design and operation, the absence of moving parts which results in little to noise during operation, as well as their compactness and reliability. Since this specific compression method is used for the purposes of the project, details on its integration will be discussed in the following paragraphs. The compressor used in this installation (Figure 5) is comprised of 6 stages and can reach pressures of up to 220 bar, while having as input hydrogen from the electrolysis at 16 bar which can be reduced to the desired input pressure by a pressure regulator. The heating and cooling medium of the compressor stages is water which flows concentrically to the metal hydride bed, through an outer jacket and an inner helical coil. The operation of the compressor can be divided in two phases which are differentiated by the stages of the compressor which are being heated and cooled. So for example, during phase A stages 1, 3 and 5 are cooled, while 2, 4 and 6 are heated.

During phase A, since stage 1 is being cooled, it is therefore adsorbing hydrogen from the buffer tank for the pre-specified time period and at the pre-specified pressure which is needed for the complete saturation of the MH. Once phase A is finished, phase B begins, meaning that the first stage is heated at a pre-specified temperature for as long as it takes for the complete desorption of the stored hydrogen while at the same time stage 2 is being cooled, absorbing in the process hydrogen leaving stage 1. What needs to be taken into account in the design of the compressor is that each stage's inlet pressure is the previous stage's outlet pressure, hinting at the desired characteristics of the MH which will be used. The same process is repeated until hydrogen leaves the sixth stage at the pressure of 200 bar and the steady state of the compressor begins.

As mentioned, the MH compressor achieves compression by providing hot and cold water to the appropriate stages during each phase, there is therefore a constant need for water of the desired temperatures. The matter of temperature is of great importance, since MH have a specific range of temperatures in which they operate optimally. In this case, the system utilizes a heat pump which simulates the waste heat flow from an industry or the hot water flow from a solar thermal/chiller unit. The sizing of the heating/cooling system is determined by the thermal needs of the MHC stages, which are calculated by taking into account the desired temperatures of the water inside the stages as well as the exothermic/endothermic nature of adsorption/desorption processes respectively. In order to estimate the mass flow of the heating/cooling medium, what should be taken into account is the mass of the MH and its reaction enthalpy, while also important are the heat capacity of the MH and of the hydride bed walls. Once all the above have been calculated for all stages of the MHC, one can estimate the required thermal energy which needs to be provided/ extracted to each stage. This can then be translated to mass flow for the heating/cooling medium leading to the optimal sizing of the hot and cold water tanks as well as of the required pumps for the medium circulation (Figure 6).

For the automation of the compression and of the station's function in general, the installation is monitored and controlled by a PLC unit. By monitoring the system's status constantly (temperatures and pressures of the complete gas network), the controller ensures the smooth operation of the installation at all

Fig. 5. Metal Hydride Compressor

Fig. 6. Hot and cold water tanks and pumps for the compressor operation

times. The automated function of the compressor is ensured by the control unit and an algorithm of successive phase transitions. The systems begins to operate only when the temperature transmitters inform the controller that the water temperature is in its pre-specified temperature. The controller then, basically switches on and off the appropriate valves which regulate the flow of water and when they are at the correct state (open or closed), it gives a signal to the pumps to start operating. The system then runs for the

pre-specified time and stops only to switch phases or in case of a detected abnormality, such as an overpressure, or the absence of the desired temperature.

2.5. Hydrogen Dispenser

After being compressed to 200 bar, the high pressure hydrogen is stored in the pressurized gas tanks which have been shown, where it is stored until a vehicle needs to be refilled. In this case, the dispenser is fitted to the vehicle's tank and the PLC initiates the refueling algorithm. Basically what happens is the comparison of the pressure inside the vehicles tank and the station's supply pressure. As long as the former is lower than the latter, hydrogen will flow to the vehicle's tank. Once the two are equal, the dispensing halts, and the dispenser is detached from the vehicle. In the process, the system has gathered data about the quantity of hydrogen which was dispensed, the time required as well as its hypothetical cost.

2.6 Gas Network

An integral part of the installation, one which ensures the automation of the system as well as its adequate monitoring at all times is the gas network (Figure 7). In Fig. 7 one can see the way hydrogen flows through the various components of the network. These include solenoid, hand and check valves, pressure and temperature transmitters and indicators, pressure regulators and a flow meter. Also there are numerous configurations for venting hydrogen to the atmosphere in order to increase the system's safety. The gas network can be divided to three parts, namely the low pressure and high pressure compartments and the dispensing compartment, which can be seen in fig x, at the bottom, upper and middle parts of the panel respectively. The low pressure compartment is responsible for monitoring the pressure of hydrogen which builds up in the low pressure tank, with the ultimate purpose of facilitating its input to the compressor, at the pressure set by the regulator. The same goes for the high pressure compartment, with the difference that it feeds the high pressure tanks. The dispensing compartment regulates the pressure of hydrogen leaving the high pressure storage and finally allows the filling of the vehicle that needs refueling, through an algorithm which opens and closes the right solenoid valves, as set by the controller. The whole process is documented by the flow meter, which transmits to the control panel the quantity of the hydrogen which was used.

2.7 System Integration

In order to determine whether the system can operate harmoniously, we need to identify potential bottlenecks or shortages. Mean hydrogen production rates have been already addressed and established as 127 grams per hour, while as seen in Diagram 1 the compressor has an output of roughly 100 grams per hour. Note that Diagram 1 shows the compressor output at 3 cycles in which the 6th and final stage is heated and 2 in which it is cooled, with the heating obviously occurring when the mass output increases. The mismatch between the two outputs seems to create a slight bottleneck, which is currently being addressed by experimenting with the compressor's temperature ranges in order to further increase its output. Regardless of that, this bottleneck doesn't seem to hinder the functionality of the system in practical use. The vehicles which are refueled in the station, have a total capacity of 161 grams in terms of wight, meaning that they can be refueled numerous times throughout the day, taking into consideration that they will not require refueling on an hourly basis. Thus it can be assumed that the station could potentially cover the needs of even more vehicles. Regardless of the vehicles which can be served in the installation in its present status, there is the ability of increasing its capacity with only minor changes. This is on the one hand due to the modularity of the electrolysis unit which can increase its output simply by adding more stacks and on the other hand due to the modular design of the compressor which can also increase its output by adding more stages in parallel with the existing ones.

One of the reasons that the installation can have such a smooth function lies in the nature of hydrogen as an energy storage medium. It is obvious that the fluctuations in the electrolysis operation which are due to the fluctuations of the solar irradiance can be

Fig. 7. Hydrogen Dispenser

Fig. 7. Gaseous Network Panel. Top to bottom: High pressure panel, Dispensing panel, Low Pressure panel

counterbalanced by the hydrogen which is already produced and stored during peak hours of solar irradiance. The fact that there is constantly a quantity of hydrogen stored both in the low pressure and high pressure tanks ensures the operation of the system even in times when the electrolysis does not operate, thus gives the ability of refueling vehicles throughout the day.

3 Conclusions

The work presented in the previous paragraphs focuses on showcasing the basic aspects of operation of a hydrogen refueling station which makes use of a metal hydride compressor. An important aspect for the system's smooth operation is the matching of the electrolysis and the compressor's flow rates, since it is vital for identifying potential hydrogen bottlenecks or shortages. The installation's hydrogen producing unit is a 4kW PEM electrolysis which was shown to be able to meet the load of 2 scooters and a golf cart on a daily basis. The system proved to be completely automated in terms of hydrogen production and compression, while the only part which needs a human presence is the refueling of the vehicles. Finally the modularity of the system which is based on the modular design of the electrolysis and the compressor leads to the conclusion that a larger number of vehicles could potentially be served in an installation similar to this, with only minor changes on the core infrastructure of the installation.

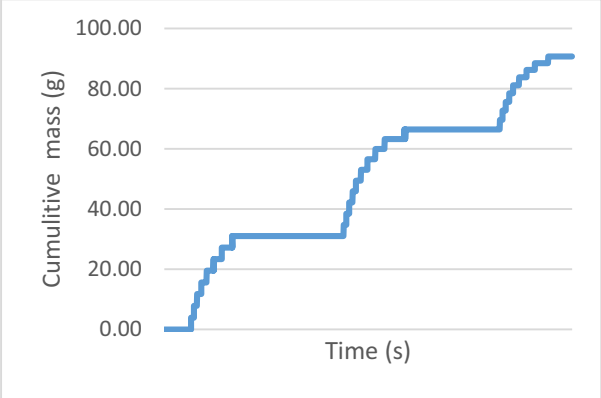

Diagram 1. Compressor mass output

Acknowledgments

This work is co-financed by the European Regional Development Fund of the EU and Greek national funds under the call RESEARCH – CREATE – INNOVATE (project H2TRANS_T1EDK-05294).

4 References

[1] D.L. Greene, J. M. Ogden Z. Lin: "Challenges in the designing, planning and deployment of hydrogen refueling infrastructure for fuel cell electric vehicles", eTransportation, **6,** 100086, (2020)

[2] P. Nikolaidis, A. Poullikkas: "A Comparative Overview of Hydrogen Production Processes", Renewable Energy and Sustainable energy reviews, **67,** 597-611 (2017)

[3] Andreas Züttel: "Materials for hydrogen storage", Materials Today,**6** (9), 24-33(2003)

[4] Almasi, A.: Reciprocating compressor optimum design and manufacturing with respect to performance, reliability and cost. World Acad. Sci. Eng. Technol. **52**, 48–53 (2009)

[5] Jiahao, C., Xiaohan, J., Chuang, et al.: Design and validation of new cavity profiles for diaphragm stress reduction in a diaphragm compressor. IOP Conf. Ser. Mater. Sci. Eng. (2015)

[6] F. Laurencelle, Z. Dehouche, J. Goyette, T.K. Bose, "Integrated electrolyser - metal hydride compression system", Int J. Hydrogen Energy **31**, 762-768, 2006.

[7] Bossel U., *"Does a Hydrogen Economy Make Sense?", Proceeding of the IEEE, 2006*.

Digital Twin of Fuel Cell Hybrid Electric Vehicle: a detailed modelling approach of the hydrogen powertrain and the auxiliary systems

Lorenzo Bartolucci[1], *Edoardo* Cennamo[1,*], *Stefano* Cordiner[1], *Vincenzo* Mulone[1] and *Ferdinando* Pasqualini[1]
Marco Aimo Boot[2]

[1] University of Rome Tor Vergata, Department of Industrial Engineering, via del Politecnico 1, 00133, Rome, Italy.
[2] Iveco Group, Electrification Technologies.

Abstract. The transport sector is today a major source of pollutant and greenhouse gas emissions. Fuel Cell Hybrid Electric Vehicles are a solution to reduce its environmental impact, thanks to the zero pollutant tailpipe emissions and longer driving ranges if compared with full electric vehicles. A Digital Twin of a FCHEV is developed in this study, through the assessment of models of mechanical and thermal systems within the vehicle. The Simulink/Simscape model here presented is able to support both the design choices and the test of control strategies. The results obtained allow characterizing the impact of the auxiliary systems on the driving range, whose relative value ranges from 28% to 40% of the overall energy demand depending on the ambient temperature, and the range is between 430 km and 356 km respectively for mild and cold temperature.

1 Introduction

Nowadays, sustainability is one of the key concepts driving the research activities on vehicles towards solutions capable of facing with global challenges, such as the limited availability of fossil primary energy sources, the global warming or the environmental pollution.

In the last decades, UE has promoted several initiatives to achieve the target of net-zero Greenhouse Gases (GHG) emissions (whose limit is 2050), to keep the global temperature increase below 2°C above pre-industrial levels [1],[2],[3]. In agreement with the aforementioned restrictions, automotive companies are acting to replace the conventional internal combustion engines with innovative powertrain systems fueled with cleaner energy sources (i.e. Battery Electric Vehicles BEVs and Fuel Cell Hybrid Electric Vehicles FCHEVs [4]).

PEM fuel cells, the mainstream technology for the utilization of hydrogen in the transport sector, are attractive for such applications due to the following advantages: high efficiency and durability, low noise, no tailpipe emissions other than water, and short refueling time [5],[6],[7] [8]. Applying such systems in a vehicle, often requires a battery pack, according then to a hybrid architecture, to exploit fully the potential advantages of coupled battery packs and PEM fuel cells stacks.

Numerous studies have been carried out on FCHEVs critical issues, such as the fuel cell integration and sizing, the drivetrain design, the battery pack design, the fuel storage system design, and the implementation of control strategies and component downsizing in general [7],[9].

For such purposes, design and control of components into more complicated systems, Digital Twins (DTs) of physical systems are an important tool, since experimental tests usually require high costs and longer development timings.

In many papers available in the literature, studies reported about the use of computational models to represent the behavior of single components into a hybrid fuel cell powertrain system. Wang et al. [10] proposed a Digital Twin of a PEMFC starting from a 3D model whose results were used to train a machine learning simpler model. Similarly, authors in [11] implemented a data-driven DT for the prediction of fuel cell Remaining Useful Life (RUL).

In other papers, the attention was focused on Energy Management Systems (EMSs), proposing different control strategies to manage the power splitting between the different energy sources (FC, batteries and ultra-capacitors). Simplified models have been adopted to study optimal control strategies for different purposes, including the maximization of efficiency or system downsizing. More in general, control strategies in the literature fall into different classes, such as rule-based strategies [12],[13], model predictive control (MPC) strategies [14],[15] and other categories.

In this study, a Digital Twin of a whole FCHEV, including powertrain and auxiliary system, is proposed to represent its actual behavior according to a driving cycle. All the important sub-systems to characterize the vehicle from the energy standpoint are considered, including the battery pack, the fuel cell stack, the thermal system, the hydrogen and air supply systems, and the HVAC system. In this paper the model is applied to discuss a fuel cell range extender control strategy based on rules defined similarly to the paper by Fernández et al. [16] [17].

Based on the above-mentioned papers, this paper aims at proposing a complete FCHEV digital twin - developed in the Matlab/Simulink/Simscape framework - with the aim of filling the following literature gaps:

- Highlighting the influence of auxiliary systems on the vehicle performance.

* Corresponding author: edoardo.cennamo@alumni.uniroma2.eu

- Highlighting the importance of a complete vehicle digital twin to elaborate power splitting strategies.
- Introducing a virtual platform for testing and designing sustainable FCHEVs.

The article has the following structure. Section 2 presents a description of the Digital Twin representing a FCHEV; numerical results and related discussion are reported in Section 3 and finally Section 4 highlights the main conclusions and future perspectives.

2 Modelling approach

The basic layout of the considered fuel cell hybrid electric vehicle (light-medium duty commercial vehicle) is shown in Fig. 1. The powertrain includes a 130 kW electric motor supplied by two energy sources: the primary one is a 104 Ah battery pack, whose rated voltage is 350 V, and a secondary energy source based on a 99 kW rated power PEM fuel cell. In particular, a parallel layout between the FC and the batteries is chosen and a DC-DC converter is used to connect the FC to the DC-bus.

The hybrid powertrain is linked to the "Vehicle dynamics" block to represent the mechanical and dynamic behavior of the vehicle (i.e. body, tires, brake system and drive axles) and the "Drive cycle data" block used to model the driver, through a PI controller receiving the speed error and converting it into a torque request signal.

As temperature is one of the main parameters determining the components behavior, thermal capacity and heat transfer effects are represented with detail into a thermal system model. The thermal system includes a radiator, a circulating pump, pipes, by-pass valves, and a fan to control the air flow to the radiator. A chiller is also considered to control the temperature of batteries, characterized by strict requirements. The HVAC (Heating, Ventilation and Air Conditioning) system is also modeled to satisfy the comfort requirements of the cabin.

The hydrogen supply system is represented with a tank, pipes and pressure regulators for pressure control purposes at the stack, including the purge feature. Air supply system and power electronics sub-systems are also represented with simplified sub-models taking into account efficiency, toward the calculation of thermal losses and electric power absorption.

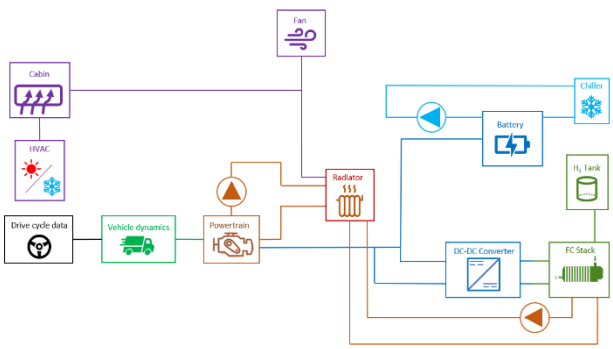

Fig. 1 FCHEV layout scheme.

2.1. PEM Fuel cell

The technical specifications of the Fuel Cell System (FCS) considered in the FCHEV Digital Twin are listed in Table 1.

Table 1. Fuel Cell system specifications [18].

Rated Electrical Power	*99 kW*
Operating Current	*0 to 500 A*
Operating Voltage	*180 to 360 V*
Peak Efficiency	*55 %*
Coolant	*Ethylene glycol and water mixture*
Operating temperature	*67°C*
Dimensions L x W x H	*955 x 1525 x 345 mm*
Mass	*327 kg*
Volume	*502 l*

Fig. 2 shows voltage, net power and efficiency of the FCS as a function of the net current.

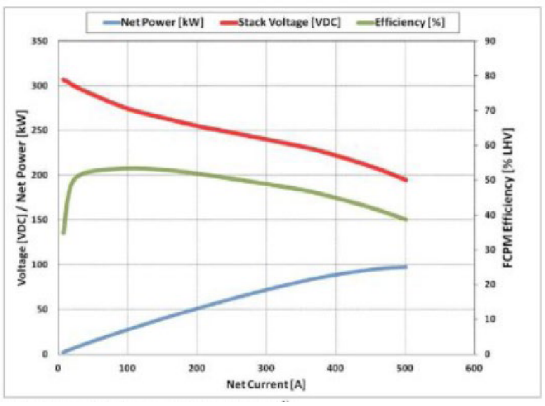

Fig. 2 FCS Datasheet performance[18].

Considering the fuel cell efficiency, the heat losses are defined by the following equation [8]

$$Q_{gen} = P_{tot}\left(\frac{1}{\eta_{stack}} - 1\right). \quad (1)$$

The layout of the FCS cooling systems is provided in Fig. 3. The required coolant flow rate is provided by a variable speed centrifugal pump, feedback controlled to target the coolant temperature value at the stack inlet. The heat power disposed from the FC is dissipated with an air-cooled radiator. The air mass flow rate is supplied by fans mounted in the front section of the radiator. A three-way valve allows the control of coolant flow splitting beetween radiator and by-pass, to manage the transient period.

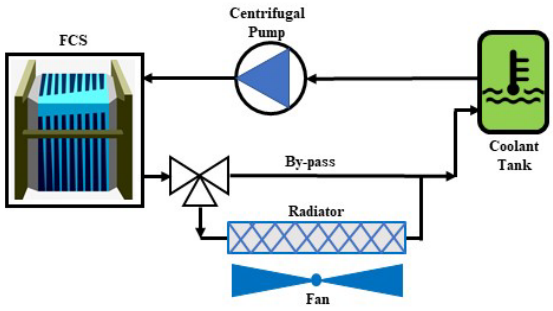

Fig. 3 FCS layout cooling system.

The Fuel Cell System is controlled to work at the optimum temperature as specified by manufacturer to maximize the conversion efficiency. The functional dependence of efficiency and power output on temperature and current is shown in Fig. 4 and Fig. 5. Moreover, a pre-heating feature is considered at cold start to further increase the hydrogen conversion efficiency.

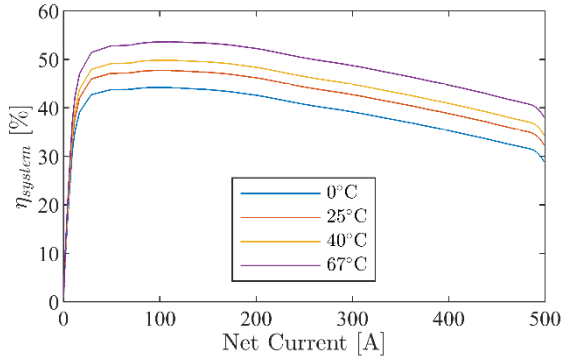

Fig. 4 System Efficiency vs Stack Temperature.

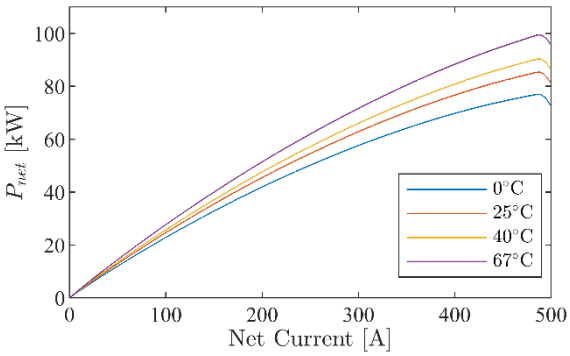

Fig. 5 Net Power vs Stack temperature.

3 Results and discussion

The analysis of results is divided into two sections. In the first one, results of a standard case are reported and commented to highlight the features of the vehicle model. In the second one, two case studies are presented, to show the differences in terms of range and auxiliary system power absorption characteristics, affecting the vehicle performances depending on:

- Ambinet temperature (winter, summer, standard case).
- Battery capacity, considering two battery packs in parallel .

3.1 Standard case

In this study the standard driving cycle WLTP is used as input datum. The cycle considers an aggregation of different driving conditions (from urban to extra-urban in terms of speed and acceleration ranges) with a total distance covered of 23 km and a duration of 30 min (1800s). The simulations are carried out according to a sequence of the WLTP until the hydrogen contained in the two 700 bar pressurized hydrogen tanks are discharged and the battery SOC is back to the starting value.

A range extender rule-based strategy has been selected to control the power splitting between the FC system and the battery. The control strategy is based on the battery SOC monitoring, with an upper and a lower bound values set *a priori*, determining the conditions to start the operation of the FC system. Whenever the upper bound is reached, the operating conditions are set as "discharge phase", according to which batteries operate as the exclusive energy source and fuel cell stops operating. In Fig. 6 the SOC profile for the *Standard case* ($T_{amb} = 25°C$) simulation is shown: SOC_{min} and SOC_{max} are set to 45% and 70% respectively.

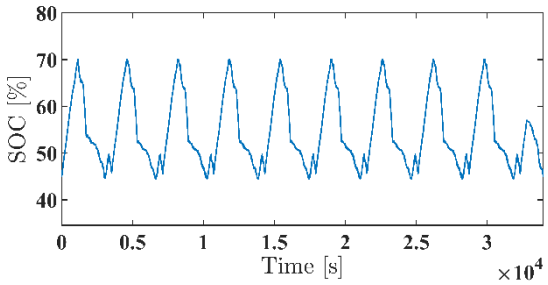

Fig. 6 Battery State Of Charge.

During the "recharge phase", the DC-DC converter is controlled by its output current, set to a constant value, meaning that the power output, as well as the input given by the fuel cell system, is not constant due to a voltage variation.

The powertrain control strategy in terms of SOC bound values and recharge current supplied by the FC system is important as the recharge efficiency of a battery is not ideal, and charging efficiency depends on the Depth of Discharge (DOD) and recharge current set-point. To avoid excessive efficiency drops , a rather strict lower bound of the SOC value (at a DOD of 35%) with a constant recharge current set to 104 A ($1C$ rate) is implemented. The latter represents an upper bound, since during operating conditions if the traction motor requests power, the net current at the battery is decreased. The value of 104 A is also chosen according to a conservative approach, to not affect the battery state of health, avoiding degradation due to high load cycling.

Fig. 7 presents the profile of the system efficiency and stack efficiency over a full simulation test.

In Fig. 8 and Fig. 9 a detail of system as well as stack efficiencies and FC temperature are shown respectevely. It is worth noting that during the warm-up, efficiencies are lower than the rated values. Again in Fig. 9 it can be observed that the FC cooling system control operates in order to maintain the temperature at the set point value (the plateau in the figure).
During the discharge phase, the FC temperature partially cools down, keeping values closer to the design ones, and enabling a faster warm-up during the following charging phase (Fig. 10).

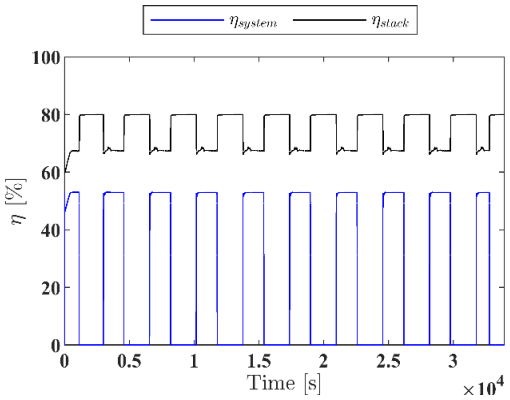

Fig. 7 System efficiency vs stack efficiency.

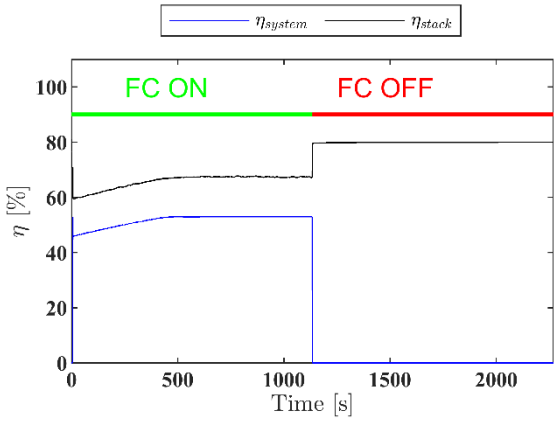

Fig. 8 Detail of System and Stack efficiencies - start up.

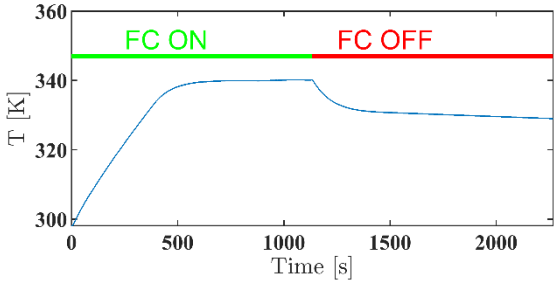

Fig. 9 Detail of FC temperature – start up.

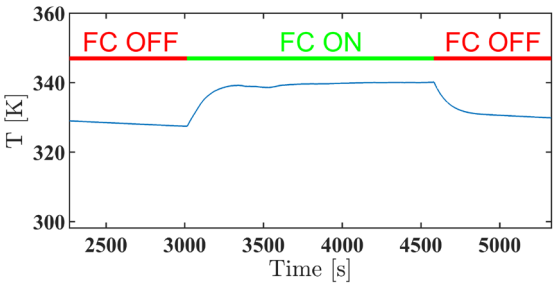

Fig. 10 Detail of FC temperature - steady state.

A detail of the power absorbed by the Fuel Cell internal auxiliaries over a single charge phase is reported in Fig. 11.

An almost constant auxiliaries request of about 10 kW is observed over the whole FC operating time and the Fuel cell System efficiency is maintained in the maximum efficiency range, as already commented for Fig. 2.

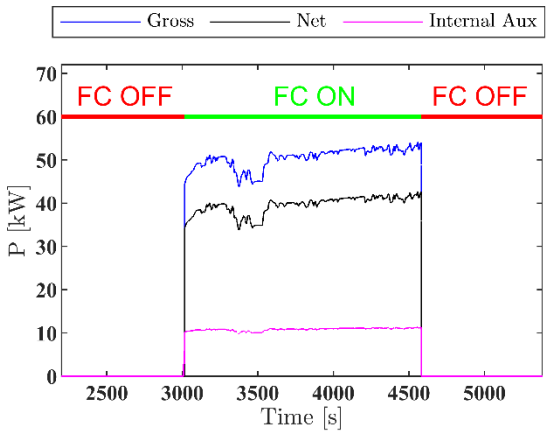

Fig. 11 Detail of Fuel cell power distribution.

As mentioned for the FC system, temperature control is also mandatory for the correct operation of other vehicle sub-systems, such as the battery packs and the electric motor. On the one hand, it affects the behavior of the components (degradation, useful life), and on the other hand, its management results into an additional power demand which must be supplied by vehicle energy sources. Fig. 12 shows the battery pack temperature during the whole simulation: the peaks of temperature over 40°C (but always below 45 °C) correspond to the last stretch of the WLTP, the extra-urban sub-cycle, which requires a greater traction power.

An important observation concerns the control logic of the chiller, since it is used for both the HVAC and the battery cooling system. The refrigerant gas flow rate is split depending on the temperature of the battery according to the following strategy:

- If $T_{battey} < 35°C$ HVAC gets the entire refrigerant flow rate.
- If $35°C < T_{battey} < 40°C$ the coolant flow rate is split between HVAC and battery cooling system.
- If $T_{battey} > 40°C$ the battery cooling system has priority in terms of refrigerant flow rate.

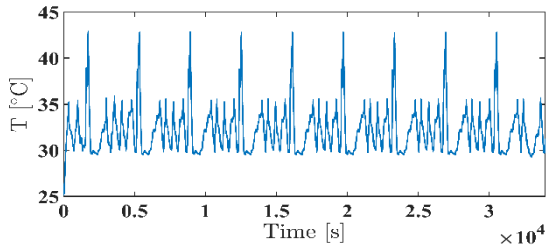

Fig. 12 Battery Packs Temperature.

Fig. 13 describes the energy fluxes distribution among the different components and the split between the auxiliary loads. It can be observed that the total energy requested by all the vehicle auxiliaries (not considering the FC internal Balance of Plant) is approximately 6.5% of the entire energy demand. The FC auxiliaries have also a great influence on the overall energy consumption, assessing their share at around 21.6% of the total demand. A significant amount of energy is also lost during the charing/discharging processes from the battery (about 6.8%). Overall, the traction accounts for 65.1% of the total energy consumption highlighting the significant impact of the other components in the global Balance of Plant (BoP) of the vehicle. Among all the auxiliaries, the most demanding are the chiller, the FC cooling system, and the motor fan, all involved in the thermal management of the vehicle system components.

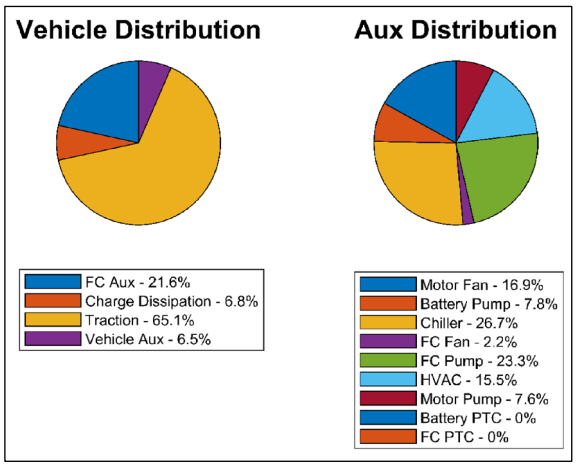

Fig. 13 Vehicle energy distribution - $T_{amb} = 25°C$.

3.2 Case study: Environmental Temperature influence

In order to highlight the influence of the ambient temperature on the vehicle performance and on the distribution of energy demand among auxiliaries, three different operating conditions are tested, and specifically the external air temperature has been set to $25°C$ (*Standard case*, equal to the previous one), $40°C$ (*Summer case*) and $0°C$ (*Winter case*).

Fig. 14 shows the results for the *summer case*. As expected, due to the increased power needed to cool the cabin, the portion of energy requested by vehicle auxiliaries is greater than *standard case* (7.9% of the overall energy demand against 6.5%).

A similar behavior, even more evident, is obtained for the *Winter case*, shown in Fig. 15. In fact, the lower ambient temperature leads to the required use of the PTCs for the battery and the FC system warming-up, as well as the cabin requests greater power ($\Delta T = 25°C$ respect to $\Delta T = 15°C$ for *summer case*) to maintain the set-point temperature. So, vehicle auxiliaries reach a overall impact of 18.6% on the overall energy demand.

The performance parameters commented are summarized in Table 2 by the variation of "Vehicle Aux" percentage between the three cases, and the consequent change in the estimated vehicle range considering the same amount of hydrogen available.

Table 2 Season results comparison.

	T_{amb} [°C]	$E_{Aux,\ Total}$ [%]	Range [km]
Winter	0	18.6	355.76
Standard	25	6.5	429.55
Summer	40	7.9	422.38

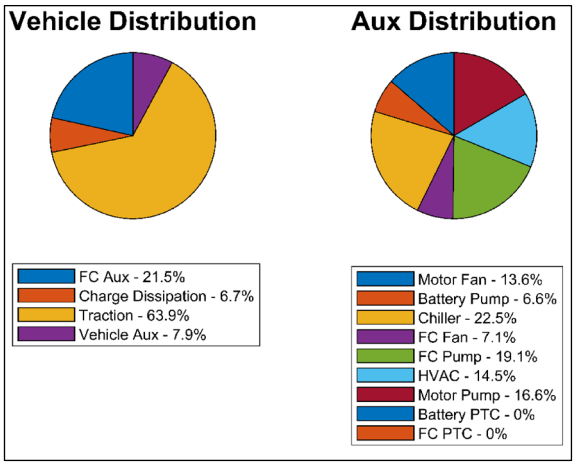

Fig. 14 Vehicle energy distribution - $T_{amb} = 40°C$.

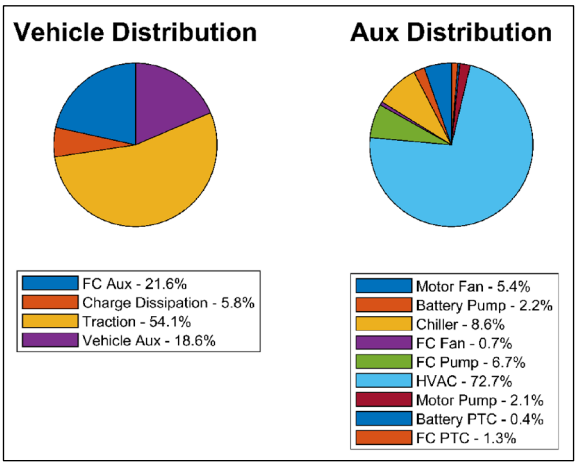

Fig. 15 Vehicle energy distribution - $T_{amb} = 0°C$.

3.3 Case study: Battery Oversizing

The model developed can be used also for the test of different vehicle configurations. In this section, starting from the single battery pack of the original vehicle, the

possibility of increasing the battery capacity by using two of the 104 Ah modules in parallel is tested to evaluate the impact on the vehicle range. The standard case is chosen to test the increased battery size. The recharge current is kept at 104 A, therefore halvening the C-Rate with respect to the reference case. Then , heat losses are reduced. Fig.16 shows the total energy distribution obtained for the new configuration. As expected, the fraction of energy required to run vehicle auxiliaries is smaller, due to a relevant reduction of the chiller energy consumption during the whole simulation, leading to an increase of the estimated range from 429.5 km to 447.3 km.

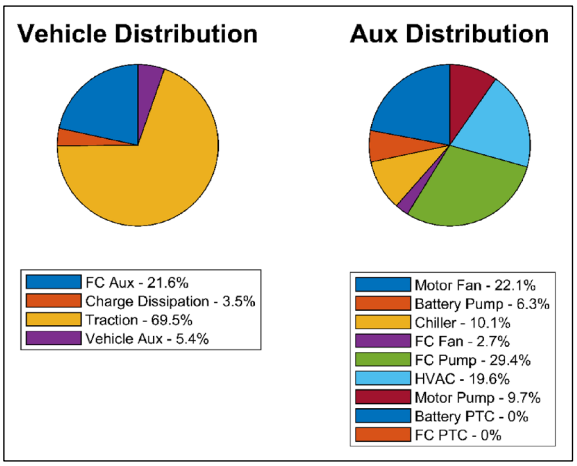

Fig. 16 Vehicle energy distribution – $T_{amb} = 25°C$ – 208Ah.

The lower internal heat generation of the 208 Ah battery pack leads to a lower mean operating temperature. In fact, the temperature peaks during the extra-urban discharge phases are avoided, as shown in Fig. 17.

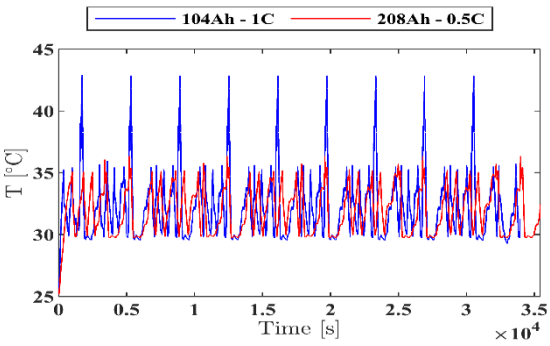

Fig. 17 Battery temperature comparison – 208/104 Ah.

It is also worth noting that comparing "charge losses" between the two cases (Fig. 13 and Fig. 16), this parameter is nearly halved in the oversized case, as evidence of the fact that the battery charge efficiency is indirectly proportional to the charging load (leaving DOD unchanged): reducing the C-rate (104 A of recharge current represents a 0.5C load with respect to the previous 1C), the recharge efficiency is increased.

4 Conclusions

In this paper, a Digital Twin of a Fuel Cell Hybrid Electric Vehicle is proposed to analyze thoroughly the physical behavior of the mechanical and thermal systems. In particular, detailed modeling of the vehicle auxiliaries has been implemented, taking into account the HVAC, the cooling systems for the main components, and adding a chiller for a better management of the battery temperature, and fuel cell stack auxiliaries.

The vehicle computational model is able to:

- Support design development,
- Analyze the performance parameters of the vehicle.
- Test different Energy Management System control strategies.

A case study, according to which the ambient temperature is set to 0°C (*winter case*), 25°C (*standard case*), and 40°C (*summer case*), has been carried out to show the potential of the digital twin and to highlight the impact of the auxiliary system energy consumption may have on such hybrid vehicles.

The major findings of the work can be summarized according to the following points:

- The thermal management of system components and FC auxiliaries have a great impact on the overall energy consumption (with a relative impact ranging from almost 28% for the standard case up to more than 40% for the winter case).
- The external air temperature has a noteworthy influence on the vehicle range that varies from about 430 km in the standard case down to 356 km for the winter case.
- Among the auxiliaries, chiller, HVAC, FC cooling pump, and motor Fan are the most demanding.
- Doubling the battery pack of the vehicle can lead to significant improvement in terms of battery efficiency and thermal management, having positive impact also on the vehicle range. Economic consideration must be introduced to evaluate the actual convenience of increasing the storage capacity with respect to the benefits illustrated.

References

1. C. D. (EU), in (2016), pp. 6–8
2. J. Enzmann and M. Ringel, (2020)
3. K. Kuklinska, L. Wolska, and J. Namiesnik, Atmos. Pollut. Res. **6**, 129 (2015)
4. G. Morrison, J. Stevens, and F. Joseck, Transp. Res. Part C Emerg. Technol. **87**, 183 (2018)
5. P. Ferreira-aparicio, J. J. Conde, and A. M. Chaparro, *2 - Fundamentals and Components of Portable Hydrogen Fuel-Cell Systems* (Elsevier Inc., 2018)
6. M. Muthukumar, N. Rengarajan, B. Velliyangiri, M. A. Omprakas, C. B. Rohit, and U. K. Raja, Mater. Today Proc. **45**, 1181 (2021)

7. A. G. Olabi, T. Wilberforce, and M. Ali, **214**, (2021)
8. P. T. Moseley, *Fuel Cell Systems Explained* (2001)
9. M. Ogburn, D. J. Nelson, W. Luttrell, B. King, S. Postle, and R. Fahrenkrog, SAE Tech. Pap. **2000**, (2000)
10. B. Wang, G. Zhang, H. Wang, J. Xuan, and K. Jiao, Energy AI **1**, 100004 (2020)
11. S. Meraghni, L. S. Terrissa, M. Yue, J. Ma, S. Jemei, and N. Zerhouni, Int. J. Hydrogen Energy **46**, 2555 (2021)
12. T. C. Do, H. V. A. Truong, H. V. Dao, C. M. Ho, X. D. To, T. D. Dang, and K. K. Ahn, Energies **12**, (2019)
13. S. Changizian, P. Ahmadi, M. Raeesi, and N. Javani, Int. J. Hydrogen Energy **45**, 35180 (2020)
14. Y. Zhou, H. Li, A. Ravey, and M. C. Péra, J. Power Sources **451**, (2020)
15. Y. Zhou, A. Ravey, and M. C. Péra, Energy Convers. Manag. **229**, (2021)
16. R. Á. Fernández, F. B. Cilleruelo, and I. V. Martínez, Int. J. Hydrogen Energy **41**, 4808 (2016)
17. R. Álvarez Fernández, S. Corbera Caraballo, F. Beltrán Cilleruelo, and J. A. Lozano, Renew. Sustain. Energy Rev. **81**, 655 (2018)
18. https://pdf.directindustry.it/pdf-en/hydrogenics/hypm-hd-90/33492-420317.html, (n.d.)

Investigation of gas purging and cold storage impact on PEM fuel cell system performance for aeronautical applications

Gema Montaner Ríos[1,*], *Florian* Becker[1], *Anna* Vorndran[1], *Christoph* Gentner[1] and *Syed Asif* Ansar[2]

[1]German Aerospace Center (DLR), Institute of Engineering Thermodynamics, Hein-Saß-Weg 22, 21129, Hamburg (Germany)
[2]German Aerospace Center (DLR), Institute of Engineering Thermodynamics, Pfaffenwaldring 38-40, 70569, Stuttgart (Germany)

Abstract. Durability of proton exchange membrane fuel cell systems under cold weather conditions is essential and a critical challenge for transportation applications. During cold storage the water remaining in the cells can freeze causing damage to the cell components. In order to avoid this degradation, fuel cells are commonly purged with dried gases during shutdown prior to its storage at subzero temperatures. This work investigates cold storage of PEMFC systems at temperatures down to -40°C with the aim of developing a shutdown procedure that leads to minimal degradation due to cold storage, while meets energy efficient and time requirements of aeronautical applications. To that end, several experiments were carried out with two different stacks (a 4 kW liquid cooled and a 100 W air cooled) under a wide range of operating parameters: cathode gas, purge temperature, anode and cathode gas purge flow rates, purge time and cold storage temperature. The fuel cell performance degradation due to ice formation was measured by the polarization curves conducted prior and after every F/T cycle. The effects of these operating parameters on the durability of the PEMFC systems under cold storage are evaluated. The obtained experimental results showed that very long purge process lead to further performance degradation at -10°C than shorter process at -40°C, which indicates that eliminating all remained water in the cells is not only inefficient, but also lead to degradation due to the drying process. Moreover, guidelines to improve shutdown procedure for cold storage of proton exchange membrane fuel cell systems for aeronautical applications are discussed.

1 Introduction

Aviation represents around 2.5% of CO_2 global emissions and 3.5% of global warming per year [1, 2]. To move away from fossil fuel combustion to a clean aviation necessary entails the use of more environmentally sustainable technologies. Over the last years, several zero-emission energy sources and technologies have been studied and developed. Among all, the use of hydrogen is extremely promising due to its higher specific energy compared to kerosene, ammonia and batteries [3]. PEMFC systems are gaining interest for the on-board generation of electrical power on aircrafts because of its higher efficiency, less weight and lower noise.

Nevertheless, fuel cells exhibit limitations for aircraft applications which need to be overcome, such as their safe use in winter scenarios. Under sub-zero temperatures, the remaining water in the cells will freeze after shut-down causing several damages to the cell components [4]. Therefore, ensuring the durability of fuel cell systems at extremely low temperatures is essential for their deployment in aircraft applications, especially for cold operators.

As it is known from the literature no fuel cell material was damaged because of freezing temperatures down to -40°C, if there were no contact with liquid water [4]. Therefore, and in order to avoid degradation due to ice formation during cold storage, the stack is commonly purged with dry gases during the shut-down. However, most of the previous experimental studies about gas purging method and cold storage were carried out on single cells and at not extremely low temperatures, whereas previous numerical models didn't focus on degradation [4-8]. Thus, further investigation about the effect of purging and cold storage on the stack performance degradation at temperatures lower than -20°C is needed.

In this investigation, we experimentally study the impact of the gas purging shut-down procedure and the cold storage on the PEM fuel cell system performance with two different stacks (a 4 kW liquid-cooled and a 100 W air-cooled) at temperatures down to -40°C. These results should assist to define an optimal shut-down procedure based on gas purging for aeronautical applications at extreme winter conditions.

2 Experimental

2.1 Test bench

This investigation was carried out with two different stacks: a 4 kW Hydrogenics (40 cells, 200 cm² of active cell area, graphite bipolar plates and liquid-cooled) and a 100 W from ZBT GmbH (5 cells, 20 cm² of active cell area, graphite bipolar plates and air-cooled). Therefore, two test benches, one for each kind of stack, were used. Details of the 4 kW stack test bench were presented by

*Corresponding author: Gema.MontanerRios@dlr.de

Montaner Ríos et al., and hence not repeated here [9]. The test bench used with the 100 W stack was developed in-house and is presented in Figure 1. The stack is fed with compressed air the cathode and with H_2 the anode, whose mass flow rates are regulated: the cathode by two mass flow controllers (MFC) of 10 nl/min maximal flow rate, and the anode by one MFC of same maximal flow rate. Both gases go through a humidifier before entering into the stack. The relative humidity of cathode inlet is regulated with a humidity control valve. The anode has a hydrogen recirculation loop by a recirculation pump to reuse the residual hydrogen and for humidification, and a valve purge to regulate the pressure at anode side as well as to remove accumulated water. A blower it is used for cooling down the stack. Cell voltages are measured with the cell voltage monitoring system (CVMS) and cell temperatures with the cell temperature monitoring system (CTMS), which consists of six thermocouples connected to the six bipolar plates of the five cells. Relative humidity (RH) of cathode inlet and outlet are measured with two relative humidity sensors, which produces reliable values at RH < 90%. A load with a maximal power of 45 W is connected to the PEMFC. The control of system components and auxiliaries, such as: blower speed, cathode relative humidity and mass flow rates are performed through a software developed in-house in LAbVIEW. For the stack cold storage was used a TT-60-375 U //logg FRYKA climate room of (150 cm x 50 cm x 50 cm), which can freeze up to -45°C.

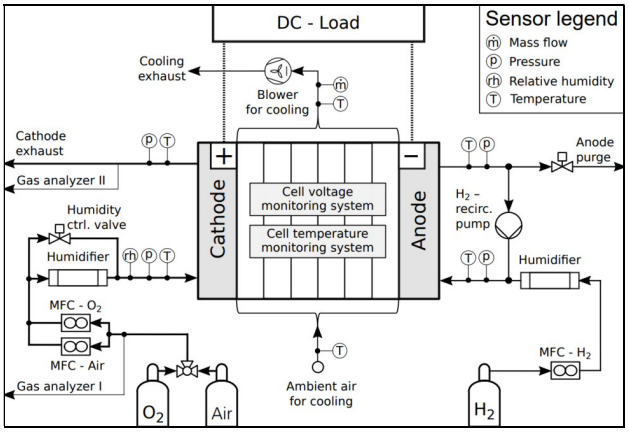

Fig. 1. PID of 100 W PEMFC system test bench.

2.2 Gas purging operating parameters

This work studied experimentally the influence of the gas purging operating parameters on the PEMFC system performance after cold storage, first with a 4 kW stack at temperatures down to -20°C, and next with a 100 W stack at temperatures down to -40°C. The selected parameters investigated with both stacks are given in Table 1. Additionally, F/T tests conducted with the 100 W stack at different purge times and cold storage temperatures are listed in Table 2.

2.3 Test protocol

Two experimental protocols were used in this investigation, a different one for every kind of stack. However, both protocols consist of six main steps: conditioning, polarisation curve, gas purging procedure, cold storage, start-up and polarisation curve again. The major difference between both protocols is that with the 4 kW stack was carried out a cold start-up, while the start-up with the 100 W stack was carried out at room temperature. Furthermore, with the 100 W stack were carried out two polarisation curves after the cold storage. Following, both experimental protocols are briefly described.

2.3.1 Test protocol used with the 4 kW stack

- Conditioning test at room temperature with dry gases, but with humidification through H_2 recirculation loop.
- Polarisation curve was carried out at room temperature with dry gases, but with humidification through H_2 recirculation loop, to get some reference points before freezing temperatures and to guarantee the same relative humidity level before purge procedure.
- Purge procedure. Stack purged with dry gases (at the cathode N_2, air or synthetic air, and at the anode H_2) to remove the remaining water before cold storage.
- Cold storage. The stack was further cooled down to the testing temperature and kept for 4 h.

Table 1. Operating parameters.

Parameter	Value with the 4 kW stack	Value with the 100 W stack
Cathode purge gas	N_2, air, synthetic air	Air
Anode purge gas	H_2	H_2
Purge temperature (°C)	15, 40, 50	25
Cathode purge flow rate (nl/min)	400	5, 10, 20
Anode purge flow rate (nl/min)	30	0.375, 0.75, 1.5
Purge time (s)	180	0, 45, 90, 300, 600, 1200, 3600, 8400, 12000, 14000
Cold storage temperature (°C)	-20	-10, -20, -40
Cold storage time (h)	4	12
Start-up temperature (°C)	-20	25

Table 2. F/T tests conducted with the 100 W stack.

Test number (procedure)	1	2	3 (A)	4 (B)	5 (C)	6 (D)	7 (E)	8 (F)	9 (G)
Cold storage temperature (°C)	-10	-20	-40	-40	-40	-40	-40	-40	-40
Purge time (s)	3600	3600	3600	1200	600	300	90	45	0

- Cold start PEMFC. In order to get a quick cold start, stack was run on potentiostatic mode and with a small cooling loop to warm it up quickly.
- Polarisation curve was repeated to get same reference points, thus measuring the performance degradation due to the freezing temperatures.

2.3.2 Test protocol used with the 100 W stack

- Conditioning test at room temperature with wet gases.
- Polarisation curve at room temperature with wet gases.
- Purge procedure. Stack was purged with dry gases (at the cathode air and at the anode H_2). For that, humidifier is set to a relative humidity of 0%. During the purge procedure, the cathode outlet RH sensor was plugged into the system, when the cathode inlet RH was 10%, to avoid that remaining water in the cathode outlet could condense at the top of the RH sensor, thus falsifying the test results.
- Cold storage. The stack was stored in the climate room to the testing temperature and kept there for 12 h.
- Polarisation curve was carried out at room temperature and with wet gases to measure the performance degradation due to the freezing temperatures.
- Conditioning test at room temperature with wet gases. Since the conditioning test is a procedure that can overcome reversible degradation, this test was repeated before carrying out other polarization curve, to prove which performance degradation due to the cold storage was reversible.
- Polarisation curve at room temperature with wet gases.

3 Results

3.1 Cold storage with the 4 kW stack

This investigation is partly based on prior studies of the purge time influence on the cold start of this 4 kW stack [10, 11]. Experimental results showed that the optimal purge time for slow cold starts was an intermediate value, so that membranes can absorb large amounts of water instead of freezing in the cathode catalyst layer (CCL), while being hydrated to guarantee proton conductivity during the cold start [10]. Additionally, a 1-cell cold start model was developed which calculates the ice fraction during cold start at temperatures down to -40°C and was used to study the influence of the purge time on its cold start ability [11]. These simulation results validated the obtained experimentally.

In this study the influence of the cathode purge gas, the purge temperature and the purge time on the PEMFC system performance after cold storage at -20°C were further investigated with the 4 kW PEMFC system, whose experimental results can be summarized as follows.

3.1.1 Cathode purge gas

Tests were carried out purging the cathode before cooling down the stack at -20°C with different gas compositions: synthetic air (O_2 20.9 Vol.-%, N_2 79.1 Vol.-%), compressed air and pure nitrogen. During cold storage stack is soaked with dry gases which can diffuse form cathode to anode, and vice versa (fuel and oxidant crossover). Thus, purging the cathode with air may lead to an air-hydrogen front that could cause material and performance degradation [4]. However, by comparing polarization curves was found neither any difference between different gases used, nor performance degradation. Therefore, and for technical reasons compressed air was defined as purge cathode gas for next tests as well as for the later study with the 100 W stack.

3.1.2 Purge temperature

The purge temperature has an effect on the amount of water removed: a higher temperature can be beneficial to take off more water, but the contrary would result from too high temperature [8, 12]. Test results of varying purge temperature from +15°C to +50°C didn't show any relevant influence, neither on the 4 kW PEMFC system performance degradation after cold storage nor on its cold start ability. But purging with a high-power size stack at high temperatures (e.g. +85°C) may result in a non-uniform drying, thus potential membrane damage [4, 12]. For this reason, and in order to increase the energy efficiency of the system by eliminating the energy consumed by gas heaters, the purge procedure in the next study with the 100 W stack was carried out at +25°C.

3.1.3 Purge time

The purge time influences the water remaining in the stack membranes. These experimental results showed, that the purge time influence on the cold start time of the PEMFC system was lower for quick cold starts than for the slow ones. Moreover, no performance degradation was measured after more than 70 cold starts by purging for 3 min (intermediate-low value) 400 nl/min of air in the cathode and 30 nl/min of H_2 in the anode before freezing the stack at -20°C, while parasitic loses during shut-down were a bit lower.

3.2 Cold storage with the 100 W stack

3.2.1 Purge gases flow rates

Purge gases volume flow rates and optimal purge time (intermediate-low value) previously selected for the 4 kW stack have been taken as reference to calculate the purge gases flow rates and time for the 100 W stack, even

though both stacks have different power sizes and fuel cell components, hence different water storage capacities. According to this estimation, the 100 W stack should be purged before freezing at -20°C for 90 s with air in the cathode at 20 nl/min and with H_2 in the anode at 1.5 nl/min. Therefore, in this study the cathode flow rate by purging was varied between 5 and 20 nl/min, as the cathode MFCs maximal flow rate is 10 nl/min, and hence the anode flow rate between 0.375 and 1.5 nl/min.

Figure 2 presents the evolution over time of the cathode relative humidities inlet and outlet (RH) at different purge gases flow rates. As Figure 2 shows, cathode outlet relative humidity decreases proportionally as the flow rate increases, thought this decrease is not linear. Indeed, cathode relative humidities decreased much faster with cathode purge volume flow rates equal to or higher than 10 nl/min. Since the cathode outlet was dried faster by purging with air in the cathode at 20 nl/min and with H_2 in the anode at 1.5 nl/min, this combination was selected for next series of tests. Moreover, and based on the previous results with the 4 kW stack, we suppose that the optimal purge time (t_{opt}) for the 100 W stack is not bigger than the corresponding time of the turning point, in which the cathode outlet RH begins to decrease slowly. For the 100 W stack this RH value was below 20% for all purge gas combinations, as illustrated in Figure 2. We assume that at this point no relevant water was remaining neither in the channels, nor in the gas diffusion layers (GDL), and that most of the water remaining in the cells is in a non-freezable state at the cold storage temperatures. So, purge times longer than t_{opt} are not necessary to assure no severe damages due to ice-formation during the cold storage. Moreover, by reducing parasitic losses of a very long purging. the energy efficiency of the system increases. To the contrary, the purge time should be long enough, so that no relevant water remains in the system that can turn into ice, thus damaging the stack and/or other components. Therefore, we expect that the minimal purge time should be the turning point in which the cathode inlet RH begins to decrease slowly. These assumptions were studied in the next series of tests.

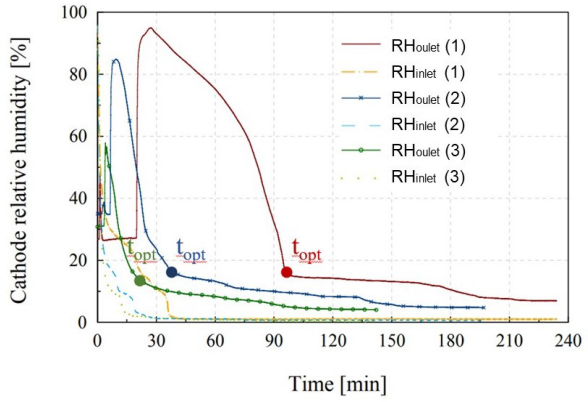

Fig. 2. Cathode relative humidities (inlet and outlet) over time during purge procedure for different combination of gases volume flow rates: (1) 5 nl/min of air and 0.375 nl/min of H_2, (2) 10 nl/min of air and 0.75 nl/min of H_2, and (3) 20 nl/min of air and 1.5 nl/min of H_2.

3.2.2 Cold storage temperature and purge time

To illuminate the impact of the cold storage and purge time on the performance degradation of a PEMFC system due to cold storage at temperatures down to -40°C, nine F/T cycles listed in Table 2 were conducted with different cold storage temperatures and purge times.

Figure 3 illustrates the effect of the first cold storage (test number 1 of Table 2) on the stack performance degradation by comparing the voltage (Fig. 3(a)) and the power density (Fig. 3(b)) as a function of current density before and after the first F/T cycle, as well as after a later conditioning test.

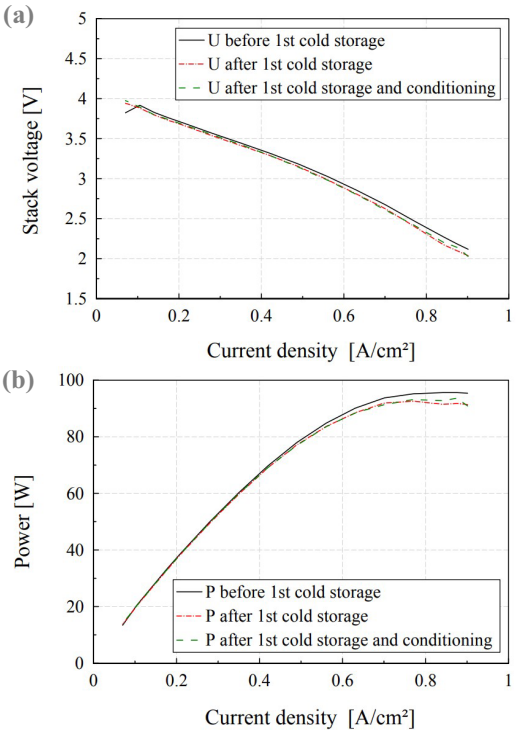

Fig. 3. Effect of the first cold storage at -10°C on the 100 W stack performance: (a) polarization curves; (b) p-j curves.

As Figure 3 shows, the stack already experienced irreversible performance degradation after the first cold storage, even though it was at a not very low temperature (-10°C). This degradation may have occurred due to the ice formation during cold storage, but it might be most likely due to the long purging procedure carried out (1 h). This performance losses may be caused mainly by two factors; the large period at open circuit voltage (OCV) during the purge procedure, and by the excessive dryness of the cells, which may cause an uneven stress distribution in the membrane, thus resulting in membrane degradation [4, 12]. By operating the stack at OCV can cause fuel and oxidant crossovers as well as cells reversal, which would lead to a higher CO_2-corrosion, thus degrading the cells irreversibly [13-15].

Figure 4 compares the polarization and power density curves of the 100 W stack before and after F/T cycles from Table 2 at different purge times and cold storage temperatures. Specifically, from before the 1st cold storage at -10°C after purging 1 h, to after the 7th cold storage at -40°C after purging 90 s.

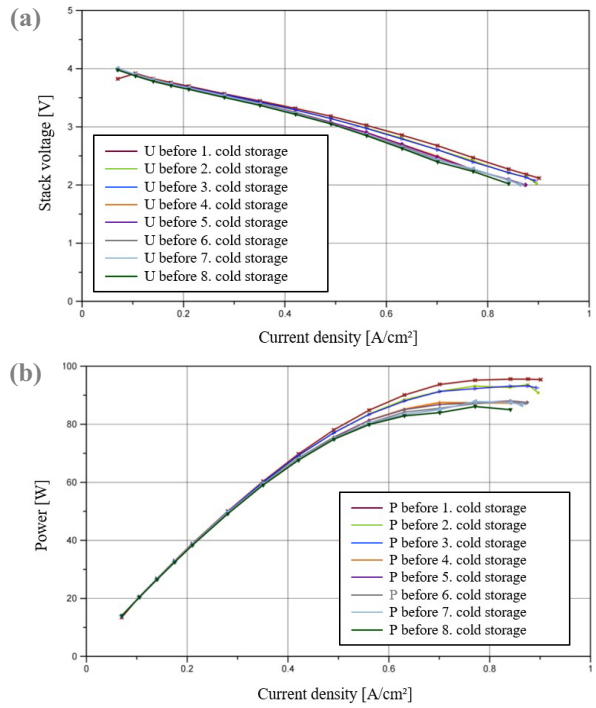

Fig. 4. Effect of the F/T cycles from Table 2 on the 100 W stack performance: (a) polarization curves; (b) p-j curves.

As Figure 4 illustrates, the greatest performance losses result from the firsts cold storages at -10°C and at -40°C, which both have the longest purging procedure (1 h). This indicates that the performance losses are likely to be influenced more by the long purging than to the freezing temperatures. Therefore, a purge time between 1.5 and 10 min seems to be more adequate for the 100 W stack, since a shorter purging reduces degradation and parasitic losses. Thus, the durability and energy efficiency of the PEMFC system can be increased. These results validate our previous assumption of optimal purge time (section 3.2.1.), and are in agreement with the results obtained for the 4 kW stack, in which the optimal purge time was defined as 3 min (400 nl/min air at the cathode, 30 nl/min H_2 at the anode). Moreover, and according to Figure 2, after purging 10 min the 100 W stack (20 nl/min air at the cathode, 1.5 nl/min H_2 at the anode), the cathode outlet relative humidity was approximately 20%. Which is also in concordance with the experimental results obtained by St-Pierre et al. [12].

By comparing performance curves before and after a F/T cycle at -40°C without purging (test 9(G) from Table 2), performance losses due to ice formation were observed, specially at current densities higher than 0.75 A/cm². These losses were mostly irreversible, not being recovered even after some conditioning tests. But these losses were lower than expected. A possible reason for that may be that the stack operated with an excess oxygen ratio of 3 at low current densities (lower than 0.1 A/cm²) for the last twenty minutes of the polarization curve. Therefore, the stack was already partly dried before freezing without conducting any purge procedure. This shows, that combining the purge procedure with the previous operation of the PEMFC system would be optimal to reduce time and energy consumption.

4. Conclusions

In this investigation, the impact of the purge procedure and the cold storage on the performance of two types of PEMFC fuel cell systems has been studied. The main findings of this experimental work are addressed below.

Results showed that the purge temperature required didn't seem to be necessary at a high temperature. Indeed, a higher temperature may lead to a non-uniform drying, thus accelerating membrane degradation [4, 12]. Hence, this temperature was chosen according to the system at room temperature, thus reducing parasitic losses and consequently enhancing the energy efficiency of the system.

Purge shutdown procedure has to be chosen very carefully. This study has shown that very long purging (e.g. more than 20 min for the 100 W stack) also lead to degradation, even at not very low temperatures, such as -10°C. This degradation may have occurred because of the large period at OCV and by the excessive dryness of the cells. Besides, a purging procedure that dries the cells completely would be extremely slow and energy inefficient because of the parasitic losses. Therefore, the optimal purge time is the one reducing remained water in the cells to a value below that at which damage occurs, but not too long to avoid membrane degradation due to internal stress generation. For the 100 W stack, the optimal purge time was found to be between 1.5 min and 10 min by purging 20 nl/min air at the cathode and 1.5 nl/min of H_2 at the anode. This is in relation with the results obtained with the 4 kW stack.

Very long purging procedures with air at the cathode and H_2 at the anode led to degradation, which may be caused due to fuel and oxidant crossover. For this reason and to enhance the safety and fuel cell efficiency of the system, eliminating anode purge or drying it with nitrogen should be consider.

In addition, the use of a microporous layer (MPL), material choice, cell components design (e.g. diffusion media thickness or channel/land) and the use of a methanol solution as antifreeze during cold storage can help to mitigate degradation due to ice formation [4, 16, 17, 18]. With the aim of reducing the degradation due to subfreezing temperatures of a PEMFC system for aircraft applications, these findings will be validated with a state-of-the-art stack, for which cold storages down to -40°C will be carried out. The design of this state-of-the-art stack together with the purge procedure are expected to reduce degradation due to ice-formation during cold storage.

This work was financially supported by the Federal Ministry of Transport and Digital Infrastructure of Germany within the framework of the BILBO project (No 03B10701C) and, by the Fuel Cells and Hydrogen 2 Joint Undertaking within the framework of the INN-Balance project (No 735969). This Joint Undertaking receives support from the European Union's Horizon 2020 research and innovation programme, Hydrogen Europe and Hydrogen Europe research. The authors would like to thank Stefan Bleeck and Vincent Hackstein for the set up hardware and software of the 100 W fuel cell test bench, as well as Dr. Johannes Schirmer for fruitful discussions.

References

1. https://www.iea.org/
2. D S Lee, et al., Atmos. Environ. **244**, 117834 (2021)
3. H Webber, S Job. (2021). https://www.ati.org.uk/
4. M M Mench, E C Kumbar, T N Veziroglu, *Polymer electrolyte fuel cell degradation*, (Elservier, Oxford; 2012)
5. E Pinton, L Antoni, Y Fourneron, S Rosini, ECS Trans. **17**, 251 (2009)
6. S-Y Lee, et al., J Power Sources. **180**, 784 (2008)
7. S Kim, C Chacko, R Ramasamy, M M Mench, ECS Trans. **11**, 577 (2007)
8. P Xu, S Xu, SAE Int. **01**,1312 (2018)
9. G Montaner Ríos, J Schirmer, C Gentner, J Kallo, Appl. Energy. **279**, 115813 (2020)
10. G Montaner Ríos G, J Schirmer, J Kallo, EFC (2017)
11. M Schröder, C Gentner, G Montaner Ríos, F Becker, S Bleeck, I Sokolov, J Kallo, MODVAL (2019)
12. J St-Pierre, J Roberts, K Colbow, et al., J. New Mater. Electrochem. Syst. **8**, 163 (2005)
13. P Reng, P Pei, Y Li, Z Wu, D Chen, S Huang. Prog. Energy Combust. Sci. **80**, 100859 (2020)
14. N Dyanti, A Parsons, P Bujlo, S Pasupathi, Mater Renew Sustain Energy. **8**, 4 (2019)
15. S Kundu, M Fowler, L Simon, R Abouatallah, N Beydokhti, J Power Sources. **183**, 619 (2008)
16. A Turhan, K Heller, J S Brenizer, M M Mench, J Power Sources. **180**, 773 (2008)
17. F Knorr, D Garcia Sanchez, J Schirmer, P Gazdizcki, K A Friedrich, Appl. Energy. **238**, 1 (2019)
18. G Montaner Ríos, J Schirmer, F Becker, S Bleeck, C Gentner, J Kallo, ECS Trans. **98**, 243 (2020)

Characterization of a metallic interconnect operated in stack during 40,000 hours in SOFC mode

Paolo Piccardo[1]*, *Roberto* Spotorno[1], *Valeria* Bongiorno[1], *Daniele* Paravidino[1], *Christian* Geipel[2], *Greta* Patrone[1] and *Francesca* Valente[1]

[1]UNIGE Chemistry and Industrial Chemistry Department, 16146 Genoa, Italy
[2]SUNFIRE GmbH, Gasanstaltstraße 2, Dresden, 01237,Germany

Abstract. An SOFC stack operated for 40,000 hours has been dismantled offering the opportunity to characterize the metallic interconnect. The metal plate was carefully investigated to define the evolution of the surfaces exposed to the air and to the hydrogen electrodes respectively. The observations of the surfaces reveal the stability of the layers applied on top of the rib at the air side while in the bottom of the channels the protective coating (i.e., Co-Mn base spinel oxide) shows large crystals. The cross section allowed to highlight the formation of a rather homogeneous layer of thermal grown oxide between the metal and the coating. The average thickness of the TGO is around 11 µm. The hydrogen side shows a superficial alteration (due to the interaction with the water vapour) changing from the inlet to the outlet where it seems thinner as if the TGO further reacted by forming volatile compounds. The cross section observations confirmed the presence of a porous TGO with a rather high content of manganese in a Cr-Mn spinel oxide. Several spots testifies the zones of contact with the Ni base contacting layer. The cross section corresponding to such zones highlighted the Ni diffusion in the metal substrate.

1 Introduction

In the perspective of an efficient decarbonisation of the energy production the usage of hydrogen as fuel for power plants seems to be a logical solution [1] due to its compliance with the renewable power sources (e.g., photovoltaic, wind power) often characterized by the intermittence of operating period and by the need of an energy storage solution. Moreover, the usage of "green hydrogen" would increase the environment friendly characteristic of power plant fuelled by such an energy vector. To reach and sustain such a goal the scientific community is widely engaged to fulfil the few issues still slowing down the trend to the ecological transition demanded by the citizens and by the planet itself.
One of the issues is the durability of the power plant and its reliability on the long lasting period with the corresponding low degradation rate.
Among the possible solutions, the solid oxide fuel cells (SOFC) are favoured for their high efficiency in energy conversion of the reaction between hydrogen and oxygen reaching more than 90% if heat and electrical power are considered [1]. The operating time needed to make the stack built around SOFCs is at least 50,000 hours even though the ideal time would be 80,000 hours at an operating temperature between 650°C and 850°C and an optimal fuel consumption of 80%. The evolution of the components inside a stack is strictly related to the efficiency of the whole system and involves materials evolution and the interaction between materials [2-4]. The interconnects, allowing the separation of cells by granting the passage of electrons from the anode to the cathode of the adjacent cell, have a key role in the stack even though they do not participate to the energy production [5-8]. The state of the art combined heat and power (CHP) devices makes use of metallic interconnects (MICs) based on ferritic stainless steel (FSS) for the following reasons: 1) high electrical conductivity; 2) shapability; 3) easiness to seal with the cells to insure the gas tightness between the cathode and anode chamber; 4) coefficient of thermal expansion (CTE) matching with the one of the cell (especially of the electrolyte); 5) high mechanical resistance; 6) chemical stability obtained by the formation of electrically conductive oxide at the air side eventually enhanced with the application of protective coatings [9]; 7) cost effectiveness.
The reliability of the MICs is fundamental to offer trustworthy power plants, this is due to the delicate and multiple roles they play in the stack and by the direct interaction they have with the cell's electrodes. The usage of FSS rich in Cr and poor in all other elements to obtain the correct CTE and conductive thermally grown oxide (TGO) makes the presence of coating at the air side mandatory to hinder the formation of volatile compounds rich in oxidized Cr. This is know as one of the most detrimental phenomenon by the rapid poisoning of the cathode three phase boundaries. The coating has the double role to keep the TGO stable in oxidizing atmospheres and to avoid its direct interaction with the

* Corresponding author: author@e-mail.org

cathode material to hinder the interdiffusion of cations between the electrode and the oxidized scale [10, 11].
Due to the high quality of the FSS used for the MICs the investigations need extremely long lasting experiments to have a correct vision of the phenomena and the reproduction of "real-life conditions" (i.e., temperature, atmospheres, materials). The validation of laboratory tests and the refining of degradation models can only occur by the comparison with components extracted from operated stacks [12-14]. The project Ad Astra offers such an opportunity SOFC stacks field operated for several thousand hours.

The present paper refers on the first results obtained by the post-mortem characterization of MIC samples extracted by a stack field operated for 40,000 hours in fuel cell mode and is an update of previous publications [12, 13] referring of interconnects operated for up to 20,000 hours. The results are of fundamental importance for the modelling of the stack performances evolution and for a better understanding of samples issued by accelerated tests.

1.1 Materials and methods

The MIC was extracted by an SOFC stack manufactured and operated by Sunfire company (Sunfire GmbH, Dresden, Germany) according to the disclosable working conditions listed in table 1.

Table 1. Operating parameters for the stack.

Operation type	SOFC (µCHP), field
Total runtime/h	40,000
Fuel gas (Co-flow)	44% N_2 34% H_2 16% CO 4% H_2O 2% CO_2
Nominal temperature/°C	850
Current density/mA•cm^{-2}	90-200

The major changes expected from inlet to outlet are the temperature gradient common to both side and the composition of the fuel stream with an increase of pH2O at the fuel side only. The stacks manufactured according to the company standards used electrolyte supported cells based on 3YSZ as electrolyte, with electrodes made of LSM (cathode) coated with a cathode contacting paste (LSCM on the ribs only) and Ni cermet (anode) connected to the MIC by a Ni metal foam. The MIC was an undulated plate of ferritic stainless steel CROFER 22 APU©, commercial grade (table 2), joined to the cell electrolyte by a proprietary glass-ceramic compliant sealant. It was coated at the air side only with a manganese cobalt spinel oxide (MCO) doped with Fe.

Table 2. Crofer22APU Chemical composition (wt.-%) according to the ThyssenKrupp datasheet [15].

Wt. %	Cr	Fe	C	Mn	Si	Ti	La	others
min.	20.0	bal.		0.30		0.03	0.04	Cu Al
max.	24.0		0.03	0.80	0.50	0.20	0.20	

The MCO protective coating covers the whole surface following the ribs/channels profile with a constant thickness; it was applied on the bare metal with an initial porosity and Fe content unknown due to the proprietary application method.

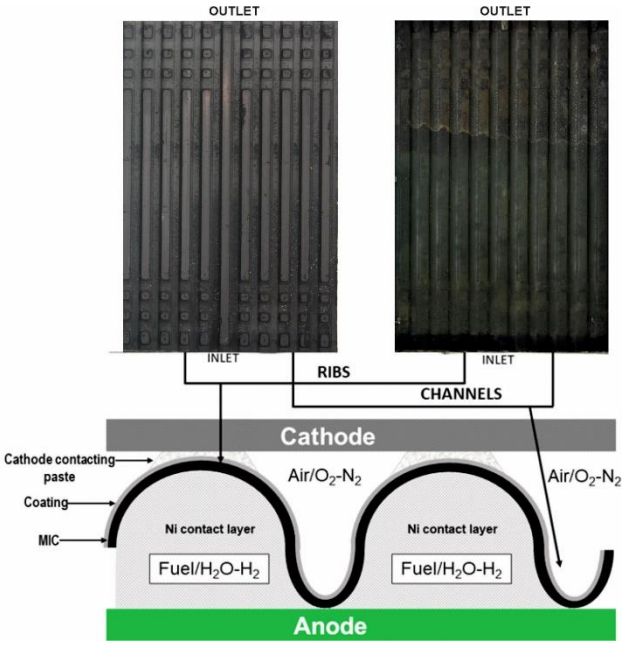

Fig. 1. *schematic representation of the MIC cross section and overall vision of the air side (top left) and of the fuel side (top right) with the INLET – OUTLET positions to indicate the co-flow direction of the streaming.*

To simplify the identification of the investigated areas on the MIC cross sections, two main positions are conventionally defined: the Ribs, as the part of the plate in contact with the cathode, and the Channels allowing the air flow from inlet to outlet. The air side is contacted with the cathode only by the ribs while at the anode side the whole surface is contacted with the electrode by a porous and compliant Ni layer. At this side therefore there is no distinction between rib and channel. According to the company information on the field operations from Inlet to Outlet the temperature range passes from ca. 1000 K to ca. 1050 K with consequences on the MIC reactivity. The interconnect was therefore divided in four samples all along the flow stream covering nearly 25 mm of length each sample: inlet, center-inlet, center-outlet, outlet. Each samples was mounted in epoxy resin and polished up to a diamond suspension with 250nm of granulometry, to expose the cross section for investigations by a scanning electron

microscopy (SEM) coupled with an energy dispersive X-ray spectroscopy (EDS) calibrated with pure Co reference. The EDS data are treated by INCA software (Oxford) with ZAF 5 correction to achieve quantitative information on metals and semiquantitative data on oxygen.

2 Results and discussion

From the characterization of the surface, it results that the fuel side is more affected by the interaction with the gas stream (fig. 1). The H2/H2O gradient is constantly evolving from the Inlet zone toward the Outlet zone with an increase of water vapour corresponding to a reduction of the hydrogen partial pressure. As already discussed in [12] the oxidation of the MIC is due to the interaction with the water vapour and corresponds to the formation of a TGO rich in Mn and Cr evolving into a Mn richer oxidized layer by the evaporation of Cr rich volatile compounds. The overall electrical conductivity is not affected by the TGO formation due to the numerous zones of welding between the Ni contacting layer and the MIC as visible in figure 2. Such zones corresponds to the interdiffusion between Ni and FSS forming an intermediate alloy rich in Ni. The cross section allowed finding a wide diffusion zone of Ni in correspondence of the spot welding area. In this zone, coherently with the Cr-Fe-Ni phase diagram [16], a second phase rich in Cr separated from the main matrix. Such phases present several cracks probably due to the compressive stress applied by the surrounding alloy that has a higher CTE due to the presence of Ni.

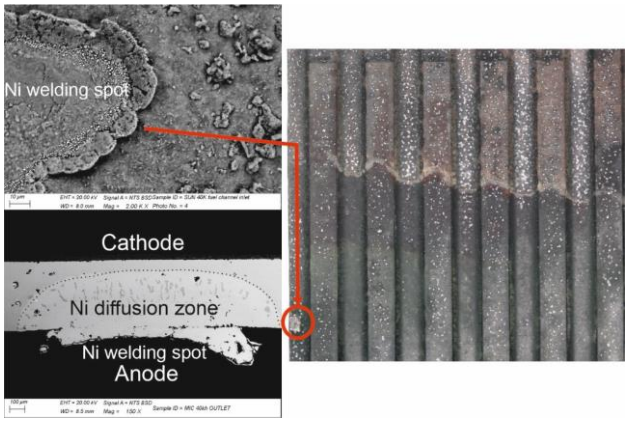

Fig. 2. *Fuel side, OUTLET zone, visible welding spot of the Ni contacting layer with the anode*

The remaining surface of the MIC at the fuel side presents various form of oxide with, in the central zone between the inlet and the outlet, evidence of the presence of conglomerates interpreted as bubbles once observed in cross section (fig. 3). This morphology is typically related to the formation of volatile compounds by the further oxidation in presence of water vapour of Cr rich oxides. The remaining scale covering the mic shows a micro porosity matching with the evaporation phenomenon.

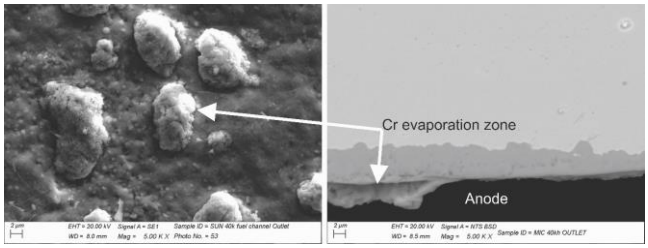

Fig. 3. *Fuel side, central area nearby the OUTLET zone, superficial bubbles with detail in cross section showing the cavity due to volatile compounds*

At the air side the macroscopic observation shows only the presence of large crystals in the ribs, where the air stream flows without obstacles from the inlet to the outlet zones. In figure 4 a detail on such crystals is presented. They formed on top of the MCO coating and correspond to spinel oxide where Cr is trapped. The MCO in cross section appears well adherent to the metal substrate and with a remaining porosity despite the 40,000 hours at high temperature. The TGO formed at the interface with the FSS.

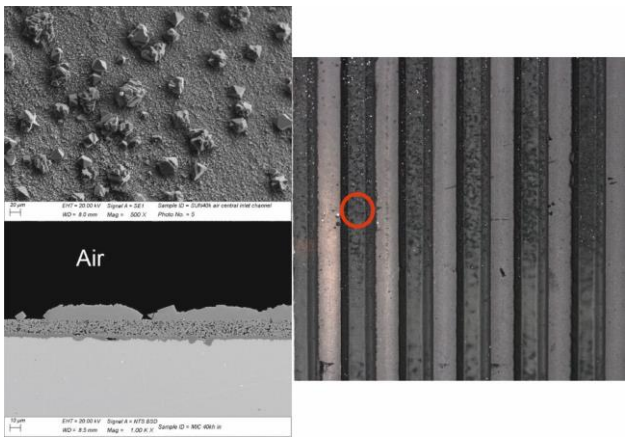

Fig. 4. *Air side, central area inside a channel with large spinel crystals containing Mn, Co, Cr, Fe on top of the MCO coating. Details are visible on the cross section image*

In figure 5 a representative image of the situation found on the rib (i.e., where the cathode enters in direct contact with the interconnect) is presented. The surface shows the homogeneous presence of crystals of contacting layer with a possible increase of the crystals size to be discussed more in details after further studies. The cross section reveals the presence of multiple interphases related to the interaction between the various layers. The contacting layer and the MCO coating have sporadic interactions with formation of dense phases but, in general, Cr remains in the coating where it enters by solid-state diffusion. The TGO formed at the interface with the MIC is mainly due to the diffusion of oxygen from the coating. This limits the TGO growth rate as results by table 3 with related graphic (fig. 6).
The TGO thickness increases on both sides but it results definitely thicker at the fuel side due to the absence of protective coating. The range of thickness observed from the inlet to the outlet is related to the differences in temperature (i.e., up to 60K) between the two zones and, for the fuel side only, by the change in favour of the

water vapour of the ratio H2/H2O due to the anodic reaction.

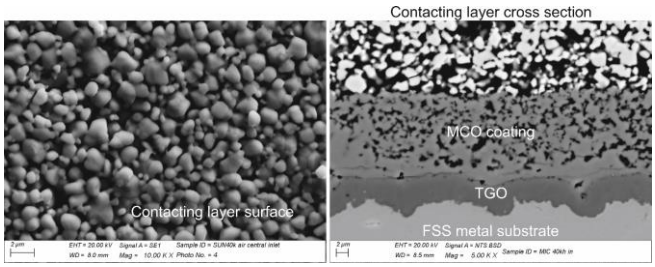

Fig. 5. *Air side, central area on top of a rib (surface view) and related cross section with all visible interphases from the metal substrate to the top contacting layer*

	TGO fuel min (mm)	TGO fuel max (mm)	TGO air min (mm)	TGO air max (mm)
inlet 0-2.5 cm	6	8	2	5
center-in 2.5-5 cm	3	9	4	11
center-out 5-7.5 cm	7	18	4	14
outlet 7.5-10cm	10	24	9	17

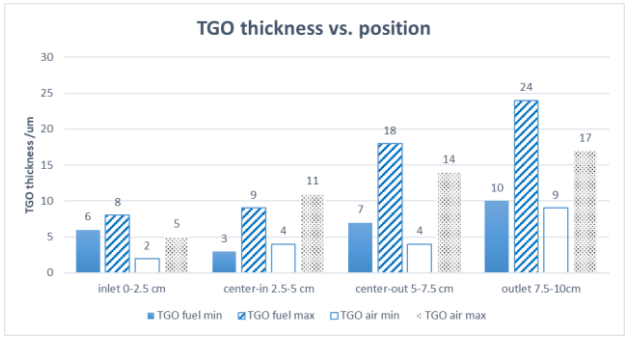

Fig. 6. *Graphic representation of the TGO thickness range at the fuel and air side respectively*

3 Conclusions

The rare opportunity to characterize components operated for a very long period allowed the investigation on a metallic interconnect extracted from an SOFC stack field operated for 40,000 hours. The preliminary results has shown the following highlights on the materials evolution:

1) The fuel side results more affected by the interaction with the gas stream than the air side

2) The protective coating confirms its efficiency on the long lasting period by gathering the Cr moving by solid-state diffusion from the metal substrate.

3) The MIC in contact with the cathode shows an evolution by the formation of a TGO with a growth rate depending by the temperature (which confirms to be an important accelerator of such an ageing process)

4) The fuel side of the MIC presents various form of oxidation with the evidence of Cr evaporation. The TGO grows faster than at the air-side but without affecting the electrons exchange between the anode and the MIC. This is due to the formation of welded spots between the MIC and the Ni contacting layer

5) In correspondence of the welded spots the MIC changes locally the composition with a remarkable increase of the Ni content provoking the formation of a differing alloy with the precipitation of hard and brittle second phase rich in Cr.

As general conclusion it is possible to suggest that the MIC observed has maintained a sufficiently satisfying functionality even after 40,000 hours of operation. However, the diffusion of Ni into the FSS matrix, which is locally transformed into an austenitic alloy with Cr rich large precipitates, and the thick TGO formed on both sides (i.e., air and fuel side respectively) are clear warning signals that some counterstrategies should be applied to reach the planned 80,000 hours for the next generation SOFC stacks.

Temperature and water vapour partial pressure confirm their key role as accelerating parameters of the ageing phenomena related to the MIC. The design of accelerated tests should take these and the previous results into account to better understand how to use the accelerating parameters to perform meaningful laboratory experiments.

The research leading to these results has received funding from the Fuel Cells and Hydrogen 2 Joint Undertaking under Grant Agreement No 825027.

References

Here are some examples:

1. J.B. Hansen, Faraday Discuss, **182** (2015)
2. Michael C. Tucker, Int. J. Hydrogen Energy, in press
3. Y. Yan, Q. Fang, L. Blum, W. Lehnert, Electrochimica Acta **258** (2017)
4. C. Chatzichristodoulou, M. Chen, P.V. Hendriksen, T. Jacobsen, M.B. Mogensen, Electrochimica Acta **189** (2016)
5. D. The, S. Grieshammer, M. Schroeder, M. Martin, M. Al Daroukh, F. Tietz, J. Schefold, A. Brisse, Journal of Power Sources **275** (2015)
6. M. Riedel, M. P. Heddrich, K. A. Friedrich, Int. J. Hydrogen Energy **22** (2019)
7. Regis Anghilante, David Colomar, Annabelle Brisse, Mathieu Marrony, Int. J. Hydrogen Energy **43** 45 (2018)
8. Juhyun Yoo, Sang-Kuk Woo, Ji Heng Yu, Siwoo Lee, Gun Woo Park, Int. J. Hydrogen Energy 34 3 (2009)

9. Xiaoyu Zhanga, James E. O'Brien, Robert C. O'Brien, Joseph J. Hartvigsen, Greg Tao, Gregory K. Housley, Int. J. Hydrogen Energy, **38** 1 (2013)
10. M.R. Ardigò, I. Popa, S. Chevalier, P. Girardon, F. Perry, R. Laucournet, A. Brevet, C. Desgranges, Int J. Hydrogen Energy **39** 36 (2014)
11. M. Bianco, J.P. Ouweltjes, J. Van herle, Int. J. Hydrogen Energy **44** 59 (2019)
12. G. Ghiara, P. Piccardo, V. Bongiorno, L. Repetto, C. Geipel, R. Spotorno, Int. J. Hydrogen Energy, **46** (2021)
13. G. Ghiara, P. Piccardo, V. Bongiorno, C. Geipel, R. Spotorno, Energies **13** (2020)
14. M. Bianco, P. Caliandro, S. Diethelm, S. Yang, A. Dellai, R. Steinberger-Wilckens, Journal of Power Sources, **461** (2020)
15. ThyssenKrupp VDM, Crofer 22 APU – Material, Data Sheet No. 4046 (2010)

I. Ansara, T. G. Chart, P.Y. Chevalier, Phase diagrams for FE-CR-NI based alloys, CD-NA-09-657-EN-C (1996)

A hydrogen generator coupled to a hydrogen heater for small scale portable applications

Dirk Hufschmidt[1], *Gisela M.* Arzac[1,2], *Maria Carmen* Jiménez de Haro[1] and *Asunción* Fernández[1,*]

[1]Instituto de Ciencia de Materiales de Sevilla (CSIC-Univ. Sevilla), Avda. Américo Vespucio 49, 41092-Sevilla, Spain.
[2]Departamento de Química Inorgánica, Facultad de Química, Universidad de Sevilla, C/Profesor García González 1, 41012-Sevilla, Spain.

Abstract. This study aims to build and test a small scale portable device able to couple a hydrogen generation system (based on a $NaBH_4$ solution as liquid H_2 carrier) to a hydrogen heater (based on the exothermic catalytic combustion of the released H_2). The hydrogen generating system is based on the hydrolysis of stabilized solutions of $NaBH_4$ (fuel solutions) which are pumped into the hydrolysis reactor. The generated H_2 feeds the catalytic combustor. Two catalysts have been developed for the H_2 generation and the combustion reactions able to operate at room temperature without need of additional energy supply. For the $NaBH_4$ hydrolysis a Co-B catalyst was supported on a perforated and surface treated stainless steel (SS316) home-made monolith. For the flameless H_2 catalytic combustion a Pt catalyst was prepared on a commercial SiC foam. The device was automatized and tested for the on-demand production of heat at temperatures up to 100ºC. In steady state conditions the $NaBH_4$ solution flow is controlling the H_2 flux and therefore the heater temperature. Once the steady-state is reached the system responds in a few minutes to up and down temperature demands from 80 to 100 ºC. The catalysts have shown no deactivation during the tests carried out in several days.

1 Introduction

For the implementation of the "hydrogen economy", challenges related to its sustainable and low-cost production, transportation and storage are under continuous investigation [1–5]. The use of $NaBH_4$, (SBH) solutions as liquid hydrogen carrier constitutes an attractive strategy for hydrogen storage [6-8]. Solid SBH is stable in dry air, can be stabilized in basic solutions and produces hydrogen through its hydrolysis reaction (Eq.1). The borate by-product is non-toxic, and must be extracted from the spent fuel for further regeneration [9,10].

$$NaBH_4 + 2H_2O \rightarrow 4H_2 + 2NaBO_2 \qquad (1)$$

The potential of SBH solutions for H_2 storage and release, coupled to PEM fuell cells for mobile or portable applications have been previously considered [11-14]. In this work we aim to couple a H_2 generation system to a reactor for the direct production of heat (e.g. cookers and heaters) based on the catalytic hydrogen combustion (CHC, Eq.2).

$$H_2 + ½O_2 \rightarrow H_2O \qquad (2)$$

The CHC is a key reaction in the "hydrogen economy" because it is safe, controllable and highly exothermic (286 $kJ.mol^{-1}$) [15]. This reaction can be employed for heat production as well as for safety purposes for the elimination of undesired hydrogen [15-17]. The catalysts in this work have been selected to operate at room temperature for both H_2 generation and combustion reactions and have been deposited on selected structured supports according to the reactors´ requirements [18]. The design of the H_2 generation and combustion reactors and the final controlled heater device are described herein, together with the operation tests.

2 Catalysts and catalytic reactors

2.1. The H_2 generation by $NaBH_4$ hydrolysis

Co-B materials are the most investigated cobalt based catalysts for the SBH hydrolysis reaction and have been prepared on a wide range of conditions in powder as well as in supported form [12-14,19-21]. As catalyst's structured support, a homemade cylindrical monolith was fabricated from commercially available perforated stainless steel (SS316) as shown in Fig.1a [13-14]. The SS support was calcined at 900ºC to produce a well adhered oxide layer according to a previous work [13]. Fig.1c shows SEM (scanning electron microscopy) images of the monolith oxidized surface at two magnifications. The Co-B catalyst was deposited by successive cycles of alternated immersions of the support on 30% $CoCl_2.6H_2O$ and stabilized 19% SBH aqueous solutions [13]. Fig.1b shows the monoliths after deposition of the Co-B catalyst. A cylindrical reactor

* Corresponding author: asuncion@icmse.csic.es

with a total volume of 11 mL (hydrolysis reactor in Fig.3) can be made of PMMA or stainless steel. Catalytic monoliths are placed inside the reactor where the hydrolysis reaction will start spontaneously upon contact of the SBH stabilized solution with the catalysts.

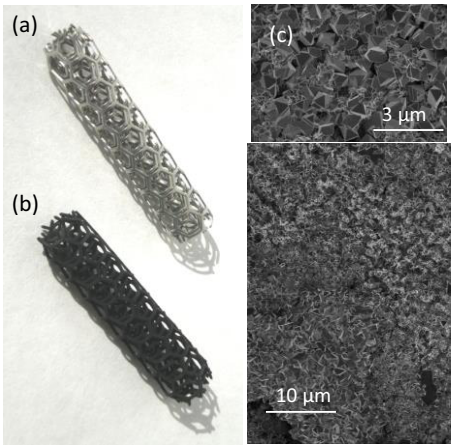

Fig.1. Stainless steel monoliths before (a) and after (b) deposition of the Co-B catalysts. (c) SEM images of monolith surface modified after thermal treatment.

2.2 The catalytic H_2 combustion

For the flameless H_2 catalytic combustion Pt and Pd are reported as the most active catalysts which permit to initiate the reaction without ignition even at room temperature [15, 22-23]. In this work a Pt deposited catalyst was prepared on commercial SiC foam by impregnation with an ethanolic solution of H_2PtCl_6 for a final Pt loading of 1.0 wt%. The catalyst was dried in an oven and further calcined in static air at 400 °C during 4 h. Fig.2 shows the commercial disc of alumina bonded SiC foam (from Lanik s.r.o., 80 pores per inch) before (a) and after (b) deposition of the Pt catalyst. Fig.2c shows SEM (scanning electron microscopy) surface images of the monolith SiC structured supports at two magnifications.

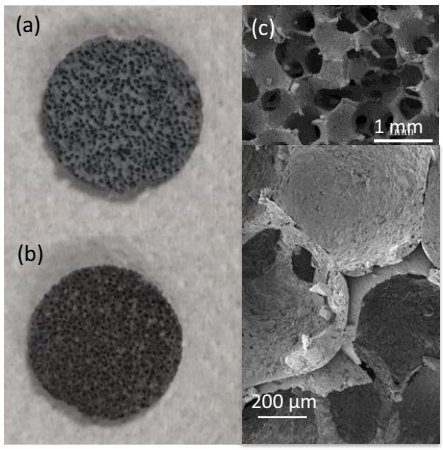

Fig.2. SiC monoliths before (a) and after (b) deposition of the Pt catalysts. (c) SEM images of the bare SiC foam surface.

The reactor (combustor in Fig.3) was made of stainless steel for 30 mm diameter and 5 mm thickness size of catalytic monoliths. H_2 generated in the hydrolysis reactor will directly feed the combustor where the CHC reaction will start spontaneously in the presence of oxygen and the Pt catalyst.

3 Controlled heater device for portable applications

3.1. The experimental design

According to scheme in Fig.3 a prototype has been designed and constructed for a portable heater powered by H_2. Stainless steel was used to fabricate the two reactors according to machining availability in the laboratory. The hydrolysis reactor and the residues tank could however be constructed with polymeric materials. The tank for the SBH fuel solution was made of PP polymer.

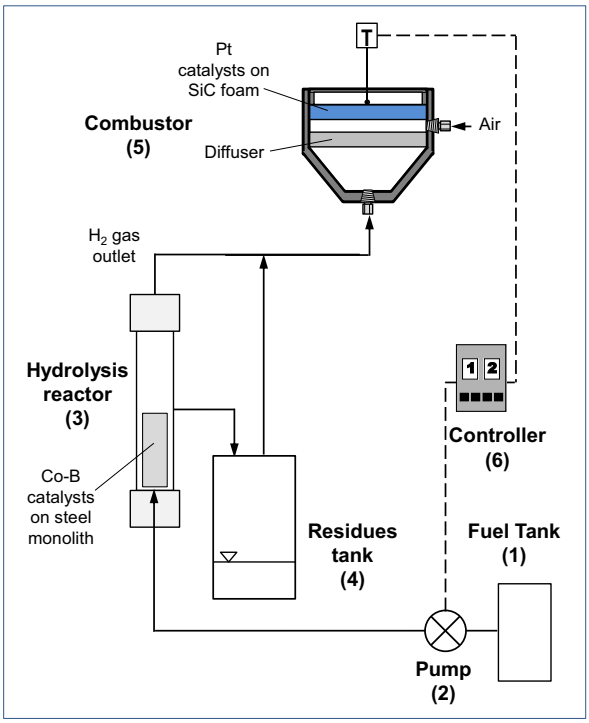

Fig.3. Scheme of the complete experimental design for a portable H_2 heater: (1) Tank for the SBH fuel solution. (2) Micropump. (3) Hydrolysis reactor with catalytic monolith. (4) Tank for the borate residues solution. (5) CHC reactor with catalytic monolith. (6) Controller

The hydrolysis reactor consists of a tube of 105 mm long and 15 mm internal diameter. The reactor has three connections, the fuel inlet on the bottom, the waste outlet on the side and the gas outlet on the top. The waste outlet is connected to the waste tank (V ca. 300 mL), which is also connected to the gas outlet line (pressure balance in the system). Inside the reactor is the home-developed stainless steel monolith with the CoB catalyst of 60 mm length and 12 mm diameter. The fuel enters the reactor from down, and in contact with the catalyst begins to evolve H_2. The gas formed exits the reactor free from residues through the head of the reactor. At a height of 75 mm there is a connection (min. 1/8") for the elimination

and separation of the reacted fuel to the waste tank. With this configuration the catalyst is wet during operation and the synergism between the high temperatures achieved and the continuous elimination of the spent fuel, prevent borates from crystallization on the surface of the CoB, which could easily cause deactivation [12,13]. Fig.4 shows the experimental realization of the portable H_2 generator which also includes a thermocouple for reaction temperature measurements. The selected micro-pump was from HNP Microsysteme with reference mzr-2921.

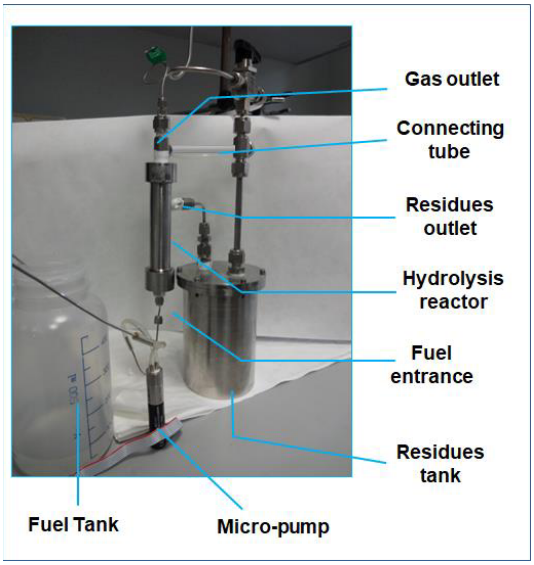

Fig. 4. Experimental realization of the portable H_2 generator**.**

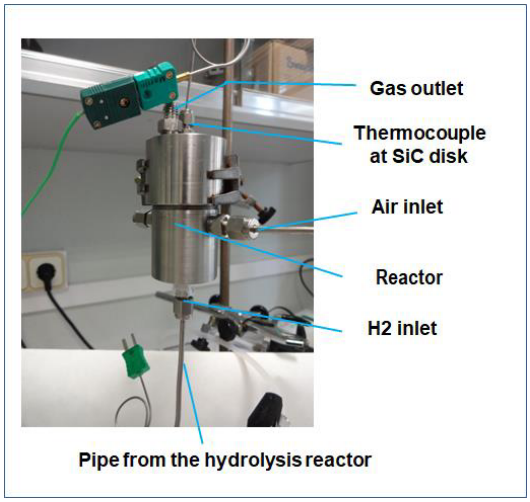

Fig. 5. Experimental realization of the H_2 combustor**.**

The catalytic combustion reactor is connected to the hydrolysis reactor (H_2) and to the air supply from a compressor (for a final device a miniature air pump may be used). The reactor consists of a stainless steel body with an internal diameter of 30 mm and a height of 50 mm. The conical bottom with the gas inlet is 20 mm high and is filled with quartz wool for free volume reduction. On top it is a disc (5 mm thick) of the bare porous SiC foam as a diffuser. Above it is a free space where the air inlet is placed and is mixed with the H_2. In the upper part the porous SiC plate with the deposited catalyst is located. The heat resulting from catalytic combustion is measured with a K-type thermocouple, which is in contact with the center of the catalytic plate. The reactor can be used in the open mode (for the final portable device) or with a cap including a gas outlet for gas chromatographic (GC) analysis. Fig.5 shows the experimental realization of the portable H_2 combustor.

3.2. The operation tests

With the objective of controlling the heater temperature by the fuel addition rate, tests were performed with the following conditions:
(i) SBH hydrolysis reaction: Fuel ($NaBH_4$) concentration 1-2 wt.%. Fuel flow between 0.5-2 mL/min. In these conditions the maximum H_2 production is 30 mL/min. Maximum usage time: determined by the capacity of the waste tank (ca. 3h in this prototype).
(ii) Catalytic hydrogen combustion: Air flow 800 mL/min, fixed to ensure a concentration of H_2 in air below 4 vol.%. H_2 flow up to 30 mL/min. H_2 conversion (determined by GC) > 99%

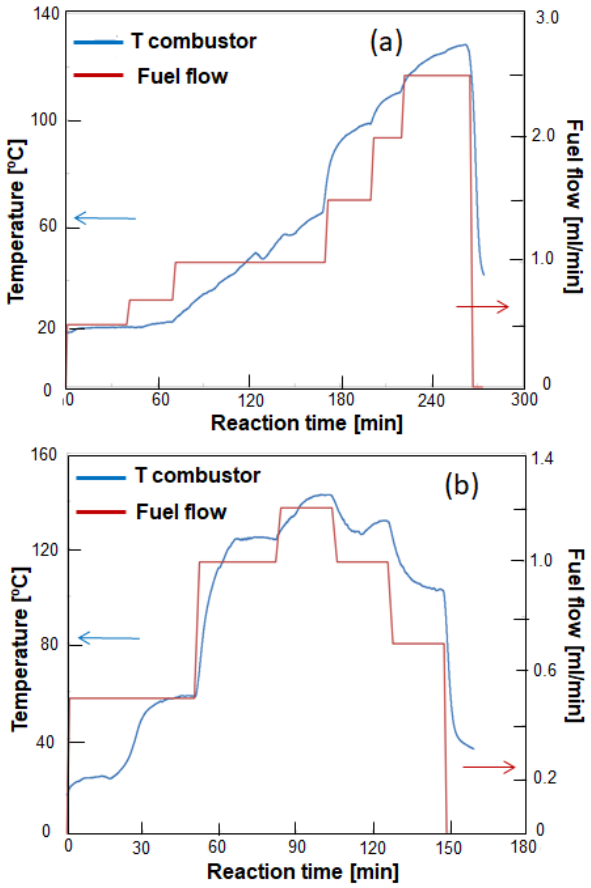

Fig. 6. Relationship (as a function of experiment time) between the combustor temperature and the SBH fuel solution flow which is feeding the H2 generator. (a) 1wt.% NaBH4, (b) 2wt.% NaBH4.

First tests were devoted to determine the relationship between the fuel flow feeding the hydrolysis reactor and the temperature resulting in the combustor. Two SBH concentrations (1 and 2 wt.%) were compared. Results are shown in Fig.6a and 6b respectively. In both cases it is observed an increase in temperature, due to the hydrogen combustion, with an increased fuel flow. The reason is that there is a correlation between the fuel addition and the hydrogen generation rates [12,13]. With the 1 wt.% fuel a maximum temperature of 128 ºC can be reached with 2.5 mL/min flow and 100 ºC is reached with 1.5 mL/min fuel. Comparatively lower flows are needed and higher temperatures are reached for the 2 wt.% fuel as expected [12-13]. With a 1.2 mL/min flow, 142 ºC can be reached while to achieve 100ºC a flow of ca. 0.7 mL/min of fuel was needed. For the range of around 100 ºC the 1 wt% SBH fuel was selected to test the application of an electronic control at these moderate temperatures.

Second tests were therefore done connecting the micro-pump to the electronic controller as shown in Fig. 3. The objective is to control the flow of the fuel in relation to the desired temperature of the combustor. Two set-point temperatures have been chosen, 100ºC and 80ºC.

To avoid a long initial induction period, observed in preliminary experiment, a quantity of 2 mL of 19wt% SBH fuel has been initially injected, resulting in the production of ca. 600 mL of H_2. This will purge the complete system from air and will stablish a base H_2 pressurization in the system. Once the combustor is at room temperature the experiments start. The set points temperatures given to the controller, along the experiment time, are indicated in red in Fig.7.

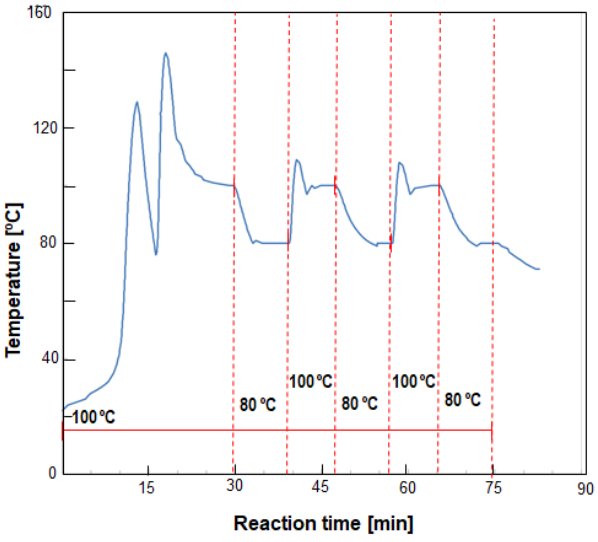

Fig. 7. Evolution of the H_2 combustor temperature upon time as a response to the set-point temperatures given to the controller in an automatic mode operation

Despite the previous injection of the concentrated fuel to purge and pressurize the system, the combustor starts to heat up slowly what results in a high flow demand of fuel. Due to this, an intense temperature increase can be observed at the beginning of the experiment until the system finally stabilizes at the predetermined temperature of 100 ºC. This peak also results in high fuel consumption. Once in the range of this temperature, the system reaches the selected temperatures in a short time (2-3 min) (80ºC-100ºC-80ºC-100ºC-80ºC), demonstrating the regulation effectiveness of the controller system.

No deactivation of the catalysts has been observed, neither in this automated experiment, nor in the previous manual experiment.

4 Conclusions

In summary, in this work a small portable heater which operates at room temperature was designed and built. The system is based on coupling a hydrogen generator with a hydrogen combustor. The controlled addition of SBH in the form of stabilized solution (fuel solution) permits to generate hydrogen in a controlled rate to feed the combustor. In steady state conditions, the temperature of the combustor was tuned with the fuel addition rate, which was controlled with the micro-pump. The system operating in an automate mode, was able to respond fastly to the desired temperature from 80ºC to 100ºC and *vice-versa*. When the system is demanded to increase the temperature, the heating is slow, resulting in the increase of a fuel addition rate which produces a peak in the temperature of the combustor. On the contrary, the system responds more efficiently to a demand for decreasing temperature. The catalysts chosen for the hydrogen generator and the combustor demonstrated to be adequate to initiate the reactions with no extra energy supply and stable during each experiment and upon cycles. For a final mobile device the system requires the integration of a small battery (or fuel cell also fed by the H_2 generator) to power the small controller and both fuel and air micro-pumps. The designed (SS monolith) and selected (SiC disk) structured supports met the geometric requirements of each reactor and the necessary surface roughness for high catalyst anchorage.

In sum, the results presented herein constitute a proof of concept which can be adapted and scaled to different temperature demand. The operation time is limited by both the fuel addition and residues tanks which could be eventually replaced during operation.

Acknowledgements

Financial support is acknowledged from the Junta de Andalucía (grant PE2012-TEP862, EU co-financed by FEDER). This study was also supported by the Spanish Ministry of Science, Innovation and Universities and co-financed by EU FEDER funds under grant RTI2018-093871-B-100. The support of V. Gallardo and B. Sarmiento (Abengoa Hidrógeno) to the integration of the system electronic control is also acknowledged.

References

1. E.S. Hanley, J.P. Deane, B.P.Ó. Gallachoir, Int. Sustain. Energy Rev. **82**, 3027 (2018)

2. L. Shlapbach, A. Züttel, Nature **414**, 353 (2001)
3. J. O. 'M. Bockris, Int. J. Hydrogen Energy **38**, 2579 (2013)
4. P. Nikolaidis, A.Poullikkas, Renew. Sustain. Energy Rev. **67**, 597 (2017)
5. T.S. Veras, T.S. Mozer, D.C. Rubin Messender dos Santos, A.S. Cesar, Int. J. Hydrog. Energy **42**, 2018 (2017)
6. H. Jiang, S.K. Singh, J. Yan. X. Zhang, Q. Xu, ChemSusChem **3**, 541 (2010)
7. P. Brack, S.E. Dann, K.G. Upul Wijayantha, Energy Sci Eng **3**, 174 (2015)
8. U.B. Demirci, Energy Technol **6**, 470 (2018)
9. D.M.F. Santos, CAC Sequeira, Int J Hydrogen Energy **35**, 9851 (2010)
10. W. Chen, L.Z. Ouyang, J.W. Liu, X.D. Yao, H. Wang, Z.W. Liu et al. J. Power Sources **359**, 400 (2017)
11. U.B. Demirci, O. Adkim, J. Andrieux, J. Hannauer, R. Chamoun, P. Miele, Fuel Cells **10**, 335 (2010)
12. G.M. Arzac, A. Fernández, A. Justo, B. Sarmiento, M.A. Jiménez, M.M. Jimenez, Journal of Power Sources **196**, 4388 (2011)
13. G.M. Arzac, D.Hufschmidt, M.C. Jiménez de Haro, A. Fernández, B. Sarmiento, M.A. Jiménez, M.M Jiménez, Int. J. Hydrogen Energy **37**, 14373 (2012)
14. G.M. Arzac, D.Hufschmidt, E. Jiménez-Roca, A. Fernández, M.A. Jiménez *et al*. Process for the production of hydrogen through catalytic hydrolysis on a continuous reactor designed for this procedure. Spanish Patent application P201230221. Priority date 14-Feb-2012. Presented by Abengoa Hidrógeno S.A.
15. M. Haruta, H. Sano, Int. J. Hydrogen Energy **7**, 737 (1982)
16. W. Choi, S. Kwon, H. D. Shin, Int. J. Hydrogen Energy **33**, 2400 (2008)
17. C. Zhang, J. Zhang, J. Ma, Int. J. Hydrogen Energy **37**, 12941 (2012)
18. A. Cybulski, J.A. Moulijn, *Structured Catalysts and Reactors* (CRC Press, 2nd edition, 2005)
19. S.S. Muir, X. Yao, Int J. Hydrogen Energy **36**, 5983 (2011) and references therein
20. U.B. Demirci, P.Miele **12**, 14665 (2010) and references therein
21. G.M. Arzac, T.C. Rojas, A. Fernández, ChemCatChem **3**, 1305 (2011)
22. F. Giarratano, G.M. Arzac, V. Godinho, D. Hufschmidt, M.C. Jiménez de Haro, O. Montes, A. Fernández, Appl. Catal. B: Environmental **235**, 168 (2018)
23. A. Fernández, G.M. Arzac, U.F. Vogt, F. Hosoglu, A. Borgschulte, M.C. Jimenez, O. Montes, A. Züttel, Appl. Catal. B: Environmental **180**, 336 (2016)

Ammonia-based Solid Oxide Fuel Cell for zero emission maritime power: a case study.

Simona Di Micco[1,*], *Mariagiovanna* Minutillo[2], *Luca* Mastropasqua[3], *Viviana* Cigolotti,[4] *Jack* Brouwer[3]

[1]Univerisity of Naples "Parthenope", Naples, Italy
[2]Department of Industrial Engineering, University of Salerno, Salerno, Italy
[3]National Fuel Cell Research Center, University of California, Irvine, CA 92697-3550, United States
[4]ENEA - Italian National Agency for New Technologies, Energy and Sustainable Economic Development, Naples, Italy

Abstract. Implementing environmentally friendly fuels and high efficiency propulsion technologies to replace the Internal Combustion Engine (ICE) fueled by fossil fuels such as Heavy Fuel Oil (HFO) and Marine Gas Oil (MGO) on board ships represents an attractive solution for maritime power. In this context, fuel cells can play a crucial role, thanks to their high energy efficiency and ultra-low to zero criteria pollutant emissions and environmental impact.

This paper performs the technical feasibility analysis for replacing the conventional diesel engine powertrain on board a commercial vessel with an innovative system consisting of ammonia-fuel-based Solid Oxide Fuel Cell (SOFC) technology.

Taking into account the size of the diesel engines installed on board and the typical cruise performed by the commercial vessel, the ammonia consumption, as well as the optimal size of the innovative propulsion system have been assessed. In particular, the SOFC powertrain is sized at the same maximum power output as the main reference diesel engine. The mass and energy balances of the ammonia-based SOFC system have been performed in Aspen Plus^{TM} environment. The gravimetric (kWh kg^{-1}) and volumetric (kWh m^{-3}) energy density features of the ammonia storage technology as well as the weight and volume of the proposed propulsion system are evaluated for verifying the compliance with the ship's weight and space requirements. Results highlight that the proposed propulsion system involves an increase in weight both in the engine room and in the fuel room compared to the diesel engine and fuel. In particular, a cargo reduction of about 2.88% is necessary to fit the ammonia-based SOFC system compared to the space available in the reference diesel-fueled ship.

1 Introduction

Maritime transport is one of the largest greenhouse gas (GHG) emitting sectors of the global economy, responsible for around 1 Gt of $CO_{2,eq}$ every year [1,2]. It is responsible for 10–15% of anthropogenic sulfur (SO_x) and nitrogen oxide (NO_x) emissions, as well as approximately 3% of the carbon dioxide (CO_2) emissions [3]. The stringent demands by the national and international authorities to reduce the environmental footprints of the shipping industry have pushed the industry towards the use and adoption of cleaner power sources as well as alternative fuels. As matter fact, the International Maritime Organization (IMO) has set ambitious goals to reduce, and eventually eliminate, greenhouse gas (GHG) emissions from international shipping [4]. Decarbonizing the maritime sector involves changes in onboard energy storage and in energy conversion systems. Therefore, the introduction of innovative technologies as well as of carbon-free fuels both on ships and in ports, can pave the way for reducing the emissions [5–8].

In this regard, new energy conversion technologies such as fuel cells can represent the key element for the decarbonization in the maritime sector [9–12]. Several studied demonstrated the viability of using FCs, H_2 and H_2 carriers in oceanic going vessels (OGVs).

Demonstration projects are underway to highlight the viability of H_2 and H_2 carriers to power ships using FCs.

The METHAPU [13] (Methanol auxiliary power unit) project foresees the implementation of a 20 kW SOFC (solid oxide fuel cell) system fed by methanol on board a Roll-on/Roll-off (RoRo) vessel. The SOFC system comprised a methanol tank, a reformer, the SOFC stack, a catalytic combustion afterburner and in-process heat exchangers.

The FELICITAS project [14], foresees to develop and to test a 250 kW LNG-powered stationary SOFC system. In addition, the coupling of SOFC system with a gas turbine and the heating, ventilation and air conditioning systems is examined.

The E4Ships SchIBZ project [15] studies a hybrid power system combining a 50 kW containerized SOFC unit with lithium-ion battery packs. It is developed for the auxiliary

* Corresponding author: simona.dimicco@studenti.uniparthenope.it

power supply onboard the general cargo ship MS Forester. The hybrid power system consists of a diesel tank, a water tank, a reformer, the SOFC stack, a catalytic combustor and lithium-ion battery packs to compensate the fluctuations of the electrical loads and power electronics.
Several studies available in literature analyze the possibility of installing fuel cells on board ships.
Dall'Armi et al. [16], proposed a process simulation study to analyze the peak shaving services that a hybrid PEMFC/Li-ion battery propulsion system can provide to a small RoRo vessel and to a passenger ferry. They also evaluated different compressed hydrogen storage solutions depending on the cruise duration.
Di Micco et al. [17] developed a techno-economic feasibility analysis for integrating a polymer electrolyte membrane fuel cell (PEMFC) technology on board Ro-Pax ferry, considering two different hydrogen storage technologies (GH_2 and LH_2). Results highlighted that, although both the hydrogen solutions were suitable in terms of weight and volume, the number of voyages (without refueling) were drastically reduced.
Strazza et al. [18] analyzed the methanol-fueled SOFCs as an on-board auxiliary system.
Gianni et al. [19] analyzed the possibility to install PEMFC and SOFC onboard a cruise vessel. They observed that the installation of PEMFC or SOFC systems, involves an increase of the space in engine and fuel rooms.
De Baldasano et al. [20] investigated a hybrid plant based on diesel engine and methane fueled SOFCs for an offshore support vessel, where the fuel cell unit is used during slow cruising operations and feature a power output four times smaller compared to the main engine.
Haseltalab et al. [21] developed a new approach to enable the use of SOFC fed by Liquid Natural Gas (LNG) as the main power source on board vessels. Results demonstrated that the integration of the SOFC with the propulsion system allowed to yield up to 53% CO_2 reduction and 21% higher fuel utilization efficiency compared to conventional diesel-electric vessels.
According to this background, it is possible to perceive the great interest in developing fuel cell-based powertrain system on board ships, even if several issues, from technical and economic points of view, must be further analyzed in depth.
In this work, the technical feasibility replacement analysis of a conventional diesel engine powertrain with an innovative power system consisting of ammonia-based SOFC technology, is presented. The analysis is carried out by comparing the two powertrain solutions in terms of volumes and weights onboard a commercial vessel.
The system design and the energy balance assessment are performed by using a simulation model developed in Aspen Plus™ environment.

2 Vessel description and operation

The selected commercial vessel is equipped with a 8.3 MW main engine (ME) and 2.8 MW auxiliary engines (AEs) [22,23]. During the navigation the load demand is approximately constant and the auxiliary engines are used for docking/in-port operation and for satisfying the electric demand. Table 1 shows the general characteristics of the target vessel and Table 2 lists the volume and weight of the engines currently installed on board.

Table 1. General characteristics of the target vessel [24]

Engine Room Volume (m^3)	3,276.0
Engines Weight (ton)	107.1
Fuel Room Volume (m^3)	1,646.0
Fuel Room Mass Capacity (ton)	1,374.4

Table 2. Diesel engine system technical characteristics

Equipment	Volume (m^3)	Weight (tons)
Main Diesel Engine [25,26]	140.4	84.9
Auxiliary Diesel Engines [26,27]	17.6	22.2
Total	158.0	107.1

Fig.1 depicts the vessel load profile as percentage of the operating power compared to the total installed power during its typical cruise, which has a duration of about 240 hours.

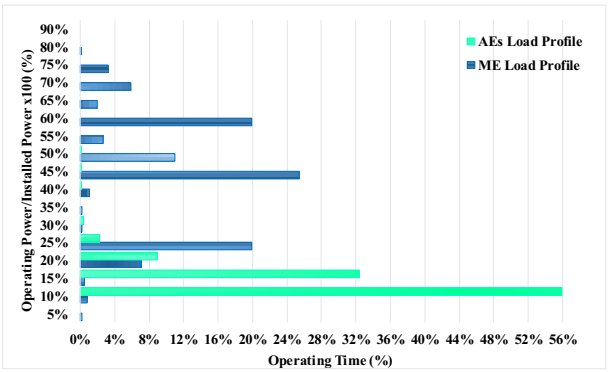

Fig. 1. Vessel load profile during its typical cruise (240 hours).

It is possible to notice that ME works at 45% of it nominal power capacity for 26% of the cruise duration, and it works at 75% for only 3% of the total time.

3 Powertrain system based on NH_3-SOFC technology

Fig.2 illustrates the schematic concept of the proposed powertrain system based on NH_3-SOFC technology. Ammonia, stored in liquid form, is vaporized and sent to the SOFC, for the power generation. To regulate the voltage from the SOFC, a DC/DC converter is applied after the cell. A DC/AC inverter is considered, since the electric motor is supplied in AC. Downstream the AC switchboard, a transformer is needed, to supply the electric utilities according to the different type of load.
The electric power needed for the electric motor is regulated with a frequency converter, which allows to operate for the entire range of speeds. The electric motor is connected to the propeller shaft by means of a gearbox. The efficiencies of these components have not been considered in this analysis.

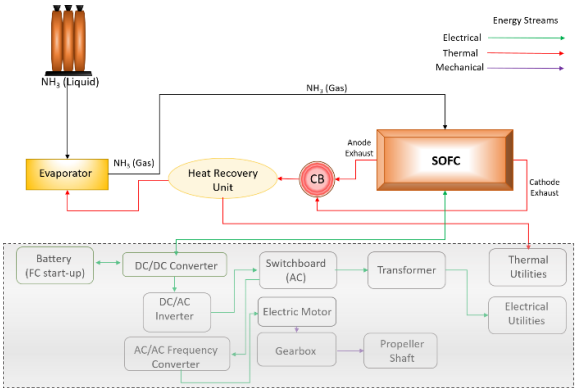

Fig. 2. Layout of NH_3-SOFC based powertrain system.

To perform the feasibility replacement analysis, for the ammonia storage the cryogenic tank developed by Linde is taken into account [28] (Table 3).

Table 3. Ammonia ISO T50 storage tank characteristics [28]

Technical data	LNH_3
External Diameter (mm)	2,500.0
Length (mm)	4,480.0
Empty Weight (kg)	11,500.0
Internal Volume (m^3)	22.0

As far as the SOFC module is concerned, the 300 kW module developed by Bloom Energy is taken into account [29].

This module is designed to be fed by natural gas (nominal condition 56.9 m^3/h). Therefore, in this study we calculated the produced nominal electric power feeding the SOFC module with the same NH_3 volumetric of natural gas (56.9 m^3/h), assuming the same conditions in terms of module volume and weight.

3.1 System modeling

The fuel cell power module and the BOP are modeled in Aspen Plus™ environment. Fig. 3 illustrates the flowsheet of the model. The ammonia, stored at 20 °C and 8.8 bar, is vaporized (HE-1) and preheated (HE-2) by using the exhaust gasses (25) coming from the catalytic burner (B2). In the throttling valve (B9) the ammonia expands before entering the anode side of the fuel cell. The exhaust gasses, before being vented to the atmosphere, are used both to preheat (HE-3) the cathodic air (AIR) and to generate (HE-4) steam for thermal loads onboard the vessel. In order to simulate the SOFC behavior from a thermodynamic point of view, the anode and the cathode are modeled by using some components, as suggested by the authors in a previous paper [30]. Table 4 describes these components.

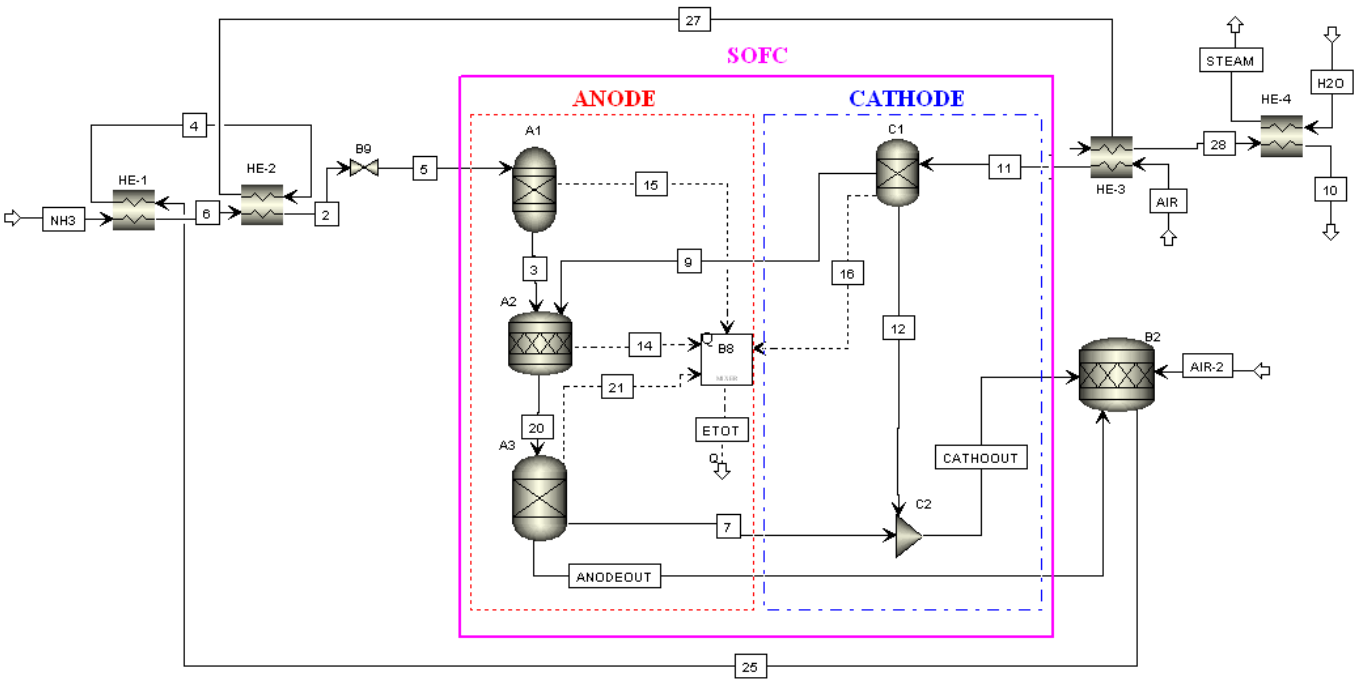

Fig. 3. NH_3-SOFC system model adapted from [30]

Table 4. Electrodes Modeling

Electrode	Aspen Components
Anode	Gibbs reactor (A1): in this reactor the ammonia cracking (46kJ/mol NH_3) occurs: $2NH_3 \rightarrow 3H_2 + N_2$ Stoichiometric reactor (A2): in this reactor the hydrogen oxidation is carried out: $H_2 + \frac{1}{2}O_2 \rightarrow H_2O$ Separator (A3): the unreacted oxygen is separated to be again mixed to nitrogen.
Cathode	Separator (C1): the oxygen is separated by nitrogen and sent to the anode side for reacting with hydrogen Mixer (C2): the unreacted oxygen is mixed with the nitrogen to get the right cathode off-gas composition.

The single cell polarization curve (Figure 4), implemented in a Fortran block calculator for estimating the fuel cell electrical performance, is taken from ref. [31]. Table 5 summarizes the fuel cell nominal operating data suggested in [31]. Finally, a thermal mixer block (B8) is used to solve the energy balance of the SOFC.

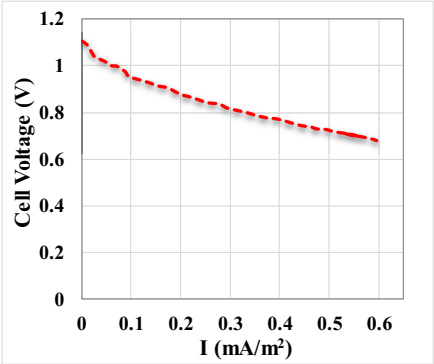

Fig. 4. NH3-SOFC module polarization curve

Table 5. NH_3-SOFC module operating data [31]

Active area (cm^2)	500
Stacks Temperature (°C)	750
UF	0.80
Cell Voltage (mV) at nominal power	714
Current density (mA/cm^2) at nominal power	513
Cell electric power (W)	183

4 Results and discussion

Results of the proposed analysis concern: i) the calculation of the NH_3-SOFC module produced nominal electric power; ii) the assessment of the thermodynamic condition for the NH_3-SOFC layout; iii) the feasibility of replacing the proposed system in terms of volume and weight for both the engine and fuel rooms.

4.1 NH_3-SOFC nominal electric power

Taking into account the characteristics of the selected SOFC module, we calculated the produced nominal electric power feeding the SOFC module with the same NH_3 volumetric of natural gas (56.9 m^3/h), assuming the same conditions in terms of module volume and weight. It results to be 118.3 kW instead of 300 kW. Table 6 lists the main characteristics of the selected SOFC module.

Table 6. SOFC module characteristics [29]

Technical data	Fuel Cell Module
Length (m)	7.8
Breadth (m)	2.6
Height (m)	2.3
Mass (tons)	15.8
Nominal power-NH_3 (kW)	118.3

Taking into account these data, for sizing the SOFC system, we have assumed that the nominal power capacity of the SOFC powertrain matches the one of the reference main diesel engine (i.e., 8.3 MW). Consequently, the SOFC powertrain system is made up of 71x118.3 kW units.

4.2 Modeling results

Starting from the performance of the single NH_3-SOFC module, the thermodynamic conditions for each point of NH_3-SOFC system are assessed. Results, referred to the nominal operating condition, are summarized in Table 7.

Table 7. Thermodynamic condition of NH_3-SOFC system

Flows	Mass flow rate (kg/s)	T (°C)	P (bar)	Composition
NH_3	0.86	20	8.8	NH_3-100%
2	0. 86	600	8.8	NH_3-100%
3	0. 86	750	1.1	H_2-75%, N_2-25%
4	31.75	807	1.1	N_2-76.9%, O_2-16.5%, H_2O-6.6%
5	0. 86	600	1.1	NH_3-100%
6	0. 86	21	8.8	NH_3-100%
7	6.08	750	1	O_2-100%
9	7.04	750	1.1	O_2-100%

10	31.75	152	1.1	N_2-76.9%, O_2-16.5%, H_2O-6.6%
11	30.24	650	1.1	N_2-79%, O_2-21%
12	23.20	750	1.1	N_2-100%
20	7.90	750	1.1	O_2-65.5%, H_2O-20.7%, N_2-8.6%, H_2-5.2%
25	31.75	833.6	1.1	N_2-76.9%, O_2-16.5%, H_2O-6.6%
27	31.75	773.7	1.1	N_2-76.9%, O_2-16.5%, H_2O-6.6%
28	31.75	215.7	1.1	N_2-76.9%, O_2-16.5%, H_2O-6.6%
AIR	30.24	20	1.1	N_2-79%, O_2-21%
AIR-2	0.65	20	1.1	N_2-79%, O_2-21%
ANODE OUT	1.82	750	1.1	N_2-25%, H_2-15%, H_2O-60%
CATHODE OUT	29.28	750	1.1	N_2-81.3%, O_2-18.7%
H_2O	0.49	20	1.1	H_2O-100%
STEAM	0.49	120	1.1	H_2O-100%

4.3 Replacement Analysis

The replacement analysis takes place by assessing the feasibility of installing the proposed system according to the available volume and the mass capacity of both the engine and fuel rooms. The weight and volume of the proposed propulsion system is assessed and compared with the ones of the diesel engine system (see Table 2). Taking into account the typical cruise performed by the selected vessel, the ammonia weight and volume needed to complete the journey are calculated and compared with the diesel.

4.3.1 Technical feasibility: engine room

The volume and the weight of each component of the proposed powertrain system are listed in Table 8.

Table 8. Equipment Volume and Weight

Equipment	Volume (m^3)	Weight (tons)
SOFC (71 modules)[29]	3451.9	1121.8
Propulsion Motor [25]	30	20
Converter [25]	2.7	1
Inverter [25]	4	2
Variable Freq. Drive (VFD) [25]	31	8
Heat Exchangers	27.1	19.2
BOP	46.9	21.2
Total	3581.2	1183.7

Comparing the results of tables 2-8, it can be noticed that the NH_3-SOFC powertrain system occupies approximately a space 22 fold-higher with respect to the diesel engine, and exceeds the available volume of the engine room of about 9%. As far as the weight is concerned, the proposed system overcomes the weight of the diesel engine system of about 91%.

4.3.2 Technical feasibility: fuel room

In order to perform the feasibility replacement analysis in the fuel room, it is needed to calculate the ammonia consumption for the considered cruise.
The ammonia consumption (C_{NH_3}) in each load condition (i) has been calculated as reported in [32]:

$$C_{NH_3}(i) = \frac{L_f(i) \cdot W_{SOFC}}{LHV_{NH_3} \cdot \eta(i)} \quad (3)$$

where, W_{SOFC} is the nominal power of the SOFC system, L_f is the load factor of the chemical tanker (Fig. 2), LHV_{NH_3} represents the ammonia lower heating value (18.8 MJ/kg), and η is the SOFC efficiency (Fig.3).
Therefore, considering the fuel cell operation during the cruise (240 hours), the total ammonia consumption (TC_{NH_3}) has been calculated as:

$$TC_{NH_3} = \int_0^{t_f} \frac{L_f(i) \cdot W_{SOFC}}{LHV_{NH_3} \cdot \eta(i)} dt \quad (4)$$

Taking into to account Eqs. 3-4, the overall ammonia consumption during the cruise is 240.2 tons. By assuming a fuel margin percentage of 10% for safety conditions, the needed ammonia amount to be stored on-board is 264.2 tons.

Considering the weight and the volume of the ammonia storage tanks (see table 3) the total volume and weight of stored ammonia is calculated. Fig.5 compares the weight and volume of the ammonia with the diesel, needed for the selected cruise.

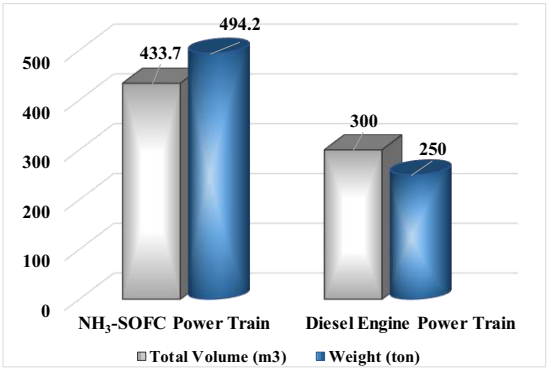

Fig. 5. NH_3-diesel weight and volume comparison

It can be noticed that, even if the volume of stored ammonia is 1.4 times higher with respect to the diesel, it is in accordance with the available volume in the fuel room. The weight of the storage technology represents the critical issue since, even if the ammonia consumption is quite similar to the diesel one (264.2 tons vs 250 tons), the storage technology involves a weight increase of about 49% (494.2 tons vs 250 tons).

Therefore, considering the weight increasing both in the engine room and in the fuel room, for installing the proposed system on board the vessel, a cargo reduction is needed. In particular, it has been calculated a cargo reduction of about 2.88%.

5 Powertrain Systems Comparison

Fig.6 compares the NH_3-SOFC system with the diesel one in terms of weight incidence of the equipment.

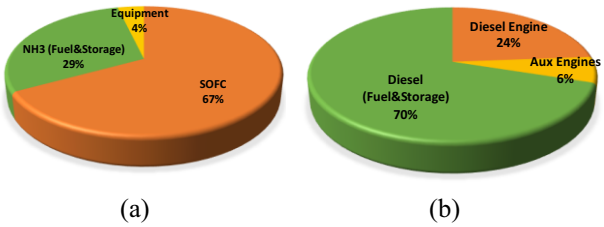

Fig. 6. NH_3-diesel weight incidence equipment comparison

It is worth noticing the greatest incidence of the SOFC weight (67%) with respect to the diesel engine system (24%), which represents the most critical issue for the cargo reduction.

Conclusion

In this paper the feasibility analysis for the integration of a solid oxide fuel cells fed by ammonia as propulsion system on-bard a commercial vessel, is carried out.

The NH_3 based-SOFC system is designed to completely replace the main diesel engine as well as the auxiliary engines, with 71 units of 118 kW each.
The results show that the proposed system occupies a space in the engine room 22 time higher with respect to the diesel engine, and exceeds the available volume of the engine room of about 9%. In terms of weight, the NH_3 based-SOFC system overcomes the weight of the diesel engine system of about 91%.

The volume of stored ammonia is 1.4 times higher with respect to the diesel but it is consistent with the available volume in the fuel room. The critical issue is represented by the weight of the storage technology. As matter of fact, even if the ammonia consumption is quite similar to the diesel one (264.2 tons vs 250 tons), the storage technology involves a weight increase of about 49% (494.2 tons vs 250 tons).

Therefore, taking into account the weight increasing both in the engine room and in the fuel room, installing the proposed system on board the commercial vessel, requires a cargo reduction of about 2.88%.

References

1. S. De Bruyn, M. Bijleveld, L. de Graaff, E. Schep, A. Schroten, R. Vergeer, and S. Ahdour, CE Delft 175 (2018)
2. K. Anderson and G. Peters, Science (80-.). **354**, 182 (2016)
3. K. Y. Bjerkan and H. Seter, Transp. Res. Part D Transp. Environ. **72**, 243 (2019)
4. D. Rutherford and B. Comer, Int. Counc. Clean Transp. 8 (2018)
5. E. A. Bouman, E. Lindstad, A. I. Rialland, and A. H. Strømman, Transp. Res. Part D Transp. Environ. **52**, 408 (2017)
6. S. Integration, H. Rail, and M. Applications, (2020)
7. S. Karimi, M. Zadeh, and J. A. Suul, IEEE Electrif. Mag. **8**, 47 (2020)
8. A. Ritari, J. Huotari, J. Halme, and K. Tammi, Energy (2020)
9. H. Bach, A. Bergek, Ø. Bjørgum, T. Hansen, A. Kenzhegaliyeva, and M. Steen, Transp. Res. Part D Transp. Environ. **87**, 102492 (2020)
10. A. Bergek, Ø. Bjørgum, T. Hansen, J. Hanson, and M. Steen, 9th Int. Sustain. Transitions Conf. 1 (2018)
11. X. Mao, D. Rutherford, L. Osipova, and B. Comer, (2020)
12. A. E. Georgeff, X. Mao, D. Rutherford, D. Ph, L. Osipova, and D. Ph, (2020)
13. Fuel Cells Bull. **2008**, 4 (2008)
14. L. K. C. Tse, S. Wilkins, and R. F. Martinez-botas, EET-2007 Eur. Ele-Drive Conf. (2007)
15. (2016)
16. C. Dall'Armi, D. Micheli, and R. Taccani, Int. J. Hydrogen Energy **46**, 13878 (2021)
17. S. Di Micco, M. Minutillo, and A. Forcina, E3S Web Conf. **312**, (2021)
18. C. Strazza, A. Del Borghi, P. Costamagna, A. Traverso, and M. Santin, Appl. Energy **87**, 1670 (2010)
19. M. Gianni, A. Pietra, and R. Taccani, E3S Web Conf. **238**, 1 (2021)
20. M. C. Díaz-de-Baldasano, F. J. Mateos, L. R. Núñez-Rivas, and T. J. Leo, Appl. Energy **116**, 91 (2014)

21. A. Haseltalab, L. van Biert, H. Sapra, B. Mestemaker, and R. R. Negenborn, Energy Convers. Manag. **245**, 114625 (2021)
22. L. Starcrest Consulting Group, Long Beach, CA (2019)
23. L. Starcrest Consulting Group, *Port of Los Angeles 2019 Air Emissions Inventory. Los Angeles, CA 2019* (2019)
24. Marine Traffic: Global Ship tracking Intelligence.
25. K. Kim, G. Roh, W. Kim, and K. Chun, J. Mar. Sci. Eng. (2020)
26. MAN Diesel & Turbo, *Marine Engine Programme* (2020)
27. Wärtsilä Generating Sets. Available online., (2021)
28. The Linde Group datasheet-01-ammonia-June-2017_tcm17-417364, Datasheet
29. Bloom Energy Energy Server 5 PRODUCT DATASHEET Always On
30. A. Perna, M. Minutillo, and E. Jannelli, Energy Convers. Manag. **159**, 381 (2018)
31. A. Perna, M. Minutillo, E. Jannelli, V. Cigolotti, S. W. Nam, and J. Han, Appl. Energy **231**, 1216 (2018)
32. C. Raucci, T. Smith, and P. Dodds, The Potential of Hydrogen to Fuel International Shipping, 2017

Four years of operational data for five hydrogen refueling stations

Roberta Caponi[1*], *Andrea* Monforti Ferrario[2], *Enrico* Bocci[3], *Kristina* Fløche Juelsgaard[4]

[1]CIRPS, Interuniversity Research Center for Sustainable Development, 00152 Rome, Italy
[2]ENEA, Italian National Agency for New Technologies, Energy and Sustainable Economic Development, TERIN-PSU-ABI, 00123 Rome, Italy
[3]Department of Engineering Science, Guglielmo Marconi University, 00193 Rome, Italy
[4]Ballard Power Systems, Majsmarken 1, 9500 Hobro, Denmark

Abstract. Worldwide about 550 hydrogen refueling stations (HRS) were in operation in 2021, of which 38%. were in Europe. With their number expected to grow even further, the collection and investigation of real-world station operative data are fundamental to tracking their activity in terms of safety issues, performances, costs, maintenance, reliability, and energy use. This paper shows and analyses the parameters that characterize the refueling of 350 bar fuel cell buses in four HRS within the 3Emotion project. The HRS are characterized by different refueling capacities, hydrogen supply schemes, storage volumes and pressures, and operational strategies. From data logs provided by the operators, a dataset of three years of operation has been created. In particular total hydrogen quantity, the fill amount dispensed to each bus, the refueling duration, the average mass flow rate, the number of refueling events and the daily number of refills, the daily profile, the utilization factor, and the availability are investigated. The results show similar hydrogen amount per fill distribution, but quite different refueling times among the stations. The average daily mass per bus is around 12.95 kg, the most frequent value 15 kg, the standard deviation 7.46. About 50% of the total amount of hydrogen is dispensed overnight and the refueling events per bus are typically every 24 hours. Finally, the station utilization is below 30% for all sites.

1 Introduction

Supported by regulators, investors, and consumers, hydrogen is strongly emerging as one of the principal protagonists among the actors for the global shift towards a decarbonized road transportation system. The European Union has identified in its Hydrogen Strategy three phases to develop a mature hydrogen market by 2050 [1]. Instead, the United States Department of Energy has launched Hydrogen at Scale, an initiative that promotes R&D projects aiming at affordable hydrogen production, transport, storage, and utilization [2]. At the same time, China has listed hydrogen among the energy sources for the first time in its latest Energy Law [3]. Jointly, Japan and Korea have set aside substantial funds for hydrogen technology [4,5].

As of 2020, the number of fuel cell electric vehicles on the road were 35 800, with Korea becoming the leading country reaching more than 10 000 vehicles in circulation [6]. Complementarily, a sufficient hydrogen infrastructure has been established. Currently, there are around 550 Hydrogen Refueling Stations (HRS) worldwide. Of these 275 are located in Asia, around 200 HRS are in Europe – of which just a little less than half are in Germany – and 75 HRS are sited in the United States, mainly in California [7]. In the majority of the HRS the hydrogen is stored as a compressed gas at pressures up to 700 bar [8] and then delivered into the onboard vehicle tanks. To charge the pressurized storages, the stations are generally equipped with a compression system. An alternative solution is to store the hydrogen in liquified form. Although studies show that this configuration reduces the stations' footprint, capital and operating costs, the lack of a global assessment over the entire liquefaction chain and the poor performance of existing pumps slow down its application [9,10]. The compressed gas delivery is conducted either by tube trailers, in which the hydrogen is generally stored at a pressure of 200 bar or is transported from the point of production until the distribution point through pipelines at pressures between 30 and 80 bar [11,12]. Otherwise, the hydrogen can be produced locally via steam methane reforming or water electrolysis. In this case, along with the compressors, the stations include buffers, filters, and a purification system [13].

Over the last years, the body of literature on hydrogen infrastructure was expanded notably, among these [11,14–19]. Nevertheless, a study that shows the HRS operational performance in terms of hydrogen quantity delivered to the vehicle, refueling duration and station utilization applied to real-world stations has been less investigated. The study of Samuelsen et al. [20] presents the performance metrics of the 180 kg/day 700 bar University of California, Irvine HRS. The data collected are compared with the National Renewable Energy

* Corresponding author: author@e-mail.org

Laboratory (NREL) dataset for all HRS in the United States [21].

This paper illustrates and analyses the operational performances of five HRS involved within the European 3Emotion project [22] during three years of activity. The project plans for the deployment of 29 articulated fuel cell buses in four cities in the UK (London), the Netherlands (Rotterdam and Province of South Holland), France (Versailles, Pau), and Denmark (city of Aalborg). The stations are characterized by different refueling capacities (kg_{H2}/day), hydrogen supply schemes (in-situ production or delivery), storage volumes and pressures, and operational strategies. The ultimate aim is to provide a

global outlook of the actual functioning of small/medium size hydrogen stations, investigating their availability, capacity utilization and technical performance and benchmarking their status.

2 Case study: the 3Emotion project

The 3Emotion Project, which stands for Environmentally friendly Efficient Electric Motion, envisages the establishment of a pan-European consortium for the deployment of 26 new buses in addition to 8 existing buses and the realization of 3 new HRS. The buses and the HRS operate in 5 leading cities: Aalborg (DK), London (UK), Pau (FR), Rotterdam (NL), Versailles (FR). By considering the lesson learned from past fuel cell bus projects, 3Emotion aims to enhance the number of operators involved paving the way to commercialization.

The sites were selected so that the most effective commercialization impact is reached, ensuring the implementation of the hydrogen refueling stations with a different supply (hydrogen is provided via pipeline in Rotterdam, by trailers in London and Versailles, and is produced locally via electrolysis in Pau and Aalborg). In addition, the HRS refuel buses of different size fleets (3 to 10 buses) that are used in different environmental conditions (urban and extra-urban roads). The design capacity is smaller for the on-site stations, 100 kg/day in Aalborg and 174 kg/day in Pau. Rotterdam and Versailles sites have both a capacity of 200 kg/day. The largest station is London, capable of dispensing 400 kg/day. All the stations are equipped with a dispenser to refuel the bus at 350 bar, whilst the Dutch and Versailles sites are the only ones that were realized with the possibility to refuel cars at 700 bar. The project aims to reach the following objectives concerning the stations' performance:

- Bus capacity 16 kg_{H2}/refueling once a day
- Refueling time 10-15 minutes
- Refueling station capacity 200-350 kg_{H2}/day
- Availability of the station 98%
- Station production efficiency >70%

3 Methods

Except for Versailles, the operational data on which this study is based have been taken from excel logbooks spreadsheets that monitor the bus refueling. The site operators fill the logbooks manually, later sharing the information to be analyzed. The spreadsheets provide qualitative and quantitative data with daily frequency and, when possible, divided by bus number. In particular, the refueling data include: date (dd:mm:yy), hour (minutes), hydrogen dispensed per fueling event (kg), refueling duration (minutes). Although, this last data cannot be obtained in the Rotterdam site. For the Aalborg station, the data on the electrolyzer operation (hydrogen produced, electricity and water consumption) were also collected and investigated. The HRS data for the Versailles come from quarterly reports provided by AirLiquide in which a preliminary aggregated analysis about the charging distribution over the day, the total and per filling quantity dispensed, the duration, and the availability divided into months are presented.

Due to slight but still relevant unevenness between the data and the activity period, further elaboration in Microsoft PowerBI was required. Indeed, London and Rotterdam were the first stations to start the operations, and their data are available from 2018. At the end of 2019 also the data collection in Versailles was put in place. The Aalborg HRS was delivered in December 2019, but it is not until March 2020 that it became fully operational. Finally, in Pau, the HRS was installed during summer 2019. However, due to the COVID pandemic, the HRS was on stand-by mode until August 2020, when its regular activity began. Albeit, it is not before summer 2021 that the HRS data transfer was set up. All the stations are currently running, except London, which has reached the demonstration goal in March 2020 and took the buses out of service.

The outcome is a complete and rich data set of four years of the real-world performance of hydrogen stations. In particular total hydrogen quantity, the fill amount dispensed to each bus, the refueling duration, the average mass flow rate, the number of refueling events and the daily number of refills, the daily profile, the utilization factor, and the availability are obtained and elaborated in Matlab, PowerBI and RStudio software.

4 Results

Fig. 1 shows the total quantity of hydrogen dispensed for each site. The longer period of operation allowed to build up a greater experience and the bigger bus fleet of London is the reason for the prevailing quantity dispensed, i.e., 67 209.9 kg, with respect to the other sites. Although, on

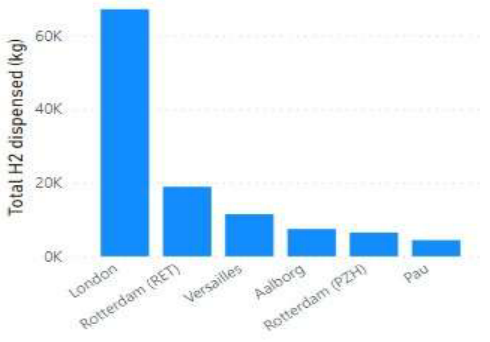

Fig. 1. Total quantity of hydrogen dispensed for each site.

Table 1. Total hydrogen amount dispended per site and relative specific values.

Site	Total H2 quantity (kg)	Bus fleet (#)	Specific H2 dispensed (kg/bus)
London	67 209.90	10	6 720.99
Rotterdam (RET)	18 917.23	2	9 458.61
Rotterdam (PZH)	6 446.12	4	1 611.53
Versailles	11 470	7	1 638.57
Aalborg	7 421.62	3	2 473.87
Pau	4 396.77	8	549.59

specific terms (hydrogen dispensed per bus), the highest amount of hydrogen was dispensed by the transport operator RET in Rotterdam. At the same time, the results for the buses of the Province of South Holland (PZH) and Aalborg are nearly balanced (Table 1). The underperformance of the Pau site is because of the smallest period of available data.

Fig. 2 shows all the daily dispensed hydrogen per site and the relative rolling 30-day average. London HRS (Fig. 2a) is characterized by a reasonably stable quantity dispensed since the beginning of the operation in 2018. The drop observed from February 2020 is related to the progressive decommissioning of the station. The HRS has a maximum capacity of up to 400 kg/day, while the estimated bus demand is approximately 160 kg/day, leading to a lower utilization rate equal to 40% in nominal operating conditions. Furthermore, the data shows that the actual demand is substantially lower. In fact, the maximum total hydrogen mass refueled is 187.92 kg/day, with a mean value of 81.86 kg/day. As a consequence, the station capacity utilization achieves 26% at best.

With respect to the initial period of operation, the quantity of hydrogen dispensed in Aalborg (Fig. 2b) has gradually increased until the beginning of 2021. Subsequently, a component breaking in the dispenser that caused zero refueling events in January 2021, in addition to COVID-19, which strongly impacted the public transportation sector, led to a reduction of the station performance. The Aalborg HRS has a maximum capacity of up to 100 kg/day, while the estimated bus demand is approximately 90 kg/day. The data shows that the maximum total hydrogen mass refueled is 67.97 kg/day, with a mean value of 16.85 kg/day. Therefore, the station capacity utilization is, on average, just 18%.

In Rotterdam (Fig. 2c), several zero refueling strong affect the moving average, oscillating around 17 kg/day. Nevertheless, an improvement of the station performance is noticed from January 2021, after implementing the buses of a second operator and the total bus circulation recovery. The total HRS capacity is 200 kg/day, while the data shows that the maximum total hydrogen refueled is 103.58 kg/day. With respect to the average amount, the aggregate utilization rate is about 9%.

Finally, for what concerns the Pau site (Fig. 2d), the data related to just three months of operation show an increase of the mass dispensed at the beginning of September 2021, followed by a stable trend. The station is designed to provide 174 kg/day, in contrast the maximum total hydrogen refueled observed is more than 170 kg/day, the mean value is 72 kg/day, leading to a station utilization of about 41%.

In Fig. 3a), is plotted the probability density function of the hydrogen amount dispensed by refueling. The buses of PZH in Rotterdam are characterized by the highest mass quantity dispended, with the majority of the refuelings above 18 kg/fill. Conversely, Aalborg, Versailles, and London HRS distributions feature a pick in correspondence of around 16 kg/fill. On average the lowest fueling amount is provided to the buses of RET. Only 26% of the total refueling events are below 10 kg/fill. Fig 3b) shows the density function of the refueling

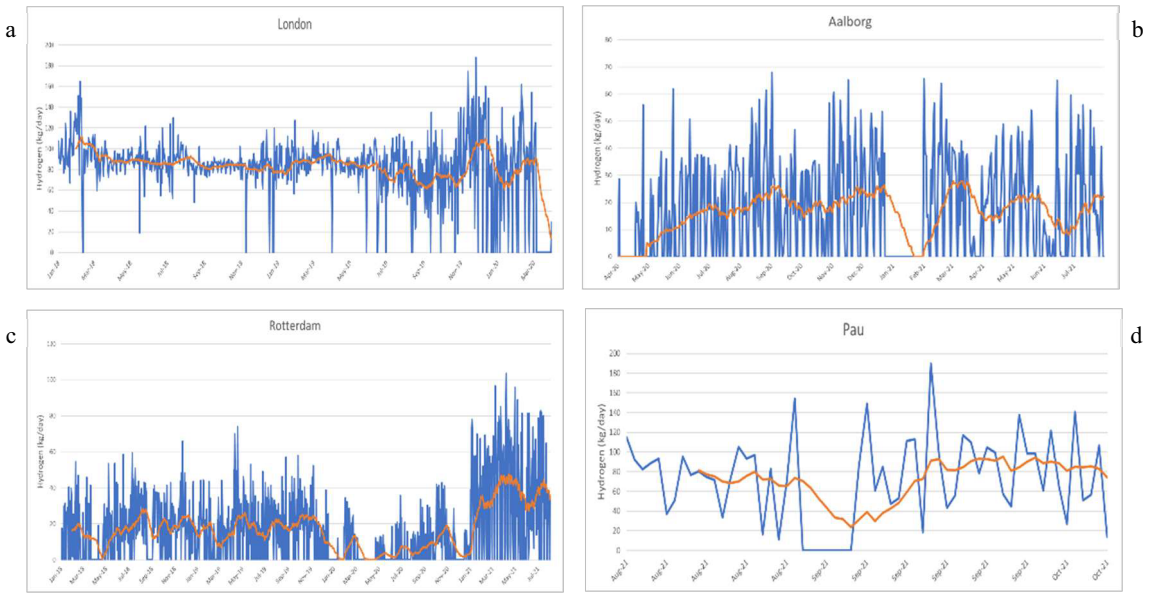

Fig. 2. Daily dispensed hydrogen and rolling 30-day average in the sites of London a), Aalborg b), Rotterdam c), and Pau d).

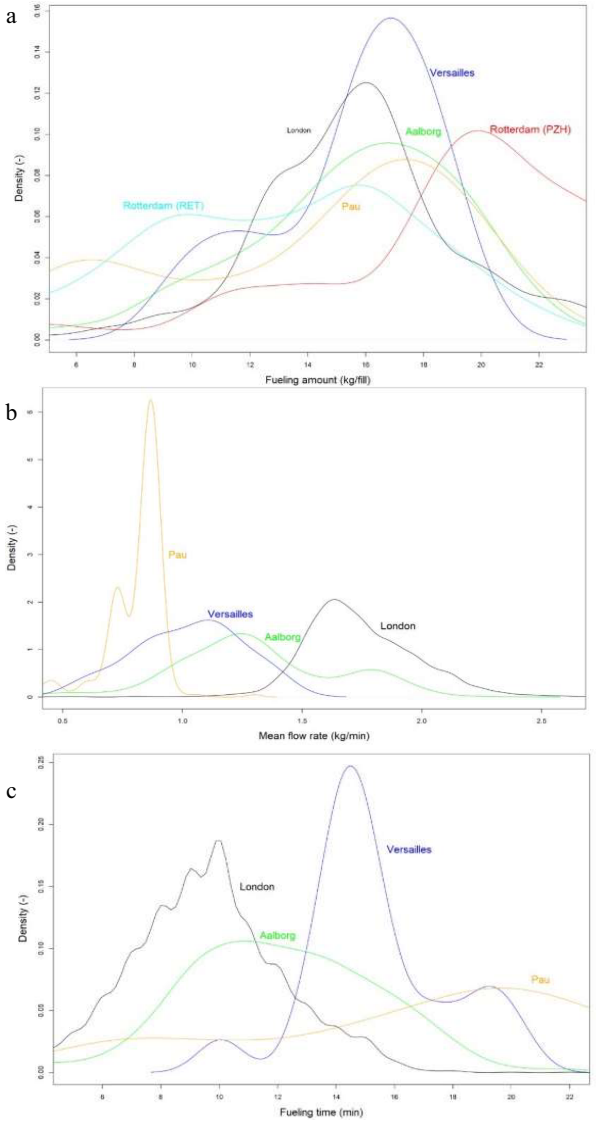

Fig. 3. Probability density function of the hydrogen quantities dispensed per fill a), duration b), and mean flow rates c).

duration. If the curve is shifted towards refueling above 15 minutes for Versailles and Pau, in Aalborg and London, the average oscillates around 11 minutes. Fig 3c) illustrates the mean mass flow rate distribution. The mean fueling rate in London is 1.74 kg/min, in Aalborg is 1.19 kg/min, in Pau is 0.80 kg/min, lastly in Versailles is 1.03 kg/min. No more than 7% of flow rates are greater than 2 kg/min, whilst the maximum value detected is 3.6 kg/min. The results are aligned with the protocol SAE J2601/2 requirements, which prescribes a maximum flow rate of 3.6 kg/min for heavy-duty vehicles [23]. More detailed information on the mean, mode, standard deviation and the 50th percentile for the three parameters analyzed above are reported in Table 2.

Fig 4 shows the correlation between the refueling time and the mass dispensed per fill during the years. In 2018 and 2019 only the stations of London and the buses of RET were running. In that period, recurrent zones are noticed in correspondence of 15 to 18 kg/fill and around 10 minutes. With the implementation of the other stations, the results show a concentration of the number of refills

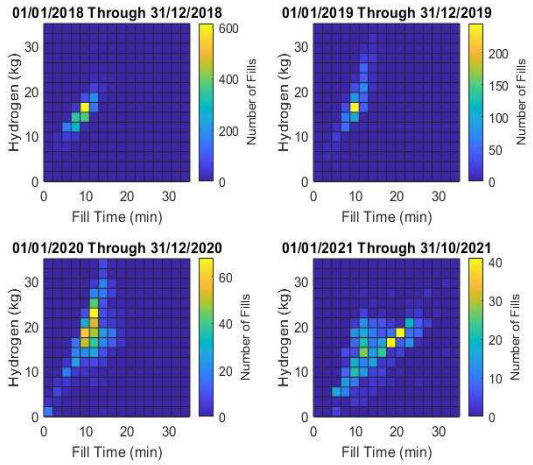

Fig. 4. Correlation of the hydrogen amount per fill vs. refueling duration during the years of operation.

between 15 to 25 kg/fill and 10 to 20 minutes, which means that the buses are refueled mainly by half-tank.

The daily load dispensing profiles with a one-hour resolution for the different sites is shown in Fig. 5. In London, Rotterdam (RET) e Pau, the buses are refueled overnight to secure capacity and availability. In particular, the majority of the refueling events are focused from 8 pm to 1 am, coinciding with about 50% of the total amount dispensed. Peaks of the refuelings are observed at 8 pm (6 248.36 kg_{H2}), 11 pm (8 364.63 kg_{H2}) and at midnight (7 326.77 kg_{H2}). Aalborg HRS mainly operates in the early morning and evening hours, especially between 3 am-5 am (1 915.18 kg_{H2}) and from 8 pm-10 pm (1 805.66 kg_{H2}). Contrarily, in Rotterdam (PZH), the refuellings are centralized in the morning, with peaks occurring at 7 am (2 225.28 kg_{H2}), and 9 am (1 784.17 kg_{H2}). In general, all the sites execute top-up refuelings throughout the day.

Finally, Fig. 6 shows the density function of the time between refuelings per site. Except for Aalborg, 50% of the fills per bus occur with a distance of 24 hours from the last refueling event. The data also shows recurrent zones in correspondence of 48 hours, thus the buses are frequently refueled two days apart. In Aalborg, the 50th percentile is 11.3 hours since it is referred not to single bus refilling but to all the events occurring at the station.

5 Conclusions

In this study, the operational performances of five hydrogen refueling stations within the 3Emotion project are presented. The analysis covers a total period of four years, even though differences within the stations' activity timeframe subsist. The results show a similar hydrogen amount per fill distribution, but quite different refueling times among the stations. The average daily mass per bus is around 14.43 kg, the most frequent value 15 kg, the standard deviation 5.05, the 50th percentile is 14.85 kg. Conversely, the average refueling time is 10.28 minutes, the mode is 10 minutes, the standard deviation is 3.26, the 50th percentile is 10 min. The average flow rate is around

Table 2. Mean, mode and standard deviation of the filled mass, refueling time and flow rate for all the sites.

Site	Mean			Mode			St deviation			50th percentile		
	Mass (kg)	Time (min)	Flow (kg/min)	Mass (kg)	Time (min)	Flow (kg/min)	Mass (kg)	Time (min)	Flow (kg/min)	Mass (kg)	Time (min)	Flow (kg/min)
London	12.58	9.55	1.74	15	10	1.66	8.39	5.03	0.82	15.95	10	1.71
Rotterdam (RET)	12.60	-	-	15	-	-	5.45	-	-	13.36	-	-
Rotterdam (PZH)	18.73	-	-	19	-	-	5.68	-	-	19.76	-	-
Versailles	15.53	15.34	1.02	15.8	14	1.13	2.88	2.43	0.22	15.8	14.57	1.09
Aalborg	14.23	11.77	1.19	15	11	1.32	6.03	6.26	0.48	15.84	12	1.25
Pau	14.08	16.77	0.80	17.03	21	0.88	5.75	6.59	0.14	15.83	18	0.85

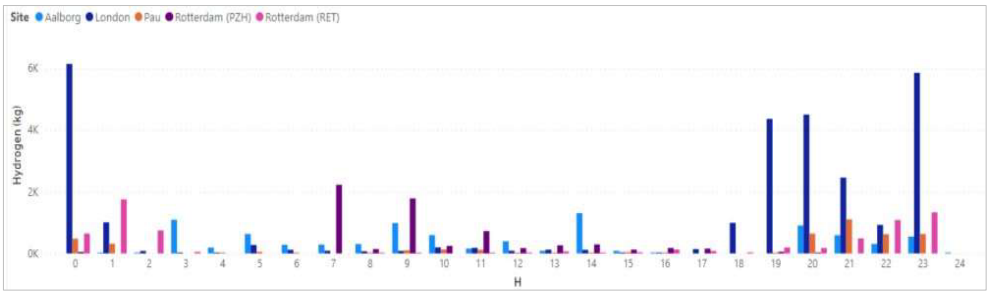

Fig. 5. Daily resampling of the hydrogen refueled amount in hourly resolution

1.68 kg/min, which is compatible with the limitations of the SAE J2601-2 maximum value of 3.6 kg/min for slow filling. The hourly dispensing profiles show that, in general, the majority of the refueling are performed overnight from 8 pm to 3 am to secure capacity and availability. Still, all the sites execute top-up fills throughout the day. Typically, the buses are refueled every 24 hours. From the investigation of the station capacity utilization, the actual demand is substantially lower than the planned maximum capacity. Indeed, the station utilization is below 30% for all the sites. Therefore, this study illustrates the HRS capability to sustain larger fleets than the current, ensuring future hydrogen bus fleets ramping up potentiality.

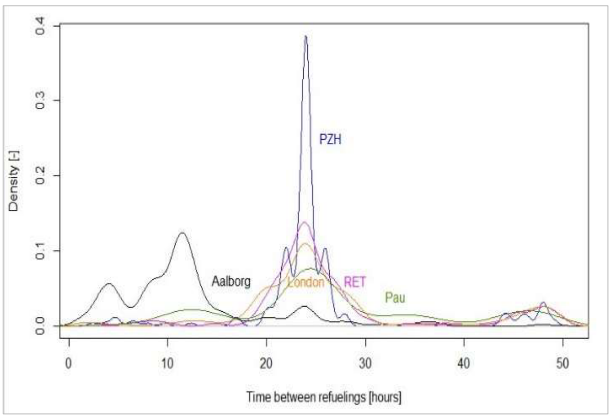

Fig. 6. Probability density function of time between refuelings.

This work was supported by CIRPS (Centro Interuniversitario per lo Sviluppo Sostenibile) and the FP7-JTI 3Emotion Project [Grant ID 633174].

References

[1] Chatzimarkakis J, Levoyannis C, van Wijk A, Wouters F. Hydrogen Act Towards the creation of the European Hydrogen Economy. 2021.
[2] Pivovar B, Rustagi N, Satyapal S. Hydrogen at Scale (H2@Scale): Key to a Clean, Economic, and Sustainable Energy System. Electrochem Soc Interface 2018:27:47-52. https://doi.org/doi:10.1149/2.F04181if.
[3] King & Wood Mallesons. Prospects for hydrogen in Asia Pacific 2021.
[4] MFAT. Japan: Strategic Hydrogen Roadmap. 2020.
[5] Ha JE. Hydrogen Economy Plan in Korea. 2019.
[6] Energy Agency I. Global EV Outlook 2021 Accelerating ambitions despite the pandemic. 2021.
[7] H2 mobility. Overview Hydrogen Refuelling For Heavy Duty Vehicles. 2021.
[8] Hosseini M, Dincer I, Naterer GF, Rosen MA. Thermodynamic analysis of filling compressed gaseous hydrogen storage tanks. International Journal of Hydrogen Energy 2012;37:5063–71. https://doi.org/10.1016/j.ijhydene.2011.12.047.
[9] Mayer T, Semmel M, Guerrero Morales MA, Schmidt KM, Bauer A, Wind J. Techno-economic evaluation of hydrogen refueling stations with liquid or gaseous stored hydrogen. International Journal of Hydrogen Energy 2019;44:25809–33. https://doi.org/10.1016/j.ijhydene.2019.08.051.
[10] Li J, Ramteke A, Youn E, Hansen E, Kratschmar K, Prakash A, et al. Liquid pump-enabled hydrogen refueling system for heavy duty fuel cell vehicles: Pump performance and J2601-compliant fills with precooling. International Journal of Hydrogen Energy 2021;46:22018–29. https://doi.org/10.1016/j.ijhydene.2021.04.043.

[11] Apostolou D, Xydis G. A literature review on hydrogen refuelling stations and infrastructure. Current status and future prospects. Renewable and Sustainable Energy Reviews 2019;113. https://doi.org/10.1016/j.rser.2019.109292.
[12] Wang A, van der Leun K, Peters D, Buseman M. European hydrogen backbone: How a dedicated hydrogen infrastructure can be created. 2020.
[13] Qin N, Brooker P, Srinivasan S, Dunn MD. Hydrogen Fueling Stations Infrastructure. 2014.
[14] Kurtz J, Sprik S, Bradley TH. Review of transportation hydrogen infrastructure performance and reliability. International Journal of Hydrogen Energy 2019;44:12010–23.
https://doi.org/10.1016/j.ijhydene.2019.03.027.
[15] Hecht ES, Pratt J. Comparison of conventional vs. modular hydrogen refueling stations, and on-site production vs. delivery. 2017.
[16] Kurtz J, Sprik S, Peters M, Bradley TH. Retail Hydrogen Station Reliability Status and Advances. Reliability Engineering & System Safety 2020:106823. https://doi.org/10.1016/j.ress.2020.106823.
[17] Reddi K, Elgowainy A, Rustagi N, Gupta E. Impact of Hydrogen Refueling Configurations and Market Parameters on the Refueling Cost of Hydrogen. 2017.
[18] Bethoux O. Hydrogen fuel cell road vehicles and their infrastructure: An option towards an environmentally friendly energy transition. Energies 2020;13. https://doi.org/10.3390/en13226132.
[19] Park S, Nam S, Oh M, Choi IJ, Shin J. Preference structure on the design of hydrogen refueling stations to activate energy transition. Energies 2020;13. https://doi.org/10.3390/en13153959.
[20] Samuelsen S, Shaffer B, Grigg J, Lane B, Reed J. Performance of a hydrogen refueling station in the early years of commercial fuel cell vehicle deployment. International Journal of Hydrogen Energy 2020;45:31341–52.
https://doi.org/10.1016/j.ijhydene.2020.08.251.
[21] National Renewable Energy Laboratory. Next Generation Hydrogen Station Composite Data Products: Retail Stations 2021.
[22] 3Emotion 2021. 3Emotion | Environmentally friendly, efficient, electric motion.
[23] SAE International. Fueling Protocol for Gaseous Hydrogen Powered Heavy Duty Vehicles (J2601/2_201409) 2016. https://saemobilus.sae.org/content/j2601/2_201409.

Characterization and modelling of air humidification in Fuel Cell System for transport sector

Amedeo Grimaldi[1,*], *Lorenzo* Villa[1], *Andrea* Baricci[1], *Stefano* De Antonellis[1], *Claudio* Oldani[2], and *Andrea* Casalegno[1]

[1]Politecnico di Milano, Energy Department, 20156 Milano, Italy
[2]Solvay Specialty Polymers SpA, R&D Centre, 20021 Bollate, Italy

Abstract. A model for the physical description of water transport through steady-state permeation and dynamic sorption within perfluoro-sulfonic acid (PFSA) membranes has been developed. A broad experimental campaign is conducted on several membranes, belonging to Aquivion class, varying both in thickness and equivalent weight (EW). The experimental data have been used to calibrate and validate water transport model and to find correlations for mass-transfer properties in low-EW PFSA membranes that describe consistently both water vapor permeation and sorption. It has been possible to identify individual contributions to mass transport resistance and to determine the optimal configuration and materials of a full-scale counter-flow membrane humidifier under a set of specific operating conditions.

1 Introduction

High durability and efficiency in state-of-the-art polymer electrolyte membrane (PEM) fuel cells are strongly dependent on membrane hydration state and external humidification of the reactant streams is essential [1]. Passive humidification techniques seem to be the most viable solution for automotive applications and could be developed using PFSA membranes, already adopted as electrolyte in PEM fuel cells where water management is a crucial phenomenon for efficient operation.

Water uptake features of PFSA ionomers have been investigated over the past few decades and water diffusion and sorption properties through membranes are generally determined using experimental methods, such as dynamic water sorption (DVS), steady state diffusion or permeability, pulsed-field gradient spin-echo (PGSE) nuclear magnetic resonance (NMR), and time-resolved Fourier transform infrared-attenuated total reflectance (FTIR) spectroscopy [2]. A complete understanding of mechanisms underlying water transport through PFSA ionomer is still under investigation. Water diffusivity values reported in literature vary up to four orders of magnitude, i.e. 10^{-14} to 10^{-9} m^2/s, depending on the experimental method [2].

In the following, starting from a batch of short-side chain PFSA membranes, belonging to Aquivion class, a transport model is developed, able to simulate two different experimental techniques, especially water permeation and DVS tests.

A unique formulation for water transport properties, independent of the experimental method is obtained. Performances and size of a full-scale automotive PEM fuel-cell humidifier under real operative conditions are estimated.

2 Experimental Setup

Prior to testing, all membrane samples have undergone a standard cleaning procedure, consisting in regenerating each sample by boiling it for 30 minutes in deionized water and letting it dry for 12 hours into a beaker before testing.

Permeation testing aims at obtaining steady-state data of the water permeation rate through the membrane-gas diffusion layer (GDL) assembly. Membrane area, A_{cell}, is equal to 8 cm^2. Dry air flow rate values on dry side, $\dot{V}_{air}^{dry}$, are 0.5, 1.0 and 1.5 SLPM, that correspond to the typical flow rates on humidifier and are scaled on membrane area. Dry air flow rate on wet side is 2 SLPM, before entering in a bubbler and getting humidified with a given dew point temperature, that is varied to test different inlet RH for wet stream. Gas flow rate values on dry side are chosen smaller than the wet-side ones to avoid very low dry-side RH conditions at the outlet. Air is fed in a co-flow configuration. The cell temperature values are chosen to match the typical operative conditions of a PEM fuel cell, from start-up to full power.

The permeated water flux rate, $\dot{m}$, is computed through Equation (1), assuming that dry air behaves as a perfect gas and that its permeation rate through the membrane is negligible.

$$\dot{m} = \frac{MM_{H_2O}}{A_{cell}} \frac{\frac{RH_{out}^{dry}}{100}}{\frac{p_{out}}{p_{H_2O}^{sat}(T_{out}^{dry})} - \frac{RH_{out}^{dry}}{100}} \frac{\dot{V}_{air}^{dry}}{22.414} \quad (1)$$

where RH_{out}^{dry}, p_{out}, T_{out}^{dry} are RH, pressure and temperature of the stream on dry side outlet.

* Corresponding author: amedeo.grimaldi@polimi.it

Absorption tests have been carried out using an automated, gravimetric, dynamic water sorption analyzer, namely AQUADYNE DVS™ 2 produced by Quantachrome Instruments. Each membrane sample is conditioned as described above, before being tested, and is placed over a balance plate of the gravimetric analyzer.

The overall dry gas fed to the machine throughout the test is kept constant at 100 Standard Cubic Centimeters per minute (SCCM). Once the drying step is completed at 80°C in a nitrogen atmosphere at ambient pressure, to obtain the reference dry mass, m_{dry}, the samples are subject to increasing-humidity conditions within the range 0% to 90% RH, with 5% intervals, at a given temperature.

The DVS instrument measures mass change over time for samples and automatically switches to the following step when the cut-off condition is reached. Tests are performed at different temperatures, 30, 50, 70 °C respectively.

The membrane water content λ is computed for each sample by knowing the dynamic mass measurement, $m(t)$, the mass of the dry ionomer, m_{dry}, and the sample's equivalent weight.

$$\lambda(t) = \frac{m(t) - m_{dry}}{m_{dry}} \frac{EW}{M_{H_2O}} \tag{2}$$

From the absorption curves over time, it is possible to distinguish a two-step process with two rate constants largely separated in time, as reported in [2],[3]. The first mechanism is generally related to mass transport resistances, mainly external gas convection and interfacial membrane resistance, and predominates at short time. The latter mechanism takes over at longer times, suggesting that water uptake becomes controlled by the polymer rearrangement and relaxation.

3 Model Formulation

3.1. Model Domain

For the water permeation test setup, framework consists of five regions that represent wet and dry gas channel, wet and dry porous media, and ionomer, similar to configuration in a typical plate and frame humidifier. For the DVS test setup, ionomer is exposed to humidified air on both sides, thus determining the presence of the external convection together with water uptake and diffusion through ionomer.

It has been assumed that transport model is isothermal since tests are performed at constant temperature; moreover, water diffusion is assumed to occur only through ionomer thickness, whereas planar diffusion is assumed to be negligible; single phase is modelled for water in porous media.

In the following, first, the governing equations for each domain will be presented, then permeation and sorption models' framework are described.

3.2 Model Equations

Generally, water transport through ionomer is described in terms of λ, that indicates the moles of water molecules per moles of sulfonic acid group, thanks to equation (3), where D_λ is the effective diffusion coefficient of water through ionomer, proportional to the hydration state of membrane.

$$\frac{\partial \lambda}{\partial t} = \nabla \cdot (D_\lambda \nabla \lambda) \tag{3}$$

$$\dot{N}_w^{int} = k_{ad} \frac{\rho_i}{EW} (\lambda^* - \lambda) \tag{4}$$

$$\lambda^* = (1 - \phi)\lambda^{eq} + s_{relax} \tag{5}$$

$$\frac{\partial s_{relax}}{\partial t} = -\frac{1}{\tau_{relax}} (s_{relax} - \phi \lambda_{eq}) \tag{6}$$

Water sorption and desorption, occurring at membrane interfaces, can be modelled by equation (4), where k_{ad} is the interfacial water transfer coefficient, assumed to be function of λ, and λ^*, described by equation (5), is the quasi-equilibrium value for water content in the ionomer, as a consequence of transient swelling of polymer backbone of ionomer [3].

Relaxation model, described in [4], has been implemented. Indeed, the quasi-equilibrium value for water content, λ^*, is obtained according to equation (6), where ϕ represents the further volume for water accumulation that becomes available as polymer relaxes over time and s_{relax} accounts for the dynamics of stress relaxation, that is assumed to be described by a first-order dynamics, as observed by Satterfield et al.[5].

Stress relaxation factor ϕ ranges between 0.15 and 0.3 whereas the relaxation time constant, τ_{relax}, is assumed to be 3500 s, close to findings in [5]. The equilibrium water content, λ_{eq}, is function of water activity and temperature and adsorption isotherms are obtained from DVS experiments.

Gas diffusion trough porous medium, adjacent to gas channels, is governed by the following equation.

$$\nabla \cdot \left(D_i^{eff} \nabla c_i \right) = 0 \tag{7}$$

$$D_i^{eff} = \varepsilon \left(\frac{\varepsilon - \varepsilon_{pc}}{1 - \varepsilon_{pc}} \right)^{n_e} \frac{1 - y_i}{\sum_{j \neq i}^{N_{species}} \frac{y_j}{D_{ij}}} \tag{8}$$

Where ε is the compressed layer porosity, c_i denotes the concentration of species i, D_i^{eff} is the effective diffusivity of species i which is calculated by accounting for molecular diffusion and for the tortuous pathway through porous layers.

In Equation (8), ε_{pc} is the percolation threshold, assumed to be 0.11 [6].

Conservation equations for mass, inside channel volumes, are solved for each species along channel direction.

$$\nabla \cdot \dot{N}_i = \frac{\dot{N}_i^{\mathrm{GDL|CH}}}{L_{ch}} \tag{9}$$

$$\nabla p = -\frac{f \mu}{2 \, d_h^2} \frac{\dot{N}}{\frac{h_{ch}}{L_{ch}} \frac{p}{R \, T}} \tag{10}$$

where c_i, $\dot{N}_i$, $\dot{N}_i^{\mathrm{GDL|CH}}$ are the molar concentration, molar fluxes along channel direction and molar fluxes at GDL/channel interface of species i, whereas $\dot{N}$ and p are the local total molar flux and pressure in gas channels. f is the friction factor evaluated according to Pant et al. [7].

$$\dot{N}_i^{\mathrm{GDL|CH}} = h_m(c_i - c_i^{GDL|CH}) \qquad (11)$$

In the case of flow inside a channel, as in the first setup, h_m is dependent upon Sherwood number, that is related to local operating conditions.

For the second setup, where humidified air is flowing externally over the ionomer sample, h_m is estimated from literature, equal to 2×10^{-3} m/s [8]. All the other gas properties are taken from literature.

The transport model has been implemented in MATLAB, and, according to the frameworks, shown above, two different versions of the transport model have been implemented. In particular, a steady-state model is used for simulating water permeation tests, whereas a transient model for the water uptake.

4 Results and Discussion

In Figure 1-2-3, water flux is plotted against mean logarithmic water vapor concentration difference, $\Delta C_{ml} = (\Delta C_{in} - \Delta C_{out})/ln\,(\Delta C_{in}/\Delta C_{out})$ that represents the driving force of the process. ΔC_{in} and ΔC_{out} denote the difference between water vapor concentration of the inlet and the outlet streams, respectively.

Focusing on membrane properties, in Figure 1(a), it is possible to observe the effect of thickness on water transport, for membranes with same *EW*, i.e. 980 g mol^{-1}. As expected, by increasing membrane thickness, water flux is lower, since diffusion through membrane is hindered. It is noticeable that, as thickness increases by three times, maximum water flux at 80°C is twofold. As visible in Figure 1(b), water sorption over time results to be affected as well. In particular, higher thickness slows down water uptake in the first step, dominated by mass transport resistance. In the second regime, dominated by ionomer relaxation, no visible effect can be noted, thus suggesting that ionomer relaxation is independent upon thickness.

In Figure 2(a), it is shown the global water flux for membranes with same thickness, i.e. 50 μm and different *EW*, for three values of membrane temperature. It can be noted that, by decreasing *EW*, water flux gets higher. As ΔC_{ml}increases, water flux increases as well, since inlet RH of wet stream is increasing. At the same time, looking at water absorption curves, in Figure 2(b), it results that water uptake is slightly faster for membrane with lower *EW*. A slight deviation among the curves is visible as well in the second regime, indicating that ionomer relaxation is faster for lower *EW*.

Effect of porous layer treatment has been analyzed and it has enlightened that using hydrophilic porous layer on both wet and dry side allows to have a higher water flux,

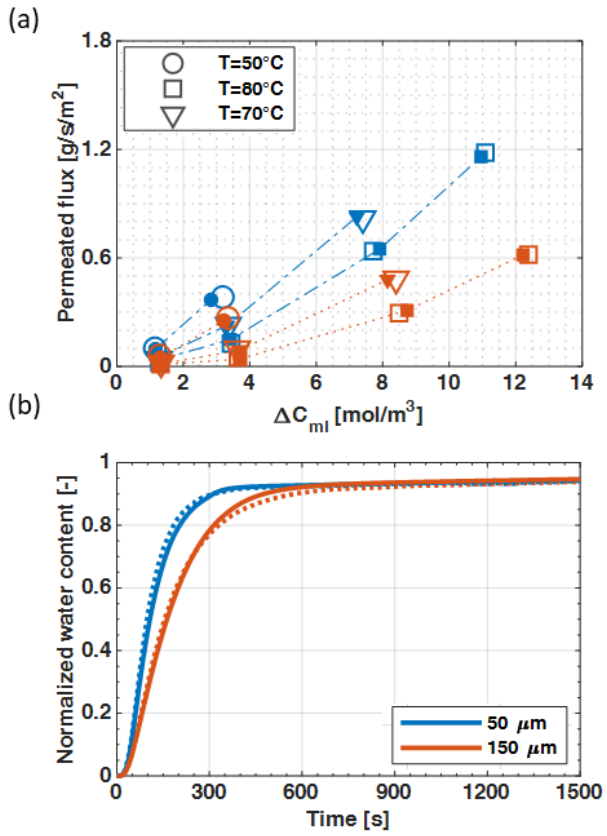

Fig. 1 Effect of membrane thickness: (a) Water permeation flux; (b) Water sorption over time. (Experimental data: void symbols in (a) and dashed lines in (b); Model simulations: solid symbols in (a) and solid lined in (b))

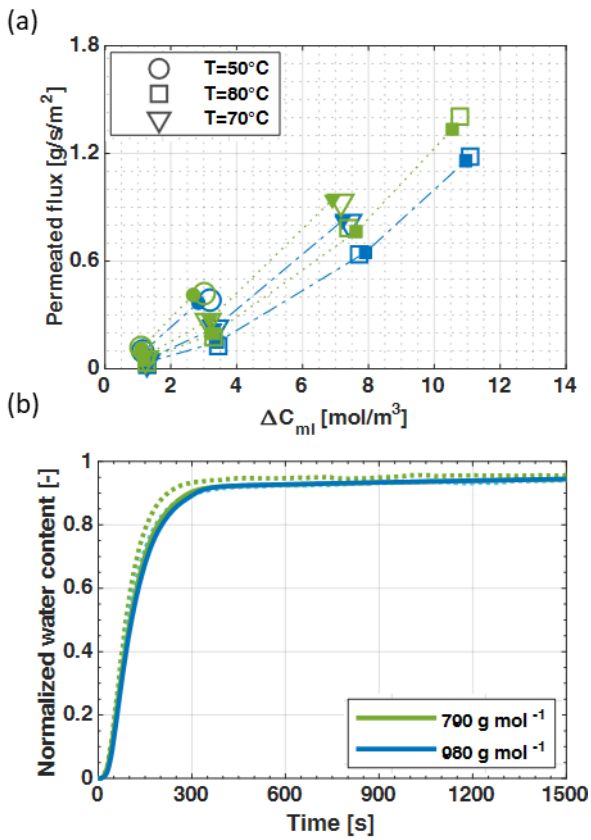

Figure 2 Effect of membrane *EW*: (a) Water permeation flux; (b) Water sorption over time. (Experimental data: void symbols in (a) and dashed lines in (b); Model simulations: solid symbols in (a) and solid lined in (b))

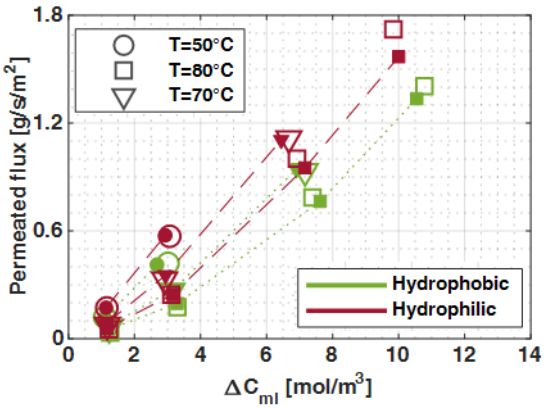

Fig. 4 Effect of porous layer treatment: Water permeation flux. (Experimental data: void symbols; Model simulations: solid symbols)

with respect to having hydrophobic one on both sides or mixed configuration with hydrophilic on dry side and hydrophobic on wet side, under every operating conditions. It is beneficial, also, to reduce thickness of the layer, thus, to reduce its mass transport resistance. Moreover, it has been observed, by overlapping several layers of porous layers, that effective vapor diffusivity through the layer itself is independent of the treatment, indicating that decrease in mass transport resistance is ascribable to diminishing of the other contributions.

Correlations for D_λ and k_{ad} are reported, obtained by fitting of the experimental data, shown in Figure 1 and 2, implemented according to Paragraph 2, exploiting the functional forms proposed by Kulikovsky [9] for D_λ and Ge et al. [10] for k_{ad}:

$$D_\lambda = \left(\frac{\lambda}{25}\right)^{0.15} [1 + tanh(\lambda - 2.1g^{0.5})] \\ 4.22 \times 10^{-10}\, g^{0.66} exp\left[\frac{15000}{R}\left(\frac{1}{343} - \frac{1}{T}\right)\right] \quad (12)$$

$$k_{ad} = 10.1 \times 10^{-5} f_v \exp\left[\frac{40000}{R}\left(\frac{1}{343} - \frac{1}{T}\right)\right] \\ \text{with} \quad f_v = \frac{1.8\times10^{-5}\,\lambda}{\frac{EW}{\rho_i} + 1.8\times10^{-5}\,\lambda} \quad (13)$$

where $g = EW/980$ accounts for the effect of EW on diffusion coefficient. For low water content, diffusion coefficient D_λ results to be slightly higher for lower EW, whereas, as λ increases, it tends to a lower maximum value. This feature could be maybe attributed to an increase in tortuosity of water channel domains, whose effect is incorporated in D_λ[2].

Table 1 DOE reference condition and geometrical dimensions of humidifier cell

Parameter	Dry Air	Wet Air
$\dot{V}_{air}^{dry}[SLPM]$	3000	2600
T [°C]	80	80
P [$mbar$]	1830	1600
RH [%]	0%	85%
$A_{cell}[cm^2]$	100	
Channel height/width [mm]	0.85/0.85	

Actually, it has been observed that, as EW decreases, width of hydrophilic channels decrease in size and water cluster distribution becomes more dispersed inside membrane volume, determining a tortuous path for water transport, especially at higher degrees of hydration [11].

On the other side, local water concentration increases, as a consequence of an increase in density of sulfonic acid groups, determining a higher water flux for membranes with lower EW membranes, with the same driving force ΔC_{ml}.

The interfacial constant, k_{ad}, considering the formulation of Ge et al. [10] is affected as well by EW, since it is related to water volume fraction, f_v, that increases as EW decreases, for the same value of water content λ.

The greater performance, associated to hydrophilic porous layer can be incorporated in the model, assuming that interfacial adsorption/desorption becomes very fast for high ΔC_{ml}, thus meaning a negligible contribution by interfacial transport resistance. It is possible to relate this aspect to the likely presence of liquid film on the membrane interfaces, whose growth is favored by hydrophilicity of the porous layer, that would determine a strong decrease in the interfacial surface resistance, as also reported in Weber et al. [2].

Validation of transport model has been performed thanks to water uptake curves from DVS analyzer.

Model simulations are well adherent to experimental data, mainly for low and medium values of RH. For higher RH, a slower uptake is generally visible, and it has been noted that a limiting factor is the slower dynamics of average RH in the weighting chamber, that is affected by a greater accumulation of water inside the ionomer. The slower uptake is consistent with a stronger growth of water domains, that must accommodate more water, and it can be correlated to swelling of membrane structure [3]. Indeed, it has been adopted a correlation for model parameter ϕ as λ increases, according to Equation 14, to account for a great membrane deformation, calibrated on specific RH steps, i.e. RH 30%, 50%, 70%.

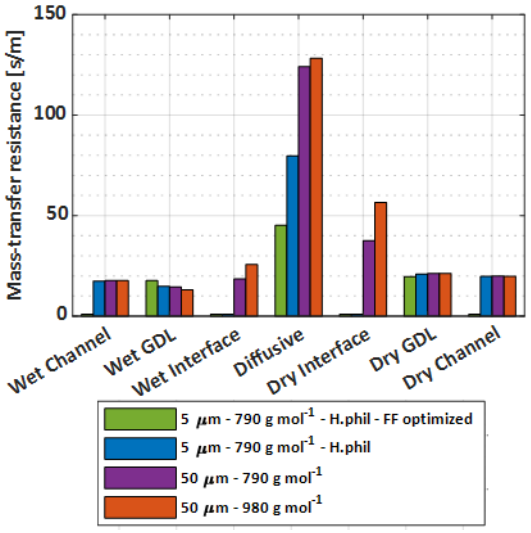

Fig. 3 Individual contribution to water transport trough membrane under several configurations

$$\phi = 0.022(\lambda - 2) + 0.05 \qquad (14)$$

Experimental data have been compared with model simulations also for different temperatures and *EW*, confirming the good adherence between the two.

Once identified PFSA water transport properties, steady state model simulations have been performed at the same operating conditions specified by DOE [12] and reported in Table 1, together with assumption on geometrical dimension of humidifier single cell, to estimate water flux and active membrane area of air humidifier. In Figure 4, individual contributions to mass transport resistance are identified for different membrane and configuration. It can be observed that the main contributions are represented by membrane diffusive resistance and interfacial resistance on dry side. The decrease in *EW* causes a significant reduction in the interfacial resistance on both wet and dry side and a slight decrease in the diffusive one.

Based on the above-mentioned results, it has been observed that counter-flow configuration with such PFSA membranes with *EW* and thickness equal to 790 g mol^{-1} and 5 μm respectively, assembled with hydrophilic porous layer, that lets to minimize membrane interfacial resistances, allows to get an average water flux of 2.3 g m^{-2} s^{-1}, representing 55% of the target proposed by DOE.

It can be observed, from Figure 4, that diffusive resistance is diminished by 38%, after a ten-fold decrease in thickness of membrane, because average membrane water content is very low, in such conditions, causing a strong decrease in water diffusivity. Since channel resistance to mass transport is not negligible, adopting an optimized channel geometry, that lets to strongly reduce its resistance, allows to get an average water flux equal to 3.4 g m^{-2} s^{-1}, in accordance with what has been obtained in [13]. Moreover, it can be seen that reducing gas transport resistance lets to decrease further membrane diffusive resistance. Thus, total water request, equal to 5 g s^{-1}, for a typical automotive stack, can be achieved with a total membrane area of 1.4 m^2. Optimization of operating conditions, as dry air inlet temperature or operating pressure, would allow to further reduce membrane diffusive contribution, increasing average water flux.

5 Conclusions

A water transport model that integrates steady-state vapor permeation and dynamic vapor sorption phenomena through PFSA membranes consistently has been implemented. Thanks to a broad experimental campaign, on low equivalent weight and short-side-chain membranes, water transport properties of such membranes have been determined and model has been calibrated and validated. It has been possible to identify the several contributions to mass transport resistance in a typical humidifier configuration, indicating that mass transfer resistances in the ionomer interfaces and the ionomer layer are of comparable magnitude. By investigating performance for a set of conditions for which air humidifier for automotive fuel cell system should transfer 5 g s^{-1}, model predicts an average value of 3.4 g m^{-2} s^{-1}, that corresponds to a total active area equal to 1.4 m^2.

References

1. D. A. Cullen, K. C. Neyerlin, R. K. Ahluwalia, R. Mukundan, K. L. More, R. L. Borup, A. Z. Weber, D. J. Myers, and A. Kusoglu, Nature Energy **6**, 462 (2021)
2. A. Kusoglu and A. Z. Weber, Chemical Reviews **117**, 987 (2017)
3. A. Kusoglu and A. Z. Weber, in *Polymers for Energy Storage and Delivery: Polyelectrolytes for Batteries and Fuel Cells* (ACS Publications, 2012), pp. 175–199
4. A. Goshtasbi, P. García-Salaberri, J. Chen, K. Talukdar, D. G. Sanchez, and T. Ersal, Journal of The Electrochemical Society **166**, F3154 (2019)
5. M. B. Satterfield and J. B. Benziger, The Journal of Physical Chemistry B **112**, 3693 (2008)
6. N. Zamel and X. Li, Progress in Energy and Combustion Science **39**, 111 (2013)
7. L. M. Pant, M. R. Gerhardt, N. Macauley, R. Mukundan, R. L. Borup, and A. Z. Weber, Electrochimica Acta **326**, (2019)
8. A. Thorell and L. Wadsö, Drying Technology **36**, 332 (2018)
9. A. A. Kulikovsky, Journal of the Electrochemical Society **150**, A1432 (2003)
10. S. Ge, X. Li, B. Yi, and I.-M. Hsing, Journal of The Electrochemical Society **152**, A1149 (2005)
11. K. D. Kreuer, M. Schuster, B. Obliers, O. Diat, U. Traub, A. Fuchs, U. Klock, S. J. Paddison, and J. Maier, Journal of Power Sources **178**, 499 (2008)
12. W. Johnson and W. Gore, *Materials and Modules for Low-Cost, High Performance Fuel Cell Humidifiers* (2012)
13. R. K. Ahluwalia, X. Wang, W. B. Johnson, F. Berg, and D. Kadylak, Journal of Power Sources **291**, 225 (2015)

Analysis of MEA's durability under Accelerated Stress Tests that mimic realistic automotive operations

Elena Colombo*, *Andrea* Baricci, and *Andrea* Casalegno

Politecnico di Milano, Department of Energy, Via Lambruschini 4, 20156 Milano, Italy

This work aims at studying MEA's ageing under single operational "mode" accelerated stress tests (AST), that were specifically designed to replicate under hydrogen/air feeding the main stressors of realistic operations in the automotive sector. A methodology for developing AST is here presented and preliminary results about the activity included. In particular, low power and high power functioning have been mimicked in a Zero-Gradient hardware, which allows a reliable materials comparison. Quantities, measurable *in-situ* and *operando*, have been tracked during ageing, like cell power, polarization curves, Pt active area, oxygen mass transport resistance, Electrochemical Impedance Spectra. The final objective is to clarify the underlying ageing mechanisms and assess the contribution of each specific operation to the MEA lifetime, focusing in particular on the cathode catalyst layer durability. Moreover, the rate of voltage loss for the new ASTs has been successfully correlated to the degradation observed under a complete driving cycle protocol.
***Index Terms* – Accelerated Stress Test, Automotive, Degradation mechanisms, PEMFC, Catalyst durability.**

1 Introduction

The typical conditions of automotive driving cause durability issues that it is necessary to overcome for a large-scale commercialization of Polymer Electrolyte Membrane Fuel Cells (PEMFC). The operating state affects lifetime since it degrades the different components of PEMFC: many degradation mechanisms could occur [1,2], which have been extensively studied and recognized. However, it is not clear how much they contribute to real ageing, considering in particular the mitigation strategies that are applied today in vehicles: identify such contributions in dependence on the operational modes is crucial for orienting the direction of research and development activities. This work presents a methodology for developing Accelerated Stress Tests (AST) for single cell (SC) starting from a realistic driving cycle. The reference driving cycle, used for designing the operative conditions of ASTs and to guarantee their validation, was obtained starting from vehicles data in the frame of the EU Horizon 2020 ID-FAST project (grant agreement No 779565)[3]. The observed and measured clue stressors of realistic operations have been successfully replicated on a Zero-Gradient hardware, by separating specific "operational modes". In particular, different state-of-the-art Membrane Electrode Assemblies (MEA's) were tested under ASTs that mimic low and high power automotive functioning, as well as under a suitable combination of these protocols, with the purpose of resembling realistic ageing and identifying correlations in terms of degradation rates of clue quantities (like *i-V* curves performance and Pt active area loss).

2 Experimental

2.1 Tools and MEA characterization

A Zero-Gradient hardware[4,5,6], developed at Politecnico di Milano, was adopted for testing different materials in a reliable way, ensuring homogenous conditions over the cell active area (from 2 to 10 cm^2). Its purpose is to minimize the influence from the testing hardware (e.g. flowfiled design) on results of performance and durability protocols. A high and accurate control of the operating conditions is guaranteed. To investigate the alterations induced by the studied protocols, electrochemical characterization methods were exploited: performance polarization curves (both under H_2/air and H_2/O_2), electrochemical impedance spectroscopy (under H_2/air, H_2/O_2 and H_2/N_2), cyclic voltammetry, linear sweep voltammetry and limiting current measurement, following a protocol close to *Baker et al.*[7]. Reference polarization curve operative conditions in H_2/air are: 80 °C, fully humidified gases both at anode and cathode, P_c/P_a = 230/250 kPa. Stoichiometry is set equal to 8 and >10 at anode and cathode respectively in case of Zero-Gradient hardware. Limiting current measurement, under excess gas feeding, was obtained at different pressures

* Corresponding author: elena.colombo@polimi.it

(P_c/P_a = 150/170 kPa, 250/270 kPa, 350/370 kPa) and diluted percentages of dry oxygen in nitrogen (1%, 2% and 3%). The results of the ASTs activity are compared to those of MEA's aged under conditions closer to stack operation. In particular, the realistic ID-FAST driving cycle protocol, used as a starting point for the ASTs design and for their validation, was carried out on a 25 cm^2 macro-segmented hardware. Hardware details are provided in references [8,9,4,10].

2.2 Tested MEA's and protocols

Different Pt/C MEA's were tested: *state-of-of-the-art* materials with different catalytic loading, ionomer and support type have been compared. They provide more generality to the drawn conclusions and highlighted possible differences during ageing among MEA's which were similarly performant at BoL (Beginning of Life). MEA's were degraded under newly developed Accelerated Stress Tests. A new *ad-hoc* protocol, designed for the specific process of air start-up, was developed and presented in a previous work[4]. It introduced realistic stressors (*i.e.* high potentials, up to 1.5 V, but ambient temperature and very fast transients) according to the mitigation strategies commonly adopted in nowadays vehicles. *Bisello et al*. successfully correlated the protocol to the realistic process. Here, another AST, named Low Power AST (LP AST), was designed to specifically mimic the low power operation. It was carried out in galvanostatic mode under hydrogen/air. For each MEA, the current densities correspondent to 0.85 V and 0.70 V have been evaluated at the BoL: voltages were selected in order to be close to real systems. Then, these current densities were imposed as a stressor for studying degradation. A single low power cycle is formed by: a basic unit of 30 s at the minimum current (*i.e*. 0.85 V at BoL) and 12 s at the high current (*i.e*. 0.7 V at BoL); the unit is repeated 6 times and it is finally followed by 30 s at the minimum current. After each set of current cycling, a short stop (110 s) is introduced. It causes voltage drop to very low values (< 0.1 V), that reduces the Pt surface, as well as pressure cycles due to the interruption of the cathodic flux. Cell temperature was set equal to 71 °C, RH_A/RH_C = 60/70% and $P_{A,in}/P_{C,in}$ = 190/140 kPa. Conditions were selected such to replicate the "mean" state of a MEA subjected to driving cycle. Constant fluxes were set such to ensure λ_A/λ_C = 8/20 at the maximum current. High Power AST (HP AST) introduces the main stressors of the high load operation. Again, the AST aims at reproducing the voltage cycling observed in a realistic process but exploiting galvanostatic mode in order to make the operation closer to actual systems and check the voltage decay in time. The current densities were defined such to correspond to 0.85 V, 0.75 V, 0.7 V, 0.65 V at BoT. Pressure cycles up to $P_{A,in}/P_{C,in}$ = 300/280 kPa and gas switch from humidified (RH_A/RH_C = 60/70%) to completely dry were included. Cell temperature was set equal to 90 °C. Every 200 cycles, a long stop have been simulated by cooling down the system for 12 h. Then, electrochemical and performance characterization were carried out. Preliminary results about these ASTs have been obtained for a total of 1000 cycles (approximately 120 hrs of testing for Low Power AST and 70 hrs for High Power AST). A Combined AST, which alternates Low and High Power, was tested too, in order to take care of the interplay between the two types of operation. Finally, the Combined AST was validated: correlations to the decay of performance and of the main electrochemical parameters of real world functioning was identified such to quantify the acceleration factors. It should be also proved that the new design does not alter the ageing mechanisms involved in realistic processes. Preliminary results about this point have been obtained but future activity will furnish further insights.

3 Results and discussion

The design of single "mode" accelerated stress tests was carried out starting from the driving cycle protocol defined in ID-FAST project. The Low Power AST was intended to include voltage cycling as the main stressors, which is consequence of load changes and short stops: a x7 acceleration factor was introduced by reducing the holding times compared to the realistic profile. The operando High Frequency Resistance (HFR approximated with impedance measured at 1000 Hz) was proved to be comparable to the value observed in the middle region of the MEA operated under the same kind of operation in the driving cycle. Pressure is set at the level of 140/190 kPa during the load cycling, while it decreases every short stop. Voltage cycling due to load changes is recognized to play a key role in cathode catalyst layer ageing since it causes Pt active area loss through mechanisms like Pt dissolution [11,12,13]; therefore, a sufficiently accurate reproduction of this stressor was considered as fundamental. The High Power AST was designed with the purpose of mimicking both voltage cycling and MEA hydration cycles, that were verified as relevant in the transitions from low to high loads. Pressure cycles were introduced as well. Pressure makes wide cycles at cathode between ambient value (short stop) up to 280 kPa, while between 150 kPa (short stop) to 300 kPa. Again, a x7 time acceleration factor was introduced. As done in case of Low Power, the MEA hydration state was verified as coherent to middle region of the realistic driving cycle. At the first stage of each High Power cycle, thanks to the growing pressure and the increasing current setpoints, the HFR drops significantly. Thereafter, the introduced drier gas feeding, combined with a decreasing load setpoint and decreasing pressure, the HFR very steeply grows. The process is repeated every High Power cycle, introducing thus hydration cycles that are expected to cause a mechanical stress for membrane and/or ionomer in the catalyst layer[14,15]. Finally, the Combined AST was realized by alternating Low and High Power AST. Preliminary results revealed that the two processes could influence one each other, therefore an alternation of 200 cycles + 200 cycles was kept. All the AST protocols cause an analogous decay of the Pt active area: largest losses occurred during the first 200 cycles and the Pt active area (ECSA) loss stabilizes

in the range of 30% ÷ 40% for all the tested materials. Checking the operando voltage profiles, the largest part of the loss is recovered by the way of long stops[16]. As preliminary observation, *i-V* performance, recorded during characterization, shows that discrepancies among the materials are minor under Low Power AST: all of them present a downwards vertical translation as the most relevant ageing impact and changes in mass transport resistance could be correlated to ECSA loss[17]. High Power AST was verified to play a major role in ageing rather than low power operation, even though the MEA operates in this condition for less time (operative time of 1 High Power AST cycle ≈ 60% 1 Low Power AST cycle). Clear differences in terms of performance loss rise among the materials under this kind of operation. In addition, the voltage profile keeps a higher rate of loss at high current densities. Some evidences indicate an increased ohmic loss.

Combining the protocols, there is no linear summation of the performance loss rates. Indeed, ECSA reaches a stabilization, that makes the voltage losses at low current values comparable among all the developed protocols. Performance decay at high current densities is instead controlled by the high power operation. As a validation of the developed design, it was proved that 1 cycle of the Combined AST matches the average losses caused by 1 operative hour of the realistic protocol: reasonable consistency was verified in terms of ECSA decay, performance loss and oxygen mass transport resistance evolution. In particular, adopting the reference polarization curve and the reference material, the rate of voltage loss was 10.8 µV/cycle in the AST case versus 8.0 µV/hr of the global driving cycle protocol loss, at the current setpoint that corresponds to 0.78 V at BoL. At larger current densities (setpoint equivalent to 0.65 V at BoL) the AST rate of 30.5 µV/cycle matches the realistic 28.8 µV/hr. Voltage loss comparison between the two testing activities is collected in Fig.1, while compatibility of catalyst active area drop is shown in Fig.2.

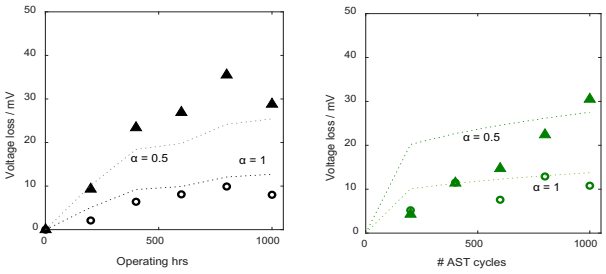

Fig. 1 (left) Voltage loss computed as the difference between the performance at BoT and after 1000 operating hours under ID-FAST driving cycle protocol[3], measured under H_2/air, T = 80 °C, fully humidified conditions, $P_{A,in}/P_{C,in}$ = 230/250 kPa, λ_A/λ_C = 2/4. Adopted hardware: triple-serpentine 25 cm^{-2} single cell. Symbols: triangle indicates current density 2 and circle current density 1 (see Table 1); (right) Voltage loss computed as the difference between the performance at BoT and after 1000 AST cycles, measured under H_2/air, T = 80 °C, fully humidified conditions, $P_{A,in}/P_{C,in}$ = 230/250 kPa, λ_A/λ_C = 8/20. Adopted hardware: Zero-Gradient cell. Symbols: triangle indicates current density 2 and circle current density 1 (see Table 1). Results are reported for one of the tested MEA's.

		i / A cm^{-2}	Voltage at BoT
Zero-G	Current density 1	0.7	0.78 V
	Current density 2	2.8	0.65 V
25 cm^2 cell	Current density 1	0.7	0.78 V
	Current density 2	1.9	0.65 V

Table 1. Current densities values used for comparison of Combined AST and driving cycle results, as indicated in Fig. 1.

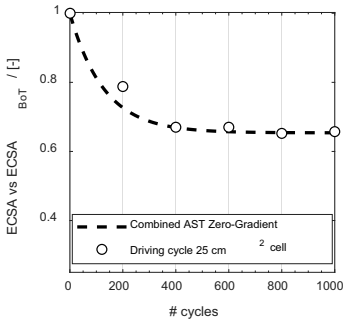

Fig. 2 Evolution of Pt active area (ECSA) with the number of AST cycles/operating hours for Combined AST and driving cycle protocol respectively. ECSA is measured from cyclic voltammetry: H_2/N_2 flow = 60/60 ml min^{-1}, RH 100/100, scan rate 0.05 V s^{-1}, 30°C, ambient pressure, minimum potential = 0.079 V and maximum potential of 0.6 V. Results are reported for one of the tested MEA's.

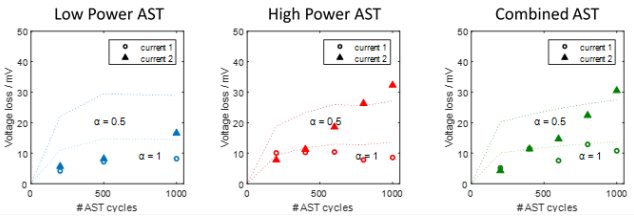

Fig. 3 Voltage loss computed as the difference between the performance at BoT and after 1000 AST cycles. The three developed ASTs are compared: Low Power (left), High Power (middle) and Combined (right). Performance loss is measured under H_2/air, T = 80 °C, fully humidified conditions, $P_{A,in}/P_{C,in}$ = 230/250 kPa, λ_A/λ_C = 2/4. Adopted hardware: Zero-Gradient cell. Symbols: triangle indicates current density 2 and circle current density 1 (see Table 1). Results are reported for one of the tested MEA's.

4 Conclusions

A methodology for designing new Accelerated Stress Tests protocols that ensure real operations representativeness has been presented. A process of

identification of the main stressors has been carried out. Each operational "mode" has been studied in a separate way and finally combined to resemble the complete driving cycle ageing. The final objective is to identify an acceleration rate without altering the realistic degradation mechanisms. New ASTs representatives has been preliminary proved and they revealed as an effective tool for clarifying the underlying degradation mechanisms under each process. In particular, as evinced in Fig.3, at Low Power conditions, the voltage loss in time reaches almost a stabilization both at low and high current densities of *i-V* curve, with largest drops in the first 200 AST cycles. The result is consistent to the profile of ECSA decay and to the consequent activation overpotential (Fig.2). Under High Power AST and Combined AST, the rate of voltage loss at high currents keeps greater, indicating an additional mechanism of degradation under high load operation, probably caused by mechanical stress. Finally, it was proved that 1 cycle of the Combined AST represents well 1 cycle of the realistic driving cycle protocol (Fig. 1 and Fig. 2). Future work will consist in analysing a larger number of cycles for the newly developed AST protocols and in further comprehending the mechanisms responsible of ageing through materials comparison and *ex-situ* analysis, that will help in validating the transfer function to "real world" too.

Acknowledgment

The work received funding under ID-FAST grant agreement No 779565. This Joint Undertaking receives support from the EU Horizon 2020 program

Bibliography

1. P. Ren, P. Pei, Y. Li, Z. Wu, D. Chen, and S. Huang, *Prog. Energy Combust. Sci.*, **80**, 100859 (2020).

2. T. Zhang, P. Wang, H. Chen, and P. Pei, *Appl. Energy*, **223**, 249–262 (2018).

3. F. Wilhelm, S. Escribano, et al, *ID-FAST - Investigations on degradation mechanisms and Definition of protocols for PEM Fuel cells Accelerated Stress Testing; Grant agreement no : 779565; Call : H2020-JTI-FCH-2017-1; D4.3 – Analysis of coupling between mechanisms and definition of comb.*, (2021).

4. A. Bisello, E. Colombo, A. Baricci, C. Rabissi, L. Guetaz, P. Gazdzicki, and A. Casalegno, *J. Electrochem. Soc.*, **168**, 054501 (2021).

5. T. Bednarek and G. Tsotridis, *Data in Bief*, **31**, 105945 (2020).

6. T. Bednarek and G. Tsotridis, *J. Power Sources*, **473**, 228319 (2020).

7. D. R. Baker, D. A. Caulk, K. C. Neyerlin, and M. W. Murphy, *J. Electrochem. Soc.*, **156**, B991 (2009).

8. C. Rabissi, P. Gazdzicki, L. Guétaz, S. Escribano, L. Grahl-Madsen, A. Baricci, and A. Casalegno, *J. Power Sources*, **397**, 361–373 (2018).

9. C. Rabissi, E. Brightman, G. Hinds, and A. Casalegno, *Int. J. Hydrogen Energy*, **43**, 9797–9802 (2018).

10. E. Colombo, A. Bisello, A. Casalegno, and A. Baricci, *J. Electrochem. Soc.*, **168**, 054508 (2021).

11. P. Zihrul, I. Hartung, S. Kirsch, G. Huebner, and H. A. Gasteiger, **163**, 492–498 (2016).

12. W. Bi and T. F. Fuller, **178**, 188–196 (2008).

13. P. P. Lopes, D. Tripkovic, P. F. B. D. Martins, D. Strmcnik, E. A. Ticianelli, V. R. Stamenkovic, and N. M. Markovic, *J. Electroanal. Chem.*, **819**, 123–129 (2018).

14. A. Kusoglu, A. M. Karlsson, M. H. Santare, S. Cleghorn, and W. B. Johnson, *J. Power Sources*, **161**, 987–996 (2006).

15. T. Morawietz, M. Handl, C. Oldani, P. Gazdzicki, J. Hunger, F. Wilhelm, J. Blake, K. A. Friedrich, and R. Hiesgen, *J. Electrochem. Soc.*, **165**, F3139–F3147 (2018).

16. P. Gazdzick, J. Mitzel, D. Sanchez, M. Schulze, and K. A. Friedrich, *J. Power Sources*, **327**, 86–95 (2016).

17. T. A. Greszler, D. Caulk, and P. Sinha, *J. Electrochem. Soc.*, **159**, F831–F840 (2012).

Hydrogen-based technologies in maritime sector: technical analysis and prospective

Mariagiovanna Minutillo[1,4], *Viviana* Cigolotti[2,4], *Giovanni* Di Ilio[3,4*], *Arianna* Bionda[5], *Erik-Jan* Boonen[6] and *Thomas* Wannemacher[7]

[1] University of Salerno, Department of Industrial Engineering, Salerno, Italy
[2] ENEA - Italian National Agency for New Technologies, Energy and Sustainable Economic Development, Naples, Italy
[3] University of Naples "Parthenope", Department of Engineering, Naples, Italy
[4] ATENA Future Technology, Naples, Italy
[5] Politecnico di Milano, Department of Management, Economics and Industrial Engineering, Milan, Italy
[6] Damen Shipyards Group, Netherlands
[7] Proton Motor Fuel Cell GmbH, Germany

Abstract. The maritime transportation sector is one of the main contributors to global emissions of greenhouse gases (GHGs). The International Maritime Organization (IMO) has adopted a strategy to reduce these emissions from international shipping >50% by 2050, compared to 2008's emissions. Therefore, ship owners need to adopt solutions to bring emissions within these and other future limits by means of environmentally friendly fuels (hydrogen or hydrogen carriers) and high efficiency propulsion technologies (fuel cells). This paper focuses on the replacement of the conventional Diesel genset installed on a hybrid small-size ferry, with an innovative system based on PEMFC technology. A real case scenario is investigated: the total energy/power demand of the vessel is determined basing on a typical operational profile. Then, a preliminary redesign of its powertrain configuration is proposed along with an energy management strategy. The analysis has allowed to define the hydrogen consumption for a daily operation. Finally, different storage technologies involving both compressed and liquefied hydrogen have been considered and compared, in order to identify ship's weight and space requirements.

1 Introduction

The International Maritime Organization (IMO) has adopted mandatory measures to reduce greenhouse gas (GHG) emissions in the maritime sector. Regulations and strategies cover several aspects ranging from hull resistance to new renewable fuels and propulsion systems. Fuel cells represent a valid option for the replacement of conventional fossil fuel-based technologies adopted for shipping and a great attention is devoted to evaluating the implementation of these technologies on board vessels.

Pivetta et al. [1], analyzed the optimal design and operation of Ro-Pax ferry on which a hybrid PEMFC/Li-ion Battery powertrain, fueled by liquid hydrogen, was installed. The study was based on the development of multi-objective optimization method that allowed to define the best operating conditions of the hybrid system components according to the performance degradation of both fuel cells and batteries. Thus, the authors developed a useful tool for carrying out a preliminary choice of the optimal energy management strategy for ships new propulsion systems. Similarly, a hybrid PEMFC-battery propulsion system, installed on a tourist boat, was proposed by Choi et al. [2] that demonstrated the reliable operation in the coastal waters of these novel hydrogen-based power trains in the maritime sector. Also, Rivarolo et al. [3], performed a time-dependent thermo-economic analysis to determine the optimal operating conditions for a PEMFC-based powertrain system on a ferry with a capacity up to 200 people and operating on the artificial lake of Itaipu (hydroelectric plant). Recently, a techno-economic feasibility study on the replacing of the conventional diesel engine powertrain of a Ro-Pax ferry with a hydrogen-based system has been presented by Di Micco et al. [4]. In that study, different storage solutions based on compressed and liquefied hydrogen technologies have been also considered to determine ship's weight and space requirements.

Thus, hydrogen in marine applications is attracting more and more attention, and feasibility assessments are necessary to define the technical characteristics that allow it to be used as an alternative to fossil fuels.

In this paper, a preliminary technical assessment of the actual feasibility of replacing the conventional Diesel genset of a small-size ferry with a fuel cell-based system is carried out. The hydrogen storage requirements are then evaluated by considering different solutions among those commercially available. The present analysis is aimed at providing a reference framework for further developments on the hydrogen-based redesign of ships.

* Corresponding author: giovanni.diilio@uniparthenope.it

Table 1. Reference vessel: hybrid waterbus – main features.

Classification	Light Ship, Passenger Catamaran
Accommodation	125 passengers, 2 crew
Propulsion Equipment	
1 x Diesel genset	
Rated power	520 kW
2 x Lithium-Titanate-Oxide (LTO) batteries	
Energy capacity	84 kWh
Max continuous C-rate	3C (discharging), 1.5 (charging)
Energy density	70 Wh/kg
Mean charging/discharging efficiency	95%
2 x Electric motors	
Max power	375 kW
Fuel tank capacity	
Volume	2.0 m^3
Weight (fuel and tank)	2.5 t

2 Case study

The considered vessel is a small ferry providing daily water-based public transport service along the inland paths of the city of Rotterdam, Netherlands. In particular, the reference vessel is a new-build hybrid waterbus by Damen Shipyards Group, which main features are reported in Table 1. The propulsion system of this hybrid waterbus is composed of a Diesel genset and two battery packs. These components jointly provide power to two electric motors, connected to the propellers of the vessel. A typical operational profile for this vessel is mainly characterized by short routes, which are repeated several times during a day. In this work, a real operational profile is considered: this consists of 8 roundtrips, each lasting for about 2 hours (that is, 1 hour one-way); the total distance covered by the vessel during a day is around 340 km. Details for the reference mission used in this study are reported in Table 2.

Table 2. Main parameters for the reference operational profile.

Distance (one-way)	20.9 km (11.3 nm)
Duration (one-way)	1 hr
Stops (one-way)	9
Total roundtrips per day	8
Max sailing speed	39.9 km/h (21.6 kn)

Fig. 1 shows the total electric power demand during a single roundtrip, that has been used in the present analysis. This power profile, which is representative of a typical duty cycle experienced by the vessel during its operation, is measured at the switchboard, and it includes both propulsion power and auxiliary power (which is a constant load, equal about to 18 kW). It should be noted that the power requested to the propulsion system depends on the specific direction of the trip: the upstream route is significantly more power demanding than the downstream route, since the two ways are affected by different sailing conditions. In Table 3, the main energy and power requirements for the reference operational profile are reported.

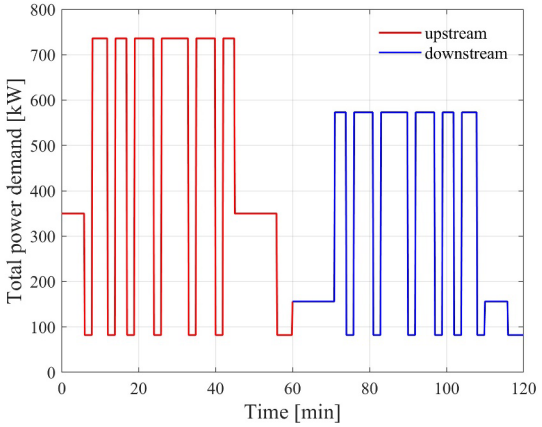

Fig. 1. Reference duty cycle: total electric power demand of the vessel (propulsion and auxiliary) during a single roundtrip. Red line: upstream route; blue line: downstream route.

Table 3. Energy and power consumptions for the reference operational profile.

Energy [kWh]	1 roundtrip	776
	8 roundtrips	6208
Mean power [kW]	Roundtrip	388
	Upstream route	452
	Downstream route	324
Max power [kW]		736
Min power [kW]		82

3 H_2-based hybrid system

The proposed hydrogen-based powertrain design is similar to the original one, in the sense that all its components are kept the same, except for the genset, which is instead replaced by a fuel cell system. In particular, the choice of using the same battery of the original vessel is justified by the need of implementing the minimum number of modifications, in order to perform a preliminary, fair evaluation of the hydrogen-fuelled vessel requirements (in terms of energy/power and fuel storage).

The fuel cell system is connected to the electric motors inverters and battery packs through DC/DC

converters, with an assumed efficiency of 93%. The fuel cell is enabled to either supply electric power to the electric motors, recharge the batteries, or accomplish both tasks simultaneously. The electric motors can be powered either by the fuel cell, the batteries, or both at the same time.

The hydrogen-fueled vessel has to accomplish the same operational profile of the Diesel-fueled one, therefore, it must ensure the same energy and power performances. Fuel cell and hydrogen storage system have to be sized based on these requirements.

3.1 Fuel cell sizing

In the hydrogen-based powertrain, the fuel cell must be able to provide at least the requested mean power, in order to avoid the battery State of Charge (SoC) depletion under continuous vessel operation. In particular, since the typical operational profile of the vessel is characterized by two clearly distinguishable route profiles (i.e. upstream route and downstream route), the minimum requirement for the fuel cell sizing must be the mean power requested during the most demanding route, that is, 452 kW. In principle, this value would be sufficient to guarantee that the hybrid powertrain is always capable of meeting the vessel electric power request, since the maximum continuous discharging power for the battery is 504 kW (Table 2), and the maximum power requested during the whole mission is 736 kW (Table 3). However, to exploit the efficient use of the fuel cell at partial loads, and to provide more flexibility in the energy management of the powertrain system, the fuel cell system has been slightly oversized with respect to the mean power demand of the upstream route. The selected fuel cell stack is the Proton Motor PM400–144 [5], whose main characteristic parameters are reported in Table 4.

Table 4. Main features of the fuel cell stack PM400–144 [5].

Power Range [kW]	5.9 – 45.2
El. System Efficiency [%]	47 – 67
Main Dimensions [mm]	436 x 279 x 860
Volume [L]	104.6
Tare weight [kg]	73

Fig. 2 shows the architecture of the FC system developed by PM (in this configuration the second stack is used to assure the redundancy of the power supply for safety reasons) and its integration within the vessel powertrain. In this study, in order to achieve a fuel cell system with 95 – 723 kW range of power output, a 16 stacks configuration must be used.

4 Energy management strategy

The fuel cell/battery hybrid powertrain must fulfil the vessel power demand during the whole mission, that is:

$$P_{FC} + P_b = P_{EM} + P_{aux} \quad (1)$$

where P_{FC} is the fuel cell output power (including DC/DC efficiency loss), P_b is the power provided by the battery, P_{EM} is the electric motors power request, and P_{aux} is the auxiliary power. To this aim, a rule-based control strategy, with a feedback control on battery SoC, is implemented. Despite not relying on an optimal approach, the proposed energy management strategy has the key advantages of being reliable and suitable for online implementation, that is, the knowledge of the operation profile is not required a-priori. This makes it ideal for a preliminary evaluation of the energy/fuel storage requirements of the vessel.

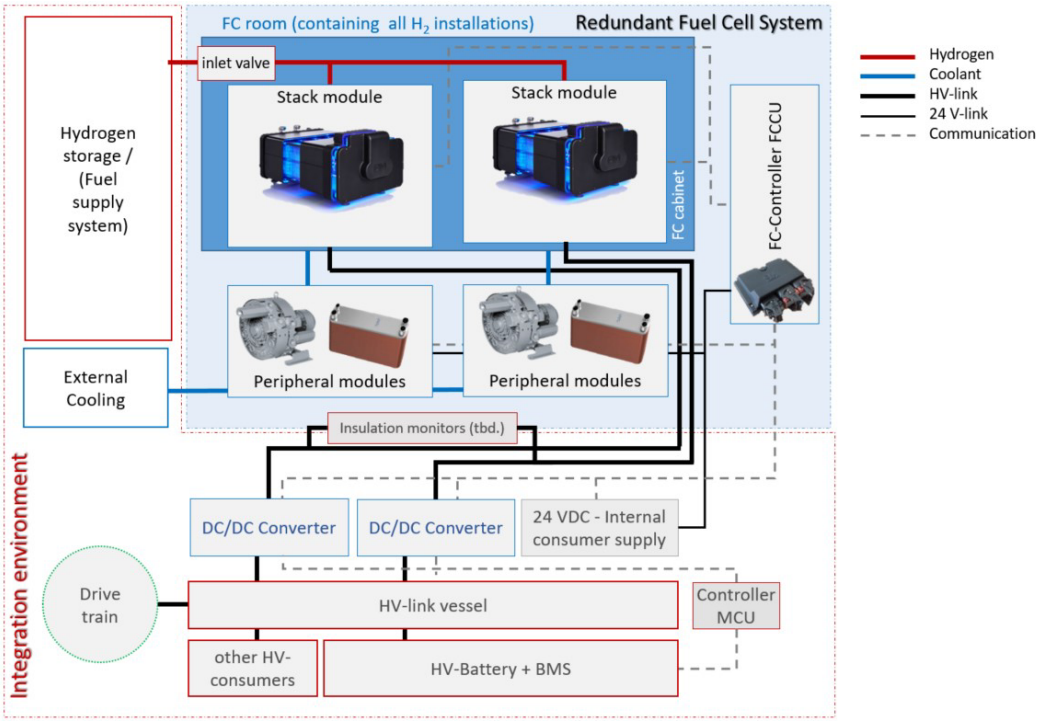

Fig. 2. Schematic representation of the hydrogen-based powertrain architecture of the vessel.

The power split between fuel cell and battery follows a Charge Sustaining (CS) mode of operation: it is assumed that the battery cannot be recharged from an external source when the vessel is at berth, therefore, its SoC must be kept around a constant value by the fuel cell during the entire duration of the trip. According to this approach, two predefined SoC control values, equal to 0.4 and 0.6, respectively, have been set. In particular, the implemented control algorithm consists in the consecutive solution of the following two equations:

$$P_{FC} = P_{bmax,charg} + (P_{EM} + P_{aux})y \quad (2)$$

$$P_b = P_{EM} + P_{aux} - P_{FC} \quad (3)$$

where $P_{bmax,charg}$ is the battery (continuous) maximum charging power, while y is a Boolean variable which distinguishes two operating modes, as follows:

- *Mode A:* $y = 0$.
  Under this mode of operation, which is activated anytime the higher battery SoC control value is hit, the battery tends to discharge, since it has a primary role to provide propulsion power, while the fuel cell operates at low constant power to support battery operation and/or partially recharge the battery. This latter event occurs whenever the overall power request is lower than the fuel cell power (negative values of P_b in Eq. 2). In particular, it is readily seen that the selected fuel cell power set-point satisfies the following condition:

  $$P_{FC} + P_{bmax,disch} \geq P_{totmax} \quad (4)$$

  where $P_{bmax,disch}$ is the battery (continuous) maximum discharging power, and P_{totmax} indicates the maximum power demand (736 kW). Eq. 4 represents indeed a mandatory requirement in order to guarantee that the vessel power demand is always met, also during the most critical condition.

- *Mode B*: $y = 1$.
  The fuel cell is the primary energy source to supply propulsion power, while the battery is used only to compensate the request of power whenever this is higher than that available from the fuel cell, since, clearly, the value of P_{FC} is bounded to its allowed maximum. This mode of operation is activated anytime the lower battery SoC control value is reached. Specifically, the fuel cell operates following the electric motor request and recharging the battery, that is, according to a load following mode.

The two modes of operation described above are alternatively enabled so to perform a hysteresis cycle between two battery SoC limits. The initial battery SoC is set to 0.5, by assumption. By this energy management strategy, the available power to charge the battery is maximized, while its damaging due to exceeding amount of charging power is prevented at the same time. In fact, when the propulsion power demand is low or near zero (i.e. docking operations or port-stay at berth), the recharging of the battery occurs at nearly the maximum allowed rate, thus favouring a fast (and efficient) restoring of its SoC.

5 Results and discussion

The control algorithm described in Section 4 has been implemented in MATLAB environment, and the hydrogen-based vessel powertrain has been simulated in order to check for correct operation of its components and to estimate the hydrogen consumption required to accomplish the predefined operational profile. This data has been then used to make assumptions on the on-board fuel storage needs, in terms of volumes and weights, by considering commercially available storage solutions. The fuel cell is modelled by means of its performance curve, retrieved from private communication with the manufacturer. The battery instead is modelled only considering a mean charging/discharging efficiency.

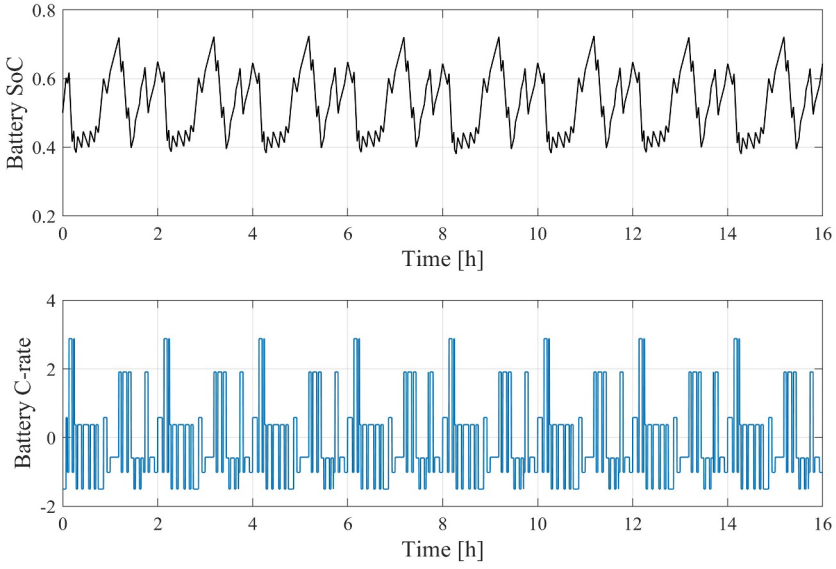

Fig. 3. Battery SoC (top) and battery C-rate (bottom) during vessel operation.

In Fig. 3 the obtained battery performances are shown, in terms of SoC and C-rate, as a function of time, for the whole duration of the vessel operation. The results show that the CS of the battery is well developed during the powertrain operation, with a Depth of Discharge (DoD) roughly equal to 0.3. This value can be considered acceptable, since it preserves battery lifetime [6]. Also, the battery C-rate never exceeds its allowed maximum value, either under charging (1.5C) or discharging (3C), as expected. Next, in Fig. 4, the obtained power profiles for battery and fuel cell, for a single roundtrip, are depicted and compared to the total electric power demand of the vessel.

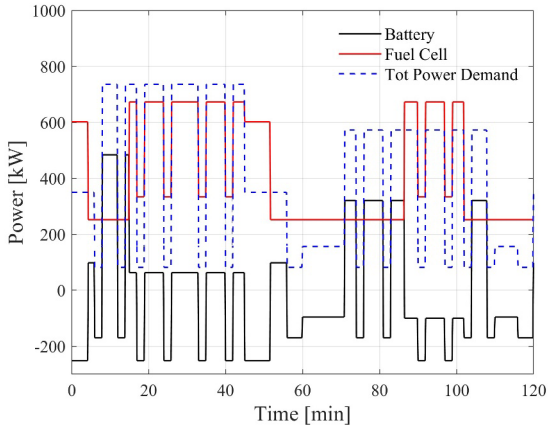

Fig. 4. Battery and fuel cell power output vs the total power demand, during the first roundtrip.

The results emphasize that the fuel cell operation is not directly related to the requested power, since the battery operates as energy buffer; thus, the proposed power unit architecture, along with the employed energy management strategy, allows components downsizing and their efficient use. In Table 5 the main results from the hydrogen-based powertrain analysis are reported.

Table 5. Estimated hydrogen overall consumption (8 roundtrips) and fuel cell performances

H_2 consumption [kg]	396
Mean fuel cell power [kW]	428
Fuel cell average efficiency [%]	52

In order to estimate on-board fuel storage requirements, different solution of hydrogen storage technologies have been considered. These include compressed gas at 350 and 700 bar, as well as cryogenic liquefied hydrogen. Thus, five solutions among those commercially available have been identified, as reported in Table 6.The computed on-board hydrogen storage volumes and weights, for each solution, are presented in Table 7. The results are provided for a single roundtrip (except for solution #5, where a single tank would be sufficient to allow 4 roundtrips) and for 8 roundtrips, that means to consider that all the amount of hydrogen required for a day of operation is carried on-board.

Table 6. Hydrogen storage technologies. Main features of a single tank.

ID	Manufacturer	Technology	Weight [kg]	H_2 capacity [kg]	Volume [L]	kg_{tank}/kg_{H_2}
#1	LUXFER [7]	compressed 350bar	95	4.96	285	19.15
#2	LUXFER [7]	compressed 700bar	61	2.15	101	28.37
#3	FABER [8]	compressed 350bar	140	5.00	270	28.00
#4	TOYOTA [9]	compressed 700bar	88	5.00	230	17.54
#5	LINDE [10]	liquid	2500	200.00	8300	12.50

Table 7. Estimated on-board hydrogen storage requirements.

ID	#1		#2		#3		#4		#5	
N. roundtrips	1	8	1	8	1	8	1	8	4	8
N. tanks	10	80	24	185	10	80	10	80	1	2
H_2 capacity [kg]	49.6	396.8	51.6	397.8	50.0	400.0	50.0	400.0	200.0	400.0
Weight tanks [t]	0.95	7.60	1.46	11.29	1.40	11.20	0.88	7.02	2.50	5.00
Total weight [t]	1.00	8.00	1.52	11.68	1.45	11.60	0.93	7.42	2.70	5.40
Volume [m^3]	2.85	22.83	2.41	18.59	2.70	21.60	2.30	18.40	8.30	16.60

The liquid hydrogen storage technology is the one providing both the lowest weight and volume, among the considered solutions. Although, solutions #2 and #4, that are, compressed hydrogen tanks at 700 bar, offer a similar volume requirement. Solution #4 is also the one among the compressed gas alternatives which owns the lowest weight. In all cases, the hydrogen storage system is significantly heavier than the Diesel tank of the original vessel configuration (between 5.40 t and 11.68 t against 2.5 t) and, especially, it requires even more than ten times its volume (22.83 m^3 for solution #1 vs 2.00 m^3 of the Diesel tank). This represents the most crucial issue when conceiving the vessel redesign to hydrogen propulsion, and it may imply the development of a well suited bunkering strategy. Regarding the power unit, the fuel cell system has volume and weight features comparable with those of the genset. In fact, basing on the tare weight only, the assumed fuel cell system should weight approximately 1.2 t, against the 3.5 t of the genset, while its volume, not considering the BoP, is around 1.7 m^3, which is in line with the space availability on-board of the vessel.

6 Conclusions

In this study, a technical feasibility analysis on the hydrogen-based redesign of a small size vessel has been carried out, with the aim of providing a clear picture on the hydrogen on-board systems requirements. The analysis is based on a realistic case scenario: a typical operational profile for a waterbus is used to evaluate energy, power and fuel storage requirements, and to setup a simple, preliminary, on-board energy management strategy. The fuel cell system has been sized to take the place of the original genset of the vessel, while the battery packs are kept the same as in the original configuration. The results confirm expectations: volume is the most critical factor related to hydrogen storage, regardless the specific choice of technical solution. This is especially true when refuelling during the daily operation is not considered an option. Hydrogen storage weight is also a crucial issue, with an increase of between two and five times with respect to the Diesel system. In contrast, all the considered hydrogen solutions are promising, if an ad-hoc bunkering strategy is conceived and/or the vessel architecture is suitably redesigned.

This research has received funding from the Fuel Cells and Hydrogen 2 Joint Undertaking (JU) under grant agreement No 101007226, project e-SHyIPS - Ecosystemic knowledge in Standards for Hydrogen Implementation on Passenger Ship. The JU receives support from the European Union's Horizon 2020 research and innovation programme and Italy, Finland, Germany, Greece, Spain, Cyprus, Netherlands.

References

1. D. Pivetta, C. Dall'Armi, R. Taccani, Int. J. Hydrog. Energy **46**, 35949-35960 (2021), https://doi.org/10.1016/j.ijhydene.2021.02.124.
2. C.H. Choi, S. Yu, I.S. Han, B.K. Kho, et al., Int. J. Hydorg. Energy **41**, 3591-3599 (2016), http://dx.doi.org/10.1016/j.ijhydene.2015.12.186.
3. M. Rivarolo, D. Rattazzi, T. Lamberti, L. Magistri, Int. J. Hydrog. Energy **45**, 25747-25757 (2020), https://doi.org/10.1016/j.ijhydene.2019.12.086.
4. S. Di Micco, M. Minutillo, A. Forcina, V. Cigolotti, A. Perna, E3S Web Conf. **312** (2021), https://doi.org/10.1051/e3sconf/202131207009.
5. PM400 Data Sheet, www.proton-motor.de, Proton Motor Power Systems.
6. S. Fang, Y. Xu, Z. Li, T. Zhao, H. Wang, IEEE Trans. Veh. Technol. **68**, 3361-3373 (2019), https://doi.org/10.1109/TVT.2019.2898461.
7. Luxfer Gas Cylinders – G-Stor™ H2 cylinders, www.luxfercylinders.com
8. Hydrogen-Faber Industry SPA, www.faber-italy.com/eng-login-vip-list.asp
9. Mirai-Toyota Europe, www.toyota-europe.com
10. Linde Engineering – Cryogenic standard tanks, www.linde-engineering.com

Design of a hydrogen-powered bicycle for sustainable mobility

Paolo Di Giorgio[1,2*], *Giovanni* Di Ilio[1,2], *Gabriele* Scarpati[1,2], *Giovanni* Erme[2,3], *Elio* Simeoni[1,2], *Elio* Jannelli[1,2]

[1] University of Naples "Parthenope", Naples, Italy
[2] ATENA Future Technology, Naples, Italy
[3] University of Cassino and Southern Lazio, Cassino, Italy

Abstract. Hydrogen-powered vehicles are emerging as a key source for a clean and sustainable mobility scenario. In particular, hydrogen technologies have a great potential for light mobility in urban areas, where traffic congestion may cause very high levels of local pollution. In this context, hybrid fuel cell/battery vehicles represent a promising solution, since they allow for extended driving range and short recharge time, which are two of the major concerns related to electric propulsion, in general. In this work, a new plug-in fuel cell electric bicycle concept is presented, where the on-board energy storage is realized by means of an innovative system integrating a battery pack with a metal hydride hydrogen tank. This solution allows to achieve very high performance in terms of riding range, which are unattainable with traditional battery electric bicycles. In particular, the hybrid energy storage system is conceived to provide an optimal thermal management of the two integrated components. The proposed design is developed on the basis of typical duty cycles acquired during on-road measurements. A prototype of the bicycle is then realized and bench-tested in order to assess design consistency and to evaluate its performances. The results show that the riding range of the new hydrogen-fuelled bicycle is about three times higher than the one for a similar electric bicycle.

1 Introduction

Hydrogen is capturing an unprecedented attention in industry as a versatile and sustainable energy carrier for a zero-emissions mobility scenario, and it is nowadays very much part of the political agenda of several Countries. Fuel Cell Electric Vehicles (FCEVs) are progressively taking hold in the market, as a viable alternative to Battery Electric Vehicles (BEVs). In particular, Plug-in Fuel Cell Electric Vehicles (PFCEVs) represents possibly an even more appealing solution than FCEVs, since they are generally more energy efficient, due to the possibility of component downsizing and optimization of control strategies [1,2]. In addition, the plug-in fuel cell/battery hybrid powertrain configuration is suitable for implementation across a wide range of road vehicle sizes and typologies, from heavy duty trucks [3–5] to lightweight vehicles such as bicycles, scooters and three-wheelers [6–8]. One crucial aspect related to PFCEVs concerns the on-board hydrogen storage. Typically, this is realized by means of a compressed gas system, given the relatively high energy density features of this technology. However, other common solutions involve the use of hydrogen carriers, like ammonia [9,10], or the adoption of metal hydrides for solid-state storage of hydrogen [11]. In particular, despite the growing interest in developing cleaner and more efficient solutions for light-mobility, the potential of hydrogen technologies for this class of vehicles has not been fully exploited yet, and only a very limited number of prototypes is available.

In this work, the authors propose the design of the power unit and of an innovative thermally integrated energy storage system for a plug-in fuel cell electric bike, hereafter referred to HyBike. In particular, the proposed energy storage solution consists of a small sized battery pack partially integrated into a MH tank for hydrogen storage. In this way, the waste heat of the battery pack can be effectively transferred via conduction to the MH tank, thus promoting hydrogen desorption and enabling a suitable thermal management of the battery pack. Moreover, the realized energy storage system has enhanced energy density, which results in an increase of about three times the riding range of the vehicle. The proposed design for the HyBike power unit and storage system is developed on the basis of power profiles acquired during road-tests for the original electric bicycle (e-bike) from which the new HyBike originates, and that are representative of typical operations. A prototype for the designed components is then realized and bench-tested using a Battery Testing System (BTS) reproducing the acquired operational profiles. The aim of the experimental tests was to assess the correct operation of the power unit and to evaluate the suitability of the new energy storage system, in terms of hydrogen consumption and achievable riding range.

2 Power unit design

The original e-bike is powered by a 250W @36V brushless electric motor (EM) mounted on the rear wheel, and it has a battery pack with capacity of 10Ah (360 Wh). The new HyBike keeps the same EM and driver, but its hybrid power unit is composed instead by a PEM fuel cell

* Corresponding author: paolo.digiorgio@uniparthenope.it

(FC) and a smaller battery pack. The hydrogen is solid-state stored in a MH tank that operates also as thermal management system for the battery pack. The FC is connected to the battery pack via a DC/DC step-up converter, that stabilizes the output voltage of the FC and controls its power output. In this way, the power produced by the FC stack can be either used by the EM or to charge the battery pack. A schematic representation of the fuel cell/battery hybrid power unit architecture is reported in Fig. 1.

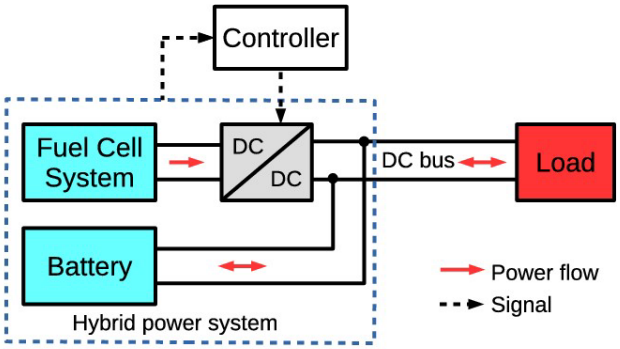

Fig. 1. Schematic of the HyBike power unit architecture.

The battery in the new power unit provides the power required by the EM during transient operations, while the FC operates basically as a range extender, providing the required average power and avoiding the battery pack State of Charge (SoC) to drop below a minimum threshold. In particular, the FC charges the battery whenever the power requested by the EM is sufficiently low, while the battery is discharged when the power demand is higher than the power output of the FC. Anyhow, the charging current of the battery pack can never be higher than its allowed maximum (that for a lithium-ion battery is usually much lower than the discharge current one).

2.1 Data acquisition

The design of power unit components was performed starting from the power profile acquired during the normal operation of the vehicle. To this aim, a large on-road data acquisition campaign has been carried out with the original un-modified model of the e-bike, powered by the 10Ah, 36V battery pack. Both battery voltage and current profiles were collected for 25-30 minutes for each test. As an illustrative example, two EM power profiles are shown in Fig. 2, which are representative of two different vehicle operative conditions: panel (a) refers to a typical urban use, hereafter referred as Urban Cycle A, with not frequent uphill and downhill, and characterized by several stops; panel (b) refers instead to a more severe path, hereafter referred as Urban Cycle B, presenting several climbs, which is consequently a more power demanding scenario. Both paths were about 7.5 km long. The duty cycle analysis revealed that, despite the nominal maximum continuous power of the electrical motor being 250 W, its measured power output reaches above 600 W during transient operations.

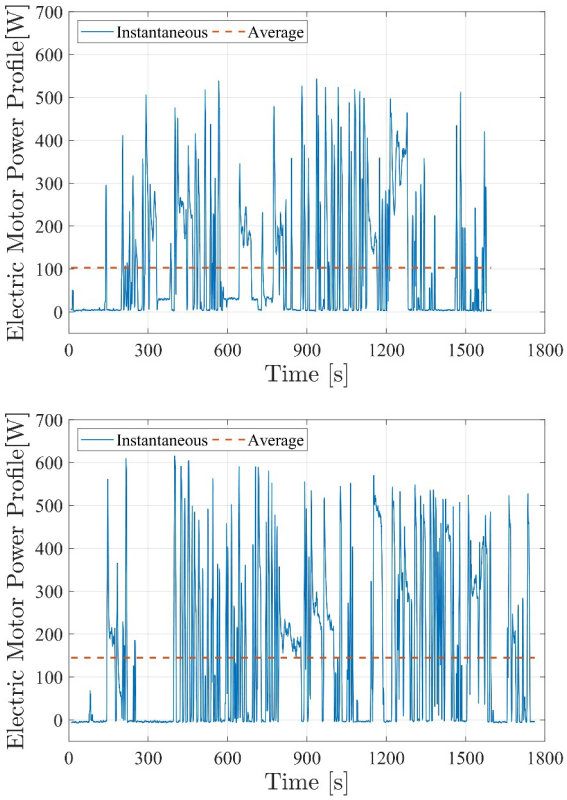

Fig. 2. EM power demand acquired during two road-tests. Top: Urban Cycle A. Bottom: Urban Cycle B.

For the two cases shown in Fig. 2, the average power consumption is equal to 103 W and 145 W, for Urban Cycle A and Urban Cycle B conditions, respectively, while the total energy requested by the EM amounts to 45 Wh and 71 Wh, respectively.

2.2 Fuel cell module

The size of the FC was determined basing on the maximum average power consumption of the EM acquired during the tests. The Horizon FCS-C200 PEM Fuel Cell [12], with a rated power of 200 W, was the final choice, since this model is able to provide the reference average power, and given also that its dimensions fit well with the available space on-board of the bicycle. Thus, this FC was bench-tested in order to characterize its performances.

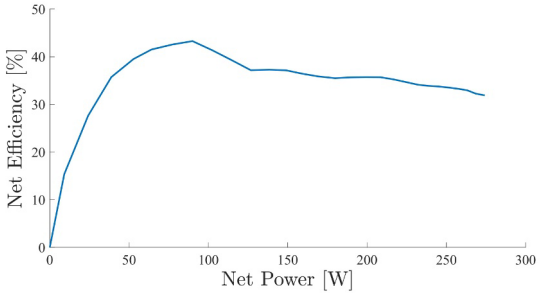

Fig. 3. Fuel cell efficiency curve.

Fig. 3 shows the measured FC net efficiency against the net power output. It is interesting to note how the peak efficiency is reached at about 100 W, while it decreases significantly for higher and, especially, lower values of power.

The power of the FC is controlled by a DC/DC converter placed between the FC and the battery pack. Since a programmable DC/DC converter that is suitable for the specific application was not find available on the market, a commercial DC/DC converter was instead used after ad-hoc modified. This is shown in Fig. 4.

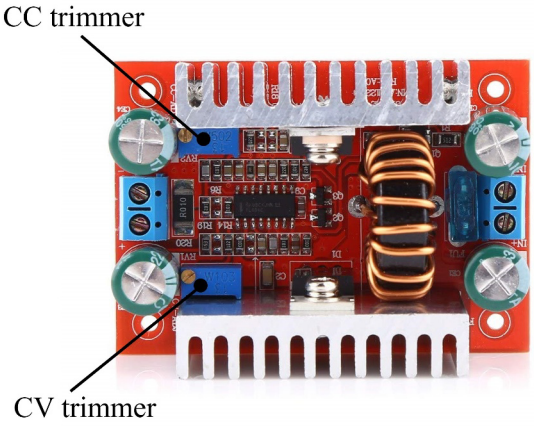

Fig. 4. The employed DC/DC converter, before the trimmer substitution.

The used converter is able to work both in CV mode (constant output voltage) and CC mode (constant output current): when the current is lower than the reference value (set through the CC trimmer), the DC/DC converter provides a constant output voltage (set through the CV trimmer); otherwise, as the current tends to exceed the reference value, the output voltage is lowered in order to maintain the output current equal to the reference value. Substituting the CC trimmer with a digital potentiometer, which is a variable resistance controlled by an electronic control unit, it is possible to control in real-time the DC/DC output current and so the power supplied by the FC. The CV trimmer was set to an output voltage of 41 V, so that the battery overcharging would be avoided in any case (the maximum operating voltage for a 36V battery pack is 42 V).

The power unit of the HyBike must be contained in a small space and arranged in such a way as not to negatively affect the comfort and drivability of the vehicle. Therefore, an extremely compact design was realized for the casing containing the power unit, which was finally positioned at the rear of the HyBike, as shown in Fig. 5.

2.3 Battery pack

The battery cells used for the new battery pack are lithium Nickel-Cobalt-Aluminum oxyde (NCA) cells provided by GWL, model LG MH1 [13], having nominal voltage of 3.67 V and maximum discharge current of 10 A. Their main features are summarized in Table 1.

Fig. 5. Casing of the HyBike power unit.

The battery pack is formed by two modules connected in series, each having a 5s2p configuration (Fig. 6-a). This allows to reach the nominal voltage of the EM and to provide the required maximum discharge current measured during the data acquisition (about 20 A, corresponding to roughly 700 W of discharge power). The total capacity of the battery pack is 6.4 Ah (230 Wh), that corresponds to about 65% of the capacity of the battery pack powering the original e-bike.

Table 1. Main characteristics of the LG MH1 battery cells used in the HyBike.

Model	LG MH1
Chemistry	NCA
Nominal Voltage [V]	3.67
Nominal Capacity [Ah]	3.2
Max continuous discharge current [A]	10 (3.125C)
Max continuous charge current [A]	3.2 (1.0C)
Recommended charge current [A]	1.6 (0.5C)

2.4 Power sharing algorithm

In order to prevent malfunctioning and damages of the battery pack, its charging current should not exceed the 3.2 A (0.5C), which corresponds to about 100 W. On the other hand, in order to avoid an excessive depletion of the battery SoC, the FC mean power output should be at least equal to the mean power required by the EM during vehicle operation (i.e. about 145 W, according to data acquisition). These considerations pose a constraint to the choice of a suitable energy management strategy. Therefore, the power split between FC and battery is setup according to a rule-based control strategy, with a feedback control on battery SoC, which distinguishes three modes of operation, as follows:

- *Charge Depleting* (CD): for a battery SoC higher than 70%, the HyBike run as a BEV.

- *Charge Sustaining – constant power* (CS-CP): the first time the battery SoC goes below 70%, or anytime the battery SoC hits the 60%, the FC is activated so to provide constant power at 100 W to support battery operation and/or partially recharge the battery, whenever the power request from the EM is lower than the FC power. This mode of operation is held until the SoC reaches a lower threshold value set equal to 50%.

- *Charge Sustaining – load following* (CS-LF): as the battery SoC reaches/is below its lower threshold (50%), the FC starts to operate by following the EM request and possibly recharging the battery, that is, according to a load following mode. Therefore, in this case, the FC power output is not constant anymore, but rather it is equal to the (variable) power requested by the EM plus a base constant load of 100 W. Under this mode of operation, the battery is used only to compensate the request of power whenever this is higher than that available from the FC, which is bounded to its allowed maximum. This approach allows for an optimal recharging strategy of the battery.

In order to ensure the proper functioning of the FC, a maximum power ramp rate given by 1.5 A/s has been imposed. The CS-CP and CS-LF modes of operation described above are alternatively activated so to perform a hysteresis cycle between the two predefined battery SoC limits.

3 Integrated energy storage system

The energy storage of the HyBike is a combined system where the battery pack and a MH tank are thermally integrated to each other into a compact device. By this design, an optimal self-sustained thermal management of the two components is realized, since the heat produced by the battery during operation is efficiently removed and transferred to the MH tank, where an endothermic hydrogen desorption process occurs.

In general, the choice for the most suitable alloy to be used as hydrogen storage material in MHs depends on the system operating conditions. Therefore, the hydride material chosen for the MH tank of the HyBike was selected among the commercially available ambient-temperature (0–30°C) alloys. Also, the maximum recharge pressure of the MH tank was set to 20 bar, in order to contain the wall thickness and the overall weight. This value for the pressure is compatible with the FC hydrogen feeding pressure, that is around 0.45–0.55 barg according to the FC technical data sheet. In addition to good absorption-desorption properties within the operating temperature and pressure conditions, the selected alloy should also i) be easy to activate, ii) have fast kinetics, iii) have high reversible gravimetric capacity, and iv) have good cyclability. Among all the intermetallic compounds responding to these requirements [14–16], the Hydralloy C5® supplied by Gesellsclhaft für Elektrometallurgie (GfE) was finally selected [17].

The MH tank of the HyBike is composed of eight aluminium cylinders, two of which are integrated with the battery cells to form a hexagonal modular structure, while the remaining six are external to the battery pack and exposed to air. Pictures for the prototypes of MH tank and assembled hybrid energy storage system are shown in Fig. 6. The cylindrical battery cells and the two integrated MH canisters are allocated in a 3D printed holder made of conductive PLA (GRAPHYLON3D) with 100% filling, which promotes the heat exchange between the two components. In particular, the size of the cylinders containing the MH was determined upon the estimation of the heat generated by the battery cells that has to be removed. This calculation led to an internal diameter of 24 mm for all the cylinders, and to a length of 450 mm for the 2 integrated cylinders, while the remaining 6 have a length of 250 mm. The external diameter of all cylinders was set to 30 mm. The final hydrogen capability of the MH tank was 50 g, for an overall weight of about 7 kg.

All the cylinders are externally threaded on one end (M30 x 1.5) so that they can be screwed-in a flange, which connect them together. The hydrogen flows through a 1 µm Swagelock filter before reaching a pressure reducer and then the FC stack. The sealing between the flange and the cylinders is guaranteed by a Teflon gasket. On the opposite end the cylinders are internally threaded and closed by an end cup with o-ring. The battery pack is enclosed in a carter and connected to the bicycle frame using screws, while the MH tank can be easily removed to be refilled.

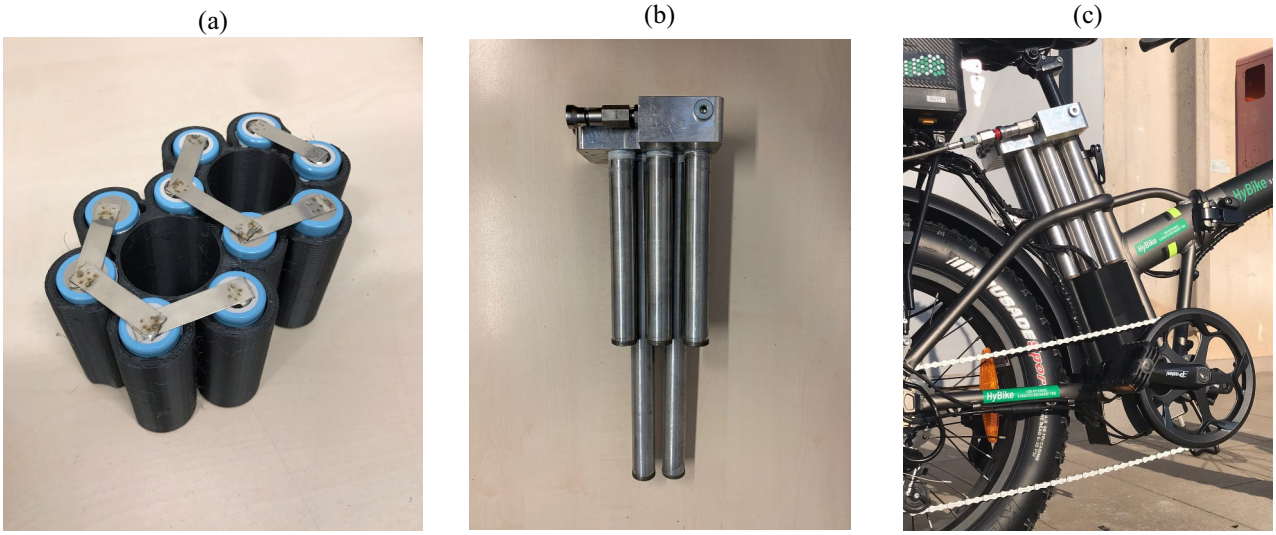

Fig. 6. Hybrid energy storage system of the HyBike: a) single module of the battery pack, b) MH tank, c) assembling of the storage system on the HyBike prototype.

4 Experimental results

In order to verify the correct operation of the designed system, two experimental tests were carried out. These were performed by using a regenerative BTS, which uses the power profiles acquired during the design phase (Fig. 2) to emulate the actual vehicle operation. The employed BTS is the IT8005-80-150 model, produced by ITECH, which has maximum power, voltage and current output equal to 5 kW, 80 V and 150 A, respectively.

Specifically, with the aim of investigating the power unit performances under the different modes of operation prescribed by the power sharing control algorithm, the two tests were carried out by imposing different initial conditions, in terms of battery SoC: for the Urban Cycle A, the initial battery SoC has been set to 39%, while for the Urban Cycle B, an initial value of 67% has been chosen. The obtained battery SoC profiles, during the two tests, are shown in Fig. 7.

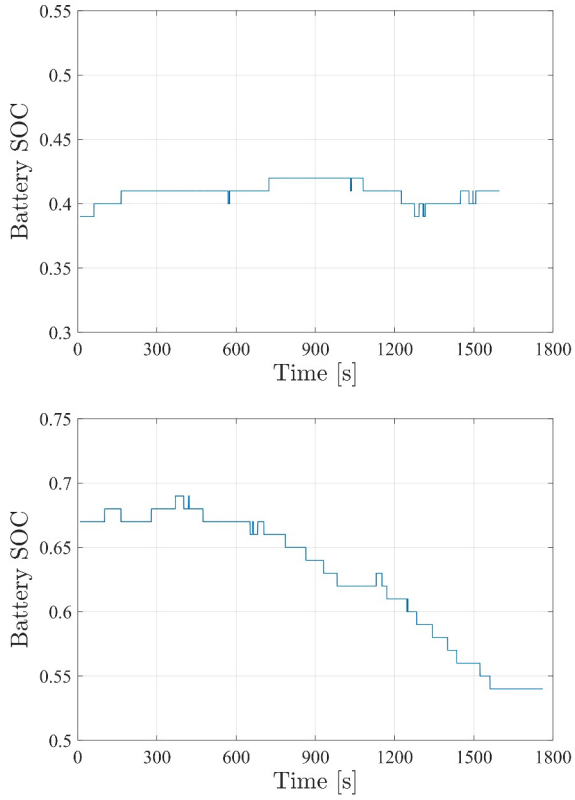

Fig. 7. Battery SoC profiles recorded during the two experiments. Top: Urban Cycle A. Bottom: Urban Cycle B.

The battery SoC remains fairly constant and always below 50% during the Urban Cycle A: in this case, the FC operates according to a CS-LF mode. In contrast, the battery SoC decreases during the Urban Cycle B, finally reaching a value of a 54%: in this case, the CS-CP mode of operation is the activated mode. Next, Fig. 8 reports the obtained power output profiles recorded during the two experimental tests. The results show that the power unit is able to provide the power requested by the EM during both the analyzed scenarios and under the two different power sharing modes, while preserving at the same time the correct operation of its components.

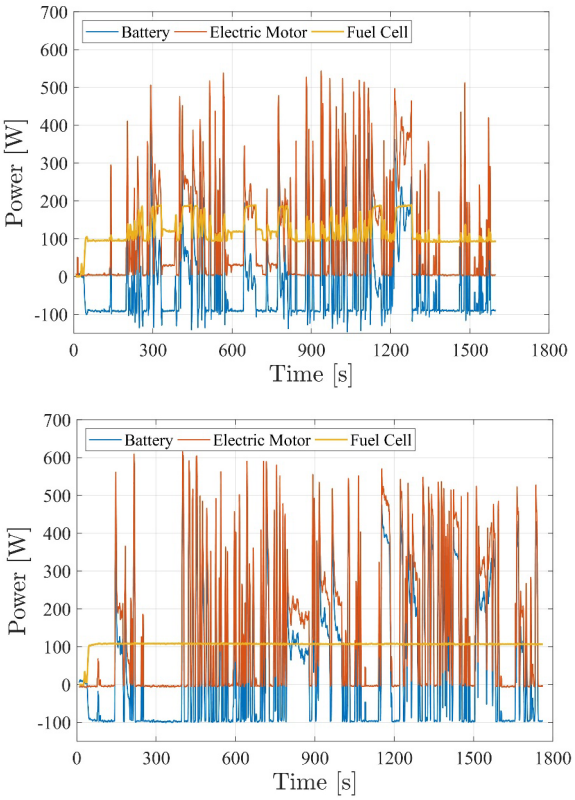

Fig. 8. Obtained power profile for FC and battery vs EM power demand. Top: Urban Cycle A. Bottom: Urban Cycle B.

In Table 2 the evaluated FC average efficiency and the measured hydrogen consumption are reported.

Table 2. Fuel cell performance and hydrogen consumption during experimental tests.

	Average FC efficiency [%]	H_2 consumption [g]
Urban Cycle A	36	4.4
Urban Cycle B	42	3.8

It should be noted that the average FC efficiency is higher for the Urban Cycle B since, in this case, the FC operates at constant power, with value close to the point of maximum efficiency (see Fig. 3). Considering that the MH storage tank has a hydrogen capacity of 50 g, the HyBike results to achieve a riding range of about 90 km in charge sustaining mode, while its all electric range, assuming a battery Depth of Discharge (DoD) of 80%, is about 25 km, thus leading to an overall estimated range of 115 km. This value is significantly higher than that for the original e-bike, for which a riding range of roughly 40 km is estimated, considering the same test conditions and under the same assumption of battery DoD.

5 Conclusions

A new hydrogen-powered bicycle has been presented in this study. The peculiarity of this vehicle lies in its on-board energy storage system: a hybrid system which is based on the thermal integration between a metal hydride

tank and the battery pack. By this way, not only the storage energy density of the vehicle is enhanced, but also an optimal thermal management of the two components may be achieved.

Specifically, the design of the power unit of the vehicle and of its hybrid energy storage system have been shown in this work. Thus, a prototype has been realized and bench-tested, in order to check design consistency and to evaluate its performances. The results are very promising: the riding range of the HyBike is about three times higher the one of the original e-bike. This may open interesting prospects towards a more sustainable urban mobility, since the new HyBike can potentially play a significant role in the light-vehicles panorama. Further investigations will be devoted to the assessment of the hybrid energy storage system, in terms of thermal management capabilities.

This research was funded by the project HyLIVE – Hydrogen Light Innovative Vehicles, grant n. B63D18000430007, under the program POR Campania FESR 2014/2020.

References

1. G. G. Nassif and S. C. A. d. Almeida, Int. J. Hydrogen Energy **45**, 21722 (2020)
2. H. Zhang, X. Li, X. Liu, and J. Yan, Appl. Energy **241**, 483 (2019)
3. Fuel Cells Bull. **2018**, 4 (2018)
4. G. Di Ilio, P. Di Giorgio, L. Tribioli, G. Bella, and E. Jannelli, Energy Convers. Manag. **243**, 114423 (2021)
5. G. Di Ilio, P. Di Giorgio, L. Tribioli, V. Cigolotti, G. Bella, and E. Jannelli, SAE Tech. Pap. 2021-24-0109 (2021)
6. M. Minutillo, A. Forcina, N. Jannelli, and A. Lubrano Lavadera, Energy **153**, 200 (2018)
7. J. L. Shang and B. G. Pollet, Int. J. Hydrogen Energy **35**, 12709 (2010)
8. P. Di Trolio, P. Di Giorgio, M. Genovese, E. Frasci, and M. Minutillo, Appl. Energy **279**, 115734 (2020)
9. A. Perna, M. Minutillo, S. Di Micco, V. Cigolotti, and A. Pianese, E3S Web Conf. **197**, 5001 (2020)
10. C. Zamfirescu and I. Dincer, J. Power Sources **185**, 459 (2008)
11. K. P. Brooks, S. J. Sprik, D. A. Tamburello, and M. J. Thornton, Int. J. Hydrogen Energy **45**, 24917 (2020)
12. Horizon Fuel Cell Technologies, *H-200 Fuel Cell Stack User Manual* (2021)
13. GWL Power, *Li-Ion Cell LG MH1 Data Sheet* (2021)
14. B. Tanç, H. T. Arat, Ç. Conker, E. Baltacioğlu, and K. Aydin, Int. J. Hydrogen Energy **45**, 26344 (2019)
15. C. H. Chao and J. J. Shieh, Int. J. Hydrogen Energy **37**, 13141 (2012)
16. L. Xu, M. Ouyang, J. Li, F. Yang, L. Lu, and J. Hua, Appl. Energy **103**, 477 (2013)
17. B. Sakintuna, F. Lamari-Darkrim, and M. Hirscher, Int. J. Hydrogen Energy **32**, 1121 (2007)

Development of a plug-in fuel cell electric scooter with thermally integrated storage system based on hydrogen in metal hydrides and battery pack

Paolo Di Giorgio[1,2*], *Gabriele* Scarpati[1,2], *Giovanni* Di Ilio[1,2], *Ivan* Arsie[1,2] and *Elio* Jannelli[1,2]

[1] University of Naples "Parthenope", Naples, Italy
[2] ATENA Future Technology, Naples, Italy

Abstract. The thermal management of lithium-ion batteries in hybrid electric vehicles is a key issue, since operating temperatures can greatly affect their performance and life. A hybrid energy storage system, composed by the integration of a battery pack with a metal hydride-based hydrogen storage system, might be a promising solution, since it allows to efficiently exploit the endothermic desorption process of hydrogen in metal hydrides to perform the thermal management of the battery pack. In this work, starting from a battery electric scooter, a new fuel cell/battery hybrid powertrain is designed, based on the simulation results of a vehicle dynamic model that evaluates power and energy requirements on a standard driving cycle. Thus, the design of an original hybrid energy storage system for a plug-in fuel cell electric scooter is proposed, and its prototype development is presented. To this aim, the battery pack thermal power profile is retrieved from vehicle simulation, and the integrated metal hydride tank is sized in such a way to ensure a suitable thermal management. The conceived storage solution replaces the conventional battery pack of the vehicle. This leads to a significant enhancement of the on-board gravimetric and volumetric energy densities, with clear advantages on the achievable driving range. The working principle of the novel storage system and its integration within the powertrain of the vehicle are also discussed.

1 Introduction

Improving energy efficiency and curbing CO_2 emissions are top priority issues that need to be addressed by the automotive manufactures in the pursuit of a sustainable mobility. The transportation sector is indeed one of the largest contributors of the world's fuel consumption, taking up 49% of oil resources [1]. Battery Electric Vehicles (BEVs) represent a sustainable solution for the mobility, even if the long recharge time and the high cost of the battery pack are critical issues for their diffusion [2]. The Fuel Cell Electric Vehicle (FCEV), on the other hand, is emerging as a promising solution given its potential to provide both longer range and shorter refueling time; however, the refueling infrastructure is still under development and has high investment costs [3-5]. In this context, Plug-in Fuel Cell Electric Vehicles (PFCEVs) overcome the drawbacks of the above-mentioned solutions in terms of recharging time, refueling infrastructure and driving range. As a matter of fact, PFCEVs have a moderately-sized battery, which is rechargeable at relatively low power from the electric grid, and a small size fuel cell stack which operates as a range extender. Since the average actual power demand is only a fraction of the peak power that the vehicle power unit can provide, in a PFCEV the fuel cell can be sized on the average vehicle power demand, thus providing the required energy, while the battery pack acts as a power buffer. Thus, this configuration allows to reduce the overall costs by downsizing both the fuel cell stack and the battery pack [6-10]. Moreover, the electric range of the battery can satisfy short commutes, reducing the need of a widespread diffusion of hydrogen refueling stations that a FCEV solution would have, with advantages on the infrastructure costs [11].

The thermal management system of the battery pack is a key element for hybrid electric vehicles, and especially for PFCEVs, since in these vehicles the battery pack undergoes more severe thermal stresses than in BEVs. In fact, in PFCEVs the battery pack typically experiences higher C-rates than in BEVs, which lead to a larger heat production. Moreover, the limited size and thermal capacity of the battery pack can further worsen the thermal management issues [12]. In particular, if the temperature in a battery cell (especially if aged) rises above 80°C, the thermal runaway can be triggered and its propagation within the pack can further result in catastrophic hazards [13]. Therefore, in these vehicles, high power battery cells (with relatively low internal resistance) and an efficient thermal management system are required.

To address this critical issue, an interesting option may be represented by the use of an integrated system which combines a metal hydride (MH) hydrogen storage with a battery pack, into a single, compact, device. The

* Corresponding author: paolo.digiorgio@uniparthenope.it

idea behind this solution is to exploit the endothermic desorption process of hydrogen in metal hydrides during vehicle operation to remove the excess heat from the battery pack. In fact, by means of an ad-hoc design, the MH tank and the battery pack can be placed in direct contact to each other, thus favouring a purely conductive heat transfer between them. At the same time, the on-board energy density of the storage system of the vehicle is enhanced, since a thermal management system is not required. In this study, a specific design configuration of such a Hybrid Energy Storage System (HESS) for a plug-in fuel cell electric scooter (Fig. 1) is developed and a prototype is presented. Also, its integration within the vehicle power-unit is discussed.

Fig. 1. The plug-in fuel cell electric scooter.

The overview of this work is as follows: the study starts with the design of a fuel cell/battery hybrid powertrain for a two-wheeler. To this aim, a vehicle dynamic model is setup and used to estimate power and energy requirements. The numerical model, along with a rule-based energy management strategy, is then used to simulate the vehicle performance in typical operating conditions and to estimate the thermal power produced by the battery pack. This is used to size the MH tank integrated into the HESS. Finally, the energy performances of the proposed storage solution, in terms of gravimetric and volumetric energy densities, are evaluated and compared to those for the conventional battery pack of the base plug-in fuel cell electric scooter configuration.

2 Plug-in fuel cell electric scooter architecture

The base vehicle is a battery electric scooter equipped with a 48V-2kW brushless DC electric motor and a 40Ah-48V lead-acid battery pack (four 12V modules connected in series). The vehicle does not enable kinetic energy recovery from braking. In the base plug-in fuel cell electric configuration of the vehicle, the lead-acid battery pack has been replaced by a more compact and performing 20Ah-48V lithium iron phosphate ($LiFePO_4$) battery pack, a Proton-Exchange Membrane (PEM) fuel cell stack and a MH tank for hydrogen storage. The fuel cell vehicle architecture keeps the same electric motor of the original vehicle. The plug-in fuel cell electric scooter was further upgraded by replacing the $LiFePO_4$ battery pack with a HESS, which is composed by a new battery pack thermally integrated with a secondary MH tank. The schematic layout of the two-wheeler powertrain configuration with the integrated HESS is shown in Fig. 2. The specific HESS design allows to downsize the battery pack, thus increasing the overall on-board energy density, as well as the hydrogen availability.

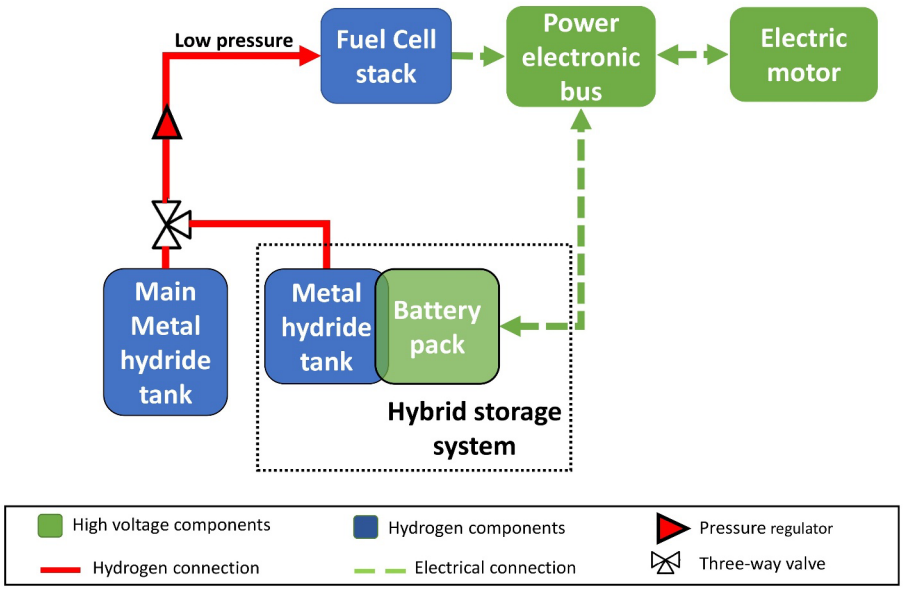

Fig. 2. Power unit and hydrogen storage system architecture for the plug-in fuel cell electric scooter.

The main MH tank is heated up by the waste heat of the fuel cell stack. The two MH tanks, are directly connected to each other by means of a three-way valve. The connection between the two tanks allows for an efficient and self-sustained thermal management of the battery pack. In fact, as shown in [14], the reaction rate for hydrogen desorption is proportional to the difference between the hydrogen pressure in tank and the desorption equilibrium pressure of hydrogen, the latter depending on temperature. Thus, depending on the battery pack temperature, the reaction rate for hydrogen desorption in the secondary tank varies: higher temperatures correspond to higher desorption equilibrium pressures, and vice-versa. Therefore, when the battery pack temperature rises above the one of the main tank, the hydrogen desorption rate in the secondary MH tank is higher than that in the main MH tank and the cooling effect on the battery pack increases. On the contrary, when the temperature of the battery pack goes below the temperature of the main MH tank, the hydrogen desorption rate is higher in the main MH tank and the cooling effect on the battery pack is reduced, as requested. During this process, the hydrogen concentration in the two tanks decreases approximately with same rate, due to the self-regulated desorption of the hydrogen content in the metal hydride. It should be emphasized that an inherent advantage from the adoption of the proposed solution is related to the hydrogen refueling infrastructure that would be required. The two MH tanks have indeed a significant lower pressure than compressed hydrogen storage systems. This would allow, in principle, a reduction of costs for the refueling infrastructure.

3 Performance analysis

In order to design the power unit of the plug-in fuel cell electric scooter, a preliminary road-test for the original battery electric scooter was made, with the aim of estimating maximum power required by the electric motor and auxiliaries power consumption. The test provided the following values: 2 kW of maximum power demand and 36 W of average auxiliary power. Since the acquired data from the road-test could not be considered as representative of a typical/mean duty cycle for the vehicle, a dynamic model was further setup to simulate the vehicle and better characterize its performance by using a standard driving cycle. According to this model, the power at the electric motor is computed as follows:

$$P_{EM} = P_t/\eta_{EM} + P_{aux} \quad (1)$$

where $\eta_{EM} = 0.85$ is the electric motor efficiency, P_{aux} is the auxiliary power, and P_t is the traction power that, assuming the road grade equal to zero, is given by:

$$P_t = 0.5\rho v^3 A C_d + f_r mgv + \delta mav \quad (2)$$

with: $\rho = 1.2$ kg/m^3 the air density, $A = 0.7$ m^2 the vehicle frontal area, $C_d = 0.7$ the drag coefficient, $f_r = 0.01$ the rolling resistance coefficient, $m = 206$ kg the vehicle mass, g the gravity acceleration, $\delta = 1.1$ the mass factor, a the instantaneous acceleration, and v the vehicle speed. Thus, an ad-hoc modified version of the Artemis urban cycle was used to assess the scooter performances. Corrections to the original Artemis speed profile were indeed necessary in order to comply with the speed constraint of the tested vehicle. The resulting driving cycle is shown in Fig. 3.

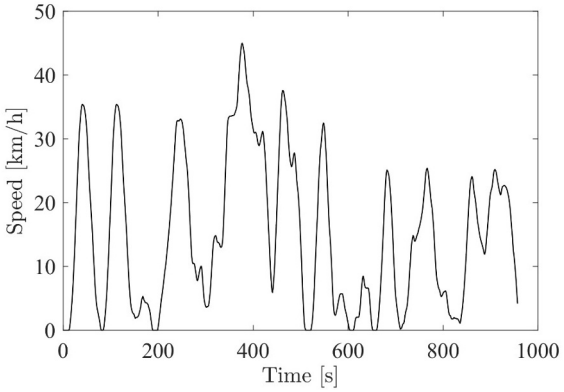

Fig. 3. Modified Artemis urban cycle, for the testing of the electric scooter performance.

The maximum and mean power obtained from the numerical model are equal to 2.8 kW and 370 W, respectively. These values have been considered to size the power unit of the new hydrogen-fueled vehicle.

4 Fuel cell design and characterization

The power unit design for the plug-in fuel cell electric scooter was made according to the following principle: the fuel cell has to be sized to provide at least the mean power requested by the electric motor, while the battery pack will satisfy the peak power requests. Therefore, a fuel cell with 1 kW of maximum power has been considered a suitable choice, since this size would allow the fuel cell to operate efficiently at values of power around the requested base load. In particular, a fuel cell system made of two Horizon FCS-C500 PEM Fuel Cell [15] modules (rated power: 500 W), connected in series, was selected. This choice leaves enough space for the main MH hydrogen storage to be placed in front of the cooling fans of the fuel cells.

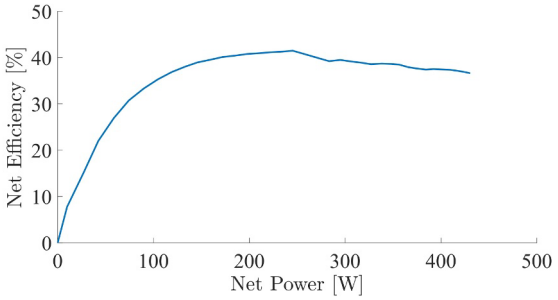

Fig. 4. Fuel cell efficiency curve.

In order to fully characterize the fuel cell performance, a bench-test was conducted: a maximum net efficiency of

40% was obtained for a value of power close to 250 W, as shown in Fig. 4.

5 Main MH tank design

The hydrogen storage in MHs is based on a reversible reaction of gaseous H_2 with a parent hydride forming metal alloy or intermetallic compound. The use of MHs allows a very high volumetric hydrogen storage density even at low pressure [16]. In addition, the endothermic nature of the MH decomposition (hydrogen desorption) results in a high inherent safety of MH-based hydrogen storage systems. The hydride material chosen for the MH tanks of the plug-in fuel cell electric scooter is the Hydralloy C5, that has been selected among commercially available room-temperature alloys. The Hydralloy C5 belongs to a class of pseudo-binary AB_2 alloys and it is produced by Gesellsclhaft für Elektrometallurgie (GfE). The hydrogen desorption characteristics of this alloy are reported in Table 1. The adopted alloy presents also a good compromise between raw material cost and hydrogen storage capacity [17].

Table 1. Hydrogen desorption characteristics of Hydralloy C5.

Parameter	Value	Ref.
Plateau pressure (@ 44 °C)	2 MPa	[18]
Max reversible H_2 content (wt %)	1.77 %	[18]
ΔH [kJ/mol$_{H2}$]	28.4	[19]
ΔS [J/(mol$_{H2}$K)]	112	[19]

In particular, the main hydrogen storage system allows to store 150g of hydrogen, and it is composed of five MyH2® SLIM 350 cartridges connected in parallel, each having a storage capacity of 30g of hydrogen. The MH cartridges are placed in front of the fuel cell fans, in order to exploit the waste heat to promote the hydrogen desorption process from the cartridges. Fig. 5 and Fig. 6 show pictures of a single MH cartridge and of a detail of the scooter prototype, where it is possible to observe the main MH tank and the fuel cell stack layout.

Fig. 5. MyH2® SLIM 350 cartridge used in the main MH tank of the plug-in fuel cell electric scooter.

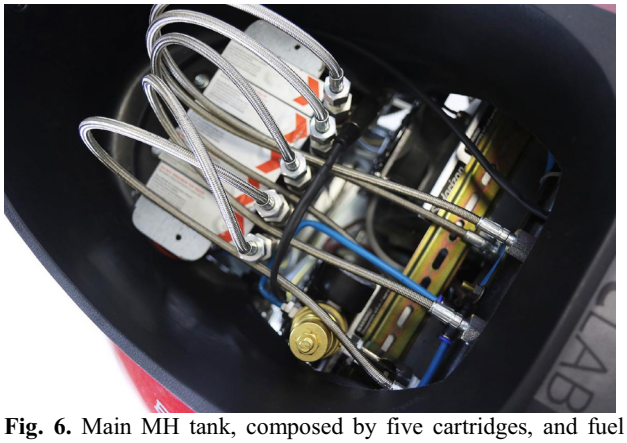

Fig. 6. Main MH tank, composed by five cartridges, and fuel cell system, on the scooter prototype.

6 Hybrid storage system design

The HESS of the new plug-in fuel cell electric scooter is composed by a battery pack integrated with a metal hydride tank. Specifically, its configuration is based on a modular hexagonal structure, shown in Fig. 7, which is used to enhance the heat transfer between the two components and increase the packing density.

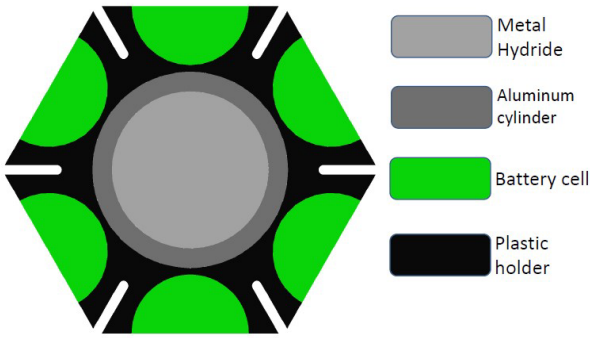

Fig. 7. 2D schematic representation of the HESS module.

In each HESS module, an aluminum cylinder containing the MH alloy is placed at the center, while six battery cells are around it. The heat transfer between the battery cells and the MH canister is purely conductive and it is ensured by a 3D-printed thermally conductive PLA holder. The reason why the holder containing battery cells and the MH canisters is made of plastic material is that it has to allow enough thermal conduction between these two components while ensuring protection to the battery cells at the same time, so to prevent spreading of thermal runway reactions. In addition, thermal insulation cavities have been included in the plastic holder between neighboring battery cells, to further reduce the risk of an undesired catastrophic thermal runaway.

In the hydrogen-fueled scooter, several hexagonal modules are combined together to form its HESS, as detailed in the following Sections.

6.1 Battery pack

The battery pack of the HESS is composed by two modules connected in series, each made of 28 Panasonic

NCR18650BD cylindrical cells (18 mm diameter, 65 mm length) in a 7s4p configuration. These are Lithium Nickel Cobalt Aluminium Oxide (NCA) cells, with 3.67 V nominal voltage and 3.2 Ah capacity. From data-sheet, these cells are able to deliver 10 A continuous discharge current, that corresponds to a C-rate of 3.125C, while the recommended charge current is 1.6 A, that is, 0.5C. The chosen battery pack configuration is designed in such a way to provide a compromise between power and energy capacity features: the overall nominal capacity of the battery pack is around 660 Wh, the maximum continuous power that it can deliver is roughly equal to 2 kW, while the maximum charging power amounts to about 330 W.

6.1.1 Battery thermal power evaluation

In order to determine the size of the integrated MH storage tank and to properly balance the HESS, the thermal power produced by the battery pack during its operation has been estimated by means of vehicle simulation. To this aim, an ad-hoc developed quasi-steady backward-looking simulator has been employed. In particular, a rule-based energy management strategy has been implemented, which consists of three different modes of operation, as follows:

- *Charge Depleting* (CD): the vehicle operates as a BEV for a battery State of Charge (SoC) higher than 60% or if the hydrogen fuel is fully depleted.

- *Charge Sustaining – constant power* (CP): the first time the battery SoC goes below 60%, and anytime the battery SoC hits the 50%, the fuel cell operates at constant power, in such a way to allow for battery partial depletion, which instead has the role of fulfilling the peak power request. In particular, the value of the fuel cell power output is set to 365 W, that, including a DC/DC efficiency of 90%, corresponds to the maximum charging power for the battery. In fact, under this mode of operation, the charging of the battery is still allowed, and it occurs anytime the overall power request is lower than the fuel cell power. Therefore, this approach allows to maximize the charging of the battery, while avoiding its damaging. The CP mode of operation is held until the SoC reaches a lower threshold value set equal to 40%.

- *Charge Sustaining – load following* (LF): whenever the battery SoC hits the lower threshold of 40%, the fuel cell operates to fully supply the electric motor and recharging the battery at the same time, that is, according to a load following mode of operation. Therefore, the fuel cell power output is made of the sum of two contributions: a constant base load equal to the CP set-point (i.e. 365 W), and a variable contribution which is equal to the electric motor power request. By this way, also this mode of operation extends battery life, since it avoids its damaging due to exceeding charging current. Clearly, the value of the power output for the fuel cell is bounded to its allowed maximum. Thus, if the electric power demand is higher than the maximum power that can be provided by the fuel cell, the request is instantaneously fulfilled by the battery.

The modified Artemis urban cycle (Fig. 3) is then used as reference driving cycle to simulate the power unit operation. The vehicle is assumed to start its journey with a battery SoC equal to 0.90. The simulation is run until the hydrogen stored on-board in the main MH tank is fully depleted and the battery SoC reaches 0.2. Fig. 8 shows the obtained battery SoC profile, with highlighted the selected power unit modes of operation.

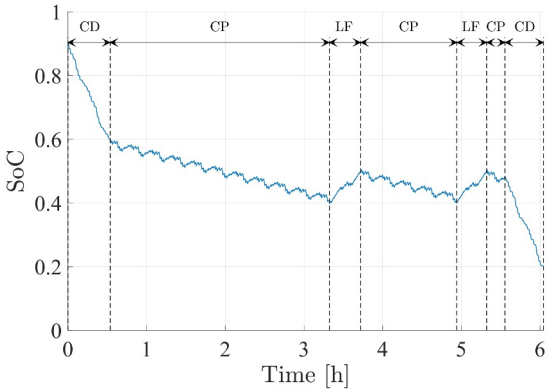

Fig. 8. Battery SoC during vehicle operation. The power unit modes of operation are reported on the top.

The driving range of the hydrogen-powered scooter –not considering the hydrogen stored into the HESS yet– is about 6 hours. The fuel cell operates near its maximum efficiency point for most of the duration of the trip, with an average efficiency of 39.5 %. Next, in Fig. 9 the fuel cell and battery power profiles are depicted against the electric motor power request, for specific time frames, corresponding to the different modes of operation, that are CD, CP and LF, respectively.

From the knowledge of the battery power output profile, the thermal power produced by each battery cell during vehicle operation has been then retrieved. To this aim, a conservative value of 55 mΩ for the battery cell overall resistance (internal resistance and connections) has been assumed. As a result, each battery cell produces on average about 0.62 W under the CD mode of operation. The battery pack heat production in charge sustaining mode is clearly lower than in CD mode. In particular, a value of 0.45 W has been obtained for the average thermal power produced per cell under the CP mode of operation, while in LF mode this value is further reduced and equal to 0.30 W since, in this case, the root mean square of the battery current is the lowest.

The thermal power produced by the battery pack must be dissipated, otherwise it can lead to an uncontrolled temperature raise which can negatively affect the battery performances and, eventually, bring to its failure. The heat removal for the battery pack of the fuel cell electric scooter is accomplished by exploiting the endothermic desorption process of hydrogen in the integrated MH tank of the HESS.

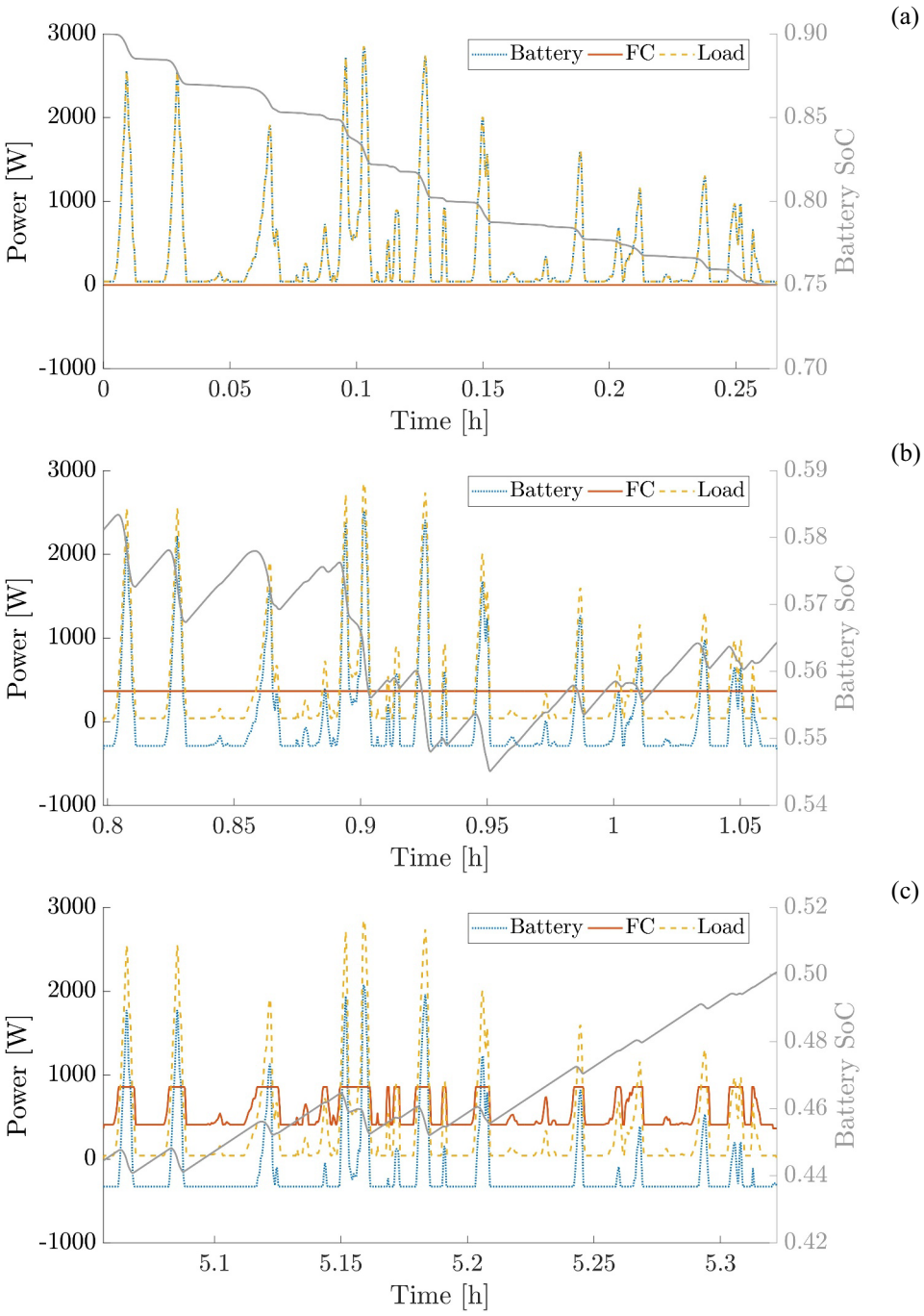

Fig. 9. Battery and fuel cell power output profiles vs the electric motor requested power, during: CD (a), CP (b) and LF (c) modes of operation. The battery SoC is also reported (grey line).

6.2 Integrated MH storage system

In order to provide an effective thermal management of the battery pack, the integrated MH tank of the HESS must be suitably designed. Therefore, the size of the cylinders containing the MH was determined taking into account the estimated amount of thermal energy produced by the battery pack during vehicle operation. Specifically, a reference cycle of 6 hours of continuous operation in CP mode (that is, the most critical condition in terms of battery thermal power production during the charge sustaining) has been assumed.

The two battery modules are stacked one on top of the other and they are crossed by seven aluminium cylinders containing the MH alloy. In Fig. 10 a prototype representation of the HESS and its components is shown.

Given the hexagonal modular geometry of the HESS, each MH cylindrical unit is surrounded by three equivalent battery cells on two rows, therefore it has to contain enough hydrogen such that its desorption ensures the thermal management of six battery cells, on average. The total heat that each MH unit must be capable of dissipating is then approximately equal to 60 kJ, according to the following equation:

$$Q = n\,\dot{Q}_b\,t \tag{3}$$

where n = 6 is the number of involved battery cells, $\dot{Q}_b$ = 0.45 W is the average thermal power produced by a single battery cell under the CP mode of operation, and t = 6 h is the assumed time of continuous operation. Such an amount of energy corresponds to the thermal energy required to desorb roughly 4.2 g of hydrogen (Table 1). By considering a maximum reversible hydrogen content of 1.77% in weight, this estimated amount of hydrogen can be reversibly stored in 232 g of metal hydride alloy, that assuming a density of the powder of about 4000 kg/m^3, is contained in about 58 cm^3. As a consequence, considering that the cylinder length is equal to 130 mm (that is, two times the battery cell height), the resulting internal diameter of each canister is around 24 mm. By setting also a 3 mm wall thickness for the aluminium cylinder (a reasonable estimate for the operating pressure range), an external diameter of 30 mm is obtained for the whole MH cylindrical unit. With this configuration, the HESS of the scooter provides an overall extra-amount of hydrogen equal to about 29 g.

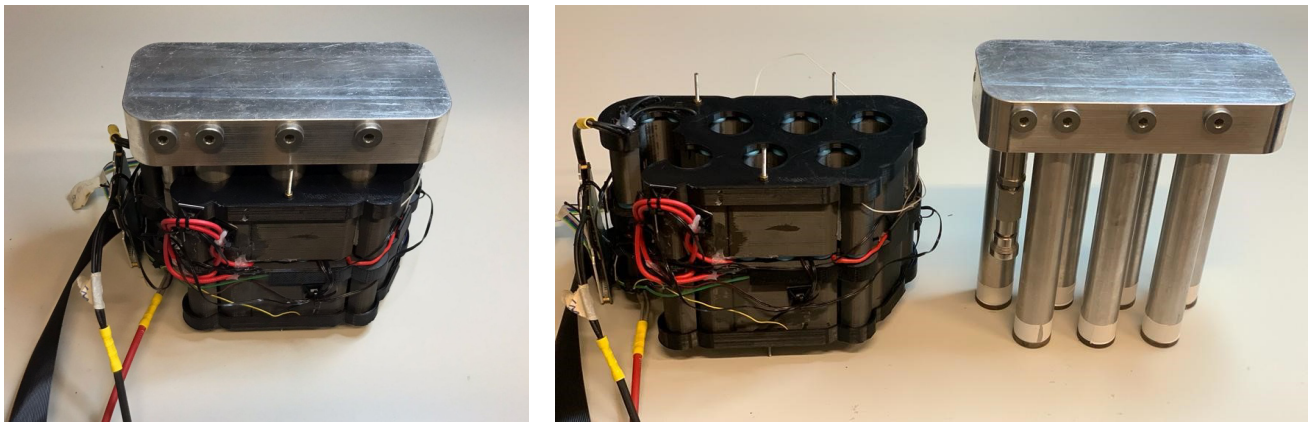

Fig. 10. HESS of the plug-in fuel cell electric scooter. Left: full system prototype. Right: detail for system components - battery pack and MH tank.

7 Energy performance

Table 2 shows the comparison between the HESS of the new plug-in fuel cell electric scooter and the battery pack of its base configuration. In particular, the values for the useful gravimetric (UED_g) and volumetric (UED_v) energy density provided in Table 2 have been calculated by assuming an 85% Depth of Discharge (DoD) for the battery pack and, in the case of HESS, by assuming an average efficiency (η_{FC}) of 50% for the fuel cell, as follows:

$$UED_g = \frac{m_{H_2} LHV_{H_2} \eta_{FC} + E_b DoD}{m_{HESS}} \quad (4)$$

$$UED_v = \frac{m_{H_2} LHV_{H_2} \eta_{FC} + E_b DoD}{V_{HESS}} \quad (5)$$

where m_{H2} is the mass of stored hydrogen, LHV_{H2} = 120 MJ/kg, E_b is the battery energy capacity, while m_{HESS} and V_{HESS} are the overall mass and volume of the HESS.

The HESS outperforms the LiFePo$_4$ battery pack solution, in terms of energy storage capabilities. In fact, the two storage systems have similar UED_g to each other but the HESS presents a significantly higher UED_v: the useful volumetric energy density of the HESS is almost the double than that of the standard battery pack. This is a key feature of the HESS, which make it particularly suitable for lightweight mobility, as in the present case, where lack of on-board space availability may represent a crucial aspect that limits the driving range.

Table 2. Main features of the HESS in comparison with the LiFePO$_4$ battery pack of the plug-in fuel cell electric scooter.

	HESS	**LiFePO$_4$ battery pack**
Overall size [mm]	90x210x240	130x160x310
Volume [L]	4.5	6.4
Weight [kg]	9	7.5
Battery pack nominal capacity [Wh]	660	960
Stored H_2 [g]	29	-
Total useful energy [kWh]	1.044	0.816
UED_g [Wh/kg]	116	109
UED_v [Wh/L]	230	127

The thermal integration of the two components, MH and battery pack, allows indeed to avoid the use of an ordinary thermal management system, in favour of additional hydrogen storage capacity. It should be also emphasized that the actual volume of the HESS is substantially lower (~3.7 L) than the one indicated in Table 2, which instead refers to the volume of the parallelepiped in which the system is inscribed, thus leading to a conservative estimation.

The overall driving range of the plug-in fuel cell electric scooter with HESS is equal to about 7 h (105 km), on the base of the reference driving cycle used in this study, while the driving range of the vehicle with

$LiFePo_4$ battery pack solution is about 6.5 h (99 km). In particular, the extra-amount of hydrogen contained in the HESS extends the range of about 1 h. In contrast, the battery electric scooter achieves 3.6 h (54 km) of driving range, under the same battery operational conditions and driving cycle.

8 Conclusions

A plug-in fuel cell electric scooter with an innovative energy storage system has been presented throughout this study. The key of such an energy storage system is the thermal coupling between a MH tank and a NCA battery pack: the two components are in direct contact to each other, thus allowing for an optimal thermal management of the system. In fact, the heat produced by the battery pack during vehicle operation is efficiently removed through the endothermic desorption process of hydrogen in the MH. Moreover, the compact design of the HESS leads to high energy density values, which in turn allow for an enhanced driving range, with respect to that achievable by the vehicle equipped with a standard battery pack. The presented solution is promising: the developed HESS prototype leaves room for further design improvement, with potential of effectively boost the performance of plug-in fuel cell lightweight vehicles.

This research was funded by the project HyLIVE – Hydrogen Light Innovative Vehicles, grant n. B63D18000430007, under the program POR Campania FESR 2014/2020.

References

1. S. Amjad, S. Neelakrishnan, R. Rudramoorthy, Renew. Sustain. Energy Rev. 14, 1104-1110 (2010)
2. E. Wood, L. Wang, J. Gonder, M. Ulsh, SAE Int. J. Commer. Veh. 6, 563-74 (2013)
3. M. Minutillo, A. Perna, P. Di Trolio, S. Di Micco, E. Jannelli, Int. J Hydrog. Energy 46, 10059-10071 (2021)
4. M. Minutillo, A. Perna, A. Forcina, S. Di Micco, E. Jannelli, Int. J Hydrog. Energy 46, 13667-13677 (2021)
5. A. Perna, M. Minutillo, S. Di Micco, P. Di Trolio, E. Jannelli, AIP Conf. Proceedings 2191, 020127 (2019)
6. P. Di Trolio, P. Di Giorgio, M. Genovese, E. Frasci, M. Minutillo, Appl. Energy 279, 115734 (2020)
7. H. Zhang, X. Li, X. Liu, J. Yan, Appl. Energy 241, 483-490 (2019)
8. G.G. Nassif, S.C.A. de Almeida, Int. J Hydrog. Energy 45, 21722-21737 (2020)
9. G. Di Ilio, P. Di Giorgio, L. Tribioli, G. Bella, E. Jannelli, Energy Convers. Manag. 243, 114423 (2021)
10. G. Di Ilio, P. Di Giorgio, L. Tribioli, V. Cigolotti, G. Bella, E. Jannelli, SAE Technical Paper 2021-09-05 (2021)
11. B. Lane, B. Shaffer, G.S. Samuelsen, Int. J. Hydrog. Energy 42, 14294-14300 (2017)
12. Q. Wang, B. Jiang, B. Li, Y. Yan, Renew. Sustain. Energy Rev. 64, 106-128 (2016)
13. H. Wang, W. Shi, F. Hu, Y. Wang, X. Hu, H. Li, Energy 224, 120072 (2021)
14. A.R. Sánchez, H.P. Klein, M. Groll, Int. J. Hydrog. Energy 28, 515-27 (2003)
15. Horizon Fuel Cell Technologies, H-500 Fuel Cell Stack User Manual (2021).
16. G. Han, Y.K. Kwon, J.B. Kim, S. Lee, J. Bae, E.A. Cho, et al., Appl. Energy 259, 114175 (2020)
17. G. Sandrock, J. Alloys Compd. 293, 877-888 (1999)
18. G. Capurso, B. Schiavo, J. Jepsen, G. Lozano, O. Metz, A. Saccone, S. De Negri, J. Bellosta von Colbe, T. Klassen, M. Dornheim, Appl. Phys. A 122, 236 (2016)
19. K. Herbrig, L. Röntzsch, C. Pohlmann, T. Weissgaerber, B. Kieback, Int. J. Hydrog. Energy 38, 7026-7036 (2013)

Bioelectricity production of PMFC using Lobelia Queen Cardinalis in individual and shared soil configurations

Grégory Bataillou*, *Naoufel* Haddour, and *Christian* Vollaire

Laboratoire Ampère (CNRS), Université Claude Bernard Lyon 1, Insa Lyon, Ecole Centrale de Lyon, 36 avenue Guy de Collongue - 69134 Ecully

Abstract. Plant Microbial Fuel Cell (PMFC) creates electricity from oxidation of root exudates by microbia anaerobic digestion, and reduction of dioxygen to water. In this study, Lobelia Queen Cardinalis was used as a plant model to investigate the impact of ionic connection between stacked Plant microbial fuel cell (shared soil). 10mm thickness carbon felt woven with stainless steel wire was used for both anode and cathode, and soil was a mix of potting soil and ground from pond banks (30\%-70\% weight, respectively). Independent performances did not show any difference between individual and shared soil PMFCs. Stacking independent PMFC in series sums both open circuit potential (OCP) and internal resistance, while stacking in parallel sums current, keeping open circuit potential to the mean of the OCPs. Although series stacking seems to output best performances, this configuration may cause voltage reversal in one PMFC when current is strong, leading to biofilm damage, so stacking in parallel is recommended.

1 Introduction

Plant Microbial Fuel cells are promising alternatives for renewable energy harvesting systems. These electrochemical systems use plants and exoelectrogenic bacteria to convert the carbon stored in the soil into electrical energy [1]. Thanks to photosynthesis, plants are able to transform carbon dioxide CO_2 into sugars such as acetate or glucose. Surplus of produced sugars are excreted by the roots, as root exudations and are therefore translocated into the soil [2]. These organic molecules are used as renewable resource in PMFC for electrical energy production. A typical PMFC comprises an anode installed deep in the soil (anaerobic region), a cathode placed on the ground surface (aerobic environment), separated by the soil which acts as a membrane, and connected by an external electrical circuit (fig.1). At the anode, anaerobic bacteria naturally grow to form a biofilm, which oxidizes organic rhizodeposits, resulting in a release of electrons and protons. Electrons transmitted to the anode are carried away by the external circuit, and protons are transferred across the cathode via soil. This flow of charges generates electrical energy. At the cathode, a reduction reaction occurs, where electrons, protons and oxygen react to form water. Dioxygen is often used as the electron acceptor, because it is abundant and has a quite good electronegativity [3]. Theoretically, the PMFC generates a maximum electrical power output of 3.2 W/m^2 (280 MWh/ha year) [4].Although this power density is lower than that of photovoltaic panels, PMFCs can generate continuous energy without need for energy storage systems, without competition for food and can be operated at any location. However, several factors limit the implementation of larger scale PMFC for real application.

Main disadvantages of PMFC are relatively low power densities production and loss of performances in scaled-up systems. The connection of multiple PMFCs in parallel and in series, is a way to boost output voltage and current of larger scale system. This stacking approach has been already described for Microbial Fuel Cells (MFCs) for wastewater treatment and sediment MFCs [5] . Only one recent study of Pamintuan's group, described the stacking behaviour of individual PMFCs [6]. This study demonstrates that a combination of series and parallel connection between cells might be the best choice to extract more performances in individual PMFCs. However, the individual configuration of PMFCs used in this study (PMFCs do not share the same soil), is not suitable for large scale application where PMFCs share the same soil. Indeed, two main configurations could be used to study PMFCs : (1) individual PMFCs planted in single pots without any ionic connection between them [7], [8] [9] ; (2) soil shared PMFCs that are directly planted in the same ground maintaining ionic connection between them, [1], [10]. The soil shared configuration is more appropriate for real application, for example, to combine agriculture and electricity production. In this configuration, ionic connection between PMFCs could greatly change stacking behaviour of connected cells as previously reported for MFCs[11].

Herein, we describe the study of the stacking behaviour of PFMCs in both individual and shared soil configurations. The primary goal of this work was the investigation of the

* Corresponding author: gregory.bataillou@ec-lyon.fr

impact of shared soil on PMFC performances. Then, performances and behaviour of stacked PMFCs in shared soil and in individual soil were compared. To the best of our knowledge, this study was never reported.

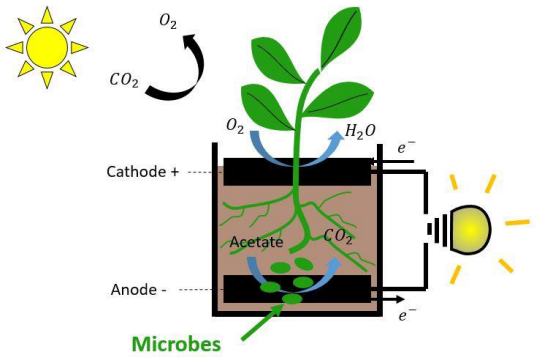

Fig. 1. Example of Plant microbial fuel cell system

2. Materials and methods

2.1. Experimental setup

Ten single-chamber PMFCs were built with 3.5 L plastic conical pot as base container (17.5cm deep). For 6 of them, pots were connected together by 3. The remaining 4 pots were independents (fig. 2) There were no holes at the bottom of the pots, in order to keep the soil constantly immersed. This prevented dioxygen to diffuse to the anode and kept ionic conductivity between electrodes. Electrodes were made with 10mm carbon felt cut in circle (Graphitech, FR). Anodes had a diameter of $13.2cm \pm 0.2cm$ (surface area $0.014m^2$) and cathodes had a diameter of $17.5cm \pm 0.5cm$, with a 5cm hole at the middle in order to let the plant grow (surface area $0.021m^2$). Distance between anode and cathode were chosen to be $7.5 \pm 0.5cm$. The choice of this distance originates from preliminary studies: pots with interelectrode distances below 7cm did not start well, certainly because of dioxygen diffusion (no membranes were used). Besides, Takanezawa et al. [12] found out that, within the same configuration, 5cm distance gave better performances than 2cm. Although it depends on the ionic conductivity, this interelectrode distance must be high. Collectors were stainless steel wire AISI316, $0.25mm$ thick (GoodFellow) woven inside the electrodes, and attached to copper wire with dominoes. As good contacts, flatness and inter-electrodes distance were not easy to reproduce, contact resistance was considered as acceptable if it was under 50 Ω (using ohmmeter between carbon and the end of the wire. Inoculation was made with acetate just once at the begining (Acetate sodium, $1g.L^{-1}$), and already living organisms in ground/potting soil. pH was not buffered, as the commonly used phosphate buffer solution (PBS) seems to have an uncleared impact on PMFC [13]. pH was measured at the end of the experiment. Plants used were *Lobelia Queen Cardinalis*, and were bought in a garden center already 5cm tall with 5 to 10 leaves. All pots were installed in a closed rack with LED attached above each floor. Temperature was left in the range of 15 to 25°C. Plants were lighted with 43W LED, $12h.day^{-1}$. As already stated above, pots were constantly immersed to respect water-logged conditions, as it is a quite important parameter [14]. To prevent chemical imbalance inside the shelf (especially abundance of CO_2), 5V fans were used to create a slight overpressure inside the shelf and aerate the place. All results were made in triplicate to avoid statistical errors and misinterpretation.

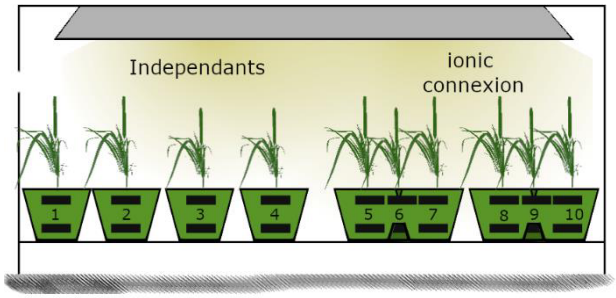

Fig. 2. Experiment plan

2.2 Potential logging

Starting from day 0, current through 680 Ω external charge and open circuit potential between anode and cathode were measured every other day with a voltmeter. Once current measurements were made, these ones were disconnected from the PMFCs, and the measurements of open circuit potential was made after waiting 15 minutes at least. Electrodes potential vs Ag/AgCl were also logged, at open circuit and with the charge connected.

2.3 Internal resistance

Internal resistance ($R_{internal}$) of each MFC was estimated with the two used functioning points, open circuit and 680 Ω external charge :

$$R_{internal} = R_{external} * \frac{OCP - V_{external}}{V_{external}} \quad (1)$$

where $R_{external}$ is the external resistance connected to PMFC (680 Ω), OCP is the open circuit potential, and $V_{external}$ is the voltage across external resistance.

2.4. Electrode contribution to internal resistance

As mentioned above, internal resistance is limiting the maximum extracted power from the Plant MFC. this

internal resistance implies voltage loss, and depends on electrolyte conductivity and resistance across electrodes (due to mass transfer, and reaction kinetics) [15]. To know which electrode contributed more to the internal resistance of the PMFC, a linear model was defined, where internal resistance can be separated into 2 contributors: anode and cathode (Fig.3).

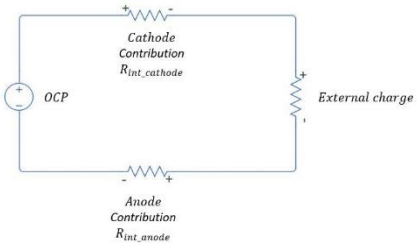

Fig. 3. Electrical model of PMFC with separated electrode contribution

It is then possible to separate the electrode contribution to internal resistance $R_{int_{electrode}}$ as following :

$$R_{int_{electrode}} = \frac{V_{electrode}}{i} = R_{external} * \frac{V_{electrode}}{V_{external}} \quad (2)$$

where i is the current flowing through the external charge, $R_{external}$ is the external charge used, $V_{external}$ is the voltage across the external charge, and

$$V_{electrode} = \left| E^{charge}_{electrode} - E^{OCP}_{electrode} \right| \quad (3)$$

Where $E^{charge}_{electrode}$ is the potential of the electrode potential (compared to $Ag/AgCl$ reference electrode) when external charge is connected, and $E^{OCP}_{electrode}$ and is the same potential on open circuit mode. Then, internal resistance is the sum of the two contributions :

$$R_{internal} = R_{int_{cathode}} + R_{int_{anode}} \quad (4)$$

It has to be stated that the result is mainly qualitative, and should be used as a comparison method only. Indeed, calculation of internal resistance with 2 points can lead to quantitative errors, especially when 1 point is outside the linear domain of the V-I PMFC curve (in this case the Open circuit potential point). Besides, this model does not take into account electrolyte and membrane (if exists) resistance, since they are included in $R_{int_{anode}}$ and $R_{int_{cathode}}$. Therefore, any difference between $R_{int_{anode}}$ and $R_{int_{cathode}}$ will imply inequalities between electrode resistance, no matter the value of electrolyte resistance, considered to be distributed evenly. Not taking this value into consideration still allows to investigate which electrode is contributing more to the internal resistance, and then is limiting the current density.

2.5. Stacking

During measurements, 3 individual soil pots were stacked together, and 3 sharing soil pots as well. Stacking of PMFCs was either in series or in parallels (fig.4). Internal resistance estimations were made, in order to compare them to single pots average.

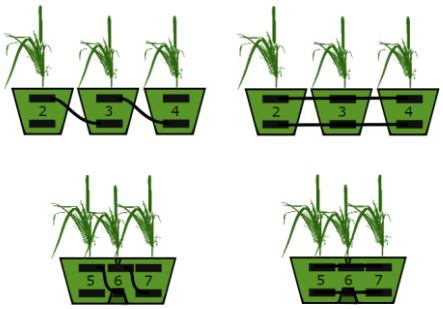

Fig. 4. Stacking combinations

Open circuit potential and current through external resistance were also logged for stacked PMFC regularly. PMFC were connected together, and measurements were made when the system was stable. This allowed to estimate global internal resistance of a stacked PMFC system. However, as different plants are used when comparing shared soil and individual soil stacking, there is a bias. Indeed, every PMFC do not have the same performances at the same time, and results of stacking will be dependent on single PMFC performances at that specific time. To avoid this bias, normalization was made on open circuit potential and internal resistance to respectively average open circuit potential and average internal resistance of used PMFC.

3 Results and discussions

3.1. Biofilm formation

All PMFC started 7 days after their implementation. These results indicate that living potting soil and ground as matrix substrate already contain exoelectrogen microorganisms, and addition of acetate made them competitive at the electrode surface. There were no differences between pots ionically connected and individual pots in terms of startup duration. These results ensure that ionic connection between PMFCs does not affect biofilm formation. Moreover, the anode potential log allowed to understand that the biofilm was stable when potential at open circuit reached about $-400mV\ vs\ Ag/AgCl$. Interestingly, when potential of anode was reached, open circuit voltage and current through external charge didn't reach the steady state yet, and a second growth phase was observed (fig. 5.a). Cathode contribution to resistance was still huge compared to the anode, but decreased during this second phase, until stability was reached (fig. 5.b). This behaviour might be explained by the development of

a aerobic biofilm on the cathode with slower kinetic than that of anodic biofilm [16] [3]. However, further investigations are required to determine the structure of this cathodic biofilm and its growth kinetics.

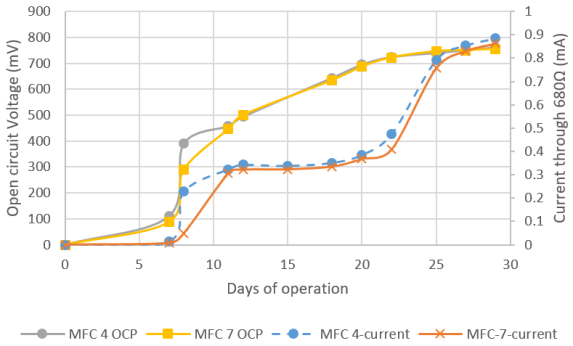

a. Open circuit potential and current through 680 Ω

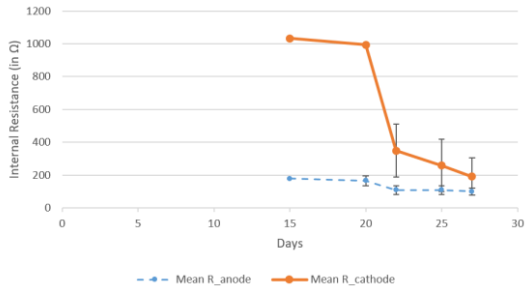

b. Evolution of each electrode contribution to internal resistance

Fig. 5. PMFC startup

3.2. Study of individual and shared soil configurations

3.2.1. Steady state

On steady state, open circuit potential and current was found to be identical between shared soil plant and unique plant. The maximum current obtained through 680 Ω external charge was 0.92 mA, and was reached by both individual (1 and 2) and soil shared (6, 8 and 10) PMFCs, showing no significant difference between the two configurations. Interestingly, it was observed that breakdown of one ionically connected plant did not interfere with other PMFC of the same ground (fig.6).

3.2.2. *Stacking*

Stacking microbial fuel cell was studied and compared with the average of related plants performances. Stacking in series with shared soil PMFC is certainly the worst configuration. Open circuit potential is slightly increased, but not as much as internal resistance, which renders the performances of the stacked PMFC system even worse than one single PMFC. When stacking in series with individual pots, open circuit potential was found to be the sum of all single open circuit potential (fig. 7.a.). However, two major concerns make that configuration not advisable. First, internal resistance is multiplied by more than 3 (fig.7.b.) which limits considerably the power output. Second, voltage reversal was observed on strong functioning current, and biofilm damage due to this polarization can be irreversible. Voltage reversal has been found when using an external charge of 50 Ω on individual soil plant in series. The PMFC on which it appeared was the weakest one in terms of individual performances.

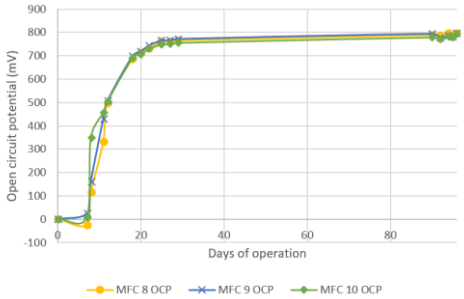

a. Open circuit potential

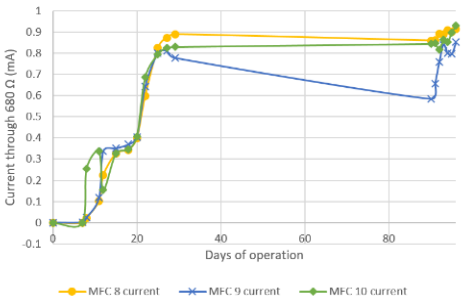

b. current through 680 Ω

Fig. 6. PMFC log in shared soil

Stacking PMFC in parallel might be the right choice, regardless of the ground connection. Open circuit potential is the mean of the three single open circuit voltage, and internal resistance is almost divided by three, which allows to drag more power.

3.2.2. *Stacking when breakdown of one PMFC*

One single PMFC voltage and current dropped from day 87 of experiment. This allowed to look at the evolution of stacking performances when one plant microbial fuel cell broke down. It appears that the stacked PMFC system reacts as previously described: the multiplication factor was not changed according to the chosen configuration. The sum of internal resistance in series show that a breakdown of one PMFC can drastically limit the current flow.

3.2.2. *Perspectives*

Cathode contribution to internal resistance was higher than the anode one, even if cathode area was larger and reduction was catalysed after 3 weeks. This result implies that, although this PMFC configuration is mainly used and other configurations have been tested [17] [18], research on low-cost and easy-to-build configuration still needs to

be done to reduce the cathode limitation. Biocathode is a really interesting way to catalyse dioxygen reaction [3]. Besides, internal resistance can be drastically reduced with higher ionic conductivity [19]. Studying PMFC stacking at different conductivities could lead to different electrons transfer limitations, and might lead to new conclusions.

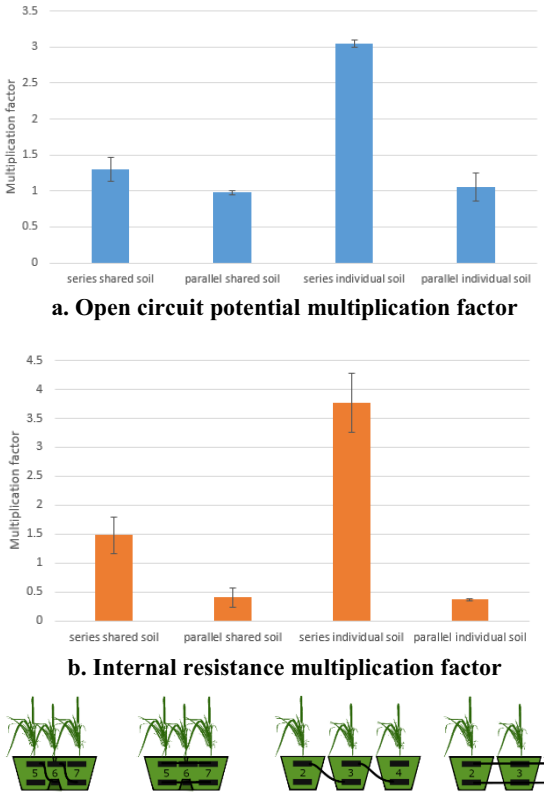

Fig. 7. **PMFC log in shared soil**

4. Conclusion

Lobelia Queen Cardinalis was used in plant microbial fuel cell systems. PMFC with another broken PMFC in the same soil is not affected by this breakdown. Cathode limitation was shown at the begining, but supposed biofilm formation at the cathode increased this one's performance to the same level as anode, when comparing contribution to internal resistance. When stacking multiple PMFC in series, both internal resistance and open circuit potential increase. In case of ionic connection, strong interferences are making the stacking even less efficient than only one PMFC. Parallel connection should be preferred in both individual and shared soil to avoid voltage reversal in one PMFC.

This work was financially supported by the “Hubert Curien Program” through the PHC MAGHREB Project number 19MAG23/41382WC.

References

[1] N. Kaku, N. Yonezawa, Y. Kodama, et K. Watanabe, « Plant/microbe cooperation for electricity generation in a rice paddy field », *Appl Microbiol Biotechnol*, vol. 79, nº 1, p. 43-49, mai 2008, doi: 10.1007/s00253-008-1410-9.

[2] T. S. Walker, H. P. Bais, E. Grotewold, et J. M. Vivanco, « Root Exudation and Rhizosphere Biology », *Plant Physiology*, vol. 132, nº 1, p. 44-51, mai 2003, doi: 10.1104/pp.102.019661.

[3] K. Wetser, E. Sudirjo, C. J. N. Buisman, et D. P. B. T. B. Strik, « Electricity generation by a plant microbial fuel cell with an integrated oxygen reducing biocathode », *Applied Energy*, vol. 137, p. 151-157, janv. 2015, doi: 10.1016/j.apenergy.2014.10.006.

[4] D. P. B. T. B. Strik, R. A. Timmers, M. Helder, K. J. J. Steinbusch, H. V. M. Hamelers, et C. J. N. Buisman, « Microbial solar cells: applying photosynthetic and electrochemically active organisms », *Trends in Biotechnology*, vol. 29, nº 1, p. 41-49, janv. 2011, doi: 10.1016/j.tibtech.2010.10.001.

[5] W. H. Tan *et al.*, « Microbial Fuel Cell Technology—A Critical Review on Scale-Up Issues », *Processes*, vol. 9, nº 6, Art. nº 6, juin 2021, doi: 10.3390/pr9060985.

[6] K. R. S. Pamintuan, J. A. A. Clomera, K. V. Garcia, G. R. Ravara, et E. J. G. Salamat, « Stacking of aquatic plant-microbial fuel cells growing water spinach (Ipomoea aquatica) and water lettuce (Pistia stratiotes) », *IOP Conf. Ser.: Earth Environ. Sci.*, vol. 191, p. 012054, nov. 2018, doi: 10.1088/1755-1315/191/1/012054.

[7] P. Chiranjeevi, G. Mohanakrishna, et S. Venkata Mohan, « Rhizosphere mediated electrogenesis with the function of anode placement for harnessing bioenergy through CO2 sequestration », *Bioresource Technology*, vol. 124, p. 364-370, nov. 2012, doi: 10.1016/j.biortech.2012.08.020.

[8] P. J. Sarma et K. Mohanty, « Epipremnum aureum and Dracaena braunii as indoor plants for enhanced bio-electricity generation in a plant microbial fuel cell with electrochemically modified carbon fiber brush anode », *Journal of Bioscience and Bioengineering*, vol. 126, nº 3, p. 404-410, sept. 2018, doi: 10.1016/j.jbiosc.2018.03.009.

[9] M. A. Moqsud, J. Yoshitake, Q. S. Bushra, M. Hyodo, K. Omine, et D. Strik, « Compost in plant microbial fuel cell for bioelectricity generation », *Waste Management*, vol. 36, p. 63-69, févr. 2015, doi: 10.1016/j.wasman.2014.11.004.

[10] K. Wetser, J. Liu, C. Buisman, et D. Strik, « Plant microbial fuel cell applied in wetlands: Spatial, temporal and potential electricity generation of Spartina anglica salt marshes and Phragmites australis peat soils », *Biomass and Bioenergy*, vol. 83, p. 543-550, déc. 2015, doi: 10.1016/j.biombioe.2015.11.006.

[11] N. Degrenne, « Gestion de l’énergie des piles à combustible microbiennes », 2012.

[12] K. Takanezawa, K. Nishio, S. Kato, K. Hashimoto, et K. Watanabe, « Factors Affecting Electric Output from Rice-Paddy Microbial Fuel Cells », *Bioscience, Biotechnology, and Biochemistry*, vol. 74, nº 6, p. 1271-1273, 2010, doi: 10.1271/bbb.90852.

[13] M. Helder, D. P. B. T. B. Strik, H. V. M. Hamelers, R. C. P. Kuijken, et C. J. N. Buisman, « New plant-growth medium for increased power output of the Plant-Microbial Fuel Cell », *Bioresource Technology*, vol. 104, p. 417-423, janv. 2012, doi: 10.1016/j.biortech.2011.11.005.

[14] N. F. Tapia, C. Rojas, C. A. Bonilla, et I. T. Vargas, « A New Method for Sensing Soil Water Content in Green Roofs Using Plant Microbial Fuel Cells », *Sensors*, vol. 18, nº 1, p. 71, janv. 2018, doi: 10.3390/s18010071.

[15] C. Xia, D. Zhang, W. Pedrycz, Y. Zhu, et Y. Guo, « Models for Microbial Fuel Cells: A critical review », *Journal of Power Sources*, vol. 373, p. 119-131, janv. 2018, doi: 10.1016/j.jpowsour.2017.11.001.

[16] K. Rabaey *et al.*, « Cathodic oxygen reduction catalyzed by bacteria in microbial fuel cells », *ISME Journal*, vol. 2, nº 5, p. 519-527, 2008, doi: 10.1038/ismej.2008.1.

[17] M. Helder, « Design criteria for the Plant-Microbial Fuel Cell », 2012.

[18] R. A. Timmers, D. P. B. T. B. Strik, H. V. M. Hamelers, et C. J. N. Buisman, « Electricity generation by a novel design tubular plant microbial fuel cell », *Biomass and Bioenergy*, vol. 51, p. 60-67, avr. 2013, doi: 10.1016/j.biombioe.2013.01.002.

[19] J.-Y. Nam, H.-W. Kim, K.-H. Lim, H.-S. Shin, et B. E. Logan, « Variation of power generation at different buffer types and conductivities in single chamber microbial fuel cells », *Biosensors and Bioelectronics*, vol. 25, nº 5, p. 1155-1159, janv. 2010, doi: 10.1016/j.bios.2009.10.005.

DEVELOPMENT OF FLEXIBLE, CONDUCTIVE AND BIOCOMPATIBLE CHITOSAN-BASED MINIATURIZED BIOELECTRODES FOR ENZYMATIC GLUCOSE BIOFUEL CELLS

Laura García-Carmona[1*], *Mireia* Buaki-Sogó[1*], *Marta* Vegas-García[1], *Mayte* Gil-Agustí[1], *Pedro* Llovera-Segovia[2], *Alfredo* Quijano-López[1,2].

[1] Instituto Tecnológico de la Energía (ITE), Avenida Juan de la Cierva 24, 46980 Paterna, Spain;
[2] Instituto de Tecnología Eléctrica, Universitat Politècnica de València, Camino de Vera s/n Edificio 6C, 46022 Valencia, Spain

Abstract. The need for new clean energy sources for portable devices in biomedical, agro-food industry and environmental related sectors boosts scientists towards the development of new strategies for energy harvesting for their application in biodevices development. In this sense, enzymatic biofuel cells (BFCs) have gained much attention in the last years. This work faces the challenge of develop new generation of BFCs able to be adapted to remote and personal monitoring devices within the framework of wearable technologies. To this aim, one of the main challenges consists of the development of conductive and biocompatible electrodes, which constitute a challenge itself due to the non-conductive capabilities of most of the biocompatible supports. Additionally, bioelectrodes may achieve good mechanical properties and resilience in order to be suitable for the envisioned application, which involves exposure to deformation during long-term use. Furthermore, it is desirable that the systems developed are versatile enough to be adapted to miniaturized supports for new personal wearable devices development. In the present work, self-standing chitosan-carbon black membranes have been synthesized and modified with suitable enzymes for the assembly of an enzymatic glucose BFC. The membranes have been adapted to be integrated in miniaturized interdigitated gold electrodes as the step forward to miniaturized systems, modified with enzymes and metallic particles clusters and tested for energy harvesting from glucose solutions. The miniaturized system produces a power density of 0.64 μW/cm2 that is enhanced to 2.75 μW/cm2 in the presence of the metallic clusters, which constitute a 76% incensement. Such preliminary demonstrations highlight the good response of metals in bioelectrode configuration. However, energy harvesting real application of the developed miniaturized electrodes need still improvements but pave the way for the use of BFC as an energy source in wearable technologies due to their good mechanical, electrical and biocompatible properties.

1. INTRODUCTION

Chitosan is a natural biopolymer obtained from the deacetylation of chitin, which can be found, for example, in shrimp shells. Chitosan has been widely used in the development of enzymatic bioeletrodes due to its capability for stabilising enzymes in the biopolymer network, hydrophilicity and biocompatibility [1][2][3]. Nevertheless, chitosan presents an insulating behaviour and need to be integrated with conducting surfaces or doped with conducting agents when developing enzymatic bioelectrodes. Thus, the main strategy in the use of chitosan to be used in enzymes immobilization consists of incorporating the enzyme in a solution of chitosan and then, cast it on the surface of common electrode such as graphite, glassy carbon or gold electrodes[4][5]. Additionally, it is usual to dope chitosan with carbon-based materials such as carbon nanotubes, graphene or carbon black to overcome the insulating barrier [4][5][6].

In this sense, the former approach of casting onto the surface of electrodic materials is useful when dealing with bioelectrodes to be used in biosensor development with analytical purpose or electrochemical characterization of enzymes and their bioelectrocatalytic activity. However, when dealing with enzymatic glucose biofuel cells (BFC) for energy harvesting aimed to be wearable or implantable, new strategies must be implemented since long-term use is required.

Glucose BFCs consist of biodevices aimed to harvest energy from human body due to the catalytic electrochemical oxidation of glucose as a result of the selective recognition of a substrate (glucose) by the enzyme, typically glucose oxidase (GOx) or glucose dehydrogenase (GDH). Thus, low cost and availability of the enzymes are required, together with stable immobilization methods on the surface such as crosslinking, entrapment, covalent anchorage to allow stability of the binding for the long term use [7].

However, advances in wearable technologies need for new electrode configurations that can be placed anywhere in the body. For this reason, miniaturization strategies are of interest for the development of small prototypes of such biodevices. In this sense, chitosan has the ability of forming films that could be used as electrodes in the form of a path or that could be integrated in existing systems such as screen-printed, interdigitated electrodes or in flexible electronics [4][5][8][9]. Thus, chitosan thanks to

* Corresponding authors: mireia.buaki@ite.es (M.B.-S.) and laura.garcia@ite.es (L.G.-C.); Tel.: +36-9-6136-6670.

their biocompatibility characteristics and its film forming ability has been used to develop a biopolymeric membrane of chitosan doped with carbon black that presents the capability of acting as a support for enzyme immobilization and as self-standing electrode at the same time [1]. The chitosan-carbon black membrane with 25% w/w or 100% w/w with respect to chitosan can be integrated in the most convenient configuration using additional conductive layers. However, taking into account the miniaturization and further use in flexible electronics, this procedure already tested for glucose BFCs and biosensor should be optimized to be integrated into miniaturized supports with conductive layers for connection already included in the support.

On the other hand, either in film or miniaturized form, chitosan-carbon black based electrode can be doped and modified using electrochemical methods for metals electrochemical synthesis in its surface. In this sense, different electrochemical methods have been used for metal deposition [10]. Specifically, double pulse potential constitutes a very convenient method since it is possible to create clusters in situ in a distributed way all along the electrodic surface. As its name suggest, two pulses are applied to the cell in which the first one (in the order of ms) is responsible of the generation of nuclei of the particles, meanwhile the second pulse (in the order of s) allow the growth of those particles [11]. This is a highly valuable synthesis feature since metals included in BFCs configuration have been proved to enhance the power input by improving the electron transfer rate [12].

Thus in this work, the chitosan-carbon black membrane composition have been optimized to be integrated into miniaturized supports to be adapted to real systems and later on tested to be used in glucose BFCs. In this context, integration of metallic clusters on the membrane surface have been tested to evaluate the feasibility of the membranes to be in situ modified but also the possible enhancement in the response of the BFCs as prove of the concept of this approach.

2. EXPERIMENTAL SECTION

2.1 Materials

Chitosan of medium molecular weight with a deacetylation degree higher than 85% (Sigma–Aldrich. St. Louis, MO, USA), glacial acetic acid reagent grade, NaOH (Scharlab, S.L.,Barcelona, Spain), and C65 Carbon black powder (Nanographi, Ankara, Turkey) were used for the preparation of membranes using water as solvent.

Glucose oxidase (GOx) from Aspergillus niger Type VII and Laccase from Trametes versicolor were used for bioelectrodes preparation (Sigma–Aldrich (St. Louis, MO, USA)). N-(3-dimethylaminopropyl)-N-ethylcarbodiimide (EDC) and N-hydroxysulfosuccinimide (NHS) were btained from Iris Biotech Gmbh (Marktredwitz, Germany), and Sigma–Aldrich (St. Louis, MO, USA), respectively. 2-(N-morpholino)ethanesulfonic acid for the MES buffer and D-Glucose (biotechnology grade) were provided by VWR LIFE SCIENCE (Radnor, PA, USA)., Na_2HPO_4 and NaH_2PO_4 were acquired from VWR LIFE SCIENCE (Radnor, PA, USA for the preparation of 0.1 M Phosphate Buffer solutions pH=7.

Gold interdigitated electrodes (IDE) from Micrux Technologies were employed as a miniaturized electrodes support.

2.2. Preparation of chitosan membranes

Self-standing chitosan membranes doped with carbon black were prepared as following a Doctor Blade strategy by way of a stainless steel casting knife protocol previously reported [1]. In brief, slurry was first prepared by mixing an appropriate chitosan solution with carbon black. The slurry was casted onto a glass surface with the aid of a casting knife and dried overnight. After a neutralization step with NaOH solution was accomplished, followed by different washing steps up to reach neutral pH. The as-prepared membranes were allowed to dry onto a flat surface overnight.

2.3. Modification of interdigitated electrodes

Gold interdigitated electrodes from Micrux Technologies (10 x 6 x 0.75) were modified with chitosan-carbon black membranes. At this purpose, slurry composition was optimized in order to ensure that the chitosan-carbon black membrane remains into the electrode surface to ensure long-term use of the bioelectrode.

For the immobilization of GOx, the interdigitated electrodes were modified with a membrane of chitosan-CB. The composition of the slurry was a chitosan solution of 1% w/w in acetic acid 0.3M with 50% w/w of carbon black. The mixture was prepared in a planetary ball mill and after a volume of 15 µl of the slurry was casted on the gold surface of interdigitated electrodes.

For the immobilization of Laccase, the slurry composition is based on a solution of chitosan 2% w/w doped with 25% w/w of carbon black with respect to chitosan. As in the case of modified interdigitated electrodes for the anode, a planetary ball mill was used for mixing the components and the same volume of 15 µl was casted onto the gold surface of the interdigitated electrode.

The incorporation of metallic clusters in order to enhance electrode response was accomplished electrochemically by double pulse potential voltammetry (1 sg for nucleation potential and 10 sg for grow potential) in $AgNO_3$ solution. Then, bioelectrodes were electrochemically oxidized using NaOH 0.1 M at 0.7 V during 120 sg.

2.4. Enzyme immobilization

GOx and Laccase were immobilized in the membranes for bioelectrode development. For the GOx-based anode 10 mg/mL GOx was immobilized in the CH-CB membranes using a covalent approach based on the use of EDC/NHS as previously reported [1]. In the case of Laccase, the enzyme was first adsorbed onto the CH-CB starting from a 10 mg/mL solution of Laccase in PB pH

6.5. For the covalent anchoring to the amino groups of the chitosan matrix, an approach based on the use of EDC/NHS was also used based on a procedure previously reported [1][13].

2.5. Electrochemical testing

An Autolab PGSTAT 12 potentiostat (Eco Chemie, Utrecht, The Netherlands) and a Zhaner IM6 electrochemical workstation provided with a PP241 module for high currents was used for cyclic voltammetry, chronoamperometry, double pulse potential voltammetry and BFC polarization curve determination. Electrochemical characterization of the GOx bioanode, Laccase biocathode were performed in a three electrode configuration using developed miniaturized bioelectrodes as the working electrode, a reference electrode of Ag/AgCl, and a platinum wire as the counter electrode under O_2 or N_2 purged PBS buffer solution.

3. RESULTS AND DISCUSSION

3.1. Miniaturization of chitosan CB membrane for bioelectrodes development.

Chitosan-carbon membrane can be prepared using different carbon nanomaterials. However, CB has been selected due to their conductive properties and tuneable surface. The chitosan-CB membrane final structure will vary depending on whether it is a film or if it is intended for integration in miniaturized supports. In case of self-standing membrane development (Figure 1A) the composition has been selected according to the resilience to mechanical strain stretching, bending, and twisting, together with its the conductivity properties [1]. However, when adapted to miniaturized supports (figure 1B) this composition should be optimized to avoid detachment from the support. In this sense chitosan – CB ratio is crucial to be optimized to find a compromise between chitosan attachment properties and conductivity capabilities thanks to CB.

The composition of the original self-standing membranes, with a 25% w/w and 100% w/w of CB for cathode of anode respectively, resulted in the detachment of the film from the gold interdigitated electrode in the case of the anode configuration. The film formed onto the gold surface of the IDE for cathode configuration remained attached onto the gold surface. To diminish the solid content on the membrane and prevent membrane folding and detachment an anode configuration with a 50% w/w of CB was checked. In this case membrane detachment was also observed.

In case of the anode, the reason for not using the same configuration as the cathode is that carbon black is oxidized to generate carboxylic acid groups that will be used later as anchoring site for the GOx. The Laccase anchorage follows a different strategy using amino groups of chitosan for its covalent attachment on the membrane surface. Thus, the role of CB in this configuration is to overcome the insulating behaviour of chitosan films. Therefore, it is better if CB particles are homogeneously distributed in the chitosan matrix and, as we observed in our previous work, this occurs for CB weight percentages of 50% or higher, when polymeric matrix is not visible at low magnification [1].

At this point, the next step for the optimization of the anode configuration in gold interdigitated electrodes was the decrease of the concentration of the chitosan solution in order to decrease film thickness and prevent detachment. When chitosan concentration was decreased to 1% w/w in the acetic acid solution, the membrane detachment was observed for CB weight percentages higher than 50%. Therefore, the anode configuration selected for the integration of the chitosan-CB membranes in the miniaturized electrodes was 1% weight percentage for the chitosan solution in acetic acid, doped with a 50% w/w of CB with respect to chitosan.

3.2. Self-standing chitosan membrane bioelectrodes for BFC development.

The self-standing chitosan-CB bioelectrodes already modified with the enzymes were tested by cyclic voltammetry in order to confirm the presence of the immobilized enzyme for anode (Glucose Oxidase) and cathode (Laccase) on the membrane surface (Figure 2). In the cyclic voltammetry experiments carried out in N_2 purged atmosphere for the membrane based bioanode, it can be observed the presence of the oxidation and reduction peaks of the redox centre (Flavin Adenine Dinucleotide – FAD) of the glucose oxidase enzyme. The formal potential of the redox peaks was 0.45 V in accordance with the values found in literature.

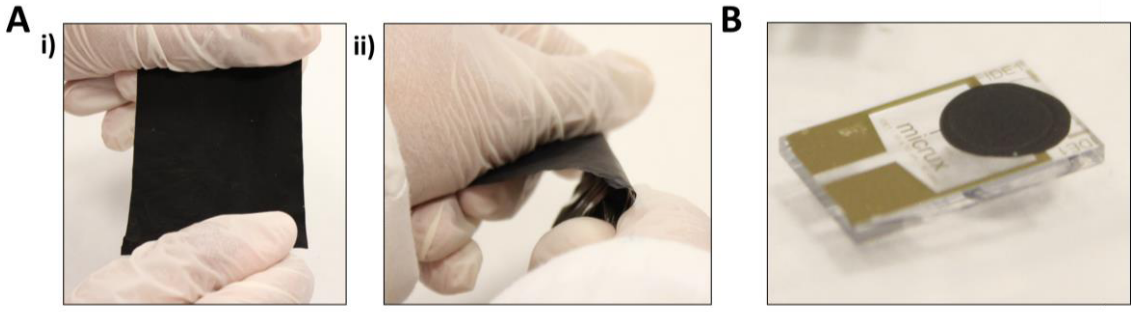

Figure 1. *Chitosan-CB membrane configuration such as (A) self-standing membrane under (i) stretching and (ii)) twisting, and (B) membrane integrated into miniaturized electrodes.*

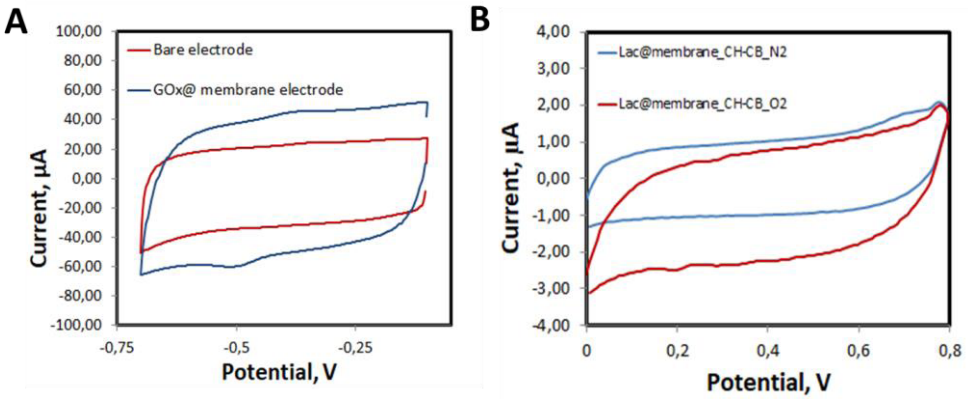

Figure 2. *Bioelectrodoes evaluation in terms of enzyme attachment for, (A) GOx bioanode and (B) Laccase biocathode. Cyclic voltammetry in PBS 0,1M and KCl 0,1M in N_2 saturated solution (bioanode) and N2/O2 saturated solution (biocathode). Scan rate: 75 mV/s*

The presence of Laccase on the chitosan-CB membrane that will be used as the cathode was ascertained using also cyclic voltammetry in the presence of oxygen and the appearance of an onset around 0.7 V for the reduction of oxygen confirmed the successful immobilization of Laccase. However, and as observed in our previous work, the onset and the current generated are of low magnitude probably due to the working electrolyte at pH 7, far from the optimum working pH reported for Laccase (pH 4.2) [14]. It is worth to mention that acid pH is not used since at that pH chitosan will become protonated and the membrane will be dissolved. Additionally, the BFCs are envisioned to be used in wearable technologies where a physiological pH is expected.

In order to evaluate the suitability of the developed self-standing bioelectrodes for energy harvesting from glucose solutions a BFC was assembled in a lab scale using the GOx based bioelectrode as anode and the Laccase bioelectrode as cathode. Polarization curve was recorded and power and current density was calculated from the results of the polarization experiment. The area used for the calculation of power and current density was the electroactive surface area obtained from Randles-Sevcik experiments for the miniaturized electrodes. The results for the polarization curve are showed below. Prior to bioelectrodes miniaturization, the geometric area of the electrodes employed was calculated as 0.6 cm^2 [1] achieving thus an electroactive area of 1.2 cm^2. After the miniaturization procedure into gold interdigitated electrodes, the electroactive area was reduced to 0.03 cm^2 compared with the electrodes used in previous work using non miniaturized suppors with additional conductive layers for connections [1].

In this sense, Figure 3 shows the polarization curves obtained by the complete configuration of glucose BFC using non miniaturized bioelectrodes from [1], with maximum power density of 62.7 µW/cm^2 at 0.19 OCV. It proves the successful enzyme immobilization technique and the retention of the specific electrocatalytic activity of the immobilized enzymes.

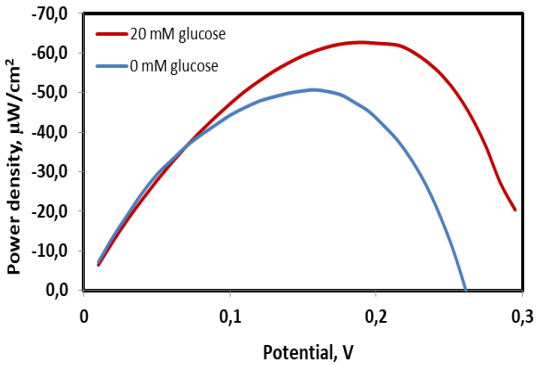

Figure 3. *Glucose BFC power density (GOx-based anode and Laccase-based biocathode) in PBS 0.1 M (blue) and 20 mM glucose (red). Results obtained in larger electrodes, before miniaturization procedure (0.6 cm^2).*

3.3. Integration of chitosan membranes in gold interdigitated electrodes

In order to integrate the developed membranes in real and miniaturized systems, the chitosan-based membranes have been incorporated in interdigitated gold electrodes. Onto these membranes, following the same immobilization strategy stated and proved above, GOx and Laccase have been incorporated on the modified interdigitated electrodes. The polarization curve has been recorded and the results obtained are shown in Figure 4.

In this case, power densities obtained are lower than those recorded with the self-standing bioelectrodes. This could be due to the fact that geometrical and electroactive surface area of the interdigitated electrodes is lower and therefore current generated in the BFC assembly is decreased. However, miniaturized electrodes required to be equally efficient in terms of energy harvesting to be used to power monitoring devices. Then, in these systems it will be necessary to enhance the electrode response to increase the power generation in miniaturized systems.

To this aim, metallic clusters on the electrode surface have been in situ synthetized into the anode in order to improve electron transfer kinetics and bioelectrode response using the double pulse potential technique

* Corresponding authors: mireia.buaki@ite.es (M.B.-S.) and laura.garcia@ite.es (L.G.-C.); Tel.: +36-9-6136-6670.

[11][1]. As it has been already explained, this method allows direct silver electro synthesis in the bioelectrodes in less than 1 minute. Additionally, this technique creates nuclei of the particles in the first pulse in a distributed way all along the electrode surface than, later on growth during the second pulse. This fact lead to a distributed and homogeneous particles disposition in the membrane that will benefit electron transfer kinetics.

Energy harvesting capabilities were evaluated to test GOx activity and the suitability of CH-CB membrane modified with silver metallic clusters. Figure 4 shows the comparison between the complete BFC composed by anode that incorporates metallic clusters on the configuration (purple line) and a bare electrode, containing just the enzymatic component (green line) with a characteristic bell-shaped curve. The biocathode employed in this study was a Laccase-modified bioelectrodes for both anode configurations. From this, it can be noticed that the maximum power density output is obtained with the silver-base anode is used, reaching a value of 2.75 $\mu W/cm^2$ at 0.2 V which represents an increase of the power density in 76 % with respect to that reached without metallic cluster in the setup.

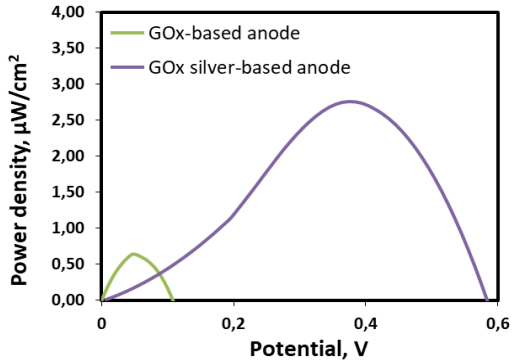

Figure 4. *Glucose BFC polarization curves using two different anodes GOx-bioanode (green) and GOx-Ag particles-bioanode (purple). Laccase-based biocathode has been used in both cases. 25 mM glucose has been used as fuel in both cases (TP 0.1M, using gold interdigitated electrodes).*

This result shows the good feasibility of the membrane to be integrated in different supports such as interdigitated electrodes. Additionally, this results suggest the good electrocatalytic behaviour of the metallic particles, due to the performance of Ag_2O to reduce O_2, paving the way to a new trend of the incorporation of metallic elements on the bioelectrodes. However, these density power outputs values should be large increased for real application in wearable technologies. In this sense, it is foreseen the connection of several miniaturized electrodes in serial in case the final application requires maximum power inputs.

4. CONCLUSIONS

In this work it has been reported the development of a biocompatible membrane that can be miniaturized maintaining good mechanical and electrical properties at the same time. This shape- and size-tailored membrane, allows its deposition in a variety of substrates such as films or rigid supports, enabling the versatility to be adapted to any design for use in multiple applications such as the production of wearable devices with flexible electronics. Moreover, its suitability to be used in the development of bioelectrodes for glucose BFCs haven been proved thanks to the positive results obtained in energy harvesting for larger electrodes (62.7 $\mu W/cm^2$, 0.6 cm^2). In this regard, and despite to the low density power output obtained with the miniaturized electrodes, an improvement of energy harvesting capabilities have been obtained by means of the incorporation of metallic particles on the bioanode, producing an increase of the final power density in a 76% when compares to the bare-electrode setup. It is also important to mention that Lacasse-based cathode is used at pH 7 which is not the optimal working condition of this enzyme.
Additionally, this development paves the way for the use metals in the anode configuration but also foresee the use of hybrid BFC, with enzymatic bioanode and metal-based cathode, to solve the issue of Lacasse-based electrode at physiological pH. However, more research is required in terms of electronics, in order to develop higher power output energy harvesting strategies.

5. ACKNOWLEDGEMENTS

This work has been supported by the Generalitat Valenciana towards Instituto Valenciano de Competitividad Empresarial (IVACE) in accordance with the IMAMCL/2020/1 agreement and within the framework of the BioSensCell and BioCell-Power projects.

6. REFERENCES

[1]. M. Buaki-Sogó, L. García-Carmona, M. Gil-Agustí, M. García-Pellicer, A. Quijano-López, Nanomaterials **11** (2021)
[2]. S. Haque, A.Nasar, Inamuddin, M. Muzibur . *Sci Rep* **10**, 10428 (2020)
[3]. S. El Ichi, A. Zebda, J.-P Alcaraz, A. Laaroussi, F. Boucher, J. Boutonnat, N. Reverdy-Bruas, D. Chaussy, M.N. Belgacem, P. Cinquin, D.K. Martin, Energy Environ. Sci., **8**, 1017-1026, (2015).
[4]. D. Talarico, F. Arduini, A. Amine, I. Cacciotti, D. Moscone, G. Palleschi, Anal Bioanal Chem **408**, 7299–7309 (2016)
[5]. A. Rabti, W. Argoubi, N. Raouafi, Microchim Acta **183**, 1227–1233 (2016)
[6]. V. Mani, M. Govindasamy, SM. Chen, TW. Chen, A. Sentil Kumar, ST. Huang, Sci Rep **7**, 11910 (2017)
[7]. M. Buaki-Sogó, L. García-Carmona, M. Gil-Agustí, L. Zubizarreta, M. García-Pellicer, A. Quijano-López, Top. Curr. Chem., **378**, 1–28, (2020)
[8]. U. Hashim, M.A. Farehanim, N. Azizah, S. Norhafiezah, M.F. Fatin, A.Rahim Ruslinda, R.M. Ayub, IEEE *ICoBE*, pp. 1-3, (2015)
[9]. P. Wang, M. Hu, H. Wang, Z. Chen,Y. Feng, J. Wang, W. Ling, Y. Huang, *Adv. Sci.* , **7**, 2001116, (2020)
[10]. Y.Tang, W. Cheng, *Langmuir*, ***29***(9), 3125-3132 (2013).

[11]. L. García-Carmona, D. Rojas, M.C. González, A. Escarpa, *Analyst*, ***141***(21), 6002-6007, (2016).
[12]. F.Qu, X. Ma, Y. Hui, F. Chen, Y. Gao, *Chin. J. Chem.* ***35***(7), 1098-1108 (2017).
[13]. C. Gutiérrez-Sánchez, W. Jia, Y. Beyl, M. Pita, W. Schuhmann, A.L. de Lacey, L. Stoica, Electrochim. Acta, **82**, 218–223 (2012)
[14]. B. Reuillard, C. Abreu, N. Lalaoui, A. Le Goff, M. Holzinger, O. Ondel, F. Buret, S. Cosnier, Bioelectrochemistry, **106**, 73–76 (2015)

Assessing the effect of the electrode orientation on the performance of soil microbial fuel cells

Jakub Dziegielowski [1,2], Gresa Bregu [1], Luke Hulse [1] and Mirella Di Lorenzo [1,2,]*

[1] Department of Chemical Engineering, University of Bath, BA2 7AY, Bath, United Kingdom
[2] Centre for Biosensors, Bioelectronics and Biodevices, University of Bath, BA2 7AY, Bath, United Kingdom

Abstract. Soil microbial fuel cells (SMFCs) are a sub-class of the microbial fuel cells family, in which the soil acts as the electrolyte, and as the source of microorganisms and organic fuel. Given the great simplicity of the system design, SMFCs show a promising avenue for energy generation in remote areas. In this study, we investigate the influence that geometrical factors, such as the electrode orientation, have on the electrochemical performance of SMFCs. Two types of electrode orientations: horizontal and vertical, were tested. Additionally, the influence of anode and cathode immersion in soil was explored too. Our results demonstrate that vertical positioning of the cathode in soil is not a viable option. The increase in cathodic immersion leads to a more rapid performance decay, attributed to more anaerobic conditions along soil's depth. The increase in anode immersion has a positive effect on the evolution of the negative electrode potential. However, with the increase in electrode spacing, the performance drops due to a greater internal resistance.

1 Introduction

The threat of climate change pushes the search for alternative energy sources that minimize carbon pollution. In this context, Microbial Fuel Cells hold great promises. Particularly interesting are Soil Microbial Fuel Cells (SMFCs), capable of deriving electricity from soil, via microbial and electrochemical mechanisms. In these systems, the soil acts as the electrolyte and as the source of both microorganisms and organic matter. With respect to other types of microbial fuel cells, SMFCs are characterized by an extremely simple and cost-effective design, with no need for fuel pumping and/or electrolyte replacement. Minimum maintenance is required since the organic matter is naturally provided in the soil by plants and/or decomposing matter, thus allowing long term operations in remote areas.

Yet, the feasibility of this technology for real life applications is often questioned, due to the low power output, which is a consequence of the inherent thermodynamic limitations. In microbial fuel cells, the electromotive force induced by the bioelectrochemical reactions is limited to a theoretical maximum potential of 1.14 V, resulting in power densities in the range of tens to hundreds of mW m^{-2} [1]. Redox kinetics is a barrier that may never be fully broken through, despite many great attempts: implementing oxygen reduction reaction catalysts at the cathode [2]; integrating membranes and gas diffusion layers [3]; selecting specific microbial strains or genetically modifying them for optimum performance [4]. Consequently, alternative approaches are necessary to try and maximise power densities.

Engineering a space efficient device could be a great breakthrough in commercialising SMFCs, since the power scale-up can only be achieve by stacking together several SMFC units [5]. The surface coverage required by a single SMFC is therefore a current challenge, due to the necessity for cathode's exposure to air [5]. Wetser et al attempted to resolve this, by developing a tubular reactor, operational underground [6]. The device, however, required pure oxygen or pressurised air to be pumped through, resulting in higher energy requirements. It also suffered from instability due to oxygen crossover from cathode to anode, which significantly lowered the electric output [6]. Walter et al showed a promising concept by submerging vertically positioned electrodes in urine fed microbial fuel cells [7]. They found the performance improving with increased immersion of the device in urine, (with optimum immersion of 75%), due to enhancements in reduction reaction rates from better contact between the cathode and the electrolyte [7].

Therefore, to test whether a similar approach can be used in soil microbial fuel cells, in this study, we investigate the effect that positioning the electrodes vertically, rather than horizontally, has on electrochemical performance. This geometrical approach has the potential to enhance output power densities, by allowing more SMFCs installed per surface area.

* Corresponding author: m.di.lorenzo@bath.ac.uk

2 Materials and Methods

2.1 Materials

All reagents used were purchased of analytical grade from Alfa Aesar and Sigma-Aldrich, unless otherwise specified, and used without further purification. The soil was collected from a maximum depth of 30 cm below the surface around the campus area of the University of Bath. Soil pH (6.44 ± 0.19) and conductivity (κ= 195.2 ± 23.3 μS cm^{-1}) were measured by using a Thermo Scientific Orion Star A325 probe. The moisture content expressed as a percentage by mass, Wm (% m/m), calculated according to Eq. 1, was 45.05 ± 0.36 %.

$$W_m = \frac{m_w - m_D}{m_w - m_0} \times 100 \quad (1)$$

where mw (g) is the mass of the wet sample in the crucible; mD (g) is the mass of the dried sample in the crucible; m0 (g) is the mass of the empty crucible. The organic matter content, 21.75 ± 0.47 % (expressed as a percentage by mass) was estimated with the Loss on Ignition analysis.

2.2 SMFC design and operation

Six membrane-less air-cathode SMFC designs were constructed. In three of the devices, the electrodes were configured vertically, while in the other three, a horizontal electrode orientation was used. Each design had three replicates to evaluate the reliability and reproducibility of the data obtained. The design specifications of the six SMFCs used in this study are summarised in Table 1.

Table 1. SMFCs tested in the study

SMFC Design	Electrode Configuration	Electrode Spacing	Cathode soil immersion
H-4	Horizontal	4 cm	-
H-6	Horizontal	6 cm	-
H-8	Horizontal	8 cm	-
V-25	Vertical	2 cm	25% (2 cm)
V-50	Vertical	2 cm	50% (4 cm)
V-75	Vertical	2 cm	75% (6 cm)

The SMFC devices were fit into PVC containers (32 x 24 x 10 cm) filled up with soil, which was kept moisturised with tap water. The anodes were buried inside the soil and the cathodes were exposed to air. In the case of the vertical designs, cathode immersion in soil varied, as shown in Figure 1. The electrodes were connected to an external resistance of 510 Ω and to a data acquisition system (DAQ6510, Keithley), by means of titanium wire (0.25 mm diameter). Polarization tests were performed by connecting the SMFCs to a resistance box (Cropico RM6 Decade) and varying the applied resistance. Ohm's law ($I=E/R_{ext}$) was used to calculate the current (I) corresponding to each externa resistance (R_{ext}).

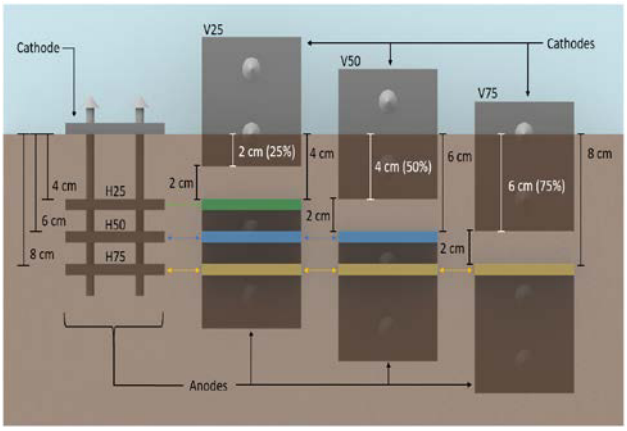

Fig.1. SMFC designs tested in this study.

3 Results

The performance of the several SMFCs was assessed and compared according to the enrichment curves (Figure 2). As shown in Fig.2A, for all the SMFCs with horizontal electrodes the lag phase took 9.65 days for H-8, followed by 10.76 days for H-6 and 11.41 days for H-4. The SMFCs with vertical electrodes (Fig.2B) experienced an average of 5% increase in microbial growth rate, and 42% decrease in lag phase duration, with V-25 (7.26 days), V-50 (6.3 days) and V-75 (4.86 days), respectively. These variances were found to be related to the anode depth and orientation. Evaluation of individual electrode potentials revealed that the reactor designs with the vertical anodes immersed deeper in the soil, reach negative values of -400 mV vs. Ag/AgCl, six days faster than the horizontal set-ups (see Figure 3).

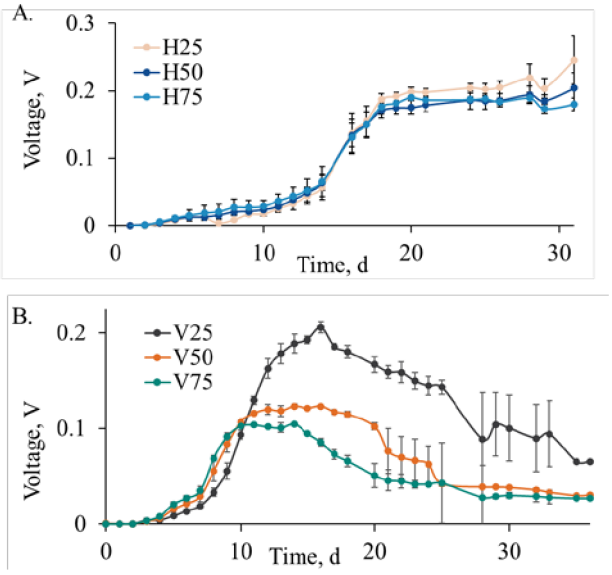

Fig.2. Enrichment curves of: (A) Horizontal reactor designs; (B) Vertical reactor designs. Data is the average of three replicates. Error bars refer to 3 replicates.

This result can be attributed to the increased anaerobic conditions, at the anode in deep soil [8], where a more rapid electroactive biofilm development allows the exponential growth phase to be reached quicker.

The other noticeable difference between the designs is in the steady-state voltage. The horizontal configuration produced a stable steady voltage for the entire duration of the experiment (Fig. 2A), whereas the voltage of the vertical configurations started to decay after only two weeks of operation (Fig. 2B). Although the exact reason for this voltage decay was not identified, individual electrode potential assessment revealed that the drop in performance is related to the cathodes. As shown in Fig. 3, following the enrichment completion, the cathode potentials in all the vertical configurations began to decrease from -0.27 ± 0.05 V to -0.41 ± 0.02 V, after 15 days.

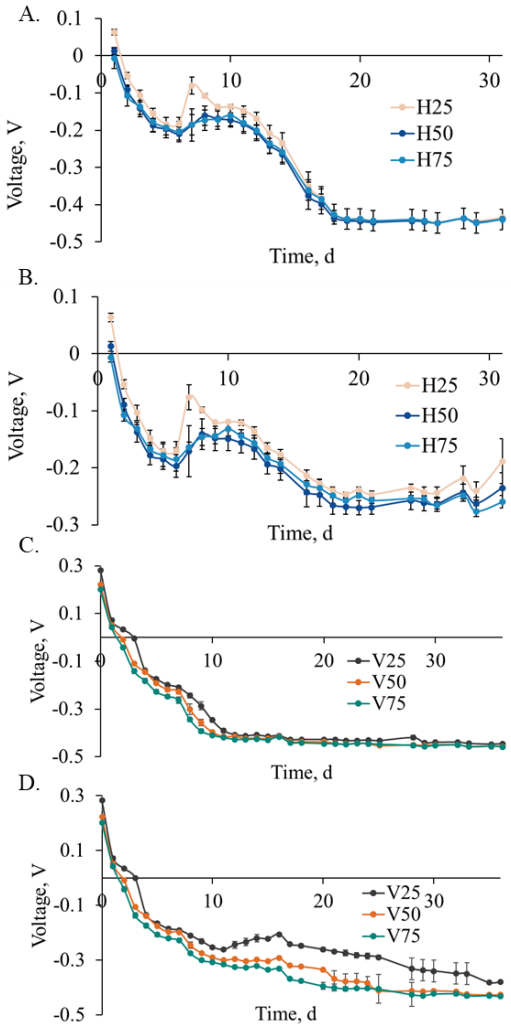

Fig.3. (A) Anode potentials of Horizontal SMFCs; (B) Cathode potentials of Horizontal SMFCs; (C) Anode potentials of Vertical SMFCs; (D) Cathode potentials of Vertical SMFCs

This voltage decay suggests increasing oxidative conditions at the cathode. A quantitative assessment of the growth curves revealed that the rate of voltage decay decreased with time. In particular, the output voltage generated by V50 and V75 dropped by 15.62% and 21.36%, respectively, compared to V25.

This result, therefore, confirms that the greater the cathode fraction immersed in soil, the higher the output voltage decay.

The voltage versus time trends obtained can be attributed to the increasingly anoxic conditions experienced at greater soil depths, which can decrease the rate of reduction reaction, due to oxygen limitations [9]. Furthermore, it is likely that a mix potential distribution occurs within the electrodes partially immersed in the soil, to the point that the part of the electrode deeper in the soil may act as the anode and transfer electrons to the upper part of the electrode, thus short circuiting the overall system [10].

Further analysis was carried out in the form of polarisation tests, which were done on day 20, after completion of the enrichment, and on day 30, following the voltage decay of vertical SMFCs. In the case of the SMFCs with horizontal electrodes, the configuration with a 4 cm electrode spacing performed best, generating 0.110 mW. Second was the configuration with a 6 cm spacing (0.082 mW), and third the configuration with a 8 cm spacing (0.079 mW). Furthermore, the performance of the H-25 and H-50 configurations increased from day 20 to day 30 by 68% and 32.5%, respectively, which can be attributed to extra developments of electroactive biofilms [11]. The performance of H-75 slightly dropped by 13% after the 10 days. This trend suggests that 4 cm is the optimal distance between the electrodes in a flat-plate configuration. Distances smaller than 4 cm can lead to oxygen crossover in the anode [12] and distances larger than 4 cm begin to inhibit proton diffusion, causing greater internal resistances, as demonstrated in Figure 4A.

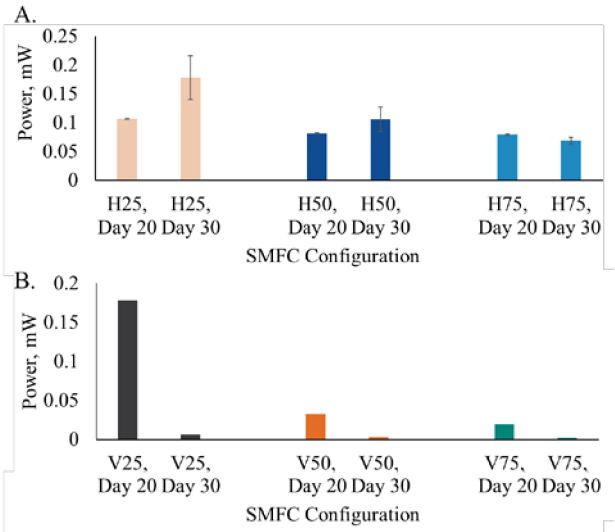

Fig.4. Maximum power generated by the SMFCs after 20 and 30 days of operation; (A) Horizontal set-up; (B) Vertical set-up

In the case of vertical SMFCs (Fig.4B), on day 20, V-25 significantly outperformed the other configurations, generating 0.178 mW. However, as a consequence of the voltage decay, the performance in all vertical SMFCs dropped. V-25, V-50 and V-75 generated only 0.006 mW, 0.003 mW and 0.002 mW, respectively, after 30 days of operation.

4 Conclusions

Soil microbial fuel cells have tremendous potential in energy harvesting applications in remote areas. In this study, the effect of the electrode orientation was investigated to identify solutions that would enhance the power density of SMFCs stacks. SMFCs with horizontal and vertical electrical configurations were tested. The tests revealed that the electrode configuration and placement in soil has clearly an effect on performance in SMFCs. Cathode immersion showed a negative influence, causing an up to 68 % voltage decay after four weeks of operation. Although the exact reason for this behaviour has not been identified, it is likely related to slower reduction rates due to oxygen limitations across the depth of soil and mixed potentials developing along the electrode. It was also demonstrated that the optimal spacing between horizontal electrodes is 4 cm, generating 58% and 158% more power than reactors with 6 cm and 8 cm spacing, resulting in power densities of 28 mWm^{-2}. Although low, such power would be able to sustain the operation of certain electronics and LEDs, or could be accumulated and stored over, to power devices with higher energy requirements.

This project was funded by the UK Research England, under the Global Challenges Research Fund (GCFR), and is part of the project GREENER funded by the European Union's Horizon 2020 research and innovation programme under the grant agreement No 826312

References

[1] C. Santoro, C. Arbizzani, B. Erable, I. Ieropoulos., Power Sources **356** (2017), pp. 225-244
[2] H. Yuan, Y. Hou, I. Abu-Reesh, J. Chen, Z. He, Mater. Horiz, **3**, (2016), pp. 382-401
[3] M. Shabani, H. Younesi, M. Pontie, A. Rahimour, M. Rahimejad, A. Zinatizadeh, J. Clean. Prod., **264**, (2020)
[4] M. Angelaalincy, R. Krishnaraj, G. Shakambari, B. Ashokkumar, S. Kathiresan, P. Varalakshmi, Front. Energy Res., (2018)
[5] J. Dziegielowski, B. Metcalfe, P. Guzman, C.A. Martinez-Huitle, A. Gotrayeb, J. Wenk, M. Di Lorenzo, Appl Energy, **278** (2020)
[6] K. Wetser, K. Dieleman, C. Buisman, D. Strik, Appl Energy, **185** (2017), pp.642-649
[7] X. Waletr, C. Santoro, J. Greenman, I. Ieropoulos, Int. J. Hydrog. Energy, **44** (2019), pp. 4524-4532
[8] Chen, C.-Y., et al., 2013. Environmental Technology 35, 2013, p. 286-293.
[9] H. Rismani-Yazdi, et al., J Power Sources, **180**, (2008), pp. 683-694.
[10] F. Harnisch, U. Schroder, ChemSusChem, **2**, (2009), pp. 921-926.
[11] G. Pasternak, J. Greenman, I. Ieropoulos, J Power Sources**, 400**, (2018), pp. 392-401
[12] J. Dziegielowski, N. Poyiatzi, M. Di Lorenzo, *EFC19* (2019)

Minimalistic soil microbial fuel cells for bioremediation of recalcitrant pollutants

Arpita Nandy[1], *Bongkyu* Kim[1,2], and *Mirella* Di Lorenzo[1*]

[1] Department of Chemical Engineering and Centre for Biosensors, Bioelectronics & Biodevices (C3Bio), University of Bath, Claverton Down, BA2 7AY, UK

[2] Division of Biotechnology, College of Environmental and Bioresource Sciences, Jeonbuk National University, Iksan, Jeonbuk, 54596, South Korea

Abstract: Increased human, agricultural and industrial activities along with improper waste disposal leads to high levels of soil contamination and accumulation of recalcitrant contaminants in the environment. This global issue demands the use of green and sustainable technologies and soil microbial fuel cells (SMFC) can be a potential solution. We adopted minimalistic designs, based on low-cost carbon materials without any expensive catalyst and membrane, which makes the SMFCs suitable for in-field applications. We investigated the ability of the indigenous microbial population of the soil to use organic contaminants as the source of carbon and the enrichment of the electroactive consortium was monitored over time onto the electrode surface of the SMFCs. We tested performance in soil contaminated with pesticide and soil contaminated with hydrocarbons and compare the microbial enrichment process with respect to the case of non-contaminated soil.

1.Introduction

Increasing human, agricultural, and industrial activities cause widespread environmental pollution across the globe, which is a serious threat to the ecosystem as well as to human and animal health. Hazardous compounds, in the form of recalcitrant hydrocarbons, pesticides, heavy metals and micropollutants, contaminate soils/sediments, ground and surface waters. About 80% of the global wastewater is released into the environment without adequate treatment [1] and 400 million tons of hazardous waste is produced annually around the globe [2]. Although there are different physico-chemical techniques to deal with such pollutions, they are often complex, energy-consuming, and expensive. Despite the scientific advancements towards reducing these pollutants, there is still huge scope and need for developing low-cost, sustainable green technologies to address these environmental issues.

Minimising the risks associated with the accumulations of harmful chemicals in the environment is key to establish low-cost sustainable methodologies for the treatment of contaminated soil and water. To exploit the excellent capability of different microbial species to utilize recalcitrant compounds and converting them to harmless end products is crucial to achieve higher remediation efficiency. The efficacy of the microbes to oxidize organic contaminants as carbon source provides an understanding on microbial enrichment patterns in different kinds of soils and can help to develop innovative techniques for bioremediation. Conventional bioremediation techniques rely on either biostimulation (addition of nutrients or O_2) or bioaugmentation (addition of microorganisms) [3, 4]. These approaches have many limitations, which include limited water solubility and high chemical reactivity of oxygen with the minerals in soil and subsurface environment. Bioaugmentation can also be ineffective because of incompatibility with the indigenous microorganisms and lack of effective electron donors/acceptors. Most contaminated sites in soil and subsurface environment are anoxic and hence relying on the activities of indigenous microorganisms is often more practical [5].

By introducing microbial fuel cell (MFC) strategy as a remediation technique, we can effectively exploit the ability of electroactive bacteria to degrade organic contaminants and simultaneously generate bioelectricity. The protons generated in the microbial oxidation, travel to the cathode and the electrons flow through the external

* Corresponding author: m.di.lorenzo@bath.ac.uk

circuit to reach the air cathode, where a terminal electron acceptor (Oxygen) is reduced, and the overall cell potential is measured. Several studies have demonstrated the ability of MFCs to degrade recalcitrant pollutants like hydrocarbons and pesticides [6, 7], thus suggesting the technology as a promising green strategy to promote advanced environmental remediation. In this study, we test the use of low-cost air-cathode soil microbial fuel cells (SMFCs) for the degradation of recalcitrant pollutants in soil. We have tested the electrochemical performance of the SMFCs in soil contaminated with the pesticide atrazine and soil contaminated with petroleum hydrocarbon, along with the pollutant degradation ability of the system. The simple design implemented for the SMFC, with no use of catalyst and no membrane, facilitates the scale-up of the technology for field tests and guarantee its cost-effectiveness.

2. Materials and Methods

2.1. Materials

The chemicals used in this experiment were purchased from Alfa Aesar/Thermo Fischer Scientific (Lancashire, UK) and Sigma-Aldrich (Merck Life Science UK Limited, Gillingham, UK). The graphite felt is purchased from Online Furnace Services Ltd (Scotland, UK), screws were procured from Bluemay Limited (Wiltshire, UK) Titanium wire (diameter 0.25 mm) was obtained from VWR International Ltd. (Leicestershire, UK). Non-contaminated soil was collected around the campus area of the University of Bath from a maximum depth of 30 cm below the surface. The soil used for pesticide study was purchased from Homebase (https://www.homebase.co.uk/). The soil used for hydrocarbon study was provided by Acciona (https://www.acciona.com/) and collected from a contaminated area in a Machinery Park in Noblejas (Toledo, Spain). The contaminated area can be classified as surface spill from a drilling machine with the oil infiltrated about 20-25 cm deep. The soil was sieved at 0-2 mm after excavation to remove stones and gravels. The non-contaminated soil, collected from the university of Bath campus, was also cleaned of visible stones, gravels, roots and leaves before use. The hydrocarbon contaminated soil was mixed with surfactant Tween-80 at 0.2 mass% [8] to enhance the bioavailability. The physicochemical properties of the three types of soils are summarised in Table 1. The percentage of organic matter is higher in non-contaminated soil, but the amount of phosphorus and potassium is higher in the soil contaminated with hydrocarbons. In addition, concentration of TPH (Total Petroleum Hydrocarbon) is very high in the contaminated soil.

Table 1: Physicochemical properties of the soils used in this study

Parameters	Non-contaminated soil [9]	Soil contaminated with Pesticide	Soil contaminated with Hydrocarbons
pH	6.5	7.4 ± 0.18	7.9±0.05
Moisture content	53%	32%	20%
Nitrogen	<0.001%	<1%	<1%
Phosphorus	<10 mg/kg	<10 mg/kg	70.7 mg/kg
Potassium	<150 mg/kg	-	1800 mg/kg
Organic matter	17.4%	7.27%	10.9%
Concentration of contaminant	N/A	5mg/kg (Atrazine)	34000 mg/kg (Total Petroleum Hydrocarbon)

2.2. SMFC Design and Operation

SMFCs for three experimental conditions were operated according to the type of soil (non -contaminated, with pesticide and with hydrocarbon), as shown in Figure 1. The SMFCs were constructed in triplicates and fitted in small polypropylene boxes (dimension: 12 cm^2 X 12 cm h), which were insulated with aluminium foil to avoid photolysis of the pesticide and hydrocarbons. The boxes were further loosely covered with lids to avoid evaporation. Graphite felt electrodes were used for both the anode and the cathode (dimension: 8 x 8 x 0.6 cm for SMFCs with non-contaminated soil and pesticides and 7 x 7 x 0.4 cm for the SMFCs with hydrocarbon contaminated soil) and kept at a fixed distance of 4 cm with nylon screws. The anodes were pre-treated to increase the hydrophilicity and the roughness of the carbon nanofibers, as previously described [10]. No external catalyst was used for the cathode. The anodes were buried in the soil and the cathodes were exposed to air. The soil itself was used as a separator for the two electrodes, while the natural stratification in soils ensures negligible oxygen transfer to the anode. The electrodes were connected to an external resistance of 500 Ω and to a data acquisition system (DAQ6510, Keithley instruments, Tektronix UK Ltd.) to monitor the output voltage over time. The current was calculated using Ohm's law $V=IR$ and was normalized to the surface area of the electrodes. The soil was kept moistened with tap water. Titanium wire was used for connecting the electrodes.

Hydrocarbon fractions from the SMFCs were analysed using Gas chromatography-mass spectrometry (GC-MS) and were performed through an external analytical company (Eurofins Chemtest Ltd, Cambridge, UK). The pesticide was collected from homogenized soil and analysed using high-performance liquid chromatography coupled with tandem mass spectrometry.

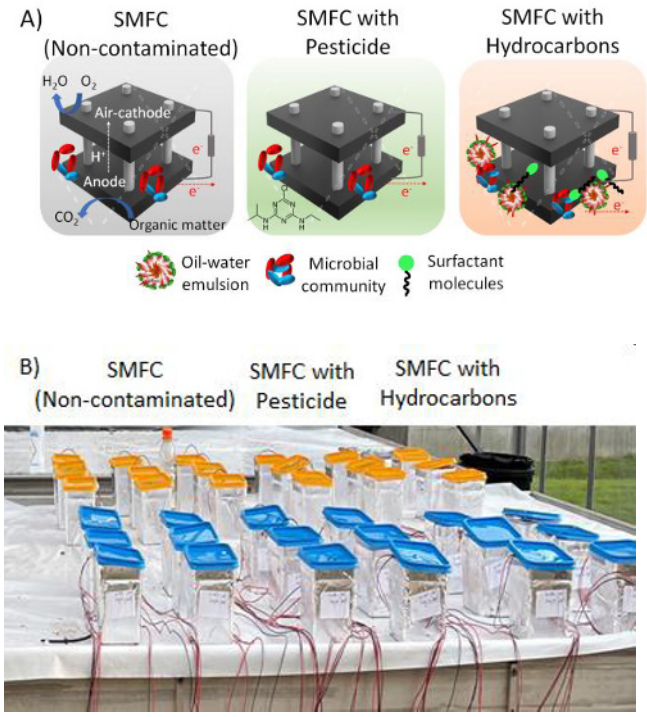

Fig. 1. A) Schematic of the SMFCs working principles and operation in different soils. B) Experimental set-up

3. Results and Discussion

The performance of the SMFCs in soils with different pollutants was investigated. The model pesticide tested was atrazine, which was used to spike non-contaminated soil. Atrazine is a herbicide widely used to control weeds. It is sprayed on row crops and sometimes also on residential lawns and highway/railroad rights-of-way [11]. Atrazine can enter water supplies from the soil and its contamination in public/private water supplies above the drinking water standards (maximum contaminant level for drinking water: 0.003 mg/L) set by United States Environmental Protection Agency-EPA raises concern as it has been linked to adverse reproductive effects in amphibians and other wildlife and reduce primary production in aquatic communities by inhibiting photosynthesis. Currently it is also being studied as a potential carcinogen to both aquatic and human life. The other soil tested was contaminated with petroleum hydrocarbons. Petrochemical contamination due to oil spills is a major concern because of its toxicity and recalcitrance. Oil companies produce billions of gallons of salty and toxic wastewater out of the oil wells and if not stored properly until treated further, there is a potential risk of spill which contaminates surface water including vegetation and drinking water [12]. The clean-up standard for TPH in soil varies on different factors, including the types of hydrocarbon present, depth of groundwater, proximity of human population and the future use of the site etc. Despite these variables, the most commonly used soil cleanup standard for TPH is 100 mg/kg [13].

The performance of the SMFCs in these two types of soils was compared with the case of non-contaminated soil. Figure 2 shows the current density generated by the SMFCs in the different soils over time. As shown, in non-contaminated soil, the enrichment of the microbial consortium at the anode occurred faster than the soil contaminated with pesticide and hydrocarbons. The initial lag-phase (with voltage below 0.05 V, current density <16 mA/m^2) lasted approx. 10 days in non-contaminated soil, while, for the case of soil with pesticides, the lag phase lasted >13 days. In the case of soil contaminated with hydrocarbons, however, the average current density remained at about 25 mA/m^2 (~ 0.06 V) for the entire duration, suggesting the microbes did not attain the state of enrichment. In the case of non-contaminated soil, an average steady output voltage of 0.204 ± 0.068V (Corresponding current density 64 ± 21 mA/m^2) was obtained, after reaching a value of 0.18 V (56 mA/m^2), while the output current density in the case of SMFC in pesticide contaminated soil decreased until a value of 34 mA/m^2 (~0.11 V) on day 19. The pesticide SMFC started to show improvements from 22nd day onwards (~ 28 mA/m^2, 0.09 V) and steadily reached to (~53 mA/m^2 ,0.17 V) in about 30 days,

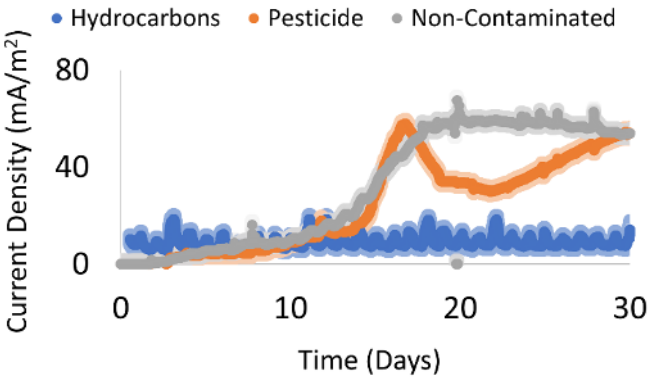

Fig. 2. Current density showing enrichment patterns over time for three SMFCs. Data is the average from three replicates. Shades show the standard error of replicates

suggesting that this is the actual exponential phase for the microbial consortium in the SMFC in soil contaminated with pesticide. The abrupt rise and fall in the potential for the SMFC in soil contaminated with pesticide may be due to some alteration in the microbial consortium or to variation in the operational conditions (such as temperature and water content in soil).

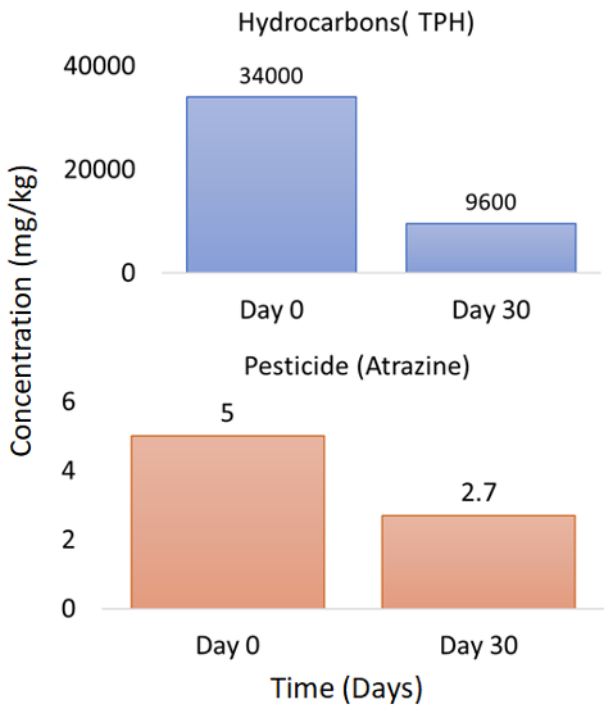

Fig. 3. Degradation pattern of Total Petroleum Hydrocarbon (TPH) and pesticide (Atrazine) in SMFCs over a period of 30 days

The poor performance of the SMFC in the soil contaminated with very high concentrations of hydrocarbons demonstrates that its toxicity prevents the development of an electroactive biofilm at the anode. No bioaugmentation (addition of enriched microbial consortium externally) strategy is adopted in this study, and the SMFC performance is uniquely dependent on the indigenous microbial consortium. It is likely that the formation of electroactive biofilm is hindered in presence of such high concentrations of hydrocarbon fractions, leading to lower output potential.

Figure 3 shows the degradation of atrazine and TPH obtained with the SMFCs. As shown, in the case of soil contaminated with atrazine, a degradation of about 46% was observed after 30 days. In the case of hydrocarbons, a much better degradation in the TPH was observed, reaching a value of about 72% on day 30. Although future investigation is required to assess the impact of bioelectrochemical routes in atrazine degradation, our results suggest that hydrocarbon degradation is achieved by other biochemical pathways. Further research must necessarily investigate the effect of different types of hydrocarbons and lower concentrations, as well as the relevance of biostimulation and bioaugmentation in the process.

4. Conclusions

There is a clear need for development of low-cost and easy-to-scale-up strategies for the bioremediation of recalcitrant pollutants in soils. Soil microbial fuel cells can be the solution, considering key features such as self-powered operations and minimum maintenance requirements. In this study, a cost-effective SMFC design was implanted and its performance in different types of soil, was investigated for the first time. Indigenous microbial population can significantly degrade organic matter of natural soil and it can also be used for the removal of contaminants such as atrazine. However, the concentration of the contaminants has crucial role in attaining microbial enrichment. Very high concentration of contaminant, as in the case of soil contaminated with hydrocarbons, can markedly limit the generation of high output voltages. Abundance of different microbial consortium plays an important role in degradation of pollutants and generation of electricity. Therefore, molecular analysis of the microbial consortium can be considered in future for more in-depth understanding.

Acknowledgement

This work was funded by project GREENER that has received funding from the European Union's Horizon 2020 research and innovation programme under the grant agreement No 826312.

References

1. United Nations, Sustainable Development Goals, *https://www.un.org/en/sections/issues-depth/water/*, accessed online on October 26, 2021

2. UNEP. UN Environment. Available online: *https://web.unep.org/,* accessed online on October 26, 2021

3. M. Tyagi, M.M.R. da Fonseca, C.C. de Carvalho, *Biodegradation*, **22**, 231-241, (2011)

4. G.O. Adams, P.T. Fufeyin, S.E. Okoro, I. Ehinomen, *Int. J. Environ. Biodeterior. Biodeg*. **3**, 28-39, (2015)

5. M. Sharma, A. Nandy, N. Taylor, S.V. Venkatesan, V.O. Kollath, K. Karan, V. Thangadurai, N. Tsesmetzis, L. M. Gieg, J Hazard Mater. **389**, 121845, (2020)

6. G. Mohanakrishna, R.I. Al-Raoush, I. M. Abu-Reesh, D. Pant, RSC Adv, **9**, 41409-41418, (2019)

7. X. Cao, H.L. Song, C.Y. Yu, X.N. Li, Bioresour Technol, **189**, 87-93, (2015)

8. 3. C.C. Lai, Y.C. Huang, Y.H. Wei, J.S. Chang, J Hazard Mater. **167**, 609-614, (2009)

9. J. Dziegielowski, B. Metcalfe, P. Villegas-Guzman, C.A. Martínez-Huitle, A. Gorayeb, J. Wenk, M. Di Lorenzo, Appl Energy **278**, 115680, (2020)

10. S. Monasterio, M. Di Lorenzo, Chem Eng Sci, **198**, 108-116, (2019)

11. United States Environmental Protection Agency (EPA*), https://www.epa.gov/national-aquatic-resource-surveys/indicators-atrazine*, accessed online on October 29, (2021)

12. A. Nandy, J.R. Radović, B. Novotnik, M. Sharma, S.R. Larter, V. Thangadurai, Bioresource Technol Reports, **11**, 100449, (2020)

13. T.C. Michelsena, C.P. Boyce, J. Soil Contam, **2**, 1-16, (1993)

.

Modelling Miniature Microbial Fuel Cells with Three-dimensional Anodes

Elisa Casula[1], *Michele* Mascia[1,*], *Giorgia* De Gioannis[2], *Mirella* Di Lorenzo[3], *Marco* Isipato[2], *Aldo* Muntoni[2], *Daniela* Spiga[2]

[1]Dipartimento di Ingegneria Meccanica, Chimica e dei Materiali, Università degli Studi di Cagliari, via Marengo 2, 09123 Cagliari, Italy
[2]Dipartimento di Ingegneria Civile, Ambientale e Architettura, Università degli Studi di Cagliari, via Marengo 2, 09123 Cagliari, Italy
[3]Department of Chemical Engineering and Centre for Biosensors, Bioelectronics & Biodevices (C3Bio), University of Bath, Claverton Down，BA2 7AY, UK

Abstract. Microbial fuel cells (MFCs) exploit the metabolic activity of electroactive microorganisms for oxidation of organic compounds and extracellular electron transfer to an external electrode. the technology is associate with very slowreaction rates, resulting in low current densities. Anodes with high specific surface should be used to increase the overall electricity generation. Carbon-based 3D materials, with high surface per unit of volume, are largely used anode materials in MFCs, although may show significant lack in efficiency due to mass transfer limitations, concentration gradients, velocity distribution and resistivity of the material. Consequently, the concomitant effect of several parameters should be assessed and quantified to design highly performing MFCs implementing 3D anode materials. In this work, miniature MFCs with 3D anodes are mathematically modelled to quantify the effect of operative parameters on performance. The model combines equations of charge conservation, mass transport phenomena, hydrodynamics, and kinetics of the involved processes under transient conditions, and provides 3D profiles with time of velocity, biofilm thickness, substrate concentration, current density and potential. The solution predicts a laminar flow, as it was expected with the low flow rates used. The concentration profiles show the consumption of substrate in the anode, with low values of local concentrations depending on organic load in the feed stream. The model also provides a versatile tool to optimise the operative conditions of the system, managing the flow arrangements to maximise either substrate removal or electricity generation.

1 Introduction

An MFCs is a fuel cell where the anode reactions are catalysed by exoelectrogenic microorganisms [1]. The typical MFC setup comprises an anode and a cathode electrode, immerged in an electrolyte and physically separated by an ion exchange membrane, . In the anodic chamber, microbial communities in planktonic state or within a biofilm that develops onto the electrode surface, oxidize an organic substrate with the result to generate electrons, protons, and other metabolites as end-products. The electrons collected by the anode are transferred to the cathode throughout the electric circuit, to power a load [2]. On the other side, the protons move to the cathode passing through the membrane or by simple diffusion throughout the electrolyte solution to be reduced by the electrons, thus closing the circuit.

Any substrate containing organic matter, including municipal or industrial and residual from food industry, can be used as fuel in MFCs [3].

Typically, MFC systems generate power at milliwatt level [4]. One of the largest prototypes reported, with capacity of 255 dm^{-3} [5], produced only 78 mW m^{-2}. [6]. Successful examples of up-scaling from the laboratory to pilot or demonstrator scale are, however, still scarce, [7].

Several biological, operational and design parameters may affect cell performance, and the literature often reports contrasting results on their effects [8]. An example is the contact time between substrate and microorganism, which is one of the most critical factors for power production and chemical oxygen demand (COD) removal in wastewaters [9,10]. Contrasting results are reported in literature on the influence of the hydraulic retention time (HRT) on cell performance. Ye et al. [9] found that increasing the HRT determines an improvement of the power output, Costa Santos et al. [10] found an optimum HRT for effective COD removal, as higher HRT results in an insufficient organic load limiting bacteria activity and growth, shorter times do not allow bacteria to efficiently degrade organic nutrients.

Conversely, Akman et al. [11] found that decreasing the HRT from 1.5 to 1 d determines an improvement of the power density from 818 mW m^{-2} to 909 mW m^{-2}. Recently, Chen et al. [12] reported an optimal HRT equal to 72 h for voltage outputs when the HRT was raised from 24 to 120 h, while the longer HRTs produced the higher COD removal.

* Corresponding author: michele.mascia@unica.it

Mathematical modelling offers a valid tool to identify and quantify the concomitant effect of the most influent operational and geometrical parameters in MFC technology and guide on its effective scale-up [13-16].

In this context, our work aims to provide a 3D mathematical model of a continuous flow air-cathode MFC. The model combines equations of charge conservation together with mass transport phenomena, hydrodynamics and kinetics of the involved processes, such as biofilm formation, bioelectrochemical and electrochemical reactions, under transient conditions. The effect of residence time and inlet substrate concentration is simulated with different anodic cell geometries to evaluate their influence on performances.

2 Mathematical model

Figure 1 show the inner part of the three in-flow MFCs simulated in this study, which corresponds to the domains of integration of the model: the inlet and outlet channels, the anodic compartment, and the membrane/cathode assembly.

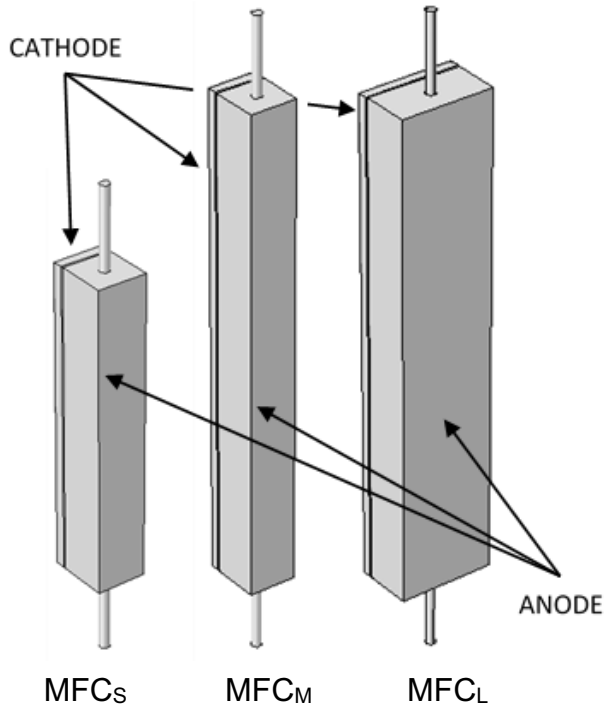

Fig. 1. Geometries of cells used in the model

Three different anode sizes are considered with dimensions of 0.5 cm x 0.5 cm x 3 cm (MFC_S), 0.5 cm x 0.5 cm x 5 cm (MFC_M), and 0.5 cm x 1 cm x 5 cm (MFC_L). The domains corresponding to the electrodes and membrane are modelled as a porous matrix, the anodic channels are modelled as a continuous medium in liquid phase.

The model numerically describes the phenomena occurring as MFCs operate, according to the following assumptions.

A single carbon source was considered, and it was modelled as equivalent acetate.

Biofilm nucleation

The anolyte containing planktonic microorganisms M_S and the substrate, enters the inlet channel then flows throughout the porous anode where microorganisms bump into and adhere to the carbon surface or leaves the cell by the exit channel. Once attached onto the carbon surface, adherent microorganisms M_A start duplicating until the bare surface is covered, and then grow layer by layer until a stable biofilm thickness is reached [17]. The model only considers adherent microorganisms as electroactive [18].

Changes in pH in the anolyte are considered as negligible.

Planktonic microorganisms adhere to the anode developing the growth nuclei of the biofilm (adherent microorganisms). The reaction rate of biofilm generation r_1 (mol m^{-3} s^{-1}) has been described using a Nernst-Monod kinetics [19]:

$$r_1 = k_1 \frac{C_{Ac^-}}{C_{Ac^-} + K_{s,S}} \frac{C_{M_S}}{C_{M_S} + K_{s,M_S}} \left[1 + \exp\left(-\frac{F}{RT}\eta_{AN}\right)\right]^{-1} \quad (1)$$

Where: C_{Ac} and C_{Ms} (mol m^{-3}) are the acetate and planktonic microorganisms concentration; k_1 (mol m^{-3} s^{-1}) is the kinetic constant; $K_{s,S}$ and $K_{s,MS}$ (mol m^{-3}) are the half saturation constants and η_{An} (V) is the anodic overpotential.

Growth of biofilm

The reaction rate of biofilm (M_A) production r_2 (mol m^{-3} s^{-1}) has been described by a Nernst-Monod kinetics, which relates the rate of substrate depletion with its concentration and the electrical potential in biofilms [19]:

$$r_2 = k_2 \frac{C_{Ac^-}}{C_{Ac^-} + K_{s,A}} \frac{C_{M_A}}{C_{M_A} + K_{s,M_A}} \left[1 + \exp\left(-\frac{F}{RT}\eta_{AN}\right)\right]^{-1} \quad (2)$$

Where: k_2 (mol m^{-3} s^{-1}) is the kinetic constant; $K_{s,S}$ and $K_{s,MS}$ $K_{s,S}$ and $K_{s,MS}$ (mol m^{-3}) are the half saturation constants.

It is assumed that the growth of biofilm onto the porous anode does not affect its porosity. In MFC models, constant values of porosity are commonly used either for carbon felt electrodes [20] or for different anodes configurations as carbon brushes [21] and graphite felt [22] to reduce the model intricacy [23].

Detachment of biofilm

The reaction rate of detachment r_3 (mol m^{-3} s^{-1}) has been described by a pseudo-first order law depending on the amount of biofilm produced:

$$r_3 = k_d C_{MA} \quad (3)$$

Cathode

Electrons are transferred to the cathode through the conductive biofilm and the external circuit. Protons H^+ cross the membrane to reach the cathode surface where oxygen is reduced. Butler-Volmer law has been used to describe the cathodic reaction

Flow

Incompressible Navier-Stokes model was used to obtain velocity profiles.

Mass, charge, and momentum conservation equations together with relevant initial and boundary conditions are summarised below. Symbols are summarised in Table 1.

Momentum Transport

$$\frac{1}{\varepsilon_j}\left[\rho\frac{\partial \boldsymbol{u}}{\partial t}+\frac{1}{\varepsilon_j}\rho\,(\boldsymbol{u}\cdot\nabla)\boldsymbol{u}\right]=\nabla\cdot\left[-p\boldsymbol{I}+\frac{1}{\varepsilon_j}\mu(\nabla\boldsymbol{u}+(\nabla\boldsymbol{u})^T)\right]-\frac{\mu}{k}\,\boldsymbol{u} \quad (4)$$

$$\rho\,\nabla(\boldsymbol{u})=0;\ j=\begin{cases}channels\rightarrow\ \varepsilon_j=1\\ anode\rightarrow\ \varepsilon_j=\varepsilon_{AN}\end{cases}$$

$$\boldsymbol{u}|_{t=0}=0$$

$$\boldsymbol{u}=-u_{in}\boldsymbol{n}\quad Inlet$$

$$[-p\boldsymbol{I}+\mu(\nabla\boldsymbol{u}+(\nabla\boldsymbol{u})^T)]n=-\mathrm{p}_{out}\boldsymbol{n}\quad Outlet$$

Mass Balances

$$\varepsilon_j\frac{\partial C_i}{\partial t}+\nabla\cdot\left(-\mathcal{D}_{i,j}^{eff}\nabla C_i\right)+\boldsymbol{u}\cdot\nabla C_i=R_{i,j} \quad (5)$$

$$i=Ac^-,M_S,H^+$$

$$j=\begin{cases}channels\rightarrow\ \varepsilon_j=1\\ anode\rightarrow\ \varepsilon_j=\varepsilon_{AN}\\ cathode\rightarrow\ \varepsilon_j=\varepsilon_{CAT},\boldsymbol{u}=0\end{cases}$$

$$C_i|_{t=0}=0$$

$$C_i|_{inlet\ channel}=C_i^0\qquad Inlet\ channel$$

$$-\boldsymbol{n}\cdot\left(\mathcal{D}_{i,j}^{eff}\nabla C_i\right)=0\qquad Outlet\ channel$$

Mass Balance of biofilm

$$\varepsilon_{AN}\frac{\partial C_{M_A}}{\partial t}=R_{M_A,Anode};\ C_{M_A}\big|_{t=0}=0 \quad (6)$$

$$\mathcal{D}_{i,j}^{eff}=\frac{\varepsilon_j}{\tau_j}\mathcal{D}_i \quad (7)$$

$$\tau_j=\varepsilon_j^{-1/3} \quad (8)$$

Reaction Rates

$$R_{Ac^-,Anode}=-\nu_{Ac^-}\,(r_1+r_2) \quad (9)$$

$$R_{Ms,Anode}=-r_1 \quad (10)$$

$$R_{Ma,Anode}=r_1+r_2-r_3 \quad (11)$$

$$R_{H^+,Anode}=\nu_{H^+}(r_1+r_2) \quad (12)$$

$$R_{H^+,Cathode}=-\frac{I_{CAT}}{F} \quad (13)$$

Currents

$$I_{CAT}=F_{H^+}\,F\,a_{CAT}\ exp\left(-0.5\frac{F}{RT}\eta_{CAT}\right) \quad (14)$$

$$F_{H^+}=\mathcal{D}_{H^+}\nabla C_{H^+} \quad (15)$$

$$I_{AN}=r_2\,z_{AN}F \quad (16)$$

$$\eta_{AN}=V_{AN}-E_{AN}^0 \quad (17)$$

$$\eta_{CAT}=V_{CAT}-E_{CAT}^0 \quad (18)$$

Electric potential

$$\nabla\cdot\left(-\sigma_j\nabla V_j\right)=f;\ j=\begin{cases}anode\rightarrow\ f=I_{AN}\\ P.E.M.\rightarrow\ f=0\\ cathode\rightarrow\ f=I_{CAT}\end{cases} \quad (19)$$

$$V_j\big|_{t=0}=0$$

$$V_j=0\qquad Ground-Anode\ interface$$

Table 1. List of symbols

Symbol	Description	Units
a_j	Electrode specific area	m^{-1}
C_i	Concentration of i-th species	$mol\ m^{-3}$
$\mathcal{D}_i$	Free diffusivity of i-th species	$m^2\ s^{-1}$
$\mathcal{D}_{i,j}^{eff}$	Effective diffusivity of i-th species in the j-th porous medium	$m^2\ s^{-1}$
E_j^0	Electrode standard potential	V
f_j	Current source at j-th domain	$A\ m^{-3}$
I_j	Electric current at the electrode	$A\ m^{-3}$
k_1	Specific rate (bacteria adhesion)	$mol\ m^{-3}\ s^{-1}$
k_2	Specific rate (substrate consumption)	$mol\ m^{-3}\ s^{-1}$
k_d	Inactivation constant for biofilm	d^{-1}
$K_{s,A}$	Half-saturation constant (substrate consumption)	$mol\ m^{-3}$
K_{s,M_A}	Half-saturation constant (biofilm growth)	$mol\ m^{-3}$
K_{s,M_S}	Half-saturation constant (bacteria adhesion)	$mol\ m^{-3}$
$R_{i,j}$	Reaction term	$mol\ m^{-3}\ s^{-1}$
u_{in}	Fluid velocity	$m\ s^{-1}$
V_j	Electric potential of j[th] domain	V
z_{AN}	Electrons generated from substrate degradation	8
Greek letters		
ε_j	Porosity of the electrode	-
η_j	Electrode over-potential	V
ν_{Ac^-}	Stoichiometric coefficient of substrate degradation	-
ν_{H^+}	Stoichiometric coefficient for H^+ generation	-
σ_j	Conductivity of j[th] domain	$S\ m^{-1}$
τ_j	Tortuosity of the porous electrode	-
p	Fluid density	$1000\ kg\ m^{-3}$
μ	Fluid viscosity	$1\ Pa\ s$
Subscripts		
Ac^-	Substrate (acetate)	
H^+	Protons	
M_S	Suspended microorganisms	
M_A	Adherent microorganisms	
i	Species (Ac^-, H^+, M_S, M_A)	
j	Domains (Anode, Catode/PEM, Channels)	

The model was implemented and solved under transient conditions with the COMSOL Multiphysics© software.

3 Model simulations and discussion

The model developed was used to predict the space time distribution of the main variable in the MFCs. In particular, simulations were carried out at different inlet flow rates and substrate concentrations to obtain space profiles of the relevant variables. Values from previous works were used for the model parameters and the process conditions; the whole set of values can be found in references 17 and 18

Figure 2 shows the 3D velocity streamlines calculated with the model for the three cell geometries. The model predicts that low velocities are reached, and a laminar flow regime is developed without dead zones or preferential flow paths.

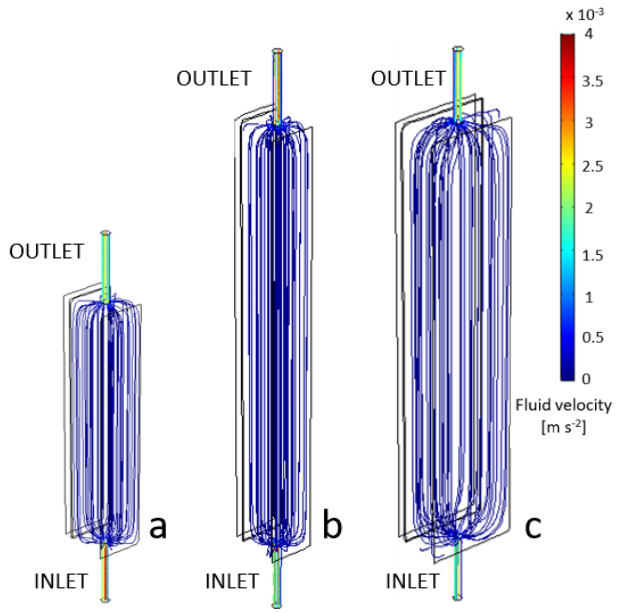

Fig. 2. Velocity streamlines for the three cells geometries a) MFC_S, b) MFC_M, and c) MFC_L at Q = 0.1 cm^3 min^{-1}.

The influence of inlet concentration on substrate degradation and average current density in the three MFCs MFC_S, MFC_M, and MFC_L was calculated with the model: an example of results obtained with a flow rate of 0.1 cm^3 min^{-1} is shown in Figure 3.

The model predicts that an increase of substrate availability determines an increase of current density production and a faster degradation of substrate. MFC_S shows the highest values of current density, due to the lower local removal with high organic load available for microbial activity, as it was also experimentally observed in a previous work [18].

Figure 4 shows the influence of the flow rate on current density and substrate degradation in the three cells at steady state conditions under the flow rates 0.01 and 0.5 cm^3 min^{-1}.

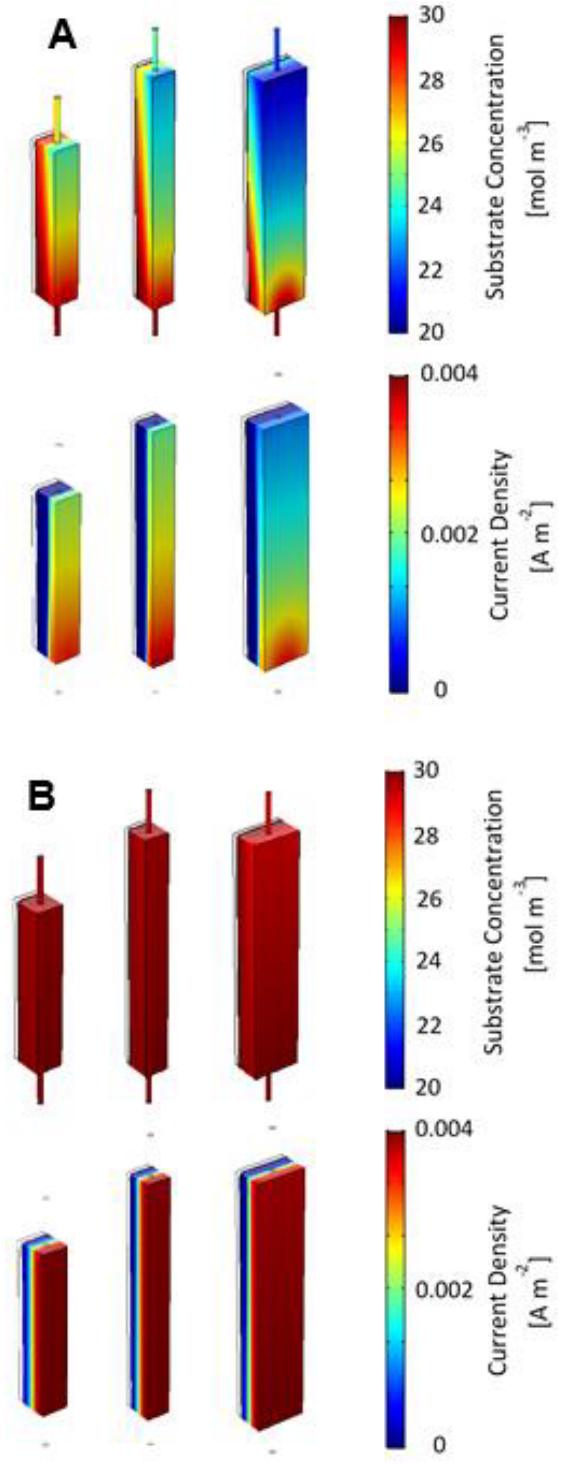

Fig. 3. Substrate concentration and current density calculated with the model for the three MFCs at 0.1 mL min-1 with C^0i = mol m^{-3} mM (A) and C^0i = 30 mol m^{-3} (B)

The model predicts an increase of current density with the flow rate due to an increase in mass transfer rate that, under the assumption of the model, leads to a higher availability of substrate for the anodic biofilm [17].

Moreover, a different distribution of the substrate is predicted, with low conversion at high flow rates, where higher local concentration of substrate lead to higher currents [11,17].

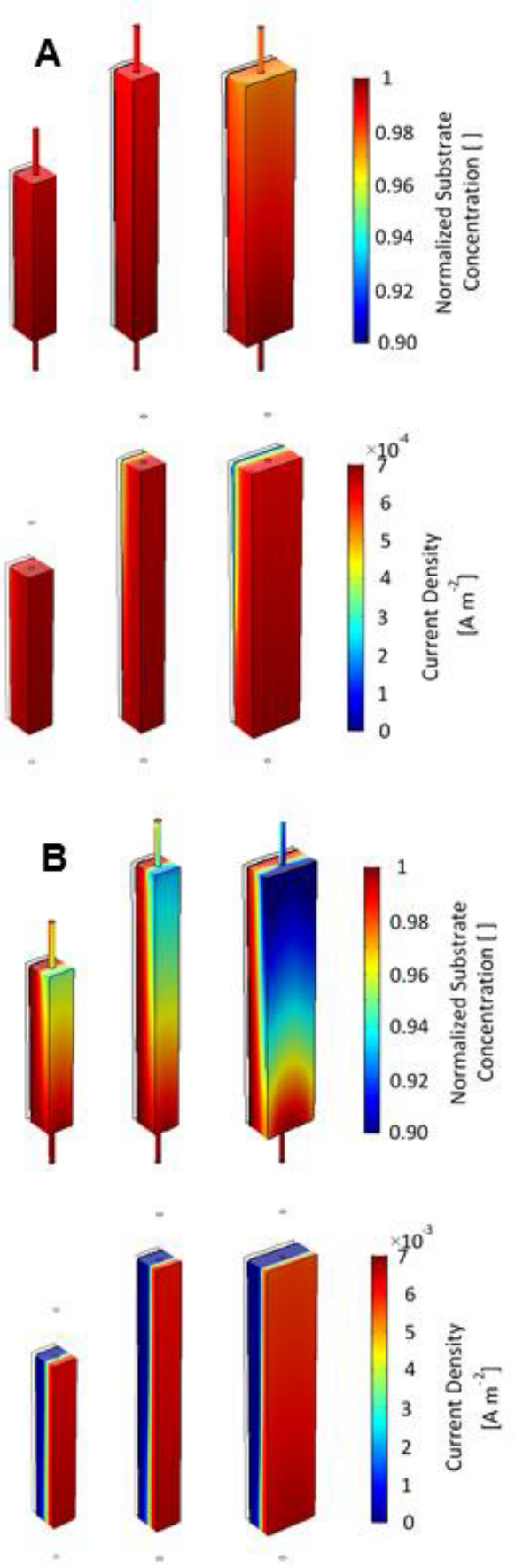

Fig. 4. 3D steady state distributions of substrate concentration and current density at two flow rates: Q = 0.01 mL min^{-1} (A) and Q = 0.5 mL min^{-1} (B).

When higher flow rates are used, there is a predominance of convective flow over diffusive flow, protons flux through the cathode is lower at higher flow rates. Conversely, the size of the anodic chamber has the opposite effect on the protons flux: at constant flow rate, the greater is the cell, the higher is the protons flux through the cathode. The protons discharge caused by the convective flux is mitigated by the increase in length and section of the cell.

Conclusions

Based on the preliminary results, the mathematical model in 3D implemented and solved of this work can be used to design modular systems, where the simulation of a single unit could be used to design cells in-parallel, while simulation and design of cells in-series can be easily implemented. The model also provides a versatile tool to optimise the operative conditions of the system, managing the flow arrangements to maximise either substrate removal or electricity generation.

The model solutions can be used to design modular systems: design of a single unit as well as of a system with MFCs in parallel can start from the simulation of a single MFC. The simulation of system with MFCs in-series can be easily implemented, so making possible the relevant design.

This work is part of a project that has received funding from the European Union's Horizon 2020 research and innovation programme under grant agreement No 826312.

References

1. M.C. Potter, A.D. Waller, Proceedings of the Royal Society of London. Series B, Containing Papers of a Biological Character 84 (1911) 260-276.
2. B.E. Logan, B. Hamelers, R. Rozendal, U. Schröder, J. Keller, S. Freguia, P. Aelterman, W. Verstraete, K. Rabaey, Environ Sci & Technol 40 (2006) 5181-5192.
3. F. Zhang, Z. Ge, J. Grimaud, J. Hurst, Z. He, Environ Sci & Technol 47 (2013) 4941-4948.
4. Y. Dong, Y. Feng, Y. Qu, Y. Du, X. Zhou, J. Liu, A, Scientific Report (2015).
5. H. Hiegemann, T. Littfinski, S. Krimmler, M. Lübken, D. Klein, K.-G. Schmelz, K. Ooms, D. Pant, M. Wichern, Bioresource Technol 294 (2019) 122227.
6. R.D. Cusick, B. Bryan, D.S. Parker, M.D. Merrill, M. Mehanna, P.D. Kiely, G. Liu, B.E. Logan, Applied Microbiology and Biotechnol 89 (2011) 2053-2063.
7. S. Babanova, J. Jones, S. Phadke, M. Lu, C. Angulo, J. Garcia, K. Carpenter, R. Cortese, S. Chen, T. Phan, O. Bretschger, Water Environment Research 92 (2020) 60-72.
8. S. Gadkari, S. Gu, J. Sadhukhan, Chem Eng J 343 (2018) 303-316.
9. Y. Ye, H.H. Ngo, W. Guo, S.W. Chang, D.D. Nguyen, X. Zhang, S. Zhang, G. Luo, Y. Liu, Sci Total Environment 734 (2020) 139220.

10. J.B.C. Santos, V.V.S. de Barros, J.J. Linares, J ElectroChem Soc 164 (2016) H3001-H3006.
11. D. Akman, K. Cirik, S. Ozdemir, B. Ozkaya, O. Cinar, Bioresour Technol 149 (2013) 459-464.
12. F. Chen, S. Zeng, Z. Luo, J. Ma, Q. Zhu, S. Zhang, Sep Sci Technol 55 (2020) 2490-2499.
13. V.M. Ortiz-Martínez, M.J. Salar-García, A.P. de los Ríos, F.J. Hernández-Fernández, J.A. Egea, L.J. Lozano, Chem Eng J 271 (2015) 50-60.
14. C. Xia, D. Zhang, W. Pedrycz, Y. Zhu, Y. Guo, J Power Sources 373 (2018) 119-131.
15. D. Recio-Garrido, M. Perrier, B. Tartakovsky, Chem Eng J 289 (2016) 180-190.
16. P. Sobieszuk, A. Zamojska-Jaroszewicz, Ł. Makowski, J Power Sources 371 (2017) 178-187.
17. E. Casula, D. Molognoni, E. Borràs, M. Mascia, J Power Sources 487 (2021) 229432.
18. S. Mateo, M. Mascia, F.J. Fernandez-Morales, M.A. Rodrigo, M. Di Lorenzo, Electrochim Acta 297 (2019) 297-306.
19. A. Kato Marcus, C.I. Torres, B.E. Rittmann, Biotechnol BioEng 98 (2007) 1171-1182.
20. R.P. Pinto, B. Srinivasan, M.F. Manuel, B. Tartakovsky, Bioresource Technol 101 (2010) 5256-5265.
21. S. Gadkari, S. Gu, J. Sadhukhan, J Power Sources 441 (2019) 227145.
22. E. Casula, B. Kim, H. Chesson, M. Di Lorenzo, M. Mascia, Electrochim Acta 368 (2021) 137568.
23. M. Quaglio, G. Massaglia, N. Vasile, V. Margaria, A. Chiodoni, G.P. Salvador, S.L. Marasso, M. Cocuzza, G. Saracco, F.C. Pirri, Int J Hydrogen Energy 44 (2019) 4533-4542.

Versatile Bioelectrochemical system for heavy metals removal

Martí Aliaguilla[1,*], *Daniele* Molognoni[1], *Pau* Bosch-Jimenez[1], *Eduard* Borràs[1]

[1]Leitat technological centre, Carrer Innovació 2, Terrassa 08225 (Catalunya, Spain)

Abstract. Industrial activity has resulted in heavy metals anthropogenic contamination of groundwater, especially in industrial or mining areas. Bioelectrochemical systems (BES) can be used for metals removal and recovery from aqueous solutions. In the framework of GREENER project, double-chamber BES have been adopted to treat groundwater from industrial sites containing copper, nickel and zinc (Cu, Ni and Zn), among other contaminants. Two operation modes, (i) short-circuited microbial fuel cell (MFC), and (ii) power supply driven microbial electrolysis cell (MEC, poisoning the cathode at -0.4 V vs. Ag/AgCl), were studied for metals removal at lab-scale. Two control reactors were run to evaluate metals adsorption on cathodes and membranes, and the effect of anolyte composition. Synthetic water containing different concentrations of Cu, Ni and Zn were treated, and metals removal pathways were studied. MEC and MFC performed similarly and the highest removal efficiencies were 97.1±3.6%, 50.7±6% and 74,5% for Cu, Ni and Zn respectively, from initial concentrations in the range of 1.1-1.5 mM.

1 Introduction

Heavy metals contamination in groundwaters, especially in industrial or mining areas, is a global concern for environment and human health. It is mandatory to answer this situation by stopping the anthropogenic contamination but also developing new cost-effective and low energy-demand techniques to treat already contaminated aquifers. Bioelectrochemical systems (BES) are within the promising technologies to tackle the challenge. BES technologies are capable to remove (and recover) metals from aqueous streams, reducing the energy and reagents consumption compared to traditional remediation processes [1].

Different bioelectrochemical reactor architectures have been described in literature, to this purpose. Double-chamber reactors with abiotic cathodes have been used to remove and recovery a wide range of different target metals ([2], [3] [4]).

Abiotic cathode removal strategies are mainly based on three pathways: (i) direct electrochemical reduction (DR) of ionic metals such as Cu(II), Pb(II), Hg(II) or Cd (II), which is the most widely reported removal pathway in BES; (ii) indirect by-product precipitation (IBP) where the cathodic reduction by-products such as OH^-, H_2O_2, and sulphide are the responsible of metal precipitation as in [5] and [6]; (iii) metal ion migration, where the electrons are the driving force for metallic ions movement through the ion exchange membrane. Thus, metallic ions can be separated from the polluted stream and later recovered by direct reduction or precipitation like in [2]. One important limitation of DR, from the water treatment point of view, is the low reduction potential of some metallic ions what could result in a higher energetic cost of the treatment. For this reason, to design an approach capable to efficiently combine the explained removal pathways could led to a sustainable integrated solution.

In BES, the cathode architecture and operation (together with the catholyte composition) defines the reduction reactions. An air-cathode reduces atmospheric oxygen to water, consuming protons from the solution, i.e., basifying the catholyte. Thus, the use of an air-cathode under specific operational conditions could lead to the removal of metals by both DR and IBP.

This work aims to study the removal of copper, nickel and zinc from groundwaters by using a double-chamber, air-cathode BES reactor that pretend to take benefit of DR and IBP simultaneously to find an efficient and low-energy method for groundwater treatment.

2 Materials & Methods

2.1 Experimental Setup

Six double chamber reactors were designed and constructed. Anionic exchange membranes (AMI-7001, Membrane International) were placed between anodic and cathodic chambers. Planar anodes were made of 25 cm^2 of battery grade carbon felt (Sigracell® KFD2.5, SGL Carbon GmbH, Meitingen, Germany). The cathodes material was unidirectional carbon fiber non-crimp fabric (Sigratex® C U200, SGL Technologies GmbH, Meitingen, Germany) with 2 mg/cm^2 of PMF-011904 catalyst from Pajarito Powder with 25cm^2 of surface. Tyvek® textile (Dupont) was placed on the external side of cathodes acting as water impermeable layer and air diffusion membrane. Stainless-steel current collectors

* Corresponding author: maliaguilla@leitat.org

were used in both anodes and cathodes, to ensure a uniform electron harvesting and distribution. The anodes' inoculation was done in single chamber reactors with three electrodes configuration, applying different potential steps in several cycles from -0.050 to -0.350 V vs Ag/AgCl. The biomass used for the inoculation was a mixed culture coming from the outflow of an operating MFC. During the inoculation reactors were fed with acetate based mineral media (ABMM) containing 2.5g /L of $NaCH_3COO$, 8.3g/L of $NaHCO_3$, 128mg/L of K_2HPO_4, 49.5mg/L of NH_4Cl, 15.3mg/L of Mg_2SO_4, 13.6 mg/L of $CaCl_2$, trace elements and Wolfe vitamins.

2.2 Experimental design and operation

Reactors were operated in batch recirculating the electrolytes to external buffer tanks. Thus, 0.5L ABBM were used as anolyte in metals removal experiments. The catholyte was 1L of 1.1 mM $CuSO_4(H_2O)_5$ solution in the first bench of experiments, 1L of 1.1 mM of $NiSO_4(H_2O)_6$ solution in the second and 1L of 1.6 mM of $ZnSO_4(H_2O)_7$ solution in the third bench of experiments.

In metals removal experiments, the reactors were operated in replicate: two control reactors, two MFCs operated under short-circuit condition (E_{cell}=0V) and two MECs, poising the cathode at -0.4V vs Ag/AgCl. The control reactors were abiotic and fed with two different anolytes: ABMM (OCV_Ac) and NaCl solution at the same conductivity of ABMM. The electric data were collected by means of a VMP3 potentiostat (BioLogic).

2.3 Analysis and Calculations

For the anolytes, liquid samples were taken at the beginning and the end of the experiment. The pH and electric conductivity were measured with HQ40D multi-meter (Hach Lange) with probes intelicall® PHC101 and intelicall® CDC401 respectively. Chemimcal Oxygen Demand (COD) was analysed using Hach Lange LCK kits. For the catholytes, liquid samples were taken at each sampling time and metals concentration determination was done by ICP-MS analysis (ICPMS Agilent 7500). Also, electric conductivity and pH were monitored every 24h.

The removal efficiency of metals and was calculated with the following equation, where C_0 represents the initial and C_F the final metal concentration.

$$R_{EF} = \frac{C_0 - C_F}{C_0}$$

Removal rate (RR) represent the removal per time and catholyte volume unit, and is calculated as follows:

$$R_R = \frac{\Delta C_M x V}{Q \cdot t}$$

Where ΔC_M is the change of metal concentration in the catholytes ($g \cdot m^{-3}$); V, the catholyte volume in m^3; representing, the product ΔC_MxV, the mass of metals removed; Q operating in batch mode is equivalent to the catholyte volume in m^3; and t, the experiment time in days.

Current density (j) represents the electron flowrate, i.e., averaged current (I in Amperes), per electrode surface unit (A in m^2) and is calculated with the following equation:

$$J = \frac{I}{A_m}$$

The Cathode coulombic efficiency (CE_{cat}) represents the fraction of electrons, i.e., the circulated charge, eventually involved in the metal removal and is calculated as follows:

$$CE_{cat} = \frac{F \times n \times V_{cat} \times \Delta C_M}{M_M \times \int Idt}$$

Where F is Faraday constant, n is the molar number of electrons required for metal reduction ($mol \cdot mol^{-1}$), V_{CAT} is the catholyte volume (L), ΔC_M is the change of metal concentration in the catholytes ($g \cdot L^{-1}$), M_M is the molar mass of the removed metal ion ($g\ mol^{-1}$).

3 Results

3.1 Copper removal experiments

Bioelectrochemical reactors successfully treated synthetic water containing 1.1mM Cu, as can be observed in Figure 1. At 24h, MEC removed 97.1 ±3.6% of Cu and MFC, a 88.1 ± 5.5%, with Cu removal rates of 64.1 ± 2.1 $g \cdot d^{-1} \cdot m^{-3}$ and 53.3 ± 0.35 $g \cdot d^{-1} \cdot m^{-3}$, respectively. These Cu removal rates are below the average values of previous studies, as 218 $g \cdot d^{-1} \cdot m^{-3}$, 504 $g \cdot d^{-1} \cdot m^{-3}$ and 7.92 $g \cdot d^{-1} \cdot m^{-3}$ were achieved in [7], [8] and [2], respectively. Regarding the current densities, MEC reactors reached 0.109±0.038 A/m^2 while MFC ones 0.078±0.027 A/m^2, with CE_{cat} of 45 ± 16% and 58 ± 24% respectively. Therefore, from an efficiency and sustainability point of view MFC operation would be more appropriate for copper removal. At 24 h, the control OCV-Ac removed 45% of copper with a removal rate of 12 $g\text{-}Cu \cdot m^{-3} \cdot d^{-1}$, while the control OCV-Na had no quantifiable removal. After 48 h of treatment, the control OCV-Ac removed almost the same copper than BES reactors (95% OCV-Na vs 98 - >99% BES). OCV-Na removal was still unquantifiable. This demonstrates that the composition of the anolyte is playing a role in the copper removal, in the absence of electrical field. Anions present in the ABMM anolyte could cross the anionic exchange membrane, by concentration gradient, having as a result the copper removal by precipitate formation. In bioelectroactive reactors, both MEC and MFC, the electrical field generated between the electrodes led to an ion migration force opposed to the concentration gradient. Thus, the effect of the anolyte is expected to be lower in the bioelectrochemical reactors, but it was not quantified.

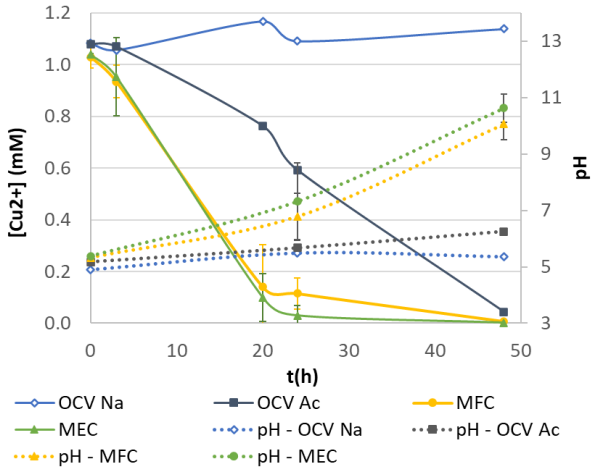

Fig. 1. Copper concentration and pH evolution of catholyte, under different operation modes

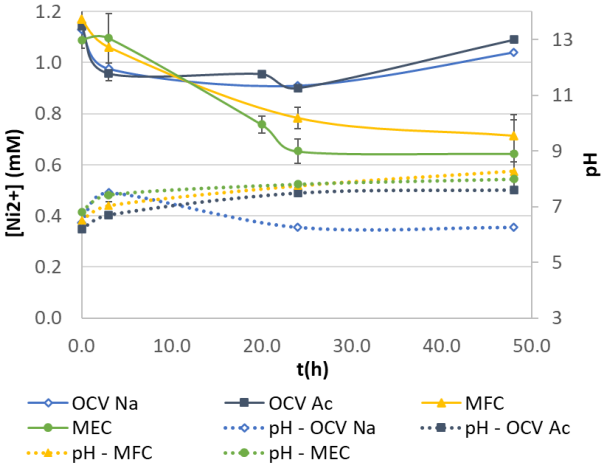

Fig. 2. Nickel concentration and pH evolution of catholyte, under different operation modes

Figure 1 also shows that pH increased during the whole experiment, in all cases except in OCV-NaCl. Moreover, in MEC and MFC reactors, after the removal of most of copper, the pH curve slope increased, indicating higher hydroxide ions production in the catholyte. This can be attributed to the lack of electrons consumption in the direct reduction of copper resulting in a higher rate of catholyte basifying reactions, and, to the lack of OH^- ions consumption to form metallic hydroxide precipitates. During the experiments, precipitate formation was observed in the buffer tanks of MEC, MFC and in lower measure in OCV-Na. After the experiments the reactors were opened, and precipitates were observed also in the cathode chamber and in the AEM surface. Cu^0 colored deposits were observed in the cathode surface of MEC and MFC reactors, suggesting that the copper removal was carried out by both DR and IBP, as it was expected given the high standard reduction potential of copper (0.06V vs Ag/AgCl).

3.2 Nickel removal experiments

Figure 2 shows similar trend between MEC and MFC in terms of nickel removal. MFC had higher averaged value of removal efficiency but there is no statistical significance due to the variations among replicates. After 48h of operation, facing an initial nickel concentration of 1.1mM, bioelectrochemical reactors achieved a removal efficiency of 41.0 ± 12.3% in MEC and 50.7 ± 6.23% in MFC removing 13.1 ± 3.5 $g \cdot d^{-1} \cdot m^{-3}$ and 17.4 ± 1.6 $g \cdot d^{-1} \cdot m^{-3}$ of Ni, respectively. The nickel concertation curves of OCV-Ac and OCV-Na reactors had more similar behaviour in this case. After 48h the removal efficiencies accounted for 4.6% and 7.9%, respectively, indicating that the effect of the anolyte in Ni removal was significantly lower compared to Cu removal experiments.

The current density was 0.08 ± 0.03A/m^2 in MEC and 0.04±0.01 A/m^2 in MFC and the CE_{cat} was 30.7±20.82% and 73.87±19.5% respectively. With less than 1/3 of electric conductivity compared with copper experiments, current density decreased 26% in MEC and 48% in MFC. However, MEC CE_{cat} was 15% lower in nickel experiments, but MFC CE_{cat} was 15% higher. The lower current density, in this case, could have an effect in the Ni removal efficiency and Ni removal rate, as the current density is the main driving force for the metal's removal in all expected pathways. Hence, it also had an effect in the pH evolution, compared with copper experiments. The final pH was 7.99±0.17, 8.27±0.34, 7.61 and 6.26 in MEC, MFC, OCV-Ac and OCV-Na, respectively. In this case, the BES (MEC and MFC) and the OCV-Ac control pH curves had a behaviour more similar between them than in the copper case, pointing that most of the hydroxide molecules produced in the reduction reactions were consumed in the nickel precipitation, still after 48h of operation.

Previous studies have reported the bioelectrochemical removal of nickel by direct reduction in MEC with similar initial concentration achieving a removal efficiency around 99% with a Ni removal rate of 118.8 $g \cdot d^{-1} \cdot m^{-3}$ [4]. Also, higher Ni concentration in acid mine drainage synthetic solution have been reported using BES in MEC and achieving an 87% of removal efficiency with a Ni removal rate of 282g-$d^{-1} \cdot m^{-3}$ [9]. Even though no previous works have been found for nickel removal by precipitation in the catholyte using BES, the bioelectrochemical induced precipitation has been described before as a potential mechanism for Nickel separation in BES [10]. $Ni(OH)_2$ or $NiCO_3$ precipitation needs a high pH to take place [10] and this could be more challenging for BES compared to the removal of other metals by precipitation. However, after the experiments the reactors were opened and green and white precipitates were observed in the cathode surface and in the cathode chamber of both MEC and MFC, but not in OCV-Na nor OCV-Ac cases. That fact suggests that the local pH

conditions of the catholyte surroundings were high enough to result in the Ni removal by precipitation.

3.3 Zinc removal experiments

Figure 3 shows that n can be removed using BES. After 48h, MEC achieved a removal efficiency of 73.17% and MFC 74,49% with Zn removal rates of 40.25 $g \cdot d^{-1} \cdot m^{-3}$ and 39.03 $g \cdot d^{-1} \cdot m^{-3}$, respectively. The current density achieved was 0.032 A/m^2 in MEC and 0.031 A/m^2 in MFC with CE_{cat} of 169.7% and 174.2%. This indicates that at least 31.1% (MEC) and 30.6% (MFC) of Zn removal efficiency was not driven by electrochemical processes. These results match with the removal efficiency achieved by the control OCV-Ac which accounted for 28.7% with a Zn removal rate of 15 $g \cdot d^{-1} \cdot m^{-3}$ suggesting that the effect of the anolyte in the zinc removal efficiency could be the same under the effect of the electrical field. The control OCV-Na positioned the zinc removal efficiency baseline due to the reactor design and materials at 10.24%.

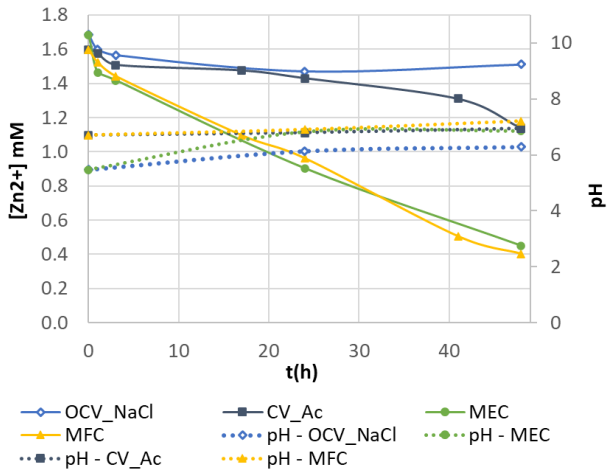

Fig. 3. Zinc concentration and pH evolution of catholyte, under different operation modes.

At the end of the experiments, when the reactors were opened, white precipitate was observed in the cathode surface and settled in the cathodic chamber. Also, a small amount of precipitate was observed in the bottom of the buffer tanks and in the AEM surface, like in copper removal experiments, where OCV-Ac had a role too in the metal's removal. Hence, IBP is a functional removal pathway for Zn with the adopted integrated metals removal approach, at least, when the initial pH is higher than 5.5.

BES for DR of Zn has been reported before in MEC as in [3] were 71.9% of removal efficiency was reached treating synthetic water with an initial concentration of 285 mg/L of Zn. Few works have reported before the bioelectrochemical zinc removal with O_2 reduction as the main cathodic reaction. In [11] 96% of removal efficiency was reached in MFC reactors treating synthetic water with a removal rate of 135.5 $g\text{-}Zn \cdot d^{-1} \cdot m^{-3}$. In this case the removal of controls was 52%. Other studies like [12] reported also relevant Zn removal in control reactors (52.1%). It is worth mentioning that the membranes used as chambers separator, in both cases, were anionic exchange membranes and the anolytes were mineral mediums containing acetate, like in the present study. These high removal in controls results would coincide with the anolyte effect demonstrated in the present work.

4 Conclusions

The experiments carried out demonstrated that the tested reactor design is capable to remove Cu, Ni and Zn under different electrochemical operation modes. Depending on the operational conditions, different removal rates could be achieved. DR evidence was found only in Cu removal experiments, while IBP evidences were found in all experiments (Cu, Ni and Zn) confirming the versatility of the bioelectrochemical reactor. It is worth to mention that in most of the experiments there was no significant differences in terms of removal efficiency between MEC an MFC. As MFC is spontaneous and produces electricity, instead of consuming it like MEC, it become an interesting low-energy operation mode for metals removal under the studied operational conditions. Moreover, MFC, which in most of cases reached lower current density, usually led to higher CE_{cat}. Thus, a higher current density does not necessary imply a greater removal efficiency. This suggests that other limitations would be acting as the concentration gradient between the electrode surface and the bulk solution (e.g. mass transport limitations). The effect of the composition of the anolyte has been demonstrated to be relevant in terms of metals removal performance when an anionic exchange membrane is separating electrolytesin BES reactors.

These first trials proved the feasibility of the reactors to remove metals from polluted waters and paved the way for the next step, treating polluted groundwaters from industrial sites.

5 References

[1] Dominguez-Benetton, X., Varia, J.C., Pozo, G., Modin, O., Ter Heijne, A., Fransaer, J., Rabaey, K., 2018. Metal recovery by microbial electro-metallurgy. Progress in Materials Science **94**, 435–461. https://doi.org/10.1016/j.pmatsci.2018.01.007

[2] Jiang, Q., Song, X., Liu, J., Shao, Y., He, W., Feng, Y., 2020. In-situ enrichment and removal of Cu(II) and Cd(II) from low-strength wastewater by a novel microbial metals enrichment and recovery cell (MMERC). Journal of Power Sources **451**, 227627. https://doi.org/10.1016/j.jpowsour.2019.227627

[3] Modin, O., Fuad, N., Rauch, S., 2017. Microbial electrochemical recovery of zinc. Electrochimica Acta

248, 58–63. https://doi.org/10.1016/j.electacta.2017.07.120
[4] Qin, B., Luo, H., Liu, G., Zhang, R., Chen, S., Hou, Y., Luo, Y., 2012. Nickel ion removal from wastewater using the microbial electrolysis cell. Bioresource Technology **121**, 458–461. https://doi.org/10.1016/j.biortech.2012.06.068
[5] Song, X., Yang, W., Lin, Z., Huang, L., Quan, X., 2019. A loop of catholyte effluent feeding to bioanodes for complete recovery of Sn, Fe, and Cu with simultaneous treatment of the co-present organics in microbial fuel cells. Science of The Total Environment **651**, 1698–1708.
[6] Wang, Q., Huang, L., Quan, X., Zhao, Q., 2017. Preferable utilization of in-situ produced H2O2 rather than externally added for efficient deposition of tungsten and molybdenum in microbial fuel cells. Electrochimica Acta **247**, 880–890. https://doi.org/10.1016/j.electacta.2017.07.079
[7] Heijne, A.T., Liu, F., Weijden, R. van der, Weijma, J., Buisman, C.J.N., Hamelers, H.V.M., 2010. Copper Recovery Combined with Electricity Production in a Microbial Fuel Cell. Environ. Sci. Technol. **44**, 4376–4381. https://doi.org/10.1021/es100526g
[8] Luo, H., Qin, B., Liu, G., Zhang, R., Tang, Y., Hou, Y., 2015. Selective recovery of Cu2+ and Ni2+ from wastewater using bioelectrochemical system. Front. Environ. Sci. Eng. **9**, 522–527. https://doi.org/10.1007/s11783-014-0633-5
[9] Luo, H., Liu, G., Zhang, R., Bai, Y., Fu, S., Hou, Y., 2014. Heavy metal recovery combined with H2 production from artificial acid mine drainage using the microbial electrolysis cell. Journal of Hazardous Materials **270**, 153–159.
[10] Hui Guo, Y.K., 2019. Mechanisms of Heavy Metal Separation in Bioelectrochemical Systems and Relative Significance of Precipitation, in: Microbial Electrochemical Technologies. pp. 128–144.
[11] Lim, S.S., Fontmorin, J.-M., Pham, H.T., Milner, E., Abdul, P.M., Scott, K., Head, I., Yu, E.H., 2021. Zinc removal and recovery from industrial wastewater with a microbial fuel cell: Experimental investigation and theoretical prediction. Science of The Total Environment **776**, 145934. https://doi.org/10.1016/j.scitotenv.2021.145934
[12] Wang, X., Li, J., Wang, Z., Tursun, H., Liu, R., Gao, Y., Li, Y., 2016. Increasing the recovery of heavy metal ions using two microbial fuel cells operating in parallel with no power output. Environ Sci Pollut Res **23**, 20368–20377. https://doi.org/10.1007/s11356-016-7045-y

Towards cost-effective soil microbial fuel cell designs

Jakub Dziegielowski [1,2] and Mirella Di Lorenzo [1,2,]*

[1] Department of Chemical Engineering, University of Bath, BA2 7AY, Bath, United Kingdom
[2] Centre for Biosensors, Bioelectronics and Biodevices, University of Bath, BA2 7AY, Bath, United Kingdom

Abstract. Soil microbial fuel cell (SMFC) is a carbon-neutral energy harvesting technology that exploits the use of electroactive bacteria naturally present in soil to directly generate electricity from organic compounds. Given the simplicity of the system design, SMFCs have great potential to be used for decentralised solutions, especially in areas where access to conventional energy sources is limited. Yet, the high cost to power ratio severely limits the translation of this technology into the market. With the aim of reducing the capital cost, in this study we explore the effect of decreasing the amounts of current collector (CC) on the performance. The results demonstrate that increasing the amount of current collector per surface area of the electrode is not a feasible way of enhancing power densities, as to increase the performance by 20% and 35%, the amount of current collector would have to be increased by 150% and 300%, respectively. This highlights the importance of economic evaluations when optimising the design of a SMFC.

1 Introduction

Biomass energy has been fuelling the world for thousands of years, far long before the industrial revolution [1]. Since then, it has, however, been replaced by fossil fuels, an unsustainable resource, responsible for a lot of the damage to our climate. there is, therefore, the urgent need for alternative sources that can meet our energy demands with clean, safe and renewable solutions.

Microbial fuel cell (MFC) is an emerging technology, with the potential of becoming one of the future sources of sustainable energy. In MFCs waste is converted into electrons and protons via metabolic pathways of electroactive microbes, which release the charged particles during oxidation of organic compounds [2,3]. By introducing electrodes and a proton exchange membrane, the electrons can be captured and driven through an external circuit, generating green electricity.

This unique feature eliminates the technology's heavy reliance on environmental conditions, which remains a huge hindrance to success of other renewable energy technologies, and brings a circular economy element to the table, by making further use of waste. For this reason, the majority of MFC applications has targeted the wastewater treatment sector, where these devices are being used for the removal of organics, generating electricity on top [2].

Nonetheless, the technology is currently faced with numerous challenges related to its successful scale-up studies, with cost being the primary one [4-6]. The capital costs of scaled-up systems can range from USD 735 m^{-3} to USD 36,000 m^{-3}. Electrode and membrane materials have been the main contributors to the high price of MFCs [5,7]. In addition, operational costs such as pumping air and effluent, as well as mixing, have also been identified as detrimental to the energy usage and to the overall operational costs of the system [8]. For this reason, among the various types of MFC, soil microbial fuel cells (SMFCs) pose an interesting alternative.

SMFCs are characterized by an extremely simple design, with no need for fuel pumping and/or electrolyte replacement. Minimum maintenance is required since the organic matter is naturally provided in the soil by plants and/or decomposing matter, thus allowing long term operations [9]. The soil acts as a membrane, allowing membrane-less operation and the geometries and materials implemented are a lot cheaper compared to what used in conventional (i.e., liquid) MFCs [5].

Nonetheless, due to the relatively low power obtained from SMFCs, cost remains a hinderance in commercialising the technology. Our previous work, on a flat plate SMFC design [10], revealed that the cost of a single SMFC device is approximately £2. Titanium wire, used as the current collector (CC), was identified as responsible for up 50% of the total price. Furthermore, weaving the wire into the electrode resulted in the most time-consuming task in the fuel cell set-up. Therefore, with the aim of reducing the price and improving the practicality of SMFC installation, in this study we investigate the effect that a reduced amount of CC has on the overall performance of a flat SMFC.

2 Materials and Methods

* Corresponding author: m.di.lorenzo@bath.ac.uk

2.1 Materials

All reagents used were purchased of analytical grade from Alfa Aesar and Sigma-Aldrich, unless otherwise specified, and used without further purification. The soil was collected from the campus area of the University of Bath, and its characteristics are summarised in Table 1.

Table 1. Physiochemical properties of the soil

Parameter	
pH	6.5
Conductivity	195.2 ± 23.3 μS cm^{-1}
Moisture content	53%
Organic matter content	17.4 ± 1.5%

2.2 SMFC design and operation

Three flat plate, membrane-less air-cathode SMFC designs were constructed, as depicted in Figure 1A. Each design comprised of two graphite felt electrodes (anode and cathode), separated from each other by 4 cm with nylon screws. The designs differed from each other by the amount of CC used. The CC, titanium wire (0.25 mm diameter), was weaved through the electrodes, with High CC, Medium CC and Low CC having respectively 32 cm, 20 cm and 8 cm of wire, as depicted in Fig.1B-D. Each design had three replicates to evaluate reliability and reproducibility of the data obtained.

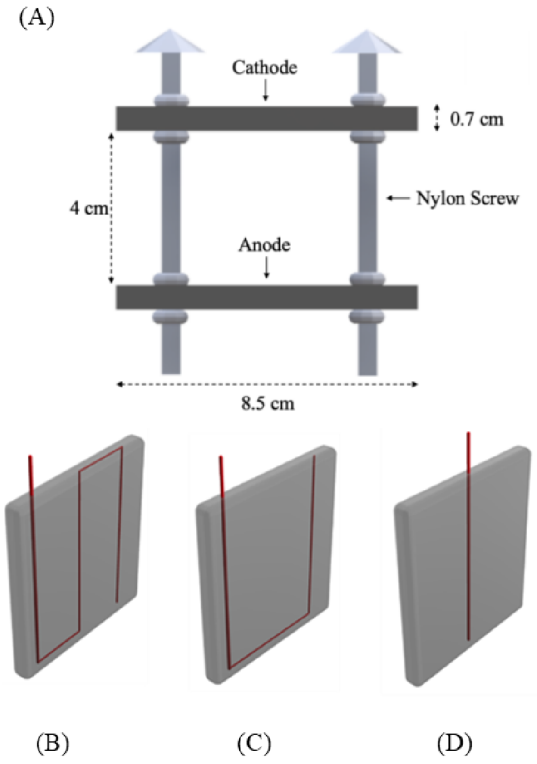

Fig.1: (A) Flat plate SMFC design; (B) High CC; (C) Medium CC; (D) Low CC

The SMFC reactors were fit into PVC containers (32 x 24 x 10 cm) filled up with soil that was kept moisturised with tap water. The anodes were buried inside the soil and the cathodes were exposed to air, as shown in Fig.2. The fuel cells were connected to an external resistance of 510 Ω and to a data acquisition system (DAQ6510, Keithley). Polarization tests were performed by connecting the SMFCs to a resistance box (Cropico RM6 Decade) and varying the applied resistance. Ohm's law (I=E/Rext) was used to calculate the current (I) corresponding to each externa resistance (Rext).

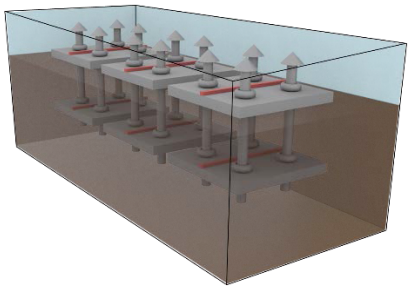

Fig.2: Example schematic of the experimental set-up showing 3 replicates of the Low CC SMFCs.

3 Results

3.1 SMFC Performance

The performance of the SMFCs was assessed and compared according to enrichment curves and individual electrode potentials. As shown in Fig.2A, the enrichment process clearly highlights the differences between the three configurations. The High CC SMFCs were the quickest to enrich, reaching a steady state of approximately 200 mV after 20 days, followed by Medium CC (23 days) and Low CC (25 days). This difference is further reflected in the anode potentials, as shown in Fig.2B. The increased contact area between the current collector and the graphite felt, improves the electrode's electrical conductivity, widening the electrochemical signal reception from a larger part of electrode surface and lowering the charge transfer resistance. This strategy in turn facilitates the electron transfer and is likely the reason why a more rapid drop in the anode potential is observed [11]. Nonetheless, eventually all the configurations reached a comparable anode potential of -400 mV vs. Ag/AgCl after 23 days, suggesting that the electrodes are inoculated with similar strains of electroactive species [12].

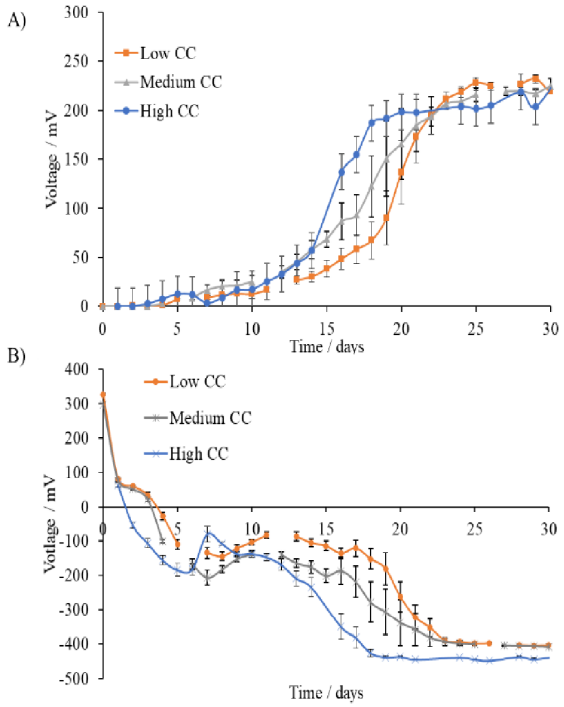

Fig.3: (A) Enrichment curves; (B) Anode electrode potentials vs. Ag/AgCl reference electrode. Data is the average of 3 replicates, with error bars referring to the standard error.

Following the completion of the enrichment, a series of polarisation tests were conducted, to understand how much power can be generated by each SMFC. As the amount of titanium wire increased from 8 cm to 20 cm and then 32 cm, the amount of power produced increased by 20% and 35% respectively (Fig.3). This result is attributed to the lower charge transfer resistance in High CC and Medium CC, due to a better contact of the CC with the electrode with respect to Low CC [11,12]. Capacitor characteristics of the electrodes could also play an important role. Paitier A. et al demonstrated that by increasing the amount of current collector, the capacitance of a microbial fuel cell increases leading to greater power densities during charge/discharge cycles [13].

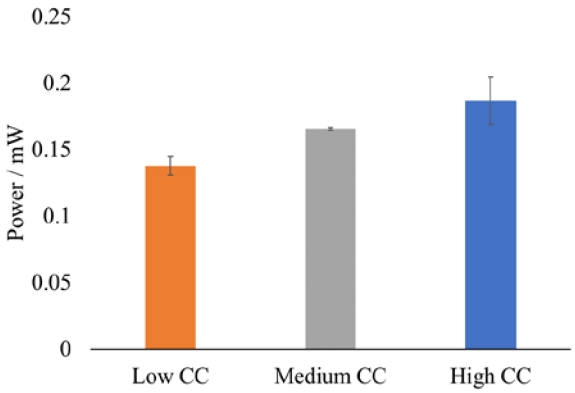

Fig.4: Bar chart of power generated by the different SMFCs. Error bars refer to three replicates.

3.2 Cost Analysis

Although increasing the amount of titanium wire has shown to enhance the power density of the flat-plate SMFC, such strategy remains questionable, due to the associated costs. At the current price point of titanium wire (£2.5 per meter), increasing its amount by 150% and 300% would lead to a proportional increase in materials costs, yet only a 20% and 35% increase in performance, respectively. This relationship can be better described by representing it as cost per Watt of power, derived as shown by eq. 1-2.

$$Cost\ of\ CC\ used\ (£) = Amount\ of\ CC\ (m) * £2.5/m \quad (1)$$

$$Cost\ per\ Watt = \frac{Cost\ of\ CC\ used\ (£)}{Power\ (mW)} * 1000\frac{mW}{W} \quad (2)$$

Considering that the power can be linearly scaled up by stacking the electrodes together [10], one can compare the cost per Watt with the amount of wire used in a single electrode (Fig.5). A scaled-up system comprising of Low CC SMFCs, would cost approximately £1450 per watt of power, whereas systems with Medium CC and High CC SMFCs would £3,020 and £4,280, respectively. This result reflects the disproportionality between the performance increase and the increase in material cost, proving Low CC to be most economically viable.

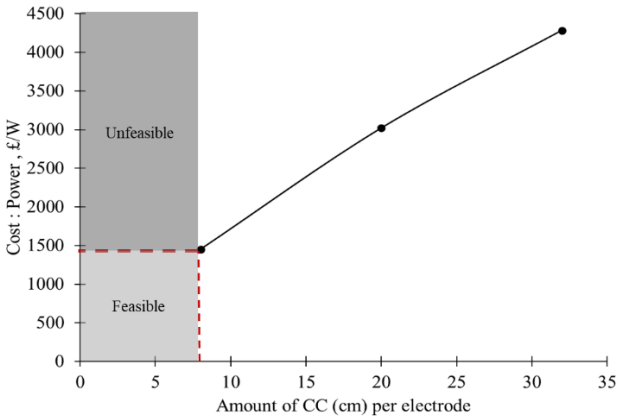

Fig.5: Relationship between the flat-plate SMFC cost per Watt of power (£/W) vs. the amount of current collector used.

To further optimise the cost of the SMFC device, a lower amount of titanium wire per electrode should be tested. In Figure 5, two regions have been identified, labelled as: Feasible and Unfeasible. The dotted red line represents the limit dictated by the Low CC configuration, of £1,450 per Watt, which indirectly sets the minimum power requirements to be generated by SMFCs with even less CC. For example, according to equations 1-2, a single SMFC with 4 cm of CC in each electrode should generate a minimum of 0.07 mW, for the cost per Watt to be roughly £1,450. For an output power lower than this limit, the overall device cost would exceed the threshold, thus entering in a so-called unfeasible region. If the SMFC generates more than 0.07 mW, the cost per Watt would accordingly drop, thus making the SMFC design more economically feasible.

4 Conclusions

Soil microbial fuel cells have great potential as energy harvesting technology for remote areas with minimum maintenance requirements. Cost-effective design solutions can markedly enhance scalability and implementation of this technology.

In this study, SMFC designs with different amounts of titanium, used as the current collector, were investigated. We showed that, while higher amounts of titanium wire would enhance the SMFC performance, the percentage increase in the power output is significantly smaller than the percentage increase in the material cost. From an economics standpoint, a large-scale system comprising of Low CC SMFCs would be significantly cheaper than Medium CC and High CC SMFC systems. Additional work is required to identify a point at which reducing the amount of CC begins to hinder the economics, in order to find the right balance between power output improvement and cost.

This project was funded by the UK Research England, under the Global Challenges Research Fund (GCFR), and is part of the project GREENER funded by the European Union's Horizon 2020 research and innovation programme under the grant agreement No 826312

References

[1] Lewis, C.W., Biomass (1981), **1**, pp.,5–15.
[2] Logan, B.E. Microbial Fuel Cells; John Wiley & Sons: Hoboken, NJ, USA, (2008).
[3] Dewan, A., Beyenal, H., Lewandowski, Z. Environ. Sci. Technol. (2008), **42**, pp. 7643–7648.
[4] Liang, P., Duan, R., Jiang, Y., Zhang, X., Qiu, Y., Huang, X. Water Res. (2018), **141**, pp. 1–8.
[5] Ge, Z., He, Z. Environ. Sci. Water Res. Technol. (2016), **2**, pp. 274–281.
[6] Wang, A.-J., Wang, H.-C., Cheng, H.-Y., Liang, B., Liu, W.-Z., Han, J.-L., Zhang, B., Wang, S.-S., Environ. Sci. Ecotechnol. (2020).
[7] Rozendal, R.A., Hamelers, H.V., Rabaey, K., Keller, J., Buisman, C.J. Trends Biotechnol. (2008), **26**, pp. 450–459. [CrossRef]
[8] Tommasi, T., Lombardelli, G. J. Power Sources (2017), **356**, 438–447.
[9] S. Maddalwar, K. Nayak, M. Kumar, L. Singh. Bioresour. Technol., **341**, (2021)
[10] J. Dziegielowski, B. Metcalfe, P. Guzman, C.A. Martinez-Huitle, A. Gotrayeb, J. Wenk, M. Di Lorenzo, Appl Energy, **278** (2020)
[11] Malvankar, N. S., et al., Applied and Environmental Microbiology 78, 16, (2012)
[12] Commault, A. S., et al., Bioresour.Technol.139,226-234 (2013)
[13] Paitier, A., et al., Biotechnology. INSA Lyon, (2017)

The different behaviour of *Thermotoga neapolitana* in the anodic and cathodic compartment of a bioelectrochemical system

Pierangela Cristiani[1*], *Laura* Malavola[2], *Silvia* Franz[3], *Massimiliano* Bestetti[2], *Giuliana* D'Ippolito[3], *Nunzia* Esercizio[3], Mariamichela Lanzilli[3], Angelo Fontana[3]

[1]Ricerca sul Sistema Energetico - RSE S.p.A., 20134 Milano, Italy
[2]Politecnico di Milano, Department of Chemistrty Materials and Chemical Engineering, 20131 Milano, Italy
[3]Institute of Biomolecular Chemsitry (ICB), National Research Council (CNR), Pozzuoli, 80078, Na, Italy

Abstract. *Thermotoga neapolitana* is a hyperthermophilic bacterium that can metabolize glucose and several organic wastes in hydrogen and lactate at a temperature of 80°C. Their high performance in producing hydrogen at so high a temperature as 80°C suggests a potential energy application of them where hydrogen is an important element of the process. In this view, experimentation of a *T.neapolitana* strain is carried out in double-chamber electrochemical systems. The aim is to explore the interaction of these bacteria with the anode and the cathode, stressing their capability to survive in presence of a polarized electrode which can drastically change the pH of the media. A culture enriched of 5 g/L of glucose, under CO2 pressure (80 °C) was used to fill both the anodic and cathodic compartments of the electrochemical system, applying a voltage of 1.5 V between the anode and the cathode. The test lasted ten days. Results clearly indicate that bacteria colonize both electrodes, but the glucose metabolism is completely inhibited in the anodic compartments. On the contrary, metabolism is stimulated in the cathodic compartment. Bacteria are alive on the electrodes in the pH interval of 3 - 9.

1 Introduction

The use of single strains in hyperthermophilic conditions is a possible innovative way to make electrochemical systems simpler to manage and efficient. Hyperthermophilic microorganisms are characterized by an extremely productive metabolism that allows them to survive in challenging conditions for life, such as a temperature of 80°C up to more than 100°C, and under a scarcity of energetic organic nutrients. *Thermotoga neapolitana* is a microorganism that produces hydrogen and lactate by metabolizing glucose at a temperature of 80°C. Previous works, [1, 2] found a great affinity of T. neapolitana to form biofilm on different materials. In principle, they can be exploited to catalyze the hydrogen evolution reaction in a microbial electrolytic cell, with the aim to improve the overall yield of the system, as recently attempted [3]. Nevertheless, the previous tests were performed in single-chamber electrochemical systems, using an alternated polarization between electrodes [2]. Those conditions could not allow differentiating the behaviour of the bacterial colony on anode or cathode. Aiming at exploring separately the interaction of the hyperthermophilic bacteria with the anode and the cathode electrodes, new tests of a *T. neapolitana* strain in double-chamber electrochemical systems have been carried out. Carbon cloth (CC) and Boron Doped Diamond (BDD) are used for electrodes. A culture enriched of 5 g/L of glucose, under CO_2 pressure, at 80 °C, is used to fill both the anodic and cathodic compartments of the electrochemical system, applying a voltage of 1.7 V (or more) between the anode and the cathode in two tests that lasted nine days each one. The metabolism of glucose to acetic and lactic acid was monitored by periodic chemical analyses in the first test. The pH of the solution of the anodic and cathodic compartments was measured in the second test, where higher polarization and BDD anodes were used to monitor the resistance of bacteria to the pH variation induced by the electrochemical reactions. The results are here reported and discussed.

2 Materials & Methods

2.1.1 Media and Inoculum

250 ml of culture broth ATCC 1977 for anaerobic microorganisms, with trace element solution (DSM medium 141) was used as media. 5 g/L of glucose (28 mM) was added before the inoculation. A stream of CO_2 gas was sparged in the culture to create anaerobic condition until the resazurin in the solution was colourless, as described for previous tests [3]. An aliquot of 7 ml of pre-acclimate batch culture (at 80 °C for 1 day) was inoculated in each electrochemical bioreactor at the beginning of the test. All transfers and sampling of cultures were performed with sterile syringes and needles. *Thermotoga neapolitana* subsp. capnolactica (DSM33033), a lab strain derived from *T. neapolitana* DSMZ 4359T [2] was tested.

2.1.2 Set-up and operational conditions

The double chamber electrochemical reactor was set up using a small glass bottle of 250 ml connected by the polymeric membrane Nafion 417. The setup of electrochemical bioreactors is shown in Figure 1.

Two electrochemical reactors were first operated with identical electrodes (anode and cathode) of carbon cloth, in duplicate. A subsequent test was carried out using Boron Doped Diamond instead of carbon cloth at the anode, to limit the current and the consequent pH decay during the polarization. Only pH variation was measured during the second test (not the metabolism's products).

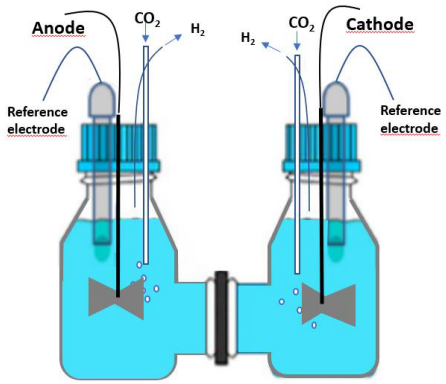

Figure 1. Schematic of double chamber electrochemical reactor used for the tests.

In the first test that lasted eight days, the same polarization of 1.7 ± 0.1 V was applied between the anode and cathode of each polarized electrochemical bioreactor.
4 more bottles were operated in the same condition of the reactor semi-cells, as follows: 2 bottles without electrodes (REF1, REF2), and 2 bottles containing one carbon cloth electrode (unpolarized) operating at the open circuit potential (OCP1, OCP2).
In a second test, the polarization was increased for A3, A4 to 6.5 V, to stimulate overproduction of hydrogen and also inverted for BDD1, BDD2 and C5, C6, to very if bacteria survived in that extreme polarization condition.
In Table 1 a summary of the tested conditions is reported.

Table 1. Experimental condition and labels.

First test	Material	Label
Reactors without electrodes	-	REF1 REF2
Unpolarized electrodes (OCP)	CC	OCP1 OCP2
Cell voltage 1.7 ± 0.1 V	Anode: CC Cathode: CC	A1, A2 C1, C2
Second test	**Material**	**Label**
Reactors without electrodes	-	REF3 REF4
Cell voltage 1.7 ± 0.1 V (6 days) + 6.5 V (2 days)	Anode: CC Cathode: CC	A3, A4 C3, C4
Cell voltage 1. 7 ± 0.1 V (6days) Inverted polarization (4days)	Anode: BDD Cathode: CC	BDD1 BDD2 C5, C6

Each electrochemical reactor is equipped with an Ag/AgCl (saturated) reference electrode (AMEL Srl, Italy, mod. 373/12). The bottle without electrodes is equipped with a red-ox (platinum combined electrode (AMEL Srl, Italy) for measuring the redox potential of the solution. A tube sealed on the cap and with the tip immersed down in the solution allows the sparging of CO2 gas into the solution at the beginning of the test and after the sampling/refilling operations in all the chambers/bottles. A syringe needle is used for the collection of produced gas, connected to a gas bag of 1 L.
0.25 L of culture medium ATCC 1977 was introduced in every reactor. T. neapolitana was inoculated at the start of the test.
The operation for each test lasted nine days, counted from the inoculum of bacteria.

2.1.3 Electrodes

Carbon cloth (CC, SAATI, Italy) is used for setting up the cathodes; the anodic materials were: i) the same CC as used for the anodes or ii) Boron Doped Diamond BDD (BDD/Nb, by NeoCoat®, Netherlands).
A carbon cloth piece of 10 × 10 cm is wrapped around and tightly fixed to a titanium wire to assemble CC electrodes. They geometrically occupy almost 1/5 of the liquid volume when immersed almost completely in the reactor (Fig1).
BDD electrodes is a plate of 5 x 2.5 x 0.1 cm. The BDD plate was suspended in the solution by a titanium collector.

2.1.4 Chemical analyses

To quantify the level of the metabolic activity, the medium was sampled during the experiment through sterile syringes and analysed.
The generated H_2 in the bioreactors was collected in a gasbag of 3L. Samples from the gasbags were collected by a gas-tight syringe at room temperature before the analysis. H_2 analysis was performed by gas-chromatography using a gas-chromatographer (Focus GC, Thermo Scientific) equipped with a thermo-conductivity detector (TCD) and fitted with a 3 m molecular sieve column (Hayesep Q). Nitrogen was used as gas carrier.
Acetic acid (AA), lactic acid (LA), and glucose concentration was determined by the dinitrosalicylic acid method calibrated on a standard solution of 1 g/L glucose [4]. Organic acids were measured by ERETIC 1H NMR as described by Nuzzo et al. (2019). All experiments were performed on a Bruker DRX 600 spectrometer equipped with an inverse TCI CryoProbe. Peak integration, ERETIC measurements, and spectrum calibration were obtained by the specific subroutines of Bruker Top-Spin 3.1 program.

2.1.4 SEM observations

A scanning Electron Microscopy SEM (Zeiss EVO 50, Carl Zeiss Jena GmbH, Jena, Germany) was used to observe the surface of electrodes. Samples were gentle rinsed with water after collection and dried in hover for 15 minutes. Then stored at 4°C until the analyses.

Observations were carried out at high vacuum and high voltage (20keV).

3 RESULTS AND DISCUSSION

The glucose metabolism during 9 days of testing is monitored during the first test. The hydrogen production and pH variation, under different polarization conditions, are estimated with the second test.
BDD, which is known to control the formation of reactive oxidant substances (ROS) at potential >1 V [4] is used in comparison with carbon cloth anodes in the second test.

3.1 First test: glucose metabolism

The results of the chemical analyses (glucose, acetate, lactate, and alanine concentrations) sampled after 30h from each cell are reported in Tables 2-4. A decrease in glucose concentration with a subsequent increase in acetate indicates that bacteria are carrying out their normal glucose metabolism. The data after 30 h indicated that the glucose metabolism in the cathodic compartment started first and overperformed vs the other condition, in the order: Cathode > Reference > OCP > Anode.

Table 2. Data of the glucose consumption, during the first test. Information on H_2 and Alanine production is also reported.

	Glucose consume (G)		**H_2**		**Alanine (Ala)**	
	mM	dev	mM	dev	mM	dev
Cathode	23.67	0.47	88*	-	1.81	0.00
REF	8.41	2.23	88*	-	1.29	0.04
OCP	2.28	3.03	-	-	0.61	0.87
Anode	1.84	1.35	-	-	1.02	0.11

*Estimated value, as gasbag exploded because an overproduction of H_2 during the night.

Table 3. Data of the acid production from the glucose metabolism during the first test.

	Acetic acid (AA)		**Lactic acid (LA)**		**LA/AA**	
	mM	dev	mM	dev	mM	dev
Cathode	25.91	0.60	3.99	0.82	0.15	0.04
REF	8.12	1.75	2.86	0.94	0.35	0.04
OCP	4.40	5.16	1.11	1.34	0.24	0.03
Anode	0.67	0.05	0.39	0.04	0.59	0.02

Table 4. Ratios of the glucose metabolism for acetic acid, lactic acid, and alanine.

	AA/G		**LA/G**		**Ala/G**	
	mM	dev	mM	dev	mM	dev
Cathode	1.09	0.00	0.17	0.04	0.08	0.00
REF	0.97	0.05	0.34	0.02	0.16	0.04
OCP	3.71	2.67	0.83	0.52	0.14	0.20
Anode	0.51	0.40	0.30	0.24	0.79	0.64

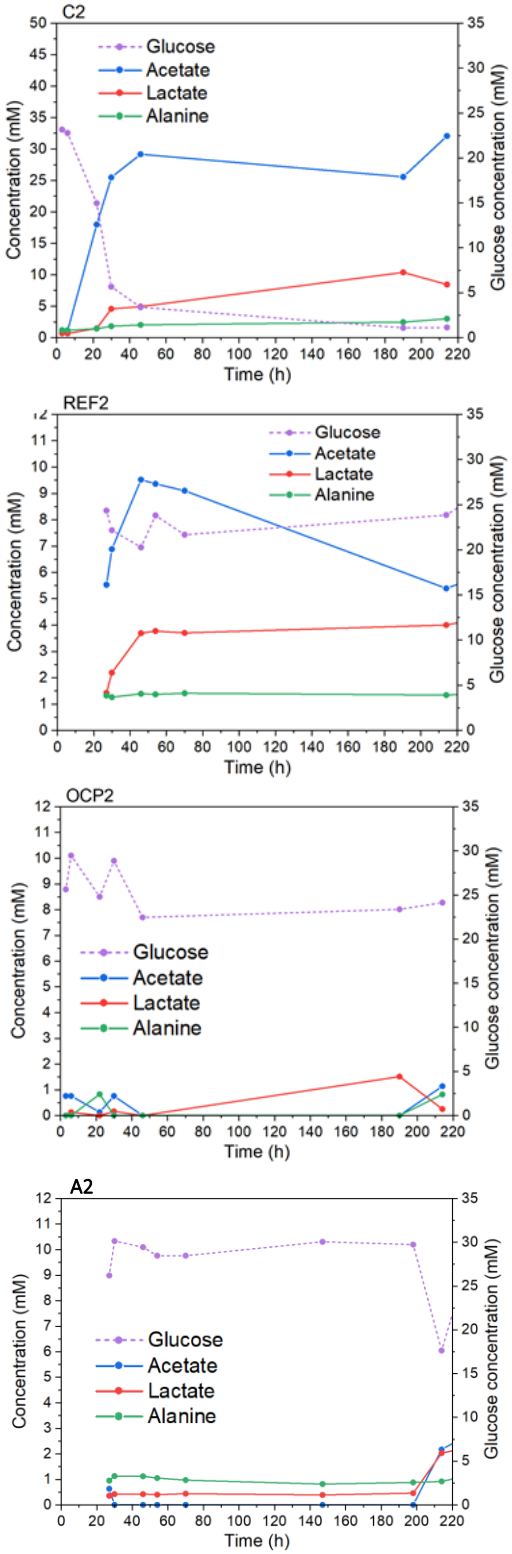

Figure 2. Trends of the metabolism products and glucose consumption in C2, REF2, OCP2, and A2, during the first test.

The trends of the chemical product and glucose consumption for the total first test (220 h, 9 days), in one of the replicates of all compartment types, are reported in the graphics of Figure 2 (replicates are similar). After 190 hours, the solution in the compartment was refilled with an aliquot of fresh media enriched with glucose. This

caused little increase in glucose concentration in compartment OCP2 and REF2.
The solution in the cathodic reactors and references become murky during the first 30 h, indicating that bacteria grew in number in the bulk of the medium.
The anodic compartments and the OCP ones, indeed, remained transparent and clear, so we assume that all the bacteria were attached to the electrode in a stasis form (Figure 3). The condition of stasis was broken in OCP cells during the rest of the test as solution went numb, while persisted in the anodic compartments until stress caused by the performing of a strong (4 cycles) of cyclic polarization probably stimulated the detachment of some bacterial cells from the anode, sudden inducing consume of glucose and acids production (Figure 2, A2).

3.1.1 Cathodic chamber

It is clearly observable from Figure 2 that in the semi-reactors where a negative polarization was present the concentration of metabolism products is way more significant than in other cells: indeed, 50 h after the inoculum, the concentration of acetate in C1 and C2 is about 30 mM (lower than 0,5 mM in the anodic compartments and in OCP2, and roughly 10 mM in all other cells).
Moreover, between 50 and 140 h, the concentration of acetate decreases from 30 to 25 mM in cell C2, while the lactate concentration increases by the same amount. This aspect, particularly, deserve more future investigation since it points to a possible induction of the capnophilic lactic fermentation pathway (1) [3,4] as a particularity of the cathodic compartment.

$$CH_3CO_2H + CO_2 + 4H^+ + 4e^- \leftrightarrow 2CH3CH(OH)CO_2 + H^+ + H_2O \quad (1)$$

It is a remarkable result as the same phenomenon was already noticed in previous experimentations with alternated polarized electrodes, where was not possible to address it to the anode or to the cathode specifically.

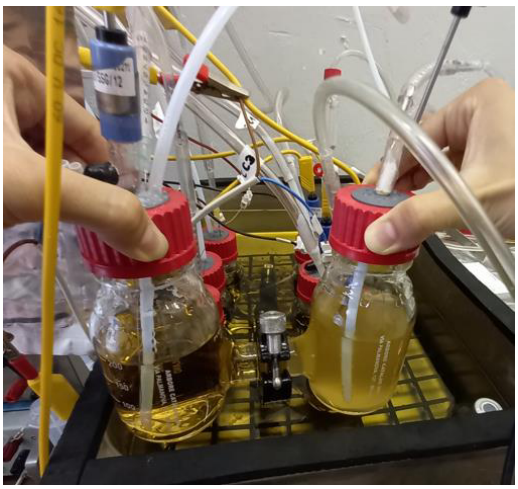

Figure 3. Image of anodic compartment (A2, on the left) and cathodic compartment (C2, on the right) after 30 h of test.

3.1.2 Anodic chamber

In the anodic compartments, the metabolism was almost negligible for all the tests. Nevertheless, a higher concentration of aniline than acetate is here detected, meaning that under anodic conditions the metabolism of microorganisms is stressed.
This fact was remarked performing cyclic voltammetry which strong polarized (with alternated polarity) the anodic electrodes, after refreshing the solution on day 6. After this, in both anodic compartments, the concentration of acetate and lactate suddenly increases, indicating that microorganisms detached from the electrode and actively start the glucose consumption similarly as in the case of the OCP2. This fact is highlighted because it proves that *T. neapolitana* survived, although in a sort of stasis, on the anode.

3.2 Second test: hydrogen production

Unfortunately, it was not possible to estimate the produced hydrogen from the volume of the gasbags (1 L) during the first test. This, because the gas bags connected to C1, C2, REF1, and REF2 broke the day after the inoculum before the sampling. Therefore, it is assumed that the production of gas in those reactors has been massive during night-time. The gasbags connected to the other cells, on the contrary, have shown an unvaried volume. The hydrogen production in these last reactors (anodes and OCPs) was indeed almost negligible during the test.
The produced hydrogen is better measured during the second test, in the cathodic compartments C3 – C6. After 5 days of the second test. The gas measured in the gasbag (1 L) was hydrogen 80 - 95% with 5-15% of CO_2.
The amount of hydrogen produced during the electrochemical process can be calculated from Faraday's law (2).

$$\Delta n_i = \frac{v_i I t}{v_e F} \quad (2)$$

In the equation, Δn_i is the amount of species reacted in the time interval in mol, v_i is the stoichiometric number of the species i, ν_e is the stoichiometric number of electrons implied, I is the current circulation, t is the time interval and F is the Faraday constant (approximatively 96500 C/mol). From this calculation, in the case of reactors with anode and cathodes of CC, the amount of hydrogen electrochemically produced in 5 days, sustained by a continue current of 6.3 mA (1.7 V), is about 14 mmol, corresponding to 316 mL in standard conditions, from the Avogadro's law of gases. This is the electrochemical condition that characterizes the first as well as the second experiment with CC electrodes (the current in the case of BDD anodes was inferior). The gas collected from the gasbags is about 1 L, which ~0.1 L consists of dosed CO_2. Therefore, only a maximum of about 500-600 mL of hydrogen is produced by microorganisms, which corresponds to about 22 mmol in

standard conditions (88 mM). The dosed glucose in 250 mL of solution is ~ 7 mmol. Considering that glucose wouldn't be completely consumed, this estimation agrees with the theoretical molar ratio of H_2/Glucose (4/1) from the Embden–Meyerhoff pathway [5] (2),

$$C_6H_{12}O_6 + 2H_2O \rightarrow 2C_2H_3O_2^- + 2H^+ + 4H_2 + 2\ CO_2 \quad (2)$$

and with a maximum of 3.85 ± 0.07 achieved from previous experiments in bioreactors [6]. It can be consequently concluded that bacteria were productive at best in the cathodic compartments of the tested systems.

3.2.1 pH variation

The pH measured in the different compartments of tested systems during the second test is reported in Figure 4. The pH variation in the references, without electrodes, declined just a little to 5. Similar behaviour has the pH of C5 and C6 coupled to BDD anodes.

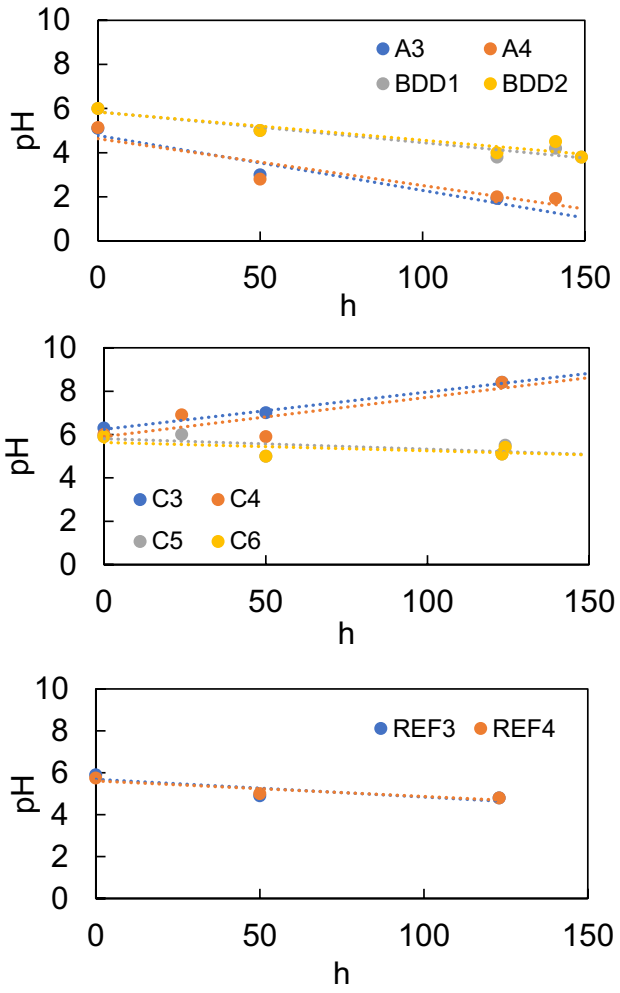

Figure 4. pH variation in the compartments of different bioreactors during the second test (see Table 1).

On the contrary, the pH raised over 9 in the cathodic compartments C3 and C4, and fell down to 2 for A3 and A4, due to the high imposed polarization in those cells. The pH in the anodic compartments of BDD electrodes, only declines to 3.8. To verify if bacteria survived the pH decline in BDD anodes, at the end of the test (150 h) the polarity between the electrodes was reversed. After few hours from the inversion, the solution of the inverted BDD compartment become mouldy, clearly indicating the presence of alive bacteria detaching from the electrode.

3.2.2 SEM images of the electrodes

SEM micrographs of the biofilm on the BDD surface pristine and covered of bacteria at the end of the test is reported in Figure 5a and 5b, respectively.

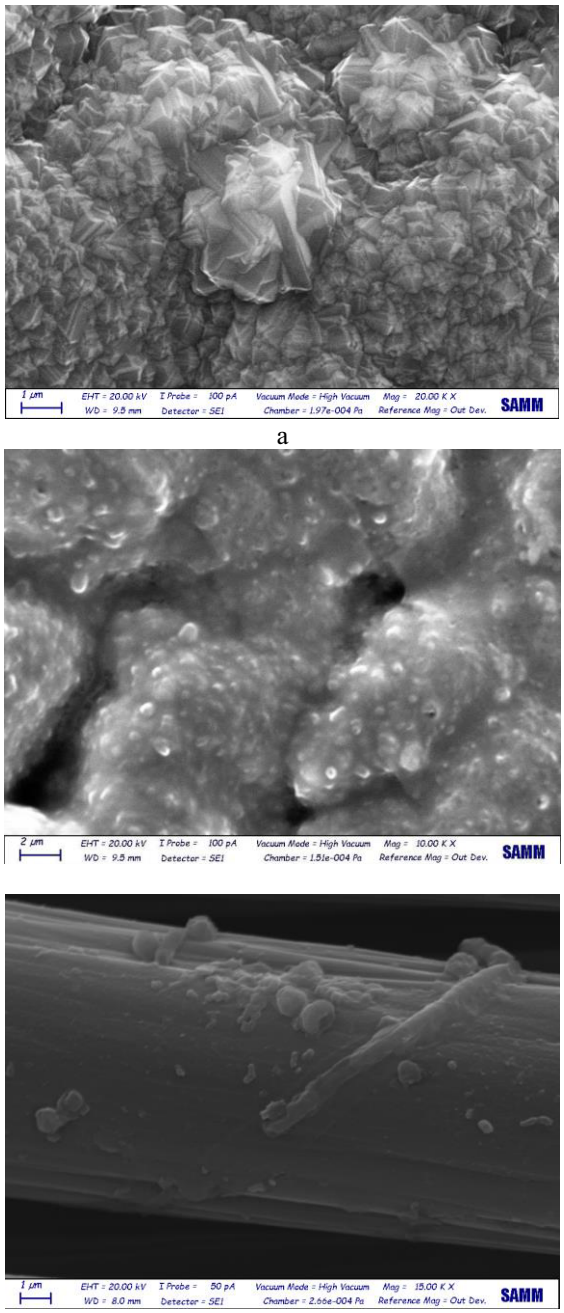

a

Figure 5. Micrographs of the biofilm on: the BDD surface pristine (a), BDD1 covered of bacteria at the end of the test (b) and CC cathode (C3) at the end of the second test.

The two images, in comparison, clearly evidenced that biofilm uniformly cover the surface, hindering the polycrystalline structure of the BDD material. Similarly, carbon cloth anode was covered by an uniform biofilm (data not reported). More uneven biofilm characterized the cathodes, where bacteria (single units or aggregates) are more evident (Figure 5c).

4. Conclusions

The data produced in this work confirmed that it is possible to drive the metabolism of hyperthermophilic bacteria T. neapolitana in polarized bioelectrochemical reactors. *Thermotoga neapolitana* confirms its strong affinity for polarized electrodes as well as for conductive materials such as carbon cloth and BDD.
The bacteria metabolism of glucose is clearly stimulated in the cathodic compartment where electrodes are negatively polarized, while it is almost completely inhibited in the anodic compartments, where a positive polarization attracts bacterial cells, forcing them in a condition of stasis.
On BDD, bacteria create a biofilm where they can survive in spite of a pH degree down to 3.
Further investigations on more cost-effective materials than BDD are proposed, which might mitigate the pH change induced by polarization, such as pH variation, preserving the bacteria vitality, as BDD does.
The enhancement of hydrogen production on cathodes stimulated by hyperthermophilic bacteria such as T. neapolitana, can find several industrial and energy applications. One example of a possible application that deserve to be investigated is the technologies of the power-to-gas, where hydrogen is the primary resource with CO_2 for methane production.

5 Acknowledgements

This work was financed by the Research Fund for the Italian Electrical System in compliance with the Decree of March 19th 2018.

References

1. G., Squadrito, G. d'Ippolito, M. Tucci, M. Vastano, N. Esercizio, A. Sardo, M. Lanzilli, A. Fontana, P. Cristiani. Bioresource Technology, **319** (2021) 124078.

2. 6.G Squadrito, P Cristiani, G d'Ippolito, M Tucci, N Esercizio, A Sardo, M. Lanzilli, A. Fontana. Data in brief **33**, (2020), 3.

3. G. d'Ippolito, L. Dipasquale, F.M. Vella, I. Romano, A. Gambacorta, A. Cutignano, A. Fontana. Int. J. Hydrogen Energy **35**, (2010), 2290.

4. P. Bernfeld, Amylases a and b. Methods Enzymol. **1** (1995), 1995149.

5. RS. Ronimus, HW. Morgan, Archaea, **1,** 3, (2003), 199.

6. N. Pradhan, G. D'Ippolito, L. Dipasquale, G. Esposito, A. Panico, P.N.L. Lens, A. Fontana. Biomass Bioenergy **125**, (2019), 17.

Performance of Reduced Titanium Oxide and Boron Doped Diamond as anodes in hyperthermophilic bioelectrochemical systems

Laura Malavola[1], *Silvia* Franz[1*], *Massimiliano* Bestetti[1], *Nunzia* Esercizio[2], *Giuliana* D'Ippolito[2], *Pierangela* Cristiani[3]

[1]Politecnico di Milano, Department of Chemistry Materials and Chemical Engineering, 20131 Milano, Italy
[2]Institute of Biomolecular Chemistry (ICB), National Research Council (CNR), Pozzuoli, 80078, Na, Italy
[3]Ricerca sul Sistema Energetico - RSE S.p.A., 20134 Milano, Italy

Abstract. This work investigates Reduced Titanium Oxide (RTO) in comparison with Carbon Cloth (CC) and commercial Boron Doped Diamond (BDD) as anodes in hyperthermophilic bioelectrochemical systems operating at 80°C by *Thermotoga neapolitana*. Two samples of RTO were synthesized by plasma electrolytic oxidation (PEO) of titanium plates and subsequent electrochemical reduction. Electrochemical performance of CC, BDD, and RTO are tested by performing cyclic voltammetry in the anodic region (0-1V, 50 mV/s), in abiotic and biotic conditions. The surface of colonized materials is observed by SEM microscopy. Results show that bacteria fast settle on all tested material, significantly affecting their electrochemical conductivity. The integration of voltammetric cycles reveals that biofilm generates capacitive effects on the anodic surfaces, particularly evident in RTO, less in CC and absent in BDD. Charge densities provided by capacitive response of RTO and CC are of the order of 5.58 and 0.77 mC/cm^2, respectively.

1. Introduction

Thermotoga neapolitana are hyperthermophilic anaerobic bacteria, which produce hydrogen and lactate by metabolizing glucose. In principle, they can be exploited to catalyze the hydrogen evolution reaction in a microbial electrolytic cell, improving the overall yield of the system, as recently demonstrated [1]. Thermophilic systems are convenient to enhance the kinetics of the reactions involved and to promote the selectivity of the process, since other microbial strains, including pathogenic ones, are not allowed to grow. Previous works [2] found a great affinity of *T.neapolitana* to form biofilm on different materials. On the other hand, the effect of an oxidative polarization is supposed to excessively disturb the bacteria metabolism, due to the formation of reactive oxygen species (ROS). Furthermore, the electrochemical behavior of the electrode is modified when the bacterial colony attaches to its surface [1]. Carbon cloth is extensively used as electrode material for bioelectrochemical systems, since it provides very high surface area and porosity, as well as good conductivity, mechanical strength and flexibility. Among metals, the most used one is stainless steel, due to lower cost. Also copper and nickel have been investigated, leading to good performances, despite copper and nickel ions can be poisonous for microorganisms [3]. Stainless steel cathodes are commonly used, providing good catalytic effect when a wide surface area is available, but corrosion resistance should be improved [4]. On the other hand, bacteria reveal to be good catalysts for the cathodic reaction, enhancing the hydrogen production rate, without the use of metals [5].
The objective of this work is to investigate the change of the electrochemical properties of different types of anodes, and in particular Reduced titanium oxides (RTO), colonized by *Thermotoga Neapolitana*.
Reduced titanium oxides (RTO) were prepared and tested in comparison with a commercial Boron Doped Diamond (BDD) and carbon cloth (CC) in a double chamber electrochemical system. BDD is an inert anode, that is it does not participate in the reaction. It is a p-doped diamond that exhibits chemical inertness, corrosion resistance, extremely high hardness, thermal conductivity and good charge carrier mobility. With an overpotential of more than 1V for oxygen evolution reaction (OER), it is able to oxidize the majority of organic compounds. Therefore, it allows the formation of oxidants on its surface that in turn will react with the organic matter [6], [7]. The main drawbacks of this material are certainly the high cost and the complex production process, that strongly limit its application on a large scale.
In this work, the performance of the BDD is used as a reference.
Cyclic voltammetry was performed before and after the colonization for each material. After the experiment, the surface of the electrodes was analyzed through SEM imaging. The results are here presented and discussed.

2. MATERIALS AND METHODS

2.1 Reduced Titanium Oxide electrode preparation

The reduced titanium oxides (RTO) were produced in three steps: starting from a c.p. titanium (Ti) plate, titanium dioxide (TiO_2) is obtained by means of plasma electrolytic oxidation (PEO), using two titanium meshes as counter electrodes and 1 L of 1.5 M H_2SO_4 as electrolyte. The operation was performed at 0°C, under a voltage of 150 V and maximum current of 10 A for 5'. Thereafter, the samples were heat treated at 450°C for 3 h

* Corresponding author: Silvia.Franz@polimi.it

in air environment. The material was then reduced through electrochemical treatment: the specimen was exposed at a current density of -10 mA/cm² for 10 min, using a platinum (Pt) wire as counter electrode. The operation was carried out at 0°C in 1 L of 1.5 M H_2SO_4. This procedure, among four different methodologies, proved to lead to the best performing material. The four samples were synthesized through PEO, then post treated as follows:

A: no post treatment
B: thermal post-treatment in air at 450°C for 3h
C: thermal post-treatment as B and subsequent electrochemical reduction (as described)
D: thermal post-treatment and reduction, as C, and, subsequently, de-hydrogenation in Ar environment at 400°C for 1 h.

The samples were characterized by means of cyclic voltammetry CV (potential interval -1.5-3 V vs SCE, scan rate 20 mV/s) and potentiostatic chronoamperometry (2.5 V vs SCE, 20 min), carried out in 0.5 M Na_2SO_4 under dark conditions.

2.2 Media and Inoculum

250 ml of culture broth ATCC 1977 for anaerobic microorganisms, with trace element solution (DSM medium 141) and 5 g/l of glucose was used as media. A stream of CO_2 gas was sparged in the culture to create anaerobic condition, until the resazurin in the solution was colorless, as described for previous tests [1]. An aliquot of 7 ml of pre-acclimate batch culture (at 80 °C for 1 day) were inoculated in each electrochemical bioreactor at the beginning of the test. All transfers and sampling of cultures were performed with sterile syringes and needles.
Thermotoga neapolitana subsp. capnolactica (DSM33033), a lab strain derived from *T. neapolitana* DSMZ 4359T [8] was tested.

2.3 Electrochemical tests

The electrochemical bioreactor was operated applying a voltage between the electrodes of 1.5 ± 0.1 V.
In order to compare the behavior of the anodic materials, four cycles of cyclic voltammetry were performed in the anodic region 0-1 V vs Ag/AgCl (50 mV/s) on the anodes, using a stainless-steel wire as counter electrode inserted in the anodic compartment. Measurements were repeated in abiotic and biotic conditions, 24 h after the inoculum of *T. neapolitana*.
The evaluation of capacitive effects generated by the biofilm has been derived from the integration of the 4th cycle of current density curves. For each material, the charge density exchanged through anodic current in abiotic conditions is subtracted from the charge density exchanged through anodic current in biotic conditions. The difference is compared to the charge density exchanged through cathodic current in biotic conditions, hence the capacitive contribution is estimated.

2.4 SEM analyses

After the test, electrodes were dried 15 minutes in the oven at 80 °C and stored at 4 °C until the analysis at Scanning Electron Microscopy (SEM). The used instrumentation is: Tescan Mira 3 – SEM field emission. The working voltage is 20KV.

3. RESULTS

3.1 Synthesis of reduced titanium oxide

Through PEO a porous TiO_2 coating of about 3 μm is obtained, that appears light grey in color [9].
After the electrochemical reduction step the color shifts to light blue, in agreement with the reduction of band gap [10]. This is a first proof of enhanced conductivity with respect to the stoichiometric TiO_2.
CV and chronoamperometry reveal that the electrochemically reduced sample (C) is the best performing in terms of conductivity (Table 1). Indeed, A and D samples appear too resistive, B appears promising in the CV, but the chronoamperometry shows a low current density at this voltage.
Hereafter, it is decided to proceed with the synthesis of the material C to be used in the bioelectrochemical system.

Table 1. Initial (i_0) and final (i_{1200}) current density and overpotential for OER (η) of the synthesized materials and commercial BDD.

	i_0 (μA/cm²)	i_{1200} (μA/cm²)	η (V)
A	143	7	3-5,8
B	0,9	0,4	1,9-2
C	56	14	1,8-1,9
D	0,9	0,1	4,1-5,5
BDD	1760	487	1,6

3.2 Cyclic voltammetry in culture medium

In figure 1, the 4th cycle obtained in abiotic and biotic medium for each material is shown (1a: CC; 1b: BDD; 1c: RTO).
In the abiotic environment, after the inversion of potential scan, it appears that Ti-based electrodes continue some oxidation reactions forming oxidant species, while boron doped diamond presents a current density almost zero. We assume that the organic species attached to the electrode oxidized themselves and the glucose present in solution.
Carbon cloth electrode shows a wider capacitive effect compared to BDD and RTO. The onset of OER is definitely higher for BDD than for the other materials, as expected.
After the inoculum, instead, the curve obtained on RTO is much wider than for CC, and this behavioral variation is not detected on BDD. The curve is integrated to obtain the charge density: the difference between the resulting

value in biotic and in abiotic medium is an estimation of the capacitive effect arisen by microbial growth. For RTO, a contribution of 5.58 mC/cm^2 is calculated, while on CC it was of 0.77 mC/cm^2. On BDD no capacitive effect is observed, indeed, only an increase in current density is measured.

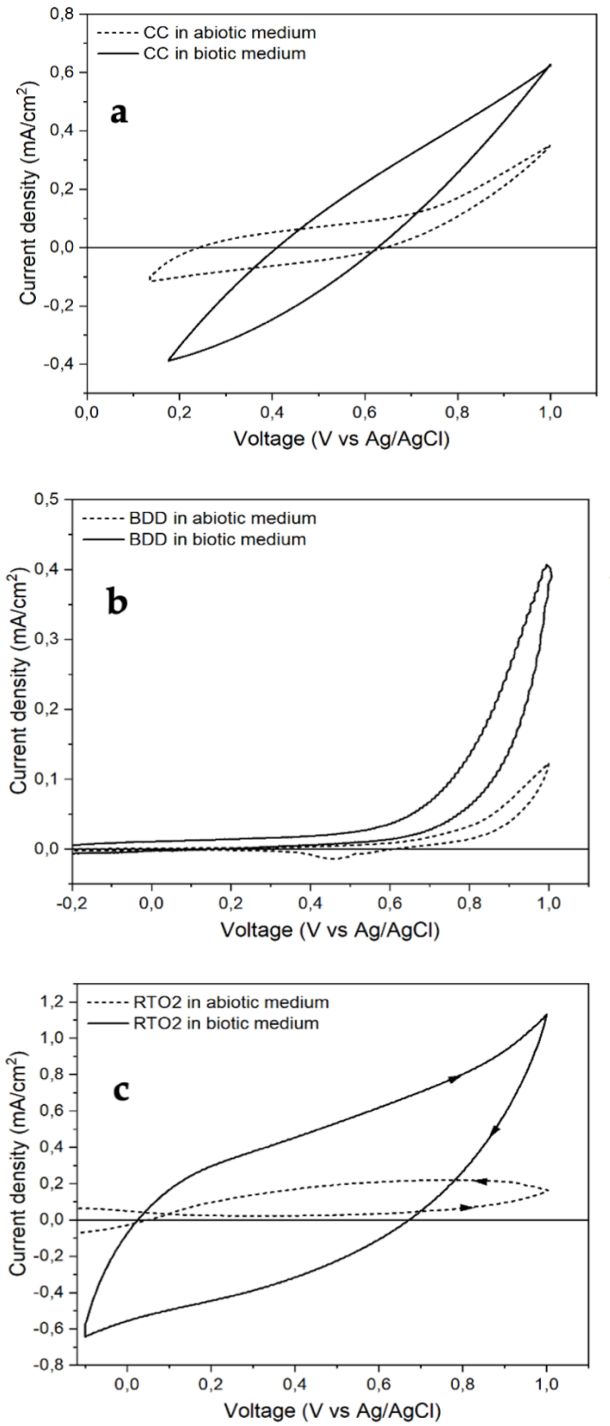

Fig. 1. Graphics of the 4th cycle of voltammetry obtained in abiotic and biotic medium for each material (1a: CC; 1b: BDD; 1c: RTO).

3.3 SEM images of the electrodes

In figure 2 SEM images of CC-PVdF1, C3, C1, RTO2, RTO1, BDD3 and A1 are reported.
SEM images of the cathodes (fig. 2.a-c) reveal that the fibers are covered by biofilm, meaning that bacteria are not only living in the bulk of the solution, but also on the electrode surface. On C3, that was subjected to a high circulating current, bacterial cells are not clearly visible in the biofilm appears different from the normal case: it is assumed that bacteria were damaged by the electrical stress, or that microorganisms detached, leaving biological matter on the surface.
From SEM images of the CC anode (fig. 2.i), it can be noticed that here bacteria have completely colonized the fibers. It is confirmed that *T. neapolitana* live on the anodic surface, thus confirming that their affinity with positive polarization is strong.
SEM images of BDD electrodes (fig. 2.g-h) reveal a uniform layer of biofilm adherent to the surface, and the typical aspect of BDD is hindered.
The inspection over RTO1 and RTO2 revealed that on both electrodes a biofilm is present, hence the edges of the porous structure are surrounded by a film (figure 2.d vs 2.e). Furthermore, in the case of RTO1 the biofilm formed was so thick (≈250 nm) that it cracked, as it can be seen in figure 2.f. Cells were not easy to detect, so that we assume bacteria were damaged by the high current circulating during the experiment.
On RTO2, the porous morphology of reduced TiO2 is observable, covered by a veil of biofilm.

4. DISCUSSION

Cyclic voltammetry in absence of bacteria confirm that BDD outperforms the other materials in terms of overpotential for OER, although RTO shows itself a good response.
The behavior of Reduced Titanium Oxide changes significantly, basing on whether bacteria are present or not: after the inoculum the material shows a capacitive behavior that was not detected before (5.58 mC/cm^2). The capacitive effect is attributed to the biofilm formation, since hyperthermophilic bacteria *T. neapolitana* possess a *toga* rich in ionic species that improve the resistance to high temperatures [11]. The increased number of ionic species can actually enhance the conductivity of a surface, improving the performances of current exchange. The presence of hyperthermophilic *T. neapolitana* is detected by means of SEM on all anodic materials, meaning that in principle all of them are feasible for the application in bioelectrochemical systems, and bacteria are attracted by their positive polarization. However, it is probable that excessively high currents damage the microorganisms on RTO, while the biofilm, rich in ionic species, stays adherent to the negatively polarized surface.

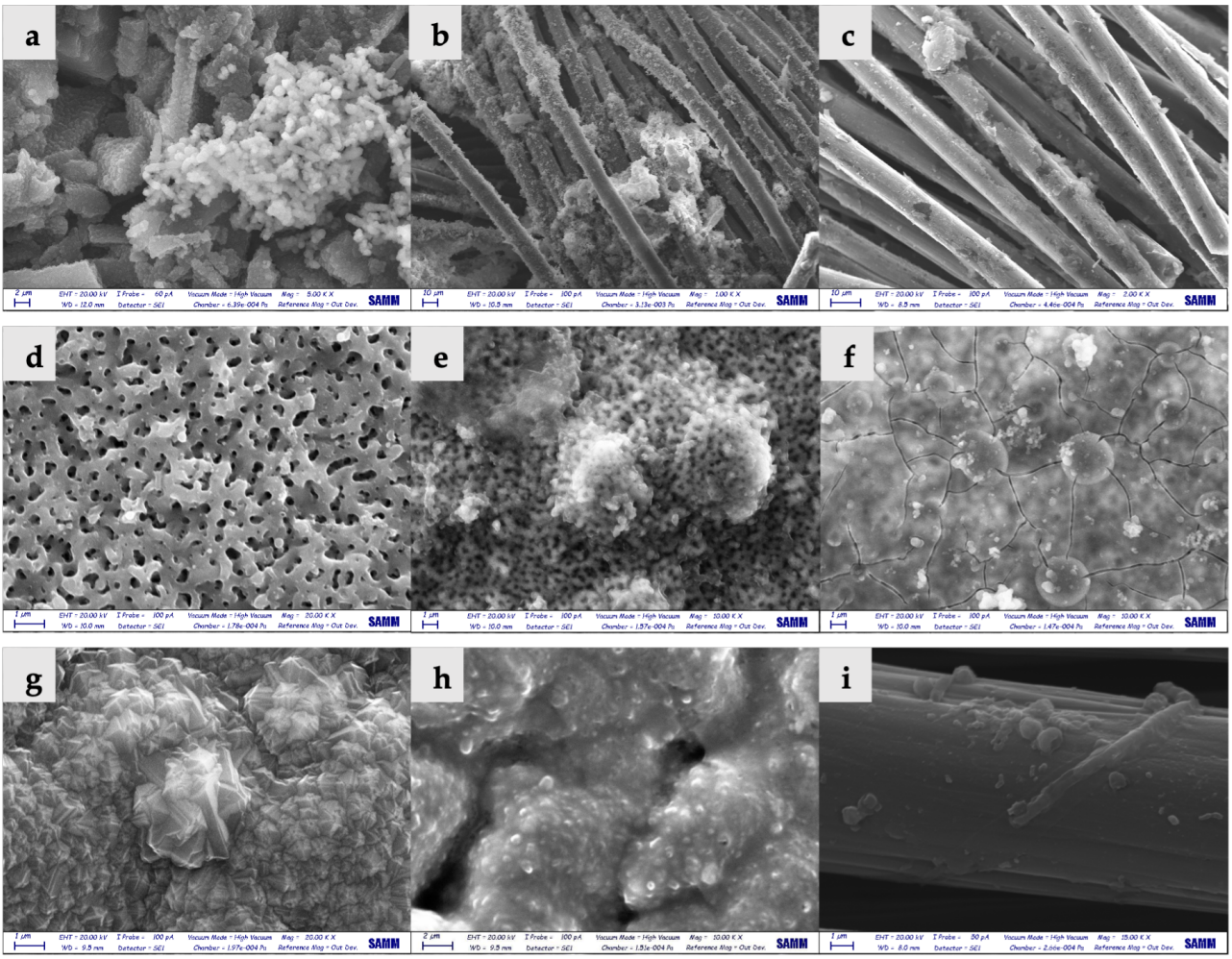

Figure 2. SEM images of cathodes: a) CC-PVdF1, b) C3 and c) C1; SEM images of anodes: d) RTO as prepared, e) RTO2, f) RTO1, g) BDD as purchased, h) BDD3, i) A1 (a fiber of carbon cloth).

Two hypotheses have been proposed on the nature of the capacitive effects of RTO and CC: either bacteria are "oxidized" on the surface, thus damaged by current circulating, or charges are simply transferred through the ionic species present in the biofilm. The latter option would be of great relevance: *Thermotoga neapolitana* strongly interact with the synthesized material, enhancing its conductivity. This would mean that RTO can be investigated more in depth even in single-chamber systems, where the damaging of cells cannot be an acceptable phenomenon. On the other hand, a sort of "cleaning" effect on the colonized electrode might be beneficial if a turn-over of active cells is preferred, for instance, to limit issues related to the mass transfer of nutrients at the interface between solid and biofilm.

The capacitive response recognized on RTO is present with lower effect on CC (0.77 mC/cm^2), and not observed at all on BDD, where only the faradaic effect of the reaction emerges from cyclic voltammetry. The comparison between RTO and CC suggests that the former could be used in high voltage regime, without the risk of corrosion, encountered on the latter.

If, instead, bacteria damaged by current circulating might reach unacceptable level, boron doped diamond would be the best performing material to be implemented in the bioelectrochemical system, due to the absence of capacitive behavior even if colonized by bacteria.

5. CONCLUSIONS

Reduced titanium oxide (RTO) has been synthesized by means of plasma electrolytic oxidation (PEO), thermal treatment and subsequent electrochemical reduction. This procedure is certainly convenient in terms of time and costs.

Comparisons have been made between RTO, BDD and CC using the ATCC 1977 medium as electrolyte.

The best material can be chosen basing on different criteria: BDD is the best performing to maintain anaerobic conditions, moreover it does not involve the biofilm in the exchange of charges with the solution. RTO could be used to enhance conductivity of the system, even further if microorganisms are present on its surface.

The tested materials offer the possibility of choosing the best solution: a material that guarantees the absence of oxygen evolution on the anode while oxidizing the

* Corresponding author: Silvia.Franz@polimi.it

organic matter (BDD), or a material which electrical performance is positively affected by the presence of microorganisms in a high current regime, and that is definitely more economic (RTO).
Further investigations on the used materials and their interaction with hydrogen-producing bacteria *T. neapolitana* are required to elucidate the effect on bacteria metabolism.

Acknowledgements

This work was financed by the Research Fund for the Italian Electrical System in compliance with the Decree of March, 19th 2018.

References

[1] G. d'Ippolito *et al.*, *"Electrostimulation of hyperthermophile Thermotoga neapolitana culture*s," Bioresour. Technol., vol. **319**, p. 124078, Jan. (2021).
[2] G. Squadrito *et al.*, *"Hyperthermiphile biofilms of Thermotoga neapolitana on different materials and electrostimulated: SEM micrographs and chemical data of the glucose fermentation in electrochemical reactors,"* Data Br., vol**. 33**, p. 106403, (2020).
[3] A. Baudler, I. Schmidt, M. Langner, A. Greiner, and U. Schröder, *"Does it have to be carbon? Metal anodes in microbial fuel cells and related bioelectrochemical systems,"* Energy Environ. Sci., vol. **8**, no. 7, (2015).
[4] P. Dange *et al.*, *"Recent developments in microbial electrolysis cell-based biohydrogen production utilizing wastewater as a feedstock,"* Sustainability (Switzerland), vol. **13**, no. 16. (2021).
[5] R. A. Rozendal, A. W. Jeremiasse, H. V. M. Hamelers, and C. J. N. Buisman*, "Hydrogen production with a microbial biocathode,"* Environ. Sci. Technol., vol. **42**, no. 2, (2008).
[6] E. Brillas and C. A. Martínez-Huitle, *Synthetic Diamond Films: Preparation, Electrochemistry, Characterization, and Applications*. (2011).
[7] M. Panizza and G. Cerisola, *"Application of diamond electrodes to electrochemical processes,"* Electrochim. Acta, vol. **51**, no. 2, pp. 191–199, (2005).
[8] L. Dipasquale, G. D'Ippolito, and A. Fontana, *"Capnophilic lactic fermentation and hydrogen synthesis by Thermotoga neapolitana: An unexpected deviation from the dark fermentation model,"* Int. J. Hydrogen Energy, vol. **39**, no. 10, pp. 4857–4862, Mar. (2014).
[9] S. Franz, H. Arab, G. L. Chiarello, M. Bestetti, and E. Selli, *"Single-Step Preparation of Large Area TiO 2 Photoelectrodes for Water Splitting,"* Adv. Energy Mater., vol. **10**, no. 23, p. 2000652, Jun. (2020).
[10] C. Hauf, R. Kniep, and G. Pfaff, *"Preparation of various titanium suboxide powders by reduction of TiO2 with silicon,"* J. Mater. Sci., vol. **34**, no. 6, pp. 1287–1292, (1999).
[11] G. Auerbach *et al.*, *"Lactate dehydrogenase from the hyperthermophilic bacterium Thermotoga maritima: the crystal structure at 2.1 å resolution reveals strategies for intrinsic protein stabilization,"* Structure*,* vol. **6**, no. 6, pp. 769–781, Jun. (1998).

Long-term experience in anoxic wastewater treatment plants of planar MFC with Ce-doped cathodes

Andrea Franzetti[1], *Anna* Espinoza[1], *Enrico* Barontini[1], *Matteo* Tucci[2], *Paolo* Bonelli[3], *Pierangela* Cristiani[4]

[1] Università degli Studi di Milano Bicocca, DISAT, 20100 Milano, Italy
[2] Water Research Institute (IRSA), National Research Council (CNR), Monterotondo (RM), Italy
[3] Ricerca sul Sistema Energetico - RSE S.p.A., 20134 Milano, Italy

Abstract. Planar MFC prototypes were constructed and experimented to operate as sensors of the anoxic condition in a denitrification tank of a wastewater treatment plant in Italy, during different times in 2018 – 2019. Electrodes were differently enriched with carbon paint containing nanotubes and CeO2 nanoparticles. Performances of different electrodes were compared. Results underline critical anoxic conditions in the tank, that caused a very low signal and phenomena of signal reversion during some period of the year. the activity of aerobic microorganisms and protozoa growing and grazing the bacteria on the electrodes strongly influenced the signal of the MFCs. The presence of nanoceria enhanced, for some extent, the MFC signal, both in presence of reversing trends and in absence of these phenomena. In absence of reversing trends, nanoceria enhanced the MFC voltage. Such signal trends from MFCs can give, in real-time, useful information to optimize the purification process without the necessity of frequent biological and chemical analyses.

1 Introduction

Microbial fuel cells (MFCs) have been extensively proposed as a valid alternative to traditional sensors for the wastewater treatment providing a comparatively cheaper and faster solution, showing high linearity, stability, and good reproducibility [1]. In fact, the electro-active microbial biofilm on electrodes can work as a low-cost quantitative biological recognition element, directly converting biochemical energy to bioelectricity, through the metabolic activity in the biofilm. However, long-term testing of microbial fuel cells in wastewater plant were seldom documented.

Previous works documented the performance of planar MFCs, demonstrating their capability of returning a signal related to physical and chemical parameters of the environment, such as light, temperature and dissolved organics [2-4]. In continuity with previous experiences carried out in Italian wastewater plants [2, 3], sets of microbial fuel cells of planar geometry were carried in a different wastewater plant (CAP Group, wastewater plant Bresso, Italy), and using different carbon electrodes for the cathode.

Electrodes were enriched with carbon nanotube, Ce-doped and/or undoped. CeO_2 nanoparticles were added through a Ce doped carbon-based powder, aiming at forcing more aerobic condition on the cathode than in undoped carbon cloth ones, to improve the intensity of the signal. Indeed, previous lab tests with Ce-doped cathodes of air breathing cathodes in single chamber microbial fuel cells demonstrated an improved performance of the electrochemical system [4], induced by the presence of Ceria nanoparticle in the air cathode. The results of monitoring in anoxic tank of the wastewater plant is here compared, aiming at the monitoring of the process during different period of the year.

2 Materials and methods

2.1 Planar MFC setup

Several triplicate sets, composed of three planar MFC prototypes, were constructed and operated in the anoxic tank of the wastewater treatment plant of Bresso-Niguarda (group CAP Amiacque, Milan, IT) during different times in 2018 – 2019 (Figure 1 and Figure 2).

The planar prototype (Fig. 1) consists of two planar electrodes separated by a polypropylene felt of 1 cm, as a sandwich, attached to a structural floating frame. The floating frame, made of polystyrene, ensured to keep a planar structure of electrodes on the water surface. In this way, one of the electrodes faces the air, while the other faces the anoxic water. The porous felt assures the wet condition for both electrodes. The same construction of floating MFCs has already been tested in previous experiments in other wastewater plants [2, 3].

For the first test performed at the beginning of 2018, the submerged anodes and cathodes were made of pristine carbon cloth (CC) (10x10 cm, SAATI P10). The same carbon cloth differently enriched with carbon nanotubes and used for anode of the subsequent tests (2018-2019). Cathodes and CeO_2 nanoparticle were added on the cathodes for those tests. A carbon paint enriched with nanotubes (Vernici Bresciane, Italy) were used to cover a face of the carbon cloth. CeO_2 nanoparticles were spread on the paint. MFC with cathodes characterized by Ce-nanoparticle and carbon nanotubes are labelled cathode Ce-Nt, the other MFCs without nanoceria particles in the cathode are labelled cathodes NT.

The electrodes were connected to an external circuit with 100 Ω load and separated by an insulating polypropylene felt attached to the frame (Figure 1).

The voltage was continuously measured using a multichannel Data Logger (Graphtech midi Logger GL820).

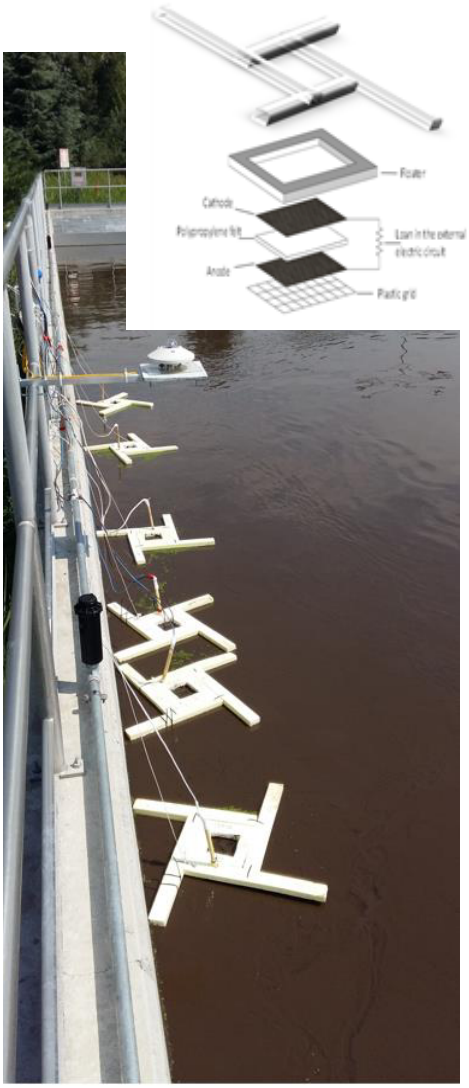

Figure 1. Planar MFCs floating in the anoxic tank of the wastewater plant during the test. The schematic of MFC components is reported right on the top.

2.2 SEM micrography of electrode samples

Electrode samples were collected to analyse the biofilm structure and nanoceria permanence.
First of all, the electrodes were washed in sterile Phosphate Buffered Saline (PBS, 0,1 M, pH 7.4) to remove the non-attached bacterial cells. For biofilm fixation, electrodes were incubated overnight at room temperature in new sterile PBS containing 2% glutaraldehyde.
To achieve dehydration, samples were washed two times in sterile water, sequentially treated with 30, 50, 70 and 96% of ethanol solution baths at 10 minutes intervals and infiltrated with 30, 60 and 100% of HMDS (hexamethyldisilazane). After this, electrode pieces were air dried and finally sputter coated with a thin layer (about 10 nm) of gold to produce a conductive surface. SEM-SE imaging was performed using Zeiss Gemini 500 operating with an acceleration voltage of 5 kV.

3 Results

The average of the voltage of each type of planar MFCs operated at Bresso wastewater plant during different period of time is shown in the graphics of Figure 2.

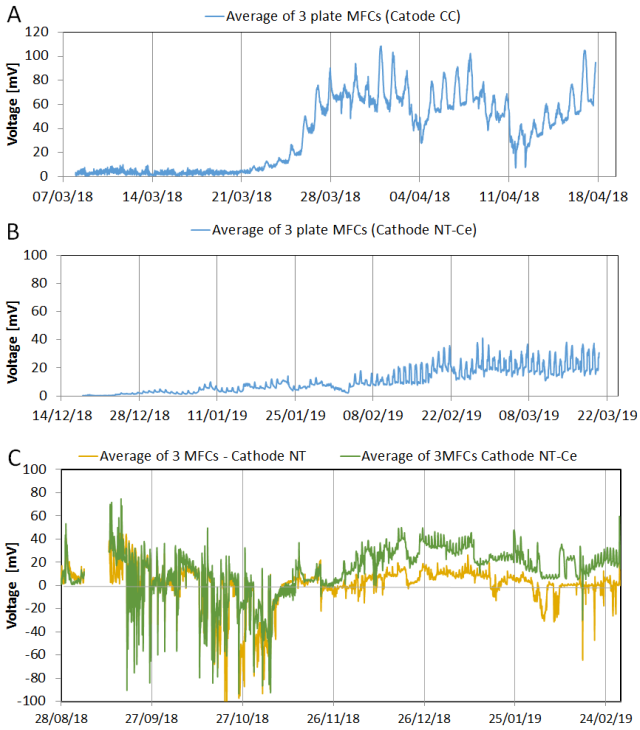

Figure 2. Voltage of planar MFCs (average of three replicates) operated at Bresso wastewater plant. A: anodes and Cathodes of carbon cloth (CC); B: anode of CC and Cathode of CC+NT+Ce; C: anode of CC+NT and cathode in CC+NT or CC+NT+Ce.

Figure 2 shows the signal trends (voltage) of the floating MFCs in the different tested configurations. In the first trial with CC anodes and cathodes made of pristine carbon cloth (Fig. 2A) we observed a typical lag phase of two weeks at the beginning of the test when the bacterial colonization of the electrodes occurred. The signal started to increase after two weeks and was characterized by regular peaks reflecting day and night periods. The dependence of the signal magnitude with temperature could be due to the increased microbial activity at higher temperatures. Conversely, the light effect could be due to the stimulation of oxygen production by phototrophic bacteria, and algae, at the cathode. These signal patterns reveal that the magnitude of the signal could be affected by other variables than the organic load of the water. A similar pattern was observed in the experiments with the cathode functionalized with NT and Ce (Fig 2 B) where a longer lag phase occurred before the signal started to rise. Therefore, the design of this floating biosensor should aim at minimizing the effect of external parameters.

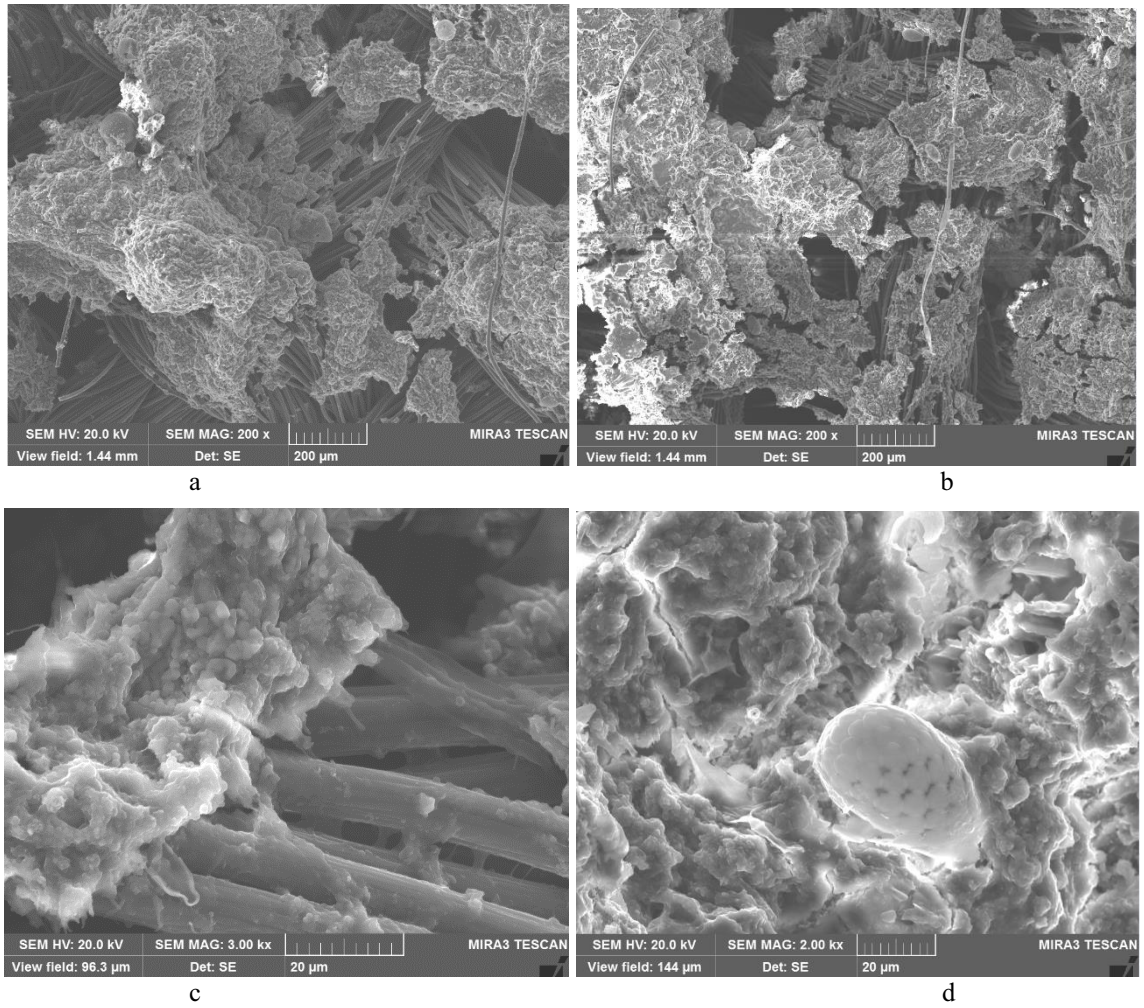

Figure 3. SEM micrographs at differnt magnitudes of biofilm on carbon cloth anodes enriched with carbon paint (CC-NT) (a-b). Details evidencing diatoms are visible in (c) and one protozoa of order *Euglyphida in (d).*

In the cell with the anodes functionalized with NT, particularly in the first part of the test, a significant inversion of the polarization of the electrodes with respect to that expected (Figure 2) was recorded. In other terms, the submerged electrodes acted as the cathode (instead of the anode), receiving the electrons from the air-exposed electrodes. This inversion of polarization documents the presence of oxic conditions in the first layer of the denitrification tank. Indeed, the measured profiles of redox potential and dissolved oxygens (data not reported) indicated that in the first centimeter of the water column oxygen is detectable and redox conditions are positive.

The oxic conditions are also witnessed by the presence of diatoms and amoebae, as the results of SEM analyses (Fig. 3). Particularly, among the visualized amoebae, SEM images allowed identifying some organisms belonging to Order *Euglyphida*, which are known to feed on bacteria. This surely has further reduced the potential electroactive bacterial communities on the submerged electrodes. Conversely, on the air-exposed electrodes, the development of oxygen-consuming bacterial biofilms should enhance anoxic conditions close to the electrode. The condition of anaerobiosis on the cathode was clearly documented in the previous lab works performed with single-chamber MFCs equipped with cathodes of carbon cloth enriched with a microporous layer of carbon powder [5, 6]. Indeed, in other similar lab MFCs tests [4] nanoceria boosted the performance of such cathodes acting as oxygen reservoirs beneath a well-established anaerobic biofilm.

The supposed mechanism of nanoceria was shorting distance between the electrode (electron donor) beneath the biofilm and the final electron acceptor (oxygen) outside the biofilm. Differently, here, the presence of nanoceria could have contributed to impeding the formation of an anaerobic biofilm, supplying further energy (oxygen and electron) to the oxygen-consuming bacteria and algae living on the cathode surface. This hypothesis is supported by the SEM images of cathodes in Figure 4. Observing the surface of the cathode CC-NT in Figure 4a-b, it evidently appears a thick layer of biofilm mixed to the nanotube coating above the carbon cloth base material.

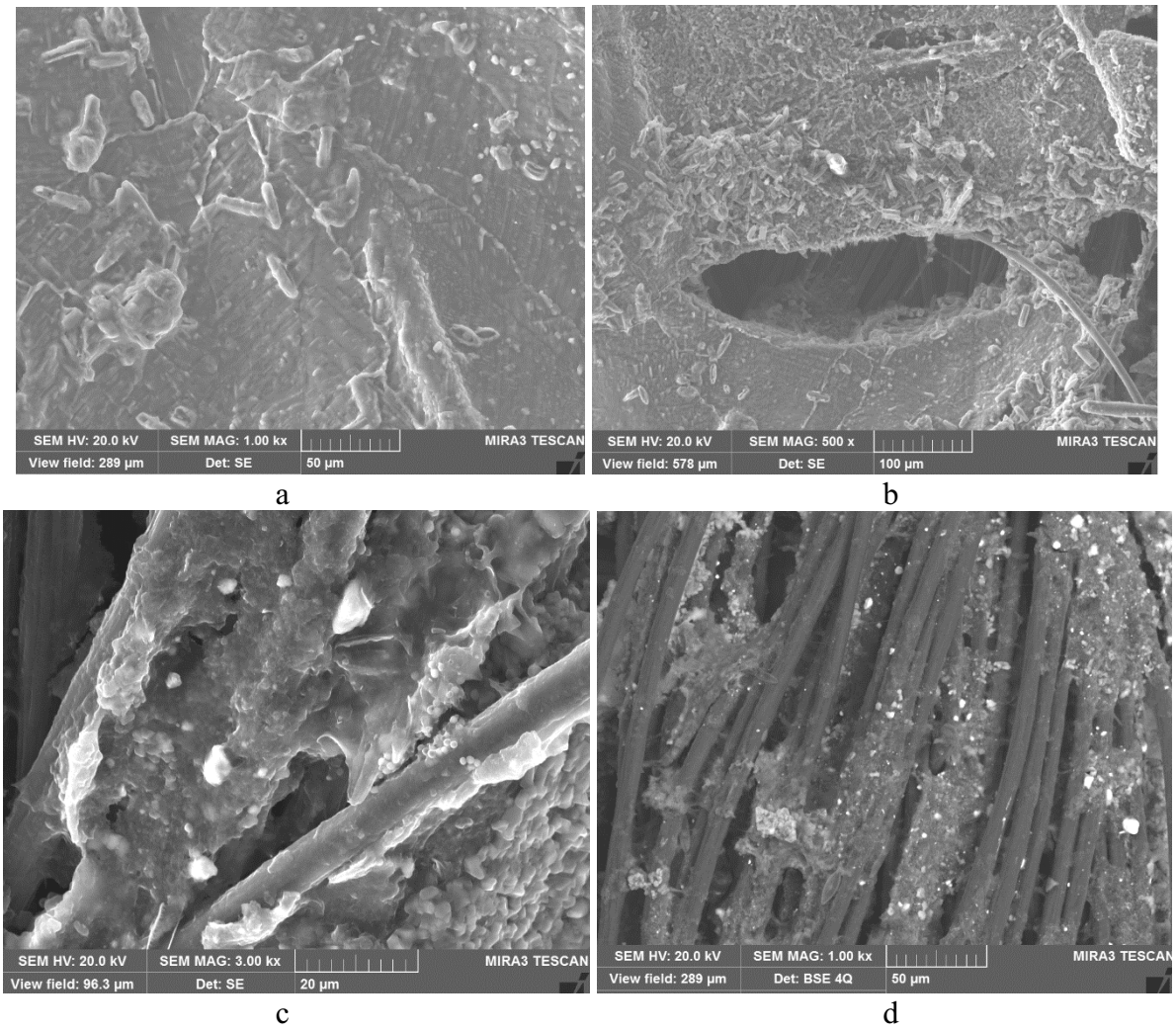

Figure 4. SEM micrographs at differnt magnitudes of biofilm on carbon cloth cathodes : enriched with carbon paint CC-NT (a-b) and also doped with nanoceria CC-NT-Ce (c-d).

A crowd of diatoms appears on the surface, which was not able to penetrate in deep, reaching the carbon cloth fibers. On the contrary, the coating is disaggregated and patchy on the sample of cathode CC-NT-Ce (Fig. 4c-d). In this case, traces of diatoms are clearly visible close to the carbon cloth fibers.

The presence of diatoms was similar as in some of the anodes (Figure 3c).

Similar aerobic conditions, therefore, persisted (and evolved in time) on the anodes as well on the cathodes, inhibiting the raising of the voltage in the MFCs. Hence, this phenomenon induced in some period the reversing of the polarity between the electrodes.

The inversion of polarization occurred mainly in the warmest months (September-October) when the bacterial growth on the air-exposed electrodes is favoured. In this first part of the test, no differences between Ce-doped cathode and non-doped cathode were observed. Conversely, in the second part of the test (November-February), the expected polarization was observed for most of the time, although the signal was lower than that in previous experiments (ref o graph). It is worth mentioning that, in this period, Ce-doped electrodes showed higher signal than non-doped ones, which underwent polarization inversion only in the last month of the test. Thus, we can suppose that in the Winter period grazing protozoa were inhibited by the low temperature, as well as photosynthetic organisms, facilitating more anaerobic conditions on both the electrodes. In this last condition, nanoceria might have enhanced the cathode performance, increasing the cathodic potential. These allowed to record a correlated signal to the organic load dispersed in the wastewater tank. To validate and confirm the achieved results, further experimentation with different types of MFC and geometry is suggested. Nonetheless, it is worthy to note the versatility of simple MFC such as the one tested here, which signal can give useful information on the biology occurring in the wastewater process, as well as on some physical-chemical parameters and nutrients, in real-time.

4. Conclusion

Planar and membraneless MFC with carbon cloth electrodes differently enriched and doped with carbon Nanotube, Ce-doped, and/or undoped, were tested. The results indicated that in absence of a strong anoxic condition in the tank, cathode and anode tend to reverse.

The weak anoxic condition in the tank was documented by the presence of a rich flora of protozoa in the water, that inhibit anaerobic conditions on the anode by grazing microorganisms. MFCs signal stays very low, independently of the season of the year, and tend to reverse when anoxic conditions are not well stabilized. The presence of nanoceria at the cathode enhances the voltage of the MFC but also the phenomenon of signal reversing, probably favouring the life of aerobic protozoa which scratch the surface of the electrode grazing bacteria and biofilm. Signal trends from such MFCs can give, in real-time, useful information on the biology occurring in the wastewater, as well as on physical-chemical parameters and nutrients which are strategic to optimize the purification process.

4. Acknowledgements

This work was financed by the Research Fund for the Italian Electrical System in compliance with the Decree of March 19th 2018.
We warmly thank the Managers and staff of the wastewater treatment plant of Bresso-Niguarda (group CAP Amiacque, Milan, IT) for promoting and support this experimentation.

References

1. M.W.A. Spurr, E.H. Yu, K. Scott and I.M. Head,. Environmental Science: Water Research & Technology, **6,** 7, (2020)

2. P. Cristiani, I. Gajda, J. Greenman, F. Pizza, P. Bonelli, I. Ieropoulos. Front. Energy Res., 01 November 2019.

3. E. Martinucci, F. Pizza, E. Guerrini, A. Colombo, S.P.M. Trasatti, A. Lazzarini Barnabei, A. Liberale, P. Cristiani. International Journal of Hydrogen Energy IJHE **40** (42), 9 (2015)

4. S. Marzorati, P. Cristiani, M. Longhi, S. P. Trasatti and E. Traversa. Electrochimica Acta, **325** (2019).

5. L. Rago, P. Cristiani, F. Villa, S. Zecchin, A. Colombo, L. Cavalca, A. Schievano. Bioelectrochemistry, **116** (2017) 39.

6. E. Guerrini, M. Grattieri, S.P. Trasatti, P. Cristiani. Journal of Hydrogen Energy. **39**, (2014)21837.

Performance assessment of stacked air-cathode microbial fuel cells under series and parallel electrical connections

Simona Di Micco[1,*], *Pasquale* De Falco[1], *Mariagiovanna* Minutillo[2], *Antonio* Bracale[1], *Pierluigi* Caramia[1], *Angelo* Gifuni[1], *Giuseppe* Grassini[1]

[1]Univerisity of Naples "Parthenope", Naples, Italy
[2]Department of Industrial Engineering, University of Salerno, Salerno, Italy

Abstract. Microbial fuel cells (MFCs) are playing an important role in the context of sustainable energy development. They represent a sustainable approach to harvest electricity from biodegradable materials. However, harvesting energy from MFCs represents a critical issue because of the low output voltage and power produced. Realizing stacked configurations may involve an increase in MFCs performances in terms of output voltage, current and electric power.
In this paper, two stacked configurations under different electrical connection modes have been designed, developed, modeled and tested. The stacked MFCs consist of 4 reactors (28 mL x4) that are connected in series, and parallel-series modes. Three different tests have been carried out, which involves: 1) performing the polarization and power curves by applying decreasing resistances; 2) assessment of the electric behavior of each reactor over time at a fixed resistance, 3) performing the polarization and power curves by applying increasing resistances. Moreover, a numerical model for predicting the transient behavior of the electrical quantities for one reactor, has been developed and validated by using the experimental data. As expected, the results highlighted that the parallel-series configuration assures the highest volumetric power density compared to the series configuration, reaching the maximum value of 1248.5 mW/m^3 (139.8 μW) at 0.291 mA. Eventually, by comparing the numerical and the experimental data, it has been demonstrated that the developed model is able to predict the reactor's electrical trend with a good accuracy.

1 Introduction

MFCs represent a sustainable approach to harvest electricity from biodegradable materials. Thanks to the capability of bacteria inside the reactor of generating electricity while consuming organic matter, the can be considered as a future option for the treatment of organic wastes, bioremediation, and the recovery of bioenergy from wastes [1–5]. However, harvesting energy from MFC represents a critical issue because of the low output voltage and power produced, which limits its use as an electricity supply system and its development on the market as renewable energy technology[6–8].
The scale-up of MFCs does not represent a valid solution for improving the MFCs performances since the greater distance between the electrodes, that can occur in bigger reactors, involves a reduction in power density.
In a previous paper [9], the authors demonstrated that increasing the reactor volume and using multiple anodes did not involve an improvement in performances because of the negative influence of the greatest geometric parameters, i.e. the ratio between anodic and cathodic surfaces, the electrodes spacing, etc.

On the other hand, realizing stacked MFCs configurations, according to different electrical connection modes, may feature a more feasible and efficient strategy for improving the performances. As matter of fact, realizing stacked MFCs in series mode allows increasing the output voltage with respect to a single cell as well as realizing stacked MFCs in parallel mode, which allows to increase the output current compared to the single MFC.
Estrada-Arriaga et al. [10] studied two different air-cathode stacked microbial fuel cells configurations connected in series for municipal wastewater treatment and electricity generation. The first stack (20 individual air-cathode MFCs) was able to produce a maximum power density of 79±0.65 mW/m^2; the second stack (40 air-cathode MFCs), was characterized by a power production of 4.2 ±0.6 mW/m^2.
Ieropulos et al. [11] tested the polarization curves trends of 10 identical MFCs connected in series, parallel and series/parallel configurations. Results highlighted that volumetric power densities were 0.45 W/m^3, 0.81W/m^3, 0.56W/m^3, for the series, parallel and series/parallel configurations, respectively.
Wang et al. [12] analyzed 4 MFCs electrical connections modes: series, parallel, series/parallel and parallel/series.

* Corresponding author: simona.dimicco@studenti.uniparthenope.it

Results, in terms of power outputs (mW) were 4.02 (± 1.01), 6.84 (± 0.24), 4.58 (± 0.30), and 5.64 (± 0.96) for the series (6 cells), parallel (5 cells), series/parallel (5 cells) and parallel/series (5 cells) connections, respectively.

In a previous paper [13], the authors tested 4 different configurations demonstrating that the best performances were measured for the parallel-series configuration.

Starting from these results, in this paper the authors study in depth the electrical behavior of two of these configurations, one which maximizes the output voltage (i.e series-configuration) and the other one which maximizes the volumetric power density (i.e parallel-series configuration). In particular, the polarization curves have been measured by applying both the conventional and the "inverse" monocyclic method, with a sampling time of 9 minutes.
Different experimental tests have been carried out: Test 1 which involves performing the polarization and power curves by applying decreasing resistances; Test 2 in which the assessment of the electric behavior of each reactor over time at a fixed resistance is evaluated; Test 3 which implies performing the polarization and power curves by applying increasing resistances.
Furthermore, in order to predict the transient behavior of the electrical quantities, a numerical model has been developed and validated by using the experimental data. During these tests, the rector's electrical behavior has been evaluated skipping from the OCV condition to the maximum power one.

2 Material and Methods

The experimental activities have involved, first of all, the design and the development of the reactors as well as the substrate preparation, the biofilm growth, and the bacteria acclimation.
For sake of simplicity, the authors reported, in the following sections, the main choices concerning the material and methods taken into account during the experimental activities. More details are widely described in the authors' previous paper [13].

2.1. MFC design and development

The investigated stacked MFCs consist of 4 single-chamber reactors operating in batch mode and fluidically isolated, i.e., fed from individual lines.
They have been manufactured by using the Poly-Lactic Acid (PLA)-based material and a 3D printer (Delta Wasp 20x40) [14], downstream the definition of their shape and design by using the CAD support.
Each MFC shows a cubic shape with an internal volume of 28 mL. Table 1 summarizes the main geometric parameters of each reactor.

Table 1. Geometric parameters of a single-chamber MFC

Geometric details	Units	Values
External Dimensions (length x height x depth)	mm	50x50x46.5
Internal Dimensions (diameter x depth)	mm	30x40
Total internal volume	mL	28
Cathode surface	cm^2	7

For each reactor, it has been selected a carbon fiber brush as anodic electrode and an activated carbon coated with both a PTFE (polytetrafluoroethylene) layer and a nickel mesh (as current collector) as cathodic one [9,15].

2.2. Substrate preparation, biofilm growth and bacteria acclimation

The substrate used for feeding the MFCs consists of a mixture containing 50 mL of sodium acetate 1M and a mineral solution, prepared according to ref [16]. Sodium acetate ensures the highest energy yield for supporting the metabolism of exo-electrogenic bacteria if compared to fermentable compounds like glucose, lactose, starch and sucrose [15,17]. For avoided criticism to the catabolic activities of anaerobic bacteria, it has been needed to verify that the pH of the prepared substrate ranged from 7-8, since it strongly affects the microorganisms' growth.
The biofilm selected in this study consists of endogenous bacterial species of the Compost, that generally are Bacillus, Geobacillus and Brevibacillus [18–20].
As concern the biofilm growth and the bacteria acclimation, a procedure consisting of 4 steps have been applied as detailed in [13].

2.3. MFC electrical transient modeling

Transient analysis for MFCs is very important since the current and the voltage values to evaluate the performance with polarization curves and to make power density analysis should be taken when pseudo-steady-state conditions have been established [21]. This condition can take several minutes or more.

The estimation of electrical voltage and currents during transient in MFCs operation can be made using proper models that allow the development of equivalent circuits able to emulate behavior of MFC in electrical network dynamic conditions.

In this paper, a simple model for the estimation of the electrical transient is proposed, according to the general solution of the step response of a first-order system:

$$x_1(t) = c_0' + c_2' \, e^{-\frac{t}{\tau}} \quad (1)$$

which can represent either a decreasing variable ($c_0' = 0$) or an increasing variable ($c_0' = -c_2'$).

An estimation of the biochemical transient is instead proposed through a simple linear function:

$$x_2(t) = c_0'' + c_1'' t \quad (2)$$

Therefore, assuming the superposition principle, the entire transient pattern can be modelled through the following equation:

$$x(t) = x_1(t) + x_2(t) = c_0' + c_2' e^{-\frac{t}{\tau}} + c_0'' + c_1'' t \quad (3)$$

where the parameters $c_0', c_2', c_0'', c_1'', \tau$ are estimated through the minimum least-square approach on the measured sample data $x_1, \dots, x_N$:

$$\min_{c_0', c_2', c_0'', c_1'', \tau} \sum_{n=1}^{N} [x_n - x(t_n)]^2 = \sum_{n=1}^{N} \left[x_n - c_0' - c_2' e^{-\frac{t_n}{\tau}} - c_0'' - c_1'' t_n \right]^2 \quad (4)$$

s.t.

$$c_0'(c_0' - c_2') = 0$$

$$\tau > 0.$$

3 Test Bench

In order to assess the performance MFCs, an experimental test bench has been developed. It includes different devices to perform accurate measurements of MFCs voltage and current. In particular, it consists of a resistance box and four multimeters.

The resistance box allows changing the electrical load to which one or more reactors are connected. The 8-digit wheel switch allows to change the resistance value and the multiple gold contact arrangement ensures low contact resistance. The multimeters consist of an alphanumeric display, an input connector and a digital viewer, and allow measuring the instantaneous values of the current and of the voltage that are recorded on a dedicated computer. Fig. 1 shows the test bench set up in the laboratory.

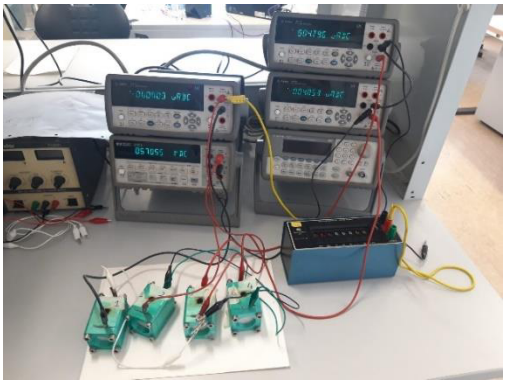

Figure 1. Test bench set up

4 MFC Configuration

In this paper two stacked configurations have been designed, developed, and tested. In the first configuration four MFCs have been connected in series mode, the second one, instead, in parallel-series mode. The performances in terms of volumetric power density (normalized with respect to the total volume of reactors) and electric power production for these configurations have been estimated and compared.

4.1. Series Configuration

Fig.2 shows the electrical circuit of the series configuration. It should involve an increase of the output voltage if compared to a single cell, since the output voltage is equal to the sum of four single-reactor output voltages.

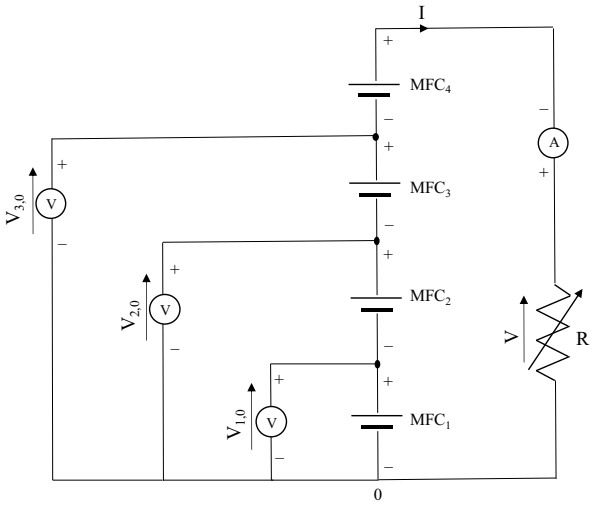

Figure 2. Electrical circuit of the series configuration

According to this electrical circuit, the test bench has been set up with three multimeters for the instantaneous voltage measurements ($V_{i,0}$ with $i = 1,2,3$), and a multimeter for measuring the instantaneous value of the current *I* flowing through the resistance. The voltage output of the MFC_1 has been the one measured directly, while the output voltages for the MFC_2 and MFC_3 have been calculated according to the following equations:

$$V_1 = V_{1,0} \quad (5)$$

$$V_2 = V_{2,0} - V_{1,0} \quad (6)$$

$$V_3 = V_{3,0} - V_{2,0} \quad (7)$$

Note the value of the applied load resistance *R* and the corresponding measured current *I*, it is possible to calculate the series stack output voltage as:

$$V = RI \quad (8)$$

where the resistance selected for this configuration ranged from 3.28 kΩ to 132 kΩ with variable steps. Eventually, the output voltage of MFC_4 has been calculated by difference:

$$V_4 = V - V_{3,0} \quad (9)$$

4.2. Parallel-Series Configuration

Fig. 3 illustrates the electrical circuit of the parallel-series configuration. It has been realized by connecting two MFCs in parallel mode and then by connecting two parallel connections in series mode. This configuration should involve an increase of the output current as well as of the output voltage if compared to a single cell.

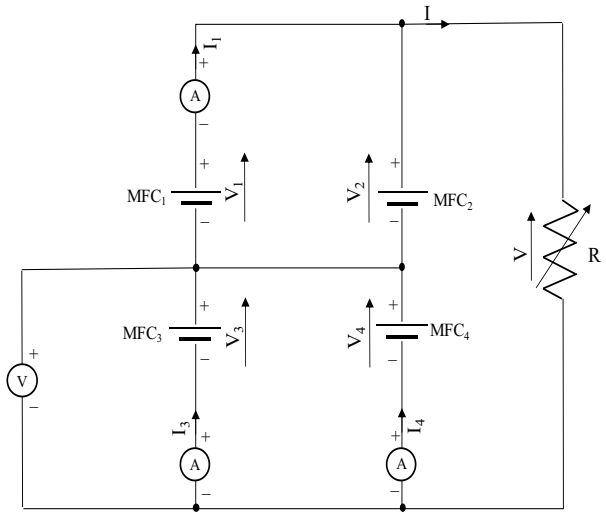

Figure 3. Electrical circuit of the parallel-series configuration

Based on this configuration, the test bench has been set up with three multimeters for measuring the instantaneous currents and a multimeter for the voltage measurement. This test bench allows to measure directly the currents of MFC_1, MFC_3 and MFC_4, i.e. I_1, I_3 and I_4 and the voltage of the cell MFC_3, i.e. V_3, which is equal to V_4 because of the parallel connection of MFC_3 and MFC_4. The other electric quantities have been calculated according to the following equations:

$$I_2 = I_3 + I_4 - I_1 \quad (10)$$

$$I = I_3 + I_4 = I_1 + I_2 \quad (11)$$

$$V_1 = V_2 = R(I_3 + I_4) - V_3 \quad (12)$$

where the resistance selected for this configuration ranged from 1.64 kΩ to 66 kΩ with variable steps.

5 MFC testing activity

For comparing the performances of the proposed MFCs configurations, the experimental activity has been organized in three tests:

- Test 1: the polarization curves for each configuration have been performed at the end of the acclimation phase. In particular, the polarization curves have been carried out starting from the monocyclic method reported in ref. [22], which consists of applying decreasing values of resistances, each one supplied for a time interval of 9 minutes. The electrical quantities are measured with a sampling time of 1s. For each test obtained with a value of resistance, the average value of stack output voltage is calculated.

- Test 2: the transient patterns of the measured currents and voltages are analyzed and characterized through the procedure described in Section 2.3. The time period considered for each analysis is of 9 minutes, i.e., the same length of the acquisition of Test 1. Only for sake of conciseness, the analysis and characterization of the transient current and voltage patterns are presented in this paper for the acquisitions corresponding to the maximum volumetric power densities of the parallel-series configuration and of the series configuration, determined by Test 1.

- Test 3: the polarization curves for each configuration have been performed considering an "inverse monocyclic method". It consists in applying increasing values of resistances, each one supplied for a time interval of 9 minutes. The electrical quantities are measured with a sampling time of 1s. For each test obtained with a value of resistance, the average value of stack output voltage is calculated.

6 Results

Before estimating the performance of the series and the parallel-series configurations, the performance of a single cell, in terms of polarization and power density curves, has been evaluated.

6.1 Single Cell Performance

Fig. 4 shows the polarization curve and the volumetric power densities measured for the single MFC. The volumetric power density has been calculated taking normalizing the produced electric power with respect to the MFC internal volume, which is equal to 28 mL. It can be noticed that the average current is in the range 0.01 - 0.03 mA and the average voltage ranges from 0.02 to 0.33 V. The maximum average volumetric power density is 131 mW/m^3 (3.66 μW) at 0.023 mA.
For the single cell, at high current densities the "power overshoot" occurs. This phenomenon refers to a "doubling back" effect of the power density curve in which a lower power than that measured for lower current densities is measured [23]. It is mainly due to the increase of internal resistance and also to the inability of bacteria (on the anode) of producing sufficient current at lower voltages [24].

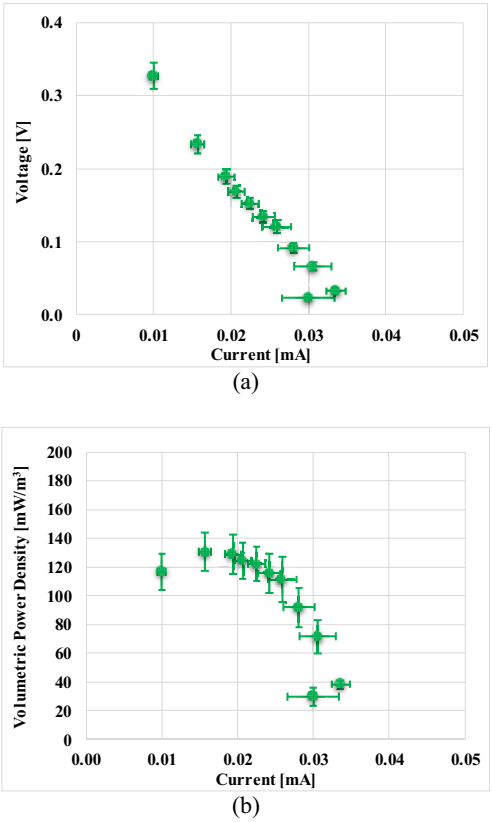

Figure 4. Polarization (a) and volumetric power density (b)curves of the single MFC

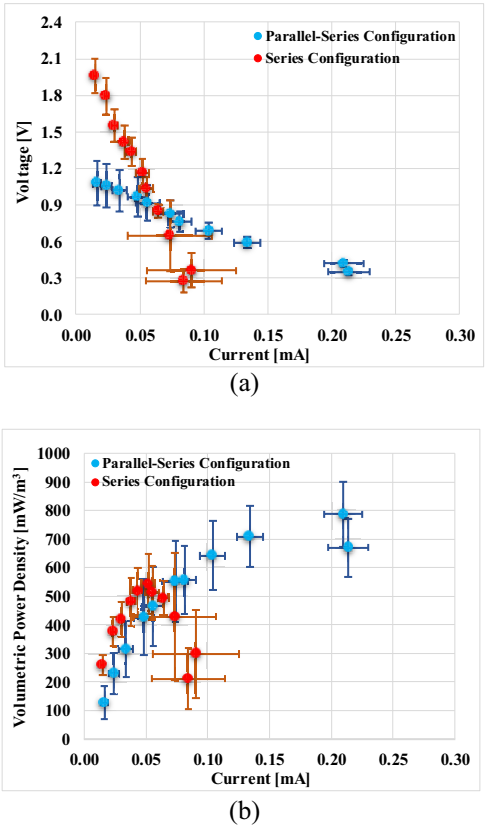

Figure 5. Polarization (a) and volumetric power density (b) curves for series and parallel-series configuration

6.2 Behavior and performance in Test 1

Test 1 has involved the measurement and the comparison of the performances for the series and the parallel-series configurations in terms of polarization and power density curves (Fig.5). It is worth noticing that the parallel-series configuration reaches the best performance in terms of volumetric power density, producing 787.8 mW/m^3 (88.2 µW) at 0.21 mA (0.419 V), by applying an external resistance of 2 kΩ. Even if the series configuration allows to have the highest voltage operating range (up to 2 V) compared to the parallel-series configuration, the maximum volumetric power density is 543.4 mW/m^3 (60.9 µW) at 0.05 mA, by applying an external resistance of 22.4 kΩ. The calculated standard deviations of the maximum power densities are equal to ±114.44 mW/m^3 and ±106.02 mW/m^3 for the parallel-series and series configurations, respectively.

It is important to highlight that the obtained performances, for both configurations, are lower compared to the ones obtained in the authors' previous paper (2451 mW/m^3 and 1799 mW/m^3 for the parallel-series and the series configuration, respectively)[13]. In particular, that the performance, in terms of produced volumetric power density decreases of about 67.9% and 69.8% for the parallel-series and series configuration, respectively. These lower performances are certainly due to the aging of the cathodes, since these tests have been carried out 5 months later

6.3 Behavior and performance in Test 2

Test 2 involves the analysis and characterization of the transient patterns of the current and voltage measured for each reactor, through the procedure described in Section 2.3. Only for sake of conciseness, the results presented here are related only to two acquisitions that correspond to the maximum volumetric power densities of the parallel-series configuration (i.e., 2 kΩ resistance load) and of the series configuration (i.e., 22.4 kΩ resistance load).

Figs. 6 and 7 show the currents and voltages versus time measured for the parallel-series and series configurations, respectively. It can be noticed that the electrical variables measured on each MFC follow both a purely electrical transient and a "biological transient" (much slower) due to the capability of bacteria to adapt themselves for delivering current under the new load conditions. In the parallel-series configuration (Fig. 6), voltages drop by about 12-14% in the first 100 seconds, whereas all currents except I_1 drop by about 4-16% in the first 100 seconds; current I_1 follows instead an initial rise (~8%) in the first 100 seconds, and a subsequential drop. In the series configuration (Fig. 7), voltages drop instead by less than 4% in the first 100 seconds, and the current drops by about 4% in the first 100 seconds. In both configurations, about 50% of the total variation of the variable that can be evidenced in the 9-minutes interval occurs in the first ~50 seconds.

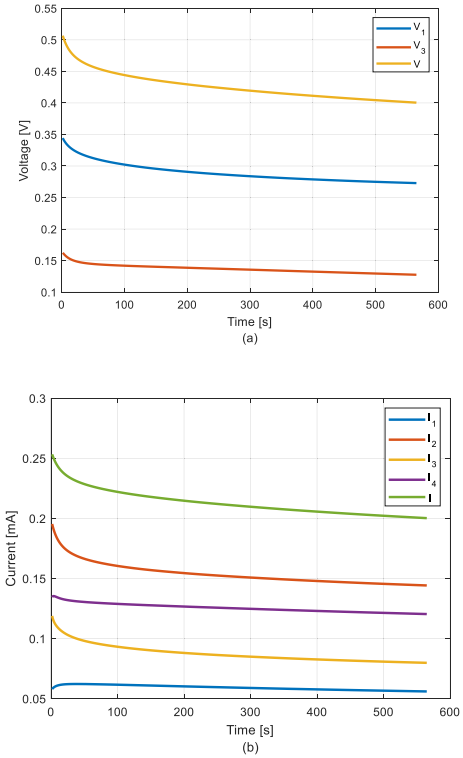

Figure 6. Voltages (a) and currents (b) versus time measured during the polarization experiment in test 1 for the parallel-series configuration

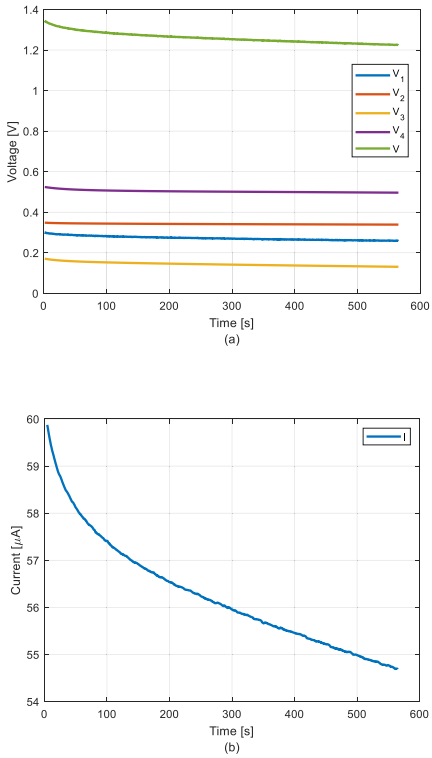

Figure 7. Voltages (a) and current (b) versus time measured during the polarization experiment in test 1 for series configuration

As an example of the estimation procedure of the electrical quantities, described in Section 2.3, the voltage and current estimations for the parallel-series configuration are reported in Fig. 8. In particular, the comparison between the measured and the estimated voltages and currents for the MFC_1, selected between the reactors of the parallel-series configuration (by applying the load resistance at which the maximum volumetric power density is reached), is depicted. From the graphical inspection of Fig. 8, it appears that the proposed transient model allows obtaining a good approximation of the actual pattern, although further improvements could be obtained using more complex models, especially for the tails of the pattern.

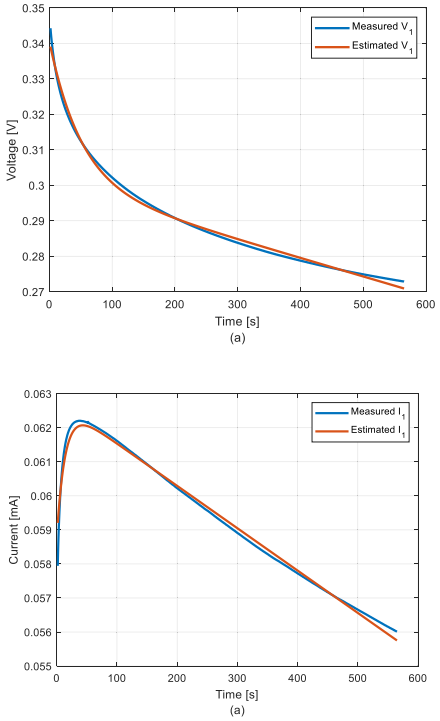

Figure 8. Comparison between the estimated and measured voltages (a) and currents (b) versus time for MFC_1 in the parallel-series configuration.

Although not reported here, for sake of conciseness, good results in terms of transient approximation are achieved also in the series configuration. Table 2 eventually summarizes the values of the parameters estimated according to eq. (4) for the parallel-series and series configuration.

Table 2. Estimated parameters

Parameter	Parallel-series Configuration		Series Configuration	
	Voltage V_1	Current I_1	Voltage V_1	Current I
c_0'	0	0	0	0
c_2'	0.040	-0.004	0.016	0.003
c_0''	0.300	0.063	0.238	0.047
c_1'	-5.218×10^{-5}	-1.244×10^{-5}	-4.269×10^{-5}	-4.653×10^{-5}
τ	50.519	13.723	80.059	64.202

6.4 Behavior and performance in Test 3

The test 3 has allowed measuring the polarization curves by applying the "inverse monocyclic method". It consists in applying increasing resistances and thus in evaluating the rectors' behaviors switching from higher to lower values of produced output currents. Fig. 9 compares the performances in terms of polarization and power density curves by applying the "inverse monocyclic method" for the tested configurations.

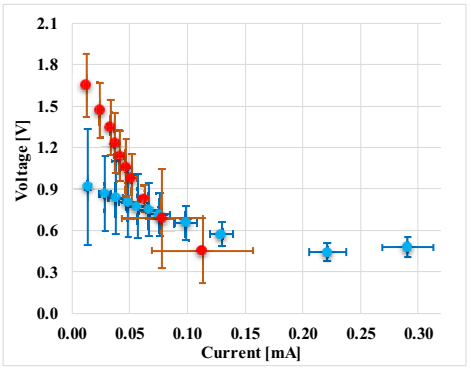

(a)

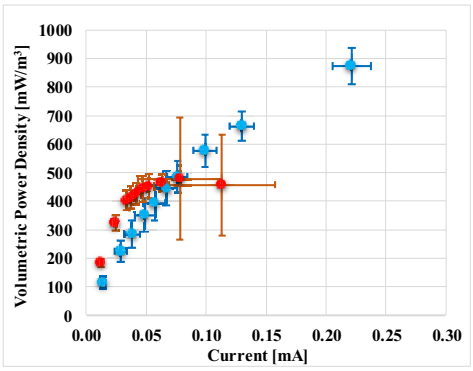

(b)

Figure 9. Inverse polarization (a) and volumetric power density (b) curves for series and parallel-series configuration.

It is worth noticing that also applying the "inverse monocyclic method" the parallel-series configuration reaches the best performance in terms of volumetric power density. Besides, by comparing the results for the test 1 and test 3, it is highlighted that:

- the power overshoot occurs for the series configuration but not for the parallel-series one;
- the current reversal does not occur for the series-configuration, unlike what happens in the test 1;
- the parallel-series configuration, has shown the best volumetric power density, 1248.5 mW/m^3 (139.8 µW) at 0.291 mA (0.477 V), by applying an external resistance of 1.64 kΩ;
- for the series configuration, the maximum volumetric power density is 478.8 mW/m^3 (53.6 µW) at 0.078 mA (0.687 V), by applying an external resistance of 8.8 kΩ. This value is lower compared to that measured during the test 1;
- the calculated standard deviations of the maximum power densities are equal to ±94.62 mW/m^3 and ±215.10 mW/m^3 for the parallel-series and series configurations, respectively.

7 Conclusion

In this study, two stacked MFCs configurations, based on different electrical connection modes, have been designed, developed, realized, and tested. The analyzed configurations consist of 4 MFCs connected in series and parallel-series modes.
Three different tests have been carried out for both the configurations. Results highlighted that the parallel-series configuration assures the highest volumetric power density with respect to the series configuration, reaching the maximum volumetric power density, 1248.5 mW/m^3 (139.8 µW) at 0.291 mA, during the test 3.
However, both in test 1 and test 3, the reached performances in terms of volumetric power density for the series and the parallel series configurations significantly exceed those obtained for the single cell. As matter of fact, in test 1 the volumetric power densities of series and parallel-series configuration are 6 and 4-fold higher with respect to the single cell, respectively. In test 3, instead, the volumetric power densities are 9.5 and 3.7-fold higher with respect to the single cell, for the parallel-series configurations, respectively.
Moreover, another result has been come out. In particular, the authors noticed that the obtained performances, for both configurations, were lower compared to the ones obtained in the authors' previous paper (2451 mW/m^3 and 1799 mW/m^3 for the parallel-series and the series configuration, respectively). As matter of fact, the produced volumetric power density, decreases of about 67.9% and 69.8% for the parallel-series and series configuration, respectively. These lower performances are certainly due to the aging of the cathodes, since these tests have been carried out 5 months later. This effect will be deeply analyzed in future studies.

References

1. M. A. Moqsud, K. Omine, N. Yasufuku, M. Hyodo, and Y. Nakata, Waste Manag. (2013)
2. D. Borello, G. Gagliardi, G. Aimola, V. Ancona, P. Grenni, G. Bagnuolo, G. L. Garbini, L. Rolando, and A. Barra Caracciolo, Int. J. Hydrogen Energy **46**, 10131 (2021)
3. E. Casula, B. Kim, H. Chesson, M. Di Lorenzo, and M. Mascia, Electrochim. Acta **368**, (2021)
4. M. Alaraj and J. Do Park, J. Power Sources **418**,

225 (2019)
5. G. Di Ilio and G. Falcucci, Int. J. Hydrogen Energy **46**, 20280 (2021)
6. R. A. Nastro, N. Jannelli, M. Minutillo, M. Guida, M. Trifuoggi, L. Andreassi, A. L. Facci, V. K. Krastev, and G. Falcucci, Energy Procedia **105**, 1102 (2017)
7. D. Frattini, G. Falcucci, M. Minutillo, C. Ferone, R. Cioffi, and E. Jannelli, Chem. Eng. Trans. (2016)
8. S. Cheng, H. Liu, and B. E. Logan, Environ. Sci. Technol. (2006)
9. M. Minutillo, R. A. Nastro, S. Di Micco, E. Jannelli, R. Cioffi, and M. Di Giuseppe, in *E3S Web Conf.* (2020)
10. E. B. Estrada-Arriaga, Y. Guillen-Alonso, C. Morales-Morales, L. García-Sánchez, E. O. Bahena-Bahena, O. Guadarrama-Pérez, and F. Loyola-Morales, Water Sci. Technol. (2017)
11. I. Ieropoulos, J. Greenman, and C. Melhuish, Int. J. Energy Res. (2008)
12. Z. Wang, Y. Wu, L. Wang, and F. Zhao, Chinese Sci. Bull. **59**, 2214 (2014)
13. M. Minutillo, S. Di Micco, P. Di Giorgio, G. Erme, and E. Jannelli, Energies **14**, 5116 (2021)
14. S. Ford and M. Despeisse, J. Clean. Prod. (2016)
15. B. Logan, S. Cheng, V. Watson, and G. Estadt, Environ. Sci. Technol. (2007)
16. H. Liu, R. Ramnarayanan, and B. E. Logan, Environ. Sci. Technol. (2004)
17. C. Gonzalez-Solino, E. Bernalte, B. Metcalfe, D. Moschou, and M. Di Lorenzo, J. Power Sources **472**, 228530 (2020)
18. F. Flagiello, E. Gambino, R. A. Nastro, and C. Kuppam, in edited by P. Kumar and C. Kuppam (Springer Singapore, Singapore, 2020), pp. 217–234
19. B. Cercado, N. Byrne, M. Bertrand, D. Pocaznoi, M. Rimboud, W. Achouak, and A. Bergel, Bioresour. Technol. (2013)
20. B. Cercado-Quezada, M. L. Delia, and A. Bergel, J. Appl. Electrochem. (2010)
21. B. E. Logan, B. Hamelers, R. Rozendal, U. Schröder, J. Keller, S. Freguia, P. Aelterman, W. Verstraete, and K. Rabaey, Environ. Sci. Technol. (2006)
22. V. J. Watson and B. E. Logan, Electrochem. Commun. (2011)
23. F. Khaled, O. Ondel, and B. Allard, J. Power Sources (2016)
24. B. Kim, J. An, and I. S. Chang, ChemSusChem (2017)

Testing novel multicomposite materials for electromethanogenesis

Giorgia Ghiara[1], *Stefano* Trasatti[1], *Andrea* Goglio[2], *Pierangela* Cristiani[3]*

[1]Università degli Studi di Milano, Department of Environmental Sciences and Policy, Milano, Italy
[2]Università degli Studi di Milano, Department of Agricuture and Environmental Sciences, Milano, Italy
[3]Ricerca sul Sistema Energetico - RSE S.p.A., 20134 Milano, Italy

Abstract. Electromethanogenesis is an innovative technology that uses a microbial electrochemical system to produce methane from CO_2, in a power-to-gas (BEP2G) concept. The results of experimental tests of new and cost-effective carbonaceous materials for electrode are presented here. The study aims at optimizing electromethanogenesis processes at laboratory level in mesothermic condition. As part of the experiments, hydrogenotrophic microorganisms (Family Metanobacteriaceae of Archaea domains) were selected from a mixed consortium taken from a biogas digestate and inoculated in double-chamber bioelectrochemical systems. The maximum amount of methane produced was 0.3 - 0.8 mol/m^2g (normalized to the cathode area) with carbon cloth electrodes. Aiming at improving the methane productivity, innovative materials for the electrodes were now studied, creating porous high-surface composites, and studying nitrogen carbons doped with Cu and hydroxyapatite (Multicomposite Cu@/HAP/C), as chemical catalysts for CO_2 reduction (CO2RR). The description of the procedure for the Multicomposite Cu@/HAP/C production is reported in detail.

1 Introduction

Electromethanogenesis also called bioelectrochemical power-to-gas (BEP2G) is an innovative technology for storing renewable electricity in the form of methane, alternative to both biochemical methanogenesis and thermochemical methanation (Sabatier process) [1,2]. The process is supported by specific microorganisms selected FROM biogas plants or from natural anaerobic environments [3]. In BEP2G carbon dioxide (CO_2) and electrical energy are converted directly into methane (CH_4) on electrodes colonized by methanogenic microorganisms of the *Archea* domain [4,5]. In general, the mechanisms for the CH_4 production, in absence of electricity are different and depend on the metabolic pathways ascribed to the selected species. Two main pathways for methanogenesis are known: i) hydrogenotrophic; ii) acetoclastic. These metabolic processes start from two main types of molecules, respectively: i) carbonate ion; ii) acetate ion (or methanol). The values of Gibbs free energy at standard conditions (25 ° C and pH 7) [6] differ by the nature of the substrate and the energy source used to produce CH_4 [7,8]. Among these, the most widespread and most metabolically efficient process for energy generation is the hydrogenotrophic one [9,10]

Using electricity, methanogenesis can be achieved using only carbon dioxide and bicarbonate as the only source of carbon and, it can be coupled to both the abiotic oxidation of water and the abiotic, or microbial, oxidation of organic molecules [11-13]. According to this set-up, microorganisms catalyze the reduction of carbon dioxide introduced into the cathode chamber to methane on a polarized cathode, which donates electrons following reaction (1):

$$CO_2+8H^+ + 8e- = CH_4+2H_2O \quad (1)$$

Furthermore, microbial electromethanogenesis can be effectively combined with the conventional anaerobic digestion (AD) process using CO_2-rich gases produced by biogas plants (methane up-grading) or using CO_2-rich industrial waste gases. However, it is a relatively recent technology, still mainly experimented at a laboratory level [1,2].

Lately, novel approaches have been proposed to solve technological problems and to make it a energy storage system more economically and industrially competitive [1,2]. Research on the optimization of the design and configuration of the bioreactors were carried out to reproduce the systems on a larger scale [2]. They manly focused on the chamber set-up (i.e., single, or dual chamber), the applied cathode potential (~1 V), the choice of microorganisms, the cathode and/or anode feeding, the pH, etc… [14-17]. An alternative, relevant, approach is the study of different materials for the cathode. Electrodes must give large surfaces to maximize the interaction with microorganisms minimizing charge transfer resistance and diffusive mass transport [15]. Carbon-based materials are particularly suitable for electrochemical systems, especially biochar, which aroused great interest for such

* Corresponding author: Pierangela.Cristiani@rse-web.it

application [18,19]. In this study the authors present the first results of the use of an innovative composite carbon based electrocatalysts (e.g., biogenic carbon) functionalized with copper nanoparticles (Cu@) and hydroxyapatite (HAP) as a cathode material where reduce CO_2 (CO_2RR) to CH_4. The choice of a carbon of biological origin (biochar) as a support for both Cu@ and HAP was made according to the necessity to have suitable performances, in terms of porosity, conductivity, biocompatibility, mechanical resistance and resilience [20,21]. Furthermore, Cu@ is an active phase that directly promotes a further reduction of CO_2 (transfers > 2 e^-) to a wide range of so-called higher order products (as CH_4, C_2 or C_3), while HAP enhances the selectivity towards CH_4 [22, 23]. The preparation of the electrode material (Cu@/HAP/C) is an important part of the experiment, and an innovative multi-phase protocol is introduced here.

2 Materials and methods

2.1 Biochar production

To obtain an electrically conductive material, giant cane (Arundo Donax. L., 1753) was employed. The canes were positioned in a quartz tube inside a horizontal furnace (Carbolite) and pyrolyzed accordingly. The pyrolysis procedure of the material was carried out according to the following protocol: 2 hours at 25 °C, slow heating (10 °C/min) up to 900 °C, 1 h held at 900 °C and cooling down to 25 °C according to [24]. During all the pyrolysis treatment, nitrogen flowed constantly at 1 NL/h. This type of procedure allows high temperatures to be reached in a short time and maximum treatment efficiency, without any heat loss.

2.2 Multicomposite Cu@/HAP/C production

The composite produced followed a multi-step protocol that involved the use of copper nanoparticles (SigmaAldrich, CAS 7440508, ø = 25 nm) and hydroxyapatite (produced at the University of Milan according to a procedure described elsewhere [25]). Firstly, biochar was pulverized using an agate mortar. The powder was subsequently used as a support for copper nanoparticles (Cu@) and hydroxyapatite (HAP). Approximately. 95 mg of biochar was dispersed in ca. 40 ml of isopropyl alcohol (IPA) (Figure 1a).

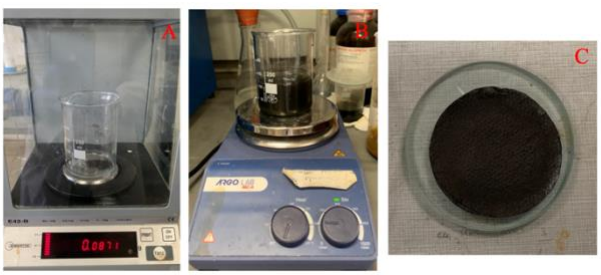

Fig. 1. Protocol to produce the multicomposite Cu@/HAP/C.

The pH of the suspension was adjusted to 10 by adding an aqueous solution of 0.1 M KOH. Similarly, approx. 5 mg of commercial Cu NP were dispersed in ca. 40 mL of IPA, adjusting the pH as indicated for the biochar suspension. Both mixtures were placed on ultrasound for 30 minutes to obtain an optimal suspension. Then, the Cu NP suspension was added one shot to the biochar suspension. The resulting mixture was stirred at room temperature for 48 hours (Figure 1b).
After the immobilization step, the powder was vacuum filtered on a 0.45 m Nylon membrane, washed with MilliQ water and dried at 110 ° C for 45 minutes. The sample obtained was labeled Cu@/C. Approximately. 100 mg of Cu@/C were suspended in ca. 90 ml of MilliQ water. The pH of the suspension was brought to 7 by adding a 0.1 M aqueous solution of KOH. Similarly, ca. 7 mg of HAP were dispersed in ca. 20 mL of MilliQ water, adjusting the pH of the suspension to 7 by adding a 0.1 M KOH solution. Both mixtures were sonicated for 45 minutes. Then, the HAP suspension was added to the Cu@/C suspension in one shot; the resulting mixture was stirred for 72 h at room temperature. Finally, the powder was vacuum filtered on a 0.45m Nylon membrane, washed with MilliQ water and dried at 110 ° C for 3 hours (Figure 1c). This sample obtained was labeled Cu@/HAP/C and the desired composition is presumed to be 5 wt. % Cu and 5 wt. % HAP.

2.3 Set-up of the bioelectrochemical cells

The dual chamber system was made with borosilicate (Pyrex) bottles. The anode and the cathode chambers, both characterized by a volume of 200 mL, were separated by a proton exchange membrane (PEM NAFION 417) (working surface: 7.0 cm^2). CO_2 was fluxed at the cathode at the beginning of the experiment for 10 minutes. The catholyte solution consisted of the inoculum retrieved from an online biogas plant and stored at University of Milan, Bicocca. The inoculum was supplied with 2.54 g/L KH_2PO_4, 11.7 g/L Na_2HPO_4 * $12H_2O$, 0.53 g/L NH_4Cl, 0.1 g/L Na2SO4, 5.0 g/L $NaHCO_3$, and vitamins. The anolyte consisted of a solution of 0.2M Na_2SO_4. The cathode was made of different materials and operated to verify, in comparison, the methane production.

Fig. 2. Set-up of the bioelectrochemical cell.

Three materials were used for the cathode: i) carbon cloth (CC); biochar (C); multicomposite Cu@/HAP/C. All electrodes had a comparable surface area of 100 cm^2. The anode was a Ti-mesh of a suitable area of 36 cm^2. Both anodic and cathodic collector wires were connected to a potentiostat (Amel S.r.l. Milan, Italy) that acted as a power supply. The recording of the potential imposed between the cell and the generated current was performed with an Agilent 4930 A data-logger. A reference electrode Ag/AgCl 3M was inserted in each cathodic compartment. The potential imposed on the cathode during the test was -1.2 V vs the reference electrode, corresponding to approximately -1V vs SHE (Standard Hydrogen Electrode). The duration of the experiments was 6 days and was replicated twice.

2.4 Analytical methods

To verify the morphology (i.e., pore size) of the pyrolyzed biochar and to characterize the multicomposite produced a Scanning Electron Microscopy analysis (SEM) coupled with Energy dispersive X-Ray measurements (EDS) was carried out at the Department of Earth Sciences of the University of Milan. The analyses were conducted at different magnifications and with an acceleration voltage of 20 KeV using secondary electrons (SE) detector.

The composition of biogas (CH_4, H_2, and CO_2) was analyzed using a gas chromatograph (GC) at the Department of Agriculture of the University of Milan. The sample for the GC was taken from the headspace of the bioreactor cathode chamber with flex-foil bags (1 and 5L) connected to the gas escape system. Numerous gas samplings were carried out on a weekly basis, lasting about 60 minutes. The quantity of CH_4 produced was expressed as a percentage of gas found. Furthermore, the pH was monitored on a three-day-basis.

3 Results

3.1 Biochar production

Firstly, A. Donax samples were weighted before and after pyrolysis to verify the success of the procedure. Figure 3 shows a sample before and after the treatment.

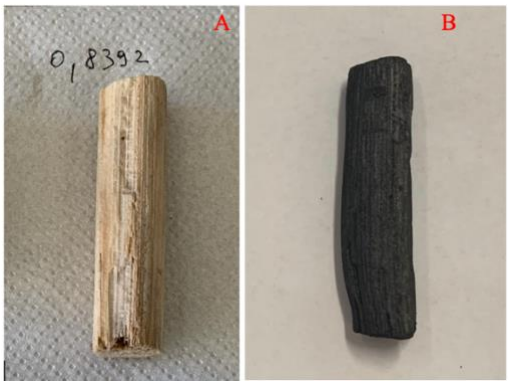

Fig. 3. Example of: A) pre pyrolyzed sample; B) pyrolyzed sample

Generally, a weight loss corresponding to approximately 75% of the initial weight was highlighted for all samples, consistent with the decomposition of the material in the absence of oxygen. During this process, the lignocellulosic components such as cellulose ($C_6H_{10}O_5$) n-hemicellulose and lignin undergo depolymerization reactions, fragmentation, and cross-linking [26]. It is in fact known from the literature that pyrolysis increases the porosity of the material and the surface area even by several orders of magnitude [26]. Porosity is formed because of the loss of water during the treatment. To define the size of the pores we proceeded with a SEM analysis. As can be seen from Figure 4, the material after pyrolysis maintained the same mechanical structure and highlighted an increasing number of pores on the surface, confirming the success of the treatment.

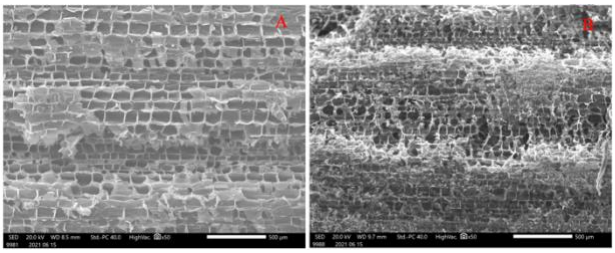

Fig. 4. SEM-SE micrographs of: A) pre pyrolyzed sample; B) pyrolyzed sample

Generally, three types of pores can be distinguished followed by various applications of biochar: i) micropores (<2nm); ii) mesopores (2-50 nm); ii) macropores (> 50 nm). As displayed by the figure the material is composed of macropores, with average dimensions around 50 ± 10 µm. This is a promising result for its use as an electrode as the presence of macropores favors: i) the diffusion of gases (CO_2 and H_2) inside the material, also allowing for a good wettability by the H_2O; ii) the extracellular transfer of electrons by microbes that catalyze the direct production reaction of methane.

3.2 Multicomposite Cu@/HAP/C production

Figure 5 displays the qualitative results obtained by the EDS analysis on the powder.

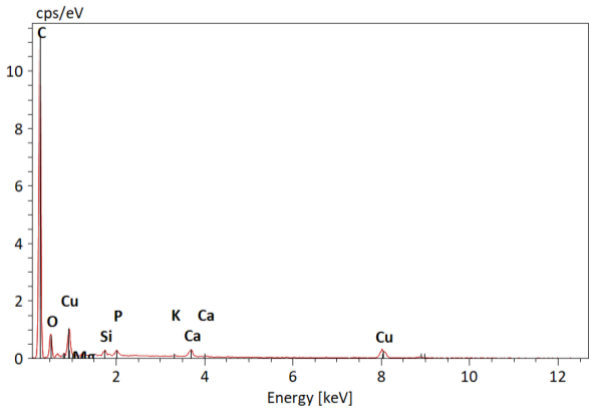

Fig. 5. EDS average spectrum of the Cu@/HAP/C multicomposite.

As expected, the spectrum indicated a high percentage of C on the surface, attributed to the biochar. However, the signals of Cu, Ca, O and P are detected, which implies the success of the methodology. In fact, hydroxyapatites bear generally the following stoichiometry: $Ca_{10}(PO_4)_6(OH)_2$. However, it was not possible to further quantify the overall percentage of the single components due to quantification limits connected to the massive presence of carbon. Further investigation will thus be dedicated to the study of the distribution of the Cu@ and HAP on the biochar and exact composition of this multicomposite material.

3.3 Bioelectrochemical cells

3.3.1 Current output

Figure 6 shows the trend of the cell current (I_{cell}) circulating for 140 h, considering the average. Red and blue arrows indicate gas and pH sampling, respectively. It should be noticed that the CO_2 dosing was carried out through a sparging method (materials and methods section) to allow all CO_2 to be consumed at the electrode and transformed into methane.

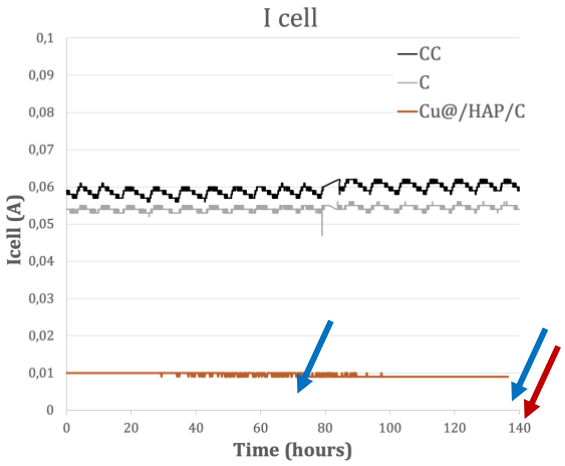

Fig. 6. Current circulating between the electrodes according to the material used. CC= carbon cloth; C= biochar.

As can be seen from the figure, the current produced is influenced by the type of material used as a cathode. An evident variability in the current output is noticed. Carbon cloth (CC) and biochar (C) exhibit higher currents than the multicomposite Cu@/HAP/C. These results are not surprising considering that with the same potential applied, the reisistivity of the multicomposite is higher due to the presence of HAP.
The moles of H_2 that could ideally be produced by the system were also calculated, considering the charge supplied to be used exclusively for the H_2 production reaction. Table 1 summarizes the results obtained in moles of H_2 per day, averaging the currents as a function of the monitoring time.

Table 1. Ideal mmol of hydrogen produced daily by the polarization.

material	H_2(mmol/d)
Carbon Cloth (CC)	23
Biochar (C)	23
Multicomposite Cu@/HAP/C	4

From the values obtained, the presence of the multicomposite catalyses the production of hydrogen at the electrode less easily, 6-times lower values of mmol produced per day.

The pH of the system varied according to the electrode used (as displayed by table 2) and it was expected to rise as a function of the hydrogen consumption due to the applied polarization.

Table 2. Measurements of pH during the experiment

material	pH		
	Day 1	Day 3	Day 6
Carbon Cloth (CC)	6.5	10	10
Biochar (C)	6.5	10	10
Multicomposite Cu@/HAP/C	6.5	6.5	7

As can be seen, a correction of the pH was necessary (0.1 M HCl each time) for both systems using carbon cloth and biochar due to the uptake of hydrogen ions from the solution. However, this trend seems not to interest the multicomposite system in which the pH results more stable, maintaining optimal conditions for the inoculum to produce methane.

3.3.2 Methane production

The gaseous methane was detected as a volumetric percentage contained within the 1 L flex-foil gasbags. The values that emerged from gas chromatography refer exclusively to the methane produced during sampling, which lasted about 60 minutes, for each experiment conducted. Figure 7 shows the results obtained from the gas chromatographic analyses at the end of the experiment.

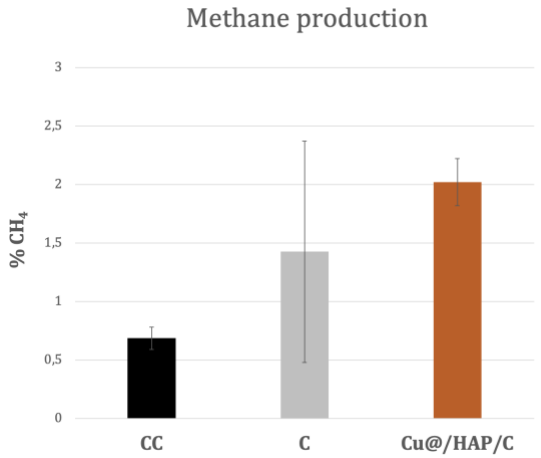

Fig. 7. CH_4 produced at the end of the experiment. CC= carbon cloth; C= biochar.

At first glance, the material effect on experimentation can be seen, characterized in general by an upward trend in methane production, showing a higher production in the presence of biochar. These results are also very promising since the highest methane production was found for the Cu@/HAP/C, in spite the current generated on the electrode was the lower one, suggesting a selectivity for the direct reduction of CO_2 into methane in presence of the inoculum.

4 Conclusion

Comparing the results from the electrochemical and analytical point of view it the better performances of the Multicomposite Cu@/HAP/C than the other materials tested (carbon cloth and biochar) point out in an evident way.
This suggests the use of a different metabolic pathway to produce methane, probably associated with a direct passage of the electron from the electrode to the methanogens, avoiding a dispersion of hydrogen into the solution. Over time, the cell currents and the differences between the different materials remain constant.
An excessive enhancement of the pH suddenly occurs in the case of carbon cloth and biochar, in a few days, while the Multicomposite Cu@/HAP/C guarantee neutral values for longer time. The effect of pH stabilization can be adduced to the presence of HAP in the composite. This phenomenon, associated to the presence of Cu nanoparticle catalysts, can be responsible for the advantage in terms of the methane production process.

References

1. N. Aryal, T. Kvist, F. Amman, D. Pant, L. D. Ottosen, Biores. Technol., **264**, (2018).
2. R. Blasco-Gomez, P. Batle-Vilanova, M. Villano, M. Balaguer, J. Colprin e S. Puig, Int J. Mol Sci, **18**, 32, (2017).
3. P. Clauwaert, Water Sci. Technol., **57**, (2008).
4. P. Clauwaert, W. Verstraete, Appl. Microbiol. Biotechnol., **82**, (2009).
5. P. Beese-Vasbender, Bioelectrochem., **102**, (2015).
6. R. K. Thauer, K. Jungermann e K. Decker, Bacteriol. Rev., **41**, (1977).
7. J.-L. Garcia, B. Patel, B. Ollivier, **6**, (2000).
8. Y. Liu, W. Whitman, Ann. N. Y. Acad. Sci., **1125**, (2008).
9. M. Lever, Trends Microbiol., **24**, 2, (2016).
10. F. Sousa, T. Thiergart, G. Landan, S. Nelson-Sathi, I. Pereira, J. Allen, N. Lane, W. Martin, Philos. Trans. R. Soc. B: Biol. Sci., **368**, 1622, (2013).
11. S. Gajaraj, Y. Huang, P. Zheng, Z. Hu, Biochem. Eng. J., **117**, (2017).
12. Q. Fu, Y. Kuramochi, N. Fukushima, H. Maeda, K. Sato, H. Kobayashi, Environ. Sci. Technol., **49**, (2015).
13. D. E. A. Park, Appl. Environ. Microbiol., **65**, (1999).
14. D. Liu, L. Zhang, S. Chen, C. Buisman A. ter Heijne, Water Res., **99**, (2016).
15. Y. Dang, D. Holmes, Z. Zhao, T. Woodard, Y. Zhang, D. Sun, L.-Y. Wang, K. Nevin, D. Lovley, Bioresour. Technol., **220**, (2016).
16. X. Guo, J. Liu, B. Xiao, Int. J. Hydr. En., **38**, (2013).

17. M. Siegert, M. Yates, A. Spormann, B. Logan, ACS Sustain. Chem. Eng., **3**, 2015.
18. A. Schievano, A. Goglio, C. Erckert, S. Marzorati, L. Rago, P. Cristiani, Detritus, **1** (2018)
19. S. Marzorati, A. Goglio, S. Fest-Santini D. Mombelli, F. Villa, P. Cristiani, A. Schievano, Int. J Hydr. En. 44 (2019)
20. C. Cruz Viggi, S. Simonetti, E. Palma, P. Pagliaccia, C. Braguglia, S. Fazi, S. Baronti, M. Navarra, I. Pettiti, C. Koch, F. Harnisch, F. Aulenta, Biotechnol. Biofuels **10**, (2017).
21. J. Mumme, F. Srocke, K. Heeg, M. Werner, Bioresour. Technol., **164**, (2014).
22. A. Rendón-Calle, S. Builes, F. Calle-Vallejo, Curr. Opin. Electrochem., **9,** (2018)
23. R. Chong, Y. Fan, Y. Du, L. Liu, Z. Chang, D. Li, Int. J. Hydr. En., **3** (2018)
24. P. Cristiani, A. Goglio, S. Marzorati, S. Fest-Santini, A. Schievano, Front. En. Res. **8** (2020)
25. M. Ferri, S. Campisi, L. Polito, J. Shen, A. Gervasini, J. Hazard. Mater., 2021, doi: 10.1016/j.jhazmat.2021.126656
26. P.R. Yaashika, P. Senthil Kumar, Sunita Varjani, A. Saravanan, Biotechnol. Reports, **28,** (2020)

Social Life Cycle Assessment of a Proton Exchange Membrane Fuel Cell stack

Eleonora Bargiacchi[1,*], *Felipe* Campos-Carriedo[1], *Diego* Iribarren[1] and *Javier* Dufour[1,2]

[1]IMDEA Energy, Systems Analysis Unit, 28935, Móstoles, Spain
[2]Rey Juan Carlos University, Chemical and Environmental Engineering Group, 28933, Móstoles, Spain

Abstract. Hydrogen systems are gaining importance in view of a progressive decarbonisation of societies, and becoming more and more cost-competitive alternatives in many sectors (e.g., mobility). However, the sustainability of these technologies must be carefully assessed following a holistic approach which embraces not only environmental but also social aspects. Social Life Cycle Assessment (S-LCA) is an insightful methodology to evaluate potential social impacts of products along their life cycle. In the frame of the project eGHOST, social risks of a proton exchange membrane fuel cell (PEMFC) stack were assessed through an S-LCA. The functional unit was defined as one 48 kW stack (balance of plant excluded), targeted for mobility applications. The supply chain was defined assuming Spain as the manufacturing country and involving from the material/energy production plants to the stack manufacturing. Beyond conventional life cycle inventory data, trade information and additional inventory data were retrieved from the UN Comtrade and PSILCA databases, respectively. Besides, working hours for the manufacturing plants of the stack and its subcomponents were calculated based on literature data. Social life cycle inventories were modelled and evaluated using openLCA and the PSILCA method. Two stakeholder categories, workers and society, were considered through the following social indicators: child labour, contribution to economic development, fair salary, forced labour, gender wage gap, and health expenditure. The choice of these indicators is in line with the eGHOST project purpose. Despite the relatively small amount contained in the product, platinum clearly arose as the main social hotspot under each of the selected indicators. At the level of component plants, the manufacturing of bipolar and end plates was also found to be relevant under some indicators. On the other hand, electricity consumption generally accounted for a minor contribution. Overall, in order to avoid burden shifting from environmental to social issues, a careful design of technologies is needed.

1 Introduction

Hydrogen technologies are expected to play a key role in achieving the decarbonisation objectives in the European energy transition (1). This will imply enormous investments in the Fuel Cells and Hydrogen (FCH) sector and a sharp increase in the number of hydrogen production and use devices. Such a ramp-up of the sector will provide beneficial environmental and societal impacts, in particular related to pollution reduction and economic development (1). On the other hand, the steep development and market penetration of FCH systems could create environmental or social issues along their whole supply chain, for instance related to the presence of critical raw materials. Hence, a careful analysis is necessary to avoid burden shifting. Regarding social issues, Social Life Cycle Assessment (S-LCA) has proved to be an effective and increasingly applied methodology to assess the potential social impacts of product systems along their supply chain (2). Updated guidelines have been developed by the United Nations Environment Programme (UNEP) (3). However, few studies have addressed the social life-cycle impacts of FCH systems (4,5), and therefore further effort is needed for a complete assessment of FCH products through a comprehensive approach including social, economic and environmental dimensions (Life Cycle Sustainability Assessment, LCSA). This paper aims at assessing the social life-cycle impacts associated with the manufacturing of a 48 kW Proton Exchange Membrane Fuel Cell (PEMFC) stack, in the framework of the EU-funded project eGHOST (6). Within this project, this S-LCA study will complement the corresponding environmental Life Cycle Assessment (LCA) and Life Cycle Costing (LCC) to build a robust LCSA that drives the eco-(re)design of the PEMFC stack.

* Corresponding author: eleonora.bargiacchi@imdea.org

2 Methodology

2.1 Definition of the case study

The reference product is a 48 kW PEMFC stack, intended for mobility applications. The stack specifications and detailed bill of materials was provided by the manufacturing company SYMBIO. In particular, the stack is designed for subsequent use as a range extender fuel cell for electric vehicles (EV) or as a dual/full-power system for light fuel cell electric vehicles (FCEV). The core of each cell of the stack, where the electrochemical reactions take place, is constituted by the Membrane Electron Assembly (MEA), composed of a Proton Exchange Membrane (PEM), two catalyst layers (made of platinum nanoparticles on a carbon support) and two Gas Diffusion layers (GDL), as shown in Figure 1a.

Gas flows are guided to and removed from the reaction sites throughout the bipolar plates, which separate the cells from one another and provide mechanical support. The power unit is obtained by stacking the unitary entities together by using conventional connectors (screws, clamps, bolts, springs…) and gaskets to ensure tightness (Figure 1b). Finally, the current collector conducts the electricity produced by the stack out of the system.

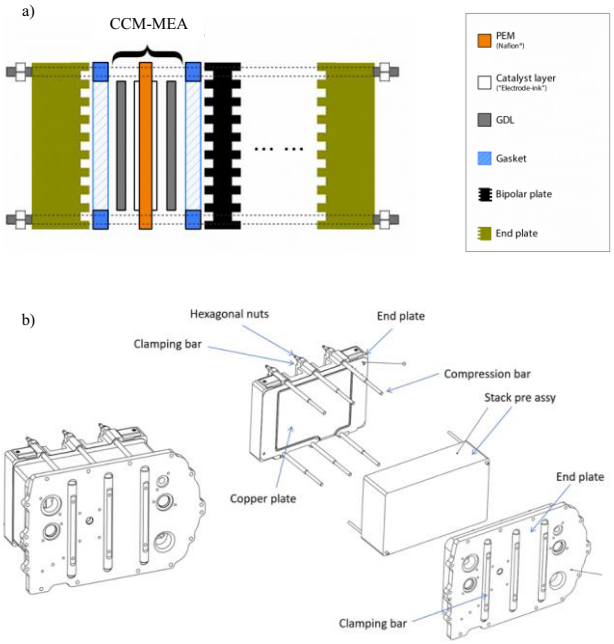

Figure 1. a) Membrane Electrode Assembly (MEA) main components. b) PEMFC stack assembly final step manufacturing. Adapted from (6)

2.2 Goal and scope

The goal of the work is to carry out a detailed S-LCA on the PEMFC stack introduced in Section 2.1. The functional unit (FU) is one PEMFC stack (Balance of Plant – BoP – excluded) The system boundaries are set according to the supply chain definition as explained below.

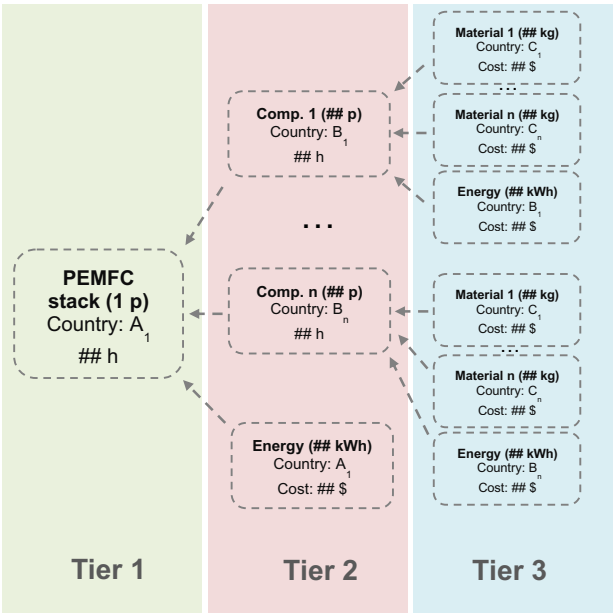

Figure 2. Inventory segmentation for S-LCA

Along the supply chain of the system under evaluation, three tiers are considered, as shown in Figure 2. Tier 1 refers to the stack manufacturing plant; tier 2 involves the plants related to the production of the stack components and the energy flows required by tier 1; and tier 3 contains the plants where the materials and energy flows required by tier 2 are produced. Spain is set as the manufacturing country in tier 1.

The protocol followed to identify the countries involved in the supply chain of the PEMFC stack is based on (7). Setting Spain (final product manufacturer) as the declarant entity, global trade data for each stack component are acquired from the UN Comtrade database (8). A component is found to be also manufactured in Spain if its monetary export-import balance is positive. On the other hand, if the balance is negative, the main exporter is identified. In the end, one manufacturing country is assigned to each of the product components.

When the previous step is completed, a similar procedure is applied to define the origin of tier 3 materials. Each component manufacturing country is set as declarant for every material flow within that component and typified analogously by its trade balance result. However, when identifying relevant exporters, a mix of the ones accounting for more than 50% of global exports to the

declarant country could be found (not necessarily focusing only on the top one as in tier 2).

Tier 2 energy flows are located in Spain. Tier 3 energy flows are located in each of the component manufacturing countries.

2.3 Data acquisition and characterisation

The main source of data for the S-LCA is constituted by the LCA and LCC inventories together with the use of the PSILCA (Product Social Impact Life Cycle Assessment) database (9), which is used as both a database and an impact assessment method. The activity variable that allows impacts calculation is *working hours*, which are retrieved from literature sources for each manufacturing process at the stack component level. The assessment is performed using the openLCA software. The choice of the social indicators to be studied is based on the specific goal of the eGHOST project (i.e. the development of eco-design criteria for FCH products), literature results from previous life-cycle studies of FCH systems (10–12) and the Sustainable Development Goals. Child labour, forced labour and fair salary are selected within the stakeholder category "workers", and health expenditure and contribution to economic development are considered within the category "society".

3 Results and discussion

3.1 Social life cycle inventory

The resultant social life cycle inventory of the 48 kW PEMFC stack, is presented in Figure 3. All values correspond to the functional unit of one stack and monetary flows are expressed in 2015 American Dollars.

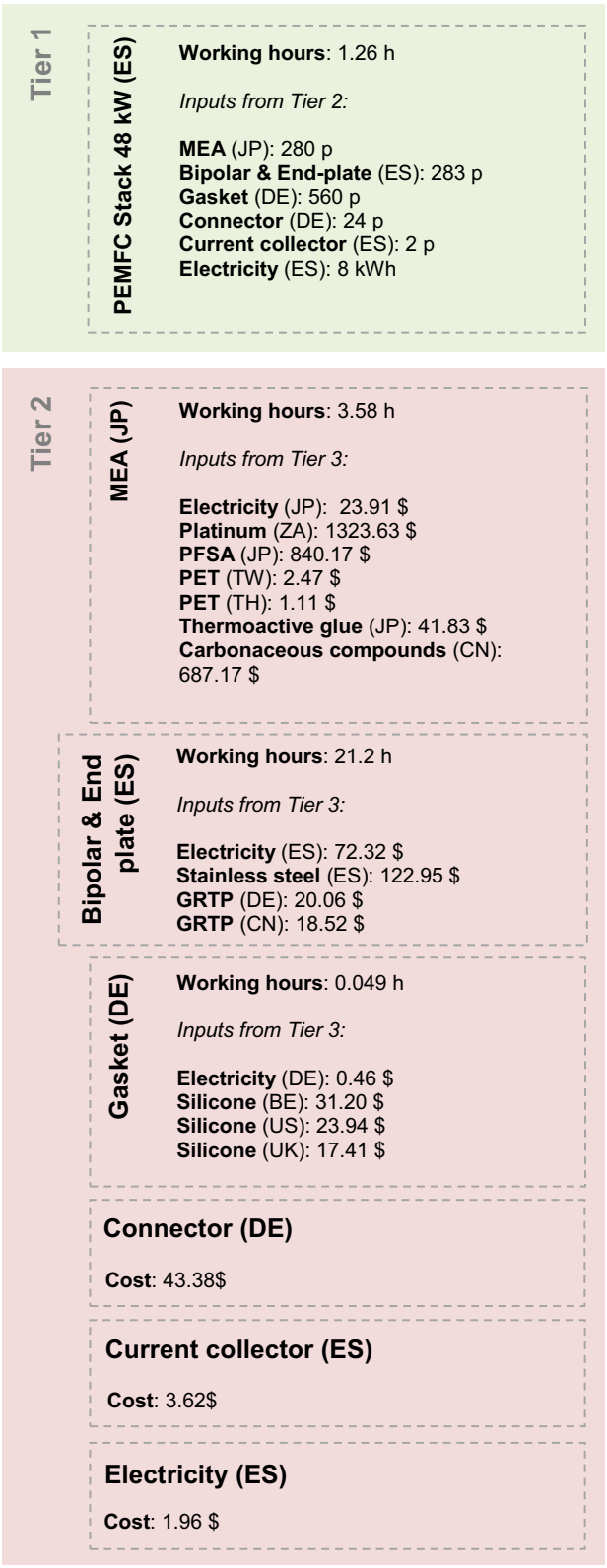

Figure 3. Social life cycle inventory of a 48 kW PEMFC Stack

3.2 Social life cycle impact assessment

The social life cycle profile and the process contribution to the selected impact categories are shown in Figure 4. Despite its low mass fraction (< 0.1% of the total mass of the stack), platinum production in South Africa arises as the main social hotspot for every impact category apart from "contribution to economic development". This is mainly linked to the high specific cost of platinum and the high sector-specific risk level in the relevant manufacturing country (South Africa). The manufacturing of carbonaceous compounds in China is the main contributor to economic development. Among the stack components, bipolar and end plates manufacturing shows a relevant contribution in 5 out of 6 indicators since these components make up 74% of the total mass of the stack. Overall, manufacturing processes at the level of materials are found to present higher social risks than manufacturing processes at the level of components, while the social risks associated with energy production plants are negligible due to the involvement of low-risk countries.

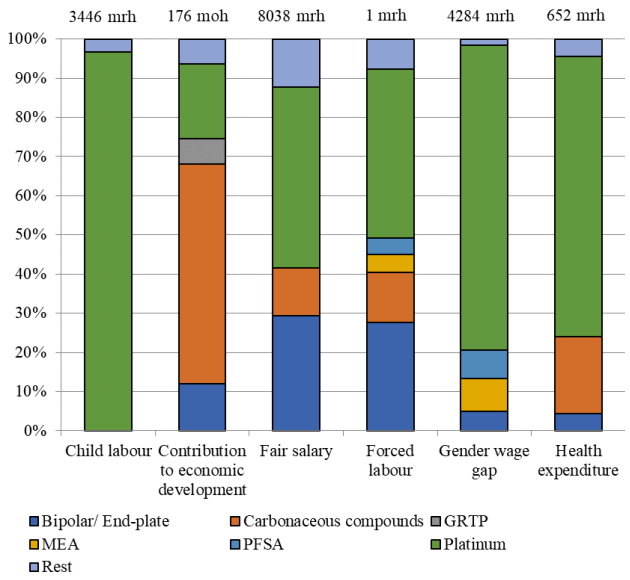

Figure 4. Impact assessment results and process contribution of the reference product

4 Conclusions

In this work the S-LCA of a 48 kW PEMFC stack was performed. Even though platinum means < 0.1% of the total stack weight, its production arises as the key social hotspot over the assessed social indicators due to its high cost and country-specific social risks. A careful eco-design aiming at reducing the catalyst loading is therefore recommended, as well as promoting its recovery in the end-of-life phase.

Acknowledgments

This work was carried out in the context of the project eGHOST. This project has received funding from the Fuel Cells and Hydrogen 2 Joint Undertaking under Grant Agreement No 101007166. This Joint Undertaking receives support from the European Union's Horizon 2020 Research and Innovation programme, Hydrogen Europe and Hydrogen Europe Research. The authors acknowledge CEA, SYMBIO and University of Ljubljana for valuable scientific exchange.

Nomenclature

BE	Belgium
BoP	Balance of Plant
CCM	Catalyst Coated Membrane
CN	China
DE	Germany
EoL	End of Life
ES	Spain
EU	European Union
EV	Electric Vehicle
FCEV	Fuel Cell Electric Vehicle
FCH	Fuel Cells and Hydrogen
FU	Functional Unit
GDL	Gas Diffusion Layer
GRTP	Glass Reinforced Thermoplastic
JP	Japan
LCA	Life Cycle Assessment
LCC	Life Cycle Costing
LCSA	Life Cycle Sustainability Assessment
MEA	Membrane Electrode Assembly
moh	medium opportunity hours
MPL	Microporous Layer
mrh	medium risk hours
PEMFC	Proton Exchange Membrane Fuel Cell
PET	Polyethylene Terephthalate
PFSA	Perfluorosulfonic acid
S-LCA	Social Life Cycle Assessment
TH	Thailand
TW	Taiwan
UK	United Kingdom
UN	United Nations
US	United States of America
ZA	South Africa

References

1. Fuel Cells and Hydrogen Joint Undertaking. Hydrogen Roadmap Europe. 2019. Available from: https://fch.europa.eu
2. Ramos Huarachi DA, Piekarski CM, Puglieri FN, de Francisco AC. Past and future of Social Life Cycle Assessment: Historical evolution and research trends. J Clean Prod. 2020;264:121506.
3. United Nations Environment Programme. Guidelines for Social Life Cycle Assessment of Products and Organizations 2020. Benoît Norris C, Traverso M, Neugebauer S, Ekener E, Schaubroeck T, Russo Garrido S, Berger M, Valdivia S, Lehmann A, Finkbeiner M, Arcese G (eds.). UNEP; 2020.
4. Schlör H, Koj J, Zapp P, Schreiber A, Hake JF. The Social Footprint of Hydrogen Production - A Social Life Cycle Assessment (S-LCA) of Alkaline Water Electrolysis. Energy Procedia 2017;105:3038–44.
5. Werker J, Wulf C, Zapp P. Working conditions in hydrogen production: A social life cycle assessment. J Ind Ecol. 2019;23(5):1052–61.
6. eGHOST. Establishing Eco-design Guidelines for Hydrogen Systems and Technologies. 2021. Available from: https://eghost.eu
7. Martín-Gamboa M, Dias AC, Arroja L, Iribarren D. A protocol for the definition of supply chains in product social life cycle assessment: application to bioelectricity. Sustain Energy Fuels. 2020;4:5533–42.
8. United Nations. UN Comtrade database. [cited 2021 Sep 10]. Available from: https://comtrade.un.org/
9. Maister K, Di Noi C, Ciroth A, Srocka M. PSILCA database v.3 documentation. Green Delta; 2020.
10. Valente A, Iribarren D, Dufour J. Comparative life cycle sustainability assessment of renewable and conventional hydrogen. Sci Total Environ. 2021;756:144132.
11. Valente A, Iribarren D, Dufour J. Life cycle sustainability assessment of hydrogen from biomass gasification: A comparison with conventional hydrogen. Int J Hydrogen Energy. 2019;44(38):21193–203.
12. Martín-Gamboa M, Quinteiro P, Dias AC, Iribarren D. Comparative social life cycle assessment of two biomass-to-electricity systems. Int J Environ Res Public Health. 2021;18(9): 4918.

Assessment of Hydrogen and LNG buses adoption as sustainable alternatives to diesel fuel buses in public transportation: Applications to Italian perspective.

Michele Vincenzo Migliarese Caputi[*1], Rossana Coccia[2], Paolo Venturini[3], Luca Cedola[4], Domenico Borello[5]*

[1-2-3-4-5] Department of Mechanical and Aerospace Engineering –DIMA- Sapienza University of Rome Via Eudossiana, 18 - 00184 Roma, ITALY

Abstract. This work deals with a technical and economical comparison between hydrogen and liquid natural gas (LNG) fueled buses with reference to the standard solution based on diesel fuel internal combustion engines. The level of service is evaluated considering the number of buses replaced and the average kilometers traveled each year for two levels. The economical comparison is made using the Total Cost of Ownership (TCO) method considering capital and operating costs. The costs of LNG and Diesel (at the pump in Italian market) are estimated with reference to the year 2020. Furthermore, an assessment of greenhouse gas emissions will be carried out starting from energy needs, adopting a "cradle to grave" approach, thus evaluating emissions from the well to the tank and from the tank to the wheel. The results show that the operating costs (0.778 €/km) of LNG solution are lower than the Diesel ones (1.072 €/km), while the hydrogen buses can become competitive in the next few .The production of hydrogen with water electrolysis considering the current electricity costs of the Italian market is expensive and involves a cost to the hydrogen pump 7,60 €/kg which makes the operating cost of the hydrogen solution is equal to about 1.420 €/km which makes this solution uncompetitive. It is also important to underline that the cost of green hydrogen production from water electrolysis strongly depends on the cost of electricity. The Life Cicle Analisis (LCA) analysis shows strong environmental benefits of the hydrogen solution in terms of CO_{2eq} if the hydrogen is produced by electrolysis using renewable energy sources. In the other cases, the advantage of using hydrogen is not very strong as it is associated with the use of fossil fuels that release climate-altering substances.

1 Introduction

Issues related to Climate Changes boost the research of innovative solutions to radically reduce emissions. Paris Conference of the Parties (COP21) represents the start point for Europe transition to a decarbonized energy system [1]. It is expected that the implementation of COP21 objectives can have a strong impact, radically transforming the EU strategies in generating, distributing, storing and consuming energy. Major stakeholders are considering all available options to limit energy-related CO_2 emissions to less than 770 Mt/y by 2050, and it is a common opinion that hydrogen can constitute a very interesting solution [2]. According to ISPRA (Italian Higher Institute for Protection and Environmental Research, 2019), in Italy 23% of greenhouse gas emissions are attributable to road transport [3]. A report of European Environment Agency (EEA) states that air pollution caused over 400.000 deaths in Europe per year [5]. Italy is the first European country for premature deaths (more than 10.000) due carbon dioxide, while it is the second one (behind Germany) for deaths due to high nitrogen concentrations (about 3.000 deaths a year) and particulate matter ($PM_{2.5}$) (more than 52.000) [5]. Focusing on the Italian case it is possible to see that most of the pollution-related diseas are related to the low efficiency (and relatively large emissions) of public transportation, pushing travelers and commuters to use private cars instead of choosing public or shared mobility [5]. In this context, the energy transition can be achieved through a gradual shift from a system mostly based on fossil fuels to a more sustainable and renewable energy mix. The use of Liquefied Natural Gas (LNG) as a fuel could significantly contribute to the energy transition [6]. A very competitive solution consists in using green hydrogen as a fuel for electric buses equipped with batteries and hydrogen fuel cells, as also stated in the "Piano Nazionale Ripresa e Resilienza" representing the Italian implementation plan of the Next Generation EU action [7] Hydrogen and fuel cells technologies were identified amongst the new energy technologies needed to achieve a 60 % to 80 % reduction in GHGs emissions by 2050, in the European Strategic Energy Technology Plan presented along with the Energy Policy Package [8]. Use of hydrogen guarantees zero emissions [8][9] at the exhaust pipe and efficient power production in stationary, portable and transport applications. Hydrogen allows a wide diversification of energy sources as it can be produced from several raw materials. In combination with fuels cells, it can also improve energy efficiency in transport and contribute strongly to mitigate climate change especially when produced by renewable primary energy sources (green hydrogen).

* Corresponding author: michelevincenzo.migliaresecaputi@uniroma1.it

Here we analyze the new emerging possibilities for reducing emissions of the transport sector through the substitution of diesel fuels with LNG or Hydrogen. Assuming a bus type and a level of service (in terms of km*bus/year) and computing the needs of the three considered fuels to satisfy such service, we present a comparison using the total cost of ownership (TCO) and Life Cycle Assessment (LCA) [10][36] methods, that allow to account for both the economic and environmental performance.

2 From Diesel to Hydrogen getting through LNG

Recent actions from the countries regulators, as mentioned before, are reducing the diffusion of Diesel fuel while increasing the viability of using alternative fuels, such as natural gas and hydrogen[11]. The effects on environmental quality, health and safety change using Diesel, LNG or hydrogen. Diesel is one of the responsible of urban areas environmental problems. In Italian cities, the urban public transport service mainly relies on the use of diesel buses. In Rome, for example, 92% of the surface service is characterized by the use of buses, most of which powered by Diesel engines [12]. To ensure a transition to a lower environmental impact, is necessary to consider the employment of LNG buses at first and later Hydrogen ones. For the supply, there are not critical problem because of the high capillary action of the Italian gas network [13] combined, with the possibility of building small NG liquefaction plants. **Table 1** show the comparison of the calorific value between different fuels

Table 1. Comparison of the calorific value between different fuels

Type of Fuel	LNG (T=-160 °C, P=1 atm)	H2 (T=25 °C, P=1 atm)	Diesel (T=25°C, P=1 atm)
Density [g/L]	446	0.0899	835
LHV [kWh/kg]	13.50	33.3	11.70
LHV [Wh/L]	6,100	3	10,000

As reported in [14] the main advantages of using LNG compared to Diesel are lower maintenance costs, greater price stability, lower polluting emissions, greater safety. LNG has an energy content per unit mass greater than Diesel fuel, but it is smaller in terms of energy per unit volume. Moreover, the low LNG storage temperature**,** needed to increases the energy contend, makes the tanks more complex than those for Diesel.

In this study the Hydrogen is considered to be employed with fuel cells, thus the only emission are water and hot air. Vehicles powered by Hydrogen fuel cells have a driving range similar to the Diesel fueled one, and they can be refueled in about the same time, which makes fuel cell vehicles suitable for long-haul. It is important to consider how the Hydrogen is produced and to assess the emissions associated to the Hydrogen (H2) transport. Nowadays, green Hydrogen is mainly produced by dissociation of water in electrolysers (using electricity from renewable sources). It can be used in the form of compressed gas or liquid cryogenic [15]. As compress gas Hydrogen can be supplied by existing natural gas pipelines. “To date, SNAM, the operator of the Italian gas network, estimates that over 70% of its pipelines are ready to transport hydrogen”[16] .

3 Methodology

Is of a paramount important establishing a balance between the three main pillars of sustainable production, namely the social, economic, and environmental aspects[15]. TCO has long been recognized as an important technique for the evaluation of the total cost of ownership of a product from cradle to grave and it has frequently been used in decision making processes. The TCO approach considers not only the initial cost of purchase but also usage, maintenance and disposal/resale value of a product. According to this approach, in the long run a product with a higher purchase cost could still be economically more advantageous than others with lower purchase cost. In Addition, an indicator that allows to evaluate environmental performance of a product is the carbon footprint. It corresponds to the entire amount of greenhouse gas (GHG) produced to support the lifestyle and activities of a person directly and indirectly, or the production, use and disposal of a product. Carbon footprint is usually measured in tons of CO_{2eq}, over the period of one year, and it can be associated with an individual, organization, product or event, among others. To evaluate this indicator the LCA approach can be used. LCA is the quantitative environmental assessment of a product over its entire life cycle, including raw material acquisition, production, transportation, use and disposal [15]. Therefore, it is a good way to measure the real environmental footprint of a product [10]. For a given transport system and with reference to the fuels used, LCA results in the so called "Well-to-Wheels" approach (WTW) [36]. For the sake of convenience, the evaluation in the present paper will be divided into two successive steps, "Well-to-Tank" (WTT) and “Tank-to-Wheels” (TTW), each considering specifics operations, as shown in (Fig. **1**).

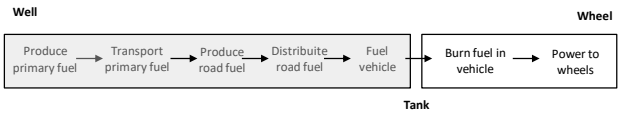

Fig. 1. “Well-to-Wheels" approach

TCO and LCA methods will be here applied to evaluate the three transport systems considered from both the economic and environmental points of view, to compare them aiming at giving an indication on the more convenient choice for the energy transition process.

4 Vehicle specifications and operating data

The present study is focus on local public transport in urban areas, are considered 12 m Buses, used in Italian

medium/big cities. The comparison is performed considering three different kind of Bus.

1. Bus powered by Diesel fueled internal combustion engine (DF Bus)
2. Bus powered by LNG fueled internal combustion engine (LNG Bus)
3. Electric Bus in which electricity is produced by hydrogen fuel cells (FC Bus)

In the present study we assume that each Bus travels 90,000 km/y (working for 300 days/y for 17 hours). To evaluate the scale effect, two fleets are considered: the first (A) is composed of 15 Buses, and the second one (B) by 30 Buses. This leads to the definition of the two global service levels reported in Table 2.

Table 2. Global service level of the two considered Bus fleets.

Fleet name	No. Bus	km/y per Bus	Fleet service level (km/year)
A	15	90,000	1,350,000
B	30	90,000	2,700,000

The main technical characteristics of the considered Buses are taken form the manufacturers web sites, and they will be presented in sections 4.1-4.3, where specific fuel consumption per 100 persons transported (SFC100) [17] will be also computed.

4.1. DF Bus

As a conventional Bus, we considered the Iveco Cursor 9, one of the newest in service in Rome. It has a range about 900 km and meets EURO VI emission limits. Table 3 reports the main characteristics of this Bus [18].

Table 3. Main characteristics of Cursor 9 Bus [18] .

Model	Cursor 9 Diesel (Iveco)
Size [m]	12
Diesel storage [kg]	371
Estimated specific consumption [kg/km]	0.49 [17]
Emissions	Euro VI

Knowing the technical data sheet (provided by the manufacturer), it is possible to easily calculate the fuel required in the two scenarios analyzed (Table 2) as shown in tab.4

Table 4. Annual consumption of diesel

Service level	kg of Diesel/year
A	661,500
B	1,323,000

4.2. LNG Bus

The LNG bus here considered is the Irizar Bus, one of the solutions recently adopted by some urban centers in Emilia-Romagna [19]. The storage pressure of 1 atm and temperature of -160 ° C occupy a volume of tanks of approximately 1.260 liters. The specific consumption value will be used in the following for the calculation of the fuel requirement for the different service levels [17]. The environmental benefits offered by coaches with this technology reduce CO_2 emissions by between 20 and 25%, NOx by up to 60% and emissions of particulate matter by over 98%. In addition to higher thermal performance than diesel, vibrations and noise emissions are also reduced by between 4-5 dB [20] [21]. The technical characteristics are shown in **Table 5**.

Table 5. Specifications of Irizar LNG Bus [21]

Model	Irizar i4
Size [m]	12
LNG storage [kg]	240
Estimated specific consumption [kg/km]	0.44 [17]
Emissions	Euro VI

The quantification of LNG needs for the two levels of service is shown in Table 6.

Table 6. Service level Bus fleet and quantity of fuel LNG

Service level	kg of LNG / year
A	594,000
B	1,1888,000

In relation to operating cost, it is estimated that its reduction can reach up to 35% of the total cost of consumption and maintenance, depending on the differential between the cost of gas and diesel. In the case under study, the specific consumption is assessed on the same database of the DF-bus [17]. The maintenance cost remains similar to that of a conventional diesel vehicle [20] [21][17].

4.3. FC Bus

The technical characteristics of the Bus, shown in Table 7, refer to the Solaris Urbino 12 Hydrogen equipped with the fuel cells supplied by Ballard. The hydrogen is stored in 5 cylinders of composite material of 312 liters at a pressure of 350 bar [22]. The actual hydrogen consumption of a FC Bus will depend on the operation of each specific Bus and will take into account passenger load, route, speed, and heating and cooling requirements. Recent Ballard publications, for the current generation of fuel cell electric buses, estimate an average fuel consumption of 8 kg kilograms of hydrogen per 100 kilometers [[23]] [[24]]. This value will be used in this study for the assessment of the hydrogen requirement for the two chosen service levels which is shown in the **Table 8**

Table 7. Specifications FC Bus [22]

Model	Solaris Urbino 12 Hydrogen
Size [m]	12
Battery power lithium-ion-phosphate [kWh]	28
Fuel cell power FCmove [kW]	70
Hydrogen storage [kg]	36.8
Fuel cell lifetime [hours]	>30,000 [23]
Emissions	Only heat and water

Table 8. Service level Bus fleet and quantity of fuel H_2

Service level	kg of Hydrogen / year
A	108,000
B	216,000

For the production of hydrogen, the case of production by SMR and electrolysis will be evaluated. For the latter case, production is based on electricity produced from renewable sources or extracted from the Italian national grid. The production costs related to hydrogen from electrolysis were estimated for two scenarios:

- electrolysers that use mains electricity,
- a direct physical connection between a renewable electricity source (RES) and the electrolysers.

In the first case, the emissions are linked to the type of network used; and in Europe and Italy electricity is not yet produced entirely from renewable sources. In the second case of direct connection, 100% of the electrolyser production is renewable.

5 TCO analysis

The methodology adopted to include economic factors in the assessment of sustainability is the Total Cost of Ownership (TCO) mentioned above. The TCO approach is implemented by considering the initial Capital Expenditure (Capex), maintenance and OPerating EXpense (Opex) incurred them in the buses lifetime (12 years) [22][23], (assuming no residual value for the assets); they are discounted at a 4% financial rate too. In fuel cell buses, after an estimated operating period of 30.000 hours (6 years see, section 4) should be considered a cost of overhauling (refurbished) (The cost of replacing the cells is estimated at € 24.000 ($ 30.000 USD) [22] with estimated downward costs in the coming years. A disposal cost equal to 1% of the purchase cost is assumed.

The Net Present Value (NPV), having expressed the Opex costs in terms of € / km, allows us to define the operating cost in the same way.

5.1. DF Bus

In Table **9** it is possible to evaluate the purchase, fuel and maintenance costs for the Bus mentioned in section 4.1.

Table 9. DF Bus Costs

Model	Diesel Urban Bus
Purchasing cost [€]	250,000 [25]
Fuel cost [€/kg]	1.576 [26]
Maintenance cost [€/km]	0.30 [27]

In **Table 10** are reported the Capex and disposal costs of the DF Bus fleet for the two scenarios.

Table 10. Capex of the DF Bus fleet

Scenario	1	2
Capex DF Bus [€]	3,750,000	7,500,000
Disposal cost estimated at 1% of the Capex DF Bus	1 %	
Disposal cost [€]	37,500	75,000

In Table 11 are reported the Opex of the Diesel Bus fleet for the two scenarios:

Table 11. Opex of the DF Bus fleet

Scenario	1	2
Fuel Costs Annual [€]	1,042,556	2,085,111
Maintenance cost [€]	405,000	810,000
Total Opex DF Bus [€]	1,447,556	2,895,111

Table **12** shows the NPV and the operating cost in €/km and the % Capex and % Opex for the DF Bus fleet. The NPV defines the present value of the Capex and Opex expenses (12 year) by discounting them (at 4% financial rate) on the basis of the rate of return.

Table 12. NPV and operating cost DF Bus fleet

Scenario	1	2
NPV [€]	17,358,839	34,717,679
Operating cost €/km	1.072	1.072
% Capex	72%	72%
% Opex	28%	28%

5.2. LNG Bus

In Table 13 are reported the purchasing, fuel and maintenance costs for the LNG Bus mentioned in section 4.2.

Table 13. LNG Bus Costs

Model	LNG Urban Bus
Purchasing cost [€]	258,000 [28]
Fuel cost [€/kg]	0.950 [26]
Maintenance cost [€/km]	0.27 [27]

In Table 14 are reported the Capex and disposal cost of the LNG Bus fleet for the two scenarios.

Table 14. Capex of the LNG Bus fleet

Scenario	1	2
Capex LNG Bus [€]	3,870,000	7,740,000
Disposal cost estimated at 1% of the Capex LNG Bus	1 %	
Disposal cost [€]	38,700	77,400

In **Table 15** is reported the Opex of the LNG Bus fleet for the two scenarios.

Table 15. Opex of the LNG Bus

Scenario	1	2
Fuel Costs Annual [€]	564,300	1,128,600
Maintenance cost [€]	364,500	729,000
Total Opex LNG Bus [€]	928,800	1.857.600

Table 16. shows the NPV and the operating cost in €/km and the % Capex and % Opex for the LNG Bus fleet.

Table 16. NPV and operating cost of LNG Bus fleet

Scenario	1	2
NPV [€]	12,611,028	25,222,057
Operating cost €/km	0,778	0,778
% Capex	81%	81%

% Opex	19%	19%

5.3. FC Bus

In Table 17 it is possible to value the purchasing, fuel and maintenance costs for the FECBs mentioned in section 4.3.

Table 17. FC Bus Costs

Model	Hydrogen Urban Bus
Purchasing cost [€]	625,000 [30]
Fuel cost [€/kg]	See the (Table **18**)
Maintenance cost [€/km]	0.32 [8][24]
Maintenance cost of Fuel Cell [€/km]	0.1 [8][24]
Cost replacement Fuel Cell [€]	24,000 [8][24]

Several options will be considered for the assessment of the cost of hydrogen. The solutions studied are shown in the Table **18** and the production costs will be explained in the next section 5.3.1 and 5.3.2.

Table 18. Hydrogen costs

Hydrogen production method	Costs €/kg
SMR with CCS	4.91
Electrolysis with electricity supplied by the Italian grid	7.60
Electrolysis with electricity supplied by FER	9.2

In Table 19 is reported the Capex of the FC Bus fleet for the two scenarios.

Table 19. Capex of the FC Bus fleet

Scenario	1	2
Capex FC Bus [€]	9,375,000	18,750,000
Disposal cost estimated at 1% del Capex	1,00%	
Disposal Cost [€]	93,750	187,500
Replacement Stack Cell [€]	360,000	720,000

For hydrogen-powered buses, the operating costs obtained with the TCO method are shown below by varying the purchase cost of hydrogen, considering three different procurement methods.

5.3.1 Case 1 Hydrogen from SMR with CCS (Blue Hydrogen)

Steam Reforming (SR) or Steam Methane Reforming (SMR) is a methodology used for the production of hydrogen exploiting the reaction of hydrocarbons with water. Therefore, if hydrogen has to play a role in reducing the impact of climate change, it will need to be produced with concomitantly low carbon dioxide emissions, which, when using natural gas as a feedstock, implies coupling it with carbon capture and storage (CCS) technologies. The estimated production costs for the EU markets today, for fossil-based hydrogen, are highly dependent on natural gas prices. In 2020 hydrogen from SMR without CO_2 capture and storage has an estimated cost of 1,41 €/kg [30]. CO_2 capture and storage process generates an additional production cost estimated at around € 0.50 / kg [31][32]. For the evaluation of the cost of hydrogen to the nozzle pump, must be evaluated the additional costs for storage and distribution. Another costs that have a significant impact is related to the Refueling station (HRS). These costs change in each different European countries. A study based in Germany [33] evaluates them in a range from 2 to 4 € / kg. In this paper an average cost of 3 € / kg is estimated. The distribution costs at the pump is therefore estimated by us at 4,91 €/kg. In Table 20 the Opex of the FC Bus fleet for the two scenarios are reported.

Table 20. Opex of the FC Bus fleet

Scenario	1	2
Fuel Costs Annual [€]	€ 530,280	€ 1,060,560
Maintenance cost [€]	€ 594,000	€ 1,188,000
Total Opex FC Bus [€]	€ 1,124,280	€ 2,248,560

Table 21 shows the NPV and the operating cost in €/km and the% Capex and % Opex for the FC Bus fleet with hydrogen produced by SMR with CCS.

Table 21. NPV and operating cost of FC Bus fleet-SMR and CCS

Scenario	1	2
NPV [€]	20,269,520	40,539,040
Operating cost €/km	1.251	1.251
% Capex	90%	90%
% Opex	10%	10%

5.3.2 Production of hydrogen by electrolysis

The production of hydrogen through water electrolysis is a process that requires a lot of energy. The consumption of electricity to produce one kg of hydrogen is in the range of 54 to 65 kWh [35] therefore the cost of electricity has a significant impact on its cost.

5.3.3 Case 2 Electrolysis with electricity supplied by the Italian grid

This scenario requires the purchase of electricity from the Italian national grid. In 2020, the costs of hydrogen production using grid electricity in the EU were estimated in the range 1.8-7.7 € / kg [31]. In Italy the cost is estimated at 4.1 € / kg [30]. Therefore, for the above cost considerations, the pump cost is valued at 7.6 € / kg.

In **Table 22** the Opex of the FC Bus fleet for the two scenarios are reported with Hydrogen produced with electricity supplied by the Italian grid.

Table 22. Opex of the FC Bus fleet

Scenario	1	2
Fuel Costs Annual [€]	820,800	1,641,600
Maintenance cost [€]	594,000	1,188,000

Total Opex FC Bus [€]	1,414,800	2,829,600

Table 23 shows the NPV and the operating cost in €/km and the% Capex and % Opex for the FC Bus fleet with electricity supplied by the Italian grid.

Table 23. NPV and operating cost of FC Bus fleet Hydrogen from electricity supplied by the Italian grid

Scenario	1	2
NPV [€]	22,996,072	45,992,143
Operating cost €/km	1.420	1.420
% Capex	87%	87%
% Opex	13%	13%

5.3.4 Case 3 Electrolysis with electricity supplied by FER (Green Hydrogen)

This scenario envisages that electricity is purchased entirely from renewable sources assuming a production cost of 5.7 € / kg [30] and a pump cost of 9.2 € / kg, due to the previous considerations on the additional cost. In Table **24** the Opex of the FC Bus fleet for the two scenarios are reported.

Table 24. Opex of the FC Bus fleet

Scenario	1	2
Fuel Costs Annual [€]	993,600	1,987,200
Maintenance cost [€]	594,000	1,188,000
Total Opex FC Bus [€]	1,587,600	3,175,200

Table 25 shows the NPV and the operating cost in €/km and the% Capex and % Opex for the FC Bus fleet

Table 25. NPV and operating cost of FC Bus fleet Hydrogen with electricity supplied by FER

Scenario	1	2
NPV [€]	24,617,812	49,235,625
Operating cost [€/km]	1.520	1.520
% Capex	86%	86%
% Opex	14%	14%

6 Carbon footprint

A carbon footprint corresponds to the whole amount of greenhouse gases (GHG) produced to, directly and indirectly, support a person's lifestyle and activities. Carbon footprints are usually measured in CO2eq, [35] during the period of one year, and they can be associated with an individual, an organization, a product or an event, among others. The GHGs whose sum results in a carbon footprint can come from the production and consumption of fossil fuels, food, manufactured goods, materials, roads or transportation. It not simple to calculate carbon footprints due to poor knowledge and short data regarding the complex interactions between contributing processes including the influence of natural processes that store or release carbon dioxide. The analysis that considers the entire cycle is the so-called "from Cradle to Grave", which in the case of fossil fuels takes the name of "Well to Wheel" (WTW) [35][36] which is increasingly used as a tool decision support to provide an effective contribution towards greater asset sustainability. The Well to Wheel, analysis is often divided into two phases respectively called: Well to tank (WTT) and Tank to Wheel (TTW). The WTT and TTW for the three types of buses powered by Diesel, LNG and Hydrogen, are reported below. The Upstream fuel emissions (WTT) are based on the extraction, refining, transport and distribution of fuels.

6.1. DF Bus

Table 26 shows the WTT emissions related to the production of Diesel [38].

Table 26. Emissions WTT DF Bus

Emissions WTT DF Bus		
Scenario	1	2
Emissions WTT CO_{2eq} [g/kg] of fuel produced	3,150 [38]	
Total Emissions WTT CO_{2eq} [t/year]	2,083.73	4,167.45

In **Table 27** show the TTW emissions related to the use of Diesel Bus [39]

Table 27. Emissions TTW DF Bus

Emissions TTW DF Bus		
Scenario	1	2
Emissions TTW CO_{2eq} [g/km]	1,129 [39]	
Total Emissions TTW CO_{2eq} [t/year]	1,524.15	3,048.30

In Table 28 show the WTW emissions for the DF-Bus

Table 28 Emission WTW for DF Bus

Emissions WTW DF Bus		
Scenario	1	2
Total Emissions WTW CO_{2eq} [t/year]	3,607.88	7,215.75

6.2. LNG Bus

In **Table** 29 shows the WTT emissions related to the production of LNG fuel (16,52 g CO_2/MJ) [40]

Table 29. Emissions WTT LNG

Emissions WTT LNG Bus		
Scenario	1	2
Emissions WTT CO_{2eq} [g/kg] of fuel produced	803 [40]	
Total Emissions WTT CO_{2eq} [t/year]	476.98	953.96

In Table **30** shows the TTW emissions related to the use of LNG Bus[39].

Table 30. Emissions TTW LNG Bus

Emissions TTW LNG Bus		
Scenario	1	2
Emissions TTW CO_{2eq} [g/km]	1,096[39]	
Total Emissions TTW CO_{2eq} [t/year]	1,479.60	2,959.20

In **Table 31** show the WTW emissions for the LNG-Bus

Table 31 Emission WTW for LNG Bus

Emissions WTW LNG Bus		
Scenario	1	2
Total Emissions WTW CO_{2eq} [t/year]	1,956.58	3,913.16

6.3.FC Bus

In Table 32 show the WTT emissions related to the production of Hydrogen from SMR with CCS [41]

Table 32. Emissions WTT Hydrogen production from SMR with CCS

Emissions WTT Hydrogen SMR-CCS		
Scenario	1	2
Emissions WTT CO_{2eq} [g/kg] of fuel produced	3,130 [41]	
Total Emissions WTT CO_{2eq} [t/year]	338.04	676.08

In **Table 33** shows the WTT emissions relating to the production of hydrogen at the pump in HRS, with electrolysis with electricity produced from the mix of the Italian national grid. The CO2eq emissions to produce one kWh of energy in Italy are estimated at 307.7 g CO_{2eq} / kWh[38].

Table 33. Production of hydrogen by electrolysis with electricity produced from Italian national network mix

Emissions WTT Production of hydrogen by electrolysis		
Scenario	1	2
CO_{2eq} [g/ kWh] electricity produced	307.7[38]	
Electricity consumed in the HRS to produce 1 kg of H2. [kWh]	60	
Emissions WTT CO_{2eq} [g/kg] of fuel produced	18,462	
Total Emissions WTT CO_{2eq} [t/year]	1,993.30	3,987.79

In Table 34 show the WTT emission related to production of hydrogen by electrolysis with electricity produced from FER (20 g CO_{2eq} /MJ H_2) [42]

Table 34. Production of hydrogen by electrolysis with electricity produced from FER

Emissions WTT Production of hydrogen by electrolysis with electricity produced from FER		
Scenario	1	2
Emissions WTT CO_{2eq} [g/kg] of fuel produced	2,400	
Total Emissions WTT CO_{2eq} [t/year]	259.20	518.40

The TTW emissions for the FC Bus are zero as there are no emissions from the tailpipes.

7 CONCLUSIONS

This paper shows that the LNG solution is, nowadays, an improvement of DF Bus solution both from economic and environmental point of view. The higher purchase price of LNG buses, consisting in bigger Capex, does not affect the quality of the solution chosen over the full operating life. The lower operating costs met advantage the LNG solution to have more profitable operating costs €/km than the DF Bus solution, see (Table **12** and Table 16). The FC Bus solution shows a higher operating cost €/km. The higher costs of this solution are linked to the higher price of acquiring buses and fuel, which, however, is needed in smaller quantities. As can be seen from tables 21, 24 and 27, the price change of hydrogen relative to the production method used, involves a significant change in operating costs. If the purchase cost of the FC Bus sees a reduction of 5% per year for the next 10 years and the price of green hydrogen does not exceed the value of 5 €/kg, a scenario would arise in which operating costs €/km of the hydrogen solution would approach those of DF and LNG Bus. A further reduction in the price of hydrogen, below 3 €/kg, would bring the operating costs of the hydrogen scenario below 1 €/km. About the environmental aspect, the LNG solution is an improvement over the Diesel solution for both WTT and TTW emissions. Furthermore, this solution involves lower WTT emissions even compared to the FC Bus solution with hydrogen produced by SMR with CCS. However, comparing the overall emissions data (WTT + TTW) of the three solutions (DF, LNG and FC Bus), with hydrogen produced by SMR with CCS, it emerges that the hydrogen solution has the least impact on the environment. The study highlights that WTT emissions related to the production of hydrogen from electrolysis are related to the method of producing electricity. In fact, the use of electricity produced by the Italian national grid involves more emission of CO_{2eq} than fossil solutions. However, the total emissions (WTT + TTW) are lower than the DF Bus solution and higher than the LNG Bus solution. The best solution, and desirable in the near future, from the environmental point of view, is represented by the production of hydrogen from water electrolysis, using the electricity produced from renewable sources. This solution have a strong environmental benefits in terms of CO_{2eq} emissions. In the other cases, the advantage of using hydrogen is not very strong. Finally, the choice of having two service levels (A-B) was made to evaluate the possible scale effect on capex, but the value of the capex remained unchanged.

References

[1] https://ec.europa.eu/clima/policies/international/negotiations/paris_en. (Accessed: April 2021).

[2] Hydrogen roadmap europe, Fuel Cells and Hydrogen 2 Joint Undertaking, 2019.

[3] D. Romano, C. Arcarese, A. Bernetti, A. Caputo, M. Cordella, R. De Lauretis, E.Di Cristofaro, A.Gagna, B. Gonella, F. Moricci, G. Pellis, E. Taurino, M. Vitullo.

[4] ISPRA, National Inventory Report, Istituto Superiore per la Protezione e la Ricerca Ambientale April 2020.

[5] Air quality in Europe 2020 report, EEA Report No 09/2020, ISSN 1977-8449

[6] https://www.ispionline.it/en/pubblicazione/leading-way-towards-successful-energy-transition-role-lng-25140. (Accessed: April 2021).

[7] https://www.governo.it/sites/governo.it/files/PNRR.pdf (Accessed: September 2021).

[8] https://ec.europa.eu/energy/topics/energy-system-integration/hydrogen_en#eu-hydrogen-strategy (Accessed: September 2021)

[9] https://www.iea.org/reports/the-future-of-hydroge (Accessed September 2021)

[10] Selin Gundes, The Use of Life Cycle Techniques in the Assessment of Sustainability, Urban Planning and Architecture Design for Sustainable Development, UPADSD 14- 16 October 2015.

[11] https://ec.europa.eu/transport/sites/transport/files/themes/strategies/doc/2011_white_paper/white-paper-illustrated-brochure_it.pdf. (Accessed: April 2021).

[12] T. Ammendola, I. Calcaterra, A. Cardoni, P. Carrozzi, R. Cipollone, C. Dionigi, M. L. Giarrizzo, E. Iegri, S. Iuliano, F. Mori, O. Noci, L. Panzali, L. Papacci, S. Pascucci, R. Polverini, G. Rauco, S. Sammarco, N.Signoretti, C. Villani, Rapporto statistico sull'area metropolitana romana, 2019.

[13] https://www.snam.it/it/trasporto/Archivio/Anno-termico_2013_2014/Info-agli-utenti/.(Accessed: September 2021).

[14] https://www.enestas.com/advantages-of-lng-vs-diesel/?lang=en. (Accessed: April 2021).

[15] https://theconversation.com/hydrogen-where-is-low-carbon-fuel-most-useful-for-decarbonisation-147696. (Accessed: April 2021).

[16] https://www.snam.it/en/energy_transition/hydrogen/snam_and_hydrogen/.(Accessed: September 2021).

[17] https://www.trentinotrasporti.it/azienda/trentino-trasporti/autoBus-e-treni/400-emissioni-e-consumi-degli-autoBus. (Accessed: April 2021).

[18] https://cdnwp.dealerk.com/eed49ed7/uploads/sites/553/2019/04/crossway-pro-scheda-tecnica.pdf. (Accessed: April 2021).

[19] https://www.regione.emilia-romagna.it/notizie/2021/marzo/mobilita-flessibile-integrato-sicuro-e-digitale-presentate-le-linee-guida-del-trasporto-pubblico-investimento-per-oltre-240-milioni-di-euro. (Accessed: April 2021).

[20] https://www.irizar.com/brasil/en/irizar-incorporates-natural-gas. (Accessed: April 2021).

[21] https://www.sustainable-Bus.com/news/irizar-is-ready-to-launch-cng-and-lng-intercity-Buses-and-coaches/ (Accessed: April 2021).

[22] https://www.solarisbus.com/en/vehicles/zero-emissions/hydrogen "Zero Emissions Powertrains Product Catalogue 2021/2022". (Accessed: April 2021).

[23] Ballard Jen 2021 Fuel Cell Electric Buses Proven Performance and the Way Forward.

[24] Roland Berger, Fuel Cell Electric Buses –Potential for Sustainable Public Transport in Europe, A Study for the Fuel Cells and Hydrogen Joint Undertaking, FCH JU – Commercialization Strategy for Fuel Cell Electric Buses in Europe,2015.

[25] Dipartimento Mobilità e Trasporti Direzione Trasporto Pubblico Locale UFFICIO GESTIONE CONTRATTI SOCIETÀ PRIVATE Determinazione Dirigenziale NUMERO REPERTORIO QG/814/2020 del 19/08/2020 NUMERO PROTOCOLLO QG/26435/2020 del 19/08/2020 "Comune di Roma".

[26] https://dgsaie.mise.gov.it/prezzi-annuali-carburanti?pid=2. (Accessed: April 2021).

[27] Roland Berger GmbH, "Fuel Cell Electric Buses - Potential For Sustainable Public Transport In Europe." München: The Fuel Cells and Hydrogen Joint Undertaking, 2015. Web. November 1, 2016.

[28] https://www.tper.it/Trasporto Passeggeri Emilia-Romagna – S.p.A Sede legale Via di Saliceto, 3 – 40128 Bologna. Accessed: April 2021. (Accessed: April 2021).

[29] Ivan Smajla, Daria Karasalihović Sedlar, Branko Drljača and Lucija Jukić, Fuel Switch to LNG in Heavy Truck Traffic,6 February 2019, Energies 2019, 12, 515; doi:10.3390/en12030515

[30] https://www.sustainable-Bus.com/news/major-fuel-cell-Bus-order-for-solaris-from-rvk-cologne-15-solaris-hydrogen-on-delivery/.(Accessed: April 2021).

[31] Hydrogen Europe Clean Hydrogen Monitor 2021, Hydrogen Europe

[32] Global Hydrogen Review 2021, International Energy Agency Website: www.iea.org

[33] IEAGHG Technical Report 2017-02, Techno-Economic Evaluation of SMR Based Standalone (Merchant) Hydrogen Plant with CCS.

[34] Markus Reußa, Thomas Grubea, Martin Robiniusa, Detlef Stoltena, "A hydrogen supply chain with spatial resolution: Comparative analysis of infrastructure technologies in Germany"

[35] John A. Turner, Sustainable Hydrogen Production Science, 305 (5686), DOI: 10.1126/science.1103197

[36] Well-To-Wheels Analysis of Future Automotive Fuels And Powertrains In The European Context. European Commission Joint Research Centre Institute for Energy and Transport. Report EUR 26237 EN 2014.

[37] V. Konecný, J. T. Settey, F. Petro, T. Skrúcaný and T. Figlus. Environmental Sustainability of the Vehicle Fleet Change in Public City Transport of Selected City in Central Europe, Energies 2020, 13, 3869; doi:10.3390/en13153869

[38] Caserini, P. Baglione, D. Cottafava, M. Gallo , F. Laio, G. Magatti , V. Maggi , M. Maugeri , L. Moreschi , E. Perotto , L. Pizzol, E. Semenzin, A. Senese; FATTORI DI EMISSIONE DI CO2 PER CONSUMI ENERGETICI E TRASPORTI PER GLI INVENTARI DI GAS SERRA DEGLI ATENEI ITALIANI dx.doi.org/10.32024/ida.v6i1.207 Ingegneria dell'Ambiente Vol. 6 n. 1/2019 Stefano.

[39] Alternative Bus Technologies August, 2018 Produced by: C40 Cities Finance Facility in collaboration with Grütter Consulting. https://cffrod.s3.amazonaws.com/storage/files/J5uOxG6boRSm6lb8EyU8lACO1Y3EhX53gx1yEKJs.pdf

[40] D. A. Hagos, E. O. Ahlgren. Well-to-wheel assessment of natural gas vehicles and their fuel supply infrastructures – Perspectives on gas in transport in Denmark. https://doi.org/10.1016/j.trd.2018.07.018.

[41] C. Antonini, K. Treyer, A. Streb, M. van der Spek, C. Bauer and M. Mazzotti Hydrogen production from natural gas andbiomethane with carbon capture and storage - A techno-environmental analysis. DOI: 10.1039/d0se00222d

[42] Fuel Cells and Hydrogen Applications for Regions and Cities Vol. 2 Brussels and Frankfurt, September 2017 Roland Berger and FCH

Comparative study of Global, European and Italian Standards on Hydrogen Refueling Stations

Matteo Genovese[1*], *Viviana* Cigolotti[2], *Elio* Jannelli[3] and *Petronilla* Fragiacomo[1]

[1]Department of Mechanical, Energy and Management Engineering, University of Calabria, Arcavacata di Rende, 87036 Cosenza, Italy
[2]Laboratory for Energy Storage, Batteries and Hydrogen Production and Utilization Technologies, Department of Energy Technologies and Renewable Sources, ENEA—Italian National Agency for New Technologies, Energy and Sustainable Economic Development, Research Centre of Portici, 80055 Naples, Italy
[3]Department of Engineering, University of Naples "Parthenope", Centro Direzionale Is. C4, 80143 Naples, Italy

Abstract. The purpose of this paper is to give a strategic overview of the existing standards governing the construction and operation of hydrogen refueling stations. A succinct and comprehensive study of hydrogen refueling station standards globally, in Europe, and in Italy is conducted and discussed in light of the new European Hydrogen Strategy and Roadmap. Among the numerous topics examined, a particular emphasis is placed on the standards in force for on-site hydrogen production via water electrolysis, hydrogen storage, both liquid and gaseous, and refueling protocols for light-duty and heavy-duty vehicles, on an international level through the provision of ISO, IEC, and SAE standards; on a European level through the examination of the CEN/CENELEC database; and on an Italian national level through the analysis of the UNI database.

1 Introduction

Hydrogen as an energy carrier has tremendous potential to address a variety of important energy issues in a variety of industries [1]. Its uses contribute to the de-carbonization of different industries, provide a flexible and efficient process [2] and act as long-term energy storage [3].

Hydrogen has the benefit of being a versatile energy carrier that enables energy generation with little or no environmental effect in a wide variety of industries that presently rely on fossil fuels. Hydrogen is certainly developing as a viable option that is garnering both academic and industrial interest.

Because transportation accounts for about one-third of worldwide carbon dioxide emissions (which contribute to climate change), hydrogen adoption in the mobility sector, coupled with fuel cell technology, such as in Fuel Cell Electric Vehicles (FCEVs), is

* Corresponding author: matteo.genovese@unical.it

worldwide recognized as an alternative fuel able to decrease greenhouse gas emissions in this sector. Additionally, hydrogen may be generated via the process of water electrolysis utilizing clean energy derived from renewable sources, being “green” and “clean” also at the source of production.

Hydrogen refueling stations (HRSs) must undoubtedly be implemented in this scenario. They are at the core of the infrastructure that enables hydrogen-based green mobility, serving as the hub for the distribution required to support the delivery of hydrogen to FCEVs. However, the success of this novel technology is constrained by some impediments to future growth and development. The most important disadvantages to this endeavor are a lack of sufficient infrastructure and a hefty initial investment cost, as well as the lack of established regulations, codes, and standards compared to other alternative fuel infrastructures, such as methane refueling stations and electric chargers.

To the best of the authors' knowledge, the latest scientific contribution on the HRS regulations and standards belongs to 2017, when Pique et al. [4] compared the laws, norms, and standards applicable to hydrogen fueling stations for light-duty vehicles. The analysis was based on 2014 data, with documents gathered through a bibliographic review and information gathered via a questionnaire distributed to authorities and IA HySafe [5] members.

Another European Project, HyLaw [6], addressed a similar issue, extended to commercial adoption of hydrogen and fuel cell technologies by providing market developers with a comprehensive understanding of relevant laws and drawing policymakers' attention to legal obstacles that need to be eliminated. The latest report [7] presented a short and overall legislative summary on HRS regulations and standards, followed by an assessment and the proposal of some recommendations.

A specific overview of standards related to HRS equipment and operation is lacking in literature, and it could be helpful to researchers, policymakers, and HRS operators to support the future HRS network expansion.

To address this research gap, the present paper aims to provide a high-level strategic overview of the current standards that regulate the design and operation of hydrogen filling stations. A concise and thorough research of hydrogen refueling station standards is performed and reviewed worldwide, in Europe, and in Italy. The standards in force for on-site hydrogen production via water electrolysis, hydrogen storage, both liquid and gaseous, and refueling protocols are among the numerous topics examined, on an international, European, and Italian level.

2 HRS Standards

Regulation, codes, and standards development is a key action needed to facilitate safe and accelerated access to the market for HRS components and technologies.
The present paper is based on the following classification on standards, codes, and regulations:

- A standard is a formal document that specifies the requirements for a certain component, or that elaborates on a specific technique or approach;
- A code is a document that specifies the desired outcome – what a product should adhere to – rather than the method by which it should be accomplished;
- Regulations are obligatory and mandatory, in contrast to codes and standards, which are voluntary.

2.1.1 International Level

The main international organizations for standard publication are ISO and IEC organizations. Within these organizations (ISO, IEC, and SAE), standards are developed by TC with national involvement from CEN members, called NSBs. The technical committee establishes a working group to complete a particular job by a certain deadline A WG is responsible for the actual standard development (working group). The main TCs for ISO hydrogen-related standards are:

- ISO/TC 197 Hydrogen technologies;
- ISO/TC 220 Cryogenic vessels;
- ISO/TC 58 Gas cylinders;
- ISO/TC 22/SC 41 Specific aspects for gaseous fuels.

Figure 1 shows the main ISO standards for HRS equipment and operation. It is worthy to mention how several standards are still under development, for different components and equipment. Liquid hydrogen storage technologies appear to have a more mature knowledge in terms of ISO standards, while several gaseous hydrogen-related standards, which include most of today and future hydrogen applications, are under drafting and work in progress.

Most IEC standards are focused on fuel cell technologies and their application in power systems. Few of them are centered on HRS operation and equipment. However, useful standards can be found for explosive gas atmospheres, as shown in Figure 2, and they found application in hydrogen station operation.
The main TCs for IEC hydrogen-related standards are:

- IEC/TC 31 - Equipment for explosive atmospheres;
- IEC/TC 69 - Electrical power/energy transfer systems for electrically propelled road vehicles and industrial trucks;
- IEC/TC 105 - Fuel cell technologies.

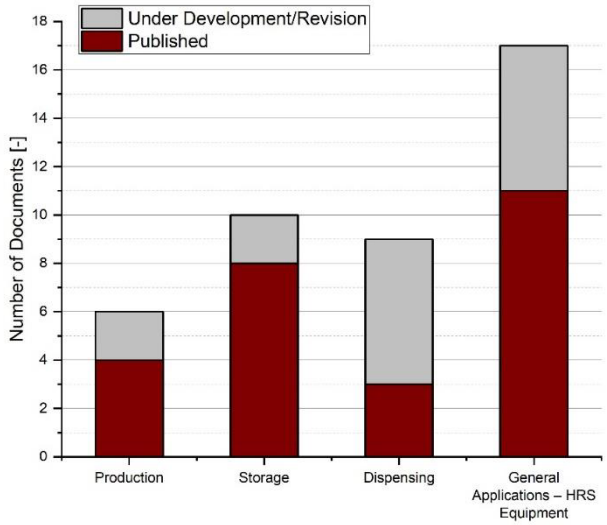

Fig. 1. HRS Equipment – ISO Standards

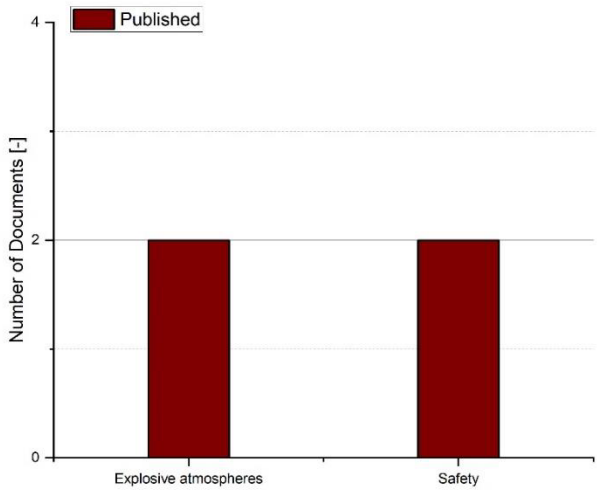

Fig. 2. HRS Equipment – IEC Standard

Apart from ISO and IEC, SAE standards are also available. The Society of Automotive Engineers (SAE) is a worldwide organization of engineers and technical specialists, and it is delivering technical protocols on hydrogen refueling processes and connecting devices, as shown in Figure 3. The main TC for SAE hydrogen-related standards is the SAE Fuel Cell Standards Committee.

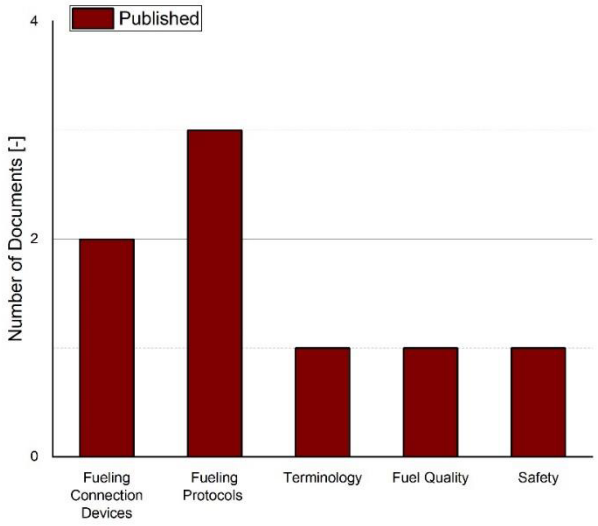

Fig.3. HRS Equipment – SAE

2.1.2 European Level

CEN or CENELEC generate and publish codes and standards at the European level, shown in Figure 4. Part of them is the transposition/implementation of ISO standards.
The main TCs for CEN/CENELEC hydrogen-related standards are:

- CEN/CLC/TC 6 - Hydrogen
- CEN/TC 23 Transportable gas cylinder
- CEN/TC 69 Industrial valves
- CEN/TC 185 Fasteners
- CEN/TC 197 Pumps
- CEN/TC 234 Gas infrastructure
- CEN/TC 235 Gas pressure regulators and associated safety devices for use in gas transmission and distribution;
- CEN/TC 236 Non-industrial manually operated shut-off valves for gas and particular combinations valves-other product
- CEN/TC 238 Test gases, test pressures, appliance categories, and gas appliance types
- CEN/TC 268 Cryogenic vessels and specific hydrogen technologies applications

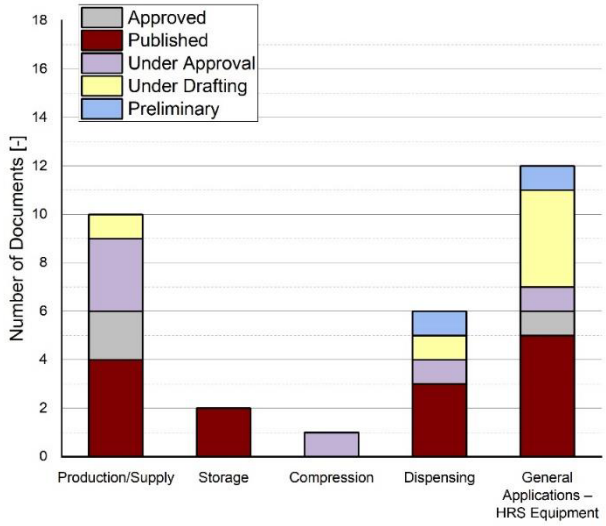

Fig.4. HRS Equipment – CEN/CENELEC

2.1.3 Italian Legislation

Considering the abundance of renewable energy sources and the presence of a capillary network for gas transport, Italy is an ideal market for the development of green hydrogen. Italy's geographical location in the Mediterranean makes it an ideal crossroads between Africa and the Middle East, big potential exporters of hydrogen, and the nations of the north, large potential consumers. Despite the huge potential, there are still significant regulatory and other barriers to the full development of green hydrogen in Italy.

The only TC National mirror group to ISO/TC 197 Hydrogen technologies is the UNI/CT 056/GL 01, which acts also as the national mirror group for CEN/CLC/JTC 6. The Italian TC is focusing on the systems, equipment, and connections used to produce and consume hydrogen from renewable energy sources.

The National Decree n. 1657 of 16 December 2016, which implements the EU Directive 2014/94/EU, recognizes hydrogen as an alternative fuel and commits Italy to develop an appropriate network of refueling stations by December 31, 2025. The lack of the implementing regulations of the Ministerial Decree of 31 August 2006 has caused a major obstacle to the spread of hydrogen refueling stations in Italy. With a new Decree from 2018, a 700 bar supply pressure is allowed and improved alignment with ISO 19880, the absence of implementing rules for the Ministerial Decree of August 31, 2006, has been overcome. The local "National Fire Corps - Corpo Nazionale dei Vigili del Fuoco" is responsible for giving an evaluation in terms of safety and fire prevention. However, a series of hydrogen-related actions are excluded, such as:

- the storage and transport of liquid hydrogen;
- safety distances aligned with the operating pressure of the equipment
- adoption of hydrogen supplied via pipelines;
- a methodology for safety distance calculations in case of ignited and un-ignited hydrogen releases;
- mitigation techniques, such as ventilation systems, passive or active.

At the time of writing, the only available national standards belong to UNI, and are:

- UNI ISO 14687:2020, Hydrogen fuel quality -- Product specification, which accepts ISO 14687:2019;
- UNI ISO 19880-1:2020, Gaseous hydrogen -- Fueling stations - Part 1: General requirements, which accepts ISO 19880-1:2020;
- UNI ISO/TR 15916:2018, Basic considerations for the safety of hydrogen systems, which accepts ISO/TR 15916:2015.

3 Conclusions

This article presents an extended overview of HRS standards:

- at an international level, by presenting ISO, IEC, and SAE standards;
- at European level, by analyzing the CEN/CENELEC database;
- and at Italian National Level.

As a result of the findings, ISO has developed numerous hydrogen standards for HRS equipment and operation. Quality, safety, production, hydrogen stations, and testing are all covered by ISO hydrogen standards. It's worth mentioning, though, that numerous standards for different components and equipment are in the works right now. Technical protocols for hydrogen refueling procedures and connected devices have previously been published by SAE. The majority of IEC standards relate to fuel cell technology and how it is used in power systems. The International Electrotechnical Commission (IEC) has developed hydrogen standards that concentrate on safety, applications, and testing. Only a small number of standards are focused on HRS operations and equipment. Effective standards, on the other hand, exist for explosive gas atmospheres.

Several European standards are being approved, drafted, or are in the early stages of development. They will, however, be published shortly to keep up with the new European Hydrogen Strategy and Roadmap.

In Italy, there are uneven and insufficient hydrogen requirements for HRS spreading out at the national level. Standards for hydrogen production, storage, transportation, and fueling should be emphasized, with a comprehensive assessment of the whole supply chain taking into account hydrogen as an energy carrier. This covers how hydrogen is generated, how it is stored on a large scale to account for seasonal intermittency in renewable energy generation, and how it is transported and distributed from a centralized production facility to HRS and within the HRS itself.

Nomenclature

CEN	European Committee for Standardization
CENELEC	European committee for Electro-Technical Standardization
EC	International Electro-Technical Commission
FCEV	Fuel Cell Electric Vehicle
GH_2	Gaseous Hydrogen
HRS	Hydrogen Refueling Station
ISO	International Standards Organization
LH_2	Liquid Hydrogen
NSB	National Standardization Bodies
SAE	Society of Automotive Engineers
SM	Steam Reforming
TC	Technical Committee
UNI	Ente Nazionale Italiano di Unificazione
WE	Water Electrolysis
WG	Working Group

References

1. You, C.; Kim, J. Optimal design and global sensitivity analysis of a 100% renewable energy sources based smart energy network for electrified and hydrogen cities. *Energy Convers. Manag.* **2020**, *223*, 113252, doi:https://doi.org/10.1016/j.enconman.2020.113252.
2. Abdin, Z.; Mérida, W. Hybrid energy systems for off-grid power supply and hydrogen production based on renewable energy: A techno-economic analysis. *Energy Convers. Manag.* **2019**, doi:10.1016/j.enconman.2019.06.068.
3. Abdalla, A.M.; Hossain, S.; Nisfindy, O.B.; Azad, A.T.; Dawood, M.; Azad, A.K. Hydrogen production, storage, transportation and key challenges with applications: A review. *Energy Convers. Manag.* 2018.
4. Pique, S.; Weinberger, B.; De-Dianous, V.; Debray, B. Comparative study of regulations, codes and standards and practices on hydrogen fuelling stations. *Int. J. Hydrogen Energy* **2017**, doi:10.1016/j.ijhydene.2016.02.158.
5. IA HySafe International association on hydrogen safety Available online: http://www.hysafe.info/ (accessed on Oct 12, 2021).
6. HyLAW HyLAW Online Database Available online: https://www.hylaw.eu (accessed on Oct 12, 2021).
7. Floristean, A. *EU Policy Paper (June 2019) HyLAW*; 2019; Vol. 2019;.
8. Tolias, I.C.; Giannissi, S.G.; Venetsanos, A.G.; Keenan, J.; Shentsov, V.; Makarov, D.; Coldrick, S.; Kotchourko, A.; Ren, K.; Jedicke, O.; et al. Best practice

guidelines in numerical simulations and CFD benchmarking for hydrogen safety applications. *Int. J. Hydrogen Energy* **2019**, doi:10.1016/j.ijhydene.2018.06.005.

9. Kim, W.; Shentsov, V.; Makarov, D.; Molkov, V. High pressure hydrogen tank rupture: blast wave and fireball. In Proceedings of the 6th International Conference on Hydrogen Safety; 2015.
10. Sasaki, K.; Li, H.-W.; Hayashi, A.; Yamabe, J.; Ogura, T. *Hydrogen Energy Engineering*; 2016; ISBN 978-4-431-56040-1.
11. Molkov, V. *Fundamentals of Hydrogen Safety Engineering I*; 2012; ISBN 9788740302264.
12. Hydrogen Tool Portal Available online: https://h2tools.org/lessons (accessed on Oct 26, 2019).
13. Molkov, V. Hydrogen Safety Research : State-of-the-Art. *Proc. 5th Int. Semin. Fire Explos. Hazards* **2007**.
14. Samsun, R.C.; Antoni, L.; Rex, M. *Advanced Fuel Cells Technology Collaboration Programme Report on Mobile Fuel Cell Application : Tracking Market Trends*; 2020;